Anil Kumar
Amit Pal
Surendra Singh Kachhwaha
Prashant Kumar Jain *Editors*

Recent Advances in Mechanical Engineering

Select Proceedings of RAME 2020

Springer

Lecture Notes in Mechanical Engineering

Anil Kumar · Amit Pal ·
Surendra Singh Kachhwaha · Prashant Kumar Jain
Editors

Recent Advances in Mechanical Engineering

Select Proceedings of RAME 2020

Editors
Anil Kumar
Department of Mechanical, Production &
Industrial and Automobile Engineering
Delhi Technological University
North West Delhi, Delhi, India

Amit Pal
Department of Mechanical, Production &
Industrial and Automobile Engineering
Delhi Technological University
North West Delhi, Delhi, India

Surendra Singh Kachhwaha
Department of Mechanical Engineering
Pandit Deendayal Petroleum University
Gandhinagar, Gujarat, India

Prashant Kumar Jain
Department of Mechanical Engineering
Indian Institute of Information Technology
Design & Manufacturing
Jabalpur, Madhya Pradesh, India

Foreword

I am pleased to know that an International Conference on "Recent Advances in Mechanical Engineering" (RAME 2020) is being organized by Department of Mechanical Engineering, Delhi Technological University (DTU), on September 18 and 19, 2020. I welcome all the delegates and participants across the globe for participating in RAME 2020 conference at DTU. I am sure that RAME 2020 conference will bring together the national and international talents.

The role of mechanical engineering is inevitable to improve productivity, product quality and safe working environment in the applied fields for the society at large. The conference shall provide excellent opportunities for researchers, scientists and industrialists to share and converse on the latest developments in the areas of mechanical engineering. The publication of the conference proceedings in *Lecturer Notes in Mechanical Engineering*, Springer, will give a new benchmark and more insight to the R&D initiatives in these areas. I also hope that the conglomeration of eminent experts will highlight the importance of research and innovation and discuss the best global practices.

I congratulate the organizing team of RAME 2020 conference and wish that the conference will be a grand success and help in branding Delhi Technological University as a leading research university.

Prof. Yogesh Singh
Vice-Chancellor
Delhi Technological University
New Delhi, India

Preface

Mechanical engineering is the application of physical principles of science and engineering to the creation of useful systems, devices, objects and machines. This basic perception of mechanical engineering still holds good, while it has evolved into various new fields. Mechanical engineering is thus deep rooted in to a vast engineering canvas and is in the service of mankind at all levels. Therefore, there is also a need to understand the design principles for environment, life-cycle design and sustainable development.

It is our pleasure to present the academicians and scholars, the proceedings of the research papers scheduled for presentation at the 2nd International Conference on "Recent Advances in Mechanical Engineering" during 18–19 September 2020 at the Department of Mechanical, Production and Industrial and Automobile Engineering and Centre for Energy and Environment, Delhi Technological University (*Formerly Delhi College of Engineering*), Delhi-110 042 (India). This conference is in series with earlier international conference RAME-2016 organized by the Department of Mechanical Engineering, Delhi Technological University (Formerly Delhi College of Engineering), Delhi-110 042 (India). The conference was very well received, both by the industry and academia.

The core organizing committee for organizing RAME-2020 is:

- **Chief Patron**: Prof. Yogesh Singh, Hon'ble Vice-Chancellor
- **Patron**: Prof. Samsher; Prof. S. K. Garg
- **Chairman**: Prof. R. S. Mishra; Prof. Vipin; Prof. S. Maji
- **Co-Chairman**: Prof. Vikas Rastogi; Prof. Raj Kumar Singh; Prof. Atul Agrawal
- **Convener**: Prof. Amit Pal
- **Co-Convener**: Prof. Vijay Gautam; Prof. Quasim Murtaza and Prof. Rajesh Kumar
- **Organizing Secretary**: Dr. Anil Kumar
- **Joint Organizing Secretary**: Dr. Girish Kumar; Dr. N. A. Ansari and Dr. N. Yuvraj
- **Treasurer**: Dr. M. Zunaid

The proceeding consists of papers contributed by leading academicians, research scholars and experts from the industries. The conference papers cover both research areas and the latest trends in the industry. 96 papers from 300+ authors and about 450 participants attended the conference. In all, qualitative papers would be selected to present during the conference. The main topics of the conference have been classified into the following four categories:

- Thermal Engineering
- Energy Science and Engineering
- Design and Development
- Industrial and Production Engineering

The technical advisory committee is pleased to mention that the papers have been received on all these topics. Such a voluminous proceedings is not possible without the generous support received from various quarters. The committee would like to put on record its deep appreciation for the persistent efforts of all reviewers.

We are grateful to all the authors of the papers for having made their contributions to enrich this international conference of RAME-2020.

It is our immense pleasure to express our heartful gratitude to Prof. Yogi D. Goswami, University of South Florida, USA; Prof. H.C. LIM, Pusan National University, South Korea; Prof. Afzal Husain, Sultan Qaboos University, Oman; Dr. Nitin Upadhyay, University of Modern Science, Dubai, UAE; Dr. Ashish Shukla, Loughborough University, UK; Dr. Shyam S. Pandey, Kyushu Institute of Technology, Japan; and Dr. Jan Banout, Czech University of Life Science Czech Republic and other colleagues in India and abroad.

Special acknowledgement is made to the support of expert papers and also the generous support received from our distinguished alumnus of DTU, the leading industrialist. We also acknowledge the excellent cooperation received from our colleagues and experts on the review panel, for their painstaking efforts in reviewing the papers.

We duly acknowledge the sponsors with thanks and extend full credit to the publisher (Springer) for accepting the proposal to publish conference proceedings with the book title 'Recent Advances in Mechanical Engineering' under the series title 'Lecture Notes in Mechanical Engineering'.

We sincerely hope that engineering community would find this publication a valuable source of knowledge to profess mechanical engineering in the knowledge age.

North West Delhi, India	Anil Kumar
North West Delhi, India	Amit Pal
Gandhinagar, India	Surendra Singh Kachhwaha
Jabalpur, India	Prashant Kumar Jain

Contents

Design and Development

Industrial and Production Engineering

About the Editors

Dr. Anil Kumar is Associate Professor in the Department of Mechanical, Production & Industrial and Automobile Engineering, with additional charge of Additional Coordinator-Centre for Energy and Environment, Delhi Technological University, Delhi, India. He has completed his Ph.D. in Solar Energy from Centre for Energy Studies, Indian Institute of Technology Delhi, India, in the year 2007. He was Postdoctoral Researcher at Energy Technology Research Center, Department of Mechanical Engineering, Faculty of Engineering, Prince of Songkla University, Hat Yai, Songkhla, Thailand, in the discipline of Energy Technology from June 2015 to May 2017. He has also served as Assistant Professor in Energy Centre, Maulana Azad National Institute of Technology Bhopal, India, from 2010 to 2018, and the Department of Mechanical Engineering, University Institute of Technology, Rajiv Gandhi Proudyogiki Vishwavidyalaya, Bhopal, India, from 2005 to 2010. His areas of specialization are energy technology, renewable energy, solar energy applications, energy economics, heat transfer, natural rubber sheet drying and environmental issues. He has completed many research projects in these areas. He has more than 15 years of experience in the field of energy technology. He has published 135 papers in international peer-reviewed journals and 75 papers in the international/national conferences proceeding. He has received more than 3500 citations with h-index = 33. He has developed thin-layer drying model with his student in 2014. It is known as "Prakash and Kumar model". This model is being used and cited by so many researchers around the globe. He has published 10 books with international/national publishers. He has also published 3 patents—one in the solar dryer and another in the solar photovoltaic thermal collector. He has supervised 9 Ph.D. scholars and 37 master students. Dr. Kumar has visited countries, namely UK, Thailand and Malaysia. He has received various awards and appreciation from reputed sources. Some of them are provided here: "Commendable Research Award 2019" for publishing quality research paper in Delhi Technological University, Delhi, India. Research Excellence Award 2016: The researcher has Top 20 Publications from the Web of Science database, honored by Dr. Chusak Limsakul, President Prince of Songkla University, Hat Yai, Thailand. "Appreciation" for Outstanding Service in the reviewer's committee and active reviewers during the year 2015 from International Institute of Engineers, Kolkata, and Elsevier. "Best Paper Award" in Global Conference on

Energy and Sustainable Development (GCESD 2015), February 24–26, 2015, at Coventry University Technology Park, Puma Way, Coventry, West Midlands CV1 2TT.

Dr. Amit Pal is currently working as Professor at the Department of Mechanical, Production & Industrial and Automobile and Production & Industrial Engineering, Delhi Technological University (Formerly Delhi College of Engineering), Delhi. He obtained his B.E. (Mechanical Engineering) from Vikram University, Ujjain and Master of Engineering from the University of Mumbai and Ph.D. from the Faculty of Technology, University of Delhi. He has more than 23 years of experience in teaching and research with major research interest areas which include IC engines, biofuels and waste management, pollution mitigation, etc. He has published 50 papers in reputed international journals. Prof. Amit Pal received commendable research award 2018 for the paper "Experimental Studies on Utilization of Prunus armeniaca L. (Wild Apricot) Biodiesel as an Alternative Fuel for CI Engine in Waste and Biomass Vaporization." He also received the first prize for the research paper "Recent Developments in Biodiesel: Part I – Biodiesel Production Technology" and the Second prize for the research paper titled "Optimization of Solar assisted Production of Biodiesel from Cottonseed Oil". He has been an expert member in various committees of CPCB India, DTC Delhi, GGSIPU, NIOS and NBOS India, etc. Prof. Amit Pal published 3 books on Renewable Energy, Advances in Mechanical Engineering, and Heat and Mass Transfer. He wrote many chapters in "Advances in Alternate and Renewable Energy Technologies". Prof. Amit Pal has also successfully completed different research projects sponsored by the Government of Delhi, Arihant Energy Solutions, Mosarbear and DTU costing over 17 lakhs (INR). He is the life-time member of the Indian Society of Mechanical Engineers, the Indian Society of Technical Education, the Solar Energy Society of India and the Ultrasonic Society of India. Prof. Amit Pal organized many workshops, conferences and faculty development programmes and also delivered over 30 expert lectures in many reputed seminars, conferences, short-term courses, QIP and FDP programmes etc. organized at DTU and other reputed organizations.

Dr. Surendra Singh Kachhwaha is Professor, Mechanical Engineering Department, School of Technology, Pandit Deendayal Petroleum University, Gandhinagar, India. He has accomplished research projects and consultancy work worth four crores. He completed his B.E. degree in Mechanical Engineering from M.B.M. Engineering College, Jodhpur. He did his M.Tech. in Heat Power from Indian Institute of Technology, BHU Varanasi, and Ph.D. in Evaporative Cooling from IIT Delhi. He has teaching experience of more than 32 years in thermal engineering at undergraduate and postgraduate levels. Dr. Kachhwaha has around 80 technical publications in reputed national and international journals and more than 100 publications in national/international conferences. His research interests include evaporative cooling, ice slurry generation, polygeneration, offshore wind energy and biodiesel production techniques. Dr. Kachhwaha has taught various thermal engineering courses at undergraduate and postgraduate levels and guided 33 M.Tech.

dissertation and 7 PhDs. He served as Faculty in Rajasthan Technological University, Kota and Delhi Technological University, Delhi, in the past.

Dr. Prashant Kumar Jain is Associate Professor and Dean (Students) at Indian Institute of Information Technology, Design and Manufacturing Jabalpur, India. He has over 25 years of research and teaching experience at UG and PG levels. He is graduated in Mechanical Engineering from Dr. H. S. Gour University Sagar in 1995 and did Master's in Advanced Production Systems from Samrat Ashok Technological Institute (S.A.T.I.) Vidisha. He has received Ph.D. Degree in the area of Rapid Prototyping/Additive Manufacturing, particularly on Part Strength studies in Selective Laser Sintering Process from Indian Institute of Technology Delhi, (IIT Delhi) Delhi in 2009. Dr. Prashant K. Jain was previously with Delhi Technological University Delhi (formerly known as Delhi College of Engineering) as lecturer in Mechanical Engineering Department. He has also served Indian Institute of Technology Delhi as project scientist and research associate where he was engaged in research work on error compensation in CNC machines and part quality improvement in Fused Deposition Modelling. Currently he is with PDPM IIITDM Jabalpur as Associate Professor and Dean (Students). He has more than 110 publications to his credit, published in International peer reviewed journals of repute, National and International conferences in India and abroad. He has guided 5 Ph.D.'s and 27 Master's and several ongoing. He has been a resource person and delivered invited lectures, chaired scientific sessions in several National and International Conferences, STTP's and QIP programs. His research interest extends from Geometric Modelling, CAD/CAM Integration, Incremental Sheet forming, Computational geometry, Rapid Prototyping & Tooling, Incremental sheet forming to Nano Technologies in Manufacturing.

Thermal Engineering

Experimental Studies of Heat Transfer Under Natural Convection in Heat Pipe Insulated with Vacuum Chamber

Sumit Kumar Rai ⓘ**, Anjaney Pandey** ⓘ**, and Alok Chaube** ⓘ

Nomenclature

Symbol

A	Surface area of HP (m^2)
C_p	Specific heat (J/(kg K))
$h_{practical}$	Practical value of CCHT (W/(m^2 K))
$h_{theoretical}$	Theoretical value of CCHT (W/(m^2 K))
k	Thermal conductivity (W/(m k))
$Q_{practical}$	Practical value of RHT (W)
$Q_{theoretical}$	Theoretical value of RHT (W

Subscript

CCHT	Coefficient of convective heat transfer
HP	Heat pipe
HPHE	Heat pipe heat exchanger
HPHEVC	Heat pipe heat exchanger insulated with vacuum chamber
RHT	Rate of heat transport

S. K. Rai (✉) · A. Pandey · A. Chaube
Department of Mechanical Engineering, Mahatma Gandhi Chitrakoot Gramoday
Vishwavidyalaya, Chitrakoot, M.P., India
e-mail: sumit.rai87@gmail.com

1 Introduction

The heat transfer systems are commonly associated with different types of heat transfer equipment who is working based on sensible heat transfer, latent heat transfer and mixed mode of these two types [1]. The heat transfer system can be designed into single tube and multi-tube type [2], cross flow heat transfer, evaporators and condensers, hollow cylindrical type heat pipe equipment [3], etc. The motivation for making an experimental setup of heat pipe insulated with vacuum chamber is to obtain high exchanger compactness in given surface area having size, position and weight limitations [4, 5]. The heat transfer systems are normally based on the transferring heat from hot fluids to cold fluids with the help of different types of equipment which are used in a variety of engineering applications. The heap pipe system has been divided into three sections, i.e., evaporator, adiabatic and condenser section.[1] The heat transfer inside the heat pipe between hot and cold fluids is by the forced convection or natural convection. The manufacturers normally depend upon the local vendors for procurement of accessories including heat exchangers working under natural or forced convection which may not be optimally designed. Since these heat exchangers are to be acquired in a new design of model with configurations and layout, therefore, even well composition of heat exchangers in a particular configuration is subjected to change in thermal performance [6]. There are a lot of methods to amplify the transferring heat from hot fluids to cold fluids with the help of heat exchanger equipment; one may look for a solution in the given situation. If the area of heat transfer is increased, then heat transfer will be increased, and the other solution is increasing the flow rate of working fluids may be increasing the heat transfer. The first solution takes more space, so it is not helpful for minimum space area and the other solution required more pressure drop between inside section of heat pipe and atmosphere. All these types of studies are limited to forced convection because they need some external forces for transferring the heat by heat pipe in heat exchanger. Therefore, to make heat pipe, heat exchanger under natural convection is required for transferring the heat without any external forces [7] (Fig. 1).

The literature survey reported that the temperature difference between the surface and the working fluids is created natural convections without any external forces. And a model can be developed for transfer the heat through a heat pipe under natural convection conditions [7]. The size and thermo physical properties of material of heat pipe also involve transferring the heat under natural convection conditions [8]. The temperature difference between surface and fluids indicates that good working conditions under natural convection conditions and huge amount of heat transfer through the heat pipe insulated with vacuum chamber. The heat transfer through the natural convection also depends on the properties of fluids, design of heat pipe, position of heat pipe [9] and working environments [3, 9]. These all are critical parameters that affected transferring the heat under natural convective conditions.
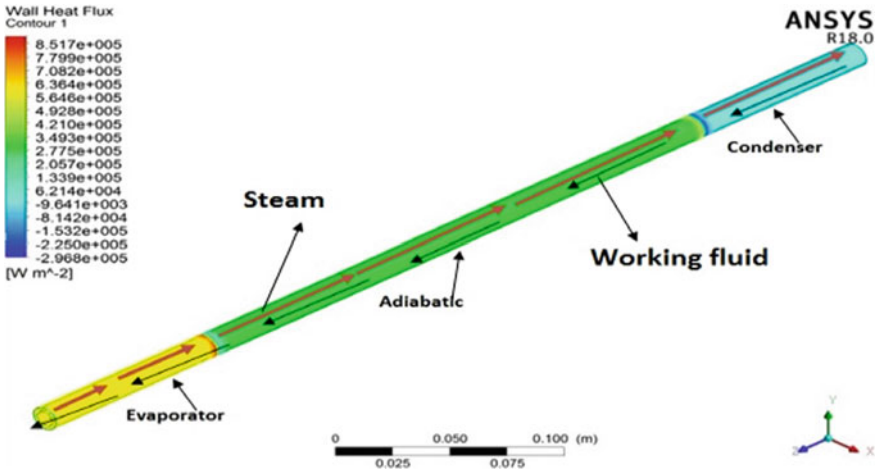
Fig. 1 Heat pipe

2 Design Considerations

The present investigation aims at low temperature application, such as cooling of transformer oil, cutting fluids and generated heat from the CPU should be dissipated, and therefore, the operating temperature range of 40–61 °C has been considered.

The availability, cost, properties and operating conditions of fluids are the basic parameters of fluids for selection as working fluids working under natural convection at low temperature range [10]. The viscosities of fluids should be low at liquid and vapor conditions. Based on all above parameters, water, ethanol, methanol and butanol are used as working fluids [11]. The maximum possible heat transfer occurs when water is used as working fluids as compared to the other working fluids.

2.1 Development of Analytical Model

An analytical model of heat pipe has been developed to calculating coefficient of heat transfer and heat transfer rate when heat pipe working under natural convection conditions at 40–61 °C inlet heating temperature range [3, 12]. The different heat transfer correlations available in the literature have been used to compute the coefficient of heat transfer, rate of heat transfer across evaporator system of the HPHE.

The analytical considerations for analyzing the HPHE are

1. Laminar flow or turbulent flow regime has been assumed in the evaporator side [2].

2. A temperature range of 40–61 °C is assumed for the heating (hot) fluid in the evaporator section for low temperature applications [3, 12].
3. The thermodynamic properties of heating fluids (water, ethanol, methanol[12] and butanol) and ambient air have been evaluated at the mean temperature of fluids [11].
4. Glass vacuum chamber is used as insulating material surrounding the heat pipe for minimum heat loss to atmosphere [13].

2.2 Mathematical Formulations

To determine the CCHT, the HPHE has been modeled as a thermal resistance network [4]. The CCHT have been computed on the internal surface of evaporator. For natural convection condition, the correlations have been taken from a text book of Engineering Thermodynamics written by G.F.C. Rogeks and Y. R. Mayhew. The calculation of CCHT and RHT across the heat pipe under natural convection is described below:

$$Nu = C(Gr \times Pr.)^n \tag{1}$$

Natural convection heat transfer from inclined tube from y-axis is computed by the correlations of

$$Nu = C(Gr \times Pr \times \cos\theta)^n \tag{2}$$

where Gr, Pr and Nu represent the value of Grashoff number, Prandtl number [10] and Nusselt number [7, 6], respectively, C and n are constant. θ is angle of inclination of heat pipe from vertical axis or y-axis [4].

The fluid flow will be laminar flow

$$Nu = 0.590 \times (Gr \times Pr \times \cos\theta)^{0.25}, \tag{3}$$

For $10^4 < (Gr \times Pr \times \cos\theta) < 10^9$.
The fluid flow will be turbulent flow

$$Nu = 0.590 \times (Gr \times Pr \times \cos\theta)^{1/3}, \tag{4}$$

For $10^9 < (Gr \times Pr \times \cos\theta) < 10^{12}$

$$Nu = \frac{(ht \times L1)}{K} \tag{5}$$

where ht or $h_{\text{theoretical}}$ represents the theoretical value of coefficient of convective heat transfer in W/m^2 °C, L1 is the length of heat pipe in m, and K represents the thermal conductivity of fluids in (W/m °C).

The heat transport rate by HPHE has been computed by following correlations:

$$Q_{\text{theoretical}} = V.I \tag{6}$$

where V = Voltage in Volt, I = Current in ampere.

3 Experimentation

The test rig has been designed in a manner such that calculates the value of coefficient of heat transfer and heat transfer rate at different tilt angles under natural convection conditions. A test setup is shown in Fig. 2. The total length of heat pipe is 500 mm, and thickness of heat pipe is 4 mm. The evaporator, adiabatic and condenser lengths are 100 mm, 300 mm and 100 mm, respectively. The evaporator section is insulated with glass chamber when the internal pressure of glass chamber is less then vacuum pressure. The adiabatic section is insulated with glass chamber when the internal pressure of glass chamber is less than vacuum pressure. The condenser is exposed to a chamber made of glass box having length, width and height are 100 mm, 100 mm and 100 mm, respectively, which filled with flowing water at ambient temperature. The condenser removes the heat by natural convection. The working fluids (water, ethanol, methanol and butanol) heated through an electrical heater. Temperature data logger has been used to measure the value of temperature with the help of thermocouples. There are ten thermocouples used for measuring the temperature

Fig. 2 Experimental setup of heat pipe insulated with glass vacuum chamber

from different–different locations of heat pipe. Two thermocouples are mounted with the external surface of evaporator, three thermocouples are mounted with the external surface of adiabatic section, and other four is mounted with the condenser section. One thermocouple is left open in the atmosphere to take a reading of atmospheric temperature. A voltmeter is used to measure the voltage reading in volt, and ammeter is used to take the reading of current in ampere.

The coefficient of convective heat transfer under natural convection was determined with the help of experimental reading. The practical value coefficient of convective heat transfer in W/m^2 °C was computed as follows:

$$\text{hp} = \frac{Q}{A * dT} \tag{7}$$

The transferring heat by the heat pipe has been calculated with the help of experimental reading. The practical heat transfer rate in W/m^2 °C was computed as follows:

$$Q_{\text{practical}} = q_1 - q_2 - q_3 \tag{8}$$

$q_1 =$ Heat input to the evaporator in W [5]

$$q_1 = \frac{m.\text{cp}.\Delta t}{\text{time}} \tag{9}$$

q_2 (Heat loss from adiabatic section) [5]

$$q_2 = h.\text{Aa}.(T\text{adiabatic} - T\text{atm}) \tag{10}$$

q_3 (Heat loss from condenser) [5]

$$q_3 = h.\text{Ac}.(T\text{condenser} - T\text{atm}) \tag{11}$$

where m represents the value of mass flow rate, cp represents the value of specific heat at given inlet heating temperature, and $\Delta t =$ temperature difference between walls of heat pipe to atmosphere, Aa = area of adiabatic section, Ac = area of condenser section, $h =$ coefficient of convective heat transfer.

4 Results and Discussions

The experimental values of CCHT and RHT of the heat pipe insulated with vacuum chamber under natural convective conditions have been calculated. The analytical values are used to validate the experimental model whether model worked under

natural convection conditions or not. This paper shows the results and comparisons of experimental values of different–different working fluids.

4.1 CCHT When Water, Ethanol, Methanol and Butanol Used as Working Fluids

The practical value of CCHT has been calculated with the help of experimental setup for different–different fluids separately. The results of practical value with respect to the inlet temperature of evaporator and tilting angles of heat pipe from vertical axis [11] for water [11, 10], ethanol, methanol [12] and butanol are used as working fluids are shown in Table 1 and Figs. 3, 4, 5, 6 and 7.

Figures 3, 4, 5, 6 and 7 show the results of practical values of CCHT with respect to the inlet heating temperature for water, ethanol, methanol and butanol used as working fluids at different inlet temperature of evaporator.

The value of CCHT is influenced by angle of inclination of heat pipe from vertical axis. It has been observed that the angle of inclination of heat pipe increases from vertical axis 0° to 15°, the coefficient of convective heat transfer increases, and it starts decreasing beyond 15° tilt angles for inlet evaporator temperature 61 °C and methanol, ethanol and butanol used as working fluids.

4.2 RHT of HPHE for Water, Ethanol, Methanol and Butanol Used as Working Fluids

The practical value of RHT has been calculated with the help of experimental setup for different–different fluids separately. The results of practical value with respect to the inlet temperature of evaporator and tilting angles of heat pipe from vertical axis [4] for water [11], ethanol, methanol [12] and butanol are used as working fluids are shown in Table 2 and Figs. 8, 9, 10, 11 and 12.

Figures 8, 9, 10, 11 and 12 show the results of practical values of RHT of HPHE with respect to the inlet heating temperature for water, ethanol, methanol and butanol used as working fluids, and the arrangements of heat pipe inclined at different–different tilt angles from vertical axis of HPHE.

The result shows that the HPHE gives the maximum heat transport rate when water is used as a working fluid as compared to ethanol, methanol and butanol. In the case of inclination of heat pipe from its vertical position, it gives good thermal execution when heat pipe is inclined at 45° tilt angles at all the range of inlet temperature of the evaporator and methanol is used as a working fluid.

Table 1 Coefficient of convective heat transfer for different working fluids under natural convection

Coefficient of convective heat transfer for different working fluid under natural convection in W/m² °C

Water

T1	Angle of inclination				
	0	15	30	45	60
	$h_{practical}$	$h_{practical}$	$h_{practical}$	$h_{practical}$	$h_{practical}$
40	1254.53	1201.03	1201.03	1115.23	373.85
43	1334.54	1334.97	1273.70	1177.20	1046.33
46	1433.12	1453.80	1388.63	1303.32	1137.87
49	1568.00	1550.37	1473.68	1368.20	1207.53
52	1601.34	1581.72	1555.95	1434.13	1280.43
55	1705.23	1646.66	1659.28	1532.38	1350.23
58	1733.83	1766.17	1632.44	1584.41	1428.78
61	1833.22	1828.98	1768.12	1644.45	1434.67

Ethanol

T1	Angle of inclination				
	0	15	30	45	60
	$h_{practical}$	$h_{practical}$	$h_{practical}$	$h_{practical}$	$h_{practical}$
40	336.83	333.12	323.64	310.62	264.84
43	365.13	365.13	337.20	322.60	291.13
46	386.70	381.99	373.24	344.54	310.62
43	408.46	413.68	387.44	376.06	325.89
52	434.82	434.82	418.76	386.71	349.89
55	458.20	453.55	432.39	406.09	363.27
58	480.97	474.40	450.97	421.16	378.22
61	486.39	434.43	476.84	435.36	336.58

Methanol

T1	Angle of inclination				
	0	15	30	45	60
	$h_{practical}$	$h_{practical}$	$h_{practical}$	$h_{practical}$	$h_{practical}$
40	467.95	465.18	441.45	419.21	367.10
43	503.06	507.50	486.92	452.62	387.42
46	541.24	529.83	497.45	469.53	434.12
43	552.30	545.95	534.08	495.33	443.35
52	580.93	572.45	551.05	521.78	471.68

Acetone or Butanol

T1	Angle of inclination				
	0	15	30	45	60
	$h_{practical}$	$h_{practical}$	$h_{practical}$	$h_{practical}$	$h_{practical}$
40	561.78	557.81	530.87	495.66	439.90
43	606.43	611.48	579.17	538.02	485.28
46	661.44	651.13	635.36	594.38	527.65
49	706.23	700.97	672.71	634.10	553.32
52	746.02	747.36	710.76	675.25	592.19

(continued)

Table 1 (continued)

Methanol

T1	Angle of inclination				
	0	15	30	45	60
	$h_{practical}$	$h_{practical}$	$h_{practical}$	$h_{practical}$	$h_{practical}$
55	600.54	598.17	582.96	540.17	486.92
58	643.44	628.93	535.58	564.77	512.02
SI	849.71	654.00	640.65	587.32	516.34

Acetone or Butanol

T1	Angle of inclination				
	0	15	30	45	60
	$h_{practical}$	$h_{practical}$	$h_{practical}$	$h_{practical}$	$h_{practical}$
55	802.72	784.80	755.93	705.35	632.79
58	837.12	825.53	809.01	745.28	663.21
61	863.11	874.32	838.73	774.85	707.37

Fig. 3 CCHT when heat pipe inclined at 0° angles and different fluid used

Fig. 4 CCHT when heat pipe inclined at 15° angles and different fluid used
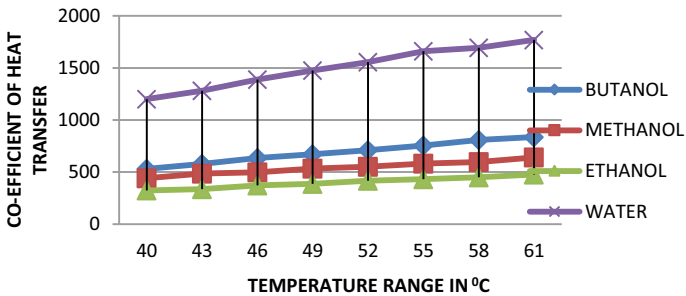
Fig. 5 CCHT when heat pipe inclined at 30° angles and different fluid used

5   Conclusions

The significant observations and conclusions obtained from this investigation are as follows:
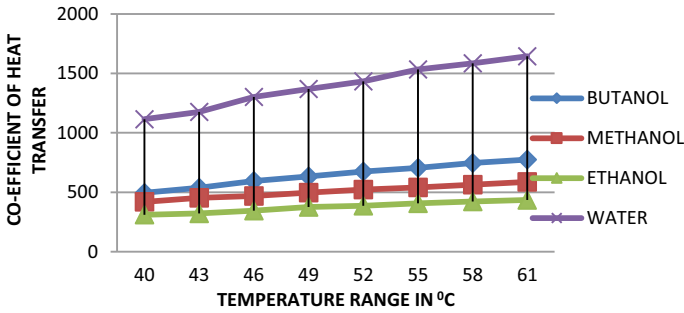
Fig. 6 CCHT when heat pipe inclined at 45° angles and different fluid used
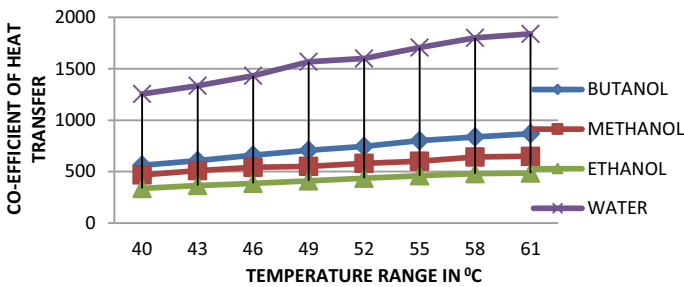
Fig. 7 CCHT when heat pipe inclined at 60° angles and different fluid used

5.1 For the CCHT of a Heat Pipe

1. The fluid temperature increases, then CCHT increases, and the inclination of heat pipe increases from vertical axis, then the CCHT decreases.
2. The maximum practical value of CCHT is 1839.22 W/m^2 °C at 0° angle of inclination of heat pipe from vertical position at 61 °C inlet fluid temperature of evaporator when water used as working fluid.
3. The minimum practical value of CCHT is 264.94 W/m^2 °C at 60° tilt angle of heat pipe from vertical position at 40 °C inlet fluid temperature of evaporator when ethanol used as a working fluid.
4. The result shows that the HPHE gives the maximum heat transport rate when water is used as a working fluid as compared to ethanol, methanol and butanol. In the case of inclination of heat pipe from its vertical position, it gives good thermal execution when heat pipe is inclined at 45° tilt angles at all the range of inlet temperature of the evaporator, and methanol is used as a working fluid.

Table 2 Rate of heat transport for different working fluids under natural convection

Rate of heal transport for different working fluid under natural convection in W

Water

T1	Angle of inclination				
	0	15	30	45	CO
	$Q_{practical}$	$Q_{practical}$	$Q_{practical}$	$Q_{practical}$	$Q_{practical}$
40	234.88	217.61	218.43	202.07	173.54
«	258.84	264.55	253.97	229.40	204.70
46	324.58	335.26	300.76	302.13	254.97
49	378.70	408.77	385.85	358.56	311.26
52	456.35	457.08	445.96	431.78	369.28
55	570.51	518.47	503.38	490.51	432.82
58	684.44	589.403	562.97	544.43	486.42
61	775.80	688.72	668.03	623.14	563.20

Ethanol

T1	Angle of inclination				
	0	15	30	45	60
	$Q_{practical}$	$Q_{practical}$	$Q_{practical}$	$Q_{practical}$	$Q_{practical}$
40	50.35	47.27	48.92	43.69	43.80
43	64.51	64.51	56.25	51.29	46.24
46	75.27	74.11	70.52	68.03	65.38
49	98.04	35.77	85.86	86.94	77.75
52	118.05	118.65	110.86	99.79	92.10
55	139.59	140.99	128.34	119.09	109.04
58	167.75	165.81	154.79	141.86	127.32
61	194.34	188.23	184.33	165.00	150.88

Methanol

Angle of inclination					
T1	0	15	30	45	60
	$Q_{practical}$	$Q_{practical}$	$Q_{practical}$	$Q_{practical}$	$Q_{practical}$
40	86.62	73.30	67.63	64.02	50.77
43	82.41	87.12	85.58	85.47	65.08
46	114.05	108.06	97.24	93.57	87.58
49	130.61	118.04	117.13	114.16	88.16
52	154.57	140.38	142.48	140.06	115.63
55	173.21	163.87	166.23	167.34	128.28
58	181.77	186.65	192.94	199.36	158.29

Acetone or Butanol

Angle of inclination					
T1	0	15	30	45	60
	$Q_{practical}$	$Q_{practical}$	$Q_{practical}$	$Q_{practical}$	$Q_{practical}$
40	100.08	93.66	90.28	88.79	79.14
43	121.17	106.68	105.88	103.08	92.74
46	143.10	128.58	133.08	132.92	122.27
49	186.16	155.65	155.82	157.97	147.60
52	227.08	187.14	181.76	186.00	172.36
55	244.16	201.44	214.28	219.03	201.45
58	274.39	242.83	238.46	246.08	228.47

(continued)

Table 2 (continued)

Methanol

Angle of inclination	0	15	30	45	60
T1	$Q_{practical}$	$Q_{practical}$	$Q_{practical}$	$Q_{practical}$	$Q_{practical}$
81	230.31	227.95	225.93	229.10	167.78

Acetone or Butanol

Angle of inclination	0	15	30	45	60
T1	$Q_{practical}$	$Q_{practical}$	$Q_{practical}$	$Q_{practical}$	$Q_{practical}$
61	324.00	283.73	275.81	272.51	263.18
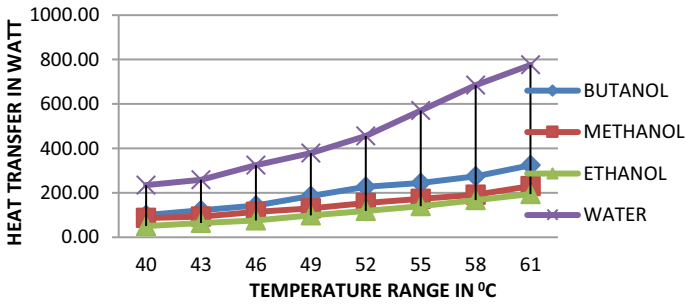
Fig. 8 RHT of HPHE when heat pipe inclined at 0° angles and different fluid used
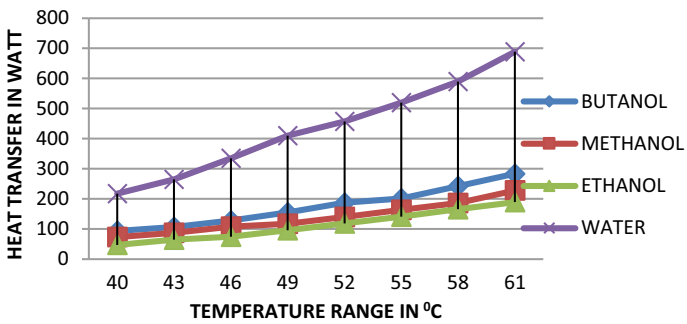
Fig. 9 RHT of HPHE when heat pipe inclined at 15° angles and different fluid used
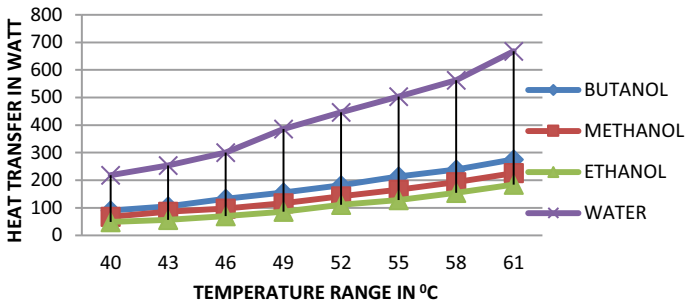
Fig. 10 RHT of HPHE when heat pipe inclined at 30° angles and different fluid used

5.2   For the Heat Transport Rate

1. The inlet heating temperature of fluids increases, then RHT also increases, and the inclination of heat pipe increases from vertical axis, then the value of RHT decreases.
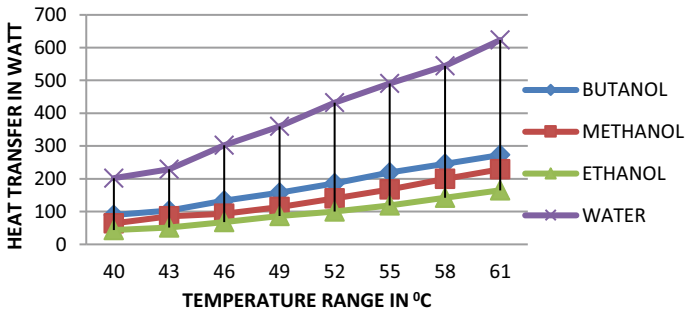
Fig. 11 RHT of HPHE when heat pipe inclined at 45° angles and different fluid used
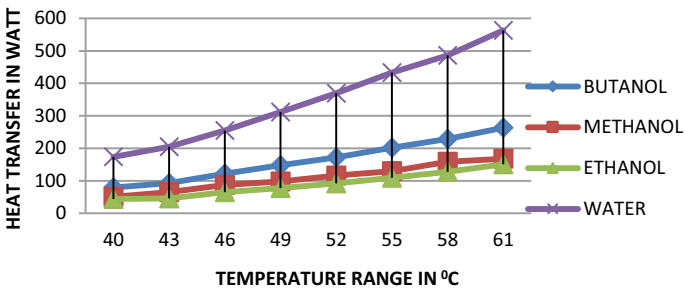
Fig. 12 RHT of HPHE when heat pipe inclined at 60° angles and different fluid used

2. The maximum practical value of RHT of HPHE is 775.90 W at 0° tilt angle of heat pipe from vertical position at 61 °C inlet fluid temperature of evaporator when water used as working fluid.
3. The minimum practical value of RHT of HPHE is 43.80 W at 60° tilt angle of heat pipe from vertical position at 40 °C inlet fluid temperature of evaporator when ethanol used as a working fluid.
4. It has been observed that water gives the good performance of heat pipe heat exchanger under natural convection condition for high heat transfer.
5. It has been observed that ethanol gives the good performance of heat pipe heat exchanger under natural convection condition for low heat transfer.

References

1. Turgut, O.E., Mustafa Turhan Çoban.: Thermal design of spiral heat exchangers and heat pipes through global best algorithm. Heat Mass Trans. **53.3**, 899–916 (2017)
2. Afzal, A., et al.: Steady and transient state analyses on conjugate laminar forced convection heat transfer. Arch. Comput. Meth. Eng. **27.1**,135–170 (2020)

3. Acharya, S., Sukanta K.D. Natural convection heat transfer from a hollow horizontal cylinder with external longitudinal fins: A numerical approach. Numer. Heat Trans., Part A: Appl. **74.7**, 1405–1423 (2018)
4. Zhang, J, et al.: A review of heat transfer enhancement techniques in plate heat exchangers. Ren. Sus. Energy Rev. **101**, 305–328 (2019)
5. Ivošević, Mi., et al.: Thermal performances and their impact on design of bayonet-tube heat exchangers–single phase plug flow. Heat Mass Trans. **55.9**, 2391–2407 (2019)
6. Nee, Aleksandr Eduardovich. Numerical analysis of three-dimensional natural convection in a closed rectangular cavity under conditions of radiant heating and conjugate heat exchange. MATEC Web of Conferences. vol. 91, Smart Grids 2017.—Les Ulis, 2017. vol. 912017. EDP Sciences (2017)
7. Sharma, K.V., Robert, S.: Frederico wanderley tavares. Natural convection heat transfer modeling by the cascaded thermal lattice Boltzmann method. Int. J. Therm. Sci. **134**, 552–564 (2018)
8. Hazbehian, M., et al.: Experimental investigation of heat transfer augmentation inside double pipe heat exchanger equipped with reduced width twisted tapes inserts using polymeric nanofluid. Heat Mass Trans. **52.11**, 2515–2529 (2016)
9. Zhang, L., et al.: Effects of the arrangement of triangle-winglet-pair vortex generators on heat transfer performance of the shell side of a double-pipe heat exchanger enhanced by helical fins. Heat Mass Trans. *53.1*, 127–139 (2017)
10. Nahar, A., et al.: Numerical investigation on the effect of different parameters in enhancing heat transfer performance of photovoltaic thermal systems. Ren. Ener. **132**, 284–295 (2019)
11. da Silva, Felipe A.S., et al.: Longitudinal vortex generator applied to heat transfer enhancement of a flat plate solar water heater. Appl. Therm. Eng. **158**, 113790 (2019)
12. Obeidat, A., et al.: Effect of cutoff radius, long range interaction and temperature controller on thermodynamic properties of fluids: Methanol as an example. Physica A: Statistic. Mech. Appl. *496*, 243–248 (2018)
13. Liu, Y., et al.: Heat transfer analysis of passive residual heat removal heat exchanger under tube outside boiling condition. Sci. Technol. Nuclear Install. (2017)

Commissioning Process and Energy Analysis in the Building: A Case Study for Ranchi City

Om Prakash ⓘ **, Bharath Bhushan** ⓘ **, Anil Kumar** ⓘ **, and Ankish Aman** ⓘ

1 Introduction

Hospitals come under the category of high electricity consuming buildings because of their high-cost operative equipment, human gathering and ecological parameters. Hospitals are the second biggest vitality buildings with energy utilization per square foot twice that of other buildings. The energy utilization of hospital buildings is intricate than that of standard commercial or corporate buildings. Its day-to-day utilization of electricity for lighting, lifts, ventilation, cooling and heating water is more. Fuel and natural gas are being used as the main source for high-temperature water, stream, sanitization and disinfectant washing and so forth. This paper uses a hospital building layout located in a composite climatic area like Ranchi city. A design case is prepared which is compared with a baseline model of the hospital building which is based on ASHRAE 90.1-2010 standards.

As per energy analysis, eQuest software is used for generating results of this building. It is analyzed that current design of the building is nearly 11.37% better than baseline. Building's energy simulation is performed to analyze annual energy consumption of the building. Energy modeling takes into account of different factors like climatic data (weather data) of the specified site location, building envelope

O. Prakash · B. Bhushan (✉) · A. Aman
Department of Mechanical Engineering, Birla Institute of Technology, Mesra, Ranchi, India
e-mail: bhushanbharath96@gmail.com

O. Prakash
e-mail: omprakash@bitmesra.ac.in

A. Aman
e-mail: ankishamansrm@gmail.com

A. Kumar
Department of Mechanical, Production & Industrial and Automobile Engineering, Delhi Technological University, North West Delhi, Delhi, India
e-mail: anilkumar76@dtu.ac.in

parameters, lighting factors, air-conditioning parameters, etc. The commissioning plan serves as a reference for the entire commissioning team includes user, design professionals, contractors, commissioning authority, vendors and various activities that comprise the commissioning process. Working together, the commissioning team will pursue the user's goals including optimizing operational performance, energy efficiency, durability, maintainability and flexibility of the building systems.

2 Methodology

2.1 Building Specifications and Commissioning

The hospital is located in the composite climatic area of Ranchi, capital city of Jharkhand state, India. The total construction area of the hospital is 35,000 ft^2. built-up area 100,000 ft^2. where operation zone is built and hospitalization area is 68,842.5 ft^2, 500 ft^2. logistics area which include laundry room, cafeteria and equipment rooms and the area of 900 ft^2. is built for apartments where doctors and nurses reside. The post-installation plan of equipment and systems is required for commissioning in this building and it includes [1]:

1. Mechanical ventilation and air-conditioning (MVAC) system

   - Terminals in owner scope.
   - Air handling units in auditorium and basement back of house (BOH).
   - MVAC controls in store.

2. Lighting system

   - Artificial lighting fixtures.
   - Emergency lighting systems.
   - Lighting controls relevant to above.

3. Electricity system

   - All distribution boxes and their accessories.
   - Two electricity meters in store.

4. Solar rooftop plant

   - I-V curve.
   - Voc, Isc measurement.
   - PV panel adjustment.

2.2 Responsibilities in Commissioning Process [2]

- Organize the commissioning team.

- Facilitate and prepare a commissioning plan that portrays the commissioning procedure to achieve the Owner Project Requirements.
- Verify that the Commissioning Process exercises are expressed plainly in all extents of work.
- Review and remark on the capacity of the plan report to accomplish the Owner Project Requirements for the authorized frameworks and congregations.
- Review the plans and specification for their fulfilment in all territories identifying with the commissioning procedure. This incorporates confirming that the Owner Project Requirements have been accomplished and there are satisfactory gadgets remembered for the structure to appropriately test the frameworks and congregations and record the presentation of each design.
- Schedule and document review, coordination of meetings, issues resolution and disposition.
- Review contractor's submittals for compliance with the Owner Project Requirements and Basis of Design.
- Prepare the pre-functional test procedures based on approved equipment and systems submittals and provide them to the contractor for execution.
- Author the Functional Performance Test procedure and provide then to the contractor for review and comments.
- Supervise and whiteness the commissioning team members in completion of testing systems and assemblies.
- Verify the results and prepare a list of deficiencies.
- Repeat implementation of tests to accommodate seasonal testing or to correct recorded deficiencies.
- Schedule initial owner training session before the contractor training.
- Prepare the final commissioning process report.
- Assemble all details of final documentation including commissioning process report and systems manual.
- Submit this documentation to the owner or user for audit and acknowledgment.
- Recommend acknowledgement congregations to the owner and executing the recommended details.

2.3 Design Professional's Responsibilities [2]

- Assist in the documentation.
- Obtain approval from the owner for revisions to the Owner Project Requirements.
- Document the Basis of Design.
- Prepare the Contract Documents, including the commissioning process requirements and recommendation by the commissioning authority.
- Respond to commissioning team plan accommodation, audit remarks and issues.
- Provide design information varying by the commissioning authority.
- Specify and confirm that the activity and support of the frameworks and congregations have been sufficiently itemized in the Construction Documents.

- Review and fuse the commissioning authorities' remarks from the submittals audit process.
- Participate in the underlying activities and support faculty and tenants' instructional courses by introducing the venture Basis of Design.
- Review and comment on the commissioning authority's commissioning reports and issues log.
- Participate in issues resolution.
- Review and comment on the last commissioning report and issues log.

2.4 Mechanical Ventilation and Air-Conditioning (MVAC) and Cx Plan

The MVAC designer by taking the responsibility to draft the Basis of Design document and reviewed it to ensure the document include all the following items [3]:

- Primary design assumptions for the MVAC system.
- Standards and guidance referred for the MVAC design.
- Narrative descriptions of the MVAC systems.

The observation is positive. The document is clear and complete and addresses the requirement raised in the documents. As indicated in the first section, Cx plan is an important guidance to the entire Cx process adopted in the project. OPR development and review process are as follows: [3]:

- BOD development and review process.
- Design review process.
- Specification development requirement and review process.
- Contractor review process including checklist.
- Testing method statements, development requirement and review process.
- Pre-commissioning review process including checklist.
- Functional testing review process including checklist.
- System manual development process and required documentation list.
- O&M training requirement and review process.
- After occupancy performance review process.

2.5 Requirements in Commissioning Process

MVAC designer and engineers develop the technical specification in tabular form. The document details include the commissioning requirements, technical acceptance level, referred standards, tools to be used, documentation requirements and O&M requirements [4]. The requirements for the commissioning process are as follows:

- **Verification of Installation and Performance**
  During construction phase, site visits need to be conducted to ensure the installation and performance of the major energy consumption systems to satisfy owner's requirement. To ensure the observation accurately, all the on-site checking including mechanical checking, electric checking, functional and performance testing shall follow the method statements/checklists as agreed by the MVAC contractor [4].
- **Activities for IGBC NB Commissioning Credit**
  The design review document issued before the construction was to ensure the design's compliance with OPR and BOD, as well as related to IGBC credits which will be pursued by the building. During the design evolving stages, regular design review should be done to ensure all the design changes will not affect the compliance with above-mentioned requirements [5].
- **Contractor Submittal Review**
  Equipment specification, construction drawings, testing documents were submitted by the main contractor. Lucas Wang conducted the review to ensure equipment to be installed, installation methods and testing methods fulfill requirements raised in OPR, BOD, design documents and specification [5].
- **Training**
  The main contractor provided operation and maintenance training for ICAI, Pune Chapter O&M staffs. Training review was conducted by Sprout through reviewing the training documents. Post-occupancy review need to be conducted at the site after 12 months to review the performance of commissioned systems [5].

3 Result and Discussion

Tables 1 and 2 explain the observations recorded for building analysis. Building resolution and its status are given by providing the issues of the building. Deadlines to the issues to be resolved and present status of the building are also discussed in Table 1.

3.1 Energy Consumption Analysis in the Building

The power feeding is acknowledged by means of three 8 kV high-voltage links and utilizes eight transformers with a diesel generator set for hardware use. Electrical energy is utilized for heating, ventilation, air conditioning, lifts, lighting, offices, kitchens and clinical. The primary energy utilization equipments are central air-conditioning framework, ventilation, lighting framework and high-temperature water heating system.

The building has cold source system of three 750-standard ton centrifugal units and a lot of one 360-standard ton screw conveyor, with COP of 5.8. The heat source

Table 1 Issue log record

S. No.	Issues	Date	Resolution	Responsible party	Status	Action deadline
1	All incandescent light bulbs must be replaced by LED	2017.11.22	Improve drawings	MEP	Solved	2018.04.22
2	Please clarify the control logics of terminals group running and controls	2018.12.22	Improve drawings	MEP	Solved	2019.02.22
3	Recommend adding proper grills for the air outlets	2018.12.22	Improve drawings	MEP	Solved	2019.03.27
4	In the MVAC schematic drawings, no amount of supplied fresh air is label	2018.12.22	Improve drawings	MEP	Solved	2019.03.29
5	The power of lighting fixtures is not consistent between the drawing sand	2018.12.24	Improve drawings	MEP	Solved	2018.12.24
6	Dust has solidified in PV panel	2018.12.24	Remove Dust through water sprinkling	MEP	Solved	2018.12.31
7	Overheating of solar PV conductors (cables)	2018.12.24	Troubleshoot faulty wiring system	MEP	Solved	2018.12.31
8	Auditorium lighting switch is not working	2018.12.26	Modify the installation	MEP	Solved	2018.12.31
9	The amount of fresh air is not marked in the drawings	2018.12.26	Improve drawings	MEP	Solved	2018.12.31

Table 1 (continued)

S. No.	Issues	Date	Resolution	Responsible party	Status	Action deadline
10	Lamps are required to replace by LEDs, as required before	2018.12.26	Replace lamps by LEDs	MEP	Solved	2018.12.31

Table 2 Construction phase

S. No.	Issue	Date	Resolution	Deadline
1	The air ducts need to protect well from dust before construction	2017.06.29	Protect the air duct	2017.06.29
2	In auditorium area, the air outlets need to protect	2017.07.05	Protect the air outlets	2017.07.07
3	The installation of wiring supporter not meet the specification	2017.08.30	Modify the installation	2017.09.06
4	All air vents need to be cleaned well before commissioning	2017.11.26	Protect the air vents	2017.11.30
5	The installation of lighting is askew	2017.12.28	Modify the installation	2018.01.10
6	Unusual noise from one terminal during operation	2018.02.12	Fix it or reduce noise by methods	2018.02.17
7	One circuit cannot self-locking when push the button	2018.02.13	Re-connect the wiring	2018.02.17
8	One switch (classroom) cannot turnoff	2018.02.13	Replace	2018.02.17
9	Two lighting circuits are different as the design drawings	2018.02.17	Modify the installation	2018.02.23
10	One emergency lighting (1F) doesn't light on when cutting out the power	2018.02.17	Re-connect the wiring	2018.02.23
11	Readings on one thermostat are difficult To read	2018.02.23	Calibrate thermostat	2018.02.27
12	Add labels for terminals as its serving area	2018.02.23	Label each controllers with its terminal	2018.02.27

is given by a lot of three 2791 kW vacuum high-temperature water boilers. Table 3 shows the building energy analysis.

Table 3 Energy analysis of the building

Parameter	Baseline case (ASHRAE 90.1–2010)	Design case
Roof U value (Btu/h f^2 °F)	0.063 Btu/h f^2 °F	0.05 Btu/h ft^2 °F (150 mm thick RCC slab + 75 mm thick XPS over deck insulation)
Wall U value (Btu/h f^2 °F)	0.124 Btu/h ft^2 °F	0.11 Btu/h ft^2 °F (U) (200 mm thick AAC blocks)
Glazing U value (Btu/h f^2 °F)	1.2 Btu/h ft^2 °F (glazing U-Value)	0.26
Glazing shading coefficient	0.29 (glazing shading coefficient)	0.31
Window-to-wall ratio (%)	5.0	5.0
LPD parking (W/f^2)	0.19	0.19
LPD corridor (W/f^2)	0.66	0.66
LPD other space	ASHRAE 90.1	Same as base case
EPD	9.35 W/ft^2	Same as base case
Fenestration	N/A	50% (glazing VLT)
Window-to-wall ratio	5.0%	5.0%
Elevator load	Same as design case	228 kW
Escalator load		327 kW
Lighting power density (space area method)	Corridor—0.66 W/ft^2	0.66 W/ft^2
	Parking—0.19 W/ ft^2	0.19 W/ft^2
	Other space: ASHRAE 90.1	ASHRAE 90.1
Occupancy	5800 ft^2/Person	5800 ft^2/Person
HVAC system	2 nos. equally sized water-cooled centrifugal chiller	2 nos. screw chiller + 4 nos. centrifugal chillers
Coefficient of performance	6.17	Chiller (multiplex)—4.68
		Centrifugal chiller—5.5
Fan power	0.0010 kW/cfm	0.0008 kW/ft^3/min
Fan control	Variable speed	Variable speed

Table 4 Proposed ECMs for energy savings in the building

Proposed ECMs	Energy savings (%)
Proposed design	11.38
Improved lighting in parking and corridor	12.1
Screw chiller COP 5.0	12.2
Centrifugal chiller COP 6.10	13.7
VSD-driven centrifugal chiller	14.9
VFD controlled pump	17.0
Centrifugal chiller COP 6.30	17.5
Centrifugal chiller COP 6.50	17.8
Screw chiller COP 5.50	17.97

3.2 Building Energy Optimization

The building analysis is done by energy simulation at first to provide the best suitable recommendation and renovation purpose of the building. The analysis simulation input parameter result is present in the given Table 4. This analysis provides insight about how the project shall perform and how the building's energy systems' performance integrated with each other. This simulation results also provides results to assess how building shall perform in its various end uses like air conditioning, lighting, miscellaneous equipment, pumps etc. Figure 1 shows the energy consumption of building components.

It is prescribed to modify the air supply as indicated by the indoor CO_2 level such that it spares energy utilization. It is prescribed to set up an air source heat siphon unit that supplies residential high temperature water as per the real needs to improve energy productivity. It is prescribed to utilize numerous channels to freely control the lighting in open territory, to rework the lighting in the zone, and to utilize the light sensor to naturally control the daylight to accomplish energy investment funds. The
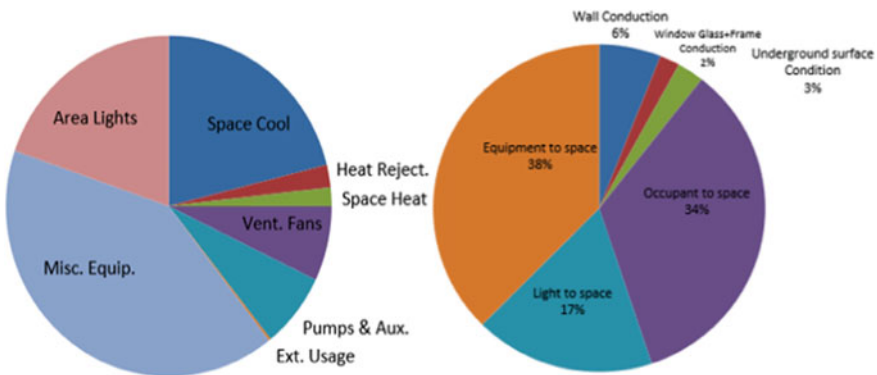
Fig. 1 Comparison of building energy components and its consumption

garage and open region lighting are consistently on for 24 h leading misuse of energy. Therefore, utilize microwave induction system and light detecting sensor in open-air lighting of the carport by this lighting is consequently controlled off in the daytime. Miscellaneous equipment consume 35% of total building energy incorporates PCs, machines, refrigerator, individual space radiators and other clinic gear stacks typically served through ordinary electrical repositories. Container power does exclude task lighting, gear utilized for HVAC purposes, open or shut refrigeration cases, stroll in coolers and fridges, lifts and electrically operated clinic hardware. In order to increase building operational, proposed ECMs if implemented can escalate the building's energy savings to 17.97%.

4 Conclusion

In this paper, the main purpose of the simulation is to find the possible energy savings of the hospital layout as baseline. The result generated in the simulation is 17.97% energy savings, and this percentage obtained is based on energy conservation and management factors. The conclusions of the study are as follows:

1. Optimum utilization of the electricity, daylight energy savings, building envelope, renewable energy generation and adopting it as a major source of electricity to the building are the parameters for energy efficiency and conservation.
2. In the process of energy conservation management techniques, design drawings of the building are reviewed before construction and documents are issued.
3. All equipment specification, construction drawings, testing documents were submitted by the main contractor. These documents focus particularly on operating the interactions between equipment and systems.
4. The on-site inspection after 12 months to review the performance of commissioned systems. As a result of commissioning work, the owner is satisfied with the performance of both MVAC system and lighting systems.

As project's commissioning for building equipment and systems succeed in getting such achievements, the further energy analysis and optimization suggestion would provide user the future trend and advanced technology.

References

1. Wahab, A.B., Omaka, K.: Investigation of the adoption of building commissioning practices in the installation of building services items. Baltic J. Real Estate Econ. Constr. Manage. **7**(1), 81–97 (2019)
2. Mills, E.: Building commissioning: a golden opportunity for reducing energy costs and greenhouse gas emissions in the United States. Energy Eff. **4**(2), 145–173 (2011)
3. Reeve, H., Jing, B.J., Zhu, Z., Chabukswar, R., Ghosh, A., Li, Y.: Field demonstration of an automated building commissioning tool. ASHRAE Trans. **125**(1), 37–47 (2019)

4. Kim, D.B., Kim, D.D., Kim, T.: Energy performance assessment of HVAC commissioning using long-term monitoring data: a case study of the newly built office building in South Korea. Energy Build. **1**(204), 109465 (2019)
5. Meruva, J., Gupta, M., Halford, A.D., Leen, C., Kolasa, R.A.: Inventors; Honeywell International Inc., assignee. Building system commissioning automation. United States patent US 10,359,745. 2019 July 23

Fabrication of Metal-Doped Polymer to Study Its Thermal and Mechanical Properties

Isha Joon, Subhra Das, and Chandra Mohan Srivastava

1 Introduction

Polymers are abundant in nature, and they are found in all the living systems. Materials like paper, wood and leather all are part of polymers only. During early civilization, all a man needed was food and shelter to protect him from extreme harsh conditions of weather. These shelters were primarily made of wood, bamboo, dry grass, animal skin/leather which may be classified as natural polymers [1, 2]. With the changing need of the people, polymers have undergone major changes in its fabrication technique, thereby leading to its usage in wide range of industries.

Natural polymers are having their intrinsic importance, but it is synthetic polymers that are widely used in today's lifestyle [3]. First manmade polymer was made by modification of natural materials in nineteenth century, whereas fully synthetic polymers were produced in twentieth century during chemical expansion. These synthetic polymers are called plastics in modern society [4, 5]. Today, synthetic polymers have become an important part of construction materials and many other applications due to its superior properties like high compressible strength, corrosion resistance, insulation properties and lower cost [6, 7].

Polymers together with ceramics are an important part of construction industry, automobile industry and household product industry. The rapid growth of these polymers is due to the availability of basic raw materials, ensemble of technical properties specific for polymers such as lightweight, stability, strength and easy, efficient and flexible processing methods [5, 8].

I. Joon · C. M. Srivastava
Amity School of Applied Sciences, Amity University Haryana, Gurgaon, India

S. Das (✉)
Solar Engineering Department, Amity School of Engineering & Technology, Amity University Haryana, Gurgaon, India
e-mail: nips.subhra@gmail.com

Research in the field of polymer has taken a greater leap with new advancement in technology and new inventions and metal-doped polymer (coordination polymer type) is one of them [9]. The metal-doped polymers find its application in major areas like aerospace industry, ship and building constructions because of high specific and compressive strength [10, 11]. Fibres in the form of metals reinforcement are the major reason for providing stiffness and strength to the composites. Several researchers have put their efforts to improve the properties of polymer composite based on the growing demand of the industry. Silica-epoxy nanocomposites are showing significant enhancement of mechanical properties such as Young's modulus, tensile stress and yield stress with increasing particle loading. Fracture toughness of silica-epoxy nanocomposite also increases with increase in particle loading [12].

The thermal conductivity of epoxy resin composites filled with combustion-synthesized hexagonal boron nitride (h-BN) particles was found to be a factor of particle size. Thermal conductivity increased with increase in filler content to a maxima and then starts deceasing with the increase in filler content because of horizontal orientation of h-BN particles at higher loadings [13]. Struzziero et al. [14] developed a methodology for the measurement of thermal conductivity of thermosetting polymers during their cure. Researchers have also studied the impact of loading epoxy resin with silicon carbide nanowires and had reported 106% enhancement in thermal conductivity [15].

In this paper, an attempt has been made to fabricate metal-doped polymer with the expectation to improve its mechanical and thermal properties. The metal-doped polymer has been fabricated using epoxy resin as base polymer which is doped with aluminium powder. Hand layup technique has been used for the fabrication of the polymer. This technique is quite cost-efficient and requires less tool to fabricate polymer in a smaller scale [6, 16]. Thermal and mechanical properties of the metal-doped polymer thus synthesized are studied and compared with epoxy resin and polyvinyl chloride (PVC).

2 Materials and Methods

2.1 Material Used

Polymer used: Epoxy resin.

Metal used: Aluminium. The main reason for combining aluminium with epoxy is because of its availability, high thermal conductivity, malleability and ductility.

Hardener used: Xin-900.

2.2 Fabrication Technique of Epoxy Resin

Hand layup technique has been used for fabrication of epoxy resin [6, 17].

Step I: **Mould preparation**: A simple wooden sheet covered with plastic sheet is used to prepare the mould. The mould of required size is cut out of cardboard sheet and is fixed on the wooden sheet using cello tape. Clay is applied inside the mould to lock it from every corner so that there is no leakage. Mixture when poured in this mould can take desired shape.

Step II: Mixture Preparation: Resin and hardener were taken in the ratio of 5:4. The resin is poured in a dry beaker. It is heated on a hot plate. The resin is rotated with glass rod in a slanted manner in order to remove air bubbles. Resin is removed from hot plate time to time so that it does not start decomposing. Temperature of resin should not exceed 70 °C else it starts decomposing. After removal of all air bubbles, the resin is removed from hot plate and hardener is then added slowly by continuously stirring the mixture to form a homogeneous mixture. The mixture is heated again for a few minutes so that excess moisture can be removed.

Step III: Sample Preparation: After removing the mixture from hot plate, it is poured into the mould and is spread evenly in a Long Line form. After pouring the sample in mould, the wooden plate is tapped gently along a table or slab so that any air bubble formed during pouring is removed and the mixture does not become brittle.

Polymerization: The mixture is allowed to set at room temperature for about 3–4 h. Then it is kept in oven for 24 h at temperature between 24 and 26 °C so that polymerization takes place completely. If polymerization is not complete (i.e. after removing sample from the mould it bends easily), then it is again kept in oven for 12 h at same temperature. After solidification, post-curing is done by putting the solidified sample at 40–50 °C in oven for 24 h more.

Step IV: Cutting of Sample: The sample is then cut using a cutter into desired shape and size.

2.3 Fabrication Technique of Metal-Doped Polymer

Hand layup technique has been used to dope aluminium to epoxy resin [16]. The steps to prepare a sample are described below:

Step I: **Mould preparation**: A simple wooden sheet covered with plastic sheet is used to prepare the mould. The mould of required size is cut out of cardboard sheet and is fixed on the wooden sheet with the help of tape. Clay is applied inside the mould to lock it from every corner so that there is no leakage. Mixture when poured in this mould takes desired shape.

Fig. 1 **a** Powered form of sample, **b** mixture poured in mould

Step II: Mixture Preparation: A beaker is taken and dried completely. No moisture should be present inside the beaker as it will lead to bubbles formation inside the resin. The resin is being poured in the beaker. It is being heated on hot plate and is rotated with glass rod in a slanted manner to remove air bubbles. It is removed from hot plate time to time so that it does not start decomposing. Temperature of resin should not exceed 70 °C else it can start decomposing.

Addition of Metal: After removal of air bubbles, the resin is allowed to cool a little and then hardener (28 ml) is added slowly by continuously stirring the mixture to form a homogeneous mixture. The resin and hardener should be taken in a ratio of 5:4. After addition of hardener, it is heated again for few minutes more and metal is added slowly by continuously stirring the mixture.

Step III: Sample Preparation: After removing the mixture from hot plate, it is poured into the mould and is spread evenly in a long line form as shown in Fig. 1. After pouring the sample in mould, wooden plate is tapped gently along a table or slab so that any air bubble formed during pouring is removed and the mixture does not become brittle.

Polymerization: The mixture is allowed to set at room temperature for about 3–4 h. Then it is kept in oven for 24 h at temperature between 24 and 26 °C so that polymerization takes place completely. If polymerization is not complete (i.e. after removing sample from the mould, the sample bends easily), then it is again kept in oven for 12 h at same temperature.

Step IV: Cutting of Sample: The sample is then cut using a cutter into desired shape and size as shown in Fig. 2. A schematic diagram for the fabrication technique is shown in Fig. 3:
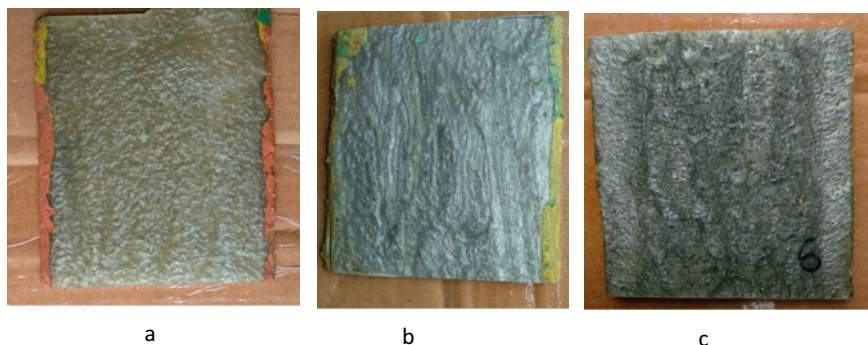
Fig. 2　**a** Sample A, **b** Sample B and **c** Sample C
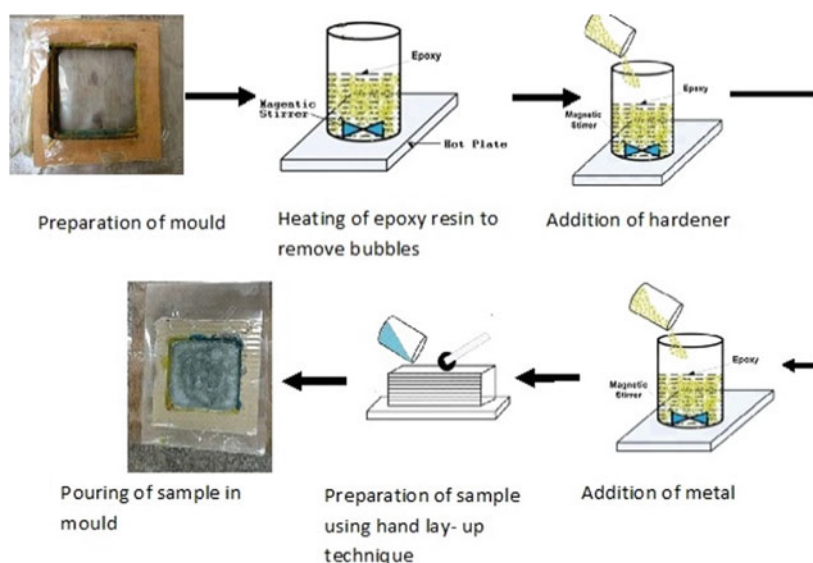
Fig. 3　Fabrication technique for epoxy resin doped with aluminium

3　Characterization Techniques

Three samples were prepared with different concentration of aluminium in epoxy resin, viz. Sample A (with 1% wt. metal in polymer), Sample B (with 3% wt. metal in polymer) and Sample C (with 5% wt. metal in polymer). A simple heat transfer test was conducted in laboratory to check thermal characteristics of the three samples. Three samples were kept under a solar simulator in such a way that only the top surface receives heat and the bottom is exposed to ambient air. Temperatures of top

Fig. 4 Simple heat transfer analysis for Samples A, B and C
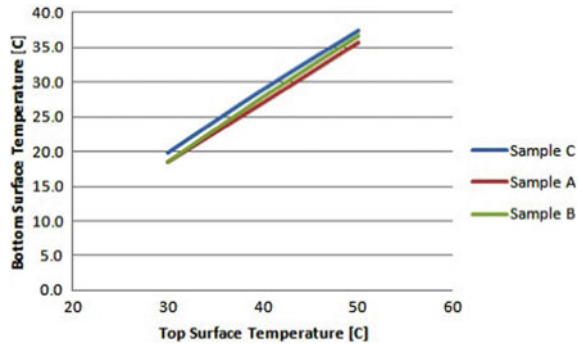
and bottom surfaces were measured at an interval of 15 min and are plotted in Fig. 4 to identify the sample which transfers heat efficiently.

It was observed that Sample C outperformed other two samples. Hence, only Sample C was sent to various laboratories for characterization.

3.1 Dynamic Mechanical Analysis (DMA)

Sample C of metal-doped polymer was first sent for dynamic mechanical analysis at Netaji Subhas Institute of Technology, New Delhi.

Composition of Sample C

Total polymer = 63 ml (9 cm/7 cm/1 cm = vol of mould).

Resin + hardener = 35 + 28 ml.

Metal = 5% of 63 ml = 3.15 ml.

The rheological material behaviour of the sample is measured as a function of temperature.

The DMA curve for epoxy resin measured at a temperature range of 30.5–93.75 °C is shown in Figs. 5 and 6. From the graph, it is clear that the drop in storage modulus (E') and peak in damping factor between 60 and 70 °C is due to glass transition temperature (T_g) of the polymer. This drop indicates that the polymer starts melting after this temperature. It can be concluded that melting point of the metal-doped polymer is around 60 °C and thus can used for applications requiring temperature below 60 °C. In Fig. 5, the viscoelastic properties were studied and the results are shown in graph. In the graph, it is clear that the value of G' is more than G''. The drop in storage modulus of the sample is due to the thermal relaxation of the polymer chain.

Glass transition temperature T_g is also observed between 30 and 60 °C which are called beta and gamma transitions. The reason for these transitions is due to the internal motion of polymer mixture as opposed to large scale motion that accompanies

Fig. 5 Storage modulus G' and Loss Modulus G'' as a function of temperature
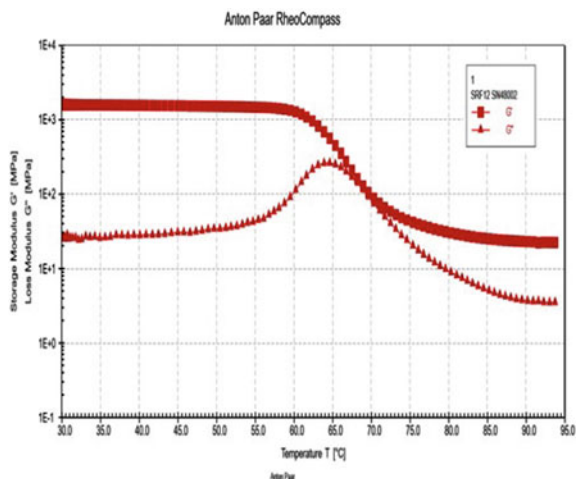
Fig. 6 Loss factor for Sample C as a function of temperature
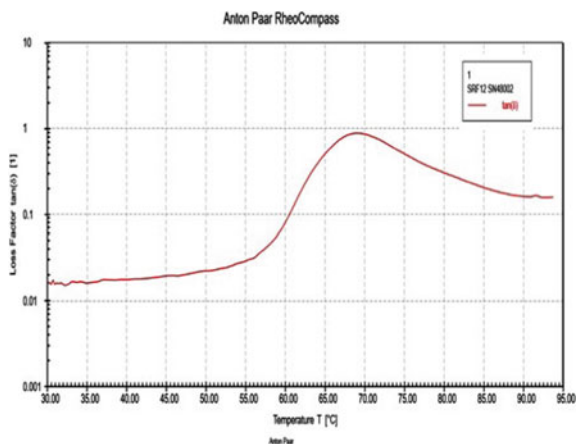
the T_g. These small transitions are very difficult to observe in differential scanning calorimetric technique but can be observed clearly in DMA. These transitions are very important as they help to determine resistance of the polymer. The glass transition temperature of the metal-doped polymer (Sample C) has shown a significant growth as compared to a polymer without metal whose T_g is less than 60 °C.

Fig. 7 Tensile stress as a function of tensile strain for Sample C
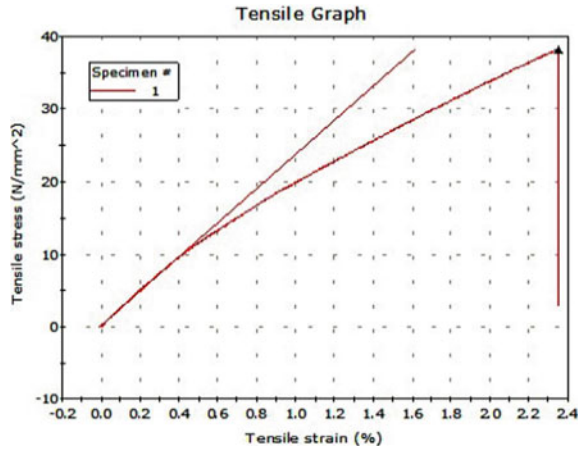
3.2 Tensile Strength

The Sample C has been tested for thermal conductivity, compressive strength and tensile strength at Laboratory for Advanced Research of Polymeric Materials, Bhubaneswar (LARPM).

When tensile strain is low, the sample obeys Hooke's law to a reasonable approximation, so that stress is proportional to strain as shown in Fig. 7. As strain is increased, the sample slowly deviates from this linear proportionality and this corresponds to 0.5% tensile strain. This nonlinearity is usually associated with stress-induced plastic flow in the sample. In this stage, the material undergoes rearrangement of its internal molecular or microscopic structure, in which atoms are moved to new equilibrium positions. Materials lacking this mobility are usually brittle rather than ductile. It has been observed that tensile stress that the sample can withstand at maximum load is 38.3 MPa.

3.3 Compressive Strength

The compressive strength is the measurement of pressure that the sample can withstand by putting a considerable amount of weight on it [7]. A weight placed on the sample at a particular point and the compression of the sample is noted down till it reaches its breaking point. The compressive strength test has been conducted on Sample C at 23 °C. A maximum load of 28,824 N has been applied on the polymer, and corresponding stress has been observed. From Fig. 8, it is observed that that the Sample C is the able to bear stress around 55 MPa with less than 1 mm of compressive extension in the sample; beyond this point with the increase in compressive stress, there is stretching of the polymer. The stretching continues till stress reaches

Fig. 8 Compressive stress of Sample C as a function of compressive extension
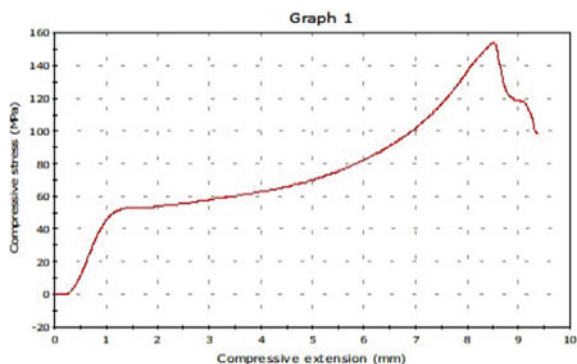
Table 1 Thermal conductivity of metal-doped polymer (Sample C)

Thickness of the sample (cm)	Temperature (°C)	Thermal resistance (m^{2}K/W)	Thermal conductivity (W/mK)
0.3450	32.89	2.05e−002	0.168
0.3450	42.91	1.85e−002	0.187
0.3450	53.04	1.79e−002	0.193

153.6 MPa which corresponds to the break point for the aluminium-doped epoxy resin.

3.4 Thermal Conductivity

Sample C was sent to LARPM to conduct thermal conductivity test. Table 1 gives thermal conductivity and thermal resistance of sample at different sample temperature. It is observed that thermal conductivity of aluminium-doped epoxy resin increased with increase in temperature.

4 Comparing Properties of Aluminium-Doped Epoxy Resin with Epoxy Resin and Polyvinyl Chloride

The tensile strength, compressive strength and thermal conductivity of aluminium-doped epoxy resin are compared with that of epoxy resin and polyvinyl chloride (PVC) and are given in Table 2. It is observed that tensile strength of aluminium-doped epoxy resin increased by 16%, compressive strength increased by almost 43% and thermal conductivity increased by 12%. This shows that there is significant increase in thermal and mechanical properties of epoxy resin due to metal doping.

Table 2 Tensile strength, compressibility and thermal conductivity of metal-doped polymer, polyvinyl chloride (PVC) and epoxy resin

Properties	Metal-doped epoxy resin	PVC	Epoxy resin
Tensile strength (MPa)	38.302	52 [18]	33 [19]
Compressive strength (MPa)	153.69	66.18 [20]	68.94 [21]
Thermal conductivity (W/mK)	0.168	0.16 [18]	0.15 [13]

The properties of aluminium-doped epoxy resin are compared with PVC which is commonly used in various industrial applications. It is observed that metal-doped epoxy resin has higher thermal conductivity and compressive strength than PVC but lower tensile strength.

5 Conclusions

This paper has dealt with fabrication and characterization of metal-doped polymer. For the fabrication of metal-doped polymer, epoxy resin is used as base polymer to which aluminium powder is added. Hand layup technique is used to fabricate the metal-doped polymer because of its simple and cost-effective technique.

Initially, three samples were made with different concentration of aluminium in epoxy resin (1 wt%, 3 wt% and 5 wt%). The samples were tested under solar simulator to test for heat transfer through these samples. It was observed that Sample C having 5 wt% concentration of aluminium in epoxy resin transfers heat efficiently compared to other two samples. Sample C was then sent to various laboratories for further characterization.

DMA of Sample C suggests that melting point of the sample is around 60 °C and thus is suitable for applications which require temperature below 60 °C. The glass transition temperature of aluminium-doped epoxy resin (Sample C) is 60 °C.

It was observed from tensile strength test that tensile stress that Sample C could withstand at maximum load is 38.3 MPa. The compressive strength test on Sample C reveals the fact that sample can bear stress around 55 MPa with less than 1 mm of compressive extension in the sample, and beyond this level, stretching of polymer was observed with the increase in compressive stress. The stretching continues till stress reaches 153.6 MPa which corresponds to the break point for the polymer. Thermal conductivity of aluminium-doped epoxy resin (Sample C) increased with the increase in temperature. It was observed that thermal conductivity varied from 0.168 to 0.193 W/mK.

Significant improvement in thermal and mechanical properties was observed in aluminium-doped epoxy resin in comparison with normal epoxy resin. Tensile strength increased by 16.06%, compressive strength increased by 121.93% and

thermal conductivity increased by 12%. Also, a comparison of these properties with PVC shows that tensile strength of Sample C is less than PVC but compressive strength and thermal conductivity of Sample C are more than that of PVC. Thus, it can be concluded that thermal and mechanical properties of epoxy resin can be enhanced by doping aluminium.

References

1. Abdellaoui, H., Bensalah, H., Echaabi, J., Bouhfid, R., Qaiss, A.: Fabrication, characterization and modelling of laminated composites based on woven jute fibers reinforced epoxy resin. MaterDes **68**, 104–113 (2015)
2. Raquez, J.M., Deléglise, M., Lacrampe, M.F., Krawczak, P.: Thermosetting (bio) materials derived from renewable resources: a critical review. Prog. Polym. Sci. **35**, 487–509 (2010)
3. Guilleminot, J., Comas-Cardona, S., Kondo, D., Binetruy, C., Krawczak, P.: Multi scale modelling of the composite reinforced foam core of a 3D sandwich structure. Compos. Sci. Technol. **68**, 1777–1786 (2008)
4. Gourichon, B., Deléglise, M., Binetruy, C., Krawczak, P.: Dynamic void content prediction during radial injection in liquid Composite molding. Compos. Part A: Appl. Sci. Manuf. **39**, 46–55 (2008)
5. Pascault, J.P., Williams, R.J.J.: Thermosetting polymers. In: Saldivar-Guerra, E., Vivaldo-Lima, E. (eds.) Handbook of Polymer Synthesis, Characterization, and Processing, pp. 519–533. Wiley, Hoboken (2013)
6. Hollaway (ed.): Polymer and Polymer Composites in Construction. Thomas Telford, London
7. Bullen, N.G.: Unified Composite Structures, Manufacturing Engineering Magazine, SME Editor, vol. 144, no. 3, March, pp. 47–55, Dearborn, MI, USA (2010)
8. Lee, L., Jain, R., Stephenson, L., Ramirez, C.: Introduction. Fiber Reinforced Polymer (FRP) Composites for Infrastructure Applications. Springer, Dordrecht (2012)
9. Sumby, C.J.: Research front on coordination polymers. Aust. J. Chem. **66**, 397–400 (2013)
10. Pegoretti, A., Accorsi, M.L., Dibenedetto, A.T.: Fracture toughness of the fibre-matrix interface in glass-epoxy composites. J. Mater. Sci. **31**, 6145–6153 (1996)
11. Paluvai, N.R., Mohanty, S., Nayak, S.K.: Synthesis and modifications of epoxy resins and their composites. Polym.-Plast. Technol. Eng. **53**, 1723–1758 (2014)
12. Islam, M.S., Masoodi, R., Rostami, H.: The effect of nanoparticles percentage on mechanical behavior of silica-epoxy nanocomposites. Hindawi Publishing Corporation, J. Nanosci. **2013**, Article ID 275037, 10 pages (2013). https://doi.org/10.1155/2013/275037
13. Chung, S.L., Lin, J.S.: Thermal conductivity of epoxy resin composites filled with combustion synthesized h-BN particles. Molecules **21**, 670 (2016). https://doi.org/10.3390/molecules210 50670
14. Struzziero, G., Remy, B., Skordos, A.A.: Measurement of thermal conductivity of epoxy resins during cure. J. Appl. Polym. Sci. (2019). https://doi.org/10.1002/APP.47015
15. Shen, D., Zhan, Z., Liu, Z., Cao, Y., Zhou, Liu, Y., Dai, W., Nishimura, K., Li, C., Lin, C.T., Jiang, N., Yu, J.: Enhanced thermal conductivity of epoxy composites filled with silicon carbide nanowires. Sci. Rep. **7**, 2606. https://doi.org/10.1038/s41598-017-02929-0

16. Bank, L.C., Gentry, T.L., Nuss, K.H., Hurd, S.H., Lamanna, A.J., Duich, S.J., Ben, O.H.: Construction of a pultruded composite structure: case study. J. Compos. Constr. **4**(3), 112–119 (2000)
17. Morey, B.: Innovation Drives Composites Production. Manufacturing Engineering Magazine, Society of Manufacturing Engineer Editor, vol. 142, no. 3, March 2009, pp. 49–60, Dearborn, MI, USA (2009)
18. https://www.vinidex.com.au/technical-resources/material-properties/pvc-properties/. Last accessed 2020/05/11
19. https://www.matweb.com/search/datasheettext.aspx?matguid=956da5edc80f4c62a72c15ca2b923494. Last accessed 2020/05/12
20. https://www.professionalplastics.com/professionalplastics/PVCPipeSpecifications.pdf. Last accessed 2020/05/11
21. https://www.epoxy.com/strength.aspx. Last accessed 2020/05/11

Investigation on Heating Load for Polyhouse Located in Agra: A Case Study

Pankaj Kumar [ID]**, Amit Yadav** [ID]**, Anil Kumar** [ID]**, Nitin Yadav** [ID]**, and Ashok Yadav** [ID]

1 Introduction

Protected cultivation is a specific horticultural framework where plants are developed by methods for controlling their typical habitat to drag out the collecting time frame, improve item quality, balance out creation, and give items when open field cultivation is limited [1]. Polyhouse development has extended during the most recent couple of years around the globe of various territories due to restriction of the ecological conditions. The general target of protected cultivation is to modify the habitat, through various procedures to identify the ideal habitat the condition of the harvest. In specific locations, the limitation of solar radiation or the insurance against the wind, slope, or other environmental conditions is additionally the goal of protected cultivation. Protected cultivation is additionally utilizing accessible soil, water, energy, space, and climatic assets; for example, sun-oriented radiation, humidity, temperature, and carbon dioxide present in the environment. Modern polyhouses are furnished with different warming and cooling gadgets, for example, radiators, coolers, fans. Since warmers and coolers expend a considerable measure of energy in inadequately protected polyhouses, sparing the energy has been a significant assignment for producing the agro-items, especially in long periods of high oil costs. Polyhouse cultivating is gradually picking up prevalence in India as well. A farmer can make immense benefits from polyhouse cultivating [2]. Be that as it may, numerous individuals do not know about polyhouse or even nursery; thus, through this study, they will become more acquainted about polyhouse and its advantages.

P. Kumar (✉) · A. Yadav
Dayalbagh Educational Institute, Dayalbagh, Agra, India
e-mail: er.pankaj2015@gmail.com

A. Kumar
Department of Mechanical, Production & Industrial and Automobile Engineering, Delhi Technological University, Delhi, India

N. Yadav · A. Yadav
Aerial Delivery Research and Development Establishment, DRDO, Agra, India

43

Polyhouse cultivations are significantly gaining popularity in India too to nourishment creation, yet require a lot of vitality to keep up their microclimate in locales with cruel atmospheres. This paper evaluated the internal heating load required to maintain ideal conditions for a polyhouse nurseries situated in DEI, Agra, during winters utilizing inside temperature changes and heat transfer coefficients. Polyhouse nurseries have a significant job in supporting stable vegetable production and supply in everywhere throughout the world. In any case, one of the significant limitations of nurseries is their energy cost because an appropriate microclimate for vegetable production must be maintained regardless of extreme climate conditions, particularly in winter [1, 2]. The increase of the world population and energy consumption has directed researchers and scientists to produce an ample quantity of food and energy by mistreatment different sources. Additionally, climate changes and inadequate water resources reveal that protected cultivation in 493 greenhouses has become the favored thanks for develop the agricultural sector. Polyhouse production is distributed, taking advantage of favorable climate (air temperature, ratio, and lighting) whereas keeping the operational price at a minimum [3].

The worldwide protected cultivation was 280,000 ha (without taking into consideration China wherever the area coated is calculated in 1,250,000 ha) in 2002. In Europe, the entire space of protected cultivation in 2005 is predictable to 126,000 ha [4]. The European nation is in the first place with 38% of the entire E.U. space of protected cultivation installations, followed by European nations with 22%. In contrast, Greece is within the sixth place with only 4%. Regarding Greece, protected cultivation production represents one among the foremost essential sectors of agriculture [5].

2 Material and Methods

2.1 Description of Polyhouse

A polyhouse generally referred to as a polytunnel has semi-circular, square, or elongated in form. It is made of steel structure and covered with polythene. The inside heats up as a result of incoming radiation from the sun warms plants, soil, and alternative things within the building quicker than heat will escape the structure. Air warm by the heat from hot interior surfaces is preserved within the building by the roof and wall. Temperature, humidness, and ventilation are controlled by instrumentation mounted within the polyhouse or by manual gap controlling of vents. Polyhouses are employed in temperate regions in similar ways that to glass greenhouses and row covers. Polyhouses are accustomed to providing a higher temperature or humidness than that is out there within the space. However, they may also shield crops from intense heat, bright daylight, winds, hailstones, and cold waves. It enables fruits and vegetables to be fully grown from time to time typically in the off season; market gardeners usually use polyhouses for season extension. The most purpose

of polyhouse is to form a microclimate that simulates the temperatures and alternative weather conditions of a location. Every aspect influencing a crop is controlled in an exceedingly polyhouse. Polyhouses are usually employed in horticulture and plant nurseries because the revenue price of the plants will justify the expense [2, 6]. There is a range of polyhouses regarding form, dimensions, and materials used for frame and coverage. Most conventional materials for the greenhouse frame are wood, aluminum, and steel, whereas for coverage are synthetic resin. The selection of polyhouses depends upon climate conditions specific location, technological development, economy characteristics, and also the nature of the crop. Because of the ecological management framework, polyhouse are of two categories: (1) Natural aired polyhouse—this sort of polyhouse or nursery does not have any ecological management framework except adequate ventilation to spare the harvests from unfavorable environmental conditions. (2) Environmental controlled polyhouse—they are developed primarily to expand the developing time of harvests or to create the slow time of the year yield by dominant the sunshine, temperature, dampness, and so on [7]. The adjustment of every variable influencing the indoor surroundings of a polyhouse could be an effective procedure. The dynamic behavior of polyhouse climate could be a combination of physical processes involving energy and mass transfer happening within the polyhouse further as between the polyhouses and also the outside surroundings. These processes depend upon the surface climate conditions, the polyhouse structure, kind and growing part of the plant. Typically, ventilation and heating will be accustomed to modifying within the temperature, humidness, and CO_2 concentrations, whereas shading and artificial lightweight to boost radiation conditions for the plants [8]. The structure of a polyhouse typically is not sufficient to stay within air temperature at an acceptable level for optimum growth, particularly in a cold climate.

Additionally, the shortage of heating systems has adverse effects on the yield, cultivation time, quality, and quantity of the polyhouse products; therefore, auxiliary heating systems must be needed [3]. Heating systems square measures either of local or central. Local heating systems accommodate heaters from biomass, diesel, or paraffin, or maybe electricity. On the opposite hand, heating system systems used alone or together, looking on depending on the particular polyhouse installation [9].

2.2 Construction and Methodology

Single span polyethylene plastic is chosen for this study. Experimental polyhouse is wrapped of a single-layered sheet of 4-mm-thick polyethylene film. It is installed in the cultivation division of DEI Agra (27.1767° N, 78.0081° E). A variety of models for polyhouse calculations are developed that classified as static, dynamic, and intermediate. Static models calculate energy consumption through overall thermal losses. They are simple, and their precision is restricted (±25% error). Dynamic models, on the other hand, show precision exactness (±10% error); however, they are complicated and challenging using in simulation over long periods [8]. Static models have
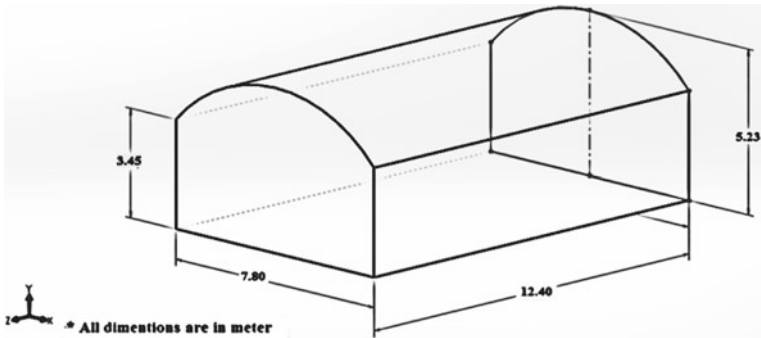
Fig. 1 Measurements of experimental polyhouse
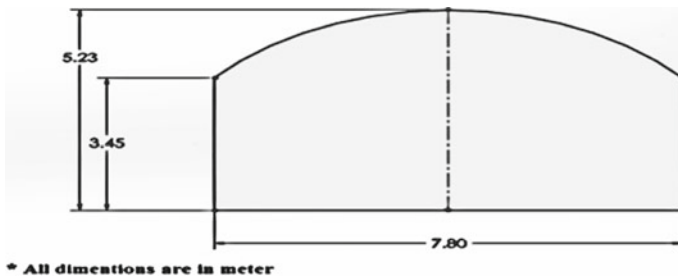
Fig. 2 Front view of experimental polyhouse [11]

been used to calculate the heating load of a reference polyhouse in Dayalbagh Educational Institute, Agra. Calculations were performed using meteorologic information (ambient air temperature, etc.), besides as thermal characteristics of the cover material. The necessary meteorologic data for the calculations data of heating loads (ambient air temperature with the help of RTD PT100 temperature indicator, the thickness of the sheet using a vernier caliper, etc.) are measured.

The polyhouse has dimensions of 12.40 m × 7.80 m × 5.23 m (Fig. 1). Total covered area is 104.34 m² with 460 m³ volume. Covering material is synthetic resin plastic (PE). The interior climate conditions consult with the optimum growing conditions for the plants that range from 25 to 32 °C for the day hours. Hence, in our calculations, the internal reference temperature to be maintained once removing additional heat from polyhouse is 30 °C [2, 10] (Figs. 2 and 3).

2.3 Measurement and Energy Analysis

The internal atmospheric temperature and outside air temperature were measured using the RTD PT100 temperature sensor. This sensor is connected with a digital

* All dimentions are in meter

Fig. 3 Side view of experimental polyhouse [11]

temperature indicator that shows the temperature with a resolution of 0.1 °C. Sensors were placed at gutter height, to avoid the shading from the crop. Temperatures were recorded at three distinct locations; at the center, and the other two are at a distance of one meter from north faced and south faced walls. All three locations are in a straight line within the polyhouse. Observations were recorded at an interval of 2 h from 8 am to 6 pm placing the sensor at 2.0 m altitude to avoid any temperature variation. Daily average temperature recorded is given in Table 1. Other measurements like height, length, width were measured using a 10-m-long measuring tap.

Volume Calculation [12, 13]
For the measurement of volume, polyhouse is divided into two parts, so that, the volume can be calculated easily. Part 1 is cuboid of size 12.4 m $\times$ 7.8 m $\times$ 3.45 m, whereas Part 2, is a Quonset having a width of 7.8 m, length 12.4 m, a radius of curvature 5.16 m and central incident angle of curvature is 98.17° (Fig. 4).

$$\text{Volume of Polyhouse} = \text{Volume of Part 1} + \text{Volume of Part 2}$$
$$= lbh + \left[\left(\text{Pi} * \theta * R^2 * l/360 \right) - \{ b * (R - h1)/2 \} \right] * l$$

where

l = length of polyhouse = 12.4 m

b = width of polyhouse = 7.8 m

H = total height of polyhouse = 5.23 m

h = Side height of polyhouse = 3.45 m

Pi = 3.143

θ = angle of intercept at center by curved part 2 = 98.17°, [12]

Table 1 Daily average temperature and heating load

Day	Average temperature in °C	Heating load (KW)	Day	Average temperature in °C	Heating load (KW)
1-Dec-19	26	17.7378	16-Dec-19	20	4.43445
2-Dec-19	28	8.8689	17-Dec-19	18	53.2134
3-Dec-19	27	13.30335	18-Dec-19	22	35.4756
4-Dec-19	29	4.43445	19-Dec-19	19	48.77895
5-Dec-19	28	8.8689	20-Dec-19	21	39.91005
6-Dec-19	27	13.30335	21-Dec-19	23	31.04115
7-Dec-19	29	4.43445	22-Dec-19	18	53.2134
8-Dec-19	27	13.30335	23-Dec-19	17	57.64785
9-Dec-19	28	8.8689	24-Dec-19	21	39.91005
10-Dec-19	26	17.7378	25-Dec-19	18	53.2134
11-Dec-19	27	13.30335	26-Dec-19	17	57.64785
12-Dec-19	28	8.8689	27-Dec-19	16	62.0823
13-Dec-19	24	26.6067	28-Dec-19	19	48.77895
14-Dec-19	23	31.04115	29-Dec-19	21	39.91005
15-Dec-19	25	22.17225	30-Dec-19	15	66.51675
Month's average temperature in °C				22.9	
December's average heating load in KW				31.484595	
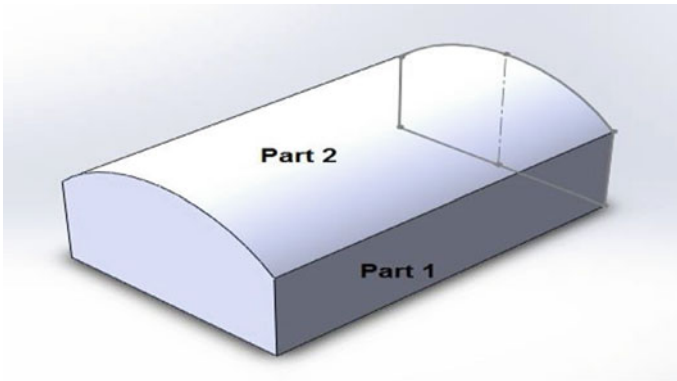
Fig. 4 Schematic diagram of experimental polyhouse [11]

$R =$ radius of curver part 2 = 5.16 m, [12]

I.e., Volume V = 460 m^3 (Approximate).

Heat flow rate in the polyhouse [14, 15]

The required heating load for maintaining the ideal environment within the polyhouse is calculated using Fourier's law of heat transfer [16].

$$Q = -K * A * dT/dx$$

where

Q = Heat flow rate per second in kW

A = Surface are of Polyhouse = 104.34 m^2, [12]

K = Thermal conductivity of polyethylene sheet = 0.17 W/m k, [13], 15]

dT = Temperature difference b/w inside and outside of the polyhouse

dx = thickness of polyethylene sheet = 4 mm.

3   Results and Discussion

Measurements were carried out during daylight hours for December 2019. The monthly average temperature was significantly lower than inside the polyhouse (22.9 °C) compared to the required average environmental temperature (30 °C) that generates a heating load of 31.5 kW. The lowest temperature was observed on 30/12/2019, where it was 15 °C that generates a heating load of 66.12 kW. In contrast, the maximum temperature was observed on 07/12/2019, where it was 29 °C, which is very close to the required temperature range and generates a heating load of 4.43 kW (shown in Table 1 and Fig. 5).
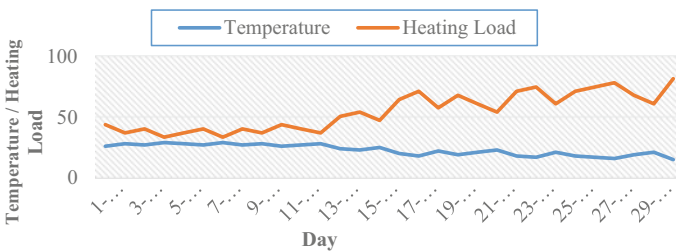
Fig. 5   Warming load pattern and temperature pattern throughout the month

4 Conclusion

The present study on heating loads of polyhouses is focused on—460 m^3 volume polyhouse used for potato cultivation. Potato is a dominant crop cultivated in the northern part of India. Meteorological data such as air temperature, solar radiation, humidity, and wind speed are in high temporal resolution (semi-hourly). Static models calculate energy consumption through the total thermal losses methodology is used to determine heating load requirements. Results show that the heating load during the whole month is quite realistic and easy to achieve with an average value of 31.5 kW. The after-effects of all heating loads vacillations during the long stretch of December are comparative.

References

1. Castilla, N.: Greenhouse Technology and Management, 2nd edn., pp. 1–10 (2007)
2. Ministry of Agriculture, Food and Rural Affairs (MAFRA). The Status of Vegetable Greenhouse Facilities and Vegetables Production in 2014
3. Hassanien, R.H.E., et al.: Advanced applications of solar energy in agricultural greenhouses. Renew. Sustain. Energy Rev. **54**, 989–1001 (2016)
4. Likoskoufis, J.H.: Development of a system to decrease relative humidity in greenhouses using GSHP and hygroscopic materials. Ph.D. thesis, Agricultural University of Athens (2011)
5. Hellenic Statistical Authority, Annual Agricultural Statistical Research for the year 2012. (2015) in Greek
6. Polytunnel, https://en.wikipedia.org/wiki/Polytunnel. Last accessed 2020/06/18
7. Horticulture: Greenhouse cultivation, https://agritech.tnau.ac.in/horticulture/horti_Greenhouse%20cultivation.html. Last accessed 2020/06/18
8. Sethi, V.P., Sumathy, K., Lee, C., Pal, D.S.: Thermal modeling aspects of solar greenhouse microclimate control: a review on heating technologies. Sol. Energy **96**, 56–82 (2013)
9. Vandiee, A., Martin, V.: Energy management in horticultural applications through the closed greenhouse concept, state of the art. Renew. Sustain. Energy Rev. **16**, 5087–5100 (2012)
10. Steduto, P.: FAO irrigation and drainage paper 66, https://www.fao.org/3/i2800e/i2800e.pdf, pp. 184–189
11. 3-D drawing, created in solid works, of experimental polyhouse installed at DEI, Agra (27.1767° N, 78.0081° E)
12. Nemali, K.: Calculating greenhouse heating requirements, https://www.purdue.edu/hla/sites/cea/article/calculating-greenhouse-heating-requirements
13. GROWSPAN greenhouse structures, https://www.growspan.com/news/how-to-size-a-greenhouse-heating-system.
14. George, N.J.,Obianwu, V.I., Akpabio, G.T., Obot, I.B.: Comparison of thermal insulation efficiency of some selected materials used as ceiling in building design. Arch. Appl. Sci. Res. **2**(3), 253–259 (2010)
15. Ettah, E.B., Egbe, J.G., Takim, S.A., Akpan, U.P., Oyom, E.B.: Investigation of the thermal conductivity of polyvinyl chloride (Pvc) ceiling material produced in Epz Calabar, for application tropical climate zones. IOSR J. Polym. Text. Eng. **3**(2), 34–38
16. Thermal conduction, https://en.wikipedia.org/wiki/Thermal_conduction. Last accessed 2020/06/18

Levelized Cost Computation of Novel Thermoelectric Modules

Pradyumn Mane and **Deepali Atheaya**

Nomenclature

TEG	Thermoelectric generator
ZT	Figure of merit of thermoelectric module
η	Performance efficiency
P_{gen}	Power generated by thermoelectric module
V	Thermoelectric voltage
R	Internal resistance
R_L	Load resistance
m	Ratio of load resistance to internal resistance
S_p	Seebeck coefficient of p-type thermoelectric material
S_n	Seebeck coefficient of n-type thermoelectric material
ΔT	Temperature difference
A	Area of the metallic plate
F	Fill factor
L	Length of thermoelectric leg
σ_p	Electrical conductivity of p-type thermoelectric material
σ_n	Electrical conductivity of n-type thermoelectric material
G	Cost-performance metric
C	Total capital cost
ρ	Density of thermoelectric material
C_B	Thermoelectric material cost

P. Mane (✉)
Engineering Physics Department, School of Engineering and Applied Sciences, Bennett University, Tech Zone-II, Greater Noida, UP 201310, India
e-mail: pradyumnmane@gmail.com

D. Atheaya
Mechanical and Aerospace Engineering Department, School of Engineering and Applied Sciences, Bennett University, Tech Zone-II, Greater Noida, UP 201310, India

C_M	Thermoelectric manufacturing cost
C_A	Areal manufacturing cost
C_{HX}	Cost of heat exchangers
U	Heat transfer coefficient
C_p	Capital cost of p-type thermoelectric leg
C_n	Capital cost of n-type thermoelectric leg
LCOE	Levelized cost of energy
C'	Overnight capital cost
O_t	Operation cost for a lifespan of t years
M_t	Maintenance cost for a lifespan of t years
F_t	Fuel cost for a lifespan of t years
E_t	Energy generated for t years
r	Discount rate
t	Duration in years
$P_{g\max}$	Maximum power generation
$G_{\max}$	Maximum cost-performance metric

1 Introduction

Thermoelectric generator (TEG) uses Seebeck principle and converts thermal energy directly into electricity, without using any moving parts [1]. Thermoelectric couple is a pair of thermoelectric legs. Thermoelectric couples connected in series form a thermoelectric module or TEG. TEG has applications in automobiles, industries, deep space exploration, thermal power plants, military, etc. It has longer lifespan, weighs less than a battery, has no moving parts, makes no noise and is a convenient power source.

In spite of longer lifespan, TEG face many commercialization challenges due to high material cost and low performance efficiency. Efficiency of typical TEG remains below 10% and has limited applications due to high toxic materials and manufacturing challenges of such materials [2]. Zhang et al. [3] have reported that organic thermoelectric materials were cost effective, easy processing and non-toxic. They have also suggested that organic polymer thermoelectric materials showed lower performance efficiency than inorganic thermoelectric materials. Wang et al. [4] suggested that the system performance with organic polymer-inorganic thermoelectric composites was good. Developments in nanotechnology resulted to achieve efficient thermoelectric materials [5]. Li et al. did a comprehensive review on the recent progress of two-dimensional nanomaterials for bulk and thin-film thermoelectric materials [6]. An extensive review of the thermoelectric characteristics of bulk phases of boron nitride, boron nitride nanotube, boron nitride nanoribbon, boron nitride quantum dots and boron nitride composites was presented by Sharma et al. [7]. Recently, superconductivity and magnets showed significant increase in performance efficiency of TEG [8–11].

Fig. 1 Global thermoelectric generator market revenue, 2015–2021 (USD Million)
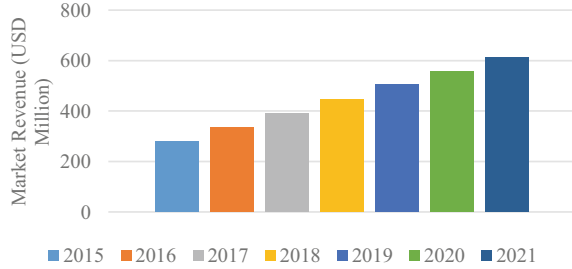
Many automotive companies like BMW, Honda, Ford, GM, Toyota, etc., have showed their interest in TEG to convert exhaust waste heat into electricity. This technology was experimentally verified to achieve fuel efficiency of 25–50% [12]. Alphabet energy invested $49.5 M into low-cost thermoelectric generator for industrial applications [13]. Their product named E1 had efficiency of 2.5% during its launch in 2014. The company assures that with further research and development, E1 will reach efficiency up to 10%. Using E1, thermoelectric generator saves 50,000 L of diesel fuel annually. NASA used radioisotope thermoelectric generators (RTGs) to power Voyager spacecrafts, Curiosity rover, Cassini spacecraft, New Horizons spacecraft, etc. [14, 15]. RTGs developed and used by NASA had efficiency of 3–7% and development cost of more than $83 M for each space missions. Thermoelectric generators have lifespan of minimum 10 years and can go up to 50 years without maintenance [15].

A research on global thermoelectric generator market was carried out by Zion Market Research [16]. The study provided historic data of year 2015 and forecasted for 2016–2021 on basis of revenue (USD Million) (Fig. 1). It displayed global thermoelectric generator market revenue from 2015 to 2021. The global thermoelectric generator market was valued at $279.3 M in 2015 and expected to be valued at $610 M in 2021, growing at a compound annual growth rate (CAGR) of slightly above 13.8%.

The study was carried by segmenting the market based on regions, applications and sources. The results indicated that TEG market is growing globally. North America was a leading region for thermoelectric generator market followed by Europe and Asia Pacific where Asia Pacific expected to show promising growth in upcoming years due increased demand of TEG by automotive manufacturers and industries. Applications of TEG in automotive, industrial, aerospace and defense sectors were studied. Applications of TEG in automotive sector shared the largest TEG market share of 57.8%, whereas TEG in industrial sectors expected to grow moderately in upcoming years. The research analyzed that the global thermoelectric generator market was dominated by waste heat recovery systems and expected to grow over the estimated period.

LeBlanc et al. [2] investigated fabrication cost, device efficiency and commercial feasibility of 30 thermoelectric materials. They have also evaluated manufacturing process and system cost was also evaluated to provide product development and

commercial feasibility contexts. Optimization and analysis of novel thermoelectric module were proposed by Mane and Atheaya [17]. The simulated results indicated $Pb_{1-x}Mg_xTe_{0.8}Se_{0.2}$ and n-type PbTe, $Pb_{1-x}Mg_xTe_{0.8}Se_{0.2}$ and $CoSb_{3-x}Te_x$, $Cu_{12}Sb_4S_{13}$ and $CoSb_{3-x}Te_x$ thermoelectric modules to show efficiency above 10%. This research paper analyzes the cost for these novel thermoelectric modules, estimating the levelized cost of TEG integrated thermal power plant and comparing the TEG with other renewable sources are the novelty of this research paper.

2 Manufacturing Process Used for TEG Production

Manufacturing is a major challenge for TEG. The manufacturing process for thermoelectric devices varies based on the type of thermoelectric material. Figure 2 displays typical manufacturing process flowchart for TEG [18]. Ball mill and spark plasma sintering (SPS) are the typical machineries used in the manufacturing process. The ball mill is a type of grinder used to grind and blend materials for use in mineral dressing process, paints, ceramics and selective laser sintering. Spark plasma sintering machine uses spark plasma sintering technique which sends pulsed or un-pulsed DC or AC current through the graphite die. Thermoelectric materials are synthesized through ball milling powders of the constituent elements. In the ball milling process, the constituent elements are completely mixed. Then, they are consolidated into ingots through hot pressing or spark plasma sintering. The consolidation process depending upon the thermoelectric operating temperature may occur at higher temperature (1000 K) in order to densify the material.
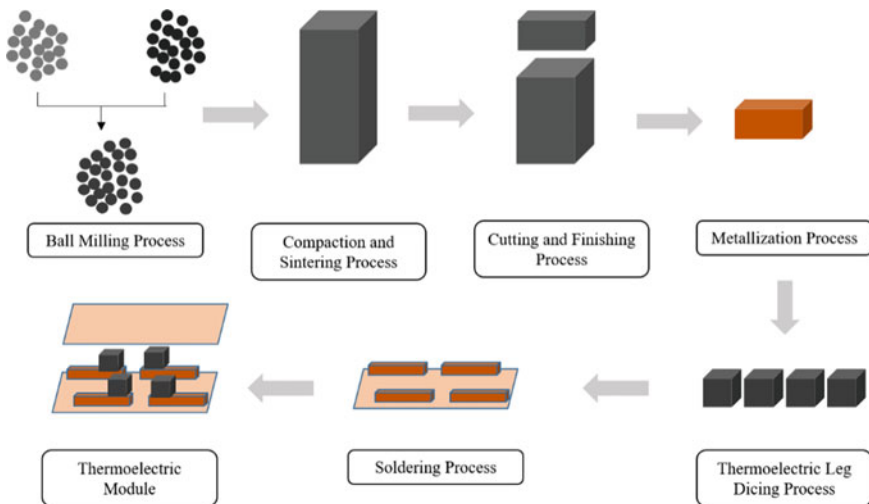
Fig. 2 Steps for manufacturing of TEG

The ingots are then diced to form the thermoelectric legs, and the material brittleness would be a primary concern in this step. Any chipping of a thermoelectric leg changes the leg surface area and influences both the leg's thermal and electrical resistance. This in turn affects the system's performance, particularly, when the geometry of each leg not same. Connections are made between thermoelectric legs and conductive metal plate. Achieving perfect contact at the interface is a major challenge. Microscopic roughness on the surfaces forms air-filled voids when the surfaces are pressed together. These voids decrease the surface area that is actually in contact. Potential surface coatings, such as oxides or other impurities, affect both the thermal and the electrical conductivity over an interface. The magnitude of the thermal contact resistances is decreased by minimizing the area of the voids, either by smoothing or softening the surfaces, or by increasing contact pressure. Another way to lower contact resistances is by filling the voids with a material with high conductivity. A thin layer of thermal grease or graphite is commonly used to fill the voids and enhance thermal contacts. Such a material has far better thermal conductivity than air, but much lower than metals. A common method for lowering electrical contact resistances is to cover the surface with a soft, electrically conducting material that is resistant to oxidization. A technically beneficial but expensive choice of coating material is gold. Studies shows, nickel (Ni) to be a best cost-efficient material to connect the semiconductor–metal surfaces [19]. Nickel (Ni) is electrically conductive material, resistant to oxidization, has diffusion ability, cost efficient and manufacturability of connection. The completed module is tested with X-ray diffractometer (XRD), laser flash apparatus (LFA), DC four-probe method and differential voltage to verify the phase structures, thermal conductivity, electrical conductivity and Seebeck coefficient, respectively.

3 Cost Analysis of Novel Thermoelectric Modules

In this research paper, three novel thermoelectric modules are proposed on basis of the simulation results achieved in previous research work. Table 1 indicates the thermoelectric materials and efficiency achieved in the simulation [17].

Here, ZT is the unitless figure of merit of thermoelectric module whose value important to identify the efficiency of thermoelectric module. The temperature difference was set at 800 K and 300 K at hot terminal and cold terminal, respectively. The power generated by thermoelectric modules is calculated by following [10].

Table 1 Simulation results of the proposed thermoelectric modules

Thermoelectric materials		ZT	η (%)
P-type material	N-type material		
$Pb_{1-x}Mg_xTe_{0.8}Se_{0.2}$	n-type PbTe	1.30	17
$Pb_{1-x}Mg_xTe_{0.8}Se_{0.2}$	$CoSb_{3-x}Te_x$	1.20	16
$Cu_{12}Sb_4S_{13}$	$CoSb_{3-x}Te_x$	0.6	10

$$P_{\text{gen}} = \left[\frac{V^2}{R}\right]\frac{m}{(m+1)^2} \tag{1}$$

where thermoelectric voltage (V) is defined to product of Seebeck coefficients of p-type thermoelectric material and n-type thermoelectric material with temperature difference, i.e., $(S_p - S_n)\Delta T$. The ratio of load resistance (R_L) to internal resistance (R) is defined to be m. The internal resistance is formulated by following [10].

$$R = \left\{\frac{2L}{AF}\right\}\left[\frac{1}{\sigma_p} + \frac{1}{\sigma_n}\right] \tag{2}$$

where L is the length of the thermoelectric leg and A is the area of the metallic plate onto which thermoelectric legs are electrically and thermally connected. The σ_p and σ_n are electrical conductivities of p-type and n-type thermoelectric materials, respectively. Fill factor (F) is the ratio of the area covered by thermoelectric material to plate area. To identify an optimum geometry of thermoelectric module, cost-performance metric (G) is formulated by following [10].

$$G = \left[\frac{C}{P_{\text{gen}}}\right] \tag{3}$$

where C is the total capital required to manufacture TEG. This capital is sum of thermoelectric material cost (C_B), thermoelectric manufacturing cost (C_M), areal manufacturing cost (C_A) and cost of heat exchangers (C_{HX}) and also depends upon the plate area, fill factor, heat transfer coefficient (U) and density of thermoelectric material. C_p and C_n are the capital cost of p-type and n-type thermoelectric legs whose sum determines the total capital cost of TEG [10].

$$C_p = \left[(C_{B,p} + C_{M,p})\rho_p L_p + C_{A,p}\right] \times AF + C_{HX} \times UA \tag{4}$$

$$C_n = \left[(C_{B,n} + C_{M,n})\rho_n L_n + C_{A,n}\right] \times AF + C_{HX} \times UA \tag{5}$$

$$C = C_p + C_n \tag{6}$$

Levelized cost of energy (LCOE) is often used to estimate the cost to generate electricity. Typically, LCOE is the ratio of total cost to power generated throughout its lifespan. The total cost includes the maintenance, financial discount, uptime, etc., for the system's lifespan. Determining LCOE is application-specific due to its input parameters and is formulated by following [10].

$$\text{LCOE} = \frac{C' + \frac{\sum_{t=1}^{n}(O_t+M_t+F_t)}{(1+r)^t}}{\frac{\sum_{t=1}^{n} E_t}{(1+r)^t}} \tag{7}$$

where C' is the initial investment or overnight capital cost and O_t, M_t, F_t are operating, maintenance and fuel cost, respectively, for a lifespan of t years. The E_t is the energy generated for t years and r is the discount rate. The unit for LCOE is \$/MW h, whereas for cost-performance metric it is \$/W [10]. The units for thermoelectric material cost, thermoelectric manufacturing cost, areal manufacturing cost and cost of heat exchangers are \$/kg, \$/kg, \$/m^2 and \$/(W/K), respectively.

4 Methodology

Figure 3 displays the flowchart of methodology which was followed throughout this research. The values for the length of thermoelectric leg, plate area and fill factor were considered to be 10 mm, 55 mm^2 and 0.91, respectively [17]. For determining the power generation, the ratio of load resistance to internal resistance was considered to be 1, i.e., defined to be maximum power generated and ΔT was considered to be 500 K. The methodology was divided into three major categories: cost analysis of novel thermoelectric module, cost analysis of TEG integrated thermal power plant and comparison of TEG with other renewables.

To analyze the cost of novel thermoelectric module, cost-performance metric was evaluated by using Eq. (3). Thermoelectric module total capital cost for the proposed thermoelectric materials was evaluated by using Eq. (6) and power generated was evaluated by using Eq. (1). The total capital cost was divided into three divisions, namely thermoelectric material cost, thermoelectric manufacturing cost
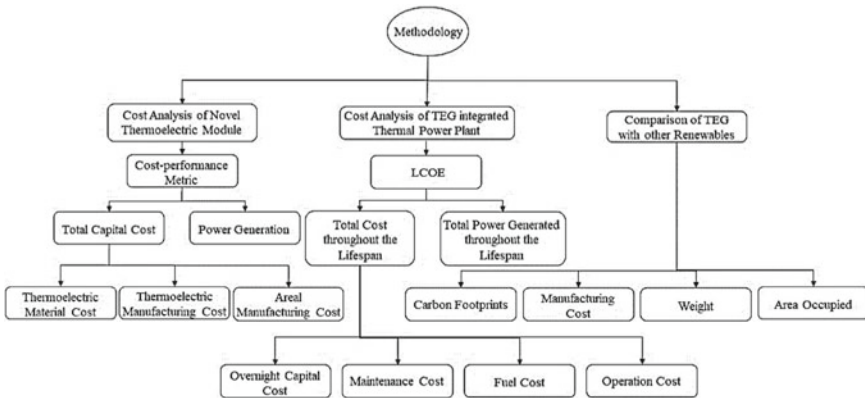
Fig. 3 Flowchart of methodology

and areal manufacturing cost. These costs were obtained through estimates provided by equipment vendors. The cost of thermoelectric material was considered for the pure form of materials. The cost of heat exchangers was assumed to be zero as water coolant would be used to maintain temperature at cold terminal whose cost would be included in maintenance of the system while determining LCOE for TEG integrated thermal power plant. The lifespan of TEG and thermal power plant were assumed to be 20 years and operating duration of 365.25 days per year and 24 h per day for determining LCOE for TEG integrated and non-integrated thermal power plant. During its lifespan, it was assumed that the TEG and the thermal power plant run in ideal conditions, i.e., with minimal maintenance and no major breakdown. The values of LCOE were determined by Eq. (7) and the discount rate was assumed to be 3%. The radius and length of the power plant's pipe was assumed to be 0.410 m and 4400 m, respectively. The TEG integrated with thermal power plant was assumed to have 200 M thermoelectric couples which were assumed on the basis of the ratio of the surface area of the plant's pipe to the area occupied by a thermoelectric couple. The load of thermal power plant was assumed to be 210 MW. The cost-performance metric is estimated to vary by maximum 5% for the proposed thermoelectric materials [10]. The TEG with lowest cost-performance metric was considered while comparing with other renewable sources. These renewable sources were compared for same power output and evaluated on the basis of carbon footprints, manufacturing cost, weight and area occupied.

5   Results and Discussion

5.1   Cost Analysis of Novel Thermoelectric Modules

The total capital cost for a thermoelectric couple and power generated by a thermoelectric couple was determined by Eqs. (6) and (1), respectively. The cost-performance metric was determined by Eq. (3) for novel thermoelectric modules. Table 2 indicates the cost summary for every cost component while determining the total capital cost for the proposed thermoelectric materials [10].

It was observed that thermoelectric material's cost is the dominant cost for manufacturing TEG as compared to other classes. Tellurium (Te) is a rare earth metal,

Table 2 Cost summary for the proposed thermoelectric materials

Thermoelectric material	ρ (kg/m^3)	C_B ($/kg)	C_M ($/kg)	C_A ($/m^2)
$Pb_{1-x}Mg_xTe_{0.8}Se_{0.2}$	8160	1200	0.06	168.23
n-type PbTe	8160	1200	0.06	168.23
$CoSb_{3-x}Te_x$	6500	1400	1.26	168.23
$Cu_{12}Sb_4S_{13}$	4900	180	1.10	168.23

Table 3 Cost analysis of novel thermoelectric modules

Module no.	Thermoelectric materials		C_p ($)	C_n ($)	C ($)	$P_{g\max}$ (W)	$G_{\max}$ ($/W)
	P-type material	N-type material					
1	$Pb_{1-x}Mg_xTe_{0.8}Se_{0.2}$	n-type PbTe	4.91	4.91	9.82	0.845	11.62
2	$Pb_{1-x}Mg_xTe_{0.8}Se_{0.2}$	$CoSb_{3-x}Te_x$	4.91	4.57	9.48	0.945	10.03
3	$Cu_{12}Sb_4S_{13}$	$CoSb_{3-x}Te_x$	0.45	4.57	5.02	0.230	21.83

hence, the cost of lead telluride-based materials and skutterudites (cobalt arsenide-based mineral) is high as compared to tetrahedrites (natural mineral with similar structure of $Cu_{12}Sb_4S_{13}$). Table 3 indicates the cost analysis of novel thermoelectric modules.

The module no. 3 was observed to be the cheapest thermoelectric module to manufacture due to the use of natural mineral tetrahedrite, whereas the module no. 1 was the costliest thermoelectric module due to the use of rare earth element Te. On other hand, the module no. 2 was observed to have highest value of maximum power generation, whereas the module no. 3 was observed to have lowest value of maximum power generation. As we have considered the maximum power generation metric, maximum cost-performance metric was determined. It was observed that the module no. 2 generates cheapest electricity as compared to other thermoelectric modules with module no. 3 to be the most costly to generate electricity. The module no. 3 has the lowest power output as compared to its total capital cost, thus, having highest cost-performance metric. The module no. 2 has the highest power output as compared to its total capital cost, thus, having a low-cost-performance metric, thus, observed to be the best thermoelectric module than others. The values of capital cost and power generation are for a thermoelectric couple. Since TEG has n number of thermoelectric couples connected in series, the capital cost and maximum power generation will be nC and $nP_{g\max}$, respectively. The value of $G_{\max}$ remains same for TEG.

5.2 Cost Analysis of TEG Integrated Thermal Power Plant

LCOE was determined for thermal power plant, TEG and TEG integrated thermal power plant for a lifespan of 20 years. Table 4 displays the total cost and energy generated throughout the lifespan of the system. LCOE in Table 4 was determined by Eq. (7). LCOE of traditional thermal power plant has been done by following Kumar et al. [20] and reported in Table 4. The overnight capital for TEG was determined by multiplying number of thermoelectric couples with the total capital from Table 3 and additional cost to integrate the TEG with thermal power plants. Module no. 3 from Table 3 was considered while determining the LCOE of TEG, since, the cost-performance metric of it is less as compared to others.

Table 4 LCOE of the proposed systems

System	C' (M$)	O_t (M$)	M_t (M$)	F_t (M$)	E_t (MW h)	r (%)	t (years)	LCOE ($/MW h)
Thermal power plant	300	500	70	430	1,840,860	3	20	838.26
TEG	2000	0	0	0	33,135,480	3	20	109.25
TEG-integrated thermal power plant	2300	500	70	430	34,976,340	3	20	147.62

It was observed that overnight capital for TEG integrated thermal power plant is 6.67 times higher than non-integrated thermal power plant. However, there was a huge increase in energy output for TEG integrated thermal power plant. Thus, decreasing the LCOE of TEG integrated thermal power plant. It was observed that LCOE decreases by 82.4%. Thus, it was observed that TEG integrated thermal power will produce electricity at a very lower cost than non-integrated thermal power plant.

5.3 Comparison of TEG with Other Renewables

In present research work solar, wind and battery technologies were compared with the proposed thermoelectric technology to analyze the capability of TEG. The renewable sources were compared (Table 5) on the basis of carbon footprints, capital cost, weight and area occupied. Solar technology was considered as a reference line and further analysis were carried. Carbon footprints analysis indicated that almost all renewable sources relatively emit same carbon footprints [21–23]. Capital cost was analyzed on the basis of cost-performance metric ($/W) [24–26] and it indicated that wind energy is relatively expensive and TEG has been found to be cheaper than wind energy but expensive as compared to battery and solar technology. Weight analysis exhibited TEG to be lightest compared to others. Area occupied was analyzed on the basis of

Table 5 Pugh chart of renewable energy sources

Evaluation criteria	Weight factor	Solar technology	Lithium–ion battery	Wind energy harvesting	TEG
Carbon footprints	10	0	0	−1	0
Capital cost	9	0	−5	−10	−2
Weight	7	0	0	−10	+3
Area occupied	8	0	+4	−10	+2
Total		0	−13	−250	+19

same power output, i.e., 1.5 MW and it showed that TEG to be second to consume less area after lithium–ion battery.

The results for individual criteria were multiplied by the arbitrary weight factor and summed to analyze the total relative score. The results from the Pugh chart indicated TEG weighted less than a battery, occupied less space than solar panels and turned out to be reliable renewable technology.

6 Conclusion

Based on present studies following conclusions have been made.

- $Pb_{1-x}Mg_xTe_{0.8}Se_{0.2}$ and $CoSb_{3-x}Te_x$-based TEG has the lowest cost-performance metric and could be used for various thermoelectric applications. This is because it has the highest power output as compared to its total capital cost, implying to be the best TEG than others.
- $Cu_{12}Sb_4S_{13}$ and $CoSb_{3-x}Te_x$-based TEG is cheapest thermoelectric module as compared to other studied novel thermoelectric modules. This is due to the use of natural mineral tetrahedrite.
- $Pb_{1-x}Mg_xTe_{0.8}Se_{0.2}$ and $CoSb_{3-x}Te_x$-based TEG has the highest power output as compared to other studied novel thermoelectric modules. This is due to their high efficiency which was observed while performing the simulation.
- Levelized cost of energy decreases by 82.4% in TEG integrated thermal power plant as compared to non-integrated thermal power plant.
- Proposed TEG weighs less than a battery, occupies less space than solar panels and is a reliable renewable technology.

References

1. Abdel-Motaleb, I.M., Qadri, S.M.: Thermoelectric devices: principles and future trends. arXiv (Apr 2017)
2. LeBlanc, S., Yee, S.K., Scullin, M.L., Dames, C., Goodson, K.E.: Material and manufacturing cost considerations for thermoelectric. Renew. Sustain. Energy Rev. **32**, 313–327 (2013)
3. Zhang, Y., Heo, Y.-J., Park, M., Park, S.-J.: Recent advances in organic thermoelectric materials: principle mechanisms and emerging carbon-based green energy materials. PMC J. **11** (Jan 2019)
4. Wang, L., Zhang, Z., Liu, Y., Wang, B., Fang, L., Qiu, J., Zhang, K., Wang, S.: Exceptional thermoelectric properties of flexible organic-inorganic hybrids with monodispersed and periodic nanophase. Nat. Commun. **9**, 3817 (2018)
5. Soleimani, Z., Zoras, S., Ceranic, B., Shahzad, S., Cui, Y.: A review on recent developments of thermoelectric materials for room temperature. Sustain. Energy Technol. Assess. **37** (Feb 2020)
6. Li, D., Gong, Y., Chen, Y., Lin, J., Khan, Q., Yupeng Zhang, Yu., Li, H.Z., Xie, H.: Recent progress of two-dimensional thermoelectric materials. Nano-Micro Lett. **12**, 36 (2020)

7. Sharma, V., Kagdada, H.L., Jha, P.K., Śpiewak, P., Kurzydłowski, K.J.: Thermal transport properties of boron nitride based materials: a review. Renew. Sustain. Energy Rev. **120** (Mar 2020) 109622

8. Zhao, W., Liu, Z., Sun, Z., Zhang, Q., Wei, P., Xin, Mu., Zhou, H., Li, C., Ma, S., He, D., Ji, P., Zhu, W., Nie, X., Xianli, Su., Tang, X., Shen, B., Dong, X., Yang, J., Liu, Y., Shi, J.: Superparamagnetic enhancement of thermoelectric performance. Nature **549**, 247–251 (2017)

9. Vaney, J.B., Aminorroaya Yamini, S., Takaki, H., Kobayashi, K., Kobayashi, N., Mori, T.: Magnetism-mediated thermoelectric performance of Cr-doped bismuth telluride tetradymite. Mater. Today Phys. **9** (Jun 2019) 100090

10. Ozaeta, A., Virtanen, P., Bergeret, F.S., Heikkilä, T.T.: Predicted very large thermoelectric effect in ferromagnet-superconductor junctions in the presence of a spin-splitting magnetic field. Phys. Rev. Lett. **112** (Feb 2014) 057001

11. Skinner, B., Fu, L.: Large, nonsaturating thermopower in quantizing magnetic field. Sci. Adv. **4** (May 2018)

12. Song, L., Zhijia, Y., Richard, S., Rui, C.: Prediction of the fuel economy potential for a skutterudite thermoelectric generator in light-duty vehicle applications. Appl. Energy **231**, 68–79 (2018)

13. Technology materials, devices and systems: technology assessment. Energy.gov (Feb 2015)

14. Schierning, G., Chavez, R., Schmechel, R., Balke, B., Rogl, G., Rogl, P.: Concepts for medium-high to high temperature thermoelectric heat-to-electricity conversion: a review of selected materials and basic considerations of module design. Trans. Mater. Res. **2**, 025001 (2015)

15. Werner, J.E., Johnson, S.G., Dwight, C.C., Lively, K.L.: Cost comparison in 2015 dollars for radioisotope power systems-Cassini and Mars science laboratory. Idaho National Laboratory (Jul 2016)

16. Thermoelectric generator market by source (waste heat recovery, energy harvesting, direct power generation, and co-generation), and application (automotive, aerospace & defence, industrial and others)—global industry perspective, comprehensive analysis, size, share, growth, segment, trends and forecast, 2015–2021. Zion Market Research (Dec 2016)

17. Mane, P., Atheaya, D.: Optimization and analysis of novel thermoelectric module. Vibroeng. Procedia **29**, 231–236 (2019)

18. LeBlanc, S.: Thermoelectric generators: linking material properties and systems engineering for waste heat recovery applications. Sustain. Mater. Technol. **1–2**, 26–35 (2014)

19. Ferreres, X.R., Yamini, S.A.: Rapid fabrication of diffusion barrier between metal electrode and thermoelectric materials using current-controlled spark plasma sintering technique. J. Mater. Res. Technol. **8** (Mar 2019) 8–13

20. Kumar, R., Sharma, A.K., Tewari, P.C.: Cost analysis of coal-fired power plant using the NPV method. J. Ind. Eng. Int. **11** (Dec 2015) 495–504

21. Jiang, Y., Bebee, B., Mendoza, A.: Energy footprint and carbon emission reduction using off-the-grid solar-powered mixing for lagoon treatment. J. Environ. Manage. **205**, 125–133 (2018)

22. Wang, C., Chen, B., Yu, Y., Wang, Y., Zhang, W.: Carbon footprint analysis of lithium ion secondary battery industry: two case studies from China. J. Clean. Prod. **163** (Feb 2016)

23. Ji, S., Chen, B.: Carbon footprint accounting of a typical wind farm in China. Appl. Energy **180**, 416–423 (2016)

24. Renewable energy technologies: cost analysis series-solar photovoltaics. IRENA Working Paper **1**(4) (Jun 2012)

25. Electricity storage and renewables: cost and markets to 2030. International Renewable Energy Agency (IRENA) (Oct 2017)

26. Renewable energy technologies: cost analysis series-wind power. IRENA Working Paper **1**(5) (Jun 2012)

Numerical Investigation of Heat Transfer Characteristics of Al_2O_3–H_2O Based Nanofluid Flow in Light Water Nuclear Reactor

Deepak Sharma

1 Introduction

At present, energy demand is rising speedily owing to growth in population [1]. Because of lesser thermal conductivities of conventional fluids like oil, water, and ethylene, glycol performed an important role for cooling and heating in several industries. They are not giving an improvement in heat transfer. With great effort, various researches have been performed in the area of improvement in heat transfer like using channels in micro form and extended surface used for enhanced in heat transfer rate. But due to rising demand of energy, rate of cooling and heating need is rising day by day. Solid metals have higher thermal conductivity when it is in nano-size. Several researchers have performed investigation on thermo-physical properties of suspended solid metals in the conventional base fluids like water and ethylene glycol. Lots of studies have been done on micrometer- and millimeter-sized particles. Due to large size of particle, various problems are raised like resistance in fluid flow, clogging, etc. When the nano-sized solid particles dispersed in base fluid like water, then that fluids are called nanofluids [2]. When particle size is smaller in size, heat transfer will be more in comparison with large particle size. Heat transfer will be also more when the volume concentration is small compare to more volume concentration. The using of nano-sized particles has various advantages like less clogging, higher heat transfer rate, large surface area, and stable in nature, that is why nanofluids are next generation fluids. Roetzel and Xuan [3] performed theoretical studies in enhancement in heat transfer of nanofluids. Nasr Esfahany [4] recently performed experiment in horizontal pipe using CuO/water nanofluid for enhancement in coefficient of heat transfer. Nanburu et al. performed numerical analysis of three distinct nanofluids

D. Sharma (✉)
Department of Mechanical Engineering, National Institute of Technology, Hamirpur, Himachal Pradesh 177005, India
e-mail: dsharma@nith.ac.in

(SiO_2, CuO, and Al_2O_3) inside a round pipe with fixed heat flux in turbulent condition. Thermal properties of nanofluid were dependent in nature with temperature. Fotukian et al. [5] research represents when little amount of Al_2O_3 nanoparticles suspended in the water, heat transfer improved, but changing particle volume fraction of Al_2O_3 nanoparticle did not signify a sensible effect on heat transfer. The key aim of present analysis is to numerically identify the consequences of varying particle concentration and varying flow rate of nanofluid at the performance in heat transfer enhancement and drop in pressure in turbulent phenomenon inside a one sixth portion of hexagonal fuel rod assembly. The reactor in this investigation is considered as VVER 440 reactor.

2   Computational Domain for Analysis

For the numerical investigation, the fuel rod assembly of VVER reactor is taken. The arrangements of rods in the fuel rods bundle are shown in Fig. 1 given below. The reactor fuel rod bundle contains 61 rods which are arranged in hexagon format. The fuel rod bundle is divided into six symmetric sectors. As the six sectors are symmetrical to each other. The single sector 1/6th segment of the computational domain is selected for computational domain, which is showing in Fig. 2. The 1/6th segment of computational domain is considered for simulation which is in triangular shape. The selected computational domain consists a central rod, four half rods, and eight full rods. The numerical parameters for computational domain are given in Table 1.

For computational domain, four meshes of different element sizes are tested. For verification, the mesh stability of annular channel and 1/6th fuel rod channel four mesh sizes are taken (MESH 1–4). The convergence criterion is satisfied very well.
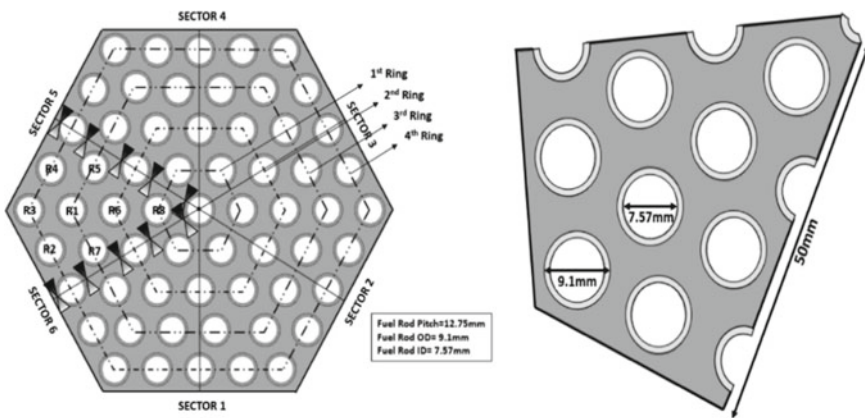
Fig. 1   VVER fuel rod assembly of 62 fuel rod and its 1/6th part
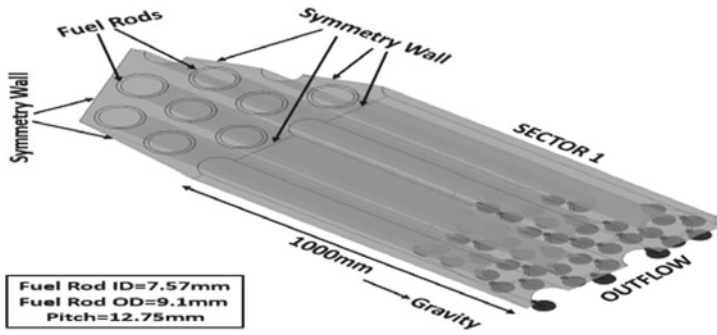
Fig. 2 Computational domain for analysis

Table 1 Numerical parameters for computational domain

Particular	Specification
Inner radius (mm)	7.57
Outer radius (mm)	9.1
Pitch (mm)	12.75
Reynolds no	10,000–30,000
Geometry type	Hexagonal
Nanoparticle size (nm)	10, 20
Heat flux (W/m^2)	50,000
Inlet temperature (K)	298
Volume concentration (%)	1, 2, 3

Number of elements, nodes, and convergence factor of computational domain are mentioned in Table 2 (Fig. 3).

A single-phase technique is considered in this present investigation, so few assumptions have been considered to solve the various governing equations for steady fluid flow:

- Non-radiation effects are considered, and viscous effect are negligible.
- The nature of flow is Newtonian, incompressible, and turbulent.
- The phase of particles and fluid are in thermal equilibrium.

Table 2 Grid test for computational domain

Details	Grid 1	Grid 2	Grid 3	Grid 4
Number of nodes	284,520	284,738	287,558	352,488
Number of elements	731,575	732,321	745,055	1,105,421
Skewness	0.88245	0.88552	0.88821	0.85254
Orthogonal quality	0.16322	0.16310	0.14630	0.16099
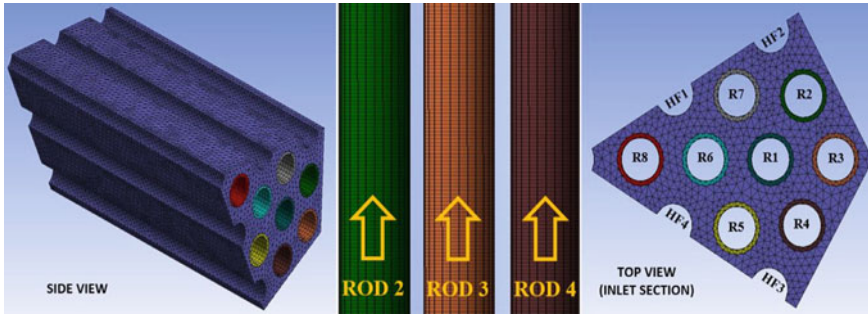
Fig. 3 Numerical grid for computational domain

Navier–Stokes equations for incompressible flow can also be presented in Cartesian coordinate that are mentioned below:

Mass conservation:

$$\nabla\left(\rho_{\text{eff}}\overline{V}\right) = 0 \tag{1}$$

Momentum conservation:

$$\nabla \cdot \left(\rho_{\text{eff}}\overline{VV}\right) = -\nabla\overline{P} + \mu_{\text{eff}}\nabla^2\overline{V} - \rho_{\text{eff}}\nabla\left(\overline{v'v'}\right) \tag{2}$$

Energy conservation:

$$\nabla \cdot \left(\rho_{\text{eff}}\,C_{p,\text{eff}}\overline{VT}\right) = \nabla \cdot \left((k_{\text{eff}} + k_t)\nabla \cdot \overline{T}\right) \tag{3}$$

3 Nanofluid Thermo-physical Properties Correlations

For heat transfer analysis in nuclear reactor, various nanofluid thermo-physical properties are required like effective thermal conductivity, effective viscosity, effective specific heat, and effective density. So the calculations of these properties have been calculated by some empirical correlations.

Effective nanofluid density:

Wang and Mujumdar have given the empirical correlation for calculation of density [6]:

$$\rho_{\text{nf}} = (1 - \varnothing)\rho_{\text{bf}} + (\varnothing)\rho_{\text{np}} \tag{4}$$

Nanofluid specific heat:

Wang and Mujumdar have also given the empirical correlation for calculation of specific heat [7]:

$$C_{p,\text{nf}} = \frac{(1 - \emptyset)\rho_{\text{bf}}C_{p,\text{bf}} + (\emptyset)\rho_{\text{np}}C_{p,\text{np}}}{(1 - \emptyset)\rho_{\text{bf}} + (\emptyset)\rho_{\text{np}}} \tag{5}$$

Nanofluid viscosity:

Corcione [8] has proposed the correlation for calculation of nanofluid viscosity.

$$\frac{\mu_{\text{nf}}}{\mu_{\text{bf}}} = \frac{1}{1 - 34.87(d_{\text{np}}/d_{\text{bf}})^{-0.3}\emptyset^{1.08}} \tag{6}$$

where d_{bf} = Molecule Equivalent diameter of base fluid, that is given below:

$$d_{\text{bf}} = 0.1\left(\frac{6M}{N\pi\rho_{\text{bf0}}}\right)^{1/3} \tag{7}$$

where N = Avogadro number, M = Base fluid Molecular weight, and ρ_{bf0} = Base fluid mass density considered at T = 293 K.

Effective Nanofluid Thermal conductivity:

Incropera [9] was proposed the correlation for determination of effective nanofluid thermal conductivity:

$$\frac{k_{\text{nf}}}{k_{\text{bf}}} = 1 + 4.4\text{Re}_{\text{np}}^{0.4}\text{Pr}_{\text{bf}}^{0.66}\left(\frac{T}{T_{\text{fr}}}\right)^{10}\left(\frac{k_{\text{np}}}{k_{\text{bf}}}\right)^{0.03}\emptyset^{0.66} \tag{8}$$

where T_{fr} = Base fluid freezing point (around 273.16 K). The relation of Reynolds number is presented as:

$$\text{Re}_{\text{np}} = \frac{2\rho_{\text{bf}}\kappa_B T}{\pi\mu_{\text{bf}}^2 d_{\text{np}}} \tag{9}$$

These relations are valid for only diameter of particles between 10 and 140 nm, particle concentration lies in the range of 0.3–9%, and temperature lies in the range of 294–324 K (Table 3).

Table 3 Properties of Al$_2$O$_3$–H$_2$O based nanofluid

Properties	Water	1 vol%	2 vol%	3 vol%
Density, ρ (kg/m^3)	994	1026	1056	1085
Specific heat C_p (J/kg K)	4176	4047	3923	3806
Thermal conductivity k (W/m^2 K)	0.623	0.631	0.649	0.672
Viscosity, μ (Pa s) $\times$ 10^{-4}	8.86	9.15	9.39	9.63

Fig. 4 Numerical versus experimental results comparison at Re = 3500
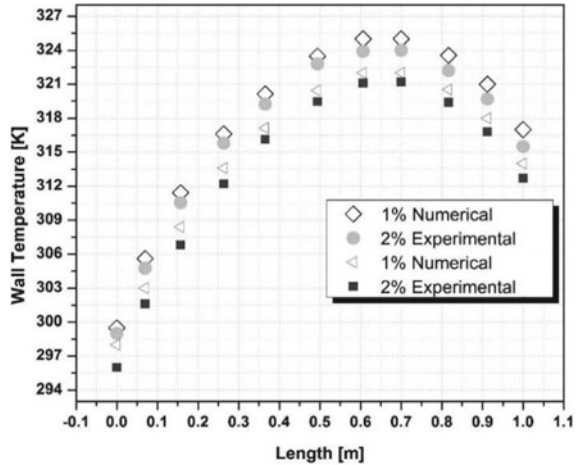
4   Verification and Validation

Numerical simulation is conducted for a set of combinations of volume concentration of nanofluid, particle sizes, and coolant flow rates. The fixed heat flux is provided to the rod wall. Nanofluid is injected at the entry of the fuel rod channel which flows upward to downward due to the gravity apply on the coolant. Initial boundary condition is provided at the innermost wall of annular channel and 1/6th fuel rod channel. The intensity of turbulence is kept fixed 10% at entry. Comparison of simulated result with analytical result signify precise in nature. Results of numerical investigation are validated by Abbassi and Talebi [10]. The wall temperature profile near walls is mentioned in Fig. 4 for constant Reynolds number at 1 vol% and 2 vol%.

5   Result and Discussion

For a triangular segment of fuel rod assembly, simulation has been performed to identify the heat transfer enhancement by using advanced fluid, i.e., Al$_2$O$_3$–H$_2$O based nanofluid. The range of Reynolds number in this analysis is in the series of
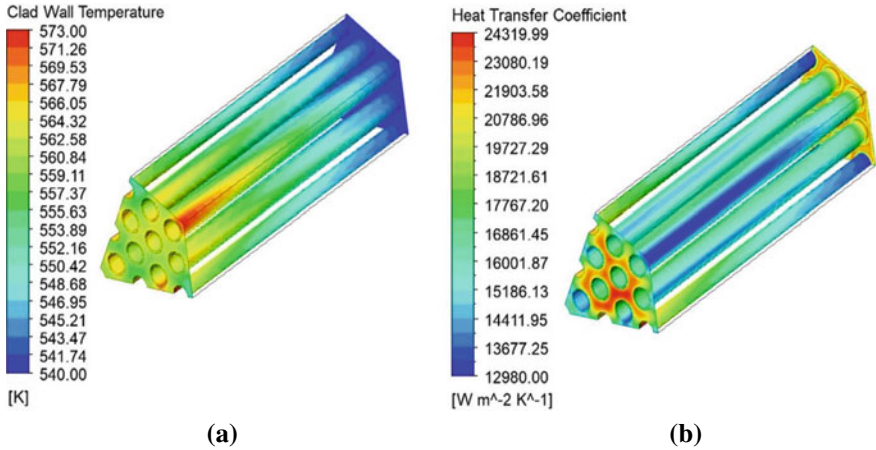
Fig. 5 **a** Clad wall temperature, **b** heat transfer coefficient at $\varnothing = 1\%$

(10,000–30,000), particle diameter is in the range of 10–20 nm, and particle volume fraction is in series of (0–3%). The consequences of volume fraction and Reynolds number on characteristics of heat transfer are discussed and analyzed in this section. Contours of clad temperature and heat transfer coefficient are shown in Fig. 5.

5.1 Effect of Reynolds Number of Al_2O_3–H_2O Based Nanofluid on Heat Transfer Characteristics

In this analysis, three distinct values of Reynolds no. have been taken to predict the consequences of Reynolds number on profiles of clad wall temperature and heat transfer coefficient. From graphs (Figs. 6 and 7), it is clear that heat transfer improvement takes place with rising Reynolds number owing to gradient of temperature rises at the wall. Wall temperature is reducing and heat transfer coefficient is rising with rise in Reynolds number.

5.2 Effect of Volume Concentration of Al_2O_3–H_2O Based Nanofluid on Heat Transfer Characteristics

In this analysis, three distinct values of particles volume fraction have been taken to predict the consequences of volume fraction on profiles of clad wall temperature and heat transfer coefficient. It can be seen from graphs (Figs. 8 and 9) as the particles volume fraction is rising wall temperature drops. But it is reducing more for 1% volume fraction of particles with compare to 2% and 3% because of greater thermal
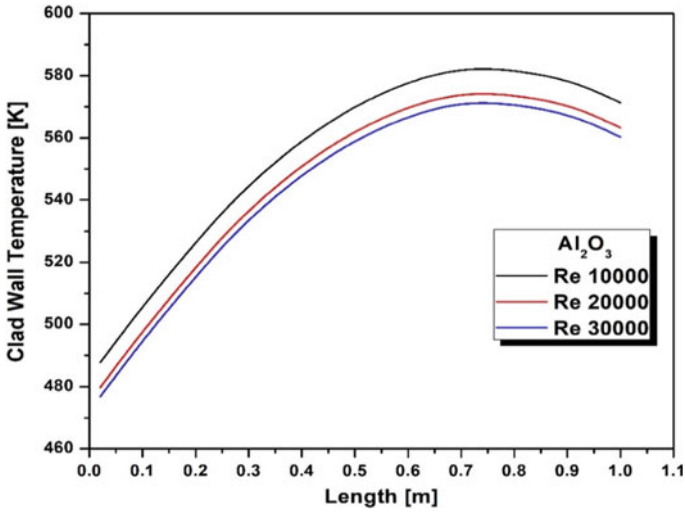
Fig. 6 Clad wall temperature at varying Reynolds no
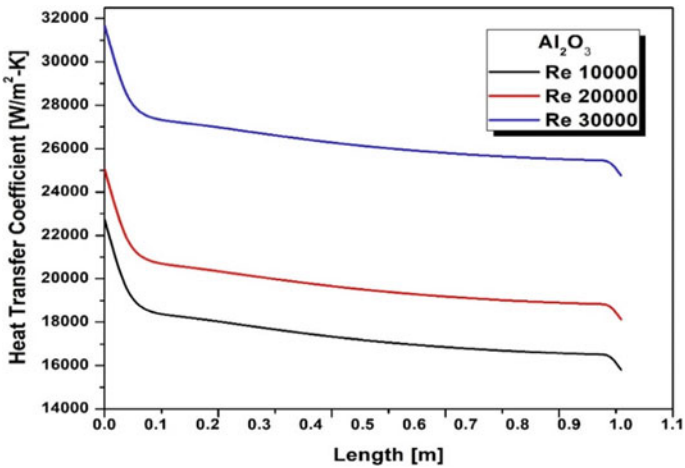
Fig. 7 Heat transfer coefficient at varying Reynolds no

conductivity of NPs. But the enhancement in heat transfer takes place as the particles volume fraction increases by reason of higher thermal conductivity of Al_2O_3–H_2O based nanofluid in comparison with pure water.
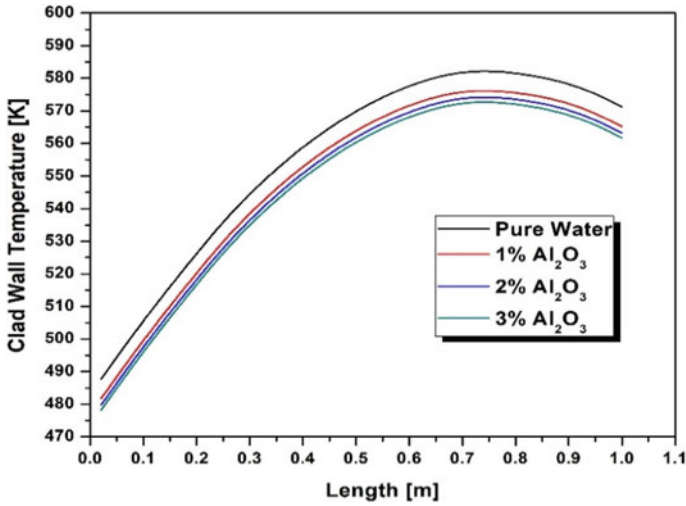
Fig. 8 Clad wall temperature for varying weight concentration of NPs
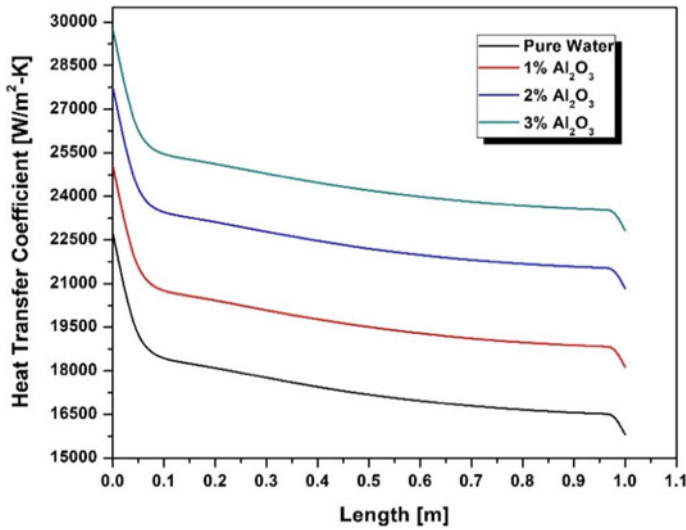
Fig. 9 Heat transfer coefficient for varying weight concentration of NPs

6 Conclusion

In this present analysis, effect of advanced fluid properties on heat transfer characteristics has been recognized. The 1/6th segment of computational domain has been considered for numerical simulation. Enhancement in heat transfer is reported in this analysis by using Al_2O_3–H_2O based nanofluid with single-phase technique

and heat flux is taken as constant. Numerical results show that enhancement in heat transfer takes place by reason of enhanced thermal conductivity of using Al_2O_3–H_2O based nanofluid compared to conventional fluid. In this analysis, HTC and clad wall temperature are compared with Al_2O_3–H_2O based nanofluid and without nanofluid. Various consequences are obtained from this numerical investigation are:

(a) Wall temperature of clad is reducing with rising in volume fraction of NPs and Reynolds number of Al_2O_3–H_2O based nanofluid by reason of higher thermal conductivity.
(b) Enhancement in heat transfer expressively rises after mixing of Al_2O_3 NPs in the base fluid in comparison with pure water.
(c) With increase in Reynolds number and varying volume fraction of NPs local HTC rises up to 25%.

References

1. Xu, Z.W.: Design strategies for optimizing high burnup fuel in pressurized water reactors. A Thesis for Doctor's Degree in MIT (2003)
2. Choi, S.U.S.: Enhancing thermal conductivity of fluids with nanoparticles. Developments and Applications of Non-Newtonian Flows FED-vol. 231/MD-vol. 66, pp. 99–105 (1995)
3. Xuan, Y., Roetzel, W.: Conceptions for heat transfer correlation of nanofluid. Int. J. Heat Mass Transf. **43**, 3701–3707 (2000)
4. Fotukian, S.M., Nasr Esfahany, M.: Experimental study of turbulent convective heat transfers and pressure drop of dilute CuO/water nanofluid inside a circular tube. Int. Commun. Heat Mass Transf. **37**(2), 214–219 (2010)
5. Fotukian, S.M., Nasr Esfahany, M.: Experimental investigation of turbulent convective heat transfer of dilute γ-Al_2O_3/water nanofluid inside a circular tube, submitted
6. Wang, X.Q., Mujumdar, A.S.: Heat transfer characteristics of nanofluids: a review. Int. J. Therm. Sci. **46**(1), 1–19 (2007)
7. White, F.M.: Fluid Mechanics, 4th edn. McGraw-Hill, New York (1999)
8. Corcione, M.: Empirical correlating equations for predicting the effective thermal conductivity and dynamic viscosity of nanofluids. Energy Convers. Manage. **52**(1), 789–793 (2011)
9. Incropera, F.P., DeWitt, D.P.: Introduction to Heat Transfer. Wiley, New York (1996)
10. Abbassi, Y., Talebi, M., Shirani, A.S., Khorsandi, J.: Experimental investigation of TiO_2/Water nanofluid effects on heat transfer characteristics of a vertical annulus with non-uniform heat flux in non-radiation environment. Ann. Nuc. Eng. **69**, 7–13 (2014)

Effect of Obstruction Aspect Ratio in a Suddenly Expanded Micro-combustor

Arees Qamareen [ID]**, Shahood S. Alam** [ID]**, and Mubashshir A. Ansari**

Nomenclature

c_p	Specific heat
u	Longitudinal velocity
v	Transverse velocity
x	Axial distance of the combustor
r	Radial distance of the combustor
k	Thermal conductivity of gaseous species
k	Turbulent kinetic energy
k_s	Solid wall thermal conductivity
T_s	Wall temperature
T_o	Temperature of combustor outer surface
h_o	Heat transfer coefficient of ambient
h	Enthalpy
p	Pressure in the gaseous zone
Y_i	Species mass fraction
q	Heat generation rate per unit volume
D_i	Diffusion coefficient of species in the mixture
ρ	Density
ε	Outer wall surface emissivity
ε	Turbulent energy dissipation
μ	Molecular viscosity
ω_i	The species mass generation rate per unit volume
φ	Equivalence ratio of the incoming mixture

A. Qamareen (✉) · S. S. Alam · M. A. Ansari
Department of Mechanical Engineering, Aligarh Muslim University, Aligarh 202002, India
e-mail: areesq@gmail.com

1 Introduction

Recently, the progress of MEMS (Micro-Electro-Mechanical Systems) technology has brought about extremely good demand for portable electronics devices [1]. These micro-scaled devices such as robots, micro-gas turbines, satellites, and propulsion devices are continuously evolving. Conventional lithium-ion batteries used as power inputs in MEMS have several drawbacks such as shorter life durations, time-consuming recharging times, bulky design, and lower energy densities.

Combustion of hydrogen or hydrocarbon fuels releases their high energy density which is utilized by the micro-power generation devices [1, 2]. The micro-scaled combustor is a vital module of these power generating systems. The conversion of chemical energy of fuels into heat energy takes place by means of combustion. The micro-combustors are required with an extensive and stable functioning range.

Researchers [2] lately have been focusing on combustion-based direct micro-power generation devices such as Micro Thermo Photo Voltaic (MTPV) and Micro Thermo Electric (MTE) generators. These power devices are better because of the greater energy densities of hydrocarbon fuels and elimination of moving parts. MTPV [3] electricity generation is appealing due to a dramatic increase in their extensive applications. They are also attractive because of the widespread range of fuel sources and high dependability.

Micro-combustor being the core component of MTPV systems needs attention to improve flame stability and conversion efficiency [4–8]. The hydrocarbon fuel releases the heat energy in the micro-combustor and the combustor wall serves as an emitter. PV cells convert this emitted thermal radiation energy from the wall into electrical energy. The conversion efficiency related to the PV cell can be increased by an enhancement of emitter temperature.

High surface to volume ratio of the micro-scale combustors offers appropriate opportunity to attain superior radiation power yield per unit of input energy as compared to the macro-scale devices. A major challenge for micro-combustor design is to achieve an optimum equilibrium between the capability of the combustor material to sustain heat and maximization of heat output per unit volume. Extreme heat loss from the outer wall of combustor not only suppresses ignition but even quenches the reaction. The combustor size reduction leads to a decrease in the residence time of the reactants hence deterring efficient mixing and combustion process.

Combustion stability can be achieved during combustion when the mixture residence time is greater than the time of chemical reaction and the combustor dimension is sufficiently larger than the thickness of adiabatic flame [9]. MTPV micro-combustors face two crucial challenges in the form of flame stability and non-homogenous temperature distribution of the wall.

Tang et al. [11] studied baffles inserted micro-planar type micro-combustor numerically and demonstrated that the combustor efficiency is enhanced because of the presence of baffles. Bluff bodies were also found to influence the micro-combustor performance positively, principally the flame stability. Bluff body shape was also found to affect the micro-planar combustor performance as investigated by Bagheri

et al. [12], who resolved that the micro-combustors having wall-blade bluffs had the maximum temperature on the outer surface and an unwavering flame. Fan et al. [13] studied the dimensional influence of the bluff body in a micro-combustor on the blow-off limit. Zhang et al. [14] investigated the conversion rate of methane along with blow-off limit in a cubical combustor of micro-scale size with a hemispherical-shaped hollow bluff body. The presence of the insert was found to enhance the limit of flame blow-off.

Though a substantial amount of literature is available related to simple micro-combustors having bluff bodies but micro-combustors with a backward-facing step and obstruction parametric study still needs to be explored in detail.

In this study, the performance of the suddenly expanded micro-combustor with an obstruction was compared with the one without any obstruction. The aspect ratio of the block insertion was varied and studies were conducted for a range of mixture inlet velocities.

2 Mathematical Model

2.1 Micro-combustor Computational Domain

Figure 1 shows the physical geometry model of a simple micro-combustor with a backward facing step used in the present numerical work. Premixed H_2 and air arrives into the micro-combustor at a particular velocity (u) and equivalence ratio (ϕ) through the inlet. Exhausted gases leave the combustor from the right side located outlet.

The swirl component of velocity is assumed to be zero, which implies that a symmetrical flow can be considered in regard to the centerline. Simplification of the geometry leads to a two-dimensional axi-symmetric model. By considering half of the geometry, the reduction in computational time is achieved.

Several assumptions are made to further simplify the problem:

(1)   Dufour effects are neglected;
(2)   Gas radiation is considered insignificant;
(3)   Pressure and viscous stress work are absent;
(4)   Combustion process is steady-state.

For the cylindrical axi-symmetric micro-combustor, the equations of continuity, momentum, species, and energy in the gaseous phase are listed [15] as:
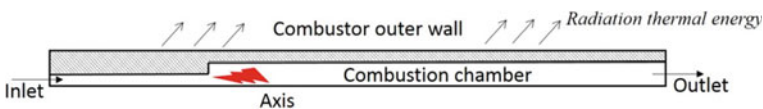
Fig. 1 Schematic diagram showing boundary conditions

Continuity equation:

$$\frac{\partial(\rho u)}{\partial x} + \frac{1}{r}\frac{\partial(\rho vr)}{\partial r} = 0 \tag{1}$$

x momentum equation:

$$\frac{\partial(\rho uu)}{\partial x} + \frac{1}{r}\frac{\partial(\rho uvr)}{\partial r} = -\frac{\partial p}{\partial x} + \frac{\partial}{\partial x}\left(\frac{4}{3}\mu\frac{\partial u}{\partial x}\right) + \frac{1}{r}\frac{\partial}{\partial r}\left(r\mu\frac{\partial u}{\partial r}\right)$$
$$- \frac{\partial}{\partial x}\left(\frac{2\mu}{3r}\frac{\partial(vr)}{\partial r}\right) + \frac{1}{r}\frac{\partial}{\partial r}\left(r\mu\frac{\partial v}{\partial x}\right) \tag{2}$$

r momentum equation:

$$\frac{\partial(\rho uv)}{\partial x} + \frac{1}{r}\frac{\partial(\rho vvr)}{\partial r} = -\frac{\partial p}{\partial r} + \frac{\partial}{\partial x}\left(\mu\frac{\partial u}{\partial r}\right) - \frac{1}{r}\frac{\partial}{\partial r}\left(\frac{2r\mu}{3}\frac{\partial u}{\partial x}\right) + \frac{\partial}{\partial x}\left(\mu\frac{\partial v}{\partial x}\right)$$
$$+ \frac{1}{r}\frac{\partial}{\partial r}\left(\frac{4r\mu}{3}\frac{\partial v}{\partial r}\right) - \frac{1}{r}\frac{\partial}{\partial r}\left(\frac{2}{3}\mu v\right) \tag{3}$$

Energy equation:

$$\frac{\partial(\rho uh)}{\partial x} + \frac{1}{r}\frac{\partial(\rho vhr)}{\partial r} = \frac{\partial}{\partial x}\left(k\frac{\partial T}{\partial x}\right) + \frac{1}{r}\frac{\partial}{\partial r}\left(k\frac{\partial T}{\partial r}r\right)$$
$$- \frac{1}{r}\frac{\partial}{\partial r}\left(r\rho\sum_{i=1}^{N}Y_i h_i V_i\right) - \frac{\partial}{\partial x}\left(\rho\sum_{i=1}^{N}Y_i h_i U_i\right) + q \tag{4}$$

Species conservation equation:

$$\frac{\partial(\rho uY_i)}{\partial x} + \frac{1}{r}\frac{\partial(\rho vrY_i)}{\partial r} = \frac{\partial}{\partial x}\left(D_i\frac{\partial(\rho Y_i)}{\partial x}\right) + \frac{1}{r}\frac{\partial}{\partial r}\left(D_i r\frac{\partial(\rho Y_i)}{\partial r}\right) + \omega_i \tag{5}$$

Energy balance equation in the solid combustor wall is:

$$\frac{\partial}{\partial x}\left(k_s\frac{\partial T_s}{\partial x}\right) + \frac{1}{r}\frac{\partial}{\partial r}\left(k_s\frac{\partial T_s}{\partial r}r\right) = 0 \tag{6}$$
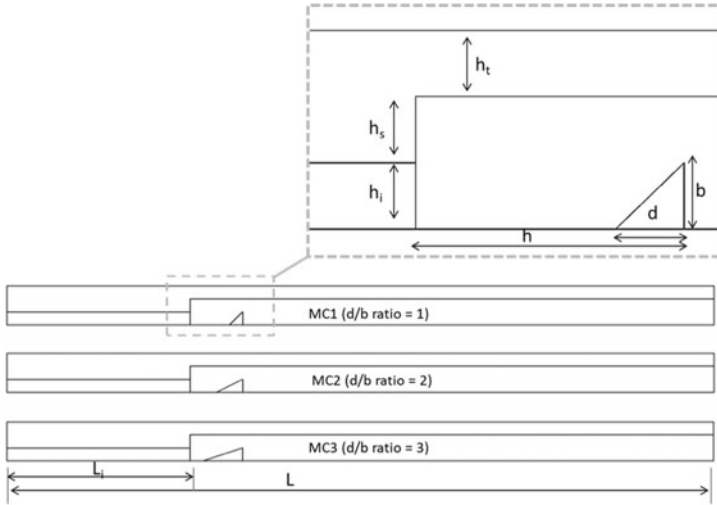
Fig. 2 Design features micro-combustors with block inserts having variable aspect ratio

2.2 Geometric Model

The design features of micro-combustors with and without triangular block insert are shown in Fig. 2. In the micro-combustor, total length (L) and inlet length (L_i) are 27 mm and 7 mm, respectively. The dimensions h_i (inlet channel height) and h_s (step height) are 0.5 mm each. The thickness of the solid combustor wall (h_t) is also 0.5 mm. A triangular block is inserted into the micro-channel which is at a distance from the combustion chamber inlet. The height (b) and location (h) of the obstruction are fixed at 0.5 and 2 mm, respectively. The length of the block (d) is a variable geometric parameter. With the intention of showing the impact of obstruction on the outer wall temperature of the micro-combustors (MC1, MC2, MC3), the dimensionless block length-to-height ratio (Aspect Ratio) is expressed as AR $= d/b = 1$, 2, and 3 respectively.

2.3 Computational Scheme

H_2 and air have been chosen as the fuel and oxidizer, respectively, and steel was considered for the combustor and block. Gas mixture density was obtained from ideal gas equation and C_p, μ, and k were calculated from mass fraction weighted average of the species properties. Piecewise polynomial fitting of temperature was done for the specific heat of each species. For stainless steel, a reduced value of thermal conductivity was used [16].

A global H_2–air oxidation mechanism is employed. Two-dimensional fully elliptic simulations based on the governing equations are carried out such that heat transfer in the solid phase besides heat and mass transfer in the gas phase is treated explicitly. The computational domain was created and discretized by using ANSYS Design Modeler and Workbench Mesh Preprocessing Software. The principal equations together with pertinent boundary conditions were resolved by using the commercial finite volume solver ANSYS FLUENT 16.0. The convergence criterion that is set for all the equations is 10^{-6}, including continuity, specie, energy, and turbulence. For the k–ε turbulence model, $k = 1 \times 10^{-3}$ and $\varepsilon = 1 \times 10^{-3}$ are fixed. A second-order upwind scheme is used for discretization of governing equations and pressure–velocity decoupling is done by the application of Semi-Implicit-Method-for-Pressure-Linked-Equations (SIMPLE) algorithm. Finite Rate/Eddy Dissipation Model is used for chemistry-turbulence interaction modelling.

Uniform H_2–air mixture velocity (4–48 m/s) and species distribution ($\phi = 0.8$), temperature (300 K) is considered. At the outlet, the species and temperature gradients are given a value of zero and a far-field pressure boundary condition is specified. Inlet and outlet walls of the combustor are considered as adiabatic as the heat losses through these surfaces are quite insignificant. Coupled boundary condition is valid at the gas–wall interfaces since the surfaces experience both conduction and convection heat transfer. At these interfaces, zero diffusive flux of species and no-slip boundary condition are indicated. The surface to surface radiation is ignored while both radiation ($\varepsilon = 0.6$) and convection ($h_o = 10$ W/m^2 K) effects are considered for the outer wall.

3 Results and Discussion

Simulations are a great means to examine the experimental results and to obtain an in-depth insight into the combustion phenomenon occurring within the micro-scaled combustors which are otherwise difficult to visualize. The present numerical study has been carried out to comprehend the crucial factors that decree the wall temperature distribution rather than to obtain an extremely refined computational model having accurate estimation. Inherent stiffness of the equations makes it difficult to obtain numerical convergence. In numerical simulations, a quad multi-zone mesh is used with 1.1×10^5 numbers of nodes (see Fig. 3). Finer grids were also verified (not presented here), with no noticeable difference of T_{out} witnessed.

The numerical result for the case with inlet velocity = 12 m/s, $\phi = 0.8$, and $\varepsilon = 0.6$ was verified against the results (Fig. 4) that were obtained experimentally by Li et al. [10]. Difference in the temperature profiles may be due to various assumptions and problem simplifications in the numerical simulations. Consideration of global H_2–air reaction scheme which does not have several intermediate reactions [6] that are otherwise considered in the detailed mechanisms also causes such differences in numerical and experimental results.
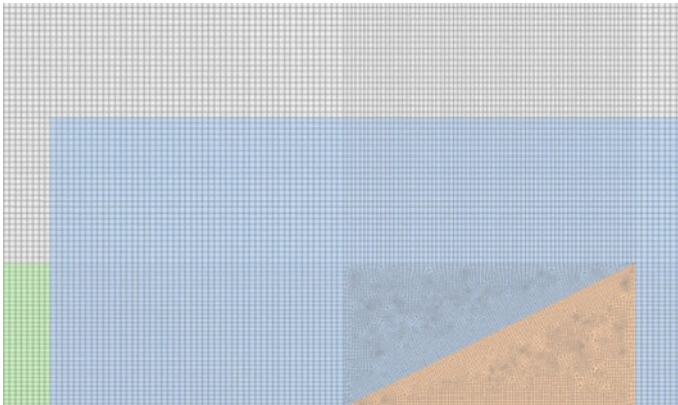
Fig. 3 Demonstration of mesh near the block inserted in the micro-combustor

Fig. 4 Validation of numerical results with experimental results of Li et al. [10]
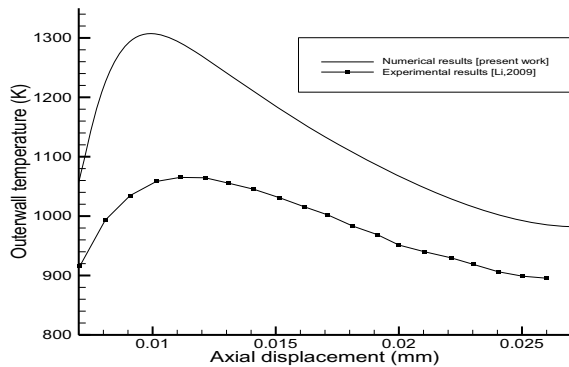
Figure 5 summarizes a comparative study of temperature distribution and T_{out} plots of different micro-combustors as the inlet mixture velocity varies from 4 to 48 m/s while the equivalence ratio of the H_2–air mixture is set to 0.8. The flame is located in the combustion chamber where the presence of maximum temperature gradient is observed. It is witnessed that as the inlet velocity is augmented, the outer wall temperature for all the micro-combustors increases dramatically. As observed from the figure, when the inlet velocity is increased, rise in T_{out} is observed with the location of peak temperature shifting downstream. With an increase in the inlet velocity, the high-temperature region behind the block gets enlarged gradually as well as its position moves downstream. The increase in the inlet velocity lowers the temperature in the area before the block but a greater temperature is observed near the micro-combustor outlet. This takes place due to shifting of the flame toward the combustor exit.

An increased amount of incoming fuel leads to larger amount of heat released in the combustion chamber as well as the lengthening of the flame. Upon further

increase in the inlet velocity, sustenance of combustion in the combustion chamber is difficult due to greater amount of heat loss from the combustor.

As also observed from the contours shown in Fig. 5a, it is shown that the flames are attached on the upper side of the backward-facing step due to the recirculation of high-temperature gases in the step corner. In this case, even though at higher velocity a lengthier and stretched flame is observed, the flame site is affected marginally, which qualitatively clarifies the reason of downstream shifting of the peak wall temperature. For Fig. 5b–d, the flame moves behind the obstruction and two recirculation zones are formed—one after the step and other behind the block.

Figure 6 summarizes a comparative study of T_{out} distribution of the geometries, at a particular inlet velocity. It is seen that for all the micro-combustors with blocks,
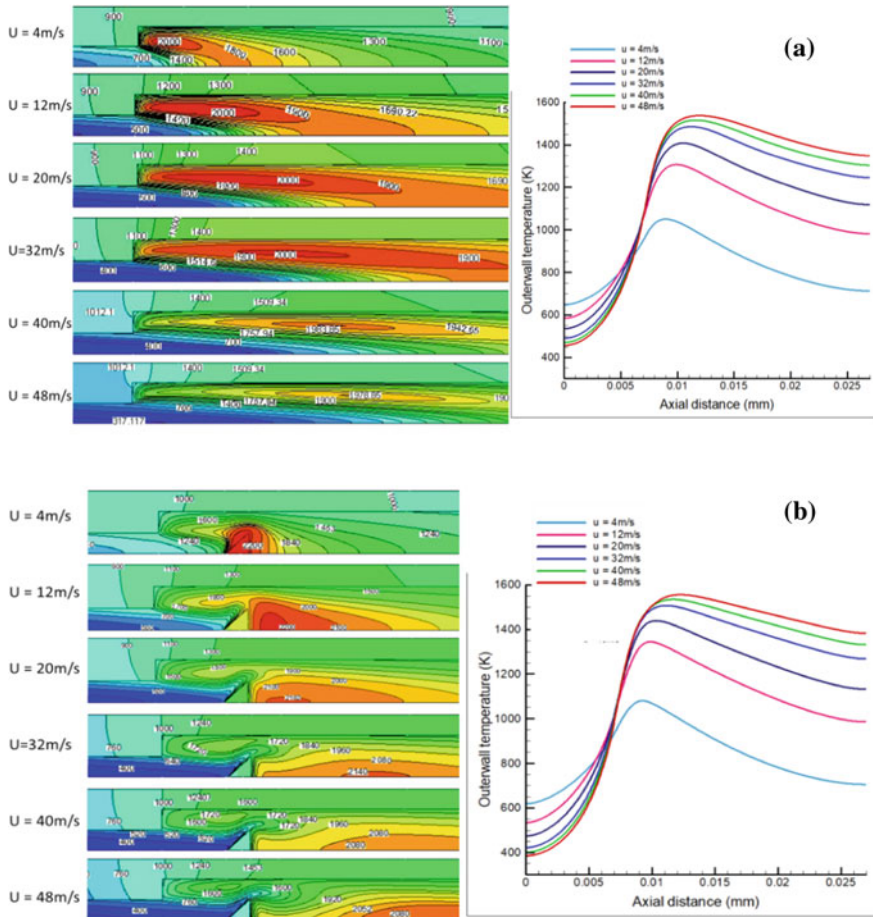
Fig. 5 Temperature contours and T_{out} plots for micro-combustors: **a** without block [MC], **b** with block of aspect ratio 1 [MC1], **c** with block of aspect ratio 2 [MC2] and **d** with block of aspect ratio 3 [MC3]
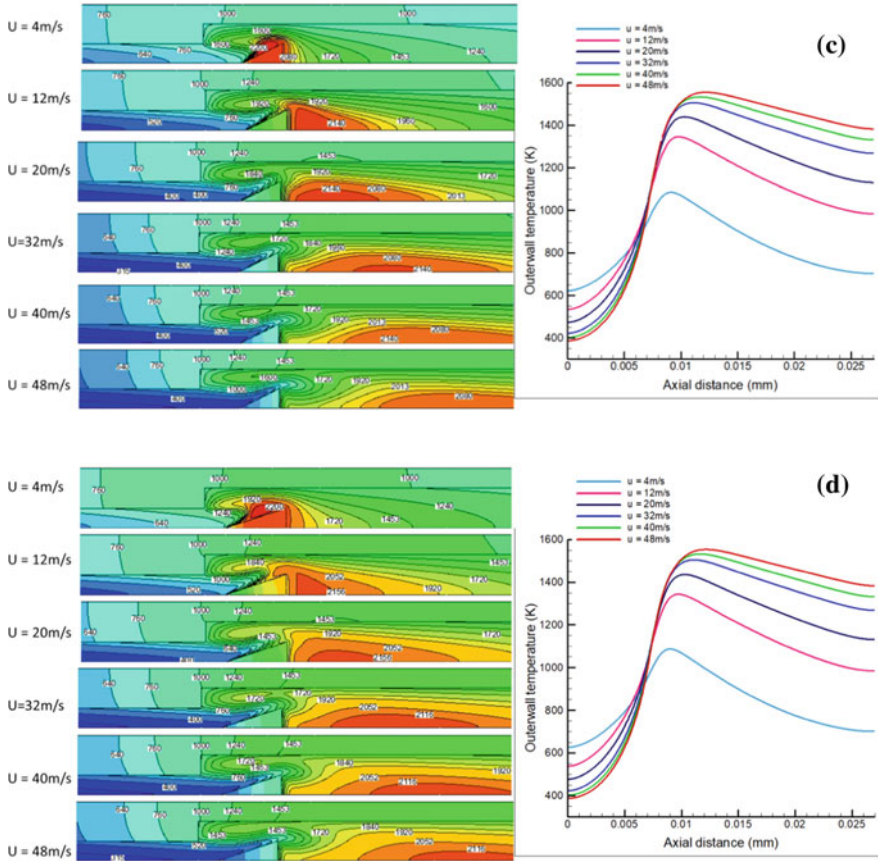
Fig. 5 (continued)

the maxima of T_{out} is more as compared to the combustor with no obstruction (of the order of 40 K) for the entire velocity range. A slight shift in the maxima with respect to the aspect ratio of block is also observed along the axial direction. Overall performance of the micro-combustors with block insertion is better and a higher T_{out} is observed as compared to the case without block.

4 Conclusions

Premixed H_2–air combustion in micro-combustors with a backward-facing step and triangular obstruction was studied numerically for varying inlet velocities and aspect ratio of block insert. The outer wall temperature was observed to increase with an escalation in flow velocity, with the peak temperature location shifting downstream.
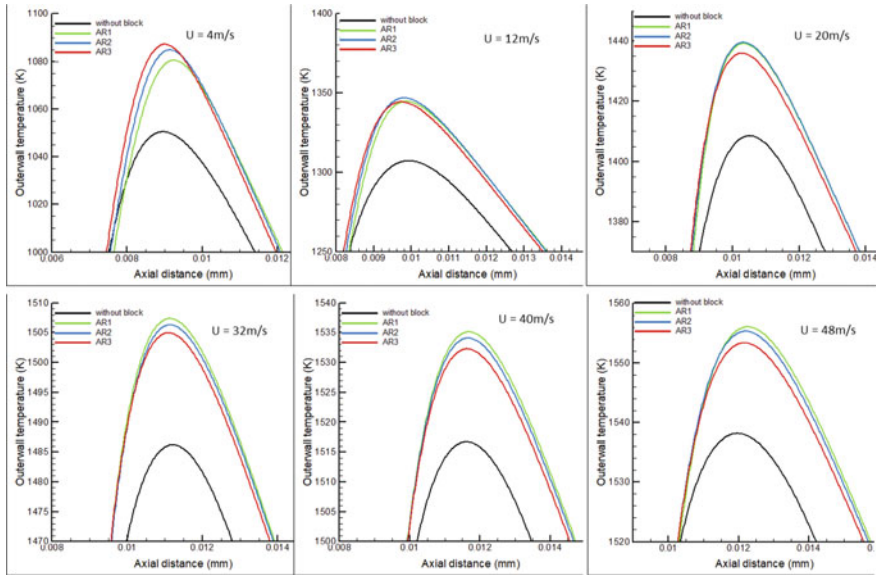
Fig. 6 Comparison of outer wall temperature distribution between different micro-combustors at different inlet velocities

The micro-combustors with block insertion performed better and a higher outer wall temperature (approximately 40 K difference) were observed as compared to the case without block but the aspect ratio of the block only slightly effected the temperature profile along the outer wall.

References

1. Wenming, Y., Siawkiang, C., Chang, S., Hong, X., Zhiwang, L.: Effect of wall thickness of micro-combustor on the performance of micro-thermophotovoltaic power generators. Sens. Actuators, A Phys. **119**(2), 441–445 (2005)
2. Jejurkar, S., Mishra, D.: A review of recent patents on micro-combustion and applications. Recent Patents Eng. **3**(3), 194–209 (2009)
3. Yang, W.M., et al.: Development of microthermophotovoltaic system development of microthermophotovoltaic system. Appl. Phys. Lett. **81**(5255), 79–82 (2002)
4. Cam, O., Yilmaz, H., Tangoz, S., Yilmaz, I.: A numerical study on combustion and emission characteristics of premixed hydrogen air flames. Int. J. Hydrogen Energy **42**(40), 25801–25811 (2017)
5. Jiaqiang, E., Zuo, W., Liu, X., Peng, Q., Deng, Y., Zhu, H.: Effects of inlet pressure on wall temperature and exergy efficiency of the micro-cylindrical combustor with a step. Appl. Energy **175**, 337–345 (2016)
6. Mansouri, Z.: Combustion in wavy micro-channels for thermo-photovoltaic applications—Part I: Effects of wavy wall geometry, wall temperature profile and reaction mechanism. Energy Convers. Manag. **198**(111155), 0–1 (2019)

7. Amani, E., Alizadeh, P., Moghadam, R.S.: Micro-combustor performance enhancement by hydrogen addition in a combined baffle-bluff configuration. Int. J. Hydrogen Energy **43**(16), 8127–8138 (2018)
8. Zuo, W., Jiaqiang, E., Peng, Q., Zhao, X., Zhang, Z.: Numerical investigations on thermal performance of a micro-cylindrical combustor with gradually reduced wall thickness. Appl. Therm. Eng. **113**, 1011–1020 (2017)
9. Hua, J., Wu, M., Kumar, K.: Numerical simulation of the combustion of hydrogen—air mixture in micro-scaled chambers Part II : CFD analysis for a micro-combustor, vol. 60, pp. 3507–3515 (2005)
10. Li, J., Chou, S.K., Yang, W.M., Li, Z.W.: Experimental and numerical study of the wall temperature of cylindrical micro combustors. J. Micromech. Microeng. **19**(1) (2009)
11. Tang, A., Xu, Y., Pan, J., Yang, W., Jiang, D., Lu, Q.: Combustion characteristics and performance evaluation of premixed methane/air with hydrogen addition in a micro-planar combustor. Chem. Eng. Sci. **131**, 235–242 (2015)
12. Bagheri, G., Hosseini, S.E., Wahid, M.A.: Effects of bluff body shape on the flame stability in premixed micro-combustion of hydrogen-air mixture. Appl. Therm. Eng. **67**(1–2), 266–272 (2014)
13. Fan, A., et al.: The effect of the blockage ratio on the blow-off limit of a hydrogen/air flame in a planar micro-combustor with a bluff body. Int. J. Hydrogen Energy **38**(26), 11438–11445 (2013)
14. Zhang, L., Zhu, J., Yan, Y., Guo, H., Yang, Z.: Numerical investigation on the combustion characteristics of methane/air in a micro-combustor with a hollow hemispherical bluff body. Energy Convers. Manag. **94**, 293–299 (2015)
15. Li, J., Chou, S.K., Li, Z.W., Yang, W.M.: A comparative study of H_2-air premixed flame in micro combustors with different physical and boundary conditions. Combust. Theory Model. **12**(2), 325–347 (2008)
16. Akhtar, S., Kurnia, J.C., Shamim, T.: A three-dimensional computational model of H_2–air premixed combustion in non-circular micro-channels for a thermo-photovoltaic (TPV) application. Appl. Energy **152**, 47–57 (2015)

Impact of Roof Colour Paints on the Indoor Temperature in a Non-conditioned Building of Composite Climate

S. P. Singh and **Mohan Rawat**

1 Introduction

Climate change creates discomfort levels in buildings due to rapid urbanization. Green areas replaced by roads, roofs and facades in cities and all of these components absorb heat from the Sun and cause the warming of these spaces to produce urban heat island effect [1]. About 45% population of the world lived in urban areas, and 60% population will shift till 2025. The temperature of the metropolitan regions is always higher than the rural areas, so the requirement of thermal comfort is an essential concern in urban areas for human health quality [2]. In buildings, thermal performance is influenced by the solar absorptance and reflectance of the roof, particularly for non-conditioned buildings. High albedo paints are a passive building strategy to reduce the energy demand in building [3]. Different strategies have adopted for energy-saving measures for buildings worldwide. An increase in solar reflectance of the outer surface of roof layers is a cost-effective technique to resolve the problem of high cooling load in buildings [4].

The peak electricity demand increased by 1.5–2.0% for every 0.5 °C increase in temperature due to the urban heat island effect in urban areas. It reduced the coefficient of performance of air-conditioning systems. An urban surface with high albedo paints is a verifiable and measurable urban heat island (UHI) mitigation strategy to cool the cities [5]. In composite climate, summer characterized by substantial solar isolation therefore, the outdoor temperature is higher with low relative humidity (10–25%) in India. Major parts of India are located in a composite climate where heat gains through the roof create indoor discomfort. Mostly construction materials used in the buildings are reinforced concrete cement (RCC) followed by concrete, brick, tiles and mud. So the requirement of thermal comfort is an essential need due to

S. P. Singh · M. Rawat (✉)
School of Energy and Environmental Studies, Devi Ahilya Vishwavidyalaya, Indore, MP 452017, India
e-mail: mrawat.seesrtc@gmail.com

the higher heat gain entered in the buildings [6]. Cool paints with higher reflectance (0.3–0.80) improved comfort and also provide opportunities for energy efficiency in non-conditioning buildings of composite climate. High albedo roof reduced energy consumption and cooling load to a large extent and maintained indoor temperature at a comfort level [7].

In this paper, the study presents a modified Fourier admittance method to see the effect of the different roof structures with cool colour paints and prediction for hourly floating room temperature for the non-conditioning building of composite climate, New Delhi. No major research work is carried out for the selection of suitable roof structures in buildings with colour paints or surface treatment of roofs for composite climates. Therefore, this study presented a comparative analysis for the selection of the roof configuration with paints in the summer season (April–July).

2 Analysis

For time-varying functions like solar radiation and ambient air temperature can be expressed in terms of the Fourier series in relationships of harmonic components [8]:

$$T_y(t) = \text{Real} \sum_{-x}^{+x} T_{y=a,R,W} \exp(in\omega t) \tag{1}$$

where $\omega = 2\pi/(24 \times 3600)$ is the daily frequency and subscripts $y = a, R, w$ represent ambient temperature, dry bulb room temperature and wet bulb room temperature, respectively.

The ambient temperature and solar radiation can be expressed individually in terms of Fourier analysis [9]

$$T_a = \sum_n T_{an} \exp(in\omega t) \tag{2}$$

$$H_s = \sum_n H_{sn} \exp(in\omega t) \tag{3}$$

The room temperature is an important parameter and determined by the net amount of heat gain loss through all its components. The energy balance equation written as follows [10]:

$$M_\tau \frac{\mathrm{d}}{\mathrm{d}t} = \left[\sum_{-x}^{+x} T_{y=a,R,W} \exp(in\omega t) \right] = \sum \dot{Q}_i \tag{4}$$

where M_τ is the thermal mass of the room air and $\dot{Q}_i$ is a heat gain due to the infiltration from ambient into room. The solution of Eq. (4) governs different harmonics of

the room air temperature, and same can be combined together to give hourly floating room temperature, i.e.

$$T_r(t) = \sum_{-x}^{+x} T_{y=a,R,W} \exp(in\omega t) \tag{5}$$

3 Results and Discussion

For simulation, a building ($7.5 \times 6.5 \times 2.7$ m) of roof area (48.75 m^2) was analysed monthly from April–July of the summer season of composite climate. A room of a building had two windows (size 1.05 m^2 each) on east and west sides and door (size 2.0 m^2), which was assumed to be located on the east side, as indicated in Fig. 1.

In the composite climate of New Delhi, the thermal performance of the non-conditioned building was characterized and demonstrated for a room using eight different roof configurations. Seven composite roof structures with a layer of cool paint (coating) and one without paint as a base case examined for the summer months (April–July). The different roof structures and details of all roof composition are described in Table 1. The climatic parameters, i.e. mean monthly radiation and an ambient temperature of New Delhi ($28.6°$ N, $77.2°$ E) have been shown in Fig. 2. In the simulation, hourly floating room temperatures are evaluated for different configurations for eight roof structures, i.e. base case, R-1, R-2, R-3, R-4, R-5, R-6 and R-7. The study assessed hourly floating room temperature for four months (April–July)
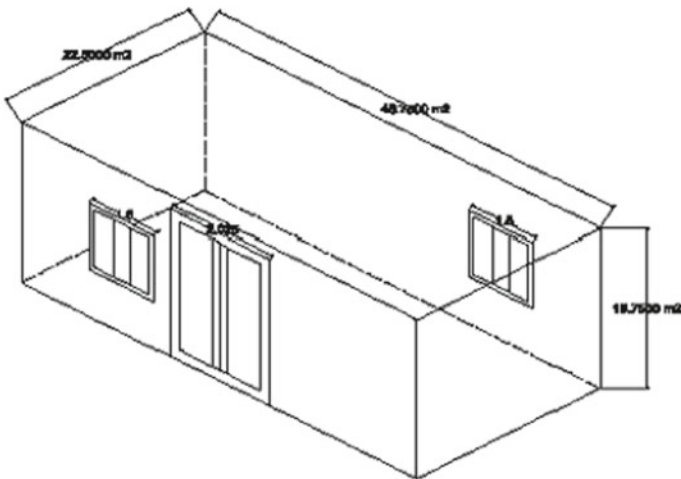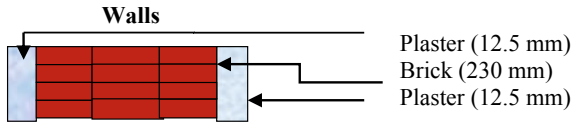
Fig. 1 Test room of a building

Table 1 Details of different roof structures

S. No.	Illustration
1	**Base Case** Brick Tile (50 mm) Mud Phuska (75 mm) RCC (120 mm) Plaster (60 mm)
2	**R-1** Cool Coating (0.5 mm) Galvanized Steel (8 mm) Concrete (100 mm) Plaster (10 mm)
3	**R-2** Albedo bright white paint (10 mm) Cement Mortar (20 mm) Dense reinforced concrete (150 mm) Cement plaster with sand aggregate (20 mm)
4	**R-3** Cool Coating (0.5 mm) Ferro Cement (30 mm) Concrete (100 mm) Plaster (10 mm)
5	**R-4** Cool Coating (0.5 mm) Plaster Concrete Block (125 mm) Plaster (10 mm)
6	**R-5** Aerogel Based Coating (40 mm) Concrete (250 mm) Glass Wool (160 mm) Plaster (13 mm)
7	**R-6** Cool Coating (0.5 mm) Mortar (20 mm)Mortar (20 mm) Concrete (250 mm) Plaster (13 mm)
8	**R-7** Aerogel Based Coating (40 mm) Mortar (20 mm) Concrete (250 mm) Plaster (13 mm)

(continued)

Table 1 (continued)

S. No.	Illustration
9	**Walls** Plaster (12.5 mm) Brick (230 mm) Plaster (12.5 mm)
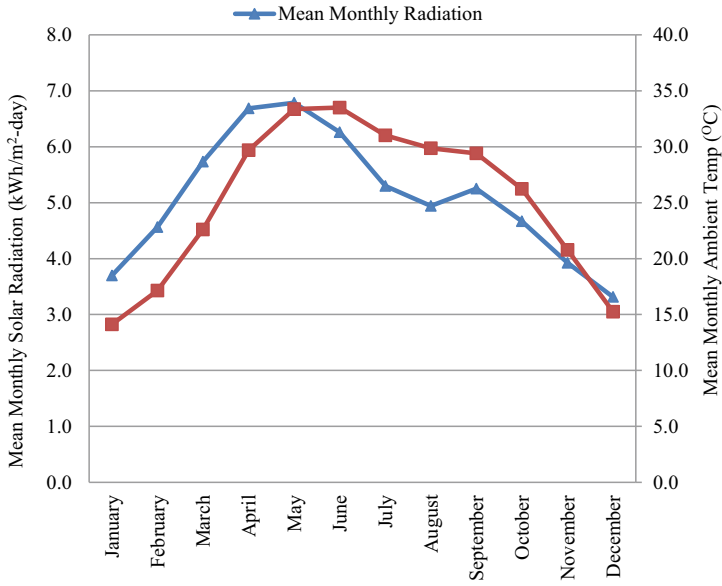
Fig. 2 Mean monthly solar radiation
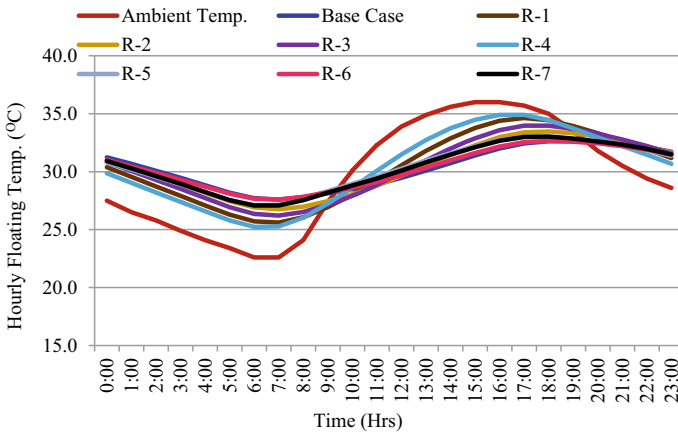
Fig.3 Hourly floating temperature in April

and its variation for twenty-four, as shown in Figs. 3, 4, 5 and 6. The thermo-physical properties of roof and wall structures used in the simulation is described in Table 2.

Figure 3 represents an hourly floating room temperature across all roof structures in April month. The maximum room temperature about 34.9 °C achieved in the roof structure, R-4 with variation in maximum and minimum temperature was 9.7 °C. On the other hand, roof structure, R-6 performed better with a maximum temperature of 32.6 °C and temperature variation about 4.9 °C throughout the 24 h cycle period.

Room temperature distribution for May is represented in Fig. 4, and the maximum temperature is attained in the roof structure, R-4 about 38.6 °C. The variation in maximum and the minimum hourly floating temperature was 9.6 °C in this structure. While the best performance found in the roof structure, R-6 with maximum temperature of 36.4 °C and variation of maximum and minimum temperature are about 5.0 °C. In June, the maximum temperature is found in roof structures, R-4,
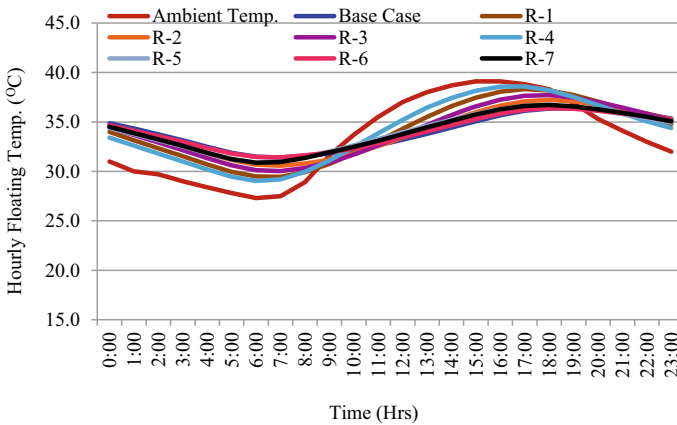
Fig. 4 Hourly floating temperature in May
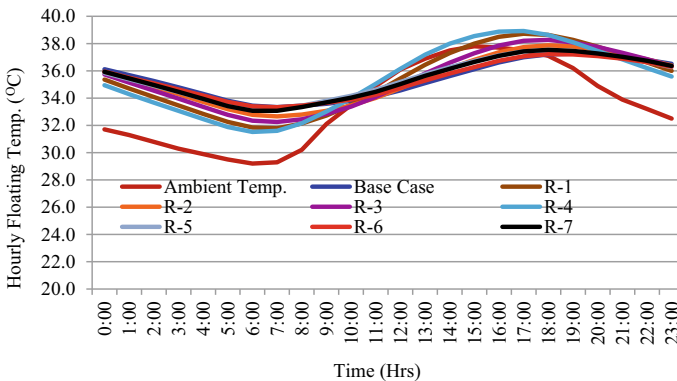
Fig. 5 Hourly floating temperature in June
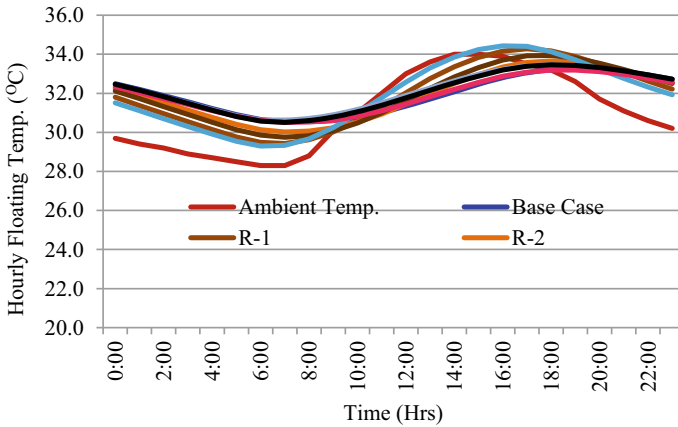
Fig. 6 Hourly floating temperature in July

about 38.9 °C with a variation of 7.4 °C of maximum and minimum temperatures, as indicated in Fig. 5. In this month roof structure, R-6 performed better in terms of maximum and minimum temperature deviation of 3.9 °C. Remaining roof structures, base case, R-5 and R-7 also have shown better results with minimal temperature variation. Roof structures, R-1, R-2 and R-3, were not performed better in this month. In July, temperature variations achieved in roof structures were quite low as compared to May and June, as shown in Fig. 6. Maximum temperature is found in the structure, R-4, around 34.4 °C with the variation of 5.1 °C hourly floating room temperature during day and night time operation. Roof structure, R-6, performed better with minimum temperature variation.

Simulation results are compared to all roof structures for hourly floating temperatures deviation in all four months (April–July). In the composite climate, the average hourly floating temperature for the roof structure, R-4, is higher in all four months. In all four months (April–July), the average maximum temperature of roof structure-R4 is 36.7 °C. Because of high thermal conductivity and lower thermal mass of plastered concrete block compared to other roof structures, it is more sensitive for heat gain in the summer period. Simulation results also assessed that average temperature variation of four months is about 7.9 °C. The comparative analysis revealed that the best thermal performance of the roof is achieved in the roof structure, R-6. The average of maximum and minimum temperature variation in all four months is 4.2 °C for this structure (R-6). This structure is a combination of concrete and mortar with a surface coating of paint with less diffusivity, and lower heat is gain entered in daytime operation. Higher reflectance and emittance properties of cool paints also reflect most of the heat flux towards the surrounding, which leads to lower temperature variation.

In the case of other remaining roof structures, thermal performance of the roof structures base case, R-5 and R-7, performed better in terms of minimum hourly variation of floating temperatures because of effective thermal conductivity and lowered thermal mass compared to other roofs. Simulation results also proved that

Table 2 Thermophysical properties of roof structures and wall

S. No.	Details	Thermophysical properties						Reference
		Material	Thickness (mm)	Thermal conductivity (W/m °C)	Specific heat (J/kg °C)	Density (kg/m³)	U value (W/m² °C)	
1	Base Case	Brick tile	50	0.80	880	1892	3.14	[9]
		Mud phuska	75–100	0.52	880	1622		
		Plaster	12	0.72	840	1762		
		RCC	120	1.58	846	2288		
2	R-1	Cool coating	0.50	0.045	800	1053	2.44	[11]
		Galvanized steel	8	15.3	500	4800		
		Concrete	100	0.85	675	2350		
		Plaster	10	1.50	750	600		
3	R-2	Albedo bright white paint	10	1.4	800	2100	3.72	
		Cement mortar	20	0.72	920	1650		
		Dense-reinforced concrete	150	1.90	840	2300		
		Cement plaster with sand aggregate	20	0.72	840	1860		
4	R-3	Cool coating	0.50	0.045	800	1053	3.13	
		Ferro cement	30	0.447	840	2000		
		Concrete	100	1.442	880	2400		
		Plaster	10	0.533	840	1568		
5	R-4	Cool coating	0.50	0.05	800	1053	3.03	

(continued)

Table 2 (continued)

S. No.	Details	Thermophysical properties						Reference
		Material	Thickness (mm)	Thermal conductivity (W/m °C)	Specific heat (J/kg °C)	Density (kg/m³)	U value (W/m² °C)	
		Plastered concrete block	125	1.10	800	920		
		Plaster	10	0.25	850	1000		
6	R-5	Aerogel-based coating	40	0.027	1100	200	2.50	[12]
		Concrete	250	2.1	800	2400		
		Glass wool	160	0.041	840	12		
		Plaster	13	0.32	800	790		
7	R-6	Cool coating paint	0.50	0.05	800	1053	1.82	[13]
		Mortar	20	1.4	840	2000		
		Concrete	250	2.1	800	2400		
		Plaster	13	0.32	800	790		
8	R-7	Aerogel-based coating	40	0.027	1100	200	0.60	[14]
		Mortar	20	1.4	840	2000		
		Concrete	250	2.1	800	2400		
		Plaster	13	0.32	800	790		
9	Wall	Plaster	12.5	0.72	840	1762	3.20	[9]
		Brick	230	0.84	800	1700		

(continued)

S. P. Singh and M. Rawat

Table 2 (continued)

S. No.	Details	Thermophysical properties						Reference
		Material	Thickness (mm)	Thermal conductivity (W/m °C)	Specific heat (J/kg °C)	Density (kg/m³)	U value (W/m² °C)	
		Plaster	12.5	0.72	840	1762		

cool paints are most effective in composite climates where maximum diurnal variation is achieved. The average variation in hourly floating room temperature for all roof structures for four months (April–July) for composite climate, New Delhi, has shown in Table 3.

4 Conclusion

The following conclusions are drawn from a simulation study aiming to evaluate the impact of using cool coatings on comparative hourly floating room temperature profiles to construct a better roof in non-conditioning buildings for composite climatic zone.

1. Roof structure (R-6), i.e. concrete, mortar with colour paint coating combinations should be preferred for composite climates for non-conditioning buildings in the composite climatic zone.
2. Roof structures, R-2, R-5 and R-7, are the best roofs in attaining a minimum hourly floating room temperature. However, roof structure, R-4, revealed the worst performance. So all types of roofs with a surface coating of paint with higher reflectance showed better thermal performance compared without surface coating of paints.

The simulation assessed that roof structures, i.e. R-2, R-5 and R-7 with aerogel-based coating are a useful technique for reducing indoor room temperatures and maintaining thermal comfort in non-conditioning buildings in composite climate.

Table 3 Monthly wise maximum and minimum room temperature (°C) for all roof structures

Roof structure	April				May				June				July			
	Max	Min	Avg	ΔT	Max	Min	Avg	ΔT	Max	Min	Avg	ΔT	Max	Min	Avg	ΔT
Base case	32.6	27.6	30.3	5.1	36.4	31.1	34.0	5.3	37.3	33.3	35.4	3.9	33.3	30.6	31.9	2.7
R-1	34.6	25.6	30.3	9.0	38.3	29.5	34.0	8.9	38.7	31.8	35.3	6.9	34.3	29.4	31.9	4.9
R-2	33.5	26.8	30.3	6.7	37.2	30.6	34.0	6.7	37.9	32.7	35.3	5.2	33.7	30.0	31.9	3.6
R-3	34.0	26.2	30.3	7.8	37.7	30.0	34.0	7.7	38.3	32.3	35.3	6.0	33.9	29.8	31.9	4.2
R-4	34.9	25.2	30.3	9.7	38.6	29.0	34.0	9.6	38.9	31.5	35.3	7.4	34.4	29.3	31.9	5.1
R-5	33.0	27.1	30.4	5.9	36.7	30.9	34.0	5.8	37.5	33.1	35.5	4.4	32.1	30.6	32.1	1.5
R-6	32.5	27.6	30.3	4.9	36.4	31.4	34.0	5.0	37.2	33.3	35.4	3.9	33.2	30.5	31.9	2.7
R-7	33.0	27.1	30.3	6.0	36.7	30.9	34.0	5.9	37.5	33.1	35.4	4.5	33.5	30.5	32.1	3.0

References

1. Mansouri, O., Belarbi, R., Bourbia, F.: Albedo effect of external surfaces on the energy loads and thermal comfort in buildings. Energy Procedia **139**, 571–577 (2017)
2. Talukdar, S.J., Khandaker, A., Hossen, M.S. Evaluation of the outdoor thermal discomfort of three major cities of Bangladesh. In: International Conference on Sustainability in Natural and Built Environment (iCSNBE2019), vol. 19, p. 22 (2019)
3. Granadeiro, V., Almeida, M., Souto, T., Leal, V., Machado, J., Mendes, A.: Thermochromic paints on external surfaces: impact assessment for a residential building through thermal and energy simulation. Energies **13**(8), 1912 (2020)
4. Fantucci, S., Serra, V.: Investigating the performance of reflective insulation and low emissivity paints for the energy retrofit of roof attics. Energy Build. **182**, 300–310 (2019)
5. Jandaghian, Z., Berardi, U.: Analysis of the cooling effects of higher albedo surfaces during heat waves coupling the weather research and Forecasting model with building energy models. Energy Build. **207**, 109627 (2020)
6. Sansaniwal, S.K., Mathur, J., Garg, V., Gupta, R.: Review of studies on thermal comfort in Indian residential buildings. Sci. Technol. Built Environ., 1–22 (2020)
7. Nihar, K., Dhaka, S., Bhatia, A., Garg, V.: Cool roof implications on thermal adaptation in built environment. In: International Symposium to Promote Innovation & Research in Energy Efficiency (2017)
8. Singh, S.P., Tulsidasani, T.R., Sawhney, R.L., Sodha, M.S.: Recent researches in indirect evaporative cooler V: relative thermal performance of buildings coupled to direct and indirect evaporative cooler. Int. J. Energy Res. **21**(15), 1413–1423 (1997)
9. Sodha, M.S., Singh, S.P., Sawhney, R.L.: Evaluation of discomfort in a room with desert cooler. Int. J. Energy Res. **14**(7), 745–756 (1990)
10. Bansal, N.K., Garg, S.N., Kothari, S.: Effect of exterior surface colour on the thermal performance of buildings. Build. Environ. **27**(1), 31–37 (1992)
11. Zingre, K.T., Wan, M.P., Tong, S., Li, H., Chang, V.W.C., Wong, S.K., Lee, I.Y.L.: Modeling of cool roof heat transfer in tropical climate. Renew. Energy **75**, 210–223 (2015)
12. Dabaieh, M., Wanas, O., Hegazy, M.A., Johansson, E.: Reducing cooling demands in a hot dry climate: a simulation study for non-insulated passive cool roof thermal performance in residential buildings. Energy Build. **89**, 142–152 (2015)
13. Zingre, K.T., Wan, M.P., Wong, S.K., Toh, W.B.T., Lee, I.Y.L.: Modelling of cool roof performance for double-skin roofs in tropical climate. Energy **82**, 813–826 (2015)
14. Zingre, K.T., Yang, X., Wan, M.P.: Performance analysis of cool roof, green roof and thermal insulation on a concrete flat roof in tropical climate. Evergreen: Joint J. Novel Carbon Resource Sci. Green Asia Strat. **2**(2), 34–43 (2015)

An Overview of Various Techniques of Atmospheric Water Extraction from Humid Air

Vikrant Mishra and **Kushal Saxena**

1 Introduction

Water is one of the most precious resource available on the earth which is essential for existence of life. Water is available in plenty amount on our earth but only 3% of the total water resources can be stated as fresh drinkable water [1]. Specially in desert areas, many people face scarcity of fresh drinkable water. Many researchers have described numerous methods to solve this problem of fresh water scarcity. There is a need to develop new sources of pure water at low cost. Extraction of water vapors from surrounding air can be a viable approach at humid locations. India have a potential of utilizing this atmospheric water extraction technique due to humid weather at many locations throughout the year [2].

The atmospheric air is an abundant source of water which has huge potential in form of water vapors. These water vapors can be restored from humid air by practice of condensation of moisture and this water can be stored for its future use in harvesting, drinking, etc. In the present work, an attempt is made to discover these techniques to condense the moisture present in air with the help of atmospheric water generator. Water extraction from the air can be done using Peltier modules or by refrigeration method, mechanical method, adsorption method, or absorption method [4]. In this paper, an overview of solar assisted chemical desiccant-based adsorption and absorption method is firstly presented in which desiccants (Mostly $CaCl_2$ and its composites) are used to adsorp or absorp the water vapors from the surrounding air and solar energy can be utilized to regenerate the water vapors and these regenerated water vapors can be condensed in the form of fresh water.

In the later part, literature review of recent work in atmospheric water extraction using Peltier modules has been presented. Peltier device is composed of

V. Mishra (✉) · K. Saxena
Rajkiya Engineering College Mainpuri, Dr. A. P. J. Abdul Kalam Technical University, Lucknow 226031, India
e-mail: mishra92vikrant@gmail.com

ceramic substrates with n-type semiconductors and p-type semiconductors sand-wiched between them. A Peltier device works upon Peltier effect in which when the device is provided an emf through an electric power source then it produces two junctions as hot and cold sides. This popular Peltier effect can be combined with a number of equipments such as heat sink, fans, cold fins to develop an atmospheric water generator as a solution to scarcity of water [19].

2 Review of Water Extraction Techniques Based on Adsorption and Absorption Methods

Fresh water can be generated from the humid air by various methods such as mechanical, refrigeration, adsorption and absorption. Many researchers have focused on adsorption and absorption method with various kinds of adsorbent and absorbent materials. In this section, an overview of some of the previous works have been presented.

Alayli et al. carried out an experiment to extract fresh water from humid air. In this experiment, authors used several mineral adsorbents to adsorb the water vapors present at the surroundings. Then, the adsorbed water vapor particles were evaporated using solar energy and lastly, 1 L of fresh water produced after condensation at the expanse of 1 m^2 composite material [3].

Abualhamayel et al. discussed an absorption method of extracting fresh water from surrounding air. In this work, authors selected $CaCl_2$ as absorbent and suggested a system with flat, one side glazed inclined surface and insulated bottom (Fig. 1). Strong absorbent, due to its less vapor pressure, absorbed the atmospheric water vapors at nighttime. Further, this weak absorbent get heated by means of solar energy in the
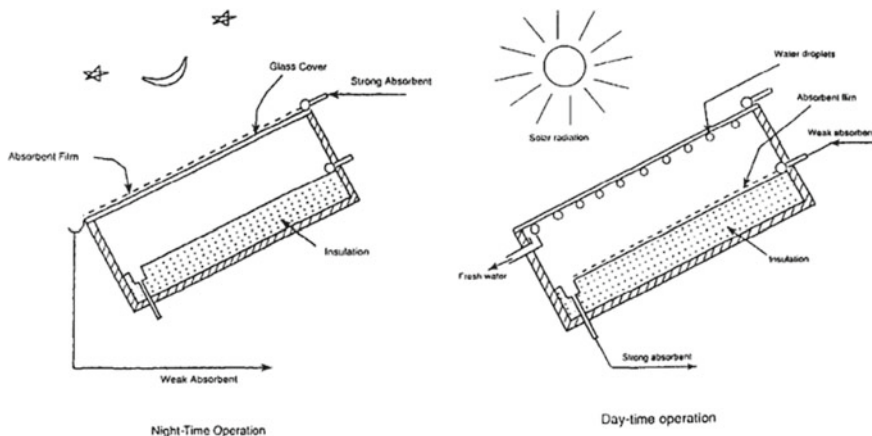
Fig. 1 Schematic diagram of model proposed by Abualhamayel et al. [4]

daytime and the regenerated water vapors get condensed under glazed layer. The temperature of glazed layer should be kept minimum to provide ease in condensation process. Authors also presented mathematical analysis to estimate the performance of water extracting system [4].

Aristov et al. proposed the use of SiO_2-based selective water sorbents in solar assisted air to water extraction process. 10 tonnes of the dry sorbents were employed in this experiment. The results showed that around 3–5 tonnes of fresh water produced after sorption and desorption stages [5].

Gad et al. used $CaCl_2$ as the working absorbent and presented a system comprised of a flat plate collector with a removable glass shield, a corrugated bed, and a condenser. The fresh water was produced after absorption and regeneration process consecutively in night and daytime. The results indicated that this system can provide 1.5 L of drinkable water per m^2 per day. In this work, mathematical analysis of absorption and regeneration process also presented and more than 17% system efficiency was estimated based on this analysis [6].

Kabeel proposed a solar assisted water extraction system of pyramidal structure with aluminum casings, glass faces, and $CaCl_2$ as employed desiccant. The system procedure included absorption of water vapors from surrounding air at night after the four sides of pyramidal structure are opened to surrounding air. All sides are shut in the daytime and regeneration of desiccant occur due to solar energy which subsequently followed by condensation of water vapors. The results showed that the volume of fresh water generated was 2.5 L per m^2 per day. The system efficiency was little less than twice the previously reported efficiency. The use of cloth bed system was recommended for greater efficiency [7] (Fig. 2).

Ji et al. proposed the use of a new composite adsorbent material which was prepared by a crystalline material MCM-41 as host material and $CaCl_2$ as a hygroscopic salt. The results indicated that this new composite material has a greater impact on performance of solar assisted atmospheric water extraction system. The amount of fresh water generated per day was more than 1.2 kg per m^2 of collector area [8].

Hamed et al. estimated the performance of solar assisted atmospheric generator using $CaCl_2$ as desiccant with sand bed. Experimental results showed that approximately 1.0 L/m^2 of fresh water can be produced using proposed system at the surrounding conditions of Taif, Saudi Arabia [9].

William et al. proposed an atmospheric water extraction system comprised of a trapezoidal prism solar collector with multi-layered bed. Hence, the surface area of bed (desiccant carter) was maximized. In this work, two types of bed, i.e., cloth bed and sand bed with $CaCl_2$ solution, were employed and the results depicted that the amount of water evaporated was 2320 g/m^2-day and 1235 g/m^2-day respectively for cloth and sand bed for initial saturation concentration of $CaCl_2$ at 30%. Similarly, system efficiency was calculated in both the case as 29.3% for cloth bed and 17.76% for sand bed [10].

Kumar and Yadav proposed the use of '$CaCl_2$/Floral foam' as desiccant in solar assisted fresh water generation from surrounding air. The system used in this work is shown in Fig. 3. The results depicted that the amount of water generated with the use of this new composite desiccant was 0.35 mL/cm^3/day [11].

Dim. in cm

Elevation view

1- pyramid sides   2- glass cover   3- pyramid base
4-collected water   5- -bed   6- collected cone
7- condenser   8- shelves   9- graduated glass   10- glass support
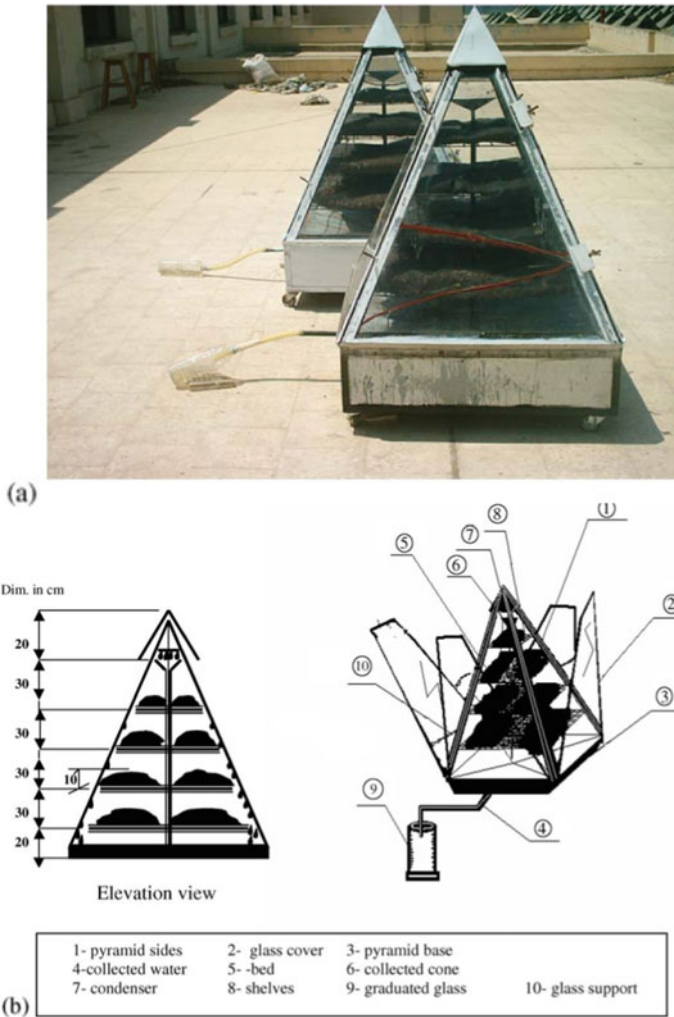
Fig. 2 a System used by A.E. Kabeel. **b** Elevation view and pyramids with open glass faces at night [7]

Kim et al. demonstrated an atmospheric water extractor even under low humidity condition (around 20%). In this work, a metal–organic framework-801 [$Zr_6O_4 (OH)_4 (-COO)_6$] was used due to its better ability of water adsorption. Solar irradiation (less than 1000 W/m^2) caused the desorption process and water vapors entered the refractive enclosure due to porous nature of MOF-801. Then these water vapors are condensed in the condenser placed at bottom and its latent heat is rejected by condenser to outside by means of a heat sink. This system could produce 2.8 L/day of fresh water at the expanse of 1 kg of MOF-801 [12].
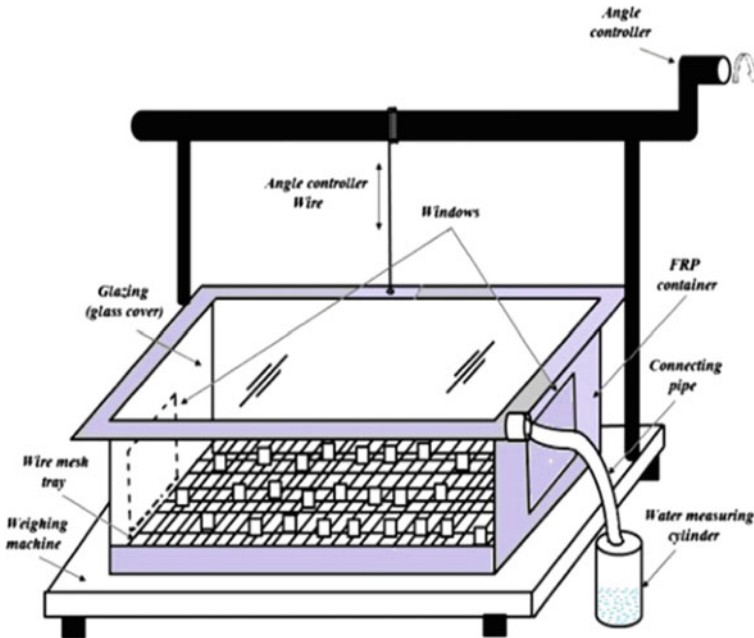
Fig. 3 Water extractor with CaCl$_2$/Floral foam desiccant [11]

Srivastava and Yadav performed experiments on solar-driven atmospheric water extraction technology at the location of NIT Kurukshetra, India. In this work, authors used sand bed as host material and three different types of materials LiCl, LiBr and CaCl$_2$, as salts to make composite desiccant. The setup used in this work is shown in figure. A Scheffler reflector (1.54 m^2 surface area) was installed with a receiver box at its focal point. Composite desiccants were placed into receiver box. All the sides of box were insulated with glass wool except the side in front of Scheffler reflector. The composite desiccant absorbed the water vapors from the surrounding air in the nighttime till the saturation condition is reached. The amount of water vapors absorbed can be determined by calculating the weight of desiccant before and after the absorption by means of a weighing machine. In the daytime, the desiccant was placed in the receiver box in front of Scheffler reflector and the regeneration of water vapors began due to solar energy. The regenerated water vapors condensed into water after passing through condensing tube and the condensate is stored in an air-tight vicker. The total water produced from atmospheric air was 90 mL for LiCl-based desiccant in 330 min at average solar irradiation 511.3 W/m^2. Similarly with LiBr and CaCl$_2$-based desiccant, water produced was 73 mL and 115 mL, respectively, in time duration of 270 min for both. The annual cost was lowest (0.53 \$/L) with CaCl$_2$-based desiccant and highest (0.86 \$/L) with LiBr-based desiccant [13] (Fig. 4).

Talaat et al. designed and studied a water extraction system at the location of Mansoura University, Egypt. This system comprised of conical see-through surface
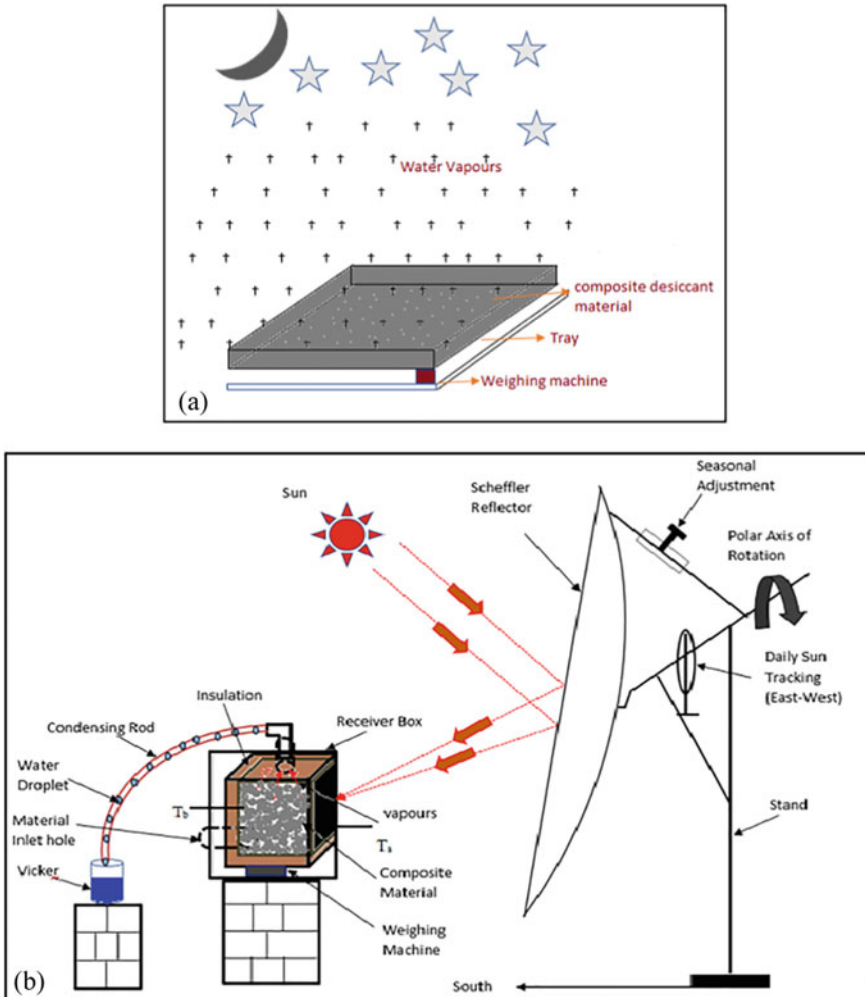
Fig. 4 Schematic diagram of **a** Absorption of water vapors at night. **b** Regeneration and condensation process using Scheffler Reflector and condensing tube [13]

which is made up of cloth bed and $CaCl_2$ (desiccant) solution. At night, when the desiccant is exposed to surrounding air, water vapors are absorbed and in the daytime, the system is enclosed with a transparent conical layer which is open to receive solar irradiation upon it. Due to heat provided from solar irradiation, water vapors evaporate and then condense into water after rejecting its latent heat to the adjacent surface. The condensed water is stored in a flask. The amount of water stored was calculated in the range 0.3295–0.6310 kg/m^2/day [14].

Elashmawy proposed an atmospheric water extraction system incorporated with tubular solar still and air circulation fan. The results depicted that the system could

generate water up to 467 mL/m^2 in a day at 4 m/s speed of air under low humidity condition (12%) at Hail city, Saudi Arabia. Under natural speed of air, 230 mL/m^2 water could be generated in a day. The maximum thermal efficiency at natural airspeed was 12.2% while in case of air circulation 4 m/s by means of a fan, thermal efficiency was 25%. Hence, authors suggested to use such system with greater speed of surrounding air to augment the performance of system [15].

3   Recent Developments in Air to Water Extraction Technique Based on Peltier Modules

Kabeel et al. proposed a solar-based atmospheric water extraction technique incorporated with thermoelectric cells to enhance the temperature difference between evaporating and condensing regions (Fig. 5). Authors also performed CFD simulation of this solar and thermoelectric-based system under three different climatic conditions. This system could produce fresh water 3.9 L per hour per square meter [16].

Suryaningsiha Sri et al. performed an experimental work on a prototype of atmospheric water generator using Peltier modules techniques at the rural areas of Indonesia. Experimental investigations led to the development of a prototype of atmospheric water generator using Peltier modules with 12 V DC supply and single unit PWM controllable Brushless DC fan. The prototype comprised of four units of Peltier modules (Model number TEC1-12706) connected in parallel. The experimental tests were conducted for different configurations of Peltier modules
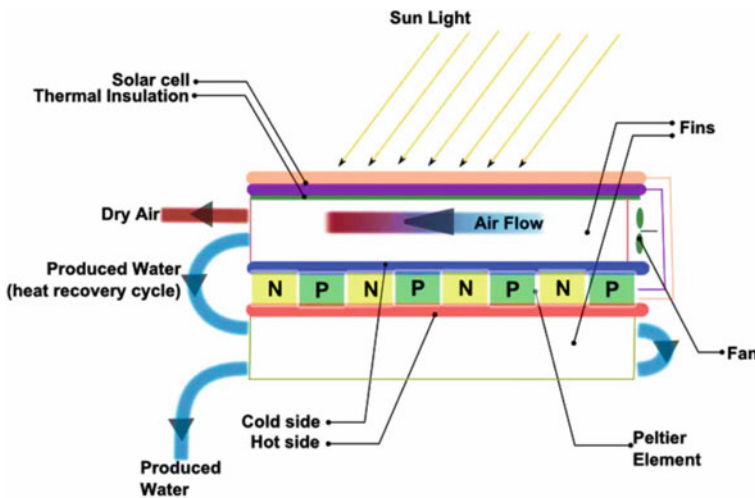
Fig. 5   Solar and TE based system used by Kabeel et al. [16]
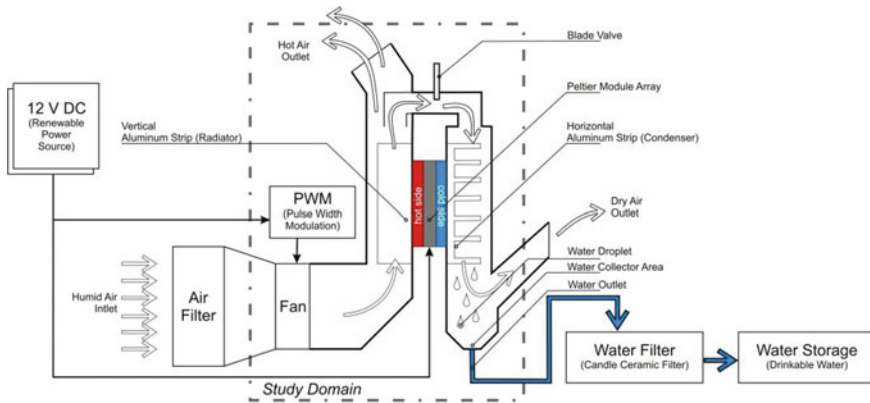
Fig. 6 Schematic diagram of the atmospheric water generator based on Peltier Module [17]

and different airflow conditions. Certain performance parameters including condensation ratio and production ratio were calculated. The results of the prototype were compared with the other available products of this category. The comparison leads to achieve a big success in the experimental effort. The production ratio for the amount of water derived from moisture of the air was obtained nearly 2 which fit the quantity of drinking water for approximately two persons. The results also concluded that the quantity of water from moisture can be increased by increasing the rate of humid airflow and also with increase in the power supply. The quality of water obtained by this method also accords to the standards of WHO [17] (Fig. 6).

Joshi et al. executed an experimental investigation to design and develop a thermoelectric fresh water generator which worked on the principle of thermoelectric cooling effect using Peltier modules. In this work, a prototype was built up consisting of a long cooling channel with ten Peltier modules arranged in an array. The experimental prototype was made to run for ten working hours. Peltier modules were arranged thermally in a parallel circuit while electrically in a series circuit. At the hot side of Peltier modules, the set up has an external heat sink serving the purpose of heat rejection. Heat sink also incorporated with four cooling fans to increase the rate of heat transfer through forced convection. An internal heat sink was used as an additional member in this set up to enhance the surface area for cooling the air and condensing the moisture. It also acts as a device which enhanced the turbulence in the motion of the moist air. In the experimental tests, observations were made on the amount of moisture condensed from the air by varying its mass flow rate, humidity and the amount of electric current supply provided. The experimental efforts derived direct proportionality relation of the amount of water condensed from the moist air with the mass flow rate of air, humidity of the air, and the electric current power supply. An important conclusion in this experiment was that the amount of water condensing from moisture rises up by 81% after employing the internal heat sink [18].

Kiara et al. projected a solution to cater the needs of a large number of human beings who are facing a very severe situation due to depleting fresh water resources. The research work explored out an experimental and numerical solution to the problem by designing two prototypes based on cross flow heat exchanger and Peltier effect, respectively. One prototype included a cross flow heat exchanger in an underground chamber where temperature was generally low, water performed as coolant cooled by the low temperature underground chamber. Another prototype was designed on the basis of Peltier effect. The prototype worked efficiently in a defined range of relative humidity of 52–100%. Mathematical modeling was executed to solve the governing equations of thermodynamics and heat mass transfer analysis to find out the variables which affect the performance of the prototypes and calculate the amount of water generated. The theoretical model results obtained from the mathematical equations were compared with experimental work. The observations concluded that the amount of water generated was nearly eight times in case of prototype based on heat exchanger model in comparison with Peltier effect-based prototype. However, the power consumption was low in case of Peltier effect-based prototype [19].

Anandhulal et al. developed a device for extraction of water from air whose working was based on the Peltier effect. The device developed for the research work was comprised of heat sink, cold sink, temperature regulator, fan and Peltier module. Fan brought the humid air in the assembly. The Peltier module was given electric force through a DC source of power due to which it produced hot and cold sides due to Peltier effect. The air when passed over the cold side, its temperature was brought down to the dew point due to which the moisture retained by the air gets condensed and can be collected. The research concluded that the device is simple in its configuration with no movable mechanical components, no harmful chemical as CFC's and a sufficient amount of drinkable water can be derived which might help for mountaineers, fishermen and several other purposes and it can also be transported easily from place to place [20].

Shanshan et al. developed a lightweight easy to transport device to generate water by condensation of the moisture present in the air with the help of two Peltier thermoelectric devices. A set up was designed to perform the research experimentally. The set up comprised of a humidifier, a mixing assembly, an air conduit, and a thermoelectric Peltier water generator. A cross flow fan led the atmospheric air into the mixing assembly where its relative humidity was controlled with the help of humidifier and forwarded to the air conduit. Finally from the air conduit, air was passed through the Peltier device where it brought down the temperature of air to its dew point. As the temperature reached the dew point, moisture in the air started to condense on the surface and for collection of water a pan was installed. Amount of water collected in the pan was measured every hour during the run of the experimental work. Three different flow rates of air were varied with the help of cross flow fan. The flow rates were quantified with the help of an anemometer. Temperature and humidity were quantified by the hygrothermographs. All the measured variables were fed to a data acquisition system. An enhancement was recorded with the increase in the relative humidity of the air for 6–7 h after the initiation of the test but afterward

experiment reached to a stage where quantity of water generated approached to a constant mark. The above result was explained as the adhesion force of water to the condensing surfaces exceeds the force of gravity so the amount of water starts to become constant. For variation of relative humidity, current power source and inlet air temperature were kept unchanged. At the initial stage of the investigation, amount of water generated was less at higher flow rates but after stabilization it starts to increase. The experimental investigation explored that two thermoelectric devices were not sufficient to offer the cooling ability and the air was not able to come in contact with the condensing surface for a sufficient time at higher flow rate. The maximum amount water generated was 25.1 g/h with two Peltier devices and less power consumption [21].

Carson et al. conducted a research work in order to utilize the water present as moisture in the air. İn this work, authors depicted the effects of fin orientation of heat sink on the amount of water extracted from atmospheric air. Four different surfaces were brought into examination—a plane plate of aluminum, a PTFE coating equipped aluminum plate, a fanned aluminum plate and a finned aluminum heat sink. All the stated surfaces were oriented vertical and the air with high humidity was forced to flow over the surface in a horizontal direction. Two conditions as clear and unclear of the surfaces were compared for all the cases. PTFE coated plate showed an enhanced rate of water condensation as compared to aluminum plate. Clearing of the surface also enhanced the rate of collection of water. Seven orientation angles starting from 0° with an increment of 15° till 90° were experimented. The orientation of 60° provided the maximum rate of water collection. Several conclusions drawn from the research including an enhancement in the rate of condensation of moisture with the use of hydrophobic materials, clearing the moisture condensing at regular intervals enhanced the performance of the device, the finned heat sinks have a high condensation compared to flat plate heat sinks, with the increase in angles of orientation the water condensing gets filled up in large quantity between the spacing of the fins [22].

Wei et al. conducted a number of experiments for evaluation of an equipment of transportable atmospheric water generator. In the experimental work, two models A and B were designed and fabricated. Their performances were compared for various factors affecting the amount of water generated from the atmospheric air. Both the models were very much similar in their geometrical constructional features. Both the models comprised of a humidifier, a mixing assembly, an air conduit and a thermoelectric cooling device for water generation. Air channels worked to transport the air through the mixing assembly on the thermoelectric cooling device. Humidifier worked to control the moisture in the air. Thermoelectric device possessed a hot side and a cold side on the basis of Peltier effect. Both the sides have extended surfaces to promote rate of convection heat transfer. The cold surface brought the temperature of the air near to its dew point which led to the condensation of moisture in the air. In model A, the cooled air is bypassed on to the hot side to support the heat rejection from the hot side while in model B, cooled air is discharged directly outside system. Besides it, a hydrophobic substance was employed over the cool side surface fin to enhance the rate of condensation in the air in model A as compared to B. Several equations were incorporated in the work based on the psychometrics to calculate the amount of

water generated and it was compared with the experimental observed values with the help of statistical graphs. The observations were taken for a test run of 10 h and the graphical comparison denotes a range of deviation between calculated and measured values. The calculated values were far above than the measured experimental values for the first 6 h run of the procedure. During the first hour the measured values ascend in a slow manner, increased in a fast manner for 2–5 h, the slope of the increment was sharp in the 5–6 h and afterward measured and calculated values have no range of differences. During the first hour, the process was just initiated so the amount was less, as the process progressed the rate of condensation got increased, the effect of gravity and air turbulence together contribute to the increased rate of condensation of moisture into water droplets. For the experimental work, an additional hydrophobic material is employed to enhance the rate of condensation. To acquire the variation of relative humidity, the airflow rate was kept constant and low. It was noticed that the amount of water accumulated due to condensation of moisture in the air gets increased up. The model A has a higher rate of condensation than model B for the above-stated variations. Graphical variation of rate of water accumulation was drawn with changing the rate of flow of air while the other parameters were kept unchanged. The yield of water was increased with increased airflow rates; it was higher for model A than B due to hydrophobic material [23] (Fig. 7).

Sajil et al. carried out an investigation to derive water from condensing the moisture present in the air. The investigation involved computational design and a model was assembled on that basis. Four Peltier devices (TEC 12706) were used for the research work carried out. The cooling draft fans were used to cool the moist air and also to create a vacuum for the moist air to enter the assembly. As the experiment was

The cross section A-A

1 – Humidified Chamber	2 – Fan	3 – Hygrographs (inlet & outlet)	4 – Room air
5 – Thermal Slug (cold side)	6 – Water Pan	7 – Thermal Slug (hot side)	8 – Cooling fan
9 – Outlet Air	10 – Humidifier		
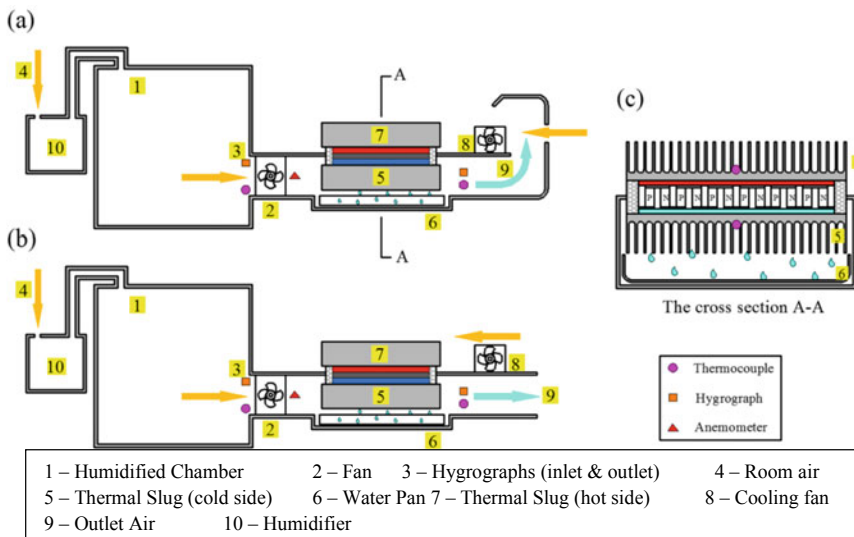
Fig. 7 Schematic diagram of Peltier module based water generator by He Wei et al. [23]

carried out the Peltier devices were provided the EMF the water starts condensing at the colder side and starts to accumulate over the surface, which decreases the rate of heat transfer and reduces the amount of moisture condensing, to prevent this to happen a wiping mechanism was incorporated in the assembly. The dew point temperature calculations were made using the data of the humidity of the air, temperature of the ambient air, and other parameters. At the completion of the experimental work the rate of work output of the assembly was recorded which was the amount of moisture condensing per unit time and it appeared as 5 mL/h. The results were not found to be very satisfactory but was a great attempt to cater the needs of the areas where a lot of lives faces the threat of scarcity of water [24].

Kadhim et al. executed an experimental research for deriving the water present in a moist air. Experiments were performed on an atmospheric water generator in which source of power was solar energy and the device for accumulation of water was based on the Peltier effect. The experimental prototype was build up on a small scale and only single thermoelectric Peltier module was used. The set up used in this experimental investigation includes a thermoelectric Peltier device, a finned heat sink, a fan, a cold side conical fin attached on the cold side of the Peltier module, a solar panel with a charge storage battery and a structural support to grasp and balance all these components. The experimentation aimed to determine the amount of moisture condensing from the air for that it includes variation of airflow velocities, relative humidity and temperature of the dry air. In the Peltier device as it receives the current from the power source one part gains temperature while other loses and becomes hot side and cold side, respectively. As the air comes into contact with the cold side and its temperature approaches dew point condensation of the air begins. A large number of observations were done for deriving any conclusion regarding the variation of the parameters on the amount of moisture condensing from the air. When airflow velocity was varied, the temperature and the relative humidity of the air were kept constant and the observations was recorded in the patterns of graphs. The graph for the variation of airflow velocity was plotted at 65% relative humidity for air temperatures 27 °C and 31 °C and an airflow velocity of 1 m/s produced satisfactory result of 10 mL/h of water condensing from the air. When the relative humidity was varied, it was observed that quantity of water generated almost gets constant with slow deviation as the relative humidity reaches 65% but when the air temperature was raised up the rate of condensation of moisture reaches double at 20 mL/h. The outcome of variation of air temperature is recorded with the time taken by the cooler surface to reach dew point of air and it was resulted into an increase of time required. To design an optimum surface for the further the experiment was concluded with the remarks that to improve the efficiency of the system more number of thermoelectric Peltier modules should be used [25].

4 Mathematical Analysis of Solar Assisted Absorption Method for Atmospheric Water Extraction

In this type of system, the desiccant solution is prepared by mixing of salt (e.g. $CaCl_2$) in distilled water. İf the mass of salt is 'm_s' and mass of distilled water is 'm_w', the total mass of desiccant solution given as:

$$m_{sol} = m_s + m_w \tag{1}$$

also,

$$X = \frac{m_s}{m_{sol}} \tag{2}$$

where 'X' is the fraction of amount of salt in desiccant solution.

The performance of system is primarily based on the rate of absorption and regeneration. The rate of absorption (G_a) and the rate of regeneration (G_r) can be calculated as [26]:

$$G_a = (m_{Sol} + m_1)\frac{d\omega}{dt} \tag{3}$$

$$G_r = m_{Sol}.\frac{d\omega}{dt} \tag{4}$$

Here, m_1 is the mass of water vapors absorbed by the desiccant in the nighttime and ($d\omega/dt$) is rate of change of moisture content. The maximum amount of water generated will be equals to m_1 when the complete water vapors absorbed by desiccant are regenerated and stored in the form of water.

The efficiency of the solar assisted absorption-based water extraction system can be estimated using the following formula:

$$\eta = \frac{M_w L}{I A(\tau\alpha)} \tag{5}$$

where

M_w mass of water produced
L Latent heat of water at mean bed temperature
I Intensity of solar radiation
A aperture area
T transmissivity
α absorptivity.

The above analysis is valid only in case of absorption method. For AWG with peltier modules, thermoelectric principles are used.

5 Conclusions

The present work has tried to summarize the different solutions to the scarcity of fresh drinkable water at remote locations. In this chapter, various methods of atmospheric water extraction have been presented. Mainly, solar assisted adsorption—regeneration or absorption—regeneration-based water extraction methods and water extraction methods using Peltier modules have been presented.

Based on the review, the adsorption method is less effective than the absorption method, as absorbents require less regeneration temperature in comparison with adsorption methods. Also the chances of mixing of dirt and dust with collected water vapors are greater in case of adsorption method. In a solar assisted absorption method, composite of $CaCl_2$ with sand bed can be effectively used as desiccant material which should absorb the water vapors up to saturated condition at the nighttime. The speed of air, surrounding temperature and the concentration of desiccant should be higher at the nighttime operation. Humidity condition also should be higher (not less than 20% relative humidity). The surface area of desiccant bed should also be higher so that maximum amount of moisture can be absorbed from the surrounding air. Once, the desiccant absorb water vapors from humid air up to saturated limit, it must be placed in an insulated box. In the daytime, solar radiations are impinged on the desiccant material in such a way that water vapors evaporate and then stored in a receiver and then water vapors are condensed into fresh water. For the better performance of this system in daytime, the surrounding air temperature and the solar irradiation should be higher and concentration and mass flow rate of desiccant should be less. It can be concluded that the quality of water produced through these methods can be safely used for drinking purpose. Still future research should be focused on chemical analysis of water produced through such methods, as when the higher ambient condition prevails, the concentration of desiccant can be high and it may possibly question the quality of water.

In this paper, a method of atmospheric water extraction using Peltier modules has also been presented. In this method, Peltier modules are arranged and incorporated with heat and cold sink fins, fan and an external power source to bring down the air to its dew point and condense the moisture present in the humid air. Future efforts should focus on design optimization of the system in such a way that more contact surface area is exposed to air. There is a need to enhance the rate of drop-wise condensation and there should be less adhesive force between contact surface and condensed water drops. Some experimental and computational works were also reviewed to discuss the Peltier effect on water generation from air. This method involves high energy consumption in comparison with absorption method. Future research should be focused to make this method cost-effective and to minimize the effects of various environmental parameters on system. With these modifications, the methods explained in the paper would be viable options to deal with the scarcity of fresh water at remote locations.

References

1. Uche, J., Martínez-Gracia, A., Círez, F., Carmona, U.: Environmental impact of water supply and water use in a Mediterranean water stressed region. J. Clean. Prod. **88**, 196–204 (2015)
2. Patel, J., et al.: Experimental investigations of atmospheric water extraction device under different climatic conditions. Sustain. Energy Technol. Assess. **38**, 10677 (2020)
3. Alayli, Y., Hadji, N.E., Leblond, J.: A new process for the extraction of water from air. Desalination *67*(C), 227–229 (1987)
4. Abualhamayel, H.I., Gandhidasan, P.: A method of obtaining fresh water from the humid atmosphere. Desalination **113**(1), 51–63 (1997)
5. Aristov, Yu.I., Tokarev, M.M., Gordeeva, L.G., Snytnikov, V.N., Parmon, V.N.: New composite sorbents for solar-driven technology of fresh water production from the atmosphere. Sol. Energy **66**(2), 165–168 (1999)
6. Gad, H.E., Hamed, A.M., El-Sharkawy, I.I.: Application of a solar desiccant/collector system for water recovery from atmospheric air. Renew. Energy **22**(4), 541–556 (2001)
7. Kabeel, A.E.: Water production from air using multi-shelves solar glass pyramid system. Renew. Energy **32**(1), 157–172 (2007)
8. Ji, J.G., et al.: New composite adsorbent for solar-driven fresh water production from the atmosphere. Desalination **212**, 176–182 (2007)
9. Hamed, A.M.: Application of solar energy for recovery of water from atmospheric air in climatic zones of Saudi Arabia. Natural Resour. **2**(1), 8–17 (2011)
10. William, G.E., Mohamed, M.H., Fatouh, M.: Desiccant system for water production from humid air using solar energy. Energy **90**, 1707–1720 (2015)
11. Kumar, M., Yadav, A.: Solar-driven technology for freshwater production from atmospheric air by using the composite desiccant material 'CaCl$_2$/floral Foam.' Environ. Dev. Sustain. **18**(4), 1151–1165 (2015)
12. Kim, H., Yang, S., Rao, S.R., Narayanan, S., Kapustin, E.A., Furukawa, H., Umans, A.S., Yaghi, O.M., Wang, E.N.: Water harvesting from air with metal-organic frameworks powered by natural sunlight, Science (2017)
13. Srivastava, S., Yadav, A.: Water generation from atmospheric air by using composite desiccant material through fixed focus concentrating solar thermal power. Sol. Energy **169**, 302–315 (2018)
14. Talaat, M.A., Awad, M.M., Zeidan, E.B., Hamed, A.M.: Solar-powered portable apparatus for extracting water from air using desiccant solution. Renw. Energy **119**, 662–674 (2018)
15. Elashmawy, M.: Experimental study on water extraction from atmospheric air using tubular solar still. J. Clean. Prod. (2019)
16. Kabeel, A.E., Abdulaziz, M., El-Said, E.M.S.: Solar-based atmospheric water generator utilisation of a fresh water recovery: a numerical study. Int. J. Ambient Energy (2014)
17. Suryaningsih, S., Nurhilal, O.: Optimal design of an atmospheric water generator (AWG) based on thermo-electric cooler (TEC) for drought in rural area. AIP Conf. Proc. **1712**, 030009 (2016)
18. Joshi, V.P., Joshi, V.S., Kothari, H.A., Mahajan, M.D., Chaudhari, M.B., Sant, K.D.: Experimental investigations on a portable fresh water generator using a thermoelectric cooler. Energy Procedia **109**, 161–166 (2016)
19. Pontious, K., Weidner, B., Guerin, N., Dates, A., Pierrakos, O., Altaii, K.: Design of an atmospheric water generator: harvesting water out of thin air. In: IEEE Systems and Information Engineering Design Conference (SIEDS '16) (2016)
20. Anandhulal, A., Athul, B.B.: Atmospherıc water generation. Int. J. Sci. Eng. Res. **7**(4) (2016)
21. Liu, S., He, W., Hu, D., Lv, S., Chen, D., Wu, X., Xu, F., Li, S.: Experimental analysis of a portable atmospheric water generator by thermoelectric cooling method. Energy Procedia **142**, 1609–1614 (2017)
22. Hand, C.T., Peuker, S.: An experimental study of the influence of orientation on water condensation of a thermoelectric cooling heat sink. Heliyon **5**, e02752 (2019)
23. He, W., Yu, P., Hu, Z., Lv, S., Qin, M., Yu, C.: Experimental study and performance analysis of a portable atmospheric water generator. Energies **13**, 73 (2019)

24. Sajil, V.P, Ameer, E.A, Anfal, P, Aswin, V.C., Masood, B.I., Ahamad, F., Vivek, V.N.: Portable atmospheric water generator. Int. Res. J. Eng. Technol. (IRJET) **07**(04) (2020)
25. Kadhim, T.J., et al.: Experimental study of atmospheric water collection powered by solar energy using the Peltier effect. IOP Conf. Ser.: Mater. Sci. Eng. **671**, 012155 (2020)
26. Kumar, A., Chaudhary, A., Yadav, A.: The regeneration of various solid desiccants by using a parabolic dish collector and adsorption rate: an experimental investigation. Int. J. Green Energy **11**(9), 936–953 (2014)

Energy Science and Engineering

Single Slope Single Basin Active Solar Still Integrated with ETCs: A Review

Manish Sanserwal and **Pushpendra Singh**

1 Introduction

With the increasing events of climate change in the world, lots of places face water scarcity and waterflood. Both the cases are not suitable for living creatures on earth because water scarcity increases the water deficiency in living creature body and flooded water become so much contaminated that unable to use for drinking purposes. According to a report presented by United Nations International Children's Emergency Fund (UNICEF) and World Health Organization (WHO) in 2015, it was found that about 663 million peoples of the world are still using untreated drinking water, which includes contaminated water from wells, springs (due to heavy rain) and unsafe surface water. According to the international energy agency, it is expected that the power consumption of the world increases by up to 35% by 2035, and for meeting this, water requirement also increases by 35%. Most of our freshwater resources are available in glaciers and ice caps foam, in which only 1.2% water is surface and other freshwater. Therefore, there is a strong requirement coming for water purification from saline or contaminated water.

Today, we are using lots of technologies for purification of water like activated carbon, electrodeioinzation, ion exchange, reverse osmosis, nano-filtration, submicron filtration, ultraviolet, etc. All these technologies required electrical energy for working, which greatly affect the environment as it is powered by fossil fuels (mostly from non-renewable resources) which again add up environmental pollution [1], and if it produced from the sun (Solar cell), then this does not remain economical.

M. Sanserwal · P. Singh (✉)
Department of Mechanical Engineering, Delhi Technological University, Delhi 110042, India
e-mail: dr.psinghs@gmail.com

M. Sanserwal
Department of Mechanical Engineering, Galgotia College of Engineering and Technology, Greater Noida, UP 201306, India

For attaining both requirements of water purification and lower energy consumption, solar still is the most suitable purification system.

Solar still is an environment-friendly attractive option to attain drinkable water from available saline/contaminated water and can be successfully used domestically. Fabricating of solar still can be done from locally available material which is also low cost, easy to operate and maintain [2]. Lots of advantages are there in using solar still over other water purification technologies, in which some of them are no need of membranes, pre or post filters, non-renewable power sources etc., and these advantages lead to the low initial investment cost and approximately no impact on the environment. Solar still works on a natural process whose working principle is same as of rain system. In the solar still, water evaporates from the basin due to absorption of sunlight and condensate on the inclined glass cover (also called condensing glass) used for the covering of solar still and finally, collected in the collecting trough which is discharged in a measuring flask. The amount of water thus collected is not up to mark concerning time, and this is the only disadvantage of solar still and makes its performance lower as compared to other purification systems. Publicly usage of solar still can be increased by enhancing its water yield productivity and also by decreasing its cost per litres [3]. However, distilled water productivity of solar still depends upon lots of parameters (solar radiations, ambient temperature, air velocity, solar still design, etc.), which ultimately affect the evaporation and condensation of water [4].

Lots of researchers studied different type of passive (stepped, spherical, hemispherical, V-shape, pyramid, wick type, tubular, etc.) [5–12] and active solar still (incorporated with reflector, PV/T system, flat plate, or evacuated tube, or inverted absorber solar concentrators and heat exchanger) [13–17] for the improvement in yield productivity. Whereas, various single-effect and multi-effect type of passive and active solar still are studied by Kumar et al. [18]. Lots of useful review on active solar stills have been done representing different aspects of solar stills like the use of reflectors, photovoltaic and integrated PV/T [15, 19, 20]. This paper reviews the different active solar still with evacuated tube collector developed by the number of researchers with a comparative study and also included the economic analysis of various active solar still.

2   Various Single Basin Single Slope Active Solar Still with ETC

The water temperature can be increased in conventional solar still by the means of additional solar–thermal technologies, which further increases the productivity of solar still. Whereas, evacuated tubular collector (ETC) is used for water heating purposes. Both systems (solar still and ETC) integration helps in improving the evaporation rate and yield output from a solar still.
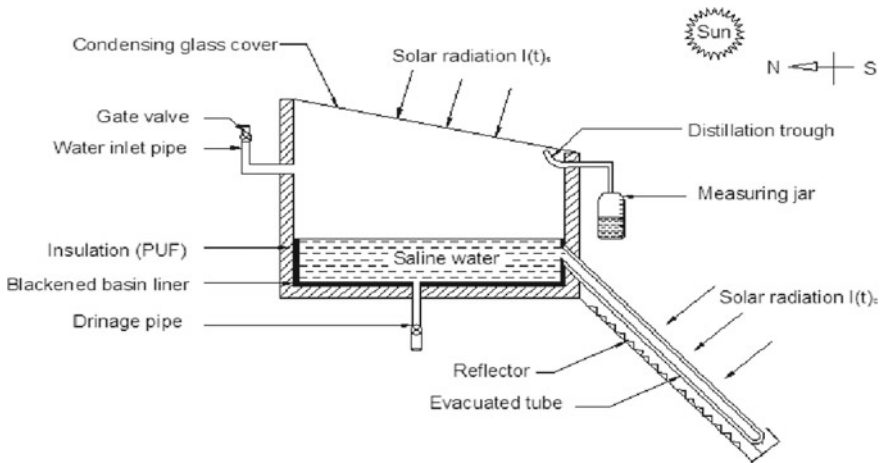
Fig. 1 Schematic arrangement of experimental set-up [21]

Sampathkumar et al. [21] investigated an active solar still incorporated with ETC and reflector plates (just below the ETCs) of corrugated structure as shown in Fig. 1. Proposed experimental still made up of aluminium with black paint on the basin and a thermal model was also developed. Also studies the effect of water depth, various heat transfer coefficients, temperature and solar radiation on the productivity of solar still. Results revealed that average daily production and energy payback time (EBT) were 72% (as compared to simple solar still) and 235 days, respectively.

An ETC integrated with single slope active solar still (EISS) has been analysed experimentally by Dev et al. [22] as shown in Fig. 2. The main purposes of EISS system are recovering the heat loss (occur off-sunshine time) for getting more distilled water from the solar still, develop a thermal model to validate experimental results and compare it with single slope solar still. Hence, this system can be used for both distillations as well as heating purpose. From the results, it is revealed that maximum overall and annual average thermal efficiency has been found 30.1% and 21.3%, respectively, on 16 May 2008 for EISS system. Also, annual distilled water produced by EISS system is 630 kg/m^2 as compared to single slope SS of 327 kg/m^2. Further, Sampathkumar et al. [23] also investigated a solar still integrated with ETC (tubes are in a horizontal direction) and without using the pump (natural mode) and compared the results with a fabricated passive solar still for comparative studies (Fig. 3). An increment in yield water productivity is found to be 129% and 83% during sunshine hours and night hours, respectively, when compared to passive solar still.

A thermal analysis of solar still is directly coupled with ETC in natural mode and forced mode (with modified geometry) done by Singh et al. and Kumar et al. [24, 25] as shown in Fig. 4. Due to disfavour condition (two water streams in tube move in opposite direction) occurs in natural mode during thermal energy extraction, force mode has been analysed later for better heat removal and avoid the effects of
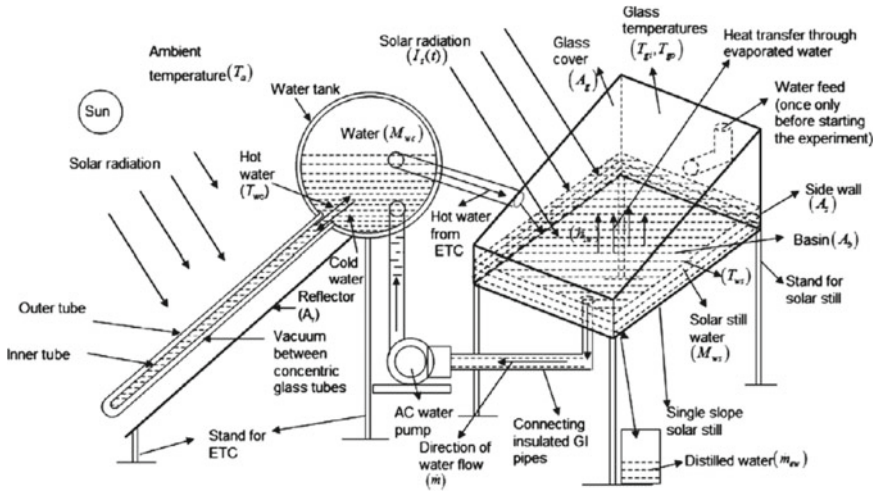
Fig. 2 Experimental set-up of EISS [22]
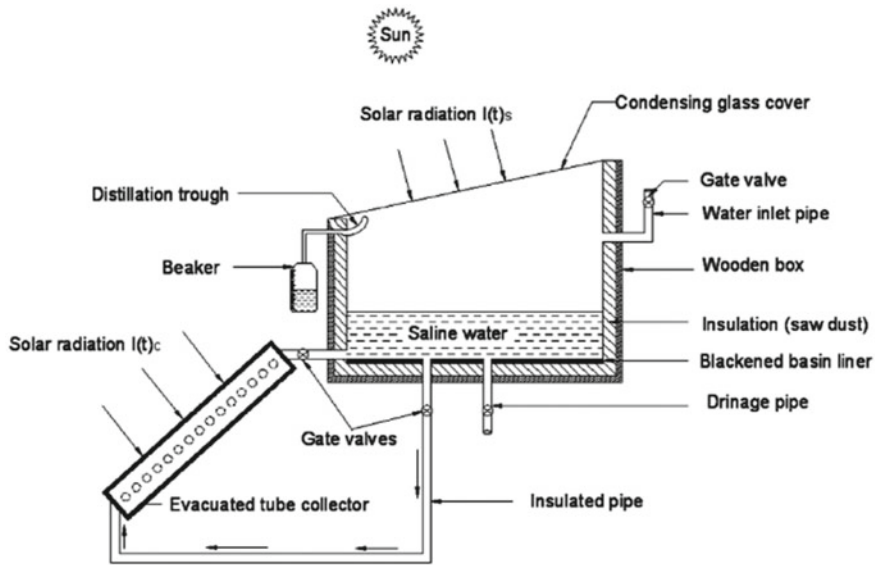
Fig. 3 Schematic of an active solar still with horizontal ETC [23]

stagnation and internal recirculation of cold water in the reservoir. Results revealed that annual yield for forced mode is 567.3 kg per m² area (radiation collector area) and it is higher than the natural mode. Moreover, forced and natural mode efficiency is found to be 33.8% and 5.1–54.4%, respectively, based on energy analysis; and 2.6% and 0.15–8.25%, respectively, based on exergy analysis.
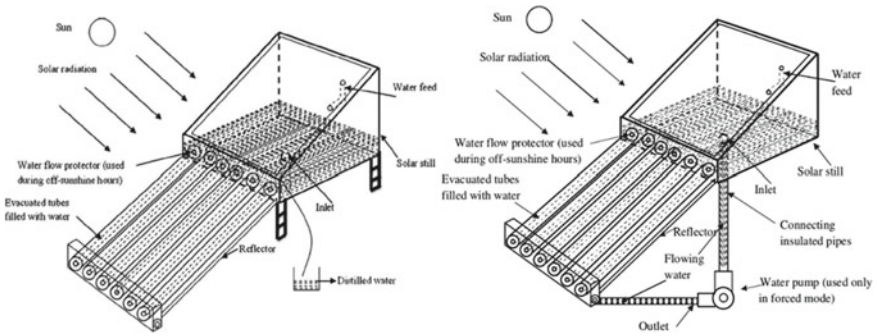
Fig. 4 Schematic diagram of EISS system in natural mode (left) and forced mode (right) [24, 25]

Panchal et al. [26, 27] experimentally analysed single slope solar still (directly coupled with vacuum tubes) over a whole year (Fig. 5) and also compared its results
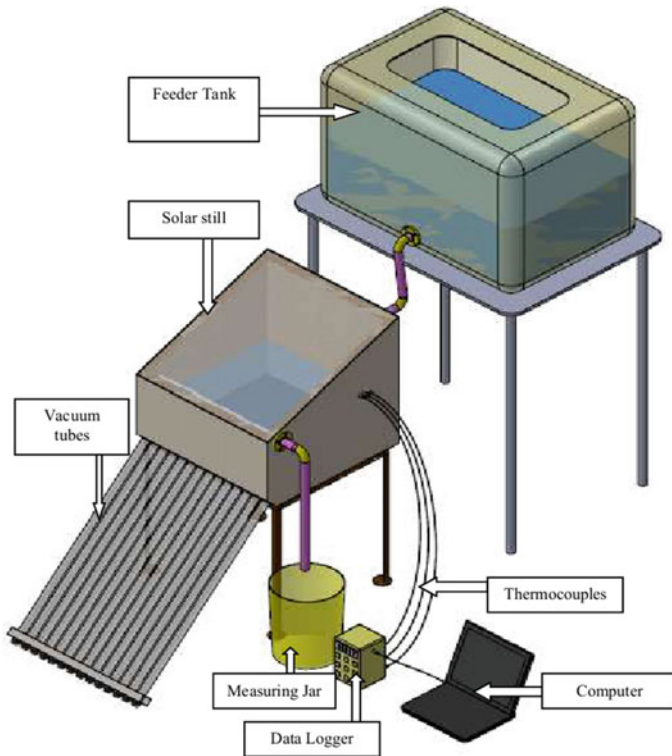
Fig. 5 Schematic arrangement of solar still with vacuum tubes [26, 27]

Fig. 6 Solar distillation system with ETC [28]

with other similar work based on distilled output. Results revealed a closed relationship between experimental and theoretical values. Moreover, EBT and the annual cost of water were found to be 176 days and 0.716 INR per litre, respectively.

An experimental study was investigated by Issa et al. [28] to evaluate the performance feasibility of a solar still under working conditions of passive and active mode (coupled with ETC using a parabolic solar energy collector) with and without using insulation (for still) as shown in Fig. 6. Results showed that, yield output of the solar still using ETC increased by a factor of 2.63 with an increment of water temperature (at least 20 °C). As per the author, EBT of 6 years is feasible for the farmers for using it in their farmland. A cost reduction of 16.8% also observed with a solar still integrated with ETC as compared to the passive solar still system.

Singh [29] theoretical investigated a single slope solar still (SS) integrated with N (found max. 12 in number) ETC (N-ETC-SS) and compared it with SS integrated with N photovoltaic thermal (PVT) flat plate collectors (N-PVT-FPC-SS), SS integrated with N-PVT compound parabolic concentrator collectors (N-PVT-CPC-SS) and conventional SS (CSS) on the basis of energy metrics (Fig. 7). Results revealed that, for the proposed system N-ETC-SS, the values of EPT are lowered by 40.38%, 102.78% and 166.58%; life cycle conversion efficiency and energy production factor are higher by 44.83%, 65.52% and 75.86%; and 28.57%, 50.79% and 61.90% than N-PVT-FPC-SS, CSS and N-PVT-CPC-SS, respectively, on the basis of exergy.

A solar still coupled with ETC using waste engine oil as a working fluid (natural flow) is experimentally investigated by Bhargva et al. [30, 31] as shown in Fig. 8. Further, for improving its yield output, four cases studied by coupling solar still with heat exchanger (HE), internal reflector (IR) and condenser and compared it with conventional passive solar still at different water depths (4 cm, 5 cm and 6 cm). Experimental results revealed that, modified solar still (consist of HE + IR + condenser) achieved maximum daily efficiency of 33.4%, whereas it is only 30.5% for still
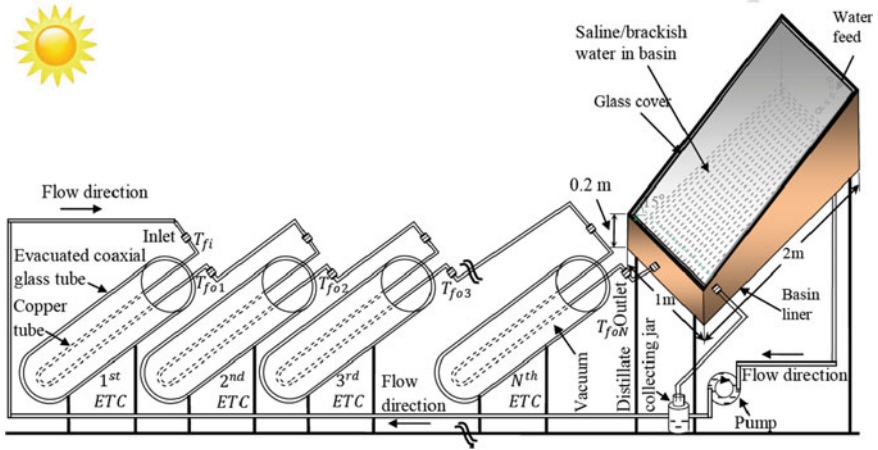
Fig. 7 Schematic arrangement of N-ETC-SS [29]

Fig. 8 Photograph of solar still using ETC with heat exchanger [30, 31]

Fig. 9 Photograph of solar still with and without ETC [32]

with HE alone and also, heat exchanger effectiveness of 0.58 at 4 m water depth. Recently, Shehata et al. [32] improve the yield productivity of a single slope solar still incorporated with the internal reflector by using ultrasonic humidifiers (USH is six in number), phase change material (PCM) and ETC (for hot water spraying inside still). Four cases were investigated by embedding different component in solar still: PCM; USH and PCM; ETC and PCM and forth case with PCM and USH combined with ETC (Fig. 9). From results, it is found that forth case having maximum daily distilled productivity of 5.34 and 7.4 kg and daily productivity in case USH integrated with ETC improved by 25 and 44% for 25 and 35 mm water depths.

Literature revealed that, yield increases with the increase of numbers and size of ETC used and decreasing water depth (during sunshine hours) in still, whereas high water depth required in off-sunshine hours due to higher storage effect (sensible heat storage capacity of water) and volumetric effect. However, it is also observed that, heat exchanger inlet temperature is independent of water depths. Moreover, ETC performance declines (up to 60%) to a great extent as the transmittance ratio of ETC glass declines (0.98–0.6). Table 1 shows general specification of various active solar stills.

3 Economic Analysis of Some Active Solar Still with ETC

Initially, cost analysis of water desalination system was introduced by Govind and Tiwari [33]. Later, Kabeel et al. [34] and El-Bialy et al. [35] presented economic analysis of different configuration of passive and active solar still. There are lots of

Table 1 General detail of various active solar still integrated with ETC

S. No.	Daily Yield (l/m²)	No. of ETC tube	Still glass angle (°)	ETC angle (°)	Productivity increment (%)	Glass inside temp	Max water temp	Ambient max temp. (°C)	Solar radiation on still	ETC (W/m²)	Location
[21]	2.472	8	11	45	72	55	62	35	1100	–	Tamil Nadu, India (11° N; 77° E)
[22]	3.328	24	30	40	92	63.9	90.8	25	680	650	New Delhi, India (28°35′ N, 77°12′ E)
[24]	3.8	10	30	45	–	90	93	39	610	560	JMI, New Delhi, India (28.5623° N, 77.2804° E)
[25]	3.9	10	15	45	6	67	89.8	39	For summer 610 / For winter 640	560 / 680	New Delhi, India (28.69° N, 77.15° E)
[27]	4.49	14	23	45	97.6	–	90	40	810	840	Gujarat, India (23° 35′ N, 72° 22′ E)
[28]	3.6	9	30	–	1571	62	80	42	870	870	Canyon, West Texas (32.7091° N, 97.9076° W)

(continued)

Table 1 (continued)

S. No.	Daily Yield (l/m^2)	No. of ETC tube	Still glass angle (°)	ETC angle (°)	Productivity increment (%)	Glass inside temp	Max water temp	Ambient max temp. (°C)	Solar radiation on still	ETC (W/m^2)	Location
[29]	12	N (max. 12)	15	30	226.5	80	95	42	950	950	New Delhi, India (28°35′ N, 77°12′ E)
[30]	7.38	15	30	30	138.9	56	87.5	43	920	–	NIT Kurukshetra, India (29.9490° N, 76.8173° E)
[32]	7.4	15	30	–	44.45	58	73	37	1090	–	Tanta, Egypt (30.79° N, 30.99° E)

Table 2 Economic analysis formulas applied for most of the still system

Economic method	Formulas
Present capital investment (P)	CRF = $i(1 + i)n/[(1 + i)n - 1]$
Capital recovery factor (CRF)	AFC = P(CRF)
Annual first cost (AFC)	SFF = $(i)/[(1 + i)n - 1]$
The sinking fund factor (SFF)	ASV = (SFF) $\times$ S (Salvage value)
The annual salvage value (ASV)	AC = AFC + AMC − ASV
Annual maintenance cost (AMC) = 15% of AFC	AC/L = AC/M (Annual Yield)
Annual cost (AC)/m^2	AUE = M $\times$ 0.65
The annual cost per litre (AC/L)	AC/kWh = (AC/m^2) $\times$ AUE
Annual useful energy (AUE)	S = $(x \times P)$
Annual cost/kWh	
Percentage of degradation rate (x)	
Cost per litres (CPL)	

cost included in economic analysis of the solar still like capital or fabrication cost, operational cost, maintenance cost (including the subsidy if provided by government). Whereas, the fabrication cost includes frame cost, sheets cost (for making still), insulation, glass and pipe cost. Also, with the increase in the rate of interest, a decrement in net cost of the system is observed due to increment of capital recovery (CR) and decrement of SFF. Economic analysis parameters can be expressed in Table 2 by Sanserwal et al. [36].

In this analysis, assumed values of i (interest per year), n (number of life years), sunny days (number of days in which availability of sun energy was there) and x are 12%, 10, 260 and 20%, respectively, taken for calculation and also prepared a excel program for the same. Table 3 shows a small overview of estimated costs analysis for some active solar stills with ETC.

Single slope solar still with materials like internal reflector, ultrasonic humidifiers, PCM and ETC shows excellent performance. These material contributions to overall price of the solar still are not as high as compared to increment in yield output from the still.

Table 3 Economic analysis of solar still with ETC

S. No.	P	M (L/m^2)	CRF	FAC	SSF	S	ASV	AMC	AC	CPL
[21]	244.89	642.72	0.177	43.342	0.057	48.978	2.791	6.5012	47.05	0.0732
[22]	694.64	865.28	0.177	122.94	0.057	138.928	7.917	18.441	133.5	0.1542
[25]	380.95	1014	0.177	67.422	0.057	76.19	4.342	10.113	73.19	0.0722
[27]	158.32	1167.4	0.177	28.02	0.057	31.664	1.804	4.203	30.42	0.0261
[28]	550	936	0.177	97.341	0.057	110	6.268	14.601	105.7	0.1129
[30]	105.8	1918.8	0.177	18.725	0.057	21.16	1.206	2.8087	20.33	0.0106
[32]	421.6	1924	0.177	74.617	0.057	84.32	4.805	11.192	81	0.0421

CPL has a great importance in economic analysis of the solar still because it gives us overall performance criteria. Even some solar still has larger distilled water output but due to their higher capital cost, CPL come out with higher value. Solar still with heat exchanger and ETC [30] shows the lowest CPL and establishment cost of 0.0106 $/l and $ 105.8, respectively.

It is also found that solar still with ETC (indirectly connected with forced flow) [22] has highest overall cost of $ 694.64 which is 82.34% higher than the solar still (directly coupled with ETC) [25] but still has 17.18% less distilled water output.

4 Conclusion

ETC integrated with active single slope single basin solar still used for improving the yield productivity and an economic analysis also carried out for different modification in stills. Above review made some following conclusions:

1. Lower angle of solar still increases the productivity. Whereas, productivity of still inversely depends upon water depth of still (for sunshine hours).
2. Use of natural convection for the circulation of water inside the active solar still integrated with ETC accelerates the scale formation inside the tubes due to saline water. Whereas, forced mode (using pump for flow) overcomes this problem but increases the cost of still with the yield productivity of 6% only.
3. Experimentally higher annual productivity of 1924 l/m^2 is found in a solar still with internal reflectors using ultrasonic humidifiers, PCM and ETC, while lower annual productivity found in EISS system of 642.72 l/m^2
4. Solar still using natural convection with heat exchanger has lowest CPL of 0.0106 $/l, whereas highest CPL of 0.1542 $/l found in solar still using forced mode without heat exchanger.

References

1. Gude, V.G., Nirmalakhandan, N., Deng, S.: Renewable and sustainable approaches for desalination. Renew. Sust. Energ. Rev. **14**, 2641–2654 (2010)
2. Malik, M.A.S., Kumar, A., Sodha, M.S.: Solar Distillation. Pergamon Press, Oxford, UK (1982)
3. Fath, H.E.S., Elsherbiny, S.M.: Effect of adding a passive condenser on solar still performance. Energy Convers. Manag. **34**, 63–73(1993)
4. Muthu Manokar, A, Kalidasa Murugavel, K., Esakkimuthu, G.: Different parameters affecting the rate of evaporation and condensation on passive solar still—a review. Renew. Sust. Energ. Rev. **38**, 309–322 (2014)
5. Flendrig, L.M., Shah, B., Subrahmaniam, N., Ramakrishnan, V.: Low cost thermoformed solar still water purifier for D&E countries. Phys. Chem. Earth **34**, 50–54 (2009)
6. Aybar, H.S., Egelioglu, F., Atikol, U.: An experimental study on an inclined solar water distillation system. Desalination **180**, 285–289 (2005)

7. Ahsan, A., Fukuhara, T.: Mass and heat transfer model of Tubular Solar Still. Solar Energy **84**, 1147–1156 (2010)
8. Farshad, F.T., Dashtban, M., Hamid, M.: Experimental investigation of a weir-type cascade solar still with built-in latent heat thermal energy storage system. Desalination **260**, 248–253 (2010)
9. Tanaka, H.: Tilted wick solar still with flat plate bottom reflector. Desalination **273**, 405–413 (2011)
10. Arunkumar, T., Denkenberger, D., Ahsan, A., Jayaprakash, R.: The augmentation of distillate yield by using concentrator coupled solar still with phase change material. Desalination **314**, 189–192 (2013)
11. Ansari, O., Asbik, M., Bah, A., Arbaoui, A., Khmou, A.: Desalination of the brackish water using a passive solar still with a heat energy storage system. Desalination **324**, 10–20 (2013)
12. Gad, H.E., El-Din, S.S., Hussien, A.A., Ramzy, K.: Thermal analysis of a conical solar still performance: an experimental study. Sol. Energy **122**, 900–909 (2015)
13. Tiwari, G.N., Yadav, J.K., Singh, D.B., Al-Helal, I.M., Abdel-Ghany, A.M.: Exergoeconomic and enviroeconomic analyses of partially covered photovoltaic flat plate collector active solar distillation system. Desalination **367**, 186–196 (2015)
14. Shafii, M.B., JahangiriMamouri, S., Lotfi, M.M., JafariMosleh, H.: A modified solar desalination system using evacuated tube collector. Desalination **396**, 30–38 (2016)
15. Omara, Z.M., Kabeel, A.E., Abdullah, A.S.: A review of solar still performance with reflectors. Renew. Sustain. Energy Rev. **68**, 638–649 (2017)
16. Pounraj, P., Prince Winston, D., Kabeel, A.E., Praveen Kumar, B., Muthu Manokar, A., Ravishankar Sathyamurthy, S., Christabel, C.: Experimental investigation on Peltier based hybrid PV/T active solar still for enhancing the overall performance. Energy Convers. Manage. **168**, 371–381 (2018)
17. Tiwari, G.N., Sangeeta, S.: Performance evaluation of an inverted absorber solar still. Energy Convers. Manag. **39**(3–4), 173–180 (1998)
18. Kumar, P.V., Kumar, A., Prakash, O., Kaviti, A.K.: Solar stills system design: a review. Renew. Sustain. Energy Rev. **51**, 153–181 (2015)
19. Muthu Manokar, A., Prince Winston, D., Kabeel, A.E., El-Agouz, S.A., Sathyamurthye, R., Arunkumar, T., Madhue, B., Ahsang, A.: Integrated PV/T solar still—a mini-review. Desalination **4351**, 259–267 (2018)
20. Kamlesh Pansal, K., Ramani, B., Sadasivuni, K.K., Panchal, H., Manokar, M., Sathyamurthy, R., Kabeel, A.E., Suresh, M., Israr, M.: Use of solar photovoltaic with active solar still to improve distillate output: a review. Groundwater Sustain. Dev. (2020). https://doi.org/10.1016/j.gsd.2020.100341
21. Sampathkumar, K., Arjunan, T.V., Senthilkumar, P.: Single basin solar still coupled with evacuated tubes—thermal modeling and experimental validation. Int. Energy J. **12**, 53–66 (2011)
22. Dev, R., Tiwari, G.N.: Annual performance of evacuated tubular collector integrated solar still. Desalin. Water Treat. **41**, 1–3, 204–223 (2012). https://doi.org/10.1080/19443994.2012.664715
23. Sampathkumar, K., Arjunan, T.V., Senthilkumar, P.: The experimental investigation of a solar still coupled with an evacuated tube collector. Energy Sources, Part A Recov. Utiliz. Environ. Effects **35**(3), 261–270 (2013). https://doi.org/10.1080/15567036.2010.511426
24. Singh, R.V., et al.: Performance of a solar still integrated with evacuated tube collector in natural mode. Desalination **318**, 25–33 (2013)
25. Kumar, S., et al.: A solar still augmented with an evacuated tube collector in forced mode. Desalination **347**, 15–24 (2014)
26. Panchala, H.N., Thakkar, H.: Theoretical and experimental validation of evacuated tubes directly coupled with solar still. Thermal Eng. **63**(11), 825–831 (2016). https://doi.org/10.1134/S0040601516110045

27. Panchal, H., Sathyamurthy, R., Pandey, A.K., Kumar, M., Arunkumar, T., Patel, D.K.: Annual Performance analysis of Single basin passive solar still coupled with evacuated tubes: Comprehensive study in climate conditions of Mahesana, Gujarat. Int. J. Ambient Energy (2017). https://doi.org/10.1080/01430750.2017.1378720
28. Issa, R.J., Chang, B.: Performance study on evacuated tubular collector coupled solar still in West Texas climate. Int. J. Green Energy (2017). https://doi.org/10.1080/15435075.2017.1328422
29. Singh, D.B.: Energy metrics analysis of N identical evacuated tubular collectors integrated single slope solar still. Energy (2018). https://doi.org/10.1016/j.energy.2018.01.130
30. Bhargva, M., Yadav, A.: Experimental comparative study on a solar still combined with evacuated tubes and a heat exchanger at different water depths. Int. J. Sustain. Eng. (2019). https://doi.org/10.1080/19397038.2019.1653396
31. Bhargva, M., Yadav, A.: Productivity augmentation of single-slope solar still using evacuated tubes, heat exchanger, internal reflectors and external condenser. Energy Sources, Part A Recov. Utiliz. Environ. Effects (2019). https://doi.org/10.1080/15567036.2019.1691291
32. Shehata, A.I., Kabeel, A.E., Khairat Dawood, M.M., Elharidi, A.M., Abd_Elsalam, A., Ramzy, K., Mehanna, A.: Enhancement of the productivity for single solar still with ultrasonic humidifier combined with evacuated solar collector: an experimental study. Energy Convers. Manage. **208**, 112592
33. Govind, J., Tiwari, G.N.: Economic analysis of some solar energy systems. Energy Convers. Manage. **24**, 131–135 (1984)
34. Kabeel, A.E., Hamed, A.M., El-Agouz, S.A.: Cost analysis of different solar still configurations. Energy **35**, 2901–2908 (2010)
35. El-Bialy, E., Shalaby, S.M., Kabeel, A.E., Fathy, A.M.: Cost analysis for several solar desalination systems. Desalination **384**, 12–30 (2016)
36. Sanserwal, M., Kumar Singh, A., Singh, P.: Impact of materials and economic analysis of single slope single basin passive solar still: a review. Mater. Today Proc. https://doi.org/10.1016/j.matpr.2019.11.289

A Review on Nuclear Energy-Based Hydrogen Production Methods

Kyu Kyu Tin [ID]**, Saumya Swarup** [ID]**, and Anil Kumar** [ID]

Nomenclature

GHG	Greenhouse gas emission
SFR	Sodium cooled fast reactor
Ni–YSZ	Nickel–zirconia
Ir	Iridium
Pt	Platinum
LSM	Strontium-doped lanthanum magnate
UOIT	Ontario Institute of Technology
MW_{th}	Megawatt $\times$ Million times
HYTHEC	Hydrogen thermochemical cycles
JAEA	Japan Atomic Energy Agency
LCA	Life Cycle Assessment
GWP	Global warming potential
AP	Acidification potential
kg CO_2 eq	Kilogram of carbon dioxide equivalent
kg SO_2-eq	Kilogram of sulfur dioxide equivalent

K. K. Tin
Languages Center, Yangon, Myanmar

S. Swarup
Department of Electrical Engineering, Delhi Technological University, Delhi 110042, India

A. Kumar (✉)
Department of Mechanical, Production & Industrial and Automobile Engineering, Delhi
Technological University, Delhi 110042, India
e-mail: anilkumar76@dtu.ac.in

Center for Energy and Environment, Delhi Technological University, Delhi 110042, India

1 Introduction

Nowadays, research momentum is focusing on the hydrogen economy because of worldwide huge energy consumption. In the energy market, clean hydrogen supply is essential. As secondary energy carrier, hydrogen is a potential candidate to meet most green energy demands replacing the hydrocarbon fuel without harming environment. Currently, the global hydrogen production mainly relies on processes that produced by using three various energy sources such as fossil fuels, renewable and nuclear energy (Fig. 1). It is important challenge to produce hydrogen as clean energy from fossil fuels which emit significant amount of GHGs; in the other hands, renewable alternative energy sources consider environmentally friendly to produce green hydrogen but still have to reach sustainable large-scale production. Therefore, nuclear energy is getting more attention because it can run a nuclear reactor without generating carbon dioxide and agree with industrial demand. However, hydrogen production for nuclear energy sector is not currently developed enough, but it will be increased attention as potential energy source because of its no greenhouse emission.

1.1 Nuclear Energy and Its Reactors

An energy which exists between an atoms' nucleus is termed as nuclear energy. A nuclear reactor is used to produce nuclear fission-based high amount of energy using uranium or thorium element. The various kinds of Generation IV nuclear reactors have received increasing attention a high level of inherent safety heat source to produce nuclear-based hydrogen for large industrial sources than previous generations. It will catch technical maturity 2030 because of its highly economical, proliferation resistant and release the lowest waste [1]. For thermochemical production, SFR system is similar to LFR, where sodium replaces leads-bismuth, GFR can produce a secondary steam and MSR have long-term potential because of its low temperature and heat delivered at high. SCWR has a higher thermal efficiency. For hydrogen
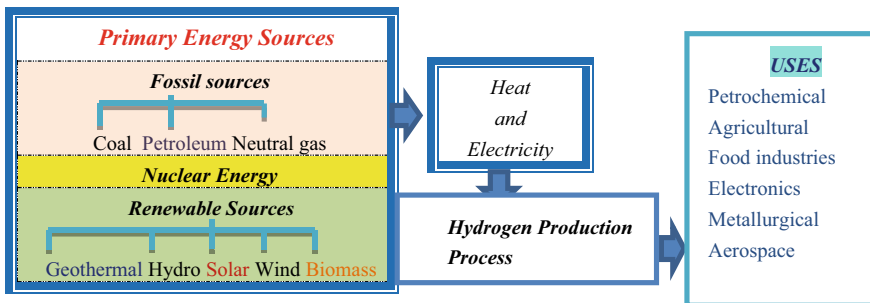
Fig. 1 Hydrogen productions methods from primary energy sources and its uses

production, it can also reduce the challenges of load balancing, either by conventional electrolysis or thermochemical water splitting. Modern version of HTGR, VHTR, can supply energy to several exothermic process, such as steam forming, electrochemical and thermochemical water-splitting processes [2, 3].

1.2 Hydrogen Storage

Hydrogen is storable which is convenient for an energy carrier. In the usage of economic source hydrogen, how to store hydrogen safely, efficiently and economically is one of the most important challenges to be overcome. Liquid hydrogen requires an extra economic cost and a complex technical plant. The good point of cold/cryogenic compression is a higher energy density than compressed gas, but cooling requires an additional energy input. The weakness is to find more economic ways. Stationary hydrogen storage in underground is the most promising materials for future hydrogen storage to play key role in hydrogen economy that can be done in large enclosed areas and kept safely away from any possible dangers [4].

2 Routes to Produce HydrogenVia Nuclear Energy

Herein, the various production pathways of hydrogen from nuclear source are introduced in (Fig. 2).

Electrolysis	Electricity +H_2O(liquid) $\rightarrow H_2$+ O_2(conventional)
	Electricity +H_2O(steam)$\rightarrow H_2$+ O_2 (HTE)
Thermochemical water splitting	Heat +$H_2O \rightarrow$ {cyclic chemical reaction}+ H_2+ O_2
Hybrid thermochemical cycle	Electricity +Heat +$H_2O \rightarrow$ {cyclic chemical reaction}+ H_2+ O_2
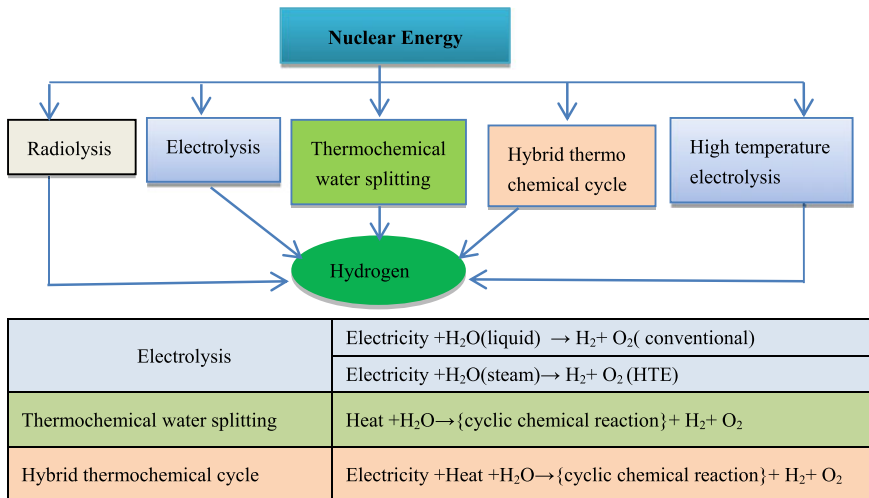
Fig. 2 Hydrogen production pathways

Nuclear radiation exits in nuclear reactors, and nuclear fuel phases processing could be applied directly to produce hydrogen from water. Generated nuclear radiation is changed to high-temperature heat. As seen in Fig. 2, five general methods are described to produce hydrogen. Directly to split water into hydrogen and oxygen, radiolysis uses nuclear radiation, and this is not practical because of its contamination of radioactive materials. To electrolyze the water, water electrolysis uses electricity derived from nuclear radiation, and it is applicable if close to standard value of temperatures. High-temperature steam electrolysis and hybrid thermochemical cycle are known as hybrid using both electricity and high-temperature heat to separate water. Thermochemical splitting directly applies high-temperature heat leading to nuclear energy [5].

Combination of O_2 and hydrogen to produce water and electricity is called electrolysis. Improved electrolysis methods include alkaline electrolysis, PEM and SOE are described in (Fig. 3). High-temperature electrolysis or solid oxide electrolysis cells can operate with steam (700–1000 °C). In SOE electrolysis process, electrode materials present at the anode (LSM) and at the cathode (Ni–YSZ), and then, conducting materials as ceramic proton represent superior ionic conductivity and high efficiency than O_2^- conductor conventionally. PEM electrolysis runs 20–100 °C and transforms liquid water. Electrodes reveal high activity of noble catalysts such as iridium as the anode and platinum Pt as the cathode. Alkaline water electrolysis operates lower temperatures such as 30–80 °C with aqueous solution KOH or NaOH as electrode, and nickel uses as electrode materials because of its availability combined with reasonable price and high activity. The interesting points are that SOE has the
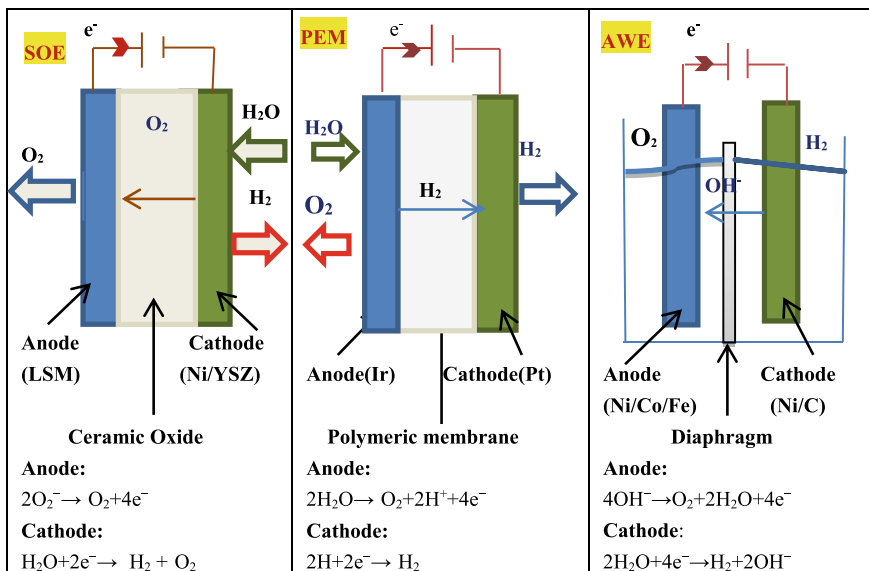
Fig. 3 Types of electrolysis

highest energy efficiency (90–100%) followed by PEM has (80–90%) energy efficiency and then AWE stands the lowest energy efficiency (70–80%). SOE has some bad points related to shortage of stability and inadequate durability, and PEM faces some challenges because of its expensive polymer membrane, while AWE also has some issues like electrode corrosions, gas permeation and decreases operation pressure. Therefore, before approaching commercial markets, some negative ascents of SOE, PEM and AWE have to be solved [6, 7].

Thermochemical cycles (TC's) has pointed combination chemical reactions with heat source to separate water into its hydrogen and O_2 efficiently. Thermochemical water-splitting cycles have major good points as the particular chemical process, no need to use catalysis, not requiring O_2–H_2 separation membranes can reach desired temperature, require low electric sources, and then, the chemical source can recycle except water [8]. Since 1960s, over 100 thermochemical cycles have been proposed. For selecting the reasonable cycle, some facts occur at the same time by following. Temperatures should be considered. The number of steps could be minimal. Each individual step with quick reaction and proportions should be similar the other steps. In chemical, the reaction products should not outcome by products, and any reaction products must be minimal to reduce the energy consumption and the price. The intermediates must be simple to handle [8].

The Hys cycle, as known as the Westinghouse cycle, hydrogen and sulfuric acid are produced by sulfur dioxide depolarized water electrolysis (SAD). To solve the challenging issue of Hys cycle, Ot–Hys process used the sulfur combustion process instead of high-temperature SAD process (Fig. 4). Ot–HyS process of the net thermal efficiency is about 25.0–30.0% higher than about 20.0% HyS cycle and then conventional water electrolysis. Due to favorable sulfur statistics, at least technical challenges and higher net thermal efficiency, as securing a bridge, Ot–HyS could introduce an important role in sustainable energy future but have to solve challenges to become economically favorable [9].

Currently, two cycles (S–I and Cu–Cl) stand as the most reliable cycles because of their costs and efficiency, while most of cycles are not feasible because of its scientific, technical or energizing reasons.

Sulfur-iodine (S-I) cycle is to produce hydrogen which has been discussed extensively (Fig. 5). Bunsen reaction is an exothermic chemical reaction that occurs at 100 °C, where H_2O, SO_2, and iodine react to form sulfuric acid and hydrogen iodide. In liquid-liquid separation, the mixed acid divide into two types of acid, which are rich phase of HI and H_2SO_4. Both type of acids are decomposed, purified and concentrated in the other two reactions after the separation of the acids. The endothermic H_2SO_4 decomposition reaction releases oxygen, sulfur dioxide and water at about 800–1000 °C. The endothermic HI, H_2 and O_2, the rest of the products are recycled alike the reactant material [10, 11]. Thermochemical water splitting with S-I cycle needs the high temperature to decompose SO_3 in SO_2 the ultimate state H_2SO_4 decomposition, the best connection with generation IV. Sulfur-iodine cycle linked to a nuclear reactor (600 MWth VHTR), operating at 950 °C but the necessary highest required temperature of the cycle, around 850 °C. Iodine losses would be noted
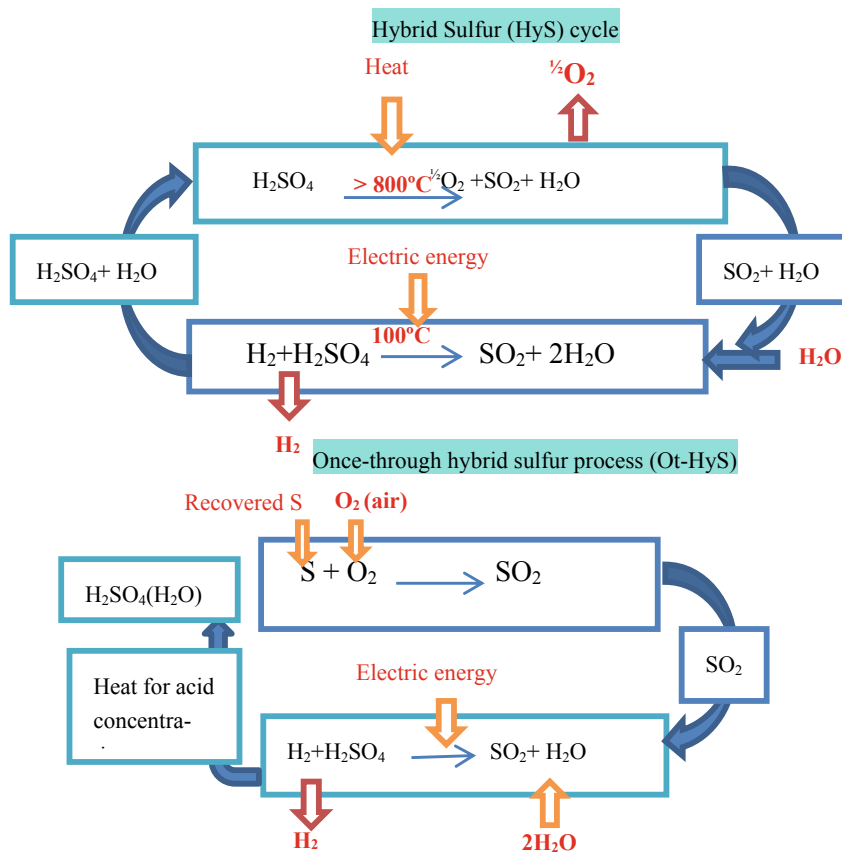
Fig. 4 Hybrid sulfur cycle and one-through hybrid sulfur process

because it is not only abundant but also really dare. And then, it only reaches an efficiency of 36% even though a thermochemical process is to achieve an efficiency of at least 50%. S–I process can produce 633 molH$_2$/s in the self-sustaining agreement of HYTHEC. For the baseline S–I plant, hydrogen production cost of 5.3 V/kg H$_2$ (6.4 $/kg H$_2$) has been accepted. At present, JAEA, Japan, can touch 0.065 kg/day of hydrogen production [12].

The copper-chlorine (Cu–Cl) cycle for green hydrogen production is currently divided into three various groups which are known three-, four- and five-step (Tables 1 and 2). Using intermediate (Cu–Cl) compounds, copper-chlorine cycle splits H$_2$O into hydrogen and O$_2$. In the five-step cycle, in a closed loop, all chemical process is performed to recycle all chemicals continuously. In the step 1, at 450 °C as an exothermic reaction, hydrogen is produced. In the step 2, at around 25 °C, producing copper from molten Cu–Cl shifts to the produced hydrogen, whereas the rest copper chloride is transferred to the next reaction. The third step of dried molten CuCl$_2$
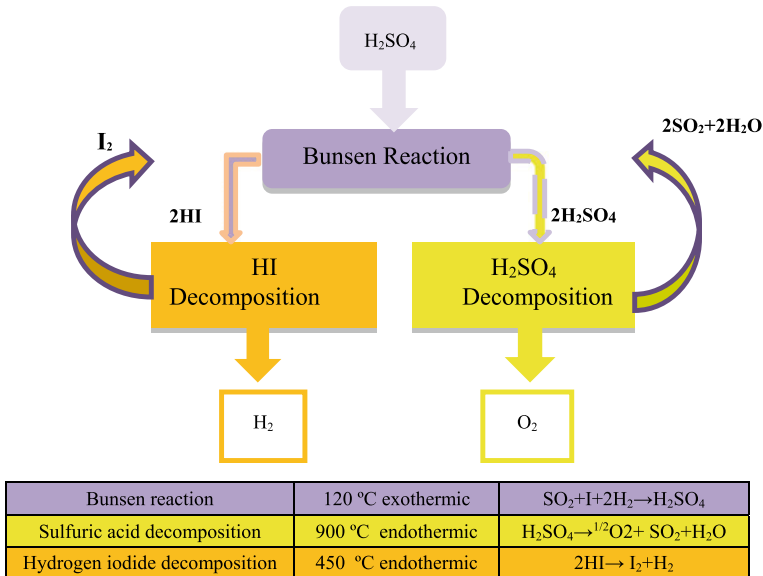
Fig. 5 S-I thermochemical cycle

is used as solid $CuCl_2$ for the fourth step. In the step four, solid $CuCl_2$ reacts with water to produce HCl and $CuOCuCl_2$, and production HCl step sees at a temperature of around 450 °C. In the final step, approximately 500 °C O_2 is produced. Heat exchanger is applied to adjust each stage of required temperature because each stage needs different temperature to complete their respective reaction.

The four-step Cu–Cl cycle, step 2(copper production) and step 3 (drying) are combined to handle the solid copper and to terminate the intermediate production. During these combinations of these two steps, the four-step copper-chlorine stands the lowest thermal energy input but higher electrical energy input than five-step Cu–Cl cycle. Therefore, among thermochemical copper-chlorine cycle, four-step Cu–Cl cycle is mentioned as the most reliable production process to support hydrogen demands. Production of hydrogen step 1 and step 2 (combine step) in the four-step cycle by providing $CuCl_2$ (aq) to water-splitting sector directly is cooperated in step 3 copper-chlorine cycle [16]. Because of its corrosive nature of products, three-step cycle is not applied for future industrialization. The Cu–Cl cycle is coupled to SCWR because of its lower temperature requirements around 550 °C which thermally decompose water into hydrogen and oxygen, through intermediate (Cu–Cl). (Cu–Cl) cycle consists of several chemical reactions that cause a closed internal loop and without generating any greenhouse gases, recycle the Cu–Cl compound continually. Then, Cu–Cl cycle has decreased construction material demands, low-cost chemical agents, solid handing insignificantly and can complete the reaction without any side

Table 1 Three main types of Cu–Cl cycle [13, 14]

Cu–Cl cycle	Step	Chemical reactions	Names of steps	Temperature (°C)
Five-step cycle	1.	$2Cu(s) + 2HCl(g) \rightarrow$ $2CuCl(l) + H_2(g)$	H_2 Production	450
	2.	$4 CuCl(aq) \rightarrow 2CuCl_2(aq) +$ $2Cu(s)$	Cu Production	25
	3.	$2 CuCl(aq) \rightarrow 2CuCl_2(s)$	Drying	90
	4.	$2CuCl_2(s) + H_2O(g) \rightarrow$ $CuOCuCl_2(s) + 2HCl(g)$	HCL Production	450
	5.	$Cu O CuCl_2(s) \rightarrow 2CuCl(l)$ $+ \frac{1}{2}O_2(g)$	O_2 Production	500
Four-step cycle	1.	$2Cu(s) + 2HCl(g) \rightarrow$ $2CuCl(l) + H_2(g)$	H_2 Production	450
	2.	$4CuCl(aq) \rightarrow 2CuCl_2(aq) +$ $2Cu(s)$	Combined Steps	25–90
	3.	$2CuCl_2(s) + H_2O(g) \rightarrow C$ $O * CuCl_2(s) + 2HCl(g)$	HCL Production	450
	4.	$Cu O* CuCl_2(s) \rightarrow 2CuCl(l)$ $+ \frac{1}{2}O_2(g)$	O_2 Production	500
Three-step cycle	1.	$Cu(s) + 2HCl(g) \rightarrow 2CuCl(l)$ $+ H_2(g)$	Combined Steps	100
	2.	$2CuCl_2(s) + H_2O(g) \rightarrow$ $CuO * CuCl_2(s) + 2HCl(g)$	HCL Production	430
	3.	$CuO * CuCl_2(s) \rightarrow 2CuCl(l)$ $+ \frac{1}{2}O_2(g)$	O_2 Production	550

Table 2 Advantages versus disadvantages reducing Cu–Cl steps [15]

Cu–Cl cycles steps	Advantages	Disadvantages
Reducing five steps to four steps	Fewer equipment material challenges; No need to separate HCl from H_2O	Current and voltage dependence on concentration not known clearly
Reducing five steps to three steps	Less to process solid particles challenges; reduce steps and less equipment	Increase heat intensity and heat great; challenges more equipment material; more unwanted side products, etc.

effect. At 500 °C, hydrogen production efficiency can achieve 33–37%. Copper-chlorine cycle can reach 3 kg/day hydrogen production under developed by UOIT, Canada [17, 18].

3   Integrated Hydrogen Production

In the near future, the coupled nuclear/solar energy sources are linked with thermochemical cycles to form hydrogen production nearly zero greenhouse gas emissions using water and either nuclear energy or sunlight. In the transition to an almost complete solar energy sector, nuclear energy can serve as a support and backup power suppliers. Generally, direct cycles start fewer steps with less complex, but its higher operating temperatures are more complicated than hybrid cycles. Thermochemical water-splitting cycles (Cu–Cl) and (S–I) are used as comparative purposes to fulfill coupling solar and nuclear energy sources because of their operating temperature range and then have less complexity and safety process in the chemical reactions. S–I cycle can be applied if it meets the required temperature by integrating nuclear and solar system because of its high operating temperature. Combining the required input from the nuclear with the output from the solar, Cu–Cl accepts constant energy, and all the time may run at its design capacity which may catch 90% or higher capacity factor significantly would decrease the cost of hydrogen and also increase the economics markets [19].

4   Life Cycle Assessment (LCA)

The LCA process is a systematic and phased approach which considers using the four main phases of LCA. LCA results are described which are based on unit product (1 kg of hydrogen [20]. Producing hydrogen from high-temperature water electrolysis of the life cycle assessment demonstrates GWP 2000 g CO_2 equivalent and AP 0.15 g eq. H + . Usage of alternative materials to improve the potential electrolysis, especially 50% reduction in the material requirements, will indicate into decrease 25% in the GWP and 30% in the AP. Therefore, scientists have to find the way for the better research for new attitudes of electrolysis [21]. S–I cycle for hydrogen production, GWP 2900 kg CO_2 eq and the AP 17 kg SO_2 are generated [19]. Four- and five-step Cu–Cl cycles of environmental impact are also mentioned. For the five-step Cu–Cl cycle, GWP as 0.346 kg CO_2-eq and AP as 5.0×10^{-3} kg SO_2-eq per kg while GWP 0.287 kg CO_2-eq and AP 2.1×10^{-3} kg SO_2-eq per kg in the four-step Cu–Cl cycle are emitted, respectively [22]. The four-step Cu-Cl cycle notices the lowest environmental impacts because of its lower heat requirement [23].

5   Conclusions

In many countries, as primary energy source, nuclear energy is introduced or being considered because it is a stable and reliable energy supply without emitting greenhouse gas. For nuclear-based hydrogen production, several types of reactors are

being introduced, and several methods are ready to participate to produce hydrogen including electrolysis and thermochemical cycles. A considerable research programs are aimed to optimize these cycles underway at the various organization in the world. Electrolysis and thermochemical cycles are used as massive hydrogen production. Electrolysis method applies as near term option. By using heat to convert water to hydrogen and oxygen, thermochemical cycle stands as long-term option because it can save cost.

Therefore, based on the articles, the Cu–Cl cycle linked SCW is very cheap hydrogen production as promising alternative production. Moreover, Cu–Cl cycle requires lower temperature (around 530 °C), while most of the cycles need process heat at temperatures above 800 °C, and then, it can reduce materials and maintenance costs. The LCA results also showed that the fourth copper-chlorine cycle has the lower environmental impact than other candidates which are based on nuclear energy to produce H_2.

References

1. Rachael, E., Ray, A.: Nuclear heat for hydrogen production: coupling a high/high temperature reactor to a hydrogen production plant. Prog. Nucl. Energy **51**, 500–525 (2009)
2. Shripad, T.: Transient analysis of coupled high temperature nuclear reactor to a therm chemical hydrogen plant. Int. J. Hydrogen Energ. **38**, 6174–6181 (2013)
3. Marques, G.: Evolution of nuclear fission reactors: third generation and beyond. Energ. Convers. Manag. **51**(9), 1774–1780 (2010)
4. Orhan, M.F., Binish, B.: Investigation of an integrated hydrogen production system based on nuclear and renewable energy sources: comparative evaluation of hydrogen production options with a regenerative fuel cell system. Energ 1–20 (2015)
5. Greg, F., Ibrahim, D., Calin, Z.: Hydrogen Production from Nuclear Energy. Springer Science and Business Media, LLC, 1–44 (2013)
6. ShivaKumar, S., Himabindu, V.: Hydrogen production by PEM water electrolysis—a review. Mater. Sci. Energ. Technol. **2**, 442–454 (2019)
7. Ibrahim, D., Canan, A.: Review and evaluation of hydrogen production methods for better sustainability. Int. Sci. J. Alternat. Energ. Ecol. **40**, 11–12 (2016)
8. Olga, B., Pavel, S.: The resources and methods of hydrogen production. Acta Geodyn. Geomater. **2**(158), 175–188 (2010)
9. Jung, Y.H., Jung, Y.H., Yong Hoon, J.: Development of the once-through hybrid sulfur process for nuclear hydrogen production. Int. J. Hydrogen Energy **35**, 12255–12267 (2010)
10. Brown, N., Seker, V., Oh, S., Revankar, S., Downar, T., Kane, C.: Transient modeling of sulfur iodine cycle thermo-chemical hydrogen generation coupled to pebble bed modular reactor. Purdue University West Lafayette, IN. (2009). https://slideplayer.com/slide/14913193/
11. Balat, M.: Energy sources, part a: recovery. Utilization Environ. Effects. **31**(1), 39–50 (2008)
12. Giovanni, C., Coriolano, S., Claudio, C., Ambra, D., Alfredo, O., Alain, L., Jean-Marc, B., Christine, M.: Sulfur–Iodine plant for large scale hydrogen production by nuclear power. Int. J. Hydrogen Prod **35**, 4002–4014 (2010)
13. Ozbilen, A., Dincer, I., Rosen, M.A.: A comparative life cycle analysis of hydrogen production via thermochemical water splitting using a Cu–Cl cycle. Int. J. Hydrogen Energ. **36**(17), 11321–11327 (2011)
14. Ozbilen, A.Z.: Life cycle assessment of nuclear-based hydrogen production via thermochemical water splitting using a copper–chlorine (Cu–Cl) cycle (Doctoral dissertation, UOIT). 49–04, 2706:144 p (2010)

15. Wang, L., Naterer, G., Gabrie, S., Gravelsins, R., Daggupati, N.: Comparison of different copper–chlorine thermochemical cycles for hydrogen production. Int. J. Hydrogen Energ. **34**, 3267–3276 (2009)
16. Marek, J., Marc, A., Tomasz, S., Michał, L.: Hydrogen production using high temperature nuclear reactors: efficiency analysis of a combined cycle. Int. J. Hydrogen Energ. **1**, 1–1 (2016)
17. Rosen, M., Naterer G., Chukwu1, C., Sadhankar, R., Suppiah, S.: Nuclear-based hydrogen production with a thermochemical copper–chlorine cycle and supercritical water reactor: equipment scale-up and process simulation. Int. J. Energ. Res. **36**. 456–465 (2012)
18. Orhan, M.F., Ibrahim, D., Marc, R.: Energy and exergy assessments of the hydrogen production step of a copper–chlorine thermochemical water splitting cycle driven by nuclear-based heat. Int. J. Hydrogen Energ. **33**, 6456–6466 (2008)
19. Orhan, M.F., Ibrahim, D., Marc, A., Mehmet, K.: Integrated hydrogen production options based on renewable and nuclear energy sources. Renew. Sustain. Energ. Rev. **16**, 6059–6082 (2012)
20. Solli, C., Stromman, H., Hertwish, G.: Fission or fossil: life cycle assessment of hydrogen production. Proc. IEEE. **94**, 10 (2006)
21. Utgikar, V., Thiese, T.: Life cycle assessment of high temperature electrolysis for hydrogen production via nuclear energy. Int. J. Hydrogen Energ. 31939–31944 (2006)
22. Ahmet, O., Murat, A., Ibrahim, D., Marc, A.R.: Life cycle assessment of nuclear-based hydrogen production via a copper chlorine cycle: a neural network approach. Int. J. Hydrogen Prod. **38**, 6314–6322 (2013)
23. Ahmet, O., Ibrahim, D., Mar, A.R.: Environmental impact assessment of nuclear assisted hydrogen production via Cu–Cl thermochemical cycles. Sustain. Cities Soc. **7**, 16–24 (2013)

Power Generation from Waste Heat Using Thermoelectric Modules

Kartik Jeph [ID]**, Keshav Kumar Tomar** [ID]**, and Kunal Lohchab** [ID]

1 Introduction

In the past few decades, attempts have been made to harness waste heat to convert it into electrical energy. The waste heat is often being derived from various technologies that are used today for human comfort. The amount of waste heat generated differs from industry to industry, for example, the automobile industry comes at the top in terms of generation of heat that is not utilized (or wasted). Other industries such as telecommunications, cooling systems, solar, and geothermal also fall into this category.

The reason behind these attempts is to save the fuel from being wasted as much as possible because of the scarcity of resources. And if the current consumption rate is not reduced, then it would not take long for our resources to get exhausted. One potential and widely used method is the thermoelectric power generation technology, for utilizing the waste heat. These generators work on the principle of the Seebeck effect which is defined as, "temperature difference between two dissimilar electrical conductors or semiconductors produces a voltage difference between the two materials" [1].

Table 1 represents some important experimental and theoretical results from previous studies on waste heat utilization using thermoelectric generators.

In this work, a theoretical model of a system is defined that uses waste heat for electrical power generation. For this system, the outer surface of the catalytic converter of passenger vehicles is considered as the heating source, and coolant from the coolant cycle of an engine is considered as the cooling source. The amount of power generated by various thermoelectric modules depends upon different parameters such as the temperature difference across the surface of the module, type of heating, and

K. Jeph · K. K. Tomar (✉) · K. Lohchab
Department of Mechanical, Production & Industrial and Automobile Engineering, Delhi
Technological University, Delhi 110042, India
e-mail: keshavkt.112@gmail.com

Table 1 Results from related literature

References and year	Temperatures (Th & Tc) (°C)	Number of modules used (N)	Power output (W)
Crane et al. [2]	Th = 90 Tc = 25	6	0.54
Niu et al. [3]	Th = 90 Tc = 25	56	146.5
Kim et al. [4]	Th = 95 Tc = 45	72	75
Remeli et al. [5]	Th = 160 Tc = 65	1	1.72

cooling source (for example, this can be water or some device). A higher temperature difference means higher power generation. The use of liquid for heating and cooling will result in high power generation because liquids have high heat capacity. The amount of power generated also increases with an increase in the mass flow rate of liquid used for heating or cooling.

2 Experimental Set-Up

The thermoelectric module uses temperature difference for power generation. In this work, this temperature difference is created by using the surface of the catalytic converter as the heat source and coolant as the heat remover or cooling source. Now as mentioned above, the surface of the catalytic converter is the heat source, and this surface will be feeding heat to the modules. But this heat input is not uniform as the surface temperature of the catalytic converter varies from point to point. Although this temperature variation is small, having a nonuniform source of heat may influence the working of modules which is not beneficial. This can be corrected by introducing a narrow metal plate just after the hot surface of the catalytic converter. This metal plate will uniformly distribute heat across its surface and will act as a good source of heat for the module. The proposed model is shown in Fig. 1.

On the other side of the module, a metal block is used which has a copper pipe embedded inside of it. This can be understood from picture given in Fig. 2.

Coolant from the cooling cycle of the engine passes through this copper pipe and takes the heat from the module. Hence, this whole assembly of metal block embedded with the copper pipe having coolant passing through it acts as a cooling system for the module. The metal block is used for better heat transfer from modules to coolant and to increase the area of heat transfer, which increases the amount of heat collected by the coolant.

A number of thermoelectric modules are sandwiched between the metal plate and the metal block to facilitate the power generation process.
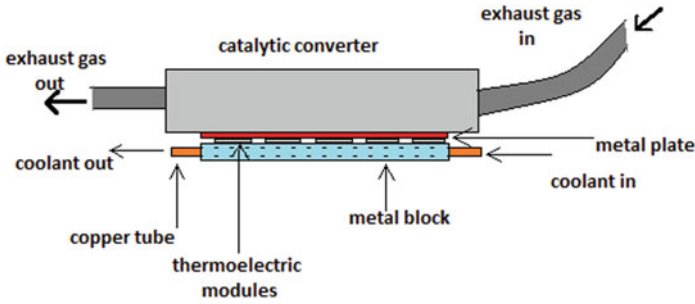
Fig. 1 Proposed model of the thermoelectric generator

Fig. 2 Lateral cross-sectional view of the aluminium block
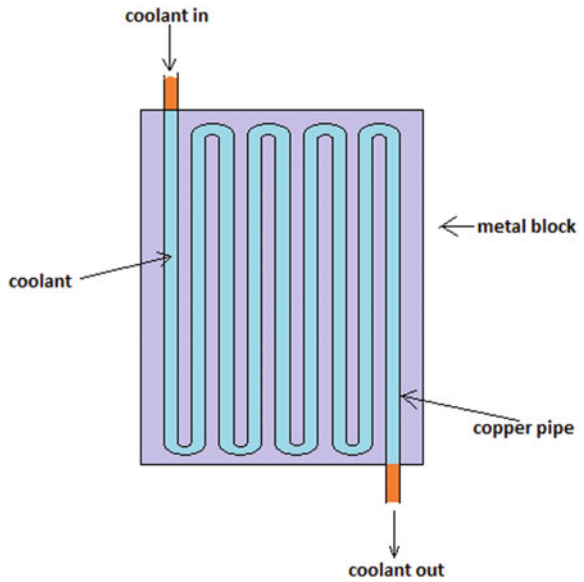
2.1 Thermoelectric Module

The maximum temperature a bismuth telluride thermoelectric module can endure is 250 °C [6]. Therefore, it is suitable for the system proposed in this work. The most common configuration that is easily available is 127 couples-6 amp. Dimensions of the selected module are given in Table 2 [7].

Length—40 mm
Width—40 mm
Height—3.95 mm

Table 2 Properties of the module at $T_h = 200$ and $T_c = 100$ [8]

S_M	Module average Seebeck coefficient (V/K)	0.04882
R_M	Module average resistance (ohms)	3.7867
K_M	Module average thermal conductance (w/K)	1.0531

Table 3 Important properties of the coolant mixture at 90 °C [9]

Dynamic viscosity (μ) (centipoise)	0.737
Specific heat capacity (C_{pc}) (KJ/kg C)	0.4335
Thermal conductivity (K_c) (W/mK)	Module average thermal conductance (w/K)
Density of mixture (ρ) (kg/m^3)	1036

2.2 Coolant

The most common coolant used in the engine cooling cycle is ethylene glycol. In the common application, it is mixed with water in 1:1 proportion to improve the cooling properties. The obtained coolant of 50% ethylene glycol and 50% of water is considered in this work.

Properties of the ethylene glycol–water mixture important for this study are given below (Table 3).

The average flow velocity of coolant in the cooling system is 5 feet per second [10], and the diameter of the coolant pipe at the radiator outlet is around 25 mm.

Mass flow rate can be expressed as

$$\dot{m}_c = \rho V A \tag{1}$$

where,

ρ (Density of the mixture) = 1036 kg/m^3. V (velocity) = 1.524 m/s

A (Area at the radiator outlet) = $\pi \times (0.025 \div 2)2$ m^2

By using the above formula and putting the values given above in it, the mass flow rate comes out to be 0.775023 kg/s.

2.3 Thermal Interface Material (TIM)

The thermal interface material is selected by considering these parameters.

1. Type of material to be connected.
2. Type of bond required.
3. Amount of heat to be dissipated.
4. Temperature.

The system proposed in this work has metal to ceramic surface connection, and it requires a TIM that can provide

1. Mechanically strong bond.
2. Can handle high temperature of about 200 °C.
3. It can transmit a high amount of heat through it easily.

Considering all the properties required for the system proposed in this work, thermally conductive epoxy adhesive is the appropriate material.

2.4 Metal Plate and Metal Block

The thickness of the metal plate is small, and the weight would not be a critical factor here. Therefore, copper is the appropriate material for the metal plate. There are over a thousand and even more commercially available grades of copper. Most of them are similar in properties with only small variations. One of the common grades of copper that can be used here is UNS C10100 that is easily available [11].

In the case of the metal block, the thickness is about 4 times the metal plate and that would significantly affect the overall weight of the system proposed. Therefore, aluminium is the appropriate material for the metal block. Priorities in descending order of their respective weights (Table 4).

Given above is a table containing properties of four most commonly used grades of aluminium. To select the best grade among these, a weighted average method is applied.

Thermal conductivity (4) > Density (3) > Tensile Strength (2) > Melting Point (1)

Weights for highest to the lowest values of thermal conductivity, tensile strength, and melting point:

4 (highest) > 3 > 2 > 1 (lowest)

Weight for highest to the lowest value of density:

4 (lowest) > 3 > 2 > 1 (highest)

It is clear from the above analysis that the Al-6063 T6 grade is the best option (Table 5).

Table 4 Aluminium grades [12]

Material	Density (g/cm^3)	Thermal conductivity (W/mc)	Melting point (°K)	Tensile strength (MPa)
Al-5052 H36	2.68	138	607	276
Al-6061 T6	2.70	167	582	310
Al-6063 T6	2.69	209	616	241
Al-1100 H14	2.71	220	643	124

Table 5 Weighted average

Grades	Weighted average
Al-5052 H36	$4 \times 1 + 3 \times 4 + 2 \times 3 + 1 \times 2 = 24$
Al-6061 T6	$4 \times 2 + 3 \times 2 + 2 \times 4 + 1 \times 1 = 23$
Al-6063 T6	$4 \times 3 + 3 \times 3 + 2 \times 2 + 1 \times 3 = 28$
Al-1100 H14	$4 \times 4 + 3 \times 1 + 2 \times 1 + 1 \times 4 = 25$

3 Standard Equations and Mathematical Modelling

3.1 Standard Equations of Thermoelectric Power Generation System [13]

With no load (R_L not connected), the open-circuit voltage as measured between terminals is

$$V_O = S_M \times \Delta T \tag{2}$$

Here, V_O is the output voltage from one module in volts, S_M is the average Seebeck coefficient in volts/°K, and ΔT is the temperature difference in °K, where

$$\Delta T = T_h - T_c \tag{3}$$

When load resistance is taken into account, the current through the load is

$$I_O = \frac{S_M \times \Delta T}{R_M + R_L} \tag{4}$$

Here, I_O is the output current in amperes, R_M is the average internal resistance of a module in ohms, and R_L is the load resistance in ohms.

Heat input to the module (Q_h) is

$$Q_h = (S_M \times T_h \times I_o) - \left(0.5 \times I_o^2 \times R_M\right) + (K_M \times \Delta T) \tag{5}$$

Here, Q_h is the heat input in watts, K_M is the thermal conductance of a module in watts/°K, and T_h is the temperature of the hot side of the module in °K. The values S_M, R_M, and K_M must be selected at the average module temperature, where

$$T_{avg} = (T_h + T_c)/2 \tag{6}$$

Power output from the module,

$$P_O = R_L \times \left[\frac{S_M \times \Delta T}{R_M + R_L}\right]^2 \tag{7}$$

Considering the modules are to be connected in a series, parallel, or series + parallel arrangement, the total number of modules in the system N_T will be

$$N_T = N_S \times N_P \tag{8}$$

Current passing through the load resistance R_L,

$$I = \frac{N_S \times S_M \times \Delta T}{\frac{N_S \times R_M}{N_P} + R_L} \tag{9}$$

Total output voltage,

$$V = R_L \times \left[\frac{N_S \times S_M \times \Delta T}{\frac{N_S \times R_M}{N_P} + R_L} \right] \tag{10}$$

Total output power from the modules,

$$P = N_T \times \frac{(S_M \times \Delta T)^2}{4 \times R_M} \tag{11}$$

Total heat input to the modules,

$$Q_h = N_T \times \left[\frac{S_M \times T_h \times I}{N_P} - 0.5 \times \left(\frac{I}{N_P} \right)^2 \times R_M + K_M \times \Delta T \right] \tag{12}$$

The total heat output from the modules

$$Q_c = Q_h - P \tag{13}$$

The efficiency of the power generation

$$E_g = \frac{P}{Q_h} \times 100(\%) \tag{14}$$

Maximum power output can be achieved when the internal resistance of the module arrangement is made equal to the load resistance R_L. This can be done by selecting a proper arrangement of modules.

3.2 Mathematical Modelling

A conceptual model has been shown in Fig. 1 which represents the overall system. The coolant flowing inside the copper tubes takes away all the heat coming from

Fig. 3 Heat transfer
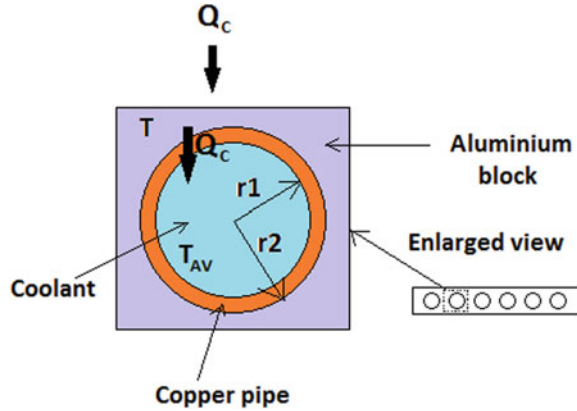
the modules. For a better understanding of the heat transfer process between the aluminium block and coolant, the cross section of the copper tube embedded inside the aluminium block is shown in Fig. 3.

Q_c is the heat coming from the modules, and this heat is transmitted to the coolant via the block. So that Q_c can be expressed as

$$Q_c = UA\Delta T_2 \tag{15}$$

Or,

$$UA = \frac{Q_C}{\Delta T_2} \tag{16}$$

(1/UA) is the overall resistance to the heat transfer between the aluminium block and coolant. For making the calculation simple, the aluminium block is assumed to have constant temperature T which is equal to Tc. And UA can be expressed as

$$UA = \frac{1}{\frac{1}{h_c A_1} + \frac{1}{2\pi K L} \ln \frac{r_2}{r_1}} \tag{17}$$

where $A_1 = 2\pi r_1 L$ and K is the thermal conductivity of copper, which is 396 W/mK at around 90 °C. ΔT_2 is the mean temperature between the aluminium block and the coolant. So, it can be expressed as

$$\Delta T_2 = \left(T - \frac{T_f + T_i}{2}\right) \tag{18}$$

T_i and T_f are the initial and final temperatures of the coolant respectively. Also,

$$Q_C = \dot{m}_c c_{pc} \Delta T_1 \tag{19}$$

Or,

$$Q_c = \dot{m}_c c_{pc}(T_f - T_i) \tag{20}$$

By using all the equations mentioned above, the heat transfer coefficient calculated in the next section leads us to the length of the copper pipe embedded inside the aluminium block.

3.3 Calculation of the Heat Transfer Coefficient of the Coolant

Reynolds number is given as

$$R_e = \frac{\rho V D}{\mu} \tag{21}$$

Or,

$$R_e = \frac{\rho V D}{\mu} \times \frac{A}{A} = \frac{\dot{m} \times D}{A \times \mu} \tag{22}$$

Putting the values from Table 3 in the above equation, R_e comes out 42,845.69 which is larger than 6000, and therefore, it is a turbulent flow.

Prandtl Number:

$$P_r = \frac{\mu c_{pc}}{K_c} \tag{23}$$

Convective heat transfer

$$h = \frac{N_u \times K_c}{D} \tag{24}$$

Now, as the flow is turbulent,

$$N_u = 0.023 \times P_r^{0.4} \times R_e^{0.8} \tag{25}$$

Convective heat transfer coefficient can be expressed as

$$h_c = \frac{0.023 \times P_r^{0.4} \times R_e^{0.8} \times K_c}{D} \tag{26}$$

After putting all the required values in the above equation, it comes out to be h_c = 5273.83 (w/m^{2}K), and here, the diameter of copper pipe is taken as 20 mm with 1 mm thickness.

4 Results

Using the standard equations for thermoelectric power generation and the mathematical modelling proposed for the system, several important characteristics are calculated for different voltage outputs keeping the temperature difference of 100 °C (T_h = 200 °C and T_c = 100 °C) and load resistance fixed, variations can be understood from the graphs given in Figs. 4, 5, 6, 7 and 8. The values that are calculated are given in Tables 6 and 7.

Table 6 Results

V (Volts)	N	E_g, efficiency	Power (W)	Q_h (W)
5.015	4	1.350	6.289	465.500
8.56	6	1.310	9.160	698.250
11.97	8	1.285	11.940	931.050
17.12	12	1.312	18.330	1396.51
20.55	14	1.227	21.120	1629.35

Table 7 Results (cont.)

V (Volts)	Q_c (W)	Length of copper pipe (m)	Temperature difference ΔT (°C)
5.015	459.211	0.1415	100
8.56	689.090	0.2132	100
11.97	919.110	0.2850	100
17.12	1378.18	0.4317	100
20.55	1609.35	0.5062	100

Fig. 4 Voltage versus
Efficiency (E_g)

$T_h = 200$ºC and $T_c = 100$ºC
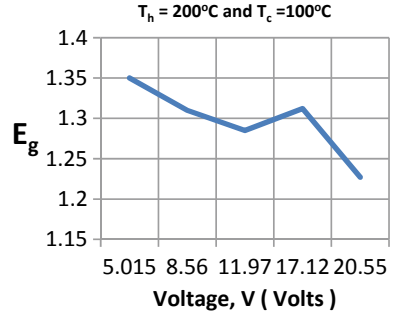
Fig. 5 Voltage versus
Number of modules (N)

$T_h = 200$ºC and $T_c = 100$ºC
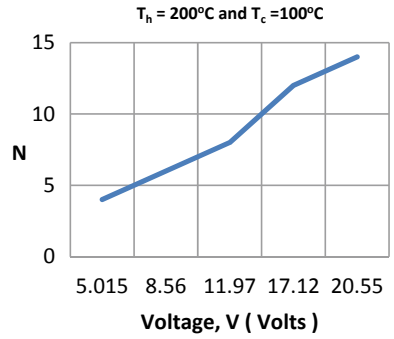
Fig. 6 Voltage versus power
output (P)

$T_h = 200$ºC and $T_c = 100$ºC
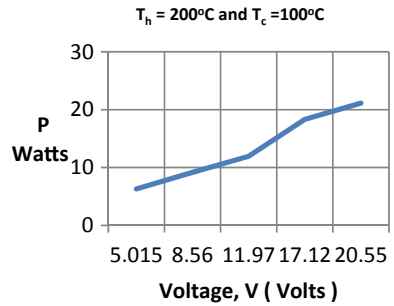
Fig. 7 Voltage versus
Length of copper pipe (L)

$T_h = 200$ºC and $T_c = 100$ºC
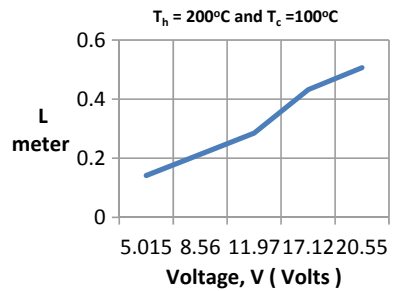
Fig. 8 Voltage versus heat input (Q_h) and Heat output (Q_c)
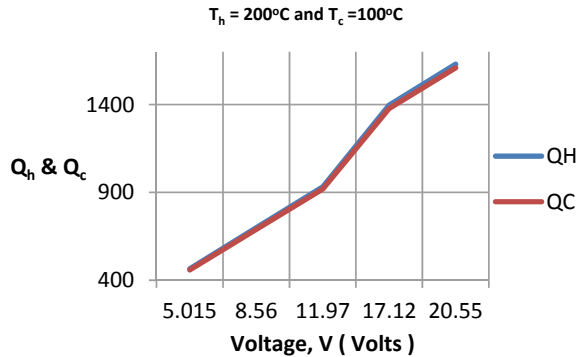
5 Conclusion

As a conclusion from this study, the power generation achieved from the excess heat using the thermoelectric module can be carried out using the model proposed. The excess heat of the catalytic converter of the passenger vehicle is utilized here. The surface temperature of the catalytic converter and coolant temperature at exit from the radiator was the main parameters. The hot side of the thermoelectric module receives heat input from the catalytic converter, while the heat from the cold side is channelled using the coolant from the engine coolant cycle. The design illustration, the power generated, generator efficiency, total heat input, heat output from the cold side, and the number of modules have been illustrated for different values of voltages and for a constant temperature difference of 100 °C ($T_h = 200$ °C and $T_c = 100$ °C) by the use of graphs. Formulas used for the calculation of all factors mentioned before have also been specified clearly. Many considerations have been studied and taken care of while undertaking this study. The study illustrates that waste heat is practically useful if it is considered as a valuable source for any reason.

References

1. IEEE Homepage: https://ieeexplore.ieee.org/document/6259167. Last accessed 12 Mar 2020
2. Crane, D.T., Jackson, G.S.: Optimization of cross flow heat exchangers for thermoelectric waste heat recovery. Energy Convers. Manag. **45**(9), 1565–1582 (2014)
3. Niu, X., Yu, J., Wang, S.: Experimental study on low temperature waste heat thermoelectric generator. J. Power Sources **188**(2), 621–626 (2009)
4. Kim, S., et al.: A thermoelectric generator using engine coolant for light-duty internal combustion engine powered vehicles. J. Electron. Mater. **40**(5), 812 (2011)
5. Remeli, M.F., et al.: Experimental investigation of combined heat recovery and power generation using a heat pipe assisted thermoelectric generator system. Energ. Convers. Manag. **111**, 147–157 (2016)
6. Li, F., Zhai, R., Yehao, W., et al.: Enhanced thermoelectric performance of n-type bismuth-telluride based alloys via In alloying and hot deformation for mid-temperature power generation. J. Materiomics **04**, 208–214 (2018)

7. Flipkart Homepage: Easy Electronics PELTIER 12706 Thermoelectric Peltier Module, https://www.flipkart.com/easy-electronics-peltier-12706-thermoelectric-module/p/itmex5fpm4ttqjgv. Last accessed 13 Apr 2020
8. Ferrotec Homepage: Mathematical Modeling of Thermoelectric Cooling Modules, https://thermal.ferrotec.com/technology/thermoelectric-reference-guide/thermalref11/. Last accessed 11 Apr 2020
9. Engineering toolbox Homepage: Ethylene Glycol Heat-Transfer Fluid, https://www.engineeringtoolbox.com/ethylene-glycol-d_146.html. Last accessed 13 Mar 2020
10. Engine Basics Homepage: Coolant flow rate, http://www.enginebasics.com/Engine%20Basics%20Root%20Folder/Engine%20Cooling%20Pg3.html. Last accessed 11 11 Apr 2020
11. Copper Development Association Inc. Homepage. https://www.copper.org/resources/properties/dbbasic-search.php. Last accessed 20 Apr 2020
12. Aalco Homepage. http://www.aalco.co.uk/datasheets/Aluminium-Alloy_Introduction-to-Aluminium-and-itsalloys_9.ashx. Last accessed 17 Mar 2020
13. Ferrotec Homepage: Power Generation. https://thermal.ferrotec.com/technology/thermoelectric-reference-guide/thermalref13/. Last accessed 17 Mar 2020

Effect of SiC Nanoparticles Concentration on the Tribological Behavior of Karanja Oil

Yashvir Singh [ID]**, Abhishek Sharma** [ID]**, Naushad Ahmad Ansari, and Nishant Kumar Singh** [ID]

1 Introduction

The increase in environmental pollution due to the extreme use of petroleum products has focused to explore alternatives [1]. One of the petroleum products is in use in the form of synthetic oil. The purpose of the synthetic oil is to minimize the friction between two sliding surfaces and enhance the energy utilized during the rubbing process [2–4]. The synthetic oils are dangerous to the environment especially aquatic as they are toxic and non-biodegradable. Most of the pollution is caused due to their improper disposal [5].

To meet the requirements of the synthetic oil and to provide effective lubrication, bio-based lubricants synthesized from the vegetable oils are suitable. They contain higher viscosity, higher viscosity index, less toxic, biodegradable and high flash point which are considered as important properties during the lubrication process [6, 7]. There are limitations associated with the vegetable oils which limit their application. Certain additives were added to the oils to improve their properties, but most of the

Y. Singh (✉)
Department of Mechanical Engineering, Graphic Era (Deemed To be University), Dehradun, Uttarakhand, India
e-mail: yashvirkankara21@gmail.com

A. Sharma
Department of Mechanical Engineering, G L Bajaj Institute of Technology and Management, Greater Noida, UP, India

N. A. Ansari
Department of Mechanical, Production & Industrial and Automobile Engineering, Delhi Technological University, Delhi, India

N. K. Singh
Department of Mechanical Engineering, Hindustan College of Science and Technology, Mathura, UP, India

additives contain sulfur and phosphorous resulting in pollution of the environment [8].

The application of the nanoparticles as an additive to the non-edible vegetable oils is one of the prominent members. The results of the nanoparticles during their application were proved to be the better one. In the previous studies, most of the studies were performed while considering them for engine oil and edible oil. Ren et al. [9] examined the tribological characteristics of the ZnO coated with graphene. The improved anti-wear mechanism was formed to maintain the capacity of the load and the lubricant film. Silica nanoparticles provided improved tribological behavior when added to the lubricant, but their application was limited due to their improper dispersibility [10]. The effect of copper nanoparticles on the serpentine powder was analyzed by Zhang et al. [11]. Up to optimum mass ratio of 7.5:92.5, improved results in the tribological analysis were seen.

In this study, SiC nanoparticle was used as additive to the Karanja oil. None of the studies was performed earlier while considering SiC nanoparticles to the tribological application with Karanja oil. The purpose of using SiC was due to its more hardness which resists in a better way to the applied pressure on the lubricant films [12]. The Karanja oil was easily available and mostly found in tropical areas. The seeds of the Karanja tree provide oil yield up to 45% as reported in the literature [13].

The objective of the study is to analyze the tribological behavior of Karanja oil during SiC nanoparticles addition. The sodium dodecyl sulfate was used as the surfactant to the Karanja oil. The test was performed at different parameters. The worn surfaces were analyzed using the scanning electron microscope (SEM).

2   Materials and Methods

Figure 1 shows the methodology adopted during the examination. It consists of the process followed for the test. The detailed description is mentioned in the subsequent sections.

2.1   Sample Development for the Characterization

The SiC nanoparticle was procured from the vendor Nano Research Lab, Jamshedpur, Jharkhand, India. The nanoparticles supplied were in the range 25–30 nm diameter having a spherical shape. The purity of the nanoparticles was 99.9% as assured by the supplier. The Karanja oil was collected through the local supplier from Dehradun City, Uttarakhand, India. To improve the properties of the Karanja oil, nanoparticles were added. The nanoparticles were added to the oil and stirred for 30 min with 300 rpm speed. For proper dispersion, the mixture was ultrasonicated for 45 min (400 W, 20 kHz). After ultrasonication, the sodium dodecyl sulfate was used as a surfactant, and proper mixing was done using the magnetic stirrer. The mixing
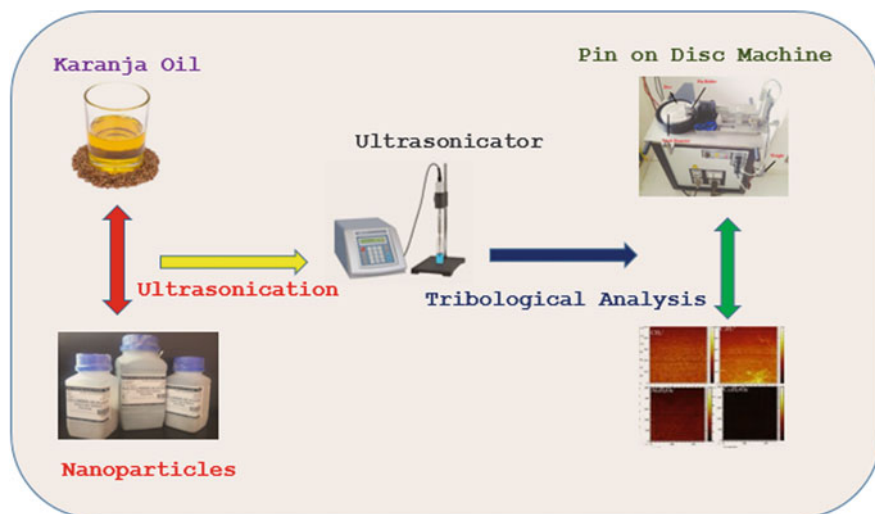
Fig. 1 Methodology of the process

process was performed for 30 min. The nanoparticles were added to the oil in the ratio 0.3–.2% (W/V). The following are the designations assigned to the different samples: 1) KO 2) KO + 0.3% 3) KO + 0.6% 4) KO + 1.2%.

2.2 Physicochemical Characterization

The physicochemical characterization was done according to the ASTM standard methods. The kinematic viscosity was evaluated through the viscometer (Swastik systems and services, New Delhi) based on the ASTM D-445 standard. The viscosity was measured at atmospheric pressure and temperatures (40, and 100 °C). The test was conducted three times, and the mean value was used to reduce the error and maintain reliability.

Flash point and pour point of the oil were measured according to ASTM D-92 (Cleveland open cup method) and ASTM D-97, respectively, using proper apparatus. The acid value was measured using GD-246B automatic tester based on potentiometric titration principle according to ASTM D664 method. Table 1 shows the properties of the lubricants.

Table 1 Characteristics of the blends used for the examination

Parameters	Viscosity @ 40 °C (cSt)	Viscosity @ 100 °C (cSt)	Flash point (°C)	Pour point (°C)
KO	239.21	16.16	253.4	−3.5
KO + 0.3%	240.13	16.88	254.6	−3.2
KO + 0.6%	241.57	17.72	256.8	−3.2
KO + 1.2%	249.41	20.63	261.2	−2.1

2.3 Experimental Setup

For performing the tribological study, pin-on-disk (POD) machine was used as shown in Fig. 2. Table 2 shows the specification of the apparatus. The POD was equipped with sensors for getting the frictional force and wear of the material. The test was performed using ASTM G99 method. During the test, 8 mm diameter and 30 mm height pin was used. The LM 13 alloy (chemical composition: Al-83.39%, Si-10.9, Fe-0.527, Cu-1.31, Mg-1.05, Ni-2.32, others-0.494) was procured from the vendor

Fig. 2 Image of the machine for the set-up
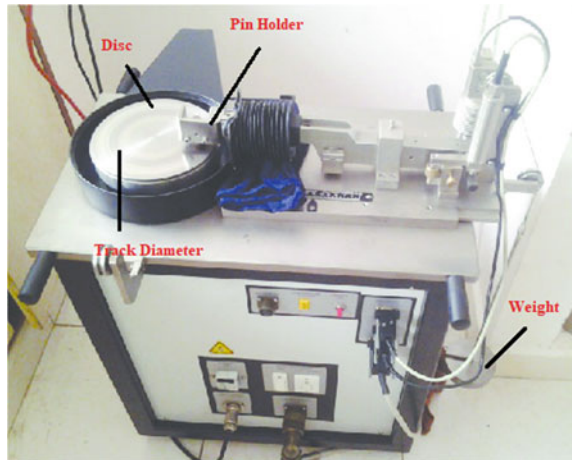
Table 2 Specifications of the experimental setup

Normal load	5–200 N
Frictional force	Up to 200 N
Disk size	165 mm × 8 mm
Rotational speed	200 rpm to 2000 rpm
Wear measurement	Range up to 2000 μm
Wear track diameter	140 mm or variable
Pin/ball diameter	3, 6, 8, 10 and 12 mm

Table 3 Conditions applied to the apparatus during analysis

Operating conditions	Quantity
Applied load	80 N
Track diameter	90 mm
Velocity	200 rpm
Time	3600 s

Raine Aluminium Private Limited, Hyderabad, which was used as pin material for the test. The purpose of consideration of this material due to its application for the piston which faces maximum friction and the hardness is 98 HRB. This type of the alloy is also capable to resist wear and corrosion. For the disk, EN 31 steel was used as it contains more amount of hardness (62 HRC) and high wear resistance [14]. Table 3 shows the process parameters undertaken for the test. The conditions are considered based on the studies in the literature, and the maximum wear on the piston rings occurs during low speed [15, 16].

3 Results and Discussion

3.1 Friction Analysis

Figure 3 shows the COF for the different samples with respect to time. Initially during the test, all the lubricant shows higher coefficient of friction up to 1000 s. This was due to the time taken by the lubricants to maintain a lubricant film on the surface. The Karanja oil shows the maximum coefficient of friction with respect to nano lubricants. The least coefficient of friction was obtained during the 0.6%

Fig. 3 Coefficient of friction of the lubricants
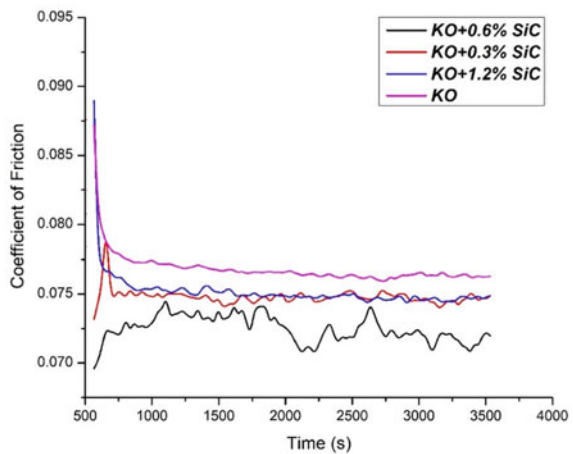
concentration. The nanoparticles up to 0.6% concentration fill up the gaps on the surfaces and provide assistance to the lubricant film in resisting the stress buildup by the applied load. When the nanoparticles concentration increases, COF also increases due to the agglomeration of the particles on the surfaces [17, 18].

3.2 Wear

The specific wear rate of the material was calculated based on Eq. (1). Figure 4 shows the specific wear rate of the materials with different lubricants. The more wear were happened with the raw Karanja oil. The nanoparticles mixing to the Karanja oil achieved less wear at 0.3 and 0.6% concentration. When more amount of nanoparticles added, it gets agglomerated on the surface which results in more amount of wear of the pin [16, 19].

$$\text{Specificwearrate} = \frac{\text{Volumeloss}(\text{mm}^3)}{\text{Load}(N)\,x\,\text{Slidingdistance}(\text{m})} \tag{1}$$

The wear scar diameter of the samples was assessed using the view 7 software employed with the microscope. The wear scar diameter was the scar formed on the surface during the various conditions. It can be observed from Fig. 5 that the maximum scar was shown when raw Karanja oil was used. It gets reduced during the application of nanoparticles, and the least scar was attained when 0.3 and 0.6% nanoparticles were added. The formation of the scar was based on the formation of the lubricant film thickness. The addition of nanoparticles up to 0.6% concentration results in the formation of effective lubricant film on the surface.

Fig. 4 Specific wear rate of the material
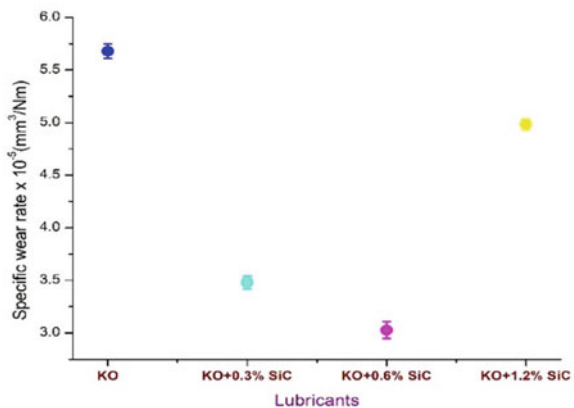
Fig. 5 Wear scar diameter
of the lubricants
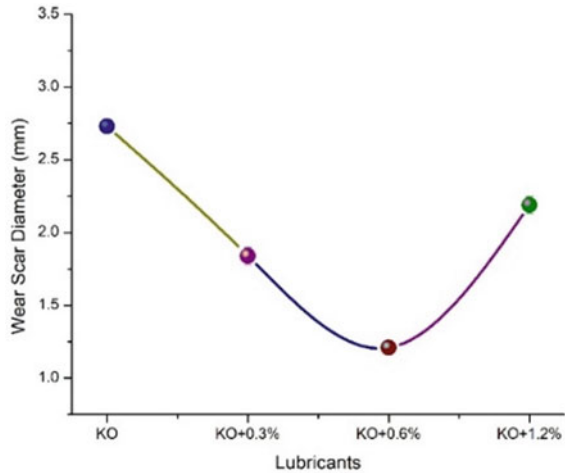
3.3 Worn Surface Analysis

Figure 6 shows the images obtained for the worn surfaces using SEM. Figure 6a
shows the images for the pin under Karanja oil lubrication. The delamination of the
surface is due to the abrasion. Figure 6b and c shows the surfaces with 0.3 and 0.6%
nanoparticles concentration. The surface gets smoother when the nanoparticles were
added up to the concentration of 0.6%. Less amount of grooves were present on the
surface which can be verified by the 3D surface. Figure 6d shows the images during
the addition of 1.2% nanoparticles. The cracks and pits on the surface were formed
due to the agglomeration of the nanoparticles on the surface resulting in more wear.

4 Conclusions

The tribological analysis of the Karanja oil with SiC nanopartciles addition was
analyzed. Following are the conclusions drawn from the study.

- The coefficient of friction gets when nanoparticles are added up to 0.3 and 0.6%,
  and an increment in the COF was observed with further addition of the nanopar-
  ticles. The SiC nanoparticles are capable to form protective layer when added up
  to 0.6% to the Karanja oil.
- The less specific wear of the material was obtained with the addition of nanopar-
  ticles to the Karanja oil up to 0.3 and 0.6%. The amount of wear rate was less
  with respect to raw Karanja oil.
- Maximum wear scar diameter was observed with the Karanja oil, and addition of
  0.6% nanoparticles provided less wear scar diameter. The highly worn surfaces
  were obtained with higher concentration of the nanoparticles.

(a)

(a)

(b)

(b)

(c)

(c)

(d)

(d)
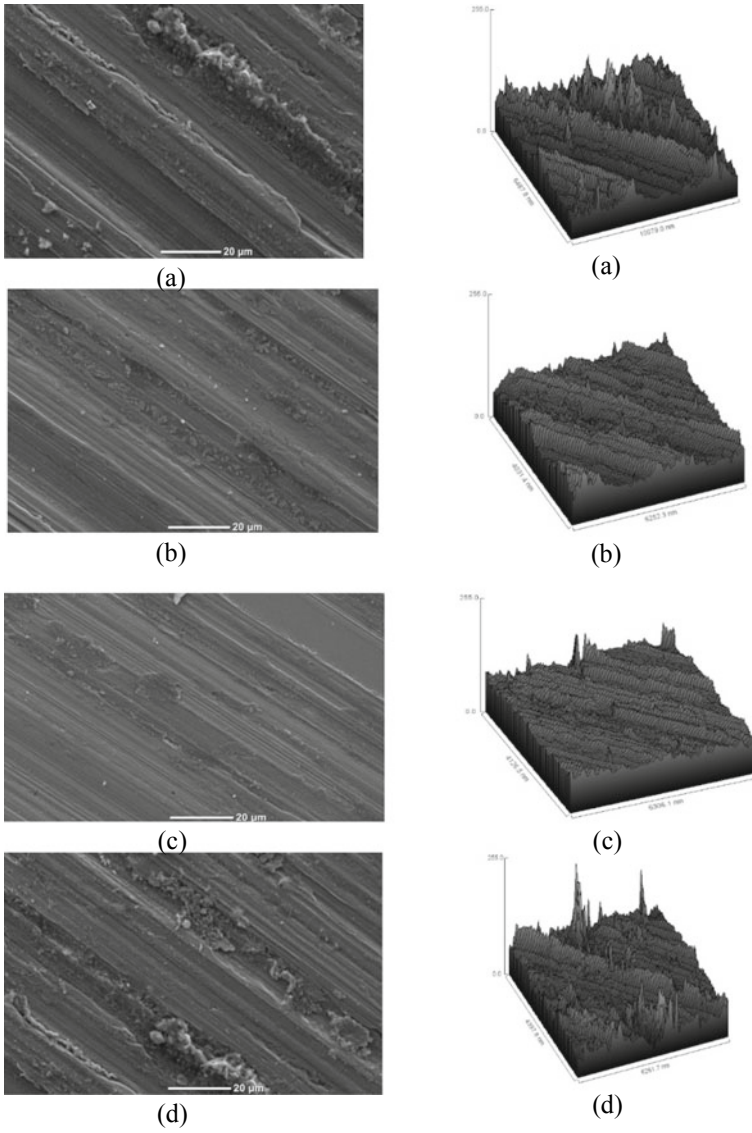
Fig. 6 Scanning electron microscope images with 20 μm zoom **a** KO **b** KO + 0.3% **c** KO + 0.6% **d** KO + 1.2%

References

1. Suresh, M., Jawahar, C.P., Richard, A.: A review on biodiesel production, combustion, performance, and emission characteristics of non-edible oils in variable compression ratio diesel engine using biodiesel and its blends. Renew Sustain. Energ. Rev. **92**, 38–49 (2018)
2. Singh, Y., Farooq, A., Raza, A., Mahmood, M.A., Jain, S.: Sustainability of a non-edible vegetable oil based bio-lubricant for automotive applications: a review. Process Saf. Environ. Prot. **111**, 701–713 (2017)
3. Singh, Y., Sharma, A., Singh, N., Singla, A., Rastogi, P.M.: Prospects of inedible plant oil-driven bio-lubricants for tribological characteristics—a review. Int. J. Ambient Energ. 1–14 (2018)
4. Singh, Y., Singla, A., Bhurat, S.: Tribological behavior of pongamia oil-based biodiesel blended lubricant at different loads. Energ. Sources, Part A: Recov. Utilization Environ. Eff. **38**, 2876–2882 (2016)
5. Sempebwa, J.C., Carpenter, D.O.: The generation, use and disposal of waste crankcase oil in developing countries: A case for Kampala district, Uganda. J. Hazard. Mater. **161**, 835–841 (2009)
6. Afifah, A.N., Syahrullail, S., Wan Azlee, N.I., Che Sidik, N.A., Yahya, W.J., Abd Rahim, E.: Biolubricant production from palm stearin through enzymatic transesterification method. Biochem. Eng. J. **148**, 178–184 (2019)
7. Aravind, A., Joy, M.L., Nair, K.P.: Lubricant properties of biodegradable rubber tree seed (Hevea brasiliensis Muell. Arg) oil. Ind. Crops Prod. **74**, 14–19 (2015)
8. Bhaumik, S., Maggirwar, R., Datta, S., Pathak, S.D.: Analyses of anti-wear and extreme pressure properties of castor oil with zinc oxide nano friction modifiers. Appl. Surf. Sci. **449**, 277–286 (2018)
9. Ren, B., Gao, L., Xie, B., Li, M., Zhang, S., Zu, G., et al.: Tribological properties and anti-wear mechanism of ZnO@graphene core-shell nanoparticles as lubricant additives. Tribol. Int. **144**, 106114 (2020)
10. Sui, T., Ding, M., Ji, C., Yan, S., Wei, J., Wang, A., et al.: Dispersibility and rheological behavior of functionalized silica nanoparticles as lubricant additives. Ceram. Int. **44**, 18438–18443 (2018)
11. Zhang, B.-S., Xu, B.-S., Xu, Y., Gao, F., Shi, P.-J., Wu, Y.-X.: CU nanoparticles effect on the tribological properties of hydrosilicate powders as lubricant additive for steel–steel contacts. Tribol. Int. **44**, 878–886 (2011)
12. Zhang, X.-Z., Wu, X.-L., Liu, G.-W., Luo, W.-Q., Guo, Y.-J., Shao, H.-C., et al.: Wetting of molten Sn-3.5Ag-0.5Cu on Ni-P(-SiC) coatings deposited on high volume faction SiC/Al composite. Trans. Nonferrous Met. Soc. China **28**, 1784–1792 (2018)
13. Kumar, D., Singh, B.: Tinospora cordifolia stem extract as an antioxidant additive for enhanced stability of Karanja biodiesel. Ind. Crops Prod. **123**, 10–16 (2018)
14. Syahrullail, S., Kamitani, S., Shakirin, A.: Performance of vegetable oil as lubricant in extreme pressure condition. Proc. Eng. **68**, 172–177 (2013)
15. Peng, Y., Xu, Y., Geng, J., Dearn, K.D., Hu, X.: Tribological assessment of coated piston ring-cylinder liner contacts under bio-oil lubricated conditions. Tribol. Int. **107**, 283–293 (2017)
16. Ali, M.K.A., Xianjun, H., Mai, L., Qingping, C., Turkson, R.F., Bicheng, C.: Improving the tribological characteristics of piston ring assembly in automotive engines using Al_2O_3 and TiO_2 nanomaterials as nano-lubricant additives. Tribol. Int. **103**, 540–554 (2016)
17. Diabb, J., Rodríguez, C.A., Mamidi, N., Sandoval, J.A., Taha-Tijerina, J., Martínez-Romero, O., et al.: Study of lubrication and wear in single point incremental sheet forming (SPIF) process using vegetable oil nanolubricants. Wear, **376–377**, 777–785, 2017/04/15/ 2017.
18. Ghaednia, H., Jackson, R.L., Khodadadi, J.M.: Experimental analysis of stable CuO nanoparticle enhanced lubricants. J. Exp. Nanosci. **10**, 1–18 (2015)
19. Awang, N.W., Ramasamy, D., Kadirgama, K., Najafi, G., Che Sidik, N.A.: Study on friction and wear of Cellulose Nanocrystal (CNC) nanoparticle as lubricating additive in engine oil. Int. J. Heat and Mass Trans. **131**, 1196–1204 (2019)

Performance Characteristics of Karanja Biodiesel Blends Using Energy Audit Technique

Sanjay Mohite , **Sagar Maji** , **and Amit Pal**

1 Introduction

Biodiesel is a mono-alkyl ester consisting of long-chain fatty acids, which is derived from renewable sources. It is an oxygenate fuel obtained from natural biological process [1]. Utilisation of inexhaustible energy technology is at a slow speed. But, biodiesel is more popular as compared to other sources because it can be used as an alternative with diesel [2]. The estimation of energy demand was 13.1473 billion tonnes of oil equivalent on 2015 in the world. This demand has been increasing at a fast pace to 17.7156 billion tonnes of oil equivalent in 2040. Now, there is 239.4 billion tonnes stock of estimated oil reserves, which is being consumed in a fast manner. Therefore, it is very essential to replace this oil fuel with alternative sources of energy. Diesel fuel is popular in the world, and it is better to replace this diesel fuel with an alternative. According to US Legislation, biodiesel production was 30.1 million tonnes in a year of 2014, and it would rise to 35 million tonnes in a year of 2020 [3].

A vehicle's energy audit is a systematic means to measure use of energy. Energy audit is used to examine and save fuel. It is a preliminary step which consists of priority set-up in a programme of energy management. Maintenance parameters decrease losses of friction, and parameters of engine performance are computed [4]. An asset's performance is judged by energy benchmarking and rating. Ships do not have any scheme of energy performance benchmarking and rating. Key performance indicators and energy rating scheme have been introduced in ships by researchers. A proposed benchmarking and rating method could be utilised for energy performance [5]. Energy audit has been investigated in fishing vessels. It has been performed

S. Mohite (✉)
Brahma Valley College of Engineering and Research Institute, Nashik, India
e-mail: smohite001@yahoo.com

S. Maji · A. Pal
Department of Mechanical, Production & Industrial and Automobile Engineering, Delhi Technological University, Delhi, India

on Australian fishing vessel for recommendation to get better efficiency. It has been investigated to make recommendation to save and propose changes to construct more efficient vessel. A vessel has been analysed for energy use in it. A sample energy audit has been proposed to fishing vessel of Australia to improve efficiency and reduce fuel consumption [6]. Energy audit is used to reduce consumption of energy and environmental impact. Green energy audit is concerned with energy and environment. It optimises building's energy performance and provides sustainability [7]. Diesel engine of heavy duty and medium duty has been analysed to find efficiency, energy losses and prospects to improve. Energy audit and technology forecasting have been used to find emerging technology for reduction of fuel. Fuel consumption has been reduced in heavy-duty diesel engine with application of future technology [8]. An energy audit is applied to get the best energy efficiency. Energy audit has been identified and communicated to get better energy conservation method [9]. There are various sectors to use energy audit. For this reason, an energy audit technique is needed for biodiesel engine, which takes into account its effect. It also illustrates the utilisation of fuel energy distributions in biodiesel engines. Currently, there is no exact energy audit of biodiesel engine. If blend is not found suitable in energy audit, further concern of blend is not required, thus saving time and money. A variety of performance and emission characteristics with heat flow analysis has been discussed. In energy audit, choice of performance and emission characteristics of biodiesel engine is one of the imperative features. In this analytical study, brake-specific energy consumption, heat flow analysis, friction power and smoke emission have been selected as key performance and emission characteristics which should be integrated in energy audit of biodiesel engine. This choice is based on their control on other parameters. This energy audit would be coordinated in research of biodiesel as fuel [10].

The documentation of biofuel performance has been known as a valuable judgment method and device to deal with biofuel utilisation and get better biofuel performance methodically. Biofuel performance certification is found to be obligatory in biofuel industry to validate biodiesel in diesel engine. In this paper, worldwide biofuel use, performance of biofuel and energy audit have been reviewed to simplify research gaps. The performance and emission characteristics of biodiesel engine have been selected as key features to judge biodiesel engine with an energy audit at the initial stage as follows [11].

1. Consumption of brake specific energy.
2. Heat flow analysis dealing with brake power, jacket cooling water, exhaust gas, radiation.
3. Friction power.
4. Smoke emission.

This might be called as preliminary energy audit to assess biodiesel engine to save time. If a blend is found practicable, then it could be used in diesel engine; otherwise, it should to discarded in total with no need to evaluate other parameters. This may be documented as a system of biodiesel certification. A preliminary energy audit method is recommended to standardise it [11].

Table 1 Diesel engine's specification [12]

S. No.	Component	Specification
1	Brand name	Kirloskar
2	Type	Four-stroke
3	Number of cylinder	Single
4	Stroke in cm	11
5	Bore in cm	8.75
6	Capacity in cubic cm	661
7	Compression ratio	18
8	Cooling arrangement	Water
9	Speed in RPM	1500
10	Rated power in kW	3.5

2 Materials and Methods

2.1 New Methodology

A new methodology is generated to evaluate performance and emission characteristics with the use of energy audit technique. This is one of the simple and fast methods to evaluate performance and emission characteristics in initial stage to save time and energy. In this method, BSEC, heat flow analysis, friction power loss and smoke analysis are evaluated to decide the utility of biodiesel blends for further investigation [10, 11].

2.2 Experimental Setup

Four-stroke single-cylinder, water-cooled, DI diesel engine was used to conduct experiments to assess characteristics of performance and emission parameters using energy audit technique. Engine was loaded with eddy current dynamometer. A vertical panel box, which consists of fuel tank, air box, manometer, fuel measuring unit, air and fuel flow measurement facilities and indicator of engine, was used. Engine and exhaust cooling water and calorimeter water flow were measured by rotameters (Table 1).

2.3 Methodology

Karanja biodiesel was prepared in the laboratory, and blends were prepared on basis of volume as 10, 20 and 30% in diesel. Karanja oil was used to produce biodiesel with

transesterification reaction. 0.696 stoke, 911 kg/m^3 and 38.416 MJ/kg were found for Karanja oil as viscosity, density and calorific value, respectively. 0.0572 stoke, 885 kg/m^3 and 37.425 MJ/kg were found as viscosity, density and calorific value of Karanja biodiesel, respectively. "Engine soft LV" was utilised in online engine measurement [12].

Engine performance characteristics were measured by Engine Soft software. The measurement of performance characteristics was done at 18:1 compression ratio with load variations from 0.5 to 3.5 kW. AVL Smoke meter measured smoke opacity.

3   Result and Discussion

3.1   *Brake-Specific Energy Consumption (BSEC)*

Brake-specific energy consumption is calculated for Karanja biodiesel blends at loads of 0.5–3.5 kW. There is highest rise of 8.52% in between B30 and diesel with the consideration of all fuels at 3.5 kW. Low calorific value, low volatile and high density would be the reasons. Brake-specific energy consumptions of fuels are shown in the bar chart at varying loads (Fig. 1). BSEC gradually decreases with increase in load which may be caused due to corresponding reduction in brake-specific fuel consumption. BSEC of biodiesel blends is found to have somewhat high values as compared to diesel. It increases with biodiesel concentration in blends which may be recognised due to lower heating value of biodiesel. This is agreed with the researchers [13–16]. It is noted that there is rise in brake-specific energy consumptions with the rise in concentration of biodiesel in blends. BSEC of biodiesel blend is higher as compared to that of diesel. BSEC might be chosen as one of the basic parameters for taking decision to incorporate energy conservation measures [10, 11]. Therefore, the biodiesel concentration in blend fuels should be reduced to bring down the value of BSEC. This is because of requirement of minimum BSEC in efficient diesel engine.

Fig. 1   BSEC of Karanja biodiesel blends
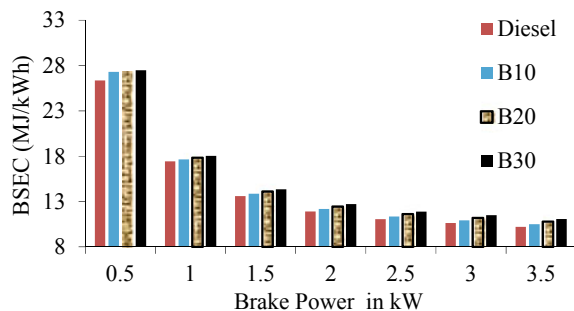
Fig. 2 HBP of Karanja
biodiesel blend
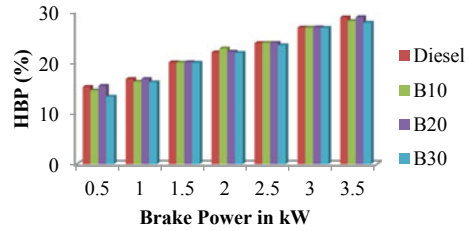
3.2 Conversion of Fuel's Heat Energy into Useful Work Output (HBP)

At a compression ratio of 18, there is significant improvement at a range of 2–4 kW brake power in brake thermal efficiency. HBP is identical to brake thermal efficiency. This happens due to the presence of oxygen in biodiesel and its higher lubricity, causing good combustion and reduced friction [17]. In heat flow analysis of Karanja biodiesel blends at 3.5 kW brake power, it is found that heat is utilised for useful work (HBP) in the range of 27.92–29.04%. Higher limit of HBP for B20 is found to be 29.04, 29% for diesel, 28.3% for B10 and 27.92% for B30 at brake power of 3.5 kW (Fig. 2). This is due to availability of sufficient oxygen in biodiesel blends for proper combustion. B20 has slightly higher HBP as compared to that of diesel. The presence of higher amount of oxygen in biodiesel causes combustion in proper way. Higher viscosity also causes increase in lubrication. Biodiesel is found to have 66% superior lubrication performance in comparison with diesel. A +30% increment in lubricity would be achieved with 1% addition of biodiesel in blend fuel. These factors would cause increment in HBP for B20 fuel. It is observed that at lower and higher loads, B10 has lower HBP in comparison with diesel which might be caused because of lower amount of oxygen content. It is also observed that HBP increases at loads of 2 kW and 2.5 kW brake power in comparison with diesel which might be the reason because of increment in lubrication at middle loads. It is also observed that B 30 has lower HBP at all loads. Higher viscosity, improper spray and improper combustion would be the reason [18, 19]. The conversion of fuel's heat energy into useful work output of B20 biodiesel blends is found to be slightly higher than that of other test fuels.

3.3 Loss of Fuel's Heat Energy to Jacket Cooling Water (HJW)

There is spontaneous climb in hotness of combustion chamber, cylinder and entire engine at time of combustion. It is noted that HJW is higher as compared to other parameters such as HBP, HEgas and HRAD. This happens because higher amount of heat is engrossed by the coolant as compared to other parameters which is because

Fig. 3 HJW of Karanja
biodiesel blend
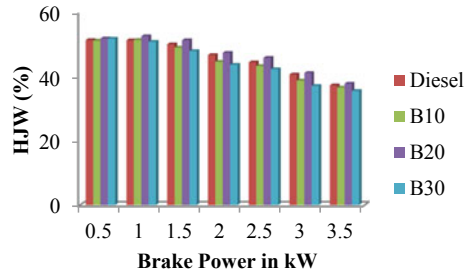
the temperature difference between cylinder and cooling medium is high, causing increase heat transfer rate. HJW is measured to be somewhat higher for B20 in comparison with other test fuels (Fig. 3). This would be caused due to higher HBP of B20 which results in better combustion and higher engine temperature as compared to that of other test fuels [20].

3.4 Loss of Fuel's Heat Energy to Exhaust Gas (HEgas)

The quantity of fraction of heat which is engrossed by exhaust gas is shown as HEgas in this paper. This is found to be lower than HJW, which depicts that smaller fraction of fuel heat energy is absorbed by the exhaust gas as compared to the cooling medium. But B20 has slightly lower HEgas as compared to other test fuels, indicating an effective use of heat energy and causing higher HBP. HEgas reduces with increment in load, which is caused because of reduction in heat losses to exhaust with increase in load. HEgas is found to be decreased rapidly at lower loads. There is more deduction in heat loss at low quantities of load because of reduction in BSEC sharply, at lower loads (Fig. 4). Reduction in BSEC depicts the reduction in heat losses also. In case of diesel fuel, heat loss to exhaust varies from 22.94 to 22.02% from 1.5 kW to 3.5 kW brake power with marginal difference of 2.92% only. This is caused due to a small reduction in heat losses with increase in load [21, 22]. It is found that heat loss in exhaust is higher for B30 in comparison with other test fuels.

Fig. 4 HEgas of Karanja
biodiesel blend
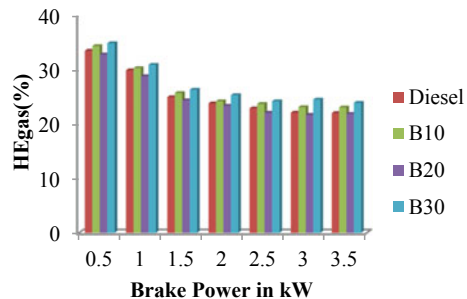
Fig. 5 HRAD of Karanja
biodiesel blend
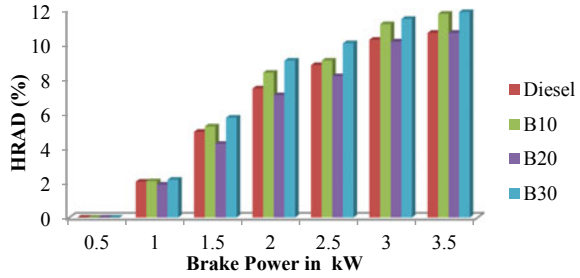
3.5 Loss of Fuel's Heat Energy to Radiation (HRAD)

It is energy of fuel heat which is lost to radiation and other non-accountable loss. It is remaining heat energy, which is not consumed in HBP, HJW and HEgas (Fig. 5). HRAD is found to be lower than that of HBP, HJW and HEgas [23, 24]. It is found to increase with increase in load. At lower load, it is found to be quite negligible. At higher loads, it is also found that B30 has more heat loss in radiation in comparison with other tested fuels, which is due to reduced amount of heat energy conversion into useful work. Heat loss in radiation is found to be higher for B30 in comparison with other test fuels.

3.6 Friction Power (FP) Loss Analysis

Friction power loss reduces with the increment of biodiesel concentration in biodiesel blends. The highest reduction in loss of friction power is observed for B30 for Karanja biodiesel blends. It may occur because of good lubricity of biodiesel [25]. It is noted that friction power loss is almost same with a slight deviation at all loads for a particular fuel (Fig. 6). Friction power loss of B 30, B20 and B10 is found to be 11.49%, 6.89% and 2.29% lower than that of diesel at 3.5 kW, respectively.

During friction power analysis, maximum decrease in friction power is observed in B30 Karanja biodiesel blend fuel as compared to other tested fuels. All biodiesel

Fig. 6 FP of Karanja
biodiesel blends
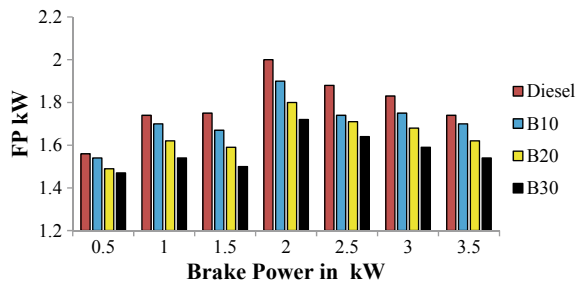
Fig. 7 Smoke opacity of
Karanja biodiesel blends
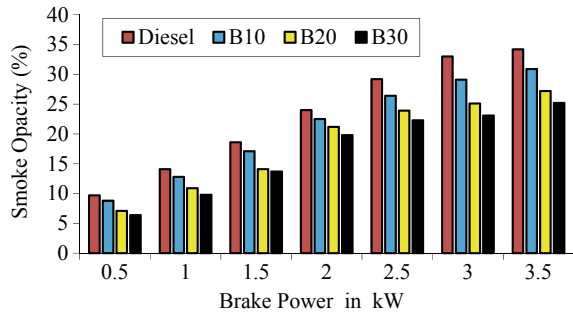
blends are found to have reduced friction power in comparison with diesel. When biodiesel concentration of blends increases, it reduces friction power loss.

3.7 Smoke Emission Analysis

There is no deterioration in trends of performance characteristics of biodiesel blends as compared to diesel, and smoke is also reduced tremendously [26]. Reduction in smoke emission is noted while using biodiesel blends of B10, B20 & B30 as compared to diesel. Minimum smoke emission is observed in case of B30 biodiesel blend which indicates that biodiesel tends to decrease smoke emission. This may be attributed because of oxygen content in biodiesel and good combustion. Smoke opacity is lower for biodiesel blends in comparison with diesel (Fig. 7). It is found to be 9.64, 20.46 and 26.31% lower than that of diesel for B10, B20 and B30, respectively, at 3.5 kW. This is in agreement with [27, 28]. During smoke emission analysis, maximum decrease in smoke opacity is measured in B30 blend fuel. All biodiesel blends are found to have reduced smoke opacity. When biodiesel concentration in blends increases, it reduces smoke opacity subsequently.

3.8 Instruments List with Accuracy

The list of used instruments is given in Table 2.

3.9 Uncertainty Analysis

Uncertainty analysis of these energy audit parameters is given in Table 3.

Table 2 Instrument's list with accuracy

S. No	Name of instrument	Accuracy
1	*Diesel engine test rig*	
	Engine load	±0.2% of Indicated value
	Crank angle	±0.1% of Indicated value
	Engine speed	±1 RPM
	Temperatures	±1 °C
	Piezo sensor	±0.1% of Indicated value
	Burette measurement	± 2 cc
2	Smoke meter	± 5% of Indicated value

Table 3 Uncertainty analysis

Name of parameter	Uncertainty in %
BSEC	±1.6
HBP	±3.6
HEgas	±3.7
HJW	±2.9
HRAD	±3.0
FP	±0.6
Smoke opacity	±1.0

Total Uncertainty = Square root of [(uncertainty of BSEC)^2 + (uncertainty of HBP)^2 + (uncertainty of HEgas)^2 + (uncertainty of HJW)^2 + (uncertainty of HRAD)^2 + (uncertainty of FP)^2 + (uncertainty of Smoke opacity)^2].

Total Uncertainty = Square root of [$(1.6)^2 + (3.6)^2 + (3.7)^2 + (2.9)^2 + (3)^2 + (0.64)^2 + (1)^2$] = (±) 6.9%.

4   Conclusion

The major conclusions of this energy audit are as follows:-

1. In BSEC, there is highest rise of 8.52% in between B30 and diesel at 3.5 kW.
2. Higher limit of HBP for B20 is found to be 29.04, 29 for diesel, 28.3% for B10 and 27.92% for B30 at brake power of 3.5 kW.
3. HJW is measured to be somewhat higher for B20 in comparison with other test fuels.
4. B20 has slightly lower HEgas as compared to other test fuels. It is found that heat loss in exhaust is higher for B30 in comparison with other test fuels.
5. HRAD is found to be lower than that of HBP, HJW and HEgas. Heat loss in radiation is found to be higher for B30 in comparison with other test fuels.

6. It is noted that friction power loss is almost same with a slight deviation at all loads for a particular fuel. Friction power loss of B 30, B20 and B10 is found to be 11.49%, 6.89% and 2.29% lower than that of diesel at 3.5 kW, respectively.

7. Smoke opacity is lower for biodiesel blends in comparison with diesel. It is found to be 9.64%, 20.46% and 26.31% lower than that of diesel for B10, B20 and B30, respectively, at 3.5 kW.

Karanja B-20 blends test fuels have been found to be more suitable in preliminary energy audit method, and it would be tested further for other parameters.

References

1. Ramadhas, A.S., Jayaraj, S., Muraleedharan, C.: Biodiesel production from high FFA rubber seed oil. Fuel **84**, 335–340 (2005)
2. Misra, R.D., Murthy, M.S.: Straight vegetable oils usage in a compression ignition engine- a review. Renew. Sustain. Energy Rev. **14**, 3005–3013 (2010)
3. Sierra-Cantor, J.F., Guerroro-Fajardo, C.A.: Methods for improving the cold flow properties of biodiesel with high saturated fatty acid content- a review. Renew. Sustain. Energy Rev. **72**, 771–790 (2017)
4. Erkut, E., Maclean, D.: Alberta's energy efficiency branch conducts transportation audits. Interfaces **22**(3), 15–21 (1992)
5. Bazari, Z.: Ship energy performance benchmarking/ rating; methodology and application. J. Mar. Eng. Technol. **6**(1), 11–18 (2007)
6. Thomas, G., O'Doherty, D., Sterling, D., Chin, C.: Energy audit of fishing vessels. Proc. Inst. Mech. Eng. Part M: J. Eng. Marit. Environ. **224**(2), 87–101 (2010)
7. Dall, G., Speccher, A., Bruni, E.: The green energy audit, a new procedure for the sustainable auditing of existing buildings integrated with the LEED Protocols. Sustain. Cities Soc. **3**, 54–65 (2012)
8. Thiruvengadam, A., Pradhan, S., Thiruvengadam, P., Besch, M., and Carder, D.: Heavy duty vehicle diesel engine efficiency evaluation and energy audit. Center for Alternative Fuels, Engines, and Emissions, West Virgina University Final report, West Virgina University, Morgantown, WV, USA (2014)
9. Anina, J.M., Rottmayer, S.P.: Virtual audits: the promise and the reality. Energ. Eng. **113**(6), 34–52 (2016)
10. Mohite, S., Maji, S.: Importance of energy audit in diesel engine fuelled with biodiesel blends: review and analysis. Eur. J. Sustain. Dev. Res. **4**(2), em0118 (2020)
11. Mohite, S., Maji, S.: Biofuel Certification performance: a review & analysis. Eur. J. Sustain. Dev. Res. **4**(3), em0124 (2020)
12. Mohite, S., Kumar, S., Maji, S.: Experimental studies on the use of Karanja Biodiesel as blend in a compression ignition engine. Int. J. Renew. Energ. Res. **6**(2), 355–360 (2016)
13. Sahoo, P.K., Das, L.M., Babu, M.K.G., Arora, P., Singh, V.P., Kumar, N.R., Varyani, T.S.: Comparative evaluation of performance and emission characteristics of Jatropha, Karanja & Polanga based biodiesel as fuel in a tractor engine. Fuel **88**(9), 1698–1707 (2009)
14. Senhur, S., Asokan, M.A., Rahul, R., Francis, S., Sreelekh, M.K.: Performance, emission and combustion characteristics of diesel engine fuelled with waste cooking oil biodiesel/diesel blends with additives. Energy **122**, 638–648 (2017)
15. Babu, D., Anand, R.: Effect of biodiesel-diesel-n-pentanol and biodiesel-diesel-n-hexanol blends on diesel engine emission and combustion characteristics. Energy **133**, 761–776 (2017)
16. Ashok, B., Nanthagopal, K., Raj, R.T.K., Bhaskar, J.P., Vignesh, D.S.: Influence of injection timing and exhaust gas recirculation of a Calophyllum inophyllum methyl ester fuelled CI engine. Fuel Process. Technol. **167**, 18–30 (2017)

17. Yadav, A.K., Khan, M.E., Pal, A.: Kaner biodiesel production through hybrid reactor and its performance testing on a CI engine at different compression ratios. Egypt. J. Petrol. **26**, 525–532 (2017)
18. Misra, R.D., Murthy, M.S.: Jatropha- the future fuel of India. Renew. Sustain. Energy Rev. **15**, 1350–1359 (2011)
19. Kumar, D.J., Binnal, P.: Performance evaluation of a single cylinder diesel engine fuelled with biodiesel produced from pumpkin oil. J. Sci. Ind. Res. **71**, 75–78 (2012)
20. Santos, T.B., Ferreira, V.P., Torres, E.A., Silva, J.A.M.D., Ordonez, J.C.: Energy Analysis and exhaust emissions of a stationary engine fuelled with diesel biodiesel blends at variable loads. J. Braz. Soc. Mech. Sci. Eng. **39**(8), 3237–3247 (2017)
21. Panigrahi, N., Mohanty, M.K., Mishra, S.R., Mohanty, R.C.: Energy and exergy analysis of a diesel engine fuelled with diesel and simarouba biodiesel blends. J. Inst. Eng. (India): Ser. C **99**(1), 9–17 (2016)
22. Yasin, M.H.M., Mamat, R., Yusop, A.F., Idris, D.M.N.D., Yusaf, T., Rasul, M., Najafi, G.: Study of a diesel engine performance with exhaust gas recirculation (EGR) system fuelled with palm biodiesel. Energ. Procedia **111**, 26–31 (2017)
23. Benajes, J., Martin, J., Garcia, A., Villalta, D., Warey, A.: Incylinder soot radiation heat transfer in direct injection diesel engine. Energ. Convers. Manag. **106**, 414–427 (2015)
24. Heywood, J.B.: Internal Combustion Engine Fundamentals. Tata McGraw Hill Edition, India (2012)
25. Dhar, A., Agarwal, A.K.: Effect of Karanja biodiesel blend on engine wear in a diesel engine. Fuel **134**, 81–89 (2014)
26. Pal, A., Kachhwaha, S.S.: Application of ultrasound energy for biodiesel production of non edibles oils and CI engine performance testing. Published in proceedings of National Symposium on Ultrasonics (NSU XIX) organized by Ultrasonic society of India and CSIR-National Physical Laboratory, New Delhi (30–31st Oct., 2012)
27. Ong, H.H., Masjuki, H.H., Mahila, T.M.I., Silionga, A.S., Chong, W.T., Leong, K.Y.: Optimization of biodiesel production and engine performance from high free fatty acid Calophyllum inophyllum oil in CI diesel engine. Energ. Convers. Manage. **81**, 30–40 (2014)
28. Pal, A., Kachhwaha, S.S., Maji, S., Babu, M.K.G.: Thumba (Citrullus colocyntis) seed oil: a sustainable source of renewable energy for biodiesel production. J. Sci. Ind. Res. **69**(5), 384–389 (2010)

Performance of Capillary Fed Wick Stove Fuelled with Blends of Butanol and Kerosene

Mohd. Yunus Khan, P. Sudhakar Rao, Md. Imran, and Sandip Kumar

1 Introduction

1.1 Need for Alternative Fuel

In India, biomass fuels (like wood, cow dung and agricultural waste) are used as a major source of energy [1]. Significant populace is living in rural areas, and a substantial amount in semi-urban and urban areas uses these fuels. Consumption of firewood is increasing at a steady rate, and deforestation is causing shortage problem. Increasing industrialization and motorization, depleting natural resources has led to a precarious ascent in the demand for petroleum [2]. Besides all this, combustion of these fuels causes environment pollution [3, 4]. In views of the above problems, search for the alternative fuels is one of the biggest needs of the hour.

Kerosene is a thin and clear fluid composed of hydrocarbons. It is derived through the process of fractional distillation of petroleum in the range of 180 and 250 °C, bringing about a mixture of carbon chains that commonly contain between 6 and 16 carbon atoms per molecule [5, 6]. Density of kerosene is about 0.78–0.81 g/cm^3. It is not miscible in water, but miscible in petroleum derivatives [7]. It is used as fuel in jet engines. In rural areas of India, kerosene is primary used as fuel to cook food and lightening purposes. Kerosene stoves have supplanted the conventional wood-based stoves which inefficient and produce cocktail of pollutants. However, kerosene contains impurities which include sulfur, aromatics and hydrocarbons. On

Mohd. Yunus Khan (✉) · P. Sudhakar Rao
National Institute of Technical Teachers' Training and Research, Chandigarh 160019, India
e-mail: yunus.mech19@nitttrchd.ac.in

P. Sudhakar Rao
e-mail: psrao@nitttrchd.ac.in

Md. Imran · S. Kumar
University Polytechnic, Aligarh Muslim University, Aligarh 202002, India

combustion, it creates pollution and extremely unpleasant odor. It also produces smoke which causes different respiratory diseases [5, 8].

Khan et al. [6] used blends of ethanol and kerosene in wick stove with no change in stove design. Stove efficiency and fuel consumption rate for fuel blends were observed to be quite close to those obtained with kerosene. Khan et al. [8, 9] evaluated performance of unmodified wick stove fueled with blends of Jatropha curcas oil and kerosene to establish the feasibility of using non-edible Jatropha oil as a fuel for wick stove. Rajvanshi et al. [10] developed pressure stove fueled with 50% ethanol–water blend. They found that the stove permits easy flame regulation and gives an output comparable with conventional fuel. Khan et al. [11] tested blends of Karanja oil and kerosene in wick stove. They found blend containing 10, 15 and 20% Karanja oil can be successfully substituted for kerosene.

After undergoing available literature, it is felt that not much work on use of butanol in kerosene stove has been conducted. The objective of this investigation is to assess performance of capillary fed wick stove fuelled on three blends of butanol (B) and kerosene (K). During experimentations, the stove was fuelled with 5, 10 and 20% butanol and kerosene blends. Unaltered kerosene was used as a baseline fuel. The fuels used for all experiments belonged to single supply, to stay away from unnecessary introduction of any variation during testing. Experimentations were conducted out on unmodified stove.

1.2 Butanol as Stove Fuel

Butanol is eco-friendly and produces significantly less pollutants in comparison with kerosene. It is a combustible fluid that is utilized as a fuel and as an industrial solvent. Butanol is a hydrocarbon, implying that it is made out of the H_2, O_2 and C. It can be conveniently used as a fuel in IC engine [12]. Table 1 compares the properties of butanol and kerosene.

It can be seen that properties of butanol are in good comparison with those of kerosene and therefore can be used in existing stove design without any alteration. The slight difference in the properties is due to the different chemical structures of these fuels, but both are composed mainly of hydrocarbons. The kinematic viscosity and density of butanol are slightly higher than kerosene. In blended form, this difference becomes very less. Hence, blends of butanol and kerosene will not cause any capillary

Table 1 Properties of kerosene and butanol [5, 13, 14]

Properties/fuel	Kinematic viscosity (cSt) at 40 °C	Calorific value (MJ/kg)	Ignition Temp. (°C)	Density (g/cm³)
Kerosene	2.50	43.5	55	0.820
Butanol	3.64	33.0	343	0.810

Fig. 1 Variation of kinematic viscosity with respect to blend ratio
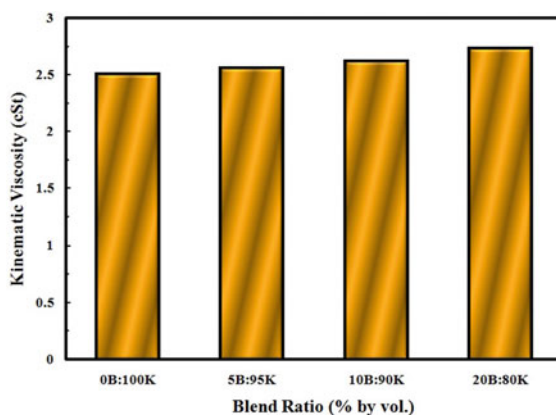
Fig. 2 Variation of density with respect to blend ratio
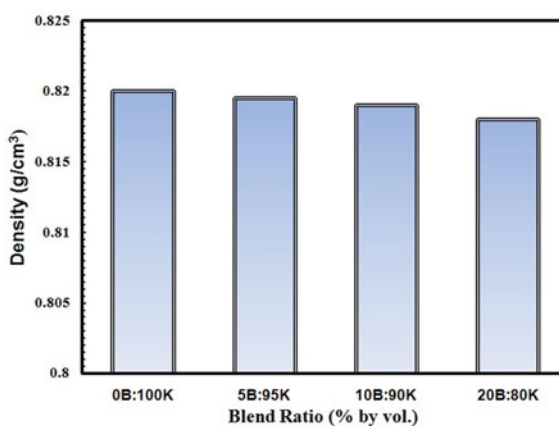
action issue. The calorific value of butanol is 33 MJ/kg, which is lower than that for kerosene. Variation of kinematic viscosity and density with respect to blend ratio is shown in Figs. 1 and 2, respectively.

2 Experimental Methodology

2.1 Test Setup

Figure 3 depicts line diagram of test setup which consists of a capillary fed wick stove, electronic weighing machine, aluminum vessel, stirrer and thermometer. Stove has eight wicks of woven cotton set inside a holder such that they can be moved up and down through a control knob. Wicks rise in an annular space encompassed by two

Fig. 3 Test setup
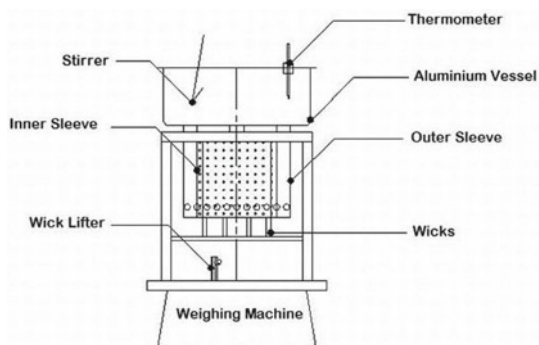
Table 2 Specifications of the stove

Product name	Manufactured by	Stove type	Fuel tank capacity	No. of wicks	Thermal efficiency (design)	Design fuel
Fargo	MVS enterprises, New Delhi	Capillary fed wick stove	1 kg	10	60%	Kerosene

concentric perforated steel walls, which are separated marginally more extensive than the wick thickness. The lower parts of the wicks are plunged into and absorb kerosene from the kerosene tank. The stove is lit by removing the perforated steel wall raising the wicks and lighting them. The holder is then put again. The flame develops at the top and fills the gap between two walls of the holder. The flame can be raised or brought down by means of the knob, when raised the flame burns with more intensity and vice versa. Specifications of the stove are given in Table 2.

2.2 Method

Thermal efficiency of stove was determined according to the guideline of Indian Standards. Water-boiling test (WBT) was performed for necessary calculations. WBT is a laboratory test that assesses stove performance while completing a standard task in a controlled environment (boiling and simmering water) to evaluate heat transfer and combustion efficiency of the stove [15].

The test fuel was filled nearly in the fuel tank. Vessel of aluminum material was chosen for testing. Measurement of water temperature during experimentation was done by alcoholic thermometer (range 0–180 °C). Aluminum stirrer was used for stirring the water so that heat is distributed uniformly. Electronic weighing machine (range 10 kg and least count 1 g) was used for measuring weight of water and stove. The weight of vessel with its cover (W_{Al}) and the weight of water filled in the vessel

(W_w) were recorded. Starting temperature of water (T_1) was also recorded. The weight of stove along with fuel (W_1) was noted. The stove was lit, and water was heated up to 80 °C with continuous stirring. When temperature of water (T_2) has arrived at 80 °C, the stove was put off. Time taken to raise the temperature from T_1 to T_2 and the weight of stove (W_2) was recorded. The difference in the weight of stove ($W_2 - W_1$) gives the mass of fuel burnt in heating water by temperature ($T_2 - T_1$). The mass of fuel burnt divided by time taken gives fuel consumption rate. Thermal efficiency of the stove is given as

$$\eta \frac{(W_w \times C_w + W_{Al} + C_{Al}) \times T_2 - T_1}{(W_1 - W_2) \times CV}$$

where C_w and C_{Al} are specific heat of water and aluminum, respectively, and CV is calorific value of fuel. By dividing, the testing was repeated thrice, and mean of the value was taken as final reading. The same procedure was adopted for all blends.

3   Results and Discussion

Figure 4 depicts variation of fuel consumption rate with respect to blend ratio. It can be seen that fuel consumption rate increases with the increase in percentage of butanol in the fuel blend. Fuel consumption rate with pure kerosene was found to be 3.22×10^{-5} kg/s while that with 20B:80 K was found to be 4.12×10^{-5} kg/s. The percentage increase in fuel consumption rate using 20B:80 K was 27.9% in comparison with baseline fuel. This is because of the low calorific value of butanol than kerosene. As result of which more fuel is consumed to produce same temperature rise.

Variation of thermal efficiency of stove with respect to blend ratio is presented in Fig. 5. It can be seen that the thermal efficiency decreases with the increasing of

Fig. 4 Variation of fuel consumption rate with respect to blend ratio
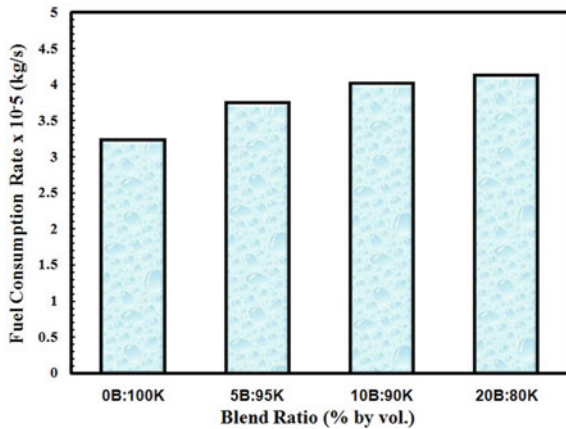
Fig. 5 Variation of thermal efficiency with respect to blend ratio
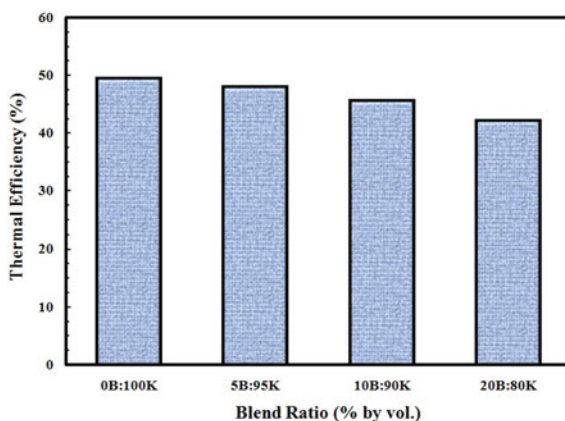
butanol concentration in the fuel blend. Thermal efficiency of stove using unaltered kerosene was found to be 49.3% while that with blend containing 20% butanol was found to be 42.1%. It can be seen that percentage decrease in thermal efficiency value was 14.6% when 20B:80 K was used in place of baseline fuel.

Among all the blends tested, the blend with the 5:95 blends of butanol and kerosene is observed to be most efficient.

4   Conclusions

In this experimental investigation, utility of using blends of butanol and kerosene as a substitute fuel for capillary fed wick stove was assessed. When blends of butanol and kerosene were used, no problem of capillary action was observed. It was observed that wick stove was successfully operated on fuel containing 5%, 10% and 20% butanol in kerosene without any alteration in stove design. It was concluded that fuel consumption rate increased and thermal efficiency decreased with increasing in concentration of butanol in blends. The blend containing 5% butanol was found to be most efficient among all blends tested.

References

1. Narang, H.P., Parashar, D.C., Bhattacharya, S.C., Salam, P.A.: A study of biomass as a source of energy in India. Int. Energy J. **21**(1), 11–23 (1999)
2. Kandpal, J.B., Maheshwari, R.C.: Combustion of biomass fuels in two cookstoves for their conservation. Energy Convers. Manage. **36**(10), 1015–1021 (1995)
3. Pandey, M.R., Neupane, R.P., Gautam, A., Shrestha, I.B.: The effectiveness of smokeless stoves in reducing indoor air pollution in a rural hill region of Nepal. Mt. Res. Dev. **10**(4), 313–320 (1990)

4. Fuller, E.G.: Chemistry and Man's Environment. Houghton-Miffin, Boston (1987)
5. Khan, M.Y., Kumar, M., Mittal, A.: Performance of wick stove fueled with used frying oil-kerosene blends. In: Proceedings of 3rd International Conference on Advances in Mechanical Engineering (ICAME-2010), pp. 55–59. Surat (2010)
6. Khan, M.Y., Khan, F.A., Beg, M.S.: Ethanol-kerosene blends: fuel option for kerosene wick stove. Int. J. Eng. Res. Appl. **3**(1), 464–466 (2013)
7. Speight, J.G., Arjoon, K.K.: Bioremediation of Petroleum and Petroleum Products. Wiley (2012).
8. Khan, M.Y., Pachuari, P.: Performance evaluation of wick stove fueled with Jatropha curcas oil-kerosene blends. NIET J. Eng. Technol. **I**, 63–66 (2010)
9. Khan, M.Y., Faraz, H.: Jatropha curcas oil fueled wick stove for rural areas. In: Souvenir of Two Day National Seminar on Growth and Social Sector Development in Uttar Pradesh Economy, Lucknow, pp. 52–53 (2017)
10. Rajvanshi, A.K., Patil, S.M., Mendonca, B.: Low-concentration ethanol stove for rural areas in India. Energy Sustain. Dev. **11**(1), 94–99 (2007)
11. Khan, M.Y., Sharma, S., Ahmad, S.: Performance of wick stove fueled with Karanja oil-kerosene blends. In Proceedings of National Conference on Recent Advances in Mechanical Engineering (RAME-2011), pp. 209–213. Mathura (2011)
12. What is butanol? https://www.wisegeek.com/what-is-butanol.htm. Last accessed 08 May 2020
13. Mehta, R.N., Chakraborty, M., Mahanta, P., Parikh, P.A.: Evaluation of fuel properties of butanol-biodiesel-diesel blends and their impact on engine performance and emissions. Ind. Eng. Chem. Res. **49**(16), 7660–7665 (2010)
14. Mack, J.H., Schuler, D., Butt, R.H., Dibble, R.W.: Experimental investigation of butanol isomer combustion in Homogeneous Charge Compression Ignition (HCCI) engines. Appl. Energy **165**, 612–626 (2016)
15. Vitali, F., Parmigiani, S., Vaccari, M., Collivignarelli, C.: Agricultural waste as household fuel: Techno-economic assessment of a new rice-husk cookstove for developing countries. Waste Manage. **33**(12), 2762–2770 (2013)

Solar-Driven Vapour Absorption (LiBr–H₂O) Cooling Systems for Commercial Buildings: A Parametric Analysis

Aseem Dubey and **Akhilesh Arora**

1 Introduction

India is developing at a continuous pace, and different sectors are undergoing facelift changes leading to increment in energy consumption at a faster rate. Driven by the expanding economy, rising population and a quest for improved quality of life, annual electricity consumption per capita in India was 543×10^3 Wh per capita in 2007 which is expected to rise to 1895×10^3 Wh per capita by 2030 [1]. The overall electricity consumption of the country was 684,324 GWh in 2010–11 [2].

The sectoral breakup of energy usage shows about 30% of total energy consumption in the residential and commercial sectors collectively. India lies in the hot climatic zone and approximately 45% of energy use in residential and 32% for commercial buildings comes under space cooling as illustrated in Fig. 1.

Electricity consumption of the commercial sector in India has risen by 50% from 2003–2004 to 2010–2011 [3]. The overall recommended yearly energy consumption for the commercial building is 120 kWh/ft², but the yearly energy consumption is 200 kWh/ft² in India [4]. The year 2012 witnessed a downturn in the growth of energy utilization globally, somewhat as a result of the economic downtrend but also because businesses and individuals have responded to price hikes by becoming extra efficient in their usage of energy. Concurrently, the literature reveals that the supply of energy is coming from various diverse sources as the world's energy market continues to evolve, innovate and adapt. USA, Russia, Japan, India, the EU, China and Brazil all saw a subpar increment in energy utilization. In fact, the growth in consumption of different forms of fossil energy was below average [5].

A. Dubey · A. Arora (✉)
Department of Mechanical Engineering, Delhi Technological University, Delhi 110042, India
e-mail: profakhilesharora@gmail.com

A. Dubey
e-mail: aseemdubey009@gmail.com
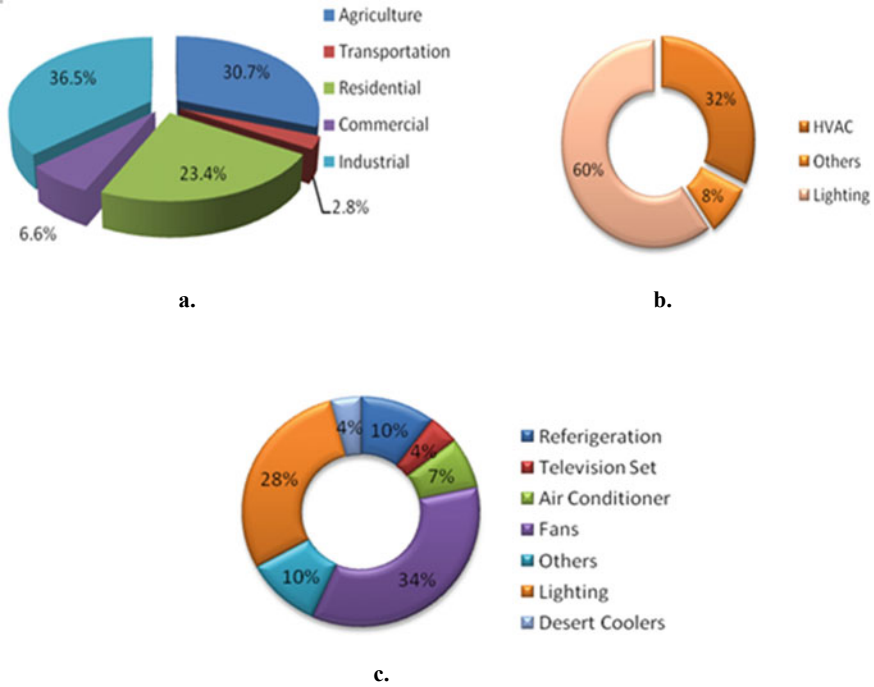
Fig. 1 **a** Energy breakup among different sectors. **b** Energy breakup of commerce-based buildings. **c** Breakup of energy usage in residential buildings

But presently, the increased energy demand can be reduced by using solar-assisted cooling systems instead of compression chillers. Solar absorption cooling systems are in use for various applications in buildings for more than a decade in European as well as Middle East countries. Solar cooling absorption system, in a tropical climate, has been used successfully and continuously without any backup and met the thermal comfort requirements as well [6]. Economic analysis shows higher initial cost of solar vapour absorption systems as compared to electric compression chillers but the annual operational cost is 14% lesser [7].

Kaushik et al. [8] carried an excellent review of hybrid absorption and conventional absorption refrigeration systems and found various gaps, including exergoeconomic viewpoint-based analysis of hybrid VAR systems for cooling applications. Alrwashdeh and Ammari [9] performed economy-based analytical comparison of photovoltaic array powered vapour compression refrigeration system and solar-powered (Evacuated Tube based) VAR system and found absorption system handy along with cost effectiveness, provided it operates under specified running conditions from waste heat (or solar-assisted). Lately, Kizilkan and Yamaguchi did practicability analysis of the new, unfamiliar solar-driven transcritical carbon dioxide (tCO_2)-based

Rankine cycle with an absorption system [10]. Researchers concluded that the absorption system (H$_2$O–LiBr) can be effectively coupled with the solar-driven transcritical (tCO$_2$) Rankine cycle for refrigeration applications and sustainable power generation.

Thus, from the survey it can be deduced that solar-driven vapour absorption system is a feasible option for cooling purposes in the commerce-based office buildings. However, energy-economic analysis of the solar-assisted absorption chiller has not been reported in the open literature for cooling applications in Indian commercial buildings.

In this paper, solar vapour absorption systems have been analysed from the energy viewpoint for commercial Indian buildings for the first time in literature, and economics of the proposed system are compared with the vapour compression cooling system.

2 Availability of Solar Energy

Average global solar radiation available in India is 19 MJ/m^2 daily (Table 1), which is higher than the average value of 10.44 MJ/m^2 for most of the European countries. Annual sunshine differs from 2400 to 3200 h in the country. The western region of India receives bright sunshine for 3000 to 3200 h in a year, and rest of the regions receive for 2600 to 2800 h except the north-eastern states and Jammu and Kashmir where the sun shines for appreciably lower period. When it comes to the availability of global solar radiation, more than 2000 kWh/m^2 year are received over western regions of the country, while east Bihar, North West Bengal and the north-eastern states receive less than 1700 kWh/m^2 year [11].

Table 1 Annual average insolation levels (Worldwide)

Country	Insolation level (MJ/m^2/day)
Belarus	7.2
France	10.9
Germany	9.0
Greece	12.7
India	19
Ireland	7.3
Italy	12.5
Norway	7.2
Russia	9.0
Spain	14.4
Turkey	14.4
UK	9.0
USA	16.2

3 Solar Absorption Cooling

In European and the Middle Eastern countries, solar-assisted absorption cooling systems (LiBr–H_2O) are being used extensively, and research shows that in the long run, this technology is superior to the conventional electric compression chiller. The absorption cooling system utilizes the solar energy through a flat plate collector (FPC) to provide the heat required in the generator, and this will replace the auxiliary boiler. A single effect LiBr–H_2O absorption chiller is shown in Fig. 2.

The single effect absorption cooling system is largely used for cooling purposes in buildings, where chilled water is fed at 6–7 °C. This operates at a generator temperature ranging from 70 to 95 °C. Mostly, the energy performance ratio (EPR) ranges from 0.6 to 0.8 [12]. Working of an absorption refrigeration system is similar to that of a conventional vapour compression refrigeration (VCR) system during process 7–8 and 9–10. Nevertheless, post evaporator, vaporized refrigerant is absorbed by the absorbent, resulting in a liquid solution which is then pumped to the generator (process 1–2 and 2–3). In generator, the mixture (absorbent–refrigerant) is heated to separate the two. Refrigerant vapour is ultimately brought to condenser which is condensed to saturated liquid while absorbent is brought back to absorber (process 4–5 and 5–6).
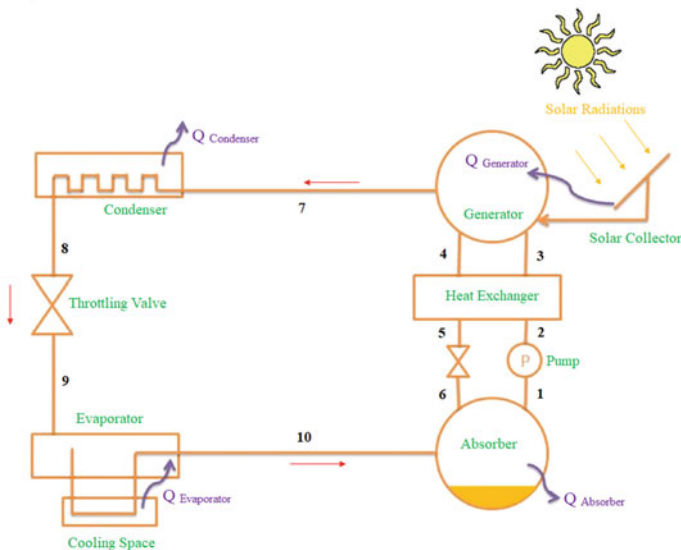
Fig. 2 Schematic of a solar-assisted absorption cooling system

3.1 Classifications

Solar-driven absorption (LiBr–H$_2$O) chiller can be classified into two types.

Single-Stage Absorption Chiller: It is the conventional type of vapour absorption chiller. The heat required by the generator is around 88 °C. The COP of the system approximately ranges between 0.65 and 0.8 [7]. The amount of heat required in a single-stage system is higher as compared to double-stage absorption chillers. The single-stage chiller system is costlier as it requires costly high-grade solar collectors to provide a generator temperature of 90 °C. Also, the single-stage system cannot always perform at its normal rating during periods of low solar radiation and high cooling water temperature. The usable temperature drop is observed in the range of 6–7 °C.

Two-Stage Absorption Chiller: This system is advantageous as it requires a lower temperature for heat supply, i.e. 65–80 °C [7] and usable temperature can range from 12 to 17 °C. Thus, it requires less expensive solar collectors. This attribute provides flexibility to the system, and there are fewer chances of the breakdown. The COP of the system ranges between 1.10 and 1.35 which is higher as compared to the single-stage system. However, the initial cost of a two-stage absorption chiller is 25–30% higher [13]. A comparison of these two chillers is presented in Table 2.

Some of the successful installations done worldwide and their comprehensive technical specifications are given in Table 3. Solar-assisted absorption cooling is not a new technique to meet the cooling demand of commercial office buildings, and it has been in use across for quite a long time now. Literature survey shows that solar cooling is working successfully and providing a huge amount of energy savings and benefits to the end-user.

Table 2 Comparison between single-stage and double-stage vapour absorption chiller

S. No.	Parameters	Single stage	Two stage
1	Absorbent/refrigerant	LiBr–H$_2$O	LiBr–H$_2$O
2	Generator temperature	88–90 °C	65–80 °C
3	Usable temperature	6–7 °C	12–17 °C
4	COP	0.65–0.8	1.1–1.35
5	Type of collector	High-grade FPC	Low-grade collector
6	Area of collector	Large	Less
7	Amount of heat required	Large	Less
8	Initial cost	Less	High
9	Operating cost	High	Less

Table 3 Worldwide installed FPC solar vapour absorption technical specification sheet

S. No.	Country	Absorption chiller type	COP	Collector Area (m²)	Generator Temperature (°C)	Evaporator Temperature (°C)	Available solar intensity (W/m²)	Cooling Capacity (TR)
1	USA	Single stage	0.75	280	98	5.5	185	43
2	France	Single stage	0.67	90	90	5	180	9
3	Spain	Single stage	0.70	49	85	5	177	3
4	Spain	Single stage	0.67	56	90	6	177	4
5	Germany	Single stage	0.76	29	85	5	124	1
6	Thailand	Single stage	0.70	72	95	5	125	10
7	Italy	Single stage	0.72	90	88	7	176	10
8	USA	Single stage	0.71	117	85	5	185	21
9	China	Two stage	0.40	500	75	5	180	29
10	China	Single stage	0.64	135	95	5	180	23
11	Portugal	Single stage	0.70	48	88	5.7	185	6
12	Portugal	Two stage	1.20	105	120	5.7	185	6

4 Case Study

Vapour absorption chillers are used in India to meet cooling demand using non-renewable fossil fuel-based energy systems, and now there is pressure due to rising fuel prices and shortage of energy to shift towards renewable energy sources. Two cases of solar absorption chiller are discussed and analysed here.

4.1 Case 1 (100% Solar-Driven Chiller)

Average load of a commercial building in India is about 200 kWh/m² per annum [4]. Although, this is very high, and it is very likely to go down in the coming years due to the use of efficient chillers and systems. But, in the present case being on the safer side a higher value of 200 kWh/m² per annum is considered for the analysis. Presently for most of the applications, people are using vapour compression chillers

for meeting the cooling demand, although its initial cost is lower but in the long run the operational cost becomes high.

On an average basis, office area is 1,023 sq. ft, and out of that 28% of the commercial office building load is for cooling end use [4, 14]. Thus, a conventional office area would require 10 tons of refrigeration load for an average commercial building. For running an absorption chiller of 10 TR capacity completely on solar energy, the required energy is 268 kWh/day. The available average horizontal global radiation is 643.38 Wh/m², and available solar energy is 272 kWh/day, which can comfortably meet the energy demand of an average size solar-driven absorption chiller. For most of Northern and Central regions of India, cooling is required for about seven months in a year, and in the analysis, this period is considered. Results of the analysis (Table 4) show that solar-driven vapour absorption chiller can bring saving up to 74% on an annual basis in comparison with compression chiller. Although the auxiliary energy usage in the equipments is higher in vapour absorption, the overall energy consumption is much lesser.

Table 4 Energy analysis (CASE 1)

HVAC system specification		
Capacity of chiller	10	TR
Generator temperature	90	°C
Evaporator temperature	7	°C
Cooling tower inlet temperature	36	°C
Solar collector specification		
Type	FPC	
Aperture area	100	m²
Collector efficiency	58%	
Storage volume	7,029	l
Per day solar energy required	268	kWh/day
Availability of solar energy	272	kWh/day
Comparison Sheet		
Compression chiller-type screw chiller		
Power consumption	18,833	kWh/year
Auxiliary power consumption	2906	kWh/year
Energy consumed by compression chillers	21,738	kWh/year
Absorption chiller type		
Power consumption	1712	kWh/year
Auxiliary power consumption	3943	kWh/year
Energy consumed by absorption chiller	5656	kWh/year

4.2 Case 2 (Offsetting Fractional Cooling Demand Using Hybrid System of Solar-Driven Absorption Chiller and Conventional Vapour Compression Chiller)

It is not practical to offset all the cooling demand by solar energy when we consider installation cost. Thus, in this scenario, some part of the cooling demand is being offset by a solar-driven vapour absorption chiller. All the other parameters of CASE 1 have been kept constant only the cooling capacity of 10 TR vapour absorption chiller has been reduced to 5 TR and the remaining 5 TR cooling is done using a conventional vapour compression screw chiller. Thus, the solar collector area is reduced to $50 \, \text{m}^2$ and storage tank volume is also downsized which reduces the initial investment (Table 5).

It is prima facie from the above calculation that solar-driven vapour absorption chiller can be a viable option and a huge amount of savings can be achieved considering both the cases. The problem lies in awareness and market conditions which are not favourable but in the coming years with new laws, the situation will improve.

Table 5 Specification sheet (CASE 2)

HVAC system specification		
Capacity of chiller	5	TR
Generator temperature	88	°C
Evaporator temperature	8	°C
Cooling tower inlet temperature	36	°C
Solar collector specification		
Type	FPC	
Aperture area	50	m^2
Collector efficiency	58%	
Storage volume	3,514	l
Per day solar energy required	134	kWh/day
Availability of solar energy	135	kWh/day
Comparison sheet		
Compression chiller-type screw chiller		
Power consumption	10,272	kWh/year
Auxiliary power consumption	1,454	kWh/year
Energy consumed by compression chillers	11,725	kWh/year
Absorption chiller type		
Power consumption	1,198	kWh/year
Auxiliary power consumption	1,971	kWh/year
Energy consumed by absorption chiller	3,170	kWh/year

5 Economic Evaluation

5.1 Case 1

As per today's market conditions, solar-driven vapour absorption chiller of capacity 10 TR will cost approximately Rs. 33 lakhs [15] including plumbing and installation cost. The major portion of the cost for a solar-driven vapour absorption chiller system comes under the solar collector field installed of 100 m^2 area costing around 3.5 lakhs and storage tank of 3.35 lakhs (Table 6). However, vapour compression chiller's total initial cost is approximately Rs. 23 lakhs. Due to this huge difference in initial cost, solar cooling is not been accepted in India and people are still using the inefficient cooling technology.

However, if its life cycle cost benefit analysis is done, the results are different. 30% subsidy is provided on purchase of a solar collector provided by Government of India to promote this form of energy. Apart from this, government also provides accelerated depreciation tax benefits on renewable energy projects. A solar-driven absorption chiller is in itself a CDM project, and if we consider this case it saves 11 tons of CO$_2$ annually. Thus, if we consider all these benefits together, the dynamic payback period of CASE 1 is 7 years with IRR of 16% (Table 7).

As shown in Table 6, the running cost is just Rs. 45,238 as compared to Rs. 1,73,898 of vapour compression chiller [16].

Table 6 Economic evaluation sheet (Case 1)

Case 1	
Vapour absorption chiller cost analysis (Rs.)	
Price of collector	3,55,250
Price of storage tank	3,35,318
Equipment cost	23,98,958
Miscellaneous cost	50,000
Installation cost	1,38,114
Total initial cost	32,77,640
Annual operating cost	45,238
Annual maintenance cost	2,762
Vapour compression chiller cost analysis (Rs.)	
Equipment cost	16,79,271
Miscellaneous cost	50,000
Total initial cost	17,29,271
Annual operating cost	1,73,898
Annual maintenance cost	33,585

Table 7 Cost benefit analysis (Case 1)

Case 1		IRR
Dynamic payback period	7	16%
Simple payback period	3	NPV
Discount Rate	12%	Rs 4,43,191

5.2 Case 2

On evaluating the second case, the results are different from Case 1, but it is encouraging. Since, in Case 2, the partial offsetting of the cooling demand is done through solar-driven vapour absorption chiller. Thus, the initial cost is Rs. 16 lakhs with solar collector and storage tank costing approximately Rs. 3.5 lakhs. On the other hand, the conventional compression chiller of 5 TR cooling capacity cost around Rs. 8.5 lakhs is shown in Table 8 [16].

Table 8 Economic evaluation sheet (Case 2)

Case 2	
Vapour absorption chiller cost analysis (Rs.)	
Price of collector	1,77,625
Price of storage tank	1,67,635
Equipment cost	11,47,079
Miscellaneous cost	50,000
Installation cost	69,052
Total initial cost	16,11,391
Annual operating cost	25,358
Annual maintenance cost	1,381
Vapour compression chiller cost analysis (Rs.)	
Equipment cost	8,02,955
Miscellaneous cost	50,000
Total initial cost	8,52,955
Annual operating cost	93,797
Annual maintenance cost	16,059

Table 9 Cost benefit analysis (Case 2)

Case 2		IRR
Dynamic payback period	6	17%
Simple payback period	3	NPV
Discount rate	12%	Rs. 2,55,899

Life cycle cost benefit analysis shows that the dynamic payback period of the system is 6 years with IRR of 17% (Table 9). The running cost of solar-driven absorption chiller is Rs. 25,358 as compared to Rs. 93,797 of a compression chiller.

Above analysis shows that using solar-driven vapour absorption chiller for meeting cooling demand is very much feasible in Indian scenario. It might appear costly during the time of installation but investing in this technology is very safe due to the magnitude of benefits it provides to the end-user.

6 Reforms in Government Policies

Indian government has already started incentive program to promote solar energy in the country. Various schemes implemented involve the following:

- Tax exemptions on purchase of solar-driven equipment
- Interest rate subsidies and easy loans on renewable projects
- Accelerated depreciation benefits
- Subsidies on custom duties.

However, still a lot more has to be done to improve the market condition in India. In Greece, the government started giving subsidies to those who are investing in oil substitution technologies [17]. This was an interesting move by the government to encourage renewable energy system in their country. The Government of India to promote solar equipment use as per MNRE notification 2019, provides 30% subsidy on benchmark capital cost for all consumers of states of India except Himachal Pradesh, Uttarakhand and Jammu and Kashmir, where the subsidy is 70%. Various financial institutions, banking sector, co-operative banks, etc., provide loan facility with interest rate 2%-5% and depends on the category of users of solar energy. However, the government should also provide hefty subsidies for those who are in the stream of manufacturing equipments for renewable energy usage.

7 Conclusions

Solar cooling has a huge potential in India. Since the country is developing; a lot of infrastructure is yet to be built. India receives 657 Wh/m² of average global radiation which is perfectly suitable for implementing solar-driven absorption cooling technology. Based on the calculations, it was found that an average commercial office can save up to 74% of energy by switching to solar cooling to meet their cooling demand. But the renewable energy market in India is in its developing stages, thus currently this option is not viable due to high initial cost. However, including the tax benefits and incentives provided by the government and incorporating CDM benefits, payback period for a 100% solar-driven cooling system is 7 years with an IRR of 16%, which is a very good return rate. Although the Government of India has already

started implementing new policies to encourage the market condition, it is a gradual process. Based on the analysis, it can be concluded that solar cooling is one of the brightest renewable energy technologies for the coming future.

References

1. Balghouthi, M., Chahbani, M.H., Guizani, A.: Feasibility of solar absorption air conditioning in Tunisia. Build Environ. **43**, 1459–1470 (2008)
2. Survey Report IEA World Energy Outlook Report 2009
3. Central Electricity Authority (CEA) 17th Electricity Survey
4. Central Authority of India Report 2010
5. Dudley, B. Energy Magzine, BP Statistical Review of World Energy, pp. 1–5 (2013)
6. Elsafty, A., Al-Daini, A.J.: Economical comparison between a solar powered vapour absorption air-conditioning system and a vapour compression system in Middle East. Renew. Energ. **25**, 569–583 (2002)
7. Hang, Y., Ming, Q., Zhao, F.: Economical and Environmental assessment of an optimized solar cooling system for a medium sized optimized office building in LA, California. Renew. Energ. **36**, 648–658 (2011)
8. Kaushik, S.C., Arora, A., Dixit, M.: Hybrid absorption cycles for solar cooling. advances in energy and built environment. Lect. Notes Civ. Eng. **36**, 223–239 (2019)
9. Alrwashdeh, S.S., Ammari, H.: Life cycle cost analysis of two different refrigeration systems powered by solar energy. Case Stud. Therm. Eng. **16**, 100559 (2019)
10. Kizilkan, O., Yamaguchi, H.: Feasibility research on the novel experimental solar-assisted CO_2 based Rankine cycle integrated with absorption refrigeration. Energ. Convers Manage. **205**, 112390 (2020)
11. Bureau of Energy Efficiency, India
12. Kalogirou, S.A.: Solar Energy Engineering: Processes and Systems. 1st edn, pp. 367–383. Elsevier Inc., London (2009)
13. Pongtornkulpanich, A., Thepa, S., Amorkitbamrung, M., Butcher, C.: Experience with fully operational solar driven 10-ton LiBr/H_2O single effect absorption cooling in Thailand. Renew. Energ. **33**, 943–949 (2008)
14. GRID-Arendal - https://www.grida.no/.
15. ISHRAE and IWEC Weather files for Indian cities (2019)
16. Berliner Energieagentur GmbH, Report April 2017
17. Tsoutsos, T., Anagnostou, J., Pritchard, C., Karagiorgas, M., Agoris, D.: Solar cooling technologies in Greece: an economic viability analysis. Appl. Therm. Eng. **23**, 1427–1439 (2003)

Comparative Performance Evaluation of Si and Ge Solar Cell Using PC1D Modelling

Apurv Yadav[ID]**, Harsha Yadav, Vineet Kumar Vashishtha**[ID]**, and Maneesh Kumar Shivhare**

1 Introduction

The societal progress, industrial growth, financial development and electrical energy capacity are the critical factors for the advancement of any nation [1]. There is a continuous growth in the demand of energy globally [2]. Energy generation from the conventional sources is not matching up to the increasing energy demand [3]. Besides, they are one of the major causes of air pollution. Various policies have been formulated and implemented by environmental protection agencies across the globe to reduce or regulate pollution [4]. The methodical application of various renewable energy sources in association with energy storage solutions may reduce the dependency on conventional energy sources [5]. Researches are being conducted on discovering more renewable energy sources and augmenting the performance of the existing sources of renewable energy. Experiments are being done to improve the performance of biofuels [6]. Effectiveness enhancement energy storage systems based on solar power is being investigated [7–12]. Various technologies to boost the output of wind-based power generation systems are being adopted [13].

A. Yadav (✉)
Amity University, Dubai 345019, UAE
e-mail: ayadav@amityuniversity.ae

H. Yadav
IIT, Delhi, New Delhi 110016, India

V. K. Vashishtha
KIET Group of Institutions, Ghaziabad, UP 201206, India

Department of Mechanical Engineering, Delhi Technological University, Delhi 110042, India

M. K. Shivhare
Gautam Budh University (GBU), Greater Noida, UP 201308, India

There are many ways to improve the performance of solar cells. Reduction of optical losses is a most efficient way to optimize a solar cell. Surface texturing on top surface is used to increase the optical path length of a light ray inside the solar cell [14]. Anti-reflection is applied on front surface of the solar cells to reduce reflection losses [15]. However, the problem in these improvement techniques is that they are either time consuming or expensive in nature. Modelling and simulation of the performance of the system using various softwares as simulation tool emerge as a promising solution.

Since the last decade, many researchers have conducted studies on modelling of photovoltaic technology with the help of variety of modelling and simulation software. Banu and Istare (2012) used curve fitting tool and empirical data to prepare the characteristics of current (I) and power (P) with respect to voltage (V) for photovoltaic (PV) module [16]. Anand et al. (2016) simulated the effect of different values of temperature and radiation of a PV panel in MATLAB [17]. Satish et al. (2020) simulated the performance of a photovoltaic plant using PVsyst software [18]. Silicon (Si) and germanium (Ge) are the most common materials in semiconductor industry. Here, in this, PC1D software is used to conduct comparison of performance parameters of a Si and a Ge solar cell for same dimension of the cell.

2 Modelling Parameters

Most of the solar cells use semiconductor to generate charge carriers. A minimum amount of energy is required to make an electron jump from its ground state to conducting state. The difference between these energy levels is termed as band gap. This property is intrinsic, and it directly affects the photovoltaic cell voltage. The suitability of a material in photovoltaic application is determined by energy of the photons incident on it, and whether that energy is more than the band gap. The energy of a photon, E_p, having a wavelength, λ_p, can be given by the following equation

$$E_p = (h * C)/\lambda p \tag{1}$$

where C is the velocity of incident photon and h is the Planck's constant.

Generation rate provides the number of electrons generated per unit time at a particular point in a solar cell. It is given by

$$G = \alpha N_0 e^{-\alpha x} \tag{2}$$

where α is the cell material's absorption coefficient, N_0 is the number of photons striking the light-facing surface of the cell per unit area in a given time and x is the distance from the front surface at which generation rate has to be calculated.

At equilibrium, the relation between the concentration of electrons and holes is given by

$$n_0 p_0 = n_i^2 \tag{3}$$

where n_0, p_0 and n_i are equilibrium material electron concentration, equilibrium material hole concentration of electrons and undoped material carrier concentration, respectively. Any variation in doping will also vary the number of charge carrier generated.

A solar cell can be visualized as a *p-n* junction diode, and the net current can be calculated using the following equation (Shockley diode equation) [19]

$$I = I_O \left[e^{[(qV)/(nkT)]} - 1 \right] \tag{4}$$

where I is the net diode current, I_O denotes the saturation dark current, q depicts electron charge, voltage is depicted by V depicts, k is a physical constant known as Boltzmann's constant, absolute temperature is denoted by T and n represents the ideality factor. In our simulation, the diode is assumed to be ideal; hence, the value of n is taken as 1. The power can be obtained by the multiple of current and voltage.

3 Design of the Model

A single-junction solar cell is designed in PC1D with 100 cm^2 cross-sectional area and 300 μm thickness, with series and shunt resistance. A shallow *N*-type emitter layer is diffused and is pyramidally textured. The texture depth is 3 μm with a front surface reflectance of 20%. The schematic for the solar cell modelled in PC1D is presented in Fig. 1. Base contact resistance is 0.15 Ω, and the conductance of internal conductor is 0.3 S. The simulation is done at one sun concentration (0.1 W/cm^2) and air mass value of AM1.5. The ambient temperature is kept at 25 °C, and the excitation of carrier is divided into 16 time steps. The values of parameters for Si and Ge are presented in Table 1. As the temperature increases beyond standard test condition (STC) temperature of 25 °C, there is a decrease in open-circuit voltage and consequently efficiency and power output of all kinds of solar cells [20].

4 Results and Discussion

Figure 2 exhibits the energy band diagrams of both of the solar cells. In Fig. 2a, Si solar cell energy levels are shown, while Fig. 2b exhibits Ge solar cell energy level diagram. The diagram depicts the position of energy levels throughout the thickness of the solar cell, and also, the position of quasi-fermi level for both electrons and holes is presented.
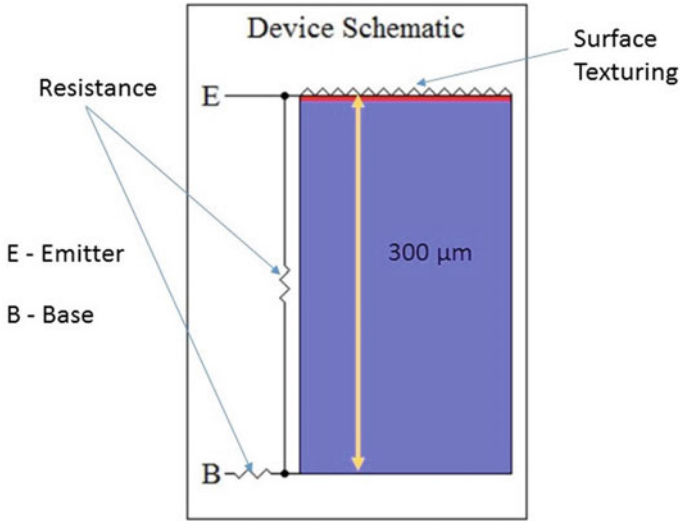
Fig. 1 Solar cell schematic

Table 1 Parameters of silicon and germanium

Parameters	Germanium	Silicon
Material refractive index	4.03	3.44
Material band gap	0.664 eV	1.124 eV
Material dielectric constant	16	11.9
Material intrinsic carrier concentration at 300 K	2.33×10^{13} cm^{-3}	1×10^{10} cm^{-3}
Material absorption coefficient at 400 nm	6.95×10^5 cm^{-1}	1.21×10^5 cm^{-1}
Material front diffusion (N-type)	2.87×10^{20} cm^{-3} peak	2.87×10^{20} cm^{-3} peak
Material carrier lifetime	7.208 µs	7.208 µs
Material P-type background doping	1.513×10^{16} cm^{-3}	1.513×10^{16} cm^{-3}
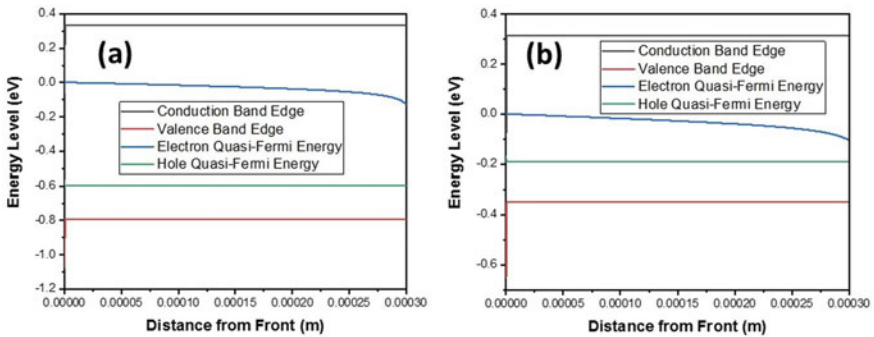
Fig. 2 Energy level diagrams of **a** Si and **b** Ge solar cell
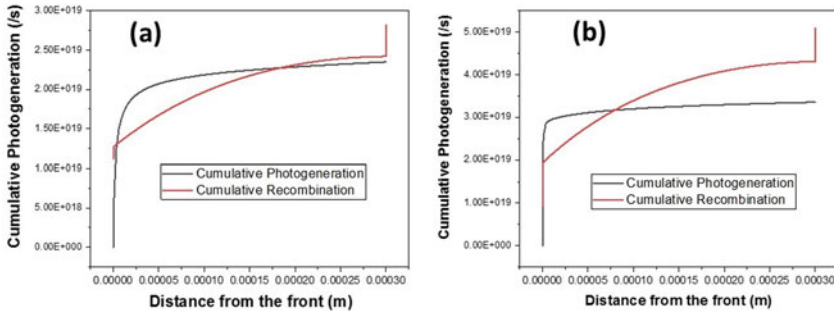
Fig. 3   Photogeneration and recombination rate curves of **a** Si and **b** Ge solar cell

Light-assisted carrier generation and recombination rate curves for both Si and Ge solar cell are presented in Fig. 3a , b, respectively. In Si solar cell, the maximum value of photogeneration rate was 2.35×10^{19} s^{-1}, while for Ge solar cell, the generation rate was 3.35×10^{19} s^{-1}. The maximum recombination rate for Si and Ge was 2.35×10^{19} s^{-1} and 5.09×10^{19} s^{-1}, respectively. In both the cells, value of generation and recombination rate increased while moving farther from front surface. But in case of Ge solar cell, the value of recombination rate was too high compared to recombination. This is the reason of reduction of power output in Ge solar cell.

The results of the power output and *I-V* characteristics are presented in Fig. 4. In case of Si solar cell presented in Fig. 4a, V_{OC} is calculated as 0.59 V, and the I_{SC} had a value of 1.36 A with a maximum power of the cell which was 0.57 W.

While in case of Ge solar cell, the values of V_{OC}, I_{SC} and maximum power was 0.18 V, 3.23 A and 0.25 W, respectively (Fig. 2b). For same amount of cell material and light concentration, the power output of Si solar cell is almost 2.36 times higher than a Ge solar cell.
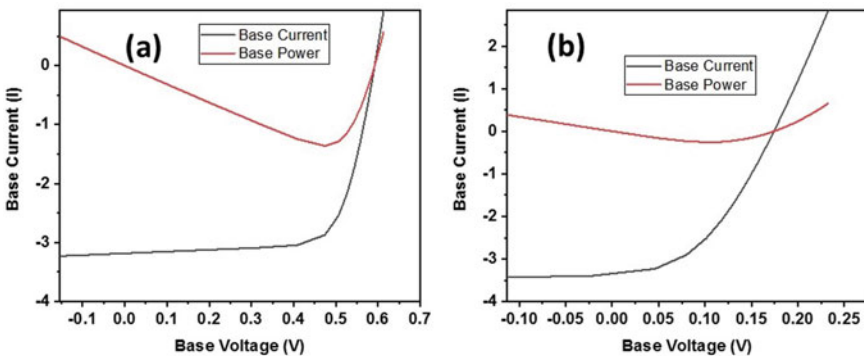
Fig. 4   Current and power versus voltage for **a** Si and **b** Ge solar cell

5   Conclusion

PC1D version 5 was used to conduct the comparative evaluation of solar cells of two different materials: Si and Ge. Same dimensions of cell were designed for each material. Ge has almost half band gap than Si, which means that for same light intensity, more charge carriers should reach conduction band in Ge, but opposite of it was observed. The generation rate of both the cells was found to be same. However, the recombination rate of Ge solar cell was almost 1.52 times more than the Si solar cell. This could be the reason of less output power. The higher value of open-circuit voltage can be also attributed to higher power output of Si solar cell. By using PC1D modelling, other materials could also be tested for their suitability in photovoltaic applications.

References

1. REN21. Renewables 2019 Global Status Report. 2019, wedocs.unep.org/handle/20.500.11822/28496. Last accessed 2020/05/23
2. Tvaronavičienė, M., Baublys, J., Raudeliūnienė, J., Jatautaitė, D.: Global energy consumption peculiarities and energy sources: role of renewables. In: Energy Transformation Towards Sustainability, pp. 1–49. Elsevier (2020)
3. Vaishak, S., Bhale, P.V.: Photovoltaic/thermal-solar assisted heat pump system: current status and future prospects. Solar Energy **189**, 268–284 (2019)
4. Solorio, I., Jörgens, H.: Contested energy transition? Europeanization and authority turns in EU renewable energy policy. J. Eur. Integr. **42**(1), 77–93 (2020)
5. Rekioua, D.: Storage in hybrid renewable energy systems. In: Hybrid Renewable Energy Systems, pp. 139–172. Springer, Cham (2020)
6. Kumar, S., Yadav, A.: Comparative experimental investigation of preheated thumba oil for its performance testing on a CI engine. Energy Environ. **29**(4), 533–542 (2018)
7. Yadav, A., Barman, B., Kardam, A., Narayanan, S.S., Verma, A., Jain, V.K.: Thermal properties of nano-graphite-embedded magnesium chloride hexahydrate phase change composites. Energy Environ. **28**(7), 651–660 (2017)
8. Yadav, A., Barman, B., Kumar, V., Kardam, A., Narayanan, S.S., Verma, A., Devinder, M., Shukla, P., Jain, V.K.: Solar thermal charging properties of graphene oxide embedded myristic acid composites phase change material. In: AIP Conference Proceedings, vol. 1731(1), p. 030030, AIP Publishing (2016)
9. Yadav, A., Barman, B, Kumar, V., Kardam, A., Narayanan, S.S., Verma, A., Madhwal, D., Shukla, P., Jain, V.K.: A review on thermophysical properties of nanoparticle-enhanced phase change materials for thermal energy storage. Recent Trends Mater. Devices 37–47 (2017)
10. Yadav, A., Verma, A., Jain, V.K., Bhatnagar, P.K., Yadav, H., Kumar, V.: Solar driven co-generation of electricity and freshwater. In: American Geophysical Union Fall Meeting 2019, GC53I-1204 (2019)
11. Yadav, A., Verma, A., Narayanan, S.S., Jain, V.K., Bhatnagar, P.K.: Carbon based phase change nanocomposites for solar energy storage. In: American Geophysical Union Fall Meeting 2018, GC23D-1226 (2018)
12. Yadav, A., Verma, A., Jain, V.K., Bhatnagar, P.K., Kumar, V.: Enhanced thermal conductivity of acetamide based nanocomposites. IJITEE **8**(10), 4227–4331 (2019)
13. Rekioua, D.: Hybrid renewable energy systems overview. In: Hybrid Renewable Energy Systems, pp. 1–37. Springer, Cham (2020)

14. Abdullah, M.F., Alghoul, M.A., Naser, H., Asim, N., Ahmadi, S., Yatim, B., Sopian, K.: Research and development efforts on texturization to reduce the optical losses at front surface of silicon solar cell. Renew. Sustain. Energy Rev. **66**, 380–398 (2016)
15. Selj, J.H., Mongstad, T.T., Søndenå, R., Marstein, E.S.: Reduction of optical losses in colored solar cells with multilayer antireflection coatings. Sol. Energy Mater. Sol. Cells **95**(9), 2576–2582 (2011)
16. Kumar, D., Mishra, P., Ranjan, A., Dheer, D.K., Kumar, L.: A simplified simulation model of silicon photovoltaic modules for performance evaluation at different operating conditions. Optik 164228 (2020)
17. Ferhati, H., Djeffal, F., Drissi, L.B.: A new approach to the modeling and simulation of multi-junction solar cells. Optik **200**, 163452 (2020)
18. Satish, M., Santhosh, S., Yadav, A.: Simulation of a Dubai based 200 KW power plant using PVsyst Software. In: 2020 7th International Conference on Signal Processing and Integrated Networks, pp. 824–827. IEEE (2020)
19. Houssa, M., Satta, A., Simoen, E., De Jaeger, B., Meuris, M., Caymax, M., Heyns, M.: Electrical performance of Ge devices. Germanium-Based Technol.: Mater. Devices 233 (2007)
20. Kumar, V., Dhasmana, H., Yadav, A., Kumar, A., Verma, A., Bhatnagar, P.K., Jain, V.K.: Theoretical analysis of temperature-dependent electrical parameters of Si solar cell integrated with carbon-based thermal cooling layer. In Advances in Solar Power Generation and Energy Harvesting, pp. 27–36. Springer, Singapore (2020)

Predicting the Output of a Wind Mill Using ANN Modelling

Swaroop Ramaswamy Pillai, Apurv Yadav , Harsha Yadav, and Vineet Kumar Vashishtha

1 Introduction

Electric capacity is a necessary factor for economic and technological advancement of any nation [1]. Generation of electricity increases energy demand globally. Energy from conventional sources is not sufficient to saturate the increasing energy demand [2]. Besides, they are one of the major causes of air and pollution. Agency across world is implementing various policies to reduce or regulate pollution [3]. This has generated a need to discover more sources of unconventional energy or enhancing the effectiveness of existing sources of renewable energy. Solar, biofuel, biomass, biofuel, geothermal, wind, etc., are some of these sources on which experiments are being conducted. Novel biodiesels blends are being prepared [4]. Effectiveness of solar thermal systems is being enhanced [5–12]. Adoption of novel solar or wind-based energy generation techniques are being explored [13, 14]. Wind energy-based energy generation is growing popular due to its modular nature [15]. A minimum average wind speed of 7 m per second is needed for proper working of a windmill. However, the nature of wind is intermittent and stochastic. Hence, the feasibility analysis of a wind mill can be done by prediction of wind power. Researchers use artificial intelligence (AI) for the assessment of the output of a proposed wind mill. At different heights of the wind turbine, wind hitting force at the turbine tip is different [16]. The performance is often gauged analytical computer codes. These computer

S. R. Pillai · A. Yadav (✉)
Amity University, Dubai 345019, UAE
e-mail: ayadav@amityuniversity.ae

H. Yadav
IIT Delhi, New Delhi 110016, India

V. K. Vashishtha
Delhi Technological University, Delhi 110042, India

KIET Group of Institutions, Ghaziabad, UP 201206, India

modelling codes involve complicated algorithms, which requires solving numerous complex differential equations. Significant amount of power and too much time are required to precisely predict the output. Artificial neural networks (ANN) provide an alternative to these confusing complex models by grasping critical information patterns from the multidimensional information field. Wind energy system has inherently noisy data, and it provides suitable problems to be managed by neural networks methodology as they are noise immune, tolerant and robust [17].

ANN's principle of operation is same as the working of brains' basic framework [18]. Neurons present in the brain accept signals from various input or nodes inputs. The importance of each input allocates a weight to that input [19]. The activation function of each node introduces network linearity. The neuron output can be connected in two ways; either to the output or to the other nodes [20]. ANN comprises many interconnecting synapses and nodes. Nodes operate in parallel, and the interconnection of synapses is used to intercommunicate [21]. ANN is nowadays integrated in various areas for the solution of several problems. Some examples are medicine, signal processing, forecasting, pattern recognition, speech recognition, speech production, control, business and also in wind energy fields. The advantages of using ANN in lieu of other intelligent systems are its simplicity in operation, high speed, uncomplicated user interface and its ability to solve complex equations by modelling a multivariate problem [22].

Wind energy problems can also be integrated with ANN. Equatorial region receives significantly more amount of sunlight and heat than polar regions. This reduces the density of air near the equator, hence it becomes lighter and rises up. Due to the pressure drop, air from polar region rushes to equation and it causes wind. Wind power generation is mostly dependent on wind speed. Power output from a windmill is calculated by

$$P = 0.5 \rho_a A_s V_w^3 \tag{1}$$

where ρ_a (kg/m^3) denotes the air density in, A_s (m^2) denotes the blade swept area for the wind turbine, and V_w (m/s) denotes the wind velocity. AI is required for forecasting the performance as these parameters are interdependent. Helbing and Ritter [23] prepared an ANN simulation to model wind power curve and reported an improvement in performance. Blanchard and Samanta [24] did a short-term forecasting of wind and found that ANN is suitable for monitoring wind power. Mustapha et al. [25] used ANN with maximum power point tracking technique on a wind turbine and found that ANN is quite effective. Pradhan and Subidhi used ANN with other techniques for wind speed prediction [26].

2 Prediction of Wind Power Curve

The hourly data for from 1 December 2019 to 7 December 2019 were taken from a wind turbine [27]. Figure 1 shows the wind rose diagram which gives the data on both wind speed and wind direction. It is evident that the wind rose shows different wind speed and direction which is fed for data training. Figure 2 represents hourly wind speed. It shows that the wind speed was constantly varying between 2 and 13 m/s.

Figure 3 shows the wind direction measured in degrees. It is also evident that the wind speed varies between 5° and 355°. These two data mainly decide the energy per unit time produced by the wind turbine. Figure 4 indicates the power curve which varies between 0 and 12 kWh. The energy theoretically depends only on the wind velocity, length of the blade and the density which both are nearly constant. There are various other parameters which decides the energy curve.

Hence, in this model neural network is utilized for power curve prediction based on the past data.

Figure 5 indicates the neural network model which shows wind speed and its direction as inputs and energy at the output. In this, it can be seen that two input layers combined with one output and one hidden layer are utilized. The updating of weights can be realized by the following formula:
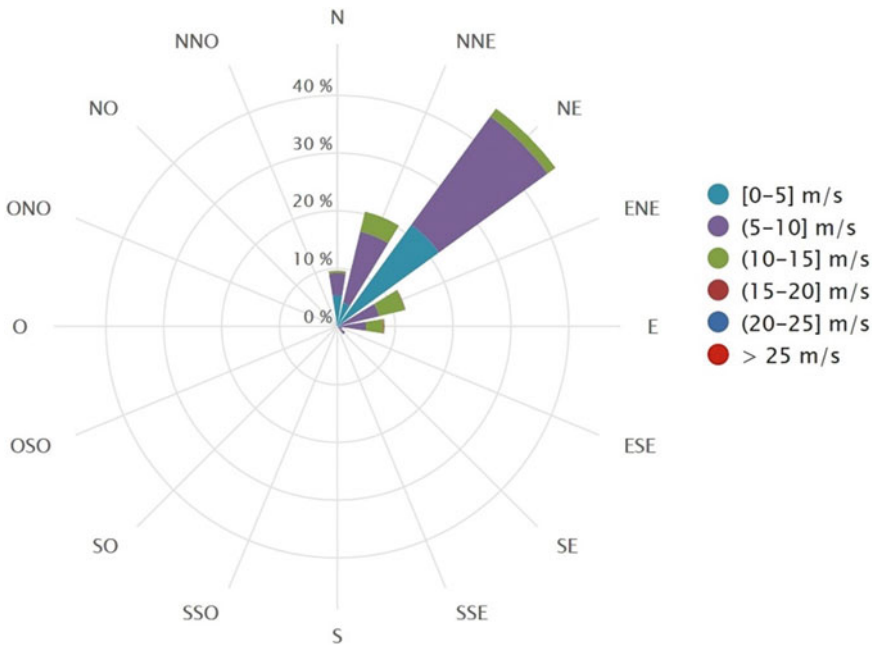
Fig. 1 Wind rose diagram
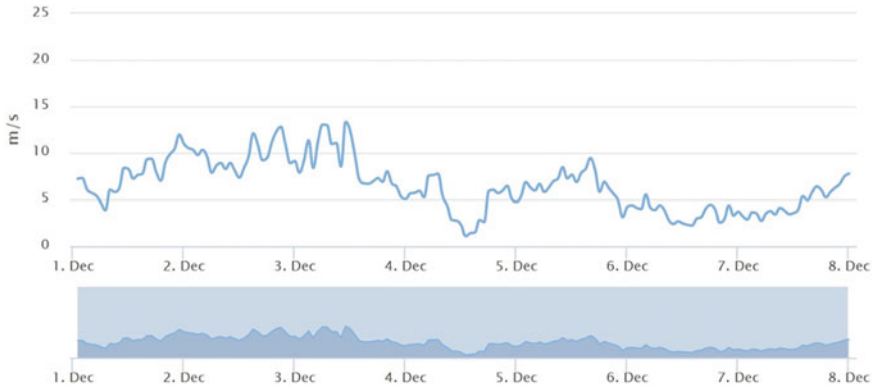
Fig. 2 Wind speed
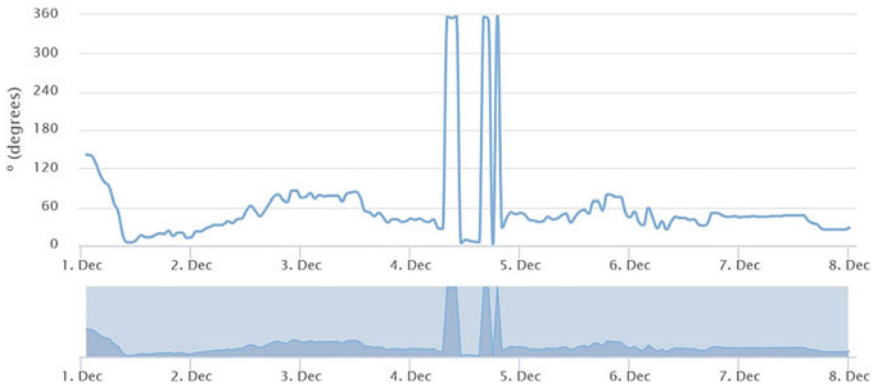
Fig. 3 Wind direction

Fig. 4 Wind power curve
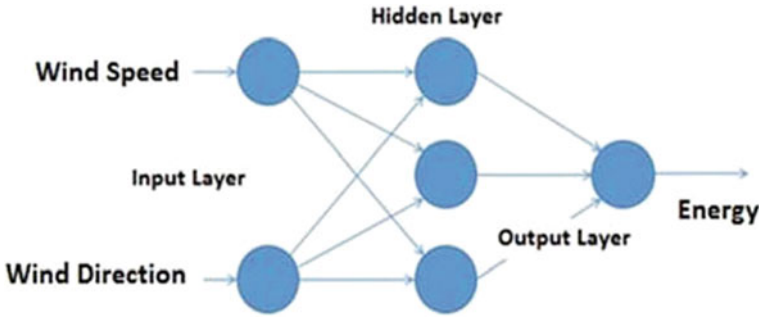
Fig. 5 Model of the neural network used for prediction

$$W_{AB(\text{New})} = W_{AB(\text{Old})} - \eta(\partial E2/\partial IB)OA \qquad (2)$$

In this equation, $W_{AB(\text{New})}$ and $W_{AB(\text{Old})}$ are the old and new weight matrix, E is the error, η is the learning rate, I is the input matrix, and O is the output matrix.

3 Results and Discussion

The learning curve from the neural networks is presented in Fig. 6. The error rate can be seen coming down with the number of iterations. The error is around 1.5 after thousand iterations. It can be also further reduced by adjusting the weights and by increasing the count of iterations. It showcases the actual and predicted power curve. It can be observed that the both actual and predicted follow the same path for little error. This can be also used for predicting the output using a newer data set.

Figure 7 also indicates the three-dimensional data for the power curve. The x- and y-axis show the wind speed and direction. The z-axis indicates the power. It can be seen how the data are distributed. The blue dots indicate the predicted data, and the red dots indicate the actual data. It can be seen how both are clustered at one place which shows the accuracy of prediction. The wind direction here is represented in degrees after multiplying the scale by 10. The energy is expressed in Kwh with scale divided by 10. This scale is adjusted to obtain more accuracy when trained with the neural network.

Energy prediction utilizing the neural network is presented in the graph of simulation results (Fig. 8). The input data in this model are wind speed and direction, which is supplied to the neural network back propagation algorithm after allotting the initial weights. After many iterations, it can be found that, based on the old data and the new data, the power is successfully predicted by the algorithm.

This model can be used forecasting the power curve and hence in the operation and management of wind power plants. ANN techniques could be range applications in the field of the modelling of wind power systems. ANN could be further
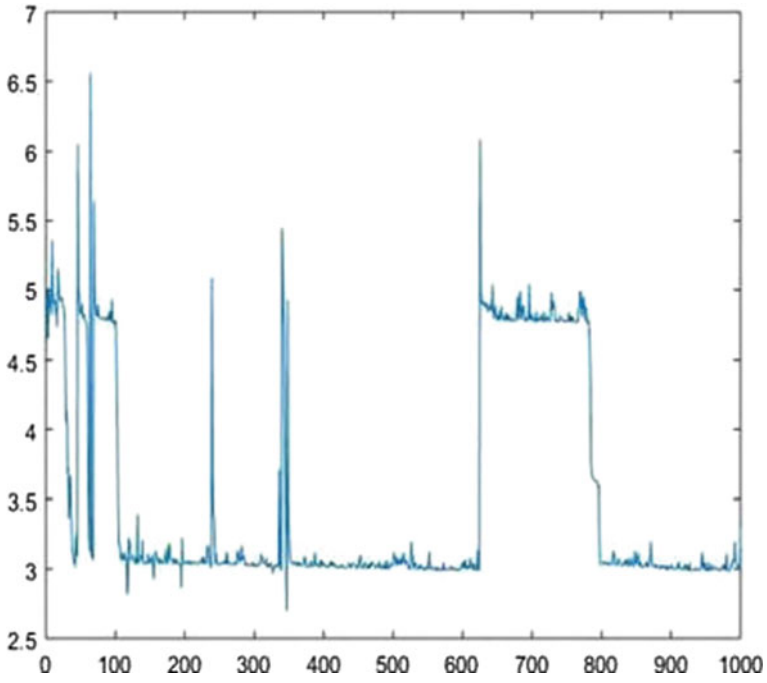
Fig. 6 Learning curve of the model
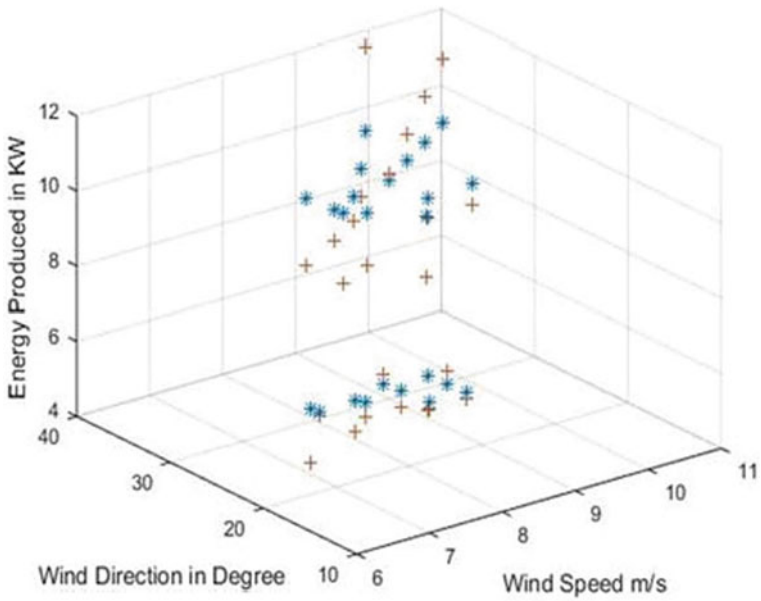
Fig. 7 3D data of the power curve
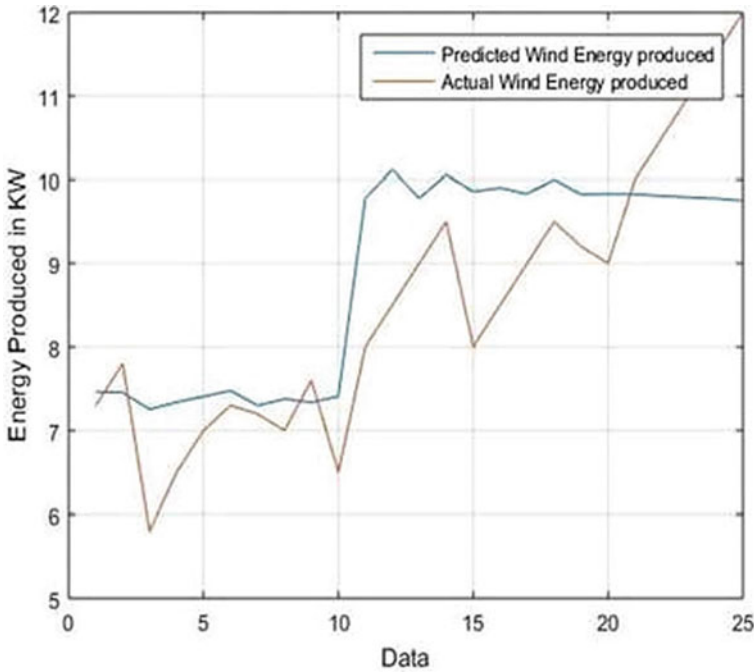
Fig. 8 Actual versus predicted energy output

extended to different functions like optimization of network configuration of large-scale wind energy conversion interconnected systems, quick security evaluation, hybridization with other intelligent systems, stability enhancement and preventive control measures. Suitable data selection is crucial for setting up of an ANN system. The training data set should be selected such that it is representing every operating mode of the system as the model performance is dependent on it. The application of ANN in wind energy systems is growing increasingly popular and expected to rise in future.

4   Conclusion

This model can be used forecasting the power curve and hence in the operation and management of wind power plants. ANN techniques could be applied in various modelling of wind energy systems to predict and evaluate the systems' performance. ANN could be further extended to different functions like optimization of network configuration of large-scale wind energy conversion interconnected systems, quick security evaluation, hybridization with other intelligent systems, stability enhancement and preventive control measures. Suitable data selection is crucial for setting

up of an ANN system. The training data set should be selected such that it is representing every operating mode of the system as the model performance is dependent on it. The applications of ANN in wind energy systems are growing increasingly popular. Research on ANN application in wind power systems is expected to grow in future.

References

1. REN21. Renewables 2019 Global Status Report. 2019, wedocs.unep.org/handle /20.500.11822/28496. Last accessed 2020/05/23
2. Vaishak, S., Bhale, P.V.: Photovoltaic/thermal-solar assisted heat pump system: current status and future prospects. Sol. Energy **189**, 268–284 (2019)
3. Kumar, S., Yadav, A.: Comparative experimental investigation of preheated thumba oil for its performance testing on a CI engine. Energy Environ. **29**(4), 533–542 (2018)
4. Solorio, I., Jörgens, H.: Contested energy transition? Europeanization and authority turns in EU renewable energy policy. J. Eur. Integr. **42**(1), 77–93 (2020)
5. Yadav, A., Barman, B., Kumar, V., Kardam, A., Narayanan, S.S., Verma, A., Devinder, M., Shukla, P., Jain, V.K.: Solar thermal charging properties of graphene oxide embedded myristic acid composites phase change material. AIP Conf. Proc. **1731**(1) 030030, AIP Publishing (2016)
6. Yadav, A., Verma, A., Narayanan, S.S., Jain, V.K., Bhatnagar, P.K.: Carbon based phase change nanocomposites for solar energy storage. In: American Geophysical Union Fall Meeting 2018, GC23D-1226 (2018)
7. Yadav, A., Barman, B, Kumar, V., Kardam, A., Narayanan, S.S., Verma, A., Madhwal, D., Shukla, P., Jain, V.K.: A review on thermophysical properties of nanoparticle-enhanced phase change materials for thermal energy storage. Recent Trends Mater. Devices, 37–47 (2017)
8. Yadav, A., Verma, A., Jain, V.K., Bhatnagar, P.K., Yadav, H., Kumar, V.: Solar driven co-generation of electricity and freshwater. In: American Geophysical Union Fall Meeting 2019, GC53I-1204 (2019)
9. Yadav, A., Barman, B., Kardam, A., Narayanan, S.S., Verma, A., Jain, V.K.: Thermal properties of nano-graphite-embedded magnesium chloride hexahydrate phase change composites. Energy Environ. **28**(7), 651–660 (2017)
10. Yadav, A., Verma, A., Jain, V.K., Bhatnagar, P.K., Kumar, V.: Enhanced thermal conductivity of acetamide based nanocomposites. IJITEE **8**(10), 4227–4331 (2019)
11. Satish, M., Santhosh, S., Yadav, A.: Simulation of a Dubai based 200 KW power plant using PVsyst software. In: 2020 7th International Conference on Signal Processing and Integrated Networks (SPIN), pp. 824–827. IEEE (2020, February)
12. Kumar, V., Dhasmana, H., Yadav, A., Kumar, A., Verma, A., Bhatnagar, P.K., Jain, V.K.: Theoretical analysis of temperature-dependent electrical parameters of Si solar cell integrated with carbon-based thermal cooling layer. In: Advances in Solar Power Generation and Energy Harvesting 2020, pp. 27–36. Springer, Singapore (2020)
13. Yadav, A., Shivhare, M.K.: Nanoparticle enhanced PCM for solar thermal energy storage. In: 2020 Advances in Science and Engineering Technology International Conferences (ASET), pp. 1–3. IEEE 2020
14. Rekioua, D.: Hybrid renewable energy systems overview. In: Hybrid Renewable Energy Systems, pp. 1–37. Springer, Cham (2020)
15. Makhdoomi, S., Askarzadeh, A.: Optimizing operation of a photovoltaic/diesel generator hybrid energy system with pumped hydro storage by a modified crow search algorithm. J. Energy Storage **27**, 101040 (2020)

16. Shao, H.: Wind power modeling wind power forecasting methods based on deep learning: a survey. Comput. Model. Eng. Sci. **122**(1), 273–301 (2020)
17. Prasad, R., Joseph, L., Deo, R.C.: Modeling and forecasting renewable energy resources for sustainable power generation: basic concepts and predictive model results. In: Translating the Paris Agreement into Action in the Pacific, pp. 59–79. Springer, Cham (2020)
18. Lee, R.S.: AI powerful tools in quantum Finance. In: Quantum Finance, pp. 159–208. Springer, Singapore (2020)
19. Ramaswamy, S.: Forecasting of power in wind energy based on back propagation algorithm in neural networks. In: Amity International Conference on Artificial Intelligence (AICAI), pp. 461–464. IEEE, Dubai (2019)
20. Trajer, J., Korupczyński, R., Wandel, M.: Assessment of wind energy resources using data mining techniques. In: Renewable Energy Sources: Engineering, Technology, Innovation, pp. 677–688. Springer, Cham (2020)
21. Reynolds, J., Clarizia, M.P., Santi, E.: Wind speed estimation from CYGNSS using artificial neural networks. IEEE J. Sel. Top. Appl. Earth Obs. Remote Sens. **13**, 708–716 (2020)
22. Pillai, S.R., Yadav, A., Vashishtha, V.K.: Prediction of wind power curve based on wind speed and direction using artificial neural network. In: International Conference on Innovative Techniques in Mechanical Engineering, 2019, Springer Publishing 2020 "unpublished"
23. Helbing, G., Ritter, M.: Improving wind turbine power curve monitoring with standardisation. Renew. Energy **145**, 1040–1048 (2020)
24. Blanchard, T., Samanta, B.: Wind speed forecasting using neural networks. Wind Eng. **44**(1), 33–48 (2020)
25. Mustapha, A., Selvaperumal, S.K., Mohd, H., Lakshmanan, R.: Ann-based maximum power point tracking of a variable-speed wind energy conversion system using sepic converter. Wind **29**(01), 189–205 (2020)
26. Pradhan, P.P., Subudhi, B.: Wind speed forecasting based on wavelet transformation and recurrent neural network. Int. J. Numer. Model. Electron. Networks Devices Fields **33**(1), e2670 (2020)
27. Historical-Sotavento, www.sotaventogalicia.com/en/real-time-data/historical. Last accessed 20120/05/23

CFD-Based Correlation Development for Artificially Roughened Solar Air Heater

Anil Singh Yadav ⬤**, Vipin Shrivastava** ⬤**, T. Ravi Kiran** ⬤**, and Mayank Kumar Dwivedi** ⬤

1 Introduction

Solar air heaters (SAH) are most widely employed to dispense the heated air at low to average temperatures. It is effectively used for space heating, timber seasoning, industrial products curing, and drying/curing of clay/concrete building ingredients and industrial applications. In a SAH, an absorber plate receives heat energy directly from the sun and transfers the radiation to the fluid flow. In SAH, a smooth absorber plate has minimal contact surface for transferring heat to flowing fluid from the absorber plate resulted in poor thermal efficiency. Implementing passive techniques like a rib, grooves, etc. in a duct creates turbulence in the laminar sub-layer; thus, thermal efficiency can be increased. Turbulence grounded on shapes of ribs, and the arrangement of ribs with varying pitch distances is crucial for the enhancement of thermal efficiency [1].

Diverse shapes and position of ribs were experimentally examined by various researchers. Detailed descriptions and progresses concerning various experimental researches on different dimensions, profiles and positionings' rib elements can be seen in excellent review papers published by various investigators [2–9]. Very few computational fluid dynamics, *(CFD)* investigations are reported for artificial roughened SAH [10–18]. Many researchers have revealed the significance of different shapes and position of ribs in heat transfer enhancement. After extensive survey of the literature, it is found that the application of numerical method in this field is very limited. It is also found that there is no CFD-based correlations reported in the literature on semicircular ribbed SAH.

A. S. Yadav (✉) · V. Shrivastava · T. Ravi Kiran
Mechanical Engineering Department, Lakshmi Narain College of Technology, Bhopal, MP 462026, India
e-mail: anilsinghyadav@gmail.com

M. K. Dwivedi
Mechanical Engineering Department, SAGE University, Indore, MP 452020, India

In this paper, we present a correlation development framework that predicts CFD simulations for investigating the transverse semicircular rib effect on thermohydraulic performance of SAH. For saving the time of computation and the memory of the computer, the 2-D flow model is considered in the present work. Yadav and Bhagoria [19] have proposed that the results obtained from two-dimensional model have the close proximity with actual results as analyzed that with 3-D flow. The primary goal of this work is to investigate numerically, heat transfer phenomena in ribbed SAH and develop a CFD-based correlation for friction factor *f* and Nusselt number *Nu*.

2 CFD Modeling and Simulation

Modeling of SAH duct having proposed geometry is done in ANSYS 16. Figure 1 represents the schematic layout of computational domain for numerical analysis. Present computational domain is identical to the computational domain used by Yadav and Bhagoria [19].

Varying rib pitch distance *P* from 10 to 25 mm with Reynolds number *Re* 3800 to 18,000 is selected for analysis. The top test wall of the SAH is associated with an absorber plate (0.5 mm thick) made of aluminium. The 1.4 mm height of the semi-circular rib on the absorber plate is taken in consideration. Turbulent airflow in SAH having artificial roughness is governed by following steady-state, incompressible, two-dimensional continuity, momentum, and energy equation with negligible heat loss by radiation [20]:

Equation of continuity:

$$\frac{\partial}{\partial x_i}(\rho u_i) = 0 \tag{1}$$

Equation of momentum:
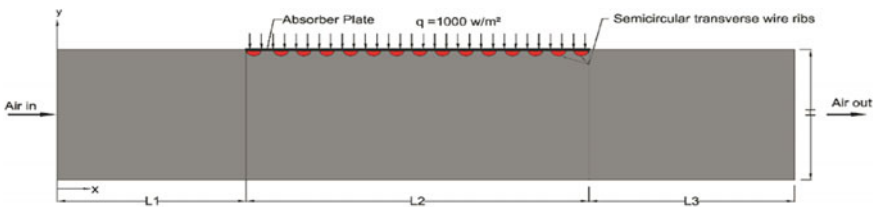
L_1 (mm)	L_2 (mm)	L_3 (mm)	W (mm)	H (mm)	D (mm)	W/H	e (mm)	P (mm)	Re	Pr	P/e	e/D
225	121	115	100	20	33.33	5	1.4	10-25	3800-18000	0.7441	7.14-17.86	0.042

Fig. 1 Schematic model of SAH
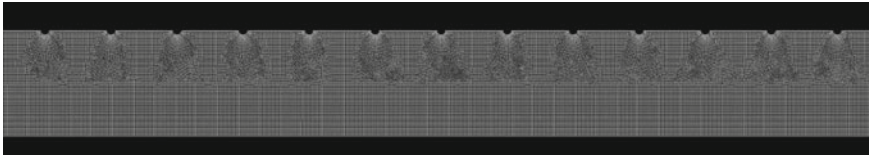
Fig. 2 Non-uniform meshing

$$\frac{\partial}{\partial x_i}\left(\rho u_i u_j\right) = -\frac{\partial p}{\partial x_i} + \frac{\partial}{\partial x_j}\left[\mu\left(\frac{\partial u_i}{\partial x_j} + \frac{\partial u_j}{\partial x_i}\right)\right] + \frac{\partial}{\partial x_j}\left(-\rho\overline{u_i' u_j'}\right) \qquad (2)$$

Equation of energy:

$$\frac{\partial}{\partial x_i}(\rho u_i T) = \frac{\partial}{\partial x_j}\left((\Gamma + \Gamma_t)\frac{\partial T}{\partial x_j}\right) \qquad (3)$$

For solving the governing continuity, energy as well as momentum equation by using ANSYS Fluent 16, finite volume methods are being utilized.

In the present analysis, the meshing was created in ANSYS ICEM CFD v16 and the size of meshing element is selected as 0.3 mm (Fig. 2). Five different element sizes are employed to check the grid-independent validation on smooth duct. The marginal variation is increased in Nus and fs when element size varying from 112,226 cells to 242,106. Therefore, in the present analysis, the grid system of 112,226 cells is considered.

The boundary conditions of the inlet velocity magnitude are set within the range of Re. Heat flux on upper wall is set as 1000 W/m^2 and outlet pressure is set as an atmospheric condition. At beginning, air temperature is considered as 27 °C. All physical fluid properties are taken constant and standard at the mean bulk temperature. A SIMPLE algorithm is chosen for the coupling of velocity–pressure [20]. The RNG, k-epsilon model, is chosen for solving the problem as per the recommendation given by [19]. A double-precision solver is chosen to solve the governing equation by a double-precision solver. The upwind discretization of second order is chosen for each and every transport equation. In residual monitoring, continuity, *x*, and *y* velocity criteria are fixed as 10e−06. Standard initialization is chosen to compute all zones. A number of iteration and report interval are varied based on proposed geometry.

3 Data Reduction

Nu$_r$ and f_r for roughened SAH duct are estimated by following equations [1]:

$$\mathrm{Nu}_r = hD/k \qquad (4)$$

Value of *h* can be obtained from CFD simulation.

$$f_r = \frac{(\Delta P/l)D}{2\rho v^2} \tag{5}$$

Value of ΔP can be obtained from CFD simulation.

Nu_s and f_s for smooth SAH duct are estimated by following equations.

Dittus–Boelter equation [21]

$$Nu_s = 0.023 \, Re^{0.8} \, Pr^{0.4} \tag{6}$$

Blasius equation [22]

$$fs = 0.0791 \, Re^{-0.25} \tag{7}$$

4 Result and Discussion

The effect of proposed shape rib on friction factor, f_r and Nusselt number, Nu_r with varying pitch distances, P is numerically investigated. Figure 3 represents the Nu_r variation as a Re function for the P/e's various values at e/D's set value.

An increment in Nu_r can be noticed with the increment of Re in all the circumstances as expected. It has been observed that there is decrease in Nu_r values as P/e value increases for a e/D set value. Hardly any exceptional cases may be found, but they don't violate this general rule significantly. A strong vortex formation occurred adjacent to the rib because of the rib's impact in flow direction, which induced turbulence in the fluid flow direction. The extreme value of Nu_r is predicted
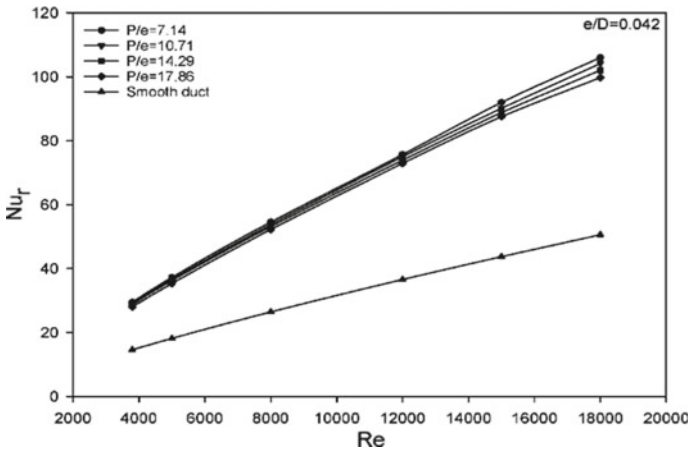
Fig. 3 Variation of Nu_r with respect to Re

(a) Re=3800

(c) Re=15000

(b) Re=8000

(d) Re=18000
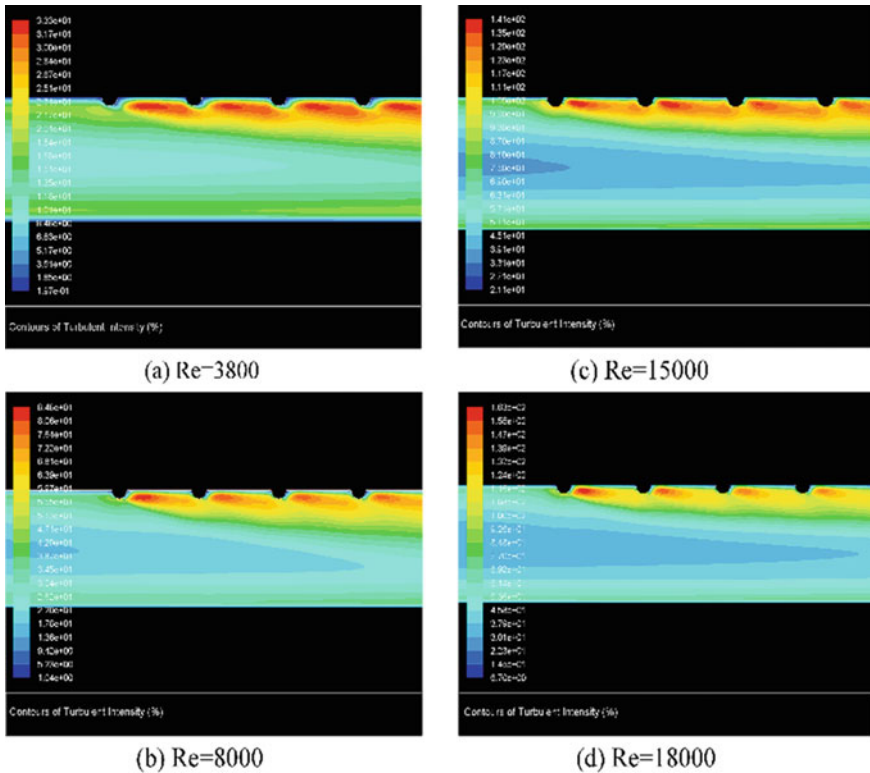
Fig. 4 Contour plot of *TI* for *P*/*e* of 10.71 at a *Re* **a** 3800, **b** 8000, **c** 15,000, **d** 18,000

for the semicircular rib with $P = 10$ mm at *Re* of 18,000 as compared with other configurations.

Figure 4 represents the *TI* contour plot of for the various *Re* values with a fixed value of *e*/*D* of 0.042 and *P*/*e* of 10.71.

It can be seen that a strong influence of *TI* in heat transfer between the couple of ribs with a heat transfer enhancement as well as average Nu_r in stream-wise distribution. As roughness is increased by *Re*, the elements start projecting outside the laminar sub-layer. Thickness of laminar sub-layer starts decreasing with any increment in the *Re*. Due to formation of eddies, an enhancement in the heat-transfer is found near to the closest laminar sub-layer of the semicircular-shaped rib. The formation of reattachment shear layer which beget strong secondary layer due to the height of the rib by increasing the *Re* is responsible for the improvement of heat transfer.

Figure 5 represents the f_r variation as *Re* function for various *P*/*e* values at *e*/*D* set value. Decrement in f_r can be seen on any increment in the *Re*. Also, it has been found that the f_r values decreases with an increment in *P*/*e* at fixed *e*/*D*. Some exceptional cases may be found, but they do not violate this general rule significantly.
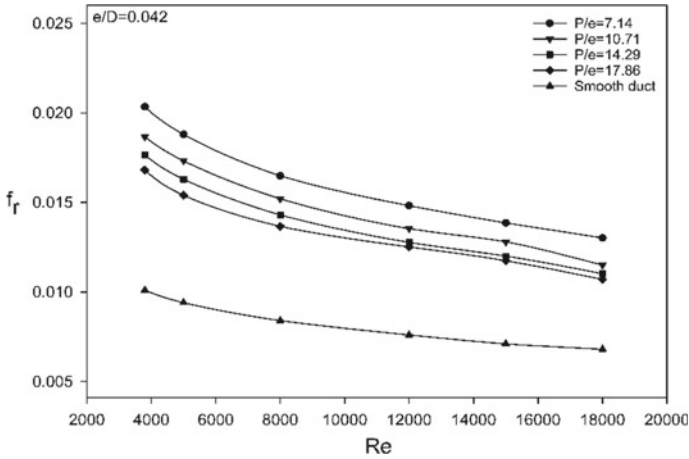
Fig. 5 Variation of f_r with respect to Re

A further energy loss results in increasing f_r due to the vortices' shedding arising from the top of the rib having semicircular section. A decrement in the value of f_r can be seen on increasing the value of *Re* because of the viscous sub-layer destruction in the duct. The extreme value of f_r is predicted for the semicircular rib with $P = 10$ mm at *Re* of 3800 as compared with other arrangements.

In order to provide credibility to the numerical results, it is extremely important to compare with available experimental data. The simulation results of the ribbed duct are compared with experimental dataset of [23]. It is observed that present predicted results found much closer to experimental results of [23]. Similar results are obtained by Nine et al. [24] who investigated the similar geometry of rib. Hence, it can be concluded that the validity of the proposed system is demonstrated by present numerical analysis results.

5   Correlation Development

Statistical correlations for Nu_r and f_r are developed by regression analysis with the help of Sigma Plot (v14.0) software. The results of this analysis show that the artificially rib-roughened SAH's heat transfer and flow characteristics are strongly influenced by non-dimensional parameters, *Re* and *P/e*. Therefore, the Nu_r and f_r can be expressed as functions of *Re* and *P/e* as given in Eqs. (8) and (9), respectively:

$$Nu_r = f(Re, P/e) \tag{8}$$

$$f_r = f(Re, P/e) \tag{9}$$

5.1 Nusselt Number Correlation

Best-fit correlation for Nu_r is established by regression analysis. All the values of Nu_r collected from CFD analysis are plotted against Re. Furthermore, for fitting a straight line via these points in regression analysis is presented as:

$$Nu_r = A_0 Re^{0.8088} \tag{10}$$

where A_0 is a constant and obtained from regression analysis.

But A_0 is a function of P/e. $A_0 (= Nu_r / Re^{0.8088})$ is designed on log-log scale as P/e function. For fitting a second-order polynomial, regression analysis is given by:

$$\ln\left(\frac{Nu_r}{Re^{0.8088}}\right) = \ln B_0 + B_1 \ln(P/e) + B_2 [\ln(P/e)]^2 \tag{11}$$

where B_0, B_1 and B_2 are constants and obtained from regression analysis.

Lastly, Eq. (11) is converted into following appropriate form

$$\frac{Nu_r}{Re^{0.8088}} = C_0 (P/e)^{0.2632} \exp\{-0.0643[\ln(P/e)]^2\} \tag{12}$$

The values of the coefficients are obtained as given below:

$$A_0 = 0.0364 \; B_0 = 0.0289 \; B_1 = 0.2632$$
$$B_2 = -0.0643 \; C0 = 0.0289$$

For the Nusselt number, these resultant values of given final correlation

$$Nu_r = 0.0289 \, Re^{0.8088} (P/e)^{0.2632} \exp\{-0.0643[\ln(P/e)]^2\} \tag{13}$$

This equation represents the correlation for Nu_r as function of Re and P/e.

Figure 6 presents a comparison between the Nu_r data obtained from CFD analysis and that of correlation developed in Eq. 13. It has been observed that points for Nu_r all data points lie in $\pm 5\%$ deviation lines which is in a good acceptable limit. It is therefore concluded that the proposed correlation accurately predicts the Nu_r for the semicircular rib roughened SAH.

5.2 Friction Factor Correlation

Best-fit correlation for f_r is developed by regression analysis. All the values of f_r obtained from CFD analysis are plotted against Re. Furthermore, for fitting a straight
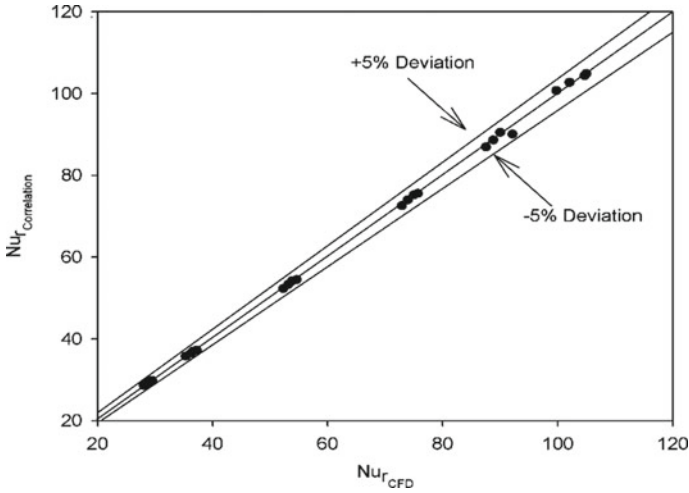
Fig. 6 Comparison of Nu_r (CFD) vs. Nu_r (Correlation-Eq. 13)

line via these points in regression analysis is presented as:

$$f_r = A_0 \mathrm{Re}^{-0.2862} \tag{14}$$

where A_0 (=0.1927) is a constant and obtained from regression analysis.

But A_0 is a function of P/e. $A_0 (= f_r / \mathrm{Re}^{-0.2859})$ is designed as a function of P/e. From regression analysis, it is obtained as:

$$f_r = B_0 \mathrm{Re}^{-0.2859} (1 + P/e)^{-0.2305} \tag{15}$$

where B_0 (=0.3463) is a constant and obtained from regression analysis.

The values of the coefficients are obtained as given below:

$$A_0 = 0.1927 \ B_0 = 0.3463$$

For the friction factor, following final correlation is resulted from these values

$$f_r = 0.3463 \mathrm{Re}^{-0.2859} (1 + P/e)^{-0.2305} \tag{16}$$

This equation represents the correlation for f_r as function of Re and P/e.

Figure 7 presents a comparison between the f_r data obtained from CFD analysis and that of correlation developed in Eq. 16. It has been observed that for f_r each data point lies in $\pm 5\%$ deviation lines which is in a good acceptable limit. It is therefore concluded that the proposed correlation accurately predicts the f_r for the semicircular rib roughened SAH.
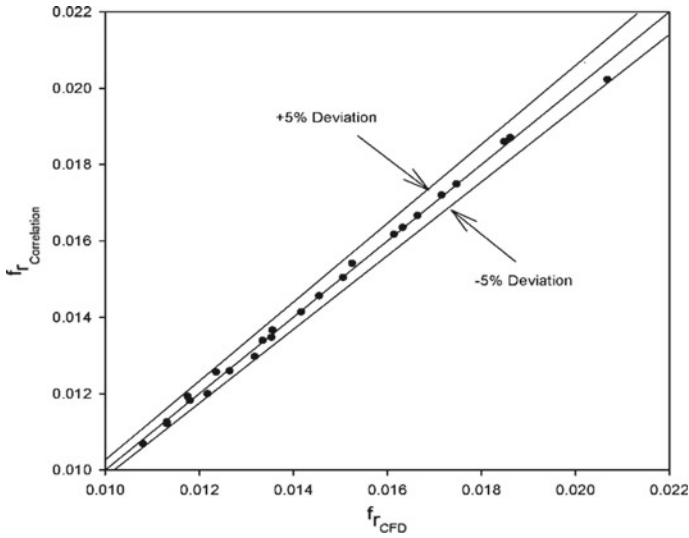
Fig. 7 Comparison of f_r (CFD) versus f_r (Correlation-Eq. 16)

6 Conclusions

2D SAH rectangular duct having one wall roughness implemented using the numerically analyzed with semicircular shape of the rib. The values of the f_r and Nu_r are obtained for varying pitch distances of various configurations of rib in the duct. The extreme value of Nu_r is predicted for the semicircular rib with $P = 10$ mm at Re of 18,000 as compared with other configurations. The extreme value of f_r is predicted for the semicircular rib with $P = 10$ mm at Re of 3800 as compared with other arrangements. In this paper, novel CFD-based correlations for f_r and Nu_r are developed by utilizing numerical data with the help of Sigma Plot (v14.0) software. To the best of our knowledge, there are no correlations for f_r and Nu_r in the literature covering chosen parameters for semicircular rib roughened SAH. Both correlations predict all data points for f_r and Nu_r lie in the $\pm 5\%$ deviation line that is in a good acceptable limit. It is therefore concluded that both the correlations are reasonably satisfactory for the prediction of the fluid flow as well as heat transfer characteristics for the semicircular rib roughened SAH.

References

1. Duffie, J.A., Beckman, W.A.: Solar Engineering of Thermal Processes. Wiley, New York (1980)
2. Bhushan, B., Singh, R.: A review on methodology of artificial roughness used in duct of solar air heaters. Energy **35**, 202–212 (2010)

3. Kumar, A., Saini, R.P., Saini, J.S.: Heat and fluid flow characteristics of roughened solar air heater ducts—a review. Renew. Energy **47**, 77–94 (2012)
4. Singh Yadav, A., Kumar Thapak, M.: Artificially roughened solar air heater: experimental investigations. Renew. Sustain. Energy Rev. **36**, 370–411 (2014)
5. Sharma, S.K., Kalamkar, V.R.: Thermo-hydraulic performance analysis of solar air heaters having artificial roughness—a review. Renew. Sustain. Energy Rev. **41**, 413–435 (2015)
6. Yadav, A.S., Thapak, M.K.: Artificially roughened solar air heater: a comparative study. Int. J. Green Energy **13**, 143–172 (2016)
7. Singh, I., Singh, S.: A review of artificial roughness geometries employed in solar air heaters. Renew. Sustain. Energy Rev. **92**, 405–425 (2018)
8. Jain, S.K., Agrawal, G.D., Misra, R.: A detailed review on various V-shaped ribs roughened solar air heater. Heat Mass Transf. (2019)
9. Patil, A.K.: Heat transfer mechanism and energy efficiency of artificially roughened solar air heaters—a review. Renew. Sustain. Energy Rev. **42**, 681–689 (2015)
10. Kumar, S., Saini, R.P.: CFD based performance analysis of a solar air heater duct provided with artificial roughness. Renew. Energy **34**, 1285–1291 (2009)
11. Yadav, A.S., Bhagoria, J.L.: A CFD (computational fluid dynamics) based heat transfer and fluid flow analysis of a solar air heater provided with circular transverse wire rib roughness on the absorber plate. Energy **55**, 1127–1142 (2013)
12. Boulemtafes-Boukadoum, A., Benzaoui, A.: CFD based analysis of heat transfer enhancement in solar air heater provided with transverse rectangular ribs. Energy Procedia **50**, 761–772 (2014)
13. Yadav, A.S., Bhagoria, J.L.: A numerical investigation of square sectioned transverse rib roughened solar air heater. Int. J. Therm. Sci. **79**, 111–131 (2014)
14. Gupta, A.D., Varshney, L.: Performance prediction for solar air heater having rectangular sectioned tapered rib roughness using CFD. Therm. Sci. Eng. Prog. **4**, 122–132 (2017)
15. Yadav, A.S., Bhagoria, J.L.: A CFD based thermo-hydraulic performance analysis of an artificially roughened solar air heater having equilateral triangular sectioned rib roughness on the absorber plate. Int. J. Heat Mass Transf. **70**, 1016–1039 (2014)
16. Gawande, V.B., Dhoble, A.S., Zodpe, D.B., Chamoli, S.: Experimental and CFD-based thermal performance prediction of solar air heater provided with right-angle triangular rib as artificial roughness. J. Braz. Soc. Mech. Sci. Eng. **38**, 551–579 (2015)
17. Gawande, V.B., Dhoble, A.S., Zodpe, D.B., Chamoli, S.: Experimental and CFD-based thermal performance prediction of solar air heater provided with chamfered square rib as artificial roughness. J. Braz. Soc. Mech. Sci. Eng. **38**, 643–663 (2015)
18. Karmare, S.V., Tikekar, A.N.: Analysis of fluid flow and heat transfer in a rib grit roughened surface solar air heater using CFD. Sol. Energy **84**, 409–417 (2010)
19. Yadav, A.S., Bhagoria, J.L.: Heat transfer and fluid flow analysis of solar air heater: a review of CFD approach. Renew. Sustain. Energy Rev. **23**, 60–79 (2013)
20. Patankar, S.: Numerical Heat Transfer and Fluid Flow. CRC Press (1980)
21. McAdams, W.H.: Heat Transmission. McGraw-Hill Book Co., New York (1942)
22. Fox, R.W., McDonald, A.T., Pritchard, P.J.: Introduction to Fluid Mechanics. Wiley, New York (1985)
23. Ahn, S.W.: The effects of roughness types on friction factors and heat transfer in roughened rectangular duct. Int. Commun. Heat Mass Transfer **28**, 933–942 (2001)
24. Nine, M., Lee, G., Chung, H., Ji, M., Jeong, H.: Turbulence and pressure drop behaviors around semicircular ribs in a rectangular channel. Therm. Sci. **18**, 419–430 (2014)

Comparative Study of the Performance of Double-Pass and Single-Pass Solar Air Heater with Thermal Storage

Vipin Shrivastava [ID]**, Anil Yadav** [ID]**, and Nitin Shrivastava** [ID]

Notation

A_p	Area of SAH (m^2)
C	Specific heat (J/kg K)
D_e	Equivalence diameter
h	Heat-transfer-coefficient (W/m^2/K)
I	Solar insolation (W/m^2)
k	Thermal conductivity (W/m °C)
$\dot{m}$	Mass flow rate (kg/s)
Nu	Nusselt number
Pr	Prandtl number $\left(\frac{\mu c_p}{k}\right)$
Q	Heat transfer rate (W)
V	Air velocity (m/s)
Re	Reynolds number $\left(\frac{\rho V D_e}{\mu}\right)$
T	Temperature (°C)
U	Overall heat-transfer-coefficient (W/m^2 °C)

Symbols

α, ε	Absorptivity and emissivity of the plate

V. Shrivastava (✉) · A. Yadav
Department of Mechanical Engineering, Lakshmi Narain College of Technology, Bhopal 462026, India
e-mail: vipin_shrivastava07@rediffmail.com

N. Shrivastava
Department of Mechanical Engineering, University Institute of Technology, Rajiv Gandhi Proudyogiki Vishwavidyalaya, Bhopal 462033, India

© The Author(s), under exclusive license to Springer Nature Singapore Pte Ltd. 2021
A. Kumar et al. (eds.), *Recent Advances in Mechanical Engineering*, Lecture Notes in Mechanical Engineering, https://doi.org/10.1007/978-981-15-9678-0_20

θ	Temperature difference (°C)
ρ	Density of air (kg/m^3)
τ	Transitivity of glass
η	Efficiency
σ	Stefan's Boltzmann constant (W/m^2 K^4)

Subscripts

a	Ambient
abs	Absorber plate
b	Bottom
c	Convective
f	Air (fluid)
g	Glass
o	Exit/outlet
i	Entrance/inlet
m	Mean
p	Plate
r	Radiative
t	Top
1, 2 and 3	1, 2, And 3 absorber plate

1 Introduction

Solar air heaters (SAH) are the best alternative in the small-scale industry where heated air of 40–120 °C is required. The SAH used in the drying of crops, herbs, room heating in hilly areas, and providing induce ventilation [1, 2]. Broad literature review about the use of SAH in solar drying reveals that effective drying by sun involves high temperature, long operational time as well as airflow to remove the moisture content from the multi tray dryer [3, 4]. The operational hours are usually extended by adopting thermal storage in the air heating unit. The temperature produced by a SAH depends on its different configurations. Wijeysundera et al. [5] investigated two-pass SAH and found that it is more efficient than SPSAH. Chabane et al. [6] compared the result of a SPSAH and DPSAH and found a substantial enrichment in the efficiency in the latter case.

Fudholi et al. [7] performed an energy analysis of a finned DPSAH collector. The authors reported an increase in efficiency with the raise in airflow. Krishnananth and Murugavel [8] used paraffin wax as a thermal storage medium and kept it in the form of a capsule in a double pass collector. The different experiment was carried out by putting the different positions of the capsule in the air heater. The result shows

that the position in which capsules were positioned on the top of absorber sheet is more efficient than others. Ramani et al. [9] experimented SPSAH and DPSAH, embedded with the porous material on the backside of the second pass. The result shows that the air heater operates on a dual-pass with porous media is 25% and 35% more thermally efficient than dual-pass without porous material and SPSAH, respectively. Saxena et al. [10] evaluate the thermal performance of SAH having four different configurations. The result show that the arrangement with thermal storage took more time to get the highest temperature as compared to without thermal storage configuration. Bhargav et al. [11] examine the three different configurations and show that in the third type of SAH heater, using two absorber plates and two channels is more efficient than other configurations.

The above literature shows that the significant heat is lost from the top absorber plate. Although the use of fin, ribs, capsules increases efficiency, but on the other side, it affects the flow rate of air, which is required in some applications such as solar drying. Therefore, a new type of DPSAH was constructed, which can maintain the temperature at a higher air flow. In the constructed DPSAH, the air is sent from the bottom of the first plate and flows out from the top of the thermal storage. Thus, it properly utilizes the heat in the sunshine and off sunshine hours.

2 Material and Methods

2.1 Experimental Setup

Both constructed SAH have the same geometry of 1.2 m × 1.2 m × 0.4 m. The only difference is in the number of air pass channels. The SPSAH has one channel, and DPSAH has two channels, of the same size, i.e., 0.06 m, to circulate the air. The gap in transparent glass cover and plate in both configurations is the same. In DPSAH, air from duct passes through the first channel and gain heat from both absorber plates; then, it moves to the second channel. The thickness of glass cover and black painted G.I sheet is 0.004 m and 0.036 m, respectively. The 8 fans of 12 V and 0.16 A supply forced air in a duct. Fans can run on variable speed. The speed of fans is gradually increased from first to last day. The acrylic sheet and glass wool layer used to prevent heat loss from the side. The constructional photographic view of DPSAH is presented in Fig. 1.

2.2 Experimentation and Instrumentation

The experimentation has been performed on for four days from 10:00 AM to 09:00 PM during winter in Energy Park of the institute, (23° 15′ N–77° 25′ E). The fan circulates the air and maintains a mass flow rate of 0.02, 0.03, 0.04, and 0.05 kg/s in
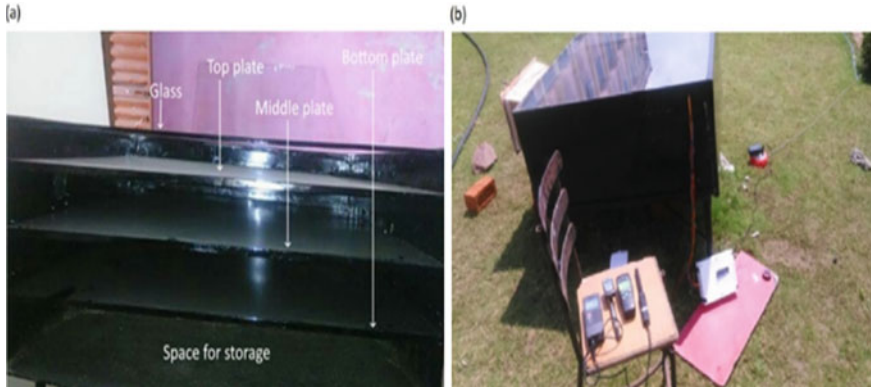
Fig. 1 A photographic view of DPSAH

Table 1 Details of instruments used in the experiment

S. No.	Instrument	Manufacturer, specification, and accuracy
1	Solar power meter	Model-TM 207, range 0–1800 W/m^2, accuracy $\pm$ 10 W/m^2, least count 0.1 W/m^2
2	Anemometer	Model Testo-490, range 0.1 m/s, least count 0.01 m/s
3	Hygrometer	Model Lutron HT-305, Resolution 0.1%RH, 0.1 °C
4	Data logger	Elimko, E-680 K type with accuracy $\pm$ 0.5 °C
5	Digital thermometer	Model HTC infrared, -50 to 550 °C and least count 0.1 °C

each consecutive experiment day. Table 1 depicts the list of the instruments used for reading purpose.

Uncertainty analysis is the most effective tool for a plan and carries out research work. The total uncertainty U_R is [12]

$$U_R = \sqrt{\left[\left(\frac{\partial U}{\partial x_1}U_1\right)^2 + \left(\frac{\partial U}{\partial x_2}U_2\right)^2 + \left(\frac{\partial U}{\partial x_3}U_3\right)^2 + \cdots + \left(\frac{\partial U}{\partial x_n}U_n\right)^2\right]} \quad (1)$$

The total uncertainty in the evaluation of temperature (digital thermometer) and reading is estimated as

$$U_{\text{temperature,total}} = \sqrt{\left[\left(U_{\text{digital thermometer}}\right)^2 + \left(U_{\text{reading}}\right)^2\right]} \quad (2)$$

$$U_{\text{temperature,total}} = \sqrt{\left[(0.1)^2 + (0.1)^2\right]} = 0.14 \quad (3)$$

The total uncertainty in the evaluation of airspeed (by anemometer) and reading error is found by Eq. 4

$$U_{\text{air,total}} = \sqrt{\left[(U_{\text{anemometer}})^2 + (U_{\text{reading}})^2\right]}$$ (4)

$$U_{\text{air,total}} = \sqrt{\left[(0.01)^2 + (0.01)^2\right]}$$ (5)

The total uncertainty in solar power meter and reading is calculated by Eq. 6

$$U_{\text{solar radiation,total}} = \sqrt{\left[(U_{\text{solar powet meter}})^2 + (U_{\text{reading}})^2\right]}$$ (6)

$$U_{\text{solar radiation,total}} = \sqrt{\left[(0.1)^2 + (0.1)^2\right]}$$ (7)

$$U_{\text{experimental,total}} = \sqrt{\left[(U_{\text{temperature,total}})^2 + (U_{\text{solar radiation,total}})^2 + (U_{\text{reading,total}})^2\right]}$$ (8)

The total uncertainty is $\pm 0.20\%$ and is in an acceptable limit.

2.3 Thermal Analysis

The solar radiation (S) on the glass surface is [13]

$$S \cong 0.97 \tau_g \alpha_{p1} I$$ (9)

Thermal efficiency of SAH depends on the rate of heat gain (Q_u) to the insolation upon the glass cover (I), and in both cases, it is given by the following equation [14]

$$\eta = \frac{Q_u}{I A_p} = \frac{\dot{m} C_p (T_o - T_i)}{I A_p}$$ (10)

Heat loss (Q_L) is given by the following equation [15]

$$Q_L = U_L A_p \theta_m = U_L A_p (T_m - T_a)$$ (11)

where U_L is overall heat-loss-coefficient

$$U_L = U_t + U_m + U_b$$ (12)

Top heat-loss-coefficient (U_t) relates with T_g, ε_p, ε_g, T_p and in present thermal network is calculated by [13]

$$U_t = \frac{1}{\left[\frac{1}{h_{r,ga}+h_{c,ga}} + \frac{1}{h_{r,gp1}}\right]} \tag{13}$$

Mid heat-loss-coefficient (U_m) between the top and a middle plate of the air heater is determined by

$$U_m = \frac{1}{\left[\frac{1}{h_{c,f1p1}} + \frac{1}{h_{c,f1p2}} + \frac{1}{h_{r,p1p2}}\right]} \tag{14}$$

Bottom heat-loss-coefficient (U_b) is

$$U_b = \frac{1}{\left[\frac{1}{h_{c,f2p2}} + \frac{1}{h_{c,f2p3}} + \frac{1}{h_{r,p2p3}}\right]} \tag{15}$$

Radiative heat-transfer-coefficient ($h_{r,ga}$) in ambient and glass [16]

$$h_{r,ga} = \frac{\sigma\left(T_g^2 + T_a^2\right)\left(T_g + T_a\right)}{\left(\frac{1}{\epsilon_g} - 1\right)} \tag{16}$$

Similarly, the radiative heat-transfer-coefficient amid the glass and first absorber plate ($h_{r,gp1}$) is [16]

$$h_{r,gp1} = \frac{\sigma\left(T_g^2 + T_{p1}^2\right)\left(T_g + T_{p1}\right)}{\left(\frac{1}{\epsilon_g} + \frac{1}{\epsilon_{p1}} - 1\right)} \tag{17}$$

Radiative heat-transfer-coefficient from the top sheet to middle plate is obtained by [16]

$$h_{r,p1p2} = \frac{\sigma\left(T_{p1}^2 + T_{p2}^2\right)\left(T_{p1} + T_{p2}\right)}{\left(\frac{1}{\epsilon_{p1}} + \frac{1}{\epsilon_{p2}} - 1\right)} \tag{18}$$

The convective heat-transfer-coefficient for air flowing inside the channel [11]

$$\text{Nu} = \frac{h_{c,p1f1}D_e}{k_{\text{air}}} = 0.0334\text{Re}^{0.8}\text{Pr}^{0.33} \tag{19}$$

Use this equation in evaluating convective heat transfer ($h_{c,p1f1}$) between the first plate and air

$$h_{c,p1f1} = \frac{\left(0.0334 \mathrm{Re}_{p1f1}^{0.8} \mathrm{pr}_{p1f1}^{0.33} k_{\mathrm{air},i}\right)}{D_e} \tag{20}$$

Similarly, the convective heat-transfer-coefficient of entering fluid to the middle plate by Eq. 19 is

$$h_{c,f1p2} = \frac{0.0334 \mathrm{Re}_{p2f1}^{0.8} \mathrm{pr}_{p2f1,}^{0.33} k_{\mathrm{air},i}}{D_e} \tag{21}$$

Radiative heat-lose-coefficient ($h_{r,p2p3}$) from the middle plate to the bottom plate is [16]

$$h_{r,p2p3} = \frac{\sigma\left(T_{p2}^2 + T_{p3}^2\right)\left(T_{p2} + T_{p3}\right)}{\left(\frac{1}{\epsilon_{p2}} + \frac{1}{\epsilon_{p3}} - 1\right)} \tag{22}$$

Convective heat-transfer-coefficient from the middle plate to the exit fluid stream ($h_{c,p2f2}$) calculated by using Eq. 19

$$h_{c,f2p2} = \frac{0.0334 \mathrm{Re}_{p2f2}^{0.8} \mathrm{pr}_{p2f2}^{0.33} k_{\mathrm{air},o}}{D_e} \tag{23}$$

Convective heat-transfer-coefficient between exit fluid stream and bottom ($h_{c,f2p3}$) from Eq. 19 will be

$$h_{c,f2p2} = \frac{0.0334 \mathrm{Re}_{p2f2}^{0.8} \mathrm{pr}_{p2f2}^{0.33} k_{\mathrm{air},o}}{D_e} \tag{24}$$

3 Result and Discussion

Figure 2 depicts the change in the environmental parameters in all four consecutive days. Solar radiations from the sun become more transparent and stronger in mid-noon. Both air heaters are inclined at 23° due to the latitude of the place. Solar radiation varies from 973–991 W/m^2 in peak hours. After 12.45 PM, solar radiation gradually decreases, and after 7 PM, radiation is almost zero. The above parameters are same for both air heaters. Relative humidity and ambient temperature are varied from 40% to 62% and 25 °C to 42 °C, respectively.
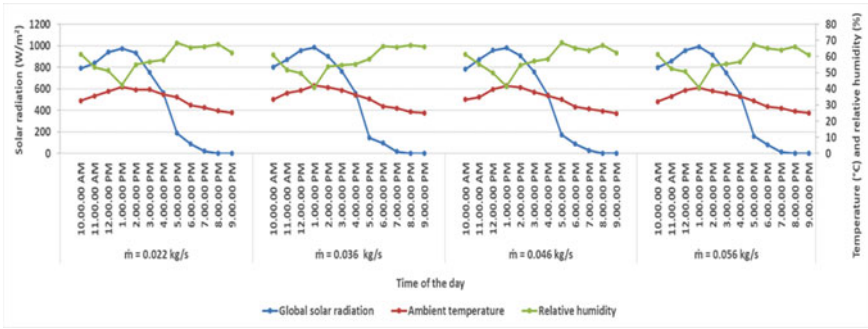
Fig. 2 Variation in environmental parameters

Figure 3a, b shows the variation of different surfaces temperature of single- and double-pass SAH. The velocity of air on a secondary axis is used because it affects the temperature of the glass surface. Observed data shows the maximum glass cover temperature in a single-pass and the double-pass mode is 60 and 67 °C. This less
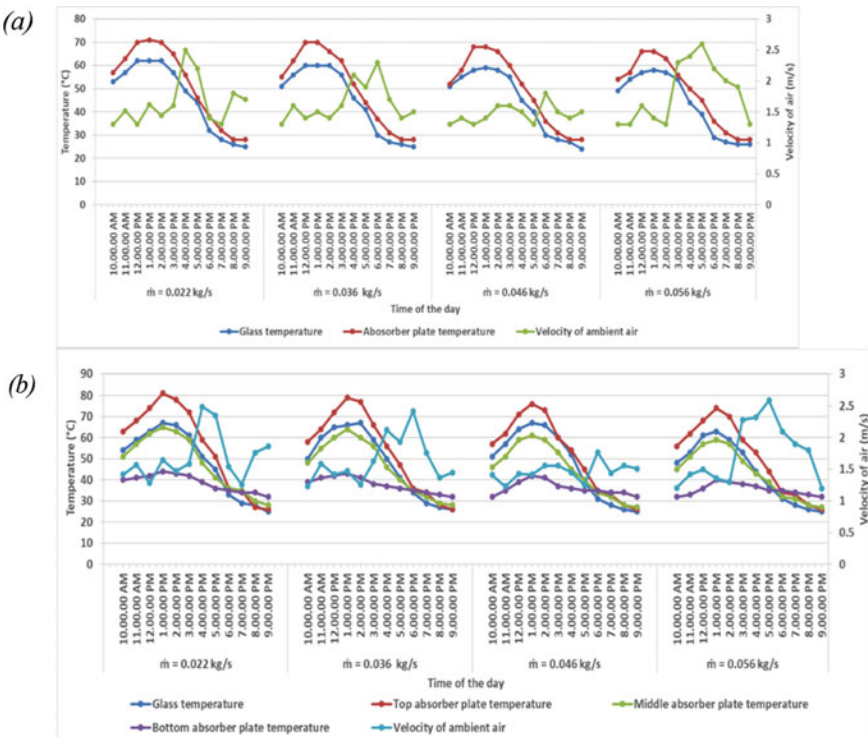
Fig. 3 Variations of the temperature in surfaces **a** SPSAH, **b** DPSAH
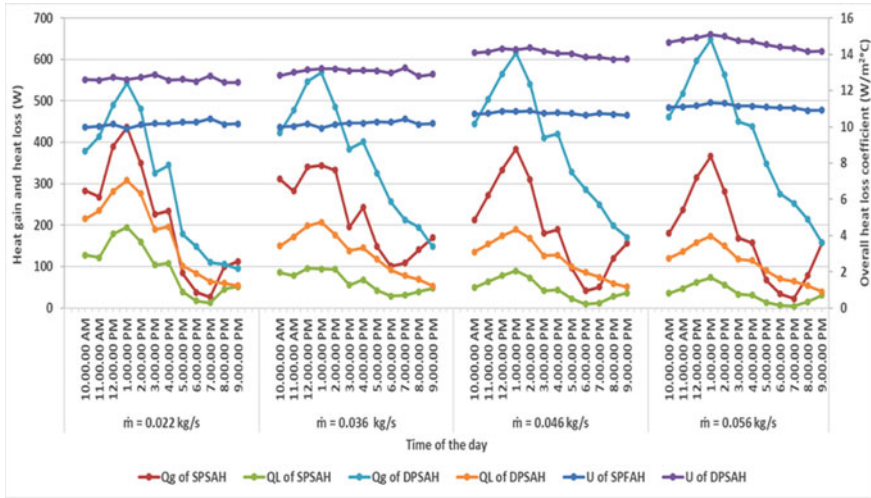
Fig. 4 Variation of heat gain, heat loss, and overall heat loss coefficient with time of the day

temperature in single pass in the same condition is due to the movement of air inside the channel. The maximum temperature of the first, second, and third plates for all days of the experimentation varied from 74–81, 59–65, and 40–44 °C. Data shows that in DPSAH, the bottom plate temperature increases, and the middle plate temperature decreases from evening to night. It is due to the storage effect. The middle plate in double-pass SAH is positioned between the top and bottom plates. Thus, it would continuously gain heat from the corresponding absorber plates.

Figure 4 shows the variation in analytically obtained values of heat gain, heat loss and heat transfer coefficient. The heat gain depends on the inlet and exit temperature. The maximum heat gain obtained in double-pass mode is 542, 568, 615, and 647 W/m^2 at consecutive days of experiments. It indicates the proposed configuration gain more heat than conventional configuration. Therefore, a rise in heat content in DPSAH with the mass flow rate of air. It is also due to the proper transfer of heat from different plates to the air. The heat-loss-coefficient (U_L) is higher in DPSAH as compared to SPSAH. Therefore, more heat is lost from DPSAH. Despite that, the maximum outlet temperature in double-pass mode is 65 °C, while in the case of single-pass mode, it is 57 °C.

Figure 5 depicts the changes in thermal efficiency during the main sunshine hours for both types of SAH with varying the airflow rate. The heat gain in single-pass SAH is decreasing, but in double-pass SAH, it increased in consecutive days of the test. The heat loss in both cases gradually decreases with increasing airflow rate. However, it is higher in the DPSAH as compared to a SPSAH. Therefore, efficiency in double-pass mode is more than single-pass SAH. The day-wise average thermal efficiency in SPSAH is decreasing from 35 to 29%, and in DPSAH, it is increasing from 49 to 61%.
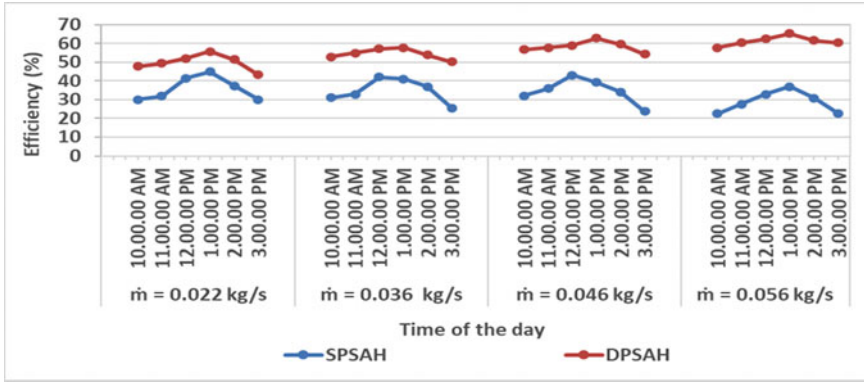
Fig. 5 Efficiency versus time of the day for SPSAH and DPSAH

4 Conclusion

- The proposed configurations can properly transfer heat to the fluid, and its thermal storage (sand) works effectively in the evening.
- Thermal storage material keeps the air warm and maintain the temperature difference of 4–5 °C till late evening.
- The DPSAH is more efficient than a SPSAH.
- The increase of air mass flow rate leads to the higher efficiency of DPSAH and reduced efficiency of SPSAH.

Appendix

Following empirical formula is used in calculations [17, 18]

$$C_p = 999.2 + 0.1434 T_m + 1.101 \times 10^{-4} T_m^2 - 6.7581 \times 10^{-8} T_m^3 \quad (25)$$

$$k_{air} = 0.024 + 0.07673 \times 10^{-4} T_m \quad (26)$$

$$\mu_{air} = 1.718 \times 10^{-5} + 4.620 \times 10^{-8} T_m \quad (27)$$

$$\rho = 353.44/(T_m + 273.15) \quad (28)$$

References

1. Shrivastava, V., Kumar, A.: Embodied energy analysis of the indirect solar drying unit. Int. J. Ambient Energy **38**(3), 280–285 (2017)
2. Shrivastava, V., Kumar, A., Baredar, P.: Kinetics of fenugreek drying in an indirect solar dryer. Heat Transf. Res. **48**(9), 787–797 (2017)
3. Hatami, S., Sadegh, M., Mireei, S.A.: Indirect forced solar drying of banana slices: phenomenological explanation of non-isotropic shrinkage and color changes kinetics. Int. J. Green Energy **14**(15), 1277–1283 (2017)
4. Kuhe, A., Ibrahim, J.S., Tuleun, L.T., Akanji, S.A.: Effect of air mass flow rate on the performance of a mixed-mode active solar crop dryer with a transpired air heater. *International Journal of Ambient Energy*. https://doi.org/10.1080/01430750.2019.1653970
5. Wijeysundera, N.E., Ah, L.L., Tjioe, L.E.: Thermal performance study of two-pass solar air heaters. Sol. Energy **28**(5), 363–370 (1982)
6. Chabane, F., Moummi, N., Benramache, S.: Experimental study of heat transfer and thermal performance with longitudinal fins of solar air heater. J. Adv. Res. **5**(2), 183–192 (2014)
7. Fudholi, A., Sopian, K., Othman, M.Y., Ruslan, M.H., Bakhtyar, B.: Energy analysis and improvement potential of finned double-pass solar collector. Energy Convers. Manage. **75**, 234–240 (2013)
8. Krishnananth, S.S., Kalidasa Murugavel, K.: Experimental study on double pass solar air heater with thermal energy storage. J. King Saud Univ.-Eng. Sci. **25**(2), 135–140 (2013)
9. Ramani, B.M., Gupta, A., Kumar, R.: Performance of a double pass solar air collector. Sol. Energy **84**(11), 1929–1937 (2010)
10. Saxena, A., Agarwal, N., Srivastava, G.: Design and performance of a solar air heater with long term heat storage. Int. J. Heat Mass Transf. **60**(8), 8–16 (2013)
11. Bhargava, A.K., Garg, H.P., Sharma, V.K.: A two-pass solar air heater. Energy **8**(4), 267–276 (1983)
12. Akpinar, E.K.: Drying of mint leaves in a solar dryer and under open sun: modelling, performance analyses. Energy Convers. Manage. **51**(12), 2407–2418 (2010)
13. Duffie, J.A., Beckman, W.A.: Solar Engineering of Thermal Processes, 2nd edn. Wiley, Hoboken (2013)
14. Kumar, R., Rosen, M.A.: Performance evaluation of a double pass PV/T solar air heater with and without fins. Appl. Therm. Eng. **31**(8–9), 1402–1410 (2011)
15. Karwa, R., Srivastava, V.: Thermal performance of solar air heater having absorber plate with v-down discrete rib roughness for space-heating applications. J. Renew. Energy (Article ID 15157), 1–13 (2013)
16. Naphon, P.: On the performance and entropy generation of the double-pass solar air heater with longitudinal fins. Renew. Energy **30**(9), 1345–1357 (2005)
17. Shrivastava, V., Kumar, A.: Experimental investigation on the comparison of fenugreek drying in an indirect solar dryer and under open sun. Heat Mass Transfer **52**(9), 1963–1972 (2016)
18. Kumar, A., Tiwari, G.N.: Effect of mass on convective mass transfer coefficient during open sun and greenhouse drying of onion flakes. J. Food Eng. **79**(4), 1337–1350 (2007)

Role of ANN in Functionality and Designing of Solar Photovoltaic Cell: A Review

Anupama Kaushik

1 Introduction

The research on photovoltaic cell has increased widely due to its extensive uses. A photovoltaic cell converts the Sun's energy into usable energy without any impact on environment. The most important component of a solar panel is photovoltaic cell, which actually generates electricity.

These photovoltaic (PV) cells are mainly divided into two categories, monocrystalline and polycrystalline, as these are most commonly used for various commercial and residential applications. A single silicon crystal is used for monocrystalline PV cell, whereas many shards of silicon crystals are used in polycrystalline PV cells. On comparison, monocrystalline PV cell is more efficient than polycrystalline PV cells. The reason being, as monocrystalline PV cell, consists of a single silicon crystal, and there is an easier flow of electrons generated through the photovoltaic effect. In polycrystalline PV cells, there are many shards of silicon aligned in many different directions which makes electricity flow slightly difficult.

The primary objective of this study is to understand the basics of PV cell and to know-how neural networks (NN) can impact its computational characteristics. The remainder of the paper will be organized as follows. Sections 2 and 3 describe the functionality and design of a PV cell. Section 4 discusses ANN in brief; Sect. 4.1 describes the earlier studies based on ANN which have modelled PV cell parameters; Sect. 5 concludes the paper and highlights the future direction.

A. Kaushik (✉)

Indira Gandhi Delhi Technical University for Women, Delhi, India
e-mail: anupama@msit.in

Department of Information Technology, Maharaja Surajmal Institute of Technology, New Delhi, India

239
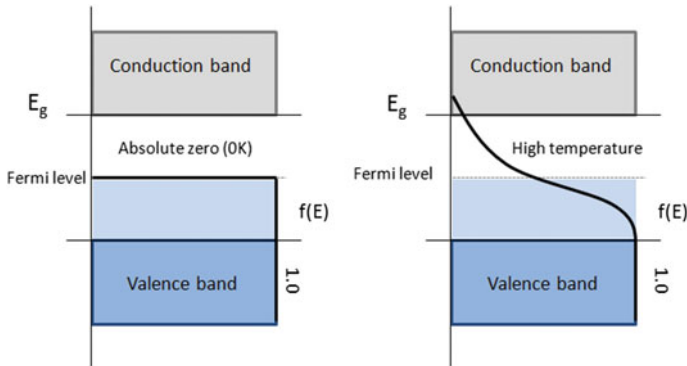
Fig. 1 Semiconductor Band Structure Plot

2 Functionality

A PV cell captures solar energy to produce electricity through a process called photovoltaic effect. Each cell operates as a semiconductor consisting of *p*-type and *n*-type semiconductor joined to form a *p-n* junction. Due to this, an electric field is formed causing negatively charged particles electrons to move in one direction and positively charged particles photons to move in other direction. When Sun rays are incident on these PV cells, photons transfer their energies to electrons in PV cell causing them to jump to a higher energy state known as the conduction band. This movement of electrons in conduction band generates an electric current in the cell.

Figure 1 demonstrates the semiconductor band structure plot. According to quantum theory, there exists a gap between valence and conduction bands of semiconductor. At absolute zero temperature, semiconductors behave as an insulator. At higher temperature, they become conductive as electrons and holes move from one band to another. This is due to the illumination of PV systems due to incident photons [1–4].

3 Designing

The PV cell design principles are affected by the working environment in which they are produced. For example, if it is developed for the research environment, then efficiency is more important, whereas for commercial environment cost weighs more.

The absorption coefficient of semiconductors also plays an important role in PV cell design. It is dependent on the material and also on the wavelength of light absorbed by the cell. The designers of PV cell use materials with higher absorption

Fig. 2 *I–V* Curve of a PV cell
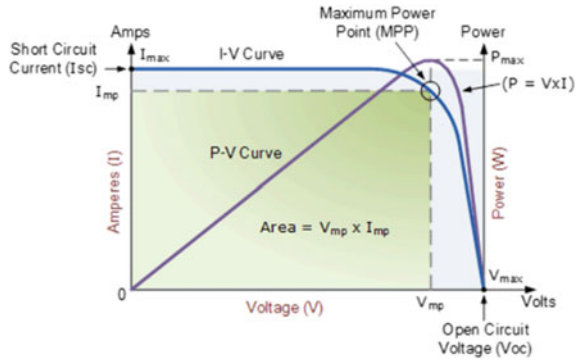
coefficients which can absorb photons readily and eventually excite electrons into the conduction band.

The main ingredient of a PV cell is silicon which causes an electric current to flow. All the PV modules are rated against standard test conditions (STC) which includes three factors: (a) Irradiance, i.e. sunlight intensity or power. The measurement standard is 1 kW per m^2. (b) Airmass, i.e. clarity and thickness of the air which affect the Sun's angle. The standard is 1.5. (c) Cell temperature. The standard is 25 °C.

The performance of solar panels can be represented by an "*I–V* curve". Every solar panel has multiple *I–V* curves which shows the relationship between current (I) and voltage (V) under prevailing conditions of, temperature, air mass and irradiance. Maximum peak power point (MPP) also depicts when a PV cell generates maximum power.

Figure 2 describes the *I–V* curve of a PV cell. At open-circuit voltage (V_{oc}), the voltage across the cell is maximum and the current is at its minimum, whereas when the cell is short circuited, the current is at its maximum known as short-circuit current (I_{sc}) and the voltage is at its minimum. As the PV cell is a *p-n* diode, the diode equations are inculcated in its designing. For achieving good conduction, the bottom layer of a PV cell should be completely covered and the topmost layer should be transparent so that the incident photons aren't blocked. A metallic cell grid is also used within the semiconductor to increase its conduction which reduces electron travel distance and thereby decreases resistance [4].

4 Artificial Neural Networks (ANN)

ANN works just like our human brain to solve a particular problem. The basic unit of brain and nervous system is the biological neurons which receives the input from the external world via dendrites, process it and gives the output through Axons. In the similar way, ANN also uses neurons to process the inputs. These neurons are connected to one another using connection link with weights assigned to them. This
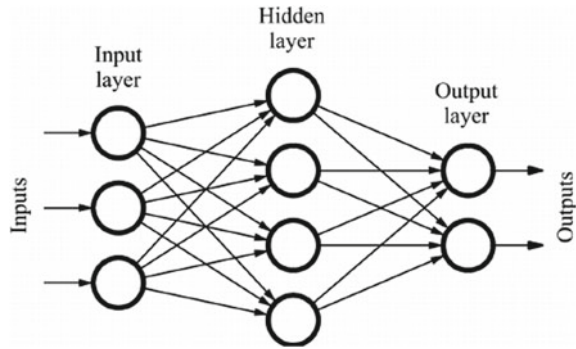
is required to solve a problem by a neural network. Every neuron has an internal state denoted by an activation function. There are many activation functions few of them are, binary step, sigmoid, tan h, ReLu, etc. There exist different kinds of ANN. The simpler one is called "perceptron" which is a single layer neural network. Later on, multilayer perceptrons with backpropogation learning algorithms are developed consisting of input, hidden and output layers. These ANNs are based on supervised learning and are used in variety of problems. Figure 3 shows a feed-forward ANN with three layers.

4.1 ANN Approaches Used in PV Cells

This section discusses various ANN approaches applied to PV cells. It also presents the discussion on various parameters of PV cell predicted through ANN modelling and the ANN framework used. The ANN modelling of a PV cell mainly uses two approaches [5, 6]: the first approach uses various irradiation and temperature values to predict the equivalent circuit parameters and then calculates current or voltage using analytical model; the second approach generates I–V curves using irradiance and module cell temperature as inputs to ANN.

Zhang and Bai [7] used genetically trained radial basis function neural networks (RBFNN) to predict the maximum power points (MPPs) and corresponding I–V curves of photovoltaic (PV) panels. The inputs to the network were radiation, ambient temperature and load voltage; and the output was load current. The hidden layer consisted of radial basis function which were trained using genetic algorithm. This model provided better results than conventional RBFNN which uses k-means algorithm in radial basis function. The genetically trained RBFNN were used to find optimal power points in PV panels.

Karatepe et al. [5] proposed feed-forward neural network with three layers. The inputs were irradiation and temperature, and the outputs were n, Is, Rs, Rp and Iph. The three kinds of activation function were used, and they were piecewise linear function, sigmoid function and piecewise linear function. In order to check the

accuracy of the proposed model, the experimental setup was used. It was found that the model provided accuracy than the conventional model.

Mekki et al. [8] proposed simulation and modelling of a PV module using ANN and VHDL language. The inputs to the model were total irradiation and mean average temperature, and the outputs were current and voltage. The NN is implemented using VHDL language. The proposed model predicted the energy from the PV panel using only the environmental factors and required less computational efforts.

Rehman and Mohandes [9] proposed feed-forward ANN for the estimation of global solar radiation (GSR). The inputs to the network were air temperature and relative humidity values of Abha City in Saudi Arabia from 1998 to 2002. The authors classified the inputs in three categories and found that ANN provided good prediction for GSR based on temperature and relative humidity.

Ghanbarzadeh et al. [10] predicted daily global solar radiation (GSR) in future time domain using ANN for Dezful City in Iran. The inputs were measured air temperature, relative humidity and sunshine hours values between the years 2002 and 2006. The entire dataset was divided into three categories. They found that the ANN model used provided promising results for GSR.

Behrang et al. [11] used MLP and radial basis function network for GSR modelling. They divided the input dataset into six categories. The inputs were daily mean air temperature, relative humidity, sunshine hours, evaporation and wind speed for Dezful City in Iran between 2002 and 2006. The training data used by them was for the year 2002–2005, and the rest of the data was used as a testing data. The results provided by ANN were good in comparison with conventional GSR prediction models.

Celik [12] used generalized regression neural network (GRNN) model to estimate the operating current of a 120 Wp of monocrystalline photovoltaic module. The inputs used in the model were solar radiation on the module, cell temperature and the operating voltage of the system. The learning algorithm used was Levenberg–Marquardt (LM) algorithm. The model's performance to estimate current was evaluated using mean absolute percentage error (MAPE). The results of GRNN model were also compared with the results of actual experiments carried out in Iskenderun, Turkey, and with the analytical model. It was found that the current predicted by GRNN model was more accurate than the analytical model and close to the real-time experimental results.

Salah and Ouali [13] proposed neural network and fuzzy logic models to estimate maximum power point (MPP) for photovoltaic modules. The inputs to both the models were solar radiation and cell temperature. The model was validated on a 100Wp PVP SM50-H panel connected to a 24 V DC load. The models were adaptable to changing solar radiations and cell temperature. The results concluded that the fuzzy logic model was better than the neural network model in estimation of maximum power point (MPP).

Bonanno et al. [14] et al. used radial basis function neural networks (RBFNN) to predict the load current. The inputs to the model were solar radiation, ambient temperature and load voltage. The model has input, hidden and output layers and, used backpropagation learning algorithm. It improved the *I–V* and *P-V* curves of a PV

module. Guede et al. [15] approximated the *I–V* curve using ANN. They modelled ATERSA A55 photovoltaic module using feed-forward network with backpropagation learning. The temperature, irradiance and the voltage were the inputs, and the current was the output. The prediction accuracy of the model is measured using mean square error (MSE). Ceylan et al. [16] used backpropagation neural network to predict the temperature of a PV module. The inputs to the ANN model were ambient air temperature and solar radiation. These inputs were determined from the experimental studies at Aegean region of Turkey with ambient air temperature at 10, 20, 30 and 40 °C and at different solar radiations. The predicted module temperature was then used to calculate the electrical efficiency and power.

Dumitru et al. [17] used multilayer perceptron and Elman neural networks to estimate the solar photovoltaic energy production. A two-year data of energy production of photovoltaic cells was analysed, and it was found that the energy production level increases in summer. This energy production was analysed using different parameters of ANN like learning rate, number of neurons and number of epochs. The accuracy prediction can also be increased by considering several factors like meteorological conditions, seasons and by increasing the dataset.

Parmar [18] used feed-forward network with Levenberg–Marquardt backpropagation (*trainlm)* as the learning algorithm. The inputs to the network were solar radiation and ambient temperature, and the outputs were voltage and current value. The network performance was measured using mean square error (MSE), and it can be used in any climatic conditions to predict the output from photovoltaic panels. The network with two hidden layers provided the best prediction performance with minimum error.

Kazem et al. [19] proposed support vector machine (SVM) for predicting the photovoltaic current. The inputs to the technique were solar radiation and ambient temperature, and the output was the photovoltaic current. The proposed model provided good accuracy in comparison with other related works.

Yassin and Harb [20] proposed neural network with differential evolution (NN-DE) technique to predict the cell operating temperature. The inputs to the network are: ambient temperature (T_{amb}), wind speed, air mass and solar radiation intensity. They used cell operating temperature to evaluate the maximum power output P_{Max} of photovoltaic modules. The obtained results of the model performed well when compared with conventional regression trees model. Durrani et al. [21] used neural networks to predict daily PV power for residential grid connected PV systems. Two forecasts models were developed for irradiation; one used multiple feed-forward networks and the other was persistence based. The NN-based irradiance forecast model performed better than persistence forecast model for all the accuracy measures used.

Sun et al. [22] used convolution neural network to relate PV cell output with the climatic conditions. The images of the sky were used to relate the current generated by the PV cell. They tested their approach with different CNN structures and proposed the future use of their model. Yousifa et al. [23] did comparative study from 2008 to 2017 on PV/T (photovoltaic thermal) energy data prediction systems which used
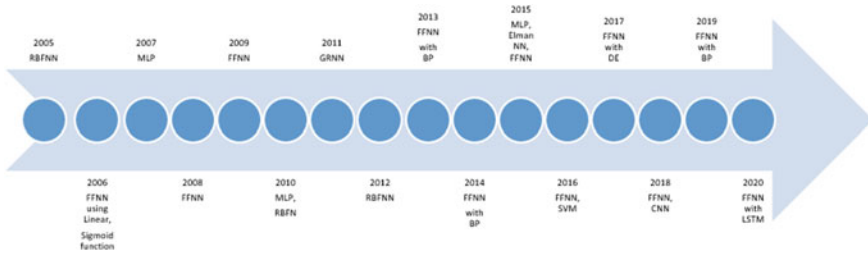
Fig. 4 Timeline of the ANNs used in the study for modelling PV cell

ANN to predict global solar radiation. The published study used different kinds of ANN and the model performed well in all the evaluation measures used.

Al-Dahidi et al. [24] proposed PV power predictions using small computational time and used ten ANN learning algorithms to train 23 datasets. They found correlations between various factors affecting PV power generation and developed an efficient prediction model. Cortés et al. [25] used multilayer perceptron network to estimate the parameters based on manufacturers datasheet. The inputs to the network are I_{sc} (short-circuit current), V_{oc} (open-circuit voltage), MPP (photovoltaic cell maximum power point), I_{mpp} (current value at the maximum power point) and V_{mpp} (voltage value at the maximum power point); the estimated parameters are I_{ph} (generated current due to photons), R_s (photovoltaic cell series resistance)and I_0 (diode reverse saturation current); the network consisted of two hidden layers and used Bayesian regularization learning method. The model can be used with any polycrystalline silicon cell, and there is no need to retrain the neural network for different PV modules made up with these cells. The synthetic data is used for training the neural network. Chen et al. [26] used long short-term memory (LSTM) learning algorithm to design a radiation classification coordinate method to select the similar time periods which are impacted by various PV power generation meteorological factors. Their proposed model was at par than the four other models compared in the work.

The ANNs used in all the above studies provided the results which were at par than the conventional models and were good in predicting the PV modules output. Figure 4 shows the timeline consisting of various ANNs used to model the PV cell. This timeline is based on the studies used in the current work.

5   Conclusion

The use of photovoltaic modules is rapidly increasing as they are based on renewable energy of sun with number environmental impact. The current study provided the base for research on photovoltaic modules and modelling their characteristics using ANN. ANNs are more capable in estimating the parameters of a PV module. The

published work on PV modules with ANN is used different types of networks. But as the new soft computing techniques are introduced, every year the future work can comprise of using these techniques in modelling PV cell characteristics.

References

1. Messenger, R.A., Ventre, J.: Photovoltaic Systems Engineering. CRC Press Technology and Industrial (2004)
2. Harmon, C.: Experience Curves of Photovoltaic Technology. IIASA Interim Report (2000)
3. American Association of Physics Teachers: Photovoltaic Cell-Sapience. Am. J. Phys. **61**, 286–287 (1993)
4. Toub, D.: A review of photovoltaic cells. https://www2.ece.rochester.edu/
5. Karatepe, E., Boztepe, M., Colak, M.: Neural network based solar cell model. Energy Convers. Manage. **47**, 1159–1178 (2006)
6. Almonacid, F., Rus, C., Hontoria, L., Fuentes, M., Nofuentes, G.: Characterisation of Si-crystalline photovoltaic modules by artificial neural networks. Renew. Energy **34**, 941–949 (2009)
7. Zhang, L., Bai, Y.F.: Genetic algorithm-trained radial basis function neural networks for modelling photovoltaic panels. Eng. Appl. Artif. Intell. **18**, 833–844 (2005)
8. Mekki, H., Mellit, A., Salhi, H., Khaled, B.: Modeling and simulation of photovoltaic panel based on artificial neural networks and VHDL-language. In: 14th IEEE International Conference on Electronics, Circuits and Systems, pp. 58–61. Marrakech (2007). https://doi.org/10.1109/ICECS.2007.4510930
9. Rehman, S., Mohandes, M.: Artificial neural network estimation of global solar radiation using air temperature and relative humidity. Energy Policy **36**, 571–576 (2008)
10. Ghanbarzadeh, A., Noghrehabadi, A.R., Assareh, E., Behrang, M.A.: Solar radiation forecasting based on meteorological data using artificial neural networks. In: 7th IEEE International Conference on Industrial Informatics, pp. 227–231. Wales (2009). https://doi.org/10.1109/INDIN.2009.5195808
11. Behrang, M.A., Assareh, E., Ghanbarzadeh, A., Noghrehabadi, A.R.: The potential of different artificial neural network (ANN) techniques in daily global solar radiation modeling based on meteorological data. Sol. Energy **84**, 1468–1480 (2010)
12. Celik, A.N.: Artificial neural network modelling and experimental verification of the operating current of mono-crystalline photovoltaic modules. Sol. Energy **85**, 2507–2517 (2011)
13. Salah, C.B., Ouali, M.: Comparison of fuzzy logic and neural network in maximum power point tracker for PV systems. Electr. Power Syst. Res. **81**, 43–50 (2011)
14. Bonanno, F., Capizzi, G., Graditi, G., Napoli, C., Tina, G.M.: A radial basis function neural network based approach for the electrical characteristics estimation of a photovoltaic module. Appl. Energy **97**, 956–961 (2012)
15. Guede, J.M.L., Hernanz, J.A.R., Graña, M.: Artificial neural network modeling of a photovoltaic module. In: International Joint Conference SOCO-CISIS-ICEUTE'13, pp. 389–397. Advances in Intelligent Systems and Computing (2013)
16. Ceylan, I., Erkaymaz, O., Gedik, E., Gürel, A.E.: The prediction of photovoltaic module temperature with artificial neural networks. Case Stud. Therm. Eng. **3**, 11–20 (2014)
17. Dumitru, C.D., Gligor, A., Enachescu, C.: Solar photovoltaic energy production forecast using neural networks. In: 9th International Conference Interdisciplinarity in Engineering, pp. 808–815. Romania (2015)
18. Parmar, H.: Artificial neural network based modelling of photovoltaic system. Int. J. Latest Trends Eng. Technol. **5**, 50–59 (2015)
19. Kazem, H.A., Yousif, J.H., Chaichan, M.T.: Modeling of daily solar energy system prediction using support vector machine for Oman. Int. J. Appl. Eng. Res. **11**, 10166–10172 (2016)

20. Yassin, A.H., Harb., M.E.: A hybrid neural network model for predicting solar cells performance. In: 12th International Conference on Computer Engineering and Systems, pp. 37–43. Cairo (2017). https://doi.org/10.1109/ICCES.2017.8275273
21. Durrani, S.P., Balluff, S., Wurzer, L., Krauter, S.: Photovoltaic yield prediction using an irradiance forecast model based on multiple neural networks. J. Mod. Power Syst. Clean Energy **6**, 255–267 (2018)
22. Sun, Y., Szűcs, G., Brand, A.R.: Solar PV output prediction from video streams using convolutional neural networks. Energy Environ. Sci. **7**, 1811–1818 (2018)
23. Yousifa, J.H., Kazemb, H.A., Alattara, N.N., Elhassanc, I.I.: A comparison study based on artificial neural network for assessing PV/T solar energy production. Case Stud. Therm. Eng. **13**, 100407 (2019)
24. Al-Dahidi, S., Ayadi, O., Adeeb, J., Louzazni, M.: Assessment of artificial neural networks learning algorithms and training datasets for solar photovoltaic power production prediction. Front. Energy Res. https://doi.org/10.3389/fenrg.2019.00130
25. Cortés, B., Sánchez, R.T., Flores, J.J.: Characterization of a polycrystalline photovoltaic cell using artificial neural networks. Sol. Energy **196**, 157–167 (2020)
26. Chen, B., Lin, P., Lai, Y., Cheng, S., Chen, Z., Wu, L.: Very-short-term power prediction for PV power plants using a simple and effective RCC-LSTM model based on short term multivariate historical datasets. Electronics **289**, 1–19 (2020)

Numerical Modelling of Thermal Cooling in PV Panels with NEPCM

Apurv Yadav , **Asha Anish Madhavan** , **Vineet Kumar Vashishtha** , **and Harsha Yadav**

List of Abbreviations

PV	Photovoltaics
PCM	Phase change material
Q_m	Latent heat of fusion
m	Mass of PCM
L	Latent heat capacity of PCM
$\dot{Q}$	Heat transfer rate from top surface to bottom surface of PCM layer
k_m	Thermal conductivity of PCM
A	Cross-sectional area of PCM layer
$\Delta T/\Delta x$	Temperature gradient from top surface to bottom surface of PCM layer
k_{HC}	Effective thermal conductivity
k_p	The thermal conductivity of dispersed carbon nanoparticles
F_p	Particle mass fraction
N	Empirical shape factor

A. Yadav (✉) · A. A. Madhavan
Amity University Dubai, Dubai 345019, UAE
e-mail: ayadav@amityuniversity.ae

V. K. Vashishtha
Delhi Technological University, Delhi 110042, India

KIET Group of Institutions, Ghaziabad, UP 201206, India

H. Yadav
Indian Institute of Technology, New Delhi 110016, India

1 Introduction

Please note that the first paragraph of a section or subsection is not indented. The first paragraphs that follows a table, figure, equation, etc., does not have an indent, either. Fossil fuel-based energy systems are not sufficient to meet the growing global energy demands and they also pose environmental concerns. This has led to aggressive research and development in the field of renewable energy technologies. Current developments in technology require the energy-efficient design of these systems. Solar, wind and biofuels are the major areas of research [1–5]. Solar photovoltaic (PV) systems are the most commonly used energy generation systems [5]. Out of the irradiation incident on the solar cell surface, only wavelengths with an energy matching the bandgap energy of the cell contribute to the direct electricity conversion. The wavelengths having high energy are dissipated as heat. The solar energy to electrical energy conversion is only about 16–20%. The remaining solar energy causes the PV panels to heat up, which could raise the PV panel temperature to around 40 °C above the ambient temperature [6]. An increase in temperature of 1 °C above 25 °C can cause the efficiency of the PV panel to drop by about 0.08% and 0.65%, respectively [7]. Cooling of PV panels is required to obtain better efficiency and prolonged life. Wide varieties of cooling methods have been explored by researchers such as cooling by fans, pumping cooled water on panels, application of high conductivity metal fins such as copper and aluminium to enhance heat transfer [8]. A preferable method of cooing is the application of phase change materials (PCMs) as it does not require additional energy and the use of expensive and bulky materials [9].

PCMs are materials absorb and release a significant amount of heat while transitioning from one phase to another. However, the low thermal conductivity of PCM poses a challenge in their application [10]. There have been numerous studies to improve the thermal conductivity of PCM [11]. The dispersion of nanoparticles has been found as the most promising technique to raise the thermal conductivity of the PCM [12, 13]. Among various nanoparticles, carbon-based nanomaterials have exhibited a considerable amount of thermal conductivity improvement of PCM [14]. Lower PV panel temperature rise has been reported with PCM and consequently higher efficiency and less material degradation [15]. A novel carbon-based PCM nanocomposite with very low concentration of additives is proposed. This study aims to describe the method of maintaining a lower PV temperature and boosting the efficiency of the PV panel. Myristic acid is selected for the absorber layer, and nanocarbon particles are used as the thermal conductivity enhancer.

2 PV-PCM Cooling Technique

This simulation assumes a panel design where the back of the panel is a flat surface and the junction box is separately connected. The model is neglecting radiative heat losses compared to the conductive heat losses to the PCM. The PV panel selected in

Table 1 PV panel parameters [16]

Parameter	Values
Model	CENTSYS
Maximum power	100 W
Short-circuit current	6.06 A
Open-circuit voltage	22 V
Maximum power current	5.56 A
Maximum power voltage	18 V
Solar cell efficiency	17.2%
Module efficiency	14.9%

Table 2 Properties of myristic acid

Parameter	Values
Thermal conductivity	0.16 W/m K [17]
Melting temperature	54 °C [12]
Latent heat of fusion	201 kJ/kg [17]
Specific heat	1.6 kJ/kg K [18]

this modelling is CENTSYS 100 W with a dimension of 1005 mm × 670 mm [16]. An aluminium foil pouch of filled with myristic acid is attached to the backside of the panel. The cross section of the pouch is kept same as panel surface area. The PCM absorber layer is 10 mm thick and the thickness of aluminium foil is negligible. The parameters for the PV panel are presented in Table 1. The properties of the selected PCM are listed in Table 2. The schematic of panel dimensions and the structure of the PV-PCM system are depicted in Fig. 1 and Fig. 2, respectively.

3 Numerical Analysis

The contact area between the PCM surface and PV panel is 0.67 m^2. The heat required to fully melt the PCM, Q_m is given as:

$$Q_m = mL \tag{1}$$

where m and L are the mass and latent heat capacity of PCM, respectively.

The heat transfer rate from the pouch surface at PV panel end to the other end, $\dot{Q}$ can be given as:

$$\dot{Q} = k_m A \Delta T / \Delta x \tag{2}$$

Fig. 1 Dimensions of the panel
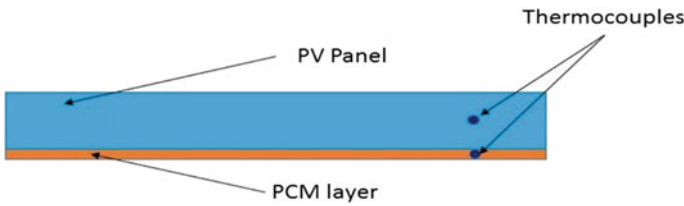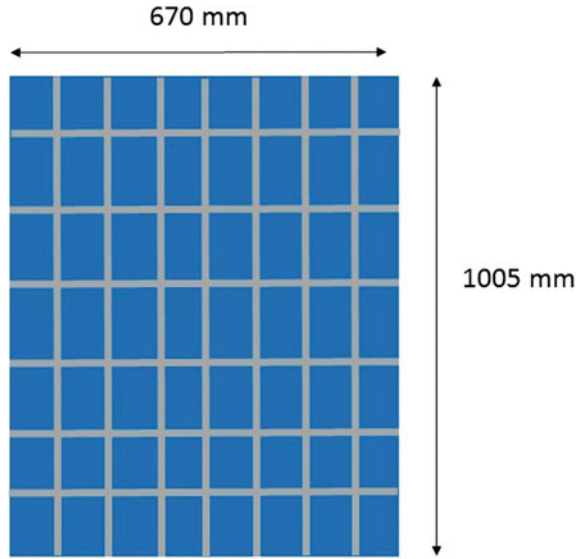
Fig. 2 PV-PCM system

where k_m, A and $\Delta T/\Delta x$ are the thermal conductivity, interfacial contact area and the temperature gradient in the PCM layer, respectively.

Myristic acid has a poor thermal conductivity with an approximate value of 0.16 W/m K. By the addition of carbon nanoparticles, it can be increased and the effective thermal conductivity, k_{HC}, can be calculated by Hamilton and Crosser (HC) approach [19] is given by the equation

$$k_{HC} = k_m \left[\frac{k_p + (n-1)k_m - (n-1)F_p(k_m - k_p)}{k_p + (n-1)k_m + F_p(k_m - k_p)} \right] \quad (3)$$

where k_m, k_p, F_p and n are the thermal conductivity of PCM, the thermal conductivity of dispersed carbon nanoparticles, particle mass fraction and empirical shape factor ($n = 3$ for sphere-shaped particles), respectively.

Fig. 3 Sensible heat of the PCM
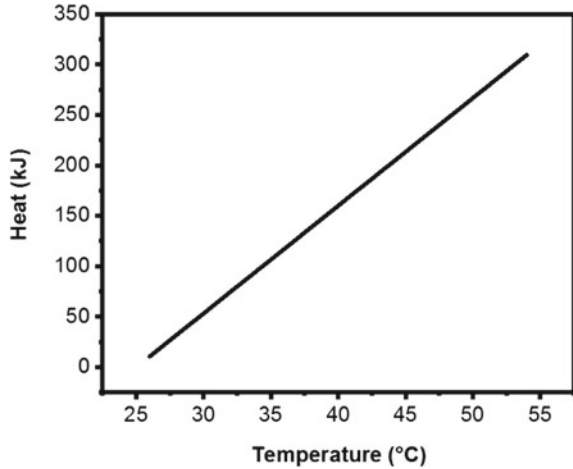
4 Result and Discussion

The front surface of the PV panel will absorb sunlight and gets heated up. As per the panel specifications, the panel will produce maximum efficiency at 25 °C (standard test conditions). If the temperature of the panel rises further, it will decrease the efficiency and consequently output of the cell. Two thermocouples will be placed on the system, one for measuring the PV panel temperature and the other for measuring the PCM temperature. The PCM layer at the back will absorb and store the excess heat from the panel, thereby reducing the panel temperature. The heat required to raise the temperature each degree till the melting of PCM is shown in Fig. 3.

PCM-PV panel cooling rate can be increased by increasing the concentration of the nanoparticles in the PCM as it will increase the heat transfer rate because of the enhanced thermal conductivity of PCM. The thermal conductivity of carbon nanoparticles is 3000 W/m K. The trend of heat transfer rate with different concentrations of carbon additives is shown in Fig. 4.

5 Conclusions

A numerical model of PCM-based cooling technique has been proposed as an efficiency-enhancing technique for a solar module. A 100 W solar panel has been selected for the study. Myristic acid is selected as the PCM cooling layer as it has the matching melting temperature range with the operational temperature of the panel. Carbon nanoparticles are selected as the thermal conductivity boosters for the PCM layer. The model showed that during the temperature rise from 25 to 55 °C, the steady-state heat rejection rate from the panel to the PCM layer will increase from 320 to 621 J/s. The application of this system can readily transfer heat from

Fig. 4 Heat transfer
enhancement due to
nanoparticle addition
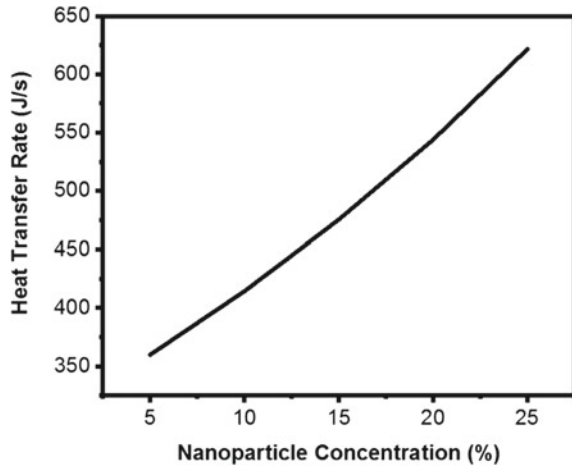
the PV panel back surface to the PCM absorber layer that will help in reducing
the temperature-related losses. It will also prove to be a cheaper and eco-friendly
solution.

References

1. Yadav, A., Verma, A., Jain, V.K., Bhatnagar, P.K., Kumar, V.: Solar driven co-generation of electricity and fresh water. American Geophysical Union Fall Meeting, GC531-1204 (2019)
2. Narayanan, S.S., Yadav, A., Khaled, M.N.: A concise review on performance improvement of solar stills. SN Appl. Sci. **2**(3), 1–15 (2020)
3. Pillai, S.R., Yadav, A., Vashishtha, V.K.: Prediction of wind power curve based on wind speed and direction using artificial neural network. In: International Conference on Innovative Techniques in Mechanical Engineering, 2019, Springer Publishing 2020 "unpublished"
4. Kumar, S., Yadav, A.: Comparative experimental investigation of preheated thumba oil for its performance testing on a CI engine. Energy Environ. **29**(4), 533–542 (2018)
5. Satish, M., Santhosh, S., Yadav, A.: Simulation of a Dubai based 200 KW power plant using PVsyst software. In: 2020 7th International Conference on Signal Processing and Integrated Networks (SPIN), pp. 824–827. IEEE (2020, February)
6. Makki, A., Omer, S., Sabir, H.: Advancements in hybrid photovoltaic systems for enhanced solar cells performance. Renew. Sustain. Energy Rev. **41**, 658–684 (2015)
7. Radziemska, E.: The effect of temperature on the power drop in crystalline silicon solar cells, Renew. Energy **28**, 1–12 (2003)
8. Chandel, S.S., Agarwal, T.: Review of cooling techniques using phase change materials for enhancing efficiency of photovoltaic power systems. Renew. Sustain. Energy Rev. **73**, 1342–1351 (2017)
9. Preet, S.: Water and phase change material based photovoltaic thermal management systems: a review. Renew. Sustain. Energy Rev. **82**, 791–807 (2018)
10. Yadav, A., Barman, B., Kumar, V., Kardam, A., Narayanan, S.S., Verma, A., Madhwal, D., Shukla, P., Jain, V.K.: A review on thermophysical properties of nanoparticle-enhanced phase change materials for thermal energy storage. Recent Trends Mater. Devices 37–47 (2017)

11. Yadav, A., Verma, A., Jain, V.K., Bhatnagar, P.K., Kumar, V.: Enhanced thermal conductivity of acetamide based nanocomposites. IJITEE **8**(10), 4227–4331 (2019)
12. Yadav, A., Barman, B., Kumar, V., Kardam, A., Narayanan, S.S., Verma, A., Madhwal, D., Shukla, P., Jain, V.K.: Solar thermal charging properties of graphene oxide embedded myristic acid composites phase change material. AIP Conf. Proc. **1731**(1) (2016)
13. Yadav, A., Barman, B., Kardam, A., Narayanan, S.S., Verma, A., Jain, V.K.: Thermal properties of nano-graphite-embedded magnesium chloride hexahydrate phase change composites. Energy Environ. **28**(7), 651–660 (2017)
14. Yadav, A., Verma, A., Narayanan, S.S., Jain, V.K., Bhatnagar, P.K.: Carbon based phase change nanocomposites for solar energy storage. American Geophysical Union Fall Meeting, GC23D-1226 (2018)
15. Hasan, A., McCormack, S.J., Huang, M.J., Norton, B.: Evaluation of phase change materials for thermal regulation enhancement of building integrated photovoltaics. Sol. Energy **84**(9), 1601–1612 (2010)
16. CENTSYS 100 W solar panel. https://www.centsys.com.au/solar-accesories/
17. Yinping, Z., Yi, J.: A simple method, the-history method, of determining the heat of fusion, specific heat and thermal conductivity of phase-change materials. Meas. Sci. Technol. **10**(3), 201 (1999)
18. Hasan, A., Sayigh, A.A.: Some fatty acids as phase-change thermal energy storage materials. Renew. Energy **4**(1), 69–76 (1994)
19. Hamilton, R.L., Crosser, O.K.: Thermal conductivity of heterogeneous two-component systems. Ind. Eng. Chem. Fundam. **1**(3), 187–191 (1962)

Intelligent Moving Machine (IMM) Based on Battery for an Efficient Regenerative Braking System

Amit Yadav , **D. K. Chaturvedi** , **Ajay Kant** , **Garima Jain** ,
and Anil Kumar

1 Introduction

This paper discusses about electric vehicle technology and development a high gain performance during runtime and also increasing attention for having distinctive features as efficiency is high, low emission, pollution-free, cost-,effective technology [1]. In electric vehicle technology, the batteries are based on different types of chemical that has been used as the main source of energy storage system in many electric vehicle programs. These are leading technologies in the electric vehicle area. However, the lead–acid batteries have limited life cycle, and this is known for shortcomings, such as limited density of electrical energy, and also, market price is very high [2–4]. The electric capacitors those have double layer are known as supercapacitors and are high capacitance capacitors that suggest several exceptional features such that power density is high, battery life is long, and high-temperature operating range. The quality lead–acid batteries and supercapacitors are compared with the help of sun shape chart (Fig. 1) [5]. Although the supercapacitor provides better outcome in most of the situations, it cannot be used as the important energy store system since its energy density is comparatively down. Similarly, the technology of the supercapacitors is developed; they are not as consistent as the conventional batteries. Additional benefits of lead–acid batteries and supercapacitors can be used in an intelligent moving machine energy storage system [6]. There are different kinds of applications of IMM discussed in detail.

A. Yadav (✉) · D. K. Chaturvedi · A. Kant · G. Jain
Dayalbagh Educational Institute, Dayalbagh, Agra, India
e-mail: amitphd2@gmail.com

A. Kumar
Department of Mechanical, Production & Industrial and Automobile Engineering, Delhi
Technological University, Delhi, India

Fig. 1 Qualitative comparison of the lead–acid battery and supercapacitor
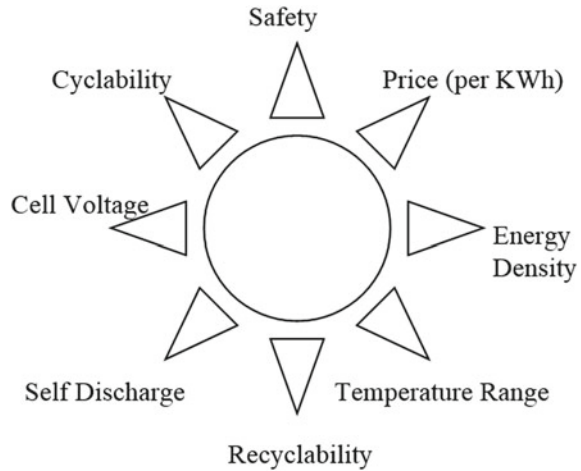
1. Supercapacitors have high power density that can be uitilized to effectively control the kinetic energy of the IMM.
2. Supercapacitor can support battery system when electrical energy demand is high, which not only prolongs the life cycle of battery but also changes the acceleration of IMM.
3. IMM drive range can be significantly increased for the regeneration braking energy which could be effectively stored [7].

During earlier innovation in electric vehicle technology, there are several techniques developed for automatic and smart vehicles. Here, the discussion for the efficient battery backup and the use of supercapacitors in development of e-vehicles to rise above the drawback of the batteries. One of the most research and development techniques in IMM is the battery and electronic devices [8], where the electrical circuit of battery pack is directly joint to the electronic driver circuit and motor. Thus, two topologies are used in individual energy storage systems, and a supportive power converter is needed for moving machine; they are generally costly. The paper discusses about the novel structure which is designed for desirable interface between the supercapacitor and battery which is proposed. The research on electrical energy storage is composed of a battery, buck converter, supercapacitor module and a diode. There are various operation modes of the proposed electrical intelligent moving machine discussed in detail. Moreover, for the proposed electrical storage system for IMM, a new regenerative braking system (RBS) is developed. RBS function performs during the braking process; using a suitable switching algorithm for the inverter, the DC link voltage is boosted. Hence, the diode modes of operation are forward biased, and the regeneration braking energy is directly harvested by the battery and the circuit module of capacitors without employing an additional converters.

The DC link is connected by the signal variations of cycle to pulse width modulation (PWM) in the inverter. Thus, when the conductor circuit module is approximately charged, the battery is realized as regenerative braking. In this method, the

IMM regenerative braking system efficiency is higher due to the removal of the utilized converters for this system performance [9]. Furthermore, an artificial neural network (ANN) is used with Simulink to complete braking energy force circulation. Meanwhile, a proportional-integrator (PI) controller is used to set the braking current to make braking torque which is kept constant.

2 Control Approach of Regenerative Braking

Control strategy of regenerative braking scheme is discussed in detail. The braking force distribution of braking energy in systematic way using ANN and PID controller is the foremost section of planned system arrangement, which is discussed in various sections as follows.

2.1 Control Algorithm for the IMM Based on ANN Technique

The idea of the planned control approach is discussed in Fig. 2. When the brake button is busy, in agreement with the slump quantity of the button, the stand in need of braking strength can be obtained during the operation of IMM. Depending on IMM conditions, such as speed (velocity) and status of the battery, secondary controllers like neural network and lookup slab are normally utilized to conclude the standards of the braking energy and involuntary braking force for the front wheels. Furthermore, in modern technology braking energy system, such as electronic braking energy system and corner brake energy, the braking force inequitably deals among dissimilar wheels of IMM to decrease the hazard of skid, rotating, and the unsteadiness. The helpful dynamics of such system cannot be simply handled by the mentioned controller.

Sigmoid function is chosen as the beginning function for the neurons in the output layer is:

Fig. 2 ANN controller for the proposed IMM
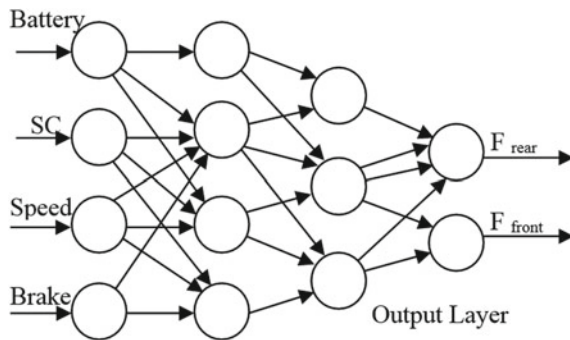
$$f(u) = 1/1 + e^{-u}/T \tag{1}$$

Similarly, linear transmit function is applied for the neurons in the output layer of the ANN.

The organization of planned multilayer close to network is shown in Fig. 2. The connections among the brake strength, the rear braking energy and the front braking energy could be considered uncomplicated by perfect allotment task using ANN. To generate the preparation dataset, a variety of simulations are approved which are absent in MATLAB/Simulink by applying diverse standards of state of charge for the battery and MOSFETs semiconductor module. IMM rate and brake power are recognized by preparation drive cycle. The selection of the drive cycle is significant for simulation of enough braking scenario. The braking scenario arises at unique IMM speed and diverse brake strength. The IMM is decelerated or blocked in specific reserve and instance resolute by the drive cycle; most regeneration energy is achieved; and charge state of battery and MOSFETs module remain with the safe limitations. The back which extends procedure with Levenberg–Marquardt process is come to teach the ANN. A clear condition to assess the performance of ANNs is the normalized root mean square error (NRMSE), which is the fault between predictable outcome and accurate outcome and can be written as follows:

$$\text{NRMSE} = \sqrt{\sum n H(n) - H'(n)} \bigg/ \sum n H'(n)2 \tag{2}$$

where $H(n)$ and $H'(n)$ are the predictable and objective principles of the output, correspondingly, and n is the number of statistics point.

3 Regenerative Braking Circuit

The regeneration braking circuit consists of a battery set and the capacitor reservoir which gives the power to the controller circuit of the IMM [7]. The battery type is lead–acid battery and made up of voltage of 12 Vs, and the ability of current rating is 7.5 Ah. A capacitor bank circuit of IMM is placed with the motor drive circuit which uses to supply the power. The MOSFET modules are linked in equal with the energy storing battery, so the whole capacitance energy of the battery will increase. The overall battery power is stored in the capacitor bank. The capacitor bank and battery are paired throughout the insulated gate bipolar junction transistor (IGBT) buck–boost converter. The buck–boost convertor is step-down converter and step-up converter. The deceleration of IMM than the buck operation takes place when IMM brakes. The boost operation is performed during the acceleration of IMM, i.e., when IMM moves to a faster rate from a lower rate. Here, this is acquired by pushing the consecutive velocity switch given in the circuit. Buck–boost convertors both of them can generate a limit of output voltages, ranging from much higher than the input
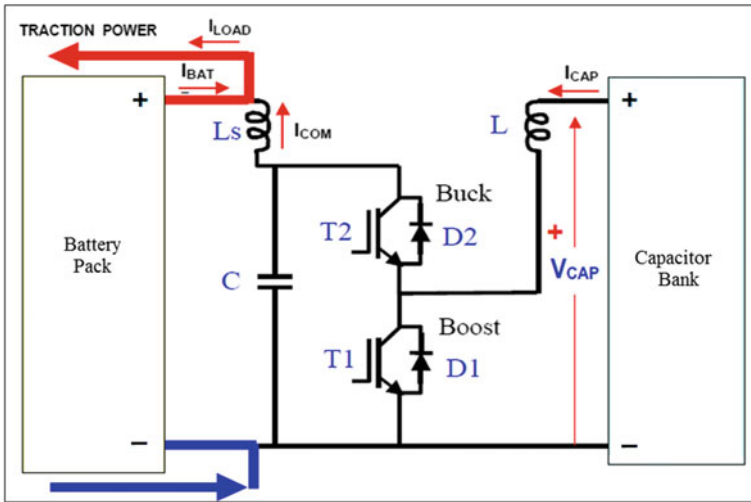
Fig. 3 Regeneration braking circuit of IMM

voltage, low to almost zero. The circuit of regenerative braking circuit is shown below in Fig. 3.

4 Simulation of Regenerative Braking System

Simulation of regenerative braking system circuit for IMM is done in Simulink/MATLAB-12 which is shown in Fig. 4. The variables of every system mechanism are located as described over. In the simulation of IMM, graph is shown on computer screen in Simulink scope for battery electrical energy, capacitor bank voltage, battery existing and PWM indication known to constrain insulated gate bipolar transistor. The output results are displayed for three sets of PWM signal which is specified to the IMM controller circuit [10]. IMM capacitor bank electrical energy goes on mounting through the buck operation (Fig. 5). IMM battery voltage is 12 volt spot through unimportant fluctuations. The existing as of battery elevation is strained toward the capacitor bank alone through the run instance of the pulsation set to the MOSFET module circuit is or else nil.

The inductor L starts storing power when the specified battery banks and MOSFET modules are fully charged or avoid transient behavior of regenerative braking.

This charge remainder in the capacitor bank and MOSFET module as it is awaiting the next boost process set and at that moment of the charge is transferred to the battery as described (Fig. 6).
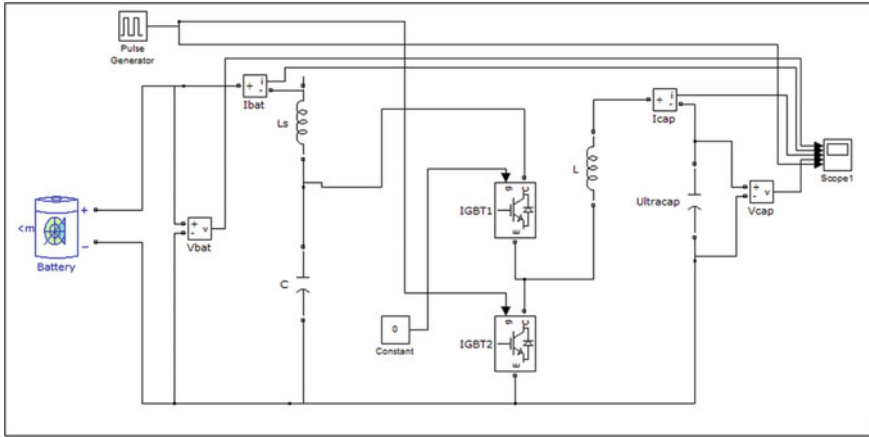
Fig. 4 Simulink module of regenerative braking system
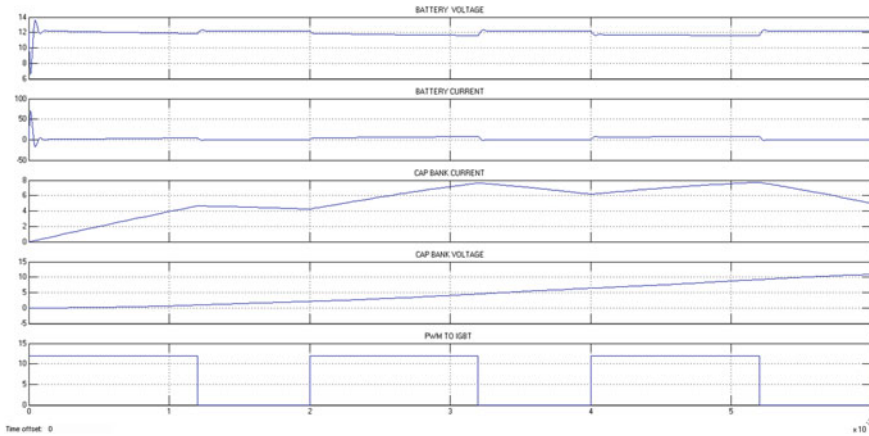
Fig. 5 Simulation results of buck operation

5 Conclusion

The regenerative braking system (RBS) track provisions and precedes the power reverse to the battery which would have been or else exhausted. The RBS is useful to generate electric power through LED. The buck–boost converter depends on signal starting the microcontroller and operates in actual instance so that the power can be stored at the precise instant of deceleration and can return support in the little second of speeding up. The capacitor reservoir also charges and discharges rapidly so that the power surge can be express and capable with no much thrashing. This makes a battery longer life as well as allows IMM to trek extra on a solitary battery charge,
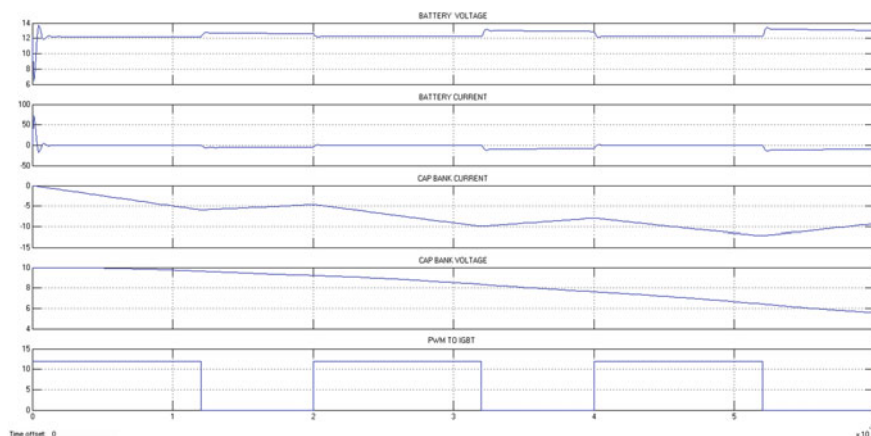
Fig. 6 Results of boost operation in Simulink

i.e., the mileage of IMM increases significantly. Regeneration all along with braking system makes IMM power well-organized as well as safer and easier to make use of and prove to be an imperative part in the suitable implementation of IMM.

References

1. Awad, F., Shamroukh, R.: Electric vehicle detection by intelligent machine urban search and rescue using image processing and neural networks. Int. J. Intell. Sci. **4**, 39–53 (2014)
2. Gold, J., Koren, K.: Hybrid vehicle with obstacle avoidance with ultrasonic sensors. IEEE J. Robot. Autom. RA **4**(2), 213–218 (2018)
3. Hook, A., Koren, K.: The vector field histogram-fast obstacle avoidance for electric vehicle. IEEE Trans. Robot. Autom. 501–518 (2011)
4. Harrol, J., Latombe, J.C.: Hybrid machine motion planning: a distributed representation approach. Int. J. Robot. Res. **10**(6), 628–649 (2018)
5. Mongin, A.K., Chatterji, B.N., Ray, A.K.: Design of a real-time tracking system for fast-moving objects with solar EV. IETE J. Res. **43**, 359–369 (2017)
6. Urzelai, J., Ezkerra, J.M.: Fuzzy controller for wall-following with a non-holonomous mobile robot. Fuzzy-IEEE/IFES, BARCELONA, July 1997
7. Yang, Y.P., Liu, L., Wang, T.J., Kuo, K.C., Hsu, P.E.: An electric gearshift with ultracapacitors for the power train of an electric vehicle with a directly driven wheel motor. IEEE Trans. Veh. Technol. **56**(5), 2421–2431 (2007)
8. Prassler, E., Bank, D., Kluge, B., Hagek, H.: Key technologies in robot assistants: motion co-ordination between a human and a mobile robot. In: Proceedings of 30th International Systems on Robotics, 2001, pp. 410–415, Mar 2001
9. Yadav, A., Chaturvedi, D.K.: Design and development of safe intelligent moving machine. Int. J. Electr. Mach. Drives (IJEMD) **2**, 16–21 (2016)
10. Zhou, H., Sakane, S.: Sensor planning for mobile EV localization based of probalistic inference using bayesian network. In: Proceedings of the 4th IEEE International Symposium on Assembly and Task Planning, pp. 7–12, May 2001

11. Nick, D., Forsyth, A.: Finding and tracking people from the autonous electric machine. In: Proceeding of Computer Vision and Pattern Recognition (CVPR), Madison Wisconnin, June 2019
12. Nian, X., Peng, F., Zhang, H.: Regenerative braking system of electric vehicle driven by brushless DC motor. IEEE Trans. Ind. Electron. **61**(10), 5798–5808 (2014)
13. Schulz, D., Burgard, W., Fox, D.: People tracking with mobile robots using sample-based joint probabilistic data association filters. Int. J. Robot. Res. 99–116 (2003)
14. Yadav, A., Chaturvedi, D.K.: Mathematical model for ground electric vehicle using Matlab-Simulink. Int. J. Autom. Control Syst. (IJACS) **2**, 26–34 (2016)
15. Yadav, A., Yadav, N., Chaturvedi, D.K.: An intelligent electric vehicle (IEV) using LabVIEW. In: IEEE 2nd International Conference on Communication, Control and Intelligent Systems (CCIS) vol. 2, ISSN 978-5090 Nov 2016
16. Yadav, A., Chaturvedi, D.K.: An autonomous ground electric vehicle using LabVIEW. In: National Systems Conference on Super Intelligent Man and Machines sponsored by IEEE (NSC-17), DEI, Agra, Dec 2017

Evaluating the Engine Emission Outcomes from a CRDI Engine Operated with Low Viscous Bio-oil Blends Under the Influence of Diethyl Ether

Mebin Samuel Panithasan , **Manimaran Malairajan** ,
Mathivanan Balusamy , **and Gnanamoorthi Venkadesan**

1 Introduction

The development activities across the world and the population increase lead to the increase in transportation. This also increases the air pollution considerably and for all these energy needs everyone depends upon the crude oil only. As a measure to reduce the increasing air pollution and to reduce the dependence upon the crude oil resources, an alternate energy source is needed [1]. If the alternate energy is made within the country itself, then it will reduce the dependency on other countries for energy needs [2]. This research paper deals to find an alternate energy source for diesel engines. As in countries like India, diesel powered automobiles are widely used due to their higher torque and efficiency characteristics [3].

When it comes to finding an alternate source for diesel engines that can be produced within the country itself, alcohols and vegetable oils comes immediately into consideration. Due to its various advantages, bio-oil is considered for the alternative fuel [4]. But the oil obtained from the vegetation sources normally has very high viscosity [5] and it is subjected to transesterification process to reduce its viscosity [6]. This is a time and cost-consuming process [7]. As a step to eliminate this process, the production of lower viscosity oils was analysed. The search for a lower viscosity oil helped in identifying the oil, which is obtained from lemon rinds which are considered as a waste in day to day usage. This lemon peel oil attracts with its lower

M. S. Panithasan (✉)
Madras Institute of Technology, Chennai, India
e-mail: mebin@mitindia.edu

M. Malairajan
K. Ramakrishnan College of Engineering, Trichy, India

M. Balusamy
Srinivasan Polytechnic College, Perambalur, Tamil Nadu, India

G. Venkadesan
University College of Engineering Villupuram, Villupuram, India

viscosity level and higher calorific values [8]. This can be directly used in the engine either solely or by blending with diesel fuel.

Even though lemon peel oil possess lots of advantageous factors, there is one major setback in terms of a very low cetane index value [9]. Since cetane index is directly proportional to the combustion quality in a diesel engine, reduction in the cetane value reduces the combustion quality of the fuel by prolonging the ignition start timing. As a measure to reduce this ignition delay period, researchers have been using different types of cetane improver additives [10]. Naptha, Xylene, di-tert-butyl, peroxide, ethylbenzene, 2-ethylhexlynitrate (2-EHN) [11], bio-ethanol [12] were few of the cetane improver additives being used for the reduction of ignition delay in the engine. Due to the oxygen availability, easy availability, lower cost and due to the absence of nitrogen atom diethyl ether was used as an additive as the measure to improve the combustion quality and thereby reduce the ignition delay period [13].

This research work portrays the usage of LPO mixed with diesel at 50% by vol. Further, diethyl ether is added at 5%. 10% and 15% by vol. with the 50% blend of LPO. Addition of diethyl ether with lemon peel oil, at these combinations to improve the performance and emission outcomes were not tried before. These blends are then experimentally analysed in a single cylinder CRDI engine for various loading values of 0, 25, 50, 75 and 100% and are compared with diesel fuel for performance (BSFC, BTE) and emission (smoke, CO, HC, CO and NO_x) results to find the influence of the low viscous lemon peel oil and diethyl ether.

2 Materials and Methodology

2.1 Low Viscous Biofuel—LPO

Lemon peel oil was procured by the process called of steam distillation. This process uses a steam chamber, condensation unit and a distillation chamber as shown in Fig. 1. The steam produced in the first chamber enters the second chamber, where all the lemon peels were kept over a perforated plate. On a constant exposure to the steam, the volatile oil molecules evaporate from the lemon peels and pass on to the next condensation chamber. The condensation chamber has water jackets which circulates cold water over the pipes conducting the vapour molecules. Due to this, the vapour molecules of water and oil condenses back into liquid form and are collected in the distillation chamber. The distillation chamber separates the liquids by its density differences. Finally, the low viscous biofuel is collected from the distillation chamber. Table 1 shows the values of the obtained LPO.
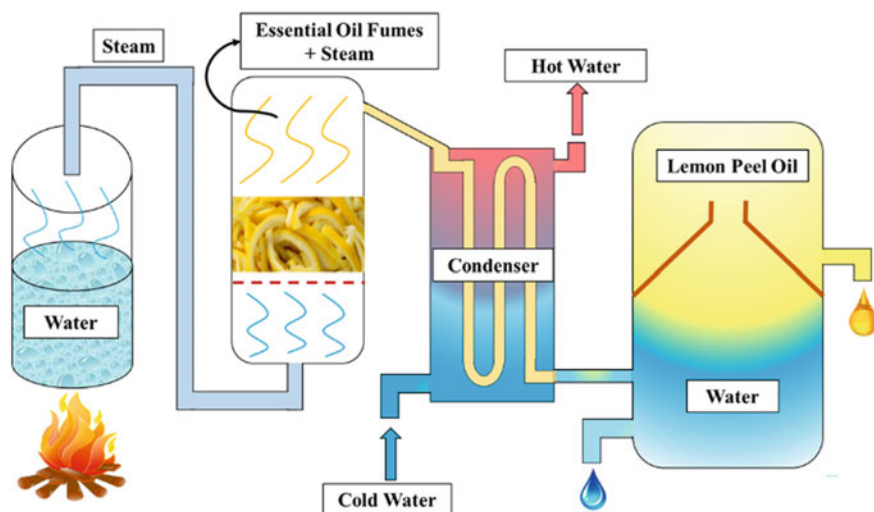
Fig. 1 Steam distillation process unit

Table 1 LPO fuel property

S. No.	Property	Unit	Diesel	Lemon peel oil
1	Density	kg/m^3	822	840
2	Calorific value	kJ/kg	43,200	41,200
3	Cetane index	–	52	15
4	Kinematic viscosity	mm^2/s	3.6	1.14
5	Flashpoint	°C	63	53
6	Fire point	°C	75	64
7	Boiling point	°C	350	174

2.2 Experimental Setup

A single cylinder water-cooled engine is used in the present study. The engine is equipped with a CRDI unit setup. It is maintained at a constant 1500 rpm speed and the fuel can be injected up to a maximum pressure of 600 bar. Exhaust emissions HC, CO and NO$_x$ were quantified with the help of a gas analyser from the make off AVL measurement systems. Similarly, the smoke opacity is estimated with the help of a smoke emission analyser made from AVL systems. All the technical specifications of the equipment used were specified in Table 2 and a schematic view is shown in Fig. 2. As we know that the variation of load values is much important, an eddy current type dynamometer was coupled with the engine to carry out the desired loading values. The specification of emission measurement equipments are given in Table 3.

Table 2 Experimental engine—technical specifications

Type	Compression ignition engine
No. of cylinder	One
Make	Kirloskar
Cooling type	Water cooled
Rated speed (rpm)	1500
Cubic capacity (cc)	661
Compression ratio	17.5:1
Injection type	Common rail direct injection
Rated power (kW)	3.5
Stroke (mm)	110
Bore (mm)	87.5
Maximum injection pressure (bar)	600
Piston bowl shape	Hemispherical type
Injection timing (°)	23° BTDC
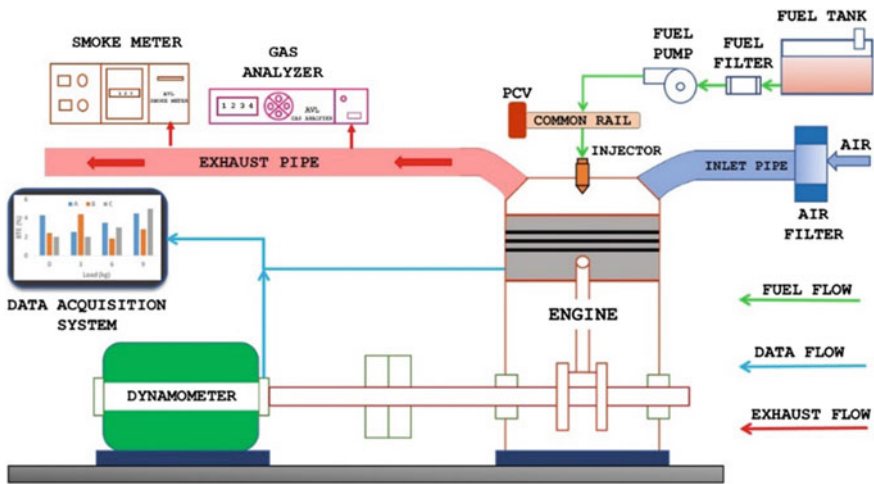
Fig. 2 Experimental setup—diagrammatic representation

Table 3 Specification of exhaust measuring instruments

Emission type	Apparatus	Range	Resolution
NO$_x$	AVL Digas 444 N five-gas analyser	0–5000 ppm	1 ppm
HC		0–20,000 ppm	1 ppm
CO		0–15%	0.01%
Smoke	AVL 437 C smoke metre	0–100%	1%

2.3 Methodology

In this study, totally, five different fuel blends were analysed, namely diesel, L50, L50D5, L50D10, L50D15. The composition of these blends is given as:

Diesel = 100% diesel

L50 = 50% diesel + 50% lemon peel oil

L50D5 = 95% L50 + 5% diethyl ether

L50D10 = 90% L50 + 10% diethyl ether

L50D15 = 85% L50 + 15% diethyl ether.

These blends were properly measured and mixed using a mechanical stirrer. The above blends are analysed in a CRDI engine by changing the load values (0, 25, 50, 75 and 100%) at a constant speed of 1500 rpm. Initially, the CRDI engine is made to run with the conventional fuel for a period of 15 min, after the engine reaches its steady-state operating condition, all the values are recorded. Also, after each blend change, the engine is operated with the corresponding fuel blend for the period of 10 min before the corresponding values are recorded.

2.4 Uncertainty Analysis

Errors occur due to the change in environmental conditions, observations, calibrations, equipment age, wear and tear of the instruments, human errors, etc. These errors are termed as uncertainty errors. To reduce these errors, the uncertainty of each parameter was calculated and neatly presented as given in Table 4. Moreover, the total uncertainty error value was calculated using Eq. (1) [14].

Table 4 Parameter uncertainties

S. No.	Uncertainty parameter	Uncertainty values (%)
1	Pressure	±1
2	Load	±0.3
3	Crank angle	±0.2
4	Air flow rate	±0.4
5	Fuel flow rate	±0.6
6	Speed	±0.1
7	Brake specific fuel consumption	±0.6
8	Hydrocarbon	±0.5
9	Brake thermal efficiency	±0.5
10	Smoke	±1
11	Carbon monoxide	±0.01
12	Oxides of nitrogen	±1.2

$$
\begin{aligned}
&= \sqrt{\left(U_{\text{BTE}}^2 + U_{\text{BSFC}}^2 + U_{\text{CO}}^2 + U_{\text{HC}}^2 + U_{\text{NO}_x}^2 + U_{\text{Smoke}}^2 + U_{\text{Load}}^2 + U_{\text{Speed}}^2 + U_{\text{AFF}}^2 + U_{\text{FFR}}^2\right)} \\
&= \sqrt{\left(0.5^2 + 0.6^2 + 0.01^2 + 0.5^2 + 1.2^2 + 1^2 + 0.3^2 + 0.1^2 + 0.4^2 + 0.6^2\right)} \\
&= \sqrt{3.92} \\
&= \pm 1.97\%
\end{aligned}
\tag{1}
$$

3 Results and Discussion

The emissions along with the performance of the engine for all the blends under study were explained in this section.

3.1 Emission Outcomes

The influence of the fuel blends used over the engine exhaust pollutants, namely smoke, CO, HC and NO_x were detailed below.

Hydrocarbon (HC). Hydrocarbon emission is a combined mixture of the fuel molecules that escapes the combustion either partially or completely and reaches the exhaust gaseous stream. The major reason for the increased level of HC emission of diesel fuel was owing to the development of many rich zones (higher concentration of fuel than the stoichiometric ratio) created because of the irregular mixing of fuel and air [8]. Figure 3 demonstrates HC emission changes for with the increase in BP. All the blends with lemon peel oil produce lesser amount of HC may be due to the lower viscosity of biofuel and the oxygen molecules in the biofuel. Also, the higher injection pressure helps in finer atomisation of fuel molecules and helps in reducing the HC emission [14]. Addition of Diethyl ether promotes and enhances the combustion characters, leading to better burning of fuel, which increases the reduction of HC. L50D10 reduces 30.26% of HC emission than conventional diesel fuel in its maximum loading value, but increasing the DEE beyond 10% increases HC by 7.5%, this may be due to the hindrance caused to the combustion process due to the increased heat of evaporation property of DEE.

Smoke Emission. It is generally the mixture of various elements such as vapours of oil, fuel and ash, but the majority part consists of soot particles [15]. Figure 4 shows the smoke opacity percentage of the blends for different values of BP is demonstrated. The oxygenated biofuel reduces the smoke opacity percentage. Improved oxygen content and lower viscosity help in finely atomising the fuel molecules, thereby reducing the amount of soot production [16]. L50 reduces smoke by 11.7% and with the addition of diethyl ether further helps in the reduction of smoke. The lowest value was seen for the L50D10 (27.05% reduction than conventional diesel at the
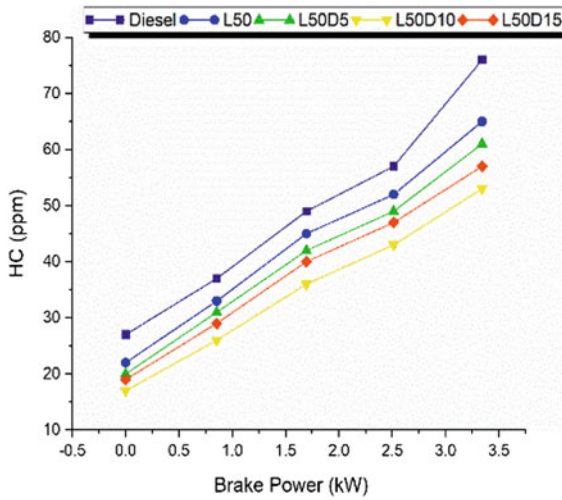
Fig. 3 Changes in HC emission versus BP
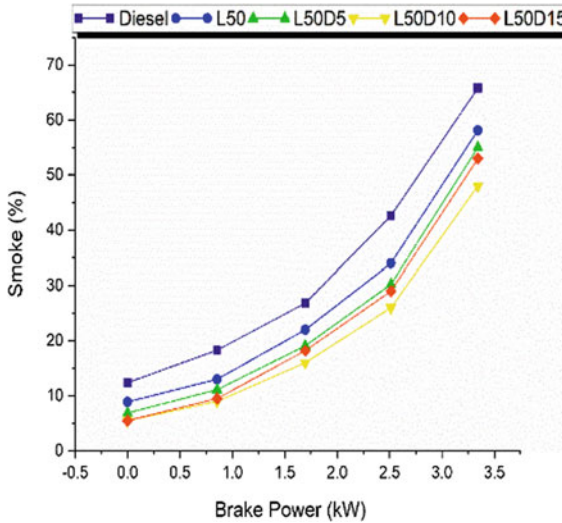
Fig. 4 Changes in smoke opacity versus BP

maximum loading value). But at higher values of DEE, due to the higher latent heat property of the additive, the smoke emission is increased by 8.63% compared to L50D10.

Oxides of Nitrogen (NO$_x$). N$_2$ present in the atmospheric air (or the fuel itself) combines with the O$_2$ (both from the air and fuel) contributes to the oxides of nitrogen emission in the exhaust. This combination requires more energy and hence it is
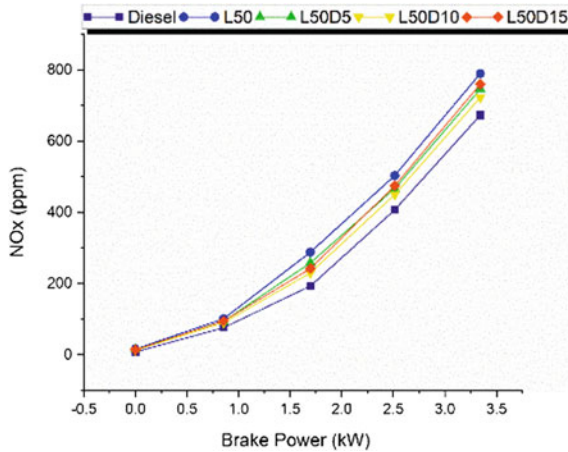
Fig. 5 Changes in NO_x emission versus BP

possible at an elevated temperature only [17]. In Fig. 5, the changes in NO_x emission of all the blends for different BP values are illustrated. It is seen clearly that NO_x emission increases for all biofuel blends than conventional diesel at all loading values. The main reason for this is the lower cetane value of the biofuel. Lower the cetane value, higher the ignition delay period. Higher ignition delay paves way for more fuel accumulation and leads to higher peak temperature within the cylinder [18]. Hence, L50 blends show the highest NO_x emission of 17.38% higher than diesel at maximum load value. Mixing of DEE helps in increasing the cetane value and reduces its ignition delay, thereby reducing the NO_x production also. L50D10 produces 7.4% higher NO_x (the lowest of all the biofuel blends). Due to higher latent heat property, adding more than 10% of DEE increases the delay time and hence leads to higher NO_x in the exhaust (5.11% higher than L50D10 at maximum load).

Carbon monoxide (CO). Incomplete oxidation of carbon molecules leads to the formation of CO emission. This incomplete process may be due to the lesser availability of oxygen molecules or time required for the transformation of carbon molecules into the carbon dioxide molecule. Figure 6 shows the level of CO present in the exhaust of all the test blends for various brake power values. CO concentration in the exhaust gases for all the biofuel mixtures is lower than conventional diesel. This may be mainly due to the increased O_2 content of the biofuel [19]. Thus, 18.75% of CO is reduced for L50 blend than the conventional diesel. Adding DEE further promotes the combustion process and reduces the CO concentration in the exhaust. Thus, the lowest CO emission value is recorded for L50D10 (37.5% lesser than conventional diesel at maximum load). Increasing DEE concentration to 15% increases CO emission due to the higher latent heat value of DEE.
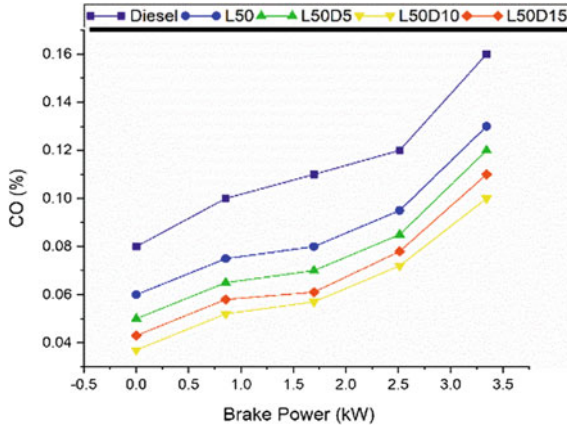
Fig. 6 Changes in CO emission versus BP

3.2 Performance Outcomes

Performance parameters are evaluated by the outcomes of BSFC and BTE values.

Brake Specific Fuel Consumption (BSFC). The quantity of fuel needed for producing 1 kW power for an hour defines the BSFC value of the engine. In Fig. 7, the changes in BSFC values for different blends for various levels of BP are displayed. It is clearly seen that diesel fuel shows the least level of BSFC. This is mainly due to the inability of the lemon peel biofuel to convert all its potential into useful work.
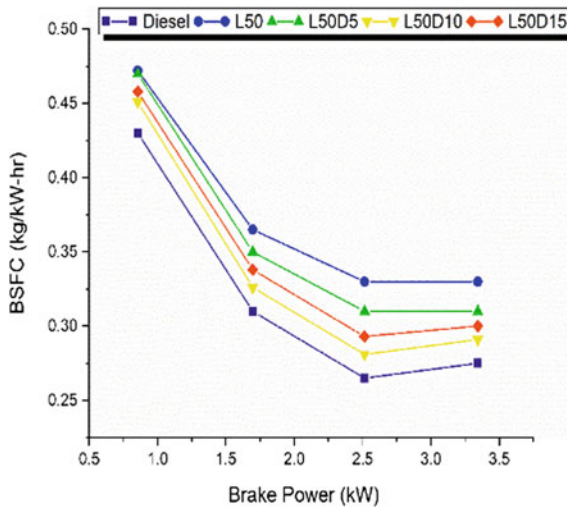
Fig. 7 Changes in BSFC versus BP
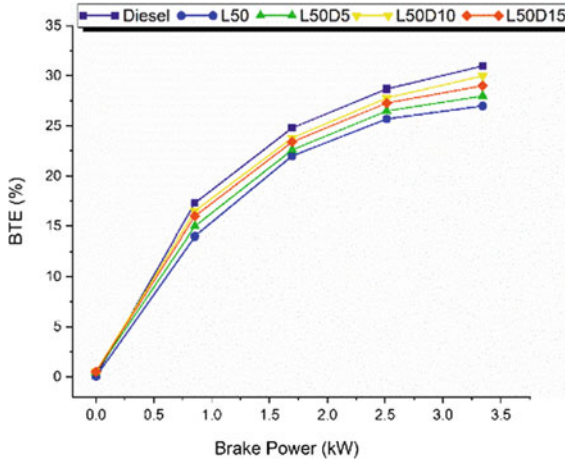
Fig. 8 Changes in BTE versus BP

The lower cetane value index may also be a reason for this. The addition of diethyl ether promotes the combustion process and reduces the fuel consumption value. These results are on par with similar works done by Yadav et al. for the same speed condition [20]. L50D10 shows 5.81% higher fuel consumption, which is the closest to diesel at maximum load value. At 15% DEE concentration, the calorific value of the fuel blend will be affected; due to this reduction in calorific value, more fuel is required for producing the same power output. Hence, BSFC is increased for L50D15 blend.

Brake Thermal Efficiency (BTE). The main property in the performance outcomes for the consideration of a fuel blend is the BTE. This is the ratio of fuel energy supplied and amount converted into mechanical power. The changes in BTE for different values of BP are seen in Fig. 8. Diesel fuel exhibits the highest BTE value of all the blends in all load condition and with L50D10 following closely with only a small difference of about 3.22% (lesser than conventional diesel at maximum load). The low viscosity of fuel helps to increase the oxygen content [21] and in enhancing the combustion but the lower cetane index value resists proper combustion of fuel molecules [22]. This is the major reason for the lesser BTE value with the usage of lemon peel oil. The addition of DEE improves the combustion process to a certain extent, but cannot move closer than 3.22% mark of L50D10 blend. This is 11.36% higher than the L50 blend. Beyond the 10% addition of DEE due to latent heat property, the thermal efficiency value is reduced [13]. Hence, L50D15 blend shows a decrease of 6.3% at maximum load.

4   Conclusions

The experimental investigation describes the use of LPO mixed with diesel is able to reduce the engine emission outcomes and also the addition of diethyl ether further helps in reducing emission values. But without DEE, the thermal efficiency of the blend is affected significantly. Moreover, the addition of DEE more than 10% provides a negative effect which may be linked with its higher latent heat of vaporisation. This research work concludes as follows:

- The addition of 10% diethyl ether with the fuel blend L50 (50% lemon peel oil and 50% diesel) reduces 37.5, 30.2 and 27.05% for CO, HC and smoke emissions, respectively, compared with diesel fuel at its full load condition. The reason might be the addition of DEE enables quicker combustion and helps in better burning of fuel molecules.
- The BTE value is increased with the addition of 5% and 10% of DEE by about 4.6% and 11.36% compared with the L50 blend at full load condition. But for 15% of DEE, BTE is reduced by 3.2% than L50D10 blend, which may be mainly due to the increase in latent heat of vaporisation value of the additive.
- The fuel consumption value of L50D5 and L50D10 are reduced by 6.81% and 11.1% compared to L50 due to the improved combustion qualities of DEE. But L50D15 increases the BSFC value by 3.1% than L50D10, which might be due to the reduced calorific value of the blend.

Thus, this study concludes that the L50D10 as the best blend combination of this research study.

References

1. Yadav, A.K., Khan, M.E., Pal, A.: Kaner biodiesel production through hybrid reactor and its performance testing on a CI engine at different compression ratios. Egypt. J. Pet. **26**(2), 525–532 (2017). https://doi.org/10.1016/j.ejpe.2016.07.006
2. Capuano, D., Costa, M., Di Fraia, S., Massarotti, N., Vanoli, L.: Direct use of waste vegetable oil in internal combustion engines. Renew. Sustain. Energy Rev. **69**, 759–770 (2017). https://doi.org/10.1016/j.rser.2016.11.016
3. Tamilselvan, P., Nallusamy, N., Rajkumar, S.: A comprehensive review on performance, combustion and emission characteristics of biodiesel fuelled diesel engines. Renew. Sustain. Energy Rev. **79**, 1134–1159 (2017). https://doi.org/10.1016/j.rser.2017.05.176
4. Yadav, A.K., Khan, M.E., Pal, A.: Biodiesel production from oleander (Thevetia Peruviana) oil and its performance testing on a diesel engine. Korean J. Chem. Eng. **34**(2), 340–345 (2017). https://doi.org/10.1007/s11814-016-0270-8
5. Panithasan, M.S., Gopalakichenin, D., Venkadesan, G., Malairajan, M.: Evaluating the working characters of a diesel engine fueled with biodiesel blends added with rice husk Nano particles. Energy Sources, Part A: Recov. Util. Environ. Effects 1–19 (2020). https://doi.org/10.1080/15567036.2020.1767726
6. Silambarasan, R., Senthil, R., Samuel, P. M.: Effect of exhaust gas recirculation on NOx emission of a annona methyl ester operated diesel engine. J Chem. Pharm. Sci. **7**(5), 723–728 (2015).

7. Yadav, A.K., Vinay, Singh, B.: Optimization of biodiesel production from Annona squamosa seed oil using response surface methodology and its characterization. Energy Sources, Part A: Recov. Util. Environ. Effects **40**(9), 1051–1059 (2018). https://doi.org/10.1080/15567036.2018.1468516

8. Ashok, B., Raj, R.T.K., Nanthagopal, K., Krishnan, R., Subbarao, R.: Lemon peel oil–A novel renewable alternative energy source for diesel engine. Energy Convers. Manage. **139**, 110–121 (2017). https://doi.org/10.1016/j.enconman.2017.02.049

9. Gnanamoorthi, V., Purushothaman, P., Gurusamy, A., Devaradjane, G..: Prediction efficiency of artificial neural network for CRDI engine output parameters. Transp. Eng **3**, 100041 (2021). https://doi.org/10.1016/j.treng.2020.100041.

10. Gurusamy, A., Gnanamoorthi, V., Purushothaman, P., Samuel, P.M., Irfan, A.M.: Evaluation of microalgae biodiesel blend along with DTBP as an ignition enhancer on diesel engine attributes. In: Proceedings of ICDMC 2019, pp. 71–82. Springer, Singapore (2020). https://doi.org/10.1007/978-981-15-3631-1_8

11. Tsesmeli, C., Dodos, G.S., Zannikos, F.: Diesel fuel improvers and their effect on microbial stability of diesel/biodiesel blends (No. 2018-01-1751). SAE Technical Paper (2018). https://doi.org/10.4271/2018-01-1751

12. Khan, O., Yadav, A.K., Khan, M.E., Parvez, M.: Characterization of bioethanol obtained from Eichhornia Crassipes plant; its emission and performance analysis on CI engine. Energy Sources, Part A: Recov. Util. Environ. Effects 1–11 (2019). https://doi.org/10.1080/15567036.2019.1648600

13. Devaraj, J., Robinson, Y., Ganapathi, P.: Experimental investigation of performance, emission and combustion characteristics of waste plastic pyrolysis oil blended with diethyl ether used as fuel for diesel engine. Energy **85**, 304–309 (2015). https://doi.org/10.1016/j.energy.2015.03.075

14. Panithasan, M.S., Gopalakichenin, D., Venkadesan, G., Veeraraagavan, S.: Impact of rice husk nanoparticle on the performance and emission aspects of a diesel engine running on blends of pine oil-diesel. Environ. Sci. Pollut. Res. **26**(1), 282–291 (2019). https://doi.org/10.1007/s11356-018-3601-y

15. Samuel, P.M., Devaradjane, G., Gnanamoorthi, V.: Performance enhancement and emission reduction by using pine oil blends in a diesel engine influenced by 1, 4-dioxane. Int. J. Environ. Sci. Technol. **17**(3), 1783–1794 (2020). https://doi.org/10.1007/s13762-019-02455-8

16. Karthic, S.V., Kumar, M.S., Nataraj, G., Pradeep, P.: An assessment on injection pressure and timing to reduce emissions on diesel engine powered by renewable fuel. J. Clean. Prod. **255**, 120186 (2020). https://doi.org/10.1016/j.jclepro.2020.120186

17. Mebin Samuel, P., Devaradjane, G., Venkadesan, G., Josan, S.: Emission reduction of a diesel engine fueled with blends of biofuel under the influence of 1,4-Dioxane and rice husk nano particle. SAE Technical Paper 2019-28-2387, (2019). https://doi.org/10.4271/2019-28-2387

18. Gobalakichenin, D., Gnanamoorthi, V.: Assessing the combined outcome of rice husk nano additive and water injection method on the performance. Emiss. Combust. Characters Low Viscous Pine Oil Diesel Engine. SAE Technical Paper 2019-01-2604, (2019). https://doi.org/10.4271/2019-01-2604.

19. Heywood, J.B.: Internal Combustion Engine Fundamentals. Mcgraw-Hill, New York (1988)

20. Yadav, A.K., Dewangan, A., Mallick, A.: Effect of n-butanol and diethyl ether on performance and emission characteristics of a diesel engine fueled with diesel–Pongamia biodiesel blend. J. Energy Eng. **144**(6), 04018062 (2018). https://doi.org/10.1061/(ASCE)EY.1943-7897.0000570

21. Khan, I.A., Singh, S.K., Yadav, A.K., Ghosh, U., Sharma, D.: Enhancement in the performance of a diesel engine fuelled with Pongamia methyl ester and n-butanol as oxygenated additive. Int. J. Ambient Energy **40**(8), 842–846 (2019). https://doi.org/10.1080/01430750.2018.1437559

22. Panithasan, M.S.: Exploring the preparation and usage of low viscous pine oil and rice husk nano additives in a CRDI engine under the effect of water emulsion. SAE Technical Paper 2020-01-2128 (2020). https://doi.org/10.4271/2020-01-2128.

Recent Advancements in Solar-Assisted Thermoelectric Generator

Princy Mishra [ID]**, O. P. Singh** [ID]**, and A. K. Katiyar** [ID]

1 Introduction

There is an intense requirement of renewable energy resources due to depletion of conventional sources of energy such as oil, coal and natural gas. Moreover, the usage of fossil fuels is the major reason for the global warming [1]. Many researchers have proposed to harness renewable sources of energy. Solar energy is one of the feasible alternatives which can be utilized by solar thermal collectors and photovoltaics. At present, solar thermal systems are being extensively used in large-scale power plants, while photovoltaics are related to the generation of electricity [2]. To enhance the viability of solar thermal applications, thermoelectric generators can be used for cogeneration of heat and electrical energy. Thermoelectric generators can directly convert waste heat of solar thermal processes into electricity on the basis of Seebeck effect [3]. In this paper, a basic phenomenon of solar-assisted thermoelectric generator (STEG) has been presented. A review of increasing conversion efficiency using thermoelectric material of higher figure of merit is also presented. Besides this, recent advancements in concentration-based solar thermoelectric generator have been reviewed.

A solar thermoelectric generator (STEG) is solid-state device in which solar energy is first transformed to heat energy by means of optical and thermal concentrator and then heat is transformed into electrical energy form by means of thermoelectric modules on the basis of Seebeck effect. When the both side of thermoelectric modules exposed to different temperatures, a voltage difference is spawned between hot and cold sides of modules due to Seebeck effect. The temperature difference is caused by the thermal or optical concentration of solar energy at hot side and through heat sink having water or air cooling at the cold side. The schematic diagram of STEG

P. Mishra (✉) · O. P. Singh · A. K. Katiyar
Institute of Engineering and Technology, An Autonomous Constituent Institute of Dr. A.P.J. Abdul Kalam Technical University, Lucknow, U.P. 226021, India
e-mail: princess.mishra07@gmail.com

with thermal and optical concentration is shown in Figs. 1 and 2, respectively. The additional thermal energy can be utilized in other applications where thermal energy is required such as Rankine cycle, solar water heating and solar distillation. Thus, this system of solar-assisted thermoelectric generator can be employed in cogeneration of both thermal and electrical power. Based on the previous researches, there can be two types of concentrators at the hot side of STEG—(i) thermal concentrator and (ii) optical concentrator.

Recent advancements in STEGs are primarily focused on increasing conversion efficiency. The efficiency of thermoelectric (TE) devices can be calculated after finding the dimensionless figure of merit value (ZT). Mathematically, the figure of

Fig. 1 Schematic diagram of STEG with large thermal concentration
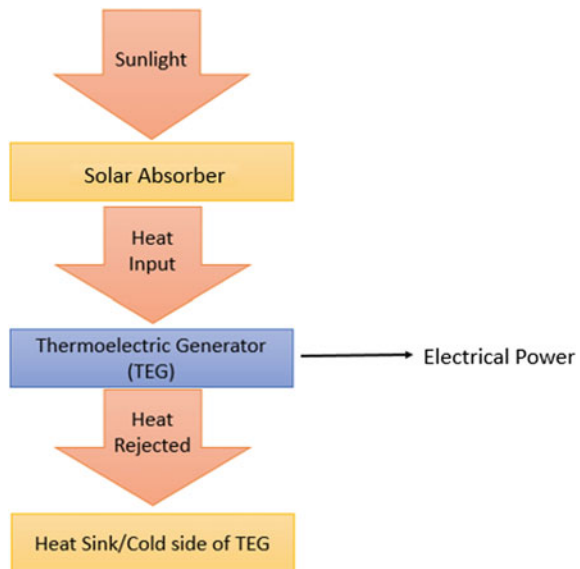
Fig. 2 Schematic diagram of STEG with large optical concentration
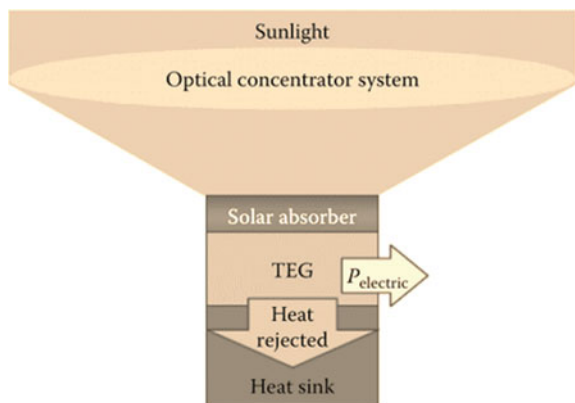
merit can be expressed as [4]:

$$ZT = \frac{\alpha^2 . \sigma}{k} T \tag{1}$$

where

Z Figure of merit of TE material in (K^{-1})
T Mean value of both side temperatures (in K)
α Seebeck coefficient
k Thermal conductivity
σ Electrical conductivity

The maximum theoretical efficiency of the TE devices can be determined by Eq. 2 [4]:

$$\eta_{TEG} = \frac{\Delta T}{T_h} \cdot \frac{\left(\sqrt{(1+ZT)}\right) - 1}{\left(\sqrt{(1+ZT)}\right) + \frac{T_c}{T_h}} \tag{2}$$

here,

T_h Temperature of hot side (K)
T_c Temperature of cold side (K)
ΔT Temperature difference between both sides $(T_h - T_c)$
ZT dimensionless figure of merit.

From the Eq. (2), it is clear that conversion efficiency is a function of figure of merit (ZT) and both side temperatures (T_h and T_c). Previous researches have shown that thermoelectric materials with ZT values around and over 2 yet to be developed but theoretically, a plot can be drawn between conversion efficiency 'η_{TEG}' and temperature difference (ΔT) for different figure of merit values as shown in Fig. 3. In this plot, hot side temperature is varied and cold side temperature is kept constant at

Fig. 3 Plot of theoretical conversion efficiency with temperature difference for various ZT values
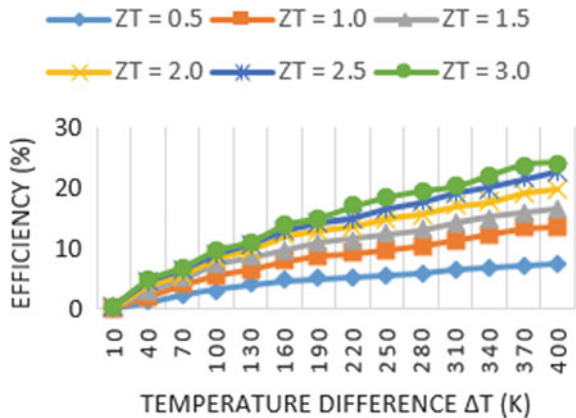
atmospheric temperature (300 K). From the diagram, it is clear that there is a need of thermoelectric material with higher value of ZT under same condition of temperature difference. In the next segment, various researches regarding the enhancement of ZT of thermoelectric materials have been discussed.

2 Enhancing Conversion Efficiency Through Improvement in Figure of Merit

In the last decades, many researchers have focused on augmentation of figure of merit (ZT) value for thermoelectric materials (TEMs) through various investigations. Amatya et al. (2010) proposed that the use of thermoelectric material (TEM) with higher ZT value can enable solar thermoelectric generator (STEG), a practicable alternative for generation of small power along heat generation in solar thermal system. In this work, the author presented thermodynamic analysis of combined system of thermoelectric generator (TEG) with cheap parabolic concentrator. The results depicted that the heat to electrical conversion efficiency of system was calculated to 4% with TEM of bismuth-telluride (Bi_2Te_3) having ZT value 0.64. Conversely, the Bi_2Te_3 module is not effective at higher temperature in the range of 800 K and above. Author also presented theoretical simulation with some TEMs of enhanced ZT such as ErAs: (InGaAs)1−x (InAlAs)x and p-type (AgSbTe)x (PbSnTe)1−x. A system efficiency of 5.64% was attained at 700 K temperature of hot side and ZT value 0.64 (Fig. 3) [5].

The figure of merit value of BiTe alloys can be enhanced by doping with Sb and Se to prepare these as p-type and n-type semiconductor, respectively. Yan et al. (2010) attained value of ZT in the range of 0.85–1.04 for n-type $Bi_2Te_{2.7}Se_{0.3}$ at 398 K [6]. Similarly, the figure of merit value was found around 1.8 at 316 K for p-type BiTe-based nano-composite doped with antimony (Sb) which was fabricated by a rapid processing method, as reported by Fan et al. (2010) [7]. The dependency of ZT on temperature ranges for various TE materials can be represented as shown in Fig. 4. It depicts that PbTe and SiGe-based alloys are more effective at higher temperature [8].

Biswas et al. (2012) proposed the use of PbTe alloys to overcome the problem of BiTe alloys in case of higher working temperature. The thermoelectric performance of PbTe-based alloys was augmented when heat-carriers phonons having long mean free paths were scattered by fine-tuning and regulating the mesoscale structure of nanostructured TEMs. The composites of PbTe-based alloys with Ag and Sb were also reported to unveil greater ZT values above 300 °C. The authors also demonstrated a p-type PbTe alloy having figure of merit value 2.2 at 642 °C which was mesostructured with precipitate processing and spark plasma sintering and nanostructure with SrTe alloy [9].

Rogl et al. (2010) proposed that thermoelectric material such as skutterudites can operate in the range of 300–800 K. These materials have virtue of scattering phonons

Fig. 4 ZT of various TE materials with respect to temperature [8]
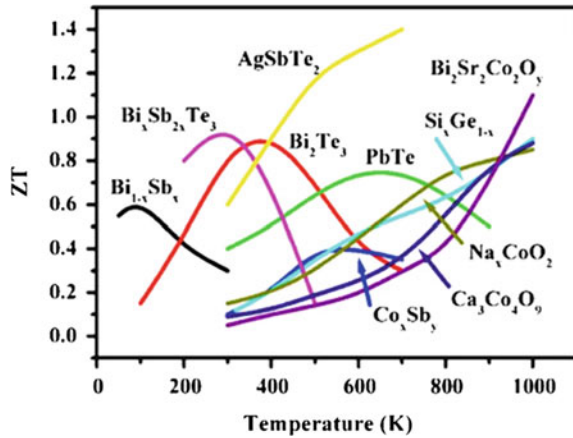
due to rattling effect. The authors reported that multi-filled nano-crystalline *p*-type didymium (Skutterudites) can have maximum value of figure of merit 1.3 at 800 K [10]. Similarly, Zhao et al. suggested a ZT value of 1.34 for *n*-type CoSb alloy at 853 K [11]. Suter et al. proposed to use SiGe-based alloys in very high temperature range such as in cavity have storage of solar heat [12].

3 Developments in Cogeneration Process Through Solar Collectors with TEG

Kraemer et al. (2011) presented a novel solar collector incorporated with thermoelectric modules to convert heat of sun directly into electricity. High concentration devices were used to increase hot side temperature of modules. The result depicted that conversion efficiency around 4.6% can be attained under the standard test condition with nanostructured TE modules and advanced solar absorber design. This efficiency was much higher than (about 7–8 times) the last best value of conversion efficiency for flat panel STEG [13].

Baranowski et al. (2012) presented a model of an optically concentrated STEG with the existing thermoelectric materials. This model could manage the theoretical efficiency of STEG up to 15.9% at the solar irradiation 0.1 MW/m^2 and 1000 °C temperature of hot side. The author suggested to use and develop the TE materials with ZT greater than or equals to 2. This enhancement in the performance of TEMs would possibly make STEG a viable option with concentration solar power (CSP) plants [14].

Olsen et al. (2014) offered a prototype of STEG with necessary optical and thermoelectric devices such as solar absorber, TEG and heat transfer system (Fig. 5). In this work, the sunlight from high flux solar furnace was concentrated to thermal

1. Concentrated sunlight from HFSF
Water-cooled quartz window

2. Thermal/optical cavity

Solar selective absorber

3. TEG (JPL)
Insulation
TEG (Bi₂Te₃)
4. Water-cooled stage

5. Feed-throughs for stage
control, electronics, cooling
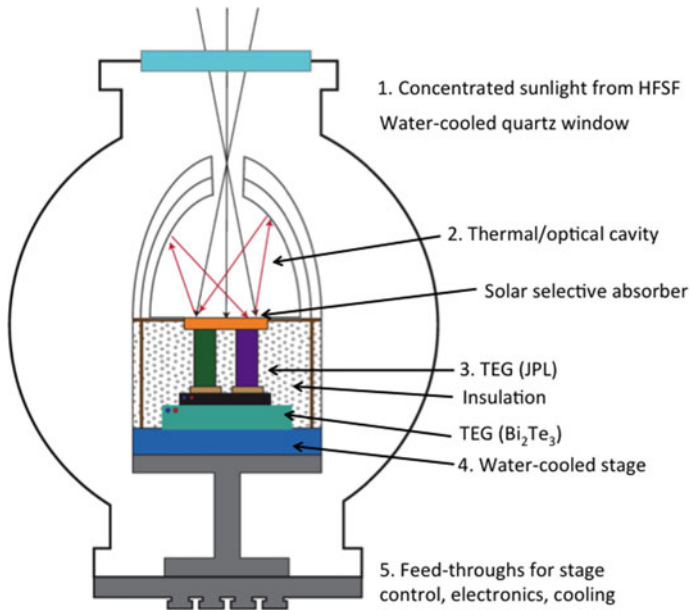
Fig. 5 Setup of STEG used by Olsen et al. [15]

cavity by means of optical devices such as lenses and solar selective absorber material was placed at high temperature side of TEG and water cooling was provided at the low temperature side of TEG. Authors conducted this experiment with the purpose of achieving approximately 15% efficiency, but due to limitation of figure of merit value of TE materials, they could achieve conversion efficiency around 5% only [15].

Nia et al. (2014) presented a cogeneration system of generating electrical and thermal energy with the help of Fresnel lens and thermoelectric modules. In this system, thermoelectric modules were placed between two reservoirs, in which upper reservoir has oil in it and lower reservoir has water. The oil was heated by concentrated solar irradiation through Fresnel lens and the other side of TE modules was cooled by water flow. This cogeneration system attained thermal efficiency 51.3% and electrical efficiency 3.2% at solar intensity of 705.9 W/m² [16].

Chao Li et al. (2014) discussed the impact of atmospheric factors on the performance of cogeneration system of TEG and parabolic trough collectors (PTC). In this setup, thermoelectric modules were placed at the focal line of the PTC and the other side of modules comprises of heat sink. The simulation results illustrated that the conversion efficiency of the combined TEG and PTC system is proportional to the amount of solar irradiation. But the increment in atmospheric temperature and wind velocity has a negative impact on conversion efficiency. A substantial increase from 1.25% to 5.68% in electrical efficiency was reported when solar intensity was varied

from around 80 to 1200 W/m^2 at constant atmospheric temperature 25 °C and wind velocity 2.5 m/s [17].

Dehghan et al. (2015) presented thermodynamic analysis of solar still incorporated with thermoelectric modules at the upper surface. The efficiency of solar still was enhanced due to enlarging temperature difference between condensing and evaporating sections. The results showed that the use of thermoelectric devices with solar still enhance its productivity and the amount of freshwater produced was 2.4 L/m^2/day with mean value of energy efficiency as 19.8% [18].

Zhu et al. (2015) designed a thin film STEG on the basis of simulation using finite element method. In this analysis, heat transfer through legs of thermoelectric modules was controlled and the heat losses were reduced. Sufficient temperature difference was maintained across TEG by reducing the temperature in the middle area of TEG legs via use of thermal conductive layer [19].

Liu et al. (2016) described a mathematical model to calculate the conversion efficiency of flat plate STEG in the space applications. The investigations showed that the conversion efficiency is significantly dependent on the length of leg geometry of modules and concentration ratio. In the Earth's trajectory, conversion efficiency could extend up to 5.5% for BiTe-based alloy while it was 5.8% and 4.7% for PbTe-based alloy in the trajectories of Mercury and Venus, respectively [20].

Guiqiang Li et al. (2016) presented a mathematical model of concentration-based STEG with the micro-passages heat pipe arrangement. The investigations depicted that the performance of this combined system is greater than the STEG system with similar area of the selective absorbing layer [21].

Kraemer et al. (2016) presented a STEG with improved performance attained by the combination of optical concentration through lenses and thermal collector of steel with copper heat spreader at the hot side of TEG. The TE materials employed in this work were skutterudite materials and doped BiTe-based alloy having figure of merits equals to 1.02. The electrical efficiency of STEG was calculated 9.60% at concentration ratio of 211 and 550 K temperature difference across TEG. The efficiency was estimated by 7.40% after consideration of optical concentration losses [22].

Kim et al. (2016) demonstrated a refraction-assisted STEG on account of phase change materials (PCMs). In this system (Fig. 6), the conversion of solid to liquid phase of PCM caused variations in the refractive index and transmittance. Authors described that the change of refractive index enabled twin focusing of the solar radiation by means of optical system and liquid PCM lens both. The PCM were helpful in storage of heat in daytime and vice versa. The investigations showed that conversion efficiencies were 60–86% higher than previously developed STEG. Moreover, the electrical energy can also be steadily generated in absence of solar energy by means of optical properties of PCMs [23].

Shen et al. (2017) offered a STEG system with cavity receiver and Fresnel lenses. In this work, various parameters including the performance of the system were analyzed by finite element method. The effects of various atmospheric factors were also discussed by the authors. The conversion efficiency reached up to 3.29% in this system, as discussed in the results [24].
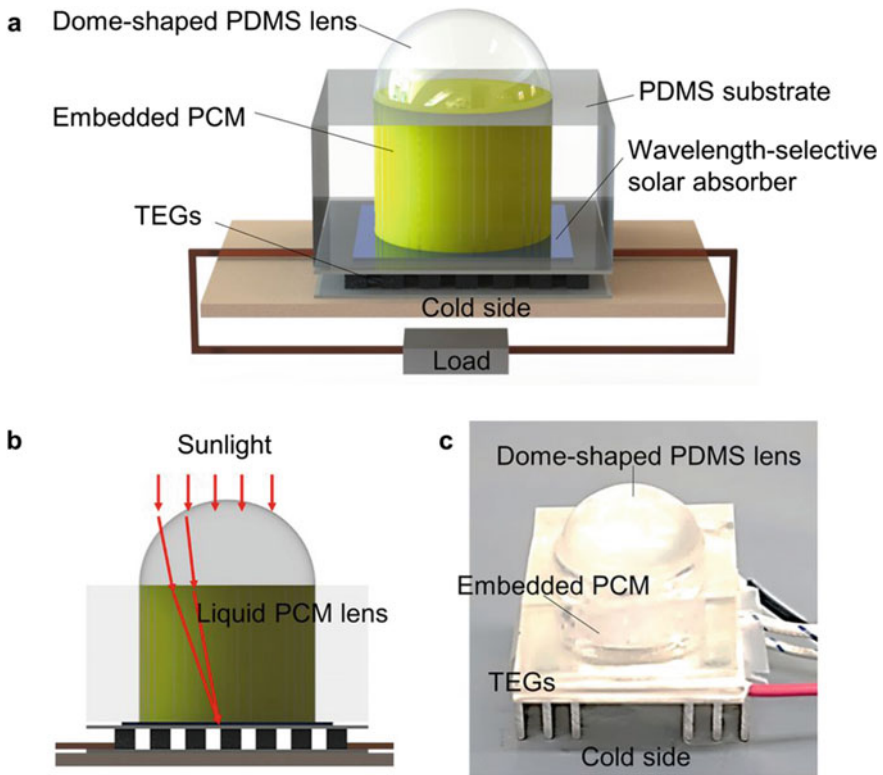
Fig. 6 Refraction-assisted STEG by Kim et al. [23]

Banakar et al. (2017) presented a combined heat and power system using TEGs and Fresnel lens. One side of TEG was heated by concentrated solar radiation by means of Fresnel lens and other side of TEG was cooled by water circulation using two configurations. In the first configuration, a pump was used to circulate water through heat pipe adjacent to the cold side, and in the second configuration, passive cooling was done using thermosiphon. The experimental analysis depicted that thermal and electrical power produced in the cogeneration system was 3.8 kW/m^2 and 70 W/m^2, respectively, with the passive technique. The combined system efficiency was 18.4% and 33.9% in case of natural and forced convective cooling, respectively [25] (Fig. 7).

Rad et al. (2018) presented the experimental validation to simulate STEG model under different ratios of diffused to direct radiations. At the ZT value 1.5 of thermoelectric material, maximum efficiency of 7.7% was noted for STEG. The results depicted that the proposed model can generate 70% of the total energy produced by parabolic trough systems at the location of greater diffused radiation [26].

Nimr et al. (2018) presented a combined system of thermoelectric generators with solar collector. In this work, two concentric cylinders were used. Water was stored in the space between inner and outer cylinder and TEGs were installed at inner cylinder.
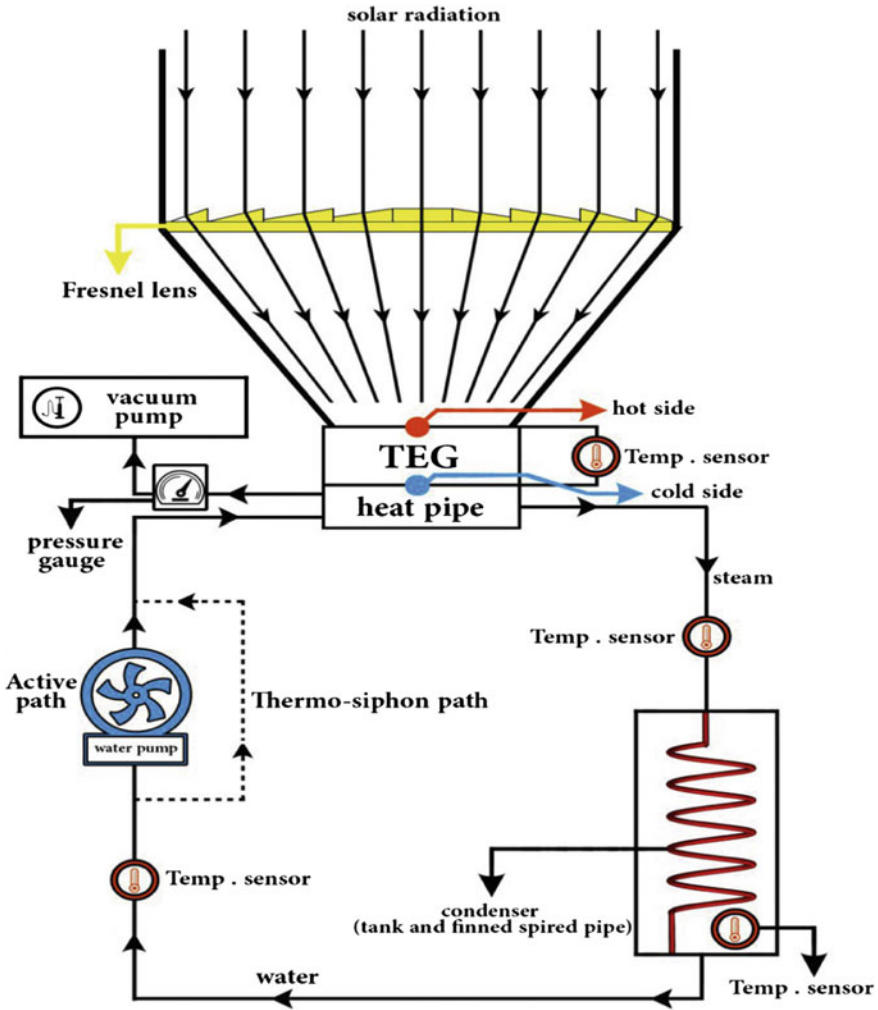
Fig. 7 Schematic illustration of combined STEG with active and passive cooling [25]

The hot side of TEG was exposed to internal cavity which was heated by reflected solar radiations from two mirrors installed, and the other side was cooled by water flow between two concentric cylinders. The analysis depicted that the combined system efficiency is around 80% at flow rate of 0.015 kg/s and intensity of solar irradiation greater than 800 W/m^2. Author also discussed that the combined system efficiency is mostly influenced by the solar irradiation on the basis of sensitivity analysis [27] (Fig. 8).

On the basis of literature review, a solar-assisted thermoelectric generator is proposed with Fresnel lens as optical concentrator and skutterudite-Bi$_2$Te$_3$ doped
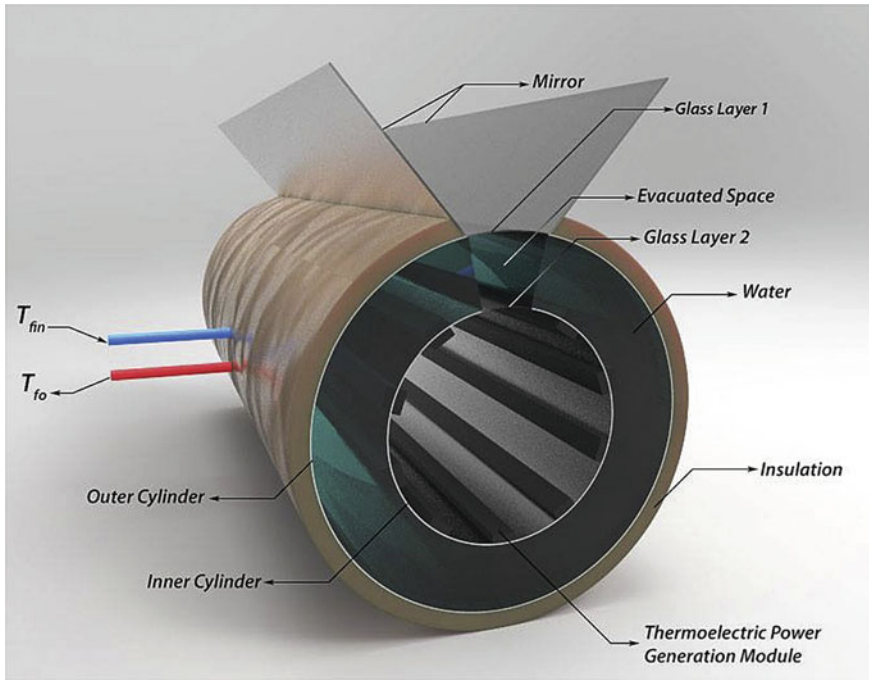
Fig. 8 Innovative solar thermal collector with cavity [27]

thermoelectric materials. These types of doped TE materials have capacity to withstand the high temperature at the hot side of TEG and the figure of merit value is also higher. The schematic diagram of the proposed model is shown in Fig. 9. The theoretical efficiency can be determined by the values of ZT and both side temperatures. Temperature sensors are used to estimate temperatures of both sides. A thermal interface material of higher thermal conductivity such as copper should be inserted between solar absorber and TE modules. This enables better heat transfer through hot side of system and temperature difference across TE modules increases. At the cold side, a heat sink with closely spaced fins should be used to reject heat from the cold side to the surroundings.

4 Summary of STEG Developed Over the Years

Many researchers worked on the combined system of solar energy and thermoelectric devices. A few have worked on the hybrid photovoltaic-thermoelectric systems and some have proposed their prototypes for concentration-based solar thermoelectric generator (STEG). The various parameters and conversion efficiencies of such STEGs are tabulated as in Table 1.
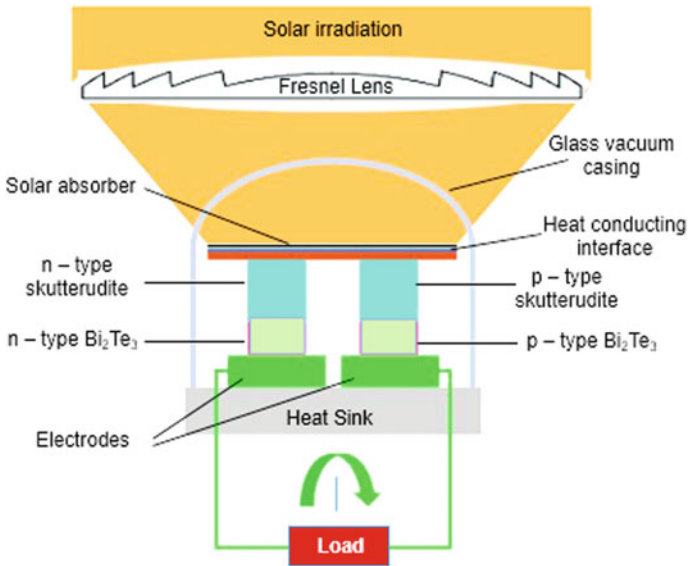
Fig. 9 Illustration of the proposed system of STEG

5 Conclusion

This paper described an overview of recent advancements in the design and performance of solar-assisted thermoelectric generators. It can be said that STEG have potential of providing thermal as well as electrical energy simultaneously. In the operations of STEG, there is no noise and environmental risk. The major factor for the commercialization of STEGs is its cost. The low conversion efficiency is a big concern for cost-effective design of STEGs. Further research must be focused on increasing conversion efficiency and STEGs must be employed in a more effective manner as discussed below:

1. Thermoelectric materials with the higher figure of merit (around $ZT = 2$ or above) should be developed. Bi_2Te_3 is the most commonly used thermoelectric material but it is not much effective at higher temperature. Hence, PbTe, SiGe-based alloys and skutterudites should be employed. BiTe materials can also be used with doping with Sb and Se to make nanostructured TE materials.
2. STEGs should be employed in cogeneration system where thermal energy is primarily produced with additional amount of electrical energy.
3. Real-time simulation of STEG can be performed so that the impact of environmental conditions can be studied.
4. TEGs should be incorporated with some other solar thermal applications such as 'solar chimney, solar water heater with storage and Trombe walls.'

Table 1 Details of STEGs developed over the years

Author	Year	Optical concentrator and thermal collector	Conc. ratio	Thermoelectric material	ZT	ΔT (K)	Heat dissipater	Conversion efficiency
Telkes [28]	1954	Flat plate + black painted Cu	1	BiSb/ZnSb	0.40	70	Heat sink	0.63
Goldsmit [29]	1980	Flat plate + black painted Al	1	Commercial BiTe	0.70	57	Heat sink	0.55
Durst [30]	1983	Evacuated tube + oil	1	Commercial BiTe	–	100	Water	0.75
Omer [31]	1998	Compound parabolic concentrator (CPC) + Al_2O_3	20	Commercial BiTe	–	100	Heat sink	0.90
Amatya [5]	2010	Parabolic dish and Fresnel lens + Si poly	66	Commercial BiTe	0.40	150	Heat sink	3.00
Kraemer [13]	2011	Evacuated flat plate + commercial multilayer spectrally–selective absorber on Cu	1	Nanostructured BiTe	1.03	200	Heat sink	4.60
Kraemer [13]	2011	Lens + commercial multilayer spectrally–selective absorber on Cu	2	Nanostructured BiTe	1.03	–	Heat sink	5.20
Suter [12]	2011	CPC + cavity storage	600	Oxides	0.05	620	Water	0.13
Zhang [32]	2013	Evacuated tube + heat pipe	1	Commercial BiTe	0.59	70	Water	1.00
Hasan Nia [16]	2014	Fresnel lens + oil flowing through tubes at hot side of TEG	1	Bi_2Te_3 (type TEP1-12656-0.6)	1	100	Water	3.2

(continued)

Table 1 (continued)

Author	Year	Optical concentrator and thermal collector	Conc. ratio	Thermoelectric material	ZT	ΔT (K)	Heat dissipater	Conversion efficiency
Kraemer [22]	2016	Lens + steel	38	BiTe-based skutterudites	1.02	400	Liquid cooled heat sink	7.40
Candadai [33]	2016	Fresnel lens + steel	62	Commercial BiTe	0.40	215	Heat sink	1.20
Kraemer [22]	2016	Lens + steel	211	BiTe-based skutterudites	1.02	550	Liquid cooled heat sink	9.60
Kim [23]	2016	Optical lens with refraction from phase change materials	1	Wavelength selective solar absorber	1		Heat sink	7.40
Nimr [27]	2018	Two flat mirrors at the aperture of two concentric cylinders		Cavity storage with black painted TEG hot side			Water flow between concentric cylinders	2.5

5. Literature depicted that concentration-based STEGs can be promising technologies if these are configured with sun-tracking mechanisms. Thermal stresses must also be reduced at higher temperature of such systems.
6. Thermal optimization of design of STEG with various sizes of thermoelectric leg should be performed.
7. Use of phase change materials (PCMs) can augment the performance of STEG system.

Future research must be focused on optimizing the number of thermoelectric modules employed in the system.

References

1. McLamb, E.: Energy's Future Today. Ecology Global Network: Energy. 2011 Sept 6. http://www.ecology.com/2011/09/06/fossil-fuels-vs-renewable-energy-resources
2. http://www.nature.com/naturematerials. Last accessed 2020/03/03
3. Babu, C., Ponnambalam, P.: The role of thermoelectric generators in the hybrid PV/T systems: a review. Energy Convers. Manage. **151**, 368–385 (2017)
4. Mesalam, R., Williams, H.R., Ambrosi, R.M., García-Cañadas, J., Stephenson, K.: Towards a comprehensive model for characterising and assessing thermoelectric modules by impedance spectroscopy. Appl. Energy **226**, 1208–1218 (2018)
5. Amatya, R., Ram, R.J.: Solar thermoelectric generator for micro-power applications. J. Electron. Mater. **39**(9) (2010)
6. Yan, X., Poudel, B., Ma, Y., Liu, W.S., Joshi, G., Wang, H., Lan, Y., Wang, D., Chen, G., Ren, Z.F.: Experimental studies on anisotropic thermoelectric properties and structures of n-type $Bi_2Te_{2.7}Se_{0.3}$. Nano Lett. **10**(9), 3373 (2010)
7. Fan, S., Zhao, J., Guo, J., Yan, Q., Ma, J., Hng, H.H.: p-type $Bi_{0.4}Sb_{1.6}Te_3$ nanocomposites with enhanced figure of merit. Appl. Phys. Lett. **96**(18), 182104 (2010)
8. Qi, Y., Wang, Z., Zhang, M., Yang, F., Wang, X., Lu, H., Yang, Y., Qiu, F., Trautmann, C., Bertsch, A., White, N.M., Paulo, A.S., Shakouri, A., Fonseca, L., Kim, K.: Thermoelectric devices based on one-dimensional nanostructures. J. Mater. Chem. A **1**(20), 6110 (2013)
9. Biswas, K., He, J., Blum, I.D., Wu, C.-I., Hogan, T.P., Seidman, D.N., Dravid, V.P., Kanatzidis, M.G.: High-performance bulk thermoelectrics with all-scale hierarchical architectures. Nature **490**(7421), 570 (2012)
10. Rogl, G., Grytsiv, A., Rogl, P., Bauer, E., Kerber, M., Zehetbauer, M., Puchegger, S.: Multifilled nanocrystalline p-type didymium–Skutterudites with ZT > 1.2. Intermetallics **18**(12), 2435 (2010)
11. Zhao, W., Wei, P., Zhang, Q., Dong, C., Liu, L., Tang, X.: Enhanced thermoelectric performance in barium and indium double-filled skutterudite bulk materials via orbital hybridization induced by indium filler. J. Am. Chem. Soc. **131**(10), 3713 (2009)
12. Suter, C., Tomeš, P., Weidenkaff, A., Steinfeld, A.: A solar cavity-receiver packed with an array of thermoelectric converter modules. Sol. Energy **85**(7), 1511 (2011)
13. Kraemer, D., Poudel, B., Feng, H.-P., Caylor, J.C., Yu, B., Yan, X., Ma, Y., Wang, X., Wang, D., Muto, A.: High-performance flat-panel solar thermoelectric generators with high thermal concentration. Nat. Mater. **10**, 532–538 (2011)
14. Baranowski, L.L., Snyder, G.J., Toberer, E.S.: Concentrated solar thermoelectric generators. Energy Environ. Sci. **5**, 9055–9067 (2012)
15. Olsen, M.L., Warren, E.L., Parilla, P.A., Toberer, E.S., Kennedy, C.E., Snyder, G.J., Firdosy, S.A., Nesmith, B., Zakutayev, A., Goodrich, A., Turchi, C.S., Netter, J., Gray, M.H., Ndione,

P.F., Tirawat, R., Baranowski, L.L., Gray, A., Ginley, D.S.: A high-temperature, high-efficiency solar thermoelectric generator prototype. Energy Procedia **49**, 1460–1469 (2014)

16. Nia, M.H., Nejad, A.A., Goudarzi, A.M., Valizadeh, M., Samadian, P.: Cogeneration solar system using thermoelectric module and fresnel lens. Energy Convers. Manage. **84**, 305–310 (2014)

17. Li, C., Zhang, M., Miao, L., Zhou, J., Kang, Y.P., Fisher, C.A.J., Ohno, K., Shen, Y., Lin, H.: Effects of environmental factors on the conversion efficiency of solar thermoelectric co-generators comprising parabola trough collectors and thermoelectric modules without evacuated tubular collector. Energy Convers. Manage. **86**, 944–951 (2014)

18. Dehghan, A.A., Afshari, A., Rahbar, N.: Thermal modeling and exergetic analysis of a thermoelectric assisted solar still. Sol. Energy **115**, 277–288 (2015)

19. Zhu, W., Deng, Y., Gao, M., Wang, Y., Cui, J., Gao, H.: Thin-film solar thermoelectric generator with enhanced power output: integrated optimization design to obtain directional heat flow. Energy **89**, 106–117 (2015)

20. Liu, L., Sen Lu, X., Shi, M.L., Ma, Y.K., Shi, J.Y.: Modeling of flat-plate solar thermoelectric generators for space applications. Sol. Energy **132**, 386–394 (2016)

21. Li, G., Zhang, G., He, W., Ji, J., Lv, S., Chen, X., Chen, H.: Performance analysis on a solar concentrating thermoelectric generator using the micro-channel heat pipe array. Energy Convers. Manage. **112**, 191–198 (2016)

22. Kraemer, D., Jie, Q., McEnaney, K., Cao, F., Liu, W., Weinstein, L.A., Loomis, J., Ren, Z., Chen, G.: Concentrating solar thermoelectric generators with a peak efficiency of 7.4%. Nature Energy **1**, 16153 (2016)

23. Kim, M.-S., Kim, M.-K., Jo, S.-E., Joo, C., Kim, Y.-J.: Refraction-assisted solar thermoelectric generator based on phase-change lens. Sci. Rep. **6**, 27913 (2016). https://doi.org/10.1038/srep27913

24. Shen, Z.-G., Wu, S.-Y., Xiao, L., Chen, Z.-X.: Proposal and assessment of a solar thermoelectric generation system characterized by Fresnel lens, cavity receiver and heat pipe. Energy **141**, 215–238 (2017)

25. Banakar, A., Motevali, A., Emad, M., Ghobadian, B.: Co-generation of heat and power in a thermoelectric system equipped with Fresnel lens collectors using active and passive cooling techniques. Renew. Energy **112**, 268–279 (2017)

26. Rad, M.K., Omid, M., Rajabipour, A., Tajabadi, F., Rosendahl, L.A., Rezaniakolaei, A.: Optimum thermal concentration of solar thermoelectric generators (STEG) in realistic meteorological condition. Energies **11**, 2425 (2018)

27. Al-Nimr, M.A., Al-Darawsheh, I.A., Al-Khalayleh, L.A.: A novel hybrid cavity solar thermal collector. Renew. Energy **115**, 299–307 (2018)

28. Telkes, M.: Solar thermoelectric generators. J. Appl. Phys. **25**(6), 765 (1954)

29. Goldsmid, H., Giutronich, J., Kaila, M.: Solar thermoelectric generation using bismuth telluride alloys. Sol. Energy **24**(5), 435 (1980)

30. Durst, T., Harris, L.B., Goldsmid, H.J.: Studies of a thermoelectric generator operating from tubular solar collectors. Sol. Energy **31**(4), 421 (1983)

31. Omer, S.: Design optimization of thermoelectric devices for solar power generation. Sol. Energy Mater. Sol. Cells **53**(1–2), 67 (1998)

32. Zhang, M., Miao, L., Kang, Y.P., Tanemura, S., Fisher, C.A.J., Xu, G., Li, C.X., Fan, G.Z.: Efficient, low-cost solar thermoelectric cogenerators comprising evacuated tubular solar collectors and thermoelectric modules. Appl. Energy **109**, 51 (2013)

33. Candadai, A.A., Kumar, V.P., Barshilia, H.C.: Performance evaluation of a natural convective-cooled concentration solar thermoelectric generator coupled with a spectrally selective high temperature absorber coating. Sol. Energy Mater. Sol. Cells **145**, 333 (2016)

Hybrid Nano-materials Properties Analysis for Solar Photovoltaic

Siddhartha Kosti [ORCID], **Chandra S. Malvi** [ORCID]**, and Sanjeev K. Vishwakarma**

1 Introduction

Powder forms of metals are called nano-particles, and when these nano-particles are reinforced into a base material, this combination is called nano-materials. As the name suggests, they are of nano-scale sizes (10–9 m). This small size helps in increasing the surface area to volume ratio and heat transfer. Nano-materials possess enhanced properties and have been widely analyzed [1]. Hybrid nano-materials are a combination of two or more types of nano-materials at 1 nm = 10–9 m scale [2]. One should be an inorganic nano-material, and other should be organic nano-material. By varying the reinforcement weight %, one can obtain different sets of hybrid nano-materials with improved properties [3]. These hybrid nano-materials are being utilized in different applications like solar cells, environment, energy, health, electronics, automotive, energy, construction, medicine, bio-medical, aerospace, etc. [4–8]. We all know that solar energy is abundant, and according to the estimations, the availability of solar energy per year on the earth's surface is around 3×1024 Joules. On the earth's atmosphere amount of solar constant received is around 1366 W/m^2 while on the earth's surface, it is around 1000 W/m^2 [9]. There are different ways and applications to use solar energy [10]. Out of all the applications, solar photovoltaic (PV) is the most widely utilized method for converting solar energy into electrical energy [11]. A variety of nano-materials of different dimensions can be utilized to produce solar energy [12]. The literature review found that the solar device's cooling

S. Kosti (✉)
Department of Mechanical Engineering, Rajkiya Engineering College, Banda 210201, India
e-mail: siddharth.kosti@gmail.com

C. S. Malvi
Department of Mechanical Engineering, Madhav Institute of Technology & Science, Gwalior 474005, India

S. K. Vishwakarma
Department of Mechanical Engineering, Jorhat Engineering College, Jorhat 785007, Assam, India

rate increases after the implementation of nano-materials [13, 14]. A variety of nano-particles are being utilized to increase the efficiency of solar devices like [15–31]. All nano-particles are utilized as reinforcement into the base fluid (H_2O/ethylene glycol) to check their effect on the properties.

The above literature review found that hybrid nano-materials have excellent properties to be utilized in solar power. Most of the studies in hybrid nano-materials are experimentally based, and few studies have been found to analyze the nano-materials' properties utilizing mathematical models. The present work focuses on the analysis of the hybrid nano-materials properties utilizing different mathematical models.

2 Materials and Methods

Present work deals with the application of nano-particles, like aluminum oxide (Al_2O_3), copper (Cu), copper oxide (CuO), and titanium oxide (TiO_2) in the solar energy devices. To analyze this, ethylene glycol (EG) is considered as a base fluid on which the nano-particles are reinforced with varying weight percentages. As ethylene glycol is an organic nano-particle, while Al_2O_3, Cu, CuO, and TiO_2 are organic nano-particle combinations of nano-particles will give hybrid nano-materials. These hybrid nano-materials (Al_2O_3-EG, Cu-EG, CuO-EG, and TiO_2-EG) properties are analyzed in the present work. Properties of these nano-particles are shown in Table 1 [32–35].

2.1 Mathematical Models

Mixture rule [36]

$$k_{hnm} = k_{np}\phi + k_{EG}(1 - \phi)$$

Maxwell model [37]

Table 1 Base material and nano-particles properties

Particle	K (W/m K)	C_P (J/kg K)	ρ (kg/m^3)
Al_2O_3	40	773	3880
Cu	401	1300	3200
CuO	33	2400	6310
TiO_2	8.9538	686.2	4250
Ethylene glycol ($CH_2OH)_2$	0.253	2089	1113.2

$$k_{hnm} = \left[\frac{(k_{np} + 2k_{EG}) + 2\phi(k_{np} - k_{EG})}{(k_{np} + 2k_{EG}) - \phi(k_{np} - k_{EG})} \right] k_{bf}$$

Yu and Choi model [38]

$$k_{hnm} = \left[\frac{(k_{np} + 2k_{EG}) + 2\phi(k_{np} - k_{EG})(1 + \beta)^3}{(k_{np} + 2k_{EG}) - \phi(k_{np} - k_{EG})(1 + \beta)^3} \right] k_{bf}$$

Hamilton and Crosser model [39]

$$k_{hnm} = \left[\frac{k_{np} + (n - 1)k_{EG} + (n - 1)(k_{np} - k_{EG})\phi}{k_{np} + (n - 1)k_{EG} - (k_{np} - k_{EG})\phi} \right] k_{bf}$$

3 Result and Discussion

3.1 Thermal Conductivity Analysis

Hybrid nano-materials considered in the present work are Al_2O_3-EG, Cu-EG, CuO-EG, and TiO_2-EG. These hybrid nano-materials are considered to be utilized in solar energy devices due to their enhanced thermal properties. The concentration of these nano-particles is varied from 0 to 30% to make different hybrid nano-materials. Al_2O_3-EG, Cu-EG, CuO-EG, and TiO_2-EG hybrid nano-materials thermal conductivity variation is shown in Table 2 and Fig. 1, 2, 3 and 4.

Figures 1, 2, 3 and 4 indicates all the hybrid nano-materials thermal conductivity increases with increment in the nano-particle weight percentage. This increment in the thermal conductivity is due to the high thermal conductivity of nano-particles (Al_2O_3, Cu, CuO, and TiO_2) compared to the ethylene glycol thermal conductivity. Maximum thermal conductivity increment is observed for $\beta = 0.3$ for Yu–Choi model. For $\beta = 0$ and n = 3 Yu–Choi model, Maxwell model and Hamilton and Crosser overlap each other. So it can be concluded that reinforcement of nano-particle into the ethylene glycol increases the hybrid nano-material thermal conductivity [39].

3.2 Density

Figure 5 and Table 3 represent the variation of the density of the hybrid nano-materials for varying weight percentages of nano-particle. The increment can be observed in density for all hybrid nano-materials with increment in the reinforcement weight percentage. CuO-EG hybrid nano-material shows a maximum increment in

Table 2 Hybrid nano-materials thermal conductivity

ϕ	Mixture	Maxwell	Yu and Choi $\beta = 0$	Yu and Choi $\beta = 0.2$	Yu and Choi $\beta = 0.3$	Hamilton and Crosser $n = 3$	Hamilton and Crosser $n = 4.9$	Hamilton and Crosser $n = 5.7$
Al$_2$O$_3$-EG hybrid nano-material								
0.000	0.253	0.253	0.253	0.253	0.253	0.253	0.253	0.253
0.100	4.228	0.336	0.336	0.408	0.533	0.336	0.386	0.407
0.200	8.202	0.438	0.438	0.642	1.139	0.438	0.551	0.598
0.300	12.177	0.570	0.570	1.039	3.442	0.570	0.762	0.841
Cu-EG hybrid nano-material								
0.000	0.253	0.253	0.253	0.253	0.253	0.253	0.253	0.253
0.100	40.328	0.337	0.337	0.411	0.539	0.337	0.390	0.413
0.200	80.402	0.442	0.442	0.653	1.172	0.442	0.562	0.612
0.300	120.477	0.577	0.577	1.067	3.750	0.577	0.782	0.868
CuO-EG hybrid nano-material								
0.000	0.253	0.253	0.253	0.253	0.253	0.253	0.253	0.253
0.100	3.528	0.335	0.335	0.407	0.531	0.335	0.385	0.406
0.200	6.802	0.437	0.437	0.640	1.131	0.437	0.549	0.595
0.300	10.077	0.568	0.568	1.032	3.377	0.568	0.757	0.834
TiO$_2$-EG hybrid nano-material								
0.000	0.253	0.253	0.253	0.253	0.253	0.253	0.253	0.253
0.100	1.123	0.330	0.330	0.396	0.509	0.330	0.372	0.388
0.200	1.993	0.424	0.424	0.607	1.027	0.424	0.516	0.552
0.300	2.863	0.542	0.542	0.945	2.619	0.542	0.694	0.753
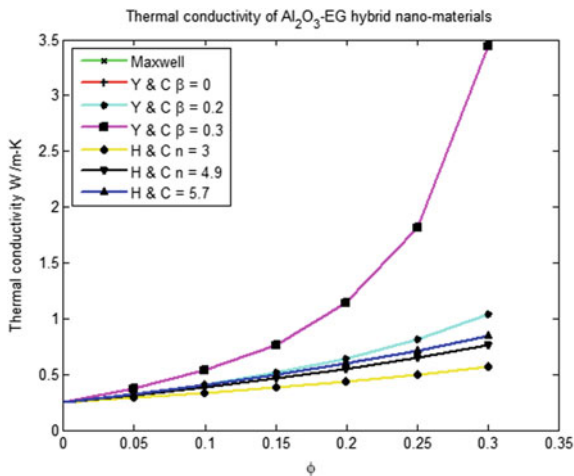
Fig. 1 Al$_2$O$_3$-EG hybrid nano-materials
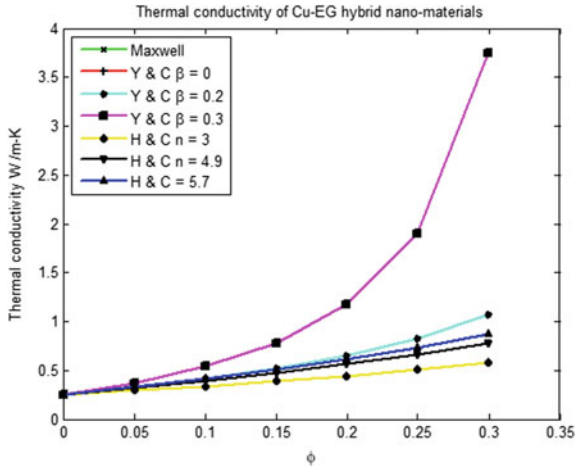
Fig. 2 Cu-EG hybrid nano-materials
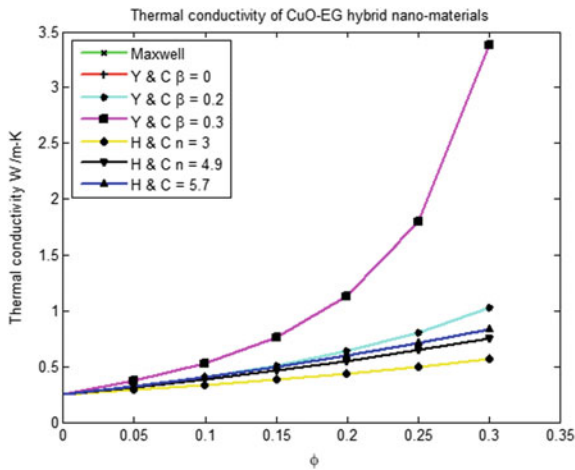
Fig. 3 CuO-EG hybrid nano-materials

the density while that of Cu-EG hybrid nano-material shows a minimum increment in the density. This is because the density of CuO nano-particle is maximum out of all the nano-particle considered while the density of Cu nano-particle is minimum out of all the nano-particle considered [40].
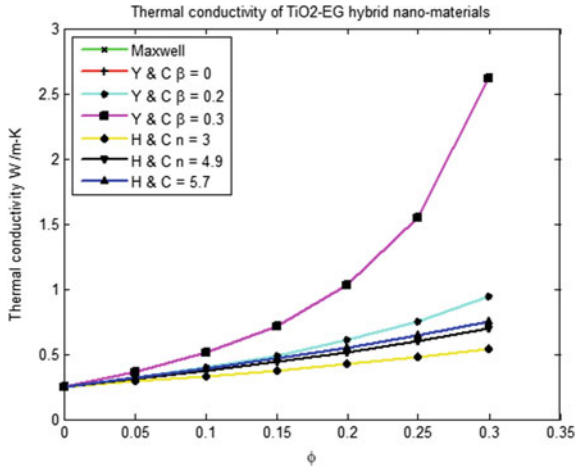
Fig. 4 TiO$_2$-EG hybrid nano-materials
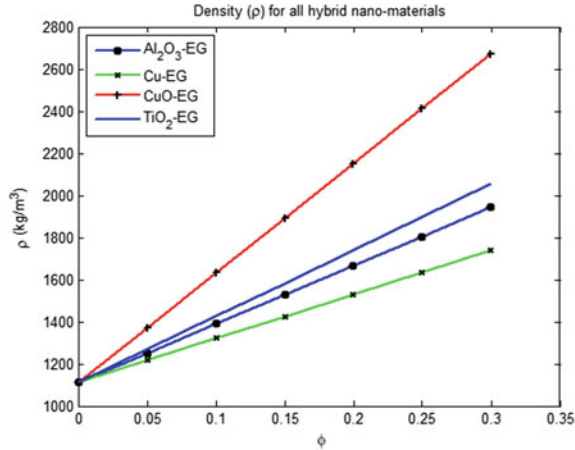
Fig. 5 Density of all hybrid nano-materials

Table 3 Density of all hybrid nano-materials

ϕ	Al$_2$O$_3$-EG	Cu-EG	CuO-EG	TiO$_2$-EG
0.000	1113.2	1113.2	1113.2	1113.2
0.050	1251.54	1217.54	1373.04	1270.04
0.100	1389.88	1321.88	1632.88	1426.88
0.150	1528.22	1426.22	1892.72	1583.72
0.200	1666.56	1530.56	2152.56	1740.56
0.250	1804.9	1634.9	2412.4	1897.4
0.300	1943.24	1739.24	2672.24	2054.24

3.3 *Specific Heat* (C_P)

Mixture rule is adopted to analyze the specific heat. Figure 6 and Table 4 show the specific heat of all hybrid nano-material (Al_2O_3-EG, Cu-EG, CuO-EG, and TiO_2-EG). From Fig. 5, it can be noticed that Al_2O_3-EG, Cu-EG, and TiO_2-EG hybrid nano-materials show an increment in the CP while CuO-EG shows decrement. It can also be noticed that CuO-EG hybrid nano-materials show a maximum increment in specific heat compared to another hybrid nano-materials [41].
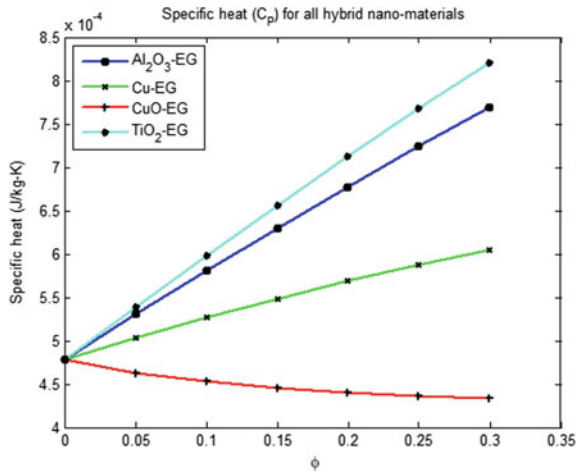
Fig. 6 Specific heat of all hybrid nano-materials

Table 4 Specific heat of all hybrid nano-materials

ϕ	Al_2O_3-EG	Cu-EG	CuO-EG	TiO_2-EG
0.000	0.000479	0.000479	0.000479	0.000479
0.050	0.000531	0.000504	0.000463	0.000539
0.100	0.000581	0.000527	0.000453	0.000598
0.150	0.00063	0.000548	0.000446	0.000656
0.200	0.000677	0.000568	0.00044	0.000712
0.250	0.000724	0.000587	0.000436	0.000767
0.300	0.000769	0.000605	0.000433	0.000821

4 Conclusion

Following results are obtained from the study:

- Hybrid nano-materials show higher thermal conductivity compared to the base material.
- Hybrid nano-materials made by reinforcing higher thermal conductivity nano-particles show higher thermal conductivity.
- Hybrid nano-materials with a more significant amount of reinforced nano-particle show a larger increment in the thermal conductivity.
- The maximum thermal conductivity increment is observed for $\beta = 0.3$ for Yu–Choi model.
- Nano-layer thickness and nano-particles shape factor affect the thermal conductivity of hybrid nano-materials.

References

1. Sharma, V.P., Sharma, U., Chattopadhyay, M., Shukla, V.N.: Advance applications of nano-materials: a review. Mater. Today: Proc. **5**, 6376–6380 (2018)
2. Loy, D.A., Shea, K.J.: Bridged polysilsesquioxanes, highly porous hybrid organic-inorganic materials. Chem. Rev. **95**, 1431–1442 (1995)
3. Hayami, R., Wada, K., Nishikawa, I., Sagawa, T., Yamamoto, K., Tsukada, S., Gunji, T.: Preparation and properties of organic–inorganic hybrid materials using titanium phosphonate cluster. Polym. J. **49**, 665–669 (2017)
4. Colombo, A., Dragonetti, C., Magni, M., Meroni, D., Ugo, R., Marotta, G., Lobello, M.G., Salvatori, P., De Angelis, F.: New thiocyanate-free ruthenium(II) sensitizers with different pyrid-2-yl tetrazolate ligands for dye-sensitized solar cells. Dalton Trans. **44**, 11788–11796 (2015)
5. Sanchez, C., Belleville, P., Popall, M., Nicole, L.: Applications of advanced hybrid organic-inorganic nano-materials: from laboratory to market. Chem. Soc. Rev. **40**, 696–753 (2011)
6. Meroni, D., Ardizzone, S., Schubert, U.S., Höppener, S.: Probe-based electro-oxidative lithography of OTS SAMs deposited onto transparent ITO substrates. Adv. Func. Mater. **22**, 4376–4382 (2012)
7. Diaz, U., Corma, A.: Organic-inorganic hybrid materials: multi-functional solids for multi-step reaction processes. Chem.-A Eur. J. **24**, 3944–3958 (2018)
8. Kosti, S., Malvi, C.S.: Cumulative influence of nano-particles on MMCs time-temperature history curve. Nano-mater. Energy **7**(1), 1–10 (2018)
9. Odum, H.T.: Energy of global processes, Handbook of energy evaluation, University of Florida, Gainesville, USA: Center for Environmental Policy, Environmental Engineering Sciences; Folio no. 2 (2000)
10. Tyagi, H., Agarwal, A.K., Chakraborty, P.R., Powar, S.: Applications of Solar Energy, Energy Environment, and Sustainability. Springer, Singapore (2018)
11. Chopra, K.L., Paulson, P.D., Dutta, V.: Thin-film solar cells: An overview. Prog. Photovoltaics Res. Appl. **12**, 69–92 (2004)
12. Theerthagiri, J., Senthil, R.A., Madhvan, J.: Design and fabrication of carbon-based nanostructured counter electrode materials for dye-sensitized solar cells. Rational Design of Solar Cells for Efficient Solar Energy Conversion, Chapter 7, pp. 193–219 (2018)

13. Al-Shamani, A.N., Yazdi, M.H., Alghoul, M.A., Abed, A.M., Ruslan, M.H., Mat, S., Sopian, K.: Nanofluids for improved efficiency in cooling solar collectors: a review. Renew. Sustain. Energy Rev. **38**, 348–367 (2014)
14. Lu, L., Liu, Z.-H., Xiao, H.-S.: Thermal performance of an open thermosyphon using nanofluids for high-temperature evacuated tubular solar collectors. Sol. Energy **85**, 379–387 (2011)
15. Yousefi, T., Shojaeizadeh, E., Veysi, F., Zinadini, S.: An experimental investigation on the effect of Al2O3–H2O nanofluid on the efficiency of flat-plate solar collectors. Renew. Energy **39**, 293–298 (2012)
16. Tiwari, A.K., Ghosh, P., Sarkar, J.: Solar water heating using nanofluids-a comprehensive overview and environmental impact analysis. Int. J. Emerg. Technol. Adv. Eng. **3**, 221–224 (2013)
17. Nasrin, R., Parvin, S., Alim, M.A.: Effect of Prandtl number on free convection in a solar collector filled with nanofluid. Procedia Eng. **56**, 54–62 (2013)
18. Tyagi, H., Phelan, P., Prasher, R.: Predicted efficiency of a low-temperature nanofluid-based direct absorption solar collector. J. Sol. Energy Eng. **131**, 1–7 (2009)
19. Otanicar, T.P., Phelan, P.E., Prasher, R.S., Rosengarten, G., Taylor, R.A.: Nanofluid-based direct absorption solar collector. J. Renew. Sustain. Energy, **2**(3) (2010)
20. Taylor, R.A., Phelan, P.E., Otanicar, T.P., Walker, C.A., Nguyen, M., Trimble, S.: Applicability of nanofluids in high flux solar collectors. J. Renew. Sustain. Energy **3**(2) (2011)
21. Saidur, R., Meng, T.C., Said, Z., Hasanuzzaman, M., Kamyar, A.: Evaluation of the effect of nanofluid-based absorbers on direct solar collector. Int. J. Heat Mass Transf. **55**, 5899–5907 (2012)
22. Khullar, V., Tyagi, H., Phelan, P.E., Otanicar, T.P., Singh, H., Taylor, R.A.: Solar energy harvesting using nanofluids-based concentrating solar collector. J. Nanotechnol. Eng. Med. **3**(3) (2013)
23. He, Q., Wang, S., Zeng, S., Zheng, Z.: Experimental investigation on photo thermal properties of nanofluids for direct absorption solar thermal energy systems. Energy Convers. Manage. **73**, 150–157 (2013)
24. Liu, Z.-H., Hu, R.-L., Lu, L., Zhao, F., Xiao, H.-S.: Thermal performance of an open thermosyphon using nano fluid for evacuated tubular high temperature air solar collector. Energy Convers. Manage. **73**, 135–143 (2013)
25. Risi, A.D., Milanese, M., Laforgia, D.: Modelling and optimization of transparent parabolic trough collector based on gas-phase nanofluids. Renew. Energy **58**, 134–139 (2013)
26. Otanicar, T.P., Golden, J.S.: Comparative environmental and economic analysis of conventional and nanofluid solar hot water technologies. Environ. Sci. Technol. **43**, 6082–6087
27. Otanicar, T.P., Phelan, P.E., Golden, J.S.: Optical properties of liquids for direct absorption solar thermal energy systems. Sol. Energy **83**, 969–977
28. Yousefi, T., Shojaeizadeh, E., Veysi, F., Zinadini, S.: An experimental investigation on the effect of MWCNT-H2O nanofluid on the efficiency of flat-plate solar collectors. Exp. Therm. Fluid Sci. **39**, 207–212 (2012)
29. Chougule, S.S., Pise, A.T., Madane, P.A.: Performance of nanofluid-charged solar water heater by solar tracking system. In: Proceedings of IEEE International Conference on Advances in Engineering Science and Management, pp. 247–253 (2012)
30. Yousefi, T., Shojaeizadeh, E., Veysi, F., Zinadini, S.: An experimental investigation on the effect of pH variation of MWCNT–H2O nanofluid on the efficiency of a flat-plate solar collector. Sol. Energy **86**, 771–779 (2012)
31. Eastman, J., Choi, U., Li, S., Thompson, L., Lee, S.: Enhanced thermal conductivity through the development of nanofluids. MRS Proc. **457**, 3 (1996)
32. Kosti, S.: Nano-particle Reinforcement Effect on the MMC's, Advances in Interdisciplinary Engineering, pp. 459–469. Springer, Berlin (2019)
33. Xie, H., Lee, H., Youn, W., Choi, M.: Nanofluids containing multiwalled carbon nanotubes and their enhanced thermal conductivities. J. Appl. Phys. **94**(8), 4967–4971 (2003)
34. Zhou, L.-P., Wang, B.-X., Peng, X.-F., Du, X.-D., Yang, Y.-P.: On the specific heat capacity of CuO nanofluid. Adv. Mech. Eng. (2009)

35. Rohatagi, P.K.: Metal matrix composites. Def. Sci. J. **43**(4), 323–349 (1993)
36. Maxwell, J.C.: A Treatise on Electricity and Magnetism, 1st edn., vol. 1, pp. 360–366. Clarendoon Press (1873)
37. Yu, W., Choi, S.U.S.: The role of interfacial layers in the enhanced thermal conductivity of nanofluids: are novated maxwell model. J. Nano-particle Res. **6**(4), 167–171 (2003)
38. Hamilton, R.L., Crosser, O.K.: Thermal conductivity of heterogeneous two-component system. Ind. Eng. Chem. Fundam. **1**(3), 187–191 (1962)
39. Sarvia, R.M., Fuskele, V.: Review on thermal conductivity of nanofluids. Mater. Today: Proc. **4**(2), 4022–4031 (2017)
40. Tay, C.Y., Setyawati, M.I., Leong, D.T.: Nano-particle density: a critical biophysical regulator of endothelial permeability. ACS Nano **11**(3), 2764–2772 (2017)
41. Hentschke, R.: On the specific heat capacity enhancement in nanofluids. Nanoscale Res. Lett. **11**, 88 (2016)

Solar Thermal Application for Crop Residue Management

Ravindra Kumar [ID]**, Anil Kumar** [ID]**, and Dang Nguyen Thoai** [ID]

1 Introduction

The energy requirement is on the rise with every passing day because of increasing technological advancements and gowning population. It is an important issue of twenty-first century to deal with the energy crisis. Energy can be in different forms, such as heat, light, electricity, and radiation. Sun has a huge potential and amount of energy, which it emits at the rate of 3.8×10^{23} kW out of which, Earth only receives approx. 1.8×10^{14} kW [1].

One of the best non-conventional and sustainable energy sources is biomass, available worldwide at scale. Biomass can be transformed into a gaseous, liquid, and solid fuel state and yields from the biological, physical, and thermal mechanisms conversion process. Agriculture dominant countries like India annually produces crop residue of more than 500 Mt. These types of residues are used at a large scale for animal feed, making houses (thatching purpose) in rural areas, as an industrial fuel, and for domestic purposes. To deal with unused crop residues after harvest, a common practice in many countries is to burn open fields because of a shortage of labor and expensive harvesting. Burning the crop residues actively contributes

R. Kumar
Department of Mechanical and Automation Engineering, ADGITM, New Delhi, India
e-mail: ravindra87kumar@gmail.com

R. Kumar · A. Kumar (✉)
Department of Mechanical, Production & Industrial and Automobile Engineering, Delhi Technological University, Delhi, India
e-mail: anilkumar76@dtu.ac.in

A. Kumar
Centre for Energy and Environment, Delhi Technological University, Delhi, India

D. N. Thoai
Department of Chemical and Food Engineering, Faculty of Natural Sciences, Quy Nhon University, Quy Nhon, Vietnam

to polluting the environment, imposes danger to health, releases greenhouse gases which cause global warming, and the loss of plant nutrients like N, K, P, and S [2].

Crop residues contain fibers, energy, and plant nutrients; their composition is cellulose, hemicelluloses, and lignin. At the global level, cellulose or fiber produce is approximately 1.3 gigatonnes from crop residues [3]. Crop residues can be converted into various types of fuels through the thermochemical process. There are many conversion processes that use thermochemical techniques like gasification, pyrolysis, direct combustion, etc. They produce economically beneficial and highly valuable fuels such as gasses, liquid, and solids or chars [4]. The best utilization of crop residue is in biogas generation, bio-oil, and bio-char by the process of pyrolysis [5]. In recent years, the use of crop residue as bagasse, rice husk, and rice straw, etc., has been receiving more attention for energy generation, and these are the vital staple food of the world [6]. Ongoing research has created protection for agriculture-based crop residue management technology innovations, which are more productive than traditional practices.

Crop residue management is an approach to making agriculture sustainable. It either partly or entirely must be used for ensuring the country's food security and keeping the soil resource base strong and healthy. The use of solar energy to aid this process can do wonders in reducing the environmental effects and increasing efficiency.

In the context of the current study, the different solar thermal applications in the crop residue management are reviewed.

2   Crop Residue Potential

Crop residues can be defined as the waste materials obtained in harvesting and while processing of vegetative agricultural crops. Crop residues can be classified into two categories.

2.1   Field Residues

These are the leftover or residual or remaining materials after harvesting the crop in agricultural land or plantation areas, which generally includes leaves, stalks, stems, and seed pods. These residual materials may be burned first or cultivated directly into the ground. If managed properly, these residues can increase irrigational efficiency and effectively control erosion.

2.2 Process Residues

These are the materials left over after the crop is converted into a resource that is usable. Process residues commonly include roots, bagasse, husks, seeds, and molasses, which could be used to feed animals and to fertilize the soil. Field residues are also commonly include beans, rice, sugar beet, maize, and wheat along with residues obtained during industrial processing of rice hull, maize cob, cottonseed hull, and sugar beet bagasse.

Crop residues are considerable, a significant cellulosic feedstock since they have bulk volumes of biomass but do not compete in food accessibility [7]. Biomass is generated from crop residues, which can be found most commonly and in large quantities throughout the world, such as rice straw, sugarcane bagasse, corn straw, and wheat straw. The availability of agriculture waste is depicted in million tons in Fig. 1 [8]. Asia globally produces the highest amount of rice and wheat straw, while America is the major producer of corn straw as well as sugarcane bagasse. The agricultural crop residues contain lignocelluloses materials, a significant source for biofuel production. The composition of elements, content of ash, and high heating values of most common agricultural residue are generated worldwide [9].

Figure 2 shows the comparison of agriculture wastes in India with Asian countries in Mt/year. Now, it is noticeable that much more burning of agriculture waste takes place in India due to the large production of agricultural waste compared to the other countries in the region [10] (Fig. 3).

3 Residue Burning

Burning of crop residue is responsible for poor air quality worldwide. Types of biomass burning are prescribed burning of savannas, crop residue burning in the open area, and forest fires [12]. Agrarian countries like India, which contribute to approximately 17% of the world population, produce enormous amounts of food
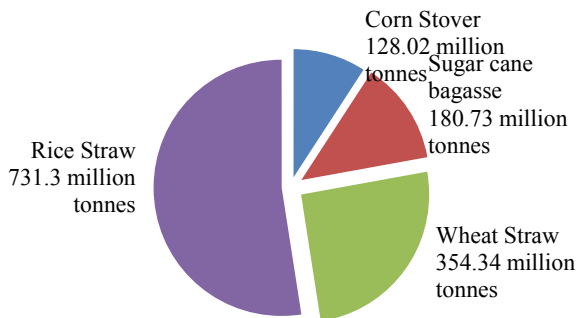
Fig. 1 Agriculture waste with different biomass and availability [8]
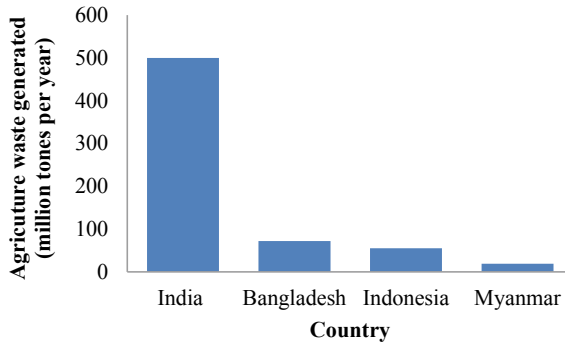
Fig. 2 Comparison of agriculture wastes in India with Asian countries in Mt/year [10]
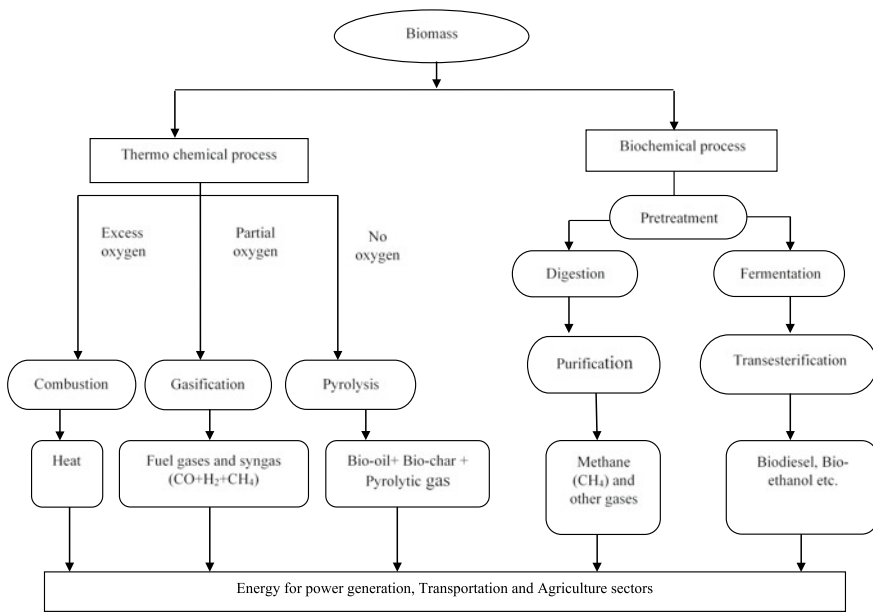
Fig. 3 Technology of producing various types of fuels through biomass [11]

grains like wheat and rice for domestic use and export. A large volume of agriculture waste is produced after harvesting and is left in the fields to be used as biomass [13].

India produced a large number of crops in 2012–2013, as stated by the Directorate of Economics and Statistics, are shown in Fig. 4.

Crop residue like cereal straw, sugarcane leaves, and woody stalks are generated every year. Residues that can be used as conventional bases for thatching homes in rural areas, animal feed, cooking fuel, and industrial fuel, still remain in large quantities as waste left on the fields.
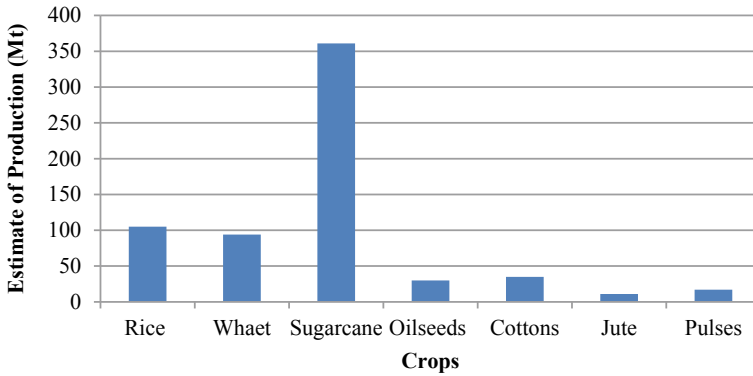
Fig. 4 Crop production in India [10]

Jain et al. [12] presented, Uttar Pradesh is contributing a tremendous amount to crop residue burning followed by other states like Haryana and Punjab, 25% residue is burned of the total amount says the record of Intergovernmental Panel on Climate Change (IPCC). The maximum range of crop residue (8–80%) of paddy is generated all over the state along with the other kinds of residues like oilseed crop (5%), sugarcane (19%), wheat (21%), and rice (43%).

There is a major challenge of disposal of crop residue. Farmers have the only option of burning the crop residue because it is inexpensive, easy, and quickly manages the massive quantity of crop residue for preparation fields on time for the next crop.

Burning of crop residue produces air pollutants like CO, SO_2, NH_3, NO_x and emits air gases such as N_2O, CO_2, volatile and semi-volatile organic compound, and particulate matter at a different rate of carbon [14].

4 Residue Crop Management

After a lot of literature study, it was found that government is focusing on biogas production from crop residues, but in most of the states of India, crop residues are used as sources of animal feed such as in Bihar, J&K, Tamil Nadu, West Bengal, Bihar, and Assam [15]. Crop residue finds its applications in cement mixes (rice husk ash), paper industry (waste of sugarcane), and mushroom cultivation (ash of bagasse and husk) [16].

4.1 Need of Burning Crop Residue

- Silica content is high in paddy straw so it is not considered as good feed, and it takes a long time to decompose.
- It is pertaining to the small interval of time between the acts of wheat sowing paddy harvesting.
- Significant cost included in using paddy straw in farms.

Wheat straw does not have the problems associated with the paddy straw because of having less of silica content. It is a significantly good animal feed, easy to chop, and there is no urgent need to sow the next crop, except maybe in a cotton belt like Gujarat and Maharashtra state.

Reason—Farmers are unable to realize the consequences of burning crop residue for the soil and their farm economics. Paid out costs are easily noticed, but indirect or long-term costs often go unnoticed and, hence, neglected.

4.2 Solutions

On Farm Use

- As animal feed.
- It can be collected and stored separately to be later used either as mulch to cover the soil or to prepare high-grade compost.
- Left to decompose on its own in due course of time.
- Changing the cropping pattern which gives some gap between crops rather than just paddy and wheat cycle.
- All three methods involve additional cost and labor. Organic farmers opt for this as they consider this additional cost a worthwhile investment. Traditional farmers do not want to wear the type of system.

Off Farm Use

- Electricity generation.
- Ethanol.
- Bio-CNG production.
- Bio-char.
- Gasification.

5 Crop Residues Management Strategies

Many technologies are available in India for crop residue management, but the limitation of these technologies is in large-scale adaptation. One of the major issues is
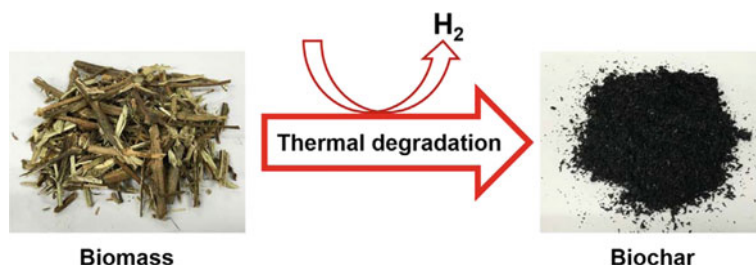
Fig. 5 Generation of bio-char through thermochemical conversion of biomass [21]

labor requirement and high cost for its transportation and collection of vast amounts of straw. Few countries have developed the techniques for crop management; for example, China annually generates 700 Mt crop residues and uses 15% for fertilizer, 19% for bioenergy, 31% for animal feed, and 31% is left in the fields [17].

6 Pyrolysis Product by Solar Thermal Application

Biomass conversion by solar assisted pyrolysis is a method of bio-refinery that produces three essential products, such as solid (Char), liquid (oil), and gas. These three products used as fuel in different sectors like power and heat production [18].

6.1 Bio-char

A form of charcoal generated by the thermochemical process of biomass under using less oxygen is called bio-char. It is not pure carbon, as it also includes H, O, N, and S. In bio-char production, different kinds of biomass are used as feedstock like agricultural crop residues, waste of wood, forestry residues, animal manure, and municipal solid waste. These types of biomass depend on the suitability of the environment, chemical composition, and economic condition [19].

Bio-char has achieved more attention to use in arable land in the last few decades because of its agronomic and environmental advantages [20] (Figs. 5 and 6).

6.2 Production Technology

Bio-char can be produced from different techniques such as gasification, slow pyrolysis, and fast pyrolysis. In the process of slow pyrolysis, the combustion of biomass takes place without oxygen approximately at the temperature of 350–800 °C, and the

Fig. 6 Utilization of bio-char [21]
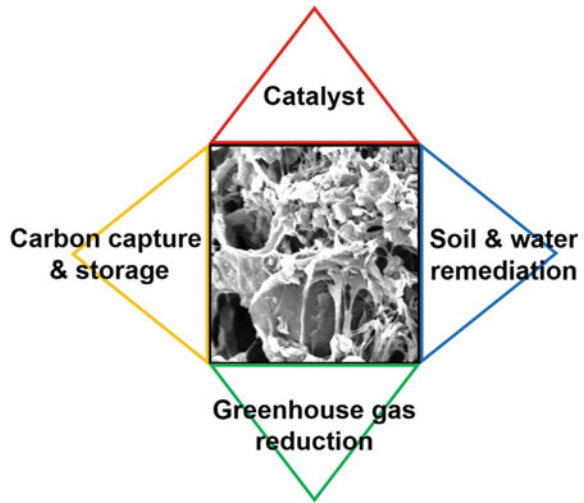
time taken for the residence can take from minutes to a couple of hours. In the process of fast pyrolysis, biomass is combusted without oxygen, at an approx. temperature of 425–550 °C. The time for residence is 2 s. In the gasification process, biomass undergoes combustion in the presence of oxygen more than a temperature at 800 °C. At the same time, the time of residence can range from a few seconds to some hours [20].

6.3 Bio-oil

Bio-oil has a dark brown color and smoky odor. It is a mixture of alcohols, acids, fatty acids, ketones, aldehydes, aliphatic hydrocarbon, aromatics, esters, etc. The availability of elements like C, N, O, H, and S in pyrolysis oil has great importance in the combustion properties. Bio-oil having higher oxygen content is comparable to fuels such as diesel and biodiesel. The following are the undesirable properties of bio-oil [22]:

- High viscosity, which leads to unwanted characteristics of fluid flow.
- High content of oxygen, resulting in high water content and lower values of heating.
- High corrosive tendency or acidic value, which can cause damage to the system components.
- High ash content.

Bio-oil derived by biomass usually involves some amount of bio-char, solid particles, and few alkali metals compared to other oils like waste tires oil and waste plastic. Solid particles present in bio-oils create problems in the utilization and storage of

fuel. Two type filters such as granular filter and glass wool hot vapor filter are used for quality purpose in term of solids particles, viscosity, ash content, and water content. Additional problems such as lower heating value and acidic nature of oil are not involved in filtration [23].

6.4 Pyrolysis Gas

Pyrolytic gas obtained from biomass consists of gases like CH_4, CO, H_2, CO_2, and other C_nH_n. In gas obtained from solar pyrolysis, the leading role is gas-phase reaction and is controlled by temperature (560 °C). Availability of hydrogen and carbon monoxide which makes pyrolytic gas applicable in different ways such as in power generation and heating. They are also present in the maximum amount of such gases. The presence of hydrogen (HHV 120 MJ/kg) gas can increase the quality of gaseous fuel in pyrolytic gas [24] (Table 1).

Table 1 Beneficial and non-beneficial aspects of pyrolyzed products as fuels [18]

Pyrolyzed products	Beneficial aspects of fuel	Non-beneficial aspects	Quality enhancement
Bio-char	Higher heating value can be compared to charcoal and wood biomass	The additional energy required to obtain the compact form (briquetting)	–
Bio-oil	1. Value of heating can be compared to biodiesel fuels 2. Density is comparable with biodiesel fuels 3. Flashpoint is comparable with diesel and biodiesel fuels 4. GC-MS composition: Alkanes, alcohols, ethers, fatty acids, esters, and aromatics which are fuel grade chemicals	1. Viscosity value is high 2. Acidic value is high 3. Temperature of re-polymerization is low	Up-gradation and distillation could enhance the quality of the fuel
Pyrolyzed gas	Presence of combustible gases such as hydrogen, methane, ethane, and carbon monoxide	Carbon dioxide and nitrogen are present in a pyrolytic gas mixture	Carbon dioxide separation required

7 Solar-Assisted Thermochemical Pyrolysis Production Technique

The production of solar bio-fuels through the thermochemical techniques depends on different kinds of biomass feedstock, operating parameters of the reactor, design of the integrated system, and pyrolysis reactor of the solar concentrator. Different types of solar concentrators or solar furnaces are used for the pyrolysis of biomass through solar radiation.

Essential types of solar concentrators are (i) Fresnel lens (Fig. 7), (ii) parabolic dish or Scheffler dish (Fig. 7), (iii) parabolic trough, and (iv) heliostat (used in solar pyrolysis technology) (Fig. 7).

In the pyrolysis reactors, for attaining low temperature, parabolic dishes are used, medium temperatures are obtained using a Fresnel lens, and high temperatures are obtained using heliostats.

Many researchers obtained the average reactor temperature approx. 360–600 °C using parabolic dishes and average reactor temperature approx. 550 °C using Fresnel lens [25].

Heliostat mirrors are utilized for receiving more radiation flux, which reflects solar radiation and makes it reach a concentrator, which further sends it to the pyrolysis reactor. The reactor is located between the concentrator and heliostat in the on-axis solar furnace because the solar radiation is distributed around the reactor symmetrically [26]. It is difficult to provide the distribution of uniform solar flux inside the pyrolysis reactor. This complicated task can be solved by using a rotating reactor working inside the area of a fixed bed reactor. Joardder et al. presented an approach sliding solar concentration and rotating reactor for solar heating [27].

Morales et al. introduced a parabolic trough for solar pyrolysis and calculated temperature profile and heat losses. Thermodynamic principles are used in the analysis of heat balance and found the temperature gradient is approx.—36.24% between ambient and reactor [28] (Table 2).

8 Conclusion

Plants use sunlight to make their food by the process of photosynthesis. Thus, a lot of energy is stored in green plants and crops. As these crops are used, they die, and the residual energy is trapped in them. While burning the residue can convert the trapped energy into biomass energy, an alternative to burning can be solar energy aided pyrolysis. Following are the conclusions:

1. Crop residue has excellent potential as industrial raw material and livestock feed.
2. Crop residues are used entirely as well as partially for making healthy soil and sustainable agriculture.
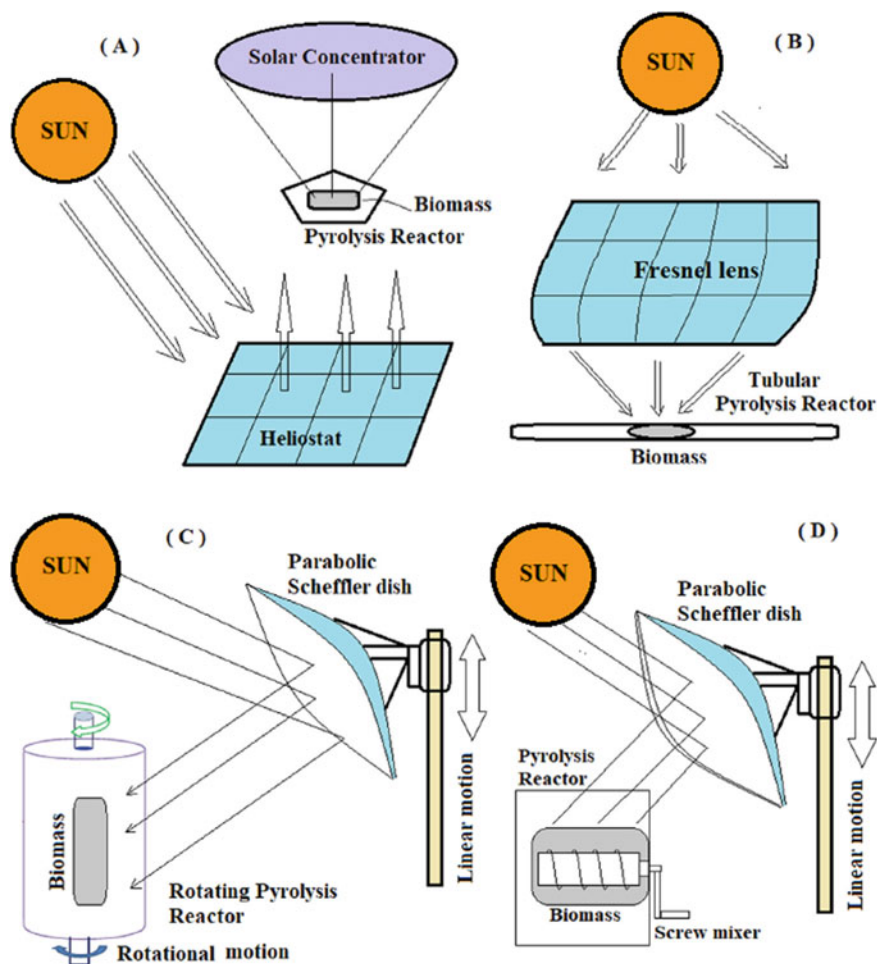
Fig. 7 Solar energy integrated pyrolysis reactor mechanisms shown with schematic diagrams; **a** solar concentrator based on heliostat, **b** solar concentrator based on Fresnel lens, **c** sliding solar concentrator with rotating reactor and Scheffler dish, and **d** biomass screw mixer and Scheffler dish [11]

Table 2 Different kinds of biomasses undergoing solar thermochemical pyrolysis

Feed stock	Type of pyrolysis reactor used	References
Date seeds biomass Fixed bed reactor	Extremely heated stainless steel	Joardder et al. [27]
Agriculture and forestry residual biomass	Transparent pyrex ballon reactor	Li et al. [29]
Beech wood biomass	Transparent pyrex ballon reactor	Zeng et al. [22]
Orange peels biomass	Tabular pyrolysis reactor	Morales et al. [28]
Beech wood biomass	Fixed bed tabular reactor	Zeaiter et al. [25]

3. Burning of crop residue has become a first issue for global warming as well as is a health issue.
4. Few techniques to use the crop residue are retaining the nutrient in the soil as bio-char, compost, and mechanization.
5. Bio-fuels (biomass) from the thermochemical process can be used successfully through solar concentrator and maximum utilization of the Fresnel lens and parabolic concentrator in solar radiation for concentrating.
6. Solar bio-fuels through the thermochemical technique depends on different kind of biomass feedstock, operating parameters of the reactor, design of the integrated system, and pyrolysis reactor of the solar concentrator.
7. Different types of solar concentrators or solar furnaces are used for the pyrolysis of the biomass process through solar radiation.
8. Pyrolysis product of agriculture waste such as bio-char, bio-oil, and pyrolytic gas used in heating, transport, and power sector but bio-oil need for up-gradation for running engines.

References

1. Kannan, N., Vakeesan, D.: Solar energy for future world: a review. Renew. Sustain. Energy Rev. **62**, 1092–1105 (2016)
2. Weldekidan, H., Strezov, V., Town, G., Kan, T.: Production and analysis of fuels and chemicals obtained from rice husk pyrolysis with concentrated solar radiation. Fuel **233**, 396–403 (2018)
3. Smil, V.: Crop residues: agriculture's largest harvest: crop residues incorporate more than half of the world's agricultural phytomass. Bioscience **49**(4), 299–308 (1999)
4. Zhang, Z., Liu, J., Shen, F., Yang, Y., Liu, F.: On-line measurement and kinetic studies of sodium release during biomass gasification and pyrolysis. Fuels **178**, 202–208 (2016)
5. Zhou, L., Yang, H., Wu, H., Wang, M., Cheng, D.: Catalytic pyrolysis of rice husk by mixing with zinc oxide: characterization of bio-oil and its rheological behavior. Fuel Process. Technol. **106**, 385–391 (2013)
6. Lim, J.S., Manan, Z.A., Alwi, S.R.W., Hashim, H.: A review on utilisation of biomass from rice industry as a source of renewable energy. Renew. Sustain. Energy Rev. **16**(5), 3084–3094 (2012)
7. Yang, L., Wang, X.Y., Han, L.P., Spiertz, H., Liao, S.H., Wei, M.G., Xie, G.H.: A quantitative assessment of crop residue feedstocks for biofuel in North and Northeast China. Gcb Bioenergy **7**(1), 100–111 (2015)
8. Sarkar, N., Ghosh, S.K., Bannerjee, S., Aikat, K.: Bio-ethanol production from agricultural wastes: an overview. Renew. Energy **37**(1), 19–27 (2012)
9. Saini, J.K., Saini, R., Tewari, L.: Lignocellulosic agriculture wastes as biomass feedstocks for second-generation bioethanol production: concepts and recent developments. 3 Biotech **5**(4), 337–353 (2015)
10. Bhuvaneshwari, S., Hettiarachchi, H., Meegoda, J.N.: Crop residue burning in India: policy challenges and potential solutions. Int. J. Environ. Res. Public Health **16**(5), 832 (2019)
11. Chintala, V.: Production, upgradation and utilization of solar assisted pyrolysis fuels from biomass—a technical review. Renew. Sustain. Energy Rev. **90**, 120–130 (2018)
12. Jain, N., Bhatia, A., Pathak, H.: Emission of air pollutants from crop residue burning in India. Aerosol Air Qual. Res. **14**(1), 422–430 (2014)

13. Deren, C.W., Snyder, G.H., Tai, P.Y.P., Turick, C.E., Chynoweth, D.P.: Biomass production and biochemical methane potential of seasonally flooded inter-generic and inter-specific Saccharum hybrids. Biores. Technol. **36**(2), 179–184 (1991)
14. Mittal, S.K., Singh, N., Agarwal, R., Awasthi, A., Gupta, P.K.: Ambient air quality during wheat and rice crop stubble burning episodes in Patiala. Atmos. Environ. **43**(2), 238–244 (2009)
15. Lohan, S.K., Jat, H.S., Yadav, A.K., Sidhu, H.S., Jat, M.L., Choudhary, M., Sharma, P.C.: Burning issues of paddy residue management in north-west states of India. Renew. Sustain. Energy Rev. **81**, 693–706 (2018)
16. Hoornweg, D., Bhada-Tata, P.: What a waste: a global review of solid waste management, vol. 15, p. 116. World Bank, Washington, DC (2012)
17. Jiang, C., Mu, X., Wang, F., Zhao, G.: Analysis of extreme temperature events in the Qinling Mountains and surrounding area during 1960–2012. Quatern. Int. **392**, 155–167 (2016)
18. Chintala, V., Kumar, S., Pandey, J.K., Sharma, A.K., Kumar, S.: Solar thermal pyrolysis of non-edible seeds to bio-fuels and their feasibility assessment. Energy Convers. Manage. **153**, 482–492 (2017)
19. Duku, M.H., Gu, S., Hagan, E.B.: Biochar production potential in Ghana—a review. Renew. Sustain. Energy Rev. **15**(8), 3539–3551 (2011)
20. Hussain, M., Farooq, M., Nawaz, A., Al-Sadi, A.M., Solaiman, Z.M., Alghamdi, S.S., Siddique, K.H.: Biochar for crop production: potential benefits and risks. J. Soils Sediments **17**(3), 685–716 (2017)
21. Lee, J., Kim, K.H., Kwon, E.E.: Biochar as a catalyst. Renew. Sustain. Energy Rev. **77**, 70–79 (2017)
22. Zeng, K., Flamant, G., Gauthier, D., Guillot, E.: Solar pyrolysis of wood in a lab-scale solar reactor: influence of temperature and sweep gas flow rate on products distribution. Energy Procedia **69**, 1849–1858 (2015)
23. Yang, H., Yao, J., Chen, G., Ma, W., Yan, B., Qi, Y.: Overview of upgrading of pyrolysis oil of biomass. Energy Procedia **61**, 1306–1309 (2014)
24. Zeng, K., Gauthier, D., Minh, D.P., Weiss-Hortala, E., Nzihou, A., Flamant, G.: Characterization of solar fuels obtained from beech wood solar pyrolysis. Fuel **188**, 285–293 (2017)
25. Zeaiter, J., Ahmad, M.N., Rooney, D., Samneh, B., Shammas, E.: Design of an automated solar concentrator for the pyrolysis of scrap rubber. Energy Convers. Manage. **101**, 118–125 (2015)
26. Yadav, D., Banerjee, R.: A review of solar thermo-chemical processes. Renew. Sustain. Energy Rev. **54**, 497–532 (2016)
27. Joardder, M.U., Halder, P.K., Rahim, A., Paul, N.: Solar assisted fast pyrolysis: a novel approach of renewable energy production. J. Eng. (2014)
28. Morales, S., Miranda, R., Bustos, D., Cazares, T., Tran, H.: Solar biomass pyrolysis for the production of bio-fuels and chemical commodities. J. Anal. Appl. Pyrol. **109**, 65–78 (2014)
29. Li, R., Zeng, K., Soria, J., Mazza, G., Gauthier, D., Rodriguez, R., Flamant, G.: Product distribution from solar pyrolysis of agricultural and forestry biomass residues. Renew. Energy **89**, 27–35 (2016)

Investigations on Ethanol as the Raw Material for Hydrogen Production, Storage, and Applications

Neeraj Budhraja[ID]**, Amit Pal**[ID]**, and Anil Kumar**[ID]

1 Introduction

The use of fossil fuel for vehicles and power generation resulted in the rapid rise in environmental pollution throughout the globe in the last few decades. Though the main source of combustion in the fossil fuels was hydrogen, a large amount of the polluting gases was generated in the burning process [1]. If the hydrogen could be extracted from fossil fuels and then the extracted hydrogen was used for combustion, then a considerably huge amount of the air pollution will be reduced. Before considering heavy hydrocarbons to generate pure hydrogen, the hydrogen was extracted from the lighter hydrocarbon compounds like ethanol. The ethanol has higher hydrogen to carbon content and it could be easily produced from the fermentation of biomass like sugarcane [2]. Thus, the source of ethanol further makes hydrogen more environmentally friendly.

The process of the ethanol conversion for the production of hydrogen might vary from high-temperature steam reforming and autothermal reforming. However, the use of catalyst considerably reduced the requirement of high temperatures in the processes [3, 4]. Although the low-temperature processes like cold plasma reforming showed better hydrogen yield. Despite the high ethanol conversion and higher hydrogen selectivity, the cold plasma processes were implemented in small-scale hydrogen production [5]. The present study discussed the pathway of the ethanol conversion to hydrogen as depicted in Fig. 1. The various hydrogen production methods included in this study were steam reforming, autothermal reforming, and few methods of cold plasma reforming, respectively. In the later part of the study, the methods of hydrogen storage and various applications were also discussed.

N. Budhraja (✉) · A. Pal · A. Kumar
Department of Mechanical, Production & Industrial and Automobile Engineering, Delhi Technological University, Delhi 110042, India
e-mail: neeraj_budhraja@yahoo.com
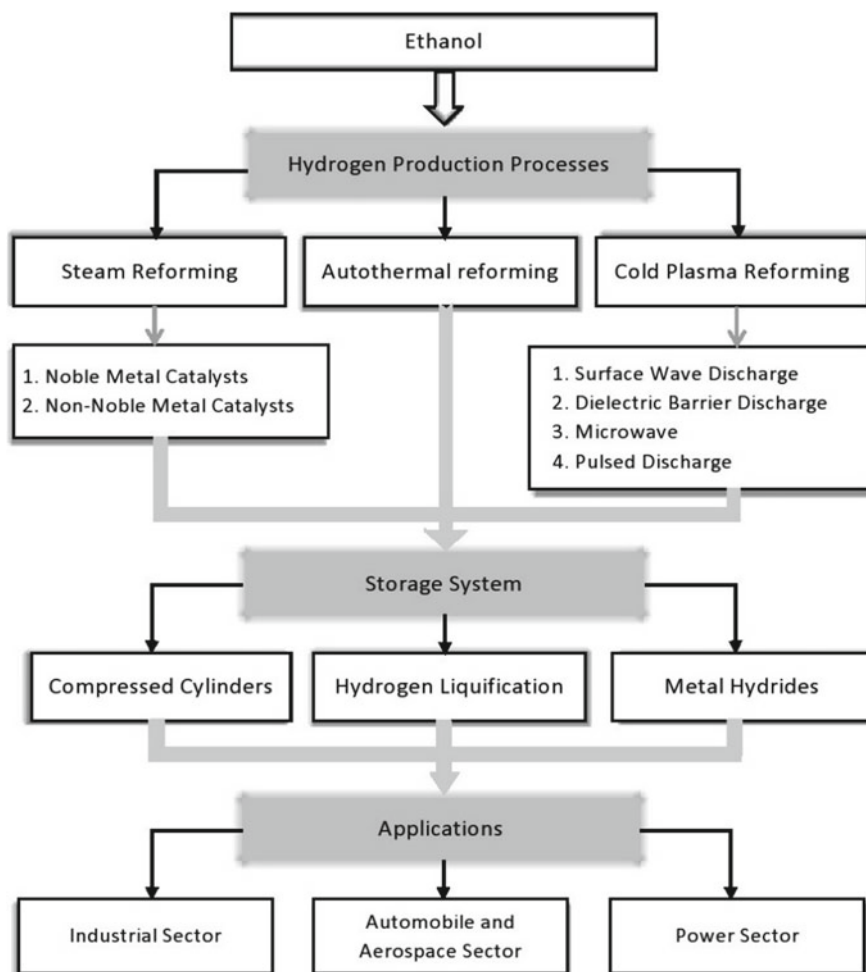
Fig. 1 Schematic block diagram of hydrogen pathway

2 Ethanol Conversion to Hydrogen

Ethanol has a renewable source and it can be easily fermented from biomass like sugarcane. Ethanol being in the liquid state has advantages of storage, handling, and transportation while non-toxic nature and low volatility are other advantages. However, the relatively high content of hydrogen to carbon confirmed ethanol as one of the best raw materials for hydrogen production [2]. The various processes of hydrogen production were discussed below.

2.1   Ethanol Steam Reforming

The steam reforming of ethanol was carried out at very high temperatures inside the reactor. The steam supply should be sufficiently high to occur the reaction (1) to produce the highest possible hydrogen yield from steam reforming of ethanol [2, 3, 6],

$$C_2H_5OH + 3H_2O \rightarrow 2CO_2 + 6H_2 \tag{1}$$
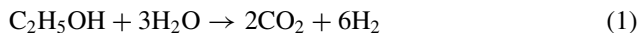
Though the insufficient supply of steam leads to the reactions (2) and (3) generating undesirable products with reduced hydrogen concentration in the product gas,

$$C_2H_5OH + H_2O \rightarrow 2CO + H_2 \tag{2}$$

$$C_2H_5OH + 2H_2 \rightarrow 2CH_4 + H_2O \tag{3}$$
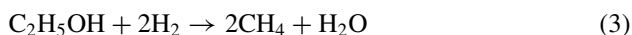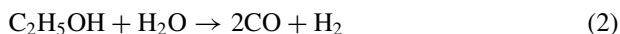
Further reduction in the hydrogen production was noticed with coke formation by the dehydration of ethanol as reactions (4) and (5),

$$C_2H_5OH \rightarrow CO + C_2H_4 + H_2O \tag{4}$$

$$C_2H_4 \rightarrow Coke(decomposition) \tag{5}$$
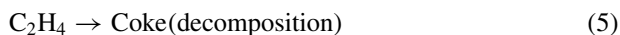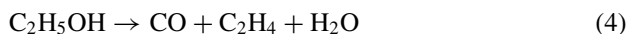
And decomposition of ethanol as the reactions (6) and (7),

$$C_2H_5OH \rightarrow CO + CH_4 + H_2 \tag{6}$$

$$2C_2H_5OH \rightarrow C_2H_6O + CO + 3H_2 \tag{7}$$
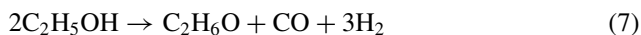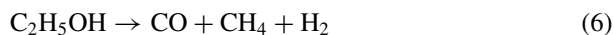
While the actual ethanol conversion reactions for the high hydrogen yield were performed by the dehydrogenation reactions (8), (9), and (10) as follows [7],

$$C_2H_5OH \rightarrow C_2H_4O + H_2 \tag{8}$$

$$C_2H_4O \rightarrow CH_4 + CO \tag{9}$$

$$C_2H_4O + H_2O \rightarrow 3H_2 + 2CO \tag{10}$$
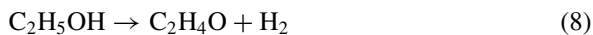
Also, the undesirable products of the above reactions were decomposed by the methanation reactions (11) and (12) as,

$$CO + 3H_2 \rightarrow CH_4 + H_2O \tag{11}$$

$$CO_2 + 4H_2 \rightarrow CH_4 + 2H_2O \tag{12}$$
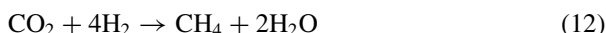
And methane decomposition reaction (13) as,

$$CH_4 \rightarrow 2H_2 + C \tag{13}$$

whereas the coke reduction was carried out by the Boudouard reaction (14) as shown below,

$$2CO \rightarrow CO_2 + C \tag{14}$$

And water gas shift reaction (15) as follows,

$$CO + H_2O \rightarrow CO_2 + H_2 \tag{15}$$

The ethanol steam reforming consists of the catalytic reactions and the catalysts used were studied below.

Noble Metal Catalysts. The high catalytic activity is the main advantage of the noble metal catalysts. The various commonly used noble metal catalysts for the ethanol steam reforming process are Rh, Ru, Pd, and Pt, respectively. The best catalytic property at low as well as high loading for ethanol conversion was shown by catalyst Rh [3]. While Ru showed similar characteristics at the high loading of above 5 wt%. About 100% ethanol conversion was achieved with the noble metal catalysts with over 95% of hydrogen selectivity [6].

Non-noble metal catalysts. The non-noble metals like Ni and Co are widely used in the catalytic ethanol steam reforming for hydrogen production. Although Al_2O_3 was considered very familiar supporting oxides for Ni or Co catalysts. Both Ni and Co are very active in breaking C–C bonds, while the high activity in the hydrogenation prioritized the use of Ni catalyst over Co [7]. However, Ni catalyst showed low activity for water gas shift reaction. This drawback of Ni was overcome by adding Cu because dehydrogenation was favored by Cu [8]. The non-noble metal catalyst also attained about 100% ethanol conversion, whereas the hydrogen selectivity was lower than the noble metal catalysts.

2.2 Autothermal Reforming of Ethanol

The steam reforming was performed under an oxygen-free environment and it was a high energy-consuming (or endothermic) process to trigger the reactions involved in the ethanol conversion [9]. Though the partial oxidation of ethanol certainly required oxygen for the hydrogen production at the comparatively lower temperature of 773 K

and the partial oxidation of ethanol was given by the reaction (16) as:

$$C_2H_5OH + {}^1/_2O_2 \rightarrow 2CO + 3H_2 \tag{16}$$
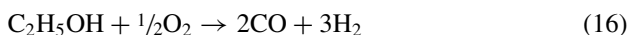
Though the reaction consumed lower energy the hydrogen yield was normally lower. The productions of the above reaction contain CO content which could be treated with steam to further enhance the hydrogen yield. Thus, the combination of the autothermal oxidation and steam reforming was performing simultaneously and the process was called autothermal reforming [4]. The reaction (17) was carried out in the autothermal reforming of ethanol.

$$C_2H_5OH + 2H_2O + {}^1/_2O_2 \rightarrow 2CO_2 + 5H_2 \tag{17}$$

This was the stable CO_2 was generated instead of CO, and thus the hydrogen production was raised. The autothermal reforming was performed with the various catalysts. Therefore, the hydrogen selectivity achieved could go beyond 100% with about 95% ethanol conversion. Additionally, the coke formation was considerably restricted in the autothermal reforming of the ethanol due to the oxidation reaction [10]. Thus, the autothermal reforming of ethanol could be performed at long-term stable operations.

2.3 Cold Plasma Reforming of Ethanol

The ionization of the neutral gas due to the supply of energy to the electrons generates plasma, which could be either thermal plasma or non-thermal plasma. The non-thermal plasma contains highly energetic electrons of the temperature lower than the neutral gas and it was also called cold plasma [5].

Surface Wave Discharge (SWD) Plasma. The surface wave discharge plasma reactor was electrode-less while the plasma consisted of the high population density of active species. Ar gas was used as the neutral gas for generating plasma torch. The ethanol conversion occurred in the plasma reactor generated hydrogen, CO_2, and H2O as the main products, respectively [11]. Though the further addition of water enhanced the hydrogen yield with reduced CO_2 production and no carbon deposit.

Dielectric Barrier Discharge (DBD) Plasma. The dielectric barrier discharge plasma reactor used the electrodes placed a few millimeters away from each other and the neutral gas was a dielectric barrier (like Ar or O_2) to generate cold plasma at the atmospheric pressure. The raw material used in the DBD plasma reactor was the combination of vaporized ethanol and water for producing hydrogen. The different by-products obtained from the DBD plasma ethanol conversion were CO, CH_4, C_2H_4, C_2H_6, and C_3H_8 [12]. However, more than 88% of the ethanol conversion was reached with about 30–40% of hydrogen yield, respectively.

Microwave Plasma. The microwave plasma reactor generated as high as 2.45 GHz frequency microwaves with only a few kW of power supply. The neutral gas (or the working gas) is commonly used as Ar, N_2, and CO_2, which carry vapors of ethanol or ethanol–water mixture into the plasma reactor. The airflow swirl was recommended and metal igniter was used to split microwave and then trigger the plasma formation [13]. About 99% of ethanol conversion was achieved with the enhanced hydrogen production at comparatively high purity.

Pulsed Discharge Plasma. The pulsed discharge plasma reactor used high current when the voltage decreased rapidly due to the formation of the spark discharge from the needle-shaped Pt electrode. The reactor was filled with the ethanol–water mixture and the sudden rise in current decomposed the ethanol/water molecules into hydrogen and oxides of carbon due to the high energy electrons. It was the light energy that was emitted from the spark discharge which initiates the photocatalysis process [14]. Thus, the small-scale production of high purity hydrogen gas was achieved with the pulsed discharge plasma.

3   Hydrogen Storage Systems

The storage system of the fuel is very important to transport the fuel from the site of production to the end-users. The hydrogen gas has good density by weight but poor density by volume, and thus the storage of hydrogen became a challenging area for the researchers [15, 16]. The few storage systems for hydrogen were discussed below.

3.1   Compressed Cylinders

The compression of gas for storage in the high pressurized gas cylinders is a very common and widely used method. The hydrogen was mainly compressed at about 20–25 MPa pressures [17]. The main characteristics of the materials used for the high-pressure cylinders include high tensile strength at low density and non-reacting nature with hydrogen. The security measures of the storage system are another concern with the pressurized gas cylinders for storing hydrogen since the hydrogen is highly explosive in nature [18]. These challenges made hydrogen gas difficult to store in large-scale using compressed gas cylinders.

3.2   Hydrogen Liquefaction

The liquid hydrogen is colorless and non-corrosive and has high liquid density storage efficiency [19]. However, the cryogenic temperature below $-253\,°C$ was required for

the liquefaction of hydrogen, and thus the highly efficient thermal insulator vessels were mandatory for the hydrogen storage. The storage vessels were made of carbon fiber, which cost about 75% of the total vessel cost. The process of hydrogen liquefaction was energy-consuming, and about 30–33% of the total energy of hydrogen was consumed in the liquefaction process only [20]. While the storage capacity through liquefaction raised to 0.070 kg/L as compared to 0.030 kg/L for hydrogen compression [21].

3.3 Metal Hydrides

Another storage medium and getting more attention nowadays for hydrogen storage was based on the metals or alloys in the form of the metallic hydrides. The hydrogen molecules got absorbed on the metal hydrides and then desorbed when the temperature was raised to about 120–200 °C, respectively [16]. The metal hydrides storage system was quick, secure, and proceed in both directions smoothly at moderate conditions. However, the high storage capacity of about 5–7 wt% was noticed [22]. Thus, the higher energy density by volume, large mass of hydrogen density, and safety labeled the metal hydrides as the promising hydrogen storage system. While hydrogen purity and low operating and maintenance costs were additional advantages of metal hydrides over other storage methods.

4 Applications

The various sectors for the hydrogen application included the industrial sector, automobile and aerospace sector, and power sector, respectively. The chemical industries utilized the hydrogen in the material refining and treatment, production of ammonia for fertilizers, and food processing. While the automobile and aerospace sectors used hydrogen or both hydrogen and oxygen as fuel. However, the power sector generated heat and electricity through either direct combustion or in the fuel cells [15, 16, 23].

4.1 Industrial Sector

Hydrogen was used in the petrochemical production in the petroleum industries for the hydrocracking of the heavy hydrocarbons. The sulfur and nitrogen compounds were hydrogenated and converted into hydrogen sulfide and ammonia [23]. Ammonia was the main raw material for the production of the fertilizers, and hydrogen was extensively used as the reactant for ammonia formation. About half of the hydrogen production was utilized in the ammonia formation throughout the globe [19]. The other important hydrogen applications in the chemical industries included

food processing, pharmaceuticals, glass purification, semiconductor manufacturing, and in the manufacturing processes like welding, annealing, and heat treatment, respectively.

4.2 Automobile and Aerospace Sector

Hydrogen was also extensively used in the aerospace sector as the propellant fuel for spacecraft. The blends of hydrogen and oxygen were used as the fuel to create enough thrust for the propulsion of the rockets into space. However, the hydrogen could also be used in both spark ignition and compression ignition engines directly as either dual fuel mode or single fuel mode [16], while the high-grade purity hydrogen was utilized in the fuel cells to generate electricity for the components of the vehicle. Although the storage of the hydrogen in the fuel tanks for the vehicles was the main challenge for the researchers due to the low energy by volume of hydrogen and also hydrogen storage required bulky and expensive storage systems [17].

4.3 Power Sector

The simplest utilization of the hydrogen in the power generation was by direct combustion in the boiler to produce steam for the turbines to generate electricity. While the other uses in the electric power sector included as the coolant for the large generators and processing of nuclear fuels. Nowadays, fuel cells have emerged the most extensively electricity-producing methods. Hydrogen was the main fuel for the fuel cells and the by-products coming out of the fuel cells were pure water and, in some cases, pure water and little carbon dioxide, respectively. The fuel cells could achieve as high as 60–70% of the energy conversion efficiency [24]. However, the additional advantages of the fuel cells included the static nature with the silent operation, i.e., operation without noise and vibrations.

5 Conclusions

The fermentation of biomass like sugarcane produces ethanol which is renewable in nature. The hydrogen to carbon content is comparatively higher in the ethanol, and thus it could be considered an effective source of hydrogen production. In the current study, the methods of hydrogen production from ethanol were discussed in brief. The steam reforming and autothermal reforming showed higher ethanol conversion with higher hydrogen selectivity, while the cold plasma processes produced hydrogen at lower temperatures. But the energy efficiency was very low in the cold plasma processes and thus could only be considered for small-scale hydrogen production.

In the later section, the storage methods for hydrogen were discussed. It was found that hydrogen has a low energy density by volume, which makes hydrogen gas difficult to store. Lastly, the applications of hydrogen gas were studied. The hydrogen was considered a very valuable component in the chemical industries for petroleum processing, pharmaceuticals, and food processing processes. The automobile and aerospace industries used hydrogen gas as fuel for vehicles and rockets. While the hydrogen in the power sector was either directly combusted or used in the fuel cells for electricity generation.

Therefore, if the cost of production and the challenges related to the storage of hydrogen will be overcome, then the hydrogen will be proved as the best fuel for industrial, automobile and aerospace, and power generation sectors, respectively.

References

1. Dawood, F., Anda, M., Shafiullah, G.M.: Hydrogen production for energy: an overview. Int. J. Hydrogen Energy **45**, 3847–3869 (2020). https://doi.org/10.1016/j.ijhydene.2019.12.059
2. Ni, M., Leung, D.Y.C., Leung, M.K.H.: A review on reforming bio-ethanol for hydrogen production. Int. J. Hydrogen Energy **32**, 3238–3247 (2007). https://doi.org/10.1016/j.ijhydene.2007.04.038
3. Liguras, D.K., Kondarides, D.I., Verykios, X.E.: Production of hydrogen for fuel cells by steam reforming of ethanol over supported noble metal catalysts. Appl. Catal. B Environ. **43**, 345–354 (2003). https://doi.org/10.1016/S0926-3373(02)00327-2
4. Deluga, G.A., Salge, J.R., Schmidt, L.D., Verykios, X.E.: Renewable hydrogen from ethanol by autothermal reforming. Science **303**(5660), 993–997 (2004)
5. Chen, F., Huang, X., Cheng, D.G., Zhan, X.: Hydrogen production from alcohols and ethers via cold plasma: a review. Int. J. Hydrogen Energy **39**, 9036–9046 (2014). https://doi.org/10.1016/j.ijhydene.2014.03.194
6. Cavallaro, S., Chiodo, V., Freni, S., Mondello, N., Frusteri, F.: Performance of Rh/Al$_2$O$_3$ catalyst in the steam reforming of ethanol: H$_2$ production for MCFC. Appl. Catal. A Gen. **249**, 119–128 (2003). https://doi.org/10.1016/S0926-860X(03)00189-3
7. Sun, J., Qiu, X.P., Wu, F., Zhu, W.T.: H$_2$ from steam reforming of ethanol at low temperature over Ni/Y$_2$O$_3$ and Ni/La$_2$O$_3$ catalysts for fuel-cell application. Int. J. Hydrogen Energy **30**, 437–445 (2005). https://doi.org/10.1016/j.ijhydene.2004.11.005
8. Mariño, F., Baronetti, G., Jobbagy, M., Laborde, M.: Cu-Ni-K/γ-Al$_2$O$_3$ supported catalysts for ethanol steam reforming: formation of hydrotalcite-type compounds as a result of metal-support interaction. Appl. Catal. A Gen. **238**, 41–54 (2003). https://doi.org/10.1016/S0926-860X(02)00113-8
9. Fierro, V., Akdim, O., Provendier, H., Mirodatos, C.: Ethanol oxidative steam reforming over Ni-based catalysts. J. Power Sources **145**, 659–666 (2005). https://doi.org/10.1016/j.jpowsour.2005.02.041
10. Wanat, E.C., Suman, B., Schmidt, L.D.: Partial oxidation of alcohols to produce hydrogen and chemicals in millisecond-contact time reactors. J. Catal. **235**, 18–27 (2005). https://doi.org/10.1016/j.jcat.2005.07.015
11. Henriques, J., Bundaleska, N., Tatarova, E., Dias, F.M., Ferreira, C.M.: Microwave plasma torches driven by surface wave applied for hydrogen production. Int. J. Hydrogen Energy **36**, 345–354 (2011). https://doi.org/10.1016/j.ijhydene.2010.09.101
12. Wang, B., Lü, Y., Zhang, X., Hu, S.: Hydrogen generation from steam reforming of ethanol in dielectric barrier discharge. J. Nat. Gas Chem. **20**, 151–154 (2011). https://doi.org/10.1016/S1003-9953(10)60160-0

13. Czylkowski, D., Hrycak, B., Miotk, R., Jasiński, M., Dors, M., Mizeraczyk, J.: Hydrogen production by conversion of ethanol using atmospheric pressure microwave plasmas. Int. J. Hydrogen Energy **40**, 14039–14044 (2015). https://doi.org/10.1016/j.ijhydene.2015.06.101

14. Xin, Y., Sun, B., Zhu, X., Yan, Z., Zhao, X., Sun, X.: Hydrogen production from ethanol solution by pulsed discharge with TiO_2 catalysts. Int. J. Hydrogen Energy **43**, 9503–9513 (2018). https://doi.org/10.1016/j.ijhydene.2018.04.062

15. Abdalla, A.M., Hossain, S., Nisfindy, O.B., Azad, A.T., Dawood, M., Azad, A.K.: Hydrogen production, storage, transportation and key challenges with applications: a review. Energy Convers. Manag. **165**, 602–627 (2018). https://doi.org/10.1016/j.enconman.2018.03.088

16. Sinigaglia, T., Lewiski, F., Santos Martins, M.E., Mairesse Siluk, J.C.: Production, storage, fuel stations of hydrogen and its utilization in automotive applications-a review. Int. J. Hydrogen Energy **42**, 24597–24611 (2017). https://doi.org/10.1016/j.ijhydene.2017.08.063

17. Zhang, Z., Hu, C.: System design and control strategy of the vehicles using hydrogen energy. Int. J. Hydrogen Energy **39**, 12973–12979 (2014). https://doi.org/10.1016/j.ijhydene.2014.06.010

18. Zhang, F., Zhao, P., Niu, M., Maddy, J.: The survey of key technologies in hydrogen energy storage. Int. J. Hydrogen Energy **41**, 14535–14552 (2016). https://doi.org/10.1016/j.ijhydene.2016.05.293

19. Barthelemy, H., Weber, M., Barbier, F.: Hydrogen storage: recent improvements and industrial perspectives. Int. J. Hydrogen Energy **42**, 7254–7262 (2017). https://doi.org/10.1016/j.ijhydene.2016.03.178

20. Niaz, S., Manzoor, T., Pandith, A.H.: Hydrogen storage: materials, methods and perspectives. Renew. Sustain. Energy Rev. **50**, 457–469 (2015). https://doi.org/10.1016/j.rser.2015.05.011

21. Zhang, Y.H., Jia, Z.C., Yuan, Z.M., Yang, T., Qi, Y., Zhao, D.L.: Development and application of hydrogen storage. J. Iron Steel Res. Int. **22**, 757–770 (2015). https://doi.org/10.1016/S1006-706X(15)30069-8

22. Schulz, R., Huot, J., Liang, G., Boily, S., Van Neste, A.: Structure and hydrogen sorption properties of ball milled Mg dihydride. Mater. Sci. Forum. **312**, 615–622 (1999). https://doi.org/10.4028/www.scientific.net/msf.312-314.615

23. Ramachandran, R., Menon, R.K.: An overview of industrial uses of hydrogen. Int. J. Hydrogen Energy **23**, 593–598 (1998). https://doi.org/10.1016/s0360-3199(97)00112-2

24. Sharaf, O.Z., Orhan, M.F.: An overview of fuel cell technology: fundamentals and applications. Renew. Sustain. Energy Rev. **32**, 810–853 (2014). https://doi.org/10.1016/j.rser.2014.01.012

Performance and Emissions Analysis of a Dual Fuel Diesel Engine with Biogas as Primary Fuel

S. Lalhriatpuia and **Amit Pal**

1 Introduction

The issues identified with the shortage of fossil fuel were witnessed all over the world. A worrying concern has been always there for a long while due to low fossil fuel reserve, which has been enhanced further when the hypothesis of peak oil production was accepted by various other studies. Most researchers and associations concur that the apex oil generation date will be in near future [1]. The generation of CO_2 from the over burning of the petroleum products contribute fundamentally to global warming [2]. Thus, to address the problems stated some alternative fuels both renewable and non-renewable were studied by many researchers to supplement either a part or all of the fossil fuels for the utilization in the internal combustion (IC) engines. The fossil fuels like petrol and diesel are commonly used as the pilot fuel for IC engines, whereas biodiesel and other alcohol fuels are considered as alternate pilot fuels. Hydrogen, syngas, and biogas are among the gaseous fuels which have studied to find an alternate gaseous fuel to be used in IC engine [3]. Thus, the sustainable energy sources and their consumption to generate heat and power were the key variables for the viable progress of the nation.

A standout among the most critical inexhaustible energizes was biogas, which basically consisted methane content of 30–70% and carbon dioxide content of 30–50% by volume. Further, the renewable and environmentally friendly nature crafted biogas very promising alternative fuel for IC engines. Although the biodiesel with insignificant sulfur and fragrant substance showed higher lubricity, cetane number, flash point, biodegradability, and non-toxicity and thus, became good contender for the liquid fuel alternative in IC engines [4]. Also, bio-alcohol achieved viability

S. Lalhriatpuia (✉) · A. Pal
Department of Mechanical, Production & Industrial and Automobile Engineering, Delhi Technological University, Delhi, India
e-mail: sactrix777@gmail.com

to be used in the CI engines for both as pilot fuel and blended fuels. The bio-alcohols mainly considered for IC engine fuels were ethanol, butanol, methanol, and propanol, respectively [5]. Biogas was also employed in the duel fueled CI engines by employing it in a dual fueled mode where biogas would act as a primary gaseous fuel [6]. Dual-fueled engine has the benefit of flexibility, i.e., the ability to transform instantly to a normal diesel engine when there is a deficit of the gaseous fuel. Also, dual fueling has the benefit of achieving lower NO_x without much of a compromise in the efficiency [7]. Dual fueling is accomplished in such a way that the engine would mostly be operated on biogas or any other primary fuel, whereas diesel or any other pilot would act as the means of achieving a combustion. The transformation of diesel to a dual fueled engine is simple and easy, and it is achieved just by the addition of two components. The first being the fuel air mixing chamber connected to the inlet of engine and secondly a regulating lever to alter the input of pilot fuel to the engine. Hence, as no alternation is needed in the engine itself, dual fueling becomes more appealing [8].

The various performance parameters for dual fuel mode and single fuel mode were computed in many research studies. Yoon and Lee [9] revealed that using biodiesel as the pilot fuel lowered the BTE in comparison with dual fueled operation system using diesel as the pilot fuel. Meanwhile, with biogas as the primary gaseous fuel in dual fuel mode using CI engine attained higher about 32% of BTE. While the marginal influence of the biogas quality was noticed in the BTE [10]. A decline on BSEC was noted when there was increase in load, in both mode of operation, i.e., only diesel and dual-fueled while study also reveals that BSEC of the blend of Jatropha biodiesel–biogas to higher than diesel–biogas [6]. However, the diesel only mode exhibit lowers BSEC than dual fueled mode for the different loading conditions [9]. The decrease in the volumetric efficiency (VE) was computed with rise in brake torque and load for dual fuel system operation. Although the reduction in VE was more for dual fueled mode when compared to diesel only fuel run [11, 12], the peak liquid fuel replacement (LFR) of 69% and 66% for diesel and jatropha pilot fuel was measured at 100% load [6].

The engine emissions were another major concern under environmental index. CO emission being the outcome of improper combustion was enhanced in dual fueled operation in comparison with the diesel only fuel mode. For dual fueled operation with biogas as the gaseous fuel, the decrease in CO emission by 50% and 16% for diesel and jatropha biodiesel, respectively, when measured in comparison with the diesel mode [6, 7]. CO_2 emission in exhaust is an implication of fuel undergone proper combustion, which was found to rise with the upsurge in load for both the modes of operation, i.e., diesel mode and dual fuel mode, though higher CO_2 emissions were detected in biogas–diesel fuel mode than biogas–biodiesel mode especially at higher loads [6, 7, 13]. The hydrocarbon (HC) emissions were the other emissions resulted from incomplete combustion of fuel, and with increase in load, the HC emissions were higher for both modes of operation, i.e., diesel and dual fueled with biogas. [13]. NO_x emission was observed with biodiesel added fuels for higher loads due to the higher temperatures. However, many after exhaust devices and methods could be implemented for the NO_x emission reduction [2, 5, 7]. An investigation

conducted with soybean–biodiesel when compared with diesel revealed that except the NO_x emission, all other emission parameters to decline. It was also recorded that the BSFC for the biodiesel to rise since the calorific value of biodiesel was lesser than diesel [14]. An investigation conducted using ethanol blend with diesel in a HCCI engine showed reduction in NO_x and smoke in comparison with the diesel only mode for all loading conditions. While the ethanol blend also showed considerably higher HC and CO in comparison with the diesel only mode [15]. A study conducted using the different ratio in blend of waste cooking oil, jatropha, and soybean with diesel revealed that all the B20 blend shows a approximal value of BTE when compared with diesel, also the NO_x is found to be the lowest for all loads. The same study also reveals the blend of waste cooking having higher NO_x than the other two blends [16]. An investigation done for varying blends of esterified Karanja oil with diesel revealed that this blend of fuel to be a good alternative fuel especially making the farmers to be more self-sufficient in ambiguous times. A lower VE was obtained using diesel for all loads in comparison with the blended fuel and BSFC being lower initially but comparable to the diesel mode with the further increase in load. BTE of diesel was higher in comparison with the blended fuel [17]. A study for performance and emission analysis was conducted using B20 blended fuels from different generation feedstock levels found that the performance parameters deteriorates while the emission was drastically reduced. In particular, spirulina microalgae and Jatropha curcas blend were found to have a significant improvement in the performance parameters while the emissions like NO_x, PM, and smoke emissions were in decline [18].

In this study, the dual fuel mode system was considered for the experimentation work and the fuel used were diesel–biogas, soya–biodiesel–biogas, and soya–biodiesel–ethanol–biogas, respectively. The proper mixing of the air and biogas was ensured with the modified air intake system of the engine [19]. Engine characteristics were observed and compared among the different dual-fueled blends.

2 Physiochemical Properties of Biogas

2.1 Biogas Chemical Composition

The chemical composition of biogas varies with the source of the waste used for production. Biogas has a corrosiveness nature due to the its constituent in the form of CO_2, H2S, and water. Also based on the input parameters in the production of biogas, the chemical composition differs. Table 1 gives the composition of the biogas generated from different biomass.

Table 1 Physiochemical properties of biogas

Composition	55–70% methane, 30–45% carbon dioxide, traces of other gases
Calorific value	4500–5000 kcal/m^3
Ignition temperature	650–750 °C
Critical pressure	75–89 bar
Critical temperature	−82.5 °C
Normal density	1.2 kg/m^3
Stoichiometric A/F ratio	10:1
Octane rating	130
Odor	Bad eggs (smell of hydrogen sulfide)

2.2 Biogas Physical Properties

Biogas is a colorless stable gas, which is non-toxic in nature, with the smell similar to rotten eggs. When the mixture of biogas was burnt, a blue flame was generated producing a substantial amount of heat and energy [20]. The various physiochemical properties of the biogas were presented in Table 1.

2.3 Physiochemical Properties of Test Fuel

The physiochemical properties of the pilot fuel used for this experiment are mentioned in Table 2.

Table 2 Physiochemical properties of pilot fuel used

S. No.	Characteristics	Diesel	SBD	SBDE
1	Density (kg/m^3)	831	859	857
2	Lower heating value (MJ/kg)	43.85	38.8	38.7
3	Kinematic viscosity at 40 °C (cSt)	2.92	3.85	3.55
4	Cetane number	45–55	43	44
5	Oxidation stability	High	No	No
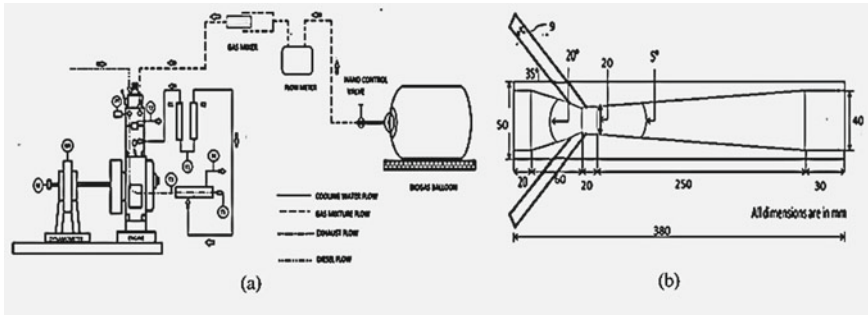
Fig. 1 Schematic diagram of **a** the experimental test setup; and **b** fuel–air mixing chamber

3 Experiment

3.1 Setup

On a four-stroke single cylinder diesel engine available in the IC engines Lab of mechanical Department of DTU, Delhi, this study was performed. To operate in dual mode, some changes were made in the test setup of constant compression ratio (CR) engine. A gas mixer was installed before the air inlet of the engine where the mixing of gaseous fuel and pilot fuel was done, and mixture is passed on to the engine as shown in Fig. 1a. In the first schematic diagram, the elements involved in the working setup for this experiment have been detailed and presented. Also, the design used for the gas mixer has been presented in the schematic diagram of the mixer in Fig. 1b.

The fuel–air mixing chamber was installed at the inlet manifold to modify the diesel engine into the dual fuel engine. The desirable quantity and quality of biogas–air mixture was delivered by the fuel–air mixing chamber and thus, the fuel–air mixing chamber proved as a dynamic component and enhanced smooth operation for all different running conditions of the engine. The design and fabrication of fuel–air mixing chamber was done through taking consideration of the different parameters of the engine, i.e., volumetric efficiency, rated power, speed, specific fuel consumption, swept volume, and manifold connection diameter of the engine. The pictorial engine test setup and key components are shown in Fig. 2. The specification of the engine used for this investigation is mentioned in Table 3.

3.2 Procedure and Process Chart

The experiment was carried out by running engine in on two modes. The first being operating it in pilot fuel only system and secondly using biogas and diesel in a dual fueled system. The modified CI engine was first made to operate on diesel at the standard diesel specification of CR 18 and ignition timing of 23° before TDC. The
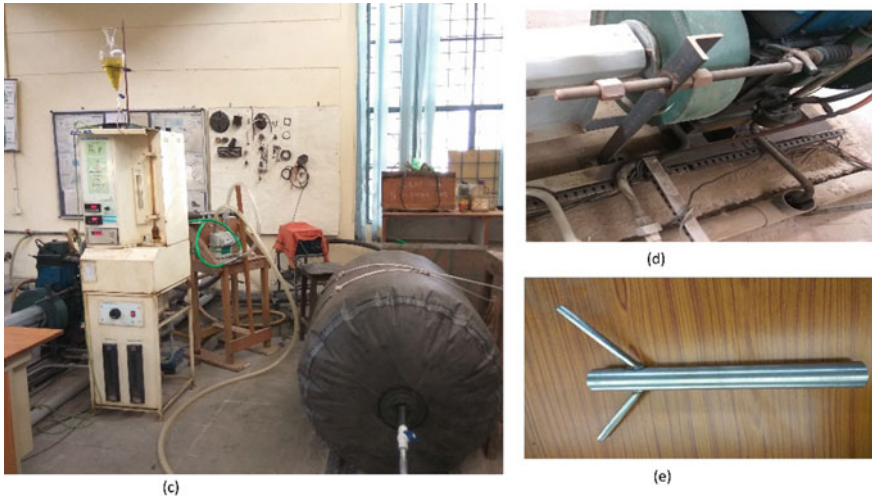
Fig. 2 Pictorial representation of **a** modified engine setup, **b** regulating lever, **c** fuel–air mixing chamber

Table 3 Specification of the VCR diesel engine

Parameter	Specification
Manufacturer	Kirloskar
Model	TV1
No. of cylinder	One
No. of stroke	4 stroke
Power	5.2 kW @ 1500 rpm
Bore	87.5 mm
Stroke	110 mm
CR	18:1
Speed	1500 rpm, constant
Injection timing	23° BTDC
Dynamometer	Eddy-current (Make: Saj, Model: AG10)
System software	'Enginesoft' engine performance analysis software

engine loads of 20%, 40%, 60%, 80%, and 100% were tested in the experimentation. 12 kg loading is considered as the 100% load, with 2.4 kg interval for each load. The engine was initially made to operate for a short period of time to stabilize before recording the temperatures, rpm and load during each test. Before each test run, the outlet valve of the tank was closed and then fuel tank was refilled. The measuring buret at the front was filled before each new run through the outlet valve of the fuel tank. The rate of diesel consumption was determined by observing the amount of fuel consumed per minute from the measuring buret in the panel.

Fig. 3 Process chart for diesel mode operation
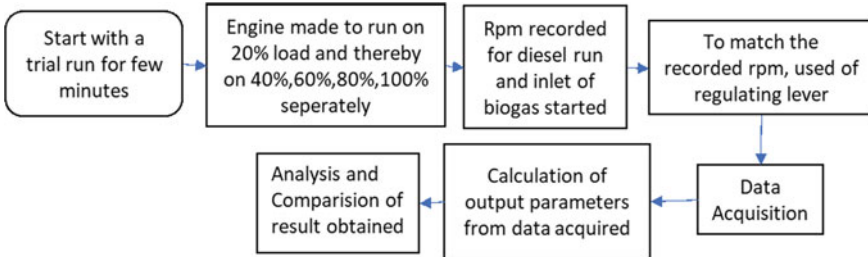
Fig. 4 Process chart for dual fuel mode operation

The rate of air flow was calculated using manometer by observing change in the heights of water column. The diesel mode rpm was noted for a particular load, and then gradually biogas supply valve was opened. The speed of the engine was boosted with the biogas inflow due to the additional energy provided by the combustion of biogas inside the engine cylinder. Until the rpm stopped increasing any further, the flow of biogas was gently raised. Meanwhile, the speed of engine is further lowered by the action of governor. Hence in dual fuel mode at any specific load to achieve the matching rpm, pilot fuel consumption was regulated by means a regulating lever. In each run, the engine was made to run for a short duration before recording the start and finish of the 30 s meter reading. The quantity of gas utilized during the experiment was determined accounting the contrast between the initial and final gas readings. AVL DiGas 444 analyzer was utilized for emission analysis from the engine exhaust.

4 Results and Discussions

The performance and emission analysis of the modified CI engine utilizing diesel, soybean–biodiesel (SBD), and soybean–biodiesel–ethanol (SBDE) as the liquid fuel and biogas as a primary gaseous fuel in a dual fueled system were discussed in the following section.

4.1 Performance Analysis

The parameters that were analyzed in the study for making a performance analysis were brake thermal efficiency (BTE), brake-specific fuel consumption (BSFC), volumetric efficiency (VE), exhaust gas temperature (EGT), and liquid fuel replacement (LFR), respectively. Performance of each parameter with load variation has been depicted in the graphs as shown in Fig. 5.

The BTE demonstrated a rise with increment in load for the entire modes of operation as demonstrated in Fig. 5a. BTE for diesel only mode exhibits the highest for all loads since it has the highest calorific value among all. Also, the BTE was establish for diesel dual fueled operation to be greater than the other dual fuel modes
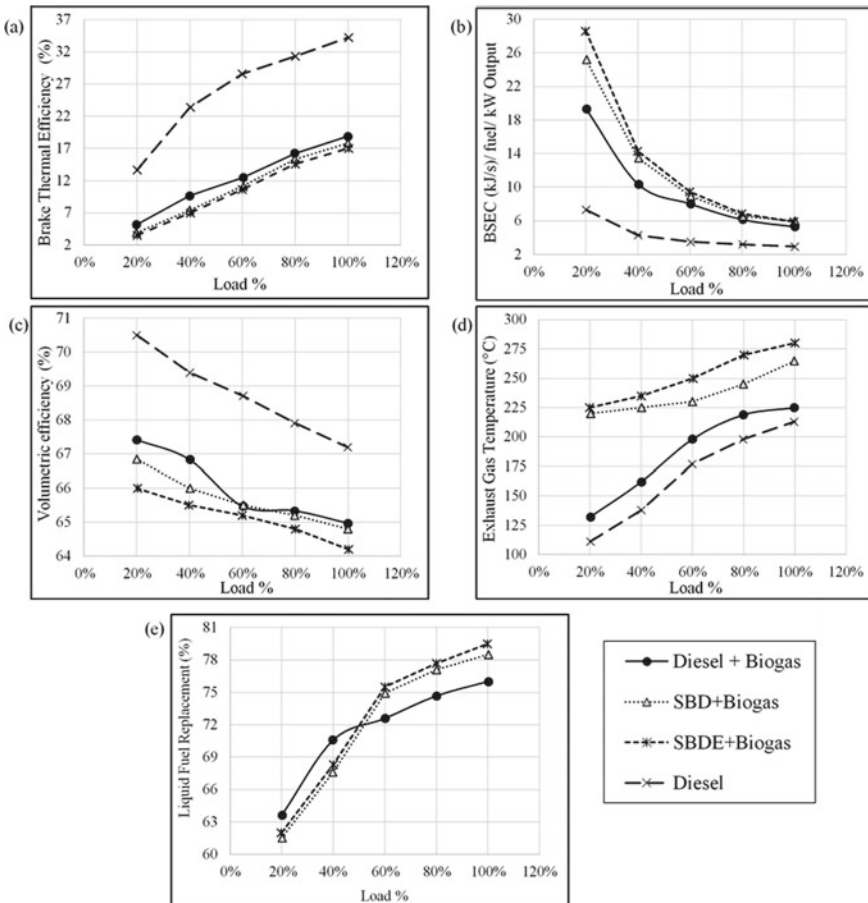
Fig. 5 Load versus the performance parameter curves for **a** brake thermal efficiency; **b** brake-specific fuel consumption; **c** volumetric efficiency; **d** exhaust gas temperature; and **e** liquid fuel replacement

of operation, because the net energy supplied being lower for dual fueled run with diesel as the liquid fuel. The reason being the other two liquid fuels has lesser calorific value which thereby increases its fuel consumption and hence resulting in lower BTE. While in full load condition among the dual fueled modes, the BTE calculated for diesel dual fuel mode was highest 18.86% followed by SBD and SBDE duel fuel modes with values of 17.81% and 17%, respectively. With the increment in load, the BSEC for all dual fuel modes as mentioned in Fig. 5b. The diesel dual fuel mode exhibits lower BSEC in comparison with the other two modes, because diesel possesses higher calorific value than that of the other two pilot fuels. For initial lower loads, the gap in the curves of diesel and dual fueled mode is found to be more which could be result of inability of transformation of biogas to energy, while for the higher loads the gap between the curves are narrow or in other words better BSEC for dual fuel mode since there is more transformation of biogas to energy. For 100% loads, an improvement of more than 50% was obtained in BSEC for the dual fueled modes in comparison with diesel mode.

In Fig. 5c, VE variation with the load has been stated. The graph showed reduction in VE with the rise in load increased for all the modes of operation. The dual modes exhibit lower VE than diesel mode because of higher substitution of air with biogas as the load increases. At about 100% load, the VE for diesel dual fueled mode was calculated as 64.96%, whereas the other dual fuel modes of SBD and SBDE were 64.8% and 64.2%, respectively. From Fig. 5d, as load increases, EGT was measured to increase for both diesel and dual fueled modes. The EGT of dual fueled mode is higher than that of diesel for all the loads, because of the late combustion of biogas thereby the exhaust products raising the temperature. The curve of SBDE was well above the curves of other modes of operation since it is the constituent of biodiesel and ethanol. This leads to the pre-heating of the inlet fuel, and thus, the VE reduction was noticed. The range of EGT for SBDE was 225–280 °C, while for diesel and SBD modes were 220–265 °C and 132–225 °C, respectively. The variation of LFR with load showed similar variation for all the dual fuel modes as demonstrated from Fig. 5e. The variation in the LFR was ranged between 61.5% and 79.5% for all the duel fuel modes. Thus, the various performance parameters confirmed that though the dual fueled modes exhibit lower BTE than diesel mode, the high LFR for dual fueled modes compensate to some sense, thereby reducing the dependence on diesel alone and making the road to more self-sufficient using alternative fuels.

4.2 Emission Analysis

The engine emission analysis was performed in Fig. 6 for various dual fuel mode and diesel mode which include the measurement of load variation with carbon monoxide (CO), hydrocarbon (HC), carbon dioxide (CO_2), and oxides of nitrogen (NO_x), respectively.
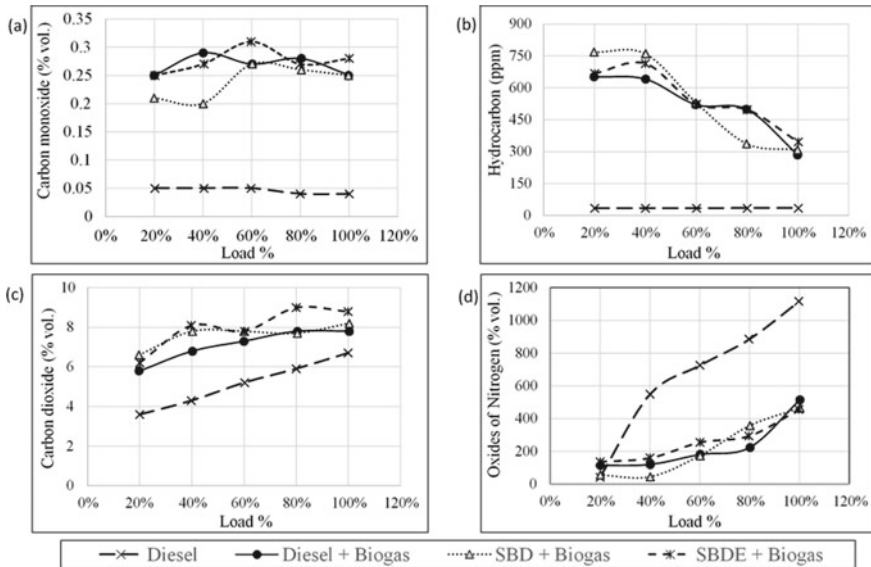
Fig. 6 Load variations with the engine emissions for different dual fuel modes measured for **a** carbon monoxide; **b** hydrocarbon; **c** carbon dioxide; and **d** oxides of nitrogen

CO for diesel was found to be higher in comparison with all the other dual fueled modes, the reason being biogas substituting air in dual fuel mode resulting incomplete combustion. Figure 6a shows the occurrence of CO in the engine exhaust with the varying loads. It was observed that CO emissions were moderately high at initial stage and then grew with the rise in the loads till the peak value was achieved at about 50–60% load, the curve turn down beyond 60% loads. However, maximum in SBDE dual fueled mode was observed for the CO emissions in comparison with the other modes. The unburned HC was another engine emission related to the poor combustion of the fuel inside the engine cylinder.

A considerably lower HC was observed for diesel mode in comparison with other modes, forming of HC in the dual fueled mode being resulted by low flame velocity of biogas. The trend of HC with the varying loads was described in Fig. 6b. The HC emission showed higher concentration in the exhaust during the starting and at lower loads since more fuel was injected during the initial stage of engine operation. But once the fuel–air mixture became leaner, the HC emissions reduced gradually.

The presence of CO_2 in the engine emissions indicated the better fuel combustion. For all the modes of operation with the rise in load, an increment in the emission of CO_2 was observed as shown in Fig. 6c. The dual fueled modes were observed to have higher CO2 emission due to the fact that among biogas composition, carbon dioxide constitutes nearly 50%. While a small reduction was observed at about 50–60% load condition where sharper elevation in the CO production was noticed, then further rise in load contributed in the CO_2 combustion. The SBDE dual fuel mode measured with the highest CO_2 emission showing better dual fuel properties than diesel and

SBD, respectively. From Fig. 6d, the variation of NO_x generation in the exhaust was demonstrated. The higher temperatures resulted in the NO_x formation in the exhaust. As seen from Fig. 6d, during the initial stage of the engine operation when temperature was low, negligible amount of NO_x formation was noticed. When the load increased, the fuel requirement also increases, thereby leading to the generation of higher temperature further leading to the formation of NO_x in the exhaust. Diesel mode exhibits higher NO_x due to its higher caloric value in comparison with other dual fueled modes.

5　Conclusions

In this current study, the objective was to study the feasibility of using soya oil through blending with biogas as the primary gaseous fuel in the CI engine. Soya oil blended with diesel (SBD) and soya oil blend with diesel and ethanol (SBDE) were used as the liquid pilot fuel. The various engine parameters, i.e., BTE, BSEC, VE, EGT, and LFR, were evaluated. There was an improvement of over 50% for the dual fuel modes in comparison with the diesel mode, the highest 56% improvement for SBDE dual fueled mode. Though the BTE of SBDE dual fueled 17% which is low in comparison with diesel mode, the SBDE also has the highest LFR with 79.5% which make it a viable alternative fuel in context of reducing the dependency on diesel fuel.

The engine emissions were also examined with the load variations for all the dual fuel modes. The various exhaust gases involved in the emission analysis were CO, HC, CO_2, and NO_x, respectively. CO and CO_2 emissions were interconnected with the fuel burning property and can be interpreted from the study. The HC reduction was noticed with the presence of ethanol due to the availableness of extra oxygen for improved combustion of fuel. Also, the NO_x emission was lower for dual fueled mode when compared with the diesel only mode, particularly the NO_x of SBDE dual fueled mode were found to be 457 ppmv in comparison with the 1119 ppmv of diesel mode.

Therefore, from this investigation it is concluded that both dual fueled mode of SBD blend and SBDE blend was successful in testing feasibility. Also, also due to obtained result of high LFR and low NO_x, SBDE blend dual fuel mode is the more attractive option to reduce the dependence of fossil fuel while also reducing the emission, thereby making it more environment-friendly.

References

1. Almeida, D.P., Silva, P.D.: The peak of oil production-timings and market recognition. Energy Policy **37**, 1267–1276 (2009). https://doi.org/10.1016/j.enpol.2008.11.016
2. Papagiannakis, R.G., Hountalas, D.T.: Combustion and exhaust emission characteristics of a dual fuel compression ignition engine operated with pilot diesel fuel and natural gas. Energy

Convers. Manag. **45**, 2971–2987 (2004). https://doi.org/10.1016/j.enconman.2004.01.013

3. Prasath, B., Leelakrishnan, E., Lokesh, N.: Hydrogen operated internal combustion engines—a new generation fuel. Int. J. Emerg. Technol. Adv. Eng. **2**, 52–57 (2012)

4. Rakopoulos, D.C., Rakopoulos, C.D., Giakoumis, E.G., Papagiannakis, R.G., Kyritsis, D.C.: Influence of properties of various common bio-fuels on the combustion and emission characteristics of high-speed DI (direct injection) diesel engine: vegetable oil, bio-diesel, ethanol, n-butanol, diethyl ether. Energy **73**, 354–366 (2014). https://doi.org/10.1016/j.energy.2014.06.032

5. Budhraja, N., Pal, A.: Production, utilization and performance of diesel-biodiesel-ethanol blends in IC engine. In: Singh, R., Pal, A., Gautam, V., Kumar, G. (eds.) Recent Advances in Mechanical Engineering, pp. 409–416. Enriched Publications Pvt. Ltd, New Delhi, India (2016)

6. Bora, B.J., Saha, U.K., Chatterjee, S., Veer, V.: Effect of compression ratio on performance, combustion and emission characteristics of a dual fuel diesel engine run on raw biogas. Energy Convers. Manag. Energy Policy **87**, 1000–1009 (2014). https://doi.org/10.1016/J.ENCONMAN.2014.07.080

7. Namasivayam, A.M., Korakianitis, T., Crookes, R.J., Bob-Manuel, K.D.H., Olsen, J.: Biodiesel, emulsified biodiesel and dimethyl ether as pilot fuels for natural gas fuelled engines. Appl. Energy **87**, 769–778 (2010). https://doi.org/10.1016/j.apenergy.2009.09.014

8. Ryu, K.: Effects of pilot injection timing on the combustion and emissions characteristics in a diesel engine using biodiesel-CNG dual fuel. Appl. Energy **111**, 721–730 (2013). https://doi.org/10.1016/j.apenergy.2013.05.046

9. Yoon, S.H., Lee, C.S.: Experimental investigation on the combustion and exhaust emission characteristics of biogas-biodiesel dual-fuel combustion in a CI engine. Fuel Process. Technol. **92**, 992–1000 (2011). https://doi.org/10.1016/j.fuproc.2010.12.021

10. Luijten, C.C.M., Kerkhof, E.: Jatropha oil and biogas in a dual fuel CI engine for rural electrification. Energy Convers. Manag. **52**, 1426–1438 (2011). https://doi.org/10.1016/j.enconman.2010.10.005

11. Duc, P.M., Wattanavichien, K.: Study on biogas premixed charge diesel dual fuelled engine. Energy Convers. Manag. **48**, 2286–2308 (2007). https://doi.org/10.1016/j.enconman.2007.03.020de

12. Barik, D., Murugan, S.: Investigation on combustion performance and emission characteristics of a DI (direct injection) diesel engine fueled with biogas-diesel in dual fuel mode. Energy **72**, 760–771 (2014). https://doi.org/10.1016/j.energy.2014.05.106

13. Mitzlaff, K.V.: Engines for Biogas: Theory, Modification, Economic Operation. Wiesbaden, Germany (1988)

14. Yusaf, T., Zamri, M.: Development of a 3D Cfd model to investigate the effect of the mixing quality on the Cng-diesel engine performance. In: Proceedings of the International Conference and Exhibition and Natural Gas Vehicles. IANGV International Association of Natural Gas Vehicles, 1–14, Yokohama (2000)

15. Gawale, G.R., Naga Srinivasulu, G.: Experimental investigation of ethanol/diesel and ethanol/biodiesel on dual fuel mode HCCI engine for different engine load conditions. Fuel **263**, 116725 (2020). https://doi.org/10.1016/j.fuel.2019.116725

16. Chaurasiya, P.K., Singh, S.K., Dwivedi, R., Choudri, R.V.: Combustion and emission characteristics of diesel fuel blended with raw jatropha, soybean and waste cooking oils. Heliyon **5**(5) (2019). https://doi.org/10.1016/j.heliyon.2019.e01564

17. Chaurasiya, P.K., Dubey, P., Bharti, M.S.: Performance evaluation of biodiesel (pongamia or karanj oil) as an alternative fuel for diesel engine. Int. J. Appl. Sci. Eng. Res. **3**(1), 288–296 (2014). https://doi.org/10.6088/ijaser.030100028

18. Krishania, N., Rajak, U., Chaurasiya, P.K., Singh, T.S., Birru, A.K., Verma, T.K.: Investigations of spirulina, waste cooking and animal fats blended biodiesel fuel on auto-ignition diesel engine performance, emission characteristics. Fuel **276**, 118123 (2020). https://doi.org/10.1016/j.fuel.2020.118123

19. Canakci, M.: Combustion characteristics of a turbocharged DI compression ignition engine fueled with petroleum diesel fuels and biodiesel. Bioresour. Technol. **98**, 1167–1175 (2007). https://doi.org/10.1016/j.enpol.2008.11.016
20. Sharma, A., Ansari, N.A., Pal, A., Singh, Y., Lalhriatpuia, S.: Effect of biogas on the performance and emission of diesel engine fuelled with biodiesel-ethanol blends through response surface methodology approach. Renew. Energy **141**, 657–668 (2019). https://doi.org/10.1016/j.renene.2019.04.031

Combustion and Thermal Performance of Dual Fuel Engine: Influence of Controlled Producer Gas Substitution with Pilot B20 (WCOME Biodiesel–Diesel) Blending

Prabhakar Sharma and **Avdhesh Kr. Sharma**

1 Introduction

Producer gas derived from waste woody biomass is a green alternative for fossil fuel with high potential [1, 2]. The producer gas can be used for thermal and motive power applications via I.C. engines after suitable modification either in single fuel operation (i.e., complete substitution) or in dual fuel operation: fumigation mode (i.e., partial substitution), where the gaseous fuel is used as main energy source, while miniscule quantity of conventional liquid fuel, i.e., *pilot* fuel. It is sprayed on charge of air and gaseous fuel when compressed just to initiate *pilot or micro-pilot* ignition [3, 4]. Toward restricting the dependency of fossil diesel fuel, a suitable green fuel (e.g., vegetable or animal fatty acid) blended with fossil diesel fuel can be used as pilot fuel. Such operation in fumigation form ensures energy sustainability with ambient harmony. Researchers have performed experimental investigations on biomass gasification system to derive good quality producer gas [1, 2, 4–7]. Numerous works were documented on dual fuel fumigation based on producer gas and diesel as guiding fuel [3, 4, 8–11]. Yaliwal et al. [8] investigated a converted dual fuel engine (DFE) by using producer gas (as main fuel) with honge oil methyl ester (as pilot fuel) to study the effect of injector nozzle and geometry of combustion chamber (hemispherical and reentrant configurations) on the performance and emission. They reported that re-entrant type combustion chamber and four holes type injector nozzle show the optimum engine performance. Nayak et al. [9] explored the study on twin cylinder engine in dual fuel mode (DFM) and diesel saving of 83% at 8 kW load and sharp decrement of NO_x and smoke level. Dhole et al. [10] investigated the combustion parameters for pilot diesel and hydrogen, producer gas and their mixture, while Banapurmath et al. [11] reported dual fuel operation with various combinations of

P. Sharma · A. Kr. Sharma (✉)
MED, D.C.R. University of Science and Technology, Murthal, Sonepat, Haryana 131039, India
e-mail: avdhesh_sharma35@yahoo.co.in

alternate fuels including honge oil with producer gas and honge oil methyl ester with producer gas.

Studies are directed on DFE using pilot biodiesel–diesel blend and producer gas as main fuel [12–16]. Yaliwal et al. [12] reported superior gas-engine efficiency at compression ratio of 17.5:1 with injection pressure of 240 bar (also comparable with injection pressure of 230 bars) for honge seed oil methyl ester-producer gas-hydrogen operation. Nayak and Mishra [13] reported optimum injection pressure of 240 bar at 25.5° bTDC for waste cooking oil in comparison with neat diesel operation. Halewadimath et al. [14] reported that dual swirl combustion chamber performs best at CR of 17.5 with the injection pressure of 240 bars at 27° bTDC. Yaliwal et al. [14] investigated the performance of a gas-engine fueled from producer gas originated from different biomass feedstocks (i.e., babool, neem and honge wood) and concluded that honge oil methyl ester gives improved performance and lower emission. Carlucci et al. [3] invested engine performance with synthetic producer gas with biodiesel and recommended that spilt pilot fuel injection system performs better especially at low loads.

Research was conducted for mathematical and empirical modeling on producer gas operated DFE using pilot diesel and/or pilot biodiesel–biodiesel fuel [4, 17]. Various designs of producer gas-air mixer or carburetor for gas-engine were developed [4, 18–20]. Kumar and Sharma [18] developed a novel gas-carburetor design using ANSYS for quality mixing without appreciable pressure drop.

Numerous studies on thermal and emission performance of DFE using best producer gas substitution and pilot diesel/biodiesel were carried out. Hardly, any comprehensive study on DFE using pilot WCOME biodiesel–diesel with controlled producer gas substitution was reported. Presently, such combination of green fuels may be an attractive alternative for clean and sustainable energy production. Thus, herein, a dual fuel engine was run to assess performances at constant engine speed with green fuel combinations (a) neat diesel mode, (b) neat B20 WCOME biodiesel–diesel blend, and (c) pilot B20 with various controlled substitution of producer gas. In response to WCOME biodiesel–diesel and producer gas, the injection pressure and injection timing are fixed at 240 bars and 25° bTDC following [12–14].

2 Materials and Methods

2.1 Test Engine

The schematics of test engine converted from a small diesel engine (capacity 5.2 kW) into gas-engine using producer gas from a downdraft gasifier and pilot fuel as waste cooking oil methyl ester (WCOME) biodiesel–diesel blend as shown in Fig. 1. To counter in variation in physical property of blending of green fuels or fuel mixture including biodiesel–diesel and producer gas, the injection pressure has been increased from 200 to 240 bars and injection timing is retarded to 25° bTDC. Test engine is fitted
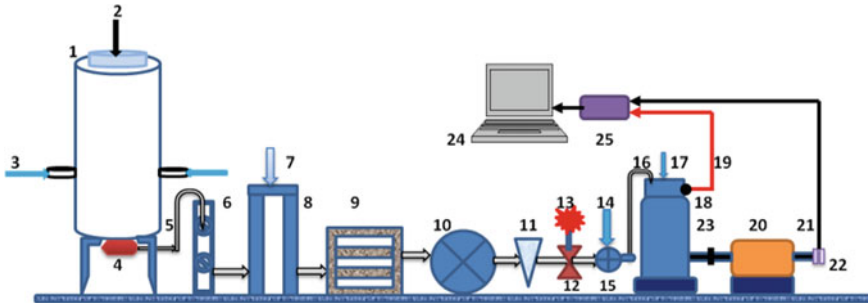
Fig. 1 Schematic diagram of gasifier-engine set up. 1: Downdraft gasifier, 2: Biomass inlet, 3: Air input, 4: Grate, 5: PG pipeline, 6: Cyclone scrubber, 7: Water spray, 8: Spray tower, 9: Sand bed filter, 10: Blower, 11: Fire arrester, 12: Gate valve, 13: Gas-burner, 14: Air induction, 15: Air-PG gas mixer, 16: Charge line, 17: Biodiesel inlet, 18: Pressure sensor, 19: Pressure line, 20: Eddy current dynamometer, 21: Crank angle sensing line, 22: Crank angle encoder, 23: Converted engine, 24/25: Laptop/KiBox analyzer

Table 1 Specification of a direct-injection, single-cylinder, diesel engine (Kirloskar)

S. No.	Parameters	Specifications engine
1	Compression ratio	17:1
2	Displacement volume	661 cc
3	Rated power	5.2 kW@ 1500 RPM
4	Nozzle pressure/ignition timing	200 bar/23° bTDC
5	Governor type	Mechanical centrifugal
6	Piston diameter/stroke	87.5 mm/110 mm
7	Dynamometer	SAJ make AG-20, water cooled eddy current

on a computerized test bench, having provision of air and fuel flow measurement. An eddy current dynamometer was used to vary load on engine through control panel. Details of specifications and instruments are given in Table 1.

2.2 In-Cylinder Combustion Analyzer

In this work, Kistler Instrument LG make "*Ki-Box To Go*" set—type 2893AK1 combustion analyzer was used to ensure high precision with real-time measurement of combustion data. A photographic view of KiBox installed on test engine is presented by Fig. 2a. It collects combustion data through a high-resolution pressure sensor installed directly on cylinder head via digital data acquisition system. The crank angle encoder (optical type) is installed at the end of engine crank shaft as exposed in Fig. 2b. The combination of pressure sensor, crank angle encoder enables
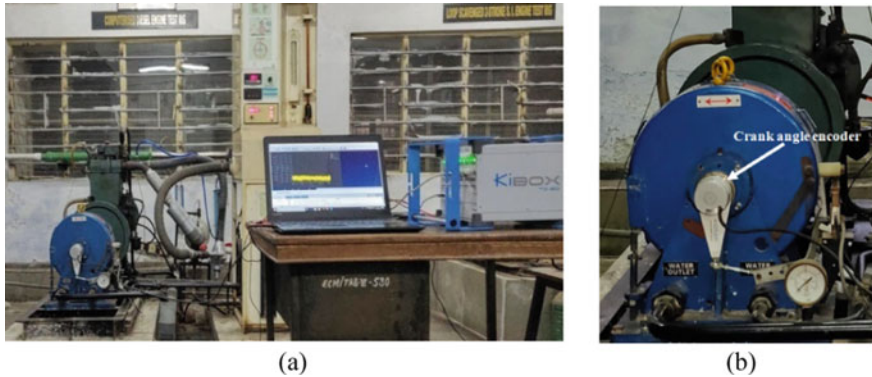
Fig. 2 View of **a** test engine with KiBox combustion analyzer and **b** eddy current dynamometer fitted with crank angle encoder

to measure in-cylinder pressure in consonance with respective crank angle in real time.

Retrofitting arrangements such as drilling and tapping the cylinder head were performed to install the pressure sensor. The synchronized analogue signal acquired through sensor and encoder is transformed into the digital signal, which is analyzed through cockpit software installed on computer. The data for cylinder pressure with respect to crank angle is used to obtain combustion performance parameters (i.e., peak pressure, rate of pressure rise, heat release rate, etc.). Technical specifications followed by measuring uncertainty, sensitivity of pressure sensor, and resolution crank angle encoder are listed in Table 2.

Table 2 Specifications of pressure sensor and crank angle encoder

Component	Specifications	Value/range
Pressure sensor	Range in bar	0–250
	Overload in bar	300
	Sensitivity in pC/bar	−17
	Acceleration sensitivity in bar/g	$\leq$0.0005
	Temperature range in °C	−20 to 400
Crank angle encoder	Resolution	720 × 0.5°
	Encoder type	Optical
	Speed range (1/min)	0–20,000
	Operating temperature range (°C)	−30 to 115
	Crank angle resolution	0.1° CA

Table 3 Properties: neat WCOME biodiesel and producer gas

S. No.	Properties	Units	ASTM D6751	WCOME	Producer gas
1	Kinematic viscosity	cStat 40 °C	1.9–6.0	3.86	–
2	Density	kg/m³ at 15 °C	860–900	868	1.01
3	Flash point	°C	>52	158	–
4	Pour point	°C	−15 to 16	−10	–
5	Calorific value	MJ/kg	>35.00	38.00	35.14

2.3 Test Fuel

2.3.1 Producer Gas

Producer gas or syngas was produced from a downdraft (biomass) gasifier using sundried babool wood, which was cut into small pieces of 2.5 cm. The wood was tested for moisture and ash contents, and it was found as 9% and 0.89%, while calorific value of feedstock worked out to be 20.28 MJ/kg. Gasifier pipeline was fitted with cooling-cleaning train to ensure the adequate cooling of hot producer gas and cleaning of particulate matters. Cooling is carried out in two water spray columns, while four tier-cleaning was done in course and fine sand bed filter. A fire arrester is provided just before the gas-burner to prevent the back fire during operation. Properly cooled and cleaned producer gas is burned at swirl-gas-burner for testing. The colorless or bluish flame ensures adequate gas quality. From gas-chromatograph available at IIT Delhi, the chemical composition of producer gas components H_2, N_2, CO, CO_2, and CH_4 is obtained as 14.8%, 47.7, 15.2%, 22.3%, and 0.0%, respectively. The properties of producer gas are listed in Table 3.

2.3.2 Waste Cooking Oil Methyl Ester

Waste or discarded cooking oil (WCO) after use was gathered out of local restaurants and cafes in Delhi. It was filtered and heated to remove impurities and converted to waste cooking oil methyl ester (WCOME) biodiesel through two-stage esterification process using methyl alcohol and potassium hydroxide [21]. After esterification, the phase separation method was used by leaving mixture in separating flasks for 16 h. Glycerol was settled at the bottom and was removed leaving behind the WCOME. Then WCOME was washed from the water to remove the catalyst impurities and heated to evaporate the excess methanol. WCOME was tested thereafter for its fuel properties at Enkay Test House, New Delhi. Table 3 presents these properties. The WCOME biodiesel and diesel blend were prepared in proportion of 20% and 80% and referred here as B20.

2.4 Experimental Procedure

Initially, the vertical shaft of gasifier is charged with charcoal and woody feedstock and then its top is closed with lid. Blower is started to create required suction to induct airflow through the gasifier without gasification for conducting the air leakage test. After test, the gasifier is fired via air tiers with lighter. Producer gas is gently formed, which is burned at the gas-burner. Initially, it burns with dark yellow–red flame and then after ~15 min the flame turns bluish or even colorless, which is an indication of enriched quality of producer gas suitable for engine use. The engine was started and waits till warming up. Subsequently, the producer gas is allowed to induct into gas-engine through a specially designed swirl-gas-carburetor as developed by Kumar and Sharma [18]. Substitution of the producer gas in gas-engine can be identified by change in sound during combustion. DFE was tested for blending of green fuel via experimentation in three different modes: neat diesel mode, B20 WCOME biodiesel–diesel mode without gas substitution and controlled producer gas substitution with Pilot B20 WCOME biodiesel–diesel blend.

3   Results and Discussion

In response to WCOME biodiesel–diesel blend and producer gas, the injection pressure and injection timing are fixed at 240 bars and 25° bTDC. The engine testing was carried out at constant engine speed of 1500 (with uncertainty of ±50 rpm) for neat diesel mode, B20 WCOME biodiesel–diesel blend and Pilot B20 WCOME biodiesel–diesel with producer gas substitutions of 1 g/s, 2 g/s, and 3 g/s. The performance parameter BTE and calorific value of B20 blend and producer gas are defined in Appendix.

3.1 Combustion Performance

Effect of B20 blending and/or controlled producer gas substitutions on cylinder pressure, heat release rate, rate of pressure change, and engine noise are presented.

3.1.1   In-Cylinder or Combustion Pressure

Trends of in-cylinder or combustion pressure against crank angle for neat diesel, neat B20 WCOME biodiesel–diesel mode and pilot B20 WCOME biodiesel–diesel with different controlled producer gas substitutions (i.e., 1 g/s, 2 g/s and 3 g/s) were compared in Fig. 3. The pressure profiles for neat diesel mode are highest followed by "neat B20 without producer gas substitution." The trends of combustion pressure
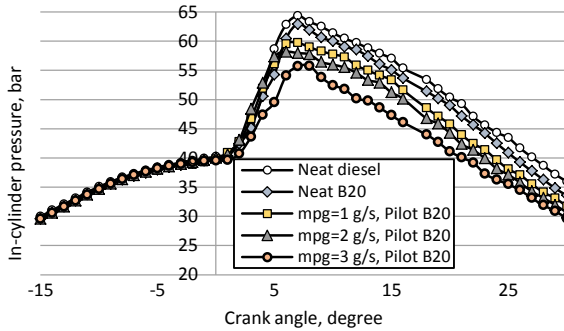
Fig. 3 Influence of blending/substitution of various green fuels on combustion pressure profile

profile decrease with increasing producer gas substitution with pilot B20 WCOME biodiesel–diesel fuel. The peak combustion pressures for neat diesel, neat WCOME biodiesel and pilot B20 with controlled producer gas substitutions, i.e., 1 g/s, 2 g/s, and 3 g/s are observed to be 64.3, 62.9, 59.7, 58.2, and 55.8 bar, respectively.

Peak combustion pressure for a given load depends on fuel mixing, combustion rate, and ignition delay. As B20 and/or lean producer gas are used as fuel, the depressed peak pressure response is expected due to their poor combustion characteristics. As substitution of lean producer gas increases more sluggish combustion pressure response is observed, as expected.

3.1.2   Rate of Pressure Change and Engine Noise

The rate of pressure change affects the engine noise and thus engine life. The trends of rate of pressure change and engine noise for all fuel combinations including neat diesel, neat B20 for B20 blending/gas substitution are highlighted. Unlike, in-cylinder pressure, in neat diesel mode, the trend for rate of pressure change is lowest, while highest for "producer gas substitution of 3 g/s with pilot B20" (Fig. 4). Similar trends are observed for engine noise (refer Fig. 5).

In engine, peak of rate of pressure change largely depends on rate of combustion during initial phase. The premixed phase or uncontrolled combustion depends upon ignition delay and mixing quality of fuel throughout the delay period. As rate of combustion for gaseous fuel is higher in premixed phase, it leads to higher rate of pressure rise and higher noise in DFM. Any visible increase in rate of pressure change indicates dependency of green fuel combinations on their combustion characteristics. The fuel with relatively poor combustion characteristic reflects higher rate change of pressure and thus higher engine noise or vibrations leading to short engine life.
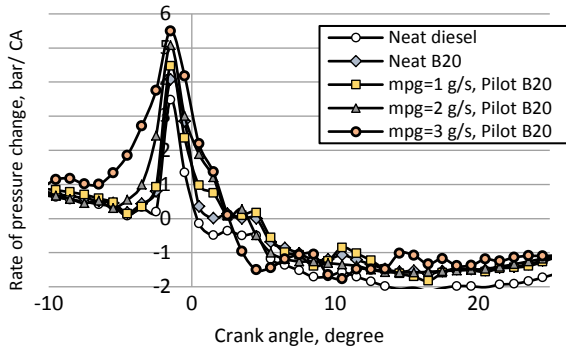
Fig. 4 Effect of blending/substitution of various green fuels on rate of pressure change profile
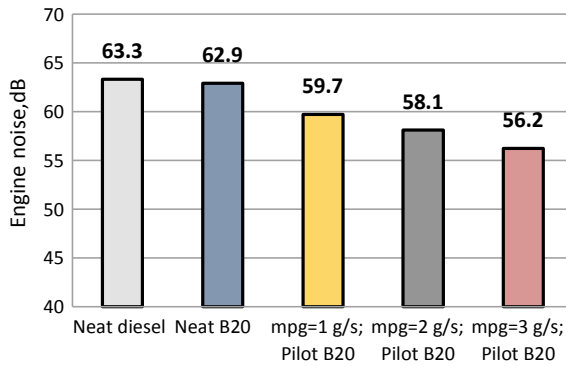
Fig. 5 Effect of B20 blending/gas substitution on engine noise

3.1.3 Heat Release Rate

Trends of heat release rate (HRR) for all fuel combinations are shown in Fig. 6. It is revealed that trend of HRR with neat diesel fuel is highest followed by neat B20 blend. In DFM using controlled producer gas substitution with pilot B20, these trends of HRR decrease further with higher producer gas substitution.

The HRR depends on ignition delay and calorific value of fuel mixture. Higher the calorific value, higher heat release rate can be expected. Such fuel combination (i.e., neat B20 and/or pilot B20 with controlled producer gas substitutions) reflects low calorific values and larger ignition delay periods, as a result lowering and late or delay heat release rate patterns is expected at 80% engine load.
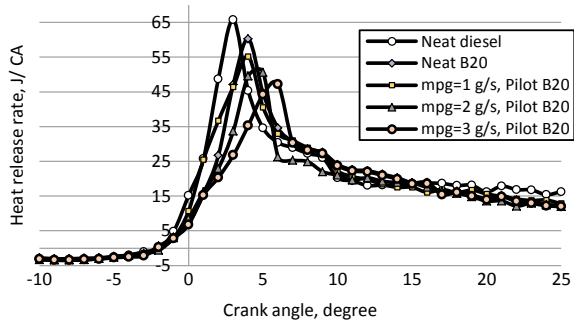
Fig. 6 Influence of blending of various green fuels on heat release rate profile

3.2 Thermal Performance

Trends of all fuel combinations (i.e., neat diesel, neat B20, and pilot B20 with producer gas substitutions) against entire engine load conditions have been discussed for liquid fuel consumption, BTE, and EGT.

3.2.1 Diesel/B20 Biodiesel–Diesel Consumption Rate

Figure 7 highlights the trends of liquid fuel consumption for all fuel combinations. The trend of fuel consumption for neat B20 is highest followed by neat diesel, while pilot B20 consumption decreases with increased substitution of producer gas.

For pilot B20 with producer gas substitution, both the producer gas and B20 contribute to total energy intake. As substitution of producer gas increases, larger
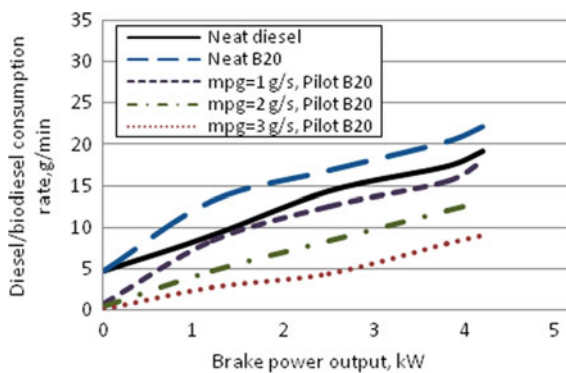
Fig. 7 Influence of blending/substitution of green fuels on diesel/B20 WCOME biodiesel consumption
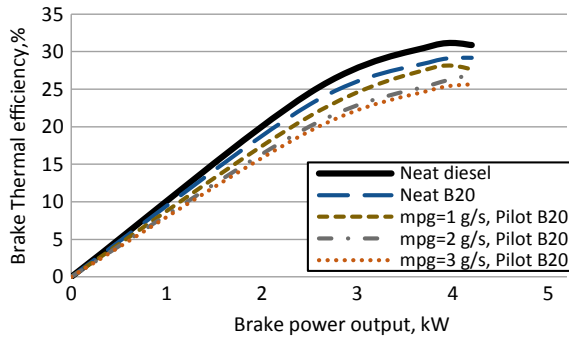
Fig. 8 Influence of blending/substitution of various green fuels on brake thermal efficiency

share of energy intake will be contributed by gas. Thus, share of pilot B20 biodiesel–diesel decreases with increasing producer gas substitution.

3.2.2 Brake Thermal Efficiency

Figure 8 presents the inclination of brake thermal efficiency (BTE) for various green fuels combination over the entire brake power range. The trends of BTE in neat diesel mode, neat B20 WCOME biodiesel without gas substitution mode, and pilot B20 with different producer gas substitutions (i.e., 1 g/s, 2 g/s, and 3 g/s) was found to be 30.9%, 29.2%, 27.7%, and 25.6%, respectively. The highest BTE is clearly reflected for neat diesel mode followed by neat B20 WCOME-diesel mode. The trends of BTE decrease with higher producer gas substitution with pilot B20 fuel in dual fuel mode.

The reason for reduction of BTE for neat B20 mode, pilot B20 with different producer gas substitutions is due to poor spray characteristics due to high viscosity of B20 WCOME biodiesel–diesel fuel followed by poor or slow combustion characteristics of lean producer gas (i.e., slow burning fuel).

3.2.3 Exhaust Gas Temperature

The effect of all fuel combinations (i.e., blending/substitution) on engine exhaust temperature (EGT) is presented in Fig. 9. In neat diesel mode, the trend of EGT is lowest followed by neat B20 mode, while for DFM using pilot B20 with producer gas substitutions, it is increase with higher producer gas substitution for entire load range.

It is understandable, as we substitute more energy input either from B20 (low calorific value fuel) and/or lean producer gas (i.e., slow burning fuel with higher ignition delay), the major part of energy release takes place during late burning/combustion phase results in higher EGT and lower engine efficiency.
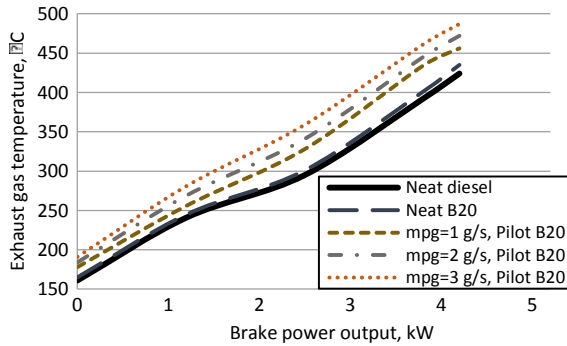
Fig. 9 Influence of blending/substitution of various green fuels on exhaust gas temperature

For gas-engine in dual fuel engine, any blending of biodiesel–diesel or substitution of producer gas results in poor brake thermal efficiency, leading to higher B20 biodiesel–diesel consumption and slow burning (facilitate heat exchange to burnt combustion products) due to higher ignition delay period and/or poor spray characteristics of B20 fuel especially in pilot mode. The fuel injector was designed originally for dedicated diesel engine for full diesel supply. In dual fuel mode, however, the supply of pilot liquid fuel is restricted due to substitution by gaseous fuel consequences of which larger droplets size flowed by oil dribbling. As a result of all such factors, in dual fuel mode, poor BTE followed by higher fuel consumption and higher thermal energy loss through exhaust leading to higher EGT as compared to neat diesel mode operation.

4 Conclusions

Dual fuel operations at constant engine speed of 1500 ± 50 rpm with neat diesel fuel, neat B20 WCOME biodiesel–diesel, and pilot B20 biodiesel–diesel with controlled producer gas substitutions were carried to analyze the combustion performance (i.e., in-cylinder or combustion pressure, peak pressure; rate of pressure change, heat release rate, and engine noise) and thermal performance (i.e., diesel/biodiesel consumption, BTH and EGT). Followings conclusions were deduced as:

1. Dual fuel engine operation is robust with pilot diesel fuel and renewable producer gas substitution. Utilization as green fuel either in blending and/or producer gas substitution is an attractive option to suppress dependency on fossil diesel fuel.
2. In dual fuel engine, any blending of green fuels either in form of WCOME biodiesel–diesel blend and/or substitution of producer gas results in

(a) Poor combustion performance (i.e., lower in-cylinder or combustion pressure, low heat release, higher rate of pressure change, and higher engine noise) and

(b) Degrade thermal performance, i.e., lower BTE leading to increased fuel consumption and higher EGT.

3. Although combustion and thermal performance of gas-engine deteriorated with B20 WCOME biodiesel–diesel blending and/or substitution of controlled producer gas, such option is benign to the ambient ensuring the sustainability by mitigating the dependency on fossil diesel fuel.

Appendix

The brake thermal efficiency of dual fuel engine can be obtained as:

$$\eta_{Th,b} = \frac{Brake\text{-}power}{\dot{m}_{Biodiesel}CV_{Biodiesel} + \dot{m}_{PG}CV_{PG}} \tag{1}$$

Here, $\dot{m}$ and CV are the mass flow rate and calorific value, respectively, their subscripts PG and biodiesel corresponds to producer gas and biodiesel respectively. The calorific value of producer gas can be calculated from relation in terms of reactive gas composition as:

$$CV_{PG} = 12.64\chi_{CO} + 10.76\chi_{H2} + 59.955\chi_{CH4} \tag{2}$$

Here χ is fraction of species in gas, its subscript is denotes the in terms of individual calorific values of reactive species.

The calorific value of pilot biodiesel blend can be obtained as

$$CV_{Biodiesel} = \lambda_{WCOME}CV_{WCOME} + (1 - \lambda_{WCOME})CV_{Wdiesel} \tag{3}$$

Here λ is mass fraction of WCOME biodiesel and diesel fuel. In this work, λ is fixed at 0.2.

References

1. Upadhyay, D.S., Makwana, H.V., Patel, R.N.: Performance evaluation of 10 kWe pilot scale downdraft gasifier with different feedstock. J. Energy Inst. **92**, 913–922 (2019). https://doi.org/10.1016/j.joei.2018.07.013
2. Ud Din, Z., Zainal, Z.A.: Biomass integrated gasification-SOFC systems: technology overview. Renew. Sustain. Energy Rev. **53**, 1356–1376 (2016). https://doi.org/10.1016/j.rser.2015.09.013

3. Carlucci, A.P., Ficarella, A., Laforgia, D., Strafella, L.: Improvement of dual-fuel biodiesel-producer gas engine performance acting on biodiesel injection parameters and strategy. Fuel **209**, 754–768 (2017). https://doi.org/10.1016/j.fuel.2017.07.100
4. Sharma, A.K.: Simulation of a biomass gasifier-engine system (2006)
5. Sharma, A.K.: Experimental investigations on a 20 kWe, solid biomass gasification system. Biomass Bioenerg. **35**, 421–428 (2011). https://doi.org/10.1016/j.biombioe.2010.08.060
6. Sharma, A.K.: Experimental study on 75 kWth downdraft (biomass) gasifier system. Renew. Energy (2009). https://doi.org/10.1016/j.renene.2008.12.030
7. Sharma, A.K.: Influence of biomass materials and gas flow rate on downdraft gasifier performance. In: 2012 IEEE 5th Power India Conference, PICONF 2012 (2012). https://doi.org/10.1109/PowerI.2012.6479570
8. Yaliwal, V.S., Banapurmath, N.R., Gireesh, N.M., Hosmath, R.S., Donateo, T., Tewari, P.G.: Effect of nozzle and combustion chamber geometry on the performance of a diesel engine operated on dual fuel mode using renewable fuels. Renew. Energy **93**, 483–501 (2016). https://doi.org/10.1016/j.renene.2016.03.020
9. Nayak, C., Achrya, S.K., Swain, R.K.: Performance of a twin cylinder diesel engine in dual fuel mode using woody biomass producer gas. Int. J. Sustain. Eng. **8**, 341–348 (2015). https://doi.org/10.1080/19397038.2014.977372
10. Dhole, A.E., Yarasu, R.B., Lata, D.B.: Investigations on the combustion duration and ignition delay period of a dual fuel diesel engine with hydrogen and producer gas as secondary fuels. Appl. Therm. Eng. **107**, 524–532 (2016). https://doi.org/10.1016/j.applthermaleng.2016.06.151
11. Banapurmath, N.R., Yaliwal, V.S., Hosmath, R.S., Indudhar, M.R., Guluwadi, S., Bidari, S.: Dual fuel engines fueled with three gaseous and biodiesel fuel combinations. Biofuels **9**, 75–87 (2018). https://doi.org/10.1080/17597269.2016.1257316
12. Yaliwal, V.S., Banapurmath, N.R., Gaitonde, V.N., Malipatil, M.D.: Simultaneous optimization of multiple operating engine parameters of a biodiesel-producer gas operated compression ignition (CI) engine coupled with hydrogen using response surface methodology. Renew. Energy **139**, 944–959 (2019). https://doi.org/10.1016/j.renene.2019.02.104
13. Nayak, S.K., Mishra, P.C.: Achieving high performance and low emission in a dual fuel operated engine with varied injection parameters and combustion chamber shapes. Energy Convers. Manag. **180**, 1–24 (2019). https://doi.org/10.1016/j.enconman.2018.10.091
14. Halewadimath, S.S., Banapurmath, N.R., Yaliwal, V.S., Nataraja, K.M.: Effect of engine variables on combustion characteristics of a dual fuel engine powered by neem oil methyl ester and producer gas. Int. J. Ambient Energy. 1–13 (2019). https://doi.org/10.1080/01430750.2019.1696889
15. Akkoli, K.M., Gangavati, P.B., Banapurmath, N.R., Yaliwal, V.S.: Comparative study of various biofuel combinations derived from agricultural residues on the performance and emissions of CI engine. Int. J. Sustain. Eng. **13**, 140–150 (2020). https://doi.org/10.1080/19397038.2019.1634774
16. Caligiuri, C., Renzi, M.: Combustion modelling of a dual fuel diesel-producer gas compression ignition engine. Energy Procedia **142**, 1395–1400 (2017). https://doi.org/10.1016/j.egypro.2017.12.525
17. Sharma, A.K.: Modelling of a CI engine operated on diesel and producer gas: an empirical approach. J. Inst. Eng. Mech. Eng. Div. **91**, 35–39 (2010)
18. Kumar, A., Sharma, A.K.: Design and development of gas carburettor for a gasifier-engine system. J. Inst. Eng. Ser. C **98**, 83–89 (2017). https://doi.org/10.1007/s40032-016-0330-1
19. Yaliwal, V.S.: Effect of mixing chamber or carburetor type on the performance of diesel engine operated on biodiesel and producer gas induction. Int. J. Automot. Eng. Technol. **5**, 25 (2016). https://doi.org/10.18245/ijaet.02009
20. Banapurmath, N.R., Yaliwal, V.S., Kambalimath, S., Hunashyal, A.M., Tewari, P.G.: Effect of wood type and carburetor on the performance of producer gas-biodiesel operated dual fuel engines. Waste Biomass Valorization **2**, 403–413 (2011). https://doi.org/10.1007/s12649-011-9083-5

21. Yeom, S.H., Go, Y.W.: Optimization of a novel two-step process comprising re-esterification and transesterification in a single reactor for biodiesel production using waste cooking oil. Biotechnol. Bioprocess Eng. **23**, 432–441 (2018). https://doi.org/10.1007/s12257-018-0209-5

Performance Enhancements of Solar Dryers Using Integrated Thermal Energy Storage: A Review

R. Senthil , **G. Vijayan** , **Gauri Phadtare** , **and Bhupendra Gupta**

1 Introduction

Solar energy is potentially available around 300 days annually in India. Solar energy utilization has increased in the past few decades due to the awareness of global warming by burning of fossil fuels for our thermal needs. Solar energy is primarily in the form of heat and readily available to heating applications with a selective energy conversion technique. Even though a diluted form, solar energy is effectively used with solar flat plate collectors toward low-temperature applications. Solar drying is popular in agriculture. The significant drawbacks of the open sun dryer are the longer dryer time, manual work and food quality affected by the varying solar radiation as well as atmospheric pollutants and weather. Mass production of dry products is in demand due to the excess production and low consumption. Solar dryer has typically employed a flat plate collector with or without secondary reflectors, dryer cabin where the food grains to be placed, the blower in the forced convection dryers. Absorber surface is one of the essential aspects to increase the temperature of flowing air.

R. Senthil (✉)
Department of Mechanical Engineering, SRM Institute of Science and Technology, Kattankulathur, Chennai, India
e-mail: senthilr@srmist.edu.in

G. Vijayan
Department of Mechanical Engineering, KSK College of Engineering and Technology, Kumbakonam, Tamil Nadu, India
e-mail: viji_laker@yahoo.co.in

G. Phadtare
Department of Mechanical Engineering, Pimpri Chinchwad College of Engineering, Pune, India
e-mail: gauri.phadtare@gmail.com

B. Gupta
Department of Industrial Production, Jabalpur Engineering College, Jabalpur 482011, India
e-mail: bhupendra243@yahoo.com
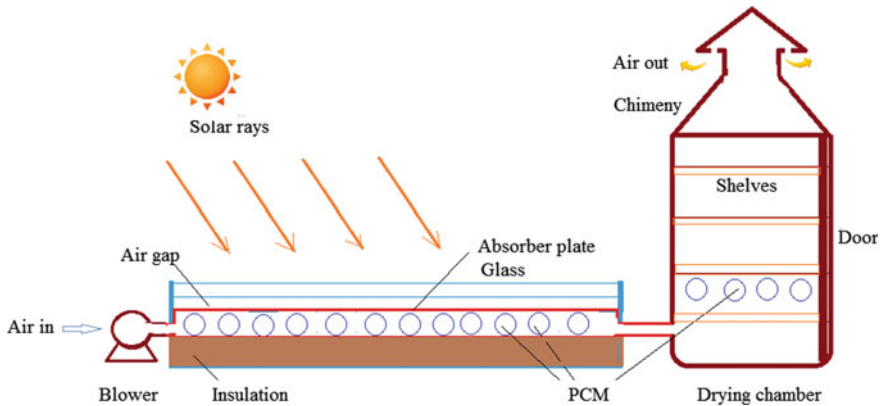
Fig. 1 Schematic layout of solar dryer and the possible locations of employing PCM in the collector and drying chamber

Absorber tubes are preferable in the liquid collectors due to higher specific heat and density. Extraction of heat energy by an air medium that is passing through the solar collector. Figure 1 shows the possible ways of employing PCM in solar air heater and dryer.

Heat transfer enhanced mainly due to an increase of collector area. The researchers tested various absorber designs. Reflectors and concentrators attached to solar dryer reduced the drying time and improved the efficiency of dryer [1]. Solar photovoltaic panels used to power the fans to make the airflow to be a forced convection dryer. Further, the chimney integrated into solar dryer improved the buoyancy of hot air through the food grains [2]. Sun-drying involves the open sun-drying at the place of harvest (in-situ) and elsewhere after post-harvest. Solar dryers are operating active and passive modes. Natural circulation of hot air occurs in the passive systems due to the buoyancy effects of air. In active systems, a blower circulates the airflow to the collector and dryer. The passive integral type of solar dryers is classified further into cabinet dryers and greenhouse dryers. PCM are used in the thermal management systems [3]. The operating temperature of suitable PCM for a dryer is around 60 °C. The selective PCMs are fatty acids, paraffin wax, salt hydrates, and eutectics. PCM possesses higher energy density than sensible storage systems. Thermal conductivity of PCM is the main drawback to the large-scale commercial deployment. In this article, the recent advances of solar dryer with PCM are discussed.

2 Previous Studies

Several researchers have been investigated solar dryers in the past decades. Varying solar intensity requires thermal energy storage (TES) to provide the required heat to applications. Sreerag and Jithish [4] investigated the solar dryer with PCM. The

incorporation of PCM provides a continuous heat supply to dryer chamber through the heat discharge from the PCM. Agarwal and Sarviya [5, 6] studied PCM-based heat exchanger to provide hot air to dry the food products. Most of the studies of dryers with PCM involve paraffin and salt hydrates for drying of food products. Vásquez et al. [7] demonstrated the use of the proper TES control system with solar drying, the potential of energy savings could be around 80% when compared to conventional drying. Jain et al. [8] developed mixtures of fatty acids to melt in the range of 40–60 °C to solar dryers. Agarwal and Sarviya [9] characterized commercial-grade paraffin wax to utilize as PCM in solar dryer instead of technical grade PCM through differential scanning calorimetry. Commercial-grade PCM is found to be a cost-effective PCM for solar dryers. The energy stored in PCM is mainly latent heat-based. Solar collectors frequently involve an absorber surface, which exchanges the heat to the air.

Krishnan and Sivaraman [10] showed the thermal efficiency of solar dryer with TES was improved by 50% than that of the conventional dryer. The effect of thermal storage was observed to sustain the required temperature for 3 h after sunset, and then it decreased gradually. El Khadraoui et al. [11] investigated a solar dryer with the PCM cavity. PCM cavity introduced in the dryer to act as a solar energy accumulator. The temperature of the drying chamber was observed to be 4–16 °C higher than ambient all over the night due to PCM. A model was used to predict the drying kinetics and observed a reduction of drying time with PCM by 50% compared to the dryer without PCM [12, 13]. Kaewpanha et al. [14] investigated 28.35 kg of paraffin wax-based dryer to dry chilies during weak sunshine. Yadav and Chandramohan [15] investigated the effect of air velocity during phase change of PCM. Melting improved by higher airflow velocity, and the discharge process requires a lower air velocity to supply hot air at 68 °C. High flow velocity was not recommended for heat retrieval from PCM. Swami et al. [16] investigated a solar dryer with two PCM to dry fish. The selection of a PCM-based dryer is to make the drying of fish around a temperature of 62 °C. Temperature control inside the drying chamber was attained with the help of the TES unit. Yadav et al. [17] investigated the hot air coming from solar collectors with PCM for drying applications, and drying process was observed to be continued up to 10.00 pm due to heat stored in PCM. The preferable air flow velocity was 1–4 m/s for charging PCM and about 1 m/s for discharging PCM. Airflow velocity influenced heat transfer. Bhardwaj et al. [18] investigated sensible and latent heat materials and showed the PCM doubled the moisture removal rate. Elbahjaoui and Qarnia [19] investigated alumina oxide-based paraffin wax for the flat plate solar collectors. Reyes et al. [20] observed the overall efficiency of dryer with PCM in a range of 56–76%. Vásquez et al. [21] studied a dynamic model of a solar dryer for agricultural products with TES, using paraffin wax.

Babar et al. [22] studied the absorber temperature profile in the dryer to employ PCM. The average temperature of the chamber was observed to be 23.5% more because of PCM. Identification of thermal zones is essential to employ the PCM to act as a thermal energy reservoir for drying. Iranmanesh et al. [23] showed the overall drying efficiency with PCM was 39.9%. The incorporation of PCM to solar

dryer improved the overall drying efficiency. Azaizia et al. [24] demonstrated PCM-based dryer was around 7.5 °C higher than the non-PCM dryer throughout the night. Reduction of moisture content of pepper about 95% was observed 30 h, 55 h, and 75 h for the non-PCM dryer, PCM-based dryer, and open sun dryer, respectively. The greenhouse solar dryer with PCM proves effective in drying.

Saw tooth-shaped absorber, along with PCM in the TES system, was investigated by Babu et al. [25]. The sawtooth shape absorbed solar radiation effectively, and the attached paraffin storage tank stores latent heat for a long time. A total of 20 aluminum pipes of 1 mm thick are used to provide hot water from 6 to 8 am. Srivastava and Shukla [26] carried out an experimental validation on solar dryer with PCM. The dryer with PCM stored heat and the drying is done for a long time with temperature regulation [27]. The temperature of PCM remains high after several cycles of operations. To make a solar air dryer reliable, the heat pipes were used during the day, containing water inside and in PCM [28]. The heat pipe helped to maintain a small temperature difference to PCM by making a flat plate solar air dryer contain heat pipes and PCM.

Atalay [29] compared a pebble-stone-based packed-bed with PCM storage in a solar dryer. The efficiency of the PCM-based dryer is minimal to the packed bed-based dryer, but the economic point of view packed-bed was about 10% lower. PCM usually is encapsulated into a container to increase the surface area available to the heat transfer. The container size and fin dimensions [30] and orientation play an essential role in the charging of PCM [31], and the arrangement of PCM is also essential to obtain the maximum benefits of TES [32, 33]. An increase in air temperature reduced the power consumption, but the mass flow rate increased the power [34]. A solar dryer using engine oil and PCM improved drying by 43.75% [35]. Khouya [36] investigated the method of reduction of drying time using several methods to dry the hardwood solar kiln. The drying time reduces with the decrease in thickness of wood-boards and increase in collector area. The use of TES reduces the drying time up to 60%. Lamrani and Draoui [37] showed a packed-bed storage reduced the drying time by about 15% and reduces the payback period by 33%. Four different concentrations of aluminum nanoparticle such as 0%, 0.5%, 1.0% and 1.55 with paraffin were used as heat energy storage element in hybrid-solar dryer [38]. The percentage reduction of drying time of dryer with and without PCM is illustrated in Fig. 2.

Fig. 2 Percentage of reduction of drying time with TES integrated with solar dryer from the literature
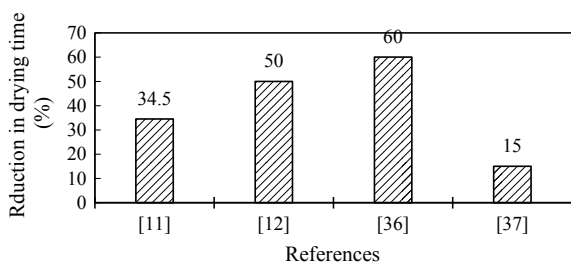
Heat energy storage capacity was improved for increased nanoparticle concentration up to 1.0% in PCM. As economics point of view, the 1.0% alumina with PCM was recommended, for drying agro-product, due to its reversibility. Ndukwu et al. [39] demonstrated wind-powered solar dryer with glycerol as PCM with lower drying time under the ambient temperature of 24–50 °C and humidity of about 10–52%. Poblete and Painemal [40] determined thermal efficiency of solar dryer with and without TES was 37.8% and 22.2%, respectively. The salient points are discussed in the next section.

3 Discussion

Utilization of PCM in dryer certainly improves the moisture removal rate from the food grains and agricultural crops. The dryer with PCM is observed to be safe and does not deteriorating the quality of food. Sometimes, the packed-bed storage using sensible heat materials like pebbles is observed economically effective when compared to PCM. However, the productivity due to longer duration for heat storage and compactness of the dryer is promising in the case of PCM. PCM with sensible heat medium and composite PCM were found to be useful to observe the faster rate of heat transfer in the TES. Most researched PCM with solar dryer is observed to be paraffin wax due to its optimum operating temperature of dryers and the organic nature as well as cost-effectiveness. The summary of the performance enhancement of solar dryer with PCM (paraffin wax) is given in Table 1.

The solar dryer with TES produced higher temperature and lower RH in dryer. Fluid flow velocity is to be optimized for the TES-based solar dryers to attain an effective drying rate. Due to low-temperature operation of solar dryers, copper tubes are preferring PCM side to enhance the heat transfer. TES unit is used as a supplementary heat source, storage for after sunshine hours, and thus, TES plays a vital role to improve the overall drying performance of solar dryers. Due to low-temperature

Table 1 Performance enhancement of solar dryer with paraffin wax as PCM

Performance enhancements	References
Lower discharge velocity of air was required to provide the heat	Yadav and Chandramohan [15]
TES unit acts as a temperature control	Swami et al. [16]
Suitable air velocity for charging and discharging of PCM was 1 to 4 m/s and 1 m/s, respectively	Yadav et al. [17]
Overall efficiency was in the range of 56–76%	Reyes et al. [20]
PCM-based dryer showed a temperature of 7.5 °C more than that of the non-PCM dryer	Azaizia et al. [24]
Drying efficiency of solar dryer with PCM was observed to be 39.9%	Iranmanesh et al. [15]

operation, nanoparticles are added as thermal conductivity enhancers to PCM. The PCM behavior is to be improved to reach large-scale commercial applications of solar dryers with PCM.

4   Conclusions

From the literature, the PCM used in solar dryer was studied by several researchers. The major conclusions are given below.

- PCM inclusion improved the drying performance of solar dryers. The reduction of drying duration was possible up to 60%.
- Solar dryer with PCM is found to be safe for foods.
- PCM container selection plays a vital role in providing heat transfer augmentation and the safety against the leakage of liquid PCM into the air.
- Heat pipes inside the PCM are a useful enhancement method used in the PCM-based solar dryer.
- Solar PV panels are used as the preheating sections for the solar dryers.
- The airflow velocity influences the PCM behavior and drying rate. Higher and lower air velocities are desirable for heating and cooling of PCM, respectively. The air velocity could be optimized to obtain a longer drying time.
- The solar dryers with TES are used for several applications ranges from domestic to industrial purposes.
- Hybrid applications like wind and biomass-powered solar dryers are observed to be fully reliant on renewable sources of energy.

References

1. Sandali, M., Boubekri, A., Mennouche, D.: Improvement of the thermal performance of solar drying systems using different techniques: a review. J. Sol. Energy Eng. Trans. ASME **141**(5), 050802 (2019). https://doi.org/10.1115/1.4043613
2. Fudholi, A., Sopian, K.: A review of solar air flat plate collector for drying application. Renew. Sustain. Energy Rev. **102**, 333–345 (2019). https://doi.org/10.1016/j.rser.2018.12.032
3. Mofijur, M., Mahlia, T.M.I., Silitonga, A.S., Ong, H.C., Silakhori, M., Hasan, M.H., et al.: Phase change materials (PCM) for solar energy usages and storage: an overview. Energies **12**(16), 3167 (2019). https://doi.org/10.3390/en12163167
4. Sreerag, T.S., Jithish, K.S.: Experimental investigations of a solar dryer with and without multiple phase change materials (PCM's). World J. Eng. **13**(3), 210–217 (2016)
5. Agarwal, A., Sarviya, R.M.: An experimental investigation of shell and tube latent heat storage for solar dryer using paraffin wax as heat storage material. Eng. Sci. Technol. Int. J. **19**(1), 619–631 (2016). https://doi.org/10.1108/WJE-06-2016-028
6. Agrawal, A., Sarviya, R.M.: A review of research and development work on solar dryers with heat storage. Int. J. Sustain. Energy **35**(6), 583–605 (2016). https://doi.org/10.1080/14786451.2014.930464

7. Vásquez, J., Reyes, A., Mahn, A., Cubillos, F.: Experimental evaluation of fuzzy control solar drying with thermal energy storage system. Dry Technol. **34**(13), 1558–1566 (2016). https://doi.org/10.1080/07373937.2015.1137001

8. Jain, A., Kumar, A., Shukla, A., Sharma, A.: Development of phase change materials (PCMs) for solar drying systems. In: Prakash, O., Kumar, A. (eds.) Solar Drying Technology. Green Energy and Technology, pp. 619–633 (2017). https://doi.org/10.1007/978-981-10-3833-4_23

9. Agrawal, A., Sarviya, R.M.: Characterization of commercial grade paraffin wax as latent heat storage material for solar dryers. Mater. Today Proc. **4**(2), 779–789 (2017). https://doi.org/10.1016/j.matpr.2017.01.086

10. Krishnan, S., Sivaraman, B.: Experimental investigations on thermal storage in a solar dryer. Int. Energy J. **17**(1), 23–35 (2017)

11. El Khadraoui, A., Bouadila, S., Kooli, S., Farhat, A., Guizani, A.: Thermal behavior of indirect solar dryer: nocturnal usage of solar air collector with PCM. J. Clean Prod. **148**, 37–48 (2017). https://doi.org/10.1016/j.jclepro.2017.01.149

12. El-Sebaii, A.A., Shalaby, S.M.: Experimental investigation of drying thymus cut leaves in indirect solar dryer with phase change material. J. Sol Energy Eng. Trans. ASME **139**(6) (2017). https://doi.org/10.1115/1.4037816

13. Aumporn, O., Zeghmati, B., Chesneau, X., Janjai, S.: Numerical study of a solar greenhouse dryer with a phase-change material as an energy storage medium. Heat Transf. Res. **49**(6), 509–528 (2018). https://doi.org/10.1615/HeatTransRes.2018020132

14. Kaewpanha, M., Wansungnern, W., Banthuek, S.: Development of thermal energy storage as a supplemental heat source for solar dryer. Key Eng. Mater. **777**, 102–106 (2018). https://doi.org/10.4028/www.scientific.net/KEM.777.102

15. Yadav, S., Chandramohan, V.P.: Numerical analysis on thermal energy storage device with finned copper tube for an indirect type solar drying system. J. Sol. Energy Eng. Trans. ASME **140**(3) (2018). https://doi.org/10.1115/1.4039273

16. Swami, V.M., Arun, T.A., Anil, T.R.: Experimental analysis of solar fish dryer using phase change material. J. Energy Storage **20**, 310–315 (2018). https://doi.org/10.1016/j.est.2018.09.016

17. Yadav, S., Lingayat, A.B., Chandramohan, V.P., Raju, V.R.K.: Numerical analysis on thermal energy storage device to improve the drying time of indirect type solar dryer. Heat Mass Transf. **54**(12), 3631–3646 (2018). https://doi.org/10.1007/s00231-018-2390-7

18. Bhardwaj, A.K., Kumar, R., Chauhan, R.: Experimental investigation of the performance of a novel solar dryer for drying medicinal plants in Western Himalayan region. Sol. Energy **177**, 395–407 (2019). https://doi.org/10.1016/j.solener.2018.11.007

19. Elbahjaoui, R., El Qarnia, H.: Performance evaluation of a solar thermal energy storage system using nanoparticle-enhanced phase change material. Int. J. Hydrogen Energy **44**(3), 2013–2028 (2019). https://doi.org/10.1016/j.ijhydene.2018.11.116

20. Reyes, A., Vásquez, J., Pailahueque, N., Mahn, A.: Effect of drying using solar energy and phase change material on kiwifruit properties. Dry Technol. **37**(2), 232–244 (2019). https://doi.org/10.1080/07373937.2018.1450268

21. Vásquez, J., Reyes, A., Pailahueque, N.: Modeling, simulation and experimental validation of a solar dryer for agro-products with thermal energy storage system. Renew. Energy **139**, 1375–1390 (2019). https://doi.org/10.1016/j.renene.2019.02.085

22. Babar, O.A., Arora, V.K., Nema, P.K.: Selection of phase change material for solar thermal storage application: a comparative study. J. Braz. Soc. Mech. Sci. Eng. **41**(9) (2019). https://doi.org/10.1007/s40430-019-1853-1

23. Iranmanesh, M., Samimi Akhijahani, H., Barghi Jahromi, M.S.: CFD modeling and evaluation the performance of a solar cabinet dryer equipped with evacuated tube solar collector and thermal storage system. Renew. Energy **145**, 1192–1213 (2020). https://doi.org/10.1016/j.renene.2019.06.038

24. Azaizia, Z., Kooli, S., Hamdi, I., Elkhal, W., Guizani, A.A.: Experimental study of a new mixed mode solar greenhouse drying system with and without thermal energy storage for pepper. Renew. Energy **145**, 1972–1984 (2020). https://doi.org/10.1016/j.renene.2019.07.055

25. Babu, S., Abishraj, V.R., Suthagar, S.: Solar thermal energy storage on PCM based integrated saw tooth collector for institutions. In: 1st International Conference on Sustainable Green Buildings and Communities, SGBC 2016, 7936078 (2017)

26. Srivastava, A.K., Shukla, S.K.: Thermal modeling of indirect solar drying system: an experimental validation. Distrib. Gener. Altern. Energy J. **32**(3), 19–51 (2017). https://doi.org/10.1080/21563306.2017.11878944

27. Gao, W.F., Lin, W.X., Liu, T., Li, M.: An experimental study on the application of polyalcohol solid-solid phase change materials in solar drying with cross-corrugated solar air collectors. IOP Conf. Ser. Earth Environ. Sci. **93**(1), 012075 (2017). https://doi.org/10.1088/1755-1315/93/1/012075

28. Bhagwat, V.V., Salve, S.P., Debnath, S.: Experimental analysis of a solar dehydration with phase changing material. AIP Conf. Proc. **1998**, 020003 (2018). https://doi.org/10.1063/1.5049099

29. Atalay, H.: Assessment of energy and cost analysis of packed bed and phase change material thermal energy storage systems for the solar energy-assisted drying process. Sol. Energy **198**, 124–138 (2020). https://doi.org/10.1016/j.solener.2020.01.051

30. Senthil, R.: Effect of uniform and variable fin height on charging and discharging of phase change material in a horizontal cylindrical thermal storage. Therm. Sci. **23**(3B), 1981–1988 (2019). https://doi.org/10.2298/TSCI170709239S

31. Senthil, R.: Effect of position of heat transfer fluid tube on the melting of phase change material in cylindrical thermal energy storage. Energy Sources Part A (2019). https://doi.org/10.1080/15567036.2019.1649751

32. Senthil, R., Cheralathan, M.: Enhancement of the thermal energy storage capacity of a parabolic dish concentrated solar receiver using phase change materials. J. Energy Storage **25**, 100841 (2019). https://doi.org/10.1016/j.est.2019.100841

33. Senthil, R.: Effect of charging of phase change material in vertical and horizontal rectangular enclosures in a concentrated solar receiver. Case Stud. Therm. Eng. **21**, 100653 (2020). https://doi.org/10.1016/j.csite.2020.100653

34. Bahammou, Y., Lamsyehe, H., Kouhila, M., Lamharrar, A., Idlimam, A., Abdenouri, N.: Valorization of co-products of sardine waste by physical treatment under natural and forced convection solar drying. Renew. Energy **142**, 110–122 (2019). https://doi.org/10.1016/j.renene.2019.04.012

35. Alimohammadi, Z., Akhijahani, H.S., Salami, P.: Thermal analysis of a solar dryer equipped with PTSC and PCM using experimental and numerical methods. Sol. Energy **201**, 157–177 (2020). https://doi.org/10.1016/j.solener.2020.02.079

36. Khouya, A.: Effect of regeneration heat and energy storage on thermal drying performance in a hardwood solar kiln. Renew. Energy **155**, 783–799 (2020). https://doi.org/10.1016/j.renene.2020.03.178

37. Lamrani, B., Draoui, A.: Thermal performance and economic analysis of an indirect solar dryer of wood integrated with packed-bed thermal energy storage system: a case study of solar thermal applications. Drying Technol. (2020). https://doi.org/10.1080/07373937.2020.1750025

38. Bahari, M., Najafi, B., Aziz Babapoor, A.: Evaluation of α-Al$_2$O$_3$-PW nanocomposites for thermal energy storage in the agro-products solar dryer. J. Energy Storage **28**, 101181 (2020). https://doi.org/10.1016/j.est.2019.101181

39. Ndukwu, M.C., Onyenwigwe, D., Abam, F.I., Eke, A.B., Dirioha, C.: Development of a low-cost wind-powered active solar dryer integrated with glycerol as thermal storage. Renew. Energy **154**, 553–568 (2020). https://doi.org/10.1016/j.renene.2020.03.016

40. Poblete, R., Painemal, O.: Improvement of the solar drying process of sludge using thermal storage. J. Environ. Manage. **255**, 109883 (2020). https://doi.org/10.1016/j.jenvman.2019.109883

Comparative Analysis of the Engine Emissions from CI Engine Using Diesel–Biodiesel–Ethanol Blends

Neeraj Budhraja [ID] **, Amit Pal** [ID] **, Manish Jain** [ID] **, and R. S. Mishra** [ID]

1 Introduction

Increasing oil prices and environmental degradation due to the burning of petroleum products is forcing us to look for energy sources which make the way for the replacement of petroleum products. Alternative source as biodiesel was suggested by many researchers [1–3]. Some of the oils used for the production of biodiesel are linseed oil [4], karanja oil [5], castor oil [6], palm oil [7], mahua oil [8], neem oil [9], and thumba oil [10], but they require some treatments before being used as CI engine fuels. Since the physiochemical properties of biodiesel are still higher than to be directly used in CI engines, blending is a better solution for this problem.

A 25% blending of biodiesel (rapeseed-based biodiesel) with diesel showed a reduction in CO_2 whereas the rise in NO_X emissions [11]. Another way is using ethanol–diesel blends, ethanol in diesel NO_X, CO_2, and smoke at higher load with the expense of reduced cetane number and high heat value [12]. Alcohol (methanol) and biodiesel (jatropha-based biodiesel) blends were also tested, thermal efficiency has been increased marginally due to the quick burning of methanol resulting in better heat releasing rate [13]. Another study showed that BE20 (80% biodiesel and 20% ethanol) reduced consumption of fuel and emissions like CO and HC were lowered due to proper combustion resulting from high exhaust temperature [14]. In the current study, the blends of diesel, biodiesel, and ethanol were prepared to test in CI engine for engine emissions. Before the test was conducted, various physiochemical properties are density, calorific value, and kinematic viscosity. Thus, the current study has determined the economical, highly efficient, and environmentally friendly biodiesel–ethanol–diesel blend for CI engines.

N. Budhraja (✉) · A. Pal · R. S. Mishra
Department of Mechanical, Production & Industrial and Automobile Engineering, Delhi Technological University, Delhi, India
e-mail: neeraj_budhraja@yahoo.com

M. Jain
Department of Mechanical Engineering, RJIT, Takenpur, Gwalior, India

2 Materials and Methods

2.1 Materials

The waste cooking oil collected from the college canteen was used to produce biodiesel and the ethanol used was of industrial grade. The blends were prepared from different fractions of biodiesel, ethanol, and diesel, respectively. The various blends thus prepared were D90B5E5, D85B10E5, D75B15E10, and D70B20E10, where D90B5E5 stands for 90% diesel, 5% biodiesel, and 5% ethanol; D85B10E5 stands for 85% diesel, 10% biodiesel, and 5% ethanol; D75B15E10 stands for 75% diesel, 15% biodiesel, and 10% ethanol; and D70B20E10 stands for 70% diesel, 20% biodiesel, and 10% ethanol, respectively.

2.2 Experimental Setup and Procedure

A schematic diagram of constant speed diesel engine test setup having 1 cylinder with 4-stroke, 661 cc diesel engine, and water-cooled; mounted with a fuel measuring unit attachment model: FF0.012 made of glass used for the test runs was shown in Fig. 1. The power at 1500 rpm was 3.5 kW, the stroke length was 110 mm, the bore diameter was 87.5 mm, and CR was about 18. The eddy current-type dynamometer Model AG10 and a Eureka made neoprene packed rotameter model PG5 having a
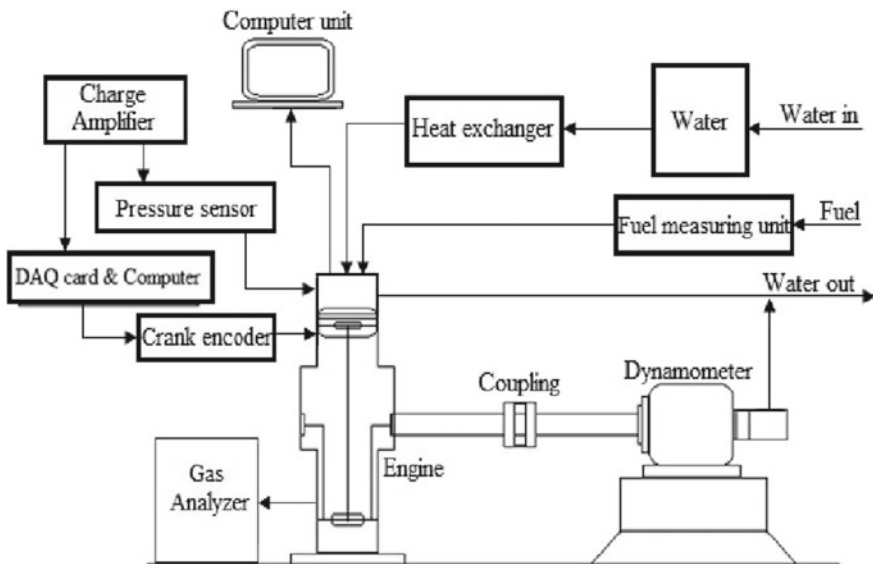
Fig. 1 A schematic diagram of the constant speed diesel engine test setup

flow rate of 25–250 lph were used. For load indication, a Selectron manufactured load indicator model PIC 152-B2 having a range of 85–270 VAC and retransmission output range 4–20 mA was mounted.

The viscometer used to measure the kinematic viscosity and density of the blends was Stabinger Viscometer-SVM 3000 manufactured by 'Anton Paar India Pvt. Ltd,' with the kinematic viscosity range between 0.2×10^{-6} and $30,000 \times 10^{-6}$ m^2/s while the density range between 600 and 3000 kg/m^3. However, the calorific value was measured by 'Parr 6100' calorimeter.

An AVL DiGas 444 with LC display and automatic water separator, with test gas fine filter, was used to measure the relative constituents of certain engine exhaust gases. High precision measurement was done for measuring the various emissions like CO, HC, CO$_2$, and oxides of nitrogen (NO$_X$), respectively. To measure the opacity of exhaust gases, an AVL437c smoke meter was used. The various blends prepared were test run on the constant compression ratio diesel engine and the composition of the gases in the engine emissions were measured.

3   Results and Discussions

3.1   Fuel Properties

The average of three readings was taken for the various properties like density, specific gravity, kinematic viscosity, and calorific value as shown in Table 1 for different samples.

The density of neat diesel was found to be 835.7 kg/m^3 whereas the density of neat biodiesel was found to be the maximum (i.e., 904.7 kg/m^3) among all samples. Ethanol was having the lowest density of 789.2 kg/m^3 among all samples. Since the ethanol content was just 5–10%, thus, the density of a blend depends on the diesel and biodiesel contents present in the blend. The blend D70 B20 E10 has 844.9 kg/m^3 and blend D90B5E5 has 836.8 kg/m^3 densities, respectively. The higher

Table 1 Desirable properties of different samples

Blends	Density (kg/m^3)	Specific gravity	Kinematic viscosity (m^2/s)	Calorific value (J/kg)
Neat diesel	835.7	0.8382	3.4526×10^{-6}	45.24×10^6
Ethanol	789.2	0.7916	1.5142×10^{-6}	29.62×10^6
Neat biodiesel	904.7	0.9074	9.9919×10^{-6}	38.28×10^6
D70 B20 E10	844.9	0.8474	4.5666×10^{-6}	42.29×10^6
D75 B15 E10	841.4	0.8439	4.2397×10^{-6}	42.63×10^6
D85 B10 E5	840.3	0.8428	4.0096×10^{-6}	43.76×10^6
D90 B5 E5	836.8	0.8393	3.6826×10^{-6}	44.11×10^6

the biodiesel content, the higher the density. Specific gravity has the same trend as density. Neat biodiesel has the highest value 0.9074, D70B20E10 has 0.8474, and D90B5E5 has 0.8393 of specific gravity, respectively. While the kinematic viscosity of neat biodiesel was measured 3 times the kinematic viscosity of neat diesel, i.e., 9.9919×10^{-6} m^2/s while kinematic viscosity of ethanol was measured minimum (1.5142×10^{-6} m^2/s). Blending reduced the kinematic viscosity in the same manner as density and specific gravity, and the reduction was considerably low as 4.5666×10^{-6} m^2/s for D70B20E10 and 3.6826×10^{-6} m^2/s for D90B5E5.

The measured calorific value (CV) of neat biodiesel was 38.28×10^6 J/kg while neat diesel has a measured calorific value of about 45.24×10^6 J/kg. The CV should be as high as possible but blending reduced the CV to 44.11×10^6 J/kg for D90B5B5 and 42.29×10^6 J/kg for D70B20E10 due to the increased biodiesel content in the blends. As seen from the above results, the blends so prepared were having very close values of desirable properties when considered with commercially available neat diesel. And thus, they can be used as IC engine fuel soon.

3.2 Engine Emissions

Carbon monoxide. The variation of CO emission with increased loading conditions is shown in Fig. 2. The CO emissions for neat diesel were higher than all the blends for loads from 0.7 to 15.2 kg. The CO emissions showed an elevation after a 3 kg load for all the samples. While at higher loads, more than 7 kg, a reduction of about 17.8% in CO emissions for D90B5E5 blend and about 50.6% reduction for D70B20E10 blend was seen as compared to neat diesel while Yilmaz et al. [3] noticed maximum 6.7% CO reduction. The extra oxygen provided by ethanol for complete combustion
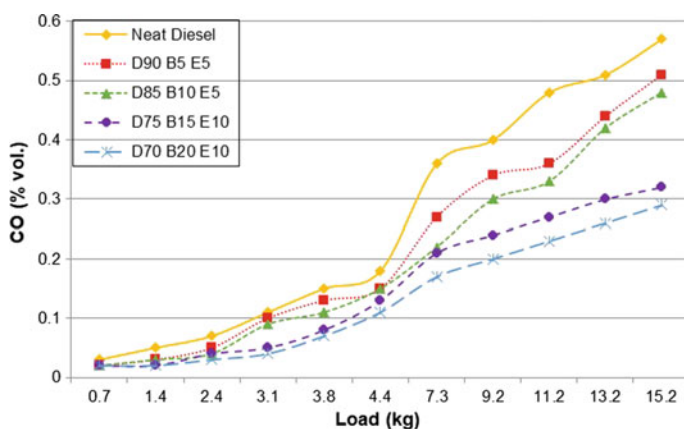
Fig. 2 Load (in kg) versus CO concentration curves for all samples
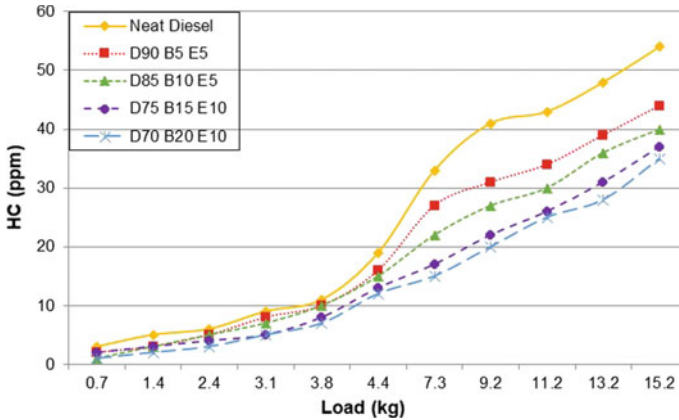
Fig. 3 Load (in kg) versus HC emissions curves for all samples

of fuel is the main reason for CO reduction. The extra oxygen oxidizes CO gas to CO_2 thus reducing CO emissions in the exhaust.

Hydrocarbon. Load (in kg) versus unburnt hydrocarbons (in vol%) curves for neat diesel and all the blends are shown in Fig. 3. From the figure, it was observed that blending reduces hydrocarbon (HC) emissions as compared to neat diesel fuel. The extra oxygen from ethanol and biodiesel structure helps in the better combustion of fuel in the combustion chamber. The maximum HC emissions measured for neat diesel fuel was about 20–30% above the different blends. Nearly 20.2% of HC emission was reduced by D90B5E5 blend and about 44.9% of HC emission was reduced by D70B20E10 blend however about 34% reduction were measured for higher load conditions by Nayak and Pattanaik [8]. Thus, making blends low polluting fuels than neat diesel.

Carbon dioxide. The curves of emissions of CO_2 with varying load for all samples are shown in Fig. 4. The CO_2 emissions from the exhaust showed a steady rise with the load from 0.7 to 15.2 kg, while it was observed that the CO_2 emissions increased with increased concentration of biodiesel and ethanol within the blends. This increase in CO_2 emission was due to the improved oxidation of fuel by extra oxygen provided by ethanol in the combustion chamber. At loads higher than 9 kg, an average increase of 3.7% is seen in the D90B5E5 blend while the D70B20E10 blend gives an average increase of 45.7% CO_2 emissions, respectively. Higher CO_2 emissions in exhaust gases are an indication of the proper burning of fuel.

Oxides of nitrogen. Another emission which increases with biodiesel concentration in the blend is NO_X emission, as clearly seen from Fig. 5. The NO_X emissions in the exhaust were measured as 1 ppm for neat diesel at 0.7 kg load and 310 ppm for D70B20E10 blend at 15.2 kg load. A considerable rise of NO_X emission was due to the high temperature achieved during the combustion of fuel in the cylinder at higher loads. An average rise in NO_X emissions was measured by nearly 10.1% for
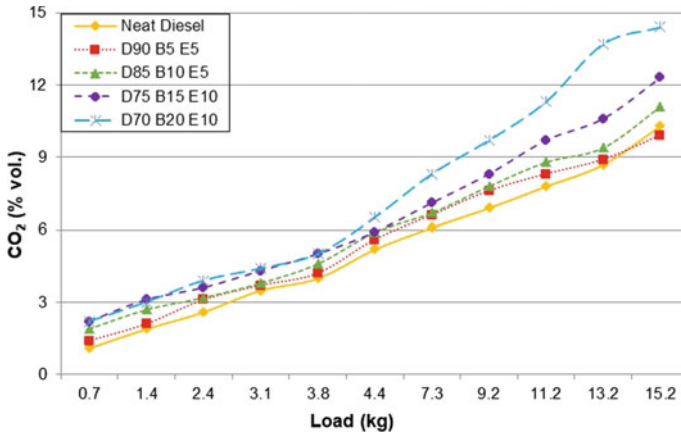
Fig. 4 Load (in kg) versus CO_2 emission curves for all samples
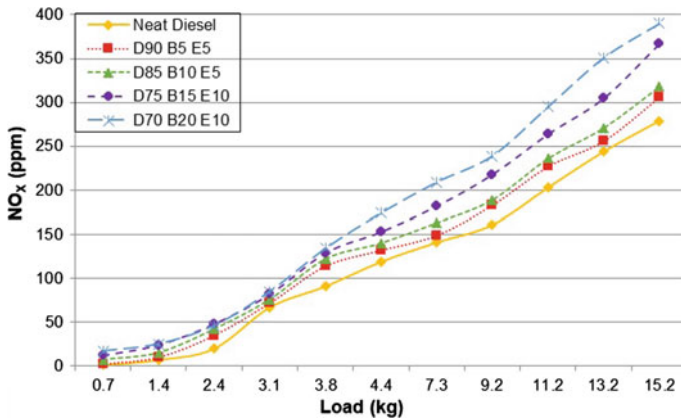
Fig. 5 Load (in kg) versus NO_X emissions curves for all samples

the D90B5E5 blend and 44.4% for the D70B20E10 blend as compared to neat diesel emissions at higher loads while Nayak and Pattanaik [8] measured 25% increase in NO_X. Thus, the various techniques can be used to minimize NO_X emissions in the exhaust gases.

Smoke opacity. To understand the smoke opacity (OPA) affect with load variation is shown in Fig. 6. The OPA is due to the soot content present in the exhaust. A consistent elevation in OPA was shown with the rise in load from 0.7 to 15.2 kg. It was seen a 11.8% reduction in OPA for D90B5E5 and a 30.3% reduction in OPA for D70B20E10 at higher loading conditions. However, Pal et al. [10] measured about 10% reduction in OPA. The extra oxygen content from ethanol helps in the proper combustion of the fuel reducing the soot content in the exhaust while the other reason
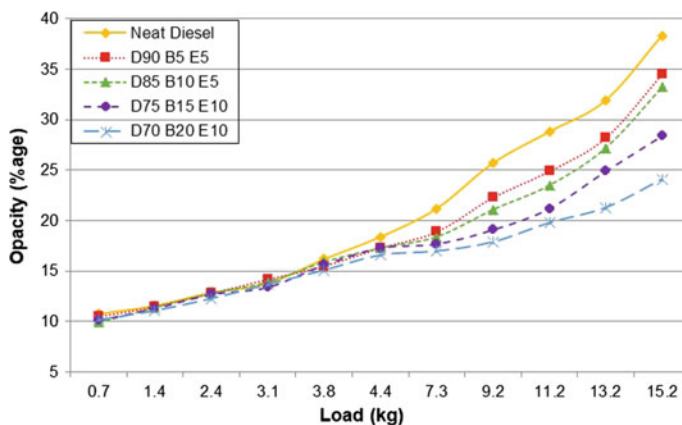
Fig. 6 Load (in kg) versus smoke opacity (in %) curves for all samples

for reduced soot content was lower chains of hydrocarbons present in the blends. This results in less smoky exhaust at higher load conditions.

4 Conclusions

The diesel, biodiesel, and ethanol blends were prepared with biodiesel in the range of 5–20 vol% and ethanol with 5% and 10% by volume. The desirable properties of all the blends were measured to see the compatibility of the blends to the CI engine without any modifications. The engine emissions were then measured to check the effectiveness of the blending for reductions in the engine emissions. The results showed that the blending reduced about 18–51% of CO emissions and nearly 20–45% of HCs at higher loads, whereas the complete combustion and the high-temperature generation in the engine cylinder raised on an average of 4–45% CO_2 emissions and 10–44% NO_X emissions with different blends. Smoke opacity (OPA) is another major issue with diesel engines which is due to the presence of soot content in the exhaust. OPA was reduced by blending with lower chains of HC. And thus, the results showed an effective reduction of about 12–30% in the OPA from engine exhaust.

The experimentation showed that a significant amount of pollution can be reduced by blending biodiesel and ethanol in neat diesel. However, various exhaust treatment methods need to be established for controlling augmented NO_X emissions.

References

1. Lapuerta, M., Armas, O., García-Contreras, R.: Effect of ethanol on blending stability and diesel engine emissions. Energy Fuels **23**, 4343–4354 (2009). https://doi.org/10.1021/ef900448m
2. Sayin, C., Uslu, K.: Influence of advanced injection timing on the performance and emissions of CI engine fueled with ethanol-blended diesel fuel. Int. J. Energy Res. **32**, 1006–1015 (2008). https://doi.org/10.1002/er.1409
3. Yilmaz, N., Ileri, E., Atmanli, A.: Performance of biodiesel/higher alcohols blends in a diesel engine. Int. J. Energy Res. **40**, 1134–1143 (2016). https://doi.org/10.1002/er.3513
4. Kumar, R., Tiwari, P., Garg, S.: Alkali transesterification of linseed oil for biodiesel production. Fuel **104**, 553–560 (2013). https://doi.org/10.1016/j.fuel.2012.05.002
5. Subramanian, K.A., Lahane, S.: Comparative evaluations of injection and spray characteristics of a diesel engine using karanja biodiesel-diesel blends. Int. J. Energy Res. **37**, 582–597 (2013). https://doi.org/10.1002/er.1947
6. Ramezani, K., Rowshanzamir, S., Eikani, M.H.: Castor oil transesterification reaction: a kinetic study and optimization of parameters. Energy **35**, 4142–4148 (2010). https://doi.org/10.1016/j.energy.2010.06.034
7. Chotwichien, A., Luengnaruemitchai, A., Jai-In, S.: Utilization of palm oil alkyl esters as an additive in ethanol-diesel and butanol-diesel blends. Fuel **88**, 1618–1624 (2009). https://doi.org/10.1016/j.fuel.2009.02.047
8. Nayak, S.K., Pattanaik, B.P.: Experimental investigation on performance and emission characteristics of a diesel engine fuelled with mahua biodiesel using additive. Energy Procedia **54**, 569–579 (2014). https://doi.org/10.1016/j.egypro.2014.07.298
9. Ali, M.H., Mashud, M., Rubel, M.R., Ahmad, R.H.: Biodiesel from neem oil as an alternative fuel for diesel engine. Procedia Eng. **56**, 625–630 (2013). https://doi.org/10.1016/j.proeng.2013.03.169
10. Pal, A., Verma, A., Kachhwaha, S.S., Maji, S.: Biodiesel production through hydrodynamic cavitation and performance testing. Renew. Energy **35**, 619–624 (2010). https://doi.org/10.1016/j.renene.2009.08.027
11. Oberweis, S., Al-Shemmeri, T.T.: Effect of biodiesel blending on emissions and efficiency in a stationary diesel engine. Renew. Energy Power Qual. J. **1**, 304–310 (2010). https://doi.org/10.24084/repqj08.314
12. He, B.-Q., Shuai, S.-J., Wang, J.-X., He, H.: The effect of ethanol blended diesel fuels on emissions from a diesel engine. Atmos. Environ. **37**, 4965–4971 (2003). https://doi.org/10.1016/j.atmosenv.2003.08.029
13. Dwivedi, G., Jain, S., Sharma, M.P.: Impact of biodiesel and its blends with diesel and methanol on engine performance. Int. J. Energy Sci. **1**, 105–109 (2011)
14. Barabás, I., Todoruţ, A., Băldean, D.: Performance and emission characteristics of an CI engine fueled with diesel–biodiesel–bioethanol blends. Fuel **89**, 3827–3832 (2010). https://doi.org/10.1016/j.fuel.2010.07.011

Nozzle Design for Intake Manifold for KTM 500 EXC Engine

Amal Nambiar , Arul Kumar , Rohan Chopra , M. Zunaid ,
and Qasim Murtaza

Nomenclature

A	Area
ABDC	After Bottom Dead Centre
ATDC	After Top Dead Centre
BBDC	Before Bottom Dead Centre
CAD	Computer-Aided Design
CFD	Computational Fluid Dynamics
EVC	Exhaust Valve Closes
EVO	Exhaust Valve Opens
IVC	Intake Valve Closes
IVO	Intake Valve Opens
M	Mach number
$\dot{m}$	Mass flow rate
p_t	Total pressure
R	Gas constant
STL	Stereolithography
T_t	Total temperature
γ	Specific heat ratio

A. Nambiar · A. Kumar (✉) · R. Chopra · M. Zunaid · Q. Murtaza
Department of Mechanical, Production & Industrial and Automobile Engineering, Delhi
Technological University, Delhi 110042, India
e-mail: arulkumar6559@gmail.com

371

1 Introduction

Formula SAE (FSAE) is an internationally renowned engineering design competition organised by SAE International. The competition is based on a concept where a fictional manufacturing firm contracts a student engineer team to conceive and fabricate a small open cockpit, open wheeled race car. The prototype race car will be evaluated on the basis of its potential as a production item. Each student team designs, builds and tests a prototype based on a series of rules, whose purpose is both ensuring on-track safety (the cars are driven by the students themselves) and promoting clever problem-solving. One of the pivotal rules of the competition is those regarding the power unit. The rules specify that all combustion power units used in the competition should be engines less than 710 cc used in conjunction with a 20 mm inner diameter restrictor placed before the intake system to limit the air entering the engine [1].

The venturi is one of the most crucial components of the of the intake manifold system as it primarily limits the amount of air that can be used by the engine. A poorly designed venturi can drastically reduce the power produced by the engine and its volumetric efficiency. Hence, it was justified to spend our resources on researching and designing the most apt venturi for our system.

The FSAE team of Delhi Technological University, Team Defianz Racing participated in FS Czech 2019. The team employed a KTM 500 EXC engine as its power unit. An intake manifold in conjunction with a restrictor was designed to compensate for the power loss caused by the restrictor. The intake manifold system that was employed in the competition included: elliptically profiled bell mouth, a throttle body of inner diameter 28 mm, a 12–6 venturi (converging angle $= 12°$ and diverging angle $= 6°$, throughout the paper this nomenclature will be used) to comply with the 20 mm restrictor rule [1], a plenum of 2.8 L volume and a runner 278 mm length and 42 mm diameter (as shown in Fig. 1). The following exercise is an attempt to optimise the design of the converging–diverging nozzle to extract maximum performance from the available manifold system.

Conventionally, in place of a 20 mm restrictor a converging–diverging nozzle or a venturi in used. The contributions made by Jawad [2] and Mattarelli [3] in this field were significant. Jawad [2] investigated the effect of diverging angles experimentally on the flow bench. Mattarelli [3] performed CFD simulations on a numerous venturi configurations. Chen [4] and Singhal [5] did a very comprehensive study of the effect of these parameters on the flow properties.

Instead of a conventional straight profile venturi, Byam [6] experimentally tested the effect of an arc shaped converging section of the venturi. He proved that a venturi with an arc-shaped converging section attained sonic flow much sooner than the conventional venturi [6]. Deshpande [7] proposed the use of De-Laval and Bell nozzle over the conventional venturi for space saving. Hence, CFD simulations have been performed on various converging and diverging angles of venturi for straight and curved arc-shaped profiles for nozzles to study their effect on flow properties.

Thereafter, to study the effect of change of venturi geometries on the engine's performance, 1-D simulations were done using Ricardo WAVE. Dragoiu [8], Ceviz [9] and Seshadri [10] studied the effects of various intake manifold parameters like plenum volume and runner length on the engine's performance with the help of 1-D modelling. Calvo [11] and Cordon [12] used the WaveMesher tool from the Ricardo suite to model the complex geometries in their intake systems and then studied the effects of varying certain intake manifold. On the other hand, Claywell [13] used 1-D/3-D coupled simulations using Ricardo WAVE and VECTIS to simulate the complex flows inside the intake manifold. WaveMesher was used to model the curved profile geometries to study the effect of change in converging and diverging angles on the brake power and torque output of the engine.

In this paper, the application of both straight and curved profiled nozzles has been studied. Furthermore, the effect of using a curved nozzle whose design is adapted from rocket nozzles instead of a straight converging nozzle on the conventional engine has been considered. Moreover, to study the effect of the varying nozzle design on the performance curves and the volumetric efficiency of the engine, these designs were simulated in Ricardo WAVE.

The ultimate aim of the whole exercise was to improve the performance of our car on-track in the competition. Conventionally, in the design of any intake or exhaust system a particular RPM range is targeted and then engine's power and torque are maximised in that particular RPM range. An alternative approach is adopted in this paper, by using the point mass lap time simulation tool, OptimumLap, to qualitatively analyse how any increase or decrease in brake power and torque, due to change in the intake nozzle design, affected the lap time of our car on-track. Hence, using OptimumLap, we were able to observe the effects of changing the geometry of the nozzle directly in the terms of the car's lap times.
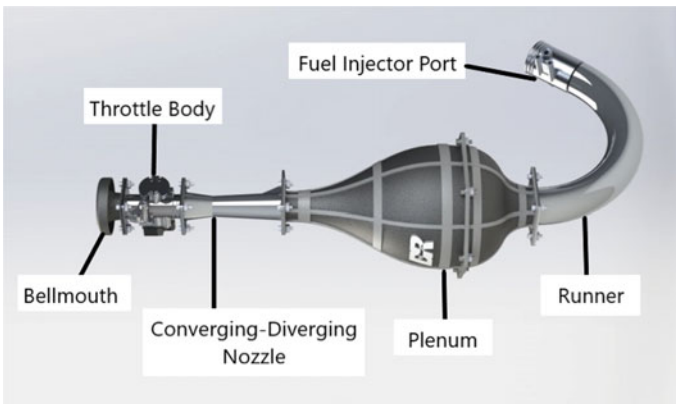
Fig. 1 Intake manifold layout

2 Computational Fluid Dynamic (CFD) Simulations

2.1 Turbulence Models

FLUENT provides the user with three different turbulence models to model viscous turbulence, i.e. Spalart–Allmaras, K-Epsilon and K-Omega.

Choosing the Correct Turbulence Model

Literature review shows that the above-mentioned turbulence models, given the right set up, are capable of simulating the flows present within the nozzle. It was observed that the Spalart–Allmaras model required least time to converge as well as least number of iterations. Both the k-ε model and the k-ω model took longer for each iteration as well as to converge to a final solution. However, upon studying the velocity profiles of the converged solutions in each case, the turbulent velocity profile of the k-ω model look much closer to a fully developed profile. Hence, it can be concluded that the k-ω model was most suited to the conditions present in the intake manifold as it provided the most accurate results despite a longer simulation period.

2.2 Meshing and Simulation

The venturi of an intake manifold is a very crucial part of the intake system as it is designed to overcome the ultimate restriction on the mass of air that can enter the engine's combustion chamber and consequently the amount of power output produced by the engine. Hence, it was necessary to extensively study and design the venturi of the intake system. Therefore, the venturi is designed as close to the choking limit as possible while still being relevant to our application. To model such a scenario, the simulation is designed with boundary conditions at its inlet as a pressure inlet with atmospheric pressure and its outlet as a mass flow outlet with fixed mass flow rate. This mass flow rate can be calculated assuming the flow is ideal compressible gas using the following formula [14]:

$$\dot{m} = \frac{A * p_\mathrm{t}}{\sqrt{T_\mathrm{t}}} * \sqrt{\frac{\gamma}{R}} * M * \left(1 + \frac{\gamma - 1}{2}M^2\right)^{-\frac{\gamma+1}{2(\gamma-1)}} \tag{1}$$

The variables are substituted with the following values:

- $A = 0.000314 \ \mathrm{m}^2$
- $p_\mathrm{t} = 101{,}325 \ \mathrm{Pa}$
- $T_\mathrm{t} = 300 \ \mathrm{K}$
- $\gamma = 1.4$
- $R = 0.286 \ \mathrm{kJ/kg \ K}$
- $M = 0.7$.

A mass flow rate of **0.069 kg/s** was calculated as a result.

The model used for the simulations is an axis-symmetric representation of the venturi to take advantage of FLUENT's capability to simulate a complete three-dimensional flow based upon a two-dimensional cross section.

As Fig. 2 shows, the two-dimensional mesh can have higher cell counts and refinement without being as computationally expensive as the three-dimensional mesh. The CAD model of the venturi was designed on SolidWorks software and the imported into the CFD software ANSYS FLUENT.

Mesh Independency

The simulation for mesh independency was done on an arbitrary venturi design with 12–6 venturi. Ten different iterations of meshes with cell counts varying from 128 to 40,331 total cells were generated. The pressure recovery at the outlet from the inlet was used as a marker for the accuracy and reliability of the mesh. Figure 3 depicts the drop in pressure across the nozzle in each iteration of the mesh. It can be seen that the pressure drops across the nozzle has varied from 1950 to 2789 Pa as the refinement of the meshes increased. It can also be observed that this variation is much lesser for
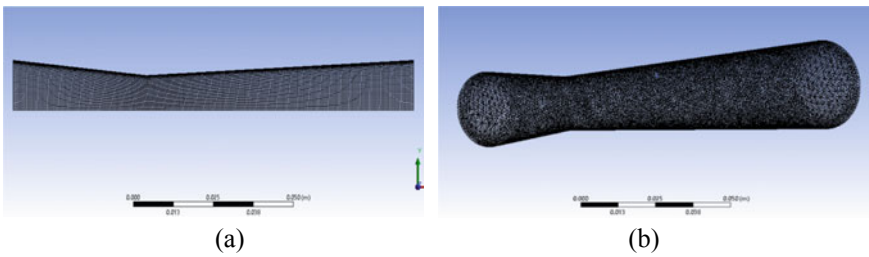
Fig. 2 Comparison of 2-D meshes (**a**) and 3-D meshes (**b**)
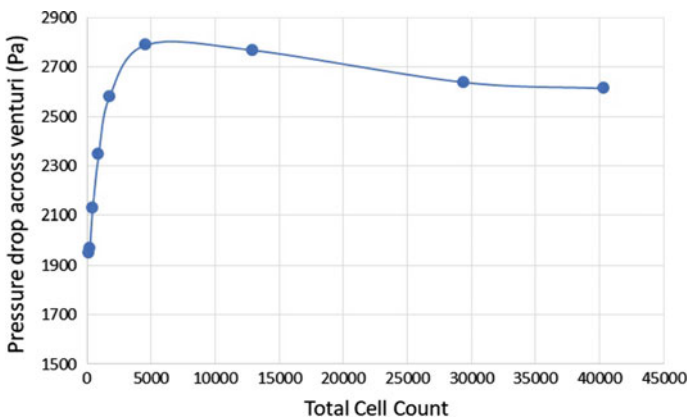
Fig. 3 Variation of pressure drop with cell count

meshes of cell count higher than 4000. It was also observed that the simulation time increased drastically for iterations of cell counts higher than 18,000.

Hence, the mesh settings used in the iteration number 6 were chosen as a standard setting for the simulations to be conducted as it provided the most accurate results with an acceptable computational time period.

Simulation

The design parameters of the venturi that could be varied were the converging angle and the diverging angle of the venturi as the radii at the throat, the inlet and the outlet were fixed due to spatial constraints, competition rules as well as the design of the plenum. The converging angle and the diverging angle of the venturi were varied in two methods. The first method involved varying the angles of the converging and diverging sections while maintaining linear, straight-line profiles. The second method involved varying the angles of the converging and diverging sections but with curved constant radius profiles. Each iteration was simulated to the same order of convergence which was when all residuals were below 10^{-6}.

3 Ricardo WAVE Simulations

WAVE is a one-dimensional engine simulation and gas dynamics software package. It is a computer-aided engineering code developed by Ricardo Software to analyse the dynamics of mass flows, pressure waves, energy losses in ducts, plenums, and the manifolds of various systems and machines [15]. Virtually any intake, exhaust and combustion system configuration can be simulated on Ricardo WAVE to find out changes in performance curves [16]. This software construes the originally intended three-dimensional simulation into numerous one-dimensional simulations [17].

3.1 Setup

The setup of the model required engine data, some of which was obtained from the service manual of the engine and the rest was measured manually by disassembling the engine, which is shown in Table 1.

Rest of the required inputs were intake and exhaust ports geometry and valve lift profiles. This was done by 3-D scanning of the cylinder head and camshafts. To capture a realistic flow of air inside the engine, it was extremely important to get the geometries of the ports. From the CAD model of the cam shaft, the valve lift profile was computed. And with the help of the CAD model of the cylinder head, intake design and geometry and the exhaust ports were computed. All of this data and engine specifications shown in Table 1 were used to create a model of the engine. In order to model and simulate the curved profiles of the bell nozzle in the WaveBuild environment, WaveMesher was used. WaveMesher is a graphical

Table 1 Engine specifications

Bore		95 mm
Stroke		72 mm
Length of connecting rod		122 mm
Compression ratio		11.8:1
Intake	Number of valves	2
	Valve diameter	40 mm
	Valve lift	10 mm
Exhaust	Number of valves	2
	Valve diameter	30 mm
	Valve lift	9 mm
Valve event timings	IVO	6.5° BTDC
	IVC	46.5° ABDC
	EVO	50° BBDC
	EVC	4° ATDC
Fuel type		Gasoline
Fuel delivery		Port fuel injection
Combustion model		SI Wiebe combustion
Heat transfer model		Woschni heat transfer

pre-processor for creating WAVE models from true 3-D, CAD-generated geometry. WaveMesher imports CAD-triangulated geometry in STL format. The CAD models of the geometries were created using SolidWorks, which were then converted into STL format and then imported into the WaveMesher environment. Cutting planes are used to chop the geometry into bodies representing ducts, y-junctions, or orifices. Once the bodies are defined, WaveMesher automatically generates a WAVE element for each body [15]. The division of the bell nozzle in to ducts is shown in Fig. 4.

The stock silencer was modelled as it was intended to be used in the competition. Disassembly of the silencer was done to measure its exact specifications for the
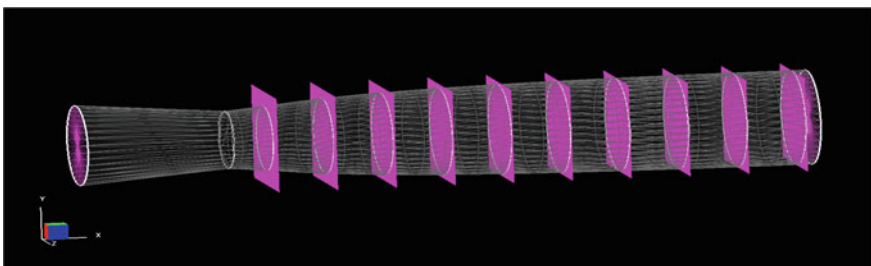
Fig. 4 Discretization of bell nozzle in the WaveMesher environment
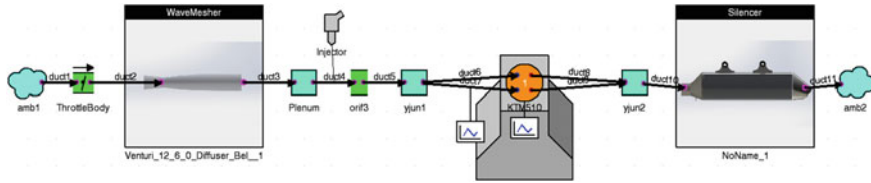
Fig. 5 Ricardo WAVE model with 3-D CAD generated geometries

perforation density. The complete model of the whole system with the intake and the exhaust configuration is shown in Fig. 5.

4 Point Mass Lap Time Simulations

The main objective of any change in the car is to get the fastest lap time possible out of it. The objectives of a race car project are always targeted towards the maximum performance out of the setup with rule constraints of the competition. Designing and manufacturing a one-of-a-kind vehicle prototype can be a very expensive and time-consuming process, especially if each change in the vehicle needs to be tested on-track for its viability. In order to avoid expensive manufacturing of different iterations and hence save time and money, the usage of lap time simulation is justified. Please note that the software does not give the absolute lap times. The key objective of the lap time simulation software is to give relative lap times on different changes made to the vehicle setup in order to get the optimum performance [18]. The software helps to get the fastest time from a particular setup which can be varied for better performance [19].

4.1 Results

Upon simulating all iterations and comparing the results of the CFD simulations, it can be noted that increasing the converging angle leads to lower pressure drops across the nozzle for curved profiles, but the converse is true for the straight-line profiles where increasing the converging angle leads to larger pressure drops across the nozzle. This can be clearly observed in the graphs depicting the pressure drops across the nozzle for varying converging angles of the nozzle (for both straight-line and curved profiles) in Fig. 6. It should also be noted that nozzles with curved profiles in their converging sections attain much better pressure recovery compared to the straight profiled nozzles at larger angles of converging sections (>20°).

In the case of diverging angles, it was observed that increasing the diverging angle of the venturi with curved profiles does lead to a drop in the pressure drop across the venturi but beyond 10°, it leads to an increase in pressure drop across the nozzle for
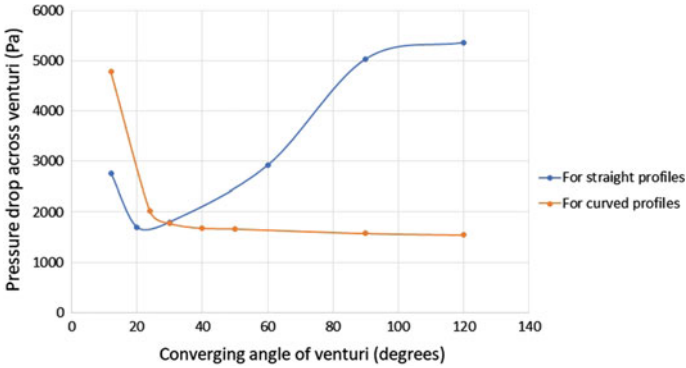
Fig. 6 Variation of pressure drop with converging angle of the nozzle

both curved profiles and hence poorer pressure recovery at the pressure outlet. The same behaviour can be observed while increasing the diverging angles of the venturi with straight-line profiles but the increase in pressure drop happens sooner at angles greater than 5°.

This has been shown clearly in the graph depicting pressure drop across the nozzle for varying diverging angles of the nozzle (for both straight-line and curved profiles) in Fig. 7. It can also be observed that the pressure drop across the nozzle is much significantly lower for nozzles with curved profiles in their diverging sections.

The torque and the power curves were observed for each of the nozzle geometries. The overall motive was to maximise the mass flow of air entering the combustion chamber, hence maximising the volumetric efficiency. It was observed that the volumetric efficiency had a direct impact on the torque produced by the engine and the power curve was relatively less sensitive to the changes in the engine's volumetric efficiency. WavePost is graphical post-processor of the Ricardo WAVE simulations.
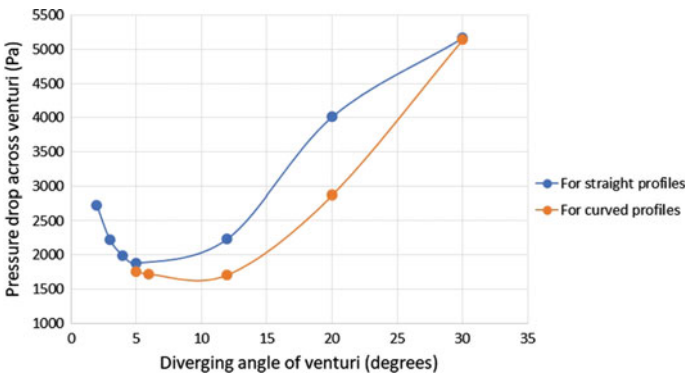
Fig. 7 Variation of pressure drop with diverging angle of the nozzle
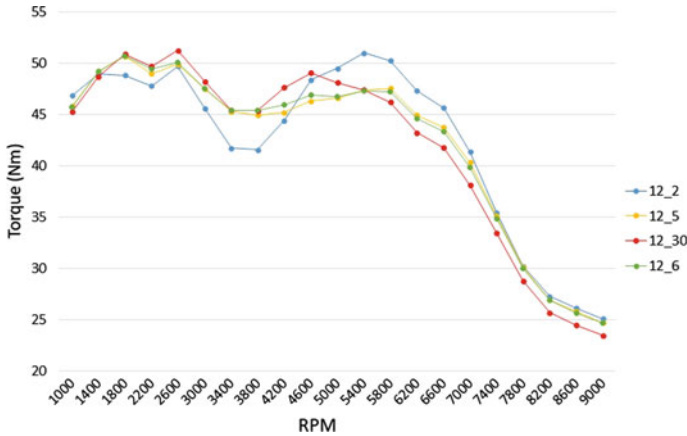
Fig. 8 Variation of torque output with RPM for different diverging angles of the nozzle

It was used to obtain the desired graphs then the visualisation and the comparison of the curves for different nozzle designs was done.

Firstly, the torque curves for different converging angles of then straight nozzle profiles were compared keeping the diverging angle to be 6°. It was observed that there was a slight increase in the torque output between 5800 and 7000 RPM for the nozzle with the converging angle of 12°. Then, the torque curves for different diverging angles of straight nozzle profiles were compared, keeping the converging angle of the nozzle to be 12°. As shown in Fig. 8, it was observed that the diverging angle of the nozzle had a substantial and considerable impact on the engine's torque output, in contrast with the effect of varying the converging angles.

The nozzle with the diverging angle of 2° showed a significant increase in the torque between 4600 and 7000 RPM.

Thereafter, the comparison of torque outputs of the bell nozzles with the straight profile nozzles was done as shown in Figs. 9 and 10.

Thereafter, lap time simulations were done to study change in lap time for varying power factors (batch simulation). Figure 11 shows the power factor batch simulation which is a stepwise increase in the power percentage in order to observe the changes in the lap time.

5 Conclusion

Upon comparing various designs of converging–diverging nozzles, simulating various angles and geometries using CFD in ANSYS, it can be concluded that a 25–10 curved converging and diverging nozzle provides the least pressure drop within the spatial as well as manufacturing constraints present. This conclusion is based on the results obtained that curved profiles nozzles provide better pressure recovery
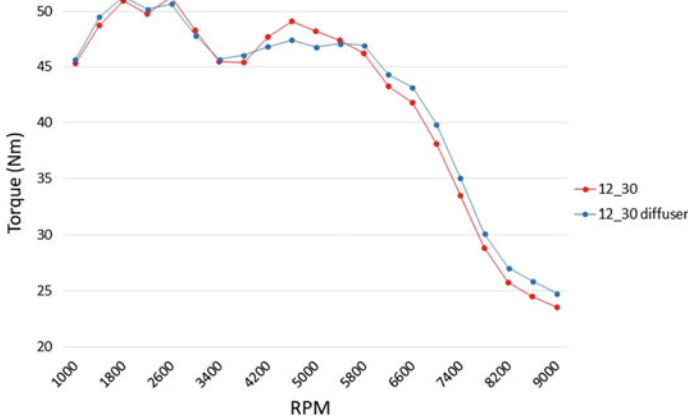
Fig. 9 Variation of torque output with RPM for a 12° converging angle for a nozzle of straight and bell profiles in their diverging sections
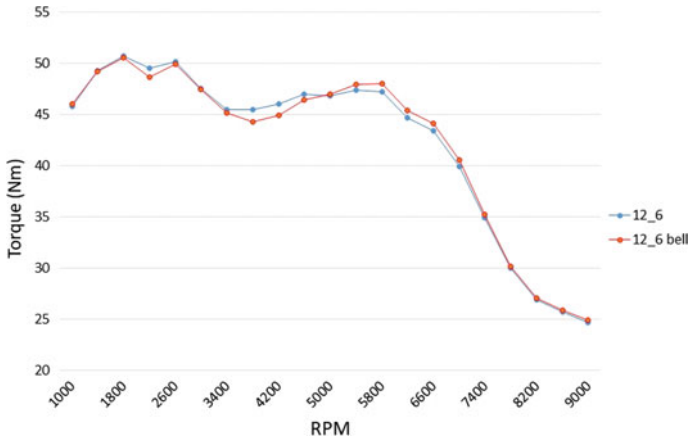
Fig. 10 Variation of torque output with RPM for a 6° diverging angle for a nozzle of straight and bell profiles in their converging sections

compared to their straight profiles counterparts and the fact that the selected 25–10 curved converging–diverging nozzle provides a 32.4% decrease in pressure drop as opposed to 12–6 straight profile nozzle.

The nozzle geometries made with the help of CFD were then simulated in Riccardo WAVE to study the effect of change in nozzle geometry on the brake power and torque output of the engine. It was found that a 25–10 bell nozzle provided a maximum of 2.6% increase in brake power at 7000 RPM and a maximum 2.6% increase in brake torque at 7000 RPM. The performance curves computed with the help of WAVE simulations were fed into OptimumLap to compute how these changes in the
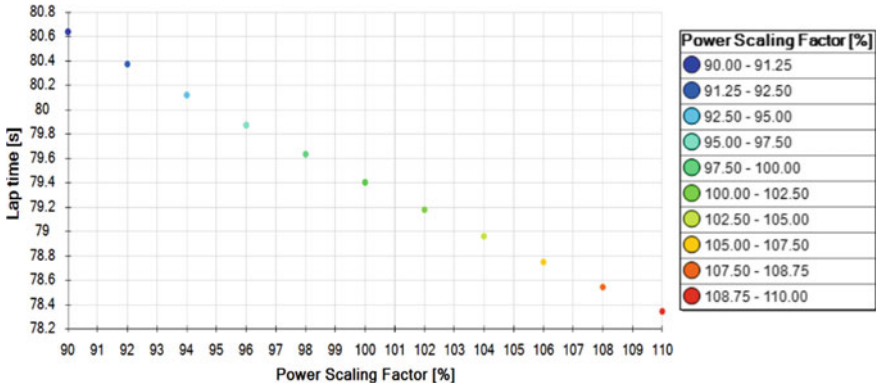
Fig. 11 Lap time(s) versus power scaling factor (1.25% steps)

performance affected the lap times of our car. It was found that the selected geometry, i.e. 25–10 nozzle, produced a lap time of 83.3 s while the base geometry produced a slower lap time of 84.03 s.

References

1. Vichi, G., Romani, L., Ferrari, L., Ferrara, G.: Development of an engine variable geometry intake system for a formula SAE application. Energy Procedia **81**, 930–941 (2015)
2. Jawad, B.A., Hoste, J.P., Johnson, B.E.: Formula SAE dual plenum induction system design. SAE Technical Paper, No. 2002-01-0457 (2002)
3. Mattarelli, E., Rinaldini, C.A., Development of a high-performance engine for a formula SAE racer. SAE Technical Paper, No. 2012-01-0833 (2012)
4. Chen, C.W., Du, W., Sun, J.Q., Liu, W., Chang, Y., Dong, W.: Simulation analysis and design of intake restrictor of FSAE race car. In: Applied Mechanics and Materials, vol. 602, pp. 751–756. Trans Tech Publications Ltd (2014)
5. Singhal, A., Parveen, M.: Air Flow Optimization Via a Venturi Type Air Restrictor. WCE, London UK (2013)
6. Byam, B., Fsadni, J., Hart, A., Lanczynski, R.: An experimental approach to design, build, and test a throttle body and restrictor system for formula SAE racing. SAE Technical Paper, No. 2006-01-0748 (2006)
7. Deshpande, O.N., Narappanawar, N.L.: Space advantage provided by de-laval nozzle and bell nozzle over venturi. In: Proceedings of the World Congress on Engineering, vol. 2 (2015)
8. Jawad, B., Dragoiu, A., Dyar, L., Zellner, K., Riedel, C.: Intake design for maximum performance. SAE Technical Paper, No. 2003-01-2277 (2003)
9. Ceviz, M.A., Akın, M.: Design of a new SI engine intake manifold with variable length plenum. Energy Convers. Manage. **51**(11), 2239–2244 (2010)
10. Seshadri, S.: Design and CFD analysis of the intake manifold for the Honda CBR250RR engine (2015)
11. Calvo, A., Garcia, H., Carbajal, G.: Design, analysis and simulation of an intake manifold. In: ASME 2013 International Mechanical Engineering Congress and Exposition. American Society of Mechanical Engineers Digital Collection (2013)
12. Cordon, D., Dean, C., Steciak, J., Beyerlein, S.: One-dimensional engine modeling and validation using Ricardo WAVE. Final Report, University of Idaho (2007)

13. Claywell, M., Horkheimer, D., Stockburger, G.: Investigation of intake concepts for a formula SAE four-cylinder engine using 1D/3D (Ricardo WAVE-VECTIS) coupled modeling techniques. SAE Technical Paper, No. 2006-01-3652 (2006)
14. Porter, M.: Intake manifold design using computational fluid dynamics. UNSW Canberra ADFA J. Undergraduate Eng. Res. **1**(2), 31 (2009)
15. Alqahtani, A., Shokrollahihassanbarough, F., Wyszynski, M.L.: Thermodynamic simulation comparison of AVL BOOST and Ricardo WAVE for HCCI and SI engines optimization. Combust. Engines **54** (2015)
16. Gilani, R.: Engine simulation model for a formula SAE race car: applied design, development, correlation and optimization (2012)
17. Ghodke, S., Bari, S.: Effect of integrating variable intake runner diameter and variable intake valve timing on an SI engine's performance. SAE Technical Paper, No. 2018-01-0380 (2018)
18. Siegler, B., Deakin, A., Crolla, D.: Lap time simulation: comparison of steady state, quasi-static and transient racing car cornering strategies. SAE transactions, pp. 2575–2581 (2000)
19. Siegler, B., Crolla, D.: Lap time simulation for racing car design. SAE Transactions, pp. 306–314 (2002)

Performance and Exergy Analysis of Single Slope Passive Solar Still in Clear Sky Condition

Ravi Kant and **Anil Kumar**

Nomenclature

A_s	Area of solar still
$\dot{E}_x$	Exergy
$I(t)$, I	Global solar radiation, solar radiation (W/m^2)
L	Latent heat of vaporization of water
$\dot{m}$	Yield (kg/h)
T	Temperature (°K)

Subscripts

a	Ambient
d	Diffused
ew	Water
g	Global
in	Input
ic	Collector input
igs	Inner glass
oc	Collector outlet
ogs	Outer glass

R. Kant · A. Kumar (✉)
Department of Mechanical, Production & Industrial and Automobile Engineering, Delhi Technological University, Delhi 110042, India
e-mail: anilkumar76@dtu.ac.in

A. Kumar
Centre for Energy and Environment, Delhi Technological University, Delhi 110042, India

385

Greek Letters

η Efficiency

1 Introduction

Water is a necessary part of life. Life is not conceivable on earth without water. There is a critical need for clean water for the survival of people on earth. Around 70% of the earth's surface is covered with water. Seas and oceans contain 97% of earth's water reserve which is salty water (30,000–35,000 ppm) and accordingly not reasonable for human utilization. Just 3% of the total water resources on the surface of the earth have freshwater. Over 2% of clean water is solidified as ice sheets and ice hinders in the polar locale and rest of clean water (under 1%) are found in the waterways, lakes, lakes, and underground water. That little piece of clean water has been the principal source of water to satisfy the need for local, agriculture, and mechanical exercises [1].

This clean water isn't clean as indicated by the national standard as it contains the destructive microorganisms and infections, which are the reason for different water-created disease, for example, cholera, looseness of the bowels, malaria, typhoid and some more, which execute over 3 million individuals consistently. Pure water is a valuable item and necessary for our survival. Because of increment in population and quick industrial improvement, the need for consumable water will expand step by step. Many water refinement systems have been created to fulfill the clean water shortage on the earth. It can be satisfied by one of the procedures known as desalination. It is a generally recognized method for converting salty or polluted water into freshwater by the utilization of thermal energy (solar or non-renewable energy sources). Solar energy is a perfect solution for fueling the distillation process, which is atmosphere friendly, freely available, never ending, and available in large quantities everywhere throughout the planet [2].

Solar desalination is a standout among other strategies for decontaminating salty water. Solar still is a gadget that is broadly utilized as a part of the solar-powered desalination process, Yet the productivity and effectiveness of a solar still are lower in comparison with other desalination processes. Therefore, it is essential to further improve the efficiency of solar still by enhancing the traditional design parameters and operational techniques.

The development of a solar still is straightforward. It can be created by individuals in the community utilizing locally accessible material. Still is a sealed pack dark-painted rectangular bowl covered with simple cover to absorb the solar energy inside it and contains polluted water. At the point when daylight falls on the straightforward cover, the water of the bowl is heated up and evaporates. The water vapor condensed on the internal side of the cover and keeps running down along the surface of cover

because of gravity and gets gathered steadily in a container through a condensate channel [3].

El-Sebaii et al. found that the daily production of distilled water from the still is measured to 9.005 (kg/m^2 day) on a summer day with a daily efficiency of 84.3% when 3.3 cm of stearic acid is used under the absorber of still. In comparison with that, the productivity of still without PCM is measured to 4.998 (kg/m^2 day) [4]. Pal et al. found that MBDSMWSS with black cotton wicks and jute had a maximum overall thermal efficiency of 28.27% and 20.94%, respectively. In December 2015, the maximum instantaneous thermal efficiency was achieved as 54.80% [5]. Elshamy et al. found that the water production rate of tubular solar still (TSS) was increased by 19.33–26.47% when a semicircular corrugated observer is used in the place of the flat absorber. The thermal efficiency of TSS with flat absorber was increased by 22.6–25.9% with the utilization of semicircular corrugated absorber [6]. Singh et al. studied and found that the yield of parallel forced mode solar still is higher than the other design of solar still. The yield was achieved as 7.54 kg/day with an energy efficiency of 17.4%. The highest hourly exergy efficiency is also obtained for the same design, and the value goes to 2.3%. The yield achieved for single slope hybrid (PVT) solar still is about 1.4 times lower than that obtained for parallel forced mode solar still comparatively [7].

Experimental work was performed to determine the yield of single slope solar still utilizing different operating parameters. A significant increment in the productivity of still of 29% was obtained with the utilization of asphalt in the basin. The combination of asphalt and sprinkler was more effective in place of asphalt alone and increased productivity by further 22%. It can also be concluded that the productivity of still is directly affected by ambient parameters (i.e., solar radiation, wind speed and temperature etc). the result shows that the distillate output of sun-powered still enhances with the decrement in the depth of water [8].

The performance of a basin type solar still has been investigated with three distinct modifications in design. The outcomes of experiments indicate that the thermal performance of conventional single slope solar still can be significantly increased through modifications in the design. The freshwater production rate was increased to 30% by installing internal reflecting mirrors in comparison with a classical rigid solar still structure. A higher production rate with an average increase of 180% is achieved when still design is modified from flat basin to stepwise basin. The productivity of distilled water increases by 380% when modified still is coupled with a sun tracking system [9].

The condensation occurs on the glass surface as well as on the four sidewalls due to the temperature difference. The efficiency of solar still can be improved by circulating water through tubes connected to the wall surface. The maximum productivity of the solar still was reached up to 1.4 l/m^2 per day with an equivalent average solar irradiance of 28 MJ/d and its efficiency reached up to 30%. The quality of condensate water was analyzed and found that it was comparable with water quality standards and against mineral water and rainwater [10].

The information on efficiency and productivity of sunlight based still depends on the area where experimentation is finished. With a specific end goal to survey the

utility and attainability of sun-powered still in the Indian focal area, single slope single basin sunlight based still were led and information attained for efficiency, productivity, and exergy efficiency. The outcomes of experiments on natural circulation mode are looked at and displayed in this paper.

2   Materials and Methods

2.1   Experimental Setup and Instrumentation

The schematic of a single slope passive sun-powered still, which is made of fiber-strengthened plastic (FRP), appears in Fig. 1. For more absorptivity, the base surface of the still was painted black and the still is covered with a glass cover of 3 mm thickness. The still area was taken as 1 and 2.014 m^2 of flat plate collector (FPC). FPC is of TATA POWER Company. The depth of solar still was 5.08 cm.

Observations were made for 24 h (6:00–18:00 h) for 3 days in March. The average spacing between the glass cover and the surface of the water is 0.25. The parameters that are measured every hour for 24 h at the full depth are as follows:

- Global radiation on the collector
- Diffused radiation on the collector
- Ambient temperature
- The velocity of air on the collector
- Inner glass temperature
- Outer glass temperature
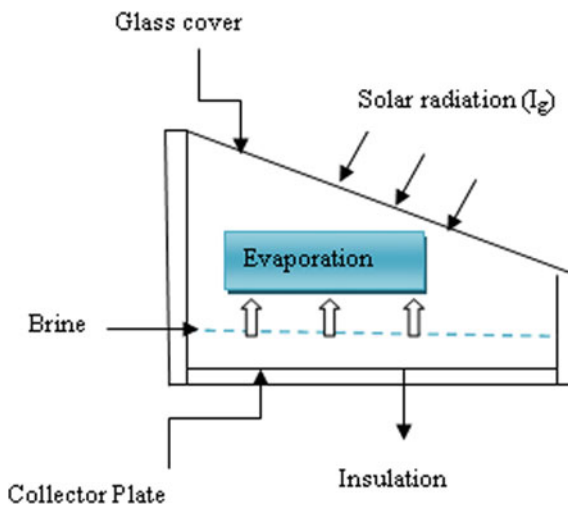
Fig. 1   Single slope passive solar still
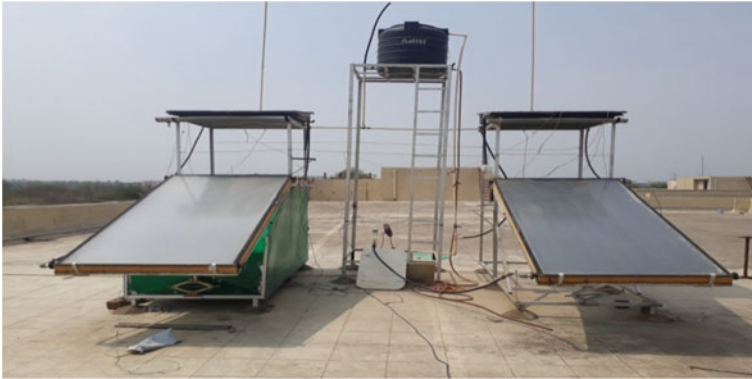
Fig. 2 Picture of the experimental setup

- Water temperature
- vapor temperature just above the water surface
- Inlet collector temperature
- Outlet collector temperature
- Distillate output.

Water, inner glass, outer glass, vapor, inlet collector, and outlet collector were measured by the calibrated iron–constantan thermocouples and a voltmeter. With the help of a voltmeter, the voltage of the above junction is recorded and then converted into temperatures by the K-type thermocouple table. The distillate output and ambient temperature were measured by the measuring cylinder of the least count of 10 ml and hygrometer, respectively. Global solar radiation and diffused solar radiation were measured by the solar power meter with least count 2 W/cm^2. Experiments were done from February to May. Inner glass, water, outer glass, vapor, solar global radiation, inlet collector, and outlet collector temperature were hourly measured for date 06, 07, and 08 in March. The experimental setup picture is shown in Fig. 2.

2.2 Methodology

2.2.1 Thermal Performance Analysis

The instantaneous thermal efficiency (η_i) can be calculated as [11]:

$$\eta_i = \frac{\dot{m} L}{I(t) A_s} \tag{1}$$

The overall thermal efficiency of a single slope passive sun-powered still can be determined as:

$$\eta_{Passive} = \frac{\sum \dot{m} L}{A_s \int I(t) dt} * 100 \tag{2}$$

2.2.2 Exergy Analysis

The exergy efficiency of a single slope passive sun-powered still can be calculated as [12]:

$$\eta_{ex} = \frac{\text{Exergy of product}}{\text{Exergy input(Exergy of fuel)}} \tag{3}$$

Exergy of product is calculated as:

$$\dot{E}_{x_{product}} = \dot{m} \times E_{x_{ew}} \tag{4}$$

In Eq. (4), $E_{x_{ew}}$ denotes the exergy of latent heat of vaporization (J/kg) which is calculated as:

$$E_{x_{ew}} = \left[L \times (1 - \frac{T_a}{T_w}) \right] \tag{5}$$

Exergy input or exergy of fuel is calculated as:

$$\dot{E}_{x_{in}} = A_s \times I(t) \times \left[1 - \frac{4}{3} \times \left(\frac{T_a}{T_s} \right) + \frac{1}{3} \times \left(\frac{T_a}{T_s} \right)^4 \right] \tag{6}$$

By putting the values of Eqs. (4), (5), and (6) in Eq. (3), the exergy efficiency is calculated as:

$$\eta_{ex} = \frac{\frac{\dot{m}}{3600} \times \left[L \times (1 - \frac{T_a}{T_w}) \right]}{A_s \times I(t) \times \left[1 - \frac{4}{3} \times \left(\frac{T_a}{T_s} \right) + \frac{1}{3} \times \left(\frac{T_a}{T_s} \right)^4 \right]} \tag{7}$$

3 Result and Discussion

The results that are obtained for different parameters are given in this section. The observations were taken in March for 24 h for 3 days.

Figure 3 shows the hourly variation of ambient parameters (relative humidity, wind velocity, ambient temperature, global solar radiation, diffused solar radiation)
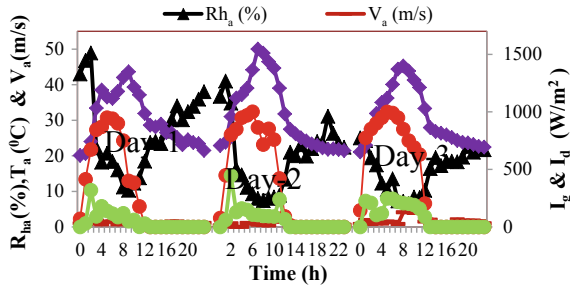
Fig. 3 Ambient parameters variation with time

with time for different days in March. The maximum relative humidity was achieved for day 1 at 8:00 h. The ambient temperature was highest for day 2 at 13:00 h and its value is achieved as 50 °C. The highest solar global radiation of 1000.5 W/m² was obtained for day 3 at 11:00 h. Wind velocity reaches up to a maximum value of 4 m/s on day 3 (Fig. 3).

Figure 5 shows the hourly variation in yield in natural circulation mode of single slope solar still in March. The yield was maximum for day 3 at 16:00 h and reaches up to a value of 990 ml. For day 2, it has a maximum value of 750 ml at 14:00 h and for day 1, it has a maximum value of 650 ml at 14:00 h.

Figure 6 shows the hourly variation in thermal efficiency in the natural circulation mode of single slope solar still in March. The highest value of thermal instantaneous efficiency was 35% for day 1.

Figure 7 shows the variation in overall thermal efficiency for different 3 days in March. Overall thermal efficiency was maximum for day 1 and reaches up to a value of 11%.

Figure 8 indicates the variation in hourly exergy efficiency to time for different three days in March. The maximum value of hourly exergy efficiency was 2.30% for day 1.
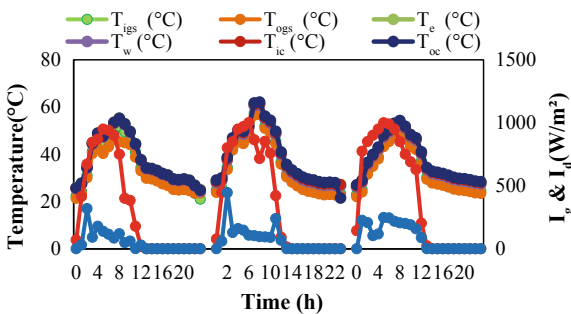
Fig. 4 Hourly variation of temperatures of different junctions of still with time
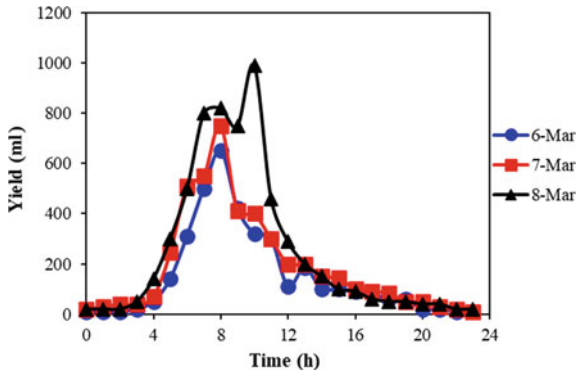
Fig. 5 Hourly variation in productivity with time
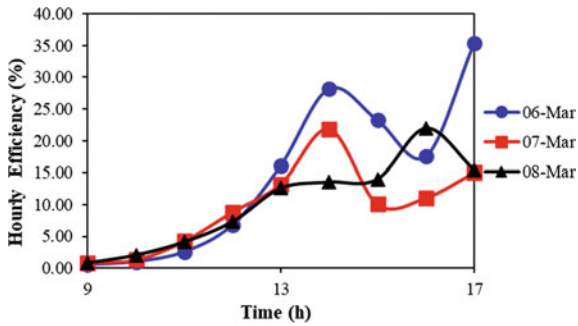
Fig. 6 Hourly variation in thermal efficiency with time
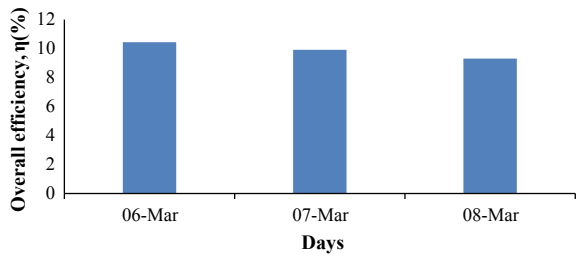
Fig. 7 Overall thermal efficiency for different days

Figure 9 shows the overall exergy efficiency for different three days. The value of maximum overall exergy efficiency reached up to 0.364% for day 1.
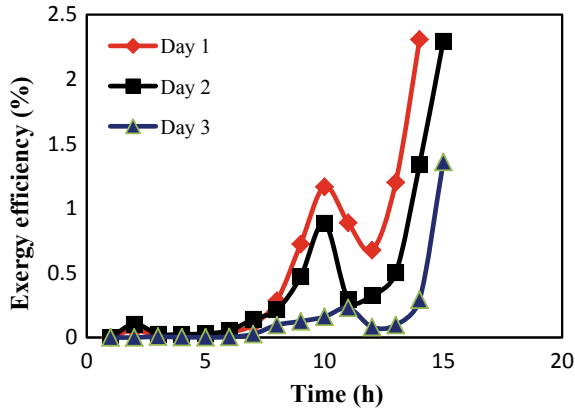
Fig. 8 Hourly exergy efficiency to time
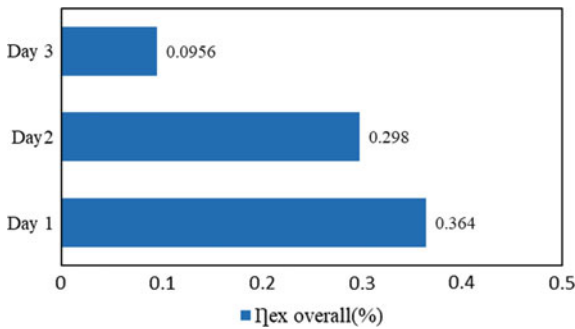
Fig. 9 Overall exergy efficiency for different days

4 Conclusions

Following conclusions have drawn after the experiments and mathematical analysis:

- Thermal instantaneous efficiency was maximum for day 1, and its magnitude was 35%.
- The highest yield was obtained for day 3 and reached up to a value of 990 ml.
- Relative humidity reaches up to the maximum value of 48.9% for day 1 at 8:00 h. The ambient temperature was highest for day 2 at 13:00 h and achieved as 50 °C. Solar global radiation reaches up to a maximum value of 1000.5 W/m^2 on day 3 at 11:00 h. Wind velocity goes to a maximum value of 4 m/s on day 3.
- Overall efficiency in March varies from 9 to 11% in passive solar still. The maximum value is obtained for day 1 (6 March).
- The highest hourly exergy efficiency was achieved for day 1, and its value was 2.30%.

- The value of maximum overall exergy efficiency reaches up to 0.364% for day 1.

References

1. Kumar, A., Prakash, O.: Solar Desalination Technology, Green Energy and Technology (2019)
2. Tripathi, R., Tiwari, G.N.: Desalination effect of water depth on intemal heat and mass transfer for active solar distillation. Desalination **173**, 187–200 (2005)
3. Tiwari, A.K., Tiwari, G.N.: Effect of water depths on heat and mass transfer in a passive solar still: in summer climatic condition. Desalination **195**, 78–94 (2006)
4. El-Sebaii, A.A., Al-Ghamdi, A.A., Al-Hazmi, F.S., Faidah, A.S.: Thermal performance of a single basin solar still with PCM as a storage medium. Appl. Energy **86**(7–8), 1187–1195 (2009)
5. Pal, P., Yadav, P., Dev, R., Singh, D.: Performance analysis of modified basin type double slope multi–wick solar still. Desalination **422**, 68–82 (2017)
6. Elshamy, S.M., El-Said, E.M.S.: Comparative study based on thermal, exergetic and economic analyses of a tubular solar still with semi-circular corrugated absorber. J. Clean. Prod. **195**, 328–339 (2018)
7. Singh, G., Kumar, S., Tiwari, G.N.: Design, fabrication and performance evaluation of a hybrid photovoltaic thermal (PVT) double slope active solar still. Desalination **277**(1–3), 399–406 (2011)
8. Badran, O.O.: Experimental study of the enhancement parameters on a single slope solar still productivity. Desalination **209**(1–3 special issue), 136–143 (2007)
9. Abdallah, S., Badran, O., Abu-Khader, M.M.: Performance evaluation of a modified design of a single slope solar still. Desalination **219**(1–3), 222–230 (2008)
10. Vinoth Kumar, K., Kasturi Bai, R.: Performance study on solar still with enhanced condensation. Desalination **230**(1–3), 51–61 (2008)
11. Tiwari, G.N.: Solar Energy Fundamentals Design Modelling and Application, 9th edn. Narosha Publishing House, New Delhi (2012)
12. Tiwari, G.N., Dimri, V., Chel, A.: Parametric study of an active and passive solar distillation system: energy and exergy analysis. Desalination **242**(1–3), 1–18 (2009)

Experimental Analysis of Four-Stroke Single-Cylinder Diesel Engine Using Biogas as a Dual Fuel

Pradeep Kumar Meena , **Amit Pal** , **and Samsher**

1 Introduction

A large amount of solid waste is generated daily in India, and according to a report, 1.5 metric tons/day and 532 metric tons/annum solid waste is generated [1]. Energy can be generated by solid waste because as we know world reserves of primary energy and raw materials are limited. According to an estimate, reserves will last 218 years for coal, 41 years for oil, and 63 years for natural gas [2].

According to a report, 999 landfill sites are identified to dump solid waste in India and in which only 204 landfill is operational [1]. This is very less according to the quantity of solid waste; it means most of the solid waste is thrown here and there without any utilization. The amount of solid waste is increasing every year with a huge increase and will reach around 250 million tons/year by 2040 [3].

Most organic wastes that originate from household, mess, and the restaurant are not as segregated. If proper separation of solid waste is done, it can be used as biogas energy for cooking, generating electricity, and running engines. India imports most petroleum products from other countries and in return pay a heavy import bill due to heavy import bill which adversely affects foreign exchange, and we know that emission of fossil fuel is very high which is the reason behind global warming. By using biogas energy more and more, the fossil fuel can be replaced because it is eco-friendly, cheap, and easy to produce [4].

Biogas is a mixture of gases developed from the digestion process of organic materials by anaerobic bacteria under anaerobic conditions, and the composition of biogas is methane, carbon dioxide [5]. Biogas plant requires cow dung and water first, once methane bacteria are produced, then any type of organic waste can be

P. K. Meena (✉) · A. Pal · Samsher

Department of Mechanical, Production & Industrial and Automobile Engineering, Delhi Technological University, Delhi 110042, India
e-mail: paru.meena@gmail.com

used in the biogas plant [6]. In this retention period, most biogas is produced by co-digestion of kitchen waste and cow dung, compared to co-digestion of kitchen waste, fruit waste, and dung [7]. Biogas that originates from the co-digestion of additive rice straw and organic waste improve the performance of the DF engine [8].

Biogas can be easily converted to DF mode without any modifications to the engine, and in DF mode, it improves engine performance [9]. Raw biogas can be converted into enriched biogas by using CO_2 and H2S scrubbers, and when the amount of CH_4 increases to 95%, these enriched biogas act as bio-CNG and give similar results to CNG gas [10]. The performance of the DF engine depends on the compression ratio and when it increases, the BTE of the DF engine increases as well as the pilot fuel saving [11].

As of 2012, approximately 4.5 million biogas plants have been set up in India, and the number of biogas plants is very small compared to the number of organic wastes [12]. To control this problem, we have to build more and more compact biogas plants, so that there is a proper use of organic waste in the form of biogas, and various applications of biogas can be used. If every citizen of India takes the initiative to properly utilize the waste generated from the kitchen or fruit waste at their home, it can make the Swachh Bharat Mission a success, i.e., the Swachh Bharat Abhiyan. In this paper, we are trying to develop a portable compact biogas plant, after which biogas is produced using homemade organic waste, and finally, it is converted to DF mode using biogas in diesel engines. In DF mode, BTE, VE, and ITE are much higher than diesel fuel, and diesel consumption rate is reduced when using dual fuel.

2   Experimental Setup and Procedure

To set up a compact biogas plant, firstly, two main plastic tanks are required, one tank has a storage capacity of 1000 L which is used for the digester, and another tank that has a storage capacity of 750 L is used for the gasholder. The gases can be produced according to the size of the plastic tank and wastage as per the requirement. The organic waste is mixed with water and the slurry is poured into the larger tank, and the smaller tank is placed upside down on the larger tank.

As the gas is formed, the small tank floats on top of the solution, and it starts to rise. The larger plastic tank has an effective volume of about 800 L. About 80% of the surface area of the digester tank is covered by the gasholder (Fig. 1).

In other words, about 20% of the gas goes through the digester surface into the atmosphere without any use. Out of the gasholder having a total volume of 750 L, only 400 L of gas can be stored, which means that the amount of usable gas in the gasholder is 400 L. After the establishment of the compact biogas plant, it produced biogas using various organic wastes (Fig. 2).

After the production of the biogas successfully, it is utilized to run a four-stroke single-cylinder diesel engine to determine the performance of the engine in terms of its power and efficiency. The diesel engine is converted into a dual-fuel engine followed by its comparative analysis. Diesel fuel supply is connected with the burette
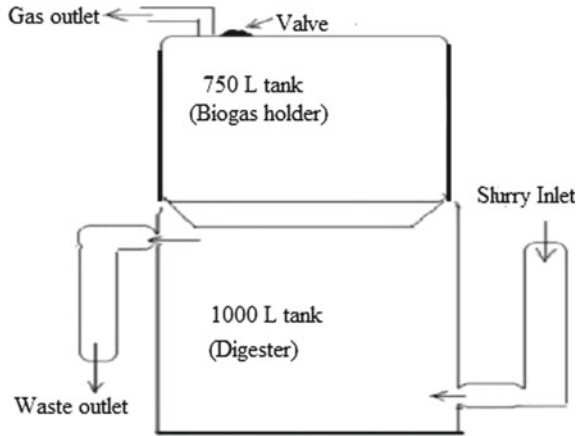
Fig. 1 Schematic view of the compact biogas plant [13]
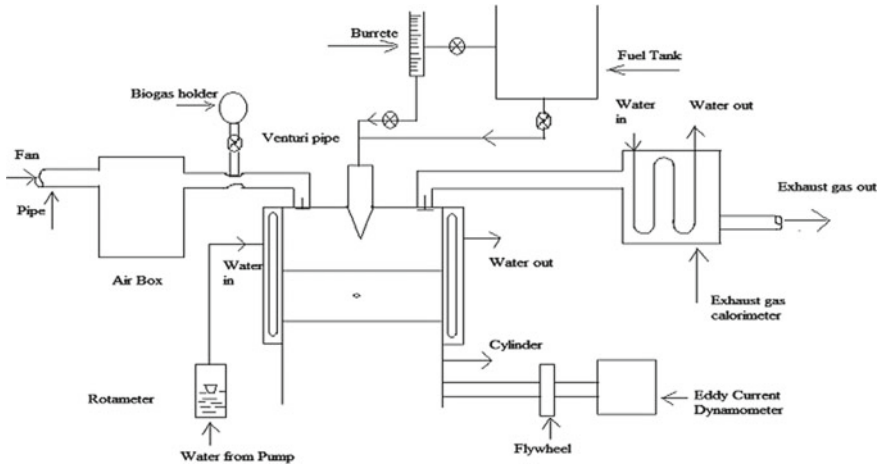
Fig. 2 Schematic diagram of the DF engine setup

through the control valve which is further connected to the injector of the engine. Fuel consumption is measured for a time through the scale on the burette (Fig. 3).

The air pipe is connected to the engine, and water from the pump is used to cool the engine, and its inlet and outlet temperature are measured at different loads as well as the inlet and outlet temperature of the water entering the calorimeter is also measured during the experiment. Exhaust gas temperature is measured at two different points, i.e., inlet and outlet of the calorimeter. A dynamometer is employed to change the load on the engine.

Venturi pipe is connected in between air pipe which is connected to the engine, and another inlet of venturi pipe is connected to the gasholder through a gas pipe. Mixing

Fig. 3 Four-stroke single-cylinder diesel engine converted into dual-fuel (biogas + diesel) mode

Table 1 Specifications of engine

Parameters	Specifications
Engine name	Comet diesel engine, Sr. no 2.7.32.8
Bore (mm)	102
Stoke (mm)	111
Compression ratio	18:1
Speed (RPM)	1500
Power output (kW)	7.4
Arm length of a dynamometer (mm)	400
Take 685 RPM at a testing time	

of biogas and air occurs in the reduced section of the venturi because of the pressure difference, and this mixture enters into the engine where it is compressed. Since the auto-ignition temperature of the biogas is much higher than of diesel; therefore, the mixture does not pre-ignite in the engine. As soon as, the mixture enters into the engine, it is compressed, and diesel is injected which further increases the overall temperature of the fuel after burning for the complete combustion of dual fuel (Table 1).

3 Calculations

First, find the average time to consume 10 cc of fuel (10 ml) at different loads (0, 2, 4, 6, 8, and 10 kg) in diesel and dual-fuel modes when the engine speed is 685 RPM. The average time in DF mode for weight 0, 2, 4, 6, 8, and 10 kg was found to be 126, 113, 80, 62, 43, and 29 s, and in diesel fuel, average time was 72, 54, 43, 35, and 27 s.

Specification and constants

Specific gravity of diesel fuel = 0.83 and biogas sp. gravity = 0.94
Specific gravity of water = 1
Water density (ρ_w) = 1000 kg m^{-3}
Specific heat of water (K) = 4.187 kJ kg^{-1} K
Characteristic gas constant for air Ra = 0.287 kJ kg^{-1} K
Calorific value of diesel fuel (C_dv) = 42,500 kJ kg^{-1}, biogas (C_bv) = 19,744 kJ kg^{-1}
Bore = 0.102 m
Stoke = 0.111 m
Maximum rated power = 7.4 kW at 1500 rpm
Speed = 1500
Radius of fan = 0.274 m
Arm length of dynamometer = 0.4 m
Diameter of pipe = 0.06 m
Compression ratio = 18.8:1
Dynamometer constant k
Mass of fuel/s = ?

Calculation for 2 kg load in dual-fuel mode

(A) Mass of fuel/s = ?, 10 cc in 113 s

So, for 1 s = 10/113 cc, and 10/113 × 10^{-6} × specific gravity of diesel fuel × density of water
So, for 1 s = 10/113 × 0.83 × 10^3 × 10^{-6} = 7.34 × 10^{-5} kg s^{-1}
In DF mode, mass flow rate for 2 kg load is 7.34 × 10^{-5} kg s^{-1}
In diesel mode, flow rate for 2 kg load is

$$1.53 \times 10^{-4}\,\text{kg/s,} \tag{1}$$

(Eq. (1) was solved at the time of diesel fuel)
Saving of diesel = 1.53 × 10^{-4} to 7.34 × 10^{-5} = 7.96 × 10^{-5} kg s^{-1} (i.e., saving of diesel means biogas used in that place.)
So, the mass flow rate is replaced by biogas is = 7.96 × 10^{-5} kg s^{-1}
It can be said that the biogas flow rate is 7.96 × 10–5 kg s^{-1}.

Similarly, mass flow rates were calculated for zero, four, six, eight, and ten kg loads in terms of diesel and dual fuel.

(B) Brake power (BP) = $\frac{2\pi NT}{60}$
Torque (T) = 2 × 9.81 × arm length = 2 × 9.81 × 0.4 = 7.848 Nm.
So, BP = $\frac{2\times3.14\times685\times7.848}{60}$ = 0.562 kW.
Similarly, it calculated brake power for zero, four, six, eight, and ten kg loads.
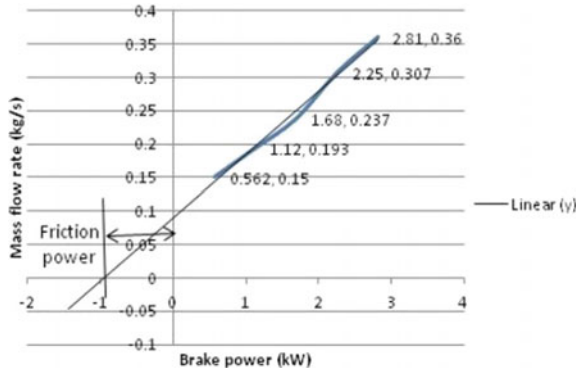
Fig. 4 Brake power versus mass flow rate of diesel testing

After calculating the mass flow rate and brake power for each load, draw a graph between the mass flow rate and BP and find out the friction power of the engine (Fig. 4).

(C) Find out the friction power (FP) which is 0.9 kW taken from the graph.

(D) Indicated power (IP) for 2 kg load = BP + FP = 0.562 + 0.9 = 1.462 kW. Similarly, it calculated the indicated power for four, six, eight, and ten kg loads for diesel and DF modes.

(E) Brake thermal efficiency

$$
= \frac{BP}{(\dot{m}d)\text{duel} \times \text{Cv of diesel} + (\dot{m}b)\text{biogas} \times \text{Cv of biogas}}
$$
$$
= \frac{0.562}{7.34 \times 10^{-5} \times 42{,}500 + 7.96 \times 10^{-5} \times 19{,}740}
$$
$$
= 11.98\%
$$

Similarly, it determined brake thermal efficiency for four, six, eight, and ten kg loads for diesel and dual fuel.

(F) Indicated thermal efficiency

$$
= \frac{IP}{(\dot{m}d)\text{duel} \times \text{Cv of diesel} + (\dot{m}b)\text{biogas} \times \text{Cv of biogas}}
$$
$$
= \frac{1.462}{7.34 \times 10^{-5} \times 42{,}500 + 7.96 \times 10^{-5} \times 19{,}740}
$$
$$
= 31.6\%
$$

Similarly, it calculated the indicated thermal efficiency for four, six, eight, and ten kg loads for diesel and DF modes.

(G) Brake specific fuel consumption (BSFC)

$$= \frac{(\dot{m}d)\text{duel} + (\dot{m}b)}{\text{BP}}$$
$$= \frac{\left(7.34 \times 10^{-5} + 7.96 \times 10^{-5}\right) \times 3600}{0.562}$$
$$= 0.980 \, \text{kg/kW h}$$

Similarly, it calculated brake specific fuel consummation for four, six, eight, and ten kg load for diesel as well as DF mode.

(H) Indicated specific fuel consumption (ISFC)

$$= \frac{(\dot{m}d)\text{duel} + (\dot{m}b)}{\text{IP}}$$
$$= \frac{\left(7.34 \times 10^{-5} + 7.96 \times 10^{-5}\right) \times 3600}{1.462}$$
$$= 0.3767 \, \text{kg/kW h}$$

Similarly, it computed specific fuel consumption for diesel and DF mode for four, six, eight, and ten kg loads.

(I) Volumetric efficiency $= \dfrac{\text{Actual volume}}{\text{Theroretical volume}}$

Volumetric efficiency for 2 kg load $= \dfrac{\frac{\pi}{4} \times 0.06^2 \times 0.0275 \times \frac{2\pi \times 470}{60}}{\frac{\pi}{4} \times 0.102^2 \times 0.11 \times \frac{685}{2 \times 60}} = 74.57\%.$

Additionally, it determined volumetric efficiency for four, six, eight, and ten kg loads for diesel, as well as DF modes.

4 Results and Discussion

The outcome of dual fuel and diesel fuel mode on single cylinder CI engine.

In Fig. 5, the BTE of diesel fuel was found to increase from 8.81 to 18.36% when the BP value was 0.5–2.8 kW, and the maximum BTE of diesel was found to be 18.36% when the BP value was 2.8 kW. In DF mode, BTE was found to increase from 11.98 to 21.79%, when the BP value was 0.5–1.68 W. Thereafter, as the value of BP increased, the BTE of DF decreased from 21.79 to 20.71%.

The maximum BTE was found to be 21.79% in DF mode when BP was 1.68 kW. Dual fuels are more effective at low loads, and diesel fuel is more effective at high loads.
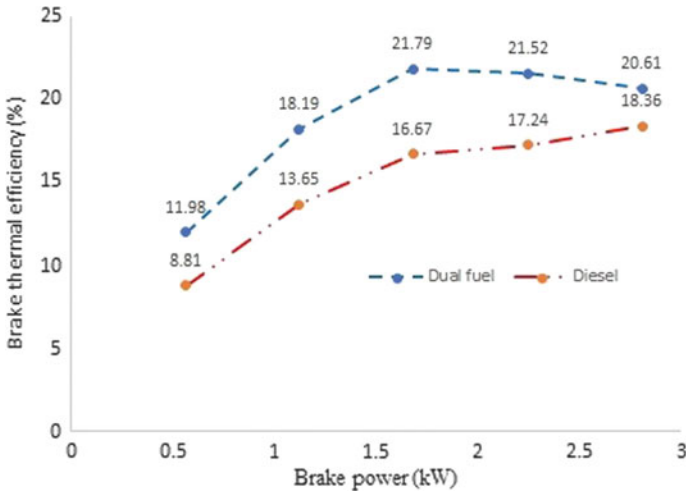
Fig. 5 BP versus BTE

In Fig. 6, the ITE of diesel fuel was found to increase by 19.25–25.61% when the IP value was 0.9–2.58 kW. ITH then decreased from 25.61 to 24.14% when IP was from 2.58 to 3.15 kW, and finally, ITH increased again when the value of IP rose from 3.15 to 3.71 kW.
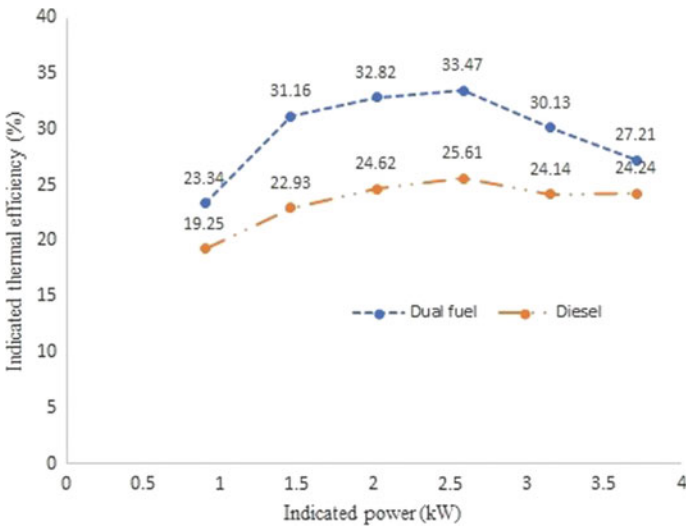
Fig. 6 IP versus ITE
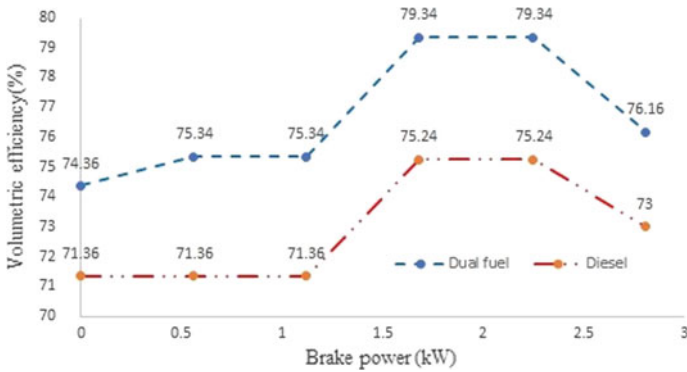
Fig. 7 VE versus BP

In DF mode, ITH increased from 23.34 to 33.47% when IP was 0.9–2.58 kW. Subsequently, ITH decreased by 33.47–27.21%, when the IP value was 2.58–3.71 kW. The maximum value of ITH was found to be 33.47% in DF mode and 25.61% in diesel fuel when the IP value was found to be around 2.58 kW, and it has been observed that the ITH of DF is much higher than that of diesel fuel.

In Fig. 7, VE of diesel fuel went from 71.36 to 75.24% when BP's value ranged from 0.56 to 2.81 kW. The VE of the diesel was found to be stable when the BP value was 0.5–1.12 kW, followed by the VE of the diesel increased from 71.36 to 75.24% when the BP was 1.12–1.68 kW. Then, the VE of at diesel 75.24% remained constant when the BP value was 1.68 kW to 2.25. Finally, the VE of the diesel decreased from 75.24 to 73% when the BP was 2.25–2.81 kW.

In dual mode, VE was found to be 74.36–79.34% when BP was 0.56–2.81 kW. The VE of DF was increased by 74.36–75.34% when BP was 0.5 kW, When the BP value has increased from 0.5 to 1.12 kW, the VF of DF is 75.34% constant.

Once again, the VE of DF is increased by 75.34–79.34% when BP was 1.12–1.68 kW. Thereafter, when BP was 1.68–2.25 kW, the dual-fuel VE was found to be constant at 79.34%. And finally, the dual-fuel VE decreased from 79.34 to 76.16% when BP was 2.25–2.81 kW. The maximum VE in DF mode was found to be around 79.34% and in diesel fuel 75.24% when BP is 2 kW, and it has been observed that VE is very high in DF mode.

In Fig. 8 BSFC was found to be about 1 kg $(\text{kW h})^{-1}$ in DF mode and diesel fuel when BP was 0.6 kW. In both cases, the BSFC value decreased from 1 kg $(\text{kW h})^{-1}$ to 0.6 kg $(\text{kW h})^{-1}$, when the BP was 0.5–1.2 kW. Thereafter, the BSFC was gradually reduced from 0.6 kg $(\text{kW h})^{-1}$ to 0.45 kg $(\text{kW h})^{-1}$ when the BP was 1.2–2.7 kW in both the conditions. The BSFC was found to be slightly higher in DF mode. In both cases, the BSFC decreases as brake power increases.

In Fig. 9, the ISFC of diesel fuel was found to be about 0.44 kg $(\text{kW h})^{-1}$ when IP was 1 kW. ISFC decreased from 0.44 to 0.36 kg $(\text{kW h})^{-1}$ when IP was 1–1.5 kW. Again, ISFC gradually decreased from 0.36 to 0.33 kg $(\text{kW h})^{-1}$, when the IP was 1.5–2.6 kW. Subsequently, when the IP was 2.6–3.25 kW, ISFC increased from 0.33
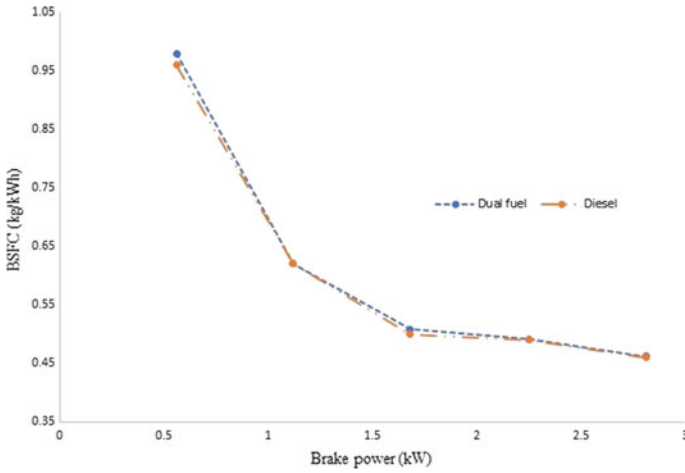
Fig. 8 BSFC versus BP
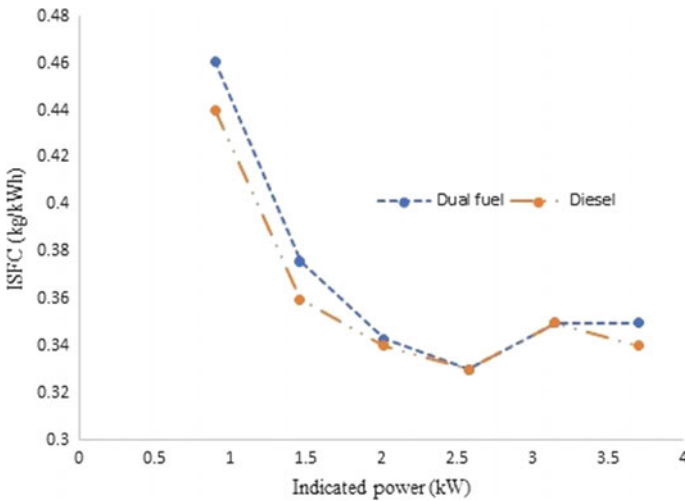
Fig. 9 IP versus ISFC

to 0.355 kg (kW h)$^{-1}$. Finally, ISFC again decreased from 0.36 to 0.34 kg (kW h)$^{-1}$ when the IP was 3.25–3.75 kW.

ISFC of dual fuel was found to be around 0.46 kg (kW h)$^{-1}$ when IP was 1 kW and when ISFC decreased from 0.46 to 0.37 kg (kW h)$^{-1}$ when IP was 1 to 1.5 kW. Again, ISFC gradually decreased from 0.37 to 0.33 kg (kW h)$^{-1}$ when the IP was 1.5–2.6 kW. The ISFC then increased from 0.33 to 0.355 kg (kW h)$^{-1}$ when the IP was 2.6–3.25 kW. Finally, when the IP was 3.25–3.75 kW, the value of ISFC was

found to be 0.355 kg $(\text{kW h})^{-1}$ constant. ISFC was found to be slightly higher in DF mode.

In the graph, it can be undoubtedly seen that BTE and VE were found to be significantly higher in DF mode at a constant speed, and BSFC and ISFC were found to be almost identical in both cases.

5 Conclusion

- In DF engine operation at a constant speed, it is found that BTE, VE, and ITE are increased.
- The consumption rate of diesel diminishes when dual fuel (diesel + biogas) is used.
- Dual fuel (diesel + biogas) is more effective at low load, when the load increases, the effectiveness of the DF starts to decrease.

The compact biogas plant can be used for the household purpose in rural as well as an urban area because it is cheap and eco-friendly. A major problem of wastage disposal can be solved if every citizen uses organic wastage in their homes to produce biogas, and it can then be used for cooking purposes, generating electricity, and running engines. Also, the slurry of the biogas plant can be used as fertilizer, which means that organic waste can be used 100%.

References

1. Central Pollution Control Board Annual report 2016–17. https://cpcb.nic.in/zobengaluru/ANNUAL_REPORT_2016-17.pdf. Last accessed 2018/11/18
2. Sharma, S.K., Mishra, I.M., Sharma, M.P., Saini, J.S.: Effect of particle size on biogas generation from biomass residues. Biomass **17**(4), 251–263 (1988)
3. Kalia, A.K., Kanwar, S.S.: Long term evaluation of a fixed dome Janata biogas plant in hilly condition. Bioresour. Technol. **65**(1–2), 61–63 (1998)
4. Jorapur, R.M., Rajvanshi, A.K.: Development of a sugarcane leaf gasifier for electricity generation. Biomass Bioenergy **8**(2), 91–98 (1995)
5. Koberle, E.: Animal manure digestion systems in Central Europe. In: Proceedings of the Second Biomass Conference of the Americas, p. 753. National Renewable Energy Laboratory, Portland, Oregon (1995)
6. Putria, D.A., Saputrob, R.R., Budiyono, B.: Biogas production from cow manure. Int. J. Renew. Energy Dev. **1**(2), 61–64 (2012)
7. Otun, T.F., Ojo, O.M., Ajibade, F.O., Babatola, J.O.: Evaluation of biogas production from the digestion and co-digestion of animal waste, food waste, and fruit waste. Int. J. Energy Environ. Res. **3**(3), 12–24 (2015)
8. Sabari Girish, G., Vijayakothandaraman, R., Prabhu, A.: Experimental investigation on a CI engine fuelled with biogas and rice straw additives. Int. J. Ambient Energy **40**(6), 610–612 (2019)
9. Roubaud, A., Favrat, D.: Improving performances of a lean-burn cogeneration biogas engine equipped with combustion prechambers. Fuel **84**(16), 2001–2007 (2005)

10. Chandra, R., Vijay, V.K., Subbarao, P.M.V., Khura, T.K.: Performance evaluation of a constant speed IC engine on CNG, methane enriched biogas, and biogas. Appl. Energy **88**(11), 3969–3977 (2011)
11. Bora, B.J., Saha, U.K., Chatterjee, S., Veer, V.: Effect of compression ratio on performance, combustion, and emission characteristics of a dual fuel diesel engine run on raw biogas. Energy Convers. Manag. **87**, 1000–1009 (2014)
12. lohan, S.K., Dixit, J., Kumar, R., Pandey, Y., Khan, J., Ishaq, M., Modasir, S., Kumar, D.: Biogas: a boon for sustainable energy development in India's cold climate. Renew. Sustain. Energy Rev. **43**, 95–101 (2015)
13. Karve, A.D.: Compact biogas plant, a low-cost digester for biogas from waste starch (2007). https://www.arti-india.org. Last accessed 2012/11/21

Effect of Bioethanol-Diesel Blends on the Vibrations of Diesel Engine

Akhilesh Kumar Choudhary (ID)

1 Introduction

The abundant consumptions of petroleum reserves are creating serious issue for energy demand and supply in future. The replacement (partial) of petroleum reserves can be possible by using alternative renewable fuels which can be a bioethanol and biodiesel. Conventionally, bioethanol has been produced by using the sugar plants as feed stock, which are mainly food crops [1, 2]. However, the increased demand of fuel supply may create the food chain disturbances, so researchers are looking for non-food crops/plants or lignocellulosic wastes for biofuel production. Water hyacinth can be a one of the feed stock for biofuel production. It is a fast-growing aquatic nuisance plant, which is usually creating problems in human activity like irrigation and navigation like activity. On the other hands, governments have spent millions of rupees every year to remove this weed plants. In this situation, these weed plants can be used for biofuel production and run the diesel engine from the developed biofuel. Diesel engine has generated the power by the combustion of fuel, and this combustion of fuel produces powerful pulses of energy which cause the engine vibration [3, 4]. Payri et al. [5] have been reported that due to combustion inside the engine cylinder, peak pressure has been rapidly increasing and produces diesel knock and results in causing vibrations in the engine block. Zhen et al. [6] have suggested that combustion noise and vibrations are emitted to the air through the outer surfaces of the engine and account for the overall engine noise and vibration levels; it can be easily measured on the cylinder head or the engine block [7, 8]. Vibration signals hold a lot of useful information concerning the engines components and their behavior. Many authors have been used the time domain and frequency domain analysis or their combinations for vibration analysis [3, 7–9]. The frequency domain

A. K. Choudhary (✉)
Mechanical Engineering Department, National Institute of Technology Hamirpur, Hamirpur 177005, India
e-mail: akhilesh@nith.ac.in

spectrum is more useful to identify the exact nature of the vibration signature in the engine [10]. The vibration can be defined by in terms of displacement, velocity, and acceleration. Vullia et al. [11] have reported that fast Fourier-transform (FFT) is capable to identifying the combustion pulses impact on engine parts and engine knock from measured acceleration [12]. Gravalos et al. [13] have observed the effect on vibration using methanol and ethanol gasoline engine blends on the engine and reported that the acceleration of the fundamental harmonics decreases with increase of load or decrease engine speeds. The sensor selection for vibration measurement and sensor mounting is very important factor for the precise diagnose of machine state. Displacement, velocity, and acceleration are common parameters for vibration monitoring and analysis. These parameters mathematically can be related with the sensor output [8, 9]. The piezoelectric accelerometer sensor is versatile, reliable, and the most popular vibration sensor [14]. The piezoelectric sensors can work at bad environmental condition, and it cannot be affected by temperatures, dirt, humidity, lubrication, and chemically harsh atmospheres. It can perform well at severe shocks and vibrations conditions. The piezoelectric-material-based bimorph sensor can be used as vibration sensor, and its signal has been proportional to acceleration [15]. In an investigation, Jung and Roh [16] have demonstrated the piezoelectric-material-based bimorph sensor for monitoring the vibration. In the above-said paper, bimorph sensor and commercial B&K accelerometer sensor outputs are compared, and the sensitivity analysis has been carried out. From the literatures, it has been elicited that very few authors has used a bimorph sensor for measuring the vibration of IC engine. The main aim of this investigation was to determine the vibrations in the internal combustion engine using different combination diesel and biofuel. In this investigation, different combination of diesel-bioethanol (fuel) blends has been used. In this study, bioethanol (fuel) has been extracted from the water hyacinth. The piezoelectric-material-based bimorph sensor has been used as vibration sensor, and frequency domain spectrum has been used to analyze the vibration signature of the engine.

2 Experimental Setup

2.1 Materials and Test Setup

For the investigation, bioethanol extracted from water hyacinth has been used to prepare blends with diesel fuel. Water hyacinth is rapidly growing weed water plant which is widely spread in ponds worldwide. For the study, two blends have been prepared (i) 80% diesel + 20% bioethanol (20BED) and (ii) 75% diesel + 25% bioethanol (25BED), by volume. The single-cylinder, water-cooled, variable compression ratio (VCR), constant speed (1500 rpm), four-stroke with Eddy current dynamometer, diesel engine has been used for the investigation.

Fig. 1 Bimorph sensor

Table 1 Factors and their levels

S. No.	Levels	Factors		
		Load	CR	FIP
1	− 1	0	14:1	180
2	0	6	16:1	225
3	1	12	18:1	270

2.2 Bimorph Sensor

The piezoelectric material based 4 V; with operating frequency 100 Hz, a bimorph sensor has been used as a vibration sensor, as shown in Fig. 1. This piezoelectric bimorph sensor is capable of converting mechanical energy to electrical energy (output). It is also a low-power electromechanical transducer. It has 1 MΩ impedance with 9^{31} ($\times 10^3$ V-m/N): 12.1 Piezo-constant. The dielectric constant and capacitance were 2000 and 750 pF $\pm$ 1%, respectively. The bimorph sensor has been pasted over the engine block and gets the signal with help of data acquisition card.

2.3 Design of Experiments (DOE)

A central composite rotatable design (CCRD) has been used to define the experimental run, and three engine-operating parameters load, compression ratio (CR), and fuel injection pressure (FIP) have been taken in to account. The three levels of these three parameters have been selected for conducting the experiments [17], as given in Table 1. Box and Hunter [18], reported that CCRD is one of the efficient methods to investigate the influence of each parameter that affects the output of the process. In this study, DOE has 20 numbers of experiments with three factors and three levels. The designed experiments are given in Table 2.

2.4 Vibration Frequency

The number of cycles per unit time is called the frequency of oscillation or the frequency and is denoted by Eq. 1 [19]:

$$f = \frac{1}{T} = \frac{\omega}{2\pi} \tag{1}$$

Fig. 2 FFT of the vibration
signal in biofuels engine
with load
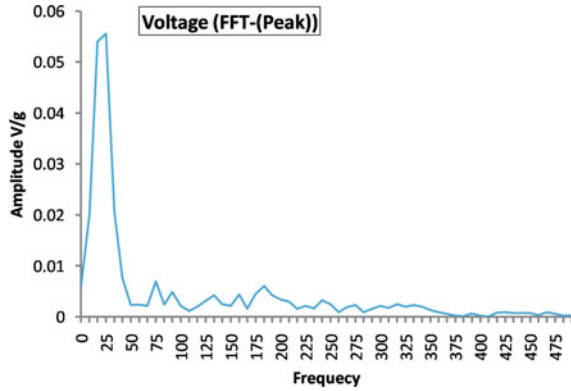
Amplitude is defined as the maximum value of a vibration, and it can be represented by displacement, velocity, or acceleration [19]. According to Eq. 1, the frequency of oscillation or frequency for engine (Speed—1500 rpm) is 25 Hz. Figure 2 shows the frequency output response from a bimorph. Over the tested range, there is dissimilarity in frequencies; however, the by and large form of the frequency response shows good regularity. The sampling frequency was selected as 1 kHz. With the help of LabVIEW 8.5, the voltage signals of the bimorph vibration sensor were sampled using DAQ system with data acquisition frequency of 1 kHz.

2.5 Experimental Methodology

Systematically designed experiments have been conducted on constant speed (1500 rpm) VCR diesel engine, which has been equipped with an electrical dynamometer. A 0.25 mm washer was placed in between spring and plunger in the fuel pump for changing the fuel injection pressure. Initially, VCR engine started with normal diesel fuel. After 30 min, fuel supply has been changed from normal diesel to bioethanol-diesel blend. The engine block vibrations data for different blend have been recorded and stored at every experiment in personal computer (PC). The experimental process diagram has been represented in Fig. 3. From the output of senor, peak-to-peak (PP) output voltage has been measured, and on the basis of response surface methodology, output voltage has been analyzed.

3   Empirical Model and Data Analysis

Response surface methodology (RSM) is a statistical technique used to develop a purposeful relationship between an output response-associated input variables [20]. After conducting experiments, the obtained experimental data were analyzed CCRD

Table 2 20 design of experiments with input parameters (Amplitude V/g)

	Factors			Experimental response			RSM response		
Run order	Load (kg)	CR	FIP (bar)	Diesel	20-BED	25-BED	Diesel	20-BED	25-BED
1	6	16	225	0.0767	0.0900	0.0898	0.0761	0.0910	0.0918
2	6	16	225	0.0767	0.0896	0.0908	0.0761	0.0911	0.0918
3	12	14	180	0.0689	0.0795	0.0890	0.0681	0.0780	0.0886
4	12	18	180	0.0459	0.0658	0.0694	0.0459	0.0691	0.0726
5	6	16	225	0.0758	0.0893	0.0907	0.0761	0.0910	0.0918
6	0	14	270	0.0823	0.0905	0.0940	0.0818	0.0920	0.0920
7	0	18	180	0.0656	0.0802	0.0879	0.0649	0.0803	0.0864
8	6	16	225	0.0768	0.0897	0.0899	0.0761	0.0910	0.0918
9	12	18	270	0.0623	0.0820	0.0825	0.0617	0.0832	0.0821
10	6	16	270	0.0801	0.0933	0.0927	0.0806	0.0916	0.0939
11	0	14	180	0.0726	0.0902	0.0914	0.0727	0.0892	0.0928
12	12	16	225	0.0725	0.0922	0.0946	0.0736	0.0883	0.0898
13	6	16	225	0.0757	0.0892	0.0938	0.0761	0.0910	0.0918
14	0	18	270	0.0771	0.0851	0.0841	0.0773	0.0831	0.0856
15	6	16	180	0.0668	0.0840	0.0893	0.0682	0.0831	0.0896
16	6	16	225	0.0787	0.0936	0.0931	0.0761	0.0910	0.0918
17	12	14	270	0.0805	0.0911	0.0955	0.0807	0.0921	0.0982
18	6	14	225	0.0741	0.0915	0.0945	0.0750	0.0915	0.0929
19	6	18	225	0.0606	0.0852	0.0845	0.0616	0.0826	0.0817
20	0	16	225	0.0829	0.0922	0.0928	0.0837	0.0938	0.0937
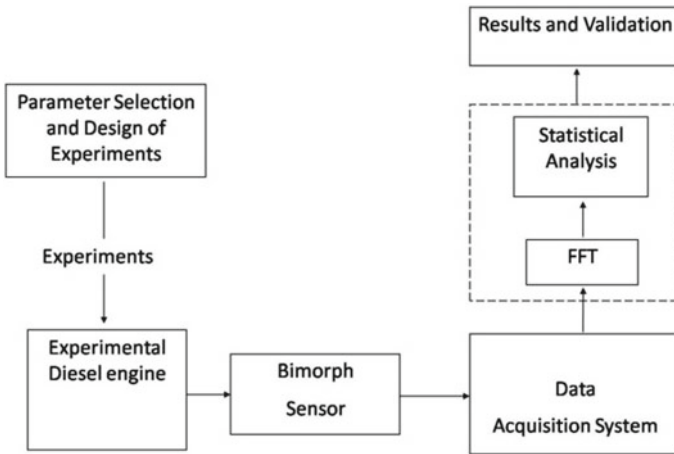
Fig. 3 Block diagram for experimental setup

by second-order polynomial equations. The equation is of the general form

$$Y = \beta_0 + \sum_{i=1}^{k} \beta_i X_i + \sum_{i=1}^{k} \beta_{ii} X_i^2 + \sum \sum_{i<j} \beta_{ij} X_i X_j \tag{2}$$

Here, Y is output response (vibration amplitude (PP) value), $\beta_0 = $ constant, $\beta_i = $ liner coefficients, $\beta_{ii} = $ quadratic coefficients, and $\beta_{ij} = $ cross-product coefficients, X_1 load, X_2CR, X_3FIP (levels k quantitative process variables). For analysis of experimental data like: regression analysis and analysis of variance (ANOVA), the design expert 7.0 software has been used. The main effect plots have been produced using the fitted quadratic polynomial equation obtained from regression.

3.1 Statistical Analysis

Analysis of variance (ANOVA) was used to see the adequacy of the established model. The ANOVA for the second-order model as shown in Eq. (3) and p-value has been presented in Table 3. For analysis purpose, 95% confidence level has been selected. From the results, it is observed that R^2 is 0.989, and in the models terms case, the p-values lower than 0.05 indicate that they are statistically significant at 95% trust level [21]. Thus, while analyzing the results, these observations are taken in account. By applying the above-said ANOVA analysis for various diesel-bioethanol blends, the following results have been obtained and demonstrated in Table 4.

$$\textbf{Diesel} = -0.426 + 0.0024 * \text{Load} + 0.0587 * \text{CR}$$

Table 3 Statistical analysis for tested blends (p-values)

Source	Diesel	20 BED	25 BED	
	p-value	p-value	p-value	
Model	<0.0001	<0.0001	0.0006	Significant
A-load	<0.0001	0.0032	0.0411	
B-CR	<0.0001	0.0001	<0.0001	
C-FIP	<0.0001	0.0002	0.0233	
AB	<0.0001	0.2793	0.0251	
AC	0.0828	0.0056	0.0177	
BC	0.0974	0.1907	0.9571	
A^2	0.0077	0.9456	0.7019	
B^2	<0.0001	0.0162	0.0432	
C^2	0.0523	0.0234	0.2148	
Residual				
Lack of fit	0.2882	0.1547	0.0924	Not significant

Table 4 Statistical analysis for tested blends

Diesel-bioethanol blends	Mean	Std. dev	R^2	Adjusted R^2
Diesel	0.072627	0.001263	0.9894	0.9799
20 BED	0.0872	0.002269	0.937362	0.880988
25 BED	0.089518	0.002588	0.901296	0.812462

$$+ 0.0003 * \text{FIP} + -0.0003 * \text{Load} * \text{CR}$$
$$+ 0.000003 * \text{Load} * \text{FIP} + 0.000009 * \text{CR} * \text{FIP}$$
$$+ 0.00007 * \text{Load} * \text{Load} + -0.0019 * \text{CR} * \text{CR}$$
$$+ -0.0000008 * \text{FIP} * \text{FIP} \tag{3}$$

$$20 - \textbf{BED} = -0.184 + -0.0015 * \text{Load} + 0.027 * \text{CR}$$
$$+ 0.0006 * \text{FIP} + -0.00007 * \text{Load} * \text{CR}$$
$$+ 0.00001 * \text{Load} * \text{FIP} + 0.00001 * \text{CR} * \text{FIP}$$
$$+ -0.000002 * \text{Load} * \text{Load} + -0.0009 * \text{CR} * \text{CR}$$
$$+ -0.000002 * \text{FIP} * \text{FIP} \tag{4}$$

$$25 - \textbf{BED} = -0.158 + 0.0005 * \text{Load} + 0.027 * \text{CR}$$
$$+ 0.0004 * \text{FIP} + -0.0002 * \text{Load} * \text{CR}$$
$$+ 0.00001 * \text{Load} * \text{FIP} + 0.000001 * \text{CR} * \text{FIP}$$
$$+ 0.00001 * \text{Load} * \text{Load} + -0.0009 * \text{CR} * \text{CR}$$

$$+ -0.000001 * FIP * FIP \qquad (5)$$

4 Results and Discussions

The bimorph sensor signals power spectrums (Peak-to-Peak) have been analyzed for the measurement of engine block vibration using different bioethanol-diesel blend. The bimorph sensor time-domain signals were converted in to frequency domain for the analysis. Typical power spectral plots with predominant frequency (25 Hz) are shown in Fig. 3. In order to investigate the most considerable contribution parameters (load, CR, and FIP), statistical analysis has been performed, and empirical models have been developed to predict the vibration response. The effects of three engine-operating parameters on the block vibration of the engine are discussed below.

4.1 *Significance of Load on Engine Vibration*

The significance of load on engine vibration are represented in Fig. 4. From the figure, it is perceived that engine block vibration levels are decreasing with increasing load. It is also observed that engine block vibrations for diesel and bioethanol-diesel blends are lower at higher load condition (12 kg) and higher engine block vibrations at zero or no-load condition. Because at higher loads condition, the translation of heat energy to mechanical work boosted with the increase in combustion temperature which provides stability to engine torque and reduces the engine block vibrations [22]. The bioethanol-diesel blends produce more vibration than diesel, and this is mainly due to the water content present in bioethanol-diesel blend which has a significant effect
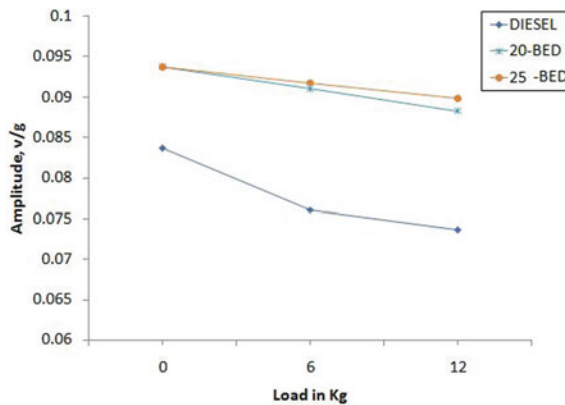
Fig. 4 Effect with different loading conditions in vibration amplitude for different blend
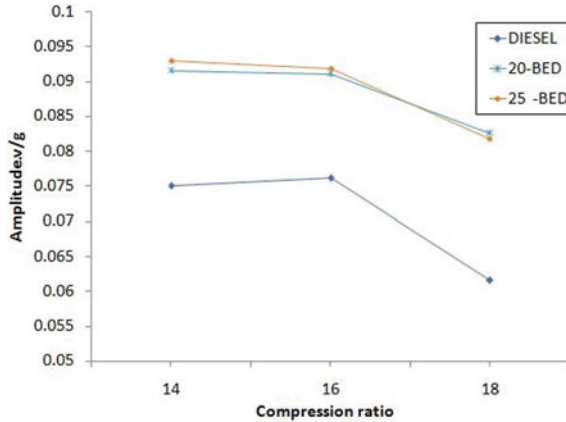
Fig. 5 Effect of compression ratio in vibration amplitude for different blend

on combustion. Water content of the blends reduced efficiency and temperature of the cylinder wall.

4.2 Significance of CR on Engine Vibration

The effects of compression ratio on engine block vibration have been observed for 20 BED and 25 BED, and from the results, it has been elicited that the engine block vibrations are decreased at higher compression ratio, and it shows lower vibrations at 18:1 CR. The significance of CR in engine block vibrations is shown in Fig. 5. Because of increased CR, the air pressure and temperature increase, which results in reduced ignition delay, and delay period has been reduced and auto-ignition temperature of the fuel [23]. At reduced compression ratio, due to lower pressure and temperature, the ignition delays large, which results in incomplete combustion and higher engine block vibrations.

4.3 Significance of FIP on Engine Vibration

Figure 6 shows the significance of fuel injection pressure on engine block vibration. The vibration signals levels are following by the different fuel injection pressure. From the results, it has been perceived that higher FIP produces higher engine block vibration for diesel and bioethanol-diesel blends. However, lower fuel injection pressure produces lower engine block vibrations. The reason behind is that when fuel injection pressure is very high, the ignition delay will be very short which reduces the combustion efficiency [23]. These bad conditions of combustion amplify the
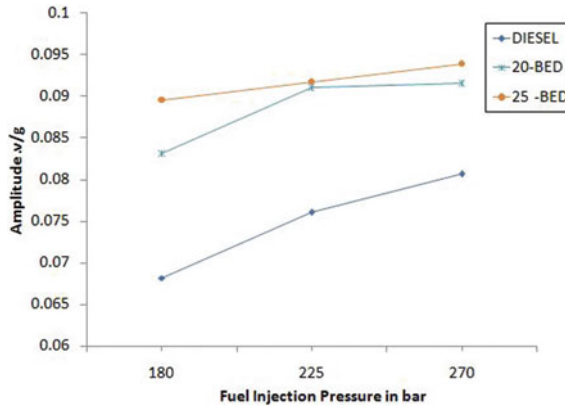
Fig. 6 Effect of fuel injector pressure in vibration amplitude for different blend

unstable waves and increase the engine block vibrations. At lower fuel injection pressure, large fuel particle diameters cause the larger ignition delay.

5 Conclusion

In this investigation, the bimorph sensor has been used to measure engine block vibration of a diesel engine which has been operated using diesel and bioethanol-diesel blends. To measure the engine block vibrations, systematically designed experiments have been conducted, and power spectrum FFT (peak to peak) of measured signals has been considered. After experimental investigation and RSM prediction model values, the following conclusions have been made:

1. Up to 25 BED (75% diesel + 25% bioethanol), the single-cylinder diesel engine can be run without any modification.
2. The RSM empirical model suggests an acceptable representation of the engine block vibration and a good correlation among experimental results and predicted results, obtained from RSM predicted model equations.
3. The 20 BED (80% diesel + 20% bioethanol) and 25 BED (75% diesel + 25% bioethanol) yielded an increase in vibration signal because during combustion the ignition delay period increases for bioethanol.
4. The piezoelectric bimorph sensor can effectively measure the engine block vibration, and these bimorph sensor signals can be used for (adoptive control) monitoring the engine-operating conditions.

References

1. Balata, M., Balata, H., Oz, C.: Progress in bioethanol processing. Prog. Energy Combust. Sci. **34**, 551–573 (2008)
2. Choudhary, A.K., Chelladurai, H., Kannan, C.: Performance analysis of bioethanol (*Water Hyacinth*) on diesel engine. Int. J. Green Energy **13**(13), 1369–1379 (2016)
3. Chen, A., Dai, X.: Internal combustion engine vibration analysis with short-term Fourier-transform. In: Proceedings of the 3rd International Congress on Image and Signal Processing (CISP2010) (2010)
4. Arroyo, J., Munoz, M., Moreno, F., Bernal, N., Monne, C.: Diagnostic method based on the analysis of the vibration and acoustic emission energy for emergency diesel generators in nuclear plants. J. Appl. Acoust. **74**, 502–508 (2013)
5. Payri, F., Torregrosa, A.J., Broatch, A., Monelletta, L.: Assessment of diesel combustion noise overall level in transient operation. J. Automot. Technol. **10**(6), 761–769 (2009)
6. Zhen, D., Tesfa, B., Yuan, X., Wang, R., Gu, F., Ball, A.D.: An investigation of the acoustic characteristics of a compression ignition engine operating with biodiesel blends. In: Proceedings of the 25th International Congress on Condition Monitoring and Diagnostic Engineering. J. Phys. Conf. Ser. **364**, 01 (2012)
7. Johnsson, R.: Cylinder pressure reconstruction based on complex radial basis function networks from vibration and speed signals. J. Mech. Syst. Signal Process. **20**, 1923–1940 (2006)
8. Elforjani, M., Mba, D., Muhammad, A.: A technical note: condition monitoring of worm gears. J. Appl. Acoust. **73**, 859–863 (2012)
9. Choudhary, A.K., Chelladurai, H., Kannan, C.: Optimization of combustion performance of bioethanol (*Water hyacinth*) diesel blends on diesel engine using response surface methodology. Arab. J. Sci. Eng. **40**(12), 3675–3695 (2015)
10. Amaranth, M., Shrinidhi, R., Ramchandra, A., Kandagal, S.B.: Prediction of defects in antifriction bearing using vibration signal analysis. IE(I) J. **85**, 88 (2004)
11. Vullia, S., Dunne, J.F., Potenza, R., Richardson, D., King, P.: Time-frequency analysis of single-point engine—block vibration measurements for multiple excitation-event identification. J. Sound Vib. **321**, 1129–1143 (2009)
12. Geng, Z., Chen, J.: Investigation into piston-slap-induced vibration for engine condition simulation and monitoring. J. Sound Vib. **282**, 735–751 (2005)
13. Gravalos, I., Moshou, D., Theodoros, G., Kateris, D., Xyradakis, P., Tsiropoulos, Z.: Vibration effect on spark ignition engine fuelled with methanol and ethanol gasoline blend. J. Agric. Mach. Sci. **7**(4), 367–372 (2011)
14. García, F., Huerta, C.I., Orozco, H., Hixson, E.L.: Design, modeling, and construction of a low frequency bimorph-piezoelectric accelerometer. https://www.carloshuerta.org/EnglishVersion/Publications/DesgModeConstLowFreq.pdf. Accessed 13 July 2013
15. https://www.wilcoxon.com/knowdesk/TN16_Sensor%20Selection%20Guide.pdf. Accessed 13 July 2013
16. Roh, Y., Jung, I.: Design and fabrication of piezoceramic bimorph vibration sensors. J. Sens. Actuators A **69**, 259–266 (1998)
17. Choudhary, A.K., Chelladurai, H., Kannan, C.: Performance analysis of diesel engine using bio ethanol (*Water hyacinth*) by response surface methodology (RSM). Appl. Mech. Mater. **737**, 53–59 (2015)
18. Box, G.E.P., Hunter, J.S.: Multi-factor experimental design for exploring response surfaces. Ann. Math. Stat. **28**(1), 195–241 (1957)
19. Ramachandran, T., Padmanaban, K.P., Vinayagamoorthy, J.: Ant colony optimization for the minimization of internal combustion engine forces and displacements. In: Emerging Trends in Science, Engineering and Technology, pp. 19–31. Springer, India (2012)
20. Myers, R.H., Montgomery, D.C., Anderson-Cook, C.M.: Response Surface Methodology: Process and Product Optimization Using Designed Experiments, 3rd edn. Wiley, Hoboken, New Jersey (2009)

21. Santos Jr., O.O., Maruyama, S.A., Claus, T., Nilson, E., Matsushita, M., Visentainer, J.V.: A novel response surface methodology optimization of base-catalyzed soybean oil methanolysis. J. Fuel **113**, 580–585 (2013)
22. Altun, S.: Effect of the degree of unsaturation of biodiesel fuels on the exhaust emissions of a diesel power generator. J. Fuel **117**, 450–457 (2014)
23. Ganesan, V.: Internal Combustion Engines. Tata McGraw-Hill Publishing Company Limited, New Delhi, India (2006)

Application of Induction Heating Technique in Biodiesel Production

Anurag Chaurasia , **Manish Jain** , **and Amit Pal**

1 Introduction

The world population in mid of the year 2017 was found to be 7.6 billion by the United Nations and is expected to rise by 1.1% per annum. By the year 2050, the population is expected to be 10 billion, Asia being the largest contributor to the rise [1]. This mammoth population is in dire need of sustainable energy resources to continue its progress to elevate the lifestyle of the people residing in it. The use of biodiesel can bring energy sufficiency to a country by increasing the production of fuel, decreasing its reliance on other countries for fuel and thus saving a large chunk of revenue from going out of the country which can then be used for the benefit of the country. The use of biodiesel should also be promoted because it is environment friendly, as it has net zero carbon dioxide turn out and very low sulphur emissions [2].

A. Chaurasia (✉)
Department of Mechanical Engineering, Gautam Buddha University, Greater Noida, India
e-mail: anurag.chrs1996@gmail.com

M. Jain
Department of Mechanical Engineering, Rustam Ji Institute of Technology, Takenpur, Gwalior, India

A. Pal
Department of Mechanical, Production & Industrial and Automobile Engineering, Delhi Technological University, Delhi, India

1.1 Conventional and Non-conventional Techniques of Biodiesel Production

Biodiesel production methods like mechanical stirring, hydrodynamic cavitation and power ultrasonics have been used for conversion of vegetable oil into its (m)ethyl-esters by transesterification for a long time. These methods can be called as conventional methods of biodiesel production.

In mechanical stirring process, mixing of oil and alcohol is carried by a motor-operated mechanical stirrer. The movement of motor rotates the mixture inside the beaker, and this rotation agitates the mixture decreasing the equilibrium of the mixture and increasing the rate of transesterification. The temperature is also controlled during the reaction. This is the most commonly used conventional technique for production of biodiesel [2]. It has limitations of the time and capacity. Usually, it is time consuming and used for small capacity biodiesel production. Mechanical stirring can also be done by the help of magnet; this process is known as magnetic stirring.

Hydrodynamic cavitation is a very efficient method for production of biodiesel. The method uses acceleration of oil and methanol mixture through a set of orifices by pumping the mixture by pump. The acceleration of mixture through orifice causes huge decrease in the pressure of the mixture which causes cavitation phenomena, and it increases the reaction rate of the mixture as explained in the case of ultrasonic cavitation method. The specific energy consumption for production of biodiesel is the lowest as compared to mechanical stirring and ultrasonic cavitation [3].

Ultrasonic cavitation is a relatively new method for transesterification of oil to form biodiesel [4]. It is a faster method than mechanical stirring, and the time of reaction is decreased by about half, as seen in the results. In ultrasonic cavitation method, mainly two processes are known to occur. First, the ultrasonic waves produced by the apparatus create sonic pressure difference creating microscopic compression and rarefactions at microscopic level which causes rapid movement of the fluid. This helps in vigorous mixing of the mixture of methanol and oil, and due to this, the reaction rate is faster than mechanical stirring. Second is the cavitation which occurs in it. Cavitation is the process of rapid formation and collapsing of vapour bubbles due to decrease in the pressure below vapour pressure. When the fluid is subjected to pressure below vapour pressure, it evaporates causing the volume to increase manifolds and form bubble, and when again it is subjected to high pressure region, the bubble collapses because of conversion of vapour back into liquid resulting in rushing of fluid towards the vacuum created by collapsing of bubble. This action of formation and collapse of microbubble results in most of the reactions [5, 6]. Ultrasounds help improve the liquid–liquid interfacial area through emulsification, which is important for viscous films containing gas-filled bubbles and cavitation bubbles [7]. Furthermore, cavitation during sonication produces extreme local conditions and a micro-environment with high temperature and high pressure, which may also create active intermediates that permit the reaction to proceed instantaneously [3]. Hence, the reaction by ultrasonic cavitation takes place at a faster rate than mechanical stirring.

The newer methods like microwave-assisted, combined process reactor, solar-assisted, etc., are not yet thoroughly tested but proves to be potential methods for industrial processing of biodiesel.

Relatively less work has been done on microwave-assisted biodiesel production. The energy associated with the microwave's frequency ranges from 300 MHz to 300 GHz, the energy related to 300 MHz is 1.24×10^{-6} and to 300 GHz is 1.24×10^{-3} eV. Microwaves transfer heat at molecular level without altering the molecular structure. One of the many advantages of this process is the time taken to initiate the reaction which is very low and it stops easily. Heating by microwave energy is a complex phenomenon. If there is a dipole moment in a molecule, and now the compound is disclosed to microwave irradiation. The dipole of molecule tries to adjust its orientation with the electric field applied to it. Due to this continuous oscillation of electric field, the dipoles regularly try to adjust with changing electric field. Therefore, dipole follows the motion of electric field. At the frequency of 2.45 GHz, the molecules have the time to adjust with the oscillating electric field, but the exact motion of oscillation is not followed by the molecule. Therefore, there is friction due to continuous relocation of the molecules of compound, and due to friction, heat is produced, and this process is very fast [8].

All these above processes have a disadvantage of time consumption; it takes about 20 min to 2 h for the transesterification reaction to reach maximum yields of biodiesel, and also the specific energy consumption is quite high for some of the methods [3]. These gaps are tried to be eliminated in this work. In this research, biodiesel has been produced by waste cooking oil by transesterification by using induction heating process.

Waste cooking oil is a promising feedstock for biodiesel production as shown by researchers [6]. Waste cooking oil is a term used to define burnt cooking oil, or the edible oil which is leftover after deep frying of food items. This oil is not fit for eating purposes. All the different oils used for frying are mixed together in a single barrel. Hence, there is no method to find out the composition of oil mixture in the waste cooking oil, which is useful in a way that we do not need to depend on a single oil to produce biodiesel, but any oil can be mixed in any composition to get biodiesel, provided that the oils have less than 3% FFA content. This is normally the case as most of the edible oil have FFA less than 2.5% excluding coconut oil and mustard oil which has high FFA content. But this is also not a problem when they are mixed with low FFA content oil, and the FFA of the mixture lowers and becomes nearly 2.5%.

Induction heating is a fairly new method for heating. Induction heating is a process which uses electricity to heat the fluids. Induction heating has reduced the time of cooking by nearly 50%. It uses the principle of eddy current for conversion of electricity to heat. The induction cooktop base has a copper coil winding at the bottom in which when the current is passed produces magnetic field all around it. The magnetic field generated in turn produces eddy currents in the pan, and this eddy current excites the electrons of the metal pan in which comes in the range of magnetic field. The excited electrons heat the pan which heats the food inside it by the process of conduction through the pan. As the eddy currents are generated by the magnetic

field, hence, it is necessary that the pan that is used on the induction cooktop must be ferromagnetic in nature, and this is why the pans that are used for induction heating are ferrous materials, like iron and stainless steel and not copper and aluminium pans though they have great heat conductivity. Because the eddy currents excite the electrons immediately when the magnetic field is turned on, there is minimal time lag when compared to the heating by conventional methods like gas cooktops and also electric heater. These conventional methods first use heat produced to heat the pan, and then, this heat is used to heat the food inside the pan. This transfer of heat causes heat losses to the surrounding which is not the case with induction heating. Hence, the heating efficiency is increased in the induction heating process. Along with better efficiency and less time, the adverse effects of radiation produced while operation of the induction heater are negligible because the radiation emitted is low level radio frequency; on its contrary, microwave emits higher frequency radiations which can be harmful to eyes, if exposed for a long period of time [9].

2 Materials

2.1 Waste Cooking Oil

WCO used in this research work was taken from DTU canteen and a local restaurant. The properties of the oil like dynamic viscosity, density, calorific value, FFA content and acid value were tested, and the results are given in Table 1 with comparison to other oils. The fatty acid profile of the oil was also found out using GC method, and the results are given in Table 2.

Basic catalyst KOH (99% pure) was used for transesterification reaction.

Table 1 Properties of WCO biodiesel

Crude oil/biodiesel/diesel	Dynamic viscosity (mPa s)	Kinematic viscosity	Crude oil/biodiesel/diesel	Dynamic viscosity (mPa s)
WCO	48.183	44.033	0.9139	35.79
WCO biodiesel	5.4035	6.1334	0.8810	39.45
Diesel	1.531	1.806	0.8476	41.50

Table 2 Fatty acid composition of WCO

Major fatty acid	% Composition (by volume)
Oleic, C18:1	43.37
Linoleic, C18:2	29.39
Palmitic, C16:0	15.78
Other acids	11.46

Methyl alcohol (CH_3OH) was used as reactant with WCO for conversion of fatty acids into methyl esters. It was also taken from DTU laboratory.

2.2 FFA Determination

Distilled water was used as solvent for determination of FFA content of WCO and WCO biodiesel, and it was bought from local shop. NaOH was used to prepare the solution, and it was taken from DTU research laboratory.

3 Methods

3.1 FFA Content Determination of WCO

To determine the FFA content of waste cooking oil and biodiesel produced from it, titration method was used. 10 ml of methyl alcohol was mixed with 1 ml of waste cooking oil and was thoroughly mixed in a beaker and 3–4 drops of indicator (phenolphthalein) was added, and then, the content was stirred. Another solution of 1 g of NaOH in 1000 ml of distilled water was prepared and put in burette. The 1% solution of NaOH was allowed to drip from the stopcock. The mixture in the beaker was titrated with stirring till the colour of mixture was changed to light pink from colour less, denoting the pH of solution to be approximately 9. The process was repeated three times to get average reading. Further, same was done to calculate the FFA of the biodiesel produced. The change in FFA of waste cooking oil and waste cooking oil biodiesel was noted. FFA content of biodiesel was found to be lower than the oil itself.

3.2 Biodiesel Production

To get the biodiesel of required BIS specification, i.e., density below 0.9 g/ml, kinematic viscosity less than 5 mm^2/s, a series of experiments were performed.

100 g WCO was weighed on an electronic balance and heated up to the temperature of 110 °C, and then, it was left to cool down to the temp of 60 °C to remove water content. Meanwhile, KOH flakes were weighed on the same balance for 1 g to get 1% catalyst concentration. Then, methanol was weighed to 22 g for getting the molar ratio of 6:1 oil to methanol ratio.

Then, methanol and KOH flakes were mixed on the magnetic stirrer, and after their complete mixing, waste cooking oil was added and kept in a pan. Then, on the induction heater, the sample was kept in a stainless-steel bowl which was covered at

the top by cardboard having a hole in it to insert the thermocouple to get the readings and weights that were kept on the top of it, so that the methanol does not evaporates away from the bowl. The induction heater was then turned on and set to a power reading of 1600 W. The power supply to the induction heater was intermittent as per the requirement of the temperature. When the temperature went above 80 °C, the induction heater was turned off by the push button provided on the front of it. And, when the temperature went below 70 °C, it was switched on, again the time of working was measured by a stopwatch using lap timings (i.e., the time when heater was consuming power), the total working time was 73 s, and the total time of operation was 19 min.

The products formed after the reaction were left in a beaker overnight to be separated to form two layers the bottom one of the glycerine formed and the top layer of the biodiesel produced.

After the separation of biodiesel from the glycerine, the biodiesel (top layer) is poured into the separating flask, and then, water is heated into a container to about 55 °C, and this warm water is poured into the separating flask and stirred for about one minute and then left to remove the dissolved KOH from the biodiesel.

After about 4 h of separation, the water and KOH form a milky white solution at the bottom and the pure biodiesel at the top.

After the formation of milky white solution at the bottom after 4 h, the water is dripped into a beaker and thrown away. The upper layer containing biodiesel is collected in a pan and heated to 110 °C and then cooled down, and properties were tested.

In the next six experiments, the time of reaction was varied from 70 to 175 s, i.e., 70 s, 175 s, 100 s, 110 s, 115 s and 130 s, though keeping all the other factors like molar ratio, power, catalyst concentration and weight of sample constant but the viscosity increased continuously with increase in time of reaction. It seemed like the reaction was being reversed with increase in time as the transesterification reaction is an equilibrium reaction. The observation in this study agrees with those of Ataya, Dube and Ternan 2006. So, in later reaction, the time was reduced from 130 to 60 s and cover was made leak-proof rest of the procedure followed was same as before. The biodiesel formed by this combination of factors (1600 W, 6:1 molar ratio, 60 s working time, 1% catalyst concentration and 100 g oil sample) had viscosity of 5.01 mm^2/s which is an acceptable value for the usage as a fuel for diesel engine.

3.3 Taguchi's Experimental Design Method

Hefty experimentation is required to find the effects of process parameters on the yield of biodiesel. But, Taguchi method is an effective way of reducing time and cost of experimentation that needs to be done while performing full factorial design method, and the results of Taguchi method are considerably accurate to those of full factorial design method [10, 11]. Many researchers have resorted to this method to optimize the control factors for maximization of yield.

Table 3 Factors and levels used in Taguchi analysis

Name of factor	Level 1	Level 2	Level 3
Molar ratio (A)	4.5:1	6:1	8:1
Time (B)	50 s	55 s	60 s
Power (C)	1000 W	1300 W	1600 W

Yield of the biodiesel produced from waste cooking oil by induction heating is to be maximized. The yield is calculated by the formula:

$$\text{Yield\%} = \frac{(\text{weight of biodiesel produced after processing}) * 100}{(\text{weight of oil taken per batch for biodiesel production})} \quad (1)$$

The effect of change in molar ratio, time of operation and power of the induction heater is studied on the yield. The factors are changed, and experiments are performed on that factor values. The experiments were performed by changing the following factors, and each factor had three levels as given in Table 3.

Rest all the factors like temperature of reaction, catalyst concentration and weight of sample of oil was kept constant. The yield is found out by performing the experiment through permutation of factors at different levels in a specific way according to Taguchi method.

The software 'Minitab 18' was used to perform calculations for the optimization of process parameters for maximization yield and formation of graphs. The graphs were formed of signal-to-noise ratio (larger is better). Larger the better method is used because the aim is to maximize the yield.

L9 orthogonal table was used for application of Taguchi technique and to find out the effect of process parameters on the yield as given in Table 4.

Table 4 List of experiments to be performed by Taguchi technique

S. No.	Molar ratio (A)	Time (B)	Power (C)
1	4.5:1 (−1)	50 (−1)	1000 (−1)
2	4.5:1 (−1)	55 (0)	1300 (0)
3	4.5:1 (−1)	60 (+1)	1600 (+1)
4	6:1 (0)	50 (−1)	1300 (0)
5	6:1 (0)	55 (0)	1600 (+1)
6	6:1 (0)	60 (+1)	1000 (−1)
7	8:1 (+1)	50 (−1)	1600 (+1)
8	8:1 (+1)	55 (0)	1000 (−1)
9	8:1 (+1)	60 (+1)	

4   Results and Discussion

4.1   Properties of Biodiesel Produced

FFA content of the waste cooking oil was found out to be 2.57%. This is nearly 2.5% which means that one step alkaline transesterification reaction can be done. The main properties of the biodiesel produced are tested and are given in Table 1. The properties of biodiesel produced are in accordance to the BIS values.

4.2   Analysis of Yield Based on Taguchi

The yield of biodiesel on various factors and levels are given in Table 5, and the yield shown is the average of three repeated experiments. Maximum yield of 94.8% is found at 4.5:1 molar ratio, 60 s of operation time and 1600 W power of induction heater. The *S/N* ratio is also calculated based on larger the better criteria for all of these results, and the results are given in Table 6.

The plot of *S/N* ratio (larger is better) and mean of means to the various factors of experiments is displayed in Figs. 1 and 2.

The time of reaction is drastically decreased by using induction-heating-assisted biodiesel production under closed vessel condition. Most of the conventional techniques require about 0.5–1 h to process same yield of biodiesel depending upon the process used and amount of chemical used, but same yield of biodiesel produced

Table 5 Calculated yield and *S/N* ratio of biodiesel produced

S. No.	Molar ratio (A)	Time (B)	Power (C)	Yield (%)	S/N ratio (larger is better)
1	4.5:1 (−1)	50 (−1)	1000 (−1)	86.37	38.7273
2	4.5:1 (−1)	55 (0)	1300 (0)	88.13	38.9025
3	4.5:1 (−1)	60 (+1)	1600 (+1)	94.79	39.5353
4	6:1 (0)	50 (−1)	1300 (0)	82.72	38.3522
5	6:1 (0)	55 (0)	1600 (+1)	92.05	39.2805
6	6:1 (0)	60 (+1)	1000 (−1)	92.88	39.3584
7	8:1 (+1)	50 (−1)	1600 (+1)	91.79	39.2559
8	8:1 (+1)	55 (0)	1000 (−1)	91.73	39.2502
9	8:1 (+1)	60 (+1)	1300 (0)	91.56	39.2341

Table 6 Ranking of factors based on their impact on increase in yield

Factor	Molar ratio (A)	Time (B)	Power (C)
Ranking	3	1	2

Main Effects Plot for Means
Data Means
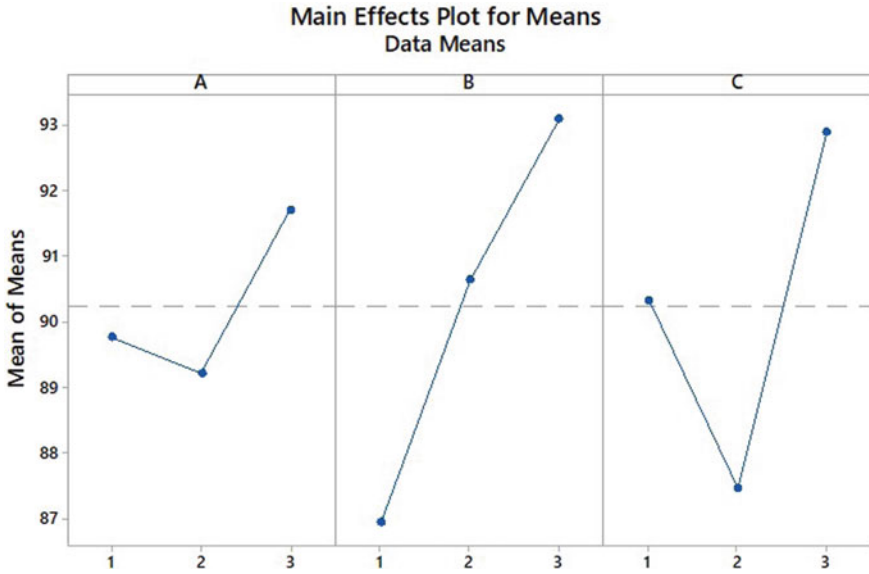
Fig. 1 Graph showing the effects of means calculated on Minitab by Taguchi method

Main Effects Plot for SN ratios
Data Means
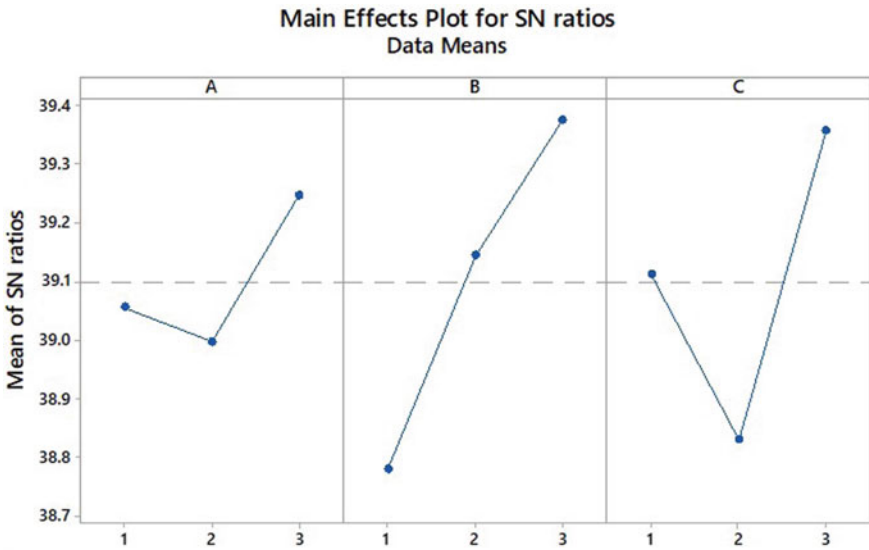
Signal-to-noise: Larger is better

Fig. 2 Plot of effects of *S/N* ratio (larger is better)

in the induction-heating-assisted process requires about 50–60 s depending upon power, catalyst and alcohol. This can be highly beneficial for industrial production of biodiesel.

4.3 Specific Energy Consumption

The SEC for the biodiesel having the highest yield is calculated.

Highest yield is found in the following sample molar ratio 4.5:1, time 60 s, power 1600 W, 1% catalyst. Yield of biodiesel in the sample for 100 g WCO is 94.79% that is equal to 94.79 g of biodiesel produced for the sample of 100 g WCO.

The energy required for its production is the product of power and time.

$$\text{SEC}\left(\frac{\text{kW h}}{\text{kg}}\right) = \frac{\text{Power(kW)} \times \text{Time(s)} \times 1\,\text{h}}{\text{Mass of Sample(kg)} \times 3600\,\text{s}} \tag{2}$$

$$\text{Energy required for production of } 94.79\,\text{g biodiesel} = \frac{1.6(\text{kW}) \times 60(\text{s}) \times 1\,\text{h}}{3600\,\text{s}}$$
$$= 0.0267\,\text{kW h}$$

$$\text{Energy required per kg of biodiesel production} = \frac{0.0267(\text{kW h}) \times 1000(\text{g})}{94.79(\text{g}) \times 1(\text{kg})}$$
$$= 0.281\,\text{kW h/kg}$$
$$= 281\,\text{W h/kg}$$

The specific energy consumption value for WCO produced by induction heating is less than values computed by using mechanical stirring and ultrasonic cavitation techniques for production of biodiesel, as referred from research paper of Yadav et al. [4] which shows that the SEC for ultrasonic cavitation is 340 W h/kg and for magnetic stirring is 450 W h/kg. It can be seen that induction heating assisted consumes less energy than both MS and UC. When compared with the results of Ji et al. [3] who found out SEC for soybean biodiesel by MS to be 500 W h/kg, PU to be 250 W h/kg and HC to be 183 W h/kg.

5 Conclusions

The research clearly shows that induction heating process can be used for production of biodiesel, and the time required for processing of biodiesel is less than the conventional methods. Power of the induction heater is found out to be the one of the most important factor on which the yield is dependent, second only to time. The effect of molar ratio is least on the yield as found out by Taguchi analysis.

The increase in biodiesel production by changing the power from 1000 to 1300 W is about 10% for 6:1 molar ratio and about 3–4% for 4.5:1 molar ratio and negligible for 8:1 molar ratio. For increase of power from 1300 to 1600 W, the yield increases to about 6% for 4.5:1 molar ratio, approximately 10% for 6:1 molar ratio and negligible for 8:1 molar ratio. The effect of change in molar ratio from 4.5:1 to 8:1 on yield of biodiesel produced is depreciating. It is also found that the SEC is comparable to PU and HC, but the time of reaction is decreased substantially.

References

1. The World Population Prospects: The 2017 Revision, published by the UN Department of Economic and Social Affairs on 21 June 2017. https://www.un.org/development/desa/public ations/world-population-prospects-the-2017-revision.html. Last accessed 2019/11/19
2. Canakci, M., Van, G.J.: Biodiesel production via acid catalysts. Trans. Am. Soc. Agri. Eng. **42**, 1203–1210 (1999)
3. Ji, J., Wang, J., Li, Y., Yu, Y., Xu, Z.: Preparation of biodiesel with the help of ultrasonic and hydrodynamic cavitation. Ultrasonics **44**, e411–e414 (2006)
4. Yadav, A.K., Khan, M.E., Pal, A.: Kaner biodiesel production through hybrid reactor and its performance testing on a CI engine at different compression ratios. Egypt. J. Petrol. **26**(2), 525–532 (2017)
5. Lin, J.R., Yen, T.F.: An upgrading process through cavitations and surfactance. Energy Fuels **7**, 111–118 (1993)
6. Pal, A., Kachhwaha, S.S.: Waste cooking oil: a promising feedstock for biodiesel production trough power ultrasonic and hydrodynamic cavitation. JSIR **72**, 387–392 (2013)
7. Kumar, G., Kumar, D., Johari, R.: Time reducing process for biofuel production from non-edible oil assisted by ultrasonication. Ultrason. Sonochem. **21**, 1618–1623 (2014)
8. Tesfaye, M., Vimal, K.: Microwave assisted synthesis of biodiesel from soybean oil: effect of poly (lactic acid)-oligomer on cold flow properties, IC engine performance and emission characteristics. Int. J. Eng. Res. Appl. Fuel **170**, 107–114 (2016)
9. European Commission Directorate-General Health and Consumer Protection (2001). Scientific Committee on Toxicity, Ecotoxicity and the Environment (CSTEE) Brussels, C2/JCD/csteeop/EMF/RFF30102001/D(01) web address: https://ec.europa.eu/health/archive/ ph_risk/committees/sct/documents/out128_en.pdf. Date accessed:23.03.2018
10. Galtonde, V.N., Karnik, S.R., Davim, J.P.: Multi performance optimization in turning of free-machining steel using Taguchi method and utility concept. J. Mater. Eng. Perform. **18**, 231–236 (2009)
11. Karabas, H.: Application of the Taguchi method for the optimization of effective parameters on the safflower seed oil methyl ester production. Int. J. Green Energy **11**(9), 1002–1012 (2014)

A Current Review on Linear Fresnel Reflector Technology and Its Applications in Power Plants

Harwinder Singh[ID], Amrik Singh[ID], R. S. Mishra[ID], and Amit Pal[ID]

1 Introduction

Because of the inadequate quantity of fossil fuel, assets and their adverse consequences on the atmosphere has put more pressure on the national economies to search for renewable resources such as solar thermal power technologies [1–3]. In the past few decades, renewable energy resources have been considered as a replacement of fossil fuels [4–6]. Apart from this, to reduce carbon dioxide emissions globally which is responsible for climate change, solar and wind both can be used as a substitute of coal [7].

1.1 Solar Energy and Concentrating Collectors

Solar energy is an alternative or renewable energy source, cheap and abundant, and even environmental friendly also [6, 8]. Nowadays, developing nations such as China and India are putting resources into sustainable power source innovations particularly in sun-based power, and in this way, worldwide commissioning and start-up of plants on the basis of concentrating solar power (CSP) can be expected in mid-term [9]. To generate base-load power, CSP can be used as alternative to traditional fossil fuels [10, 11]. In India, there are some areas which are suitable for deployment of CSP plants as these parts have greater exposure to solar radiation. In addition, solar thermal power plants of more than 400 MW are available these days, and this capacity can be increased [12]. Moreover, systems such as linear Fresnel reflector (LFR), parabolic trough collector (PTC), power tower, and parabolic dish are main

H. Singh (✉) · A. Singh · R. S. Mishra · A. Pal
Department of Mechanical, Production & Industrial and Automobile Engineering, Delhi Technological University, Bawana Road, Delhi 110042, India
e-mail: harrymehrok14@gmail.com

CSP in which PTC technology is an advanced and widely proven on commercial basis [12, 13]. As compared to other solar power plant, LFR power plant has reasonable and acceptable price for exploitation [14, 15], which makes it smart solution for thermodynamic power plant, but its performance still needs to improved [16].

1.2 Applications of Solar Thermal Energy in Various Power Plants

In this section, recent studies on the applications of solar thermal energy for different types of power plants have been discussed in brief. Jradi et al. [17] stated that cleanness, safety, and the economic and environmental aspects make solar energy more favorable, and the aim of study is to store solar energy for which an underground soil-based thermal energy storage system has been utilized that was further integrated with a combined heat and power generation system. Shabgard et al. [18] demonstrates that heating, cooling, and hot water system which is powered by solar thermal energy and further integrated with latent heat storage has a capability to reduce the auxiliary energy input significantly to satisfy the demand of residential building in Phoenix region of Arizona. Pinamonti and Baggio [19] analyzed the solar-driven heat pump along with energy storage systems in order to examine the factors which decline the systems' energy requirement, growth in solar energy's self-consumption, and lessening the cost of installation. Li et al. [20] proposed a mid-temperature sun-based heat and exhaust heat-driven novel sun-powered heat and power combined system directly attached to the absorption heat pump driven as a purpose to advance the use of solar energy as well as generation of electricity power and found that due to the regenerative cycle, recommended system produces the surplus power of 217 kWh. Kizilkan and Yamaguchi [21] concluded from the feasibility analysis that solar-driven transcritical carbon dioxide based Rankine cycle can be successfully integrated with an absorption refrigeration system which is working with H_2O-LiBr for the generation of sustainable power and refrigeration applications. Ehsan et al. [22] coupled a dry cooled recompression cycle based on supercritical carbon dioxide with the central receiver and also designed a cooling tower, but prior to this an optimization process for the various parameters of solar system and power block has been followed. Wang et al. [23] conducted a broad design and rating examination of the supercritical carbon dioxide and process of air cooling on the basis of cooling towers. Zeygham and Khalili [24] improved the productivity of air-cooled super-critical carbon dioxide cycles solar power plant by assistance of daytime radiative cooling so as to reduce the air cooling's negative effect. Milani et al. [25] reveal in their findings that contingent upon the local content situation, proposed CSP advancement could produce between 45.40 and 61.21 occupations, and 0.94 to 1.29 million of American Dollar (revenue) per MW installed. Evangelisti et al. [26] carried out a review study on solar collector and their functional elements which are important

for improving the efficiency. Further study investigated the absorbers related innovations and heat transfer fluids. Buker et al. [27] introduced the concept of building-integrated solar thermal collectors and also discussed the standards for assessing their thermal performance. Li et al. [28] examined the feasibility of a novel CSP collector to provide heat of medium-temperature to commercial buildings for the purposes of heating and cooling, so that reduction in consumption of non-renewable energy could be achieved.

1.3 Linear Fresnel Reflector (LFR) System

The non-imaging LFR is a linear concentrating collector that has many resemblances with the PTC system. In term of difference between these two technologies, there are discrete mirrors in LFR that have been placed close to the ground; however, a continuous moving reflector is present in the PTC which is situated far from the ground [29–31].

The LFR receiver is situated at a distance of about 3–5 m above the ground, and also it is non-movable. To increase the solar radiation amount approaches to absorber, a secondary reflector also presented in many cases. The tubular absorber and a secondary reflector of trapezoidal or parabolic shape can be used. However, a flat or may be curved structure especially for increasing optical efficiency can be selected for primary reflector [31]. Moreover, the design of LFR vary in terms of receiver assembly (i.e., horizontal, vertical, or triangular) and mirror arrangement [29, 32–36]. This LFR technology also possesses low cost, and without huge mechanical problems, it can achieve high concentration ratios [31, 37, 38].

1.4 LFR Comparison with the PTC

As compared to PTC, the LFR has lower optical performance in term of design differences, and reason for this lower optical efficiency is shape and spaces between the primary reflectors, effect of shading, shading effects, and the requirement of secondary reflector [31, 39]. In another way, the reason for a lower optical/thermal efficiency of LFR is a greater cosine losses which is due to the combination of a fixed receiver and the one-axis tracking mirror panels in a horizontal plane [29, 40].

2 Recent Studies on LFR Analysis

In this section, various types of past studies regarding LFR analysis have been listed. Rovira et al. [41] compares the annual performance and economic feasibility of PTC and LFR driven integrated solar-combined cycles, and it has been mentioned that

LFR is a good option for reducing the cost of CSP. Additionally, study reveals that PTC have higher thermal contribution; however, economic feasibility of the plant may be improved by LFR. Momeni et al. [42] considered the effects of employing parabolic reflectors in LFR instead of flat reflectors. Their comparison results showed that wider reflectors can be used in parabolic system which is examined under equal solar energy radiation and absorber pipe diameter that further reduced the reflectors' number and makes control system simpler. Barbon et al. [43] conducted an analysis of longitudinal movement effect on the functioning of small-scale LFR and found that with longitudinal movement, both primary cost and energy absorption through the absorber tube increases; however, a decrease in reflector area ratio has been noticed. Said et al. [44] examined the optical behavior of a LFR, and their results reveal that there is a direct impact of number of the reflective mirrors on the optical efficiency.

Dabwan et al. [45] performed a thermo-economic analysis of LFR integrated with cooling, heat, and power tri-generation system and also analyzed the annual performance of system with gas turbine of having different sizes along with area of solar collector. Their results revealed that the proposed system showed more economic feasibility for the locations having high solar radiation. Sahoo et al. [46] performed a study to investigate the heat loss for a LFR which can be due to radiation and trapezoidal cavity's steady laminar natural convection flow which is further associated with eight absorber tubes and found that losses from the cavity due to radiative component was found to be around 80–90%. Barbon et al. [47] analyzed the effects of longitudinal inclination of the mirrors' rows and/or the absorber tube on the LFR performance and study demonstrate that with longitudinal tilt angles, energy absorbed by the absorber tube strongly increases as well as weakly increases the primary cost. Lin et al. [48] experimentally and theoretically investigated the LFR with modified V-shaped cavity receiver. Their results reveal that for the tested surface temperature range, overall heat loss coefficient varied from 6.25 to 7.52 W/m^2 K. Zhu et al. [49] proposed a scalable LFR solar system and along with two stage mirrors and found that maximum thermal efficiency after adjustment was about 64%. Pulido-Iparraguirre et al. [50] studied an optically optimized LFR design for heat process applications based on solar energy, and achieved a significant enhancement ranging from 22 2% to 61% in the monthly power on the receiver. Bellos and Tzivanidis [51] investigated an enhanced thermal performance of LFR through the CuO and Syltherm 800 based nanofluid at high temperatures, and finally, it has been found that maximum enhancement in thermal efficiency is nearby 0.8%.

3   Application of LFR in Power Plants

In this section, studies available on utilization of LFR as a heat source for the various power plants have been discussed. Wang et al. [52] proposed a solar concentration photovoltaic and compact LFR based combined system, and their analysis reveals that the PV and thermal combined system has higher PV conversion and overall energy efficiencies. Dabwan and Mokheimer [53] investigated the changes of a current gas

turbine cogeneration plant, which has a gas turbine with a generating capacity of electricity, i.e., 150 MWe, and further by incorporating with CSP system, it generates steam for an industrial procedure at a rate of 81.4 at 394 °C and 45.88 bars. Sait et al. [54] carried out an optical and thermal analysis of the solar power plant in which Fresnel arrays are compared with the PTC and found that with the similar maximum flux intensities, the Fresnel array's optical performance is very nearby to PTC. Marefati et al. [55] performed an energy and exergy analysis of integrated combined cooling, heating, and power system which is made up from solid oxide fuel cell, Stirling engine, steam turbine, LFR solar field, and double effect absorption chiller and found that thermal power produces by LFR solar field is 961.7 kW as a heat exchanger. Also, their findings reveal that energy and exergy efficiencies of the proposed system are 67.5% and 55.6%, respectively.

Alhaj and Al-Ghamdi [56] proposed an LFR plant design to provide the heat for a multi-effect distillation integrated thermal vapor compression plant. Their results reveal that for per year production of 8.5 m^3 distillate, there is a requirement of 1 m^2 of the solar area. Bishoyi and Sudhakar [57] evaluated the thermal performance of 100 MW LFR plant design along with the facility of thermal energy storage of up to 6 h and found plant efficiency of about 18.3%. Marefati and Mehrpooya [58] investigated an energy, exergy, and thermodynamic assessment of combined heat and power process made up from molten carbonate fuel cell, thermoelectric generator, LFR, and power turbine. Their results indicated that the proposed system have overall and electrical efficiencies of 64.93% and 31.57%, respectively. Xu et al. [59] evaluated the performance of a LFR driven supercritical organic Rankine cycle for direct vapor generation. Their results showed that the proposed coupling not only decreases the evaporator irreversibility, but it also reduces the system's heat loss and cost.

4 Performance Optimization of LFR

Various studies on optimization of LFR have been listed in this section. Bellos et al. [60] performed Bezier polynomial parametrization-based optimization on the secondary reflector of an LFR and found that LFR's optimum optical efficiency is about 72.84%, whereas for the initial design, optical efficiency was 61.01%. Ajdad et al. [61] conducted an optical-geometric optimization of LFR through the particle swarm optimization method. Their results showed that the solar field's module allows to concentrate 60% of the solar energy incident on the mirrors' surface. Moghimi et al. [62] carried out an optimization study of a trapezoidal cavity absorber of LFR and found that top insulation thickness and cavity depth were the most sensitive parameters. Vouros et al. [63] performed a ray-tracing optimization for the secondary reflectors of LFR, and their results reveal that for secondary reflectors which are located 5 and 12.5 cm above the receiver, the maximum value of successful rays' ratio reaches to 0.97 and 0.84, respectively. Marugán-Cruz et al. [64] considered a 50 MWe solar-only LFR power plant and also analyzed the effects of the size of both

solar field and thermal storage on the annual production of the plant. Boito and Grena [65] presented the methods and results regarding the optical optimization of a LFR, and their results showed that with respect to the initial configuration, the suitable strategies of optimization can lead to an estimated gain around 12%.

5 Economic Analysis

Some recent studies on economic analysis of LFR also have been discussed here. Soomro and Kim [66] investigated a direct contact membrane distillation system driven by 111 MWe LFR plant and found that levelized cost of energy was 0.34 ¢/kWh and with a water production cost of $0.425/m^3, the average production capacity of freshwater through the distillation system was 31,844.6 L/day. In another study, Askari and Ameri [67] technically and economically considered the LFR solar field for a multi-effect desalination thermal vapor compression, and their results reveal that for the systems without thermal storage and with thermal storage, production costs of water were 1.63 $/m^3 and 3.09 $/m^3, respectively. Khajepour and Ameri [68] evaluated the effect of exercising three solar fields in a solar thermal plant, and their findings reveal rather than one solar field, employing three solar fields reduces electricity utilization by 1.83%-13.78% for the natural gas price of 9 $/MMBtu. Barbon et al. [69] studied a relationship for estimating cost of a novel small-scale LFR, for which they utilized the cost estimation software tool to determine the cost factors and found that movement components of the proposed system were influence the most to the total cost. In a different study, Bayon-Cueli et al. [70] proposed a new methodology to evaluate the both geometrical parameters and optimal distribution of small-scale LFR and computed the optimal value of both mirror width and number of mirrors at each side of the central mirror to minimize the cost of each reflector.

6 Conclusion

This review work mainly provides a short review on the solar energy and concentrating collectors especially of LFR technology and the use of solar thermal energy in power plants, and also present a solid view point for the LFR deployment instead of PTC system. It has been concluded from the past literature work that LFR could have able to prove itself in terms of low cost, less mechanical problems, and high concentration ratio [31, 37, 38]. Furthermore, various past studies related to the thermal, exergy, and optical analysis of LFR system and its application along with a power plant have been listed in this work. Moreover, some discussion on the optimization and economic analysis of LFR on the basis of recent literature has been made in this study.

References

1. Avila-Marin, A.L., Fernandez-Reche, J., Tellez, F.M.: Evaluation of the potential of central receiver solar power plants: configuration, optimization and trends. Appl. Energy **112**, 274–288 (2013)
2. Behar, O., Khellaf, A., Mohammedi, K.: A review of studies on central receiver solar thermal power plants. Renew. Sustain. Energy Rev. **23**, 12–39 (2013)
3. Lin, B., Ouyang, X.: Energy demand in china: comparison of characteristics between US and China in rapid urbanization stage. Energy Convers. Manage. **79**, 128–139 (2014)
4. Solangi, K.H., Islam, M.R., Saidur, R., Rahim, N.A., Fayaz, H.: A review on global solar energy policy. Renew. Sustain. Energy Rev. **15**(4), 2149–2163 (2011)
5. Mekhilef, S., Saidur, R., Safari, A.: A review on solar energy use in industries. Renew. Sustain. Energy Rev. **15**(4), 1777–1790 (2011)
6. Saidur, R., BoroumandJazi, G., Mekhlif, S., Jameel, M.: Exergy analysis of solar energy applications. Renew. Sustain. Energy Rev. **16**, 350–356 (2012)
7. Leonard, M.D., Michaelides, E.E., Michaelides, D.N.: Substitution of coal power plants with renewable energy sources—shift of the power demand and energy storage. Energy Convers. Manage. **164**, 27–35 (2018)
8. Basunia, M.A., Abe, T.: Thin-layer solar drying characteristics of rough rice under natural convection. Food Eng. **47**, 295–301 (2001)
9. Lisbona, P., Bailera, M., Hills, T., Sceats, M., Díez, L.I., Romeo, L.M.: Energy consumption minimization for a solar lime calciner operating in a concentrated solar power plant for thermal energy storage. Renew. Energy **156**, 1019–1027 (2020)
10. Ma, Y., Morosuk, T., Luo, J., Liu, M., Liu, J.: Superstructure design and optimization on supercritical carbon dioxide cycle for application in concentrated solar power plant. Energy Convers. Manage. **206**, 112290 (2020)
11. Zhang, H.L., Baeyens, J., Degrève, J., Cacères, G.: Concentrated solar power plants: review and design methodology. Renew. Sustain. Energy Rev. **22**, 466–481 (2013)
12. Elmohlawy, A.E., Ochkov, V.F., Kazandzhan. B.I.: Thermal performance analysis of a concentrated solar powersystem (CSP) integrated with natural gas combined cycle (NGCC)power plant. Case Stud. Thermal Eng. **14**, 100458 (2019)
13. Dersch, J., Geyer, M., Herrmann, U., Jones, S.A., Kelly, B., Kistner, R., Ortmanns, W., Pitz-Paal, R., Price, H.: Trough integration into power plants—a study on the performance of integrated solar combined cycle systems. Energy **29**, 947–959 (2004)
14. Bachelier, C., Stieglitz, R.: Design and optimisation of linear Fresnel power plants based on the direct molten salt concept. Sol. Energy **152**, 171–192 (2017)
15. Sait, H.H., Martinez-Val, J.M., Abbas, R., Munoz-Antonb, J.: Fresnel-based modular solar fields for performance/cost optimization in solar thermal power plants: a comparison with parabolic trough collectors. Appl. Energy **141**, 175–189 (2015)
16. Ghodbane, M., Boumeddane, B., Said, Z., Bellos, E.: A numerical simulation of a linear Fresnel solar reflector directed to produce steam for the power plant. J. Cleaner Prod. **231**, 494–508 (2019)
17. Jradi, M., Veje, C., Jørgensen, B.N.: Performance analysis of a soil-based thermal energy storage system using solar-driven air-source heat pump for Danish buildings sector. Appl. Therm. Eng. **114**, 360–373 (2017)
18. Shabgard, H., Song, L., Zhu, W.: Heat transfer and exergy analysis of a novel solar-powered integrated heating, cooling, and hot water system with latent heat thermal energy storage. Energy Convers. Manage. **175**, 121–131 (2018)
19. Pinamonti, M., Baggio, P.: Energy and economic optimization of solar-assisted heat pump systems with storage technologies for heating and cooling in residential buildings. Renew. Energy **157**, 90–99 (2020)
20. Li, X., Wang, Z., Yang, M., Yuan, G.: Modeling and simulation of a novel combined heat and power system with absorption heat pump based on solar thermal power tower plant. Energy **186**, 115842 (2019)

21. Kizilkan, O., Yamaguchi, H.: Feasibility research on the novel experimental solar-assisted CO_2 based Rankine cycle integrated with absorption refrigeration. Energy Convers. Manage. **205**, 112390 (2020)

22. Ehsan, M.M., Guan, Z., Gurgenci, H., Klimenko, A.: Novel design measures for optimizing the yearlong performance of a concentrating solar thermal power plant using thermal storage and a dry-cooled supercritical CO_2 power block. Energy Convers. Manage. **216**, 112980 (2020)

23. Wang, X., Li, X., Li, Q., Liu, L., Liu, C.: Performance of a solar thermal power plant with direct air-cooled supercritical carbon dioxide Brayton cycle under off-design conditions. Appl. Energy **261**, 114359 (2020)

24. Zeyghami, M., Khalili, F.: Performance improvement of dry cooled advanced concentrating solar power plants using daytime radiative cooling. Energy Convers. Manage. **106**, 10–20 (2015)

25. Milani, R., Couto, L.C., Soria, R., Szklo, A., Lucena, A.F.P.: Promoting social development in developing countries through solar thermal power plants. J. Cleaner Prod. **246**, 119072 (2020)

26. Evangelisti, L., Lieto Vollaro, R.D., Asdrubali, F.: Latest advances on solar thermal collectors: a comprehensive review. Renew. Sustain. Energy Rev. **114**, 109318 (2019)

27. Buker, M.S., Riffat, S.B.: Building integrated solar thermal collectors—a review. Renew. Sustain. Energy Rev. **51**, 327–346 (2015)

28. Li, Q., Zheng, C., Shirazi, A., Mousa, O.B., Moscia, F., Scott, J.A., Taylor, R.A.: Design and analysis of a medium-temperature, concentrated solar thermal collector for air-conditioning applications. Appl. Energy **190**, 1159–1173 (2017)

29. Zhu, G., Wendelin, T., Wagner, M.J., Kutscher, C.: History, current state, and future of linear Fresnel concentrating solar collectors. Sol. Energy **103**, 639–652 (2014)

30. Morin, G., Karl, M., Mertins, M., Selig, M.: Molten salt as a heat transfer fluid in a linear Fresnel collector—commercial application backed by demonstration. Energy Proc. **69**, 689–698 (2015)

31. Bellos, E., Tzivanidis, C., Papadopoulos, A.: Daily, monthly and yearly performance of a linear Fresnel reflector. Solar Energy **173**, 517–529 (2018)

32. Negi, B.S., Mathur, S.S., Kandpal, T.C.: Optical and thermal performance evaluation of a linear fresnel reflector solar concentrator. Solar Wind Technol. **6**(5), 589–593 (1989)

33. Negi, B.S., Kandpal, T.C., Mathur, S.S.: Designs and performance characteristics of a linear fresnel reflector solar concentrator with a flat vertical absorber. Solar Wind Technol. **7**, 379–392 (1990)

34. Gordon, J.M., Ries, H.: Tailored edge-ray concentrators as ideal second stages for fresnel reflectors. Appl. Opt. **32**, 2243–2251 (1993)

35. Abbas, R., Montes, M.J., Piera, M., Martinez-Val, J.M.: Solar radiation concentration features in linear Fresnel reflector arrays. Energy Convers. Manage. **54**, 133–144 (2012)

36. Abbas, R., Munoz, J., Martinez-Val, J.M.: Steady-state thermal analysis of an innovative receiver for linear Fresnel reflectors. Appl. Energy **92**, 503–515 (2012)

37. Montes, M.J., Barbero, R., Abbas, R., Rovira, A.: Performance model and thermal comparison of different alternatives for the Fresnel single-tube receiver. Appl. Therm. Eng. **104**, 162–175 (2016)

38. Montes, M.J., Abbas, R., Muñoz, M., Muñoz-Antón, J., Martínez-Val, J.M.: Advances in the linear Fresnel single-tube receivers: hybrid loops with non-evacuated and evacuated receivers. Energy Convers. Manage. **149**, 318–333 (2017)

39. Nixon, J.D., Dey, P.K., Davies, P.A.: Design of a novel solar thermal collector using a multi-criteria decision-making methodology. J. Cleaner Prod. **59**, 150–159 (2013)

40. Munoz, J., Martinez-Val, J.M., Ramos, A.: Thermal regimes in solar-thermal linear collectors. Sol. Energy **85**, 857–870 (2011)

41. Rovira, A., Barbero, R., Montes, M.J., Abbas, R., Varela, F.: Analysis and comparison of integrated solar combined cycles using parabolic troughs and linear Fresnel reflectors as concentrating systems. Appl. Energy **162**, 990–1000 (2016)

42. Momeni, S., Menbari, A., Alemrajabi, A.A., Mohammadi, P.: Theoretical performance analysis of new class of Fresnel concentrated solar thermal collector based on parabolic reflectors. Sustain. Energy Technol. Assessments **31**, 25–33 (2019)

43. Barbon, A., Bayon, L., Bayon-Cueli, C., Barbon, N.: A study of the effect of the longitudinal movement on the performance of small scale linear Fresnel reflectors. Renew. Energy **138**, 128–138 (2019)
44. Said, Z., Ghodbane, M., Hachicha, A.A., Boumeddane, B.: Optical performance assessment of a small experimental prototype of linear Fresnel reflector. Case Stud. Thermal Eng. **16**, 100541 (2019)
45. Dabwan, Y.N., Pei, G., Gao, G., Li, J., Feng, J.: Performance analysis of integrated linear fresnel reflector with a conventional cooling, heat, and power tri-generation plant. Renew. Energy **138**, 639–650 (2019)
46. Sahoo, S.S., Singh, S., Banerjee, R.: Analysis of heat losses from a trapezoidal cavity used for Linear Fresnel reflector system. Sol. Energy **86**, 1313–1322 (2012)
47. Barbon, A., Bayon-Cueli, C., Bayon, L., Rodríguez, L.: Investigating the influence of longitudinal tilt angles on the performance of small scale linear Fresnel reflectors for urban applications. Renew. Energy **143**, 1581–1593 (2019)
48. Lin, M., Sumathy, K., Dai, Y.J., Wang, R.Z., Chen, Y.: Experimental and theoretical analysis on a linear Fresnel reflector solar collector prototype with V-shaped cavity receiver. Appl. Therm. Eng. **51**, 963–972 (2013)
49. Zhu, Y., Shi, J., Li, Y., Wang, L., Huang, Q., Xu, G.: Design and thermal performances of a scalable linear Fresnel reflector solar system. Energy Convers. Manage. **146**, 174–181 (2017)
50. Pulido-Iparraguirre, D., Valenzuela, L., Serrano-Aguilera, J.J., Fernández-García, A.: Optimized design of a linear Fresnel reflector for solar process heat applications. Renew. Energy **131**, 1089–1106 (2019)
51. Bellos, E., Tzivanidis, C.: Multi-criteria evaluation of a nanofluid-based linear Fresnel solar collector. Sol. Energy **163**, 200–214 (2018)
52. Wang, G., Wang, F., Shen, F., Chen, Z., Hu, P.: Novel design and thermodynamic analysis of a solar concentration PV and thermal combined system based on compact linear Fresnel reflector. Energy **180**, 133–148 (2019)
53. Dabwan, Y.N., Mokheimer, E.M.A.: Optimal integration of linear Fresnel reflector with gas turbine cogeneration power plant. Energy Convers. Manage. **148**, 830–843 (2017)
54. Sait, H.H., Martinez-Val, J.M., Abbas, R., Munoz-Anton, J.: Fresnel-based modular solar fields for performance/cost optimization in solar thermal power plants: a comparison with parabolic trough collectors. Appl. Energy **141**, 175–189 (2015)
55. Marefati, M., Mehrpooya, M., Mousavi, S.A.: Introducing an integrated SOFC, linear Fresnel solar field, Stirling engine and steam turbine combined cooling, heating and power process. Int. J. Hydrogen Energy **44**, 30256–30279 (2019)
56. Alhaj, M., Al-Ghamdi, S.G.: Reducing electric energy consumption in linear Fresnel collector solar fields coupled to thermal desalination plants by optimal mirror defocusing. Heliyon **4**, e00813 (2018)
57. Bishoyi, D., Sudhakar, K.: Modeling and performance simulation of 100 MW LFR based solar thermal power plant in Udaipur India. Resource-Efficient Technol. **3**, 365–377 (2017)
58. Marefati, M., Mehrpooya, M.: Introducing and investigation of a combined molten carbonate fuel cell, thermoelectric generator, linear fresnel solar reflector and power turbine combined heating and power process. J. Cleaner Prod. **240**, 118247 (2019)
59. Xu, G., Song, G., Zhu, X., Gao, W., Li, H., Quan, Y.: Performance evaluation of a direct vapor generation supercritical ORC system driven by linear Fresnel reflector solar concentrator. Appl. Therm. Eng. **80**, 196–204 (2015)
60. Bellos, E., Tzivanidis, C., Papadopoulos, A.: Secondary concentrator optimization of a linear Fresnel reflector using Bezier polynomial parametrization. Sol. Energy **171**, 716–727 (2018)
61. Ajdad, H., Filali Baba, Y., Al Mers, A., Merroun, O., Bouatem, A., Boutammachte, N.: Particle swarm optimization algorithm for optical-geometric optimization of linear Fresnel solar concentrators. Renew. Energy **130**, 992–1001 (2019)
62. Moghimi, M.A., Craig, K.J., Meyer, J.P.: Optimization of a trapezoidal cavity absorber for the linear Fresnel reflector. Sol. Energy **119**, 343–361 (2015)

63. Vouros, A., Mathioulakis, E., Papanicolaou, E., Belessiotis, V.: On the optimal shape of secondary reflectors for linear Fresnel collectors. Renew. Energy **143**, 1454–1464 (2019)
64. Marugán-Cruz, C., Serrano, D., Gómez-Hernández, J., Sánchez-Delgado, S.: Solar multiple optimization of a DSG linear Fresnel power plant. Energy Convers. Manage. **184**, 571–580 (2019)
65. Boito, P., Grena, R.: Optimization of the geometry of Fresnel linear collectors. Sol. Energy **135**, 479–486 (2016)
66. Soomro, M.I., Kim, W.S.: Performance and economic evaluation of linear Fresnel reflector plant integrated direct contact membrane distillation system. Renew. Energy **129**, 561–569 (2018)
67. Askari, I.B., Ameri, M.: Techno economic feasibility analysis of linear Fresnel solar field as thermal source of the MED/TVC desalination system. Desalination **394**, 1–17 (2016)
68. Khajepour, S., Ameri, M.: Techno-economic analysis of using three Fresnel solar fields coupled to a thermal power plant for different cost of natural gas. Renew. Energy **146**, 2243–2254 (2020)
69. Barbon, A., Sanchez-Rodríguez, J.A., Bayon, L., Bayon-Cueli, C.: Cost estimation relationships of a small scale linear Fresnel reflector. Renew. Energy **134**, 1273–1284 (2019)
70. Bayon-Cueli, C., Barbon, A., Bayon, L., Barbon, N.: A cost-energy based methodology for small-scale linear Fresnel reflectors on flat roofs of urban buildings. Renew. Energy **146**, 944–956 (2020)

Economic Feasibility of Refrigeration Waste Heat-Assisted Solar Hybrid Drying System

S. P. Singh and **Ankur Nagori**

Nomenclatures

VCRS	Vapor compression refrigeation System
RH	Relative humidity
DBT	Dry-bulb temperature
IMC	Initial moisture content
FMC	Final moisture content
ORC	Organic Rankine cycle
SMER	Specific moisture evaporation rate
COP	Coefficient of performance
NPV	Net present value
IRR	Internal rate of return
SR	Sizing ratio
IR	Investment ratio
TR	Tons of refrigeration
ERR	Energy efficiency ratio
PUF	Polyurethane foam
wb	wet basis
m^2	Square meter
m^3	Cubic meter
kg	kilo gram
KJ	Kilo Joule
MJ	Mega Joule
H	hour

S. P. Singh · A. Nagori (✉)
School of Energy and Environmental Studies, Devi Ahilya University, Indore 452011, India
e-mail: ankur411@yahoo.co.in

1   Introduction

The reduction of post-harvest losses for fresh vegetables is a prime importance for the sector. It was observed that there is a loss of 1/3 of total food production annually [1, 2]. Most of the fresh vegetable produce are lost due to lack of management practices such as inadequate storage and preservation facilities after harvest [3]. Drying and refrigeration are two main vital methods of preservation to reduce the post-harvest losses just after harvesting. Conventional drying is prevailed worldwide along with its limitation of hygiene and product quality. Solar drying is very common, and many designs of solar dryers such as greenhouse dryer, tray dryer, and convective tunnel dryer are available for drying with individual and hybrid mode and utilized successfully [4]. On the other hand, cold chain facilities are essential for food security as well as for quality of perishable items, despite of energy intensive operation which tends to increase total energy consumption [5]. According to Global cold storage Capacity Report [6], the total capacity of refrigerated warehouses worldwide was reported as 616 million cubic meters in 2018, and India was leading as largest country market, with 150 million cubic meters, followed by the USA (131 million cubic meters), and China (105 million cubic meters). Also, 17% of total global CO_2 emission is presently coming from cold chain industry alone [7]. Therefore, there is a huge potential for waste heat utilization through cold chain industries of the global market for application in drying. Hybridization of waste heat from vapor compression refrigeration system and solar hot air drying systems could be applied where low temperature and well-controlled drying conditions are needed [8]. It was observed that drying using refrigeration waste heat is the more sophisticated method regarding product quality, efficiency, drying rate, process control, and operating cost than solar hot air drying [9]. Earlier drying studies were performed using refrigeration waste heat through commonly used refrigeration systems individually or hybrid mode for clothes, grapes [10–13]. Parameters like drying rate, SMER, COP, moisture content, energy efficiency, and mass flow rate were studies and reported. There were a very few literatures available on economic studies especially with VCRS-based solar hybrid drying systems. The studies concluded the economic benefit in terms of reduction in electrical energy consumption by using waste heat of refrigeration at condenser side [14]. Also, in combination with solar heat the hybrid system could be utilized for various applications. [15] studied about technoeconomics of different solar dryers and described various methods of economic analysis for hybrid, direct, and indirect solar drying systems. Annualized cost method, lifecycle cost saving, and payback period are the three main methods of cost analysis and economic feasibility. These methods include cost variables like net present value (NPV), salvage value, capital recovery factor (CRF), cost–benefit ratio (CBR), and internal rate of return (IRR).

The authors [16] optimized the size and cost of waste heat-based organic Rankine cycle (ORC)-powered cascaded vapor compression–absorption refrigeration system using nonlinear programming based on conjugated directions method. The simple break even and payback period was calculated and optimized. Team of investigators [17] studied about economic optimization of the air collector and evaporator area

in solar-assisted heat pump drying. The maximum amount of savings was found at minimum payback period of the system. The researchers [18] performed an economic analysis of solar-assisted heat pump drying system for 10 kg sample of Reddish. The economic feasibility was based on product pricing and payback period. Economic analysis based on net present value (NPV) and payback period was done for solar-assisted heat pump fluidized bed dryer integrated with biomass furnace for rice drying [19]. Most of the research works are available with refrigeration-based heat pump drying which utilizes low and high grade of waste energy in the form of heat for drying purpose. Research works on direct utilization of low grade heat from condenser exhaust integrated with solar energy in hybrid mode for drying applications are rarely found. Also, literatures are limited on hybrid drying system with optimum sizing and cost and its feasibility in present scenario. In order to choose the hybrid solar drying system utilizing vapor compression-based refrigeration waste heat and ensuring its economic feasibility, a theoretical attempt has been made. A simple investment ratio and sizing ratio (solar collector area in m^2 to refrigeration capacity in TR) have determined and predicted the sizing of individual units for a specific quantity of material to be dried.

2 Materials and Method

The mathematical calculation based on empirical relations and theory is performed for sizing of individual units of system to be made hybrid and heat availability for drying at outlet of each system. The hybrid system consists of VCRS and natural convection detachable solar drying unit assembly. A detachable flat plate solar heat collector would be located at the condenser outlet of VCRS. The combination of heat from refrigeration condenser and solar collector would be utilized for dehydration purpose. Let us assume a hybrid system for drying of 50 kg fresh vegetables using one TR refrigeration unit in combination with solar dryer (Fig. 1).
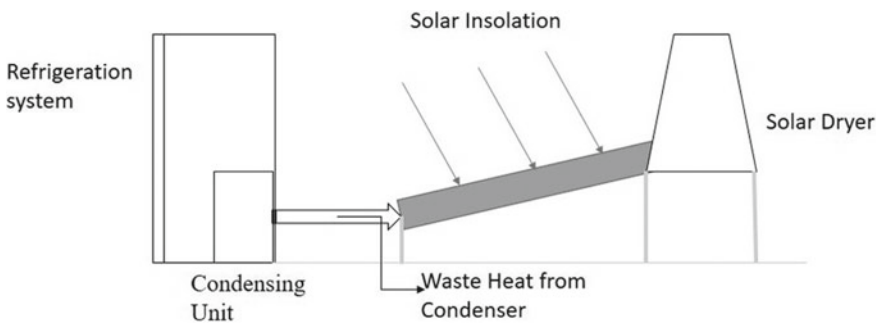
Fig. 1 Block diagram of refrigeration waste heat-assisted hybrid solar drying system

2.1   Drying of Vegetables Through Solar Heat

Product to be dried	Fresh vegetables
Initial and final moisture content (average)	88% and 7%, respectively, on wet basis
Average dry bulb temperature (DBT) and relative humidity (RH) [for composite climate like Indore (m.p.) India]	26 °C and 50.6%
Drying unit	Natural convection solar tray dryer
Collector type	Solar flat plate collector of 40% efficiency [20]
Area of solar collector % Moisture content on wet basis	$Ac = \frac{ma*(Hw-Ha)}{\eta*I}$ (1) [21] Ac: Area of solar collector (m^2) m $_a$: mass flow rate in kg/s Hw-Ha: Enthalpy difference of air at respective temperatures (kJ/kg) η: efficiency of flat plate collector I = Solar irradiation (KWh/m^2/day)
Enthalpy of ambient air	$Ha = 1.007T + \omega[251.2131 + 1.5524T]$ (3) [23] Ha = Enthalpy of moist air in kJ/kg ω = Humidity ratio in kg/kg of dry air T = Dry bulb temperature in °C
Density of air is assumed	1.20 kg/m^3

From the above-mentioned relations, heat required for natural convection solar drying and area of solar collector could be determined for different vegetables with same sample size.

2.2   Size Prediction for Vapor Compression Refrigeration System (VCRS) Utilizing Waste Heat for Drying

Product to be stored	Fresh vegetables
Quantity of vegetable to be stored	750 kg (using average density of fresh vegetables)
Capacity of chilled storage	1 TR
The temperature difference between ambient and inside storage chamber	40 °C
Insulation material	PUF having thickness 80 mm
Net heat load	Transmission load + product load + respiration load + infiltration load + misc load

(continued)

Product to be stored	Fresh vegetables
Transmission load	$Q = U * A * \Delta T$ (4) Where Q = heat transmission, A = area in m^2 and U = overall heat transfer coefficient, and ΔT = temperature difference
Product load	m*Cp*ΔT + (heat of respiration * mass of product) (5) where m = mass of product in kg and Cp is specifc heat in KJ/kgk
Overall heat transfer coefficient (U) (only conductive resistance would be taken into account)	$\frac{1}{U} = \frac{tm}{km} + \frac{ts}{ks} + \frac{tins}{kins}$ (6) Where t_m, t $_s$, and t_{ins} are the thickness of outer, inner, and insulating sheets of the chamber and k_m, k_s, k_{ins} are thermal conductivities, respectively
Infiltration Load	Total infiltration load: Sensible infiltration load + latent infiltration load sensible infiltration load = V_{inf} * ρ* C_{pv} *ΔT (7) latent infiltration load = V_{inf} * ρ*C_{pv}*(w$_o$-w$_i$)*h$_c$ (8) Total volume of infiltration = V_{inf} = 0.48*number of air change per day Number of air change = 3 (assumed) [24] w$_o$ and w$_i$—inside and outside humidity's in kg/kg of dry air h$_c$ is the latent heat of condensation for water, i.e., 2257 kJ/kg Density of moist air (ρ) and specific heat capacity of vapour (C_{pv}) will be taken as 1.20 kg/m^3 and 1.88 kJ/kg, respectively
Miscellaneous load (10–20% of total load)	Condenser fan load, light load, and load due to moisture loss from vegetable could be taken into consideration as miscellaneous load. Other loads like solar load, sensible as well as latent heat from fan motors, loss due to improper insulation, convection loads, etc., are not taken into consideration for the ease of calculations

For the sake of simplicity in calculations, the losses in refrigeration system are neglected and total heat content at condenser exhaust is assumed as equal to the total cooling load.

From Table 1 and Table 2, it is clear that heat required for drying of vegetables using solar dryer varies between 4.85 and 8.65 MJ/kg. It is seen here that the heat requirement for the onion is maximum and bitter gourd is minimum for the same sample size. The average amount of heat available with solar energy for drying of vegetables would be calculated as 5.76 MJ/kg.

Amount of heat extracted that will be available theoretically at condenser exhaust of one TR refrigeration system would be 5.64 MJ/kg with energy efficiency ratio

Table 1 Moisture content, heat requirement, and heat collector sizing for solar drying of various vegetables

Vegetable (1 kg)	Moisture content (%)		Volum-etric flow rate (m³/h)	Mass flow rate (kg/h)	Enthalpy of air kJ/kg		Heat requir-ed for drying kJ/s	Area of solar collector (m²)	Heat required for drying per batch in KJ
	IMC (wb)	FMC (wb)			Ambient air	Warm air			
Tomato	96	10	19.24	23.09	36.31	66.40	0.19	0.44	5472
Potato	75	13	21.65	25.98	41.75	66.66	0.18	0.37	5184
Onion	80	4	45.19	53.32	42.80	63.29	0.30	0.57	8640
Brinjal	95	6	21.99	26.17	67.33	91.78	0.18	0.41	5184
Bitter-gourd	92	7	20.28	24.14	72.12	96.96	0.17	0.49	4896

Table 2 Recommended temperature and humidity conditions, bulk density, specific heats, and heat of respiration for storage: [4, 6, 25, 26]

Vegetable to be stored	Recommended storage conditions temperature (°C) and relative Humidity (%)	Approximate storage life	Bulk density kg/m³	Specific heat kJ/kg K	Heat of respiration kJ/kgh
Tomato	13–15 and 85–90% RH	4–7 days	550	3.98	0.284
Potato	4.5–13 and 90–95% RH	5–10 months	675	3.43	0.072
Onion	0–2 and 65–75% RH	1–8 months	620	3.77	0.064
Brinjal (eggplant)	12 and 90–95%	1 week	295	3.94	0.736
Bitter gourd	12–13 and 85–90%	2–3 weeks	400	3.76	0.768

(ERR) of 0.4. From condenser exhaust of one TR refrigeration system, about 35 kg product could be dried.

2.3 Economic Prediction of Hybrid System

Fresh vegetables to be dried	50 kg
Refrigeration capacity	1 TR
Maximum quantity could be dried using refrigeration heat of 1 TR	35.9 kg
Dried material quantity in kg through refrigeration waste heat	3.6 kg
Remaining product to be dried with solar dryer in kgs	14.1 kg
Area of solar flat plate air collector required (m²)	6.41m²
Dried material quantity in kg through solar heat	1.41 kg
Fresh material to be stored in refrigeration system in kg	750 kg
Average cost of fresh material in Rs	@40 per kg
Average cost of dried material in Rs	@300 per kg
Cost of solar dryer in Rs	106,094.00 (a)
Cost of refrigeration system in Rs	375,000.00 (b)
Operating cost/year in Rs	43,992.00 (c)
Cost of drying through refrigeration waste heat in Rs	179,271.00 (d)
Total cost of refrigeration Rs. (b) + (c) + (d)	418,992.00

(continued)

(continued)

Fresh vegetables to be dried	50 kg
Total cost of hybrid system Rs. (a) + (b) + (c) + (d)	704,357.00
Annual saving in solar dryer Rs	63,656.28
Annual saving with refrigeration system Rs	4,661,344.00
Total savings in hybrid system Rs	4,725,000.00

3 Result and Discussion

There are various combinations of systems which could be tried for specific quantity of product to be dried. Here, we have tried to make a hybrid system by predicting the average values of total costs and savings for the individual units and plotting them for various combinations of refrigeration capacity and solar heat collecting areas. The economic feasibility of the any system is based on size and overall investment. Simple investment ratio (saving/cost) and size ratio are plotted to represent the predicted hybrid system for its feasibility on economic point of view. Here, we are trying to select the better option of hybrid drying system based on selected sample size that is 50, 100, 150, 200, 250, 300, 400, and 500 kg. Size ratio (SR) was represented on abscissa and simple investment ratio (IR) on ordinate. The almost similar trends were found for each sample sizes. The gradient of slope found steeper for small size ration in every sample size than that of higher one. For sample size of 50 kg, it seems to be flatten near 30 SR with IR of 4.5, for 100 kg it showed between 70 and 80 SR with IR of 3 (Figs. 2 and 3). It was found near 100–120 SR with IR of 2 for sample size of 150 and 200 kg, respectively (Figs. 4 and 5). For sample size of 250 and 300 kg, the
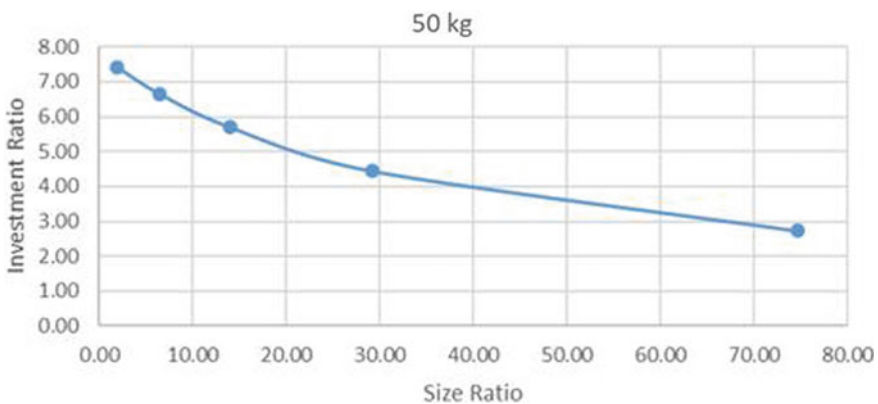
Fig. 2 Representation of IR versus SR for 50 kg sample to be loaded for drying
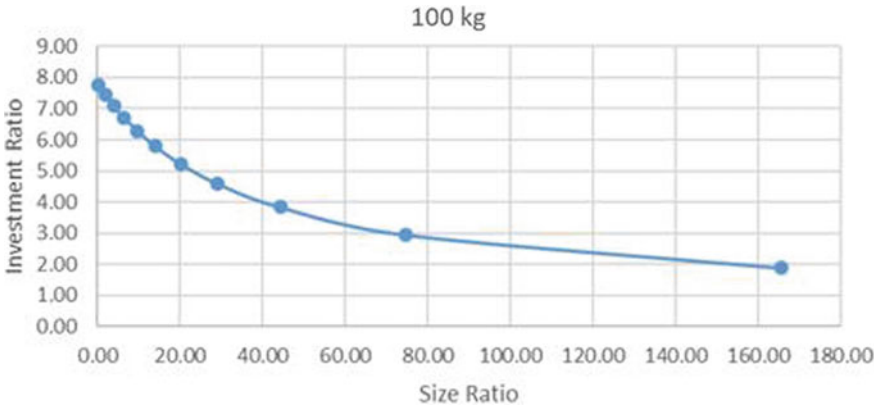
Fig. 3 Representation of IR versus SR for 100 kg sample to be loaded for drying
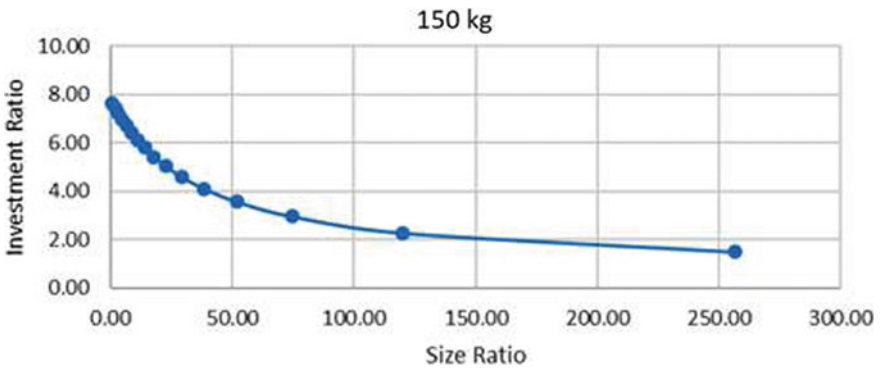
Fig. 4 Representation of IR versus SR for 150 kg sample to be loaded for drying
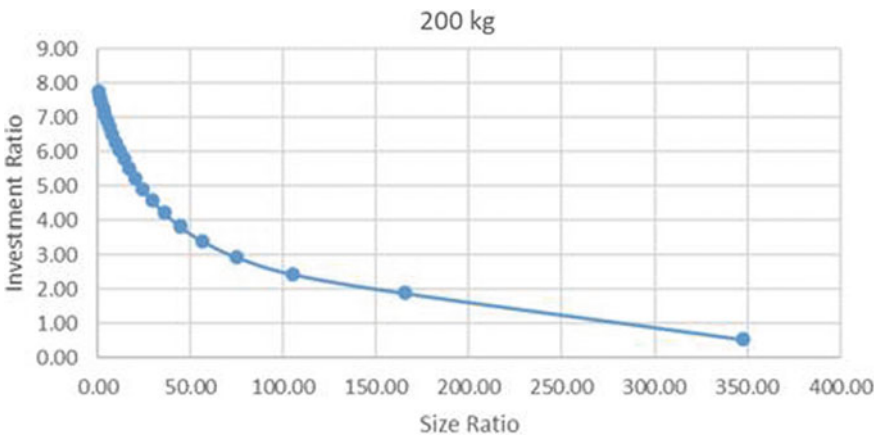
Fig. 5 Representation of IR versus SR for 200 kg sample to be loaded for drying
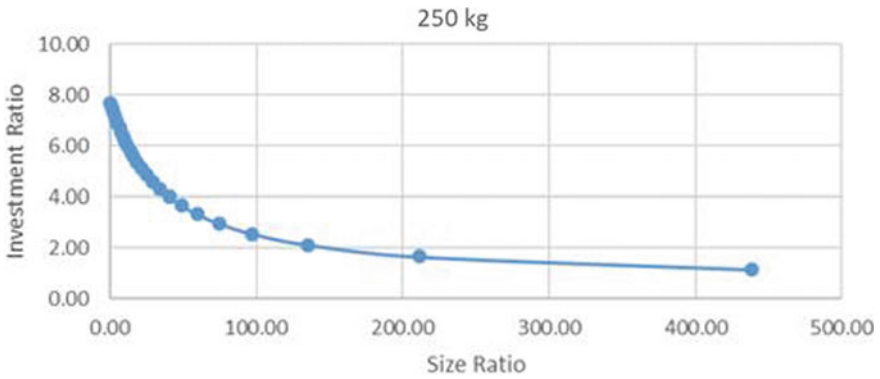
Fig. 6 Representation of IR versus SR for 250 kg sample to be loaded for drying
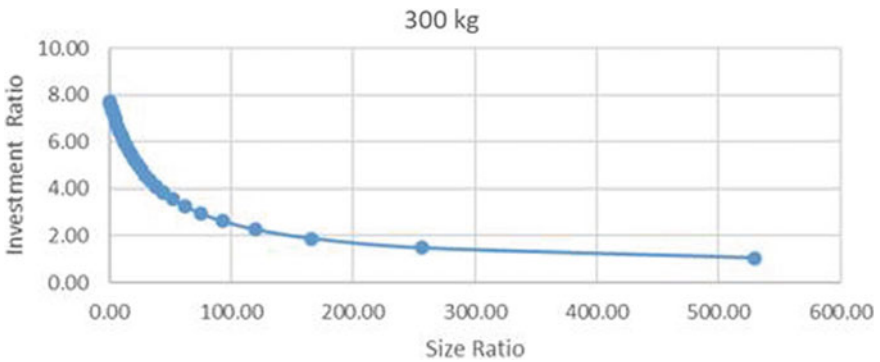
Fig. 7 Representation of IR versus SR for 300 kg sample to be loaded for drying

slope was get flattened at high SR (200–250) even though 1.5 times of IR (Figs. 6 and 7). High values of SR would not be feasible practically.

For large sample size like 400 and 500 kg (Figs. 8 and 9), the IR ration found unity, and this means savings and investment would be equal and increasing size ration would be impractical for huge quantity of drying with this hybrid mode.

By plotting the values of SR and IR with quantity of product to be dried, an intersection point is obtained by which it could be able to find the feasible option for sizing of hybrid system using overall costing and savings. Here, the point is obtained in between 200 and 250 kg where SR value would be 165.70–211.18 and IR in between 1.89 and 1.65. From Fig. 10, it is clear that the hybrid system sizing would be made feasible practically and economically for the product sample size to be dried up to 200 kg. Above 200 kg, IR would be decreased with increased SR, which may not be feasible practically. Therefore, for the economic feasibility, the sizing ratio of 29.20, 74.70, 120.20, 165.70, 211.18, 256.68, 347.68, and 438.66 and
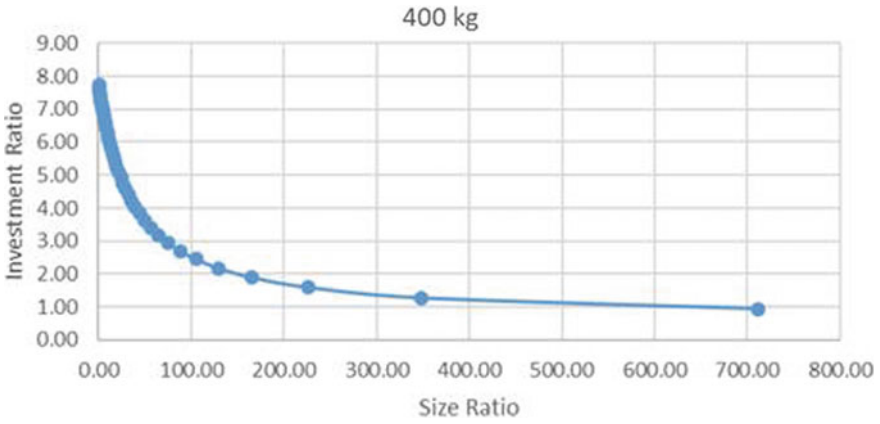
Fig. 8 Representation of IR versus SR for 400 kg sample to be loaded for drying
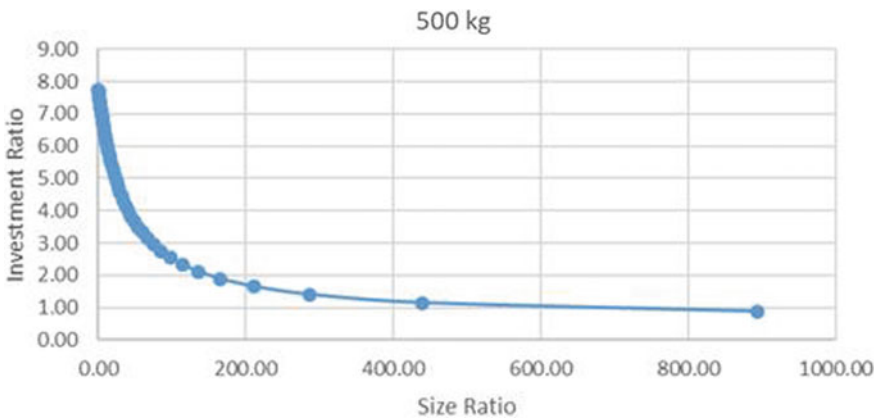
Fig. 9 Representation of IR versus SR for 500 kg sample to be loaded for drying

the respective simple investment ratio would be 4.44, 2.95, 2.27, 1.89, 1.65, 1.49, 1.29, and 1.16.

It is clear from the above results that for the economic and practical feasibility of hybrid system, the sizing ration plays an important role. By harnessing the refrigeration waste heat with existing installed systems for drying applications through combining solar heat, the size selection of individual units is crucial. It also depends on crop production and availability of refrigerated storage capacity.
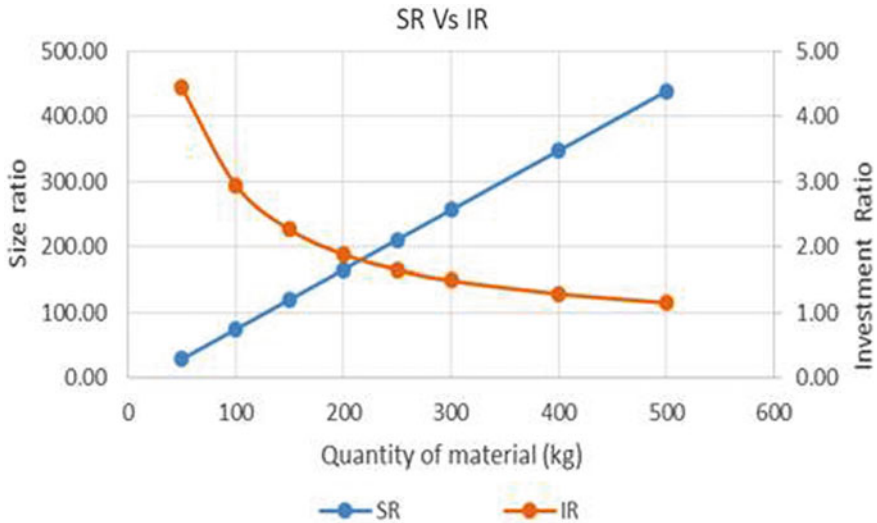
Fig. 10 Representation of optimum ration for hybrid drying system with different sample size

4 Conclusion

- Size ration (SR) and simple investment ration (IR) could be utilized for getting the economic feasible hybrid system. Economic feasible size would be obtained in between SR value of 165.70–211.18 and IR of 1.65–1.89.
- Drying of vegetable only on small scale (up to 250 kg) might be feasible practically and economically with refrigeration waste heat of VCRS, utilizing solar energy as a hybrid mode. The total saving of combined system would be found nearly two times of total investment.
- Theoretical heat available for per kg drying of selected vegetables with above-mentioned hybrid mode would be 11.4 MJ. The VCRS (0.5TR to 10TR) could be chosen in combination with solar natural convection dryer for the development of hybrid system.
- Hybrid system might be mostly preferred for small capacity drying (up to 250 kg) as total cost would be more dominant on large scale. The incremental change in size would led to insignificant change in savings so that for large-scale drying IR plot shows decreasing trend with SR.
- Refrigeration waste heat acts as alternate energy backup for drying process on unavailability of solar heat during nighttime or rainy season. Refrigeration waste heat if used in hybrid form might boost up the drying rate and thereby reducing drying time.

References

1. FAO: Global food losses and food waste. Extent Causes Prev. https://www.fao.org/fileadmin/user_upload/ags/publications/GFL_web.pdf.2011
2. ASSOCHAM: Horticulture Sector in India—State Level Experience. The Associated Chambers of Commerce and Industry of India, New Delhi (2013)
3. Yahia, E.M. (ed.): Postharvest Technology of Perishable Horticultural Commodities. Woodhead Publishing (2019)
4. Rao, C.G.: Engineering for Storage of Fruits and Vegetables: Cold Storage, Controlled Atmosphere Storage, Modified Atmosphere Storage. Academic Press (2015)
5. Kader, A.A.: Increasing food availability by reducing postharvest losses of fresh produce. V Int. Postharvest Symp. **682**, 2169–2176 (2004)
6. Hardenburg, R.E., Watada, A.E., Wang, C.Y.: The Commercial Storage of Fruits, Vegetables, and Florist and Nursery Stocks (No. 66). US Department of Agriculture, Agricultural Research Service (1986)
7. World Energy Outlook. https://www.worldenergyoutlook.org/ 2002 & 2004
8. Daghigh, R., Ruslan, M.H., Sulaiman, M.Y., Sopian, K.: Review of solar assisted heat pump drying systems for agricultural and marine products. Renew. Sustain. Energy Rev. **14**(9), 2564–2579 (2010). https://doi.org/10.1016/j.rser.2010.04.004
9. Mujumdar, A.S., Jangam, S.V.: Some innovative drying technologies for dehydration of foods. In: Proceedings of ICEF, Athens, Greece, pp. 555–556 (2011)
10. Mahlia, T.M.I., Hor, C.G., Masjuki, H.H., Husnawan, M., Varman, M., Mekhilef, S.: Clothes drying from room air conditioning waste heat: thermodynamics investigation. Arab. J. Sci. Eng. **35**(1), 339 (2010)
11. Deng, S., Han, H.: An experimental study on clothes drying using rejected heat (CDURH) with split-type residential air conditioners. Appl. Therm. Eng. **24**(17–18), 2789–2800 (2004). https://doi.org/10.1016/j.applthermaleng.2004.03.016
12. Ambarita, H., Nasution, A.H., Siahaan, N.M., Kawai, H.: Performance of a clothes drying cabinet by utilizing waste heat from a split-type residential air conditioner. Case Stud. Thermal Eng. **8**, 105–114 (2016). https://doi.org/10.1016/j.csite.2016.06.002
13. Chandrasekar, M., Senthilkumar, T., Kumaragurubaran, B., Fernandes, J.P.: Experimental investigation on a solar dryer integrated with condenser unit of split air conditioner (A/C) for enhancing drying rate. Renew. Energy **122**, 375–381 (2018). https://doi.org/10.1016/j.renene.2018.01.109
14. Ramadan, M., Murr, R., Khaled, M., Olabi, A.G.: Air dryer using waste heat of HVAC systems–code development and experimental validation. Appl. Therm. Eng. **147**, 302–311 (2019). https://doi.org/10.1016/j.applthermaleng.2018.10.087
15. Selvanayaki, S., Sampathkumar, K.: Techno-economic analysis of solar dryers. In: Solar Drying Technology. Springer, Singapore, pp. 463–493 (2017)
16. Patel, B., Desai, N.B., Kachhwaha, S.S.: Thermo-economic analysis of solar-biomass organic Rankine cycle powered cascaded vapor compression-absorption system. Sol. Energy **157**, 920–933 (2017). https://doi.org/10.1016/j.solener.2017.09.020
17. Rahman, S.M.A., Saidur, R., Hawlader, M.N.A.: An economic optimization of evaporator and air collector area in a solar assisted heat pump drying system. Energy Convers. Manage. **76**, 377–384 (2013). https://doi.org/10.1016/j.enconman.2013.06.058
18. Qiu, Y., Li, M., Hassanien, R.H.E., Wang, Y., Luo, X., Yu, Q.: Performance and operation mode analysis of a heat recovery and thermal storage solar-assisted heat pump drying system. Sol. Energy **137**, 225–235 (2016). https://doi.org/10.1016/j.solener.2016.08.016
19. Yahya, M., Fahmi, H., Fudholi, A., Sopian, K.: Performance and economic analyses on solar-assisted heat pump fluidised bed dryer integrated with biomass furnace for rice drying. Sol. Energy **174**, 1058–1067 (2018). https://doi.org/10.1016/j.solener.2018.10.002
20. Sodha, M.S., Bansal, N.K., Kumar, K., Bansal, P.K., Malik, M.A.S.: Solar Crop Drying 1, West Palm Beach (1987)

21. Tonui, K.S., Mutai, E.B.K., Mutuli, D.A., Mbuge, D.O., Too, K.V.: Design and evaluation of solar grain dryer with a back-up heater. Res. J. Appl. Sci. Eng. Technol. **7**(15), 3036–3043 (2014)

22. Sharma, V.K., Sharma, S., Ray, R.A., Garg, H.P.: Design and performance studies of a solar dryer suitable for rural applications. Energy Convers. Manage. **26**(1), 111–119 (1986). https://doi.org/10.1016/0196-8904(86)90040-3

23. Brooker, D.B., Bakker-Arkema, F.W., Hall, C.W.: Drying and storage of grains and oilseeds. Springer Science & Business Media (1992)

24. Prasad, M.: Refrigeration and Airconditioning Data Book. New Age International (1989)

25. McGregor, B.M.: Tropical Products Transport Handbook. US Department of Agriculture, Office of Transportation; No. 668 (1989)

26. Sharan, G., Rawale, K.: Physical Characteristics of Some Vegetables Grown in Ahmedabad Region (No. WP2003–12–01). Indian Institute of Management Ahmedabad, Research and Publication Department (2003)

Thermal Analysis of Solar Air Heater by Using Pebbles as an Absorber Material

Atul Gautam [ID]**, Pramod Kumar Sharma** [ID]**, Mayank Srivastava** [ID]**, G. Phaldessai, Vilas Warudkar** [ID]**, and J. L. Bhagoria** [ID]

1   Introduction

Since there is a significant gap in demand and supply of energy in the state of Goa, there is a very high rate of depletion of exhaustible resources. So, there is a need to develop an alternative solution in order to cope with exhaustible resource. There is plenty of renewable energy available but we lack ideas to significantly avail it. Therefore, it is necessary to develop eco-friendly way in order to use renewable energy efficiently. There are various ways by which solar energy is being used to fulfill various purposes. [1] But in conventional methods, the various absorbing material which is being used is less efficient and are not having much conversion efficiency (Fig. 1). Hence, proper analysis of various absorber materials is required. Solar air collector is a simple device which converts solar energy into heat energy. This heat can be used for various purposes.

[4] investigated solar collector experimentally with the two media such as air and pebble bed in different operating modes. [5] Thermal performance of the packed bed using 8500 kg rock pebbles filled and solar heat storage system was studied. [6] In this work, two types of packed bed collectors, one with wire mesh screen matrix bed and other with pebble bed, were optimized on the basis of minimum cost per unit energy delivered. [7] Analyzed performance parameters such as solar radiation intensity, temperatures at various positions in solar air heater, and daily thermal and exergy. Efficiency is based on trapezoidal corrugated solar air heater with the use of sensible heat. [8] studied different types of solar air collectors and

A. Gautam (✉) · P. K. Sharma · V. Warudkar · J. L. Bhagoria
Department of Mechanical Engineering, M.A.N.I.T, Bhopal, India
e-mail: atul1993gautam@gmail.com

M. Srivastava
Deparmant of Mechanical Engineering, NIT, Jamshedpur, India

G. Phaldessai
Mechanical Engineering Department, PCCE, Goa, India
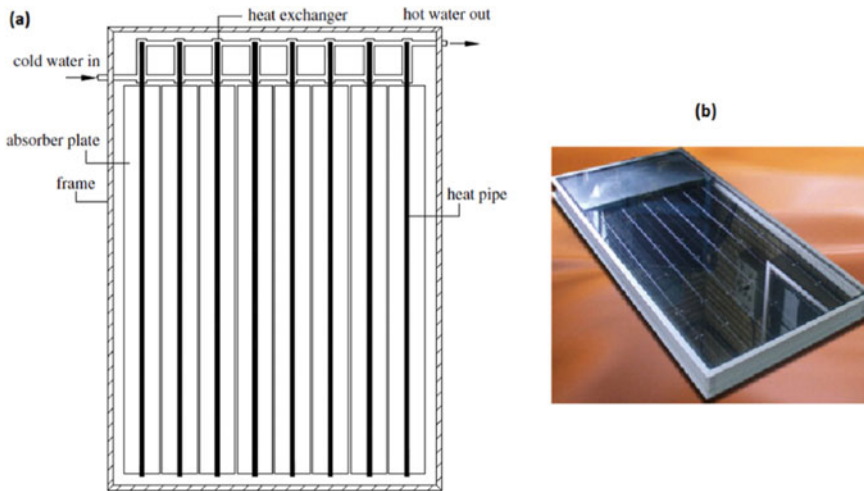
Fig. 1 A flat plate heat pipe solar collector: **a** schematic view and **b** general view [2, 3]

the paper also talks about design and fabrication of different air heaters for comparison of their thermal performance. Different factors that affect the performance were studied. Factors considered were orientation, humidity, wind speed, and intensity. [9] studied heat transfer coefficient between absorber and the air stream of an air heater. Effect of various materials like wire mesh, gravels, sand, wood, etc., in the absorbing chamber was studied. [10] studied the need for performance by studying different type of collector having different material, shapes, dimensions, and layouts. Modifications were done to improve the heat transfer coefficient between absorber plate and air using absorbers with fins, matrix type absorbers, etc. [11] studied a hybrid photovoltaic/thermal (PV/T) solar collector, and a simple analytical model was developed based on energy balance equations between PV/T components. Study of various parameters affecting efficiency was carried out. [12] studied various modes of solar drying and classification of solar drying techniques and compared with one another to find the best method. Various types like mixed mode, natural circulation, forced circulation, green house type, and tunnel type of solar dryer were reviewed with design parameters. [13] designed and constructed a forced convection indirect solar dryer for drying moringa leaves. All the parameters were calculated, and conceptual designs were made. Based upon the availability, all the materials were chosen. Plywood was used for the body, black-coated aluminum was used as solar collector, and wire mesh was used for racks. [14] developed a forced convection solar drier and compared it to direct solar drying in terms of quality to help small holders. The collector plate was painted with black paint. Glass wool was used as insulation. Gravels were used to store heat during day time which was then supplied to the flowing air during nighttime. [15, 16] The authors reviewed the integration of PCM with solar thermal that has been very beneficial in terms of reducing energy

consumption by conserving energy in the form of latent heat, decreasing temperature fluctuation by absorbing excess energy, reducing electricity consumption, and shifting the peak loads of cooling energy demands.

2 Material and Methods

2.1 Experimental Setup and Measurements

An experimental setup for the solar air heater was developed. Temperature sensors were used at different points inside the air heater. Marine plywood was selected as the construction material taking into consideration factors like weight, ease of fabrication, and moisture resistance. Channel sections were used to make support for the collector. Acrylic sheet was used as the glazing over the absorber surface. Space between the collector and the glazing was selected taking into consideration the various absorber materials. The absorber base was made of marine plywood coated with black paint. Entire setup was coated with black paint. Collection chamber was attached to the outlet of the absorber chamber as shown in Fig. 2. The collection chamber has a door at the back through which various things for drying can be put. Chimney is provided on the top of the collection chamber to let hot air move out of the chamber which also creates the draft required. Inlet vent for the absorber was made adjustable to control the amount of air entering the absorber. Insulation was provided on the sides and bottom to minimize heat loss.

Different absorber materials compared were the plywood, pebbles, wire mesh, and sand. Resistance-type temperature sensors were placed at different locations:

(1) At the absorber inlet (T1)
(2) Surface of the absorber (T2)
(3) Outlet of the absorber (T3)
(4) Collection chamber (T4)
(5) Outlet of the collection chamber (T5) in Fig. 3.

2.2 Useful Energy

Solar energy available at the earth's surface is called as solar insolation. It is possible to convert this entire energy into useful energy. That is because of the various losses taking place. Also, 100% absorption is not possible. The losses which are considered in this study are convective and radiative losses.

- $T_a = 29\,°C$

Fig. 2 Solar air heater
prototype

- $T_s = 50\,^\circ\text{C}$

- $T_f = 45\,^\circ\text{C}$

- length $= 1\,\text{m}$

- width $= 0.7\,\text{m}$

- Gap $= 0.05\,\text{m}$

- $A_s = 1*0.7 = 0.7\,\text{m}^2$

- $I = 650\,\text{W/m}^2$

Fig. 3 Bed of pebbles as absorber

- $\tau = 0.89$

Properties of air were determined at the average air temperature (i.e., 45 °C).

$$\text{Volume compressiblity} = \frac{1}{T_{\mathrm{f}}}$$

$$\text{Characteristic length} = \frac{A_{\mathrm{s}}}{\text{parameter}}$$

Rayleigh's number,

$$\mathrm{Ra} = \frac{\mathrm{g}*\beta(T_{\mathrm{s}} - T_a)*L_{\mathrm{c}}^3}{\nu^2}*\mathrm{Pr} \tag{1}$$

Nusselt number,

$$\mathrm{Nu} = 0.15*R_{\mathrm{a}}^{1/3} \tag{2}$$

Heat transfer coefficient,

$$h = \frac{k}{L_{\mathrm{c}}}*\mathrm{Nu} \tag{3}$$

Heat transfer by convection,

$$Q_{\text{conv}} = h*A_{\text{s}}*(T_{\text{s}} - T_{\text{a}}) \tag{4}$$

Heat transfer by radiation,

$$Q_{\text{rad}} = \varepsilon * \text{As} * \sigma \left(T_{\text{s}}^4 - T_{\text{u}}^4\right) \tag{5}$$

$$Q_{\text{total}} = Q_{\text{conv}} + Q_{\text{rad}} \tag{6}$$

Solar energy incident,

$$Q = \tau * I * A_{\text{s}} \tag{7}$$

$$Q_{\text{useful}} = Q_{\text{i}} - Q_{\text{t}} \tag{8}$$

Useful energy was coming out to be 45.72 W which will be absorbed by the air flowing over the absorber surface.

3 Result and Discussion

Comparison of surface temperatures of different absorber materials is plotted over a period of time.

Absorber surface temperatures of different absorbing materials were plotted as shown in Fig. 4. It was found that the absorber surface temperature was maximum in the case of pebbles and it attained highest temperature of 85 °C at 12.00 pm. Wood was having lowest absorber surface temperature among all others. We can also see from Fig. 4 that at the start of the experiment, temperature of the pebbles is less which is because of the high specific heat of pebbles. But as time progresses, temperature builds up due to heat absorption by the pebbles. This heat is then transferred to the
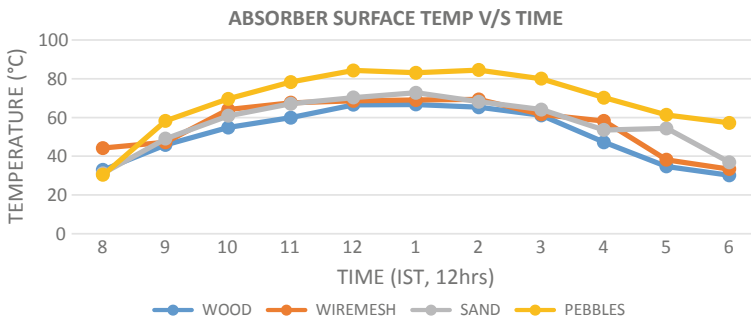
Fig. 4 Variation of surface temperatures of different absorber materials

flowing air. We can also see that pebbles could retain a temperature of 57 °C at the end of the sunshine hours.

A similar plot of variation was obtained for collection chamber temperature for varying sunshine hours as shown in Fig. 5. It was observed that the collection chamber temperature was highest at 2 P.M. and the maximum temperature recorded was 67 °C obtained for wire mesh absorber. Temperatures developed for all the materials were almost same except for wood for which it was less. Temperatures developed by pebbles have lesser variation compared to that of sand and wire mesh.

Figure 6 shows temperatures recorded at various locations inside the solar air heater for different absorber materials at 12 P.M. We can see from the results that the temperatures recorded at every location are more for pebbles compared to other materials at 12 P.M. followed by sand and then wire mesh. Temperature of the air is also more for the pebbles. This is because of the increased surface area in pebble
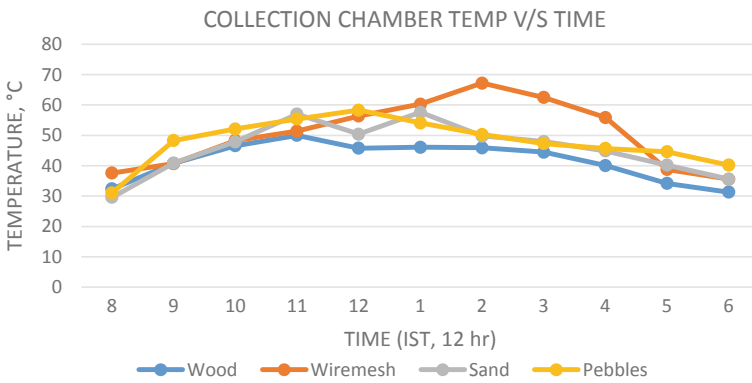
Fig. 5 Variation of collection chamber temperatures for different absorber materials
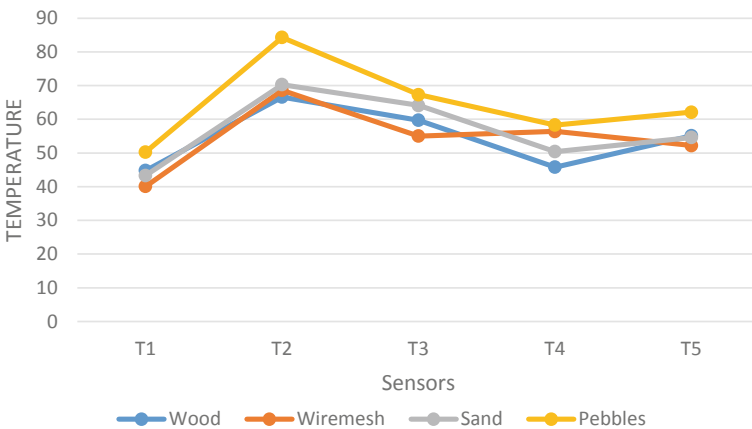
Fig. 6 Temperatures at various locations at 12 P.M. for different absorber materials
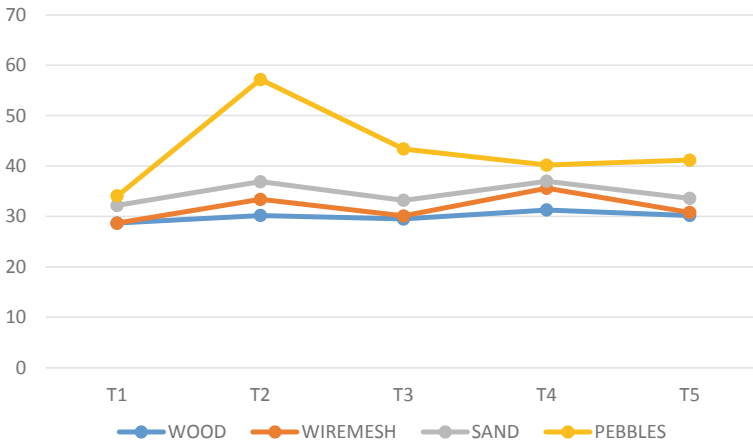
Fig. 7 Temperatures at various locations at 6 P.M. for different absorber materials

bed. Air flows through the interstitial spaces between the pebbles which increases the heat transfer coefficient. Air temperature developed in the case of wire mesh was less compared to that of sand because of the use of only one wire mesh layer. Multiple layers would have increased the heat transfer and the temperature.

Figure 7 shows the temperatures developed in different absorber materials at various locations at 6 P.M. and it can be seen clearly from the graph that the pebbles could retain high temperature of around 57 °C at the absorber surface and the temperature of air in the collection chamber was 40 °C. This is because of the high heat storage capacity of the pebbles. Hence, pebbles can heat up air even after sunshine hours. Sand and wire mesh could also retain temperature of 35 °C in the collection chamber at 6 P.M. But the air temperature will decrease after a while for wire mesh as the heat storage capacity is less. Sand will still continue to heat air for a time longer than that of wire mesh. High heat storage capacity of the pebbles is clearly indicated in Fig. 7 as a high temperature can be seen at the absorber surface, whereas for other materials, it can be seen that the absorber surface temperature is coming in equilibrium with the air temperature developed at 6 P.M.

Collector efficiency is defined as the ratio of useful energy gain by the air to the solar radiation incident on the absorber of the solar collector [17]:

$$\eta_c = \frac{m_a * c_p * (T_3 - T_1)}{I * A_s} \tag{9}$$

From Table 1 we can see that the collector efficiency for pebbles was highest followed by the wire mesh. Wood and sand had almost same collector efficiencies.

Table 1 Collector efficiencies using different materials

S. no.	Material	η_C
1	Wood	31.07%
2	Wiremesh	34.75%
3	Sand	31.90%
4	Pebbles	37.08%

4 Conclusion

Various absorbing materials were studied and analyzed. Form the results obtained, we can clearly see that some materials have better heat storage capacity while some have better specific heat. Pebbles have high specific heat as well as high thermal capacity. Hence, the time taken by the pebbles to gain sufficient temperature was more compared to other materials. However, the temperatures developed were also higher for pebbles and they could retain high temperature for longer time making it suitable in applications after sunshine hours. For single wire mesh, the temperature developed very fast because of the lower specific heat of the stainless steel. Also, the thermal storage was less because of the lesser volume of the metal used. By using sand as absorber, temperatures developed were high and comparable to those obtained using wire mesh. Also, sand could retain temperatures higher than those for wire mesh but lesser than the ones obtained using pebbles. It was observed that some of the sand particles were carried along with the air into the collection chamber making it unsuitable for drying food items. The best absorber material out of the used was then determined based on the collector efficiency, max temperature obtained, and ability to retain higher temperature after the sunshine hours. The various absorbing material will be coated by black paint for higher heat absorption. Since the natural convection mode of heat transfer takes place, the inlet ambient temperature will be kept at room temperature to maximize the drying chamber temperature.

References

1. Shafieian, A., Khiadani, M., Nosrati, A.: A review of latest developments, progress, and applications of heat pipe solar collectors. Renew. Sustain. Energy Rev. **95**, 273–304 (2018)
2. Azad, E.: Theoretical and experimental investigation of heat pipe solar collector. Exp. Therm. Fluid Sci. **32**, 1666–1672 (2008)
3. Azad, E.: Assessment of three types of heat pipe solar collectors. Renew. Sustain. Energy Rev. **16**, 2833–2838 (2012)
4. Zhao, D.L., Li, Y., Dai, Y.J., Wang, R.Z.: Optimal study of a solar air heating system with pebble bed energy storage. Energy Convers. Manag. **52**, 2392–2400 (2011)
5. Singh, P.L., Deshpandey, S.D., Jena, P.C.: Thermal performance of packed bed heat storage system for solar air heaters. Energy Sustain. Dev. **29**, 112–117 (2015)
6. Paul, B., Saini, J.S.: Optimization of bed parameters for packed bed solar energy collection system. Renew. Energy. **29**, 1863–1876 (2004)

7. Lakshmi, D.V.N., Layek, A., Kumar, P.M.: Performance analysis of trapezoidal corrugated solar air heater with sensible heat storage material. Energy Proc. **109**, 463–470 (2017)
8. Koyuncu, T.: Performance of various design of solar air heaters for crop drying applications. Renew. Energy **31**, 1073–1088 (2006)
9. Aldabbagh, L.B.Y., Egelioglu, F., Ilkan, M.: Single and double pass solar air heaters with wire mesh as packing bed. Energy **35**, 3783–3787 (2010)
10. Karsli, S.: Performance analysis of new-design solar air collectors for drying applications. Renew. Energy **32**, 1645–1660 (2007)
11. Tonui, J.K., Tripanagnostopoulos, Y.: Performance improvement of PV/T solar collectors with natural air flow operation. Sol. Energy **82**, 1–12 (2008)
12. Chaudhari, A.D., Salve, S.P.: A review of solar dryer technologies. Int. J. Res. Advent Technol. **2**, 2321–9637 (2014)
13. Amedorme, S.K., Apodi, J., Agbezudor, K.: Design and construction of forced convection indirect solar dryer for drying moringa leaves. Sch. J. Eng. Technol. **1**, 91–97 (2013)
14. Mohanraj, M., Chandrasekar, P.: Drying of copra in a forced convection solar drier. Biosyst. Eng. **99**, 604–607 (2008)
15. Srivastava, M., Sinha, M.K.: Computational analysis of encapsulated phase change materials latent heat thermal energy storage system. J. Eur. Des Syst. Autom. **50**, 227 (2017)
16. Javadi, F.S., Metselaar, H.S.C., Ganesan, P.: Performance improvement of solar thermal systems integrated with phase change materials (PCM), a review. Sol. Energy **206**, 330–352 (2020)
17. Chen, M., He, Y., Zhu, J., Wen, D.: Investigating the collector efficiency of silver nanofluids based direct absorption solar collectors. Appl. Energy **181**, 65–74 (2016)

Bio-diesel Production from Kalonji (*Nigella sativa* L.) Seed Oil Using Microwave Oven-Assisted Transesterification: A Sustainable Approach

Naveen Kumar Garg and Amit Pal

1 Introduction

The uni-alkylic ester of vegetable or animal oils has been bio-diesel. Bio-diesel has very comparable relational parameters to petroleum diesel and often greater cetane number that makes it possible to be utilized straightforwardly as a potential alternative energy source for compression ignition engines without amendments or as a diesel fuel mixing ingredient [1]. Bio-diesel has been a cleaner burning fuel than diesel, which could well be an acceptable substitute [2]. Since it is processed from non-fossil and locally cultivated biomass materials, the requirement for petroleum-based fuels can indeed be brought down and the costs associated with petroleum diesel may be significantly lowered [3]. Bio-diesel has almost no sulfur and therefore provides commitment to mitigate harmful by-products of combustion [4]. Bio-diesel has long-chain fatty acid esters and has been metabolized by plant and vegetable oils, algae [5] of shorter-chain alcohol transesterification process [6]. It is compliant with conventional petroleum diesel and has become a commercial product in Europe even [7].

Kalonji (*Nigella sativa* L.) has been a yearly flowering seed spice of the Ranunculaceae family, native to Southern and Southwestern Asia. Other identities which also include black cumin in English, kalonji in Hindi and Urdu, krishnajirika in Sanskrit, kalajira in Bangali and shonaiz in Persian also correspond to kalonji [8]. It emerges in the Mediterranean countries and has been widely grown in India and Pakistan. The plant was reported to be considerate to salt and could be considered a glycophyte. Kalonji increases to 200–300 mm height, with straight leaves precisely segregated. The plant has bright, light blue, and white-colored flowers as shown in Fig. 1 [9]. The

N. K. Garg (✉) · A. Pal

Department of Mechanical, Production & Industrial and Automobile Engineering, Delhi Technological University, Delhi 110042, India
e-mail: gargnk1973@gmail.com
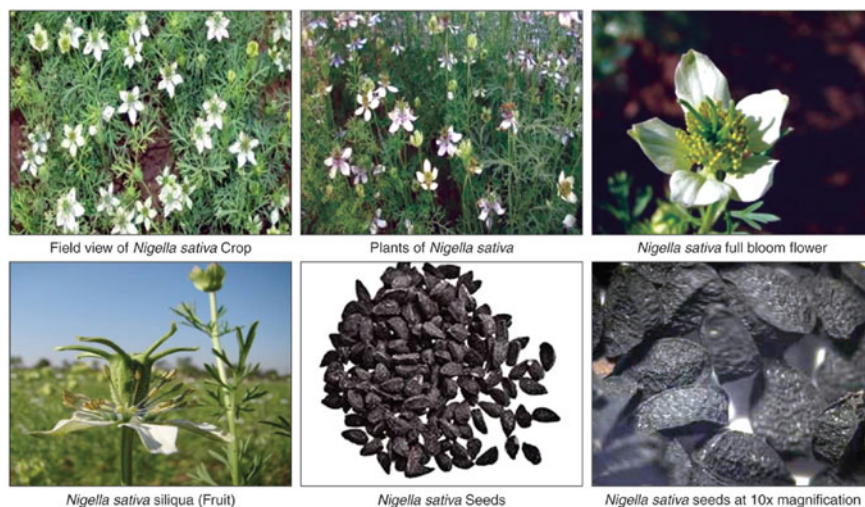
Fig. 1 Plant, flower, fruit, and seeds of kalonji (*Nigella sativa* L.) [9]

fruit of the kalonji plant has been a big and bloated capsule, which contains multiple seeds utilized for spice.

Many homogeneous alkaline, acidic [10], heterogeneous, and enzymatic catalysts have been used to commercially revolutionize plant oil to bio-diesel [11]. Alkali-catalyzed transesterification has been one of the favored pathways due to: (1) the reaction conditions were comparatively benign (moderate temperature and atmospheric conditions), (2) fewer ingredients associated, and (3) fairly low reaction time and expense especially in contrast to some of the other counter-processes involved [12]. That being said, the above approach was only appropriate for oils possessing less than 3 percent FFA ingredients. Larger FFA disrupts the catalyst, which leads to the undesirable evolution of soap, consequently reducing the efficiency percentages [11].

A novel, innovative, and faster method for transesterification of kalonji oil into bio-diesel was used in this study through microwaves assistance via a modified domestic microwave oven and two-step transesterification [13–15].

2   Materials and Methods

2.1   Samples and Chemicals

The kalonji (Nigella sativa) seed oil used for the present work was extracted from the seeds sourced from Delhi's wholesale grain market. After thorough cleaning and removal of foreign ingredients, the seeds were kept in impermeable vessels

Fig. 2 Kalonji seed oi

to sidestep the influence of humidity, and then retained at room temperature before further use. The processing of Kalonji (Nigella sativa) oil into bio-diesel was initiated out utilizing methanol of potency—99%, Sulphuric acid (99% purity) and potassium hydroxide flakes (Fischer chemical, of potency—99.5%).

2.2 Extraction of Oil from Kernels

Soxhlet extraction method has been used for extraction of oil from the seeds. The oil content was extracted using the Soxhlet apparatus by taking 100 g of crushed seeds at 60 °C for 7 h with 500 ml of n-hexane. The fixed oil was collected and concentrated in a revolving evaporator and then placed for 20 min in a vacuum oven at 100 °C, followed by cooling in a desiccator and refrigerated awaiting more exploration (Fig. 2). The yield of crude kalonji oil extract from black seed ranged from 35 to 40%.

2.3 Conversion of Specimen Oil into Bio-diesel

Initially, the FFA of kalonji oil was tested and determined to be 4.7%. Transesterification in two steps was implemented for such feedstocks. 23-L domestic microwave oven, with specifications as power/source—230 V, 50 Hz, power (microwave output)—800 W, 2.45 GHz and power consumption—1250 W has been updated

Fig. 3 Experimental setup and esterification

appropriately for experimental procedures. Throughout the first leap of esterification reaction, the extracted kalonji oil, methanol, and also the sulfuric acid (conc.), as catalyst, were mixed and steadily stirred for 15 min using modified domestic microwave oven under controlled conditions such as 60–65 °C temperature and atmospheric pressure. The mixture was then moved to the separating funnel for 10–15 min to isolate glycerin from the mixture (Fig. 3). The content of FFA has been reduced to 1.7%. With the integration of the KOH as catalyst in a fixed molar ratio of oil and methanol, the kalonji oil was further transesterified, a steady temperature of around 60–65 °C for 5 min. For the transesterification cycle, the oil:methanol was as taken as 9:1 with a catalyst concentration of 1.5 percent w/ w. In addition, the oil has been kept for the separation of methyl ester from glycerol in the separating funnel for about ten minutes. The methyl ester was washed with water and dried up to 110 °C to eliminate water content from the oil before filtering.

Flow diagram for domestic microwave oven enriched bio-diesel production process is shown in Fig. 4.

2.4 Physical and Chemical Properties

Following the laboratory exercise, standard procedures established the methyl ester's physical and chemical properties including the density, refractive index, iodine (Wij's), saponification value, and unsaponifiable matter of specimen.
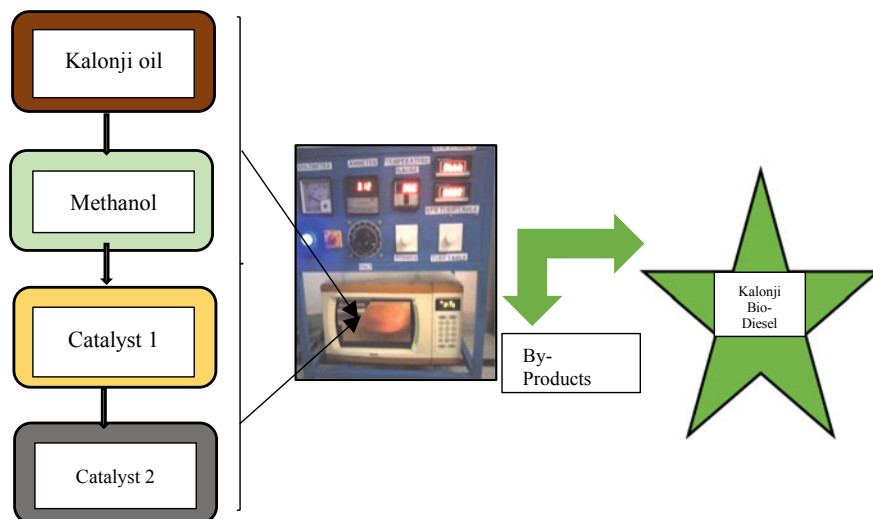
Fig. 4 Flow diagram for domestic microwave oven enriched bio-diesel production process

2.5 Fatty Acid Configuration

For determining the fatty acid profile of the oil, Centurion Scientific Gas Chromatographer (Model-GC 5770), equipped with a flame ionization detector (FID), column BPX-70, length-30 m, inner diameter-0.25 mm, and film thickness 0.25 microns, is being used for the gas chromatography (GC) of kalonji seed oil. The helium gas now for carrier gas feature was being supplied at 1 ml/minute, and the split ratio was maintained at 1:50. Primarily, oven temperature was set at 150 °C, with a holding time of 2 minutes. The temperature in the oven was increased to 240 °C @ 4 °C per minute. At this temperature, the samples had been kept now for 6 minutes. Atomizer and detector temperatures were continued to hold at 260 °C and 280 °C, respectively. The mass spectrometer was executed in the electron impact mode at 70 eV together within scanning range of 50–550 m/z.

Table 1 summarizes the entire experimental investigation, along with the yield of bio-diesel. Therefore, microwave technology has been demonstrated to be an important strategy to process bio-diesel in far less time.

2.6 Statistical Investigation and Estimates

Every statistical investigations were carried of minimum in triplicate and reported as a mean ($n = 2 * 3$).

Table 1 Experimental runs with corresponding yield

Experiment no	Variable 1 methanol: oil molar ratio	Variable 2 catalyst (wt%)	Variable 3 temp. (ºC)	Variable 4 time (minutes)	Yield (%)
1	3	1	63	37	63.585
2	3	1	62	35	62.362
3	3	1	65	35	63.445
4	3	1.5	60	32	66.995
5	3	1.5	59	33	65.568
6	3	1.5	61	32	68.995
7	3	0.75	58	38	64.238
8	3	0.75	60	37	63.951
9	3	0.75	60	39	63.124
10	6	0.75	62	32	81.417
11	6	0.75	65	31	81.138
12	6	0.75	58	30	79.721
13	6	1	59	31	83.562
14	6	1	64	30	83.399
15	6	1	62	31	83.725
16	6	1.5	65	28	87.064
17	6	1.5	60	26	88.531
18	6	1.5	55	29	88.089
19	9	0.75	61	25	90.765
20	9	0.75	60	26	91.231
21	9	0.75	62	23	91.101
22	9	1	61	24	93.475
23	9	1	57	23	92.695
24	9	1	59	25	92.755
25	9	1.5	59	21	96.423
26	9	1.5	62	20	95.425
27	9	1.5	63	19	95.159

3   Result and Discussion

3.1   The Physical and Chemical Properties of the Specimen Oil

The physicochemical properties of the specimen oil have been described, compared with those available in the literature and reported in Table 2. The kalonji seed

Table 2 Comparative analysis of physicochemical characteristics of kalonji oil/specimen

Physicochemical properties	Test method	Present study	Aftab, A. K et al. [16]	Gharby et al. [17]	Wahidu Zzaman, et al. [18]
Color	–	Deep Amber	–	–	Green- Yellow
Acid value (mg KOH/g oil)	D 664	0.35 ± 0.01	–	–	0.41 ± 0.01 (as oleic %)
FFA content (%)	D 664	4.75 ± 0.02	4.69 ± 0.15	2.3 ± 0.5	0.20 ± 0.01 (as oleic %)
Iodine value (Wij's)	EN 4214	127 ± 2	123.4 ± 1.52	126 ± 4	–
Saponification value (mg of KOH//g oil)	ISO385-1:1977	195 ± 3.2	205.21 ± 2.46	–	132.75 ± 10.02
Kinematic viscosity at 40 °C (mm^2/s)	D 445	64.6	–	–	–
Relative density at 25 °C (g/cm^3)	D 1298	0.9167 ± 0.07	0.9158 ± 0.02	–	0.93 ± 0.04
Refractive index	–	1.425 ± 0.003	1.465 ± 0.05	1.473 ± 0.002	–
Unsaponifiable matter (%)	–	–	0.33 ± 0.01	–	–

contained 35.62% oil content in it and has been extracted using the Soxhlet apparatus.The average relative density of the extracted virgin kalonji oil recorded to be 0.9167 g/cm3, measured at 25 °C. No substantial difference in relative density was observed among the various specimen oil samples. The relatively higher density would then be an outward sign of greater molecular weight and unsaturation. When the density of an oil raises, thereby an increment in molecular weight and un-saturation of the oil has been reported.

The average values of refractive index for the oil were measured with the refractometer and found to be at par with the values available in the previous studies. The iodine valuation typically explains the level to which a fat or oil is unsaturated. The volume of gram of iodine which is ingested by 100 g of fat has been called the oil's iodine value. These very measures explain the high degree of unsaturation and thus a greater vulnerability to oxidative rancidity. Maximum iodine value identified through this study's test oil was 127 which appeared to be significantly higher than the previous studies.

One of the essential factors for determining the suitability of the oil to process for the transesterification has been the FFA content imbedded in the oil. In this work, the levels of free fatty acids were measured by titrimetric method. The average recorded value for the present study was 4.7%. The FFA amount leads to a higher level of oil hydrolysis. Unsaponifiable content involves some such compounds that are often soluble in fats and oils that have not been saponifiable by caustic alkali but get dissolved in ordinary fat solvents like hydrocarbons.

3.2   GC–MS Analysis of the Specimen Oil

The peak assessment of the fatty acids in the investigated samples was done by comparing the mass spectra. Concentration of saturated and unsaturated fatty acid average proportion present in the specimen kalonji oil samples was reported in Table 3. All of the studied samples of kalonji oil included seven saturated fatty acids and five unsaturated fatty acids, including mysteric, pentadecanoic, palmitic, margaric, stearic, arachidic and behenic and palmitoleic (C16:1), oleic (C18:1), linoleic (C18:2), eicosenoic, (C20:1) and eicosadienoic (C20:2). Also, one unknown peak was observed ($\times$1). Saturated fatty acids including carbon chains of (C12:0–C16:0) carbon atoms were observed to be atherogenic, stearic acid was observed to have unbiased impacts, whereas oleic and polyunsaturated fatty acids deliver a significant decrease in the blood lipids.

Among all the saturated acids, palmitic (C16:0) observed to be influential, whereas unsaturated fatty acids including mono-unsaturated and polyunsaturated fatty acids (PUFA) linoleic (C18:2) and oleic (C18:1) fatty acids were measured to be 28.94 and 37.01%, respectively.

Regulating the levels of LDL cholesterol has been reported because of the oleic acid, whereas PUFA has favorable impacts on both decent health and terminal illnesses, such as control of lipids.

Table 3 Average proportion of saturated and unsaturated fatty acids in kalonji oil specimen

Parameter	Present study	Aftab, A. K et al. [16]	Mohammed Yahya Hadi et al.[19]	Gharby et al. [17]
C14:0 (Myristic)	3.30	0.12 ± 0.004	0.312	0.2 ± 0.1
C15:0 (Pentadecanoic)	0.55	–	–	
C16:0 (Palmitic)	20.59	12.68 ± 0.5	13.775	11.9 ± 0.1
C16:1(Palmitoleic)	0.52	0.12 ± 0.005	1.651	0.2 ± 0.1
C17:0 (Margaric)	0.13	–	–	–
C18:0 (Stearic)	6.23	3.99 ± 0.15	1.817	3.2 ± 0.1
C18:1(Oleic)	28.94	28.55 ± 0	18.643	24.9 ± 0.5
C18:2(Linoleic)	37.01	51.80 ± 1.45	18.061	56.5 ± 0.7
C20:0 (Arachidic)	0.35	0.21 ± 0.003	20.43	0.2 ± 0.1
C20:1(Eicosenoic)	0.53	0.48 ± 0.01	0.69	–
C20:2 (Eicosadienoic)	1.84	2.05 ± 0.05	3.085	–
C22:0 (Behenic)	–	–	21.536	–
X1	1.85	–	–	–

Table 4 Values of different physicochemical properties of kalonji bio-diesel

Parameter	Standard	Sample	Sample2	Sample3	Sample4	Test equipment
Saturated fatty acid (%)	EN 14103	30.15	32.6	30.43	33.12	
Polyunsaturated fatty acid (%)	EN 14103	38.85	37.23	38.45	30.2	
Saponification value (mg of KOH//g oil)	ISO 1385–1:1977	204.268	205.586	200.942	190.736	
Iodine value (Wij's)	ISO 1385–1:1977	100.156	95.168	96.375	81.535	
Cold filter plugging point (°C)	D6371	0.878	5.267	5.367	2.524	Automatic NTL 450 (Normalab, France)
Cloud point (°C)	IS: 1448 [P: 10]: 1970	5.838	6.349	4.229	5.938	
Pour point (°C)	IS: 1448 [P: 10]: 1970	−0.483	0.071	−2.23	−0.375	
Oxidation stability (hr)	EN 14112	5.777	5.758	5.658	6.495	873 Rancimat (Metrohm, Switzerland)
Calorific value (CV)	D240	39.408	39.669	38.874	36.658	Parr 6100 calorimeter (IKA, UK)
Viscosity (mm²/s)	D445	3.721	3.797	3.695	3.445	SVM 3000
Density (g/ml)	1298	0.877	0.882	0.864	0.814	SVM3000

3.3 Characterization of Kalonji Bio-diesel

Different properties of the bio-diesel obtained from specimen oils were measured and presented in Table 4.

3.4 Effects of High Saturated Fatty Acid Content in Kalonji Bio-diesel

Sample 4 exhibited the maximum saturated fatty acid content among all the samples. Bio-diesel derived from oil seeds with a large concentration of saturated fatty acids does seem to have a strong oxidation stability and a greater heating value but its cold flow properties are weaker than many bio-diesels due to the fatty acids being

solidified at elevated degrees. The greater proportion of such acids enhances the freezing temp. and exhibits high CFPP and CP, leading to the solidification of the biofuel, providing the potential for its use in hotter climate territories [20].

3.5 Effects of High Unsaturated Fatty Acid Content in Kalonji Bio-diesel

The amount of unsaturated fatty acid content in the present study reported to be 38.85%, 37.23, 38.45, and 30.2%, respectively. The sample 1 contained the highest amount of polyunsaturated fatty acid content in it. Earlier studies revealed that the bio-diesel with most unsaturated fatty acids release more NOx, and showed lower thermal performance compared to more saturated acids in bio-diesel [6]. There were no major variations in emissions of HC and smoke among the bio-diesel fuels observed [5].

3.6 Measurement of Acid Number in Kalonji Bio-diesel

The titration method was employed to determine the bio-diesel's acid number. 0.1–0.5 ml of bio-diesel was placed in a beaker. Added and thoroughly mixed with 50 ml solvent mixture (95% ethanol and diethyl ether in equal proportion). Using 1% phenolphthalein indicator, this solvent–oil mixture has been titrated with 0.1 M KOH.

3.7 Calorific Value in Kalonji Bio-diesel

The calorific value of the kalonji bio-diesel was measured using a bomb calorimeter (Parr 6100). Bio-diesel (0.5 g) was placed in a vessel in the bomb, and a thread of length 80 mm of cotton hanging from 80 mm nichrome wire was dipped into the bio-diesel specimen. At 400 psi, the bomb was filled up with oxygen. Then, the insulated vessel containing distilled water was positioned within. The fuse wires had been put at the bomb in their location. The nichrome wire fastened to two sticks connected to the wires of the fuse. To make a short circuit on the nichrome string, the fire button was pressed and the bio-diesel ignited.

3.8 Cold Filter Plugging Point and Cloud Point

The CFPP has been attributed to the lowest temperature under which a given volume of pure bio-diesel will still transfer within 1 minute across a criterion—referenced filtration system.

3.9 Effect of Microwave Power

Increasing trend in microwave power and methanol: Oil ratio helped in reduction of the free fatty acid content toward a critical threshold below which it fell. The alcohol may also be evaporated by intense microwave power resulting in inadequate esterification. Mostly as the overall power of the microwave rises, the temperature as well rises the speed of the reaction; even so, the time slot and the reversible rate also enhance as a consequence, thereby actually reducing the yield. Sufficient methanol: Oil volume fraction would consume microwave heating leading to a reduction triggering energy due to dipolar amplification rises. Greater strength of microwaves applied over a lengthy span of time also results in yield loss and quicker reversible reaction progression.

4 Conclusion

A two-step facilitated sulfuric acid–alkali-aided microwave transesterification was performed to obtain a low-cost bio-diesel from kalonji (Nigella sativa L.) oil. The very first step with acid-catalyzed esterification had been performed to minimize the level of free fatty acid content, thus mitigating catalyst inhibition, soap formulation which contributes directly to lower the processing cost. It obtained the lowest free fatty acid amount under the arrangement of oil: methanol molar ratio of 9:1, microwave power of 500 W.

1. Using microwave heating, the best possible bio-diesel changeover from kalonji (Nigella sativa L.) seed oil was accomplished with a yield of 95.47% using 1.5 (%w/w) and methanol: oil ratio of 9:1, 500 W, 30 rpm, and reaction time of 20 minutes.
2. The physicochemical properties of the bio-diesel were also comparable to the different standards.
3. Though many bio-diesel production techniques need longer reaction time, besides being energy-intensive and cost-intensive.
4. Bio-diesel produced had significant amount of fatty acid methyl esters indicating its suitability as engine fuel.
5. Microwave irradiation has become a preferable technique because it encourages lesser response time and a significant decline in the quantity of residue-products

and higher output yields, at the same time, microwave assistance may not be easy to deploy from small-scale laboratory production to mass sector, and security may be another downside of using this methodology.

Finally, it can conclude that kalonji oil can be exploited as an alternative feedstock for biodiesel production with two-step acid-alkali based microwave-supported transesterification.

References

1. Agarwal, A.K.: Biofuels (alcohols and biodiesel) applications as fuels for internal combustion engines. Progr. Energy Combustustion Sci. **33**(3), 233–271 (2007)
2. Mofijur, M., Rasul, M.G., Hyde, J., Bhuyia, M.M.K.: Role of biofuels on IC engines emission reduction. Energy Proc. **75**, 886–892 (2015)
3. Demirbas, A., Bafail, A., Ahmad, W., Sheikh, M.: Biodiesel production from non-edible plant oils. Energy Exploration Exploitation **34**(2), 290–318 (2016)
4. Gupta, J.G., Agarwal, A.K.: Unregulated and regulated emissions from biodiesel fuelled CRDI SUV engine. SAE Tech. Pap. 2015-April, 1–13, (2015)
5. Karmakar, R., Kundu, K., Rajor, A.: Fuel properties and emission characteristics of biodiesel produced from unused algae grown in India. Petroleum Sci. **15**(2), 385–395 (2018)
6. Yadav, A. K., Khan, M.E., Pal, A., Dubey, A.M.: Experimental investigations of performance and emissions characteristics of Kusum (Schleichera Oleosa) biodiesel in a multi-cylinder transportation diesel engine. Waste Biomass Valorization **8**(4), 1331–1341(2017)
7. Kim, D., Seol, S.K., Chang, W.S.: Energy efficiency of a scaled-up microwave-assisted transesterification for biodiesel production. Korean J. Chem. Eng. **33**(2), 527–531 (2016)
8. Liu, X., Abd El-Aty, A.M., Shim, J.-H.: Various extraction and analytical techniques for isolation and identification of secondary metabolites from *Nigella sativa* Seeds. Mini-Rev. Medicinal Chem. **11**(11), 947–955 (2011)
9. Dubey, P.N., Singh, B., Mishra, B.K., Kant, K., Solanki, R.K.: Nigella (*Nigella sativa*): a high value seed spice with immense medicinal potential. Indian J. Agric. Sci. **86**(8), 967–979 (2016)
10. Yunus Khan, T.M., Badruddin, I.A., Ankalgi, R.F., Badarudin, A., Hungund, B.S., Ankalgi, F.R.: Biodiesel production by direct transesterification process via sequential use of acid–base catalysis. Arab. J. Sci. Eng. **43**(11), 5929–5936 (2018)
11. Thoai, D.N., Tongurai, C., Prasertsit, K., Kumar, A.: Review on biodiesel production by two-step catalytic conversion. Biocatalysis Agric. Biotechnol. **18** (Feb.) 1–23 (2019)
12. Singh, A., Gaurav,K.: Advancement in catalysts for transesterification in the production of biodiesel: a review. J. Biochem. Technol. **7**(3), 1148–1158 (2018)
13. Sharma, A., Kodgire, P., Kachhwaha, S.S.: Biodiesel production from waste cotton-seed cooking oil using microwave-assisted transesterification: optimization and kinetic modeling. Renew. Sustain. Energy Rev. **116**(Aug) 1–17 (2019)
14. Kumar Garg, N., Pal, A.: An experimental study & analysis of effects of different parameters of microwave in production of bio-diesel. Proc. Inst. Mech. Eng. Part E J. Process Mech. Eng. **234**(4), 394–401 (2020)
15. Supraja, K.V., Behera, B., Paramasivan, B.: Optimization of process variables on two-step microwave-assisted transesterification of waste cooking oil. Environ. Sci. Pollution Res. June 2019, 1–12 (2019)
16. Aftab, A.K., Mahesar, S.A., Khaskheli, A.R., Sherazi, S.T.H., Sofia, Q., Zakia, K.: Gas chromatographic coupled mass spectroscopic study of fatty acids composition of Nigella sativa L. (KALONJI) oil commercially available in Pakistan. Int. Food Res. J. **21**(4), 1533–1537 (2014)
17. Gharby, S., et al.: Chemical investigation of *Nigella sativa* L. seed oil produced in Morocco. J. Saudi Soc. Agric. Sci. **14**(2), 172–177 (2015)

18. Zzaman, W., Silvia, D., Nadiah, W., Abdullah, W., Yang, T.A.: Physicochemical and quality characteristics of cold and hot press of *Nigella sativa* L seed oil using screw press. J. Appl. Sci. Res. **10**(12), 36–45 (2014)
19. Hadi, M.Y., Mohammed, G.J., Hameed, I.H.: Analysis of bioactive chemical compounds of *Nigella sativa* using gas chromatography-mass spectrometry. J. Pharmacognosy Phytotherapy **8**(2), 8–24 (2016)
20. Knothe, G.: Dependence of biodiesel fuel properties on the structure of fatty acid alkyl esters. Fuel Process. Technol. **86**(10), 1059–1070 (2005)

Experimental Investigation of Performance and Emission Characteristics of a Common Rail Diesel Engine (CRDe) Fueled with Cottonseed Bio-diesel and Diesel Blends

Naveen Kumar Garg and **Amit Pal**

Abbreviation

Abbreviation	Description
CRDe	Common rail diesel engine
Bte	Brake thermal efficiency
Bsfc	Brake-specific fuel consumption
Bp	Brake power
UBHC	Unburnt hydrocarbons
NO_X	Oxides of nitrogen
rpm	Revolutions per minute
B10	Blend with 10% bio-diesel and 90% petro-diesel
B20	Blend with 20% bio-diesel and 80% petro-diesel
B30	Blend with 30% bio-diesel and 70% petro-diesel
B100	100% Bio-diesel
PM	Particulate matter
16V	16 Valve
SOHC	Single overhead cam
N-m	Newton meter
WC	Water column
lph	Liter per hour
Cst	Centistoke
TCI	Turbocharged intercooled
NEF	New engine family

N. K. Garg (✉) · A. Pal
Department of Mechanical, Production & Industrial and Automobile Engineering, Delhi Technological University, Delhi 110042, India
e-mail: gargnk1973@gmail.com

1   Introduction

In the early days of its creation, plant oils were assumed to be a potential source of energy for stationary diesel-fueled engines and vehicles. Rudolf Diesel ran his first diesel engine on peanut oil in 1893 [1]. Initial results regarding the use of plants and vegetable oils in diesel engines were not very motivating because of different problems such as engine fouling, oil worsening, and flow resistance. It has been ended up finding that these plant oils can be converted through transesterification into a product somewhat more appropriate when compared to petro-diesel fuel. In a transesterification reaction, these plant and vegetable oils react with an alcohol to produce an ester and glycerin. The esters formulated through the transesterification process possess characteristics that make it acceptable to be used in diesel engines. During the reaction, the bio-diesel is being produced through chemical reaction in which the plant oil reacts with an alcohol in the appearance of a catalyst that can be an acid or alkali generally, an alkali. The product formed has become a synthesis of methylesters and glycerol. The by-product of the reaction is found to be glycerol [2]. Bio-diesel could be used in its pure form, and is widely recognized as B100. The pure bio-diesel can however be blended with conventional diesel. The blend thus formed is termed BXX, in which XX symbolizes the proportion of bio-diesel in it. The commonly accepted approach has always been the B5, B10, B20…. and B100. B100 is regarded as pure bio-diesel where as B5 represents 5% bio-diesel blended with 95% conventional petro-diesel and likewise other blends have their significance. The transesterification of the ingredients effectively enhances the different characteristics related to its cold-weather stability, viscosity, and thermal steadiness. Thus transesterified plant and/or seed oils seem to be more suitable to be used as alternative fuels for diesel engines than pure vegetable oils [3].

Power generation and transportation sectors are primarily dominated by diesel-fueled engines and are gaining popularity because of their higher thermal efficiency, as compared to gasoline or petrol-fueled engines [4]. The other advantages are higher energy density, more torque, and the susceptibility toward becoming propelled by a range of fuels, including those from renewable sources. Intensive utilization of diesel-fueled engines, aimed at meeting increasingly complex and stringent emission requirements, was observed in recent years. The development of innovative injection control technology and post-treatment exhausts resulted in a significant reduction in exhaust emissions [5].

Ever since bio-diesel has been used as an optional propellant for diesel-fueled engines, the performance and emission character traits such as Bte, Bsfc, and Bp however are retained whereas elements like UBHCs, CO, and PM are substantially reduced. Low concentration of NO_x was thus reported [6].

While data on the impact of bio-diesel on performance and emissions including unburnt hydrocarbons, carbon monoxide, nitrogen oxides, and particulates are available, most of this data have been produced on engines using typical diesel engines with mechanical fuel injection pump, governor, and mechanical atomizer [7]. Very limited experiments have been conducted on the latest technology engines to date using bio-diesel as fuel [6, 8–12]. Therefore, in this experimental investigation of performance and emission characteristics of a BS-IV CRDe fueled with petro-diesel and different blends of cottonseed bio-diesel with it is being conducted. In recent years, the downside of using bio-diesel or biofuels in general has been strengthened. Thus, the cottonseed bio-diesel used in this study is obtained through the process of microwave transesterification [13].

1.1 Research Objective

The combined effects of different mixture proportions, engine rpm, and load have been used as process parameters in this specific activity. An overview of the literature suggested that the synthesis of microwave tranesterified cottonseed bio-diesel with the mineral-diesel and being used as a substitution fuel for a CRDe has not been very significant.

2 Materials and Methods

2.1 Experimental Setup

The engine tests have been carried out on a diesel-fueled engine of the BS-IV, CRDe technology. The fundamental configurations and features of the engine used during the experimental work are described in Table 1.

Research engine was connected with a dynamometer to regulate the load and rpm of the engine. Table 2 describes the fundamental configurations and features for the dynamometer being used.

The experimental setup found to be competent of syncing and evaluation of flow of air and fuel beside the temperature and the load. The system possesses a panel box comprised of air-box, dual fuel test fuel tanks, manometer, units for measurement of fuel and air, process signifier and indicator for engine. Rotameters were made available for calculating the flow of water from the cooling and calorimeter. The experimental setup facilitates measurement of brake power, mean effective pressures (brake and indicated), thermal efficiencies (brake and indicated), efficiency (mechanical, volumetric), Bsfc, air-to-fuel ratio (A/F) beside heat equilibrium sheet.

The arrangement mainly comprises of stator and onto that stator, handful of electromagnets and a rotating disc have been fitted and the disc is paired with engine's

Table 1 Fundamental configurations of the engine used

Engine description	Specifications
Type	2.5-L, 105 bp, 16 V, NEF, TCI-CRDe engine
Fuel type	Diesel
Engine type	NEF TCI-CRDe engine
No. of cylinders, cylinder arrangement	4, Inline
Turbocharger	Turbocharger with intercooler
Cylinder head (configuration)	SOHC
Max power	105 bhp @ 3800 RPM
Max torque	247 N-m @ 1800 RPM
Fuel injection system	Common rail
Bore × stroke	94 × 90 mm
Compression ratio	17.8:1

Table 2 Fundamental configurations of the dynamometer

Description	Specifications
Type	Eddy current, water cooled, with loading unit
Piezo sensor	Limit up to- 5000 psi, with little noise cable
Sensor (crank angle)	Resol.- 1°, 5000 rpm with TDC pulse
Data acquisition device	NI USB-6210, 16-bit, 250 kS/s
Temperature sensor	PT100 and thermocouple, Type K
Load indicator	Digital, 0–50 kg, supply 230 V AC
Load sensor	Load cell, strain gauge type, 0–50 kg
Fuel flow transmitter	DP transmitter, 0–500 mm WC
Airflow transmitter	Pressure transmitter, (−) 250 mm WC
Software	"Enginesoft"
Rotameter	Coolant flow For engine (minimum 40 lph, maximum—400 lph) For calorimeter (minimum 25 lph, maximum—250 lph)

throughput shaft. Due to magnetic flux laid down by the route of field strength in the electromagnets, eddy currents have been produced in the stator then when rotor starts turning. Such eddy currents impede the motion of the rotor and hence the engine is loaded. After generating heat, these eddy currents were mostly drained away, so that this type of dynamometer demands arrangement for cooling of the system. The torque was being determined by rotation of knob. The load has been controlled by the management of the current in electromagnets. Figure 1 displays schematics of the experimental setup. Studies were conducted out on the CRDe engine fueled with mineral diesel and various cottonseed bio-diesel blends with it. Using a direct exhaust gas emission analyzer, various output and emission parameters were analyzed.
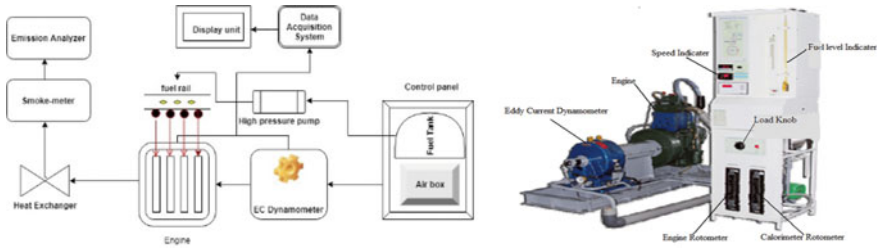
Fig. 1 Schematic and actual CRDe diesel engine test setup

Table 3 Measurement ranges of AVL gas analyzer

Element to be measured	Range	Resolution
CO	0–10% vol	0.01% vol
CO_2	0–20% vol	0.1% vol
HC	0–20,000 ppm vol	1 ppm
NO_X	0–5000 ppm vol	1 ppm
O_2	0–25% vol	0.01% vol

AVL gas analyzer is being used to measure the amount of CO, HC, CO_2, NO_x, and O_2. AVL gas analyzer is a non-dispersive infrared type analyzer. The carbon monoxide, unburnt hydrocarbons, and carbon dioxide measurements were measured by the principle of infrared measurement and the oxygen and oxides of nitrogen were measured using the electrochemical measurement principle. The measurement ranges of the gas analyzer are given in Table 3.

Managed to start the experimental test rig and maintained the engine for 4–5 minutes at no-load operating condition before the operating temperature has been attained. The throttle incrementally increased to full open position, while sustaining engine pace at 3800 RPM. Waited for a little while and allowed the engine to become stable. The reading was recorded as provided for in the observations. Gradually increased the load in steps to decrease the speed, and repeated the observations. The fuel was switched from petro-diesel to bio-diesel blends, and three consecutive readings were taken at selected RPM after interval of every 5 min. The data for each series of time were compared with the observation of the petro-diesel, and the discrepancy in the output parameters was taken as average variation. The same procedural sequence was followed with different speed ranges and different bio-diesel blends and observation tables were prepared.

3   Result and Discussion

Measured physical characteristics of investigated fuels, to be exact petro-diesel, B100, B10, B20, and B30 were tabulated in Table 4.

Investigations were performed out on a four-cylinder CRDe engine that used petro-diesel and cottonseed bio-diesel and its combinations as an alternative energy source to examine the engine's performance and emissions characteristics [14] at the speeds of 1500, 2500, and 3500 RPM under different engine loads. The findings were examined as:

3.1   Brake Power

The braking power observed to be higher for all B10 blend as compared with other formulations of the test fuel, i.e., B20, B30, at all speeds. The explanation for this performance noticed to be the various entities of the blended B10 like viscosity, cetane number, and heating value has been comparable to those of petro-diesel. It was identified that the brake power was reduced by 1.63%, 3.56%, and 3.53% for B10, B20, and B30 formulations. It was also inferred that because bio-diesel has a heating value lower than the petro-diesel, it was also likely because of adequate oxygen in the fuel, but at the same time the bio-diesel had a greater specific gravity than petro-diesel. The cumulative effect, thus, found to be around 5% lower fuel energy per unit volume due to a lack of bio-diesel heating value.

3.2   Brake-Specific Fuel Consumption

Compared to petro-diesel, an increase in Bsfc of B10, B20, and B30 blends was found to be around 5.79%, 6.82%, and 7.29% respectively (Fig. 2). It can be concluded from the increase that the B30 blend own the maximum specific fuel consumption value out of the three blends and munches extra amount of energy per kW of power than the petro-diesel. The larger Bsfc with the blends having more bio-diesel in it came to

Table 4 Measured physical properties of test fuels

Fuel	Viscosity (Cst)	Density (g/cm^3)	LCV (MJ/kg)	Cetane number
B0 [13]	2.70	0.827	42.53	51.3
B100 [13]	4.71	0.883	39.49	50.9
B10	2.92	0.832	42.30	–
B20	3.35	0.841	41.53	–
B30	3.51	0.853	41.23	–
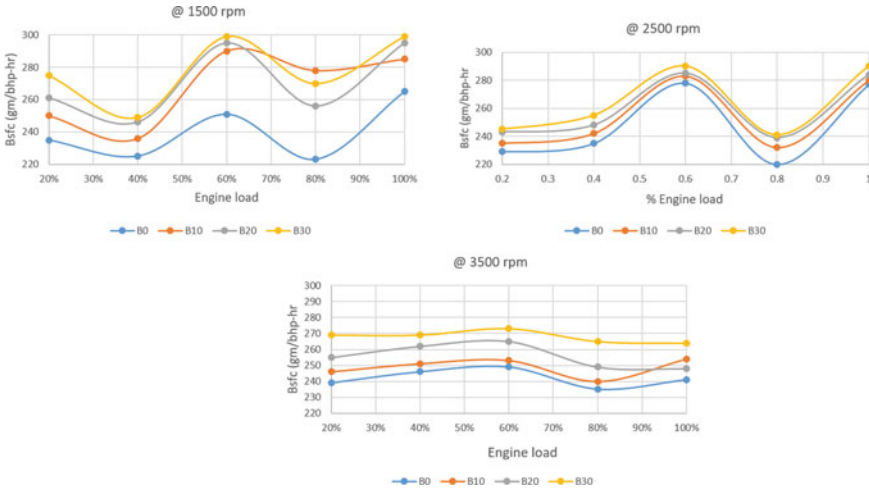
Fig. 2 Bsfc Vs % engine load at different engine speed

the conclusion, because the bio-diesel has lesser energy content in it as compared to the petro-diesel. It has been observed that at 80% of the total load the brake-specific fuel consumption found to be the least.

3.3 Brake Thermal Efficiency

For most of the speed ranges, B20 blend showed maximum increment in brake thermal efficiency than others, that can be delegated to the better combustion because of higher amount of oxygen content in the blend and additional lubricity provided by the bio-diesel.

Further it was concluded from the graph (Fig. 3) that at higher injection pressure, efficient injection timing control by the engine control module, higher speeds the B_{the} increased for all blended fuels. Higher injection pressure, consequent engine injection timing retardation, homogeneity in air–fuel mixture formation and spray pattern improved the combustion process. On the basis of tests, it has been identified that the engine output in terms of brake thermal efficiency with bio-diesel blends had been comparable with petro-diesel. The increment in the B_{the} of B20 blend is matched to petro-diesel found to be around 0.25% however for B10 and B30 it was decreased by 1.0% and 0.4%, respectively.
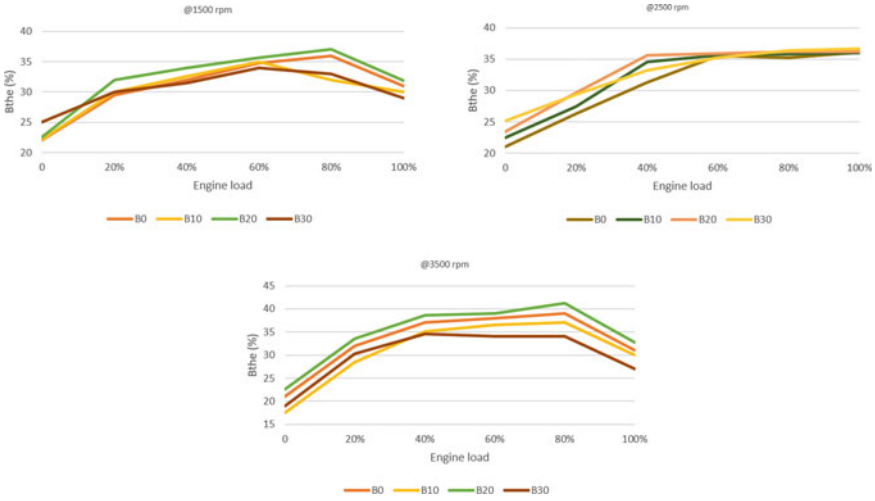
Fig. 3 B_{the} Vs % engine load at different engine speed

3.4 Carbon Monoxide

From the findings (Fig. 4) it has been shown that in the event of B20 combination of the test fuel at 2500 RPM the decrease in the percentage of carbon monoxide was maximum. The explanation behind such behavior that the CO formed during
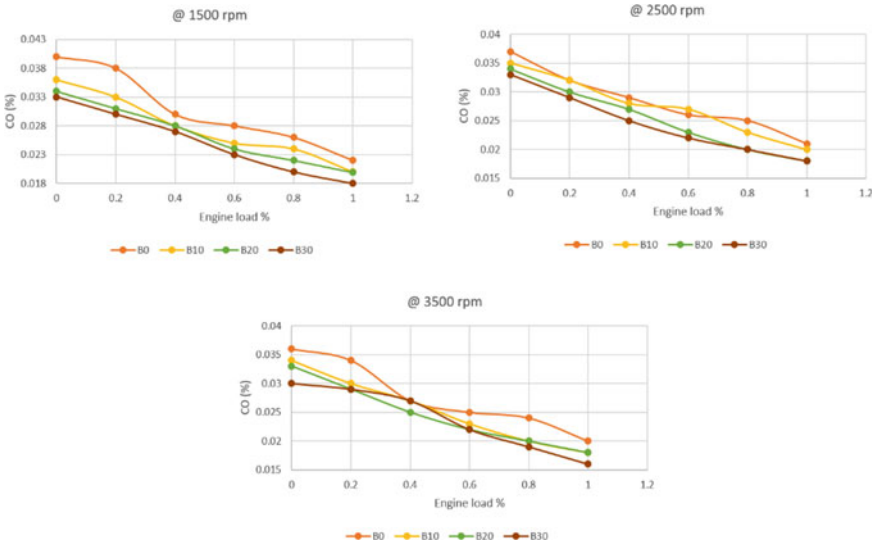
Fig. 4 CO Vs % engine load at different engine speed

bio-diesel combustion has sometimes transformed to CO_2 by captivating the extra molecules of oxygen present in the blended fuel. Nevertheless, it began to change at 2500 RPM, which will further be attributed to the enlarged fuel–air ratio at greater loads as greater volumes of oil were inoculated into the incineration compartment, resulting in lower A/F ratio. The CO percentage of B10, B20, and B30 blends was decreased by about 28.61%, 38.72%, and 54.18% relative to petro-diesel.

3.5 Unburnt Hydrocarbons

A specimen of flue gases coming out of the diesel engine can indeed be free of unburnt fuel particles yet at the same time having its large concentration due to the type of engine.

Figure 5 represents the emission of UBHC for both the mineral-diesel and blended diesel fuel. At 3500 RPM, the B20 blend recorded the least UBHC emission, followed by the B10 blend and petro-diesel. The reduction in UBHC was found chiefly as established by combustion characteristics of the B20 blend of test fuel within the combustion period. UBHC with B10, B20, and B30 compared to petro-diesel found to be reduced.
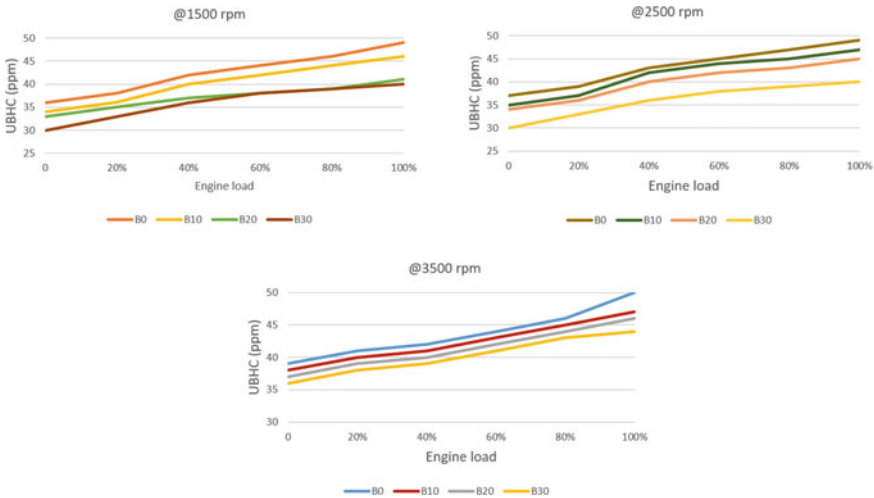
Fig. 5 UBHC Vs % engine load at different engine speed

3.6 Oxides of Nitrogen

Sustained high temperatures and nitrogen abundance in air reported to be primary factors behind the production of oxides of nitrogen [1]. The effect of bio-diesel blends with mineral-diesel on NOx emission has been seen in the graph (Fig. 6).

At the cylinder's extraordinary high combustion temperature, the hydrocarbon's long chain splits into shorter one, involves larger energy in the differentiated form, and promotes the formation of NO_x. In fact, by retarding the timing of the fuel injection, the issue of increased NO_x emissions had been effectively tackled in conventional diesel engines. The boost in NO_x emissions in B10, B20, and B30 blends to nearly 11.45%, 10.5%, and 14.54%, respectively, compared with petro-diesel.
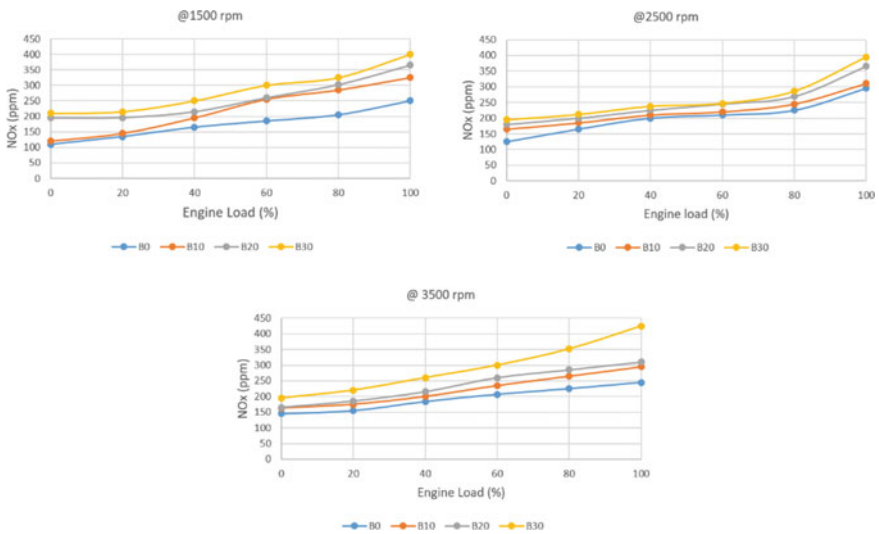
Fig. 6 NO_x Vs % engine load at different engine speed
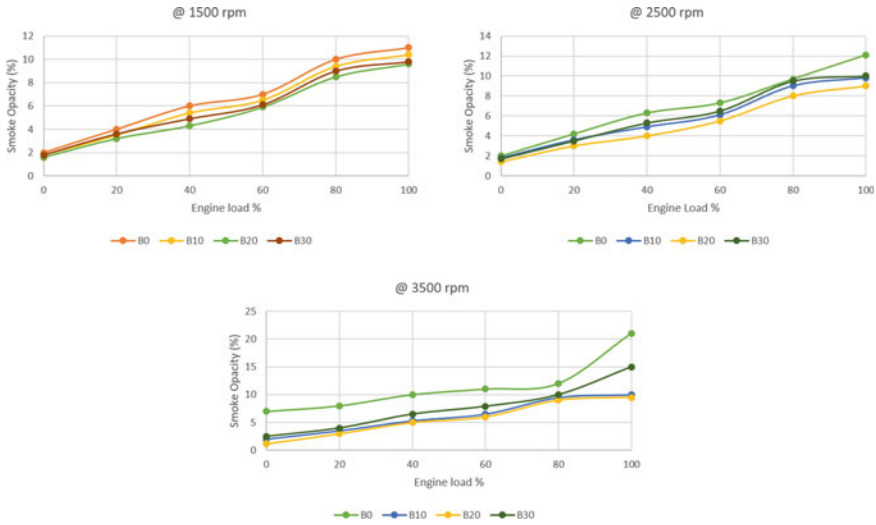
Fig. 7 Smoke opacity VS % engine load at different engine speed

3.7 Smoke Opacity

Smoke opacity can be defined as a direct measure of smoke and soot [15]. It was observed from Fig. 6 that bio-diesel and its blends with petro-diesel produced lesser smoke than the petro-diesel. It may be because of the fundamental structural distinction like lack of sulfur concentration and appearance of oxygen in the blended fuel molecule. The oxygen content helped in its complete burning. It can also be perceived that with all fuel sources examined, smoke intensities amplified abruptly above 2500 RPM (Fig. 7).

It had been owing to the diminished A/F proportion during high load conditions when more amount of energy is being supplied through fuel into the chamber of combustion, much of it goes unburnt into the exhaust.

4 Conclusions

Following conclusions can be taken on the basis of the findings obtained:

1. The calorific value of the different blends decreased with the rise in the amount of bio-diesel. It was identified that the brake power was reduced by 1.63%, 3.56%, and 3.53% for B10, B20, and B30 formulations.
2. Compared to petro-diesel, an increase in specific consumption of B10, B20, and B30 blends was found to be around 5.79%, 6.82%, and 7.29% in order.

3. The greatly improved injection pressure, an effective engine timing delay, efficient spray pattern, and homogeneity during development of air–fuel mixture have improved the mechanism of combustion with increased B_{the}.
4. The amount of CO with B10, B20, and B30 blends as compared to petro-diesel was reduced by around 28.61%, 38.72%, and 54.18%, respectively.
5. The unburnt hydrocarbons with blended test fuels were found to be substantially reduced relative to petro-diesel.
6. With the rising engine load, nitrogen oxides were found to increase and were observed to be minimum for B20 test blend at lower speed ranges.
7. Test fuel blend (B20) has shown promising blend for several harmful emissions to offer optimum performance.

References

1. Agarwal, A.K.: Biofuels (alcohols and biodiesel) applications as fuels for internal combustion engines. Progr. Energy Combustustion Sci. **33**(3), 233–271 (2007)
2. Marchetti, J.M.Ã., Miguel, V.U., Errazu, A.F.: Possible methods for biodiesel production. Renew. Sustain. Energy Rev. **11**, 1300–1311 (2007)
3. Pal, A., Kachhwaha, S.S., Maji, S., Babu, M.K.G.: Thumba (Citrullus colocyntis) seed oil: a sustainable source of renewable energy for biodiesel production. J. Sci. Industrial Res. **69**(5), 384–389 (2010)
4. J. E. et al.: Effect of different technologies on combustion and emissions of the diesel engine fueled with biodiesel: a review. Renew. Sustain. Energy Rev. **80**(May), 620–647(2017)
5. Mofijur, M., Rasul, M.G., Hyde, J., Bhuyia, M.M.K.: Role of biofuels on IC engines emission reduction. Energy Proc. **75**, 886–892 (2015)
6. Duda, K., Wierzbicki, S., Śmieja, M., Mikulski, M.: Comparison of performance and emissions of a CRDI diesel engine fuelled with biodiesel of different origin. Fuel **212**(Sept.-2017), 202–222 (2018)
7. Khan, O., Yadav, A.K., Khan, M.E., Parvez, M.: Characterization of bioethanol obtained from Eichhornia Crassipes plant; its emission and performance analysis on CI engine. Energy Sources Part A Recovery Utilization Environ. Effects August 2019, 1–11 (2019)
8. Gupta, J.G., Agarwal, A.K.: Unregulated and regulated emissions from biodiesel fuelled CRDI SUV engine. SAE Technical Paper. 2015-April, 1–13 (2015)
9. Lamani, V.T., Yadav, A.K., Gottekere, K.N.: Performance, emission, and combustion characteristics of twin-cylinder common rail diesel engine fuelled with butanol-diesel blends. Environ. Sci. Pollut. Res. **24**(29), 23351–23362 (2017)
10. Mikulski, M., Duda, K., Wierzbicki, S.: Performance and emissions of a CRDI diesel engine fuelled with swine lard methyl esters-diesel mixture. Fuel **164**, 206–219 (2016)
11. Kanthasamy, P., Selvan, V.A.M., Shanmugam, P.: Investigation on the performance, emissions and combustion characteristics of CRDI engine fueled with tallow methyl ester biodiesel blends with exhaust gas recirculation. J. Thermal Anal. Calorimetry May 2020, 1–9 (2020)
12. Agarwal, A.K., Gupta, P., Dhar, A.: Combustion, performance and emissions characteristics of a newly developed CRDI single cylinder diesel engine. Sadhana Indian Academy of Sciences, Acad. Proc. Eng. Sci. **40**(6), 1937–1954 (2015)
13. Kumar Garg, N., Pal, A.: An experimental study & analysis of effects of different parameters of microwave in production of bio-diesel. Proc. Inst. Mech. Eng. Part E J. Process Mech. Eng. **234**(4), 394–401 (2020)

14. Shirneshan, A.: HC, CO, CO$_2$ and NO$_x$ emission evaluation of a diesel engine fueled with waste frying oil methyl ester. Proc. Soc. Behav. Sci. **75**(2013), 292–297 (2013)
15. Raheman, H., Ghadge, S.V.: Performance of compression ignition engine with mahua (Madhuca indica) biodiesel. Fuel **86**(16), 2568–2573 (2007)

Heterotrophic Cultivation of Microalgae in Wastewater

Chhavi Aggarwal [ID]**, Dushyant Singh** [ID]**, Himanshu Soni** [ID]**, and Amit Pal** [ID]

1 Introduction

Algae encompasses many different types of plant; they are mainly aquatic but some can grow on soil as well [20]. They capture energy from light to make complex substances, by converting inorganic substances into simpler sugar molecules, and this process is defined as photosynthesis. Algae can be a single-celled organism to multicellular organisms with eukaryotic cells (cells with single nucleus, organelles and plastids). Different types of algal species have different blends of chlorophyll ranging from singular pigments to a combination of pigments.

Most algal species are phototrophs which use light as the source of energy for their growth. Various design structures for algal growth are developed by researchers and industries to maximize the production of it by using light to produce microalgal biomass like open ponds and photobioreactors. Outdoor pond cultures are more viable, but they raise issues like water availability, land-use and appropriate climate conditions, thereby increasing the cost of production. In addition to this, there is competition from other microorganisms like fungi, bacteria and protozoa present in the external environment that can contaminate the microalgae, hence contaminating the entire culture [22]. Photobioreactors provide a closed culture environment, protected from direct degradation and relatively safe from the attack by microorganisms present in the open air. They can also regulate the temperature and CO_2 that bubbles through the culture medium. This technique is more expensive compared to open ponds due to the increased cost of infrastructure [38].

Early efforts to raise algae in open ponds were considered by the Germans in World War II for use as a food supplement. After industrialization started, some

C. Aggarwal (✉) · D. Singh · H. Soni · A. Pal
Department of Mechanical, Production & Industrial and Automobile Engineering, Delhi
Technological University, Delhi 110042, India
e-mail: chhaviabc@gmail.com

groups of workers at the Carnegie Institute in Washington, USA, implemented large-scale algae cultivation for CO_2 dissolution [9]. The late 1970s saw a rise in commercially produced algae in Japan, Eastern Europe and Israel. The algae was grown commercially in an open pond system to provide healthy food during these times. Moreover, in countries like Africa, Lake Chad and Lake Texaco, spirulina biomass is cultivated as a major food source. In the USA, an algal pond system for water treatment was developed amidst the energy crisis of the 1970s [45, 60] was found to be a more cost-friendly method than the conventional systems which rely heavily on expensive methods, large energy inputs and high-cost chemicals. Moreover, it was also observed that wastewater treatment with algae was a much better option for decreasing biochemical oxygen demand (BOD), nitrogen and phosphorus contents and eliminating pathogens with other pollutants [36]. Cultivation of algae provided a new outlook for energy production along with protecting the environment.

Research on the use of algae cultivation as a tertiary wastewater treatment process began in the early 1970s [34, 37, 47]. The initial goal of initiating the algae pond process is to treat the secondary environment to prevent eutrophication [35, 54]. However, it was observed that this treatment removes nutrients from populated domestic wastewater rather than the active wastewater process, which indicated that the algal system permits more than the tertiary system. It is more economical and can be considered secondary rather than a tertiary process [54]. Effluent treatment plants using algae have been shown to be more effective in eliminating biochemical oxygen demand (BOD), pathogens, nitrogen and phosphorus compared to activated sludge against conventional wastewater treatment processes, which have high mechanical gas and requires more energy costs to provide oxygen for aerobic bacteria to consume organic compounds in wastewater [46].

Among the algal strains, Chlorella has been widely applied for wastewater treatment and has shown the potential to eliminate chemical oxygen demand (COD), nitrogen and phosphorus, with varying retention times ranging from a few hours to some days. This shows that it has the ability to replace an active sludge process in the secondary or tertiary phase in terms of nutrient deficiency and biomass production [63].

There are three major components of algal biomass: carbohydrates, proteins and natural oil. The oil content percentages along with the profile of the oil may vary depending on the strain of algae. There are some algal strains which contain around 40% oil of their overall mass [61]. With the global fossil fuel shortage, oil and natural gas, in particular, the world is increasingly focusing on renewable biofuel production [2]. And algae have a much higher unit oil output than the conventional terrestrial oilseed crops; therefore, they are a promising biofuel feedstock [45]. Moreover, biodiesel oil produced from microalgae can be blended with other biofuel sources without any hindrance. In addition, it is possible to refine algae oil with water to produce other fuels such as JP-8 and other jet fuels. The resulting algae biomass is a source of useful products such as biodiesel. Algae can be used for the production of bioethanol and biobutanol, and according to some estimates produce a better amount of vegetable oil than terrestrial crops grown for the same purpose [36].

Algae provides a solution to another major problem of greenhouse gas emissions that arises from the burning of fossil fuels and will continue to accelerate with technological advancements [33].

Recently, algae has garnered much attention due to its ability to produce fine chemicals that are used in various industries and as a useful product for both humans and animals [6, 15, 32]. Algae has also been applied to other fields, such as in the stabilization system for the production of certain extracellular compounds [12], and to accumulate heavy metals from wastewater through metabolically mediated [27, 31, 65]. Some studies have suggested the importance of algae in carbon dioxide fixation [3, 10, 52].

There has been a tremendous rise in the number of publications after 2005 in the algal fuel sector. Research article by Chisti Y has been one of the most cited research articles in the microalgae field [12]. After 2005, approximately 15-fold acceleration of publication rate was observed. The research concepts range from photosynthesis, zooplankton, chlorophyll, coastal, ecosystem, distribution, diatoms, bloom, community, phytoplankton and primary production in the study of microalgae. The top emerging concepts range from biostimulants and bioplastics to animal feed, agricultural advancements. The most studied species were Chlorella sp. and Scenedesmus sp. [41]. The objective of this paper is to analyse the use of microalgae species in wastewater medium.

The paper has been divided into four sections. Section 2 discusses the definition, cultivation process and wastewater-specific algae strains followed by a brief comparison between the different types of cultivation process in Sect. 3. Heterotrophic cultivation of algae has been discussed in Sect. 4 followed by a brief discussion on external carbon sources in Sect. 5. The last section concludes the study.

2 Algae

Microalgae is a very diverse group of plants and is found all over the world [58]. It has been estimated that there are about 200,000–800,000 species in many different genera out of which only around 50,000 species are described [43]. The Linnaean system was given by Linnaeus in 1754, divided the plant kingdom into 25 classes and defined 14 genera of algae [49]. However, due to the constant change in definition, only 4 contained organisms that are now regarded as algae. During the eighteenth and nineteenth century considerable attempts to classify the algal kingdom was done. Lamouroux separated the groups on the basis of colour in 1813 and in 1863, Harvey divided the algae in 4 on the basis of their pigmentation—Chlorospermae (green algae), Melanospermae (brown algae), Rhodospermae (red algae) and Diatomaceae [17]. Since then the definition and classification of algae kept on changing and altering. Today, no definition of algae is generally accepted. One of the definitions that is widely accepted is that algae "have chlorophyll as their primary photosynthetic pigment and lack a sterile covering of cells around their reproductive cells" [29].

2.1 Cultivation

Algae are persistent organisms that can survive a wide range of habitats and adapt to extreme environmental conditions with respect to geographical conditions, exposure to sunlight, availability of nutrients and growing conditions. They can be found in both land and water systems; however, they are mainly distributed in the water bodies [18, 29]. There are two types of algae-based on their visibility by the naked eye—macroalgae and microalgae. Macroalgae, also known as seaweed, is a macroscopic, multicellular, marine algae that live near the seabed. Microalgae are microscopic algae with size ranging from a few micrometres to a few hundred micrometres and are often found in marine and freshwater systems [51, 56]. Although algae are generally independent and free-living, some microalgae species live in symbiotic association with a variety of other organisms including ciliates, sponges, molluscs and fungi [40].

Algae is responsible for generating almost half of the world's atmospheric oxygen given its ability to carry out photosynthesis by simultaneously consuming CO_2 to grow photoautotrophically [44]. The main inputs required for the algal growth is an algal strain, sunlight, water, CO_2 and minerals [64]. Algae species present in the algal media upon exposure to sunlight absorb the rays to carry out photosynthesis; however, the penetration of these rays depends on algal concentration. High algal concentrations restrict the access to sun rays for algae cells present deeper inside the cultivator or pond systems. Therefore, these algaculture systems are designed and optimized to catch maximum sunlight [66].

Moreover, depending on the variable conditions like temperature, up to 25 per cent of the biomass produced during the day may be lost again at night due to the dependency on sunlight [12]. Upon catching the sunrays, algae absorb CO_2, a greenhouse gas, essential for algal growth. An insufficient supply of CO_2 is often the limiting factor in productivity as it acts as a carbon source required for optimum growth. However, heterotrophic algae species require an external source of carbon for growth like sugars (such as glucose).

Nitrogen and phosphorus are the most important minerals required for growth of algae. These minerals can be supplied in the form of agricultural fertilizer, which is simple, easily available but can be a significant cost factor [7, 13]. In low N systems, drift macroalgae are also present in low abundance but are ecologically important as they may provide protection from predation and aid in the dispersal of invertebrates and fishes [21, 42].

In India, there are 7310 algal species recorded belonging to 855 genera which are placed under 10 classes 95 order and 252 families (BSI ENVIS) [16].

2.2 Wastewater-Specific Microalgal Strains

Wastewater could be the result of usage of water for domestic, industrial, agricultural activities or natural causes like surface runoff or storm water, or a combination of all [57]. It contains physical, chemical or biological pollutants that make the water unfit for use and also reflecting the lifestyle and technologies practised in the area. It is a mixture of man-made, organic and inorganic and natural compounds. Majorly amino acids, volatile acids, carbohydrates, proteins and fats are found in sewage as organic carbon, whereas chlorine, magnesium, potassium, bicarbonate, phosphate, sulphur, calcium, sodium, ammonium salts and heavy metals constitute the inorganic substituents found in sewage [23, 30, 55]. The presence of these pollutants in wastewater makes it suitable for use as the growth medium for algae, usually without the addition of any more nutrients and thereby, reducing the cost of algal biomass production simultaneously opening up a new potential market for the biomass produced [39]. Moreover, the algae are also capable of metabolizing some heavy metals present in the wastewater making it suitable for further usage [5]. Hence, this method provides "free" nutrients while simultaneously recycling the nutrients in the wastewater, helping in meeting the wastewater treatment plant water-quality requirements.

There is a chapter in the Richmond (1986) edition of the microalgal handbook [40]. On algae in wastewater oxidation ponds which proposes the use of wastewater as a medium for algae cultivation and the treatment of wastewater. However, the sustainability of this approach requires selecting algae strains that grow rapidly, adapt to the varied conditions in the cultivation system, and produce valuable bioproducts like lipids or proteins that can be marketed profitably [48]. A 1:1 ratio of municipal wastewater with purified water can support 146% more algae growth when compared to standard BG 11 medium [4].

Different microalgae species have different growth rates in different wastewater types. Chlorella sp. growth was found to be best in agricultural wastewater with polystyrene foam and agricultural wastewater mixed with diluted dairy waste in 1:4 ratio. The biomass productivity and lipid productivity observed in both wastewater types are (2.6 g/m^{2}per day, 230 mg/m2per day) and (81.4 g/m^{2}per day, 11 mg/m^{2}per day), respectively [26, 62].

In a research by Lau et al. [28], it was reported that Chlorella Vulgaris removed more than 80% of phosphorous content and 90% of nitrogen content from primary treated sewage. A similar microalgal strain, Chlorella pyrenoidosa, removed 70% of total phosphate, 89% of total nitrogen, and 78% of soluble organic carbon and achieved 0.64 g/L·d average biomass productivity and 37% average lipid content in soybean processing wastewater [25, 50, 53] studied the growth of Botryococcus braunii in treated domestic wastewater and reported that it was able to remove nitrogen and phosphorus nutrients (79.63%) and accumulate oil with dry biomass of up to 36%. Moreover, the lipid profile of oilseed feedstocks was similar to the extracted oil.

Table 1 Difference between heterotrophic and autotrophic algal cultivation

Heterotrophic Algal Cultivation	Autotrophic Algal Cultivation
Algae uses organic carbons like glucose and sucrose as the carbon source and organic chemicals like lipids, proteins and carbohydrates as their electron and energy sources	They obtain energy from the environment in the form of inorganic chemicals or sunlight and use it to create energy-rich molecules such as carbohydrates
Cultivation process of an organism which cannot synthesize its own food, the external source for organic carbon needs to be provided	Cultivation process for organisms that can create nutritional organic substances even from simple inorganic substances such as carbon dioxide
Yield in heterotrophic cultivation is higher and can be controlled depending on the nutrients provided externally	Yield in autotrophic cultivation is lower than heterotrophic cultivation as the process relies on sunlight and the environment
Less requirement of space and maintenance	High requirements of space and maintenance
The reactor can be made deeper and denser, as sunlight does not need to penetrate because the energy source is provided externally. Hence the large surface area is not needed	The reactor needs a large surface area for sufficient sunlight exposure. As sunlight is the basic source of energy so these reactors cannot be made deeper and denser, because light cannot penetrate and the lower algae would not cultivate

3 Cultivation Process-Heterotrophic, Autotrophic Growth

There are two major ways to cultivate algae—photoautotrophic and heterotrophic. In photoautotrophic, the algal strain is cultivated in the presence of sunlight, whereas in the heterotrophic mode of cultivation, the sun rays are limited and cannot penetrate the growing medium. Table 1 gives the difference between a heterotrophic and autotrophic algae cultivation.

4 Heterotrophic Cultivation of Algae

Heterotrophic cultivation is a way of cultivating algae in which microalgae only use organic compounds for both carbon and energy sources in dark conditions, like bacteria. The basic composition of culture medium for heterotrophic cultures is similar to the autotrophic culture; however, heterotrophic cultures require an additional source of organic carbon [59] which is instigated by adding sugars. In heterotrophic cultivation, lipids move towards maturation phase which increases the total productivity and makes the final biodiesel profile similar to fossil fuel based diesel. Wastewater nutrients like nitrogen, phosphor, ammonia, sulphur, iron, toxins and essential metals present in wastewater help in reducing production costs of microalgae biomass.

Heterotrophic algal cultivation is advantageous as compared to photobioreactor (PBR) or outdoor pond system in achieving a higher specific growth rate, increased lipid content, higher cell density, and it also enhances the ability to preserve axenic monoculture to obtain metabolites with better purity [8, 11, 19, 24] Apart from this, a fast-growing microalgal strain has to be chosen with high lipid content to ensure that algal biomass extraction process is industrially and economically viable. Also, the microalgae strains should have a high cell division rate, should be able to metabolise the carbon sources in the absence of any light, grow easily in organic substrates, can change depending on changing environmental conditions and can resist hydrodynamic stresses during bioreactor operation [19].

The various types of microalgae capable of heterotrophic cultivation along with the various processes and technologies employed for the same are listed in Appendix A. The list demonstrates working of algal strains in ideal working conditions, practical success can differ. The list also shows that the Chlorella strain, particularly Chlorella protothecoides, has been studied by many researchers and innovators because of the possibility of large quantities of biodiesel production. The cells are non-motile, asexual and spherical unicellular chlorophyte, which in order to reach a particular cell density multiply during cultivation and that cell density is more than ten times more than other microalgae. Furthermore, most of the species which are present in the list manifest a two-trophic working (employing both photoautotrophic and heterotrophic mode of cultivation) instead of "true" heterotrophic procedure. The change of conditions from photoautotrophic to heterotrophic is best described by a simple two stages process. In reality, it can be very dangerous to some microalgae strains when they are suddenly illuminated with stress of 24 h light and then introduced to total darkness for another 24 h, even if they are cultivated in a medium which is enriched with nutrients and additives which support their growth.

In recent studies, it was found that Tetraselmis suecica cannot survive a completely dark environment. But, somehow the cell go through several biochemical changes in order to fit in with heterotrophic conditions by decreasing the amount of chlorophyll, size of cell walls and making some changes in carbohydrate, protein and lipid profile when put through the stated photoperiod cycle (12 h Light: 12 h Darkness, 8 h Light: 16 h Darkness, 4 h Light: 20 h Darkness and 24 h Darkness) over a period of long cultivation time [1].

Chlorella vulgaris when grown according to heterotrophic cultivation (Light, DCMU, Glucose experiment, Dark, DCMU, Glucose experiment, and Dark, Glucose experiment) has the highest lipid yields of 6.7% DCW, 5.3% DCW, and 4.7% DCW, respectively. C. vulgaris when grown according to the mixotrophic cultivation (Light, Glucose experiment) has the highest growth rate of 0.2124 day-1. Therefore, from the experiments we can conclude, the relation between high lipid yield and stresses placed on the algae, and the relationship between the highest growth rate and mixotrophic "luxury" growth condition [21].

The heterotrophic cultivator comprises a method of growing algae suitable for heterotrophic growth in a closed dark bioreactor. This requires liquid media that includes a carbon source such as sugar and various nutrients including, but not limited to nitrogen, phosphorus, potassium and trace metals such as silica and iron which can

be obtained by the wastewater media. Fermenter receives wastewater, algae strain and other nutrients to produce algae culture. After a predetermined time, the algae culture is optionally moved to a stress reactor wherein one or more nutrients are provided in limited amounts, thereby forcing the algae to produce a greater percentage of lipids [14]. After a predetermined time, the algae culture is ready to be harvested. It is then transferred to a harvesting tank where optionally a flocculation agent is added to the algae culture. Then the algae culture is transferred to the harvester and a flocculation agent is added. After a predetermined time, this flocculated algae culture is dewatered.

5 External Carbon Sources in Heterotrophic Mode of Cultivation

Like other autotrophic organisms, heterotrophs also require the essential elements like phosphorus, nitrogen, oxygen and other trace elements for their growth and productivity. Heterotrophic growth of microalgae is often referred to as fermentation, specifically aerobic fermentation pertaining to the requirement of oxygen. Though while using wastewater, external carbon sources are rarely required, however, wastewater composition varies from place to place and hence, sometimes an external carbon source is added to make the medium suitable for algal growth. There are three different types of additives that can be used as a carbon substrate—acetate, disaccharides and monosaccharides. Monosaccharides are individual sugar subunits which include galactose, glucose and fructose, whereas disaccharides are basically a combination of those monosaccharides which includes lactose, maltose and sucrose. Polysaccharides and oligosaccharides are not generally used as additives because of their high molecular size and hence, a hindrance in transportation of molecules by transporters to the cytocell of algae. Acetates are another class of smaller organic carbon substrate that can be added in the growth medium. Some of the additives from different classes are discussed below.

5.1 Monosaccharides and Disaccharides

Glucose is the simplest among all the monosaccharides and disaccharides with its size around 8.5 Å. Due to its large size, when glucose is added in the growth medium, it requires transporters that help the organic substrate to enter the cytocell. For entering the chloroplast, it needs another transporter which is similar to changing buses running on different routes, to reach a destination. After entering the chloroplast, the reduced organic carbon substrate will undergo a metabolic process that results in the generation of gluconeogenesis (GNG), and ultimately, it will form a substrate called GP3 which ultimately converts to acetyl coenzyme A (acetyl-CoA).

The acetyl-CoA will ultimately reach the mitochondria, i.e. the powerhouse of any cell, and once it is in the mitochondria, it releases stored energy by undergoing a series of chemical reactions by oxidation of acetyl-CoA which is derived from the organic carbon substrate, and this process is called citric acid cycle (CAC) or tricarboxylic acid cycle (TCA). It generates adenosine triphosphate (ATP), which are the energy storage molecules of any cell. ATPs are basically formed due to a process called oxidative phosphorylation, in which oxygen molecules are combined with the acetyl-CoA coming from the CAC/TCA cycle to produce large amounts of adenosine triphosphate (ATP). The amount of ATP produced affects and drives heterotrophic growth. Higher amount of ATP is associated with high growth rates and hence, higher algal densities. Other monosaccharides and disaccharides follow the same process with the help of transporters.

5.2 Acetate

Acetates are simpler organic carbon substrates and do not require transporters because acetates can diffuse in and out of the cell quite easily due to its small size. When acetate enters the cell, it is converted into acetyl-CoA using an enzyme known as acetyl-CoA synthetase. Upon the formation of acetyl-CoA, it can either go into the mitochondria following the TCA cycle or CAC cycle to produce adenosine triphosphate (ATP) similar to glucose breakdown cycle or it can undergo another process known as the glyoxylate cycle or glyoxylate pathway which is a variation of TCA cycle. In the glyoxylate cycle, acetyl-CoA is converted into a compound known as succinate. This cycle helps algae to satisfy their carbon requirement at a cellular level when simple organic carbon substrates like monosaccharides or disaccharides are not available. Later the synthesized compound succinate can undergo TCA cycle/CAC cycle inside mitochondria and produce energy storage packages, i.e. ATPs, which supports organisms to grow.

6 Conclusions

This paper presents a way for cultivating algae in heterotrophic mode with wastewater as the growth media that can be more cost-effective and produce more yield. Algae can metabolize the unwanted pollutants in the air as well as water bodies, thereby eliminating the need of a special water treatment facility. It can produce biomass and oil that can be further utilized by various industries, thereby making the entire process economical. Moreover, different algal strains can react differently when subjected to varying conditions and produce different products that can be further utilized in subsequent production units. Special strains can be used to produce products that are in demand by industries like omega-3 fatty acids or proteins using wastewater as the growth medium which gives clean water that can be further utilized. However,

no practical experimentation was done to prove the various proposed results. Experimental data is needed to complete and validate the hypothesis presented in this paper.

Apart from this, there are various research topics rising in the microalgal field including the use of nanoparticles as an additive in algal biofuels, microalgal immobilization to enhance the removal of pollutants and addition of nano-additives during growth to improve outcome. This highlights the rising microalgal field of study and its importance in the coming future that can revolutionize various domains like fuel, nutraceuticals and pharmaceuticals.

Appendix Technologies Employing Heterotrophically Cultivated Microalgae to Produce Biodiesel

Microalgal Strain	Technology employed	Inventor (s) and Year
Chlorella *species pluralis* Dunaliella *species pluralis*	2-staged procedure for algal oil production	Oyler, James R.—2011
Nannochloropsis *species pluralis*	Integrated method for heterotrophic and photoautotrophic algae	Bianchi D, Bellussi, G.,Bosetti A, Rispoli, G., Gioventu G.—2010
Auxenochlorella protothecoides	Algae cultivated with lignocellulosic degrading microorganism species	Valerie de Crecy-Lagard—2010
C. vulgaris Spirulina maxima C. *species plurali* Euglenoidea *species plurali* Spirulina *species plurali* Euglenoidea	Algal products improved by symbiotic diazotrophs attenuated stress co-cultivation	Srisuda D.—2011
Auxenochlorella protothecoides	Increasing lipid yield by genetic modification of Auxenochlorella	Richard T. Sayre, Suzette L. Pereira—2010
Auxenochlorella protothecoides Dunaliella salina	Agriculture waste is used to grow algae which is then used to produce biofuels	Valerie de Crecy-Lagard—2010
Prototheca moriformis Prototheca krugani Prototheca stagnora Prototheca zopfii Chlorella luteoviridis	Merging of lipid moderation genes and sucrose utilization genes into compelling heterotroph for producing medium chain of fatty acids	Rudenko G, Somanchi A, Espina K, Franklin S, Chua P.—2010
Auxenochlorella protothecoides	2-staged process for changing photoautotrophic cultivation into heterotrophic cultivation	Zhou W, Xiong, Wu Q—2011

(continued)

(continued)

Microalgal Strain	Technology employed	Inventor (s) and Year
Auxenochlorella protothecoides *species plurali*	Oil extraction method with cultivation from carbohydrate feed	Wu Q, Zhou W, Xiong—2008
Schizochytrium limacinum	Production of highly dense crude glycerol	Chi et al.—2009
C. *species pluralis*	Photoautotrophic culture to heterotrophic culture	Charlsberg Jr TW. Jr, Hackworth CA—2009
Phaeodactylum tricornutum	Tropic transformation of photoautotroph with the help of metabolic engineering	Kirk Emil APT, F.C. Thomas Allnutt—2007
Chlamydomonas globose C. protothecoides C. minutissima C. saccharophila C. vulgaris Criscosphaera carterae Dunaliella tertiolecta Nannochloropsis oculata *Scenedesmus bijuga* *Spirulina maxima* *Spirulina platensis* *Tetraselmis chuii* Tetraselmis suecica Phaeodactylum tricornutum Pleurochrysis carterae Botryococcus braunii	Mixotrophic microalgae cultivation by using wastewater from carpet mill effluents	Bhatnagar A, Hunt RW, Chinnasamy S, Das KC.—2010

References

1. Azma, M., Mohamad, R.: Improved protocol for the preparation of Tetraselmis suecica axenic culture and adaptation to heterotrophic cultivation. In: Rahim, R.A., Ariff, A.B. (eds.) Open Biotechnol J. **4**, 3646 (2010)
2. Barbara, J.S.: The false promise of biofuels. Special Report from the International Forum on Globalization and the Institute for Policy Studies, p. 30 (2007)
3. Benemann, J.R.: CO_2 mitigation with microalgal systems. Energy Convers. Manage. **38**, 475–479 (1997)
4. Bhatnagar, A., Bhatnagar, M.: Das Chlorella minutissima—A Promising Fuel Alga for Cultivation in Municipal Wastewaters. In: Chinnasamy K. C. (2009)
5. Bilal, M., Rasheed, T.: Biosorption: an interplay between marine algae and potentially toxic elements—a review. In: Hernández, J., Raza, A., Nabeel, F., Iqbal, H. (eds.) (2018)
6. Borowitzka, M.: Commercial production of microalgae: ponds, tanks, and fermenters. Prog. Ind. Microbiol. **35**, 313–321 (1999)
7. Braun, A., Reith, J.: Algae in Dutch Energy Management, Commissioned by the Novem Energy Recovery from Waste and Biomass (EWAB) Program. Braun Consultants, Utrecht (1993)

8. Brennan, L., Owende, P.: Biofuels from microalgae-a review of the technologies for production, processing, and extractions of biofuels and co-products. Renew. Sustain. Energ Rev. **14**, 557–577 (2010)

9. Burlew, J.S.: Algal Culture from Laboratory to Pilot Plant. Carnegie Institution of Washington, Washington, DC, p. 357 (1953)

10. Chae, S.R., Hwang, E.J.: Single cell protein production of Euglena gracilis and carbon dioxide fixation in an innovative photobioreactor. In. Shin, H.S. (ed.). Bioresource Technology, vol. 97, pp. 322–329 (2006)

11. Chen, F., Chen, G.Q.: Growing phototrophic cells without light. Biotechnol. Lett. 607–616 (2006)

12. Chetsumon, A., Maeda, I.: Antibiotic production by the immobilized cyanobacterium. In: Umeda, F., Yagi, K., Miura, Y., Mizoguchi, T. Scytonema sp. TISTR 8208, in a seaweed-type photobioreactor. J. Appl. Phycol. **6**, 539–543 (1994)

13. Chisti, Y.: Biodiesel from microalgae. Biotechnol. 294–306 (2007)

14. Chisti, Y.: Response to reijnders: do biofuels from microalgae beat biofuels from terrestrial plants? Trends Biotechnol. **26**(7), 351–352 (2008). https://doi.org/10.1016/j.tibtech.2008.04.002

15. Dallaire, V., Lessard, P.: Effect of algal incorporation on growth, survival and carcass composition of rainbow trout (Oncorhynchus mykiss) fry. In: Vandenberg, G., de la Nou¨e, J. Bioresource Technol. **98**, 1433–1439 (2007)

16. Dhup, S., Kannan, C.: Understanding Urea Assimilation and its Effect on Lipid Production and Fatty Acid Composition of Scenedesmus Sp. In: Dhawa, V. (ed.) (2016). https://doi.org/10.15226/2376-4589/2/1/00108

17. Dixon, P.S., Irvine, L.M.: Seaweeds of the British Isles, Vol. 1, Part 1. British Museum (Natural History), London (1977)

18. Fritsch, F.E.: The Structure and Reproduction of the Algae (1935 & 1945)

19. Garcia, O., Escalante, F.M.E.: Heterotrophic cultures of microalgae: metabolism and potential products. In. Bashan, L., Bashan, Y. (eds.). Water Res. **45**, 11–36 (2011)

20. Giordano, M., Raven, J.: Algae. Curr. Biol. **24**(13), R590-R595 (2014)

21. Grimes, K.L., McFarland, A.R.: Algae-derived biofuels: comparative algal yield of autotrophic, heterotrophic, and mixotrophic growth conditions. Energy Proc. **52**, 371–376 (2012)

22. Holmquist, J.G.: Benthic macroalgae as a dispersal mechanism for fauna: influence of a marine tumbleweed. J. Exp. Mar. Biol. Ecol. **180**(2), 235–251 (1994). https://doi.org/10.1016/0022-0981(94)90069-8

23. Horan, D.P., Chilvers, G.A.: Chemotropism—The Key to Ectomycorrhizal Formation? (1990)

24. Huang, G.H., Chen, F.: Biodiesel production by microalgal biotechnology. In: Wei, D., Zhang, X.W., Chenm, G. (eds.). Appl. Energ. **87**, 38–46 (2010)

25. Ji, M., Shanab, R.: Cultivation of microalgae species in tertiary municipal wastewater supplemented with CO_2 for nutrient removal and biomass production. In: Kim, S., Salama, E., Lee, S., Kabra, A., Lee, Y., Hong, S., Jeon, B. (eds.). Ecological Engineering, vol. 58, pp. 142–148, September 2013

26. Johnson, M.B., Wen, Z.Y.: Development of an attached microalgal growth system for biofuel production. Appl. Microbiol. Biotechnol. **85**, 525–534 (2010)

27. Karthikeyan, S., Balasubramanian, R.: Evaluation of the marine algae Ulva fasciata and Sargassum sp. for the biosorption of Cu(II) from aqueous solutions. Iyer, C.S.P. Bioresource Technol. **98**, 452–455 (2007)

28. Lau , P.S., Tam, N.F.Y.: Wastewater nutrients (N and P) removal by Carrageenan and Alginate immobilized chlorella vulgaris. In: Wong, Y.S. (eds.). Environ. Technol. **18**(9), 945–951 (1997). https://doi.org/10.1080/09593331808616614

29. Lee, R.E.: Phycology. Cambridge University Press (2008)

30. Lim, S., Chu, W.: Use of Chlorella vulgaris for bioremediation of textile wastewater. In: Phang, S. (ed.). Bioresource Technol. **101**(19), 7314–7322 (2010). https://doi.org/10.1016/j.biortech.2010.04.092

31. Lodeiro, P., Cordero, B.: Biosorption of cadmium by biomass of brown marine macroalgae. In: Barriada, J.L., Herrero, R., Sastre de Vincente, M.E. (eds.). Bioresource Technol. **96**, 1796–1803 (2005)

32. Lorenz, R.T., Cysewski, G.R.: Commercial potential for Haematococcus microalgae as a natural source of astaxanthin. TIBTECH **18**, 160–167 (2000)

33. Marland, G., Boden, T.A.: Global, regional, and national CO_2 emissions. In: Trends: a compendium of data on global change. Carbon Dioxide Information Analysis Center, Oak Ridge National Laboratory, United States Department of Energy, Oak Ridge, TN, USA. In: Andres, R.J. (eds.). (2007)

34. McGriff, E.C., McKenney, R.E.: Activated algae: a nutrient process. Water Sewage Works, 118–377 (1971)

35. McGriff, E.C., McKinney, R.C.: The removal of nutrients and organics by activated algae. Water Res. **6**(10), 1155 (1972)

36. Oilgae.: Guide to Algae-based Wastewater Treatment: A Sample Report (2010)

37. Oswald, W.J., Lee, E.W.: New wastewater treatment method yields a harvest of saleable algae. In: Adan, B., Yao, K.H. (eds.). WHO Chronicle **32**(9), 348–350 (1978)

38. Patil, V., Tran, K.: Towards sustainable production of biofuels from Microalgae. In: Giselrød, H. (ed.). Int. J. Mol. Sci., **9**, 1188–1195 (2008)

39. Pittman, J.K., Dean, A.P.: The potential of sustainable algal biofuel production using wastewater resources. In: Osundeko, O. (ed.). Bioresour. Technol., **102**, 17–25 (2011)

40. Richmond, A.: Handbook of Microalgal Mass Cultures, CRC Press, Boca Raton, p. 528 (1986)

41. Rumin, J., Nicolau, E.: A bibliometric analysis of microalgae research in the world. In: Gonçalves, R., Grünewald, C., Flynn, K., Picot, L. (eds.). Europe, and the European Atlantic Area (2020)

42. Salovius, S., Nyqvist, M.: Life in the fast lane: macrobenthos use temporary drifting algal habitats. In: Bonsdorff, E. (2005). https://doi.org/10.1016/j.seares.2004.05.001

43. Starckx, S.: A Place in the Sun—Algae is the Crop of the Future, According to Researchers in Geel Flanders (2012)

44. Serrano, O., Jeffrey, J.: Conservation of blue carbon ecosystems for climate change mitigation and adaptation. In: Kelleway, Lovelock, C., Paul, S. (eds.). Coastal Wetlands, pp. 965–996 (2019). https://doi.org/10.1016/b978-0-444-63893-9.00028-9

45. Sheehan, J., Dunahay, T.: A look back at the U.S. Department of Energy's Aquatic Species Program: Biodiesel from Algae. In: Benemann, J., Roessler, P. (eds.). Close-Out Report, National Renewable Energy Laboratory, NREL/TP-580-24190. Borowitzka, M.A.: Commercial production of microalgae: ponds, tanks, tubes and fermenters. J. Biotechnol. 70, pp. 313–321 (1998)

46. Shekhawat, D., Bhatnagar, A.: Potential of treated dairy waste water for the cultivation of algae and wastewater treatment by algae. In: Bhatnagar, M., Panwar, J. (eds.). (2012)

47. Shelef, G., Moraine, R.: Photosynthetic biomass production from sewage. In: Oron, G. (ed.). Ergebn. Limnol. **2**, 3–14 (1978)

48. Show, P., Tang, M.: A Holistic Approach to Managing Microalgae for Biofuel Applications. In: Nagarajan, D., Ling, T., Ooi, C., Chang, J. (eds.) (2017)

49. Stöver, H.D., Trapp, J. (ed.). The life of Sir Charles Linnæus. London: Library of Congress.OCLC 5660395 (1794)

50. Su, Y., Mennerich, A.: Municipal wastewater treatment and biomass accumulation with a wastewater-born and settleable algal-bacterial culture. In: Urban Brigitte, U. Water Research, Vol. 45, issue 11, May 2011, pp. 3351–3358 (2011)

51. Suganya, T., Varman, M.: Macroalgae and microalgae as a potential source for commercial applications along with biofuels production: a biorefinery approach. Renewable and sustainable energy reviews. In: Masjuki, H.H., Renganathan, S. (eds.). (2016)

52. Sung, K.D., Lee, J.S.: CO_2 fixation by Chlorella sp. KR-1 and its cultural characteristics. In: Shin, C.S., Park, S.C., Choi, M.J. (eds.). Bioresource Technol. **68**, 269–273 (1999)

53. Sydney, E.B., Silva, T.E.: Screening of microalgae with potential for biodiesel production and nutrient removal from treated domestic sewage. In: Tokarski, A., Novak, AC., Carvalho, JC., Woiciecohwski, AL., Larroche, C., Soccol, CR. (eds.). Appl. Energy, **88**, 3291–3294 (2011)

54. Tam, N.F.Y., Wong, Y.S.: Wastewater nutrient removal by Chlorella pyrenoidosa and Scenedesmus sp. Environ. Pollut. **58**, 19–34 (1989)
55. Tebbutt, T.H.Y.: Principles of Water Quality Control, 3rd edn (1983)
56. Thurman, H.V.: Introductory Oceanography. New Jersey, USA: Prentice Hall College. ISBN 978-0-13-262072–7 (1997)
57. Tilly, E., Lüthi, C.: Compendium of sanitation systems and technologies, 2nd edn. In: Morel, A., Zurbrügg, C., Schertenleib, F. Swiss Federal Institute of Aquatic Science and Technology (EAWAG), Switzerland (2014)
58. Tomaselli, L.: Microalgal Culture. Black well publications (2004)
59. Tsavalos, A.J., Day, J.G.: Development of media for the mixotrophic/heterotrophic culture of Brachiomonas submarina. J. Appl. Phycol. **6**, 431e433 (1994)
60. Ugwu, C.U., Aoyagi, H.: Photobioreactors for mass cultivation of algae. In: Uchiyama, H. (ed.) (2007)
61. Uma, B., Kim, Y.: A chance for Korea to advance algal biodiesel, JIEC-156; pp. 1–7 (2009)
62. Wang, L., Li, Y.C.: Anaerobic digested dairy manure as a nutrient supplement for cultivation of oil-rich green microalgae Chlorella sp. In: Chen, P., Min, M., Chen, Y.F., Zhu, J., Ruan, R.R. (eds.). Bioresour. Technol. **101**, 2623–2628 (2010)
63. Wang, L., Min, M.: Cultivation of Green Algae Chlorella sp. in Different Wastewaters from Municipal Wastewater Treatment Plant. In: Li, Y., Chen, P., Chen, Y., Liu, Y., Wang y., Ruan, R. (eds.). (2009)
64. Wijffels, R.H., Barbosa, M.J.: An Outlook on Microalgal Biofuels. Science **329**(5993), 796–799 (2010). https://doi.org/10.1126/science.1189003
65. Wilde, E.W., Benemann, J.R.: Bioremoval of heavy metals by the use of microalgae. Biotechnol. Adv. **11**, 781–812 (1993)
66. Zhang, Y.-M., Zhang, Y.-C.: Influence of lake hydrodynamics on blue algal growth. In: Zhang, L.-J., Gao, Y.-X., Zhao. Y. (2007)

Optimization of Biodiesel Production Using Supercritical Solvent by Taguchi's Technique and CI Engine Testing

Kartikkumar Thakkar , **Pravin Kodgire** , **Surendra Singh Kachhwaha** , and **Pavit Shah**

1 Introduction

Biodiesel is one of the valuable renewable sources produced from vegetable (including edible and non-edible) oils and animal fat. It can safely be used as an alternative to gasoline diesel without applying changes in engine operating variables. Further, due to non-toxic and biodegradable nature of biodiesel, sulfur and aromatic compounds are negligible which leads to reduction in emission of sulfur dioxide (SO_2) and particulate matters. Petroleum products like gasoline, diesel and natural gas are driving force for any economy in today's era. But their limited resources are raising questions for its future use. Biodiesel can be proved to be a potential alternative in near future. An indicative target of 5% blending of biodiesel in diesel has been set by the ministry of petroleum and natural gas working under central Government of India [1].

Vegetable oils have higher viscosity compared to petroleum diesel, which restricts its direct use in CI engines [2]. Therefore, to lower the viscosity of vegetable oil generally four processes are used, viz. dilution, micro-emulsification, pyrolysis, and transesterification [3]. Among these, transesterification is the most commonly used

K. Thakkar · S. S. Kachhwaha (✉)
Mechanical Engineering Department, Pandit Deendayal Petroleum University, Gandhinagar, India
e-mail: surendra.singh@sot.pdpu.ac.in

P. Kodgire
Chemical Engineering Department, Pandit Deendayal Petroleum University, Gandhinagar, India

K. Thakkar · P. Kodgire · S. S. Kachhwaha
Center for Biofuels & Bioenergy Studies, Pandit Deendayal Petroleum University, Gandhinagar, India

P. Shah
Mechanical Engineering Department, LDRP Institute of Technology and Research, Gandhinagar, India

507

process in the biodiesel industries today. Transesterification is the chemical conversion of the oil into its corresponding fatty esters with methanol and oil being reactants in the presence of catalyst. Rice bran oil is extracted from rice husk which is considered as non-edible oil in most of the countries except some Asian countries.

The existing biodiesel production process has many limitations. It requires more than one multiple steps during post-processing operations such as separation of glycerol layer and improves the purity of esters by removing residual reactants and recovery of catalyst [4]. The prerequisite for transesterification process using alkali catalyst is that free fatty acid content (FFA) of raw oil should be below 2% limit to avoid start of saponification reaction. On the other hand, the performance of acid catalyst is relatively less efficient when compared with alkali catalyst. Further excess glycerol production as a byproduct is causing fall in price and becoming difficult to consume the same for industrial applications.

Transesterification process using supercritical solvents (in the absence of catalyst) has potential to substitute conventional methods. Further, speedy reaction rates and simplified separation process of products is the key feature of this process [5]. Further, the final yield remains unaffected by the water and FFA content unlike conventional procedures. Interesterification process using methyl acetate at supercritical conditions eliminates glycerol production [6].

In summary, conventional ways of biodiesel productions have certain limitations which are restricting its popularization. It has several stages of production and purification as previously discussed. Also, the conventional catalytic processes cannot work well if the raw oil has high FFA content or contamination by moisture. Thus, pretreatment or purification of raw oil is required. Therefore, the prime objective of the present experimental investigation is to develop a glycerol and catalyst free biodiesel production technique which can utilize the unrefined raw oil and convert it into biodiesel irrespective of the presence of FFA content in the oil. Finally, the prepared biodiesel is blended with gasoline diesel, and performance testing using compression ignition engine has been performed.

2 Materials and Methods

2.1 Materials

Fortune Adani Wilmar brand rice bran oil was purchased from the local market. Methyl acetate and n-heptane were procured from Sigma-Aldrich of 99.5% purity, and ethyl acetate was procured from Rankem Lab of 99.7% purity. Methyl acetate and ethyl acetate were used as supercritical co-reactant.

2.2 Autoclave Specification

Autoclave (250 ml volume capacity) with a design temperature of 350 °C and design pressure of 200 bar was used for the reaction. An external ceramic band heater (1 kW) is used for the heating which has insulation at the bottom to prevent heat loss. The magnetic stirrer rotates at 1450 rpm and is driven by ¼ HP AC motor. A representation diagram of the autoclave experimental set-up is shown in Fig. 1, whereas actual setup of the autoclave is given in Fig. 2.
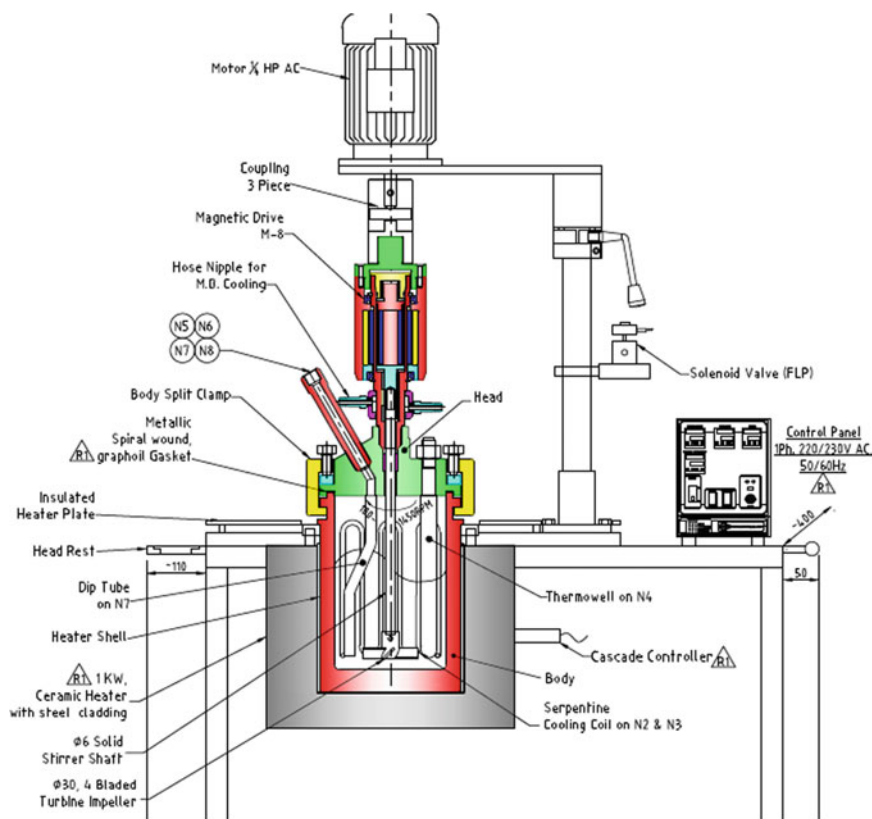
Fig. 1 Schematic diagram of autoclave setup
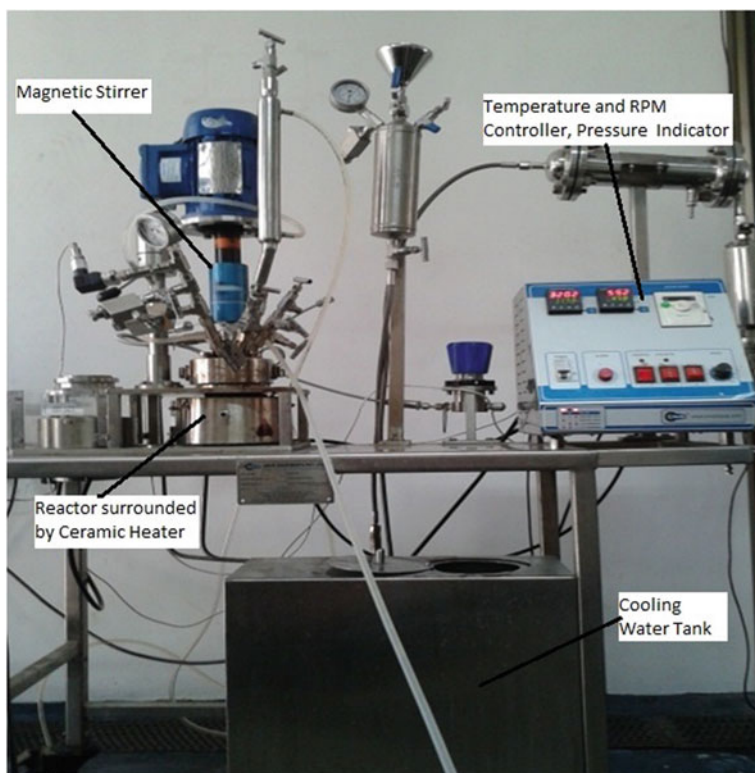
Fig. 2 Actual setup of autoclave

2.3 Design of Experiments

Taguchi's orthogonal array (L9) was selected for design of experiments. 0th experiment (Preliminary experiment) was conducted to decide the factor levels of experiments. Table 1 shows different reaction parameters, i.e., reaction temperature (A), reaction time (B) and solvent-to-oil molar ratio (C) and their levels decided after initial experiments.

Table 1 Reaction parameters and their levels using methyl/ethyl acetate

Factors	Low level	Intermediate level	High level
Reaction temperature (A), °C	325/300	335/320	345/340
Reaction time (B), min	30	45	60
Methyl/Ethyl acetate-to-oil molar ratio (C)	40	45	50

2.4 Experimental Procedure

The autoclave was thoroughly cleaned with methanol. After that autoclave was charged with required amount of raw oil (rice bran) and methyl/ethyl acetate according to molar ratio. The temperature of autoclave was set to desired point to start heating. The pressure in the autoclave was increased due to the vapor pressure of reactant liquid. Once the pressure was achieved, the time for reaction was counted and the reaction was allowed to take place for desired time (30–60 min). After the predefined reaction time, the heating was stopped and the pressure was released. Immediately the pump was started to circulate water in the water jacket of the autoclave. At last the autoclave was dismantled, and the product mixture was withdrawn. The product is now a mixture of biodiesel, triacetin, and excess ethyl acetate. In order to get the final product, excess methyl/ethyl acetate was recovered via rotary evaporator operated at 70 °C under vacuum heating. This excess methyl/ethyl acetate can also be reused.

2.5 GC–MS Procedure and Yield Calculation

All the qualitative and quantitative analysis of methyl ester of the sample was carried out using gas chromatography and mass spectrometry—GCMS (Agilent Tech. Inc Model: 7890A) fitted with a capillary column (HP-5MS, 30 m L x Diameter of 0.25 mm) and a FID (Flame ionization detector(FID). The injector and detector temperatures were set to 300 °C and 330 °C, respectively. The column temperature was fixed to 45 °C for 1 min and then increases to 55 °C at a speed of 2 °C/min, and which then hold for 1 min. Temperature was raised up to 100 °C at a speed of 10 °C/min and held for 1 min, then lastly raised to 220 °C at a speed of 25 °C/min and held for 15 min. The total investigation time was 32.3 min. 1 ml /min flow of helium as a carrier gas was used, and a split ratio of 1:50 was maintained in the analysis. 1 μl of test sample was injected into the column for analysis. Biodiesel yield and FAME/FAEE yield were calculated from Eqs. (1) and (2), respectively.

$$\text{FAME or FAEE yield} = \frac{\text{Total weight of esters}}{\text{Total weight of oil in the sample}} \times 100\% \qquad (1)$$

$$\text{Biodiesel yield} = \frac{\text{Weight of esters} + \text{Triacetin}}{\text{Total weight of oil in the sample}} \times 100\% \qquad (2)$$

2.6 Engine Test Setup

A four-stroke single-cylinder CI engine test setup coupled with eddy current dynamometer was used to perform engine experiments. The illustration of the engine setup is shown in Fig. 3. The CI engine specifications along with uncertainty in measurements are listed in Table 2. The overall uncertainty calculated using the procedure prescribed in [7] is found to be ±2.76%, which is well below the acceptable limit of ±5%.
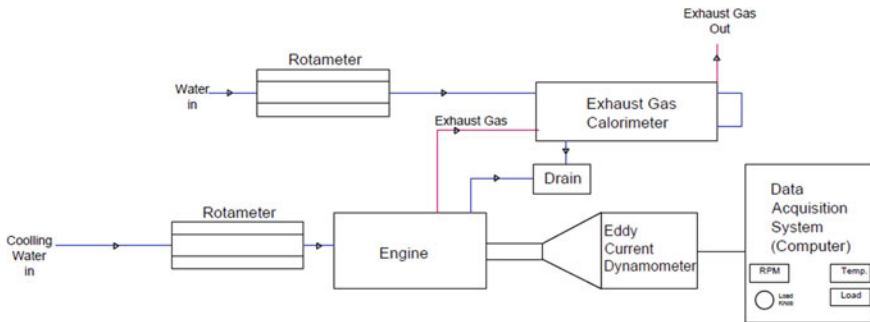
Fig. 3 Schematic diagram of test engine setup

Table 2 Engine specifications and uncertainty in measurements

Specifications of the engine coupled with eddy current dynamometer		Uncertainty in measurements		
		Parameter	Accuracy	Uncertainty
No. of cylinder	1	Speed sensor (0–9999 rpm)	±1 rpm	±0.07
No. of strokes	4	Engine load indicator (0–20 kg)	±0.1 kg	±0.5
Piston diameter	0.08 m	Temperature sensor	± 0.1 °C	±1.0
Stroke length	0.11 m	Burette system (0–100 cc)	±0.1 cc	±1.0
Engine max. power	3.5 kW	Stop watch (digital)	±0.1 s	±0.3
Engine speed (N)	1500 rpm	Brake power (0–3.5 kW)	±0.03 kW	±0.5
Compression ratio	17.5:1	Brake specific fuel consumption	–	±1.284
Volume	661 cc	Brake thermal efficiency	–	±1.284

3 Results and Discussion

3.1 Rice Bran Oil Methyl Ester Analysis

Yield data given in Table 3 were analyzed in Minitab software to calculate the signal-to-noise ratio. It is clear from the Table 4 that most influencing variable on FAME biodiesel yield is reaction temperature followed by methyl/ethyl acetate-to-oil ratio and reaction time. Similarly, for FAEE biodiesel also reaction temperature is observed to be highly influencing factor. However, unlike FAME biodiesel solvent-to-oil ratio is less significant factor compared to reaction time. The same can be inferred from the slope by means of S/N ratio plots shown in Fig. 4a for FAME and Fig. 4b for FAEE biodiesel, respectively. Moreover, increase in reaction temperature above 325 °C decreases the product yield as observed from signal-to-noise (S/N) ratio (refer

Table 3 Yield data (rice bran oil methyl/ethyl ester)

Exp No	A	B	C	FAME yield (%)	FAEE yield (%)	FAME biodiesel yield (%)	FAEE biodiesel yield (%)
1	325/300	30	40	91.20	34.65	92.13	34.65
2	325/300	45	45	87.61	39.73	87.84	40.00
3	325/300	60	50	89.51	56.49	89.89	56.64
4	335/320	30	45	88.63	65.94	88.90	66.17
5	335/320	45	50	99.48	80.06	102.93	80.65
6	335/320	60	40	87.74	83.62	88.21	84.90
7	345/340	30	50	86.41	90.06	87.47	93.15
8	345/340	45	40	86.50	93.64	87.08	99.19
9	345/340	60	45	88.60	97.15	89.86	103.56
Validation (FAME)	**325/340**	**45**	**50**	**99.52**	–	**102.95**	–
Validation (FAEE)	**340**	**60**	**50**	–	**99.39**	–	**104.01**

Table 4 Means of signal-to-noise ratio for FAME (FAEE) biodiesel

	FAME biodiesel			FAEE biodiesel		
Level	A	B	C	A	B	C
1	39.03	38.96	38.93	32.63	35.53	36.43
2	39.26	39.18	38.92	37.71	36.70	36.47
3	38.81	38.95	39.24	40.09	38.20	37.53
Delta	0.45	0.23	0.32	7.46	2.67	1.09
Rank	1	3	2	1	2	3
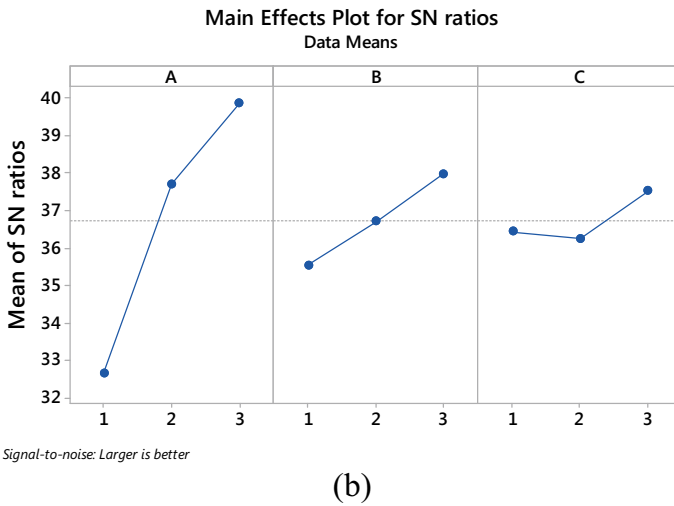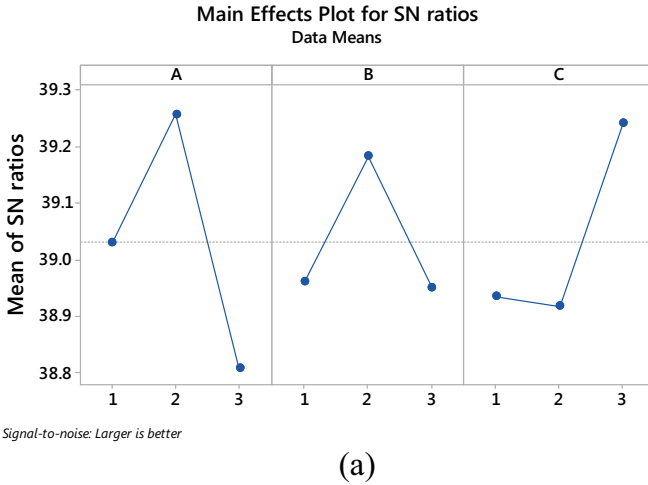
Fig. 4 Main effects plot for S/N ratio for **a** FAME biodiesel and **b** FAEE biodiesel

Fig. 4). S/N ratio (larger is better) for maximization of the response was calculated using Eq. (3).

$$\text{Signal to noise ratio} = -10 \log \left(\frac{1}{n} \sum_{i}^{n} \frac{1}{y_i^2} \right) \tag{3}$$

Signal-to-noise ratio is the measure of desired product output. Optimum values of the parameters were obtained by plotting graphs of signal-to-noise ratio vs. factor levels and observed to be temperature: 325 °C, time: 45 min and methyl acetate-to-oil

Table 5 Physicochemical properties of biodiesel

Property	ASTM standard for biodiesel	Rice bran oil biodiesel (B100)	ASTM method
Density (kg/m^3)	875–900	875	ASTM D4052
Calorific value (MJ/kg)	38 (min)	38.13	ASTM D240
Viscosity (cP)	1.9–6.0	6.56 ± 0.05	ASTM D445
Flash point (°C)	>130	207	ASTM D93
Cloud point (°C)	Report	7	ASTM D2500
Pour point (°C)	Report	−1	

ratio: 50:1 with a maximum FAME yield of 99.52% and biodiesel yield of 102.95%. Similarly, for FAEE biodiesel optimum factor settings for desirable output (99.39% FAEE yield and 104.01% FAEE biodiesel yield) is: 340 °C reaction temperature, 60 min reaction time and 50:1 ethyl acetate-to-oil molar ratio. Several confirmations run on the optimum condition were taken. In the case of ethyl acetate as a reactant, the favorable condition is on higher side. The long chain of ethyl acetate requires stringent conditions to react with fatty acids. Here temperature is the most influential factor followed by reaction time and molar ratio.

3.2 Physicochemical Properties of Biodiesel

Biodiesel produced was tested for various properties to meet ASTM standards specified for biodiesel and can be considered as a compatible fuel to be utilized in an existing CI engine without any modification. All the fuel property tests have been executed according to procedures specified as per ASTM standards as shown in Table 5.

3.3 Engine Performance Characteristics

B5 and B10 blends of biodiesel were prepared using rice bran oil methyl and ethyl esters and utilized for engine performance testing. There was no detrimental effect observed in the engine performance for blending up to 10% of biodiesel. Figure 5 and 6 shows effect on brake specific fuel consumption (BSFC) and brake thermal efficiency (BTE), respectively, with change in blending proportion of biodiesel with diesel. Improvement in BTE and BSFC was observed for B10 FAME, which can be due to improvement in combustion phenomena. It is important to note that biodiesel
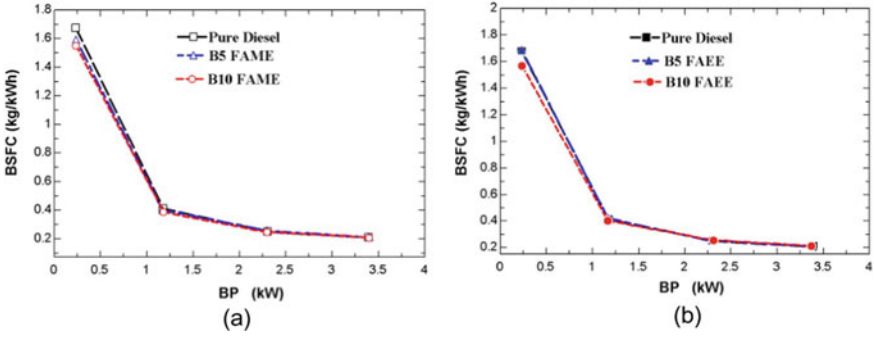
Fig. 5 Influence of various blends of **a** FAME biodiesel and **b** FAEE biodiesel on brake specific fuel consumption (BSFC)
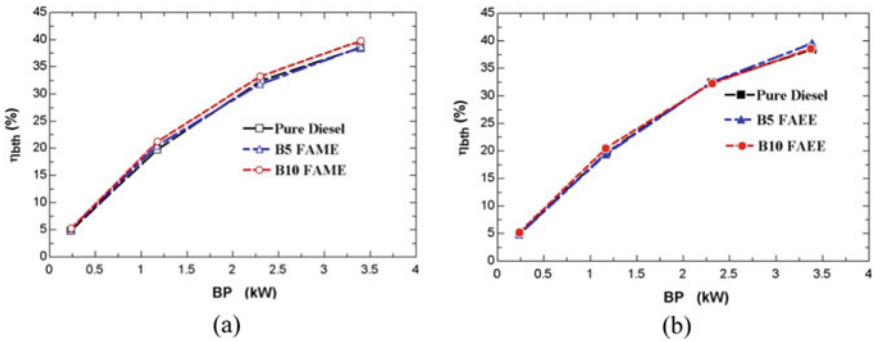
Fig. 6 Influence of various blends of **a** FAME biodiesel and **b** FAEE biodiesel on brake thermal efficiency (BTE)

has oxygen in its molecular structure which plays a vital role in improved combustion. Similarly [8] also observed improvement in BTE for the used biodiesel. However, no significant effects on BTE of BSFC were observed for B5 blends of FAME and FAEE.

4 Conclusions

Instead of transesterification process, alcohols like methanol or ethanol, in interesterification process were used to avoid production of glycerol. Triacetin, a valuable additive in diesel fuel is produced as a byproduct. Using methyl acetate as a supercritical co-reactant maximum biodiesel yield of 102.95% was achieved. Favorable condition for maximum yield were experimentally found as temperature 325 °C, time 45 min, methyl acetate to oil molar ratio 50:1. In the experiment using methyl

acetate, temperature was identified as the most influential factor, followed by molar ratio and time. When ethyl acetate was used as reactant to make biodiesel production process completely renewable, the maximum yield achieved was 104.01% at temperature 340 °C, time 60 min, and ethyl acetate to molar ratio: 50:1. For the case of ethyl acetate as reactant, the favorable condition are on higher side as the long chain of ethyl acetate requires stringent conditions to react with fatty acids. Here temperature was found to be the most influential factor followed by reaction time and molar ratio. Engine performance study using B5 and B10 shows promising result. There is no significant change in BSFC up to B10. Brake thermal efficiency increases by 3% for B10, and no detrimental effect compared to gasoline diesel on engine performance was observed.

References

1. Ministry of Petroleum and Natural Gas G of I: The Gazette of India: Extraordinary. New Delhi (2018)
2. Mehta, R.N., Chakraborty, M., Mahanta, P., Parikh, P.A.: Evaluation of fuel properties of butanol−biodiesel−diesel blends and their impact on engine performance and emissions. Ind. Eng. Chem. Res. **49**, 7660–7665 (2010)
3. Demirbas, A.: Biodiesel production from vegetable oils via catalytic and non-catalytic supercritical methanol transesterification methods. Prog. Energy Combust. Sci. **31**, 466–487 (2005)
4. Thakkar, K., Shah, K., Kodgire, P., Kachhwaha, S.S.: In-situ reactive extraction of castor seeds for biodiesel production using the coordinated ultrasound—microwave irradiation: process optimization and kinetic modeling. Ultrason. Sonochem. (2018). https://doi.org/10.1016/j.ultsonch.2018.08.007
5. Lim, S., Lee, K.T.: Process intensification for biodiesel production from Jatropha curcas L. seeds: supercritical reactive extraction process parameters study. Appl. Energy **103**, 712–720 (2013)
6. Saka, S., Isayama, Y.: A new process for catalyst-free production of biodiesel using supercritical methyl acetate. Fuel **88**, 1307–1313 (2009)
7. Yesilyurt, M.K.: A detailed investigation on the performance, combustion, and exhaust emission characteristics of a diesel engine running on the blend of diesel fuel, biodiesel and 1-heptanol (C7 alcohol) as a next-generation higher alcohol. Fuel **275**, 117893 (2020)
8. Haşimoğlu, C., Ciniviz, M., Özsert, İ, et al.: Performance characteristics of a low heat rejection diesel engine operating with biodiesel. Renew. Energy **33**, 1709–1715 (2008)

Energy and Exergy Analysis of a Hybrid Renewable Energy Source

Pratik Shah, Rishabh Agrawal, and Surendra Singh Kachhwaha

1 Introduction

Energy is the prime necessity for any activity in the known universe. There has been a considerable and unprecedented surge in the energy demands over the recent years, primarily due to industrial and economic revolutions and population growth. It is expected that population of the world will grow at 1% accompanied by a proportionate increase in energy demand [1]. The conventional energy sources currently in use, though meet the requirements now, pose a threat greater than their depletion, the carbon emissions. The resulting climate change is expected to further increase the energy demands. This has motivated the scientific community to look for renewable energy sources that renew after use and reduce the carbon footprints to align with the global agenda. Countries globally have implemented policies for advancement and encouragement of renewable energy. Renewable sources though very efficient have a substantial amount of exergy loss, which can be brought down using optimization techniques and installing hybrid systems. Numerous research and development in the field of renewable have established the edge, hybrid systems have over stand-alone systems. A study on energy and exergy analysis could lead to a better utilization of available energy in the field of electricity generation primarily and reap better returns and decreased energy waste. There is ample research on energy as well as exergy analysis-based improvement in stand-alone renewable systems; however, not much has been done to compare the hybrid systems with heavily optimized stand-alone systems, which seem to reap good results. The study could open research areas in the field of optimized design of renewable energy harnessing modules and could define the base standards for harnessing adequate energy for hybrid systems.

P. Shah · R. Agrawal · S. S. Kachhwaha (✉)
Mechanical Engineering Department, Pandit Deendayal Petroleum University, Gandhinagar, India
e-mail: surendra.singh@sot.pdpu.ac.in

Theoretical mathematical models were developed to compare the actual energy efficiency with the proposed theoretical models [2–4]. Study [3] compared thermodynamics and photochemical approach for assessing efficiency, while study [2] was developed to optimize exergetic PV array which showed increase in array temperature leads to reduction in efficiency. Models were proposed to remove heat from array to achieve higher efficiency. Apart from that, various potent materials, like perovskite, CdTe, organics cells, were not introduced owing to sustainability issues [5]. Over a period of time, these optimizations have not shown tremendous results, and optimization of module efficiency has reached its saturation so researchers are implementing other ways for better performance one of which is hybrid energy system. A novel concept of solar PVT-ST system is introduced which leads to increase in both exergy and energy efficiency [6]. Study [7] defined a benchmark to calculate maximum energy efficiency of wind turbine. However, exergy and not energy proved to be a more efficient tool to measure the efficacy of a system and its ability to harness wind power. Over the course, many breakthroughs were made in the field of exergy analysis and various developments were made to improve the accuracy of the system. In the coming years, study [8] developed relations through experimental and simulation models to predict the behavior of efficiency vs. the input parameters. Study [9] shows that at higher wind speeds the amount of avoidable exergy destruction increases. The study was then extended to development of a storage system owing to large fluctuations in power of a hybrid system.

There has been a rich research and development in the field of hybrid systems and their capabilities to harness the freely available energy sources to the fullest. The present studies deal with the development of energy analysis and development of exergy as a tool to measure the efficiency of a system. This study will show difference between efficiency (including energy as well as exergy) for stand-alone PV cell with wind turbine. Also, an estimation of exergy converted into useful work along with distribution in losses. Finally, results of stand-alone renewable systems are compared with a hybrid renewable energy system.

2 Mathematical Formulation

2.1 Energy and Exergy Analysis of Solar PV

The ratio of electric energy generated to solar energy falling on a PV cell is defined as energy efficiency. Absorbed solar flux (S) is represented by:

$$S = A_{\text{arr}}G = (A_{\text{mod}}N_s N_m)G \qquad (1)$$

where A_{arr}, N_s, N_m represents surface area of array, total number of strings, sum of modules arranged in series for one string, while module surface area is $A_{\text{mod}} = L_1 L_2$ (L_2 and L_1 are module dimensions).

Fig. 1 A generalized current–voltage performance curve [2]
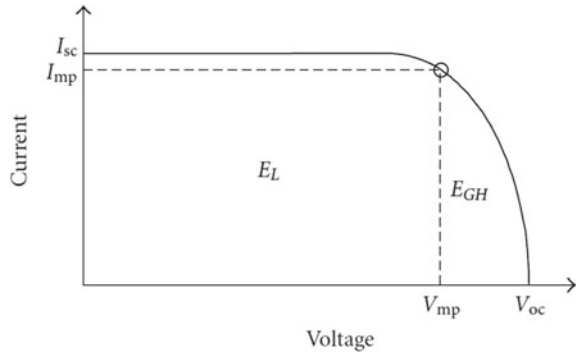
A generalized I-V curve and the associated variables are represented in Fig. 1 [2]. Electrical efficiency for PV array can be defined as:

$$\eta_{\text{ele}} = \frac{V_{\text{mp}} I_{\text{mp}}}{S} \tag{2}$$

where V_{oc} and I_{sc} are open-circuit voltage and short-circuit current respectively, while V_{mp} and I_{mp} are maximum voltage and current. Exergy is the highest amount of work potential that is produced by the system when the system achieves the equilibrium with the ambient conditions [10]. Exergy efficiency is ratio of total output exergy to total input exergy:

Change in the total exergy of the system = Total exergy in − Total exergy out

$$\hspace{6cm} - \text{ Total exergy destroyed} \tag{3}$$

$$\eta_{\text{ex}} = \frac{Ex_{\text{out}}}{Ex_{\text{in}}} = 1 - \frac{I_{c-v}}{Ex_{\text{in}}} \tag{4}$$

where Ex_{in}, Ex_{out}, I_{c-v}. are exergy at inlet, exergy at outlet and irreversibility generated inside control volume, respectively. Using Petela theorem [4]:

$$Ex_{\text{in}} = S\left(1 - \frac{T_{\text{amb}}}{T_{\text{sun}}}\right) \tag{5}$$

T_{sun} = the temperature of sun (K). T_{amb} = the ambient tempeature (K).

The total control volume irreversibility consists of exergy losses from control volume (external) and exergy destruction in control volume (internal) [4]:

$$I_{c-v} = \sum (Ex_{\text{loss}} + Ex_{\text{des}}) \tag{6}$$

The external exergy losses Ex_{loss} are due to heat transfer and represented by [4]:

$$Ex_{\text{loss}} = U_L A_{\text{arr}} (T_{\text{cell}} - T_{\text{amb}}) \left(1 - \frac{T_{\text{amb}}}{T_{\text{cell}}}\right) \tag{7}$$

The internal exergy losses involves: electrical exergy destruction $Ex_{\text{des,ele}}$, optical losses $Ex_{\text{des,opt}}$ in PV array surface, exergy destruction due to temperature gradient for PV array and sun temperature, $Ex_{\text{des},\Delta T_{\text{sun}}}$ and temperature variation of PV array w.r.t. to reference condition $Ex_{\text{des},\Delta T_{\text{arr}}}$ is given by [4]:

$$Ex_{\text{des,ele}} = \left(I_{\text{sc}} V_{\text{oc}} - I_{\text{mp}} V_{\text{mp}}\right) \tag{8}$$

$$Ex_{\text{des,opt}} = S(1 - (\zeta\alpha)) \left(1 - \frac{T_{\text{amb}}}{T_{\text{sun}}}\right) \tag{9}$$

$$Ex_{\text{des},\Delta T_{\text{sun}}} = (\tau\alpha) S T_{\text{amb}} \left(\frac{1}{T_{\text{cell}}} - \frac{1}{T_{\text{sun}}}\right) \tag{10}$$

$$Ex_{\text{des},\Delta T_{\text{arr}}} = \frac{m_{\text{cell}} C_p T_{\text{amb}}}{\Delta T} \left(\ln\left(\frac{T_{\text{cell}}}{T_{\text{amb}}}\right) - \frac{(T_{\text{cell}} - T_{\text{amb}})}{T_{\text{cell}}}\right) \tag{11}$$

2.2 Energy and Exergy Analysis of Wind Turbine

Model considers the following results and relations derived as:

$$E_{\text{in}} = W_{\text{out}} + KE \tag{12}$$

$$E_{\text{in}} = 0.5 * \rho * A * t * v^3 \tag{13}$$

where E_{in}=Energy at inlet,t=time (s),v=wind velocity.A. Betz gave the maximum power that can be harnessed as 0.59 times the input energy [7]:

$$Ex_{\text{flow 1}} = W_{\text{out}} + Ex_{\text{flow 2}} + Ex_{\text{des}} \tag{14}$$

$$Ex_{flow1} = Ex_{(\text{kinetic})} + Ex_{(\text{physical})} \tag{15}$$

Ex_{flow1} = Exergy at inlet , Ex_{flow2} = exergy at outlet , Ex_{des} = exergy destroyed, $T_{\text{iwindchill}}$ factor is a composite temperature considering the effective wind transfer capability given by [11]:

$$T_{i,\text{windchiill}} = 13.12 + 0.6215Ta - 11.37v^{0.16} + 0.3965Tav^{0.16} \tag{16}$$

Outlet velocity behind the wind turbine was defined by the following formula defined by [12]:

$$V_2 = ((E_{\text{in}} - W_{\text{out}})/(\rho * A))^{0.333} \tag{17}$$

The exergy destroyed and exergy distributed in irreversibility is accounted for in $E_{\text{(physical)}}$ by [13]:

$$E_{\text{(physical)}} = T_0 \left(cp \ln \frac{T_{\text{windchill\_2}}}{T_{\text{windchill\_1}}} - R \ln \frac{p_2}{p_1} - mcp \frac{(T_a - T_{\text{avg}})}{T_a} \right) \tag{18}$$

Exergy efficiency is given by [13]:

$$\eta_{\text{ex}} = \frac{W_{\text{out}}}{Ex_{\text{flow 1}}} \tag{19}$$

Energy efficiency is given by [13]:

$$\eta = \frac{W_{\text{out}}}{E_{\text{in}}} \tag{20}$$

3 Input Conditions

In this study, we have considered Kutch, India as our location with 23.632′N latitude and 69.960′E longitude. Figure 2 shows average daily irradiance of the month May for the location.

We have used Siemens SM55 photovoltaic module is used. It has maximum power rating of 55 W under STP conditions which is 25 °C ambient temperature having solar intensity equal to 1000 W/m². It consists of 36 single monocrystalline cells

Fig. 2 Variation of solar radiation intensity during the day
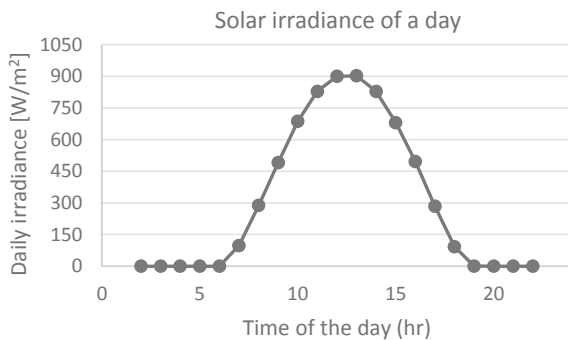
Table 1 Design data specification sheet of Siemens SM-55

PV Module variable	Values
Brand of PV module	Siemens SM55
Total modules arranged in series per string (Nm)	2
Total strings (Ns)	6
Reference state solar radiation intensity	1000 W/m^2
The ambient temperature at NOCT conditions	293.15 K
The cell temperature at the reference conditions	298.15 K
The sun temperature	5760 K
The PV array emissivity	0.88
Solar module dimension L1	1.293 m
Solar module dimension L2	0.329 m
The effective product of transmittance–absorptance	0.9
Wind speed	0.5 m/s

with manufacturer warranty of 25 years. Environment, operation, and system design variables are mentioned in Table 1.

Wind speed variation for the month of May is shown in Fig. 3 which gives a brief idea of peak speeds and minimum speeds required to calculate power characteristics and hence governs the number of turbines to be installed (Table 2).
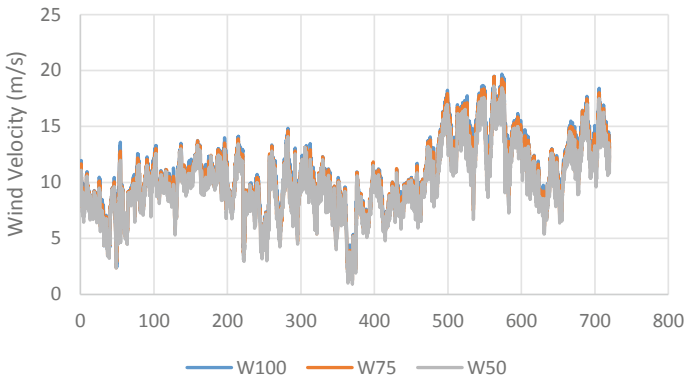
Fig. 3 Wind speed in May for hub heights of 100 m, 75 m, 50 m

Table 2 GE Gamesa 1.5 MW wind turbine specification sheet [9]

Characteristics	Value
Rated capacity	1500 W
Hub height	100 m
Rotor diameter	77 m
Swept Area	$4657 m^2$
Ambient Temperature	298 k
Cutting/cut out speed (m/s)	3.5/25
Capacity factor	29%
Rated energy efficiency	25%

4 Results and Discussions

4.1 Energy and Exergy Analysis of Solar PV

Figure 4 shows the variation of energy and exergy efficiency for Siemens SM-55 during the test day. Trend shows that energy efficiency decreases as the cell temperature increases. Hence, between 12 and 1 pm efficiencies are lower than that of between 11 to 12 pm and 1 pm to 2 pm. Also, Fig. 4 shows exergy efficiency for SM-55 depending upon the duration of the day.

Figure 5 shows the distribution of exergy during the test day. Exergy inlet in the system is distributed among external exergy losses, internal exergy losses due to temperature difference, electrical exergy losses, optical exergy losses, and exergy out which is work output. On an average, external exergy loss is 2.5% of overall input exergy; similarly, internal exergy losses due to temperature difference is around
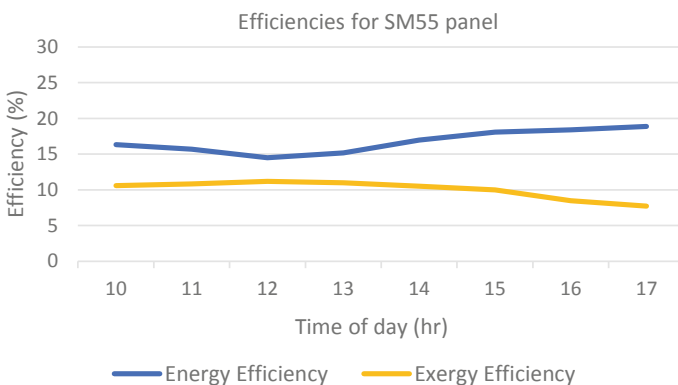
Fig. 4 Variation of Thermodynamic efficiencies of SM-55 during a day in May
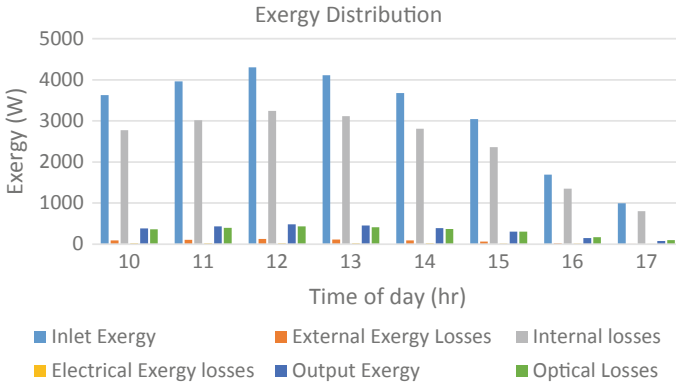
Fig. 5 Exergy distribution during the day in May

76.5%, electrical exergy losses 0.5%, optical exergy losses are 10%, and exergy out 10.5% in May.

4.2 Energy and Exergy Analysis of Wind Turbine

Exergy distribution of the input exergy signifies the part of exergy going into generation of heat and entropy generation and work output (Figs. 7 and 6).

The stand-alone exergy and energy variation vs. the time for a day in May, for the wind turbine stand-alone system was plotted to signify the variation and need to design a robust and flexible system to account for the fluctuations (Fig. 8).
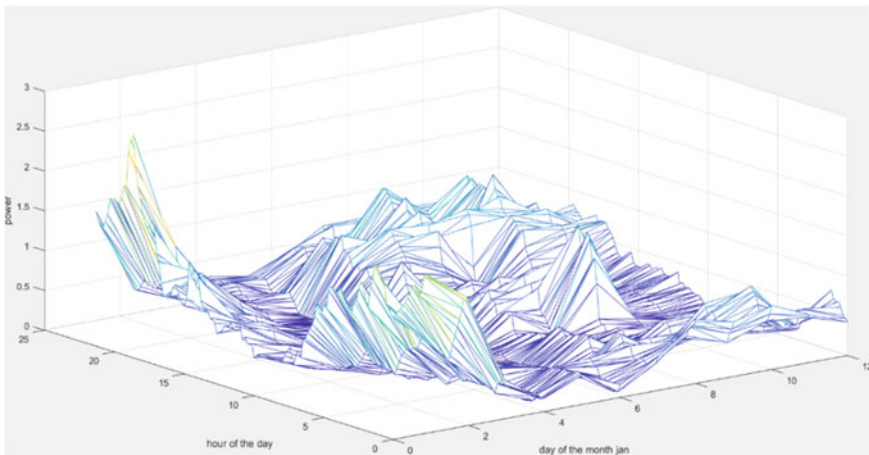
Fig. 6 Characteristic power output curve
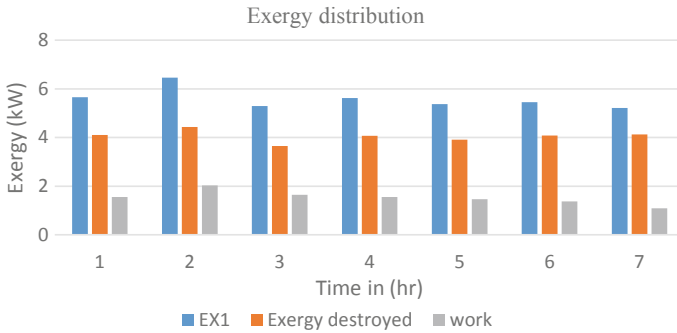
Fig. 7 Exergy distribution of exergy at inlet EX1
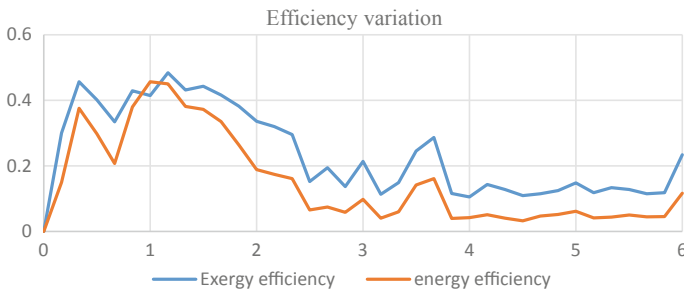
Fig. 8 Energy and exergy variation with time of the day (hr)

4.3 Energy and Exergy Analysis of Hybrid (Solar PV and Wind Turbine)

The study done for stand-alone systems was extended to estimate the efficiencies for a hybrid system.The calculations estimate the average energy efficiency of wind turbine systems to be 23.58% (rounded off to 25% for the further studies) and 34.78% as wind exergy, whereas for the solar PV cell system the average energy efficiency was found to be 16.74% and 10.04 % was found to be exergy efficiency (Fig. 9).

5 Conclusions

The study defines exergy as a more potent tool to quantify the efficiency of a renewable energy system. The solar PV cell module has the energy efficiency between 15 to 18% and exergy efficiency between 8 to 12%. Various losses which proportionately rise as in the case of rising inlet exergy. To optimize exergy efficiency, various losses should be optimized and it is seen that with increase in inlet exergy, proportionate
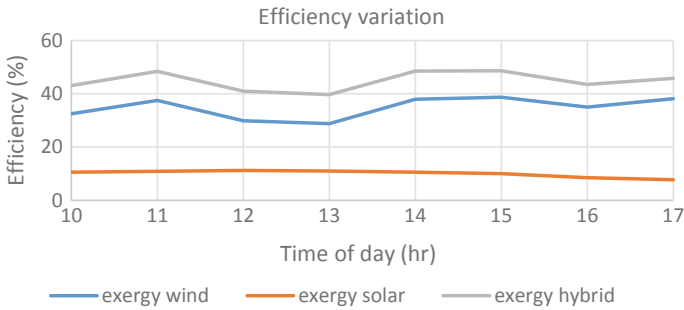
Fig. 9 Energy and exergy efficiency

increase in losses is less as compared to increase in output exergy. Hence, the system becomes more efficient.

In the case of wind turbine stand-alone system, the energy efficiency is found to be 23.58% and exergy efficiency is 34.78%. The corresponding percentage increase in the exergy loss is less in case of high inlet exergy to the system which establishes the fact that as inlet exergy or the wind speed increases there is a rise in exergy efficiency.

The hybrid system comprising of the two mentioned stand-alone system is much more exergy efficient since for the same inlet conditions, there is a combined output from the two systems. The exergy efficiency of these hybrid system lies in between 40 and 45%.

References

1. Sumathi, S.L.A.: Solar PV and Wind Energy Conversion systems: An Introduction to Theory, Modeling with MATLAB/SIMULINK, and the Role of Soft Computing Techniques. Springer, Switzerland (2015)
2. Joshi, A.S.I.D.: Thermodynamic assessment of photovoltaic systems. Solar Energy **83**, 1139–1149 (2009)
3. Sahina, A.D.I.D.: Thermodynamic analysis of solar photovoltaic cell systems. In: Elsevier Solar Energy Materials & Solar Cells, pp. 153–159 (2007)
4. Faramarz Sarhaddi, S. F.: Exergetic optimization of a solar photovoltaic array. J. Thermodynamics **11** (2009)
5. Daniel de B. Mesquita, J. L.: A review and analysis of technologies applied in PV modules. In: Marcelo, M., Villalva, G. (ed.). IEEE. Brazil (2019)
6. Meng Lia, D.Z.: Photovoltaic thermal module and solar thermal collector connected in series: energy and exergy analysis. In: Elsevier Energy Conservation and Management, pp. 206–218 (2020)
7. Betz, A.: Introduction to the Theory of Flow Machines. Pergamon Press, pp. 167–174 (1966)
8. Dincer, I.M.R. (n.d.).: Exergy: Energy, Environment and Sustainable Development
9. Ehyaeia, M.A.A.A. (n.d.).: Energy, Exergy, Economic and Advanced and Extended Exergy Analyses of a Wind Turbine
10. Cengel, Y.: Thermodynamics an Engineering Approach. United States of America, 8th edn. McGraw-Hill Education (2015)

11. Tsatsaronis, A.B.: Thermal Design and Optimization. John Wiley & Sons (1996)
12. Sahin, A.D.D.: Thermodynamic analysis of wind energy. Int. J. Energy Res, 553–566 (2006)
13. Khosravi, A.R.K.: Energy, exergy and economic analysis of a hybrid renewable energy with hydrogen storage system. Elsevier (2018)

A Short Review on Oil Palm Biomass as Feedstock for Pyrolysis Process

Pranshu Shrivastava ⬡, **Anil Kumar** ⬡, **and Arkom Palamanit** ⬡

1 Introduction

Oil palm, originated from West Africa, is one of the leading oleaginous perennial food crops because of ample precipitation (1600–2000 mm/yr.) and daylight hours (5–7 h/day) which is widely grown in tropical regions of Southeast Asia [1]. The countries like Thailand, Malaysia, and Indonesia mainly produce edible cooking oil from oil palm. The favorable conditions for the abundance of oil palm include its high oil yield nearly 5 t/ha per year, which higher than soybean, sunflower, and rapeseed, also support provided in terms of initiatives and policies of government for the palm oil production. These are the key factors in order to record a rocketing growth production of oil palm crop over the years. According to report, Southeast Asia region accounts for approximately 50 million tonnes of palm oil, about 90% of global exports and 85% of the total world production [2].

The development and growth in palm oil production result in a large quantity of oil palm biomass both from industries and plantation area which can pose a severe environmental menace. The oil palm biomass (OPB) includes oil palm trunk (OPT), oil palm fronds (OPF), and oil palm roots (OPR) from the plantation area while oil

P. Shrivastava
Energy Technology Program, Faculty of Engineering, Prince of Songkla University, 15 Karnjanavanich Rd., Hat Yai, Songkhla 90110, Thailand

A. Kumar
Department of Mechanical, Production & Industrial and Automobile Engineering, Delhi Technological University, Shahbad Daulatpur, Delhi 110042, India

Centre for Energy and Environment, Delhi Technological University, Shahbad Daulatpur, Delhi 110042, India

A. Palamanit (✉)
Energy Technology Program, Department of Specialized Engineering, Faculty of Engineering, Prince of Songkla University, 15 Karnjanavanich Rd., Hat Yai, Songkhla 90110, Thailand
e-mail: arkom.p@psu.ac.th

palm kernel shell (OPS), oil palm fiber (OPFB), oil palm decanter cake (OPDC), empty fruit bunches (EFB), and sewage sludge (OPSS) from the industries. This leads an interest in utilization of oil palm biomass as source of renewable energy which can produce various value-added products because it contains preferably rich nutritional values and high physicochemical properties. The inspiration to convert oil palm biomass is due to the fact that biomass approximately constitutes up to 90% from the palm oil production facility, while the palm oil is 10% only [3]. The oil palm biomass (OPB) includes oil palm trunk (OPT), oil palm fronds (OPF), and oil palm roots (OPR) from the plantation area while oil palm kernel shell (OPS), oil palm fiber (OPFB), oil palm decanter cake (OPDC), empty fruit bunches (EFB), and sewage sludge (OPSS) from the industries.

Biomass is converted into biofuels or bioenergy by using various process such as mechanical conversion, thermochemical conversion, biochemical conversion, and some hybrid systems. These different processes provide different final forms of bioenergy (heat or power) or biofuels (liquid, gas, or solid). Amongst these processes, pyrolysis is a thermochemical conversion process which thermally decomposes the feedstock at higher temperatures ranging from 300 to 600 °C in the absence of oxygen or air [4]. The pyrolysis process converts biomass into mainly bio-oil while biochar and pyrolysis gas as by-products. Depending upon the heating rate, pyrolysis can be classified generally as slow and fast pyrolysis. Moreover, there are many factors such as reaction temperature, heating rate, and vapor residence time also play an important role in pyrolysis process [5].

In the era of advancements in technologies to develop alternative fuel, fast pyrolysis is a good option to produce bio-oil. The bio-oil obtained from slow pyrolysis is lower than from fast pyrolysis. Moreover, there are several other factors such as the reactor type, operating conditions (heating rate, pyrolysis temperature, vapor residence time, etc.), biomass property, biomass type, etc., which influences the yield and quality of the products obtained from pyrolysis process [6].

The product obtained from the pyrolysis process, i.e., bio-oil has a higher heating value and high energy density compared to raw biomass. Moreover, storage, handling, and transportation are very easy for bio-oil in comparison with the raw biomass [7]. It can be used as fuel in an engine after upgradation, direct fuel in boiler furnaces and converted into value-added products for chemical, medicine, and food industries. Biochar can be used as soil nutrient, water absorbent, generates heat for use in other processes. Pyrolysis gas can be used as reheating the reaction chamber or generate heat energy for pyrolysis process. There are various major aspects and future challenges for the sustainable utilization of OPB as a renewable resource are discussed in the subsequent sections.

2 Oil Palm Biomass and Its Characterization

Biomass is abundant in most of the Asian countries whose prime industry is agricultural-based. Thailand has a high dependency on the agriculture and thus has a

high potential for biomass applications. Primarily, Thailand is rich in biomasses such as corn stalks, rubber wood bark, rice husks, oil palm shell, cassava roots, rubber wood sawdust, and empty fruit bunches. These biomasses can be obtained from the replantation, harvesting, and industries associated with agricultural products. Oil palm is one of the most grown crops in Thailand, and it is one of the top ranked exporters for palm oil, after Indonesia and Malaysia. For example, the government of Thailand encourages the participation in the field of oil palm industries by setting a target of 1,632,000 ha plantation by 2036. The biomass from oil palm is mainly found from the harvesting area and waste from palm oil industries. The replantation of oil palm tree provides OPT, OPF, and OPR, while the processing of fresh fruit bunches provides OPFB, EFB, OPS, OPDC, and OPSS from wastewater treatment. Reports indicated that milling 1 tons of fresh fruit bunches generates approximately 300 kgs of EFB, 200 kgs of OPFB, and 60 kgs of OPS [8]. These values are observed by a lot of research works in the field oil palm biomass processing. However, EFB, OPT, OPF, OPR, and OPDC from oil palm residues both from industries and plantation can be utilized for biofuel or bioenergy applications.

There are some physical, chemical, and thermal aspects need to be considered for obtaining physicochemical properties of OPB, and some of them are mentioned in Table 1. Particularly, OPT, OPF, and EFB have high amount of volatile matter in the range of 75.43–79.98% (wt.) [4]. The OPDC and OPSS possess high ash contents, while OPS and OPR have high amounts of fixed carbon contents. The main elemental compositions from OPB were in line with the proximate analysis results. The higher heating value (HHV) was found very low, i.e., around 15–20 MJ/kg, which needs upgradation to be used as a potential fuel. The OPF, OPR, OPT, and OPFB had high percentage of cellulose and hemicellulose contents in the range of 49 and 23% (wt.), respectively [4, 7]. The thermogravimetric analysis showed that the thermal decomposition of OPB depends on the lignocellulosic components. The inorganic elements in OPB such as potassium, calcium, magnesium, iron will act as catalyst during pyrolysis process and also influence the product yield and quality.

3 Technological Advancements for OPB Conversion

There are a lot of technologies which involved thermochemical conversion, and pyrolysis is one of the commonly used methods to convert OPB to bio-oil. Mostly, pyrolysis is done at higher temperatures in the absence of air or oxygen to produce bio-oil, biochar, and syngas. OPB can be converted to bio-oil by using fast or slow pyrolysis. The fast pyrolysis is carried out at a higher temperature of over 500 °C with a shorter residence time of less than 30 s. It is more favorable process as it provides higher liquid product rather than solid or gas product. Several research works are reported for the conversion of OPB into bio-oil, and the focus is basically on the conversion for EFB only rather than considering other potential parts from OPB. Pyrolysis reactors further classified into fluidized type, fixed bed type, agitated bed

Table 1 Physiochemical properties of biomass samples [4]

Properties	Type of biomass samples							
	OPT	OPF	OPS	OPR	OPDC	EFB	OPFB	OPSS
Proximate Analysis								
Moisture content	8.21	8.11	8.92	11.92	10.38	8.93	9.53	14.42
Volatile matter	79.98	78.90	72.58	68.32	72.13	79.16	75.43	51.70
Fixed carbon	16.17	17.87	26.14	22.28	12.75	15.43	18.24	11.42
Ash	3.69	3.12	1.35	8.49	14.79	5.48	5.82	36.43
Ultimate Analysis (wt.%, dry basis)								
Carbon	45.91	45.54	53.29	50.58	45.60	49.73	50.85	32.39
Hydrogen	6.38	6.39	6.15	6.28	6.41	6.92	6.71	4.83
Nitrogen	0.42	0.19	0.30	0.28	2.38	1.01	1.05	5.07
Oxygen*	33.19	33.24	41.54	44.60	36.40	32.61	42.14	32.08
Sulfur	0.01	0.01	0.01	0.01	0.24	0.07	0.09	0.77
Lignocellulosic content (wt.%, dry basis)								
Cellulose	39.40	54.35	37.95	49.00	21.85	37.82	33.58	2.59
Hemicellulose	25.97	20.72	11.52	19.19	13.51	21.85	25.41	8.25
Lignin	6.64	8.96	38.15	29.26	20.91	12.16	21.38	30.47
Extractives	27.99	15.96	12.38	2.55	43.73	28.17	19.63	58.69
Elemental composition (mg/kg)								
Silicon (Si)	142.07	353.18	143.71	426.18	364.44	330.54	375.41	10,907.68
Iron (Fe)	1086.96	581.11	2438.06	7959.66	1525.26	533.80	889.73	5915.44
Calcium (Ca)	1668.57	3817.10	21,407.33	841.39	14,366.06	5103.02	4042.47	38,886.73
Magnesium (Mg)	10.98	1630.22	744.80	1311.93	4737.85	2705.57	2026.11	18,892.55
Sodium (Na)	431.83	209.15	47.87	99.01	96.85	285.67	63.02	526.18
Potassium (K)	175.63	20,994.0	2708.62	7909.73	27,435.65	46,331.60	7362.17	70,791.31
Higher heating values and lower heating values (MJ/kg)								
HHV	17.41	17.62	20.21	19.42	18.68	17.90	18.72	19.53

type or auger type systems, although the process can be catalytic and non-catalytic depends on the operating conditions and required output.

3.1 Fast Pyrolysis

The fast pyrolysis is a process which often used to convert biomass into bio-oil by thermal cracking process from OPB. Some researchers derived bio-oil using OPB with fast pyrolysis process which particularly focusses on high yield by reduction of ash contents in OPB. For example, Abdullah treated ash content in EFB by water which reduces the ash contents and determined the effect on bio-oil yield [9]. With an increase in ash contents in the biomass, the bio-oil yield is decreased because of the presence of potassium which favors secondary reactions inside the reaction chamber. This leads to increase in the production of aqueous liquid, non-condensable gases, and char yields. There are many factors other than ash content in biomass which influences the yield of bio-oil, some of them are pyrolysis reaction temperature, heating rate, vapor residence time, particle size, biomass type, etc. [4, 7]. It was found that at higher pyrolysis temperatures and high heating rates the overall yield of bio-oil is higher because of the maximum thermal decomposition of the feedstock. Kim et al. investigated the highest yield from EFB around 36.47%, in comparison with palm kernel and jatropha seed shell cake with very low yields of 30.26 and 27.18%, respectively [10]. The catalytic fast pyrolysis gives good quality of bio-oil rather than non-catalytic provides comparatively poor quality of bio-oil.

3.2 Slow Pyrolysis

Slow pyrolysis is traditionally used for charcoal making and now modernly used as biochar production process. Generally, it is associated with low heating rates, relatively high vapor residence times, and a lower pyrolysis reaction temperature than fast pyrolysis in the range of 400 °C [5]. The yield of the slow pyrolysis includes biochar (solid product) accompanied with liquid and gaseous products. Palamanit et al. investigated the effects of pyrolysis process OPT, OPF, and OPS. The pyrolysis of OPS provided the highest amount of biochar. The obtained liquid product contained highly oxygenated compounds as indicated by GC-EI/MS and also high water content with low pH. The HHV of the liquid product was low (18–23 MJ/kg), while HHV of the solid product was relatively high (25.14–28.45 MJ/kg). The biochar obtained from slow pyrolysis can be considered as an alternative for activated carbon or bio-filter applications as indicated by scanning electron microscope (SEM) [7]. The slow pyrolysis produces pyrolysis gas which has a low potential for fuel applications.

4 Comparison Between Petroleum Fuel Oil and Bio-Oil from OPB

Table 2 shows the fuel properties of bio-oil obtained from pyrolysis of OPB in comparison with the fuel oils to determine the potential application and quality of the product obtained from pyrolysis process. Instead of the pyrolysis process involved, the product obtained from pyrolysis of OPB which contains comparatively high amounts of moisture and oxygen contents than the fossil fuel. Also, these traits are unfavorable for a fuel for engine because it contains high moisture and ash contents which reduces the heating value and ignition rate as well as the combustion delay; high solid contents also possess a problem for injection systems and valves, while higher oxygen contents provoke to thermal instability, which will affect the storage properties of bio-oil obtained from pyrolysis process [12]. Although these problems can be overcome by using additional methods such as water washing of OPB prior to pyrolysis and fractional distillation process to decrease the moisture content of the raw biomass and also results in low solid contents in the final product [13]. Moreover, there are some positive aspects which overcome the side effects of high water contents in the product obtained from pyrolysis process for use as a fuel in engine. Bio-oil is used to upgrade the flow characteristic of oil, which contributes a uniform temperature profile in the combustion chamber of engine and also reduces the NO_x emission. These parameters improve the combustion characteristics by reducing the CO_2 emission [14]. Furthermore, the low sulfur contents in bio-oil in comparison with petroleum fuel oil will involve in immediate health and environmental benefits. Petroleum fuel oils are lighter than the bio-oil when compared with HFO, but bio-oil viscosity lies between diesel/LFO and HFO as mentioned in Table 2. These are the main properties which will influence the bio-oil properties. The flash and pour points for bio-oil are nearly same to diesel/LFO, while acidic nature of bio-oil is much higher than either diesel/LFO or HFO. This is because of the presence of carboxylic acids mainly palmitic, lauric and acetic acids in the bio-oil [15]. Therefore, the bio-oil obtained from OPB has a tendency to corrode during transportation of fuels [14].

5 Future Scope and Challenges

Bio-oil, obtained from pyrolysis of biomass has been popularly known as a potential renewable source because of producibility and universal availability. Currently, the research works are associated with the bio-oil production in laboratory scale, although pilot scale production is limited because of limited scope. Bio-oil is considered to be a substitute fuel for power generation using diesel engines, gas turbines, steam power plants, etc., while it is more in the early stages to be used as a transportation fuel [16].

Over the few years, a lot of research works has been employed to utilize the large amount of OPB generated from industries and plantation areas, especially in

Table 2 Properties of bio-oil from OPB compared with petroleum fuel oils [11]

	Bio-oil from pyrolysis		Petroleum fuel oils		
	Fast pyrolysis	Slow pyrolysis	Diesel/LFO	Low sulfur HFO	High sulfur HFO
Moisture (%)	6.66–24.3	5.2	0.025	–	0.1
Proximate analysis (%)					
Volatile matter (VM)	42.3–60	–	–	–	–
Fixed carbon (FC)	41–58.7	–	–	–	–
Ash contents (AC)	0.39–3.22	0.1	0.01	-	0.03
Total solid contents (TSC)	24.1	–	0	–	0.2–1
Ultimate analysis (%) C	35.29–69.35	68.26	86–86.52	87.3	82.79–85.6
H	5.08–9.61	8.02	13.3–13.6	12.19	10.3–12.98
O	20.02–57.02	21.57	0.03	0.17	0.48–0.6
N	0.0113–2.74	2.02	0.04–0.2	0.06	0.2–0.6
S	<0.1	0.03	0.11–0.18	0.28	2.5–3.55
HHV (MJ kg^{-1})	20.23–36.06	31.44	45.8	44.7	43.4
Density (kg m^{-3}) @ 15 _°C	900–1548	1031	853–890	939	940–979
Kinematic viscosity ($mm^2\ s^{-1}$)	38.4 @ 25 °C	13.52 @ 50 °C	3–7.5 @40 °C	–	351 @ 50 °C
Flash point (°C)	–	65	60–98	–	100
Pour point (°C)	–	12	15	–	21
Total acid number	67.75–110	102.9	–	0.451	–
KOH (g kg^{-1}) pH	2.33–3.4	3.6	Neutral	–	–

Southeast Asia. This will help to improve the shape of national economy as well as achieve the environmental benefits globally. The various encounters correlated with the oil palm industry related with health issues, land issues, conservation of biodiversity and replantation which endangers the sustainable supply of OPB also result in the development of bio-oil industry [11].

In addition to these challenges, there are a lot of continuous efforts in order to improve the bio-oil quality produced from OPB by using hydrocracking, catalytic upgrading, hydrotreating, and steam reforming which will enhance its competency as engine fuel. It is important to optimize cost for OPB pre-treatment and pyrolysis technologies, which will nurture public sector which involves in equipment handling and efficient pyrolysis process. Furthermore, subsidy and financial support must be provided to oil palm stakeholders, simultaneously involves in growth of marketing strategy [17]. Finally, proper collaboration from public and private sector is necessary to support the bio-oil industry with OPB as feedstock to finish it in sustainable manner.

6 Conclusion

There is a concern regarding awareness for environmental sustainability and energy security along with the huge supply of OPB (mainly in Southeast Asia), and favorable physicochemical characteristics are the driving forces which attract the researchers to utilize it as a potential feedstock to convert biomass into biofuels like bio-oil in recent years. The trend shows that the fast pyrolysis shows potential to convert OPB into useful form of energy in a convenient and sustainable manner by extensive utilization as an incipient process. The bio-oil obtained from OPB has less heating value, more acidic than fuel oil and slightly heavier despite either slow or fast pyrolysis used. More research works should be done in order to upgrade the fuels from pyrolysis of OPB. The flash and pour points are nearly similar to the light fuel oil, while the viscosity lies between heavy and light fuel oils. Till now, the inadequate triumph of oil palm biomass conversion using pyrolysis process has many challenges in this research area could be focused in the future.

References

1. Palm, O., Fruit, E., Fibres, B.: Effect of Silica Bodies on the Mechanical Behaviour of Oil Palm Empty Fruit Bunch Fibres **9**, 7041–7058 (2014)
2. Preechajarn, S., Prasertsri, P.: Thailand Biofuels Annual, Washington, DC, USA (2018)
3. Misson, M., Haron, R., Kamaroddin, M.F.A., Amin, N.A.S.: Pretreatment of empty palm fruit bunch for production of chemicals via catalytic pyrolysis. Bioresour. Technol. **100**, 2867–2873 (2009). https://doi.org/10.1016/j.biortech.2008.12.060
4. Shrivastava, P., Khongphakdi, P., Palamanit, A., Kumar, A., Tekasakul, P.: Investigation of physicochemical properties of oil palm biomass for evaluating potential of biofuels production

via pyrolysis processes. Biomass Convers. Biorefinery (2020). https://doi.org/10.1007/s13399-019-00596-x

5. Mckendry, P.: Energy production from biomass (part 2): conversion technologies **83**, 47–54 (2002)

6. Leng, L., Huang, H.: An overview of the effect of pyrolysis process parameters on biochar stability. Bioresour. Technol. **270**, 627–642 (2018). https://doi.org/10.1016/j.biortech.2018.09.030

7. Palamanit, A., Khongphakdi, P., Tirawanichakul, Y., Phusunti, N.: Investigation of yields and qualities of pyrolysis products obtained from oil palm biomass using an agitated bed pyrolysis reactor. Biofuel Res. J. **6**, 1065–1079 (2019). https://doi.org/10.18331/BRJ2019.6.4.3

8. Mushtaq, F., Abdullah, T.A.T., Mat, R., Ani, F.N.: Optimization and characterization of bio-oil produced by microwave assisted pyrolysis of oil palm shell waste biomass with microwave absorber. Bioresour. Technol. **190**, 442–450 (2015). https://doi.org/10.1016/j.biortech.2015.02.055

9. Abdullah, N., Sulaiman, F., Gerhauser, H.: Characterisation of Oil Palm Empty Fruit Bunches for Fuel Application **22**, 1–24 (2011)

10. Kim, S.W., Koo, B.S., Ryu, J.W., Lee, J.S., Kim, C.J., Lee, D.H., Kim, G.R., Choi, S.: Bio-oil from the pyrolysis of palm and Jatropha wastes in a fluidized bed. Fuel Process. Technol. **108**, 118–124 (2013)

11. Chang, S.H.: An overview of empty fruit bunch from oil palm as feedstock for bio-oil production. Biomass Bioenerg. **62**, 174–181 (2014). https://doi.org/10.1016/j.biombioe.2014.01.002

12. Zhang, L., Liu, R., Yin, R., Mei, Y.: Upgrading of bio-oil from biomass fast pyrolysis in China: a review. Renew. Sustain. Energy Rev. **24**, 66–72 (2013). https://econpapers.repec.org/RePEc:eee:rensus:v:24:y:2013:i:c:p:66-72

13. Capunitan, J.A., Capareda, S.C.: Characterization and separation of corn stover bio-oil by fractional distillation. Fuel **112**, 60–73 (2013)

14. Oasmaa, A., Czernik, S.: Fuel oil quality of biomass pyrolysis oilsstate of the art for the end users. Energy Fuels **13**, 914–921 (1999). https://doi.org/10.1021/ef980272b

15. Khor, K.H., Lim, K.O., Zainal, Z.A.: Characterization of bio-oil: a by-product from slow pyrolysis of oil palm empty fruit bunches. Am. J. Appl. Sci. **6** (2009). https://doi.org/10.3844/ajassp.2009.1647.1652

16. Chiaramonti, D., Oasmaa, A., Solantausta, Y.: Power generation using fast pyrolysis liquids from biomass. Renew. Sustain. Energy Rev. **11**, 1056–1086 (2007). https://doi.org/10.1016/j.rser.2005.07.008

17. Umar, M.S., Jennings, P., Urmee, T.: Strengthening the palm oil biomass Renewable Energy industry in Malaysia. Renew. Energy. **60**, 107–115 (2013). https://doi.org/10.1016/j.renene.2013.04.010

Performance Analysis of Savonius Hydrokinetic Turbine with Stationary Deflector Plates Using CFD

Pawan Kumar Pulijala and **Raj Kumar Singh**

1 Introduction

A hydrokinetic turbine [1, 2] is a turbine which transforms the kinetic energy of flowing water in rivers, streams, canals, etc., into electrical energy or electricity. This renewable source of electricity production can be harnessed from a low head of moving water. Savonius HKT, a drag-based rotor comprises of curved blades positioned in manner such that it is S-shaped due to which it experiences less drag while moving against the flow than when moving with the water flow. The differential drag is responsible for the rotation of the turbine [3]. The advantages associated with this turbine are attributed by the low construction cost of the turbine, less noise while operation and the ability to accept fluid from any direction. However, the main disadvantage is its low efficiency in comparison with other HKTs such as the Darrieus turbine [2]. It can be utilized for low speed applications as it has low starting torque because simple making and the economic factors suggest its use in electricity generation coupled with a generator involving minimal and easier maintenance.

Numerous research works [4] to improve the performance of the turbine setup have been performed such as multistage rotor, changing the overlap ratio [5], increasing the number of blades [6], positioning the rotor in various inclinations [7], positioning moving deflector blades to the rotor [8], varying the blade profiles and rotational speed of turbine [9] were all considered to increase the efficiency of the HKT.

However, in this paper, we have considered a vertical axis Savonius HKT whose 3D computational model has been developed for simulating its performance. The numerical simulation has been done using the realizable k-ε turbulence model, and the solution of transport equations was done using the commercially available ANSYS CFX (vR19.0) which uses finite volume method (FVM) to describe the flow field.

P. K. Pulijala (✉) · R. K. Singh

Department of Mechanical, Production & Industrial and Automobile Engineering, Delhi Technological University, Delhi 110042, India
e-mail: pawankumarpulijala@gmail.com

The investigation proceeds to identify the upstream and downstream flow conditions and aims to find out about the magnitude of velocity variation upon the installment of the static deflector plates across the flow channel [10–12]. Based on the above observations, suitable calculations such as torque and coefficient of power were calculated by keeping a fixed rotational speed of the rotor. These results were tallied with the experimentation [11] and deviation was found. The paper also compares the extent of improvement in the performance of the turbine with deflector plates in a closed water channel to that of a turbine without these plates.

2 Methodology

A conventional two-blade Savonius rotor has been developed used the ANSYS design modeler considering the various design parameters as shown in Table 1.

The geometry file is imported to the ANSYS mesh module and is suitably meshed (Figs. 1 and 2).

A similar procedure is adopted in the design for stator. The stator here is a rectangular channel ($300 \times 300 \times 2000$ mm^3) of water flowing along the z-direction. Later named sections have been assigned for the purpose of interfacing and applying boundary conditions. The stator is later meshed accordingly with a resolution of 7.0 for the default size set by the module (Figs. 3, 4 and 5).

The boundary conditions have been specified with almost negligible speed of the rotor (Table 2).

The fluid problem is preprocessed with the aid of ANSYS CFX-PRE setup module, wherein all the necessary criteria and constraints have been provided and initialized. Rotor and stator domains have been created and assigned to the corresponding mesh profiles along with the interfacing between the two domains and were later initialized.

Similarly, the stator having stationary deflector blades (advancing blade-180 $\times$ 150 mm^2 and returning blade-120 $\times$ 150 mm^2) is modeled, meshed and preprocessed with the same criteria as mentioned earlier (Figs. 6, 7 and 8).

Table 1 Design parameters

Parameter	Value
Height of the rotor (H)	140 mm
Blade arc angle (Ψ)	124°
Diameter of blades (d)	135.9 mm
Thickness of blades (t)	2 mm
Diameter of the rotor (D)	240 mm
Height of cylindrical enclosure (H')	150 mm
Diameter of cylindrical enclosure (D')	250 mm
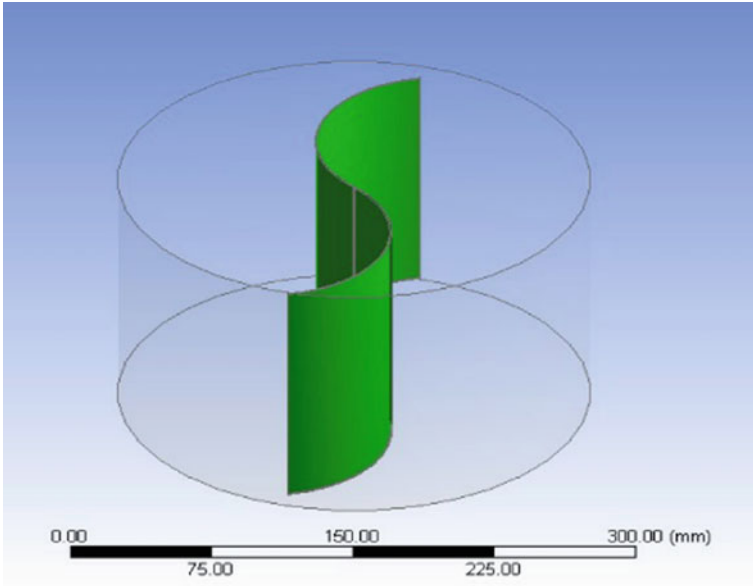
Fig. 1 Creation of geometry of rotor
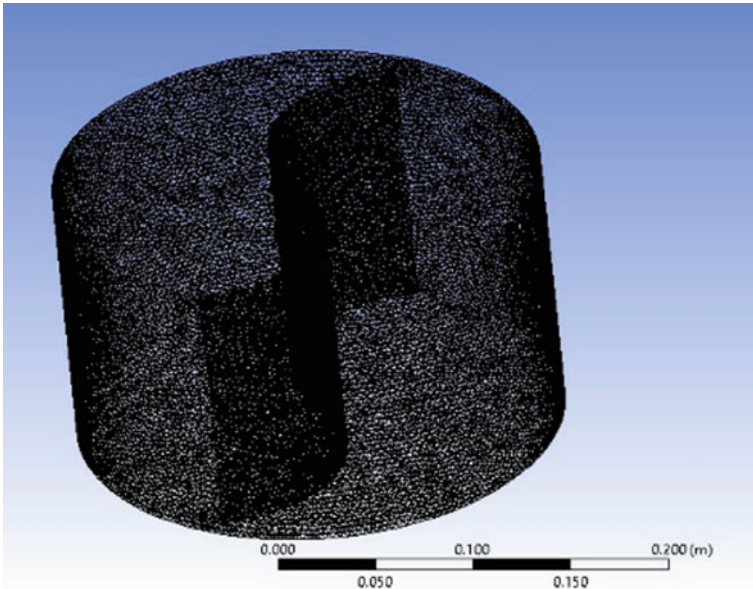
Fig. 2 Meshed rotor
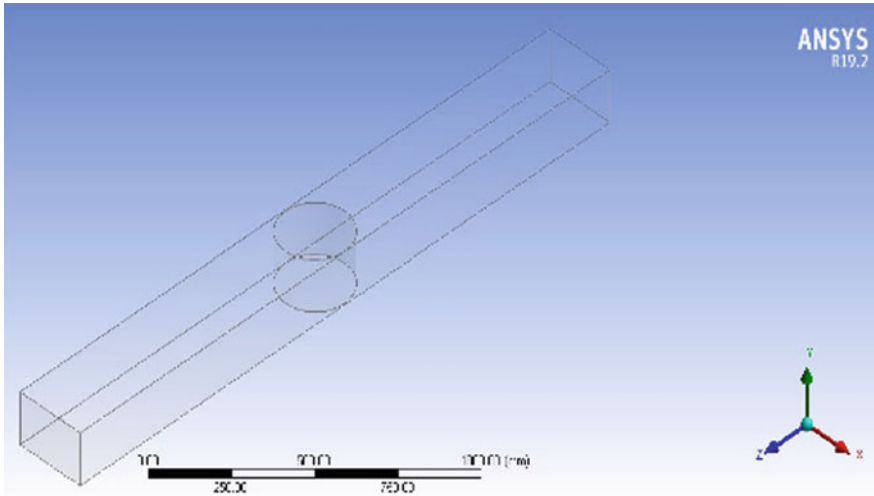
Fig. 3 Creation of geometry of water channel
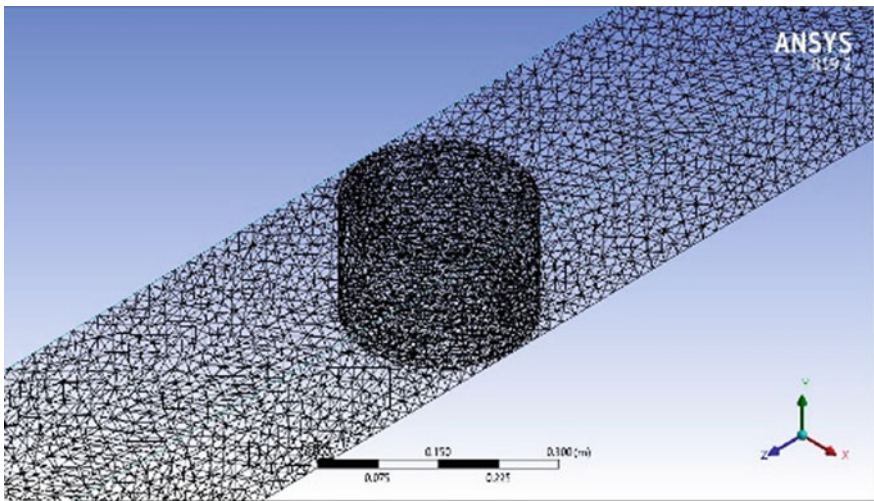
Fig. 4 Meshed stator

The energy flux of the flowing water is dependent on its density, cross-sectional area of the channel and of course the velocity of the water. Therefore, power produced by the turbine can be written as:

$$P = \frac{1}{2} x \rho A v \tag{1}$$
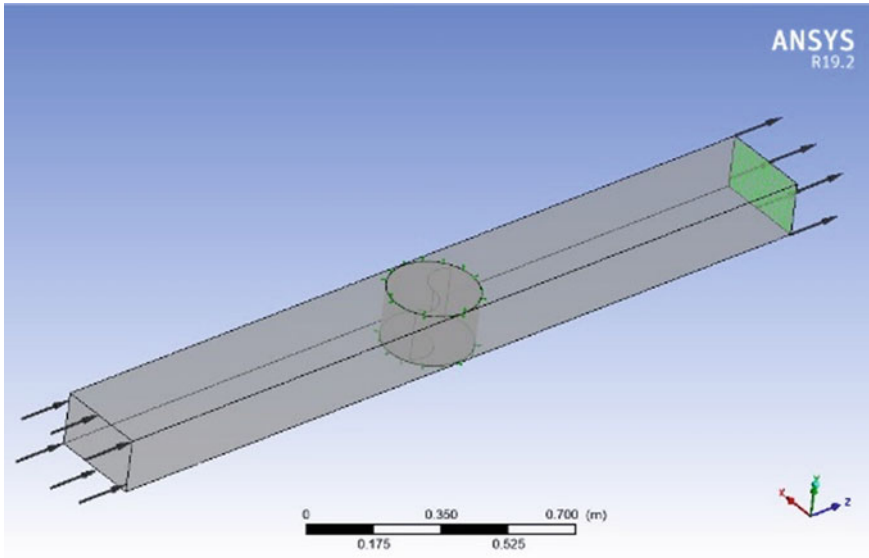
Fig. 5 Preprocessing through ANSYS CFX-PRE

Table 2 Boundary conditions

Location	Boundary condition
Inlet	Velocity $v = 2$ m/s; Re 1.32×10^5 [11]
Outlet	Static pressure $= 1$ atm
Stator's wall	No slip wall conditions
Domain motion (rotor)	Rotating (with almost zero angular velocity)
Domain motion (stator)	Stationary
Buoyant model	9.81 m/s^2 along negative Y-direction
Analysis type	Transient blade row (with medium intensity)

The torque obtained through the simulation can be verified using the below equation comprising of V_1 and V_2 which are upstream and downstream velocities of the flowing water and radius (r) of the rotor as 0.06795 m.

$$T = \tfrac{1}{2}\rho A r (V_1^2 - V_2^2) \tag{2}$$

Coefficient of torque (Ct) and coefficient of power (Cp) are given by:

$$C_t = 4T/\rho U^2 D^2 H \tag{3}$$
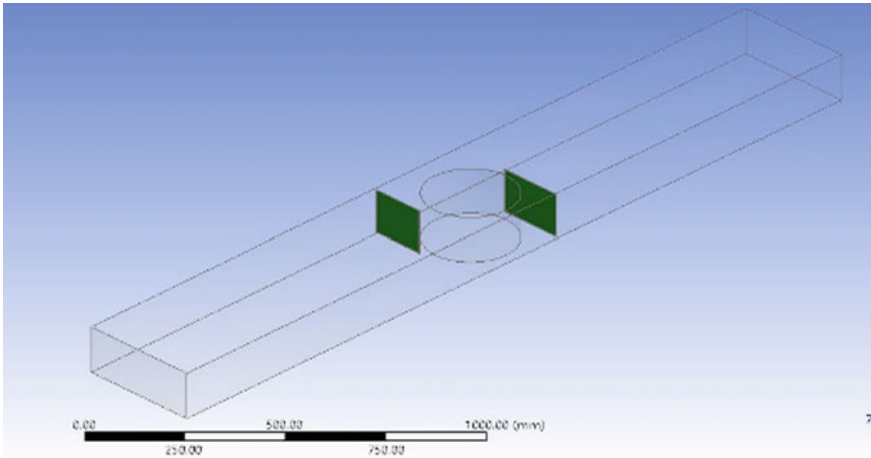
Fig. 6 Geometry with stationary deflector blades
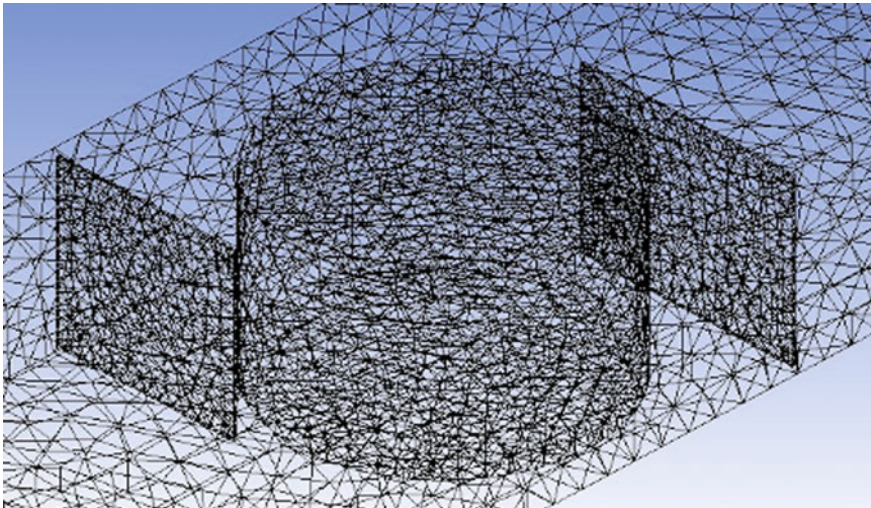
Fig. 7 Meshed stator

$$Cp = TSR \times Ct \tag{4}$$

The tip speed ratio can be calculated with U being the free stream velocity

$$TSR = \omega D/2U \tag{5}$$

Therefore,
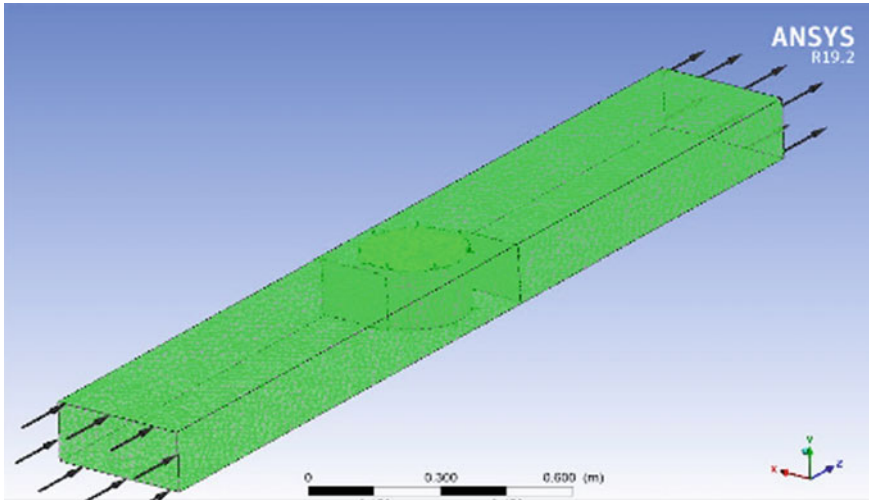
Fig. 8 Preprocessing through ANSYS CFX-PRE

Power can be written as:

$$P = Tx\omega. \tag{6}$$

Based on the above mathematical formulae, the results obtained by Golecha et al. [11] were validated. Also, keeping the rotational speed of the rotor to 2.79 rad/s, the improvement in the performance due to deflector plates was gauged and has been tabulated.

3 Results and Discussion

The various contours of pressure, velocity and turbulence kinetic energies are indicated below when a free stream velocity of 2 m/s was chosen (Figs. 9 and 10).

The above velocity contours clearly depict an increment in the horizontal velocity component when the deflector plates are positioned across the water channel as they block the passage of fluid which causes a sudden increase in the velocity of water striking the vanes and thus enabling the turbine to rotate with a much higher angular velocity. The upstream velocity is found to be doubled when the deflector plates have been positioned as a result a 2 m/s water flow turns out to be nearly 4 m/s. This increase contributes to the increase in the rotational speed of the turbine.

Similarly, once the turbine completes one full rotation the presence of a returning deflector blade causes the fluid to be directed out with a tremendous increase in its velocity from 4 m/s to 7 m/s.
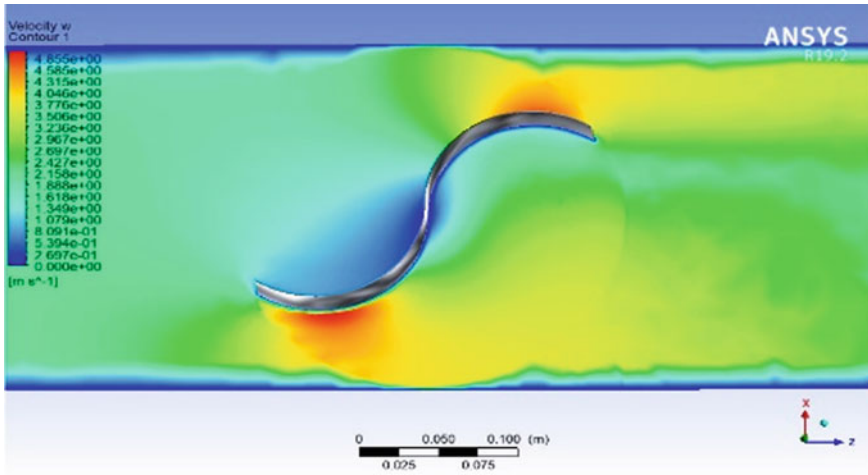
Fig. 9 Velocity distribution
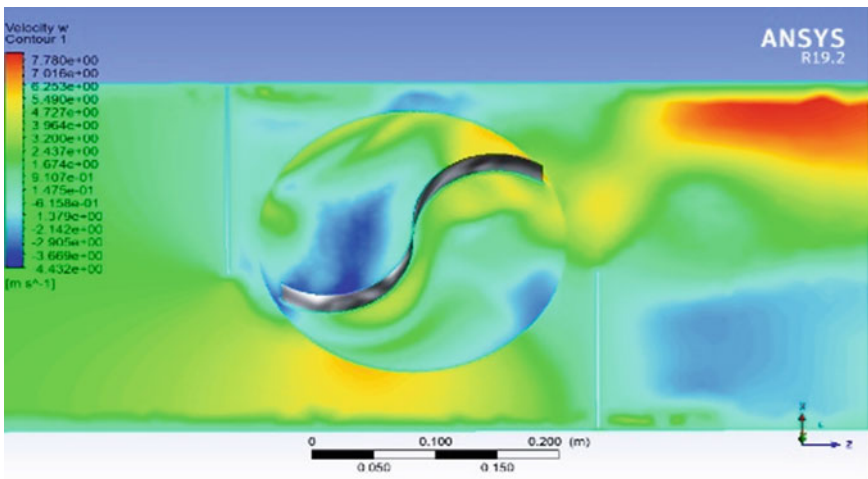
Fig. 10 Velocity distribution with deflector plates

The presence of these deflectors not only impacts velocity but also the pressure acting on the vanes of the turbine. There is a significant amount of increase in the pressure on the upstream side of the turbine arising due to the advancing deflector plate which creates a pressure difference which is the driving factor of the sudden increase in its inlet velocity and also is the cause for the rotation of the turbine (Figs. 11 and 12).
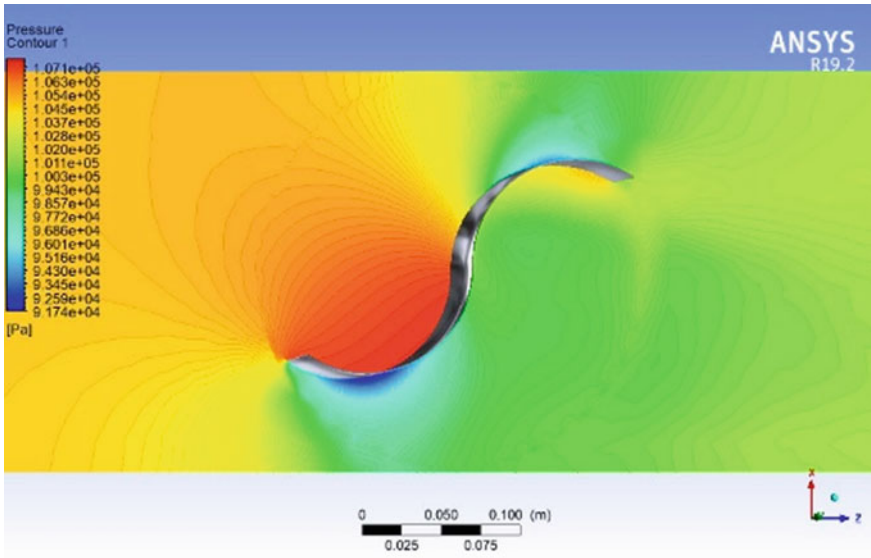
Fig. 11 Pressure distribution
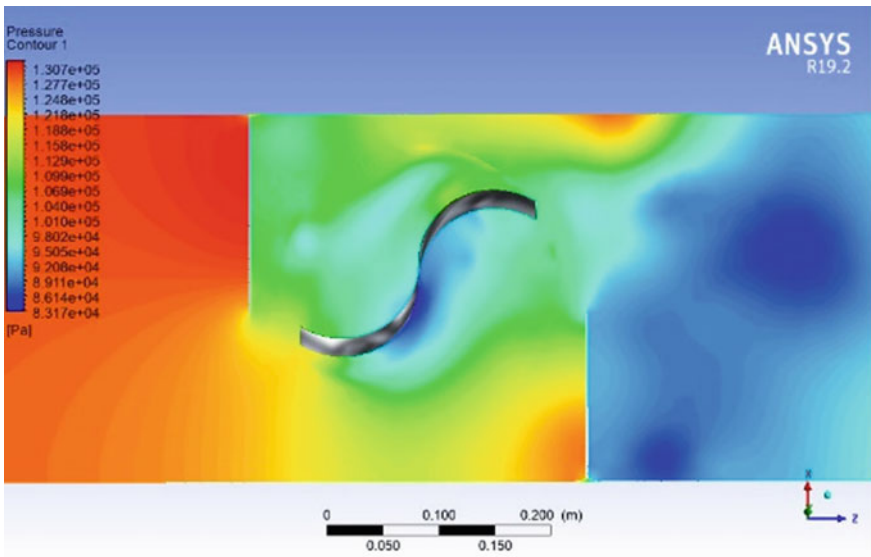
Fig. 12 Pressure distribution with deflector plates

The below simulated results also show that there is some increment in the turbulence when the deflector plates have been placed along the flow water channel (Figs. 13 and 14).
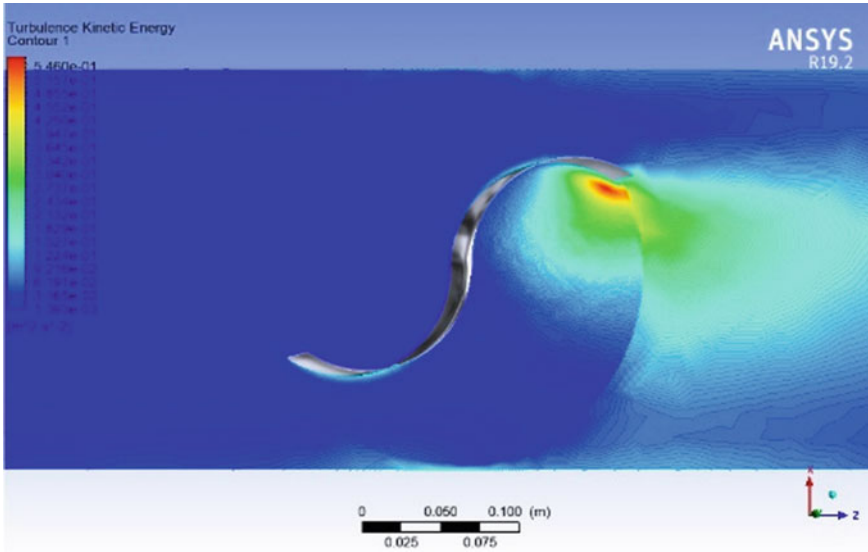
Fig. 13 Turbulence kinetic energy (KE)
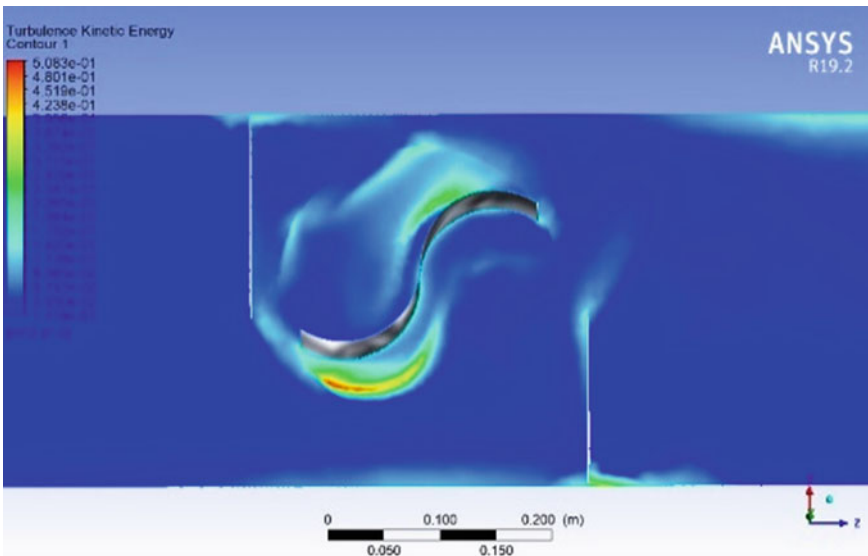
Fig. 14 Turbulence KE with deflector plates

Table 3 Comparison of the performance of rotor with and without the presence of deflector plates in the channel with a flow of Re 1.32×10^5 [11]

Performance parameter	Rotor without deflector plates in the channel	Rotor with deflector plates in the channel
Torque about Y-axis	0.15 N-m	0.18 N-m
Torque (experimental)	–	0.138 N-m
Coefficient of power (Cp)	0.23	0.27
Cp (experimental)	–	0.18
Rotational speed of rotor (kept fixed)	2.97 rad/s	3.97 rad/s

Now, the free stream velocity of the water flowing to the channel is kept at Reynold's number of 1.32×10^5 and the simulation was once again carried out on the basis of the criteria taken by Golecha et al. [11] and the results have been validated and tabulated in Table 3.

4 Conclusion

The CFD simulation of the Savonius rotor presented us with clear visual representations of flow pattern and property contours of water flowing in the channel. As it was earlier aimed, this paper gauges the performance of the SHKT under free and restricted flow circumstances. Based on the earlier experimental values, the speed of the turbine was held constant and the torque and Cp were computed. From the comparison, the following conclusions can be drawn:

i. Positioning the deflector plates along the flow path showed an increase in the magnitude of the upstream velocity striking the blades of the turbine.
ii. The flow restriction caused the input velocity to be double its initial value.
iii. Although there is no significant improvement in the turbine alone, by positioning the plates externally indicated the improvement in the turbine setup on the whole.
iv. There is an improvement in the coefficient of power (Cp) by positioning deflector plates from 0.23 to 0.27.
v. There is a marginal deviation of 0.09 observed from both experimental and simulated results.

Nevertheless, the scope for further improvisation in the performance, thereby leading to effective and higher power extraction is still wide open for future research work and definitely takes us forward to cope up with the increasing power demand by means of achieving green energy.

References

1. Author, F.: Article title. Journal **2**(5), 99–110 (2016). Mahmud, M.S., Reza, K.N., Rahman, M.Z.: Performance study of a small scale water current turbine. Int. Res. J. Eng. Technol. (IRJET) e-ISSN: 2395–0056 **05**(05), 4419–4423
2. Laws, N.D., Epps, B.P.: Hydrokinetic energy conversion: technology, research, and outlook. Renew. Sustain. Energy Rev. **57**, 1245–1259 (2016)
3. Verma, A.K., Saini, R.P.: Efficiency measurement techniques of hydro kinetic turbines: a review. In: Alternate Hydro Energy Centre, International Conference on Hydropower for Sustainable Development ICHPSD-201
4. Gejendhiran, S., Arulkumar, D., Gnanasekar, S., Gokul, C., Gokulraj, M.: Experimental investigation of modified Savonius rotor: a review. Int. J. Res. Eng. Sci. Manage. **2**(1), 203–206. January-2019 ISSN (Online): 2581-5792
5. Mabrouki, I., Driss, Z., Abid, M.S.: Performance analysis of a water Savonius rotor: effect of the internal overlap. Sustain. Energy **2**(4), 121–125; 122–124
6. Thiyagaraj, J., Rahamathullah, I., Suresh Pabu, P.: Experimental investigations on the performance characteristics of a modified four bladed Savonius hydro-kinetic turbine. Int. J. Renew. Energy Res. **6**(4), 1533–1535 (2016)
7. Bagre, N., Patel, V.: Experimental analysis of Savonius hydro turbine at various inclinations. J. Thermal Energy Syst. **2**(3.5), 2–6
8. Wahyudi, B., Adiwidodo, S.: The influence of moving deflector angle to positive torque on the hydrokinetic cross flow Savonius vertical axis turbine. Int. Energy J. **17**, 11–22 (2017)
9. Hemrom, R.D., Sarkar, S.: Performance analysis of Savonius hydrokinetic turbine in array based at same input velocity at different speed, (India), pp 5–7, ISBN: 978-93-86171-39-9
10. Mohamed, M.H., Janiga, G., Pap, E.: Optimization of Savonius turbines using an obstacle shielding the returning blade. D. Thévenin Lab. of Fluid Dynamics and Technical Flows, University of Magdeburg "Otto von Guericke", Germany www.elsevier.com/locate/renene
11. Golecha, K., Eldho, T.I., Prabhu, S.V.: Influence of the deflector plate on the performance of modified Savonius water turbine. Appl. Energy **88**, 3207–3321 (2011)
12. Kailash, G., Eldho, T.I., Prabhu, S.V.: Performance study of modified Savonius water turbine with two deflector plates. Int. J. Rotating Mach. Volume 2012, Article ID 679247, 12 pages https://doi.org/10.1155/2012/679247

Design and Development

Experimental Investigations on Bubble Detection in Water–Air Two-Phase Vertical Columns

Abhishek Saraswat [ORCID]**, Ashok K. Prajapati, Rajendraprasad Bhattacharyay, Paritosh Chaudhuri, and Sateesh Gedupudi**

1 Introduction

Two-phase flow is a commonly observed phenomenon in numerous industrial applications like heat and thermal power plants, boilers and evaporators, hydrocarbon recovery systems, etc. In some processes, ingress of gas in liquid-phase is intentional and desirable [1, 2]. In specific to nuclear applications, a two-phase flow may occur due to specific configurational constraints within the facility or due to accidental scenarios. For instance, charging of a molten-metal facility in presence of an inert cover gas may lead to trapped gas zones/dead pockets in inclined sections like nozzles for wetted configuration pressure transmitters [3]. Formation of re-circulation zones in complex structures and manifolds could also result in localized trapped gas regions. Even with proper gas venting arrangements, accidental scenarios like break in the heat sink (molten-metal/water or molten-metal/helium heat-exchangers) could lead to ingress of gas-phase within molten-metal. An additional scenario [4] could lead to the formation of helium bubbles within a lithium/lithium-based coolant like eutectic lead–lithium (Pb–16Li, hereafter, referred to as PbLi) due to interaction with neutrons to produce tritium, which is the fuel for nuclear fusion reaction. Presence of gas-phase leads to hot-spots within the reactor, reduced tritium breeding ratio (TBR) as well as an improper shielding [4]. It is, therefore, critical and imperative to detect the occurrence of such a phenomenon to initiate proper remedial measures. Though the requirements for two-phase detection are well identified [5–8], a lack of proper

A. Saraswat (✉) · A. K. Prajapati · R. Bhattacharyay · P. Chaudhuri
Institute for Plasma Research, Gandhinagar 382428, India
e-mail: asaraswat@ipr.res.in

P. Chaudhuri
Homi Bhabha National Institute, Trombay, Mumbai 400094, India

A. Saraswat · S. Gedupudi
Heat Transfer and Thermal Power Laboratory, Department of Mechanical Engineering, Indian Institute of Technology Madras, Chennai 600036, India

diagnostics tools for high-temperature applications (350–400 °C) with corrosive molten PbLi cannot be overlooked in specific to nuclear fusion applications.

As a first step to address some of the complexities involved in two-phase flow detection, experimental studies have been carried out in static water columns for detection and quantification of air-pockets. Numerous tools, ranging from non-contact techniques like induction-based measurements, gamma-ray attenuation methods, ultrasound absorption technique, etc., to contact techniques like electrical conductivity-based and capacitance-based detection probes, are readily available for low temperature two-phase flow detection and characterization studies [9–18]. However, the present study takes into account the benefits and constraints in view of further adaptability towards molten PbLi applications. Here, we have explored, in detail, electrical conductivity-based principle because of its better response, easier fabrication, relatively simpler operation, high-temperature operational feasibilities and reduced installation requirements where non-contact techniques may prove challenging. For molten-metal application, electrical conductivity principle is rather advantageous because of high electrical conductivity of the fluid itself. Secondly, only one probe is needed to be inserted; as the second conducting electrode can be configured using metal pipes of facility. In this view, a prototype sensor probe is fabricated and simultaneous high-speed imaging is performed to quantify relevant dimensions of air-pockets colliding with the probe. Leverage of transparency from water medium in the present study provides visual corroboration before proceeding towards completely opaque molten-metal applications.

2   Experimental Method and Apparatus

To fabricate the electrical conductivity sensing probe, two solid SS rods of 1.6 mm diameter are shaped in needle-point configuration and embedded in a slotted solid nylon tube. The slots are filled with an epoxy-resin based binder to provide electrical insulation and to hold the rods rigidly. Overall diameter of the sensor after fabrication is ~7.4 mm. The length of conducting bare SS electrodes are visually identified to be 1.5 mm and further confirmed by a handheld multimeter. Basic electrical circuit diagram with assembled components to gather output voltage signal, with and without interaction with an air bubble, along with principle of probe operation is demonstrated in Fig. 1.

The red section (AB) indicates electrically conducting exposed part of one SS rod in the medium, while the grey circles depict a vertically rising air bubble. For bubble positions (a) to (c), the voltage signal read by the data-acquisition (DAQ) will remain the same due to the availability of conducting path between exposed lengths of both the electrodes. Voltage signal dip across sensing resistor will begin as soon as the bubble completely encapsulates conducting portion of at least one of the electrodes, i.e. position (d) because of high resistivity of surrounding air. At this point, conduction current through the encapsulated electrode is nil, but very low insulation leakage current flows, giving rise to a drop in circuit current. After point
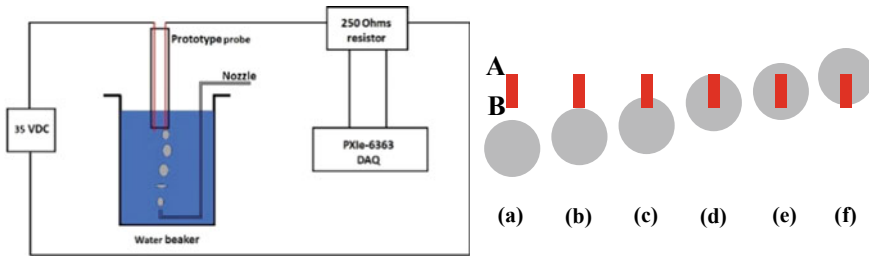
Fig. 1 Basic circuit diagram and operational principle of electrical conductivity probe

(f), when some of the conducting portion of electrode is exposed, the voltage will rise rapidly to achieve its normal value. Hence, a detectable air-pocket requires thickness greater or at least equal to the exposed length of conducting electrode. To carry out proof of concept studies, an experimental facility is fabricated which consists of a glass beaker with dimensions 150 mm (L) × 150 mm (W) × 200 mm (H). A square cross section reduces lens effects, ensuring correct dimensional measurements of injected air-pockets using camera and ruler arrangements. A primary nozzle with a 3-mm bore is installed with a provision to vary bore diameter by installing a 24-gauge hypodermic needle on top of primary nozzle. An air compressor with downstream pressure regulator and needle valve assembly is used to regulate injected airflow into static water column. High-speed imaging is performed at 60 frames per second (FPS) to register the trajectory of traversing bubbles through optical facility. For a fixed pressure downstream, nozzle generates an array of bubbles with fixed time interval in between. A LabVIEW platform-based application is developed to log and display real-time data at 5 ms interval using PXIe-6363 module. To capture finer details of interactions between the bubble and electrode, developed application also provides data logging at 1.5 MHz sampling rate.

3 Data Analysis, Results and Discussion

3.1 Trajectory and Probe Interaction Analysis for Bubbles Generated Using Hypodermic Needle

The probe location is fixed in a manner that all the ejected bubbles hit one of the electrodes. The captured flow trajectory is shown in Fig. 2 and number of distinct V-shaped voltage dips is shown in Fig. 3 against time axis (in seconds) for one such array of 07 bubbles confirm the detection of all the bubbles.

The encircled region (red) after second voltage dip depicts the residence-time of a bifurcated portion of second bubble, stuck at the probe bottom, interacting intermittently with the electrode before getting hit by the third bubble. This phenomenon
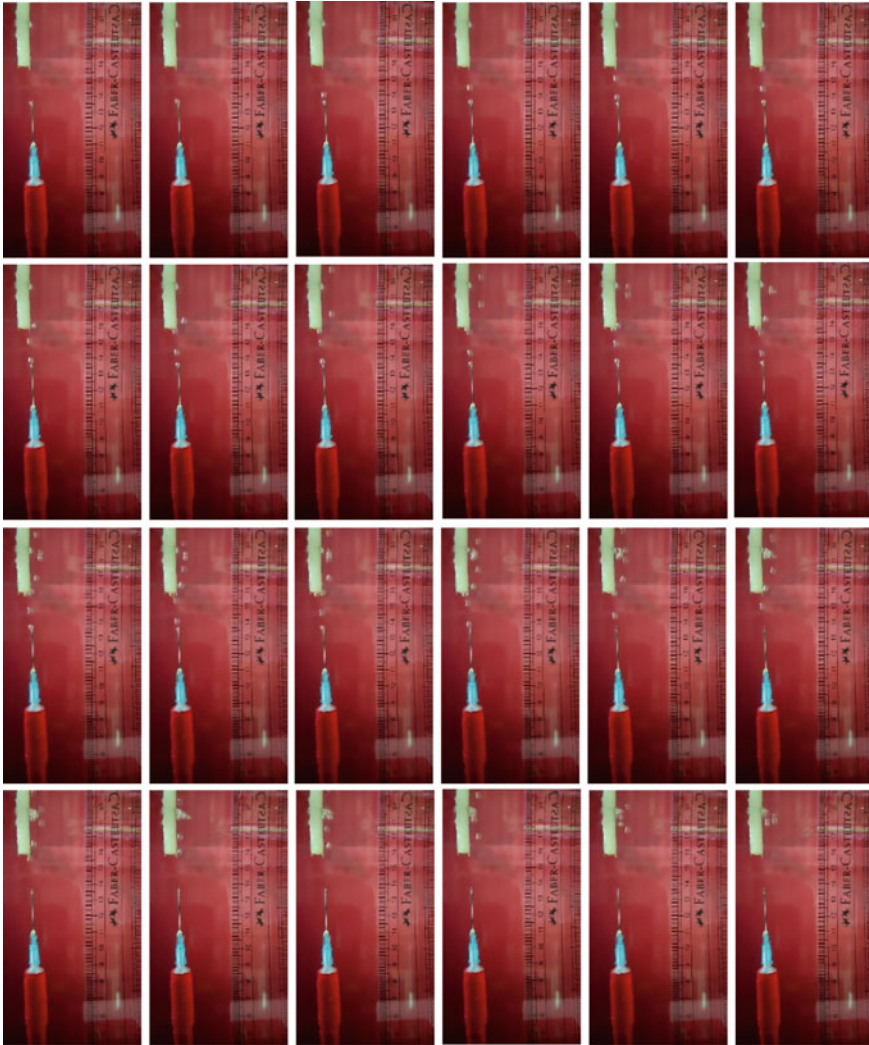
Fig. 2 Trajectory of bubbles generated from hypodermic needle towards probe

is clearly visible at 120 FPS. Such observation further corroborates sensitivity of fabricated probe towards two-phase detection.

An arbitrary threshold voltage sets a datum to calculate voltage dip time and therefore bubble traversing time. Impact of the threshold selection is discussed later during air-pocket thickness estimations. A ruler set within the plane of generated bubbles coupled with imaging field-view normal to this plane provides necessary means to measure dimensions of air-pocket just after ejection, and thereafter, to analyse distortions during rise in the column. Representative sets of extracted frames
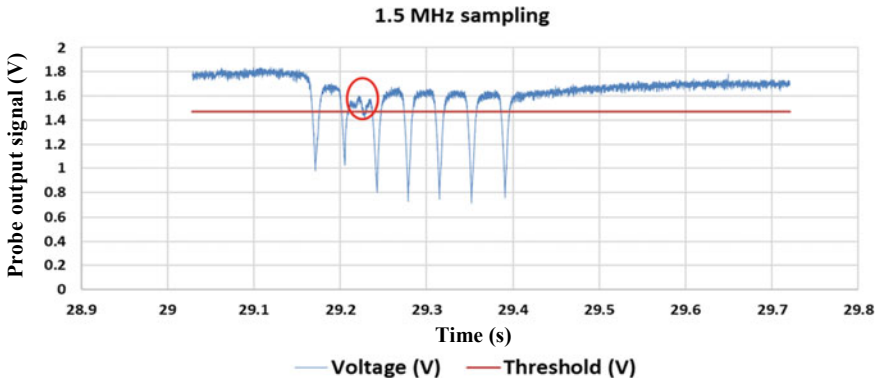
Fig. 3 High frequency sampling of probe voltage for bubbles generated through hypodermic needle

are further used to calculate average vertical velocity component of rising air-pockets from projected vertical displacement against the ruler and number of image frames to estimate the time utilized for that displacement. For each bubble analysed, vertical velocity is calculated using top reference, bottom reference and centre reference with reference to bubble profile. Average vertical velocity is then calculated using average of the velocities for analysed bubbles of selected sets for a selected reference position.

An important observation from visualization study is that smaller diameter bubbles do not tend to distort much, but acquire a convex shape, which could be accounted for vertical differential pressure. This observation is highlighted in Fig. 4 for frames taken just after release of a bubble and just before its impact with the probe, respectively. Estimated envelope dimension for the air-pocket is approximately 4 mm using projections (yellow) against the ruler. However, as the top and bottom of the pocket have nearly similar convex curvatures, it can be seen that along the conducting electrode axis, the air-pocket thickness is always less than 4 mm (~approximately 3 mm).

(a)   (b)
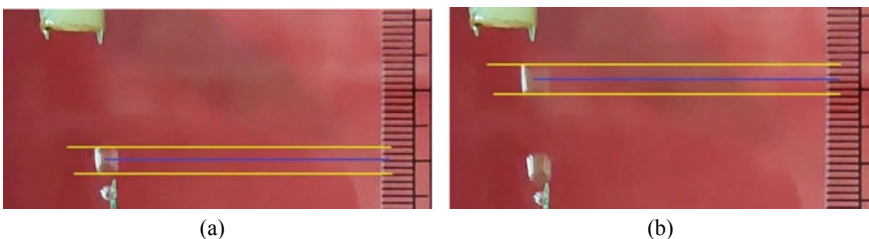
Fig. 4 Close-up views of an air bubble show a convex shape: **a** just released from the hypodermic needle; **b** after ~33 ms from the first frame

3.2 Trajectory and Probe Interaction Analysis for Bubbles Generated Using 3-mm Bore Nozzle

Similar methodology is applied to the bubbles generated from 3-mm bore nozzle and the logged voltage data for an array of 2 bubbles is presented in Fig. 5. Variation in the magnitude of voltage dips can be explained by the difference in sizes and difference in the ways of interactions. A smaller sized air-pocket generates a lower magnitude voltage dip as it traverses across the electrode relatively faster compared to a bigger sized pocket.

Figure 4 may be contrasted with Fig. 6 to analyse distinctly visible distortions and flattening for air-pockets of larger diameter within same time frame. Another critical observation is that the air-pockets tend to have a non-zero horizontal velocity component, which may depend on the density of surrounding liquid phase. A higher liquid–gas density ratio (similar to molten-metal scenario) may force the air-pockets to rise vertically upwards along least resistance path.
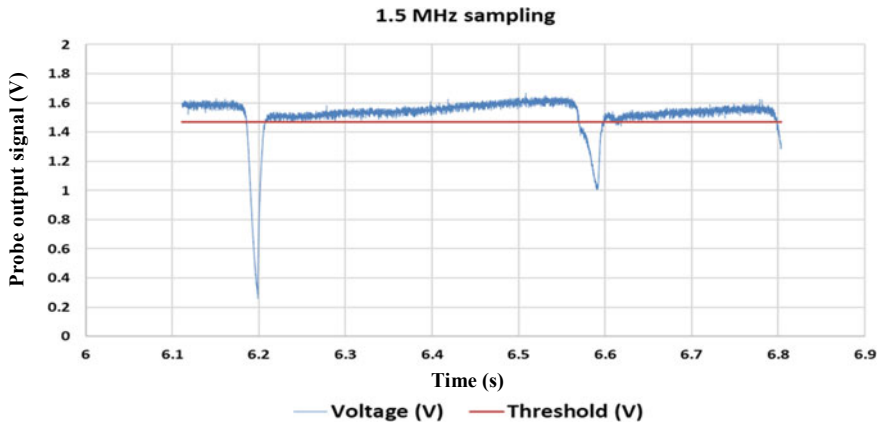
Fig. 5 High frequency sampling of probe voltage for larger diameter bubbles

(a)   (b)
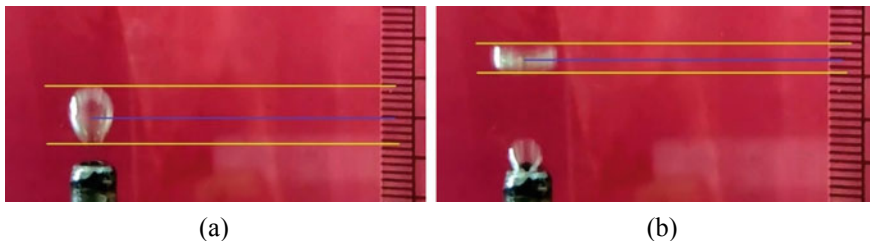
Fig. 6 Close-up views of visible dimensional distortions in an air-pocket: **a** just released from 3-mm bore nozzle; **b** after ~33 ms from the first frame

Table 1 Calibration details for prototype probe

Condition	No. of sample sets	No. of samples	Weighted average (V)
Water medium (no bubble)	–	>5,00,000	1.872
Bubble from 3-mm bore nozzle	05	1098	1.053
Bubble from hypo. needle	10	1107	1.397

3.3 Calibration of Probe Prototype

Although sub-microsecond logging is strikingly advantageous for offline data processing to gain detailed insights, it is highly desirable to monitor and detect the presence of bubbles in real-time during facility operations. To achieve this, a 0.2 kHz sampling rate is selected based on the analysis of characteristic V-shaped voltage dips from previous samples so as to acquire enough information for conclusive detection of an air-pocket. This calibration, performed with an input supply of 35 VDC and output tapped across a 250 Ω resistor, holds true for a sampling interval of 5 ms. A precise calibration may be obtained with higher sampling frequency. Table 1 reports the weighted average for a number of sample sets to arrive at the calibration voltage output signals.

It should be noted that for same sized air-pocket, voltage dip depends on the way of interaction between bubble and electrode(s) and on the sampling rate. A low frequency sampling may result in an over-estimation of output voltage during bubble interaction (refer data from Table 1 at 0.2 kHz sampling and magnitude of dips from Figs. 3 and 5 at 1.5 MHz sampling). Dip in the voltage also depends on the distorted profile and vertical alignment of an air-pocket along sensing probe. However, average dips measured (~820 mV for 3-mm bore nozzle and ~ 475 mV for hypodermic needle) at 0.2 kHz sampling suffice to detect the presence of an air-pocket in the water column. Figure 7 presents the voltage data against representative samples for continuous ingress of high-pressure gas-phase into liquid-phase, approximately, simulating a loss of heat sink accident. As observed from the logged voltage data, the flow configuration appears to be churn flow with extremely disordered bubble motions and a wide variety of bubble diameters corroborated by voltage dips of different magnitudes. A continuous 3-h duration performance test in a bubbly column corroborates no drift/degradation in the calibration signal for the fabricated probe.

3.4 Estimations of Air-Pocket Thickness

Assuming symmetricity in the V-shape dips of voltage profiles, voltage dip time is estimated as half of the total time between the points where the voltage curve intersects preset threshold. Product of the calculated average vertical velocity with estimated voltage dip time gives effective air void thickness (d) additional to the encapsulated conducting portion of electrode (l). Thus, the total effective air-pocket

(a)   (b)
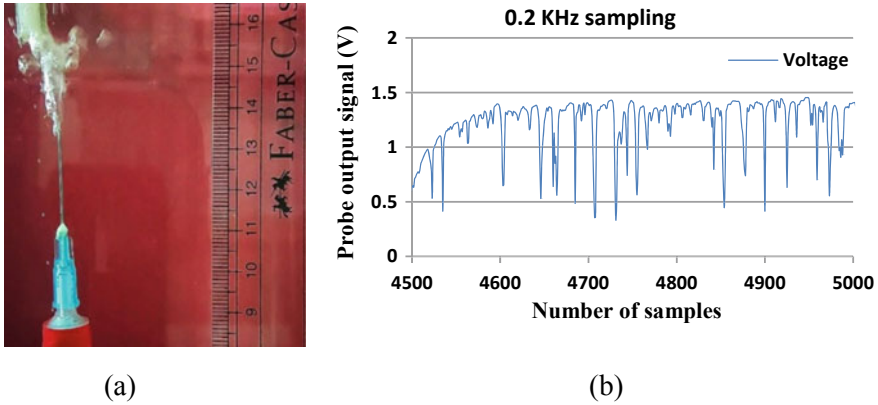
Fig. 7 Performance of prototype probe for extreme bubbly flow (similar to churn flow): **a** frame for generated extreme bubbly flow; **b** logged voltage data for flow characterization

thickness is estimated by summing the two components $(l + d)$ as elaborated in Fig. 8. Average velocity for smaller bubbles varied between 0.32 and 0.35 m/s while those for larger bubbles varied between 0.25 and 0.26 m/s.

Estimated average air-pocket thicknesses (Y-axis) against samples (X-axis) for two sets each of bubbles generated from hypodermic needle and 3-mm bore nozzle with different thresholds are shown in Fig. 9. For a given threshold, samples 1 to 3 represent average pocket thicknesses for the first set considering bottom, centre and top references for velocity calculations. Similarly, samples 4 to 6 represent corresponding quantities for the second set. As observed, a change in threshold level significantly impacts estimated pocket thickness. In these calculations, for a given case, the pocket thickness is calculated by using a common threshold level for all the voltage dips.

However, for an exact thickness calculation, each air-pocket must be analysed individually because the dip for each pocket depends on its way of interaction with the probe. In the present case, threshold levels of 1.45 V and 1.47 V seem to predict air-pocket thicknesses with relatively higher accuracy as could be confirmed from projected dimensions against the ruler for the case of smaller bubbles. However, an exact error analysis requires considerably higher frame rate imaging tools along with

(a)   (b)

Fig. 8 Estimations of air-pocket thickness: **a** spherical pocket; **b** distorted pocket
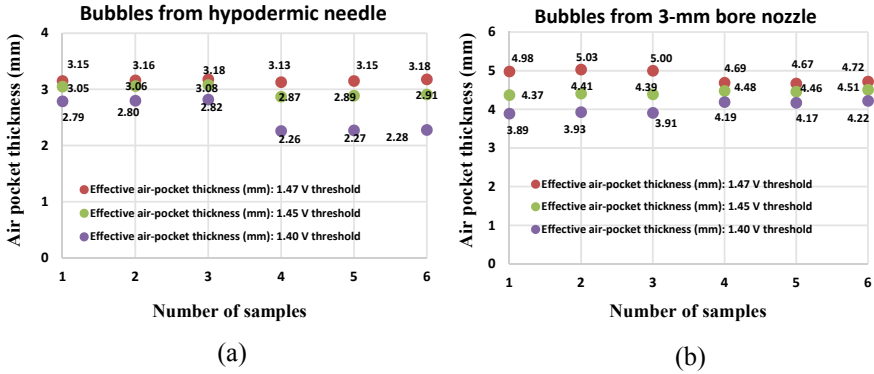
Fig. 9 Impact of threshold voltage selection on estimated air-pocket thicknesses for bubbles generated: **a** from hypodermic needle; **b** from 3-mm bore nozzle
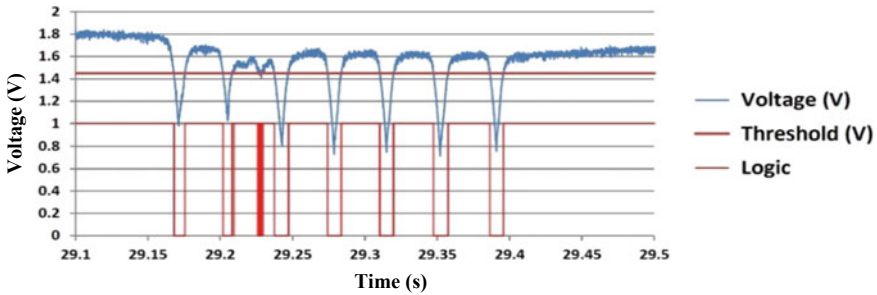
Fig. 10 Threshold method to estimate local void fraction in two-phase water–air column

ruler measurements at sub-mm level, which are limited in the present study. In the present study, exact error quantification may not be possible but it can be concluded that the thickness of air-pockets could be estimated within sub-mm accuracy.

3.5 Preliminary Attempts to Estimate Local Void Fractions

Threshold method is utilized to estimate local void fractions in the static water column using an excel logic, which assigns normalized values of 0 or 1 by comparing probe voltage with preset threshold. Basic underlying assumption is that during the rise time, till the voltage intersects threshold limit, the air-pocket encloses point A of electrode ("A" defined in Fig. 1).

Ratio of time duration for which logic remains LOW (0) to the total time duration under consideration is defined as local void fraction at the point "A". For the particular
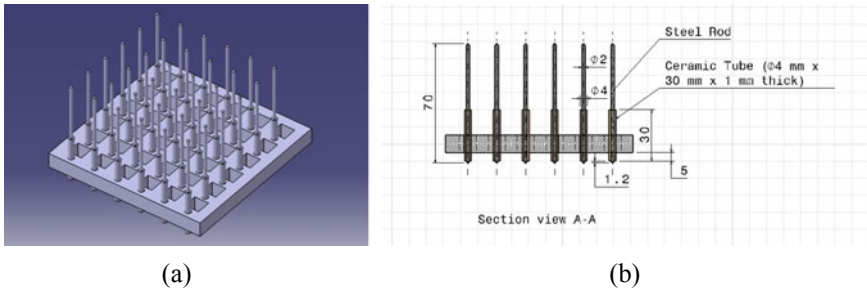
Fig. 11 Proposed sensor array assembly for detection of gas bubbles over a wider cross section: **a** 3D view of sensor assembly; **b** dimensional schematic for sensor array assembly

case for a time duration of 0.4 s and a threshold of 1.45 V, as shown in Fig. 10, a local void fraction of ~16.15% is estimated using the method described.

4 Future Plans

Future activities include gas-pockets detection in flowing water facility with forcedly injected bubbles. Additionally, to cover a wider flow detection area, a sensor array assembly is being fabricated as shown in Fig. 11, which will be initially validated with gas sparger arrangements. Further, the sensor concept will be adapted for high-temperature molten PbLi applications with application of alumina coating. A promising coating must provide an electrical insulation characteristic, corrosion resistance and high-temperature compatibility up to 400 °C to render it useful for molten-metal applications relevant to nuclear fusion power plants.

5 Conclusion

An extensive experimental study is successfully performed towards the quantification of air-pockets in water–air two-phase vertical columns. A test facility suitable to address experimental requirements is fabricated with provisions of generating different diameter bubbles and different injection frequencies. The prototype sensor based on electrical conductivity principle shows promising performance towards two-phase detection. It is observed that the prototype probe could detect all colliding bubbles. Analytically, the estimated air-pocket thicknesses along the sensing direction of probe match reasonably well with visualized thickness using imaging techniques. Present study sets a reference towards further planned activities in molten PbLi two-phase flow detection experiments.

References

1. Zheng, S., Zhu, M.: New process with argon injected into ladle around the tapping hole for controlling slag carry-over during continuous casting ladle. Metals **8**(8), 624 (2018)
2. Gajjar, P., Haas, T., Owusu, K.B., Eickhoff, M., Kowitwarangkul, P., Pfeifer, H.: Physical study of the impact of injector design on mixing, convection and turbulence in ladle metallurgy. Eng. Sci. Technol. Int. J. **22**(2), 538–547 (2019)
3. Saraswat, A., Sahu, S., Rao, T.S., Prajapati, A., Verma, S., Gupta, S., Kumar, M., Bhattacharyay, R.P., Das, P.: Development of sensors for high-temperature high-pressure liquid Pb/Pb-16Li applications (Proceeding of IAEA Fusion Energy Conference-2016) (2016)
4. Kordac, M., Kosek, L.: Helium bubble formation in Pb-16Li within the breeding blanket. Fusion Eng. Des. **124**, 700–704 (2017)
5. Handbook on Lead-bismuth Eutectic Alloy and Lead Properties, Materials Compatibility, Thermal hydraulics and Technologies, NEA, 2015 Edition
6. Lobanov, P.D., Pakhomov, M.A.: Experimental and numerical study of heat transfer enhancement in a turbulent bubbly flow in a sudden pipe expansion. J. Eng. Thermophys. **26**, 377–390 (2017)
7. Martsiniouk, D.Y., Sorokin, A.P.: The questions of liquid metal two-phase flow modelling in the FBR core channels, State Scientific Centre of Russian Federation, Institute of Physics and Power Engineering, Obinisk, Kaluga Region, Russian Federation. https://inis.iaea.org/collection/NCLCollectionStore/_Public/31/032/31032888.pdf
8. Characterization and Testing of Materials for Nuclear Reactors, Proceedings of a Technical Meeting held in Vienna, May 29–June 2, 2006 (IAEA-TECDOC-1545, March 2007)
9. Walker, S.A.: An investigation of Gas bubble generation and measurement in water and mercury. Master's Thesis, University of Tennessee, Knoxville (2010). https://trace.tennessee.edu/utk_gradthes/668
10. Anderson, J. L., Fincke, J.R.: Mass flow measurements in air/water mixtures using drag devices and gamma densitometer. In: Advances in Test Measurement, International Instrumentation Symposium, vol. 15, pp. 587–598. 24/1978/ALBUQUERQUE N.M. Instrument Society of America, Pittsburgh, USA (1978)
11. Stefański, S., Kalawa, W., Mirek, K., Stępień, M.: Visualization and research of gas-liquid two phase flow structures in cylindrical channel. E3S Web of Conferences 14, 01026 Energy and Fuels 2016 (2017)
12. Gundrum, T., Büttner, P., Dekdouk, B., Peyton, A., Wondrak, T., Galindo, V., Eckert, S.: Contactless Inductive bubble detection in a liquid metal flow. Sensors **16**(1), 63 (2016)
13. Stefani, F., Eckert, S., Gerbeth, G., Giesecke, A., Gundrum, T., Räbiger, D., Seilmayer, M., Weier, T.: The DRESDYN project: planned experiments and present status. Proc. Appl. Math. Mech. **17**, 123–126 (2017)
14. Saito, Y., Mishima, K., Tobita, Y., Suzuki, T., Matsubayashi, M.: Measurements of liquid–metal two-phase flow by using neutron radiography and electrical conductivity probe. Exp. Thermal Fluid Sci. **29**(3), 323–330 (2005)
15. Ariyoshi, G., Ito, D., Saito, Y.: Experimental study of flow structure and turbulent characteristics in lead–bismuth two-phase flow. In: Nuclear Back-End and Transmutation Technology for Waste Disposal, pp. 107–115 (2014)
16. Huang, S., Wu, X., Zong, B., Ma, Y., Guo, X., Wang, D.: Local void fractions and bubble velocity in vertical air-water two-phase flows measured by needle-contact capacitance probe. Sci. Technol. Nucl. Installations, Article ID 7532618 (2018)

17. Ratajczak, M., Hernández, D., Richter, T., Otte, D., Buchenau, D., Krauter, N., Wondrak, T.: Measurement techniques for liquid metals. IOP Conf. Series: Mater. Sci. Eng. **228**, 012023 (2017)
18. Krull, B., Strumpf, E., Keplinger, O., Shevchenko, N., Fröhlich, J., Eckert, S., Gerbeth, G.: Combined experimental and numerical analysis of a bubbly liquid metal flow. IOP Conf. Ser.: Mater. Sci. Eng. **228**, 012006 (2017)

Design Optimization and Comprehensive Study of Three-Way Cylindrical-Shaped PPE Sterilizer

Kunal Raghuvanshi , **Jashanpreet Singh Sidhu** , **Jatin Sharma** , **and Rajiv Chaudhary**

1 Introduction

Personal protective equipment (PPE) is protective gear or equipment used by a worker to protect against hazards. PPE restricts interaction with potentially contagious material by establishing a physical boundary between possible contagious material and healthcare staff. PPE, including surgical mask and N95 respirator, is vitally important to the safety of both patient and medical personnel [1]. The demand for this necessary equipment is currently outpacing supply [2]. Sterilization is an efficient method to solve this issue.

Sterilization is a process involving the destruction of all micro-organisms (such as fungi, bacteria, viruses, spore, a unicellular eukaryotic organism such as plasmodium, etc.) and is the highest level of microbial elimination that is possible. Sterilization can be done by physical, chemical, and physiochemical means [3]. This article focused on the physical and chemical methods of sterilization for cleaning and reuse of PPE. Before proceeding to the process of sterilization, general cleaning is a must. Cleaning involves the removal of visible particles (e.g., organic and inorganic material) from equipment.

The sterilization of PPE involves three stages in the order namely general cleaning, ultrasonic sterilization, and ultraviolet sterilization. General cleaning is a precursor to the main events to be followed. The focus of general cleaning remains on cleaning the equipment of all the inorganic and organic materials present on the surface of the equipment in such a way that further stages of sterilization are not hampered by the presence of such materials on PPE equipment. The PPE equipment is placed over the blades which rotate at a predetermined speed and a mixture of warm water and a neutral pH detergent is poured over it. This rotational movement allows the

K. Raghuvanshi (✉) · J. S. Sidhu · J. Sharma · R. Chaudhary
Department of Mechanical, Production & Industrial and Automobile Engineering, Delhi Technological University, Delhi 110042, India
e-mail: raghuvanshikunal3@gmail.com

PPE to be cleaned off all the unwanted materials. The second stage is ultrasonic sterilization which employs high-frequency pressure waves produced with the help of an immersible ultrasonic transducer operating at a moderate frequency. A mixture of water and an oxidizing agent is added to increase the effectiveness of sterilization. The last and most important stage is the ultraviolet sterilization. The higher-energy UV rays are used to kill the RNA of the SARS-CoV-2 which disables the microbes to increase.

2 Problem Formulation

Due to ongoing pandemic like novel coronavirus spread, PPE equipment is necessary more armor for the healthcare worker to fight this novel virus. The COVID-19 pandemic has greatly stretched our healthcare infrastructure. One of the most significant issues is the rising shortages of personal protective equipment (PPE), which is used in health care. It is a big problem for the health and safety of healthcare staff. Sterilization is an effective process to alleviate this problem [4]. The concern behind this paper is inactivating the SARS-CoV-2, the single-stranded RNA (ssRNA) virus that causes COVID-19 along with other harmful bacteria, fungi, pathogens, microbes, etc., through cleaning and sterilization. Currently, without any proper strategy, most of the hospitals are dumping their used PPEs, and demand is outpacing supply. To overcome this problem, this article proposed the design of a three-way cylindrical-shaped PPE sterilizer.

3 Design

3.1 CAD Modeling

CAD modeling of any device/machine is one of the most time-intensive processes. CAD modeling software is dedicated to the specialized job of 3D modeling.

The generic model of a three-way PPE sterilizer was made in AutoCAD 14.0 software. The design of the model is shown in Figs. 1 and 2.

As shown in Fig. 3, sterilizer holds a compact design of a 304 SS cylindrical-shaped container with a shaft in the middle. The shaft holds eight polytetrafluoroethylene plastic straight-line blades each at $\pi/4$ radians to the adjacent. 304 SS hooks are present on the blades for holding the PPE equipment. The shaft is also connected to the induction motor from the bottom. This induction motor gets AC supply from the source for the rotation of the blades. These blades help in general cleaning of the PPE equipment. It has a ring-type transducer attachment (see in Fig. 5) where immersible ultrasonic transducer of 30 kHz frequency is fixed, at the bottom of the container. The ring-type transducer attachment has two rings. The inner ring has 350 mm diameter

Fig. 1 3D model of sterilizer
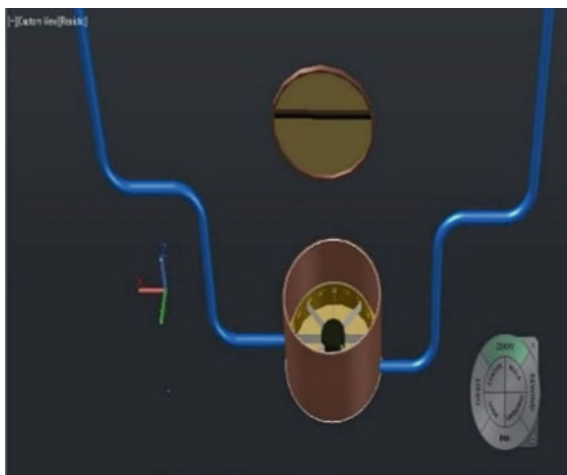
Fig. 2 2D model of sterilizer
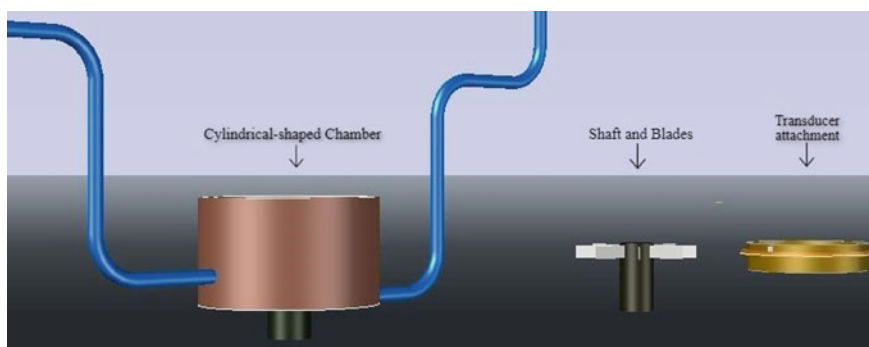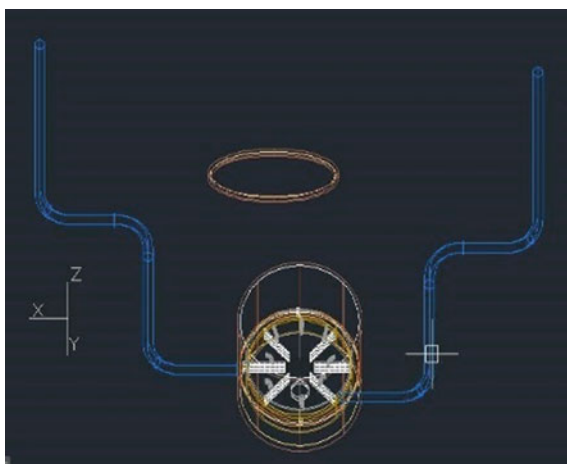
Fig. 3 Main parts of sterilizer

and 50 mm height and the other 15 mm outer ring which is attached around, and the first ring has an outer diameter of 420 mm and an inner diameter of 350 mm. The transducer also gets an AC supply from an external source and is responsible for the ultrasonic cleaning of the equipment. The UV bulb is attached to the hood of the container and causes complete decontamination with ultraviolet germicidal irradiation (UVGI). There are two pipes attached to the cylinder. The left pipe is attached with a one-way inlet valve of 25 mm at the vicinity for the entrance of water or cleansing agent while general wet cleaning and ultrasonic cleaning, respectively. The pipe on the right side is attached with an exit valve of 25 mm. Exit valve has a pressure variant fixed at the pipe exit for causing a difference in pressure whenever required for complete removal of liquid from the container and for drying the equipment before exposing them to UV-C rays. Dimensions of components are shown in Figs. 4, 5 and 6 and Table 1.
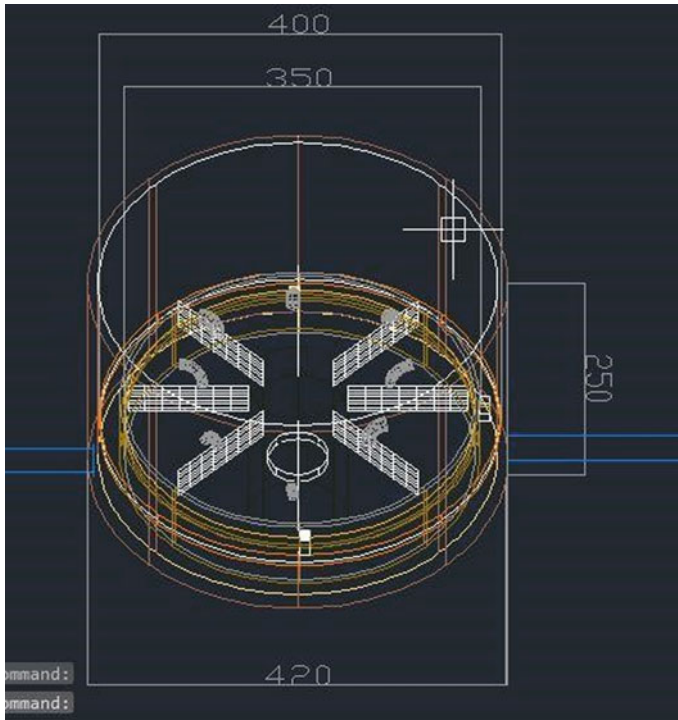
Fig. 4 2D model of cylindrical chamber

Fig. 5 2D model of shaft and blades
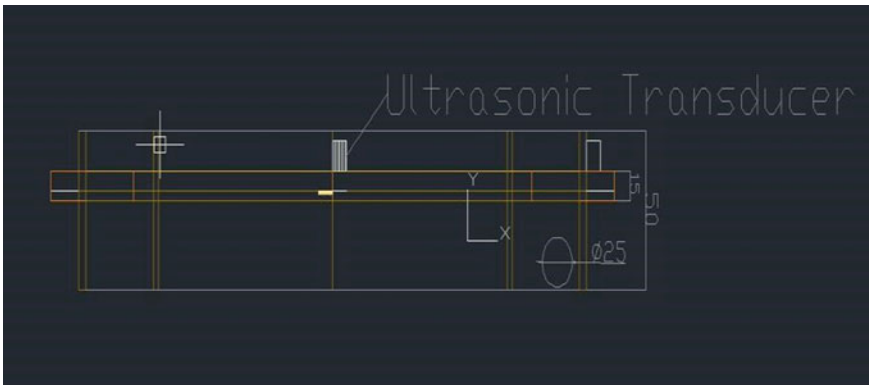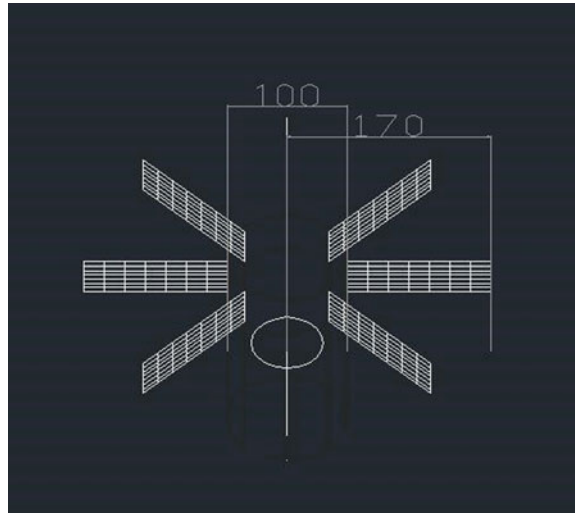
Fig. 6 D model of transducer attachment

3.2 Material

Cylindrical-shaped chamber. Corrosion resistance, durable standards, and dimensional accuracy are the critical properties required for the material selection of the cylindrical-shaped chamber of the sterilizer. 304 Stainless Steel is an austenitic type of stainless steel. It has approximately 0.08% of carbon content by weight. The additional alloying (see Table 2) elements provide excellent drawing, forming, and spinning properties. The added chromium helps to increase the corrosion resistance, heat resistance, and hardenability. The added nickel enhanced the formability and ductility of the material. 304 Stainless Steel is more susceptible to corrosion when

Table 1 Dimensions

Title	Size (mm)
Cylindrical base diameter	420
Shaft diameter	40
Blade length	170
Blade width	40
Height of cylinder	250
Hood diameter	440
Shaft diameter	100
Portion of shaft in the chamber	40
Thickness of chamber	2
Diameter of inner ring of transducer attachment	350
Height of inner ring	50
Outer diameter of outer ring of transducer attachment	400
Inner diameter of outer ring of transducer attachment	350

Table 2 Composition of 304SS [6]

Component	Weight (%)
C	Max 0.08
Cr	18–20
Fe	66.345–80
Mn	Max 2
Ni	8–10.5
P	Max 0.045
S	Max 0.03
Si	Max 1

illuminated by UV light. 304 Stainless Steel shows no sign of corrosion such as pitting in UV light [5].

Blades. Impact-resistance, durability, and corrosion resistance are the essential properties required for the material selection of blades. Polytetrafluoroethylene (PTFE) is a synthetic fluoropolymer of tetrafluoroethylene. PTFE is a durable fluorocarbon, as it is a compound with high molecular weight composed primarily of carbon and fluorine. Due to its hydrophobic nature, it does not corrode in the mixture of warm water and neutral pH detergent. It is highly reflective material and has a reflectivity percentage between 85 and 95 at 2 mm thickness against UV radiation of 250–400 nm range [7].

4 Mechanism

4.1 General Cleaning

Before high-level sterilization, proper cleaning is required because inorganic and organic matter that lingers on the surface of PPE equipment is equipment interferes with the efficacy of these processes [8]. The focus of this paper is the mechanical cleaning of PPE equipment. For proper cleaning, PPE equipment is placed over the PTFE blades with the help of 304 SS hooks. The blades are attached to the shaft (see in Fig. 4) which gets supply from single phase 220 V AC motor. To maintain the grade of a surgical mask and N95 respirators, the rotational speed of the motor is set between the range of 1500–2000 RPM. Warm water along with any neutral pH detergent is to be added via inlet pipe to the sterilizer. When power is supplied to the motor, the shaft along with blades and PPE equipment rotates. This rotational movement of the shaft causes a cleaning effect on equipment with the aid of water and neutral pH detergent mixture. The complete process of cleaning takes about four to five minutes. After completion of the process, dirty water can be removed from sterilizer via outer valve by creating pressure difference (by pressure variant) in the chamber.

4.2 Ultrasonic Cleaning

In this article, the next stage of sterilization after general cleaning is ultra-sonication (or ultrasonic cleaning) of PPE equipment. Ultrasonic cleansing uses high-frequency pressure (sound) waves caused cavitation bubbles to agitate a liquid. The ultrasonic waves and vibrations are produced by an immersible ultrasonic transducer fixed to the transducer attachment (see in Fig. 5). The ultrasonic transducer of moderate frequency (20–40 KHz) is an appropriate device for cleaning surgical masks and N95 respirators. The moderate frequency does not degrade the quality of PPE equipment. The ultra-sonication of PPE equipment can be completed with water, but to enhance the effect of cleaning on equipment an oxidizing agent should be mixed. The mixture of water and an oxidizing agent (hydrogen peroxide) is added to the sterilizer via inlet pipe. After the completion of the process, the mixture is removed via outlet pipe with the aid of pressure variant. The whole process of ultra-sonication with 35% of H_2O_2 takes approximately 5–6 min for the cleaning of respiratory equipment [9].

4.3 Ultraviolet Germicidal Irradiation

Most important and final stage of sterilization is ultraviolet germicidal irradiation (ultraviolet sterilization). Ultraviolet light is an electromagnetic form of radiation

with more energy than visible light but less energy than X-rays. It can be categorized into UV-A (315–400 nm), UV-B (280–315 nm), and UV-C (100–280 nm). UVGI uses UV-C at around 200–300 nm. The higher-energy UV-C radiations can damage DNA and RNA by crosslinking thymidine and uracil nucleotides, respectively, thereby preventing replication of microbes such as bacteria and viruses. The degree of pathogen inactivation at these wavelengths is directly proportional to the dose of UV radiation, with dosage being measured as the product of irradiance (W/m^2) and the time of exposure (seconds). Therefore, ultraviolet germicidal irradiation (UVGI) is a reasonably easy sanitation procedure, which does marginal harm to the respirator and avoids harmful chemicals from being used. Although there is no accurate amount of UV radiation needed to inactivate SARS-CoV-2, the single-stranded RNA (ssRNA) virus which causes COVID-19, the UV dose required for 90% inactivation of single-stranded RNA viruses is 5.8 mJcm^{-2} [10]. An ultraviolet lamp emits UV radiations of wavelength 254 nm is fixed at the hood of sterilizer. The surgical mask or N95 respirator mounted on the blades with the help of hooks is exposed to the ultraviolet radiation radiations. The estimated time of this stage of sterilization is calculated to be 105.45 s for both side of the mask. It totally depends upon the intensity of the bulb used along with the distance between the source and equipment.

5   Calculations

Due to the very recent nature of this topic as well as lack of ample literature, the authors have taken the liberty to assume certain values to convey the process more clearly.

a.   **Estimated cost of three-way cylindrical-shaped sterilizer**

The current pricing of all the materials used in the proposed sterilizer is given in Table 3. The authors have estimated components cost according to the current market value and can vary accordingly in the future.

According to the sources [11–13], the costs of these practices (i.e., general cleaning, ultrasonic cleaning, and ultraviolet germicidal irradiation) are Rs. 15000, Rs. 28500, Rs. 12500, respectively. The total cost of all these practicing is Rs. 56,000. As it can be seen that the estimated cost of the proposed design with error calculation is Rs. 27,800, which is a significant reduction in the total amount as compared to current system. It shows 50.35% in the price of the system which would enable its usage in developing countries. It is a conservative estimate and can be changed due to the unforeseen costs that come during manufacturing.

Estimated time to sterilize surgical mask or N95 respirators by Ultraviolet germicidal irradiation

The wavelength is 254 nm of ultraviolet lamp

Table 3 Costed bill of materials

Component	Amount (INR)
304 Stainless Steel	1900
Eight PTFE blades L180mm	2500
Immersible ultrasonic Transducer	12,000
Ultraviolet bulb	3000
Single phase A/C motor	2000
One-way inlet valve	200
One-way outlet valve	200
Wiring cost	1000
Miscellaneous/error	5000
Total	27,800

$$\text{Energy of photon } (E) = \frac{hc}{\lambda}$$

$$= \frac{6.626 \times 10^{34} \times 3 \times 10^8}{254 \times 10^{-9}} = 7.825 \times 10 \text{ J per photon} \quad (1)$$

The degree of pathogen inactivation at this wavelength is closely proportional to the dosage of UV radiation. The dosage ($\mu J/cm^2$) is calculated by the product of irradiance ($\mu W/m^2$) and the time of exposure (seconds). Amount of pathogen inactivation α dosage of radiation [14].

$$\text{UV Dosage} = \text{Intensity} \times \text{Exposure time} \quad (2)$$

$$\text{Exposure time} = \text{Dosage/Intensity} \quad (3)$$

The term intensity (or irradiance) is used to define the rate at which light diffuses to some distance from a source over a surface of a specific area. Theoretically, taking an ideal condition, that is, no energy is absorbed or scattered by the medium. The mathematical equation [15] for irradiance on small surface given by ASHRAE is

$$E = \frac{\phi}{2\pi^2 La}(2\alpha + Sin2\alpha) \quad (4)$$

At shorter distances ($a < 0.5L$), the equation simplified as

$$E = \frac{\phi}{2\pi La} \quad (5)$$

Electric power of UV lamp = 2 W
Conversion efficiency of low-pressure UV lamp is 30–40% [16]
The actual power of UV lamp (ϕ) = 0.6 W

Table 4 Estimated
sterilization time

Type	Time (min)
General cleaning	5
Ultrasonic sterilization	8
Ultraviolet sterilization	6
Total time of sterilization	19

Length of UV lamp $(L) = 41$ cm
Distance of exposed surface to the bulb $(a) = 20$ cm.

Using Eq. (5), intensity (E) of UV-C lamp $= 116.5\ \mu W/cm^2$.
The required dosage to inactivate 90% of SARS-CoV-2 (COVID-19) is 58 J/m^2
[10]. Taking unforeseen predictive error in the calculations, the estimated intensity
was taken as 110 $\mu W/cm^2$.

Required dosage $= 5800\ \mu J/cm^2$.
Intensity of UV lamp (E) $= 110\ \mu W/cm^2$.

Irradiation time was calculated by the given formula [17]

$$\text{Exposure time} = \text{Dosage/Intensity} = 5800/110 = 52.73 \text{ s for one face} \qquad (6)$$

For both sides of medical masks, the exposure time will be 105.45 s.
So, the total time for three medical masks: $105.45 \times 3 = 316.35$ s $= 5.27$ min.

b.   **Total estimated time of sterilization**

This paper proposed an estimated time of complete sterilization of surgical mask
and N95 respirators. For complete sterilization, three used surgical masks or N95
respirators have to go through all the sterilizing processes sequentially. The total
time given in Table 4 is for sterilization of three surgical masks or N95 respirators
or combination of both.

Table 4 concludes that each procedure of complete sanitation of three medical
masks takes 19 min (conservative estimated time).

6   Result and Discussion

6.1   Impact of Design

During the course of this paper, the design of a three-way cylindrical-shaped PPE
sterilizer is proposed and a comprehensive study is carried out to analyze estimated
sterilization time and estimated cost of the sterilizer. CAD modeling of the steril-
izer was performed on AutoCAD 14.0. The materials selected for the cylindrical
chamber and blades were 304 Stainless Steel and polytetrafluoroethylene plastic,

respectively, both the materials are designed to endure UV radiation and corrosion. The major advantage of the proposed design is 50.35% of cost reduction which would a supportive factor during manufacturing for developing countries. The authors have created a novel design of sterilizer in which three effective and reliable processes of sterilization can be performed sequentially.

6.2   Wavelength of UV-C Bulb

As it can be seen that the advantages of taking a low-pressure UV-C lamp of 254 nm wavelength lie in the data from the graph below. Low-pressure UV lamps radiate approximately 95 percent of their radiation at a wavelength of 253.7 nm, which is equivalent to the DNA absorption spectrum (260–265 nm) of high germicidal efficacy [18]. The most effectual way to produce UV energy is by using a low-pressure mercury arc in which the mercury atoms are energized to a high energy level. The atoms radiate intensely a distinctive spectral line with a wavelength of 254 nm when reduced to low intensity. This wavelength is close to 265 nm, by a fortunate coincidence, which is deadly to micro-organisms.

According to the requirement and optimal cost of the sterilizer, the estimated intensity taken was 110 μW/cm^2 for the ultraviolet germicidal irradiation. Outcome of the estimated time calculation (Eq. 6), i.e., 52.73 s can validate by the graph given below.

Depending on the value of surgical masks and N95 respirators in fighting COVID-19, the authors believe that the constant sanitation procedures can be successfully implemented. Calculation of sterilizer masks per day was done by the given equation [14].

$$\frac{24 \text{ h}}{\text{day}} \times \frac{3 \text{ procedures}}{\text{hour}} \times \frac{3 \text{ masks}}{\text{procedure}} \times N = \frac{216 \text{ masks}}{\text{day}} \times N \tag{7}$$

where N can be the number of sterilizers manufactured according to the proposed design. The WHO reported that approximately 89 million medical masks would be needed per month for COVID-19 response [19]. WHO reports that manufacturing has to ramp up production by 40 percent to satisfy the increasing demand. However, nearly 6.48 thousand medical masks per month can be sanitized by the proposed sterilizer ideally. If N reaches 100, the impact will increase by several folds.

7 Conclusion

Through a carefully methodical approach validated with numerous previous research papers and Web sites, a novel design of sterilizer is presented in the article, i.e., three-way cylindrical-shaped sterilizer. Three-way, i.e., general cleaning, ultrasonic sterilization, and ultraviolet germicidal irradiation are chosen to maximize the cleaning of surgical masks and N95 respirators. Ideally, each person will use a new mask or respirator to minimize the spread of airborne or transmitted infectious diseases by means of respiratory droplets. It is estimated the time to clean and sterilize three surgical masks and N95 respirators which is 19 min for both sides. Performing all three processes by a single device will be a huge advantage during the ongoing pandemic as it reduced the cost of sterilization.

References

1. Howard, J., Huang, A., Li, Z., Tufekci, Z., Zdimal, V., Van Der Westhuizen, H.: Face masks against COVID-19: an evidence review, pp. 1–8 (2020). https://doi.org/10.20944/preprints202004.0203.v1
2. FDA: FAQs on shortages of surgical masks and gowns during the COVID-19 pandemic. https://www.fda.gov/medicaldevices/personal-protective-equipment-infection-control/faqs-shortages-surgical-masks-and-gowns-during-covid-19-pandemic. Accessed 31 May 2020
3. Sridhar Rao, P.N.: Sterilization and Disinfection. www.microrao.com. Accessed 19 May 2020
4. The Economic Times: AIIMS issues guidelines on reuse of PPE, citing depletion of stocks. https://economictimes.indiatimes.com/industry/healthcare/biotech/healthcare/aiims-issues-guidelines-on-reuse-of-ppeciting-depletion-ofstocks/articleshow/75045797.cms?from=mdr. Accessed 16 May 2020
5. Forsyth, J.K.: The Effect of Ultraviolet Light on Aqueous Corrosion, FTMSA. April 20, 2000
6. ASM Aerospace Specification Metals Inc.: AISI Type 304 stainless steel. https://asm.matweb.com/search/SpecificMaterial.asp?bassnum=mq304a. Accessed 17 May 2020
7. Porex Corporation: Ultraviolet reflectance of microporous PTFE. https://www.porex.com/wpcontent/uploads/2020/04/Ultraviolet-Reflectance-of-Microporous-PTFE.pdf (2020, April)
8. Centre for Disease Control and Prevention, Disinfection and Sterilization: https://www.cdc.gov/infectioncontrol/pdf/guidelines/disinfection-guidelines-H.pdf. Accessed 26 April 2020
9. The Times of India: Covid-19: IIT Ropar comes up with equipment clean and reuse PPE kits. https://timesofindia.indiatimes.com/home/education/news/covid-19-iit-ropar-comes-up-with-equipment-clean-andreuse-ppe-kits/articleshow/74930786.cms. Accessed 29 April 2020
10. Kowalski, W., Walsh, T.. Petraitis, V.: 2020 COVID-19 Coronavirus Ultraviolet Susceptibility (2020). https://doi.org/10.13140/RG.2.2.22803.22566
11. Indiamart: Washer-disinfector. https://www.indiamart.com/proddetail/washer-disinfector-19531079530.html. Accessed 31 May 2020
12. Indiamart: Ultrasonic bath (sonicator). https://www.indiamart.com/proddetail/ultrasonic-bath-sonicator-capacity-3-lit15956335733.html. Accessed 31 May 2020
13. Indiamart: HALLY double wall UV C sterilizer. https://www.indiamart.com/proddetail/uv-c-sterilizer-with-timer22252953173.html. Accessed 31 May 2020
14. Card, K.J., Crozier, D., Dhawan, A., et al.: UV sterilization of personal protective equipment with idle laboratory biosafety cabinets during the COVID-19 pandemic. medRxiv. March 27, 2020. https://doi.org/10.1101/2020.03.25.20043489.

15. ASHRAE: Ultraviolet lamp systems. https://www.ashrae.org/file%20library/technical%20resources/covid19/si_s16_ch17.pdf. Accessed 1 June 2020
16. Schalk, S., Adam, V., Arnold, E., Brieden, K., Voronov, A., Witzke, H.-D.: UV-Lamps for Disinfection and Advanced Oxidation—Lamp Types, Technologies and Applications. UV Congress in Whistler, BC, Canada (2005)
17. UV-Technik: Disinfection with UVC. https://www.uv-technik.co.uk/assets/Uploads/product-documents/Disinfection-UVC-Explained2.pdf. Accessed 28 May 2020
18. Kowalski, W.: Ultraviolet Germicidal Irradiation Handbook: UVGI for Air and Surface Disinfection. Springer Science & Business Media (2010)
19. World Health Organization: Shortage of personal protective equipment endangering health workers worldwide. https://www.who.int/news-room/detail/03-03-2020-shortage-of-personal-protective-equipment-endangering-healthworkers-worldwide. Accessed 16 May 2020

Design and Development of Single-Sided Front Suspension Girder Fork for Bicycle

Ayush Shrivastava, Aman Kumar, Ayush Bansal, and Vijay Gautam

1 Introduction

Suspension parameters primarily affect the ride comfort and handling by keeping the rider isolated from road noise, bumps, and vibrations. Most commonly, two-wheeler front suspension has a pair of fork tubes and is of telescopic type, as shown in Fig. 1. In the old times, girder fork design was quite popular, it consists of a pair of uprights attached to the triple clamp by linkages with a spring usually between the top and bottom triple clamps, also as shown in Fig. 1. But telescopic is now ubiquitous as it offers simpler design, easy manufacturing, and lower cost. Still, many custom modifications by consumers involve girder forks assembled onto the stock motorcycles, owing to its retro-appeal, an aesthetic justification. In the performance environment, race bikes undergo wheel changing many times, taking up crucial seconds. For making wheel fastening and unfastening faster, a single-sided swing arm for rear wheels is mostly used. Besides, it has a lightweight advantage too. Hence, the idea of single-sided girder fork is sought for and attempted. Apart from custom makers, there has been no authoritative literature in the public domain or a similar design attempted by any manufacturer.

This paper discusses the development of a single-sided girder fork, mentioning all the engineering design decisions, from kinematic upfront to material selection, and

A. Shrivastava (✉) · A. Kumar · A. Bansal · V. Gautam
Department of Mechanical, Production & Industrial and Automobile Engineering, Delhi Technological University, Delhi 110042, India
e-mail: xjinenzo.dce.dtu@gmail.com

A. Kumar
e-mail: aman.gdg@gmail.com

A. Bansal
e-mail: ayushbansaldtu@gmail.com

V. Gautam
e-mail: vijaygautam@dce.ac.in

Fig. 1 Telescopic fork versus girder fork [1, 2]

sizing. Finally, computational stress analysis is performed over the design, giving suitable results. For prototyping over a test mule, the Firefox MTV Dirt bicycle has been chosen for specifications.

2 Method

The development process is based over the geometry and stock front suspension specifications of the bicycle. Requisite geometric parameters of the bicycle are obtained from some brochure data and manual measurements [3, 4]. This gives the castor angle of 18.77°, required travel of the fork-hub mount point; suspension travel of 60 mm, and also the fixed pivots relative positions: distance between them being head tube length of 160 mm.

2.1 Kinematic Synthesis

Girder fork modeled as a four-bar pin-jointed linkage is graphically synthesized, using coupler path point prescribed positions by inversion technique, on a 2D CAD software [5, 6]. Since no input crank motion is present, hence transmission angle verification is avoided. Figure 2 shows the resulting mechanism and its positions for 60 mm suspension travel. The graphically synthesized mechanism required for achieving the said 60 mm of suspension travel. The dashed line represents the coupler link, whose end is the fork end holding the wheel. Green corresponds to the full suspension travel of 60 mm from the normal position represented by black.

Fig. 2 Mechanism synthesis
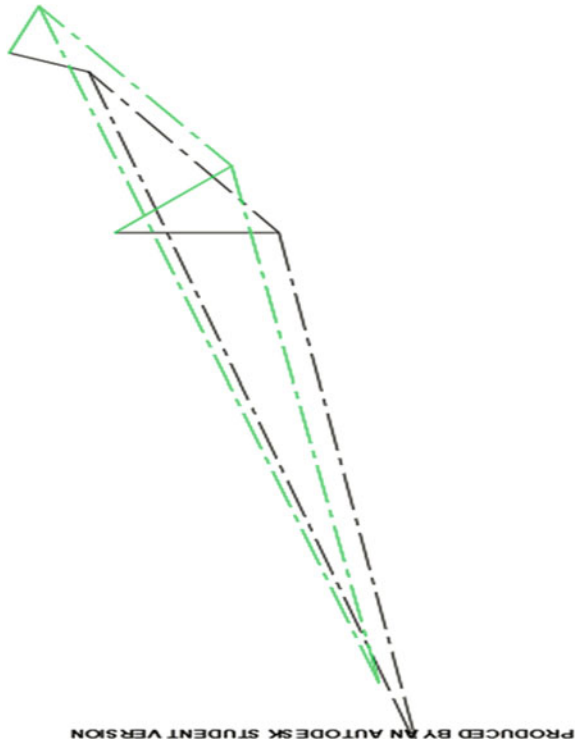
2.2 Material and Shape Co-selection

Since the cross-sectional shape can affect the material usage, material-shape co-selection is performed over the material property charts generated by CES EduPack software [7]. To proceed ahead, functional requirements of the component are needed; its function as a structural member.

Load Specification. As per the Bureau of Indian Standards (BIS) specification and safety requirement standards [8, 9], the various test loads—static, impact, and fatigue—as mentioned are taken as design loads for our case. Applying these loads to the synthesized mechanism, assuming it as a rigid frame, with a cross member. Design loads coming in the member or links are, hence, evaluated. It is interpreted that the coupler link holding the front wheel hub carries mostly bending loads and the rest of the two links have axial loading.

Since in the axial loading case, section area is the only parameter, shape has no influence over the efficient material usage. Whereas in bending, the maximum stress depends on the shape via section modulus. Also, since the slope of the index guideline in bending is greater than in axial, the former is a better criterion of excellence.

Translation: Deriving criterion of excellence. Firstly, specifying the objective(s), constraint(s), and functional requirement(s), consequently a material efficiency coefficient or material index, is obtained along with the corresponding shape efficiency factor, given in Table 1. For strength-limited design and bending loads, we consider bending shape factor ϕ_b^f [10]. Index M^* maximizes the performance of the material, fulfilling the objective of minimum mass (or cost), where ρ is the material density and σ_f is the failure stress, yield strength in static and fatigue strength in dynamic loading.

Screening and Ranking: Using CES. With the help of CES EduPack software, material property charts were plotted according to the Index M^*, and the selection guidelines drawn over them narrowed the search window giving a handful number of candidates, as shown in Figs. 3 and 4.

Table 1 Specification for material-shape co-selection

Objective(s)	Functional requirement(s)	Constraint	Material index (M)	M^* with bending shape factor (ϕ_b^f)
Minimum mass	Bending load	Strength-limited design	$\sigma_f^{2/3}/\rho$	$(\phi_b^f \sigma_f)^{2/3}/\rho$
Minimum mass	Axial load	Strength-limited design	σ_f/ρ	Not applicable
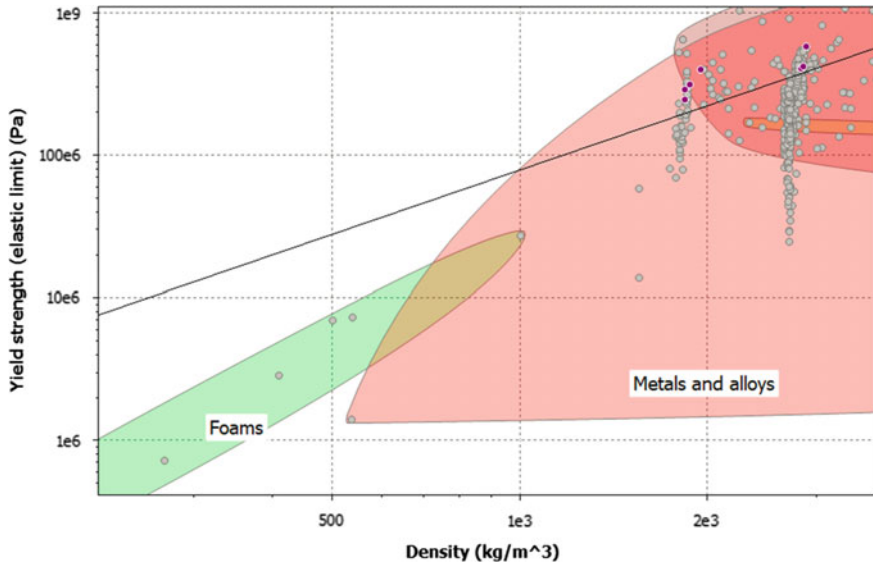
Fig. 3 The guideline narrows the search window over yield strength versus density chart, giving few shortlisted materials represented by the purple dots
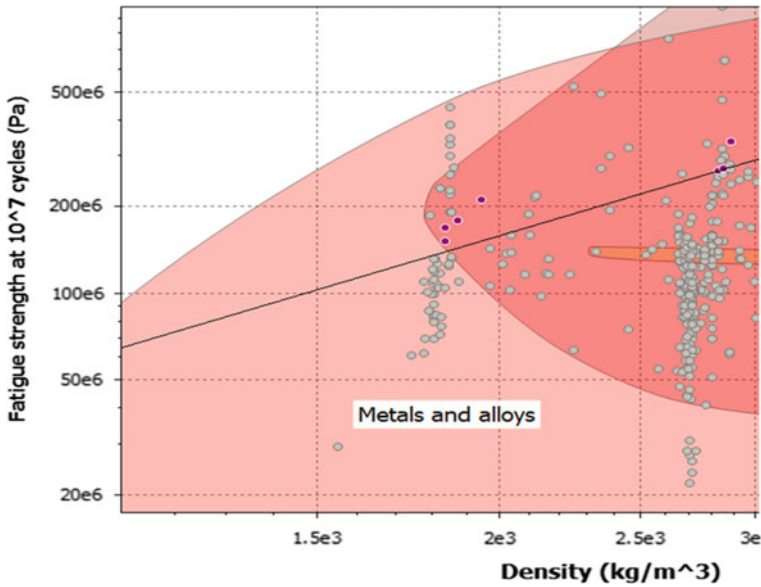
Fig. 4 The same selection guideline now over the chart for fatigue strength versus density

Ranking. The shortlisted materials are then ranked as per their index values, material with the highest index value is, thus, chosen. The maximum limiting bending shape factor ϕ_b^f for strength-limited design is found from the chart as shown in Fig. 5.

2.3 Vibrational Characteristics

Road excitations, considered as random vibrations, influence the suspension characteristics. As per BIS, the standard sinusoidal inputs were chosen for developing the vibrational model of the road [11]. Taking the speed of the bicycle 5.5 m/s, gives the spatial frequency band in range of 0.09–6 cycles/m. For B-class roads and spatial frequency of 1 cycles/m, the corresponding mean r.m.s. displacement is 0.00067 m.

Human comfort is more sensitive to vertical acceleration rather than vertical displacement. BIS standard defines tolerable limits of a seated human at a single vertical frequency for exposure durations [12, 13] using Eq. (1) [14]:

$$X_0/Y_0 = \left(1 + (2\zeta r)^2 \Big/ \left((1 - r^2)^2 + (2\zeta r)^2\right)\right)^{0.5} \tag{1}$$
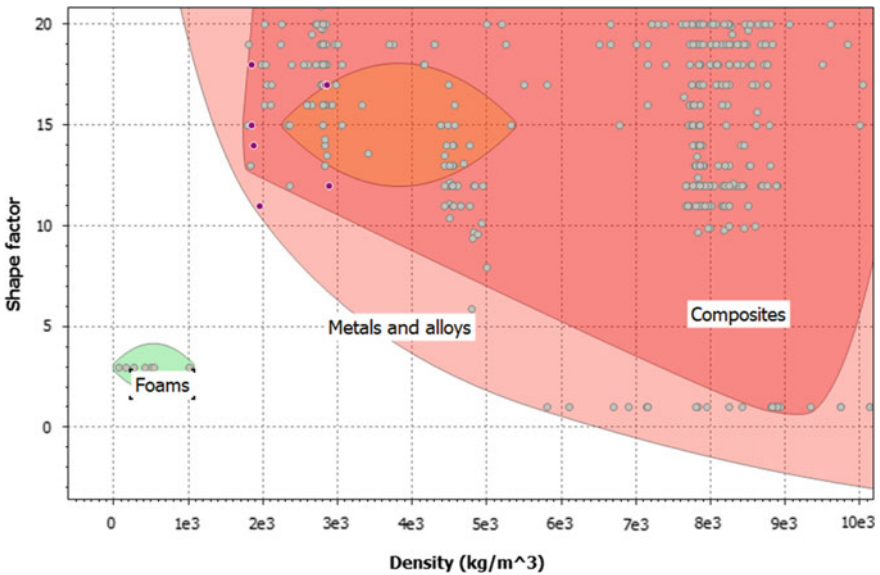
Fig. 5 Limiting shape efficiency factor versus density chart

where X_0 and Y_0 are dynamic and mean r.m.s amplitude, respectively, ζ is damping ratio and r is ratio of road frequency and natural frequency (ω/ω_n), vertical accelerations for different values of suspension parameters—stiffness and damping ratio—are obtained. Those giving acceleration lying in the comfort zone are, thus, selected.

2.4 Strength Design and Analysis

Having the material selected and shape factor determined, sizing is performed by designing for strength using the BIS standard loads and safety factor. The load values are vertical 235 N (Impact) and horizontal $600^{+5\%}$ N (Static and Fatigue), both applied at Fork end.

Safety factor selection. Factor of Safety (FOS) for the design is evaluated as per the criteria given in design data [15]. Suitable value is given to each criterion as per design data. The safety factor of 3.5 is obtained.

3 Results and Discussions

Ranking the material candidates provided us with the following comparison chart, as shown in Fig. 6.
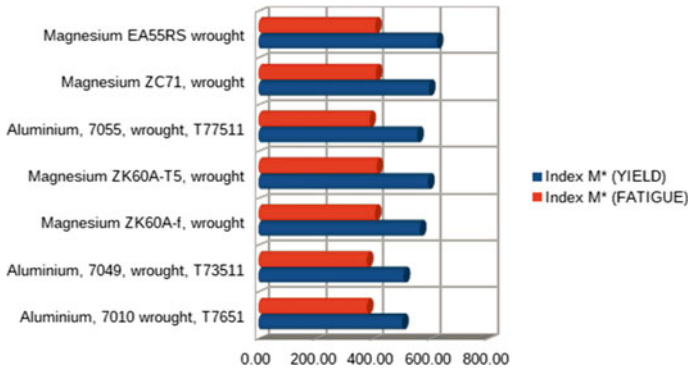
Fig. 6 Shortlist of candidate materials. Index values along the horizontal axis

Table 2 Mechanical properties of Aluminum, 7055, wrought, T77511

Designation	7055
Condition	T77511 (Solution heat-treated and overaged or stabilized)
Yield strength	583 MPa
Tensile strength	616 MPa
Compressive strength	605 MPa
Flexural strength	583 MPa
Fatigue strength (at 10^7 cycles)	339 MPa

Magnesium alloys, even though having the highest values of indices, are not preferred in our case due to the scarce market availability. Also, aluminum alloys have a price advantage over them. Aluminum, 7055, wrought, T77511, is therefore, the most rational choice, mechanical properties given in Table 2. The maximum limiting bending shape factor ϕ_b^f for strength-limited design for AA 7055 is found to be 3.46.

3.1 Shock Absorber Selection

Manufacturer data specifying stiffness and damping ratio values of four shockers, available in the market, and the calculated resulting vertical accelerations are tabulated in Table 3. Consequently, shock 1 having lowest vertical acceleration is chosen for achieving maximum ride comfort.

Table 3 Values of shock parameters

Parameters	Shock 1	Shock 2	Shock 3	Shock 4
K (N/m)	35,025.367	43,781.708	70,050.734	96,319.75
Equivalent K (N/m)	21,015.22	26,259.024	42,030.44	57,791.85
ω_n (rad/s)	22.92	25.62	32.41	38.01
ω/ω_n	1.50	1.34	1.06	0.90
ζ	0.5	0.5	0.7	0.5
Y_0 (m)	0.00067	0.00067	0.00067	0.00067
X_0 (m)	0.00061	0.00071	0.00080	0.00097
Vertical acceleration ($\omega^2 X_0$)	0.73	0.85	0.95	1.16

3.2 Stress Analysis

The fork is modeled and analyzed on Autodesk Inventor 2020. The simulation performed for vertical 235 N load gave the following stress distribution shown in Fig. 7. Since the application of load is impact in nature, the maximum stress, as calculated (Eq. (2)) for static analysis, is multiplied by a factor i [16]:

Fig. 7 Von-Mises stress distribution. Maximum stress 11.53 MPa
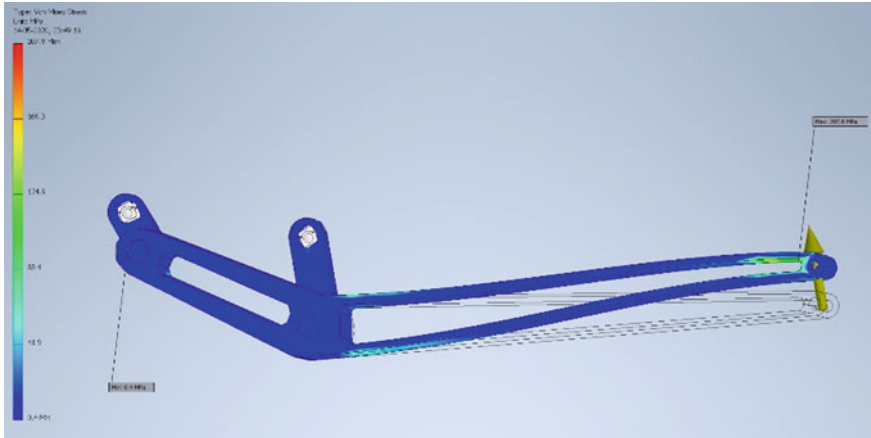
Fig. 8 Von-Mises stress distribution. Maximum stress 207.81 MPa

$$i = \left(1 + (1 + 2h/e)^{0.5}\right)^{0.5} \tag{2}$$

where h is the height of the load drop and e is the deflection by the same static load. The factor i evaluated is 4.38, thus, maximum impact stress (Von-Mises) comes out to be 50.51 MPa, which is well under the elastic limit. For 600 N load, the stress analysis results shown in Fig. 8. The material fatigue strength at 10^7 cycles is 339 MPa and since the maximum stress amplitude coming is 207.81 MPa, the design is satisfactory as per BIS specification for 50,000 cycles.

4 Conclusions

The design realized is a satisfactory one, having design stress well within the limits to prevent failure. With respect to the detailed assembly design, these following major conclusions are drawn:

- The kinematic design upfront has been given due importance in the development process, correctly determining geometry of the girder fork linkage using mechanism synthesis technique.
- A comprehensive quantitative computer-aided method for material and cross-section co-selection is used, giving efficient lightweight design and a low-cost inexpensive material having ready availability in the market.
- Loading conditions chosen for strength design comply with the BIS specifications and safety requirements for bicycle forks.
- Finite Element Analysis (FEA) for the assembly is done, and the maximum limit for impact load is 50.51 MPa and fatigue is 207.81 MPa, which indicates that stresses are within the safe limits, for the material so selected.

- The shock absorber complying with the BIS standard human health limits is selected, for ride comfort.

The multibody dynamics (MBD) for motion analysis of the resulting design remains to be performed for evaluating characteristics, with realistic conditions input to the software. Hence, MBD results would provide a way for design optimization. Further, the selection of linkage pivot bearing or bushings material and rating has to be determined, as per the technical load-size chart of the respective manufacturer. Design of the suitable mounting arrangements for retro-fitting of the girder fork assembly to the frame head tube for steering remains to be done.

References

1. BAL LAND: https://bl-graph.com/?p=1126
2. Autocurious: https://www.autocurious.com/2019/02/motorcycle-suspension.html
3. Cossalter, V.: Motorcycle Dynamics, 2nd edn. (2006)
4. Foale, T.: Motorcycle Handling and Chassis Design. Spain (2002)
5. Soni, A.H.: Mechanism Synthesis and Analysis. Scripta Book Co., Washington (1974)
6. Eckhardt, H.D.: Kinematic Design of Machines and Mechanisms. McGraw Hill (1998)
7. Ashby, M.F.: Materials Selection in Mechanical Design, 4th edn. Oxford, Butterworth Heinemann (2010)
8. IS 2061:1995 Bicycle-Front Forks-Specifications
9. IS 10613:2014 Cycles-Safety Requirements for Bicycles
10. Weaver, P.M., Ashby, M.F.: The optimal selection of material and section-shape. J. Eng. Des. **7**(2), 129–150 (1996). https://doi.org/10.1080/0954482960890793
11. IS 15592:2005 Mechanical Vibration—Road Surface Profiles—Reporting of Measured Data
12. IS 13276-1:2000 Mechanical Vibrations and Shock—Exposure to Whole Body Vibration, Part 1
13. Dixon, J.C.: The Shock Absorber Handbook, 2nd edn. Wiley (2007)
14. Rao, S.S.: Mechanical Vibrations, 5th edn.
15. Mahadevan, K., Balaveera Reddy, K.: Design Data Handbook for Mechanical Engineers, 4th edn. CBS Publishers (2018)
16. Siegel, M.J., Maleev, V.L., Hartman, J.B.: Mechanical Design of Machines, 4th edn. Scranton International Textbook Co. (1965)

Vehicle Safety System Using Fingerprint Scanner and Driving License Data

Sudeeksha Agrawal ⓘ**, Shubham Bhardwaj** ⓘ**, Raghav Tyagi** ⓘ**, and Vikas Rastogi** ⓘ

Abbreviations

ARM 7	Advanced RISC Machine
ASCII	American Standard Code for Information Interchange
CCD	Charged Coupled Devices
CMOS	Complementary Metal Oxide Semiconductor
CSI	Camera Serial Interface
DSI	Display Serial Interface
DSP	Digital Signal Processing
DTMF	Dual Tone Multi-Frequency
FTIR	Frustrated Total Internal Reflection
GND	Ground
GNSS	Global Navigation Satellite System
GPIO	General Purpose Input Output
GPS	Global Positioning System
GSMGSM	Global System for Mobile Communication
HAT	Hardware Attached on Top
HDMI	High Definition Multimedia Interface
I/O	Input Output
LAN	Local Area Network
LCD	Liquid Crystal Display
MEMS	Micro-Electro-Mechanical Systems
RAM	Random Access Memory

S. Agrawal (✉) · S. Bhardwaj · R. Tyagi
Mechanical Engineering with Specialization in Automotive Engineering, Delhi Technological University, Delhi 110042, India
e-mail: sudeeksha17@gmail.com

V. Rastogi
Mechanical Engineering Department, Delhi Technological University, Delhi 110042, India

RFID	Radio Frequency Identification
RXD	Receive Data
SD	Secure Digital
SIM	Subscriber Identity Module
SMS	Short Message Service
TIR	Total Internal Reflection
TTL	Transistor-Transistor Logic
TXD	Transmit Data
UARTUART	Universal Asynchronous Receiver/Transmitter
USB	Universal Serial Bus

1 Introduction

In the twenty-first century with rapid industrialization and modernization at its peak, within the technological aspects, automotive security has been one of the foremost necessary issues because of the alarming rise in the number of car thefts and unauthorized driving by unlicensed individuals resulting in road accidents and misuse of vehicles. The increasing cases of accidents caused by under age, inexperienced drivers pose a serious threat to the issue of road safety.

Moreover, nowadays car thefts are on the increase, particularly the lower variant cars having a keyless entry feature that doesn't seem to be equipped with high-end security systems. The current alarm system has various flaws that help thieves seek entry into the vehicle and once stolen away, it becomes a troublesome task to find the automobile [1]. In an endeavor to look out for an answer to the current downside, a unique methodology of the fingerprint and driving license-based security system to improve car safety is proposed.

For fingerprint detection, generally, the fingerprints are taken, the differentiating features of the same are found, and a digital model of the fingerprint is saved for the comparison of this image with the stored templates [2]. The strength of fingerprint identification is that it may be deployed during varied environments. Also, it is a verified core technology and the power to enter multiple fingers increases the system accuracy and suppleness [3, 4].

Each fingerprint is related to a unique authorized driving license number that enables that no person below 18 years is driving the vehicle, also no-one who is unskilled at driving is at the driver's seat. This ensures road safety and avoids accidents [5]. The device enables setting up of one owner with many trusted users for offline retrieval. For emergencies, the owner is also supplied with a password that starts the vehicle via manual override [6].

2 Literature Review

In several prior pieces of research, authors have described the circuits used in different experiments whereas, in another work, GPS is employed as a worldwide navigation satellite system to find the automobile and conjointly to protect it against theft. Many improvements have been done in the past in automobile security systems and a few of the related ones are given underneath.

Joshi and Mahajan have used ARM7 (Advanced RISC Machine) microcontroller, GSM, and GPS module along with an accelerometer and temperature sensing element [7]. GPS and GSM are used for tracing the realm of the automobile. The additional component is enclosed in the accelerometer containing the MEMS (Micro-Electro-Mechanical Systems) sensor providing a low pass filter and is essentially used for Shake, Orientation, and Tap Detection.

Al-Khedher made an advanced GPS-GSM Automobile Tracking System [8] which shows an incorporated GPS-GSM system to trace automobiles with the help of the Google Earth app. The obtained GPS directions are shifted using a Kalman filter to update the exactness of the measured position. Once the information has been processed, Google Earth is employed to look at the present space and standing of each automobile.

Ishan et al. [9] describe in their paper the successful implementation of IoT to prevent thefts and accidents. They have used GSM-GPS technology to send the owner a message in case of an attempt of theft after which the owner can either stop fuel supply or track the vehicle in real-time using a tracker app.

Pethakar et al. have used a security system supporting GPS, GSM, and RFID (Radio Frequency Identification) [10] combines the institution of an electronic widget within a car, justifiably planned machine programming to enable tracing of the vehicle's space. The place where the automotive picks, the employee, the RFID card is swapped. The microcontroller looks for a match between the RFID card number and its information records and returns the representative's id, cab id, and the cab position to the organization with the help of the GSM module.

Wankhade and Dahad have mentioned the configuration and advancement of a theft control system for a vehicle that is employed to prevent the stealing of an automobile [11]. The created framework uses a deep-rooted framework based on GSM technology, placed within the automobile. An interfacing movable is attached to the microcontroller attached with the engine. After the automobile is robbed, the information is used by the car owner for additional action. Shaikh et al. [12] mention an advanced vehicle safety system employing ARM7. The main focus of this enterprise is to supply an improved security framework in a vehicle, including a face location subsystem, a GSM module, a GPS module, and a control stage. The face detection subsystem will look out automobile resistances during which nobody should be in the vehicle and warns without sound.

Kaushik et al. [13] have shown an anti-burglary automobile security framework that allows entry to the automobile simply if the person's fingerprint matches the one already in the framework. The correlation happens in MATLAB and the result

shall be displayed on the Liquid Crystal Display (LCD). On the rare likelihood when the automobile is illicitly accessed, the automobile's fuel tank shall be fastened by a Relay circuit so whenever the tank is empty, an unauthorized person can't ever refill it.

Ibrahim et al. [14] have used an anti-robbery system that employs an installed structure using a GSM and Dual Tone Multi-Frequency (DTMF) for protecting a vehicle. Nagaraja et al. [15] define the improvements upon a GSM-based automobile theft management framework for a vehicle. This framework is based upon an inserted framework built using GSM. A GSM modem or interfacing mobile is attached to the microcontroller, conjoined with the engine using a relay. In case the automobile is robbed, the information to the owner is sent that someone has purloined the automobile. Following which the user sends the SMS to a GSM modem that is conjoined with motor ignition through a relay which then turns off the engine.

The proposed system deals with this issue by employing a Raspberry Pi-based fingerprint security system with driving license matching of verified users.

3   Materials and Methods

The connection of Raspberry Pi3: Model B with optical fingerprint scanner (R307) for the operation of the project is shown in Fig. 1. Also, the specifications of each of the hardware components (viz. Raspberry Pi 3—Model B, Optical Fingerprint Scanner, LCD (Liquid Crystal Display), Jumper Cables, GSM-GPS Module, and Keypad) are described in further subsections.
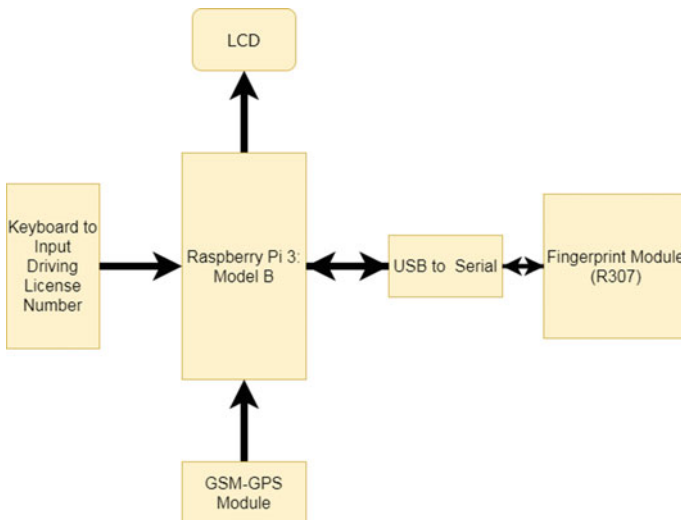
Fig. 1 The operation of fingerprint scanner with Raspberry Pi

3.1 Raspberry Pi 3: Model B

Raspberry Pi foundation initially made unit-board tiny computers called Raspberry Pi in the UK for primary education. The speed of the processor is between 700 MHz to 1.4 GHz in Pi3 Model B and is 1.5 gigahertz for Pi4 while the memory on-board varies between 256 MB and 1 GB RAM (Random Access Memory) in Pi3 and 4 GB on Pi4. To save programs and operating systems, SD (Secure Digital) cards are employed. The number of USB ports varies from 1 to 5. HDMI and composite videos enable video output while the audio output is possible through a typical 3.5 mm tip-ring-sleeve-jack. Various GPIO (General Purpose Input Output) pins enable lower range output. An 8P8C Ethernet port is provided on B variants while Wi-Fi 802.11n and Bluetooth are supported on Pi 3, Pi 4, and Pi Zero W variants. The Raspberry Pi 3: Model B employed by us is the Raspberry Pi of the third generation. It is a small unit-board computer which can be successfully employed in a variety of processes and is superior to its predecessors, Pi B + and Pi 2: Model B. Raspberry Pi 3: Model B has a powerful processor, that is ten times quicker than the Pi of the first generation. Besides, as it also supports wireless LAN (Local Area Network) and Bluetooth connectivity, it is easily the best option for connected designs [16].

Raspberry Pi 1: Model B that is 1st Generation Pi was launched in February 2012. Then Raspberry Pi 2 came, which included extra RAM, in February 2015. Raspberry Pi Zero having reduced size, lesser input/output (I/O) requirements and general input/output (GPIO) options came in November 2015.

The current model, Raspberry Pi: 3 Model B launched in February 2016, is equipped with a 1.2 GHz 8-byte quad-core processor; 802.11n Wi-Fi, Bluetooth, and USB link options. The Raspberry Pi is provided with 2 pins (GPIO pin 14, 15) that work at 3.3 V. A USB UART (Universal Asynchronous Receiver/Transmitter) converter is used for connecting the fingerprint sensor easily. The pinout diagram of Raspberry Pi 3: Model B is shown in Fig. 2 [17]. The Raspberry Pi Foundation gives an Operating system called the Raspbian that is a Debian-based (32-bit) Linux distribution besides various third-party options [18]. Due to these exceptional features as shown in Table 1, at a relatively cheap price, which the Raspberry Pi 3: Model B offers, it is the foremost choice for use as the microcontroller for the project. R307 fingerprint scanner.

The optical fingerprint scanner and reader (R307) employed is for input and scanning of the fingerprint to save it for later searches. It is based on the principle of Total Internal Reflection (TIR) by a glass prism. R307 Optical Fingerprint Reader device (Fig. 3) [19] includes a TTL (Transistor-Transistor Logic)—UART interface that allows direct connections to microcontroller UART or the computer with the assistance of the MAX232/USB-Serial adapter.

Technical specifications of R307 are in Table 2. The R307 Fingerprint Module includes a superior fingerprint alignment code, good capacity FLASH chips, extremely fast DSP (Digital Signal Processing) processor and different hardware and software packages, consistent performance, easy structure, with image processing,
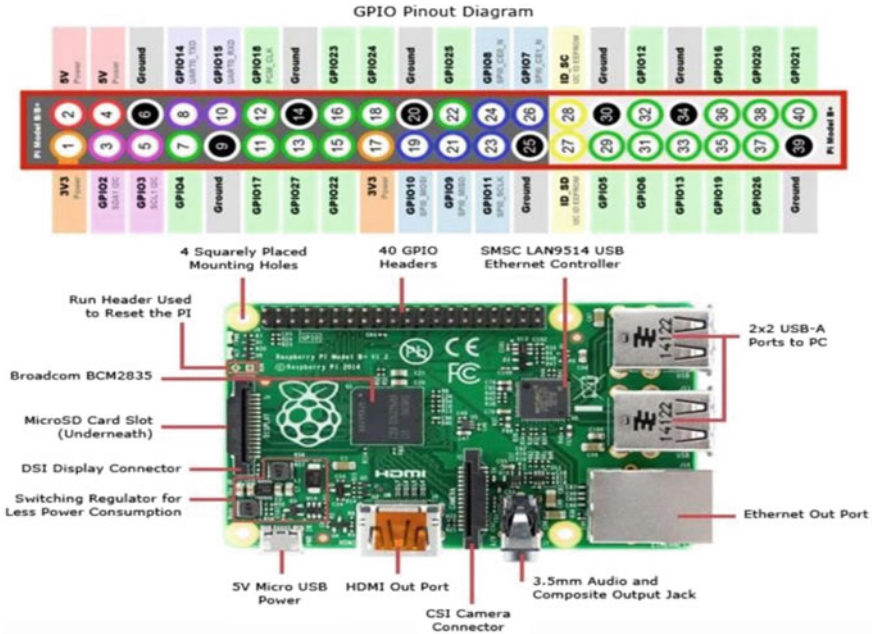
Fig. 2 Pin description of Raspberry Pi 3: Model B

Table 1 Raspberry Pi 3: Model B technical properties	Technical properties
	Broadcom BCM2387 chipset
	Ethernet Connection via 2 ports
	1.2 GHz Quad-Core ARM Cortex-A53
	802.11 Wireless LAN and Bluetooth 4.1
	1 GB RAM
	64 Bit CPU
	4 USB ports
	4 pole Stereo output with a Composite video port
	Full-size HDMI
	10/100 Base T: Ethernet socket
	Raspberry Pi camera attached via CSI (Camera Serial Interface) camera port
	Raspberry Pi's touch screen display via DSI (Display Serial Interface) display port
	Micro SD port enables the loading of the operating system, saving information
	Micro USB power supply
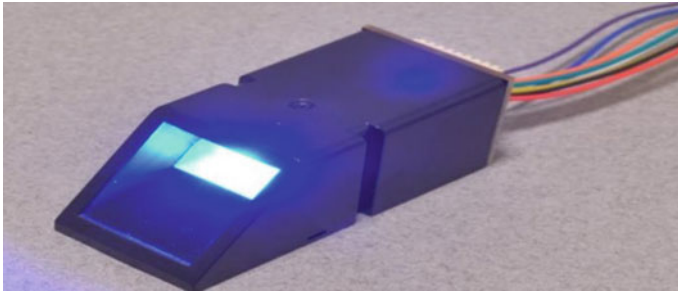
Fig. 3 R307 fingerprint module

Table 2 Technical parameters of fingerprint scanner

Property	Corresponding value
Power supply	DC 4.2 V–6 V
Current consumption	~50 mA
Interface	UART/ USB
Baud rate	(9600 * N) bps, $N = 1$–12, default is 6
Image acquiring time	<0.5 s
Verification speed	~0.3 s
Matching modes	1:1, 1:N
Character file size	256 bytes
Template size	512 bytes
Storage capacity	1000
Security levels	1–5
FAR (false acceptance rate)	<0.001%
FRR (false recognition rate)	<0.1%
Average searching time	<1 s, 1:1000
Weight	18 g
Working environment	Temp = −10 °C ∓ 40 °C, RH = 20–80%
Storage environment	Temp = −40 °C ∓ 85 °C, RH ≤ 85%
Outline dimensions	Split Type, 44.1 * 20 * 23.5 mm

fingerprint's feeding, comparing, finding, and model storage besides various other functionalities. Also, its price is low compared to other biometric scanners.

Operation Principle. Fingerprint processing is made up of 2 components: Enrollment of fingerprint and its matching (which may be 1:1 or 1:N). The individual is supposed to feed the finger twice, at the time of feeding. After the enrollment, the system processes the pictures of the finger (entered twice), prepares a model of the finger with these results, and saves its [20]. In 1:1 matching, the current finger is compared with a designated template of the module while in the case of 1:N

matching, to find the match of the finger, the entire library is searched. In either of the situations, the matching result in the form of failure or success is given back.

Distinctive Features:

- It can be easily used in various products that imply secondary development possible.
- The price, size, and power used are low with exceptional performance.
- The picture collection and algorithm chip are all in one, hence fewer faults.
- The manufacturing of the module is precise and application development is easy.
- Great pictures up to 500dpi resolution can be taken easily.
- Adjustable security level for ease of users.
- High functionality: Independent functions for fingerprint entry, save, comparison (1:1), and search (1:N) processes [3].

3.2   LCD

A basic 16*2 LCD is used which has sixteen pins and two connectors. Due to its ease of programming and ability to display all forms of ASCII (American Standard Code for Information Interchange) characters (alphabets, numbers, and symbols), animations, this LCD (shown in Fig. 4) has been chosen over other variants like the seven-segment one. With the help of DSI Connector, the Raspberry Pi connects to the touch Display that is an LCD. Raspberry Pi models 2, 3, and 4 have mounting holes in the HAT (Hardware Attached on Top) footprint with which DSI display can work while for Model 1 A/B boards, extra mounting is needed on display PCB. The pins of 16*2 LCD named RS, EN, d4, d5, d6, d7 are attached, respectively, to the GPIO pins 18, 23, 24, 25, 8, 7 of Raspberry Pi 3 [21].

Fig. 4   LCD display screen

3.3 Jumper Cables

Jumper cables are colored cables that can be distinctly identified for connecting to the USB converter. Just four cables are required for connection from the fingerprint sensor to the Raspberry Pi. The connections are described by the color as follows: Red: Based on sensor voltage White: RXD (Receive Data) Green: TXD (Transmit Data) Black: GND (Ground). When no other device is attached firstly no result comes and after the attachment with the fingerprint scanner, the display shows /dev/ttyUSB0 [22].

3.4 GSM-GPS Module

GSM: It stands for the Global System for Mobile Communications. GSM converts data to digits and compresses it after which it transmits it through a channel along with 2 other streams of user data in different time slots. The operation is at 900 MHz and 1,800 MHz, frequencies. Both internet and audio connectivity is enabled through this service [23, 24]. The GSM module is employed to send SMS to the owner's mobile and to inform the police in case of an attempt of entry into the vehicle by an unauthorized person.

GPS: It is employed to track the automobile in real-time and to detect its current position coordinates which would help us to send this data to the owner and the police in case of detection of unauthorized driving [26]. A USB cable has been employed for the connection of the Raspberry Pi with the HAT module which provides optimum power and establishes a serial communication between them [25, 26]. After USB connections, a SIM (Subscriber Identity Module) card is inserted in the HAT module for GSM to work. The SIM 808 module is employed here that is a Quad-Band GSM/GPRS module with GNSS (Global Navigation Satellite System). The code in python is run for GPS after a GPS antenna is inserted into the GNSS antenna connector on the HAT module [27].

3.5 Keypad

A small keypad is attached to the Raspberry Pi for the input of driving license number by a user and also for entering the password for manual override option. It is a basic keypad having digits and alphabets, generally used on mobiles. It is connected via the Bluetooth option (to let the USB ports be free) available on Raspberry Pi 3: Model B employed here.
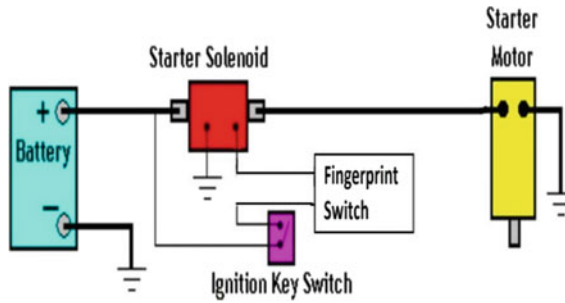
Fig. 5 The circuit diagram of fingerprint scanner and driving license data

3.6 Hardware Design

The Circuit Diagram as shown in Fig. 5 has the Fingerprint Scanner and Driving License Data Input Keyboard attached in line with the starter ignition circuit of the automobile. When the ignition switch will be turned on, current from the battery will flow through the switch to the system. At this point, user will be asked to put his/her finger on the fingerprint scanner. It ensures that unless a match is found by Raspberry Pi after authorization, the circuit will not complete and charge flowing from the battery won't reach the starter motor.

4 Working

4.1 Software Design

The flowchart as shown in Fig. 6 highlighting the algorithm is used to build upon the software framework and fed into the Raspberry Pi's Memory to enable successful feeding, scanning, searching, and matching of fingerprints. Each fingerprint is converted into binary codes and saved in the memory to ensure faster and simpler retrieval. In all the cases, the program returns a success or failure code (i.e., 1 or 0) corresponding to which the vehicle starts or displays an error without starting it along with sending vehicle location data to the owner's mobile and nearby police station through SMS.

4.2 Fingerprint Scanning Process

Principle. Total Internal Reflection (TIR) is the underlying principle of an optical fingerprint scanner. It has a glass prism for the same. The light source (a LED here)
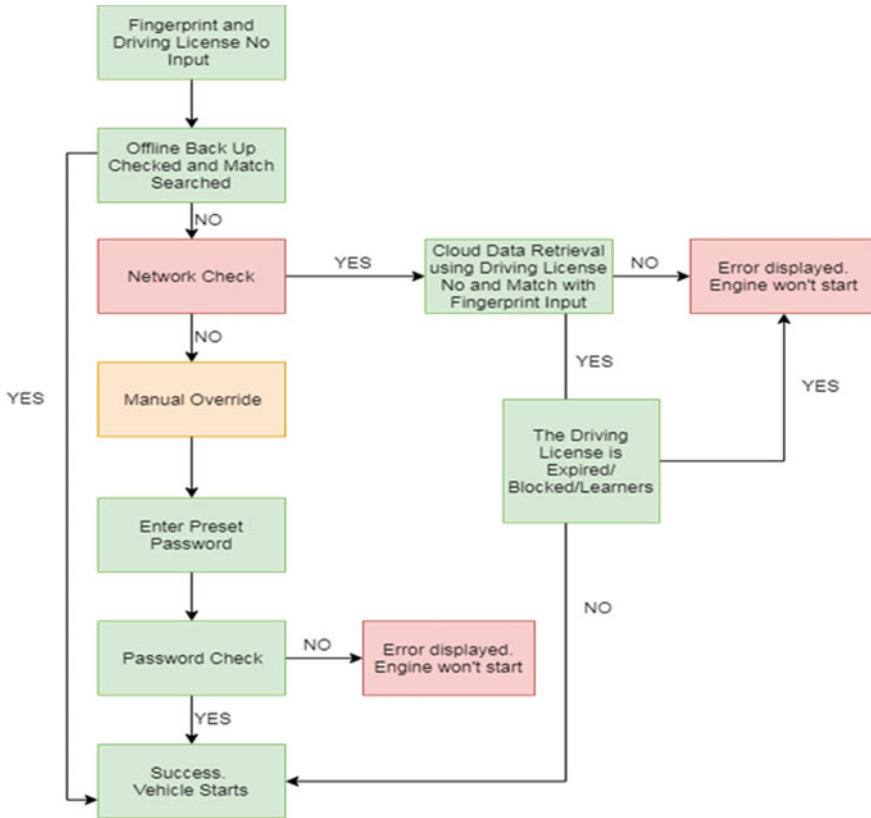
Fig. 6 The flowchart highlighting the algorithm

transmits light that enters the prism at a specific angle for the occurrence of TIR and the reflected light comes out from another face of the prism and falls on a lens and image sensor (a camera, here) (as shown in Fig. 7). In the absence of a finger on the prismatic part of the scanner, complete reflection without refraction occurs from the surface, and in the image sensor, a plain picture is obtained.

In the occasion of TIR, a fraction of the light that leaks in the external atmosphere is known as an Evanescent wave that has different types of interactions with different materials, depending on their respective refractive indexes (RI) [28].On coming in contact with the surface of the glass, the raised portion of the skin (called ridges) makes proper contact with it while the lower portion or valleys have air gaps between them and the glass. This information gets processed to generate an image with good contrast and is the fingerprint's digital copy [3].

Working of the Scanner. The optical sensing device reads and forms the finger-print image by deciding the varying light intensity areas formed by the raised part of the fingerprint. The sensing method begins once someone puts a finger on the touch surface made of glass. Optical sensors largely employ 2 varieties of
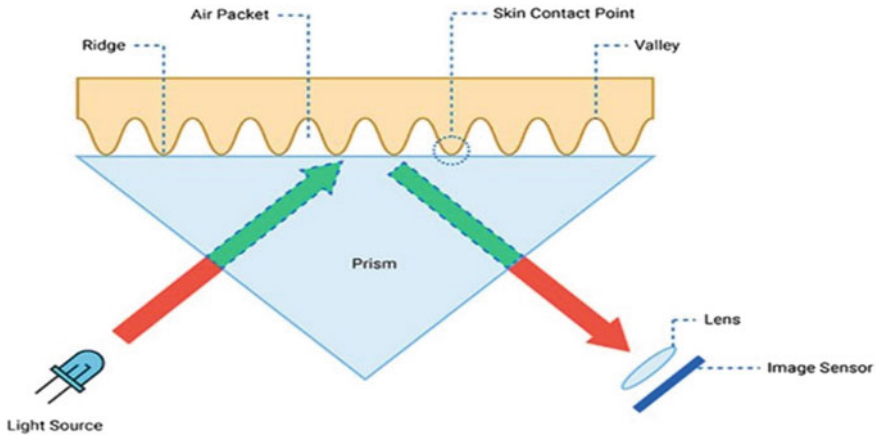
Fig. 7 Working of an optical fingerprint scanner

detecting devices: CMOS (Complementary Metal Oxide Semiconductor) and CCD (charge-coupled-devices) optical imagers.

Before examining one's fingerprint with the impression already stored, the processor of the scanner confirms that the CCD has recorded a transparent picture. It looks for numerous traits like the mean picture element blackness or complete trial values. Once there is proper darkness level, the scanner confirms the image definition to work out the scan intensity. The fingerprint scanner system serves 2 basic functions—to urge a picture of the user in addition to the licensed person's finger and scans the pattern, the ridges, and valleys and puts it within the algorithmic rule as given in computer code design [29]. The particular characteristics, distinctive to every fingerprint, are altered and kept as an encrypted biometric key or as binary codes. The image of fingerprints is not saved; rather verification is finished by the series of numbers (binary code) solely. None will be able to modify the fingerprint image from the series of binary codes or using the algorithmic rule.

If the captured picture is clear with good exposure, the scanner processor goes on to check the captured driving license card. It is a government-issued card provided to citizens above 18 years of age who have the basic acumen to drive a vehicle, given after clearing a driving test. The Smart Card for Driving (shown in Fig. 8) essentially contains the individual's name, date of birth, address, the blood group, year of issue, date of license expiry and biometric templates (taken in the form of fingerprint and iris scan at the time of issue) and every individual is identified by a unique 13 digit number known as the driving license number.

Fig. 8 Driving license smart card (the owner's details hidden for secrecy sake)

4.3 Searching Template, Matching and Starting the Vehicle

After the owner has at first kept the reliable fingerprints of licensed individuals, whenever an individual desires to begin the vehicle, the finger must be placed on the fingerprint scanner. This is repeated twice to reduce the chances of errors due to physical issues. The person also has to enter the license number to reduce the iterations of search online and to make the search operation faster.

First, the search is carried out on the pre-saved database and if not found, it is matched to check online on the cloud database accessed using the driving license number. The device enables setting up of one owner with many trusted users for the offline retrieval database. The match of previously stored and fed fingerprint images is done by finding a central point in the fingerprint image and comparing both templates for match percentage which is cumulative of orientation, brightness, angle, and direction. These make the entire comparison process lengthy and slow [2].

Feature-based matching is employed in which minutiae; primarily ridge ending and ridge division are taken from the stored fingerprint image and the entered image. The matching minutiae pairs between 2 pictures determine the authenticity of an input fingerprint. This method of comparison based on minutiae is more efficient than the non-linear method but is limited by problems like a weak fingerprint impression and poor-quality images (caused by the dry, wet, cut, allergic fingertips) [29]. In case an unauthorized person tries to start the vehicle, immediately after the check fails, an SMS is sent to the owner's mobile and nearest police station, with the location of the person and input details, with the help of the GSM-GPS Module [30].

5 Results and Discussion

The proposed model implementing a Raspberry Pi 3: Model B for vehicle safety was successfully tested and working is found to be satisfactory. In this system, it was

not only ensured that fingerprints match with the stored ones but also the validity of the driving license of the individual driving the vehicle was verified. The device enables setting up of one owner with many trusted users for offline retrieval, keeping in mind the network connectivity issues in India. A manual override option that is password protected is also provided, for emergencies. In case of illegal intervention by an unlicensed individual, the vehicle does not start due to incomplete ignition circuit and the GPS-GSM system installed helps the owner as well as the police to track the automobile.

6 Conclusions

This paper highlights the novel vehicle security system involving Fingerprint scanning and driving license verification, with the help of Raspberry Pi 3: Model B, for starting the automobile. Through an online database (with an offline backup of trusted users), the details of the user are checked and granted access only when a high accuracy match is found in the fingerprint scans and the driving license is found to be valid. In the case of an unlicensed person trying to operate the vehicle, the starter motor does not start. Also, the owner and the police are notified by an SMS with details of the car's location, sent via the GPS-GSM system installed. As the system is easy to install, operate, and involves less cost, it can be set up on any vehicle's dashboard without difficulty.

As shown in previous sections, with our system, underage and unauthorized people will be prohibited from starting a vehicle unless their fingerprint match with the stored templates of licensed individuals and thus, there would be enhanced safety on roads with reduced accidents, that too at a low overall cost.

References

1. Sayantam, S., Aritra, A., Rajendra, P.: Car security system based on fingerprint and IOT. Indian J. Sci. Technol. **10**(40). https://doi.org/10.17485/ijst/2017/v10i40/109854
2. Omidiora, E.A., Fakolujo, A.: A prototype of a fingerprint based ignition systems in vehicles. Eur. J. Sci. Res. **62**, 1450–2216 (2011)
3. Fingerprint Reader Technology Comparison: Optical Fingerprint Scanner; Capacitive-based Fingerprint Reader and Multispectral Imaging Sensor, by Danny, https://www.bayometric.com/fingerprint-reader-technology-comparison. Accessed on 12 Jan 2020
4. Bonthu, B., Kar, A., Hilda, J.J.: Optimized warning and protection system for a vehicle using RFID-based networks. Indian J. Sci. Technol. **9**(28), 1–5 (2016)
5. Pritpal, S., Tanjot, S., Bibhuti, B.B.: A smart anti-theft system for vehicle security. Int. J. Mater. Mech. Manuf. **3**(4) (2015). https://doi.org/10.7763/IJMMM.2015.V3.205249
6. SriAnusha, K., SaddamHussain, S., Kumar, K.P.: Biometric car security and monitoring system using IOT. In: 2019 International Conference on Vision Towards Emerging Trends in Communication and Networking (ViTECoN) (2019). https://doi.org/10.1109/vitecon.2019.8899370

7. Joshi, M.S., Mahajan, D.V.: ARM 7 based theft control, accident detection and vehicle positioning system. Int. J. Innov. Technol. Explor. Eng. **4**(2), 29–31 (2014)
8. Khedher, M.A.A.: Hybrid GPS-GSM localization of automobile tracking system. Int. J. Comput. Sci. Inf. Technol. **3**(6), 75–85 (2011)
9. Ishan, K., Gandhar, D., Saurabh, K.: Intelligent anti-theft tracking and accident detection system for automobiles based on internet of things. Int. J. Innov. Res. Comput. Commun. Eng. (2016). https://doi.org/10.15680/IJIRCCE.2016.040
10. Pethakar, S.S., Srivastava, N., Suryawanshi, S.D.: RFID, GPS and GSM based vehicle tracing and employee security system. Int. J. Adv. Res. Comput. Sci. Electron. Eng. **1**(10), 91–96 (2012)
11. Wankhade, P.P., Dahad, S.O.: Real-time vehicle locking and tracking system using GSM and GPS technology-an anti-theft system. Int. J. Technol. Eng. Syst. **2**(3), 272–275 (2011)
12. Shaikh, J.R., Kate, S.M.: ARM7 based smart car security system. Int. J. Eng. Trends Technol. **3**(2), 210–212 (2012)
13. Kaushik, N., Veralkar, M., Parab, P.: Anti-Theft vehicle security system. Int. J. Sci. Res. Dev. **1**(12), 2845–2848 (2014)
14. Ibrahim, V.M., Victor, A.A.: Microcontroller based anti-theft security system using GSM networks with text message as feedback. Int. J. Eng. Res. Dev. **2**(10), 18–22 (2012)
15. Nagaraja, G., Rayappa, R., Mahesh, M.: Design and development of a GSM-based vehicle theft control system. In: International Conference on Advanced Computer Control. Singapore (2009). https://doi.org/10.1109/ICACC.2009.154
16. Raspberry Pi-3 Model B. https://en.wikipedia.org/wiki/Raspberry_Pi#Model_B. Accessed on 4 Dec 2019
17. Raspberry Pi 3: Description and diagrams. https://www.jameco.com/Jameco/workshop/circuitnotes/raspberry-pi-circuit-note.html. Accessed on 17 Dec 2019
18. Specifications of Raspberry Pi 3. https://thepihut.com/products/raspberry-pi-3-model. Accessed on 17 Dec 2019
19. Fingerprint Scanner R307. https://www.bc-robotics.com/shop/fingerprint-sensor-jm-101/. Accessed on 5 Jan 2020.
20. Working of Fingerprint Scanners. https://www.androidauthority.com/how-fingerprint-scanners-work-670934/. Accessed on 20 Feb 2020
21. Vikhankar, D., Chaudhari, R.P.: Advanced vehicle security system with theft control and accident notification. Int. J. Innov. Res. Sci. Eng. Technol. (2016). https://doi.org/10.15680/IJIRSET.2016.0507149
22. Connecting Raspberry Pi to Fingerprint Scanner. https://tutorials-raspberrypi.com/howto-use-raspberry-pi-fingerprint-sensor-authentication. Accessed on 8 Jan 2020
23. Chandan, K.S., Bhavani, K., Aveena, G., et al.: Antitheft protection of vehicle by using Raspberry Pi & GPS with fingerprint verification. Int. J. Innov. Technol. **06**(01), 0249–0252 (2018)
24. GSM/GPS Architecture. https://en.wikipedia.org. Accessed on 9 Feb 2020
25. GPS-GSM Module Integration. https://robu.in/product/sim808-gsm-gprs-gps-bluetooth-compatible-development-board-with-gps-antenna/. Accessed on 12 Jan 2020
26. Narayanasamy, K., Latha, L., Thangasamy, S.: Real-time biometrics based vehicle security system with GPS and GSM technology. Procedia Comput. Sci. **47**, 471–479. https://doi.org/10.1016/j.procs.2015.03.231
27. GSM-GPS Connection and Working. https://www.rhydolabz.com/wiki/?p=18639%20obu.in/product/sim808-gsm-gprs-gps-bluetooth-compatible-development-board-with-gps-antenna. Accessed on 7 Feb 2020
28. Working of Optical Fingerprint Scanner. https://www.vishnumaiea.in/projects/hardware/interfacing-r307-optical-fingerprint-scanner-with-arduino. Accessed on 16 Feb 2020
29. Koichi, I., Ayumi, M., Takafumi, A., et al.: A fingerprint recognition algorithm combining phase-based image matching and feature-based matching. In: ICB'06: Proceedings of the 2006 International Conference on Advances in Biometrics by Springer, pp. 316–325 (2006). https://doi.org/10.1007/11608288_43

30. Jain, L.H., Pankanti, S., Bolle, R.: An identity-authentication system using fingerprints. In: Proceedings of the IEEE, vol. 85, pp. 1,365–1,388

Crash Sensing Seat Belt Release System

Sagar Jaggi (iD)**, Divyanshu Jaggi** (iD)**, and Pardeep Kumar Rohilla** (iD)

1 Introduction

Over the past decade, vehicle crashes instances have increased on the road surface and lead to the loss of many passengers' lives due to drastic injuries. Recent studies of the transport reveal that the number of crashes has increased. To overcome this problem, the vehicle occupant restraint system (VORS) and three-point seat belt have been implemented by vehicle manufacturing organizations [1, 2]. The VORS confers the energy-absorbing surface between the vehicle occupants and the interior of the car, whereas the three-point seat belt system works in the combination of airbags [3, 4]. It generally consists of a buckle to hold the seat belt, a grip tongue latch plate, and retractors which according to the locking mechanism hold the spool, and webbing which is generally made of polyesters material for the seatbelt as shown in Fig. 1 [5]. The functioning of the seat belt system is as follows; when the seat belt is applied, the seat belt webbing goes from one corner to another and holds the occupant firmly so that the person is in a stable position, and when there is a sudden change in acceleration, webbing gets tighten which resists the motion of the occupant which is the main role of a seatbelt system [6, 7]. The three-point seat belt system has been widely used in vehicles [8]. However, the three-point seat belt system has a limitation, which during collisions the seat belt retractor gets locked up due to extensive load on latch plate and buckle setup [9]. Due to this effect of extensive load, latch plate and buckle get stuck; and the occupants are unable to come out of the vehicle after a collision.

S. Jaggi (✉) · D. Jaggi · P. K. Rohilla
ADGITM (Formerly NIEC), GGSIPU University, New Delhi 110053, India
e-mail: jaggisagar4175@gmail.com

D. Jaggi
e-mail: divyanshu.jaggi@yahoo.com

P. K. Rohilla
e-mail: pardeeprohilla@rediffmail.com

Fig. 1 Existing seat belt locking system (Maruti Wagon R)

To solve this problem, a crash sensing seat belt release system (CSSBRS) has been proposed. In this system, the occupant's seatbelt will release automatically in a predetermined time interval and ensures that the occupants can easily come out from the vehicle after the accident. The CSSBRS consists of various components such as an accelerometer for impact calculation, a gyroscope for orientation sensing, a developer board for sending signals, and a solenoid to generate a magnetic field. It is a way forward in the field of automation as a mechanical latch system (MLS) has a high chance of malfunctioning when a crash of a sudden impact takes place. Sometimes, under a tense situation, the occupant is unable to act swiftly, which may restrict the occupants to use equipment like seat belt cutters, etc. In many cases, the occupants could not release the seat belt due to injury or other reasons like malfunctioning of the conventional mechanical buckle. This leads to the occupant being trapped inside the vehicle, which could be dangerous. The proposed CSSBRS system enhances the passenger's safety when a collision/crash takes place. So, the MLS can be replaced with CSSBRS, which has a more reliable locking system.

2 Design of Crash Sensing Seat Belt Release System [CSSBRS]

The CSSBRS consists of a solenoid instead of a convectional buckle used in a three-point seat belt system. Emergency release system of CSSBRS consists of an accelerometer, a gyroscope, and a developer board along with a solenoid actuator. The accelerometer senses the impact of crash and gyroscope evaluates the vehicle orientation after the crash and if there is no modification in the orientation, the gyroscope generates a signal which ultimately causes the timer to actuate, a timer is used in this system to produce a delay of 20 s so that the impact of forces induced due to collision can come to rest. After a suitable time, the solenoid actuator will actuate cause releasing of seat belt [10].

Fig. 2 Block diagram of
CSSBRS
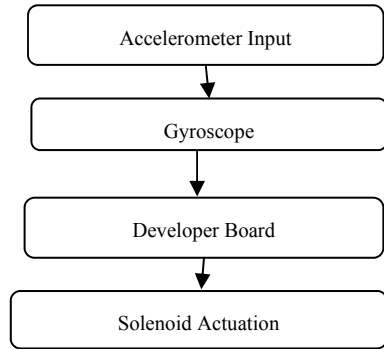
The working of the CSSBRS is shown with the help a of block diagram as shown in Fig. 2. Firstly, instant change in the inertia of the vehicles (due to collision) is detected by an accelerometer which sends a signal to the controller. Once the collision is detected, the gyroscope computes the orientation of the vehicle. When the vehicle's orientation is stable, the gyroscope sends a signal to the controller. After receiving the signal from the gyroscope, a delay is produced by the controller this delay is provided to make sure that the vehicle's internal forces became stable after a collision. After the predetermined time expires, the controller sends a signal to the actuator to release the seatbelt. To release the seatbelt, the current input of the solenoid is cut and thus the seat belt is released (as the magnitude of magnetic force reduces). The controller is designed in such a manner that it will not release the seat belt until the orientation of the car is in a secure position so that no neck or shoulder injury is faced by the occupant.

3 Amendment in Seat Belt Buckle

As we know the function of a seat belt buckle to absorb the impact of the collision and try to restrict the motion of the passengers, which can be achieved by holding the latch placed inside the buckle stationary. In CSSBRS, an electromagnetic buckle is used in place of a conventional mechanical buckle used in three-point seat belt system, and the electromagnetic buckle consists of a cylindrical coil which contains a certain number of turns which are sufficient to produce an adequate magnetic field which can easily bear the impact of the collision of the vehicle. The material used to construct the cylindrical coil is generally copper because it has a greater value of thermal stability and magnetic properties in comparison with other materials. The advantage of using the modified buckle in comparison with the ordinary buckle is that it reduces the chance of malfunctioning when a crash of sudden magnitude takes place.
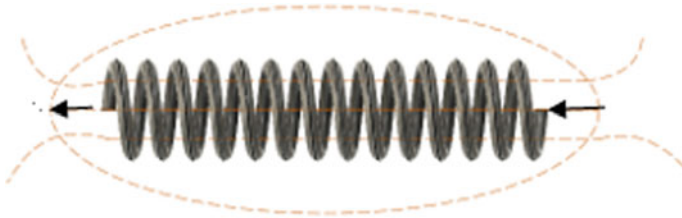
Fig. 3 Solenoid (used as modified buckle)

4 Components Used in CSSBRS

4.1 Solenoid

A solenoid is a long coil of wire which consists of a certain number of turns, as shown in Fig. 3. When current is passed through the coil, a uniform magnetic field is produced inside and the magnetic force can be used as a locking agent that holds the latch stationary like a mechanical lock. The strength of the magnetic force is adequate to withstand the impact of force generated due to a crash. As we know solenoids convert electric current into magnetic action when a current is passed through the coil, the implementation of the CSSBRS became fairly easy as the process of releasing the seat belt can take place just by cutting the supply of current in the solenoid.

4.2 MPU 6050

MPU 6050 is a combination of three axes gyroscope and a three axes accelerometer with an onboard digital motion processor. The accuracy of this sensor is greater as compared to other sensors. When the sensor is rotated, a signal is generated due to vibration, and this signal is further amplified and demodulated to produce a potential difference that is proportional to angular deviation. An accelerometer is used to detect the change in the value of acceleration which is the measurement of the change in velocity divided time. This helps to detect whether a crash has occurred as when a crash took place there is a sudden change in the value of acceleration which can be detected by an accelerometer and also accelerometer is able to measure the impact of collision irrespective of the impact point of a collision.

4.3 Developer Board

Arduino Uno is used as a developer board. It has a total of 20 digital input/output pins. The main function of this board is to evaluate the circumstances and decide

Table 1 Arduino Uno specifications	Operating voltage	5 V
	Input voltage	12 V
	I/O digital pin	Pin No-13
	Clock speed	16 MHz
	Analogue input pins	6 Pins
	DC per I/O pins	40 mA

whether a vehicle has experienced a crash and if so then evaluate other parameters like the orientation of the vehicle and produce a delay of a certain period of time in which the conditions became suitable for the seat belt to be unfastened. Programs can easily be loaded using the Arduino computer program. The pin used for transmission of data from developer to the solenoid is Pin-13 in this given system (Table 1).

5 Programming of Developer Board

```
#include <Wire.h>
const int MPU = 0x68;
float AccX, AccY, AccZ,GyroX, GyroY, GyroZ,accAngleX, accAngleY, gyroAngleX,
gyroAngleY, gyroAngleZ,roll;
    float elapsedTime, currentTime, previousTime;
    int c = 0,flag = 0,threshold_acc = 315;// Value of Threshold Acceleration is taken as
315 meter/second square, So if the value of acceleration ever became greater than
threshold value then the system will detect a crash.
    int Device_active = 13;
    void setup() {
    Serial.begin(9600);
    Wire.begin();
    Wire.beginTransmission(MPU);
    Wire.write(0x6B);
    Wire.write(0x00);
    Wire.endTransmission(true);
    delay(20);
    }
    void loop() {
```

```
Wire.beginTransmission(MPU);
Wire.write(0x3B);
Wire.endTransmission(false);
Wire.requestFrom(MPU, 6, true);
AccX = (Wire.read() << 8 | Wire.read()) / 16384.0; // X-axis value
AccY = (Wire.read() << 8 | Wire.read()) / 16384.0; // Y-axis value
AccZ = (Wire.read() << 8 | Wire.read()) / 16384.0; // Z-axis value
GyroX = (Wire.read() << 8 | Wire.read()) / 131.0;
GyroY = (Wire.read() << 8 | Wire.read()) / 131.0;
GyroZ = (Wire.read() << 8 | Wire.read()) / 131.0;
GyroX = GyroX + 0.56;
GyroY = GyroY - 2;
GyroZ = GyroZ + 0.79;
gyroAngleX = gyroAngleX + GyroX * elapsedTime;
gyroAngleY = gyroAngleY + GyroY * elapsedTime;
roll = 0.96 * gyroAngleX + 0.04 * accAngleX;
int absolute = abs(AccX);
if (absolute > threshold_acc)
  flag = 1;
if ((flag == 1) && (roll < 30)) //Accident Detected

{ delay(20000);// To Produce Delay of 20 Seconds
  digitalWrite(Device_active, HIGH);
}
}
```

The desired result of this program is to calculate the magnitude of the collision as well as the orientation of the vehicle; these parameters are further evaluated and then compared to the values of threshold acceleration and roll of the vehicle. If the results obtained reflect that an accident has occurred then a timer is initiated, which is required to produce a delay of certain duration of time.

6   Conclusions

Vehicle crashes instances have increased on the road surface and lead to the loss of many passengers' lives, one of the causes being the inability to release seatbelt because of the deficiency of mechanical buckle. The latch plate and the buckle get stuck due to extensive load, which leads to restrict the motion of the occupants after the collision. Hence, for the safety of the occupants, the CSSBRS system is proposed. The CSSBRS is designed in such a way that it ensures the safety of the passengers in all possible means, and this system automatically releases the seatbelt when it is assured that the vehicle is in a secure position. The main motivation of this system is to overcome the limitations of the existing three-point mechanical buckle and ensure that no severe injuries are caused to the occupants.

References

1. Davee, D., Raasch, C., Moralde, M., Van Arsdell, W.: Seat Belt Buckle Release by Inadvertent Contact. SAE Technical Paper 2008-01-1236). https://doi.org/10.4271/2008-01-1236
2. Nowak, W., Nowak, Z., Nowak, J.: Device for emergency cutting off fastened seatbelts (2016, Nov 22). US Patent 9,499,122 [Online]
3. Ammons, A.: Seatbelt Q-Release (2014, Aug 14). US Patent Application 14/170,421 [Online]
4. Ammon, A.C.: Seatbelt safety release (2011, Dec 29). US Patent 13/134,366 [Online]
5. Roy, J.E., Cruthirds, D.C.: Safety belt release mechanism (2011, May 17). US Patent 7,941,902 [Online]
6. Van Rooyen, R., Roelof, T.I.: Automatic safety belt release (2010, May 18). US Patent 7,717,216 [Online]
7. Meurer, W.K.: Seatbelt cutter (1987, Jul 21). US Patent 4,680,861 [Online]
8. Alcidi, L., Grassi, G.: Apparatus for the automatic release of a motor-vehicle safety belt after a collision (1992, June 23). US Patent 5,123,498 [Online]
9. Jogdhankar, S.R., Rahul Bhardwaj, S.D.: Seatbelt safety feature using sensor to protect occupant. Int. Rev. Appl. Eng. Res. **4**(4), 349–354 (2014)
10. Thomas, G.D.: Automatic seat belt release system (2009, Jun 4). US Patent Application 11/998,789 [Online]

Vibration Control Using Two Electromagnetic Actuators on a Simply Supported Beam

P. Abhijit Mitra and Sankha Bhaduri

1 Introduction

The structures that we see in our everyday life are always exposed to some kind of external force or wearing agent such as any impact force or a jerk or sometimes maybe even the load it is supposed to lift or carry and which results in the deformation or breaking of the structure. It is a natural phenomenon or sometimes forced and has both useful and harmful effects. Mechanical vibrations can cause a lot of damage to solid objects or structures. The vibration that is observed is basically the constant to and fro motion of the body about its fixed static position when provided any exciting force.

The magnitude of the vibration causing force may vary from time to time, place to place, situation to situation, or perhaps even on the type of body we are considering in the environment. The force may be one which acts like a sine wave or which comes from two different directions time to time or maybe even a force that has a periodically changing magnitude to itself. The frequency even at which the force comes may even vary or remain constant. The frequency of this force might come at its natural frequency as studied by Ziegler et al. [1] in 2005. The magnitude of the force may be small or equal to weigh of the body or a large load that begins to act on the body, creating damage as expressed by Johnson et al. [2] in 1960 in their book.

The control of this vibration can be done in two ways, that is, active vibration control and passive vibration control. The methods of passive vibration control make use of spring or viscous dampers or stuff to absorb the vibration of the body. It does not depend on the magnitude of the exciting force but is expected to act as per the specification of the damper itself studied by Zolkiewski [3] in 2011 and Gaul [4] in 1999.

P. A. Mitra (✉) · S. Bhaduri
Department of Mechanical Engineering, Birla Institute of Technology, Mesra, Ranchi, India
e-mail: mechanicalkbatch7@gmail.com

But the method that is being discussed in this paper is the active vibration control method in which a counter force to the initial force will be applied so as to nullify the displacement of a simply supported beam. Simulation work is done in MATLAB to observe the change in the displacement due to the application of the actuators. Two electromagnetic actuators are applied in such a manner that one actuator is placed below and one above the beam and the electromagnetic force that acts on the beam will reduce the displacement of the beam after application of the input force.

2 Mathematical Modeling of Simply Supported Beam

A simply supported is considered of length 70 cm, and its cross section is considered as length 2.6 cm and breadth 0.6 cm. This is done so as to help visualize the beam properly and try find out its physical proper ties. Its area moment of inertia is calculated [5] using following mathematical formula:

$$I = \frac{1}{12} \text{breadth} * (\text{height})^3$$

This came out to be 8.4×10^2 cm⁴.

Next the material of the beam is selected as mild steel which is widely used steel. The Young's modulus of elasticity of the material happens to be 200 GPa. Hence, the stiffness of the beam so calculated is:

$$k = 48 \frac{E * I}{l^3} \tag{2.1}$$

So, the stiffness comes to be 1309.90 N/cm and mass is 0.85 kg.

The beam is modeled as a single degree of freedom system. The first natural frequency (ω_n) of the beam as calculated based on the above stiffness and mass is 20 Hz. This is done because most of the real-life structures that we see around us are one degree of freedom systems [6]. The equation of the motion of single degree of freedom model of a simply supported beam [5] is:

$$\ddot{x} = -\frac{c}{m}\dot{x} - \frac{k}{m}x + \frac{F}{m} \tag{2.2}$$

This above equation can be written in matrix form as:

$$\begin{Bmatrix} \ddot{x} \\ \dot{x} \end{Bmatrix} = \begin{bmatrix} \frac{-c}{m} & \frac{-k}{m} \\ 1 & 0 \end{bmatrix} \begin{Bmatrix} \dot{x} \\ x \end{Bmatrix} + \begin{bmatrix} \frac{1}{m} \\ 0 \end{bmatrix} * F \tag{2.3}$$

$$\{x\} = \begin{bmatrix} 0 & 1 \end{bmatrix} \begin{Bmatrix} \dot{x} \\ x \end{Bmatrix} + \{0\} * F \tag{2.4}$$

3 Simulation Model

The simulation work is executed in MATLAB–Simulink using suitable operators and functions. The simulation model that is created has been shown in Fig. 1. As it is clear from it, the two actuators are being placed one above and one below the beam. The initial gap between the beam and the magnets is considered 4 cm. One of the actuators is placed 4 cm below the beam and another one is placed 4 cm above the beam. The Simulink model that is created consists of a sine signal input force, a state-space block in which the single degree of freedom model of the beam is mathematically defined. Current is controlled with a manual switch provided with a knob and finally an oscilloscope to take readings of the displacement of the beam. This displacement reading is taken with a displacement sensor and is shown with the help of oscilloscope in the simulation.

The state-space block used here operates using the following equations to take input and give output:

$$\dot{X} = Ax + Bu \tag{3.1}$$

$$Y = Cx + Du \tag{3.2}$$

Comparing Eq. 2.3 with Eq. 3.1 and Eq. 2.4 with Eq. 3.2, it is found that matrices A, B, C, and D can be defined in the state-space block in the following manner:

$$A = \begin{bmatrix} -c/m & -k/m \\ 1 & 0 \end{bmatrix} \quad B = \begin{bmatrix} 1/m \\ 0 \end{bmatrix}$$
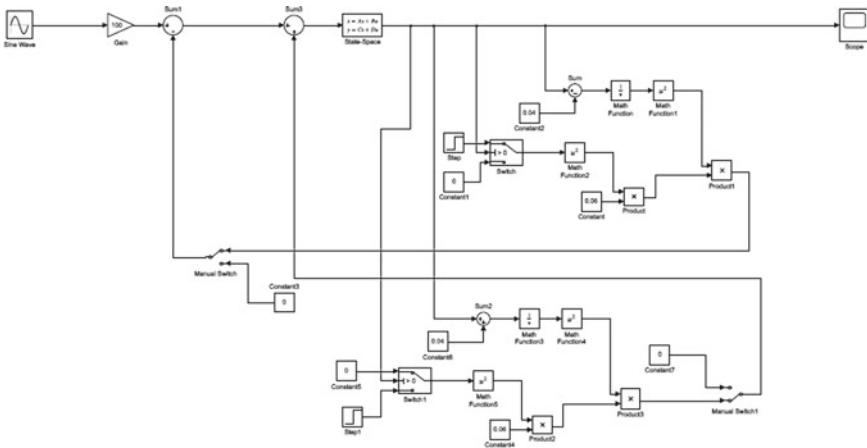
Fig. 1 Simulation model for beam and actuators

$$C = \begin{bmatrix} 0 & 1 \end{bmatrix} \quad D = 0$$

It is clear from Fig. 1 the output of the state-space block is displacement which is used to calculate the gap between beam and the top actuator and gap between beam and bottom actuator. The feedback force or actuating force is basically the electromagnetic force comes from either the top or bottom actuator. When the beam is below the equilibrium line, the top actuator is switched on, and when it is above the equilibrium line, the bottom actuator is on and applies the electromagnetic force. The output displacement of the beam is observed in oscilloscope.

3.1 Actuator Used in Simulation

The double electromagnetic actuators are used in this study where one electromagnetic actuator is placed below and one electromagnet is placed above the beam. The actuator that is used here is a coil of wire wrapped around a metallic core. The distance between the actuators and the beam is 4 cm, respectively.

The current in the actuators is a DC current that will be passed. The wires that carry the current are connected to a knob or a switch such that it can be put on and off as per our need and timing. Moreover, the source of the current is such that the magnitude of the current could be changed manually as per the wish of the operator.

4 Numerical Analysis

In this paper, the vibration of a simply supported beam is controlled whose dimensions are length 70 cm and cross section of the beam is taken as width 2.6 cm and height 0.6 cm. The state-space matrices in MATLAB are defined as follows to model the beam:

$$A = \begin{bmatrix} -0.248 & -15410.588 \\ 1 & 0 \end{bmatrix} \quad B = \begin{bmatrix} -1.166 \\ 0 \end{bmatrix}$$

$$C = \begin{bmatrix} 0 & 1 \end{bmatrix} \quad D = 0$$

The magnet that is being used has a cross-sectional area of 2.00 cm^2 and is characterized by its properties. It will have 100 turns in its coil. These parameters are useful in calculating the permittivity of the magnet used in the actuators. This will be calculated by using the formula:

$$k' = \mu_0 a_m n^2 \tag{4.1}$$

Table 1 Excitation force parameters

S. No.	Working frequency of force		Time (s)	Magnitude (N)
	(rad/s)	(Hz)		
01	125.66*	20*	10	20

*Natural frequency of the beam

Here, a_m is the area of cross section of magnet and n is the number of turns in the magnet. So the value of k' comes to be:

The value of k' comes to be:

$$k' = 0.0628 \text{ N/m}^2\text{A}^2$$

The simulation work is conducted with the beam whose specifications have been discussed above. The magnets are applying an electromagnetic force on the structure to control its movement. The magnitude of force will be determined by the current and gap between the beam and actuators given by the working formula:

$$F = k' * \frac{i^2}{\text{gap}^2} \tag{4.2}$$

Here, in the above formula, i is the current in the coil of electromagnet and *gap* is the distance from the beam to the center of magnet in consideration.

An external sinusoidal load whose magnitude is 20 N and frequency is 20 Hz is applied on the beam to take the vibration readings from the structure and observe its behavior (Table 1). The frequency of operation is the natural frequency so as to help obtain the first mode shape of the beam and determine the maximum shift in position of the beam. The oscilloscope here is used to take the displacement and velocity readings.

The current values can be changed depending on the time of application of the current. The variable is time in step input operator and the sine signal which is giving a vibration force of constant frequency all the time. This helps us find the actual force that would be provided by the actuators after different intervals of time. The time of changing of the current is set to 1.5 s.

5   Result and Discussion

The graphs obtained in the oscilloscopes have been shown in Figs. 2 and 3. As it is evident from the curves itself maximum displacement of beam comes to be 0.6 cm from its mean static position (Table 2). Its velocity is also observed throughout its motion. This force is acted upon the structure for a time span of 10 s.
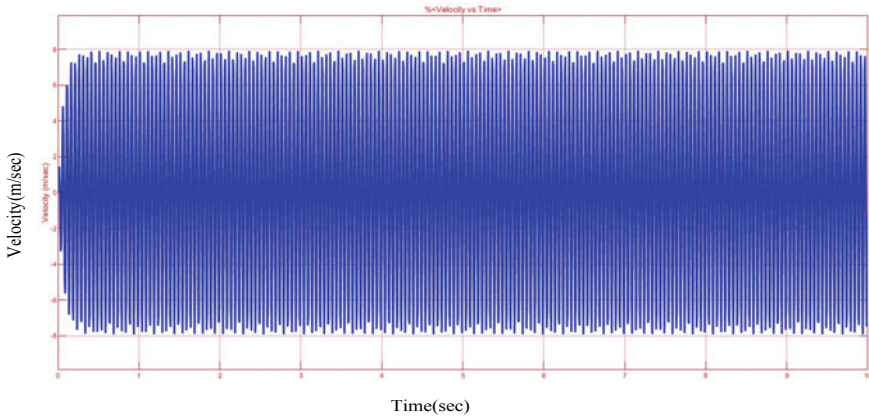
Fig. 2 Velocity versus time curve with actuator switch 'OFF'
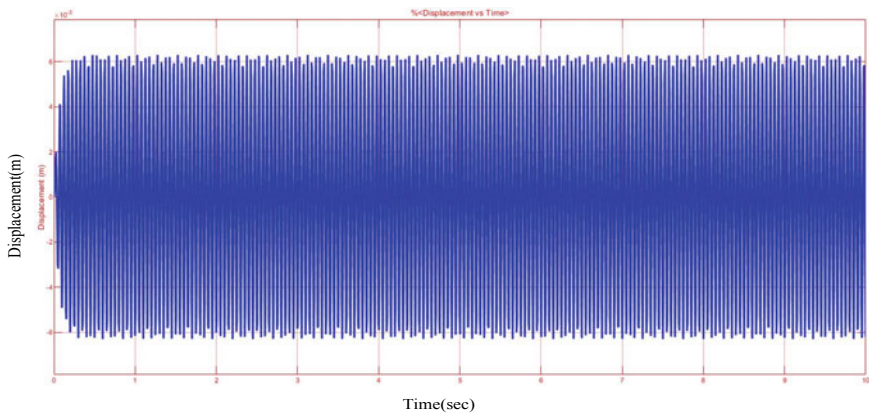
Fig. 3 Displacement versus time curve with actuator switch 'OFF'

	S. No.	Time (s)	Mode shape	Maximum displacement (cm)
Table 2 Displacement of beam for uncontrolled vibration	01	10	1st mode	0.6

The output on the scope when actuator switch is off is a simple displacement time curve of body having a vibrating motion in Y-axis (Fig. 3). The maximum displacement is observed in the natural frequency zone as expected. The frequency of the sine signal is given at ω_n so as to see the maximum effect of the force on beam. The nature of the velocity time curve is almost the same with a different scale on the Y-axis of course and the frequency as provided.

The uncontrolled displacement of beam due to application of force is shown in Fig. 2 and tabulated in Table 2 and uncontrolled Fig. 3 as received from the sensors.

Now the actuators that are switched on the controlled displacement are observed and are shown in Fig. 4, and that maximum value of displacement is observed as 0.1 cm and tabulated in Table 4. The displacement is taken as the parameter to determine the efficiency of the control method used. The shift in position of the beam has been reduced by many folds. It is quite clear that the beam is now under the influence of two counter forces which are nullifying the effect of each other.

The time after which the current changes is applied is 1.5 s. The initial current value is 0.4 A and the final magnitude is 0.8 A as tabulated in Table 3. Hence, the displacement is reduced by 90% as shown in Table 4. It is also visible from the curve seen in Fig. 4 is that the mean position of the structure almost does not shift from its initial static mean position.

It must be mentioned here that the excitation force has been applied in a manner that the first mode shape (Table 2) of the beam modeled is seen in the oscilloscope. However, by applying a load of higher frequency, the second and third mode shapes may be obtained as well. But the model created is applicable to all the situations discussed and is useful by just changing the current as per need.
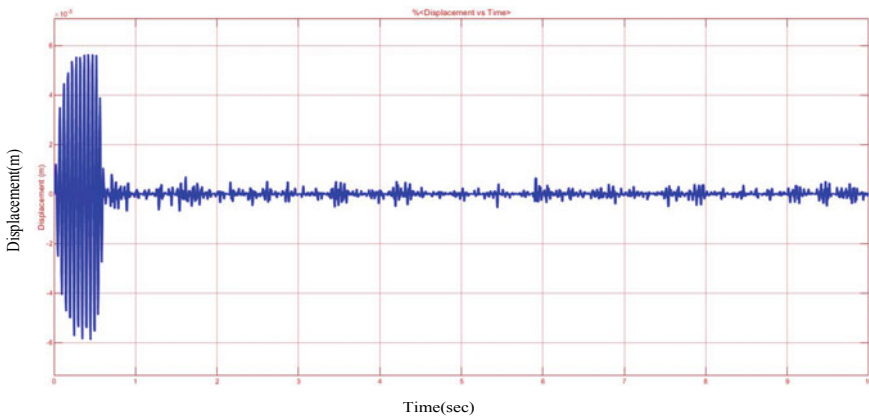
Fig. 4 Displacement versus time curve with actuator switch 'ON'

Table 3 Current in actuator

S. No.	Initial current (A)	Time (s)	Final current (A)
01	0.4	1.5	0.8

Table 4 Result and efficiency

S. No.	Displacement (cm)		Difference (cm)	Efficiency (%)
	Initial	Final		
01	0.6	0.1	0.5	90

It is seen that a good efficiency is obtained in reducing the beam displacement. The curve is sooth curve with no real rise suddenly in the movement and the maximum and minimum were reduced to almost a uniform value. In simple word from the initial situation where the beam is shifted to a large extent to damage the structure, the actuators restricted the motion to a limit where there is almost no sudden up or down motion of the structure modeled.

6　Conclusions

Finally, it is concluded from the above observations that the electromagnetic actuators so designed are very useful tools to control the vibration of a simply supported beam [7]. They are quite effective in its work and are useful in the sense that the current can be controlled as per the requirement and the beam.

It might be said that the beam in consideration was a single degree of freedom system and is not always applicable to a few complex real-life situations. Most of the industrial and urban designs have only one degree of freedom. The frequency of the vibrating forces in everyday life may vary and different mode shapes are observed which doesn't depend upon the magnitude. All of this is successfully tackled by the actuators used. Considering this the model is useful for the simple machines and structures by varying the control force.

The current that was supplied was a DC current as it is easy to supply and control the vibration of the structure. The model is also applicable to various other structures like rotor or other types of beams etc. It is also useful to reduce vibration for different degrees of freedom of beams and frequencies by increasing the current values. Finally this model is proving to be useful in the manner it was intended. This model is also applicable to various different vibration causing sources too.

References

1. Reiterer, M., Ziegler, F.: Control of pedestrian induced vibrations of long span bridges. Struct. Control Health Monitor. (2005)
2. Bishop, R.E.D., Johnson, D.C.: The Mechanics of Vibration. Cambridge University Press, Cambridge, UK (1960)
3. Zolkiewski, S.: Damped vibrations problem of beams fixed on the rotational disk. Int. J. Bifurcation Chaos **21**, 3033–3041 (2011)
4. Gaul, L.: The influence of damping on waves and vibrations. Mech. Syst. Signal Process. (1999)
5. Rao, S.S.: Chapter 9, Vibration control. In: Mechanical Vibration, vol. 5, pp. 819–830 (2009)
6. Ghodgi, V., Bhattu, A.P., Patil, S.B.: Vibration analysis of beams. Int. J. Eng. Trends Technol. **55**(2), 81–86 (2018)
7. Benning, R.D., Hodgins, M.G.: Active control of mechanical vibrations. Bell Labs Tech. J. **2**(2), 246–257 (1997)
8. Chin H.C., Pang X., Wang Z.: Analysis of bus ride comfort using smartphone sensor data. Comput. Mater. Continua, 455–463 (2019)

9. Krehel, R., Pollak, M., Kocisko, M.: Research on impact of mechanical vibration on the production machine. Adv. Mech. Eng. **8**(7), 1–10 (2016)
10. Zhou, N., Guang, B., Jiang, H.H., Bai, S.: Active vibration control simulation research of carbody vibration using piezoelectric actuators. Machinery Design and Manufacture, Southwest Jiaotong University, p. 10 (2015)
11. Huang, S.-c., Lin, K.-a.: A new design of vibration absorber for periodic excitation. Shock Vibr. **2014**, article ID 571421, 1–11 (2014)
12. Vogneshwaran, K., Behra, R.K.: Vibration analysis of simply supported beam with multiple breathing cracks. In: 1st International conference on Structural integrity, ICONS-2014, pp. 835–842
13. Hosseinabadi, A.H.H., Altintas, Y.: Modeling and active damping of structural vibrations in machine tool. CIRP J. Manuf. Sci. Technol. **7**(3), pp. 246–257 (2014)
14. Macdonald, J.H.G.: Lateral excitation of bridges by balancing pedestrians. Proc. R. Soc. A, 1055–1073 (2008)
15. Zheng, J., Luo, R.: Vibration analysis of railway passenger car systems by considering flexible carbody effect. J. China Railway Soc., p. 06 (2007)
16. Barcik, M., Koneczny, J., Kowal, J., Sapinski, B.: Vibration control of mechanical systems—introduction to the problem. Acta Montanistica Slovaca, Rocnk **3**, 504–509 (1998)
17. Johnson, C.D.: Design of passive damping systems. ASME J. Vib. Acoust. **117B**, 171–176 (1995)
18. Bicos, A.S., Springer, G.S.: Analysis of free damped vibration of laminated composite plates and shells. Int. J. Solids Struct. **25**(2), 129–149 (1989)
19. Forward, R.L., Griffin, W.S.: Wideband electromagnetic damping of vibrating structures. US Air Force, application no. 49358, January 1989
20. Forward, R.L.: Electronic damping of vibration in optical structures. Appl. Opt. **18**(5), 690–697 (1979)
21. Abdel-Ghaffar, A.M.: Free torsional vibration of suspension bridges. J. Struct. Div. (1979)

CFD Analysis of an Airfoil Due to the Influence of Active Airflow

Asim Ahmad , **Om Prakash** , **and Anil Kumar**

1 Introduction

CFD stands for computational fluid dynamics, and it is a part of fluid mechanics. It helps in analysing the behaviour of the physical system of fluid. CFD analysis has become popular after analysing the increasing rate of difficulties in applying the different laws of physics in real life. Fluid mechanics tells us about the forces acting on the fluid body and its changes Such as density, velocity, temperature and pressure. These types of relationships have also been shown through differential equations [1].

By applying numerical modelling, CFD changes differential equation into two linear equation form which will further solve the values of different fields such as pressure, velocities and temperature. Although numerical modelling is not a new method, CFD gives the facility to store a large amount of data and faster performance which helps the engineer and scientist to solve the practical problems easily [2].

A wing blade which consist of sail, turbine, rotor and propeller that has cross-sectional shape is termed as airfoil. An aerodynamic force is generated by the body having airfoil-shaped moving through a fluid. The part of the force which is perpendicular ($\perp$) to the direction of motion is termed as lift and the part which is parallel to the direction is termed as drag [3]. The schematic diagram of airfoil is shown in Fig. 1.

A. Ahmad · O. Prakash (✉)
Department of Mechanical Engineering, Birla Institute of Technology, Mesra, Ranchi 835215, India
e-mail: 16omprakash@gmail.com

A. Ahmad
e-mail: asimlife91@gmail.com

A. Kumar
Department of Mechanical, Production & Industrial and Automobile Engineering, Delhi Technological University, Delhi 110042, India
e-mail: anilkumar76@dtu.ac.in
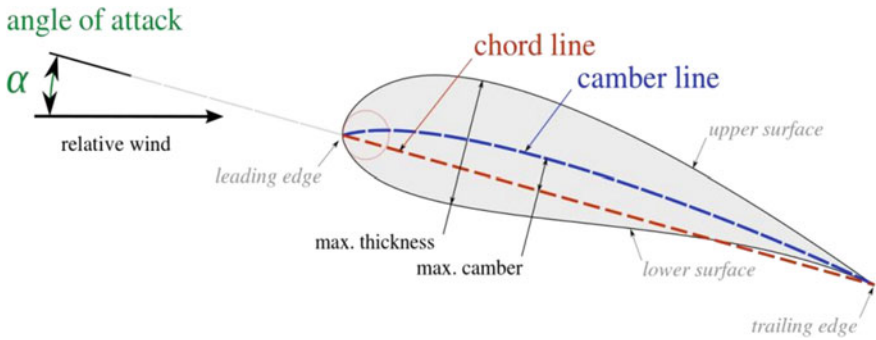
Fig. 1 Schematic diagram of an airfoil

The point at the front position of airfoil has maximum curvature which is termed as leading edge, and the point at the rear position of airfoil is termed as training edge. The chord line is the straight line joining trailing edge and leading edge, and it refers about the dimension of airfoil section. The mean line is the point at the midway between lower surface and upper surfaces. The maximum distance between the chord line and camber line is referred as maximum camber [4].

Airfoils are divided into three classes: high speed, general purpose and high lift. The example of high-speed section is high-speed aircraft. It has very low thickness, sharp leading edge and no chamber. The maximum thickness of high-speed aircraft is 50% chord point. The airfoil section of general purpose has lower thickness, sharper leading edge and less chamber. The airfoil section of high lift used in aircraft and sail planes is having short field operation [5]. The classification of airfoil is shown in Fig. 2.

The airfoil under study is NACA (National Advisory Committee for Aeronautics) 63-212. NACA 63-212 falls under the category of "high-speed" airfoil. The specifications of NACA 63-212 to be used in the analysis are length: 190 mm, chord length:

Fig. 2 Classification of airfoils
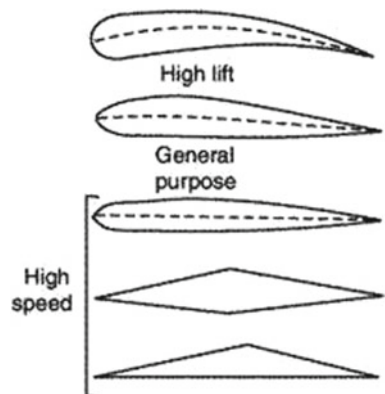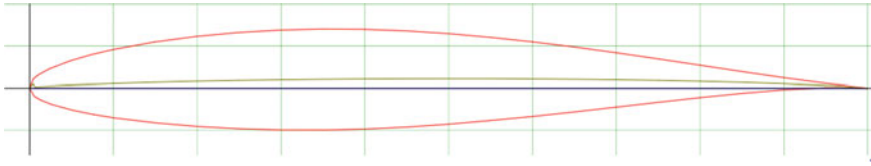
Fig. 3 Cross section of NACA 63-212

254 mm, max. thickness 12% at chord of 34.9% and max camber. 1.1% at chord of 55% [6]. The cross section of NACA 63-212 is shown in Fig. 3.

Askari et al. [7] has done the CFD analysis to analyse the compressible flow around the biconvex and double-wedge airfoil and concluded that the coefficient of aerodynamic gained from both numerical and analytical methods. Olejniczak et al. [8] have analysed the heat transfer coefficient and surface pressure of double-wedge airfoil experimentally and numerically. Raghunathan et al. [9] have found the significant impact of shock-induced separation by considering the shock oscillation on the origin. From the above literature survey, it was observed that very few or none of the researcher has worked towards the CFD analysis of the airfoil NACA 63-212. The present research work deals with the results obtained from aerodynamic testing of the airfoil NACA 63-212. The modification was done on the upper layer of the airfoil while preparing 3D CAD model. This will allow testing with and without additional active airflow on the upper portion.

2 Methodology

2.1 Preparation of CAD Model

For designing the CAD model, the steps were followed such as the coordinates of the cross section of the NACA 63-212 airfoil were obtained from the NACA online database and extracted to the 3D CAD modelling software SOLIDWORKS as shown in Fig. 4. The generated cross section was extruded to a length of 190 mm (length of the leading edge). Next, a horizontal slit of length 180 mm was cut along the leading edge. Finally, 36 holes (in the arrangement of 4×9) of diameter 6 mm each were cut on the upper portion of the airfoil and extended depth-wise to meet to slot. This allows the air to enter from the horizontal slot and leave from the holes on the upper surface, thus creating an additional active airflow on the upper surface of the airfoil.
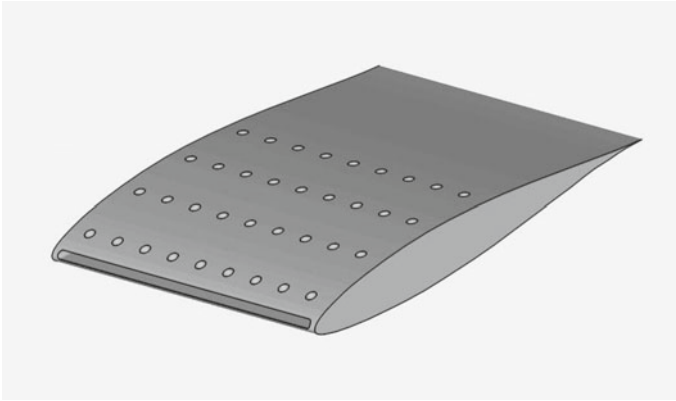
Fig. 4 3D CAD model of the modified airfoil

2.2 CFD Simulation and Analysis

To generate the CFD simulation and conduct the analysis, an online CFD simulation software SimScale is used [10, 11]. The following steps were carried out in the process:

i. A new project was created on the SimScale user dashboard. The 3D CAD model was uploaded in the STL file format, and the standard unit was set as mm (millimetres).

ii. A new simulation was created, the flow was assigned as incompressible flow, and air was selected as the fluid material.

iii. In the initial conditions option, the (P) gauge pressure was set to the atmospheric pressure, i.e., 101,325 Pa; the (U) velocity was set as $10\,\text{ms}^{-1}$ in the positive x-direction.

iv. In the boundary conditions options, the inlet velocity was set as $10\,\text{ms}^{-1}$ in the positive x-direction on the entire volume, and the outlet pressure was set as 0 kPa (corresponding to the case of testing without additional active airflow).

v. Now, the geometric model is complete, and the mesh is generated.

vi. After the generation of mesh, the simulation is run to get the results.

vii. Finally, post-processing option is selected after the simulation ends to get the resulting fields, make numerical analysis on different surfaces of the geometry along different directions and to generate plots.

viii. The process is repeated for the following values of outlet pressure: 0.5 kPa, 2.5 kPa, 1 kPa, 10 kPa, 7.5 kPa, 5 kPa (corresponding to the case of overpressure) and −0.5 kPa, −2.5 kPa, −1 kPa, −10 kPa, −7.5 kPa, −5 kPa (corresponding to the case of underpressure).

ix. The post-processing generates the values of absolute pressure on each section of the airfoil as shown in Fig. 5. The lift and drag force were directly obtained
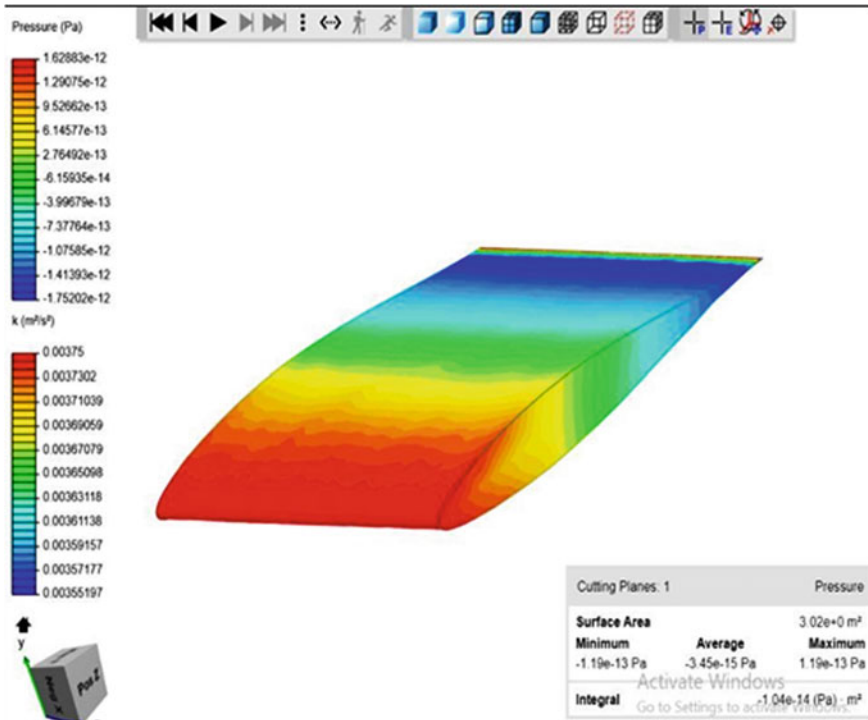
Fig. 5 Post-processing of the simulation on SimScale software

by integrating the respective pressure difference over the reference area of the airfoil for each case of computation.

2.3 Lift and Drag Coefficients

The lift coefficient (C_l) is a dimensionless coefficient that associates with the lift produced by an object to the fluid density throughout the body, the fluid velocity and related reference area. Similarly, the drag coefficient (C_d) is a dimensionless quantity that is used to quantify the drag or resistance of an object in a fluid environment and its relation to the fluid velocity, the fluid density and the related reference area.

The expression for drag and lift coefficients are as follows [12, 13]:

$$C_d = \frac{D}{\frac{1}{2}\rho A v^2} \tag{1}$$

$$C_l = \frac{L}{\frac{1}{2}\rho A v^2} \tag{2}$$

where

C_l Lift coefficient
v Velocity of fluid (air)
C_d Drag coefficient
ρ Density of fluid (air)
A Reference area
D Drag force
L Lift force.

3 Result and Discussion

The CFD simulation was carried out with some of the research parameters being fixed as given in Table 1. These parameters and their respective values are given in Table 1.

3.1 Values Obtained After Post-processing

The values obtained for lift force and drag force from the simulation's post-processing for different values of pressure for cases of overpressure and underpressure are given in Table 2.

The values of drag and lift forces obtained from the simulation are substituted in the lift equation and drag equation, respectively, to get the drag and lift coefficients for each case of underpressure and overpressure. The resultant values are given in Table 3.

3.2 Graphical Representation and Interpretation

The variation of lift force and drag force over different values of overpressure and underpressure is represented in the graphs below, i.e., Figs. 6 and 7. The graphs indicate that both the drag and lift forces increase by increasing the underpressure

Table 1 Research parameters

Parameter	Value
Fluid velocity (v)	$10 \ \mathrm{ms^{-1}}$
Reference area (A)	$0.19 \ \mathrm{m} \times 0.254 \ \mathrm{m}$
Angle of attack (α)	$0°$
Fluid density (ρ)	$1.225 \ \mathrm{kgm^{-3}}$

Table 2 Lift and drag forces for different values of overpressure and underpressure from the simulation's post-processing

Pressure (kPa)	Lift force—underpressure (N)	Lift force—overpressure (N)	Drag force—underpressure (N)	Drag force—overpressure (N)
0	2.63	2.63	0.66	0.66
0.5	2.63	2.62	0.66	0.655
1	2.64	2.61	0.665	0.65
2.5	2.65	2.6	0.67	0.645
5	2.66	2.59	0.675	0.64
7.5	2.67	2.58	0.675	0.64
10	2.67	2.57	0.68	0.635

and decrease by decreasing the overpressure. However, the variation of both the forces in both the cases of additional active airflow is not very large from the case of normal flow, i.e., flow at 0 kPa (absence of additional active airflow).

The variation of the drag and lift coefficients follow for different values of overpressure and underpressure follows the same trend as the variation of lift and drag forces, respectively, as shown in Figs. 8 and 9. The drag and lift coefficients increase by increasing the underpressure and decrease by decreasing the overpressure. Once again, the variation of both the coefficients in both the cases of additional active airflow is not very large from the case of normal flow, i.e., flow at 0 kPa (absence of additional active airflow).

4 Conclusions

This observation is mainly focused on the impact of aerodynamic forces. It was observed that lift and drag are not impacted by the application of additional active airflow on the upper portion of the airfoil to a great extent. Although it was observed that the both the drag and lift forces tend to increase with the increase of underpressure (i.e., vacuum) and tend to decrease with the increase of overpressure, i.e., increase of drag coefficient and lift coefficient from 0 to 10 kPa is 0.0067 and 0.0135 in underpressure while decrease of drag coefficient and lift coefficient from 0 to 10 kPa is 0.0084 and 0.0202 in overpressure. The variation drag and lift coefficient is shown in Figs. 8 and 9. The trends followed by the lift and drag coefficients also indicate towards the same thing as lift and drag forces. The desired case would be to increase the lift and decrease the drag to be useful in the aviation sector. The further analysis should be done in the larger scale at wider range of air flow.

Table 3 Drag and lift coefficients for different values of overpressure and underpressure from the simulation

Pressure (kPa)	Lift coefficient—underpressure	Lift coefficient—overpressure	Drag coefficient—underpressure	Drag coefficient—overpressure
0	0.889738407	0.889738407	0.223280361	0.223280361
0.5	0.889738407	0.886355371	0.223280361	0.221588843
1	0.893121443	0.882972335	0.224971879	0.219897325
2.5	0.896504478	0.879589299	0.226663396	0.218205807
5	0.899887514	0.876206264	0.228354914	0.216514289
7.5	0.90327055	0.872823228	0.228354914	0.216514289
10	0.90327055	0.869440192	0.230046432	0.214822771
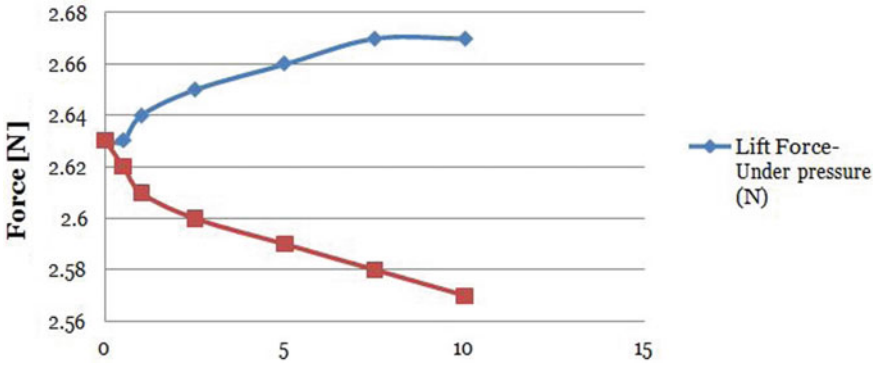
Fig. 6 Variation of lift force for different values of overpressure and underpressure
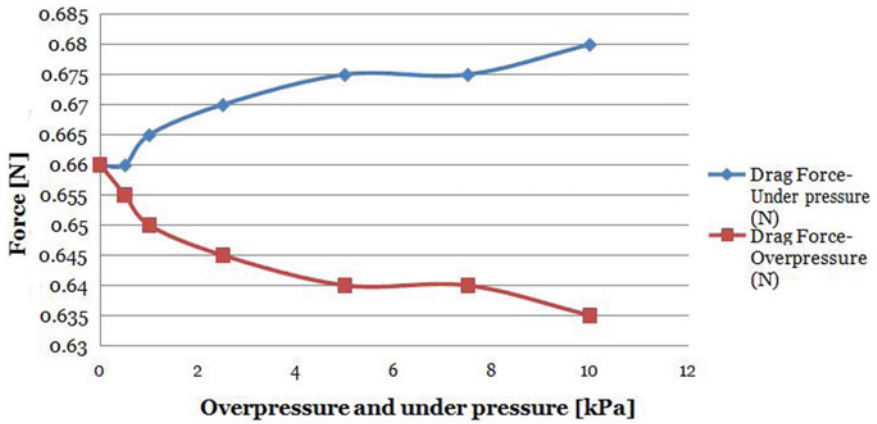
Fig. 7 Variation of drag force for different values of overpressure and underpressure
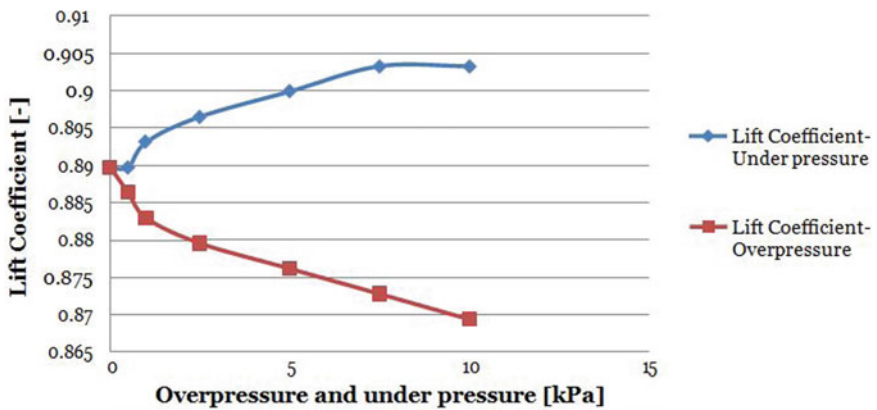
Fig. 8 Variation of lift coefficients for different values of overpressure and underpressure
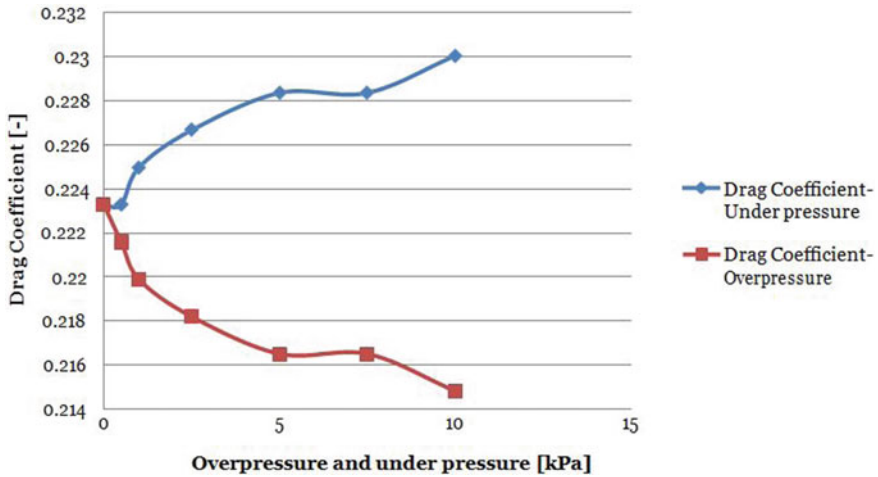
Fig. 9 Variation of drag coefficients for different values of overpressure and underpressure

References

1. Hirata, K., Kawakita, M., Iijima, T., Koga, M., Kihia, M., Funaki, J.: Numerical and experimental study on aerodynamic characteristics of basic airfoils at low Reynolds numbers. Trans. Jpn. Soc. Mech. Eng. **77**(776), 1111–1126 (2011)
2. Findanis, N., Ahmed, N.A.: Three-dimensional flow reversal and wake characterisation of a sphere modified with active flow control using synthetic jet. Adv. Appl. Fluid Mech. **9**(1), 17–76 (2011)
3. Brunner, M.S., Blaylock, M., Cooperman, A.M., Van Dam, C.P.: Comparison of CFD with wind tunnel tests of microjets for active aerodynamic load control. In: 50th AIAA Aerospace Sciences Meeting Including the New Horizons Forum and Aerospace Exposition, Nashville, United States (2012)
4. Ran, H., Mavris, D.N., Kirby, M.: Rapid-prototyping method for modeling a circulation-control wing at low speeds. J. Aircraft **49**(5), 1480–1484 (2012)
5. Traub, L.W.: Effect of rapid-prototyped airfoil finish on loading at low Reynolds numbers. J. Aircraft **50**(1), 307–311 (2013)
6. Standish, K., Rimmington, P., Laursen, J., Paulsen, H.N.: Computational prediction of airfoil roughness sensitivity. In: 48th AIAA Aerospace Sciences Meeting Including the New Horizons Forum and Aerospace Exposition, Orlando (2010)
7. Askari, S., Shojaeefard, M.H., Goudarzi, K.: Numerical and analytical solution of compressible flow over double wedge and biconvex airfoils. Eng. Comput. Int. J. Comput.-Aided Eng. **28**(4), 441–471 (2011)
8. Ovsyannikov, M.P.: Allowance for gas blowing in supersonic flow over a wedge. J. Eng. Phys. **30**(6), 663–668 (1976)
9. Raghunathan, S., Gillan, M.A., Cooper, R.K., Mitchell, R.D., Cole, J.S.: Shock oscillations on biconvex aerofoils. Aerosp. Sci. Technol. **3**(1), 1–9 (1999)
10. Hasen, D., Elangovan, S., Sundararaj, M., Parammasivam, K.M.: CFD analysis of controlling the airflow over airfoils using dimples. Int. J. Vehic. Struct. Syst. (IJVSS) **11**(5) (2019)
11. Cahyono, S.I., Anwar, M., Dihardjo, K., Hapid, A., Kaleg, S., Santoso, B.: Computational fluid dynamic simulation on bladeless fan as active cooling application. In: 2018 International Conference on Sustainable Energy Engineering and Application (ICSEEA), pp. 1–5. IEEE (2018)

12. Fatahian, H., Salarian, H., Nimvari, M.E., Khaleghinia, J.: Computational fluid dynamics simulation of aerodynamic performance and flow separation by single element and slatted airfoils under rainfall conditions. Appl. Math. Model **83**, 683–702 (2020)
13. Yue, W., Xue, Y., Liu, Y.: High humidity aerodynamic effects study on offshore wind turbine airfoil/blade performance through CFD analysis. Int. J. Rotating Mach. (2017)

New Approach for Evaluating Different Concrete Mixer Based on Concrete Slurry Property

Rushikesh Kamble , **Prashant Baredar** , **Anil Kumar** ,
and Bhupendra Gupta

1 Introduction

When two or more compounds are poured together and stirred using an external energy to obtain a required mixture possessing with marked property, it is known as processes of mixing and same happens in case of concrete mixing. A concrete mixer exerts energy into a heterogeneous mixture (cement, sand, aggregate, water, plasticisers, binders, etc.) to form a homogeneous mixture; concrete. Basically, concrete is a heterogeneous mixture but when cement and binder spread equally around sand and aggregate evenly, then it is considered as homogeneous mixer. Concrete mixers are the instrument where an external energy is provided to the mixture. In drum type low capacity mixer, a raw material is feed into rotating drum which is continuously rotating at fix rpm with optimum torque. A particle of this raw material is incident on each other because of external energy provided to them and result into equal distribution of material present in concrete. Whole process is marked into three phase dry mixing, wet mixing and mixing [1]. Mixture reflects properties of its components as it is, and same is true with concrete. Hence, proportion of component and sequence of putting them into processes is always considered as key factor of mixing. All this happen in first two phases, more precisely, most of constituents are poured itself in dry mixing phase, and only water and some plasticisers remain for wet mixing phase as shown in Fig. 1 [1, 2].

R. Kamble (✉) · P. Baredar
Energy Centre, Maulana Azad National Institute of Technology, Bhopal, India
e-mail: rushikesh.d.kamble@gmail.com

A. Kumar
Department of Mechanical, Production & Industrial and Automobile Engineering, Delhi Technological University, Delhi, India
e-mail: anilkumar76@dtu.ac.in

B. Gupta
Department of Industrial Production, Jabalpur Engineering College, Jabalpur, India
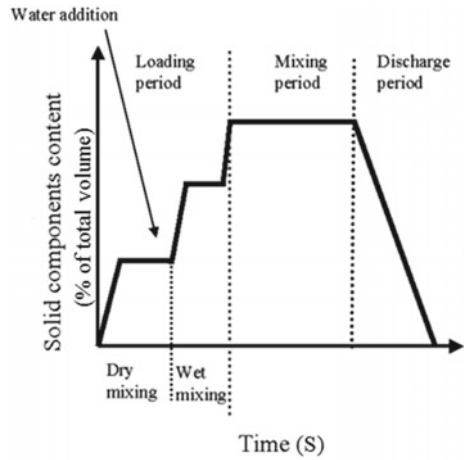
If roughly seen, most of the good concrete consists of components mentioned
in Table 1. Every individual has a proper time and proper amount for injection
into a mixture to attire a desire result. This component of concrete has taken from
concrete batch processing plant which seem as most quality concrete developed in
any processes. Initially, gravel or aggregate and sand is loaded into a plant or a drum
for small-scale batch concrete mixer, and then, it is dry mix for time period as shown
in mixing schedule in Fig. 1. Meanwhile, cements and fillers are poured into it and
dry mix till all components get properly coated with cement and binder layer; at that
time, water is poured and wet mixing is started, which is most energy-consuming
phase of whole process. After that, mixing phase begins where molecules of cements
reflect their property and started binding sand and aggregate together. Generally, in
drum which is tilted by 15° angle, this mixture is rotated at 10–20 rpm for nearly
120 s results into formation of homogeneous concrete [3].

Figure 2 represents schematics of rotating drum-type tilted-axis portable concrete
mixer. Here as shown in fig., mixture falls on itself while rising and get mixed. A
mechanical energy provided by drum to mixture helps to raise the material which
sticks exact to rotating drum. Due to ample cohesive force and self-weight, mixture

Table 1 Concrete
components [3]

Component (kg/m^3)	SCC-A	SCC-B
Cement	295	311
Limestone filler	85	109
Sand 1 (0/4)	300	332
Sand 2 (0/4)	552	522
Gravel (4/14)	886	854
Superplasticizer	4.37	5.28
Total water	184–202	185–206
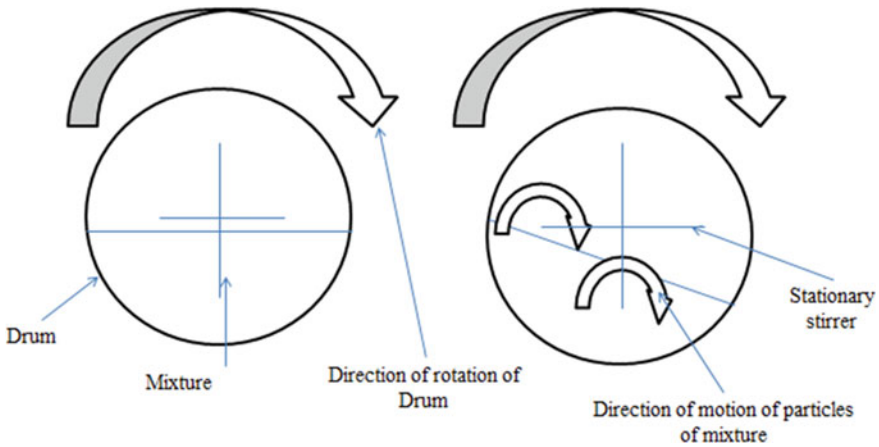
Fig. 2 Representation of motion of mixture particle in rotating drum type mixture [1–4]

falls on material present below. In another point of view, it looks like material pushes some potential energy at a height and falling from there, it reminds processes of gravity hammering. And it is seen that it is happening in drum. From that, it can be said that mixing in rotating drum may happen because of hammering or compressing of one part of material on another using self-weight and given mechanical energy.

The phenomenon of mixing in pan type mixer is little different. Instead of rotating drum, there is a central set of mixing blades which rotates with required RPM and torque to mix the mixture. Instead of free-fall, this phenomenon may look like direct compression. Blades compresses the material presents in front of him to next to him, and this wave goes on. Hence, from this, it definitely says that if a material is compressed properly in cycle of compression and dispersion, mixing processes seem as quite efficient.

The new 2n mixing theory was developed with the concept of the Japanese noodles (UDAN) mixing method [5, 6]. For making of UDON, flour and water are spread in proportion to certain thickness. Half of the part of this mixture is taken on that of other half and spread again to original thickness. This cycle is repeated for number of times to obtain UDAN [6]. Similarly, using theory of kneading and lapping, concrete is mixed. This was proved using a MY box continuous concrete mixer. Figure 4 represents the 2n theory of mixing. With use of an external energy molecules of mixture get collide with each other followed by collision with slope of wall of mixer, re-collision of same particles and final collision of similarly formed particle. In MY box gravity mixer, same mechanism is used to prepare concrete [5] (Fig. 3).
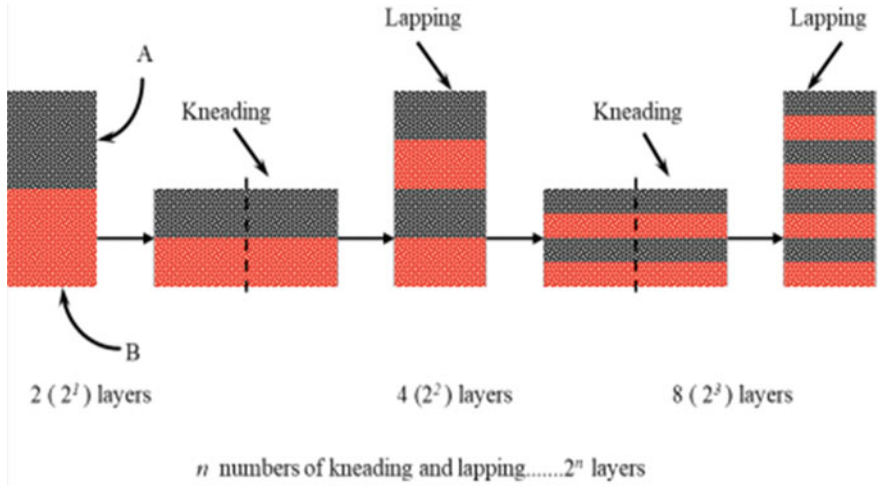
Fig. 3 Kneading and lapping mechanism in 2n theory of mixing [6]
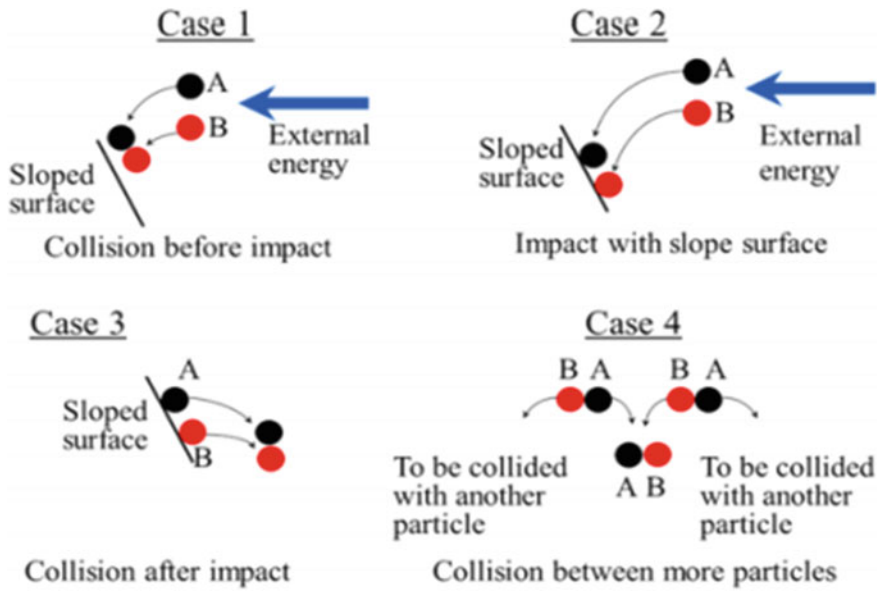
Fig. 4 Concept of new mixing technology [5]

2 Asset of Good Concrete Mixer

2.1 Homogeneity of Concrete

According to Merriam Webster, "Homogeneity is the quality or state of being of a similar kind or of having uniform structure or the composite throughout". If concrete possess uniformity of composition throughout its structure or developed mixture, then it must be called as homogeneous concrete. It gives knowledge about quality of a concrete. It depends on wide variety of components right from constituent of mixture to the processes of mixing. Every minor change affects the quality, and hence, homogeneity gives note about concrete mixer, and hence, it is more important in processes of evaluation of them. The cohesive forces present between heterogeneous molecules of concrete help to bind them up. The more homogeneous mixture means more cohesive forces [7], which results into the tight binding of molecules that ultimately results into strength; otherwise, heterogeneous constituents play its role and get separated out from mixture that results into strength failure, water bleeding, cracks in structure, etc. Hence, homogeneity of concrete is considered as key factor.

2.1.1 Factors Affecting Homogeneity of Concrete

If cement added in bulk homogeneity is more while it is reverse in case for water, and hence to achieve preferable range of homogeneity water to cement ration must be optimum. Superplasticiser plays an important role in reducing usage of water without disturbing required trade of workability, but many time, it is seen that it does print little effect on homogeneity. It is also seen that change of mixing processes changes the trade of homogeneity [8].

2.1.2 Homogeneity Test

The most convincing and worldwide adapted test for homogeneity is slump expansion together with sight, feel and experience. This is simple but judge concrete qualitatively it has lack of quantitative approach. Theory of barycentre helps here. An actual centre of shape of container and a same container filled with fresh prepared concrete is compared in instrument. If concrete is completely homogeneous, homogeneity modulus comes to 1, and if value deflects more, it states that the mixture is not homogeneous. This method is known as barycentre comparison method [7] (Fig. 5).

Following equation gives homogeneity modulus [7]:

$$C_V = \frac{2(G_X - G_1)}{G_2 - G_0} \tag{1}$$
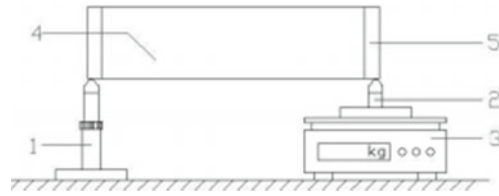
1: high strand whose height could be regulated, 2: low strand, 3: Electronic Scale,
4: Hollow Cylinder, 5: Lead

Fig. 5 Barycentre comparison homogeneity test [7]

According to Liu and Yang, form range of 1–1.05 comes under preferable cohesiveness, from 1.06 to 1.09 comes under normal cohesiveness and above 1.10 segregation and poor cohesiveness. And from this, they conclude that homogeneity near 1 is always better [7].

2.2 Workability of Concrete

Ability to turn into required mould of structure irrespective of its shape is known as its workability. Workability signifies lubrication in between particles of concrete which reduces friction between them, and it helps to reduce some unnecessary energy loss in construction processes. Skyscrapers, towers, malls, flyover, etc., are some examples of mega-constructions happening all around the world. To keep flow of this construction smooth; concrete is created in huge quantity and pump from the place of production to the point of crafting. Again, irrespective of shape and size, concrete should disperse evenly thoroughly in mould of structure; otherwise, strain prone zone is crated result into decrease in life of structure. Concrete must be pumpable as well as flowable. Workability of concrete is property which takes this in confidence. Compatibility, consistency and mobility are defining workability of concrete [9].

2.2.1 Factors Affecting Workability of Concrete

Percentage of water in concrete is a one of prime reason for workability of concrete. Plasticiser and superplasticiser are seen as some additive which adds to maintain workability of concrete in absence of water; ultimately saves a notable amount of water. Mixing processes also affect workability. Size, shape and amount of aggregate present in concrete reflect effect on workability of concrete. If round shape aggregate is used instead of spiky, more workability is achieved. Same is in sense of amount of aggregate; if cement to aggregate ration is lower, it means that more cement paste is available for lubrication results into more workability [9].

Fig. 6 Slump test apparatus
(ASTM C143)
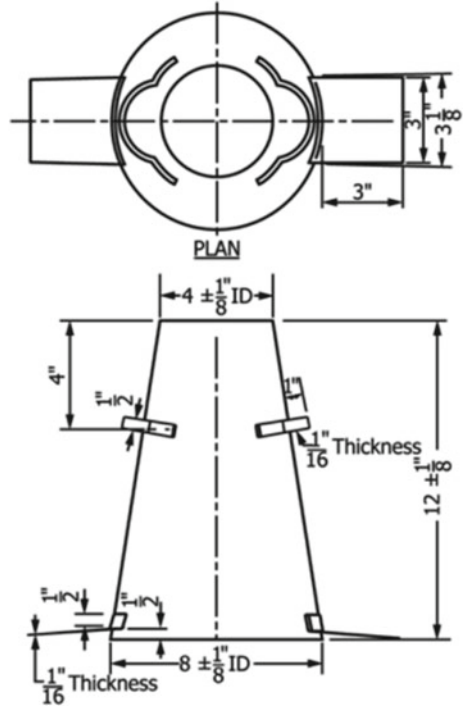
2.2.2 Workability Test

Slump test is one of the most simple and worldwide accepted tests for workability. Here, fresh concrete is poured into a conical hollow instrument name as slump cone of height nearly 300 mm. Figure 6 represents slump test apparatus ASTM C143. IS1199-1959, ASTM C143, ASTM C143-10, BS 1881:103:1993, etc., give various guideline and standard in context of slump test.

This equipment has top diameter 4″ (100 mm), bottom diameter of 8″ (200 mm) and of height 12″ (300 mm) made either from metal or plastic with wall thickness 0.06″ and 0.1″ wall thickness, respectively. 15 mm is maximum diameter of tamping rod use, and height must be more than 12″ and less than 24″. Processes are simple, fill the 25% of cone initially, ram it with taming rod, again do it till whole cone is filled with concrete, and then slowly remove cone and measure the slump height using measuring scale. The more the slump height represents lesser the workability, and hence, optimum workability range is chosen which gives sufficient cohesive force together with flowability and pumpability. Slump test categorises developed slump into four types named as true slump, zero slump, collapsible slump and shear slump. True slump is only measurable structure formed. It signifies that workability to homogeneity ration is good. Zero slumps indicate that dry mixture is due to less water. Mostly, this type is used for construction of roads. Collapsible slump

signifies more water percentage with less cohesive bonds between molecule results into not holding shape of moulding. Shear slump results failure of homogeneity which signifies that concrete is yet to be prepared. Compacting factor test, flow test, Vee-Bee consistometer test and Kelly ball test are available for workability measurement, but mostly they are laboratory tests, and hence, slump test is most popular one. For more accurate result, one of above method is referred.

2.3 Mixing Energy

Mixing energy is a product of average energy consumed and duration of mixing throughout the process. Mixing energy affects the quality of concrete developed, and it is always demanded to achieve a good quality concrete with minimal consumption of energy. Despite energy consumption, it thoroughly depends of n type of mixing and type of mixer use, and it is always considered as important factor in comparison of two mixers. Mixing processes is categorising in three phases, i.e., dry mixing, wet mixing and mixing.

In initial phase of dry mixing, aggregate, sand, fillers and cement are mixed in a mixer. Due to difference in their shape and sizes, they started to get mixed with each other compactly with every turn, and hence, with increase in time in dry phase, it results more consumption of energy as shown in Fig. 7. Just before beginning
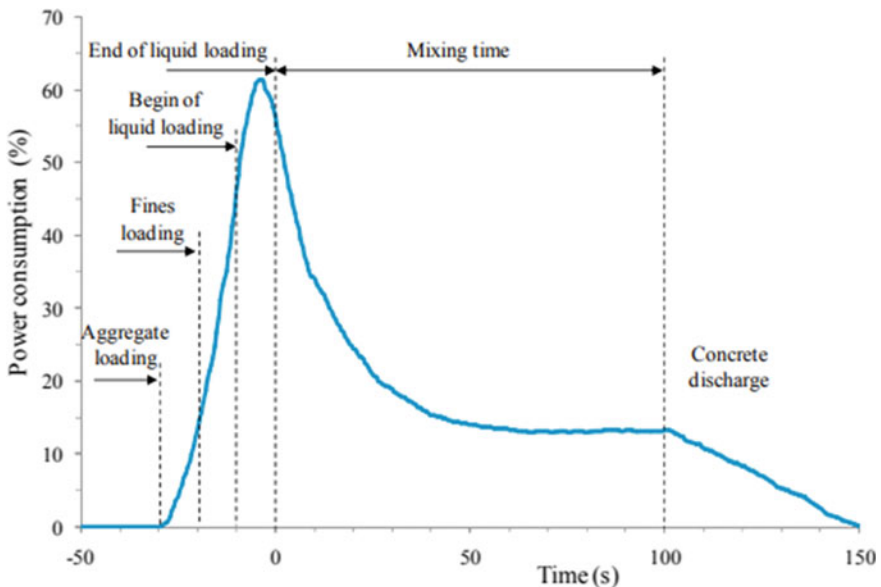
Fig. 7 Power consumption versus time graph together with component loading sequence of batch concrete mixing plant [3]

of wet mixing, water is sprayed into a rotating mixture. As seen in graph, due to water and its surface tension, cement started to create bonds between sand, fillers and aggregate which result into a thickening paste that is created, and at that time, more torque is required to mix them which results in peak energy consumption. In mixing phase, power consumption graph is heading to low down as water and superplasticisers play their role; increase the workability of that slurry; result into lower friction, lower resistance and lower in torque. This is actual mixing phase, and it lasts from nearly 50–150 s.

As the definition of mixing energy, mechanical energy provided by a mixer to slurry is given as [10]:

$$E = T \times w \times t \tag{2}$$

where T: applied torque by motor, w: rotation speed and t: duration of mixing process. It is found that torque T applied on propellers of mixer or a rotating container is directly proportional to its rotational speed w and density of ρ. Hence, equation of energy consumption while mixing processes becomes [10]:

$$E = k \times \rho \times w^2 \times t \tag{3}$$

where k is experimentally found to be equal to 6.4×10^{-9} Nm/kg m^{-3}/rpm.

Specific energy consumption is given as [10]:

$$E/M = k \times \rho \times w^2 \times t/\rho \times V = k \times w^2 \times t/V \tag{4}$$

It represents energy consume by mixing process per unit kg of concrete. And with this correlation by comparing homogeneity and workability as output parameter, one can easily say which mixer is performing well. Equation 4 represents that at constant volume energy, consumption is directly proportional to square of rotational speed and duration of time. This provides scope of reduction in consuming energy while mixing processes. Reduction in time duration is one of its ways. Workability affects consumption of mixing energy. When concrete is more workable, it provides well lubrication in slurry result into low inter layer friction; which ultimately reduces rated required torque and results into lowering of power consumption. By monitoring power consumption pattern, one can predict workability of concrete [1]. To obtain more homogeneity, it is preferred to mix a slurry for more time duration or at more speed which implies that if more energy is consumed, processes result into good homogeneity. But it is found that, after particular point, homogeneity gets saturated, and hence, after that point, there is no meaning of providing unnecessary energy for mixing [3]. More supply of energy may result into evaporation of organic fluids, and in mean time, it is seen that it affects free water present in slurry. Increasing specific mixing energy from 0 to 1 significantly improves quality of cement slurry, from 1 to 2, it remains stabilised, and above 2, it started deteriorating [10]. Mixing energy can be directly measured using motor consumption using equipped energy meter.

3   Theoretical Relations

3.1   Relation Between Strength—Homogeneity—Workability

Homogeneity is nothing but an amount of similarity present in slurry while the workability number signifies ease of handling of concrete. Strength is last and most required attribute of concrete. Whatever the processes, it happens right beginning from creation of cement to development of concrete which is done to obtain good strength. Homogeneity has direct relation with strength [1]. Homogeneity signifies the cohesive forces present in between slurry and developed structure. Cohesive forces are these forces which hold hetero particles of concrete slurry together. If in any part due to insufficiency of any constituent lack of cohesive forces is seen, then that part or area is the weakest among whole structure. Hence, it can be said that more the homogeneity in concrete signifies more the strength. On the other hand, workability plays role in handling of concrete. Workability is result of presence of fluid in slurry [9]. Due to variety of shape, size and quantity of constituents of concrete, a friction is always there. If these frictional forces are more, it says that concrete is non-workable, and if it is less because of presence of water–cement paste, which lubricates this particle of concrete, then it is notated as workable concrete. Workability is directly related to presence of water in concrete. If water percentage is more, it means workability is more and vice versa. A barycentre homogeneity test is done by Liu et al. at China Construction Ready Mixed Concrete Co. Ltd., Wuhan, China [3]. Table 2 contains proportion of constituent use in barycentre homogeneity test, and Table 3 contains results of this test in term of strength, slump, flow slump and C_v, i.e., homogeneity module.

From obtained result, they categorise samples in preferable cohesive, normal cohesive, little segregation poor cohesive and obvious segregation poor cohesive category [3]. It says that near to 1 homogeneity is preferable. According to data sample, C30-1, C30-2, C30-4 and C30-6 have 200 mm of workability. If this workability is kept constant, it is found that C30-4 have highest compressive strength (37 MPa) among all four samples. Similarly, it happens with sample C30-5 and C40-1. C40-1 (1.05) is more homogeneous as compare to C30-5 (1.06) with constant workability of 210 mm results into higher strength (46.5 MPa). Sample C40-1 (1.05) and C40-6 (1.05) have same homogeneity modulus with workability 220 mm and 250 mm, respectively. Among this, C40-6 have more strength (49.1 MPa), and from this, it can be concluded that at constant homogeneity with increase in workability strength decreases [7].

Hence, it can be stated that in an accepted range of homogeneity, i.e., from 1 to 1.09; if homogeneity is kept constant and workability is set to vary, then with increase in workability, strength decreases.

Table 2 Concrete mixture proportion used in barycentre homogeneity test [7]

Sample	Amount (kg/m^3)						Admixture dosage (%)	
	Cement	Fly ash	Slag powder	Sand	Gravel	Water	Superplasticizer	Viscosity modifier
C30-1	165	90	70	830	1070	152	IS	0
C30-2	165	90	70	830	1070	152	2.0	0
C30-3	165	90	70	830	1070	152	2.0	0.2
C30-4	180	100	75	800	1070	162	1.6	0
C30-5	180	100	75	800	1070	162	1.3	0
C30-6	180	100	75	800	1070	162	2.0	0
C30-7	180	100	75	800	1070	162	2.0	0.1
C30-8	180	100	75	800	1070	162	2.0	0.2
C40-1	215	80	90	790	1080	147	1.8	0
C40-2	225	80	100	760	1080	155	1.6	0
C40-3	225	80	100	760	1080	155	1.3	0
C40-4	225	80	100	760	1080	155	2.0	0
C40-5	225	80	100	760	1080	155	2.0	0.1
C40-6	225	80	100	760	1080	155	2.0	0.2

Strength of concrete proportional (Workability)$^{-1}$

Again, in a frame of acceptable homogeneity modulus (1 to 1.09); by keeping workability constant and homogeneity modulus varying; it is found that with increase in homogeneity strength is increased [1, 3, 7, 9].

Strength of concrete proportional to (Homogeneity)

Plateau is point beyond which homogeneity will not increase, so it can be said that homogeneity of concrete plays role in strength of concrete up to its plateau point [3].

Mathematically,

$$\text{Strength of concrete} = k + H_p x\left(h/h_p\right) + (1/W) \tag{5}$$

where k represents as % of contribution to strength of concrete happen because of change in constituent's shape, size and percentage in slurry; H_p: maximum % of contribution to strength of concrete happening because of homogeneity at plateau; h: homogeneity at present level; h_p: homogeneity at plateau point; W: % contribution to strength of concrete happening because of present workability level.

Expression (4) represents relation between contribution of strength shared by homogeneity and workability of concrete.

Table 3 Results of barycentre homogeneity test [7]

Sample	28d strength (MPa)	Slump (mm)	Slump flow (mm)	C_v	Tester's subjective judgment
C30-1	36.2	200	490	1.07	Normal collusiveness
C30-2	35.1	200	510	111	Obvious segregation, poor cohesiveness
C30-3	36.8	220	520	1.08	Normal cohesiveness
C30-4	37.0	200	480	1.04	Preferable cohesiveness
C30-5	37.0	210	510	I.06	Normal cohesiveness
C30-6	35.9	200	520	1.10	Little segregation, poor cohesiveness
C30-7	36.8	220	530	1.07	Normal cohesiveness
C30-8	37.2	240	550	1.06	Normal cohesiveness
C40-1	46.5	210	510	1.05	Normal cohesiveness
C40-2	49.1	220	510	1.03	Preferable cohesiveness
C40-3	49.3	240	550	1.06	Normal cohesiveness
C40-4	47.0	220	540	1.10	Little segregation, poor cohesiveness
C40-5	48.9	240	560	1.07	Normal cohesiveness
C40-6	49.1	250	560	1.05	Preferable cohesiveness

3.2 Relation Between Mixing Energy—Homogeneity—Workability

Mixing energy is a product of total energy required by duration of mixing processes. It is represented by Eq. 2. If a mixer operates for more duration with constant rpm or with usually more rpm with constant duration of mixing, then it results into higher homogeneity. Equation 3 justifies this statement. As mixing energy is directly proportional to duration of mixing and square of revolving speed, increment in any of them causes change in consumption of energy directly, and hence, it can be said that mixing energy is directly proportion to homogeneity but up to plateau. Plateau is a point of saturation of homogeneity, above which whatever amount of energy is put homogeneity do not change significantly.

When concrete is more, workable requirement of mixing energy is less; as friction force or resistance to rotation of blades or rotating drum of mixer is less which decreases load on motor coupled for locomotion and results into lesser consumption of energy. Equation 3 represents that mixing energy depends on density, rotation speed and duration of mixing. Change in workability gives change in density.

Table 4 Check table of relation between homogeneity, workability, mixing energy and strength [1, 3, 5, 7, 9, 10]

Case	A	B	C	D	E
K	0	0	0	0	0
Homogeneity	−1	1	0	0	0
Workability	0	0	0	−1	1
Mixing energy required	−1	1	0	1	−1
Strength achieved	0	1	1	1	0

−1: Low, 0: Optimum, 1: Higher

Hence, it can be said that with increase in workability, energy consumption decreases [3, 9, 10].

Mathematically,

$$\text{Consumption of mixing energy} = k + H_{Ep}(h/h_p) + (1/W_E) \qquad (6)$$

where k represents as % of consumption shared in mixing processes of concrete happen because of change in constituent's shape, size, percentage in slurry and mixing processes; H_{Ep}: maximum % of consumption shared in processes of concrete mixing because of homogeneity at plateau; h: homogeneity at present level; h_p: homogeneity at plateau point; W_E: % of consumption shared in processes of concrete mixing because of present workability (Table 4).

Case 'C' is most optimum case for concrete preparation. It signifies a preferable homogeneity with maximum/optimum workable value which provides good strength with optimum energy consumption. Throughout this comparison, 'k' factor is kept at optimum level. It covers affect occurs on above attribute because of presence of quality improving constituent like superplasticisers, viscosity maintainer, fillers, m-sand, mixing processes, etc.

4   Conclusion

Mechanical energy is provided to concrete mixer in sense to achieve marked properties, i.e., workability, homogeneity, mixing energy and strength. Equations 4 and 5 say that, instead of looking broadly towards consumption of energy and obtained strength, part them in line of scale of measurement of properties of concrete slurry like homogeneity and workability. Properties of concrete contribute their share to obtain compressive strength and requirement of mixing energy. This approach helps to find a state of mixing energy and strength at particular point in scale of measurement of homogeneity and workability. This helps to generate a library which states the strength and energy consumption at a particular homogeneity and workability. And on account of this, various newly developed concrete mixers are easily compared

irrespective of their mixing processes which make ease in evaluation. Nowadays, 3D concrete printing technology is in boom. Every printer required a special quality ink, and this methodology is useful to optimise an energy required to produce them in mixers.

References

1. Ferraris, C.F.: Concrete mixing methods and concrete mixers: state of the art. J. Res. Natl. Inst. Stand. Technol. **106**, 391–399 (2001)
2. Charonnat, Y., Beitzel, H.: RILEM TC 150 ECM: efficiency of concrete mixers; report: efficiency of concrete mixers towards qualification of mixers. Mater. Struct. **30**(Suppl. 196), 28–32 (1997)
3. Ngo, H.-T., Kaci, A., Kadri, E.-H., Ngoa, T.-T., Trudel, A., Lecrux, S.: Energy consumption reduction in concrete mixing process by optimising mixing time. In: ICOME 16, 17–20 May 2016, La Rochelle, France
4. Dils, J., De Schutter, G., Boel, V.: Influence of mixing procedure and mixer type on fresh and hardened properties of concrete: a review. Mater. Struct. **45**, 1673–1683 (2012)
5. Gyawali, T.R.: Mixing efficiency of energy saving gravity mixer (ESG mixer) for high slump concrete. Civil Eng. Res. J. **9**(2) (2019)
6. Gyawali, T.R., Joshi, B.R.: Mixing of dam concrete in continuous energy saving gravity mixer. J. Adv. Res. Civil Environ. Eng. **5**(4), 13–17 (2018)
7. Liua, Li., Yang, W.: The method to test the homogeneity of concrete. Key Eng. Mater. **633**, 485–489 (2015)
8. Rawarkar, K., Ambadkar, S.: A review on factors affecting workability of concrete. IJIRSET **7**(8) (2018)
9. Hoang, N.-D., Pham, A.-D.: Estimating concrete workability based on slump test with least squares support vector regression. J. Constr. Eng. **2016**, Article ID 5089683, 8 p (2016)
10. Orban, J., Schlumberger, A., Parcevaux, P.A., Guillot, D.J., Schlumberger, D.: Specific mixing energy: a key factor for cement slurry quality. In: SPE 15578

Development of Distance-Measuring System for Person-Following Robot

C. Mohan and **H. K. Verma**

1 Introduction

Several assistive devices and technologies are being developed and used to help elderly and physically challenged people in performing routine tasks of life with less effort. One such assistive device, namely an automated robot cart, was proposed by the authors in reference [1] for use by elderly people to carry their belongings to nearby places, like shopping area, bus stop, or railway station. It could be utilized with zero effort from the elderly user. The robot cart is automatically driven by motors and keeps following the elderly user. The motors are controlled by a tracking system, so that the robot cart tracks the user and keeps at a preset safe distance from him/her. The tracking systems developed for such purposes have been classified as (a) visual tracking systems, (b) non-visual tracking systems, and (c) hybrid systems and reviewed in reference paper [2]. A brief review is presented in the next paragraph.

A single type of sensor or system or combining more than one sensor or system has been used by researchers to develop person or target-following robots or robot carts. The sensor or system can be like a camera, laser range finder (LRF), infrared-based obstacle detector, and ultrasonic-based obstacle detector. In reference [3], a non-visual target tracking has been reported. To find the target's position, time difference of arrival (TDoA) principle has been used. The system has been developed using ultrasonic sensors and RF modules. This reference has been used as base paper of present work, and the features have been compared in Sect. 5. In reference [4], a visual-tracking system has been reported, and a monocular camera was used. The main disadvantage of the visual-tracking system is that it cannot be used in a

C. Mohan (✉) · H. K. Verma
Department of Electrical and Electronics Engineering, School of Engineering and Technology, Sharda University, Greater Noida, India
e-mail: c.mohan@sharda.ac.in

H. K. Verma
e-mail: hk.verma@sharda.ac.in

dark environment. A non-visual tracking system has been developed and reported in reference [5, 6] using Microsoft's Kinect sensor. The processing of the sensor data has been done using a PC. Practically, a computer cannot be used in an economical scale robot. It can be replaced by a higher-end version microcontroller. A combination (hybrid) of a camera, LRF, and sonar sensors has been used to develop a person-following system of assistive robot and reported in reference [7]. The total cost of the system will increase by combining more than one system. It may not affordable by a common user. The challenge of a researcher lies in the selection of a sensor system for a person or target tracking system of a robot that should work in all types of environments and should not be expensive.

An automated person-following robot cart should be equipped with an appropriate direction-sensing and distance-measuring systems to follow the walking user and maintain a certain desirable distance from him/her, respectively. A distance-measuring system (DMS) has been developed and tested in static mode. Its design and development details along with test results are reported in this paper. The DMS is combined with a direction sensing system, and the overall performance of the person-following assistive robot (PFAR) in static mode is also evaluated. The principle of distance measurement is discussed in the next section. Important circuit details of the person-following assistive robot (PFAR) are presented in Sect. 3, and the results of performance evaluation are given in Sect. 4. Features of the system have compared with previous work in Sect. 5. Outcome of the work and scope of extending the research future are discussed in the last section.

2 Principle of Distance Measurement Used

The distance measurement technique developed by the authors uses two pairs of ultrasonic transmitter and receiver (T/R), as shown in Fig. 1. The target here acts as a passive reflector only. The distance between PFAR, on which the ultrasonic modules have been mounted, and the target (the person to be followed) is measured on the basis of the time taken by an ultrasonic pulse emitted by an ultrasonic transmitter (T) to travel to the target and reach back to the companion ultrasonic receiver (R) after getting reflected from the target. When the target is on the left of the robot, the left-side T/R pair is active; Fig. 1a. The microcontroller calculates the distance from the following equation:

$$\text{Distance} = (\text{time taken} \times \text{velocity of sound in open space})/2 \qquad (1)$$

The velocity of sound in open space has been taken as 340 m/s in the calculation [8]. Similarly, if the target is on the right of the robot, the right-side T/R pair is active. In case, the target is in front of the robot, both left- and right-side T/R pairs are active; Fig. 1b. In the last case, the microcontroller calculates the distance on the basis of measurements made by the two pairs individually and compares them. If the difference between the values of the distance measured by the two pairs is within
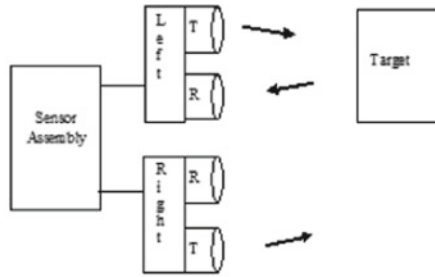
(a) Target on the left of the robot
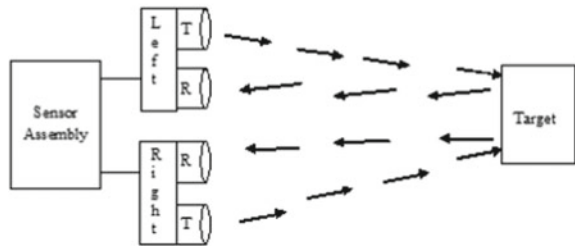
(b) Target in front of the robot

1% of each other, their average is taken as the final value of distance. In case the
difference is more than that, the measurement is rejected assuming that the difference
is because of noise, and the measurement is repeated. Reference [2] gives guidelines
to be followed for placement of ultrasonic sensor modules, which are very important
for ensuring good performance.

3 PFAR Details

The PFAR consists of the following systems and modules for performing the task of
person following:

(a) Measurement and control system (MCS)
(b) Alert and indication system (AIS)
(c) Motor driver module
(d) Power supply unit

Circuit details of MCS, including power supply unit, and those of AIS are
discussed in the following subsections.
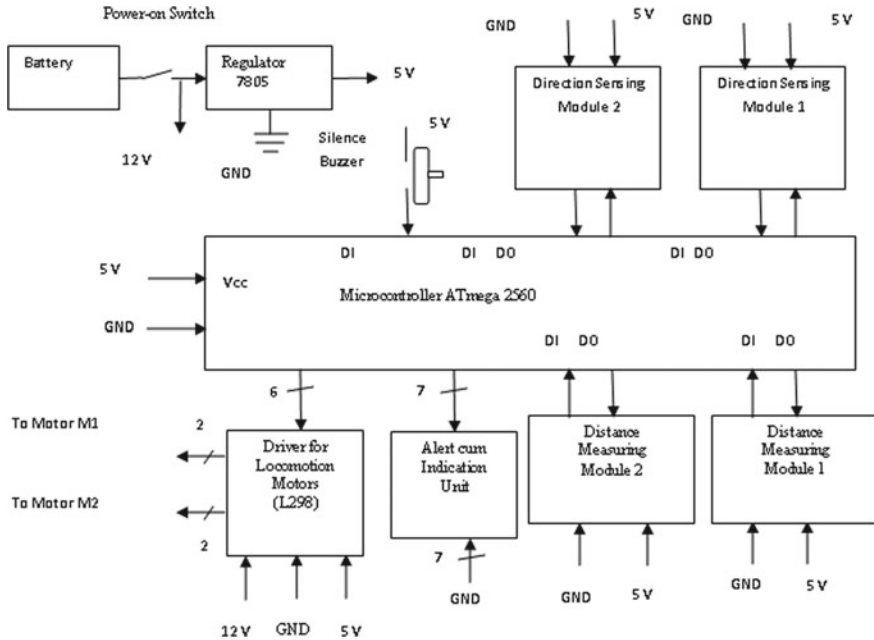
Fig. 2 Complete circuit diagram of MCS including power supply unit

3.1 Circuit Diagram of MCS

The circuit diagram of MCS, including power supply unit, is shown in Fig. 2. It shows connections between the main controller (ATmega-2560 microcontroller) and other units of the MCS. Four ultrasonic sensor modules are used for measurement: two for direction sensing and two for distance measurement. All the four ultrasonic modules work with 5-V supply. Each module has four pins, out of which two pins are used for power supply, third pin for trigger input from the main microcontroller to the small microcontroller of the ultrasonic module, and the fourth pin for connecting the output of the emitter to the main microcontroller. For controlling motors of the robot, a driver module has been used. The driver circuit has been developed with L298 and few other electronic components.

3.2 Circuit Diagram of AIS

A schematic diagram of AIS is shown in Fig. 3. An alert signal is given by the main microcontroller to a buzzer (a) when the target comes very near to the robot or (b) when there is a loss of signals between the robot and the target. Three of the six LEDs shown in the left part of the figure are used by the main microcontroller to indicate
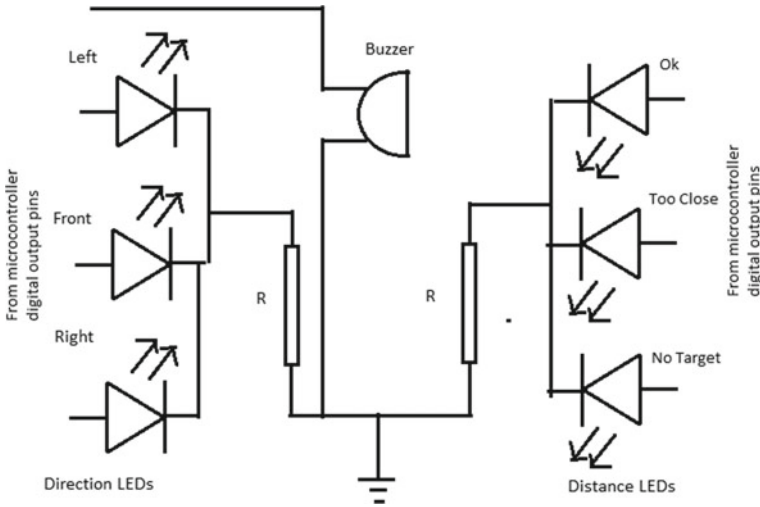
Fig. 3 Schematic diagram of AIS

the direction status of the target with respect to the robot. These LEDs indicate the target position as "left," "front," or "right." Similarly, the other three LEDs shown in the right side of the circuit diagram indicate the distance status of the target with respect to the robot. They indicate the status as "far," "near, or "no target." The "no target," indication means that either the target has moved far away from the robot or it is too close to the robot and lies within the blind zone of the sensing modules.

4 Testing and Evaluation of MCS

The performance of MCS was evaluated in the laboratory, first in direction-sensing and distance-measuring modes individually and then in a combined mode. A grid of lines was marked along with two mutually perpendicular directions, X and Y, on the floor of the laboratory. Y-direction is meant for the position of the target in the front of the cart while X-direction represents its position on the left and right sides of the cart. The PFAR was kept fixed at X = Y = 0, while the target was positioned in the front and sideways as per the requirement of the test.

4.1 Sensing Pattern in Distance Measuring Mode

For carrying out this test, the ultrasonic modules containing both emitter and receiver were used, and the center of the assembly was kept fixed at X = Y = 0. The target required in this mode needs to be only a passive reflector. Therefore, a whiteboard

was used as the target. It was moved in small steps in the front and on two sides of the PFAR. The response of the system along with alert audio output on the buzzer and visual indications on the distance LEDs were noted. The data was used for plotting for the distance sensing pattern of the MCS, and the same is shown in Fig. 4. There is a blind area in the form of a rectangle near the robot. The reason is that neither of the ultrasonic receivers gets the beam emitted by the respective transmitter after reflection from the passive target. Distance measuring also fails when the target is far away in front of the robot or it is at a large angle with respect to the robot. When the target is on the front of the robot but faraway (beyond 300 cm), the amount of the energy reflected as received by any of the two sensors is too small to be sensed. When the target is on a side of the robot making a large angle with the centerline, the sensor fails to receive enough energy in the reflected beam to enable sensing. This explains the presence of a no-sensing area (entire white area outside the sensing zone in Fig. 4).

Fig. 4 Sensing pattern in distance measurement mode as determined experimentally
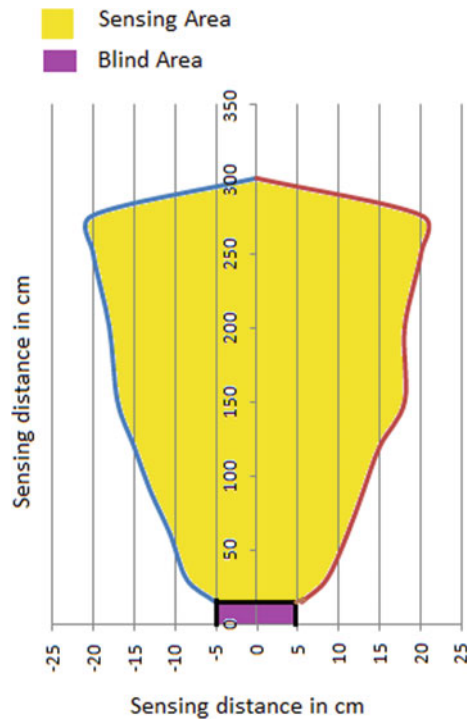
Table 1 Calibration of ultrasonic distance sensors

Actual distance	Reading based on right-side sensor module	Reading based on left-side sensor module
15	18	17
30	32	31
45	44	45
60	59	59
75	74	73
100	103	102
150	149	147
210	210	209
270	272	269
300	302	299

4.2 Error in Distance Measuring Mode

To evaluate errors in distance measuring, the target was moved in steps in front of the PFAR between 15 and 300 cm. The distance measured by the main microcontroller was read on a PC through a USB port. Table 1 shows the actual distance on the floor in its first column and the PFAR readings based on right-side and left-side ultrasonic modules in the second and third columns, respectively. These results are plotted in Fig. 5 at (a) and (b), respectively. Each figure shows the ideal response as a straight line at 45° angle to the horizontal axis and the PFAR readings as dots. The maximum positive and negative errors for the right-side module are +3 cm and −1 cm, respectively, and those for the left-side module are +2 cm and −3 cm, respectively. The errors are clearly random in nature and can be attributed to (i) human error in measuring the actual distance on the floor, and (ii) rounding-off error in the final calculation of distance by the microcontroller software (±0.5), rather than the error of PFAR in measuring the pulse-echo time.

As explained earlier under the Direction and Distance Unit (DDU), the pulse-echo time is converted by its microcontroller into pulse width and passed on to the main microcontroller. The latter measures the pulse width using clock pulses of 16 MHz frequency and ±1 ppm accuracy. Therefore, the maximum error in echo time measurement can be ± (half the cycle time or 0.03 ms + 1 ppm), which is extremely small compared to the errors mentioned above.

4.3 Testing of MCS in Combined Mode

To verify that the MCS can perform both the tasks, viz. direction sensing and distance measurement, the PFAR was further tested after installing both direction sensing and

Fig. 5 Response of PFAR in distance measuring mode as determined experimentally
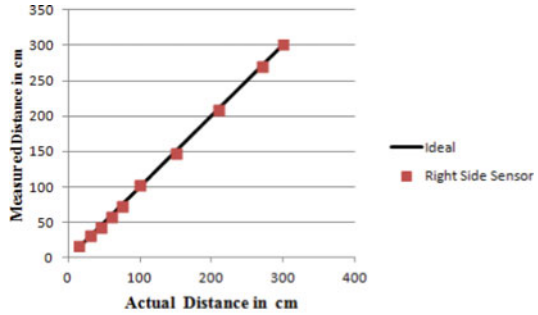
(a) Response of the right side sensor module
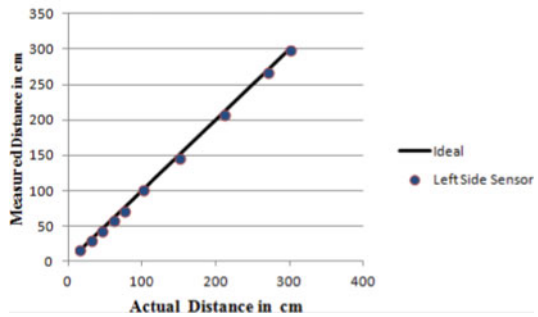
(b) Response of the left side sensor module

distance-measuring modules. The target was kept at different coordinates, and both the direction and distance of the target as sensed/measured by the MCS were noted. The noted readings are given in Table 2. The distance-sensing area is narrower than the direction-sensing area. The MCS can operate in the combined mode only for the target positions within an area common to these two areas. The test was conducted for $Y = 30, 50, 100,$ and 150 cm. For each value of Y, the value of X was varied such that the target position was initially inside the distance-sensing area, and then, it was positioned outside this area, but every time within the direction-sensing area.

The tabulated results show that the MCS gives both direction and distance when the target position is inside both the areas, but it gives only the direction and not the distance when the target is poisoned inside the direction-sensing area but outside the distance-sensing area. Some remarks are given in the last column of Table 2, which are meant for designing the locomotion unit of the PFAR. For example, if the MCS is showing left direction but no distance value, then the robot needs to be turned in the left direction until the MCS starts sensing the distance, after which the robot has to be moved forward.

Table 2 Results of testing of MCS in combined mode

Coordinates of the target			MCS readings			
Y	−X (left side)	+X (right side)	Direction sensed	Distance based on right-side module	Distance based on left-side module	Remark
30	0	0	Front	29	29	OK
30	0	8	Front	30	–	OK
30	8	0	Front	–	29	OK
30	15	0	Left	–	–	Turn the robot left
30	0	15	Right	–	–	Turn the robot right
50	0	0	Front	49	48	OK
50	0	15	Front	50	–	OK
50	15	0	Front	–	52	OK
50	30	0	Left	–	–	Turn the robot left
50	0	30	Right	–	–	Turn the robot right
100	0	0	Front	97	98	OK
100	15	0	Front	–	101	OK
100	0	15	Front	102	–	OK
100	50	0	Left	–	–	Turn the robot left
100	0	50	Right	–	–	Turn the robot right
150	0	0	Front	148	146	OK
150	15	0	Front	–	149	OK
150	0	15	Front	150	–	OK
150	75	0	Left	–	–	Turn the robot left
150	0	75	Right	–	–	Turn the robot right

5 Comparision

In this section, structure, principle. and features reference [3] have compared with current work in Table 3. In the distance measurement range, the reference has higher range than the current work. It is because of TDoA. Both direction and distance parameters are based on TDoA of emitted signal in the reference. But in the current

Table 3 System comparative

Features	Reference[3]	Present work
Target detection principle	Time difference of arrival of two different signals	Arrival of signal only
Target-finding sensors	Need ultrasonics and RF modules	Need ultrasonic modules only
Processing controller	Two microcontroller are required	Only one microcontroller is required
Precaution	Time calculation is very important to find target position	No need of time calculation
Programming	To find exact TDoA, an assembly language program has been used along embedded C	Embedded C is used
Customization of system	Need more customization	Need less customization
Additional features	Finding position of target only	The AIS can be used for troubleshooting of system
Maximum measured distance	8 m	3 m

work, direction depends on arrival of emitted signal, and distance depends on passive reflection. So, the distance measurement range has gone down.

6 Conclusion

The distance measuring system developed and described here has been evaluated in individual mode and combined mode with direction-sensing system, after mounting it on a person-following assistive robot. This evaluation was repeated at different conditions of the ambient light, and the results were found to be unaltered. This demonstrates the big advantage of the ultrasonic sensors. The distance-measuring sensor system has been calibrated, and its results have been discussed. The sensing pattern of the distance-measuring system determined experimentally can be used directly for automatic locomotion control of the PFAR. The PFAR has an additional feature of AIS. The AIS can be used for the troubleshooting of PFAR and to evaluate its performance in the field further. The ultrasonic sensors used in this work are inexpensive as well as readily available in the market. The technique developed and reported in this paper can be extended to a hybrid tracking system by adding a non-visual sensor module or a visual-system in order to improve its performance further.

References

1. Mohan, C., Verma, H.K.: Futuristic integrated assistive system for elderly population of India. Int. J. Online Biomed. Eng. **15**(13), 34–45 (2019)
2. Mohan, C., Verma, H.K.: Direction and distance sensors and sensing system for elderly people. Mater. Today Proc. no. April (2020)
3. Sales, J., Witkowski, U., Cervera, E., Nomdedeu, L.: Localization of networked mobile sensors and actuators in low-visibility conditions. In: IARP/EURON Workshop on Robotics for Risky Interventions and Environmental Surveillance (2010)
4. Koide, K., Miura, J., Menegatti, E.: Monocular person tracking and identification with on-line deep feature selection for person following robots. Rob. Auton. Syst. **124**(November), 2020 (2019)
5. Tomoya, A., Nakayama, S., Hoshina, A., Sugaya, M.: A mobile robot for following, watching and detecting falls for elderly care. Procedia Comput. Sci. **112**, 1994–2003 (2017)
6. Olatunji, S., Oron-Gilad, T., Sarne-Fleischmann, V., Edan, Y.: User-centered feedback design in person-following robots for older adults. Paladyn J. Behav. Robot. **11**(1), 86–103 (2020)
7. Portugal, D., Alvito, P., Christodoulou, E., Samaras, G., Dias, J.: A study on the deployment of a service robot in an elderly care center. Int. J. Soc. Robot. **11**(2), 317–341 (2019)
8. Sdn, C.T.: Product user's manual-HCSR04 ultrasonic sensor user's manual product user's manual-HCSR04 ultrasonic sensor index. Cytron Technologies, pp. 1–10 (2013)

Power Generation at the Security Check Point Gate Using Rack and Pinion Arrangement

Bateendra Kumar , **Mukul Yadav** , **Navneet Meena** ,
and Rajiv Chaudhary

1 Introduction

With the use of conventional resources or fossil fuels, environment gets polluted because we need electricity for day-to-day activities. Great part of electricity is generated with the help of fossil fuels, and the pollutants that escape after burning are the major cause of pollution. Among world, a great question arises "Is there any other alternative to produce electricity in a sustainable way without polluting the environment and also are the available fossil fuel reserves sufficient for the world". Growing consumption of energy has resulted in me being more dependent on fossil fuels such as gas, oil, and the major contributor among them, i.e., coal. The answer to this question comes out that to shift toward use of non-conventional fuels because fossil fuels are insufficient and costly, and their prices are increasing continuously at an alarming rate, so alternative is carried out. Aside from this, we just want to contribute a little among this to generate electricity through day-to-day activities, i.e., climbing the platform up and down and installing a setup which convert mechanical energy into electrical energy through dynamometer [1].

When a person stands on the platform of the security gate indicated in Fig. 1, the platform moves down due to weight of human being through which displacement is finally passed to dynamo, and the dynamo results in the production of current. Hence, current is produced by the rotation of dynamo. This platform is very useful in crowded areas, where there are more. Power generation by this platform or something

B. Kumar · M. Yadav · N. Meena (✉) · R. Chaudhary
Department of Mechanical, Production & Industrial and Automobile Engineering, Delhi
Technological University, Delhi 110042, India
e-mail: navneetmeena_bt2k16@dtu.ac.in

B. Kumar
e-mail: bateendrameena@gmail.com

M. Yadav
e-mail: mukul05yadav@gmail.com

Fig. 1 General design of rack and pinion arrangement
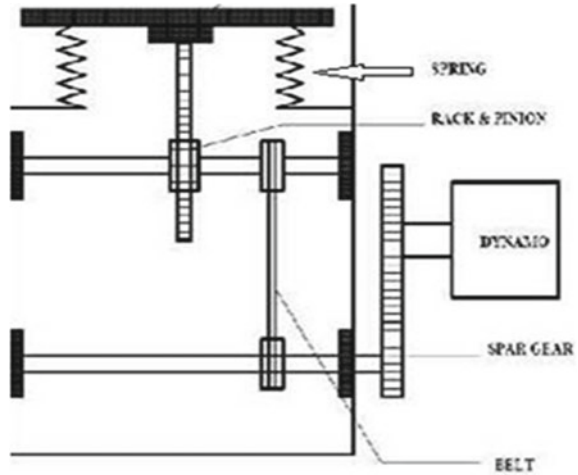
similar to this kind of setup is directly proportional to number of people and their body weight. Greater the number of people, greater will be the movement of the surface, and hence, greater the power (energy). By using these kinds of setups, we can use the human motion energy effectively and minimize the wastage of human energy. Power producing platforms will be a great initiative and will be very useful in crowded places like markets, malls, metro stations, etc.

2 Problem Summary

Electricity has become one of the regular requirements of life. It is necessary to boost the sum of alternative sources of energy as soon as possible. This framework can be used for the use of footstep energy to provide electricity during power outages in places like gyms or public places where large gatherings are happening.

3 Literature Review

Vinod et al. [2] described the generation of electrical energy from mechanical energy by the use of rack and pinion assembly and chain drive mechanism which is a part of simple drive mechanism. Conversion of pressure or force energy of the walking footsteps of people is used and converted into electrical energy with the help of dynamometer when the rotation of gears through rack and pinion arrangement takes place after applying pressure on the footstep. Both, including its power generation and cost of its manufacturing/making is high but can be compensated if it is use in large scale like in universities, schools, bus stops and specially at worship places where the

crowd is at its peak and is very advantageous to generate large amount of energy. It also does not require any type of non-renewable type of fuel for its working, and this system may solve the power crisis in future as demand of electricity is increasing at an alarming rate. As no fuel is used in this system, there is also no fear of generation of pollution from it, so it is also an alternative to save the environment by replacing use of non-renewable fuel by this method. This apparatus or system is very much useful at crowded places, and generated electricity can be stored in batteries for later use. It just requires time to time lubrication for its maintenance. Just like cycle which goes forward only in paddling clockwise, this also generates electricity in downward direction return stroke which is idle, i.e., there is no generation of electricity in it [3]. Tiwari et al. [4] described the following components along with their workings and are as follows: rack and pinion, gears, springs, ball bearing, dynamo, battery, and inverter. When force is applied on the footstep plate by foot attached to it when completely pressed springs makes full movement of rack vertically downward and causes one full revolution of pinion gear, and after removal of load from the plate, reverse motion of pinion gear takes place which causes which causes rotation of gear pair and the dynamo attached to last gear converts movement into DC power which is stored in 12 V rechargeable battery connected to inverter. In this experiment, we are able to generate 588.6 W and practically 122.3 W of power, and this can be used in many rural areas where the availability of power supply is less [5]. Kumar et al. [1] tried to find out which method of footstep power generation is better out of piezoelectric method, rack and pinion method, and fuel piston method comparative. Then, it is found that with moderate cost of operation and maintenance, rack and pinion arrangement is most efficient. Azhar et al. [6] used regulated supply of 5 V power, 500 mA power supply. Conversion of pressure energy of footstep into electrical form takes place. A controller mechanism and a bridge-type full-wave rectifier is also used in this mechanical arrangement. Since in this mechanical arrangement, there is no use of any type of non-renewable source of energy and also does not require power supply from mains and hence cause low generation of pollution. We can try to fix this mechanical arrangement across the college premises, highways, and in many places to get the best possible use of wasted energy by our foots [7]. Munaswamy et al. [8] designed a prototype of footstep to generate electricity from footstep and developed it successfully just for demonstration and cannot be used in real-life application until higher power rating generators with proper gearing systems are not used.

As it is a non-conventional source of power generation, we can opt this source of non-conventional power generation instead of solar as power generation through solar requires a very high budget. This setup is installed at crowded place with proper design and gearing system, which can able to replace the present system of non-conventional and conventional power generation. All the street lights of the roads can be lighten up or energized through this arrangement, and no requirement of electricity for this purpose is needed [9]. Raja et al. [10] tried to show that when we climb the stairs, a large amount of human energy is dissipated into the environment due to friction and heat loss, and thus, human energy is wasted in it. In developed countries like USA, Russia, they have elevators at their houses instead of staircase to climb, but in India, still we have staircase to climb which produces scope for

Indians to utilize the wasted energy and generate electricity from climbing which is wasted earlier. Mostly, buildings have footsteps to reach to their terrace, some has less, whereas some have more. Through dissipation of heat and due to friction, every time when a person climb shows that a large amount of energy is wasted in it.

We can tap out or obtain the wasted energy through installment of footstep power generator on every staircase, and the generated power can be stored in battery which can be used for domestic purpose. Also, this arrangement is pollution free and does not require any type of fuel for power generation [11].

4 Components Descriptions

4.1 Rack and Pinion Arrangement

It is a combination of two gears called rack and pinion and works on linear actuator that comprises a pair of gears. Rack is a gear of infinite circle diameter and is called biggest gear, and pinion is a circular wheel having teeth on it. Rack and pinion comprise of a circular gear engaged with an infinite circle diameter gear called rack. Rack translates linear motion into circular motion, whereas pinion is able to translate circular motion into translational motion. Table 1 drawn below shows the proportions of rack and pinion systems.

Specification of Pinion

Material: Cast iron
Outside diameter: 75 mm
Circular pitch: 4.7 mm
Tooth depth: 3.37 5 mm
Module: 1.5 mm
Pressure angle: 21°
Pitch circle diameter: 72 mm.

Table 1 Standard proportions of rack and pinion system

S. No.	Particulars	14 ½° composite or full depth in volute system (m)	20° full depth involute system (m)
1	Addendum	1	1
2	Dedendum	1.25	1.25
3	Working depth	2	2
4	Minimum total depth	2.25	2.25
5	Tooth thickness	1.5708	1.5708
6	Minimum clearance	0.25	

Specification of Rack

Material: Cast iron
Module: 1.5 mm
Cross-section: 75×25 mm.

4.2 Gear

Gears are the device used in power transmission. It is a rotating wheel having cut teeth which will mesh with another gear to transfer the torque. Two gears which are meshed rotate in opposite direction to one another. We are using spur gear in which teeth's are parallel to the axis of rotation and teeth is straight. It is a classification based on axis of shaft connected.

For no slipping condition, i.e., pure rolling

$$V = W1$$

Gears should always be meshed according to law of gearing, i.e., line of action must always pass through the fixed point (pitch point) on the line joining center of rotation of gears.

4.3 Spring

Spring is a mechanical device which is used to store energy when load is applied and return to its natural length without distortion after releasing of load. There is different type of springs, but we have used helical spring. Table 2 depicts the properties of spring that has been used in this experiment, and Fig. 1 shows the basic structure of rack and pinion and spring.

Table 2 Properties of spring

S. No.	Properties	Value
1	Height (H)	100 mm
2	Outer diameter (D_o)	30 mm
3	Inner diameter (D_i)	24 mm
4	Wire diameter (D_w)	3 mm
5	Total no. of turns (ni)	12
6	Active no. of turns (n)	10
7	Spring index (C)	1.10
8	Free length (L)	92.96 mm
9	Pitch of coil (P)	10.32 mm

4.4 Battery

In our research, we are using a rechargeable battery. Battery is a component which stores energy in the form of chemical energy and converts it into electrical energy when required to operate some appliance.

4.5 Dynamo

Dynamo is used to convert the energy generated by rotation of gears into electrical energy by using Faraday's principle of electromagnetism. It is able to produce DC into electric power. Figure 2 shows the basic structure of battery and dynamo.

5 Working Principle

Here, with the help of this project, we are converting the chemical energy of food consumed by humans which changes to mechanical energy when he does work into useful electrical energy. When a person stands on the platform of the security checkup

FOOT STEP POWER GENERATION :

LIGHTING LOAD

INVERTER

1.RETURN SPRING
2.RACK
3.PINION
4.BEARING
5.SPRACKET
12.PEIZOELECTRIC CRYSTAL

6.CHAIN DRIVE
7.GEAR WHEEL
8.BATTERY
9.FLY WHEEL
10.P.M.D.C.GENERATOR
11.SHAFT
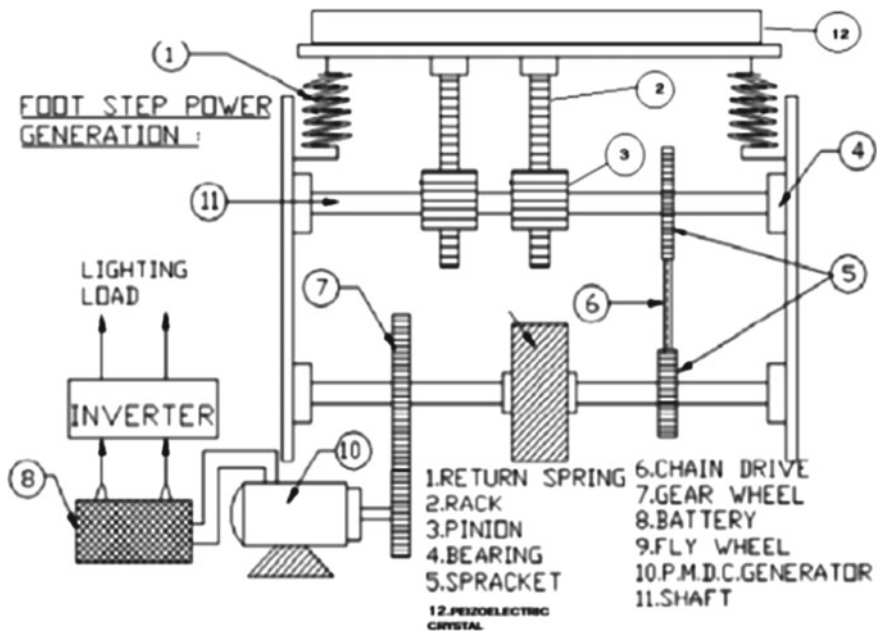
Fig. 2 Model of footstep power generation of electricity

Fig. 3 Block diagram for
generation system
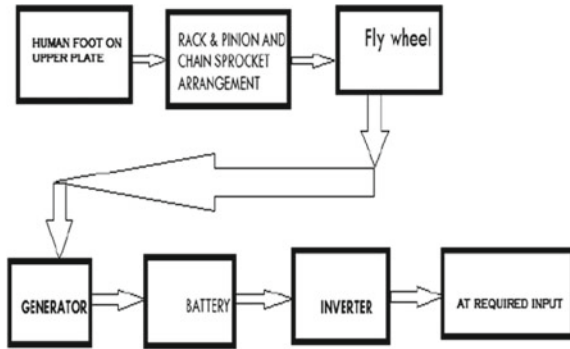
gate during security check, the surface of the platform moves down because of the
body weight which induces pressure on the surface. The general design of platform
is shown in Fig. 3. Springs present below the surface get compressed when a person
stands on the platform. As the person moves ahead, the surface retains its original
position as before because of the springs. Springs move the platform back to its
original position when pressure is removed. Rack and pinion arrangement is present
on the underside of the platform that helps in converting to and fro motion into the
rotational motion [2]. The basic structure of the security check platform has been
shown in Fig. 4. Rotational energy is converted into electrical energy with the help
of dynamo. For better efficiency, chain drive mechanism is used [4].

6 Design Calculation

6.1 Spring Design Calculations

- Material: steel wire
- Ultimate tensile strength (S_{ut}): 1090 N/mm^2
- Modules of rigidity (G): 81,370 N/mm^2
- Permissible shear stress for spring wire should be taken as 50% of ultimate tensile
  strength $\tau = 0.5\ S_{ut}$
- $P = 60 \times 9.8 = 588$ N (assume 60 kg)
- Spring index (c) = 6

  I. Wire diameter
  $\tau = 0.5 S_{ut}$.

  $= 0.5 \times 1090 = 545\ \text{N/mm}^2$

$$k = \frac{4c - 1}{4c - 4} + \frac{0.615}{c} = 1.25$$

$$\tau = k\left(\frac{8pc}{\pi d^2}\right)$$

$$d^2 = \frac{k(8pc)}{\tau \times \pi}$$

$$d^2 = \frac{1.2525(8(598)(6))}{545 \times 3.14}$$

$$d = 4.54 \approx 5 \text{ mm}$$

1. Mean coil diameter

$$D = cd = 6 \times 5 = 30 \text{ mm}$$

where
d = wire diameter
D = mean coil diameter.

2. Number of active coils

$$\delta = \frac{8PD^3N}{Gd^4}, \text{ where } \delta \text{ is deflection which is 5 cm here}$$

$$50 = \frac{8 \times 589 \times 30^3 \times N}{81370 \times 5^4}$$

$$N = 19.9 \approx 20$$

3. Total number of turns

It is assumed that spring has square and ground ends. The number of inactive coils is 2.
Therefore, $N_t = N + 2 = 20 + 2 = 22$ coils.

4. Free length of spring

The actual deflection of the spring is given by,
$$\delta = \frac{8PD^3N}{Gd^4} = \frac{8 \times 589 \times 30^3 \times 20}{81370 \times 5^4}$$
$\delta = 50.032$
Solid length of Spring $= N_t \times d = 22 \times 5 = 110$ mm
It is assumed that there will be a gap of 1 mm between consecutive coils when the spring is subjected to the maximum force. The total number of coils is 22.
The gaps between the coils will be $= (22 - 1) \times 1 = 21$ mm
free length = solid length + total axial gap + δ
$$= 110 + 21 + 50.032 = 181.032 \text{ mm} \approx 182 \text{ mm}$$

5. Pitch of coil

$$\text{pitch of coil} = \frac{\text{free length}}{(N_t - 1)}$$
$$= \frac{181.032}{(22 - 1)} = 8.62 \text{ mm.}$$

6.2 Platform Design Calculations

1. $\frac{m}{i} = \frac{\sigma}{y}$
2. $i = \frac{bd^3}{12} = \frac{300 \times 4^3}{12} = 1600 \text{ mm}^4$
3. $\sigma_b = \frac{638 \times 300}{1600}$ using Eq. 1.

$\sigma = 119.625 \text{ N/mm}$

4. $\sigma_b \ll \sigma_{\text{allow}}, \sigma_{\text{allow}} = 210 \text{ N/mm}$

So, design is safe.

6.3 Rack and Pinion Design Calculation

1. $f_n = f_t \tan \theta$ \hfill (1)

   $f_t = \text{tangentialforce.}$
   (Weight of human $= 60$ kg. This is the standard value from trusted source).
   $f_t = 60 \times 9.81 = 588.6 \text{ N.}$
   $f_n = 5.88 \times \tan 2\theta$
   $\quad = 2142 \text{ JN}$ using Eq. 1

2. $f_r = \frac{f_t}{\cos \theta} = \frac{588.6}{\cos 2\theta} = 626.38 \text{ N}$

   Power $(P) = \dfrac{\text{force} \times \text{displacement}}{\text{time}}$

3. $\quad\quad = \dfrac{588.6 \times 0.05}{1}$

   $\quad\quad = 29.43 \text{ W}$

   $P = \dfrac{2\pi N T}{60}$

4. $T = \dfrac{60 \times 29.43}{2 \times \pi \times 30}$

   $T = 9.37 \text{ Nm}$

5. $T = f_t \times r$

   $r = 15 \text{ mm}$

6. $r = 15$ mm, $SoD = 30$ mm

$\sigma_t = \frac{f_t \times P_d}{y.b}$
$P_d = \frac{T}{D} = \frac{18}{30} = 0.6$ mm^{-1}
$\sigma_t = \frac{588.6 \times 0.6}{30 \times 0.308} = 38.22$ N$/$mm^2
$\sigma_{\text{allow}} = 0.5ut = 0.5 \times 210 = 105$ N/mm^2
$\sigma_t \ll \sigma_{\text{allow}}$, So design is safe

7. $m = \frac{D}{T} = \frac{18}{30} = 1.66$

Therefore the module at pinion $= 1.66$; Also of rack is 1.66.

8. Pinion dimension: Outer dia. $= d_o = 2$ m $+ D$ 2 $\times$ 1.66 $+ 30 - 33.32$ mm
9. Root dia. $(d_r) = D - (2$ m $+ 2C) = 30 - (2 \times 1.66 + 2 \times 0.25) = 26.18$ mm
10. Addendum, Ad $= m = 1.66$ mm
11. Dedendum, Dd $= m + c = 1.66 + 0.25 = 2$ mm
13. Linear displacement of rack for one rotation of piston,

$$L = \pi m \times T = \pi \times 1.66 \times 18 = 94.44 = 100 \text{ mm (approx.)}$$

Maximum length of rack is 100 mm; Width of rack is 10 mm.

7 Experimental Setup

The project arrangement components include following:

- Four springs fixed below the platform.
- Two sprockets, i.e., first larger on main shaft and second smaller on secondary shaft.
- Chain drive mechanism to connect two sprockets.
- Rack and pinion.
- Dynamo to produce electrical energy.
- LED to detect power output.

When a person stands on the platform of security check up gate (foot impressions being most on security gate as it is mandatory used at entrance), the platform surface moves down due to pressure of foot below which four springs are present.

The purpose of springs is to move platform back to original position when foot pressure is released. On the underside of platform, rack and the pinion arrangement is present, where rack is coupled to the underside of platform. The shaft of pinion (main Shaft) is supported by end bearings. By using rack and pinion arrangement, we are converting to and fro motion of the platform into rotational motion of shaft. This in turn rotates a big gear (larger sprocket) coupled on main shaft which is connected to smaller gear (smaller sprocket) on secondary shaft through chain drive motion.

On the main shaft, pinion and larger sprocket are present, whereas on secondary shaft smaller sprocket is present. Larger sprocket is used to transfer the force of rotation to the smaller sprocket coupled on secondary shaft. We are using chain drive mechanism to obtain better efficiency. At last, secondary shaft is connected through dynamo through which the rotational energy is converted into electrical energy. Dynamo wires are connected to LED to detect the power output [6].

8 Result and Discussion

Output power.
   Let,
   Mass of pedestrian $= 60$ kg.
   Distance traveled by plate [6] $= 5$ cm.
   So,

$$\text{work done on plate by impact} = \text{weight of body}(\text{mass} \times \text{force due to gravity})$$
$$* \text{distance}$$
$$= 60 * 9.81 * 0.05 = 29.43 \text{ J}$$

So,

$$\text{power output} = \text{work done/s}$$
$$= 29.43/60 \text{ W} = 0.4905 \text{ W}$$

This much power is generated in 1 min.
Power developed for 60 min (1 h) $= 0.4905 * 60 = 29.43$ W

$$\text{Power produced in 24 h} = 24 * 29.43$$
$$= 706.32 \text{ W}$$

9 Advantages, Disadvantages, and Applications

As we have mentioned earlier that power generation is our primary objective to fulfill our need, and by using this mechanism, we can generate electricity which can provide many advantages as well like: the components used during this process are very cost effective, and the power produced by utilizing human energy is converted and stored which will go wasted if have not utilized. It is pollution-free and able to solve the power crisis in the locality which is not fulfilled by conventional methods. There is no usage of fuel; hence it is cost effective and economic friendly.

On the other side, it has fewer disadvantages like the initial cost for the setup is bit high and care should be taken care of for batteries which also requires maintenance at regular intervals. And most importantly, it can be used at a place where crowd density is high; otherwise, it will not result in cost efficient.

The power generation by this method has various applications like it can be used in hospitals where it can give backup for power supply failure, and it can effectively be used in producing energy for street lights. It also can be used in an automobile suspension mechanism in motor vehicles. And it is designed to utilize human energy so can be implemented where crowd gathering happens like railway station, malls, hospitals, metro station, airports, etc.

10 Conclusion

Although the amount of power produced by the effect of a single footprint is meager when this model is used extensively in crowded places like metro stations, schools, hospitals, etc., the amount of power produced will be very high. The most significant advantage of this project is that the electricity produced is a green form of energy which is utilized, which otherwise had gone wasted. This paper also tries to highlight the advantages that we can achieve from a simple mechanism and we have calculated the approximate watts of energy which can be produced and verified the same with the experiment. The components used in this project are very cost effective and requires less maintenance; thus, it can be simply implemented in practice.

References

1. Boby, K., Paul, K.A., Anumol, C.V., Thomas, J.A., Nimisha, K.K.: Footstep power generation using piezo electric transducers. Int. J. Eng. Innov. Technol. **3**(10), 264–267 (2014). [Online]. Available: https://www.ijeit.com/Vol3/Issue10/IJEIT1412201404
2. Rattan, S.: Theory of Machines. McGraw-Hill Education (India) Private, New Delhi (2014)
3. Vino, J.A.: Power generation using foot step. Int. J. Eng. Trends Technol. (IJETT) **1**(2) (2011)
4. Khurmi, R., Gupta, J.: Theory of Machines. Eurasia Pub. House, Ram Nagar, New Delhi (2008)
5. Ranjan Tiwari, R., Bansal, R., Gupta, P., Paul, D.: Foot step Power generation. IRJET **06**(05) (2019)
6. Tiwari, R.R., Bansal, R., Quamruzzaman: Foot step power generation. Int. Res. J. Eng. Technol. (IRJET) **06**(05) (2019)
7. Rajpurohit, J., Saif, A., Abhinay, N., Chandu, P.: Generation of electrical energy from foot step using rack and pinion mechanism. Int. J. Mag. Eng. Technol. Manage. Res. **3**(4) (2016)
8. Bhandari, V.: Design of Machine Elements. McGraw-Hill Education (India), New Delhi (2017)
9. Munaswamy, B., Prudhvi, Ch., Srikanth, V., Kirankumar, B., Pradeep Kumar, E.: Mechanical footstep power generation. Int. J. Eng. Trends Appl. (IJETA), **5**(2) (2018)
10. Rani: Foot step power generator. Slideshare.net, 2020. [Online]. Available: https://www.slideshare.net/mobile/deepa_rani9/foot-step-power-generator. Accessed 22 May 2020
11. Raja, R.: Power Generation from Staircase (Steps), vol. 3, no. 1 (2014)

Design and Fabrication of Planetary Transmission System and Simulating Torque Vectoring on Rear-Wheel Drive Vehicle to Increase Lateral Maneuverability

Sagar Kumar [ID]**, Saurabh Kumar** [ID]**, and Sarthak Lakra** [ID]

1 Introduction

1.1 Motivation

The motivation for this project lies in the increasing demand of eco-friendly vehicles which have good performance characteristics as well. Using multiple motor vehicles provides precise and fast torque generation, efficient feedback information on motor torque and speed output, and ease of producing torque in both forward and reverse directions with better control for the distribution of torque among the driving wheels. One of the effective methods to improve the dynamics of vehicle is by controlling the yaw rate of the vehicle which involves a controller to be design with the objective of bringing the vehicle's measured yaw rate into conformity with the optimal yaw rate by calculating and producing a corrective yaw moment via torque vectoring control.

2 Design and Methodology

2.1 Calculations of Single-Stage Planetary Transmission

Longitudinal Vehicle Dynamics. The vehicle is a rear-wheel drive (RWD) vehicle, so the torque is provided to the rear wheels by the motor [1]. For a constant power

S. Kumar (✉) · S. Kumar · S. Lakra
Department of Mechanical, Production & Industrial and Automobile Engineering, Delhi
Technological University, Delhi 110042, India
e-mail: sagarpanchal71619@gmail.com

S. Kumar
e-mail: saurabhk1512@gmail.com

Fig. 1 Longitudinal vehicle dynamic

Fig. 1 Longitudinal vehicle dynamic
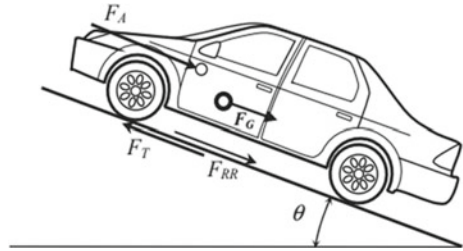
output, if we decide upon a value of reduction, so that tractive torque is maximum similarly, if we design according to maximum output speed, vehicle will probably fail due to low gradeability [2]. Therefore, we had to decide an optimum value of gear reduction.

Here, gradeability factor will not be that much required as it is a formula student car [1]. Thus, it is seen that nominal grade angle that any vehicle experiences are 10 degrees. From Fig. 1:

$$F_{RR} = mg(\sin 10 + \mu \cos 10) \tag{1}$$

where F_{RR} = Total resistive force on vehicle, g = acceleration due to gravity, m = mass of the vehicle, and μ = Coefficient of friction = 585.14 N.

So, rolling resistance came out to be approx. 585.14 N on an incline of 10. Aerodynamical drag came out to be approx. 20 N in the worst-case conditions. Hence, a net tractive force of approximately 605 N was required in the worst-case conditions.

The wheel dynamic radius was assumed to be 22.86 cm or 0.2286 m.

Tractive torque required $(T_{OUT}) = 605 \times 0.228 = 137.94$ N m.

Torque provided by the motor at rated condition $(T_{IN}) = 39$ N m.

Hence, gear ratio = 3.53–3.5.

The top speed vehicle would be able to achieve = 30.188 m/s or 108.67 km/h.

The acceleration achieved by the vehicle, say in 5 s is 6.0376 m/s^2.

Motor specifications. The specifications of motor used, i.e., Lynch rags D135 (DC brushed motor), are as follows [3] (Table 1).

Gear Train Analytical Calculations. The mechanical properties of AISI 8620 [4] is listed in Tables 2 and 3.

Using planetary gears relation [5], above-listed gear parameters have estimated, and CAD models are prepared in SOLIDWORKS using above-mentioned parameters

Table 1 Motor specifications

Maximum power	16.97 kW
Maximum torque	39 N m @ 3687 rpm
Maximum speed	4416 rpm @ 1.10 N m
Operating voltage	96 V

Table 2 Gear material-AISI 8620h

Tensile strength, ultimate	1157 MPa
Tensile strength, yield	833 MPa
Modulus of elasticity	205 GPa

Table 3 Gear parameters

Module (m)	2.5 mm/teeth
Number of teeth (n) (sun/planet/ring)	28/21/70
Pitch-diameter (sun/planet/ring) (P_d)	70/52.5/175
Face width (b)	20 mm
Pressure angle	20°

Fig. 2 Ring gear
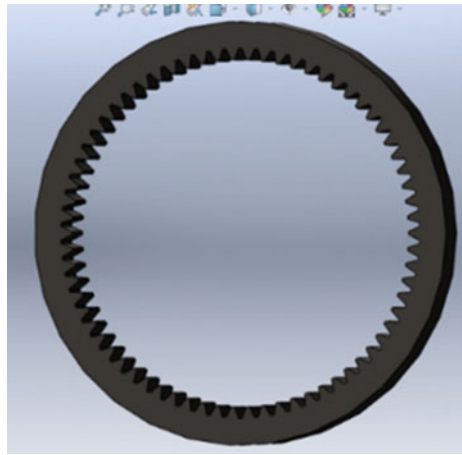
Fig. 3 Sun gear
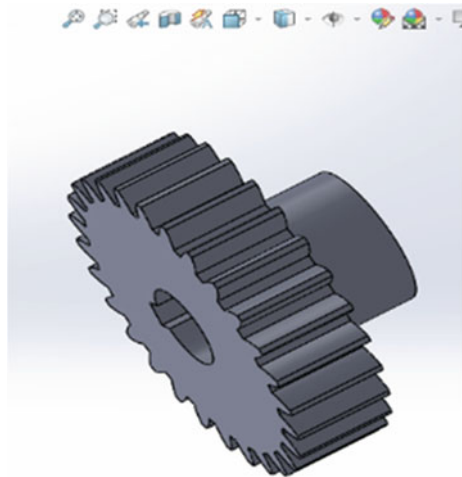
Fig. 4 Planet gear
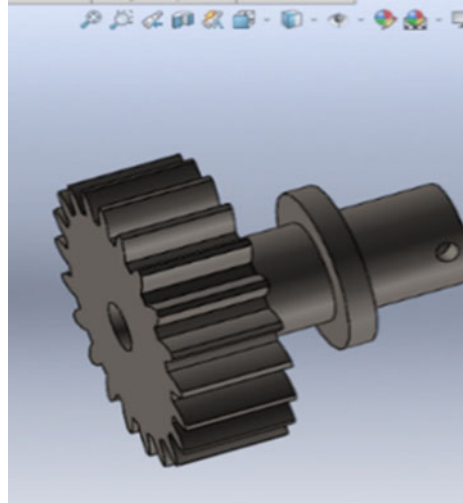
of all three gears (sun gear, planer gear, and ring gear) and are shown in Figs. 2, 3, and 4.

Using the empirical formulae for gear tooth design [1, 2], following calculations have been made:

Beam strength of the tooth:

Considering gear tooth to act as a cantilever beam [2]:

$$S_b = mb\sigma_b y \tag{2}$$

where S_b = beam strength of gear, m = module of gear, b = face width, y = form factor based on $20°$ pressure angle, and σ_b = bearable stress.

$$S_b = 8639\,\text{N}$$

Effective load on the tooth:

$$P_d = 21v(Ceb + T)/\left(21v + \sqrt{(Ceb + T)}\right) \tag{3}$$

where P_d = Dynamic load on the gear. C = Deformation factor = 954.06 N.

$$P_{eff} = C_s P_t + P_d \tag{4}$$

where C_s = Service factor. P_{eff} = Effective load on the tooth.

$$P_{eff} = 5914.67\,\text{N}$$

Factor of safety: To resist the failure, FOS should be greater than 1

$$\text{fos} = S_b/P_{\text{eff}}$$
$$\text{fos} = 1.46 \tag{5}$$

Since, the factor of safety is 1.46, module design is satisfactory, and design against static load is safe.

Wear strength of tooth:

$$S_w = bQd_pk \tag{6}$$

where S_w = wear strength of the gear, Q = velocity ratio factor, and K = combination factor.

$$S_w = 7095.99 \text{ N}$$

Factor of safety against pitting: To resist the failure, FOS should be greater than 1

$$\text{fos} = S_w/P_{\text{eff}}$$
$$\text{fos} = 1.29 \tag{7}$$

Factor of safety is 1.29. Hence, the design is satisfactory, and factor of safety is adequate against pitting failure.

Shaft analysis. Transmission shafts experience bending loads due to gears' tangential and radial forces. Shafts are generally made up of mild steel and analyzed on the basis of maximum stress theory to evaluate the strength of the shafts against failure [6].

Carrier/output shaft.

Torsion moment—140 N-m or 140×10^3 N-mm.
Bending moment—2.7 N-mm.
Here, bending moment is so small compared to torsion [7]. So, we consider only torsion here and assumed shaft to be weightless.
Shear stress,

$$\sigma = \frac{16T}{\pi D^3 \{1 - c^3\}}$$
$$= \frac{16 \times 140}{\pi \times 42^3 \{1 - 0.714^3\}}$$
$$= 84.28 \text{ N/mm}^2 \tag{8}$$

Shear stress$_{\text{material}}$ = 295 N/mm^2.

Factor of safety = 295/84.28 = 3.5.

Sun gear/input shaft.
  Torsion moment—39 N-m or 39×10^3 N-mm.
  Bending moment—3.1 N-mm.
  Using same Eq. 12 for shear stress, we get is 69.6 N/mm^2.
  Factor of safety = 295/69.6 = 4.14.

Planet gear/intermediate shaft.

Torsion moment—140 N-m or 140×10^3 N-mm.
  Bending moment—1.7 N-mm.
  Using Eq. 12 for shear stress, we get is 75.8 N/mm^2.
  Factor of safety = 295/75.8 = 3.89.
  The diameters of shafts (inner and outer) are estimated and have been designed using these parameters on SOLIDWORKS. The components have been assembled, and the assembly CAD models are shown in Fig. 5.

Gearbox Casing. In the design of the present gearbox, Al 6061 T6 is used as the casing material for its light weight and easy machinability. Gearbox casing endures bearing loads and hence must not fail under that. An analysis is performed on SOLID-WORKS to see the same. The bearing loads are taken as maximum of the bearing static load capacity and the stresses and deformation evaluated. It was found that the stresses induced are in limits, and the deformation is also small. The mechanical properties of Al 6061 T6 is listed in Table 4.

Bearing Calculations. The bearing to be used b/w the intermediate gear and the carrier shaft is finalized using the equations given below, from the SKF Bearing
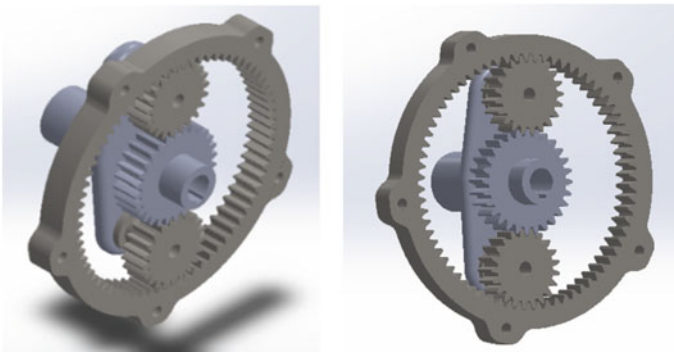
Fig. 5 Gear train assembly

Table 4 Gear casing material—Al 6061-T6

Tensile strength, ultimate	310 MPa
Tensile strength, yield	276 MPa
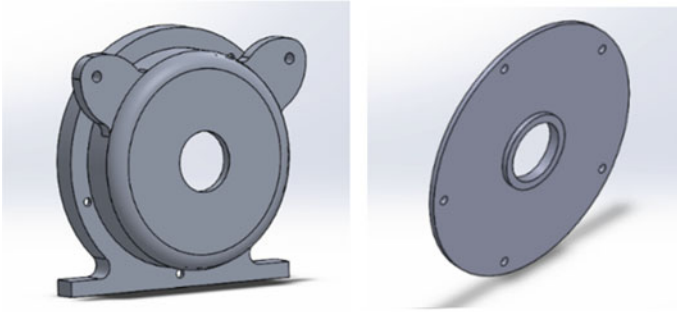
Fig. 6 Gear casing CAD

Handbook [8]. The bearing used is the ball bearing. The life of the bearing (L_{10h}) is assumed according to the required time. In our case, the life was 5000 h, and the radial force experienced by the carrier shaft (P) is 1.365 kN. For the selection of bearing, following calculations have been done (Fig. 6):

$$L_{10} = \frac{60 n L_{10h}}{10^6}$$
$$L_{10} = 378 \text{ million rev.} \tag{9}$$

$$C = P\left(L_{10}\right)^{\frac{1}{3}}$$
$$C = 1365\left(378\right)^{1/3}$$
$$= 9869.53 \text{ N} \tag{10}$$

The bearing selected by assessing over values is the SKF 6301 [8], and its feature of the single groove ball bearing are as follows:

Inner diameter $(d) = 12$ mm, outer diameter $(D) = 37$ mm, dynamic load factor rating $(C_o) = 9850$ N, and race width $(b) = 10$ mm.

Lubricant Selection. The lubricant used here to minimize friction and wear between the mating surfaces, and to transfer heat generated by the mechanical action of the system at the contact from the contact area, is [8] SKF LGHB due to property of highly viscosity, withstanding high temperature and extreme loads.

2.2 Torque Vectoring

Vehicle Parameters
See Tables 5 and 6.

Table 5 Measurable vehicle parameters	Wheelbase (L)	1575 m
	CG height (h)	305 mm
	Front track width of vehicle (T_f)	1357.8 mm
	Rear track width of vehicle (T_r)	1335 mm
	Distance b/w front wheel and CG (l_f)	945 mm
	Distance b/w rear wheel and CG (l_r)	630 mm
	Total vehicle weight (m)	2450 N

Table 6 Empirical vehicle parameters	Front stiffness coefficient (C_F)	1121.275 N/rad
	Rear stiffness coefficient (C_r)	2050 N/rad
	Moment of inertia (I_z)	1200 kg/m^2
	Front axle weight (W_f)	981 N
	Rear axle weight (W_r)	1471.5 N
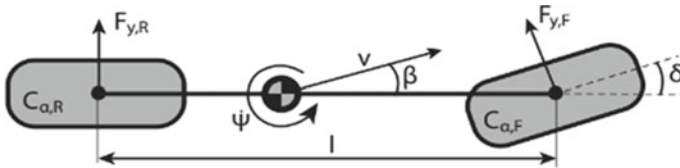
Fig. 7 Lateral dynamic model of bicycle

Vehicle Equations of Motion. Applying Newton's second law along the y-axis [9] (Fig. 7).

$$ma_y = F_{yf} + F_{yr} \tag{11}$$

where $a_y = \left(\frac{d^2 y}{dt^2}\right)_{\text{inertial}}$ is the inertial acceleration at c.o.g. in the y-axis and F_{yf} and F_{yr} are the lateral tire forces on front and rear tires, resp. a_y constitutes of two terms:

$$a_y = \ddot{y} + V_x \dot{\psi} \tag{12}$$

where $\ddot{y}$ is acceleration due to motion along y-axis and $V_x \dot{\psi}$ is the centripetal acceleration. Substituting Eq. (14) into Eq. (15)

$$m\left(\ddot{y} + V_x \dot{\psi}\right) = F_{yf} + F_{yr} \tag{13}$$

Balance of moment along the z-axis generates the eqn. for the yaw dynamics as

$$I_z \ddot{\psi} = l_f F_{yf} - l_r F_{yr} \tag{14}$$

where l_f and l_r are the distances of c.o.g. of vehicle from front and rear tires, resp. [10]. The next is to model the lateral tire forces F_{yf} and F_{yr} that is been acting on the vehicle. The lateral tire force of a tire is proportional to the "slip angle" for small slip angles. Slip angle is the angle between the orientation of tire and the velocity vector of the wheel, and the slip angle of the front wheel is:

$$\alpha_f = \delta - \theta_{Vf} \tag{15}$$

where θ_{Vf} is the angle made by velocity vector with the longitudinal axis of vehicle and δ is the angle of steering of the front wheel. The rear slip angle is given as:

$$\alpha_r = -\theta_{Vr} \tag{16}$$

The acceleration is proportional to slip angle, so the lateral force is also proportional to the slip angle. Therefore, the lateral tire force for the front wheels can be written as:

$$F_{yf} = 2C_f(\delta - \theta_{Vf}) \tag{17}$$

where C_f is called cornering stiffness of each tire, δ is the steering angle of front wheel, and θ_{Vf} is the front tire velocity angle. As there are two front wheels, so the r.h.s. is multiplied by 2. Similarly, the lateral tire force on the rear wheels of vehicle is:

$$F_{yr} = 2C_r(-\theta_{Vr}) \tag{18}$$

where C_r is cornering stiffness of rear tire and θ_{Vr} is the front tire velocity angle. The following relations can be used to calculate θ_{Vf} and θ_{Vr} and considering small angle approximations and using the notation $V_y = \dot{y}$:

$$\theta_{Vf} = \frac{\dot{y} + l_f\dot{\psi}}{V_x} \tag{19}$$

$$\theta_{Vr} = \frac{\dot{y} - l_r\dot{\psi}}{V_x} \tag{20}$$

Substituting from Eqs. (17), (18), (19), and (20) into Eqs. (13) and (14), the state space model of vehicle can be written as [6]:

$$\frac{d}{dt}\begin{Bmatrix} y \\ \dot{y} \\ \psi \\ \dot{\psi} \end{Bmatrix} = \begin{bmatrix} 0 & 1 & 0 & 0 \\ 0 & -\frac{2C_f+2C_r}{mV} & 0 & -V - \frac{2C_fl_f-2C_rl_r}{mV} \\ 0 & 0 & 0 & 1 \\ 0 & -\frac{2C_fl_f-2C_rl_r}{I_zV} & 0 & -\frac{2C_fl_f^2-2C_rl_r^2}{I_zV} \end{bmatrix}$$

$$+ \left\{ \begin{array}{c} 0 \\ \frac{2C_\mathrm{f}}{m} \\ 0 \\ \frac{2l_\mathrm{f}C_\mathrm{f}}{I_z} \end{array} \right\} \delta \qquad (21)$$

The state space matrix (Eq. 21) derived from above equation contains no physical input. The algorithm is described for difference between torques on left and right actuated motor of car. This *d/f* in torques creates yaw moment M_z about z-axis of car. To act as an input, additional yaw moment is added to the equation which is:

$$M_z = \frac{(Tq_\mathrm{l} - Tq_\mathrm{r})T_\mathrm{r}}{2r} \qquad (22)$$

where T_r is rear track width of car, r is the diameter, and Tq_l and Tq_r are the left and right torque on the wheel, respectively. For linear model of constant vehicle velocity with yaw rate as input:

$$\begin{bmatrix} \dot{\beta} \\ \ddot{\psi} \end{bmatrix} = \begin{bmatrix} -\frac{C_F + C_R}{mv} & -\left(1 + \frac{C_F l_\mathrm{f} - C_R l_\mathrm{r}}{mv^2}\right) \\ -\frac{C_F l_\mathrm{f} - C_R l_\mathrm{r}}{I_z} & -\frac{C_F l_\mathrm{f}^2 - C_R l_\mathrm{r}^2}{I_z} \end{bmatrix} \begin{bmatrix} \beta \\ \dot{\psi} \end{bmatrix} + \begin{bmatrix} \frac{C_F}{mv} & 0 \\ \frac{C_F l_\mathrm{f}}{I_z} & \frac{1}{I_z} \end{bmatrix} \begin{bmatrix} \delta \\ M_z \end{bmatrix} \qquad (23)$$

Data Acquisition and Estimation Techniques. Taking into account available data acquisition methods to the project and the benefits that they could provide, MATLAB virtual driving scenario is selected and used further in this project. MATLAB provides an essential tool regarding to virtual testing environment of the vehicles [9]. It has an in-built block set which creates virtual environment for test car. It provides output as a MATLAB function which basically output vehicle positions, velocity, and yaw rate generated during entire travel over the test road.

Linear Analysis of Vehicle Model. The linearization of model is successful and working perfectly. The individual step response for yaw moment and lateral velocity is nice and beautiful step response. Now, the linear vehicle model is analyzed on different vehicle speed, and their pole-zero and step response of linear vehicle model under different vehicle speed is generated below in Figs. 8 and 9.

TV Control System. The vehicle model is generated and upper most layer of torque vectoring control system in Fig. 10. Here, [10] the torque vectoring system is described for difference in the torques distributed on the right and left electric motor of the vehicle [7]. This difference of torques creates the yaw moment M_Z about the z-axis of the vehicle. This additional yaw moment can be computed. The linear state space vehicle model is generated on different velocity and made it to act as a SISO model.
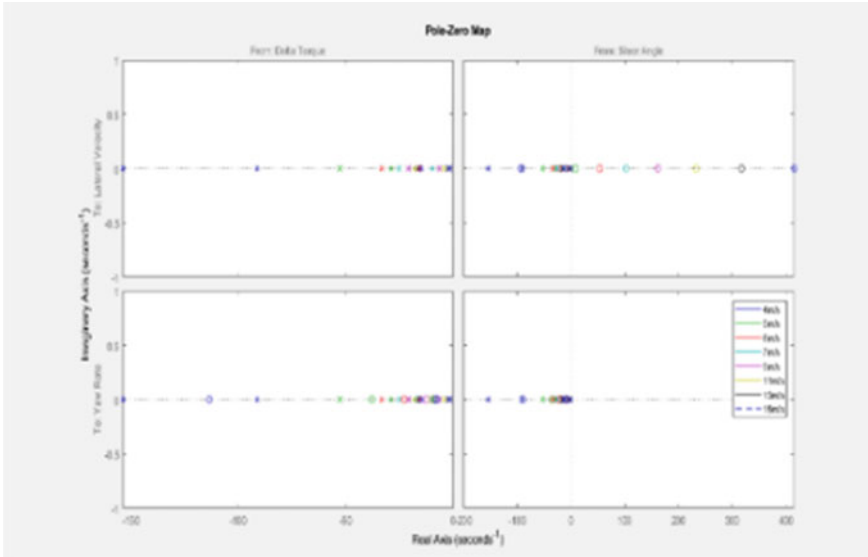
Fig. 8 Pole and zeros linear vehicle model
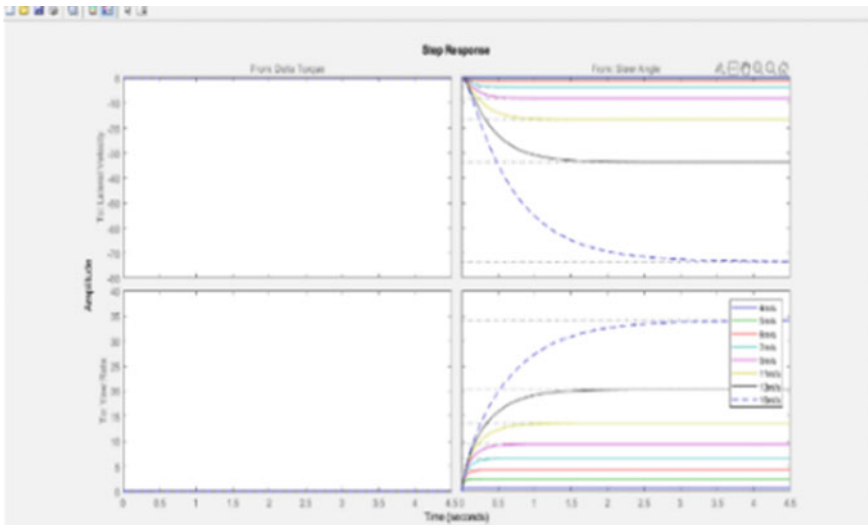
Fig. 9 Step response of linear model in different V in diff. velocity
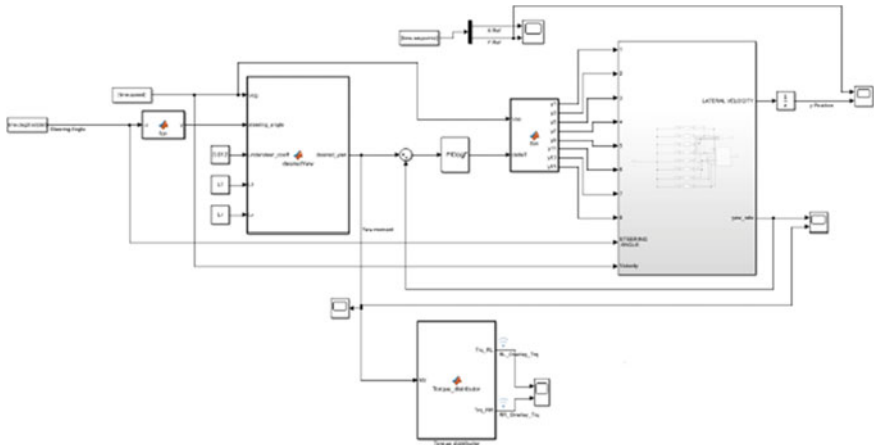
Fig. 10 Topmost layer of TV control system

3 Result and Discussion

3.1 Result Summary of Gear Train Components

Static Stress Analysis. The gears and gear casing model prepared are analyzed for the static stress on SOLIDWORKS separately, and following result provides the data which tells that the models are safe on working conditions. The simulated results are provided as (Figs. 11, 12, 13, 14, 15, 16, 17 and 18):

Manufactured Components. According to the estimated parameters of different gears, these have been manufactured on CNC milling machine (Fig. 19).

3.2 Result Summary of Torque Vectoring Control System

After simulating TV control system block in Simulink, we have got these results. It contains graph between reference lateral velocity and measured lateral velocity, graph between torque distributed on left wheel versus torque distributed on right wheel during taking turns on virtual environment, graph between reference Y position versus measured or calculated Y position, and graph between ref. yaw rate and measured yaw rate (Figs. 20, 21, 22 and 23).

The pursuit of reference yaw rate and measured yaw rate tells that yaw rate is actually the one who is been feedback controlled though PID controller and is been sending to the plant back to eliminate yaw rate error (Fig. 24).
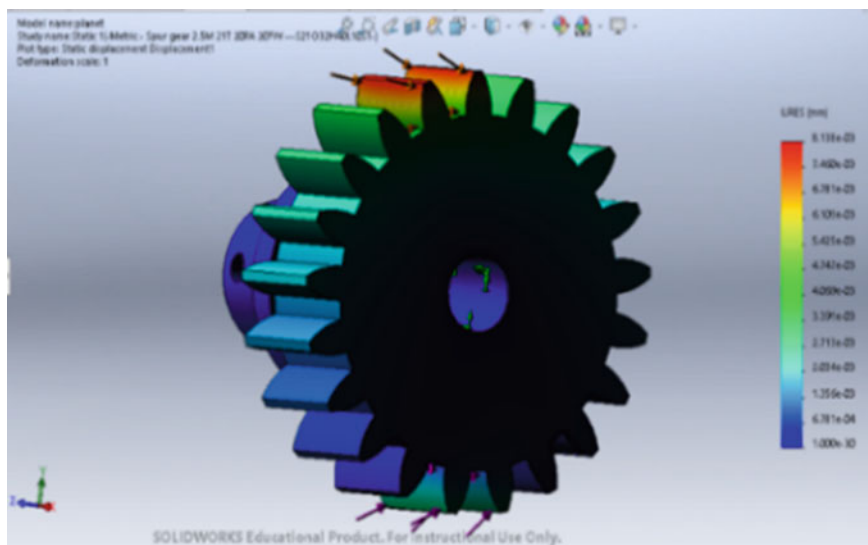
Fig. 11 Static stress simulation of sun gear
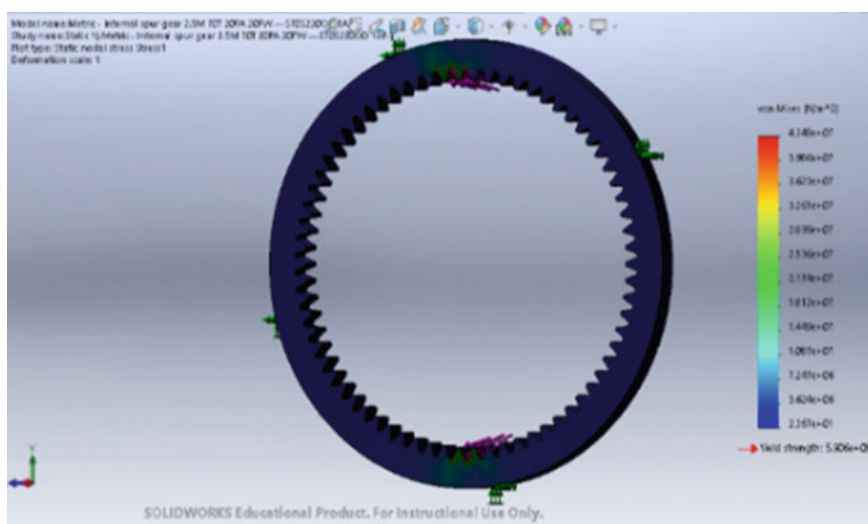
Fig. 12 Static stress simulation of ring gear

4 Conclusions

In this project, the gear box is designed and analyzed under static and wear load point of view keeping the optimum light weight and volume design in the mind.
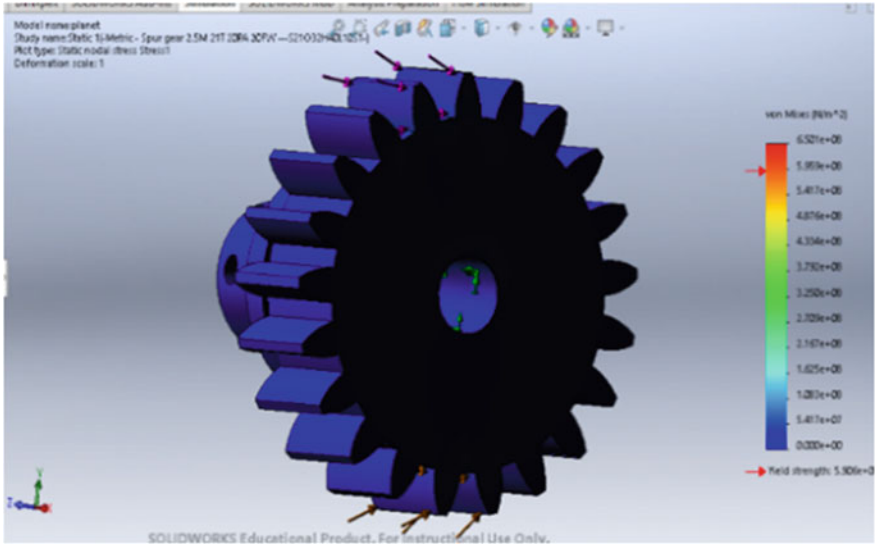
Fig. 13 Static stress simulation of planet gear
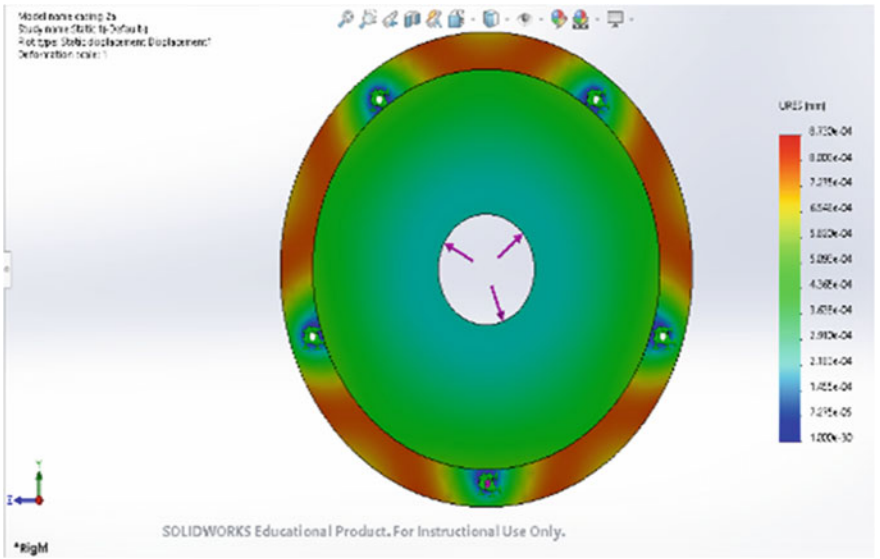
Fig. 14 Static stress simulation of gear casing 1
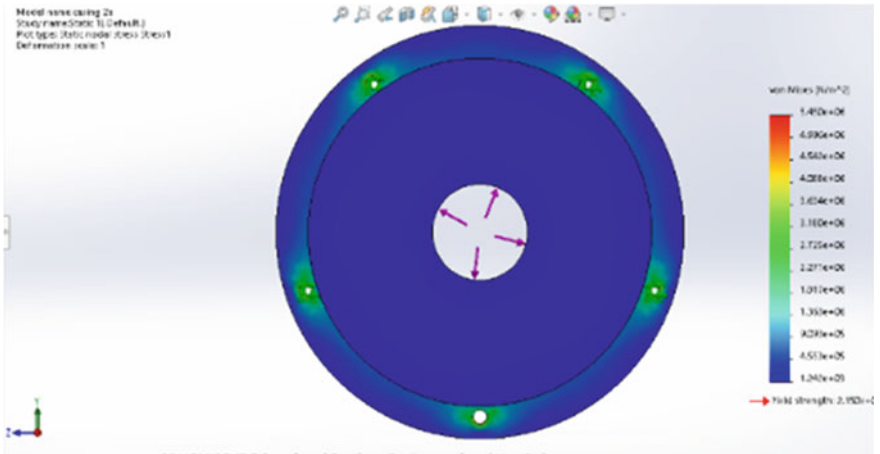
Fig. 15 Static stress simulation of gear casing 2
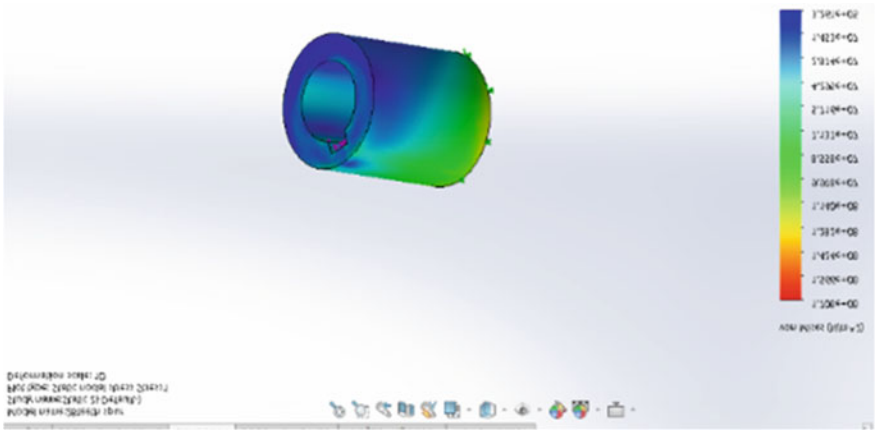
Fig. 16 Static stress simulation of sun gear shaft

From the analysis performed using SOLIDWORKS and comparing the results for different materials used in design of gearbox and gear casing, following conclusions were made:

- A total reduction of 3.5 is achieved using the single-stage reduction in the gearbox.
- All the material selected withstood various stress developed on it during simulation and result in a compact and lightweight gearbox which weighs 6.7 kg.

The torque vectoring control system is successfully designed for lateral vehicle dynamics in different velocity condition, and result generated shows control algorithm of torque vectoring is successfully designed.
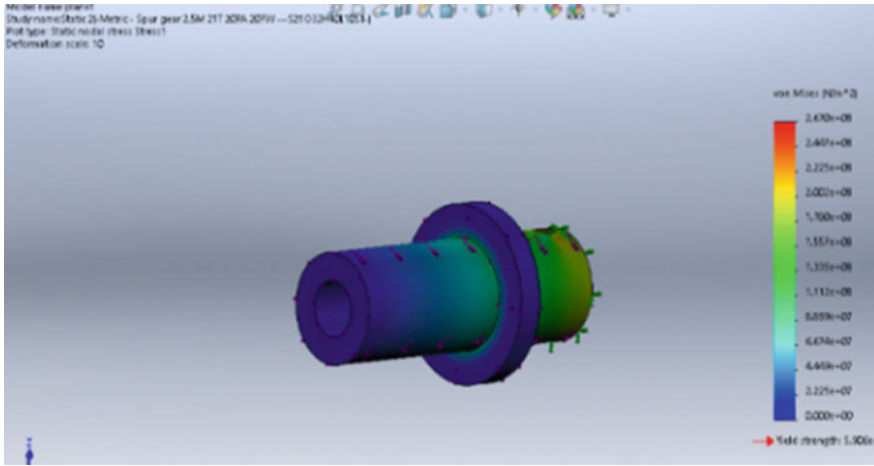
Fig. 17 Static stress simulation of planet gear shaft
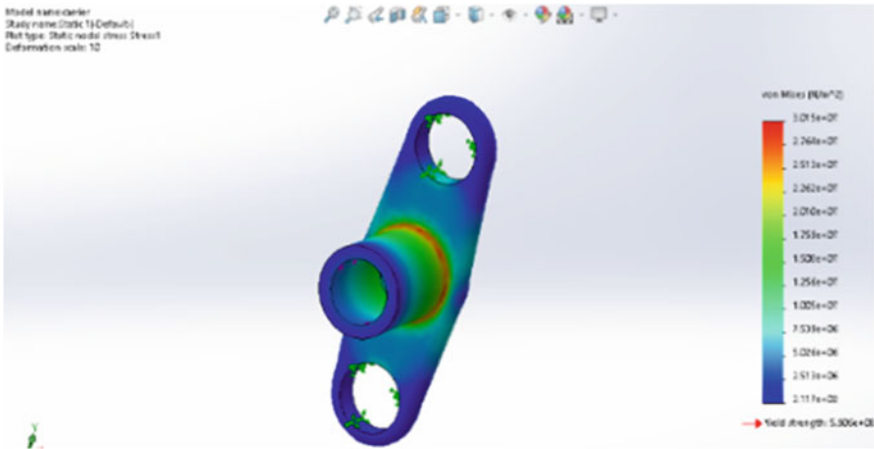
Fig. 18 Static stress simulation of carrier

Fig. 19 Manufactured components of gear train components
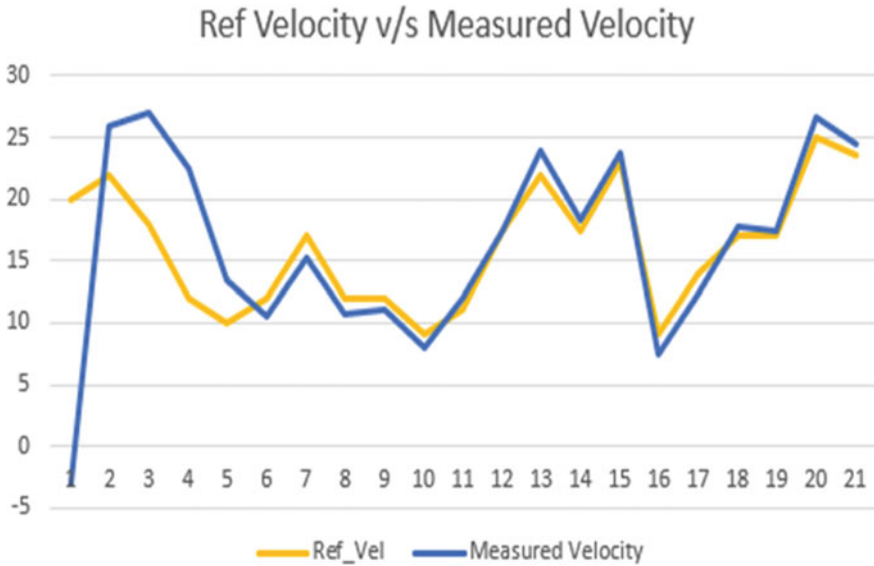
Fig. 20 Graph between Ref. and measured velocity
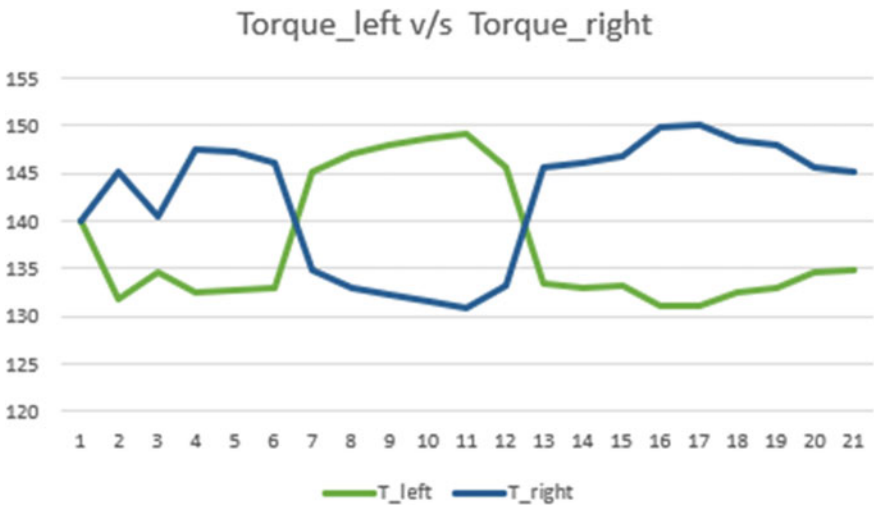
Fig. 21 Torque distribution at each wheel while turning

4.1 Future Scope

The gear manufactured on the basis of hand calculations and analysis is done on virtually on SOLIDWORKS. It is not been tested yet in working conditions and gear

X_Ref V/s Y Ref
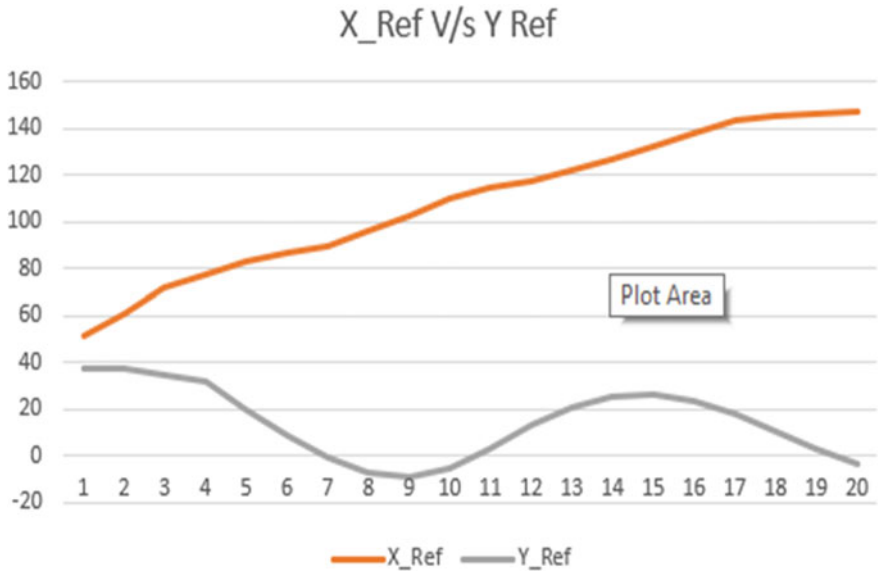
Fig. 22 Graph between *X* and *Y* Ref.

Y_ref v/s Y_measured
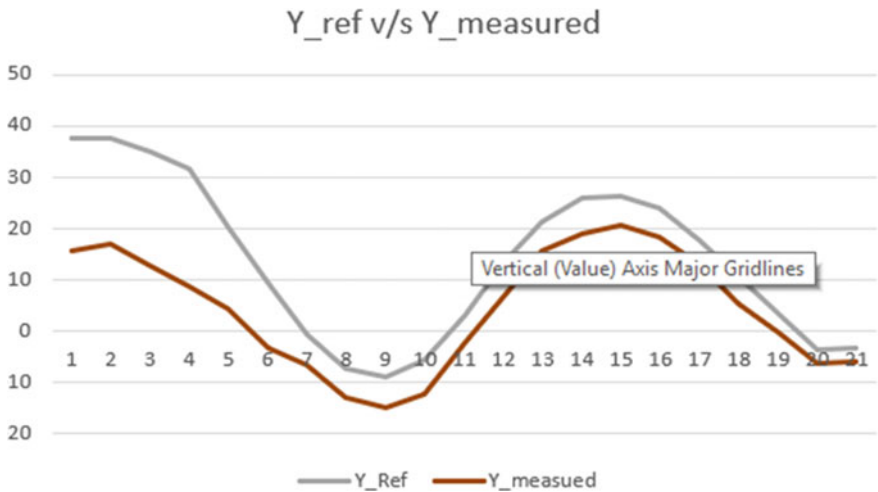
Fig. 23 Graph bet. Ref. and measured *Y* position

testing machine. So, testing in real conditions will give confirmation to the analysis of gear train. Torque vectoring's input data is not been acquired by any sensor. It has been created on MATLAB. So, the implementation of algorithm is to done yet and can be done by using motor controller and then encoding the code generated by
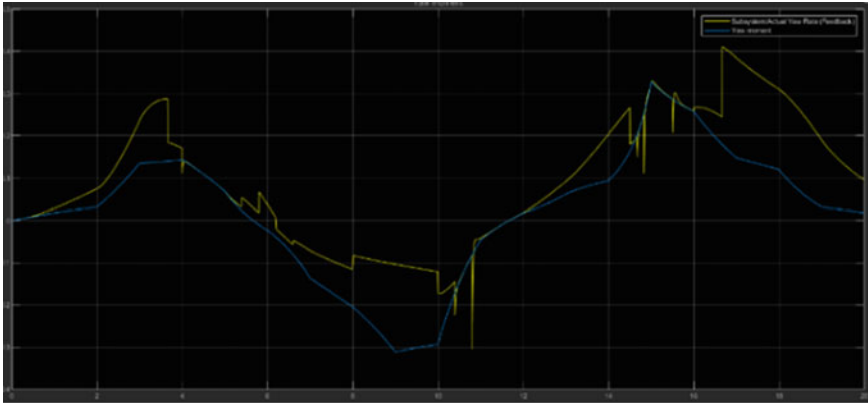
Fig. 24 Graph between reference yaw rate and measured yaw rate

control algorithm on MATLAB. It will verify our result even further, and then, it can be implemented on all four-wheel drive.

References

1. Milliken, W.F., Milliken, D.L.: Race Car Vehicle Dynamics, vol. 400. Society of Automotive Engineers Warrendale (1995)
2. Bhandari, V.B.: Design of Machine Elements, 3rd edn. McGraw-Hill Publications (2010)
3. [Online]. Available: https://lynchmotors.co.uk/. Accessed on 22 Jan 2020
4. [Online]. Available: https://asm.matweb.com/search/SpecificMaterial.asp?bassnum=MA6 061T6. Accessed on 12 Feb 2020
5. Lynwander, P.: Gear Drive Systems: Design and Applications
6. Trustry, M., Christifor, S.: Modelling and control of electric vehicles with individually actuated in-wheel motors. Master of Philosophy thesis, School of Mechanical, Materials and Mechatronic Engineering, University of Wollongong (2016). https://ro.uow.edu.au/theses/4737
7. Falcone, P., Borrelli, F., Asgari, J., Tseng, H.E., Hrovat, D.: Predictive active steering control for autonomous vehicle systems. IEEE Trans. Control Syst. Technol. **15**(3) (2007)
8. [Online]. Available: https://www.skf.com/group/products/rolling-bearings/ball-bearings/deep-groove-ball-bearings/single-row-deep-groove-ball-bearings. Accessed on 28 Feb 2020
9. Mondek, M.: Active torque vectoring systems for electric drive vehicles. Czech Technical University in Prague (2018)
10. Na, S.D., Jang, J.S., Kim, K.S., Yoo, W.S.: Dynamic vehicle model for handling performance using experimental data. In: Editor, F., Editor, S. (eds.) Conference 2016. LNCS, vol. 9999, pp. 1–13. Springer, Heidelberg (2016)

Effect of Non-Newtonian Behavior of Lubricant on Performance of Externally Pressurized Thrust Bearing

Vivek Kumar , **Vatsalkumar Ashokkumar Shah, Kuldeep Narwat, and Satish C. Sharma**

Nomenclature

A_b	Area of bearing; $\left(\pi r_o^2\right)$, mm^2
A_p	Area of recess; $\left(\pi r_i^2\right)$, mm^2; $\left(\frac{A_b}{A_{\mathrm{poc}}} = 4\right)$
D	Damping coefficient of fluid film, N s/m; $\overline{D} = \frac{h_o^3}{r_o^4 \mu}$
F_z	Fluid film reaction, N; $\overline{F}_z = \left(\frac{F_z}{p_s r_o^2}\right)$
h	Lubricant film thickness, mm; $\left(\overline{h} = h/h_o\right)$
$\dot{h}$	Squeeze velocity, mm/s; $\left(\overline{\dot{h}} = \frac{\partial \overline{h}}{\partial \overline{t}}\right)$
h_o	Reference film thickness, mm
Ω	Rotational speed parameter
K	Stiffness coefficient of fluid film, N/mm; $\left(\overline{K} = \frac{h_o}{p_s r_o^2} K\right)$
p	Fluid film pressure, MPa; $\left(\overline{p} = \frac{p}{p_s}\right)$
p_o	Lubricant pressure in the recess $\left(\dot{h} = 0\right)$, MPa
p_s	Supply pressure, MPa
r_i	Recess radius, mm
r_i and r_o	Recess and external radius of pad, mm
μ	Viscosity of the lubricant, Pa s
$\dot{\gamma}$	Shear strain rate

V. Kumar (✉) · V. A. Shah
Department of Mechanical Engineering, School of Technology, PDPU, Gandhinagar, India
e-mail: vivek.kumar@sot.pdpu.ac.in

K. Narwat
School of Mechanical Engineering, Galgotias University, Greater Noida, India

S. C. Sharma
Mechanical and Industrial Engineering Department, IIT Roorkee, Roorkee, India

τ Shear stress, N/m^2

1 Introduction

Thrust bearing are commonly used to position rotors in lightly loaded applications such as electric motors or to produced hydrostatic lift in extremely heavy turbomachines/structures [1, 2] such as telescope, observatory domes, and turbo-rotors. An externally pressurized thrust bearing (vis-à-vis hydrodynamic bearing) provides superior performance under severe operating environment such as to support extremely heavy load at low operating speed. An externally pressurized thrust bearing not only avoids metal-to-metal contact at low (or even zero) operating speed but also imparts excellent dynamic characteristics to the bearing system.

The performance of an externally pressurized thrust bearing largely depends on choice of compensating devices, pocket geometry, and type of lubricant employed in the bearing system [2, 3]. The response of thrust bearing under dynamic state can be effectively controlled by the use of a compensating device. The commonly used compensating devices are capillary tube, an orifice plate, membrane, and control flow valve. The circular and rectangular shape are most preferred recess geometry used in thrust bearing, due to their ease in manufacturing. However, with the advent of sophisticated machining techniques [4, 5] such as stereolithography, micro-machining, and laser surface texturing, complex pocket geometry with intricate contours can now be produced relatively with ease. These technologies have the ability to produce even micro-feature such as micro-dimple and micro-groove with high accuracy and dimensional repeatability. The depth of these micro-features is of order of magnitude of fluid film thickness. As a result, a number of studies [6–8] have been reported exploring the usefulness of laser surface texturing (LST) on the performance of thrust bearing operating in hydrodynamic lubrication regime as well as hydrostatic/hybrid lubrication regime. It has been reported that use of micro-texturing is quite beneficial in terms of reducing the friction coefficient as well as enhancing load supporting ability [5–8] of such bearing system. Contrary to this, pocket geometry is a macro-feature [2, 3] produced on the surface of thrust pad. The dimensions of pocket, i.e., cross-sectional area and depth, is very large as compared to the dimensions of nominal fluid film thickness. Some studies have reported that an adequate selection of pocket/recess shape and its location/orientation can significantly improve the static performance of bearing. Normally, the hydrostatic thrust bearing operates under parallel alignment of bearing surface. It has been found that presence of even small amount of tilt has adverse effect on load-supporting capacity [9] of such bearing system.

Industrial lubricants are usually blended with different package of additive agents such as rust inhibitors, anti-wear additives, and viscosity improvers, to improve the lubricant performance specific to some particular applications. Some experimental studies have been reported investigating the influence of viscosity index improving additives on the friction and wear behavior of tribo-pairs [10–12] such as journal

bearings and frictional clutch. These studies reported that blending of such additives impart a non-Newtonian character to the lubricant. Many theories have been postulated to describe non-Newtonian nature exhibited by the commercial lubricants. A number of studies have been reported dealing with numerical simulation of thrust bearings using power law [13], MHD-couples stress [14], cubic law [15], and Herschel–Bulkley [16] fluid model. Wu and Dareing [17] carried out an experimental investigation on circular pocket thrust bearing operating with non-Newtonian lubricant. The non-Newtonian lubricant is formulated by adding traces of graphite powder in ethylene glycol as stock lubricant. The author predicted the performance of bearing system, using an analytical model based on power-law lubricant. A good agreement between experimental results and analytical model suggested suitability of power-law model to describe non-Newtonian character of lubricant under given operating conditions. Sharma and Yadav [18] have derived closed-form solution for circular thrust bearing operating with cubic law fluid. Recently, Kumar and Sharma conducted a numerical simulation to optimize the annular [19] and elliptical [20] pocket geometry in thrust bearing operating with couple-stress lubricant. The authors have reported that presence of tilt between bearing surface and couple-stress in lubricant strongly affects the dynamic performance characteristics of the bearing.

The literature review presented above indicates that the performance of an externally pressurized thrust bearing can be effectively maintained by compensating device, pocket geometry, and use of non-Newtonian lubricant. The capillary tube and orifice restrictor are commonly used compensating device in hydrostatic bearing system. Some studies [18–20] are reported employing non-conventional recess shapes (elliptical and annular) in such bearing system. Wu and Dareing [17] investigated the steady-state performance of thrust bearing operating with a control flow valve device. However, a comprehensive literature review suggest that no study has been reported investigating the combined effect of pocket geometry, CFV device, and power-law lubricant on the dynamic performance indices of an externally pressurized thrust bearing. Therefore, this study has been planned to address these above-mentioned research gaps.

2 Mathematical Formulation

Figure 1a shows an externally pressurized thrust pad bearing system under investigation in presented work. The lubricant is supplied to the pocket through a control flow valve serving as compensating device. The lubricant is assumed to be non-Newtonian in nature, which has been described using power-law fluid model. The flow condition in bearing space is considered to be steady-state, laminar, isothermal, and incompressible. Figure 1b shows various pocket shapes investigated in present work. A generalized Reynolds equation governing flow of non-Newtonian lubricant in the bearing system can be expressed as:
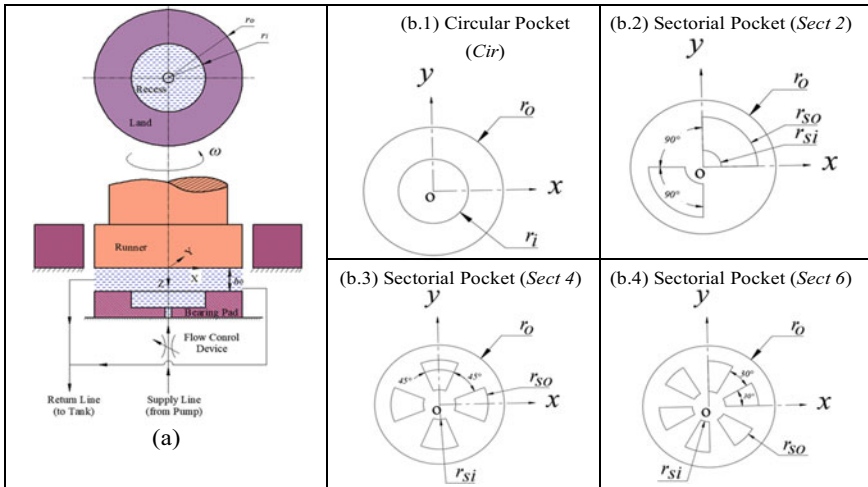
Fig. 1 **a** Hydrostatic thrust bearing and **b** pocket geometric shapes

$$\frac{\partial}{\partial \alpha}\left(\overline{h}^3 \overline{F}_2 \frac{\partial \overline{p}}{\partial \overline{x}}\right) + \frac{\partial}{\partial \beta}\left(\overline{h}^3 \overline{F}_2 \frac{\partial \overline{p}}{\partial \overline{y}}\right) = -\Omega \overline{r} \sin\theta \frac{\partial}{\partial \overline{x}}\left[\left(1 - \frac{\overline{F}_1}{\overline{F}_0}\right)\overline{h}\right]$$

$$+ \Omega \overline{r} \cos\theta \frac{\partial}{\partial \overline{y}}\left[\left(1 - \frac{\overline{F}_1}{\overline{F}_0}\right)\overline{h}\right] + \frac{\partial \overline{h}}{\partial \overline{t}} \quad (1)$$

$$\overline{x} = \frac{x}{r_o}; \; \overline{y} = \frac{y}{r_o}; \; \overline{h} = \frac{h}{h_o}; \; \overline{r} = \frac{r}{r_o}; \; \overline{p} = \frac{p}{p_s}; \; \overline{\mu} = \frac{\mu}{\mu_r}; \; \Omega = \frac{\mu_r \omega r_o^2}{h_o^2 p_s}; \; \overline{t} = t\frac{h_o^2 p_s}{\mu r_o^2}$$

where $\overline{F}_0$, $\overline{F}_1$, and $\overline{F}_2$ represent viscosity integrals of lubricant and describe as follows:

$$\overline{F}_0 = \int_0^1 \frac{1}{\overline{\mu}}d\overline{z}; \quad \overline{F}_1 = \int_0^1 \frac{\overline{z}}{\overline{\mu}}d\overline{z}; \quad \overline{F}_2 = \int_0^1 \frac{\overline{z}}{\overline{\mu}}\left(\overline{z} - \frac{\overline{F}_1}{\overline{F}_0}\right)d\overline{z}$$

Finite element technique is used to obtain numerical solution of generalized Reynolds equation. The bearing surface is discretized using four-node quad elements. The degree of approximation of primary field variable and geometry is assumed to be varying bi-linearly within an element. Fluid film pressure is approximated as follows:

$$\overline{p} = \sum_{j=1}^4 [N_j \overline{p}_j]; \quad N_j = \frac{1}{4}(1 + \xi_i \xi)(1 + \eta_i \eta) \quad (2)$$

Weighted residual approach is used to obtain weak form of Reynolds equation, and weights are substituted with Langragian shape functions of primary field variable. The residue of the approximate solution is obtained as follows:

$$\frac{\partial}{\partial \overline{x}} \left(\frac{\overline{h}^3}{\overline{\mu}} \overline{\varphi} \frac{\partial}{\partial \overline{x}} \left\{ \sum_{j=1}^{4} (\overline{p}_j N_j) \right\} \right) + \frac{\partial}{\partial \overline{y}} \left(\frac{\overline{h}^3}{\overline{\mu}} \overline{\varphi} \frac{\partial}{\partial \overline{y}} \left\{ \sum_{j=1}^{4} (\overline{p}_j N_j) \right\} \right)$$

$$+ \Omega \overline{r} \sin \theta \frac{\partial}{\partial \overline{x}} \left[\left(1 - \frac{\overline{F}_1}{\overline{F}_0} \right) \overline{h} \right]$$

$$- \Omega \overline{r} \cos \theta \frac{\partial}{\partial \overline{y}} \left[\left(1 - \frac{\overline{F}_1}{\overline{F}_0} \right) \overline{h} \right] - \frac{\partial \overline{h}}{\partial \overline{t}} = R_{\text{es}} \tag{3}$$

The minimization of residue over flow domain will lead to global system of algebraic equations. Simplification of above-mentioned equation yields:

$$\left[\overline{F}_{ij}^e \right] \{ \overline{p} \} = \left[\overline{Q}_i^e \right] + \left[\overline{RH}_i^e \right] + \overline{\dot{h}} \left[\overline{RS}_i^e \right] \tag{4}$$

Afterward, lubricant flow equation through a CFV device is incorporated in the global system of equation. This is achieved by first identifying all nodes lying on pocket periphery and then assigning them the supply pressure ($\overline{p}_{oj}$). Later, sum of lubricant flow rate through all these nodes has been equated to fluid flow through a CFV device. Reynolds boundary condition is used at outer edge of thrust pad, which implies that fluid pressure approaches to ambient pressure at the thrust pad boundary.

$$\begin{bmatrix} \overline{F}_{11} & \overline{F}_{12} & \dots & \overline{F}_{1j} & \dots & \overline{F}_{1n} \\ \overline{F}_{21} & \overline{F}_{22} & \dots & \overline{F}_{2j} & \dots & \overline{F}_{2n} \\ \vdots & \vdots & \vdots & \vdots & \vdots & \vdots \\ \overline{F}_{j1} & \overline{F}_{j2} & \dots & \overline{F}_{jj} & \dots & \overline{F}_{jn} \\ \vdots & \vdots & \vdots & \vdots & \vdots & \vdots \\ \overline{F}_{n1} & \overline{F}_{n2} & \dots & \overline{F}_{nj} & \dots & \overline{F}_{nn} \end{bmatrix} \begin{bmatrix} \overline{p}_{o1} \\ \overline{p}_{o2} \\ \vdots \\ \overline{p}_{oj} \\ \vdots \\ \overline{p}_{on} \end{bmatrix} = \begin{bmatrix} \overline{Q}_1 \\ \overline{Q}_2 \\ \vdots \\ \overline{Q}_R \\ \vdots \\ \overline{Q}_n \end{bmatrix} + \overline{\dot{h}} \begin{bmatrix} \overline{RS}_1 \\ \overline{RS}_2 \\ \vdots \\ \overline{RS}_j \\ \vdots \\ \overline{RS}_n \end{bmatrix} \tag{5}$$

The lubricant supply via a CFV device can be described [17] as:

$$\overline{Q}_R = \overline{CS}_2 \tag{6}$$

The viscosity of non-Newtonian lubricant is assumed to govern by power-law fluid model.

$$\tau = \mu \dot{\gamma}^n \tag{7}$$

where n is power-law index. Experiments need to be performed to obtain value of power-law index for Pseudo-plastic lubricants ($n < 1$), Newtonian lubricants ($n = 1$) and dilatant lubricants ($n > 1$). A generalized expression for strain rate of non-Newtonian lubricant is expressed as:

$$\overline{\dot{\gamma}} = \sqrt{\left[\frac{\overline{h}}{\overline{\mu}}\frac{\partial\overline{p}}{\partial\overline{x}}\left(\overline{z}-\frac{\overline{F}_1}{\overline{F}_0}\right)+\frac{\Omega}{\overline{\mu h F}_0}\right]^2+\left[\frac{\overline{h}}{\overline{\mu}}\frac{\partial\overline{p}}{\partial\overline{y}}\left(\overline{z}-\frac{\overline{F}_1}{\overline{F}_0}\right)\right]^2} \quad (8)$$

The bearing performance indices such as film reaction force, film stiffness, and damping coefficient can be evaluated once film pressure, and its derivatives are computed.

$$\text{Fluid film reaction:}\quad \overline{F}_z = \sum_{e=1}^{n_e}\left\{\int_{-1}^{+1}\int_{-1}^{+1}\left(\sum_{j=1}^{4}\overline{p}_j N_j\right)|\overline{J}|\mathrm{d}\xi\,\mathrm{d}\eta\right\}+\sum_{e=1}^{n_p}\overline{A}_p\overline{p}_r \quad (9)$$

$$\text{Stiffness coefficient:}\quad \overline{K} = \sum_{e=1}^{n_e}\left\{\int_{-1}^{+1}\int_{-1}^{+1}\left(\sum_{j=1}^{4}\frac{\partial\overline{p}_j}{\partial\overline{h}}N_j\right)|\overline{J}|\mathrm{d}\xi\,\mathrm{d}\eta\right\}+\sum_{e=1}^{n_p}\overline{A}_p\frac{\partial\overline{p}_r}{\partial\overline{h}}$$

$$(10)$$

$$\text{Damping coefficient:}\quad \overline{D} = \sum_{e=1}^{n_e}\left\{\int_{-1}^{+1}\int_{-1}^{+1}\left(\sum_{j=1}^{4}\frac{\partial\overline{p}_i}{\partial\dot{\overline{h}}}N_j\right)|\overline{J}|\mathrm{d}\xi\,\mathrm{d}\eta\right\}+\sum_{e=1}^{n_p}\overline{A}_p\frac{\partial\overline{p}_r}{\partial\dot{\overline{h}}}$$

$$(11)$$

3   Solution Procedure

Numerical simulation of bearing system has been performed by finite element formulation of flow governing equations. A source code is developed, employing finite element method, Newton–Raphson method, and Gauss–Legendre quadrature to solve set of algebraic equation for film pressure. The input to the numerical model is listed in Table 1. Four pocket shape specifically circular and sectorial recess having two, four, and six pockets are investigated in present work. The ratio of bearing area to pocket area is kept uniform (four) across all pocket shapes. The bearing surface is divided into subdomains using iso-para quad elements. Grid size is selected for each recess shape, after performing grid independence test. The numerical solution of Reynolds equation is based on solution scheme illustrated in Fig. 2. The solution scheme is grid-independent and able to render converged (tolerance on fil pressure = 10-04) numerical results. Next step is to check ability of source code to reproduce available results on hydrostatic thrust bearings. The developed program has been

Table 1 Bearing geometric and operating conditions

Input parameters	Dimensional value
Bearing pad outer radius (r_o)	100 mm
Circular pocket radius (r_i)	50 mm
Sectorial recess outer radius (r_{so})	75 mm
Sectorial recess inner radius (r_{si})	25 mm
Nominal fluid film thickness	0.05 mm
Lubricant supply pressure	5 MPa
Lubricant dynamic viscosity (40 °C)	0.034 Pa.s
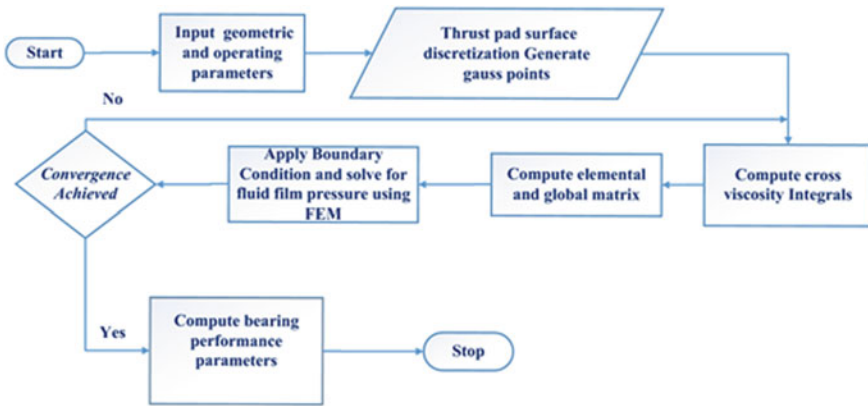
Fig. 2 Solution scheme

used to simulate the performance of hydrostatic thrust bearing [21]. Table 2 present a comparison between performance indices of thrust bearing, from the analytical solution of reference study [21] and using present approach. It can be seen that results from two studies follow closely with one another (maximum deviation below 5%). This justifies the accuracy and ability of developed source code to numerically simulate hydrostatic thrust bearing.

Table 2 Validation of solution scheme

H	($\bar{l} = 0$)		($\bar{l} = 0.1$)		($\bar{l} = 0.2$)	
	Fatima et al. [21]	Present	Fatima et al. [21]	Present	Fatima et al. [21]	Present
0	7.9641	7.7996	22.753	22.165	37.527	36.241
1	17.843	17.498	22.916	22.511	37.689	36.832
2	18.3202	18.727	23.407	23.544	38.173	38.468
3	19.1149	19.532	24.218	25.175	38.992	40.095

4 Results and Discussions

The analysis of present work deals with numerical solution of an externally pres-surized thrust bearing operating with non-Newtonian lubricant. Fluid film pressure, film reaction force, stiffness, and damping coefficient are numerically computed as performance indices of the bearing. These performance parameters are plotted as a function of power-law index. The numerical values of power-law index vary from 0.8–1–1.2, representing lubricant behavior transition from shear-thinning to Newto-nian to shear-thickening nature. Influence of geometric shape of recess is also plotted for the above-mentioned performance indices.

Figure 3 depicts influence of pocket geometry and non-Newtonian nature of the lubricant on film pressure distribution over the surface of thrust pad. All the pressure plots are depicted for a constant film thickness for the bearing system. It can be easily visualized that circular pocket thrust pad generates a bigger film pressure envelope as compared to multi-pocket (sectorial) pad. It can also be observed that film pressure envelope gets shrink with an increase in number of sectorial pocket in pad. Figure 4 presents influence of power-law index and pocket geometry on film pressure within the recess/pocket of bearing system. It has been noticed that shear-thinning ($n < 1$) and shear-thickening ($n > 1$) behavior tends to reduce and enhance pocket pressure respectively, as compared to Newtonian lubricant ($n = 1$). This is because of an increase and decrease in apparent viscosity of lubricant.

This is because of an increase and decrease in apparent viscosity of pseudo-plastic and dilatant lubricants respectively. An increase in apparent viscosity tends to decrease film velocity profile which can lead to accumulation of higher amount of

Pocket Geometry	Shear thinning lubricant (n=0.8)	Newtonian Lubricant (n=1)	Shear Thickening Lubricant (n=1.2)
Circular (*Cir*)			
Sectorial (*Sect 2*)			
Sectorial (*Sect 4*)			
Sectorial (*Sect 6*)			
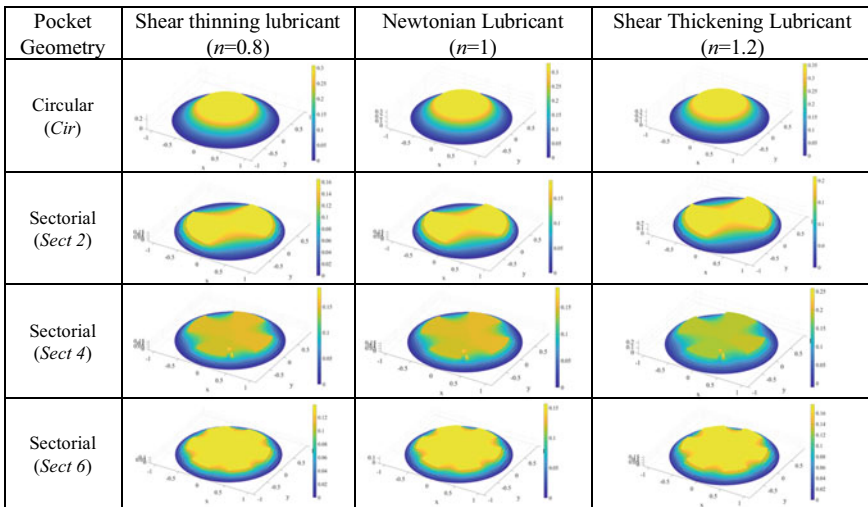
Fig. 3 Fluid film pressure for thrust with various pocket geometry

Fig. 4 Pocket pressure versus power law index
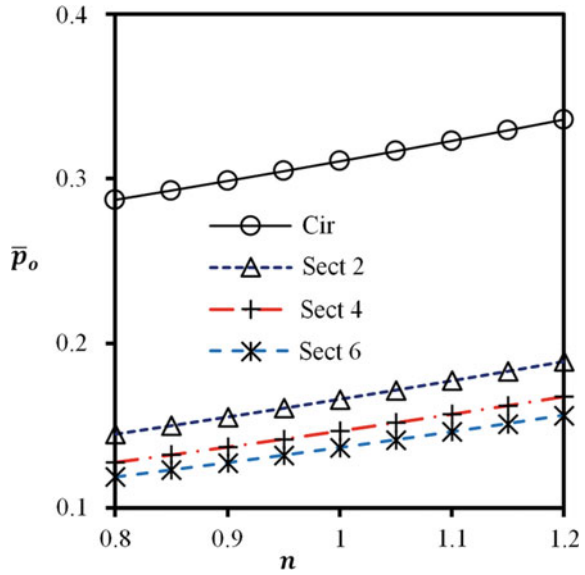
lubricant in the system and consequently film pressure envelope rises. This enhancement in film pressure (owing to use of shear-thickening lubricant) is quite beneficial in generating higher film reaction force in the bearing system. Conversely, use of shear-thinning lubricant leads to reduction in apparent viscosity, film pressure, and ultimately a reduction in load-supporting ability of the bearing system. The trends presented in Figs. 3, 4 and 5 can be summarized as follows:

$$\left| \overline{p}_o/\overline{F}_z \right|_{\text{Psuedoplastic}} < \overline{p}_o/\overline{F}_z \big|_{\text{Newtonian}} < \overline{p}_o/\overline{F}_z \big|_{\text{Dilatant}} \Big|$$

$$|\text{Sect } 6 < \text{Sect } 4 < \text{Sect } 2 < \text{Circular}|_{\overline{p}_o;\overline{F}_z}$$

The percentage change in film reaction force w.r.t use of shear-thickening ($n = 1.2$) and shear-thinning behavior of lubricant for each pocket geometry has been found as follows:

$$|+9.25_{\text{Circular}} < +12.08_{\text{Sect } 2} < +12.3_{\text{Sect } 4} < +12.37_{\text{Sect } 6}|_{\overline{F}_z(n=1\to1.2)}$$

$$|-11.12_{\text{Sect } 2} \sim -11.08_{\text{Sect } 4} < -10.84_{\text{Sect } 2} < -8.41_{\text{Circular}}|_{\overline{F}_z(n=1\to0.8)}$$

Figure 6 illustrates the variation in film stiffness coefficient with respect to power-law index of non-Newtonian lubricant. It can be seen that shear-thickening and shear-thinning nature of lubricant leads to enhancing and reducing the stiffness capabilities of the bearings system. Further, it has been found that use of circular pocket (as compared to multi-recess bearing) impart better stiffness capabilities to the bearing system. The numerical results for film stiffness and damping coefficient in the form of trends can be summarized as follows:

Fig. 5 Film reaction force versus power law index
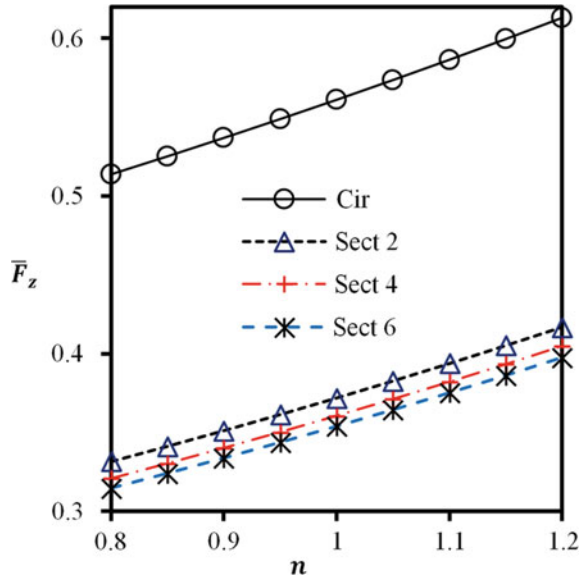
Fig. 6 Stiffness coefficient vs power law index
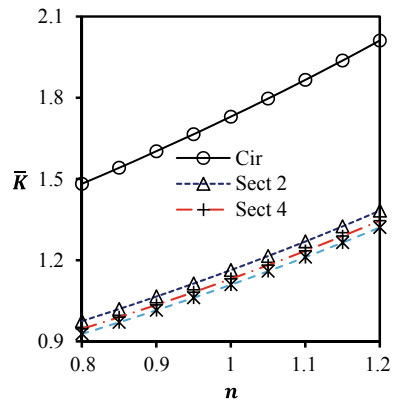
$$\left| \overline{K}; \overline{C} \right|_{\text{Psuedoplastic}} < \overline{K}; \overline{C} \big|_{\text{Newtonian}} < \overline{K}; \overline{C} \big|_{\text{Dilatant}} \right|$$

$$|\text{Sect } 6 < \text{Sect } 4 < \text{Sect } 2 < \text{Circular}|_{\overline{K};\overline{C}}$$

Under combined effect of circular pocket and dilatant lubricant ($n = 1.2$), a maximum enhancement of 85.1% has been reported in film stiffness coefficient. On the other hand, use of psuedo-plastic lubricant is found to have detrimental effect (−14.7%) on stiffness coefficient of bearing system. The numerical results for film damping coefficient of bearing system is shown in Fig. 7. It can be seen here that shear-thinning behavior of lubricant have an adverse effect on damping properties

Fig. 7 Damping coefficient
reaction vs power law index
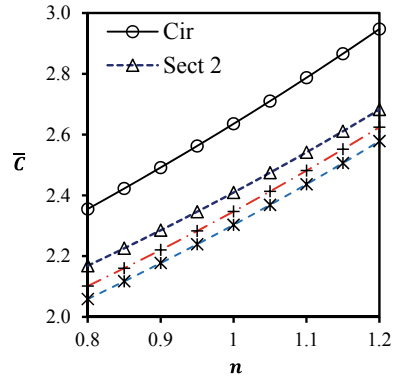
of bearing system. On contrary, shear-thickening nature of lubricant can substantially enhance the damping coefficient of bearing. Although, maximum damping coefficient is noticed for circular pocket thrust bearing, yet maximum percentage enhancement in damping coefficient owing to use dilatant lubricant ($n = 1.2$) has been reported for six-pocket sectorial recess.

5   Conclusions

Following consolidated conclusion can be drawn from the results and discussions presented in the preceding section.

- The recess/pocket geometry and non-Newtonian character of lubricant significantly affect the load-supporting capacity of a CFV controlled thrust bearing.
- Under given simulated condition, it has been found that circular pocket (vis-à-vis sectorial recess) should be preferred for generating higher fluid film reaction or load support in the bearing.
- The shearing-thinning nature of lubricant have an adverse effect on film stiffness and damping coefficient in hydrostatic thrust bearings.
- It has been noticed that providing or increasing number of sectorial-pockets adversely affect the performance indices of CFV controlled thrust bearings.

References

1. Stachowiak, G.W., Andrew, W.B.: Engineering Tribology. Butterworth-Heinemann, Australia (2013)
2. Rowe, W.B.: Hydrostatic and Hybrid Bearing Design. Elsevier, London (2013)
3. Sinhasan, R., Jain, S.: Lubrication of orifice-compensated flexible thrust pad bearings. Tribol. Int. **17**(4), 215–221 (1984)

4. Yang, H., Ratchev, S., Turitto, M.: Rapid manufacturing of non-assembly complex micro-devices by microstereolithography. Tsinghua Sci. Technol. **14**, 164–167 (2009)
5. Etsion, I.: State of the art in laser surface texturing. Trans. ASME J. Tribol. **127**(1), 248–253 (2005)
6. Brizmer, V., Kligerman, Y., Etsion, I.: A laser surface textured parallel thrust bearing. Tribol. Trans. **46**(3), 397–403 (2003)
7. Kumar, V., Sharma, S.C.: Effect of geometric shape of micro-grooves on the performance of textured hybrid thrust pad bearing. J. Braz. Soc. Mech. Sci. Eng. **41**(11), 508 (2019)
8. Kumar, V., Sharma, S.C., Narwat, K.: Influence of micro-groove attributes on frictional power loss and load-carrying capacity of hybrid thrust bearing. Ind. Lubr. Tribol. (2019). https://doi.org/10.1108/ILT-07-2019-0278
9. Safar, Z.S.: Design of tilted hydrostatic thrust bearings. Wear **70**, 243–248 (1981)
10. Oliver, D.R.: Load enhancement effects due to polymer thickening in a short model journal bearing. J. Non-Newton. Fluid Mech. **30**, 185–196 (1988)
11. Spikes, H.A.: The behaviour of lubricants in contacts: current understanding and future possibilities. J. Proc. Inst. Mech. Eng. Part J: J. Eng. Tribol. **28**, 3–15 (1994)
12. Scott, W., Suntiwattana, P.: Effect of oil additives on the performance of a wet friction clutch material. Wear **181**, 850–855 (1995)
13. Singh, C., Nailwal, T.S., Sinha, P.: Elastohydrostatic lubrication of circular plate thrust bearing with power law lubricants. J. Lubr. Technol. **104**, 243–247 (1982)
14. Kumar, V., Sharma, S.C.: Dynamic characteristics of compensated hydrostatic thrust pad bearing subjected to external transverse magnetic field. Acta Mech. **229**(3), 1251–1274 (2018)
15. Singh, U.P., Gupta, R.S., Kapur, V.K.: On the steady performance of hydrostatic thrust bearing: Rabinowitsch fluid model. Tribol. Trans. **54**, 723–729 (2018)
16. Bouyahia, F., Hajjam, M., Khlifi, M.E., Souchet, D.: Three-dimensional non-Newtonian lubricants flows in sector-shaped, tilting-pads thrust bearings. J. Proc. Inst. Mech. Eng. Part J: J. Eng. Tribol. **220**, 375–384 (2006)
17. Wu, Z., Dareing, D.W.: Non-Newtonian effects of powder-lubricant slurries in hydrostatic and squeeze film bearings. Tribol. Trans. **37**, 836–842 (1994)
18. Sharma, S.C., Yadav, S.K.: Performance of hydrostatic circular thrust pad bearing operating with Rabinowitsch fluid model. Proc. Inst. Mech. Eng. Part J: J. Eng. Tribol. **227**(11), 1272–1284 (2013)
19. Kumar, V., Sharma, S.C.: Study of annular recess hydrostatic tilted thrust pad bearing under the influence of couple stress lubricant behavior. Int. J. Surf. Sci. Eng. **11**(4), 344–369 (2017)
20. Kumar, V., Sharma, S.C.: Finite element method analysis of hydrostatic thrust pad bearings operating with electrically conducting lubricant. Proc. Inst. Mech. Eng. Part J: J. Eng. Tribol. **232**(10), 1318–1331 (2018)
21. Fathima, S.T., Naduvinamani, N.B., Hanumagowda, B.N., Kumar, J.S.: Modified Reynolds equation for different types of finite plates with the combined effect of MHD and couple stresses. Tribol. Trans. **58**, 660–667 (2015)

IoT-Enabled Automatic Floor Cleaning Robot

Vibha Burman and **Ravinder Kumar**

1 Introduction

Floor cleaning robots are an essential application in a domestic environment. In a domestic environment, people want a reliable source of technology to make their house clean in every part and every corner. Also, in the name of floor cleaning robot, mostly dry cleaners (i.e., vacuum cleaners) are obtainable in the market. Wet cleaners are not available in the market. In this section, a brief introduction about various floor cleaners is discussed. The authors proposed a self-governing cleaning robot [1] that are dry and wet cleaning robots. Using the Northstar navigation system, it navigates and cleans the home steadily. A survey was conducted by the authors [2] to understand the experience of individuals on new appliances coming in the markets. The main findings of the above survey included that people prefer robotic vacuum cleaner which possess the composed, well-mannered and mutual qualities and also at the operational facade robotic vacuum cleaner possess proficient, organized and similar schedule. The researchers reported a design-specific Roomba, a floor cleaning vacuum [3] consisting of the capabilities of roaming freely inside the house and performs a sweeping action throughout roaming freely. It performs three cleaning categories, namely mopping the floor, pull dust particles, and cleansing of mopboards and walls. Movement-based on end-to-end locomotion can be done with the help of autonomous navigation. An autonomous mobile robot cleaner system [4] contains a map creating system and memory system. The map creating system consists of detail of cleaning areas on the floor and memory space consist of stored details of the mapping. Researchers [5] have worked for 6 months on Roomba to understand the living in Switzerland of human life with a vacuum cleaning robot. Research

V. Burman (✉) · R. Kumar
Department of Mechanical and Automation, Indira Gandhi Delhi Technical University for Women, Delhi, India
e-mail: vibhaburman1025@gmail.com

concluded that the Roomba vacuum cleaner is adapted to the culture of human–robot interaction (HRI) under this concept work needs to be moral and harmless and reliable. The control module of the proposed cleaning robot by the authors [6] consist at least a movement module and cleaning module. The cleaning robot involves movement of robot, production of recognition signal and controlling the procedure of the robot according to recognition signal. Mint robotic cleaner [7] is an electric appliance that operates under two modes, automatic and manual mode. It is a wet cleaner, not a vacuum (dry) cleaner. Clothes are attached to mapping places of work and are easily detached or reused. For navigation, an indoor localization system is utilized like a Global Positioning System (GPS) module. Smart obstacle avoidance [8] used in fully automatic service robot for floor cleaning using an FPGA-based hardware algorithm. The behavior-based algorithm is used for the navigation of pathways, obstacle avoidance, and distance-measuring techniques. Some plans of attacks toward the floor cleaning robots operated through voice are done using HRI. To assist the cleaning robot from a distance, voice recognition can be used. The field of IoT is an outgrowing area which possesses the capabilities of designing innovations every day [9].

2 Literature Review

The Floor cleaning robot is employed as a domestic application. The proposed arrangement will be helpful to maintain cleanliness in indoor environments. In this part, the previous work is discussed below and also the case of floor cleaner, hardware parts, i.e., wireless mediums, sensors, and microcontrollers are discussed in the tabular form listed as Tables 1, 2, 3, 4 and 5. Mint floor cleaner robot contains two cleaning method, namely dry and wet. The floor cleaning robot brushes the floor in neat and parallel line's direction in dry mode cleaning, whereas robot mops the floor in forward and backward directions in wet mode cleaning [1]. The behavior of robot vacuum cleaners is described based on gesture, sound and luminosity. The authors utilized Roomba vacuum cleaner robot which they manually operated via Bluetooth link [2]. The Roomba vacuum cleaner [3] is a domestic service built in human-friendly environment and standardize a self-governing robot that fits into the operating environment. The intent and research of the self-governing robot results in

Table 1 Categories of floor cleaners

Types of floor cleaners	Authors
Wet cleaners	Gutmann et al. [1], Tani [4], Fink et al. [5], Hung and Leng [6], Kaur and Abrol [7], Vishaal et al. [15]
Dry cleaners	Gutmann et al. [1], Hendriks et al. [2], Forlizzi and DiSalvo [3], Tani [4], Fink et al. [5], Hung and Leng [6], Lee and Banerjee [10], Yatmono et al. [11], Bhingare et al. [12], Garud et al. [14], Vishaal et al. [15], Pandey et al. [16], Jain et al. [17], Das et al. [18]

Table 2 Wireless mediums used in floor cleaners

Wireless medium	Authors
RF modules	Kaur and Abrol [7]
IoT	Lee and Banerjee [10]
Bluetooth	Bhingare et al. [12], Vishaal et al. [15], Das et al. [18]
WiFi	Bhingare et al. [12], Garud et al. [14]

Table 3 Sensors used in floor cleaners

Sensors	Authors
IR sensor	Kaur and Abrol [7], Bhingare et al. [12]
Infrared sensor (TSOP1738)	Pandey et al. [16]
Dust sensor (DSM501)	Lee and Banerjee [10]
Ultrasonic sensor	Jain et al. [17], Bhingare et al. [12], Garud et al. [14], Das et al. [18]
Level sensor	Bhingare et al. [12]

Table 4 Microcontrollers used in floor cleaners

Microcontrollers	Authors
AT89S52	Kaur and Abrol [7]
PIC 16F877A	Garud et al. [14]
Arduino UNO	Yatmono et al. [11], Vishaal et al. [15], Pandey et al. [16], Das et al. [18], Dubey et al. [19]
Arduino Mega	Vishaal et al. [15]
ATMEGA 328P	Jain et al. [17]

Table 5 Motor drivers used in floor cleaners

Motor drivers	Authors
L293D	Kaur and Abrol [7], Jain et al. [17], Vishaal et al. [15], Das et al. [18]

human–robot interaction (HRI). An autonomous mobile cleaner system [4] constitutes a mobile robot cleaner and remote controllers. The robotic cleaner incorporates diverse sensors to offer self-governing locomotion. The remote controllers assist as an indicator of lead the way of mobile cleaner system to different rooms through the wireless medium of communication. Cleaning robot [6] including the shock sensor module helps in cleaning with less duration of time. The robot consists of broom and mop. The cleaning robot consists of modules, namely locomotion, cleaning, a shock sensor, and a controller. Cleaning robot [7] is a self-guided robot used to perform wet cleaning, like mopping or sweeping the base surface. The robot receives the main feature of systematic cleaning of the base surface. Learning provided by the

robotic domestic agent [8] consists of dual views. Foremost, the agent (energetic agent) spends its energy on all the parts involved in the scheme. The agent carries out all the projects concerning energy use. Second, the agent (social agent) works together with the various components present in the surroundings. Simulation-based optimization [10] technique to solve the cleaning device problem. The cleaning device problem possesses all the information about floor cleaning using IoT technology. Detection of dust is acquired using a dust sensor attached in the workspace of the cleaning system. Service-type floor cleaning robot [9] works under the algorithm which is executed for navigation to avoid obstructions. Since service robots are fully self-governed, it is detached from human intervention. Diverse speed variations in the robot are also incorporated like small, medium and fast modes based on the client's requirements. Floor cleaning robot is developed with the assistance of mechanical elements for holding in the robot, and android application software for controlling robot's motion is proposed [11]. The developed robot is hit along the hardware consisting of omnidirectional wheels. The controller of the developed robot is based on the Arduino microcontroller. Authors [12] have proposed their system of a vacuum cleaner using ATMEGA 256 (Arduino Mega) microcontroller. The proposed scheme consists of various advantages which include the purpose of the system is simple and easy to understand, data gathering is possible from a distance, all the compiled system is cost-effective and lastly, the whole architecture reduces the human efforts. Floor cleaning mops cannot move independently. In the area of work, the authors [13] have discussed and directed at the overall portal design, architecture, maintenance, operating ease and making out the complex mechanism of cleaning the floor. An autonomous vacuum cleaner operated with an android application proposed by researchers in [14]. Characteristics of this vacuum cleaner system include mode selection which includes manually operated and mechanically operated with the assistance of the android application. Floor cleaning architecture depicted in [15] shows the cleaning process with the aid of Bluetooth Serial Controller (BSC) android application. The above architecture performs dry and wet cleaning. In the dry cleaning mechanism, an electric duct fan (EDF) serves as a vacuum device. After the cleanup mechanism is executed, the filter is transferred. In the wet cleaning mechanism, the vacuum pump is switched ON. Except that, every mechanism is the same as the dry cleaning procedure.

Gaps identified are Many researchers have worked separately in wet and dry cleaning. No evidence is found of the autonomous wet and dry cleaning robot together in an existing system [11]. Objectives are defined as to design and simulate an IoT-enabled autonomous floor cleaning robot. Floor cleaning robot would comprise wet and dry cleaning in a single existing system.

3 Proposed Methodology

The proposed FCR will possess different sub-blocks for performing cleaning applications, i.e., dry as well as the wet cleaning process. Figure 1 illustrates the block
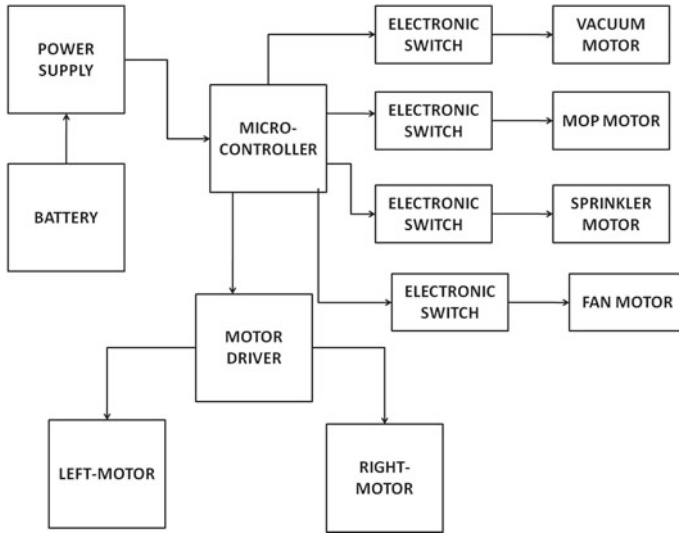
Fig. 1 Block diagram of the proposed FCR

diagram of the proposed system. Microcontroller and motor driver are powered through the power supply. Microcontroller will send the controlling signal to the motor driver. The motor driver sends the controlling signals to the attached left motor and right motor. These motors will provide actuation to perform vacuum, mop, sprinkler and fan actions. Figure 2 demonstrates the flow of information in the proposed floor cleaning robot system. The microcontroller will ultimately switch ON the motor driver and will broadcast the control signal for vacuum cleaner, mopping, fan and sprinkler, respectively.

3.1 Schematic Diagrams

Schematic diagrams of the proposed model floor cleaning robot with their dimensions in mm (millimeter) are illustrated below in Fig. 3a, b. Schematic diagrams for illustrating the dimension in mm (millimeter) of the buckets are shown from Fig. 3c–f. In top view of CAD model shown in Fig. 3b does not show the assemblage box placed above the vacuum. It is done for better visibility of the vacuum.

3.2 CAD Drawings

The proposed floor cleaning model's CAD has been prepared in AutoCAD 2007 software. All the dimensions are specified in mm (Millimeters). No electrical circuit is
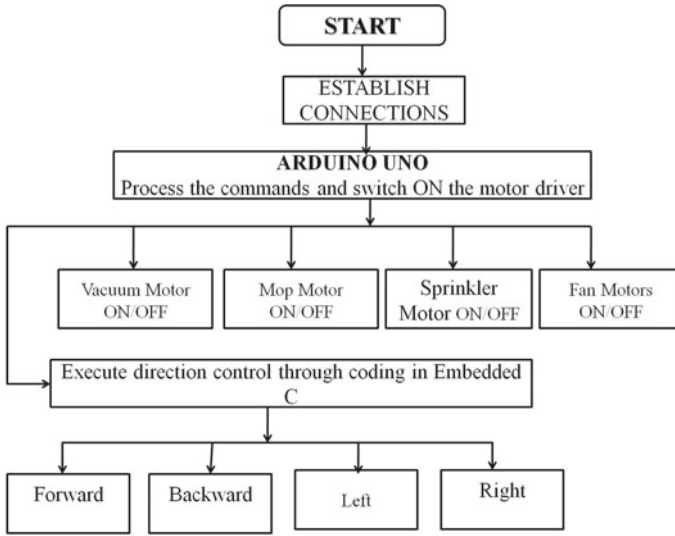
Fig. 2 Flow of information in the proposed FCR
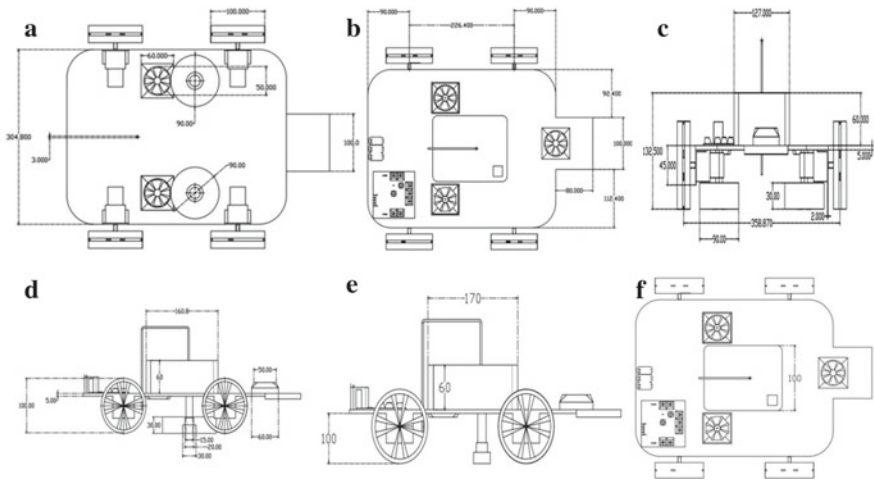
Fig. 3 Schematic diagram for **a** bottom view, **b** top view, **c** front view, **d** right view, **e** dimensions of bucket in right view, and **f** dimensions of bucket in a top view of the floor cleaning robot

shown in the CAD models of the floor cleaning robot. Figure 4i shows the top view of the floor cleaning robot with the numbering specified on them. The following numbers ares depicting the following components: (1) vacuum consisting vacuum box, (2) water tank, (3) dryer fan, (4) wheel, (5) mop, (6) mixed density fiber (MDF) frame, (7) batteries, (8) motor driver, and (9) water supply pipe, respectively. Following CAD drawings consist of bottom view (shown in Fig. 4a), front
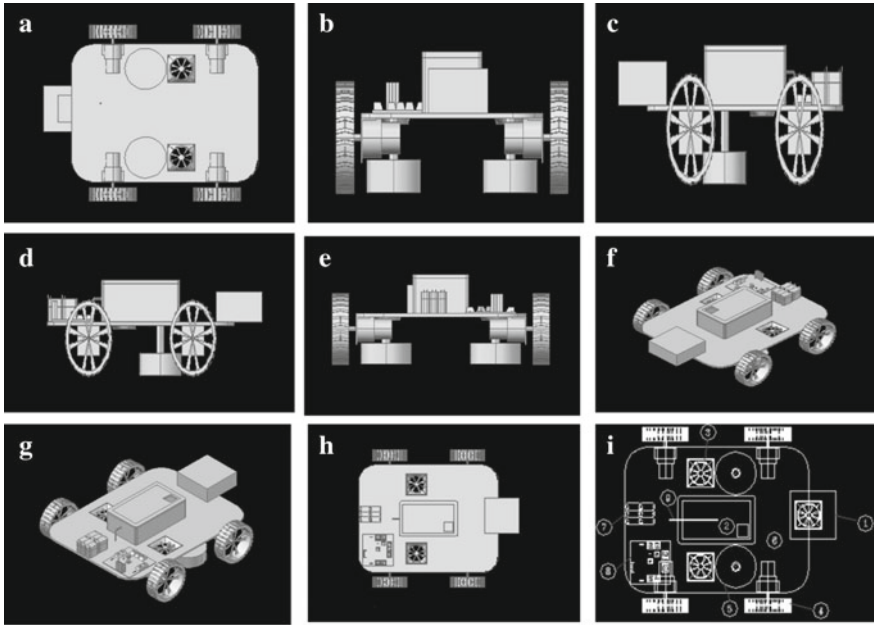
Fig. 4 CAD model for different views of the floor cleaning robot

view (shown in Fig. 4b), left-hand side view (shown in Fig. 4c), right-hand side view (shown in Fig. 4d), rear view (shown in Fig. 4e), left angluar view (shown in Fig. 4f), right angular view (shown in Fig. 4g) and top view (shown in Fig. 4h), respectively.

Concluding points from CAD Model and Schematic Diagram of the floor cleaning robot.

1. **Vacuum**: Corners present in the room are cleaned up with the help of vacuum placed at the beginning of the floor cleaning robot.
2. **Bucket**: The bucket's upper surface with a hole is covered as shown in Fig. 4h to isolate the electric circuit from water. The hole is created on the bucket lid to refill the bucket. The bucket contains level sensor and pump motor. The volume of the bucket is 1020 cc with reference to Fig. 3e, f. The water tank is full with 1.02 L (1020 cc) water. This amount is sufficient to clean a room.

   - **Bucket Consisting Level Sensor**: The level sensor will provide the level of water present inside the bucket. Level sensor is producing an alarm whenever water is less than a specified level.
   - **Bucket Consisting Pump And Motor**: The pump motor will pump the water so that through the inlet pipe water can be transferred to the mops.

   MOP: Mop size is large for better cleaning. The mops can be detached whenever they are deteriorating. The operator can command to the for cleaning process to move into the washing area or any appropriate area where the robot should clean its mops.

Table 6 Components resulting in the total weight of the floor cleaning robot

Components	Specifications	Weight (approx.)
Battery	4 V, 1.5 Ah	100 g
Bucket (with water)	Vol. 1020 cc	1.02 kg (1.020 L)
Arduino	Arduino UNO Operated at 5 V	25 g
Motor driver (L298N)	Operated at 12 V and 0.3 A	30 g
Fan (AD0812HS)	Operated at 12 V and 0.25 A	170 g
Vacuum (DF128S)	Operated at 12 V and 0.1 A	

1. **Fan**: The fans accumulated at the end of the floor cleaning robot are drying the floor surface sufficiently.
2. **Wheel**: To prevent the slippage of the floor cleaning robot because of water, we have added the grooving on the outer surface of the wheels.
3. **Load Carrying Capacity**: The area of the floor cleaning robot is 1200 cm^2. The approximate weight, carried by the floor cleaning robot is encountered with the help of main components included that has some specific weight by themselves. All these main components are illustrated in the below Table 6. The load carrying capacity of the floor cleaning robot is approx 3–4 kg as shown in Table 6.
4. **Working Efficiency Of Floor Cleaning Robot**: If the battery utilized is 1.5 Ah rated batteries, motor drivers have 0.3 A draw. By dividing both of them, we can get the total working capacity of the floor cleaning robot, i.e., approximately 5 h. The battery used is rechargeable. But if the battery is not fully charged or some fault occurs, the total working capacity can be reduced by some less hours. To increase the total working capacity by using heavy batteries. By utilizing the heavy batteries, the working hours can be extended. From, heavier batteries will result in more weight; therefore, they are not utilized to avoid non-essential load on the floor cleaning robot. Power bank can be used up to 5 V.
5. **Prevention From The Obstacles**: Whenever an obstacle is detected, the '**STOP**' signal will be sent, i.e., only '0' as an interrupt signal to all the motors. The obstacle detection can be done by an ultrasonic sensor which would be mounted on the surface of the floor cleaning robot. Edges and corners of the floor cleaning robot are changed to round shape so that it can easily avoid obstacles and would not find difficulties in moving along the path during the cleaning process.
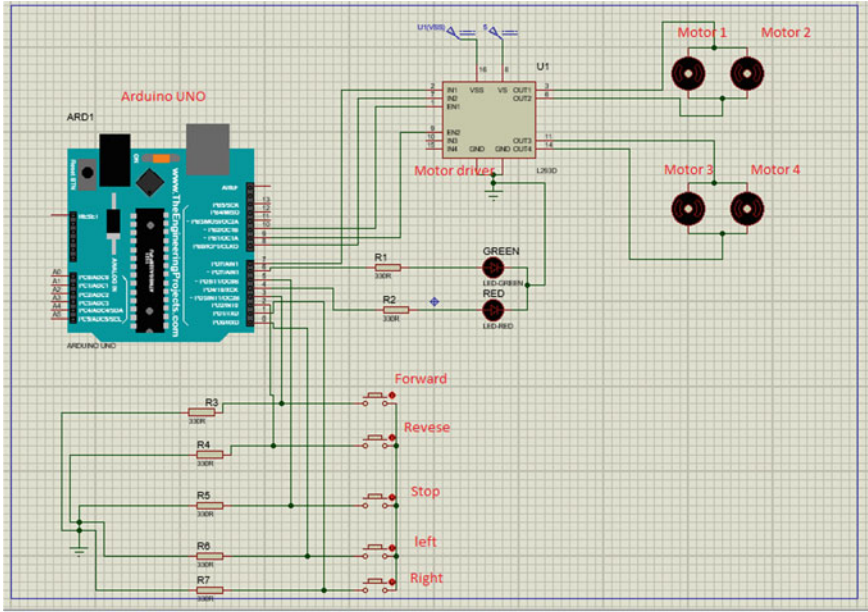
Fig. 5 Proteus circuits of the proposed system of the floor cleaning robot

3.3 *Proteus Circuit*

The Proteus circuit demonstrates the working of the wheels of the floor cleaning robot. The virtual circuit diagram is prepared in the software as illustrated in Fig. 5.

3.4 *Online Market Survey*

The online market survey is carried out for generating the estimated cost to build a prototype for the floor cleaning robot as illustrated above in Table 7. The main components are included in the cost estimation. Total estimated cost comes out to be approximately Rs. 5000/- to Rs. 6000/-. As per the requirements, different components can be added or replace from Table 7.

3.5 *Tinkercad Simulation*

The tinkercad simulations are done for the logic applied to the floor cleaning robot. Therefore, electrical simulation is executed on the Tinkercad software.

Table 7 Online market survey for components to be included

Hardware components	Quantity	Price (INR/piece)
Motor driver (L298)	1	Rs. 300/-
Lead acid battery (12 V)—15 Ah	3 (3 V)	Rs. 400/-
DC motor (30 rpm)	4	Rs. 250/-
Drill bit (4 mm and 3 mm)	2	Rs. 50/-
Nut, bolt (3 mm size)	15–20	Rs. 10/-
Clamp (iron rods)	4	Rs. 50/-
Wires	10–20	Rs. 10/-
Wheels	4	Rs. 200/-
Arduino UNO	1	Rs. 445/-
DC motor fans	2	Rs. 245/-
Relay module	1	Rs. 70/-
Water level sensor	1	Rs. 150/-
Mop, sprinkler and vacuum	1	Rs. 200/-
Ultrasonic sensor	1	Rs. 189/-
Bo motor	2	Rs. 120/-
Water level sensor	1	Rs. 99/-
Pump motor (12 V)	1	Rs. 99/-
Water splitter	1	Rs. 40/-
MDF (mixed density fiber) frame	1	Rs. 300/-

3.6 3 Relay Circuit

The electrical circuit is prepared to start the vacuum, mop and fan, dryer motors through relay as shown in Fig. 6. The circuit comprises of Arduino microcontroller, three relays attached to three bulbs, respectively. These three bulbs depict
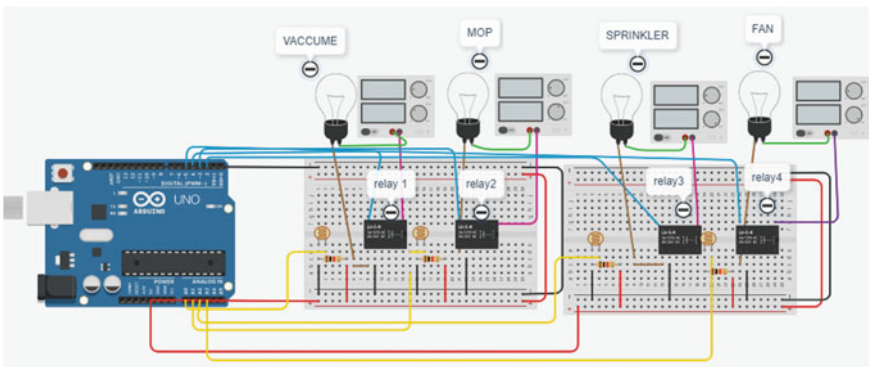
Fig. 6 Circuit of FCR when the relay is OFF
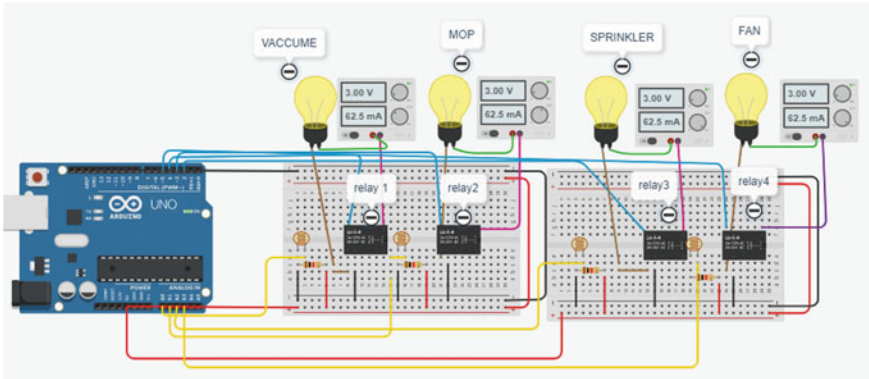
Fig. 7 Simulation of FCR when the relay is ON

the functionality of vacuum, mop and fan. Figure 7 shows the simulation results after providing power supply to the circuit.

3.7 2 Relay Circuit

The circuit shown in Fig. 8 depicts the scenario for cleaning the mop. The conclusive result would be that relay named as fan should be OFF after performing whole simulation process. All the relays are on, therefore, sprinkler, mop and fan all are at working stage. Since for cleaning the mop, only sprinkler and mop relay are required to be ON. Hence, the required logic circuit is achieved in Fig. 9.
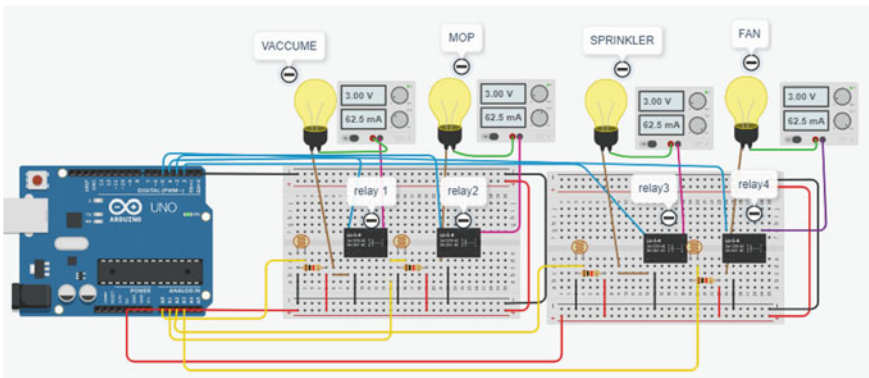
Fig. 8 FCR circuit when fan circuit is OFF
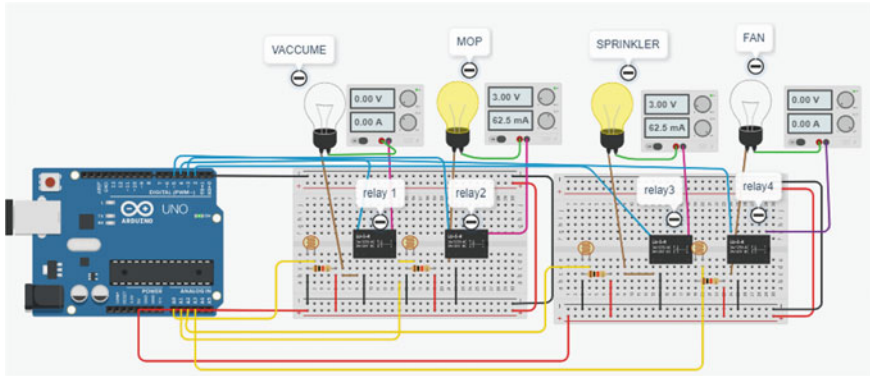
Fig. 9 FCR simulation when fan circuit is ON

3.8 Ultrasonic Sensor

The circuit shown in Fig. 10 depicts the scenario for an obstacle avoidance using an ultrasonic sensor. The conclusive result would be how far an obstacle is at distance from the floor cleaning robot during the whole simulation process is achieved in Fig. 11. The output illustrates that the maximum range of the obstacle detection is shown in serial monitor.

4 Conclusion and Future Scope

In this paper, the design of an IoT-enabled automatic floor cleaner is proposed. The proposed design architecture is beneficial in providing cleaning help for all the individuals of the society. The automatic floor cleaner will perform the cleaning methods of both dry and wet cleaning. The designed architecture is cost-effective (shown in Table 6) and easy to use. The design is structurally sound as it has sufficient weight carrying capacity of the bucket filled with water installed on the frame of the floor cleaning robot. However, with the ease in performing cleaning methods daily, this invention is an indeed requirement at this time of the hour. Therefore, its structure is acceptable at home and office workplaces.

A brief interpretation of architecture has been introduced with the help of schematic diagrams and CAD drawings featured with the circuit diagram of the electronic setup in the Proteus and Tinkercad simulation software. For future scope, the designed robot is based on HRI which can be done with the help of Blynk application. Hardware fabrication can be done for the proposed work by adding different sensors according to the user's requirement.
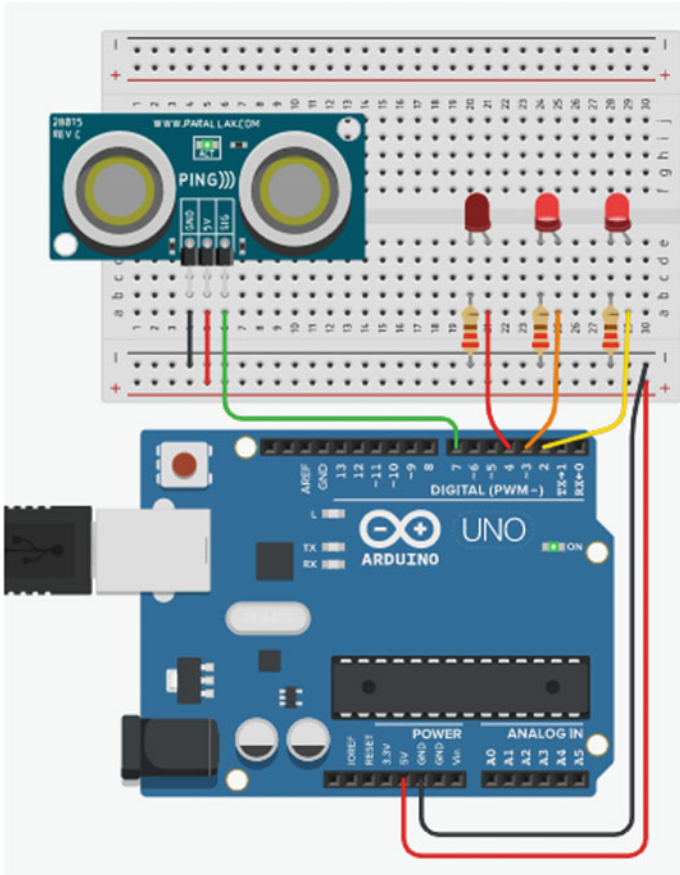
Fig. 10 Circuit for an obstacle avoidance

Fig. 11 Simulation result
showing distance
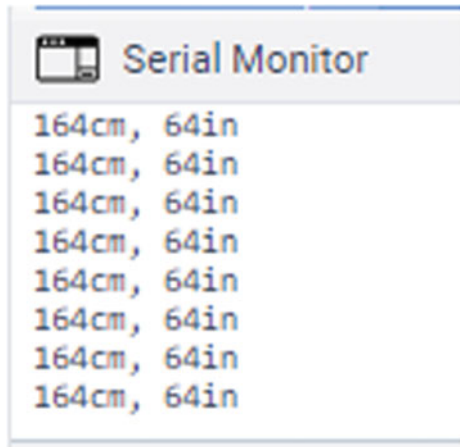
References

1. Gutmann, J.-S., Culp, K., Munich, M.E., Pirjanian, P.: The social impact of a systematic floor cleaner. In: Proceedings of the 2012 IEEE International Workshop on Advanced Robotics and its Social Impacts, pp. 50–53. IEEE (2012)
2. Hendriks, B., Meerbeek, B., Boess, S., Pauws, S., Sonneveld, M.: Robot vacuum cleaner personality and behavior. Int. J. Soc.Robot. **3**, 187–195 (2011)
3. Forlizzi, J., DiSalvo, C.: Service robots in the domestic environment: a study of the roomba vacuum in the home. In: Proceedings of the 1st ACM SIGCHI/SIGART Conference on Human-Robot Interaction, pp. 258–265 (2006)
4. Tani, T.: Autonomous Mobile Robot Cleaner System. United States Patent Application Publication, Patent No. US 2005O171636A1 (2005)
5. Fink, J., Bauwens, V., Kaplan, F., Dillenbourg, P.: Living with a vacuum cleaning robot. Int. J. Soc. Robot. **5**, 389–408 (2013)
6. Hung, S.-C., Leng, Y.-S.: Cleaning Robot and Control Method Thereof. United States Patent Application Publication, Patent No. US 20130228199A1 (2013)
7. Kaur, M., Abrol, P.: Design and development of floor cleaner robot (automatic and manual). Int. J. Comput. Appl. **97**, 32–38 (2014)
8. Vaussard, F., Fink, J., Bauwens, V., Retornaz, P., Hamel, D., Dillenbourg, P., Mondada, F.: Lessons learnt from robotic vacuum cleaners entering home ecosystem. Robot. Auton. Syst. **62**, 376–391 (2014)
9. Walters, M.L., Syrdal, D.S., Koay, K.L., Dautenhahn, K., te Boekhorst, R.: Human approach distances to a mechanical-looking robot with different robot voice styles. In: Proceedings of the 17th IEEE International Symposium on Robot and Human Interactive Communication, pp. 707–712. IEEE (2008)
10. Lee, H., Banerjee, A.: Intelligent scheduling and motion control for household vacuum cleaning robot system using simulation-based optimization. In: Proceedings of the 2015 Winter Simulation Conference, pp. 1163–1171 (2015)
11. Yatmono, S., Khairudin, M., Pramono, H.S., & Asmara, A.: Development of intelligent floor cleaning robot. ICE-ELINVO J. Phys. Conf. Ser. **1413**, 1–7 (2019)
12. Bhingare, K.M., Ransing, V.S., Palve, A.B., Misal, H.M.: Vacuum cleaner using microcontroller. Open Access Int. J. Sci. Eng. OAIJSE **3**, 15–17 (2018)
13. Parmar, H., Meena, A., Bhovaniya, J., Priyadarshi, M.: Automatic smart mop for floor cleaning. Int. Res. J. Eng. Technol. IRJET **6**, 3159–3165 (2019)
14. Garud, M.J., Shinde, V.R., Dudkekar, V.S., Thorat, S.S., Aldar, K.M.: A review wireless floor cleaning robot. Int. J. Sci. Res. Comput. Sci. Eng. Inf. Technol. **3**, 648–652 (2018)
15. Vishaal, R., Raghavan, P., Rajesh, R., Michael, S., Elara, M.R.: Design of dual purpose cleaning robot. In: International Conference on Robotics and Smart Manufacturing (RoSMa2018). Procedia Computer Science **133**, 518–525 (2018)
16. Pandey, A., Kaushik, A., Jha, A.K., Kapse, G.: A technological survey on autonomous home cleaning robots. Int. J. Sci. Res. Publ. **4**(4), 1–7 (2014)
17. Jain, M., Rawat, P.S., Morbale, J.: Automatic floor cleaner. Int. Res. J. Eng. Technol. IRJET **4**(4), 303–307 (2017)
18. Das, N.R., Daga, R., Avte, S., Mhatre, K.: Robotic automated floor cleaner. Int. Res. J. Eng. Technol. IRJET **6**(3), 4715–4721 (2019)

19. Dubey, S., Chinnaaiah, M.C., Kiran, C.S., Sai Priyanka, B., Punna Rao, P.: An FPGA based service robot for floor cleaning with autonomous navigation. In: International Conference on Research Advances in Integrated Navigation Systems (RAINS—2016). IEEE (2016)

Design and Fabrication of Suspension System of Formula SAE Vehicle Whilst Using Matrix Method for Force Estimation

Sawan Kumar [iD]**, Tushar Choudhary** [iD]**, and Varun Raizada** [iD]

1 Introduction

The suspension system defines the handling characteristics of the vehicle. Understanding the loads that the suspension carries is necessary for designing of a safe and effective suspension system. This study is done for the purpose of devising a safe methodology using the 3-D equations of static equilibrium to calculate forces in suspension members. This data is then used in analysis of suspension members and designing of the suspension system and its fabrication. First aim is to design a suspension system for Formula SAE vehicle with the help of various engineering criterions. Secondly, simulation of the suspension system is designed using the Solid-Works software. Finally, manufacturing of the suspension system so that the system can be used on a Formula SAE vehicle for practical purposes. So that the theoretical simulations can be validated practically.

2 Suspension Geometry

2.1 Designing the Suspension Geometry Using Lotus SHARK

A detailed and iterative approach was followed for designing the suspension geometry of the Formula SAE vehicle in the Lotus SHARK software module [1]. The Lotus Suspension Analysis SHARK module is a suspension geometric and kinematic modelling tool, with a user-friendly interface, which makes it easy to apply

S. Kumar (✉) · T. Choudhary · V. Raizada
Department of Mechanical, Production & Industrial and Automobile Engineering, Delhi Technological University, Delhi 110042, India
e-mail: sawankr02@gmail.com
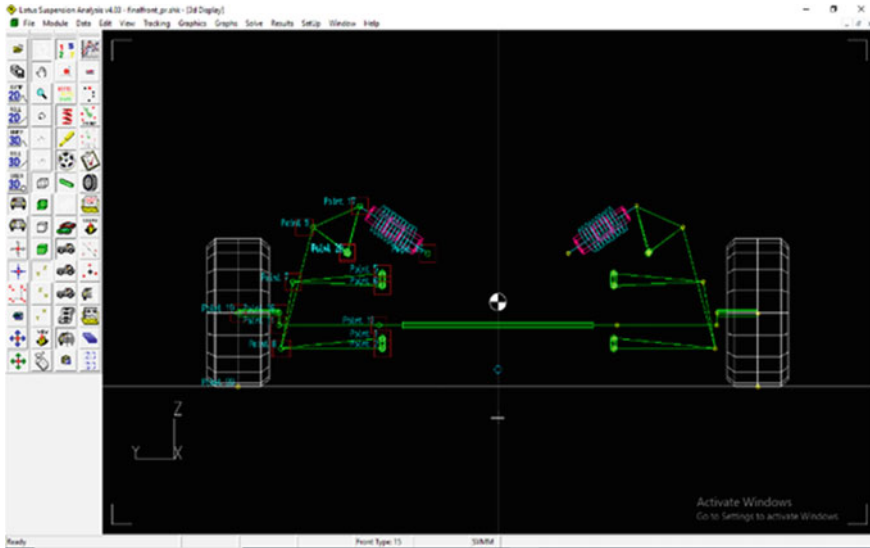
Fig. 1 Geometry of the front suspension system designed in Lotus SHARK

changes to proposed geometry and instantaneously assess their impact through graphical results. Note: For the simplicity of the suspension design and due to the lack of reference data to work with, the values of static camber and toe angle were taken to be 0° while designing the preliminary suspension geometry (Fig. 1).

From the graphs obtained after the kinematic analysis of the designed suspension geometry, it can be articulated that even in the severe dynamic conditions (extreme bump and droop) the suspension travel follows the desired geometry. The results can be validated from the fact that the rate of camber change in 40 mm jounce (bump) and 30 mm rebound (droop) is found to be 8.857°/m or ~9°/m, whereas the rate of caster and toe angle change for the same jounce and rebound is found to be 11.119°/m and 11.797°/m, respectively. Pertaining to different sources and various FSAE forums, these values are completely within the acceptable range [2]. After finalizing the suspension geometry in the Lotus SHARK suspension module, the hard points in the 3D space can be obtained very easily, and with the help of these hard points, the CAD model of the suspension system would be made in SolidWorks software later (Figs. 2, 3 and 4).

The final hard points of the suspension geometry obtained from the iterative process in Lotus SHARK suspension module are given in Table 1.

Fig. 2 Camber angle versus bump-droop
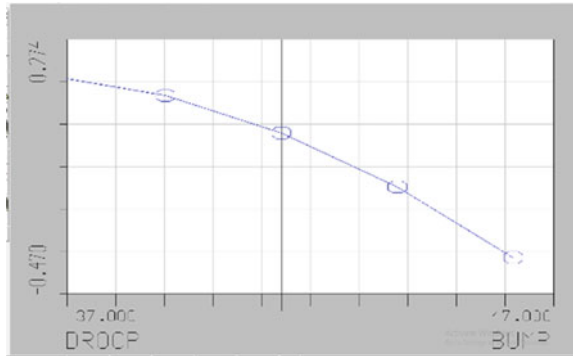
Fig. 3 Toe angle versus bump-droop
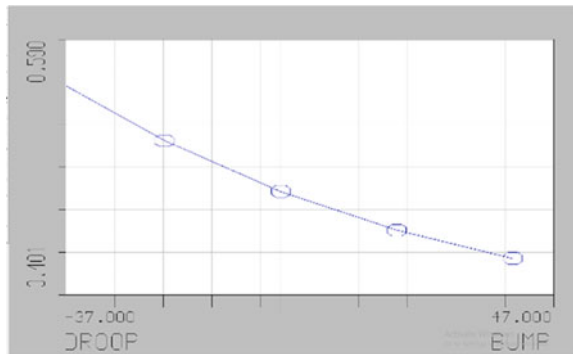
Fig. 4 Caster angle versus bump-droop
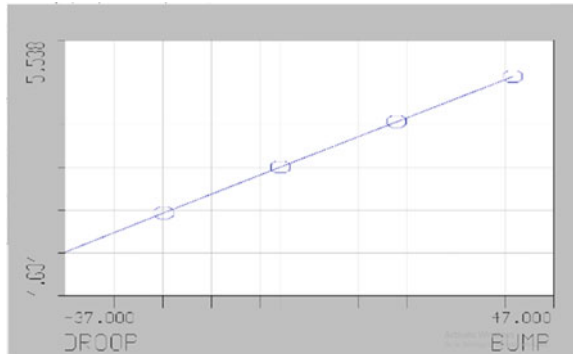
3   Force Estimation at the Tyre Contact Patch

For the calculation of force at the tyre contact patch, we need to take certain parameters that are already set/defined in the FSAE vehicle (Tables 2 and 3).

Table 1 Hard points of the front suspension geometry of the vehicle

	X	Y	Z
J, Lower arm (outer)	5.9604673	−125.24976	5.0001982
M, Upper arm (outer)	43.339	70.266536	−12.363334
P, Tie rod (outer)	0.4717	−55.8911	−88.8949
Q, Push rod arm side	82.41325	−98.55842	1.3584335
I, Lower arm (front)	425	−95	131
K, Lower arm (rear)	425	−125	−135
L, Upper arm (front)	425	95	112
N, Upper arm (rear)	425	60	−134
O, Tie rod (inner)	417.03783	−46.185511	−89.979273
R, Push rod rocker side	360.34123	415.0035	−34.867921

Table 2 Parameters of the FSAE vehicle

Parameters	Magnitude	S.I unit
Wheel base	1575 mm	1.575 m
Front track	1357.8 mm	1.3578 m
CG height	270.03 mm	0.27 m
Weight	300 kg	–
Front weight distribution	128 kg (40%)	–
Rear weight distribution	192 kg (60%)	–
Tyre diameter	18″	0.4572 m
Tyre width	6″	0.1524 m
Coefficient of friction	1.7	–

3.1 g-Force Estimation

Acceleration. For this manoeuvring condition, some speed exceptions were made and were accepted by the transmission department. It was assumed that time taken to reach a maximum speed of 70 km/h is 4 s [3].

$$v = u + a \times t$$
$$19.44 = 0 + a * (4), \quad a = 4.86 \text{ m/s}^2$$
$$\text{g - force} = 0.495 \sim 0.5 \text{ g} \tag{1}$$

Table 3 Force moment matrix

−0.9553648	−0.9484654	−0.9524693	−0.9997253	−0.475037		F-JI		F_X	−2420.17
−0.0689662	−0.0005653	0.0256211	0.0232926	−0.8777847		F-JK		F_Y	1883.52
−0.2872659	0.3168802	0.3035552	0.0026024	0.0619184		F-ML	=	F_Z	−2069
28.56072	−29.831383	30.646579	−1.7430017	11.793329		F-MN		M_X	481,789.9
3.4926535	−47.578746	−41.34465	71.831249	−18.627281		F-PO		M_Y	8055.5589
−95.823346	−89.374244	88.655051	99.649806	−26.66136	−173.59091	F-QR		M_Z	570,875.4

Braking. For this manoeuvring condition, some speed exceptions were made and were accepted by the transmission department. It was assumed that time taken to stop the vehicle from a maximum speed of 60 km/h is 2 s, with the distance to stop being 15 m [3].

$$s = u \times t + \frac{1}{2} \times a \times t^2$$
$$15 = 16.67 * 2 + (a * (4))/2, \quad a = 9.17 \text{ m/s}^2$$
$$\text{g - force} = 0.934 \text{ g} \tag{2}$$

Cornering. For this manoeuvring condition, lateral acceleration is calculated assuming the maximum cornering speed as 40 km/h and skid pad event is kept in mind. The maximum cornering speed was assumed to be 40 km/h with the radius of skid pad known to be 9.125 m [3].

$$a = \frac{v^2}{r}$$
$$a = (11.111 * 11.111)/9.125, \quad a = 13.53 \text{ m/s}^2$$
$$\text{g - force} = 1.38 \text{ g} \tag{3}$$

Bump/Droop. For this manoeuvring condition, the g-force was assumed to 3 g owing to different FSAE forums.

3.2   Load Transfer and Force Estimation

Longitudinal Load Transfer and Longitudinal force (F_Z). For longitudinal load, transfer braking is taken into consideration because it pertains to more load transfer than acceleration owing to higher g-force. Longitudinal load transfer is calculated from Eq. (4) [4].

$$(\text{Mass Transfer}) \times g \times \text{wheelbase} = (\text{Mass of vehicle}) \times g$$
$$\times \text{g - force} \times (\text{centre of gravity}) \tag{4}$$

The total longitudinal load transfer is found to be 43.71 kg, so for one wheel it comes out to be 21.86 kg. With this longitudinal load transfer atone of the front wheel, we can now find the longitudinal force (F_z) [5].

$$F_z = \mu \times m \times g$$
$$F_z = 1.7 * (21.86 + 64) \times 1.44 \times 9.81$$
$$F_z = 2069 \text{ N} \tag{5}$$

Lateral Load Transfer and Lateral force (F_X). For lateral load transfer cornering is taken into consideration. Lateral load transfer is calculated from Eq. (6) [4] below.

$$\text{(Mass Transfer)} \times g \times \text{front track} = \text{(Mass of vehicle)} \times g$$
$$\times \text{g - force} \times \text{(centre of gravity)} \quad (6)$$

The total lateral load transfer is found to be 88.32 kg, so for one wheel it comes out to be 41.16 kg. With this lateral load transfer at one of the front wheel, we can now find the lateral force (F_x) [5].

$$F_x = \mu \times m \times g$$
$$F_x = 1.7 * (41.16 + 64) \times 1.38 \times 9.81$$
$$F_x = 2420.17 \text{ N} \quad (7)$$

Vertical force (F_Y). For vertical load transfer bump/droop is taken into consideration. With this known vertical load at one of the front wheel, we can now find the vertical force (F_y) [5].

$$F_y = m \times g$$
$$F_y = (64) \times 3 \times 9.81$$
$$F_y = 1883.52 \text{ N} \quad (8)$$

4 Force Estimation on Suspension Members

The calculations used to determine the forces in suspension members begin with calculation of forces on the Tyre Patch under the combined condition of cornering and braking. These forces are transferred to the wheel centre, providing three forces and three moments along the three axes. Suspension structure is assumed to be a rigid body connected to six rigid truss members pinned at both the ends resulting in only axial forces in each of the members. Then, the force in each member can be solved by using 3D equations of static equilibrium [6]. Using vector geometry and statics equations, the loads at the wheel centre can be used to solve for the axial forces in each of the suspension arms (Fig. 5).

Member JI will be used as an example in calculating force in members [6]. Let J and I represent the corresponding suspension points. Coordinates for these points can be represented by Eqs. (9) and (10).

$$J = \left(J_x, J_y, J_z \right) \quad (9)$$
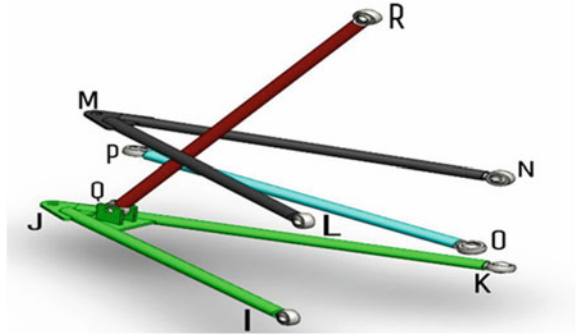
$$I = \left(I_x, I_y, I_z\right) \tag{10}$$

where J_x, J_y, J_z represent x, y, z coordinates for point J. Similarly, coordinates for all the points (J, I, M, N, P, O, Q and R) can be written.

JI in Eq. (11) will represent the vector connecting point J to point I and represented as,

$$\overrightarrow{JI} = \left(JI_x, JI_y, JI_z\right) \tag{11}$$

Magnitude of this vector is represented by Eq. (12)

$$|JI| = \left[(J_x - I_x)^2 + \left(J_y - I_y\right)^2 + (J_z - I_z)^2\right]^{1/2} \tag{12}$$

Unit vector for this vector can be calculated as in Eq. (13)

$$\widehat{JI} = \frac{\overrightarrow{JI}}{|JI|} \tag{13}$$

This same procedure is used to calculate a unit vector for each of the six suspension members.

Therefore, force vector for arm JI can be written as in Eq. (14),

$$\vec{F}_{JI} = F_{JI}\widehat{JI} \tag{14}$$

Since structure is assumed to be static, the sum of the forces must equal 0. The summation of forces in the X-direction as in Eq. (15),

$$\sum F_x = 0 = F_{JI} + F_{JK} + F_{ML} + F_{MN} + F_{PO} + F_{QR} + F_x \tag{15}$$

where F_{JI} represents magnitude of force in Arm JI in x-direction. F_x represents the force acting on upright in X-direction. Similar equations can be written for forces in Y, Z direction. This gives three force equations.

Three additional static equations are derived by equilibrium of moments about a point. Wheel centre is selected as centre point for this purpose, and moments are calculated about it. Using the wheel centre as a starting point, vectors are created joining wheel centre to each of the inward suspension points. These vectors act as the radius vectors in the cross product of the r and F used to calculate the moments. As an example, the r_j vector defined from wheel centre, T_{wc}, to point J, can be calculated by Eq. (16)

$$\vec{r}_J = J - T_{\text{wc}} = \left(r_x, r_y, r_z\right)_j \tag{16}$$

where r_x, r_y, r_z represent x-, y-, z component of r_j vector, respectively. Similar process is applied for each of the four suspension points (J, M, P, and Q). To sum the moments, cross-product is done according to Eq. (17)

$$\sum M = 0 = \left(\vec{r}_J \times \vec{F}_{JI}\right) + \left(\vec{r}_J \times \vec{F}_{JK}\right) + \left(\vec{r}_M \times \vec{F}_{ML}\right) + \left(\vec{r}_M \times \vec{F}_{MN}\right)$$
$$+ \left(\vec{r}_P \times \vec{F}_{PO}\right) + \left(\vec{r}_Q \times \vec{F}_{QR}\right) + M \tag{17}$$

This process will give moment along all three axes, i.e., x, y, z axes. This gives three moment equations.

This will give us six equations of static equilibrium (three force equations and three moment equations) and forces in each of the six members can be calculated.

An Excel program has been created to solve these equations in a short amount of time. Excel provides powerful calculation tool such as matrix inverse function which can be used to calculate inverse of 6×6 matrix quickly. It also allows changes to be made easily. The program solves system of linear equation using matrix algebra which results in loads for each of the six arms.

The resulting overall Eq. (18) for member loads is given as [6],

$$[A]\{x\} = \{b\} \tag{18}$$

where

$$[A] = \begin{bmatrix}
\hat{J}_{L_X} & \hat{K}_{R_X} & \widehat{ML}_X & \widehat{MN}_X & \widehat{PO}_X & \widehat{QR}_X \\
\hat{J}_{L_Y} & \hat{K}_{R_Y} & \widehat{ML}_Y & \widehat{MN}_Y & \widehat{PO}_Y & \widehat{QR}_Y \\
\hat{J}_{L_Y} & \hat{K}_{R_Z} & \widehat{ML}_Z & \widehat{MN}_Z & \widehat{PO}_Z & \widehat{QR}_Z \\
\left(\hat{J}_{L_Z} r_{J_Y} - \hat{J}_{L_Y} r_{J_Z}\right) & \left(\hat{K}_{R_Z} r_{J_Y} - \hat{K}_{R_Y} r_{J_Z}\right) & \left(\widehat{ML}_Z r_{M_Y} - \widehat{ML}_Y r_{M_Z}\right) & \left(\widehat{MN}_Z r_{M_Y} - \widehat{MN}_Y r_{M_Z}\right) & \left(\widehat{PO}_Z r_{O_Y} - \widehat{PO}_Y r_{O_Z}\right) & \left(\widehat{QR}_Z r_{Q_Y} - \widehat{QR}_Y r_{Q_Z}\right) \\
\left(\hat{J}_{L_Z} r_{J_X} - \hat{J}_{L_X} r_{J_Z}\right) & \left(\hat{K}_{R_Z} r_{J_X} - \hat{K}_{R_X} r_{J_Z}\right) & \left(\widehat{ML}_Z r_{M_X} - \widehat{ML}_X r_{M_Z}\right) & \left(\widehat{MN}_Z r_{M_X} - \widehat{MN}_X r_{M_Z}\right) & \left(\widehat{PO}_Z r_{O_X} - \widehat{PO}_X r_{O_Z}\right) & \left(\widehat{QR}_Z r_{Q_X} - \widehat{QR}_X r_{Q_Z}\right) \\
\left(\hat{J}_{L_Y} r_{J_X} - \hat{J}_{L_X} r_{J_Y}\right) & \left(\hat{K}_{R_Y} r_{J_X} - \hat{K}_{R_X} r_{J_Y}\right) & \left(\widehat{ML}_Y r_{M_X} - \widehat{ML}_X r_{M_Y}\right) & \left(\widehat{MN}_Y r_{M_X} - \widehat{MN}_X r_{M_Y}\right) & \left(\widehat{PO}_Y r_{O_X} - \widehat{PO}_X r_{O_Y}\right) & \left(\widehat{QR}_Y r_{Q_X} - \widehat{QR}_X r_{Q_Y}\right)
\end{bmatrix}$$

$$\{x\} = \begin{Bmatrix} F_{JI} \\ F_{JK} \\ F_{ML} \\ F_{MN} \\ F_{PO} \\ F_{QR} \end{Bmatrix} \text{ and } \{b\} = \begin{Bmatrix} F_X \\ F_Y \\ F_Z \\ M_X \\ M_Y \\ M_Z \end{Bmatrix}$$

Table 4 Resultant force in N on six suspension members

F-JI	6837.9577
F-JK	−4988.2383
F-ML	−1112.8917
F-MN	4237.9165
F-PO	−1200.0095
F-QR	−2446.2881

There are six unknowns represented in column 7, 6 knowns in column 9 and 6 × 6 directional matrix. Hence, six unknowns can be calculated using matrix algebra (Table 4).

5   Design, Analysis and Optimization of the A-Arms

5.1   CAD Modelling of Suspension Members

There are a vast number of choices available that can handle the designing with ease. The software should provide various analysis options, which are needed for the iterative design methodology. The designing of the suspension members begins with the help of the hand calculations done which provide the basis of the initial basic dimensions required to start the modelling and act as an anchoring point. The complete designing process is iterative in nature and divided into stages. It begins with CAD models of the suspension members based on the initial hand calculations [7]. The second stage of designing the CAD of suspension members is carrying out the multiple iterations, i.e., changing the outer diameter and thickness until an acceptable value of the load factor is achieved.

5.2   Analysis of CAD Models

The suspension members designed (upper and lower A-arms, push rod and tie rod) were then analyzed for static, fatigue and buckling failures under the SolidWorks simulation option. The analysis is executed multiple times for the different dimensions obtained due to the various iterations done during the CAD modelling. The analysis is performed until an acceptable value of factor of safety and life cycle is obtained.

End Conditions Used for the Buckling Analysis. Hollow circular mild steel tubes are used for the suspension members; these are physically connected to the chassis with the help of Heim joints or ball and socket joint (because it restricts suspension translation but allows for articulation about the chassis side). For the analysis process,

these members are subjected to one end pinned and one end fixed condition for upper and lower control arms, while both ends fixed for push rod and tie rod [8]. It is a valid assumption for the control arms as it complies with the attachment method. The end conditions are kept same for the rear as well as front suspension members. Orientation of each and every suspension member is aligned, and displacement constraints and externally applied loads need to be added to the model for the analysis [8].

Methodology for Optimization of the Dimensions. Firstly, the load is applied to the initial/reference geometry of the link according to the results which are obtained during the hand calculation process. The analysis is then done according to the respective end condition. The results obtained in the first iteration are then used to modify the dimensions further.

To start off the suspension members' design and analysis, the worst affected members in buckling and yielding were taken into consideration. Using the Euler's formula of critical buckling load [7].

$$P_{\text{CR}} = \frac{\pi^2 E I}{(KL)^2} \tag{19}$$

where P_{CR}: Critical load (N), E: Elastic modulus (MPa), I: Area moment of inertia (mm^4), K: Column effective length factor, L: Unsupported length of column (mm).

For buckling, the worst affected member is JK, i.e., the rear member of the lower control arm, and hence, from the above Euler's formula of critical buckling load, the required area moment of inertia comes out to be 2887.40 mm^4.

Using the yielding criteria [7], we know

$$\sigma_y = \frac{F}{A} \tag{20}$$

where σ_y: Yield strength, F: Tensile force on the member (N), A: Cross-sectional area of the member (mm^2).

For yielding, the worst affected member is JI, i.e., the front member of the lower control arm and hence from the above formula the required cross-sectional area comes out to be 128.21 mm^2. Looking at the area moment of inertia and cross-sectional area of different standard sized hollow circular tubes available in the market, the tube having dimensions 16 mm outer diameter and 3 mm wall thickness was chosen to be the reference of the design and analysis process, because the magnitude of its area moment of inertia and cross-sectional area, i.e., 2726.1170 mm^4 and 122.522 mm^2 is closest to what obtained from the above hand calculations then compared to other standard sizes. Optimization of the suspension links was done using buckling analysis; the factor of safety values is taken higher to account for the static model used for the force calculation and the standardize the dimensions of links according to availability of tubes of standard dimension. The dimension of each suspension member in the first iteration was taken to be 16 mm outer diameter and 3 mm wall thickness, whereas in the final iteration the dimensions were reduced

Table 5 Summary of buckling analysis on the final optimized dimension

Links	JI	JK	ML	MN	PO	QR
Stress	2.85×10^7	5.61×10^7	6.61×10^7	4.88×10^7	2.82×10^7	2.48×10^7
Deformation	0.045	0.092	0.062	0.070	0.043	0.054
Load Factor	9.5	9.5	6.8	8.2	7.8	7.6

to 14 mm outer diameter and 2.5 mm wall thickness. Table 5 summarizes the final analysis results of the optimized dimensions obtained on the second iteration.

Structural Analysis of the Suspension Control Arms. The fatigue analysis was conducted [9], for the upper and lower control arms using the boundary condition and loading, to obtain the results for stress life. Fatigue analysis of the upper control arms was done followed by the static analysis on SolidWorks software. From the static analysis maximum stress, deformation and factor of safety plots were obtained.

Upper control arm. The maximum stress developed in the upper control arms was obtained to be 8.43×10^7 N/m^2 for a material having yield strength 3.5×10^8 N/m^2 (or 350 MPa). The maximum deformation in the upper control arms was found to be 7.9×10^{-2} mm (or ~8×10^{-2} mm) which is acceptable compared to the size of the control arm(s). The minimum factor of safety was obtained to be 4.2. From the fatigue analysis, load factor and life cycle plots were obtained. The minimum life cycle for the upper control arms was found to be 751,000 cycles, whereas the load factor was found to be 2.947 (or ~3).

Lower control arm. The maximum stress developed in the lower control arms was obtained to be 1.12×10^8 N/m^2 for a material having yield strength 3.5×10^8 N/m^2 (or 350 MPa). The maximum deformation in the lower control arms was found to be 1.6×10^{-1} mm, which is acceptable compared to the size of the control arm(s). The minimum factor of safety was obtained to be 3.1. From the fatigue analysis, load factor and life cycle plots were obtained. The minimum life cycle for the lower control arms was found to be 184,000 cycles, whereas the load factor was found to be 2.246 (or ~2.5).

6 Material Selection for Fabrication of Suspension System

The Formula SAE suspension members (A-arms, push rod and tie rod) are generally designed and fabricated out of the material that is machinable, weldable and could withstand all the static and dynamic forces without failure. Considering the factors such as the price, availability and the desired mechanical properties, we selected AISI 1020 steel for the fabrication of A-arms, push rod and tie rod. Table 6 shows the general mechanical properties of the AISI 1020 steel [10]. The manufacturing process of the suspension members (A-arms, push rods and tie rods) is critical and should be done with a high accuracy.

Table 6 Material properties AISI 1020

Density	7.87 g/cm^3
Tensile strength, ultimate	450 MPa
Tensile strength, yield	320 MPa
Modulus of elasticity	205 GPa
Bulk modulus	140 GPa
Poisson's ratio	0.29

7 Result and Discussion

7.1 Result Summary of Suspension Members

Static stress analysis. The suspension members, i.e., the upper control arm, lower control arm, push rod and steering rod, are analyzed for the static stress and deformation on SolidWorks separately, and following results provide the data which tells that the suspension system is safe and robust in the desired working conditions. The simulation results are shown in Figs. 6, 7, 8, 9, 10, 11, 12 and 13.

Fatigue Stress Analysis. The suspension members are also analyzed for the fatigue stress on SolidWorks because fatigue stresses are one of the most prominent causes of failure in suspension members. The fatigue analysis is performed on the members at 10,000 cycles of full reversed. The simulation results are shown in Figs. 14, 15, 16 and 17.
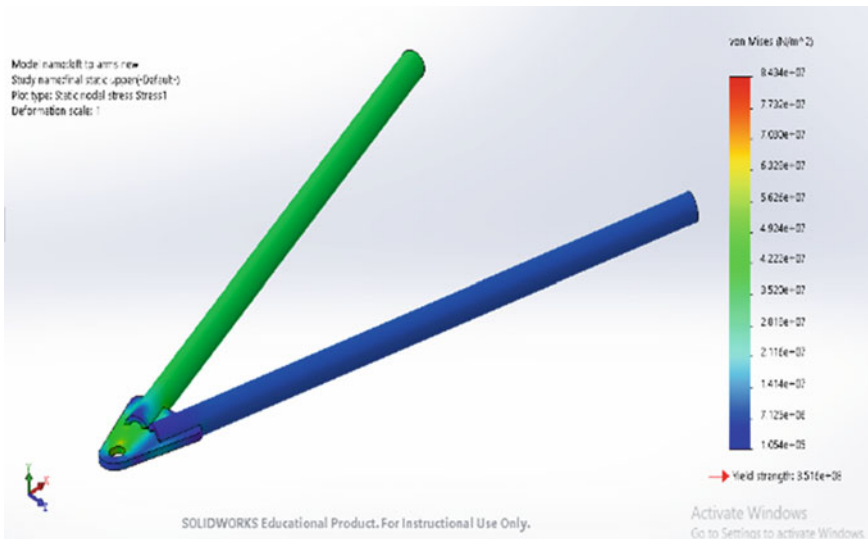
Fig. 6 Static stress simulation of upper control arm
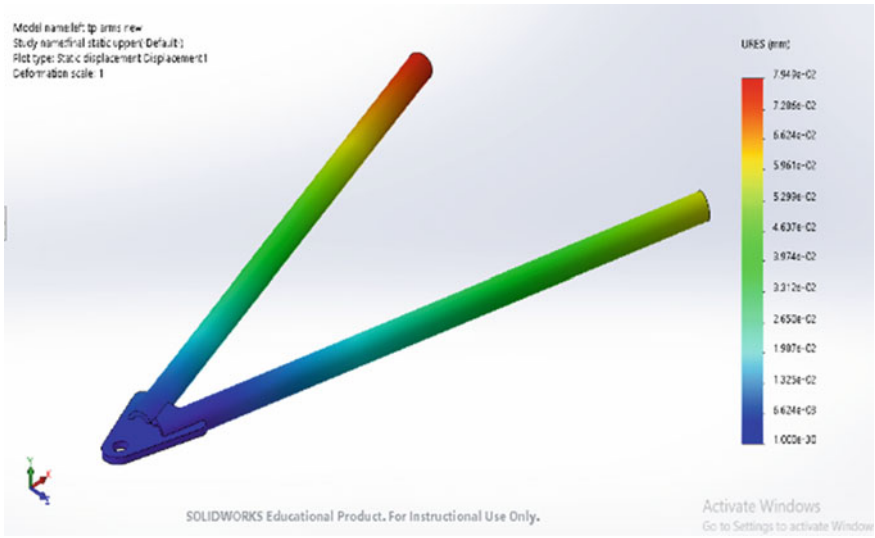
Fig. 7 Static deformation in upper control arm
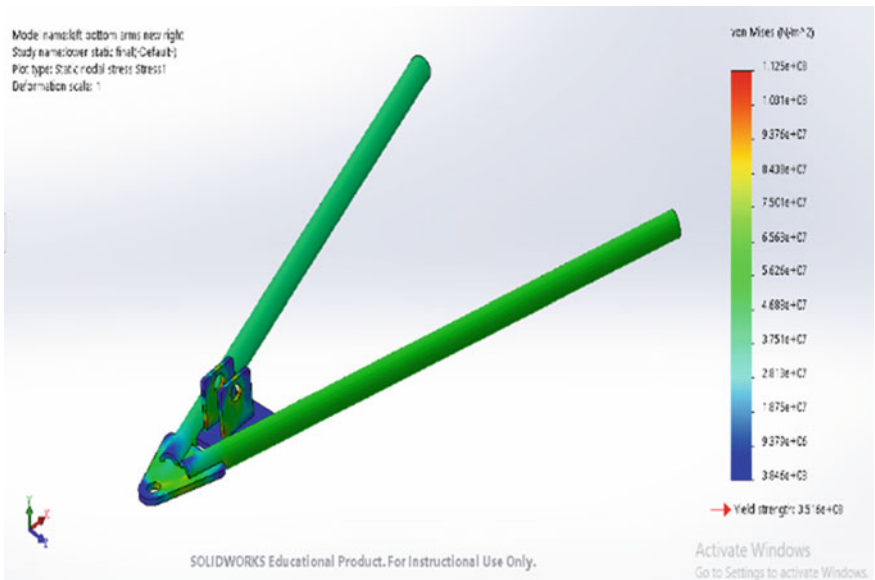
Fig. 8 Static stress simulation of lower control arm
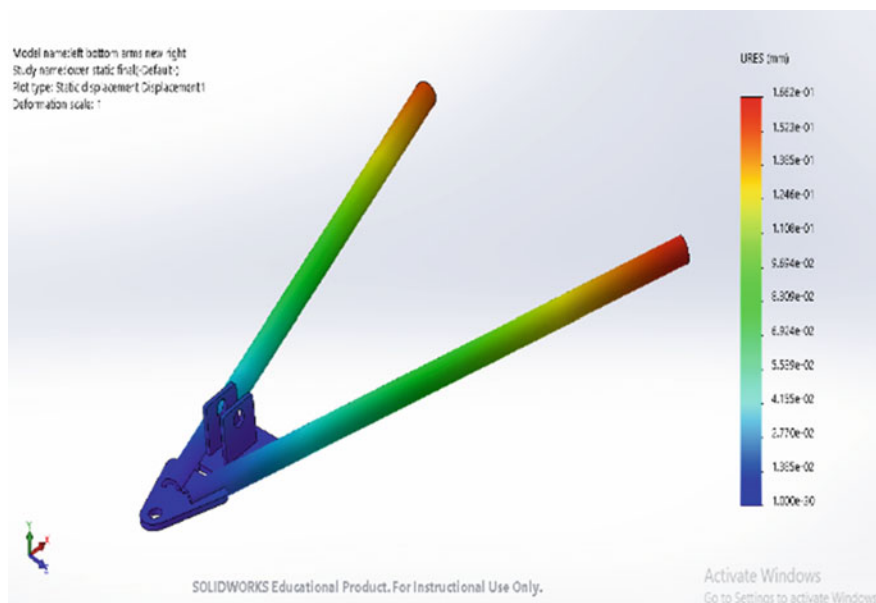
Fig. 9　Static deformation in lower control arm
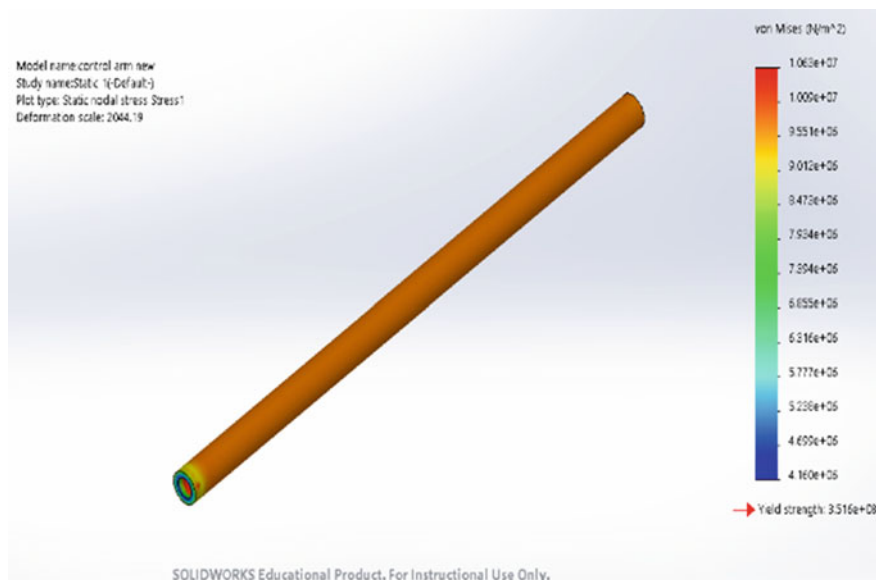
Fig. 10　Static stress simulation of tie rod
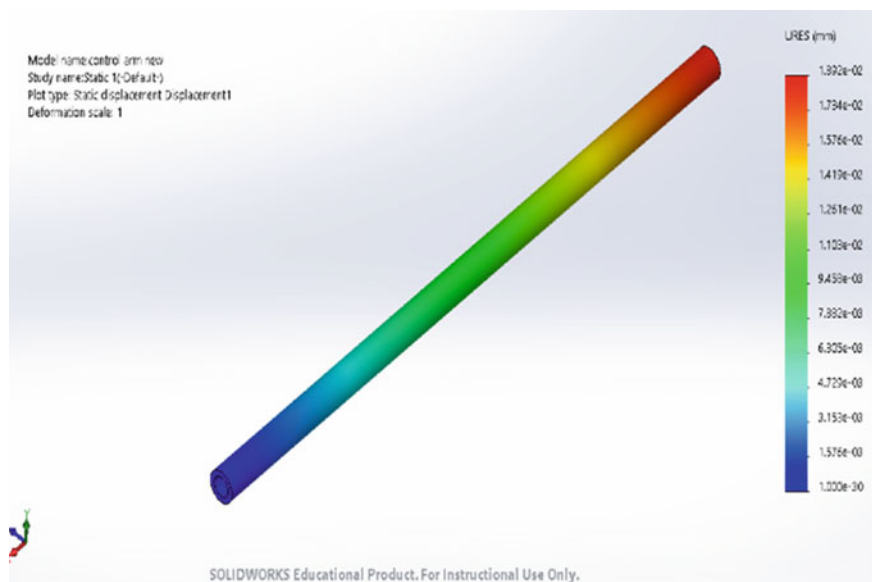
Fig. 11 Static deformation in tie rod
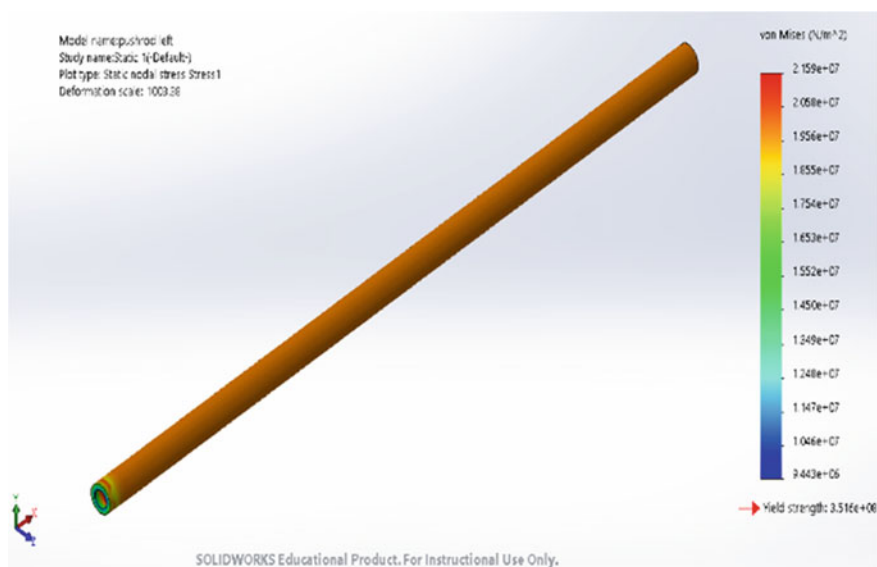
Fig. 12 Static stress simulation of push rod
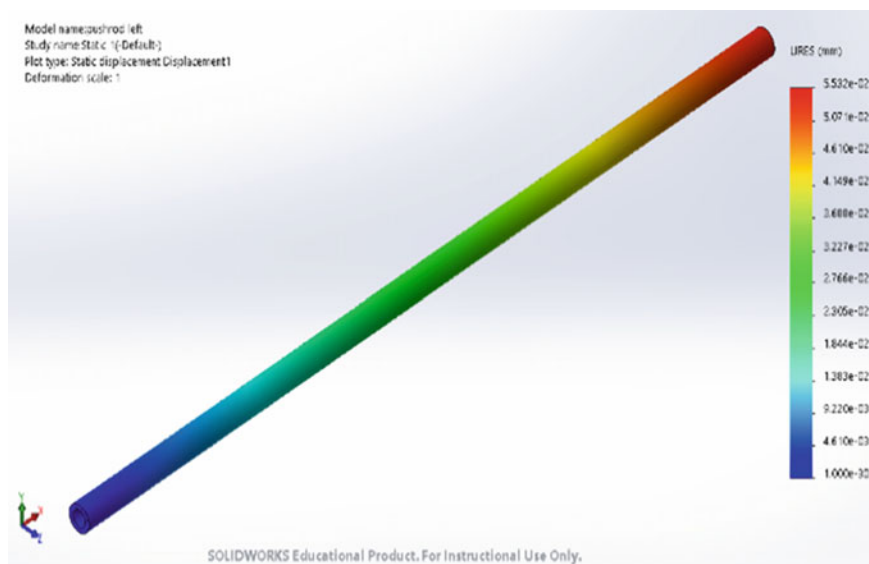
Fig. 13 Static deformation in push rod

Fig. 14 Fatigue stress simulation of upper control arm

Fig. 15 Fatigue stress simulation of lower control arm
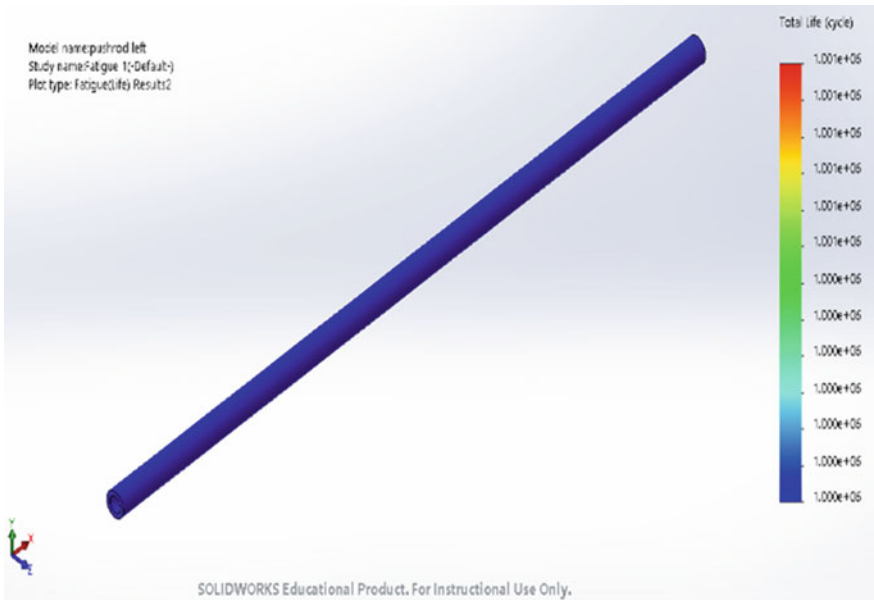
Fig. 16 Fatigue stress simulation of tie rod
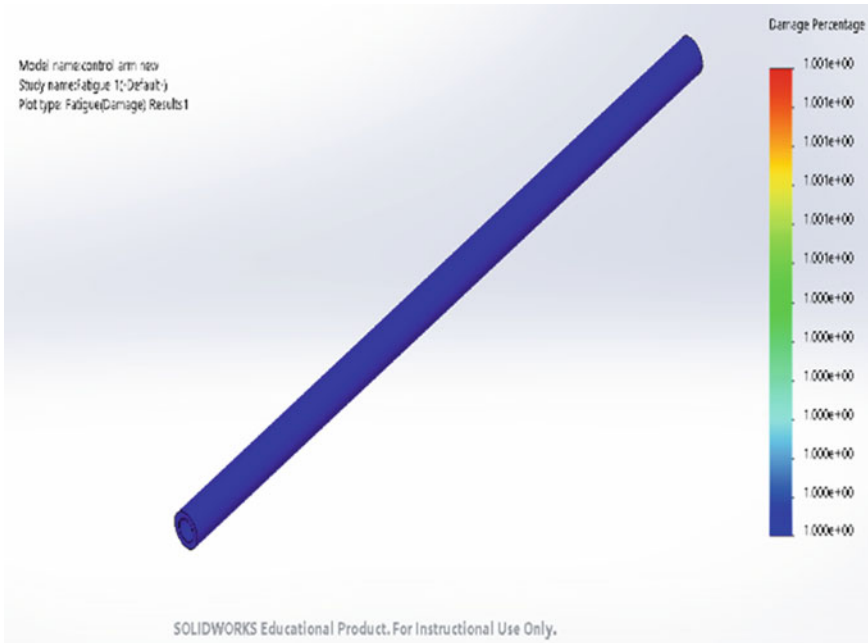
Fig. 17 Fatigue stress simulation of push rod

CAD Model of the Front Suspension System. After finalizing the cross section of all the members of the front suspension system, CAD model of the final assembly was prepared in the same SolidWorks software (Figs. 18 and 19).

8 Conclusions

In this project, a complete model of suspension system is designed including all its components. The CAD modelling and complete analysis are performed on Solid-Works which is then fabricated, and then its assembly is done on the chassis. The following conclusions were made after the completion of the designing, analysis and fabrication of the suspension system:

- The initial working values of forces in suspension system are obtained by applying 3D equations of static equilibrium to solve the static structure model assumed for the suspension system.
- The optimization of the design resulted in the overall material reduction of about 16% which in turn benefitted in weight and cost reduction as well.
- The CAD modelled on SolidWorks based on initial working values obtained from static model reduces the number of iterations significantly to optimize the CAD.
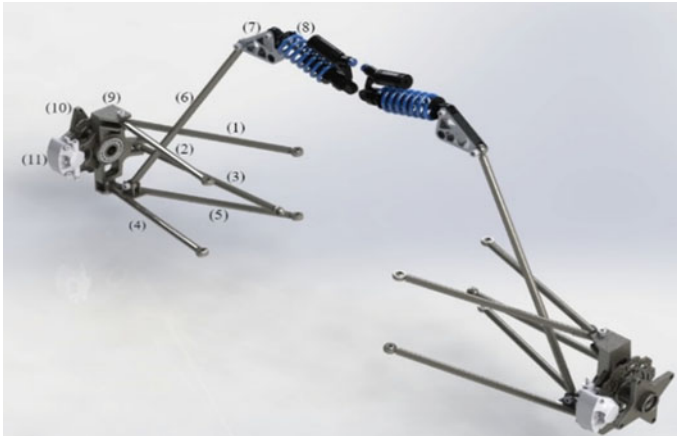
Fig. 18 Final CAD model of the front suspension system. 1: Rearward member of the upper control arm, 2: forward member of the upper control arm, 3: tie rod, 4: forward member of the lower control arm, 5: rearward member of the lower control arm, 6: push rod, 7: rocker assembly, 8: DNM RCP-2s damper, 9: wheel upright, 10: wheel hub, 11: brake calliper and brake rotor assembly

Fig. 19 Complete assembly of the suspension system

Suspension members are successfully fabricated according to the CAD model designed. The fabrication of the suspension system involved various advance machining processes. The final analysis and accuracy obtained indicate a successfully designed suspension system.

References

1. Mokati, A.R., Mittal, S.: A review of procedure of FSAE suspension design. Int. J. Inf. Comput. Sci. (2018) ISSN NO: 0972-1347
2. Ellis, J.R.: Vehicle Handling Kinematics. Mechanical Engineering Publication Limited, London (1994)
3. Dhakar, A., Ranjan, R.: Force calculation in upright of a FSAE race car. Int. J. Mech. Eng. Technol. (2016)
4. Milliken, W.F., Milliken, D.L.: Race Car Vehicle Dynamics, vol. 400. Society of Automotive Engineers Warrendale (1995)
5. [Online]. Available: https://www.slideshare.net/rohansahdev/dynamic-weight-transfer-in-vehicle
6. Borg, L.T.: Approach to using finite element models to predict suspension member loads in a formula SAE vehicle. Virginia Polytechnic Institute and State University (2009)
7. Popov Eger, P.: Engineering Mechanics of Solids, 2nd edn. Prentice Hall, New Delhi. ISBN-0135713560
8. [Online]. Available: https://www.fsae.com/forums/showthread.php?11179-analysis-of-wishbones
9. Savage, G.: Formula 1 composites engineering. Eng. Fail. Anal. **17**(1), 92–115 (2010)
10. Vadhe, A.A.: Design and optimization of formula SAE suspension system. Int. J. Curr. Eng. Technol. (2018)

Simulation-Based Designed Process for Optimization of Blank Shape in the Deep Drawing Process

Rahul Rai and **Vijay Gautam**

1 Introduction

In deep drawing operations, the material is clamped using a blank holder. The blank holder serves to clamp the material with enough force to reduce the risk of wrinkles, but not so much that no material can flow into the die during pressing. After clamping, punch applies the stroke, which will cause the blank to deform. The blank takes the shape of the punch and die when it is forced into the cavity of die by the punch. Thus, cups are formed. If the sheet is anisotropic in nature, then the top edge of the cup will be wavy. If the sheet is highly anisotropic, then these waves will form ears in the cups. This is called an earing defect. Earing in the deep drawing is produced due to the presence of anisotropy in sheet metal. Sheet metals possess anisotropy because they are produced by rolling operation and rolling operation produces texture in the sheet. The effects of rolling on textures have been studied extensively [1].

Several investigations have been done in the area of optimization of blank shape to minimize the height of ears. One of the initial works where the finite element method was used to optimize the blank shape was done by Chung and Richmond [2]. In their work, they used ideal forming design theory to calculate initial blank shape. Then, the finite element analysis was used to adjust the initial shape of the blank. It was called a sequential design process. Kishor and Ravi Kumar [3] proposed a procedure to modify the blank by considering the flow of material in different directions during the deep drawing process and also the anisotropy of the material. The procedure reduced the height of the ears in the first modification. This method could only be used for cylindrical cups with circular blanks because it used four

R. Rai (✉) · V. Gautam
Department of Mechanical, Production & Industrial and Automobile Engineering, Delhi Technological University, Delhi 110042, India
e-mail: b.rahul.rai.b@gmail.com

V. Gautam
e-mail: vijaygautam@dce.ac.in

arcs to modify the blank. Patel et al. [4] use a method similar to Kishor and Ravi Kumar [3]. Yang and Shyu [5] used a reverse forming method. They obtained the initial blank's shape according to the forward square cup drawing simulation. For their method, a very fine mesh was required to reduce ears significantly which leads to very large computation time. Vafaeesefat [6] optimized the blank shape using the boundary projection method. The method produced the optimum blank shape in three iterations. This method required searching for elements to project boundaries. Mole et al. [7] proposed a method for determining optimal blank shape in sheet metal forming based on numerical simulation. Their method required that the initial blank edge geometry should not have too much deviation from the formed product edge geometry. So, this method had a very limited application in deep drawing processes. Golshani and Jabbari [8] optimized the initial blank shape for a twin elliptical cup. They used the reduced basis technique with Taguchi design of experiments model for optimization. The maximum error was 0.07 mm, but a large number of simulations were required for optimum blank shape as compared to other methods. Kitayama et al. [9] did blank shape optimization by multi-objective optimization in which two objective functions were considered: The first was the area above the target contour, while the other was the area below the target contour. In conjunction with this, they also optimized the blank holding force. The optimized blank shape resulted in a deep-drawn square cup with shorter ears. But those ears were still significantly as compared to produce by other methods. Pegada et al. [10] proposed an algorithm to optimize blank shape for cup drawing using finite element analysis. Their algorithm was similar to the algorithm presented in this work. But in their work, no method on how to choose scaling factor was proposed. And also after each iteration, they had to adjust the scaling factor. Vahdat et al. [11] also used a similar algorithm. But they used this algorithm to optimize the draw beads contour. Also, they used a constant scaling factor. Here also no method on how to choose the scaling factor was mentioned.

2   Algorithm for Optimization

The algorithm optimizes the shape of the blank shown in the flowchart of Fig. 1.

The flowchart can be broken down into two parts: (1) initiation and (2) iteration. In the initiation part, ABAQUS/CAE was used to create the model for the simulation of the deep drawing process. ABAQUS/Explicit solver was used to do the finite element analysis. Several points on the circumference were selected to control the shape of the blank. The height of the ears at these points was measured. Error at each point was calculated by subtracting target height from measured height at that point. The target height was the required height of the cup. In iteration, part Isight was used for automation of the process. The model of simulation and the output of the solver was used as input for Isight. Then, a calculator component was used to calculate the error, maximum error, and modified shape of the blank. The loop component was used to check the condition for continuing the iteration. The workflow of the Isight software is shown in Fig. 2.
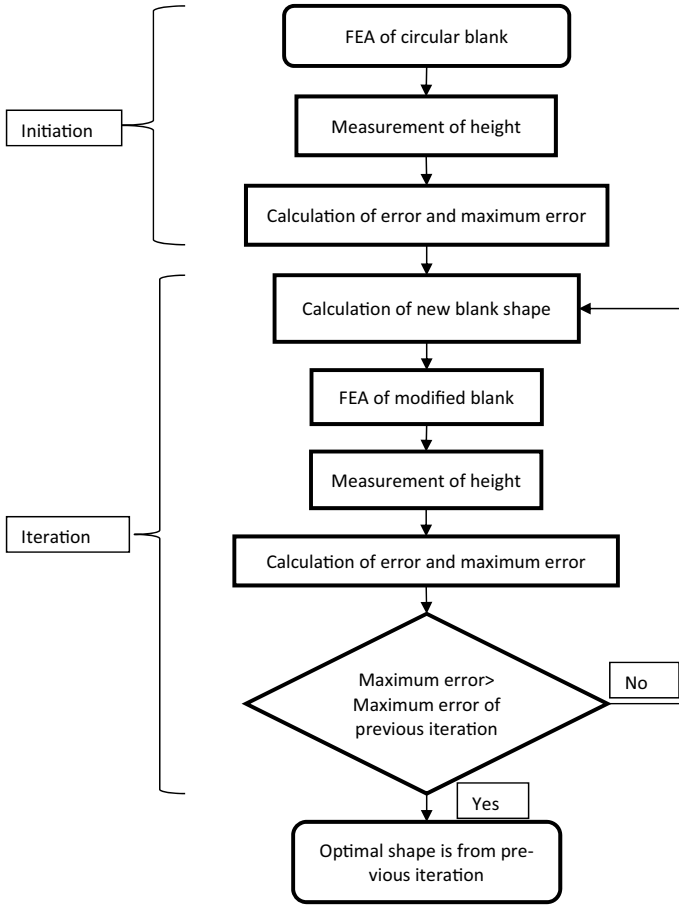
Fig. 1 Algorithm flowchart
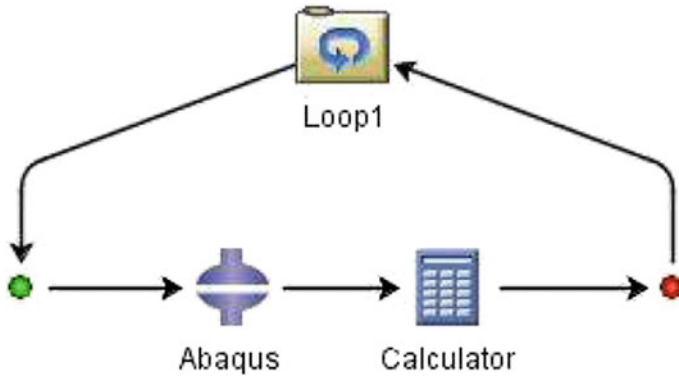
Fig. 2 Workflow of isight

The modification of the blank shape was done in a very simple way. If at a point the height of the cup was less than target height, then the material was added at that point and if the height was more than target height, then the material was deducted. The amount of material added or subtracted was done by changing the radial dimension of that point. A quarter of the circular blank and radial dimension (R_i) at the point i is shown in Fig. 3.

The variation of the height of the cup and target height concerning the points on the circumference is shown in Fig. 4. As mentioned earlier, the target height was the required height of the cup. Hence, E_i is the error at the point i. Finally, a new radial dimension was obtained by adding $K * E_i$, where K is the scaling factor. K was used to prevent overcompensation. Its value should be less than the minimum elongation of circumferential elements. The method to calculate the scaling factor is given in Sect. 2.1.
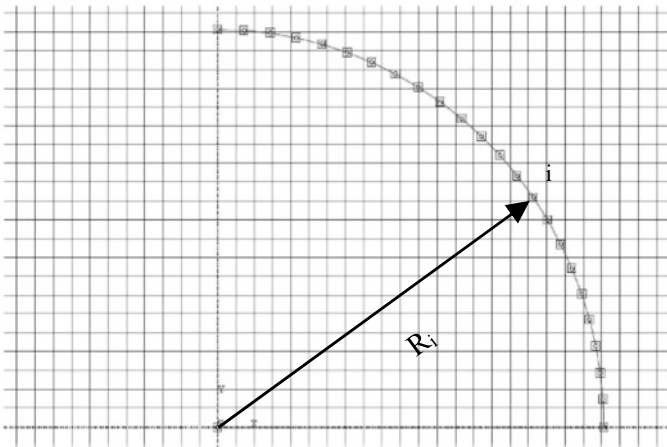
Fig. 3 A quarter of the circular blank

Fig. 4 Variation of the height of the cup and target height concerning the points on the circumference
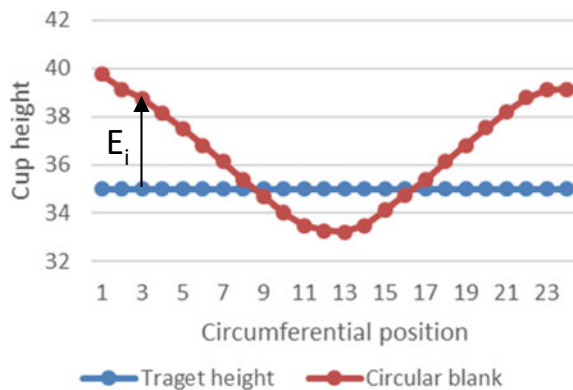
The modified shape was again deformed in the ABAQUS/CAE. This time creation of the model and running the simulation were done by Isight automatically. Also, the calculation of height and error was done by Isight. The Isight compare that if the current maximum error was greater than the maximum error of the previous iteration. If the answer was no, then the process was repeated and if yes then the blank shape of the previous iteration was the optimum blank shape.

The minimized maximum error depends on the number of points selected on the circumference. Greater will be the number of points on the circumference, minimum will be the minimized maximum error.

2.1 Scaling Factor

The scaling factor controls the convergence and rate of convergence of the algorithm. The scaling factor was used to project the error in height of cup on the blank. For the accurate projection of error in height at all points, the unique scaling factor for each point had to be defined. To simplify this, a constant scaling factor was selected. This common scaling factor should be the minimum of all the unique scaling factors so that algorithm should converge. Because, if the selected common scaling factor was greater than any unique scaling factor, then at that point the error will increase with iterations. If that error was too small, then at first convergence will happen, but in a later iteration, the solution will diverge. By observing the flow of material, it was found that there was the least material flow in the blank in 90° direction from the rolling direction. Also, it was observed that the material below the punch does not flow and the rest of the material form wall of the cup. So the initial length of the wall of the cup was the difference of radial dimension in this direction and punch radius which was shown in Fig. 5a. To calculate the scaling factor, the height of the wall
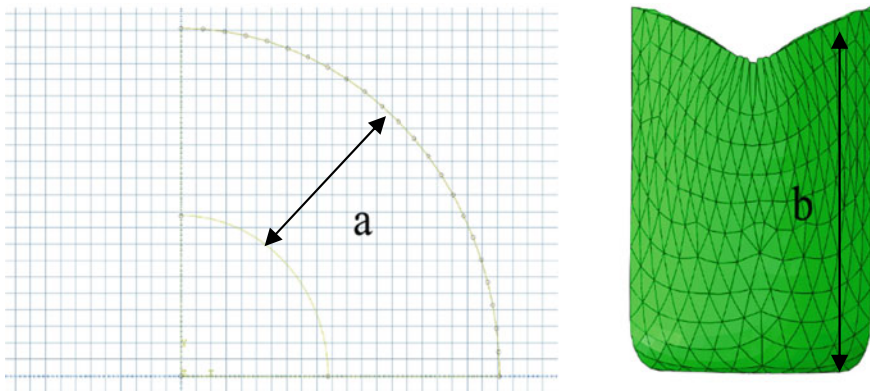
Fig. 5 Initial blank and deep-drawn cup

in this direction (shown in Fig. 5b) was divided with the initial length, which equals 0.57. To be on the safe side, value of the scaling factor was selected as 0.53.

3 FEA Simulation

ABAQUS (version 2019) is a Computer-Aided Engineering (CAE software), which was used for the simulations of the engineering real-life problems. The software uses three different stages that are pre-processing, solution, and post-processing to solve problems.

  In sheet metal forming, contact dominates the solution. Explicit procedures solve the complicated contact problems with greater ease than the implicit procedure. Therefore, in the present work explicit technique was used for analysis. In the ABAQUS/Explicit technique, the time increment step size was extremely small. This small step size leads to a very long time required to complete the simulation in natural time. To reduce the simulation time, the loading rate was increased as long as the solution remained nearly the same as the true static solution and dynamic effects remained insignificant. This was done by determining the minimum total step required to complete the simulation. Second, to reduce the simulation time, the mass scaling of the blank was done. Mass scaling increases the density of the material which leads to a decrease in stress wave speed. Decreased stress wave speed increased the stable time increment. And bigger was the stable time increment faster will be the solution. To validate that the simulation was close to real physical processes, various energies were checked. The kinetic energy and artificial strain energy of the model were negligible compared to the total internal energy of the model. And also the difference between total internal energy and total plastic strain energy was very small. Various energies of the first iteration are shown in Fig. 6.

3.1 Determining an Appropriate Step Time

The time period of the lowest mode whose deformed shape corresponded to the deformation of sheet metal blank was used as a guideline for total step time. For that, a frequency analysis in ABAQUS/Standard was used. A circular blank was created in the part module. Blank was a 3D deformable solid part with an extrusion base type, and its thickness was 1 mm. Only elastic properties and density were required to do frequency analysis. So a material named EDD with density 7.8 tonne/mm^3, Poisson's ratio 0.3 and Young's modulus of 200 GPa was assigned to the blank. An assembly of only blank was created. A single frequency extraction step was added after the default initial step. The lowest mode whose deformed shape corresponds to the deformation of sheet metal blank had a frequency of 2.32 Hz and shown in Fig. 7. The time period of this mode of vibration was 0.43 s. Hence to be on the safe side, the total step was selected to be 0.5 s.
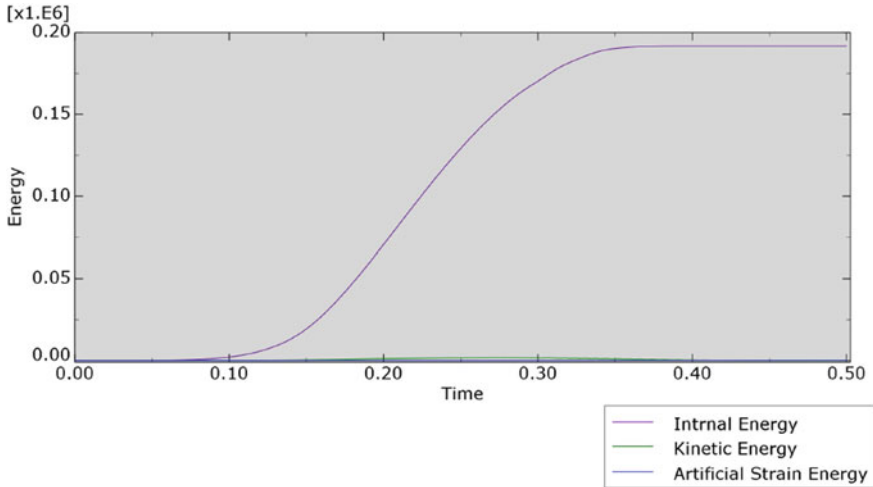
Fig. 6 Various energies of simulation in the first iteration
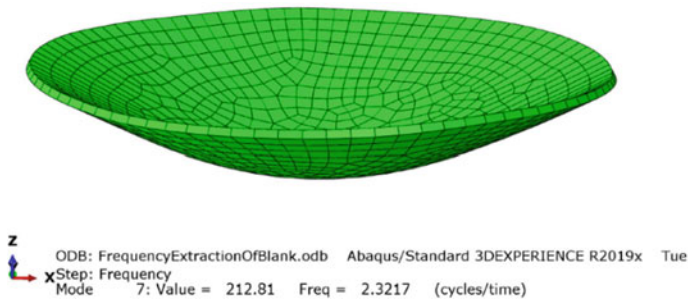
Fig. 7 Shape of lowest mode whose deformed shape corresponds to the deformation of sheet metal blank

3.2 Part Module

To simulate the deep drawing process, five parts were required: (1) blank, (2) punch, (3) die, (4) holder, and (5) stopper. All the parts are shown in Fig. 8 (the die and the holder had the same geometry, so only one part is shown).

Blank was a 3D deformable solid part with an extrusion base type. Only a quarter of blank was considered because of orthogonal symmetry. Sketch of the blank is shown in Fig. 3. Construction lines were made starting from the center of blank to the points on the circumference, and all these construction lines were dimensioned. The order of dimensioning was noted to use in Isight for mapping of data. These dimensions were going to be used to modify the blank shape. Also, a geometric set of these points was created to define an output request for the height of the cup at

Fig. 8 **a** Blank, **b** die/holder,
c punch, **d** stopper

(a)

(b)

(c)

(d)
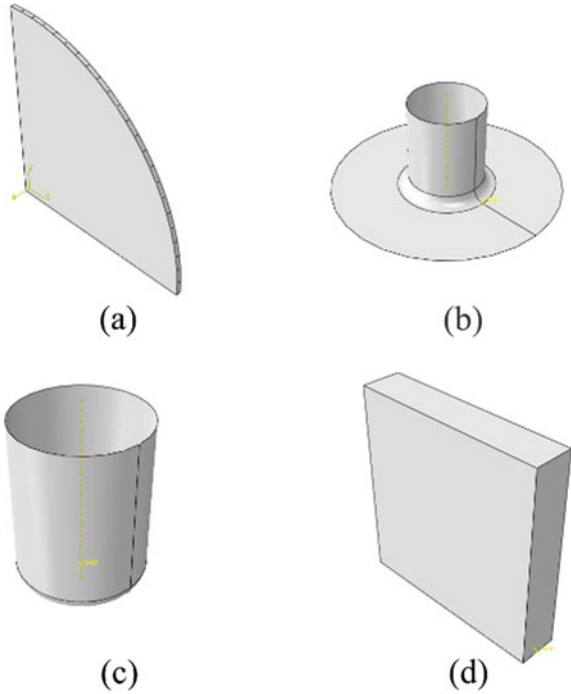
these points. The thickness of the blank was 1 mm. Punch, die and holder were 3D
analytical rigid revolved shell. Holder's was a mirror image of die in the x–y plane.
Each of these bodies was assigned a rigid body reference point. A concentrated force
will be applied to the blank holder. Therefore to compute the dynamic response of
the holder, a point mass must be assigned to its rigid body reference point. The actual
mass of the holder was not important; what important was that the mass should be
of the same order of magnitude as the mass of the blank.

The reason to make punch, die and holder as analytic rigid bodies was that contact
with analytical rigid surfaces tends to be less noisy than contact with discrete rigid
bodies. It was because analytical rigid surfaces can be smooth, whereas discrete rigid
bodies were inherently faceted. Therefore, by defining rigid bodies as analytical
rigid saved a lot of computation time. But analytical rigid surfaces cannot have
contact properties. This created a problem because the holder was constantly applying
pressure on the blank. So, when there was no blank in-between die and holder, the
holder will accelerate indefinitely. Because of which stopper was used. The stopper
was used only to restrict the motion of the blank holder. The stopper was a 3D discrete
rigid part with an extrusion base feature.

Table 1 Material properties

Material	Yield stress (MPa)	Ultimate stress (MPa)	n (Strain hardening exponent)	K (Strength coefficient) (MPa)
EDD steel sheet	155	250	0.237	431

Table 2 Lankford coefficients and plastic potentials

R_o	R_{45}	R_{90}	R_{11}	R_{22}	R_{33}	R_{12}
1.67	1.16	1.76	1.0	1.01	1.17	1.11

3.3 Property Module

As punch, die, holder and stopper were rigid bodies, they did not require any material to be assigned. Only blank was assigned material properties. The material of blank was extra deep drawing steel. This material was used because it is widely used in parts subjected to deep drawing. Material properties are shown in Table 1. To model the anisotropy of material, plastic potentials were calculated from Lankford coefficients, and both are shown in Table 2. After defining the material, a section was defined with the same material. Because our material was anisotropic, a material orientation for blank was defined before assigning this section property to the blank. To define the material orientation of the blank, a global coordinate system was used as a reference.

3.4 Assembly Module

All the parts were created as dependent instances with auto off-set from other instances toggled on. Blank was placed such that the global z-axis was perpendicular to the blank plane. Then die, holder and punch was assembled around blank with assembly constraints. The stopper was assembled on the die and away from blank, so that stopper will not create problem in future iterations with modified blank shape. The assembly of all five parts is shown in Fig. 9.

3.5 Step Module

The first step was the initial step which was auto-generated to solve the boundary conditions without any loading. Then, the second step was created to apply holder force on the blank and named as Hold force. It was an explicit dynamic step. Step time for Hold force was 0.0001 s. This time period was suitable for the application of the holder force because it was long enough to avoid dynamic effects but short
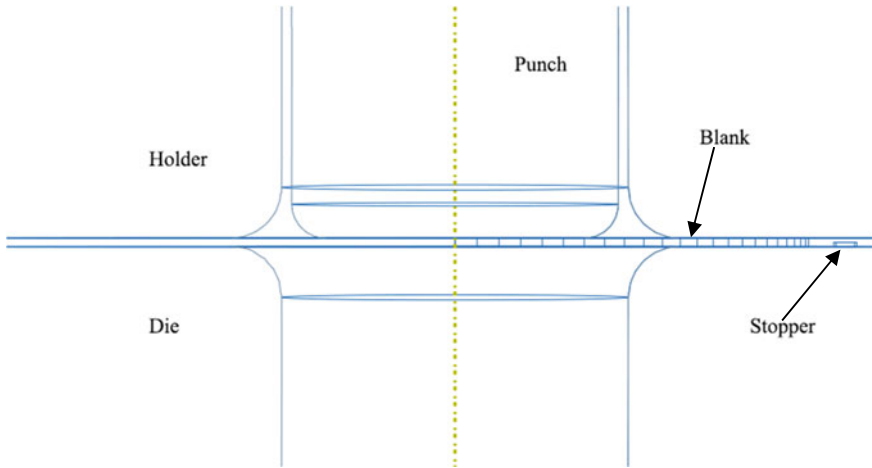
Fig. 9 Assembly of deep-drawn simulation parts

enough to prevent a significant impact on the run time for the job. The third and final step was deep-drawn. It was also an explicit dynamic step. Its time period was calculated earlier and was 0.5 s.

In addition to default field output request and history output request, one more history output request was defined. This output request was defined for a deep-drawn step. Domain for this request was the set created in the blank part of all points. The output variable was U3. U3 was the global z-coordinate. From this, we calculated the height of the cup at points in the set domain. As we need the height of the cup at the end of the simulation, the frequency of the output was set for a single evenly spaced time interval.

3.6 Interaction Module

Here two interaction properties were required. One for friction contact between blank and tools. And second for hard contact between blank holder and stopper. All interaction properties are shown in Table 3. For friction interaction, the static coefficient of friction was 0.15, and the dynamic coefficient of friction was 0.05. The decay coefficient for exponential decay was 1. The pressure overclosure for stopper interaction was "Hard" contact.

Table 3 Interaction properties

Interaction property	Contact property	Friction formulation	Mechanical constraint formulation
Friction	Tangential behavior	Static-kinetic exponential decay	Kinematic contact method
Stopper	Normal behavior	–	Penalty contact method

3.7 Load Module

In this module, loads and boundary conditions were to be defined for the analysis. For the reference point of die and stopper, ENCASTER was defined in the initial step and propagated to subsequent steps. For the reference point of the holder, all degrees of freedom except U3 was constrained to zero and also propagated to subsequent steps. For the reference point of the punch, all the degrees of freedom in the initial step was constrained and was propagated to hold force step. But this boundary condition was modified in deep-drawn step and U2 was set to be -50 with a smooth amplitude. As earlier mentioned that only a quarter of the blank was considered because of orthogonal symmetry. Symmetry boundary conditions were applied at the faces of the blank. Also because an only quarter of the blank was considered, 1/4th of the blank holding force was applied. At the reference point of the holder, -5000 N was applied in CF3 with a smooth amplitude.

3.8 Meshing

As mentioned earlier punch, die and holder were not required to mesh. For stopper, default mesh settings were used, because rigid bodies and elements that were part of a rigid body do not affect the global time increment. The blank was modeled using a 10-node modified quadratic tetrahedron element. Blank was seeded by number method so that the order of nodes at the edge of blank does not change with modification in iterations. Because the output used in Isight was defined by node numbers. Meshed blank is shown in Fig. 10a.

3.9 Job Module

Defaults setting were used to submit the job. The name and location of the output of the job were noted because these files were used as input of Isight.

Fig. 10 **a** Meshed blank,
b ears in the deep-drawn cup
from a circular blank

(a)   (b)
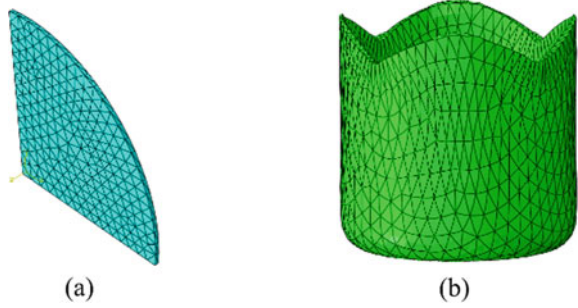
3.10 Visualization Module

In this module, the deformed shape of blank and various output variables was plotted. The set of nodes corresponding to the set of points created in the blank part was plotted, and node number corresponding to each point was noted for mapping of data in Isight. The deformed shape of blanks in various iterations is shown in Fig. 11. A plot of various energies of the first iteration is shown in Fig. 6.

(a) Iteration 1   (b) Iteration 2   (c) Iteration 7
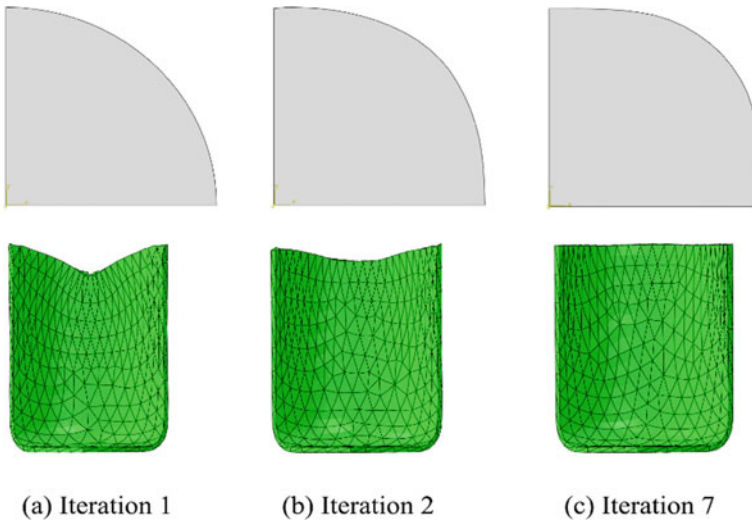
Fig. 11 Blank shape and their corresponding deep-drawn cups

4 Automation of Algorithm

Isight is a powerful tool for effectively and efficiently managing simulation-based design processes. In this work, Isight was used to automate the flow of data. Two application components: (1) ABAQUS and (2) calculator and one process component Loop were used. The workflow of Isight is shown in Fig. 2.

ABAQUS component was configured to take the.cae file created for simulation of deep-drawn process to read for input variables. Radial dimensions of all the points were selected as the input variable. The.obd file which was the output of the simulation was selected to read the output variables. The U3 value of the last frame for all the nodes noted in the visualization module of ABAQUS was selected as output variables.

The calculator component was used to calculate the error in height at various points and then corresponding new radial dimensions. In this component, six parameters were created: (1) Dim, (2) Height, (3) Error, (4) NewDim, (5) MaxError and (6) PMaxError. Except for MaxError and PMaxError, the structure of all the parameters was an array. The radial dimensions from the ABAQUS component were mapped to the Dim parameter in order, and the U3 value of nodes was mapped to the Height parameter in the same order. Then, Error parameter was calculated from the U3 parameter. The MaxError was defined as the absolute maximum value of the Error parameter. NewDim was calculated from the addition of the Dim parameter and 0.53 times of Error parameter. The value of PMaxError was set to be more than MaxError for the first iteration.

The Loop component iterates the process until the value of MaxError was greater than the PMaxError. MaxError was mapped to PMaxError of the calculator component for new iterations.

5 Numerical Results

The effectiveness of the optimization algorithm presented above was demonstrated with the almost absence of ears in the final result. Here the drawing of a cylindrical cup was considered. The assembly of the simulation is shown in Fig. 9. The initial blank shape was a circle. When this circular blank was subjected to a finite element deep drawing simulation, the cup that forms showed earing as can be seen in Fig. 10b.

This shape of Fig. 10b is very different from the target shape of a cup of uniform height. The shape of the quarter cup is shown in Fig. 7a. The error was calculated in the first iteration of the quarter cup using the procedure mentioned earlier. The maximum error was found to be 4.75 mm.

The errors at each point were used to modify the shape of the initial circular blank. A value of 0.53 was chosen for the scaling factor, K, to calculate the new radial dimensions of these points. The new finite element model with the modified

blank was subjected to finite element analysis again. The modified quarter blank shape and its corresponding cup are shown in Fig. 11b.

Once again the errors were calculated at each point. In this iteration, the maximum error was 1.33 mm which was less than that in the first iteration using the circular blank. The iterative process was repeated until the maximum error in the present iteration was greater than the previous iteration. This happened at the 8th iteration. So, the optimal shape of the blank was the shape of the blank in the 7th iteration. The maximum error in the 7th iteration was 0.08 mm. The blank shape and corresponding deformed shape of the 7th iteration are shown in Fig. 11c.

The reduction in the maximum error as iterations progress is shown in Fig. 12. The modification of the radial dimension with iteration is shown in Fig. 13.

The maximum error dropped quite rapidly in the first three iterations after which a point of diminishing returns was reached. Error reduction was achieved with greater difficulty over the next four iterations. At the end of the 7th iteration, the maximum deviation was about 0.08 mm from the target height, and convergence was achieved.
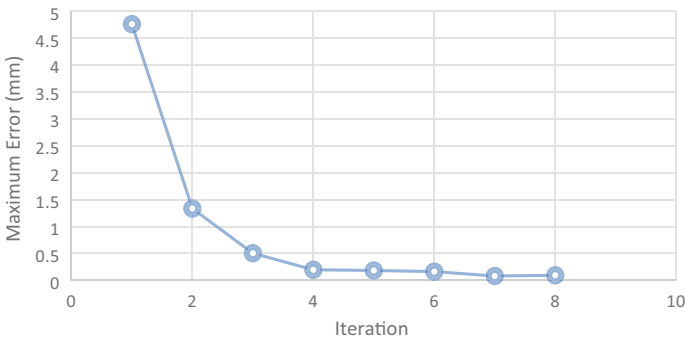
Fig. 12 Reduction in the maximum error with each iteration
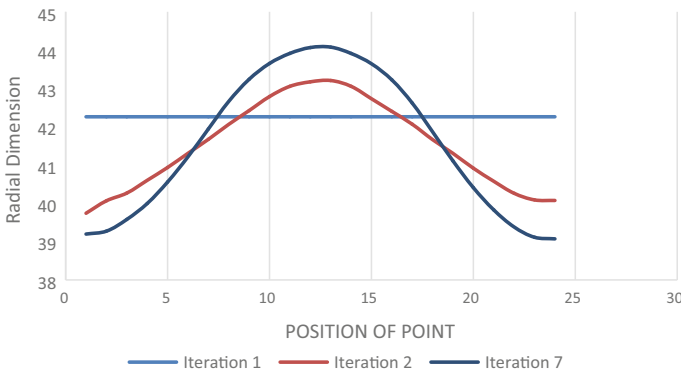
Fig. 13 Modification of radial dimension with iteration

6 Conclusions

A simple but very effective algorithm has been mentioned and used here for the optimization of blank shape problem for deep drawing of cups without ears. The algorithm used an iterative process to arrive at the optimum blank shape. Each iteration involved a finite element simulation to generate a deformed shape from a blank. An error measure was used to generate new radial dimensions that were used to modify the blank shape for the next iteration. The effectiveness of the method has been demonstrated with the almost absence of ears in the cup drawn at 7th iteration. The number of iterations required was less than other optimization methods. The method's simplicity coupled with its effectiveness makes it a very viable procedure for ear minimization in practical deep drawing problems.

Use of ABAQUS/CAE to prepare the model for simulation and then use of Isight to automate the process decreases the design time and load on the designer. Isight provides a very easy way to do a simulation-based design process.

References

1. Wilkinson, A.J.: Encyclopedia of Materials: Science and Technology. Elsevier, Amsterdam (2001)
2. Chung, K., Barlat, F., Brem, J.C., Lege, D.J., Richmond, O.: Blank shape design for a planar anisotropic sheet based on ideal forming design theory and FEM analysis. Int. J. Mech. Sci. **39**(1), 105–120 (1997)
3. Kishor, N., Ravi Kumar, D.: Optimization of initial blank shape to minimize earing in deep drawing using finite element method. J. Mater. Process. Technol. **130–131**, 20–30 (2002)
4. Patel, R., Dave, H., Raval, H.: Study of earing defect during deep drawing process with finite element simulation. Key Eng. Mater. **639**, 91–98 (2015)
5. Yang, T.S., Shyu, R.F.: The design of blank's initial shape in the near net-shape deep drawing of square cup. J. Mech. Sci. Technol. **21**, 1585–1592 (2007)
6. Vafaeesefat, A.: Finite element simulation for blank shape optimization in sheet metal forming. Mater. Manuf. Processes **26**(1), 93–98 (2011)
7. Mole, N., Cafuta, G., Štok, B.: A method for optimal blank shape determination in sheet metal forming based on numerical simulations. Strojniški Vestn. J. Mech. Eng. **59**, 237–250 (2013)
8. Golshani, M.H., Jabbari, A.: Blank shape optimization on deep drawing of a twin elliptical cup using the reduced basis technique method. Adv. Sci. Technol. Res. J. **9**, 72–77 (2015)
9. Kitayama, S., Saikyo, M., Kawamoto, K., et al.: Multi-objective optimization of blank shape for deep drawing with variable blank holder force via sequential approximate optimization. Struct. Multidisc. Optim. **52**, 1001–1012 (2015)
10. Pegada, V., Chun, Y., Santhanam, S.: An algorithm for determining the optimal blank shape for the deep drawing of aluminum cups. J. Mater. Process. Technol. **125–126**, 743–750 (2002)
11. Vahdat, V., Santhanam, S., Chun, Y.W.: A numerical investigation on the use of drawbeads to minimize ear formation in deep drawing. J. Mater. Process. Technol. **176**, 70–76 (2006)

Performance of Hydrodynamic Journal Bearing Operating with Shear-Thinning Lubricants

Vivek Kumar , **Kush Shrivastava, Kuldeep Narwat, and Satish C. Sharma**

1 Introduction

Hydrodynamic journal bearing is generally used for supporting radial load acting on rotating machines [1, 2] such as turbines, pumps, compressors, etc. In such bearings, the mating surfaces are separated by a thin film of lubricant. The film pressure required to support external load is generated by churning of lubricant in narrow passage between the bearing surfaces. Therefore, converging passage, viscous media and sufficient operating speed are prerequisite for safe and reliable operation of hydrodynamic journal bearings [2].

Since the first use of journal bearing [3], numerous theoretical/experimental investigations were carried out to examine and improve the performance of such bearing system. The performance of journal bearing significantly depends upon the geometry of bearing and lubricant employed during its service. Initial design of journal bearing system is mostly confined with circular shape of shaft and bearing. However, ever rising demands of higher production rate made the machines to operate under extremely heavy load and high speed. Under such stringent conditions, the conventional circular bearings are unable to produce desirable performance. Therefore,

V. Kumar (✉) · K. Shrivastava
Department of Mechanical Engineering, School of Technology, PDPU, Gandhinagar 382007, India
e-mail: vivek.kumar@sot.pdpu.ac.in

K. Shrivastava
e-mail: Kush.smtmd19@sot.pdpu.ac.in

K. Narwat
School of Mechanical Engineering, Galgotias University, Greater Noida 203201, India
e-mail: Kuldeep.narwat@galgotiasuniversity.edu.in

S. C. Sharma
Mechanical and Industrial Engineering Department, IIT Roorkee, Roorkee 247667, India
e-mail: sshmefme@me.iitr.ac.in

761

with the advancement in manufacturing technologies, non-circular bearings were more frequently produced and employed in turbo-machine applications. These non-circular bearing such as pressure dam bearing [4], elliptical bearings [5], multi-lobe bearings [6], titling pads bearings [7], etc. provides better rotor-dynamic performance and stability as compared to conventional circular bearings.

Recently, laser surface texturing [8, 9] is establishing as a new way of improving the tribo-performance of hydrodynamic bearings. In these techniques, micro-dimple and grooves patterns are generated over the bearing surface. These dimples act as numerous micro-bearings [8] and has the ability to enhance the performance level of tribo-pairs operating in different lubrication regimes. Many studies [8–14] have been reported examining the performance of textured surface fluid film bearing. Majorities of these studies reported a marked increase in the load carrying capacity [8, 11, 14] and reduction in coefficient of friction [8–10, 12], provided optimization of texture attributes under given operating conditions. Once the journal bearing is manufactured and employed in engineering applications, its performance can be effectively managed by an appropriate selection of type and quantity of lubricant. In most engineering applications, certain additives such viscosity improver agents, anti-friction, anti-wear agents, rust inhibitors, etc. [1, 2] are added to the base stock oil. This is done to impart specific characteristics to the lubricant. As a results of this, the lubricant during its intended use exhibits nonlinear behavior for shear-stress versus strain rate. Some experimental studies have been reported examining the effect of additives on coefficient of friction between tribo-pairs such as journal bearings [15, 16], sliding surface [17] and friction clutch [18]. Experimental and theoretical study from Wada and Hayashi [15] recommended that cubic shear-stress fluid model satisfactorily describes the non-Newtonian characters of lubricants blended with viscosity index improvers. However, then many theoretical investigations [19–26] have been reported investigating the effect of nonlinear behavior of lubricant on performance of fluid film bearings. The nonlinear behavior of lubricant in these studies has been characterized using theories/law such as couple-stress theory [19–24], micropolar theory [25], power law [26], cubic shear-stress law [15], etc. The couple-stress and micropolar theories are mainly concerned with effect of size of additives [18–24] on the performance of fluid film bearing systems, operating with non-Newtonian lubricant. It has been reported that an increase in characteristic length of additives and coupling number can enhance the load carrying capacity, increase minimum film thickness and decrease lubricant flow rate through the journal bearing system. Other theories such as power law, cubic shear-stress law, etc., define nonlinear relationship between shear-stress and strain rate. Numerical investigations [15, 24] have been reported on journal bearing operating with shear-thinning and shear-thickening lubricants, as described by cubic shear-stress law and power law fluid model.

The available published literature discussed above indicates that the non-Newtonian lubricants are commonly employed to enhance the performance of hydrodynamic journal bearing. It was reported that cubic shear-stress fluid model [15] satisfactorily approximates the shear-thinning behavior of commercial lubricants, containing long-chain polymer additives as viscosity index improvers. Some studies [15, 19, 23–25] are reported examining the steady-state performance of journal

bearing, operating with non-Newtonian lubricants. To the best of author knowledge, very few studies are available dealing with influence of shear-thinning lubricant on dynamic performance of hydrodynamic journal bearing. In view of above, this study has been planned to examine the effect of shear-thinning nature of lubricant on the rotor-dynamic coefficient of hydrodynamic journal bearing system.

2 Mathematical Formulation

Figure 1 depicts the configuration of hydrodynamic journal bearing system under consideration. The non-Newtonian lubricant exhibiting shear-thinning behavior is supplied from a supply hole located at top of the bearing. The lubricant flow condition between journal and bearing is considered laminar, incompressible and iso-viscous. In steady-state operation, the flow of lubricant inside the clearance space is governed by generalized Reynolds equation described as flows:

$$\frac{\partial}{\partial \overline{x}}\left(\overline{h}^3 \overline{F}_2 \frac{\partial \overline{p}}{\partial \overline{x}}\right) + \frac{\partial}{\partial \overline{z}}\left(\overline{h}^3 \overline{F}_2 \frac{\partial \overline{p}}{\partial \overline{z}}\right) = \Omega \frac{\partial}{\partial \overline{x}}\left[\left(1 - \frac{\overline{F}_1}{\overline{F}_0}\right)\overline{h}\right] + \frac{\partial \overline{h}}{\partial \overline{t}} \quad (1)$$

$$\overline{x} = \frac{x}{r_j}; \overline{z} = \frac{z}{r_j}; \overline{h} = \frac{h}{c_r}; \overline{r} = \frac{r}{r_j}; \overline{p} = \frac{p - p_a}{p_r}; \overline{\mu} = \frac{\mu}{\mu_r}; p_r = \frac{\mu_r \omega r_j^2}{c_r^2}; \overline{t} = t\omega$$

where $\overline{F}_o$, $\overline{F}_1$ and $\overline{F}_2$ represent viscosity integrals of lubricant and describe as follows:
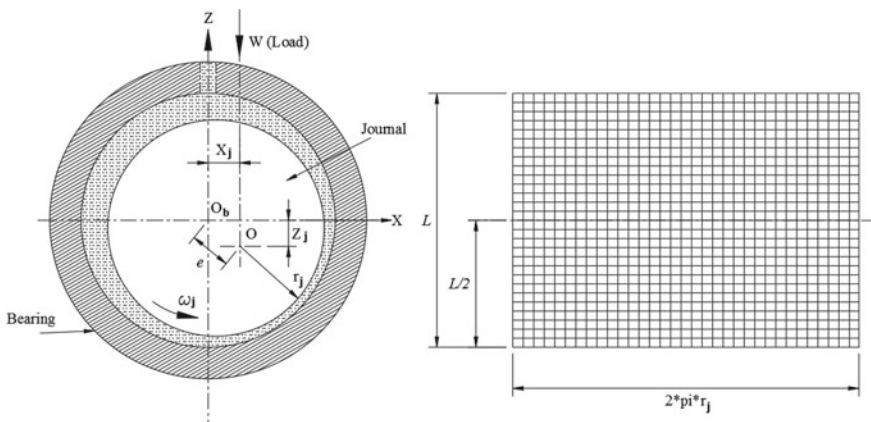
Fig. 1 Journal bearing system and unwrapped bearing surface

$$\overline{F}_0 = \int_0^1 \frac{1}{\overline{\mu}}\mathrm{d}\overline{z}; \quad \overline{F}_1 = \int_0^1 \frac{\overline{z}}{\overline{\mu}}\mathrm{d}\overline{z}; \quad \overline{F}_2 = \int_0^1 \frac{\overline{z}}{\overline{\mu}}\left(\overline{z} - \frac{\overline{F}_1}{\overline{F}_0}\right)\mathrm{d}\overline{z}$$

The film thickness expression for journal bearing configuration is described as follows:

$$\overline{h} = 1 - \overline{x} * \cos(\alpha) - \overline{z} * \sin(\alpha) \tag{2}$$

The shear-stress versus strain rate relationship for lubricant is governed by Rabinowitsch fluid model.

$$\overline{\tau} + n\overline{\tau}^3 = \overline{\gamma} \tag{3}$$

$$\overline{\gamma} = \sqrt{\left[\frac{\overline{h}}{\overline{\mu}}\frac{\partial\overline{p}}{\partial\overline{x}}\left(\overline{z} - \frac{\overline{F}_1}{\overline{F}_0}\right) + \frac{\Omega}{\overline{\mu}\overline{h}\overline{F}_0}\right]^2 + \left[\frac{\overline{h}}{\overline{\mu}}\frac{\partial\overline{p}}{\partial\overline{y}}\left(\overline{z} - \frac{\overline{F}_1}{\overline{F}_0}\right)\right]^2} \tag{4}$$

where n is known as fluid nonlinearity index.

In present work, finite element approach is used to solve Eq. 1 for computing film pressure distribution. The bearing surface is divided into sub-domains using 2D quadrilateral elements. The pressure within an element is assumed to be distributed linear along x- and z-direction.

$$\overline{p} = \sum_{j=1}^4 [N_j\overline{p}_j]; \quad N_j = \frac{1}{4}(1 + \xi_i\xi)(1 + \eta_i\eta) \tag{5}$$

The weak form of Eq. 1 has been obtained using weighted residual approach. The shape function of primary variable is taken as weights.

$$\iint_A \left(\frac{\partial}{\partial\overline{x}}\left(\frac{\overline{h}^3}{\overline{\mu}}\overline{\varphi}\frac{\partial}{\partial\overline{x}}\left\{\sum_{j=1}^4(\overline{p}_jN_j)\right\}\right) + \frac{\partial}{\partial\overline{z}}\left(\frac{\overline{h}^3}{\overline{\mu}}\overline{\varphi}\frac{\partial}{\partial\overline{z}}\left\{\sum_{j=1}^4(\overline{p}_jN_j)\right\}\right)\right.$$
$$\left. -\Omega\frac{\partial}{\partial\overline{x}}\left[\left(1 - \frac{\overline{F}_1}{\overline{F}_0}\right)\overline{h}\right] - \frac{\partial\overline{h}}{\partial\overline{t}}\right)d\overline{x}d\overline{z} = 0 \tag{6}$$

The simplification of above Eq. 6 yields set of algebraic equations, and these elemental equations can be assembled in matrix form as described below.

$$[\overline{F}]\{\overline{p}\} = [\overline{Q}] + \Omega[\overline{H}] + \dot{\overline{x}}_j[\overline{S}_j] + \dot{\overline{z}}_j[\overline{S}_j] \tag{7}$$

The above equation depicts assembly of fluidity matrix, pressure vector, flow term, hydrodynamic term and squeeze terms along x- and z-direction, respectively.

Boundary condition:

1. At axial boundary: $z = \pm L/2;\ p = p_a$
2. At lubricant supply location: $x = 0;\ 2\pi r_j;\ \overline{p} = p_a$
3. Gaseous cavitation (Reynolds boundary condition) [26]: $x = x_c;\ \overline{p} = 0;\ \frac{\partial p}{\partial x} = 0$.

The solution of Eq. 7 under steady-state operation $\left(\overline{\dot{x}}_j = \overline{\dot{z}}_j = 0\right)$ provides film pressure distribution on bearing surface. The integration of film pressure values on bearing area provides fluid film reaction.

$$\text{Film reaction:}\quad \overline{F} = \left[\left(\overline{F}_x\right)^2 + \left(\overline{F}_z\right)^2\right]^{1/2}; \tag{8}$$

$$\overline{F}_x = \int\limits_{-1}^{1}\int\limits_{0}^{2\pi} \overline{p}\cos\alpha\, d\overline{x} d\overline{z};\quad \overline{F}_z = \int\limits_{-1}^{1}\int\limits_{0}^{2\pi} \overline{p}\sin\alpha\, d\overline{x} d\overline{z};$$

$$\text{Frictional Torque:}\quad \overline{T}_f = \int\limits_{-1}^{+1}\int\limits_{0}^{2\pi} \left(\overline{h}\frac{\partial \overline{p}}{\partial \overline{x}}\left(\overline{z} - \frac{\overline{F}_1}{\overline{F}_0}\right) + \frac{\Omega}{\overline{h}\,\overline{F}_0}\right) d\overline{x} d\overline{z} \tag{9}$$

Newton–Raphson method is used to obtain dynamic state $\left(\overline{\dot{x}}_j \neq 0;\ \overline{\dot{z}}_j \neq 0\right)$ solution of Eq. 7. This will provide fluid film pressure gradient along x- and z-direction, which can be used to describe film stiffness and damping coefficients.

$$\overline{k}_{ij} = -\frac{\partial \overline{F}_i}{\partial \overline{x}_j} \Rightarrow \overline{K} = -\begin{bmatrix} \overline{k}_{11} & \overline{k}_{12} \\ \overline{k}_{21} & \overline{k}_{22} \end{bmatrix} = -\begin{bmatrix} \frac{\partial \overline{F}_x}{\partial \overline{x}} & \frac{\partial \overline{F}_x}{\partial \overline{z}} \\ \frac{\partial \overline{F}_z}{\partial \overline{x}} & \frac{\partial \overline{F}_z}{\partial \overline{z}} \end{bmatrix} \tag{10}$$

$$\overline{D}_{ij} = \frac{\partial \overline{F}_i}{\partial \overline{\dot{x}}_j} \Rightarrow \overline{D} = \begin{bmatrix} \overline{D}_{11} & \overline{D}_{12} \\ \overline{D}_{21} & \overline{D}_{22} \end{bmatrix} = \begin{bmatrix} \frac{\partial \overline{F}_x}{\partial \overline{\dot{x}}} & \frac{\partial \overline{F}_x}{\partial \overline{\dot{z}}} \\ \frac{\partial \overline{F}_z}{\partial \overline{\dot{x}}} & \frac{\partial \overline{F}_z}{\partial \overline{\dot{z}}} \end{bmatrix} \tag{11}$$

The dynamic coefficients of bearing system are used to compute the threshold speed (ω_t) margin of journal bearing.

$$\omega_t = \left[\frac{\overline{m}_c}{\overline{F}}\right]^{1/2} \tag{12}$$

where $\overline{m}_c$ is critical mass of journal, whose value depend upon the film direct and cross-couple stiffness and damping coefficients. The system becomes stable if mass of journal becomes lesser than the critical mass of the bearing system.

3 Solution Procedure

The analysis presented in preceding section has been used to simulate hydrodynamic journal bearing. The analytical solution of Reynolds equation (Eq. 1) is a cumbersome process due to nonlinear nature of partial differential equation. Therefore, finite element numerical technique is used to obtain solution of problem. The bearing input parameters are listed in Table 1. Bearing surface is divided into discrete regions using 4-node quad elements, and film pressure has been computed iteratively, using Newton–Raphson's method. A grid size of 50*.

A total of 20 nodes have been taken to generate mesh-free numerical results. The solution scheme adopted to perform finite element simulation of bearing is presented in Fig. 2. The convergence of iterative scheme is based on eccentricity of the bearing. A convergence (Eq. 13) of order of 10^{-05} is defined on eccentricity between successive iteration. Once the convergence criteria are satisfied, film pressure and performance indices mentioned in previous section of the manuscript will be computed.

Table 1 Bearing geometric and operating condition

Input parameters	Dimensional value	Input parameters	Dimensional value
Shaft radius (r_j)	50 mm	Radial clearance	0.05 mm
Axial length of bearing (L)	100 mm	Supply pressure	0.101325 MPa
Operating speed (N)	500 RPM	Lubricant viscosity	0.0345 Pa s
External load (W)	6.77–9.94 kN	Lubricant density	860 kg/m^3
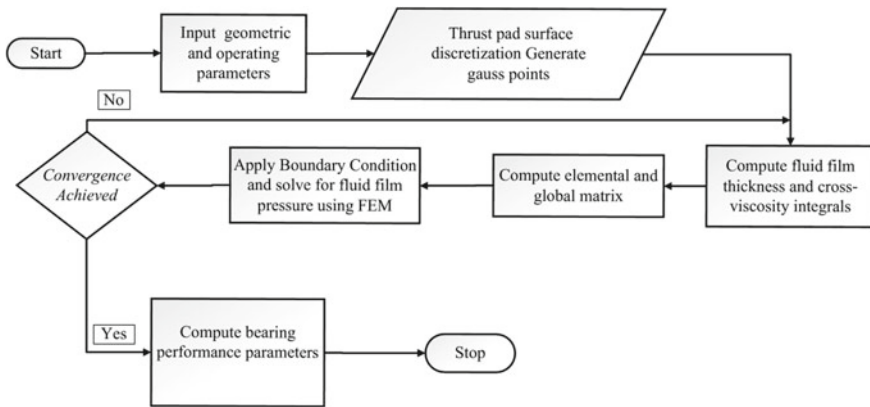
Fig. 2 Solution scheme
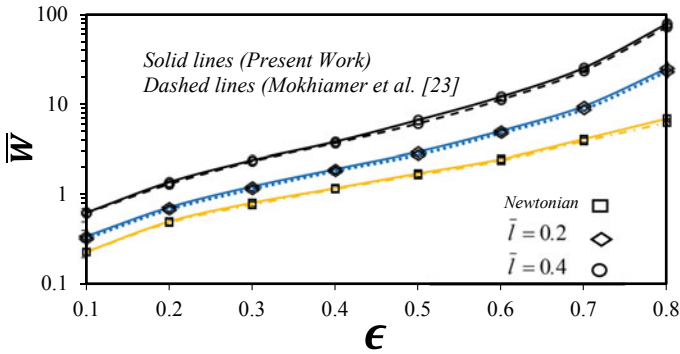
Fig. 3 Load supporting capacity versus eccentricity ratio [23]

$$\left| \frac{\left[\left(\Delta \bar{x}_j^i \right)^2 + \left(\Delta \bar{z}_j^i \right)^2 \right]^{1/2}}{\left[\left(\bar{x}_j^i \right)^2 + \left(\bar{z}_j^i \right)^2 \right]^{1/2}} \right| \leq 10^{-05} \tag{13}$$

Figure 3 depicts validation of mathematical model/numerical solution scheme with available published [23] results for hydrodynamic journal bearings. The finite element method based solution scheme depicted in Fig. 2 has been used to reproduce the numerical results of reference study [23]. Figure 3 shows variation in load supporting capacity of finite journal bearing with respect to eccentricity ratio. It can be clear seen that result from two schemes are in good agreement with each other. This justifies the accuracy of solution scheme to numerically simulate hydrodynamic journal bearing.

4 Results and Discussion

In this section, numerical results are discussed, obtained following numerical simulation of hydrodynamic journal bearings. Influence of external load and shear-thinning (n) behavior of lubricant is examined on the performance indicators of the hydrodynamic journal bearing. With a value of fluid nonlinearity index (n) approaching to zero, the lubricant is going to exhibit Newtonian character. The performance of bearing is examined in terms of physical quantitates such as film pressure, min. film thickness, film frictional torque and film rotor-dynamic coefficient.

Figure 4 depicts influence of lubricant nonlinearity index (n) on fluid film pressure distribution for bearing operating under varying external load. It can be seen that for a given external load, an increase in nonlinearity has very little effect on maximum value of fluid as well as pressure distribution. However, an increase in external load value significantly affects peak value of film pressure and its distribution in bearing domain. This might be due to that fact that to sustain heavy low, the fluid has
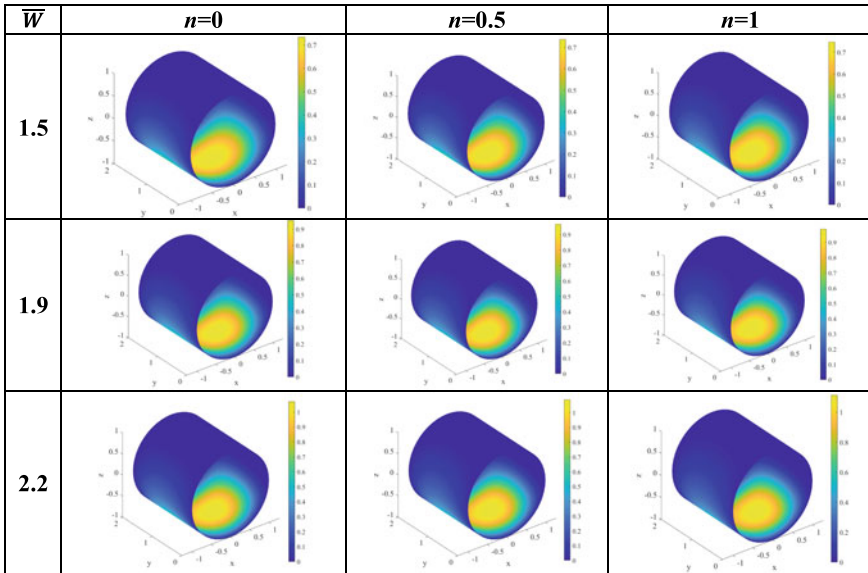
Fig. 4 Pressure distribution in bearing for Newtonian and shear-thinning lubricant as a function of external load

to generate higher magnitude of fluid film pressure values on the bearing surface. The effect of lubricant nonlinearity index (n) and external load on minimum film thickness is depicted in Fig. 5. A continuous reduction has been observed with respect to increase in the external load imposed on bearing system. Also, as lubricant nonlinearity index is increased, a significant reduction in min. film thickness has been reported. This is because an increase in n leads to a reduction in the apparent viscosity of lubricant. The reduction in min. film thickness with respect to n is noticed to be lying in the range of -22.83 to -31.88%, as the non-dimensional external load is increased from 1.5 to 2.2 (Fig. 5).

Figure 6 presents the influence of external load and shear thinning behavior of lubricant on film frictional torque. It has been found that by increasing the external load, the frictional torque of system continuously increases. Further, it was observed that with an increase in shear-thinning coefficient/fluid nonlinearity index (n), the frictional torque in the system reduces significantly. This can be accounted for the reduction in the apparent viscosity of the lubricant for an increase in n. Although the use of non-Newtonian lubricant ($n = 0.5, 1$) reduces friction torque in the bearing system, maximum percentage increase in frictional torque w.r.t external load is noticed to be maximum for non-Newtonian lubricant (31.8, 32.5%) as compared to Newtonian lubricant (+20.4%).

The numerical results for direct film stiffness coefficient ($\overline{K}_{xx}$ and $\overline{K}_{zz}$) are presented in Figs. 7 and 8. It has been observed that an increase in external load leads to a reduction the stiffness coefficient $\overline{K}_{xx}$. The shear-thinning nature of lubricant is reporting to enhancing the value of $\overline{K}_{xx}$. On the contrary, the stiffness coefficient

Fig. 5 Min. film thickness versus load
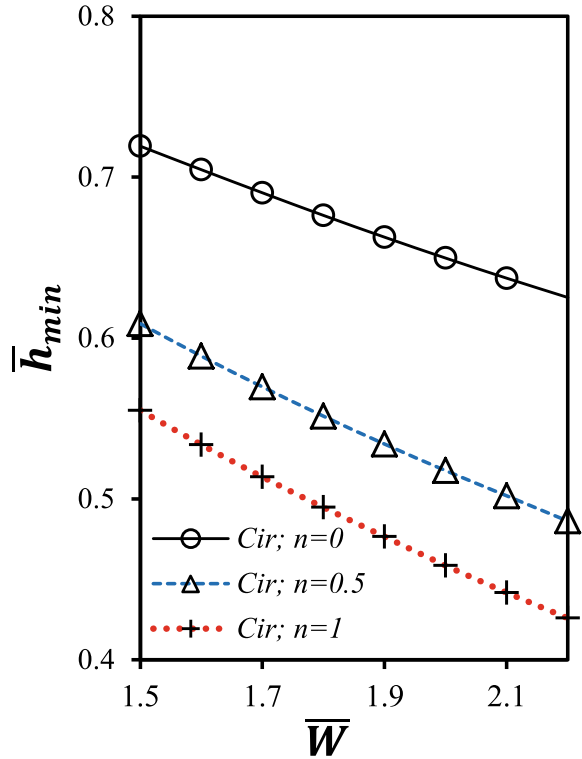
$(\overline{K}_{zz})$ is noticed to be enhanced with an increase in external load. Also, the shear-thinning behavior of lubricant is noticed to reduce the direct stiffness coefficient $\overline{K}_{zz}$. However, this effect is found to be diminished progressively with an increase in external load. Figures 9 and 10 depicts the influence of fluid nonlinearity index on direct film damping coefficient $(\overline{D}_{xx}$ and $\overline{D}_{zz})$ of the bearing system operating under a wide range of external load. It has been found that increase in external load tends to increase the damping coefficients of journal bearing. Further, the shear-thinning behavior $(n = 0.5, 1)$ of lubricant is also noticed to be enhance the damping coefficients. The effect of n on damping coefficient is noticed to profound at higher values of external load acting on the system. The $\overline{D}_{xx}$ is reported to gradually increase from 1.8% to 4.5%, with an increase in external load from 1.5 to 2.2. A substantially higher gain (6.7–18.7%) has been observed in $\overline{D}_{zz}$ by the use of shear-thinning lubricant $(n = 1)$, when external load has been increased from 1.5 to 2.2.

Figure 11 depicts variations in the threshold speed margin of bearing for an increase in external load acting on the system. The threshold speed margin depends upon direct and cross-coupled stiffness and damping coefficients. It can be seen that threshold speed margin of bearing system almost decreases linearly with a gradual increase in the external load. Further, it has been found that shear-thinning behavior of

Fig. 6 Frictional torque
($\overline{T}_f$) versus load
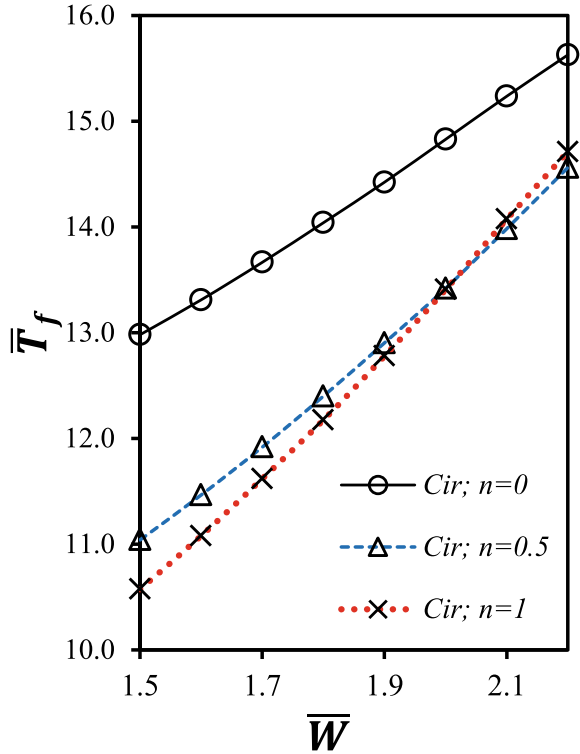
lubricant slightly reduces (-0.3 to -0.38%) the threshold speed of the hydrodynamic journal bearing system.

5 Conclusions

Following conclusion can be drawn from the numerical simulation of hydrodynamic journal bearing operating with shear-thinning lubricant.

- The shear-thinning of lubricant has minimal effect on maximum film pressure but significantly reduces (-31.88%) the min. fluid film thickness of journal bearing system under given operating conditions.
- The film frictional torque significantly reduces (-18.5 to -5.8%) owing to the use of shear-thinning lubricant. The reduction in frictional torque is noticed to be larger at lower values of external load acting on the system.
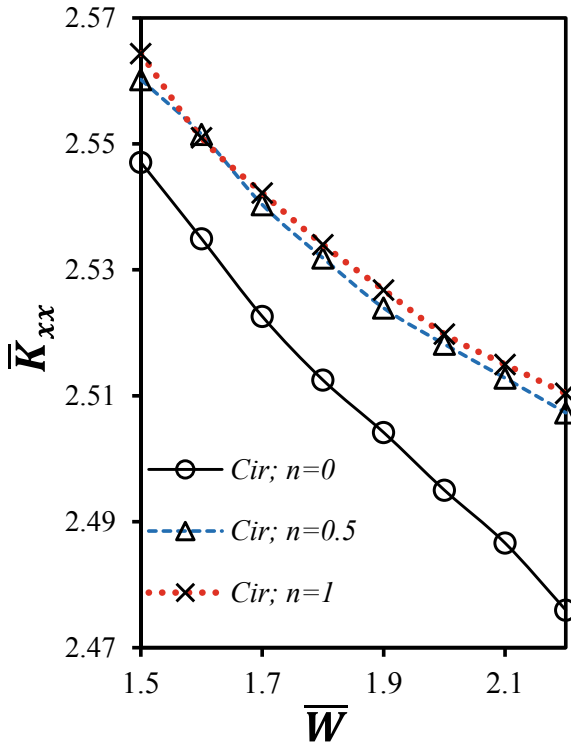
Fig. 7 Stiffness coefficient ($\overline{K}_{xx}$) versus load

- The shear-thinning of lubricant and external load is noticed to be beneficial in enhancing the film rotor-dynamic coefficients stiffness ($\overline{K}_{zz}$, $\overline{D}_{xx}$ and D_{zz}) of the hydrodynamic journal bearing.
- An increase in external load is reported to significantly reduces the threshold speed margin of the journal bearing; however, threshold speed margin is noticed to be almost invariant to shear-thinning of lubricant.
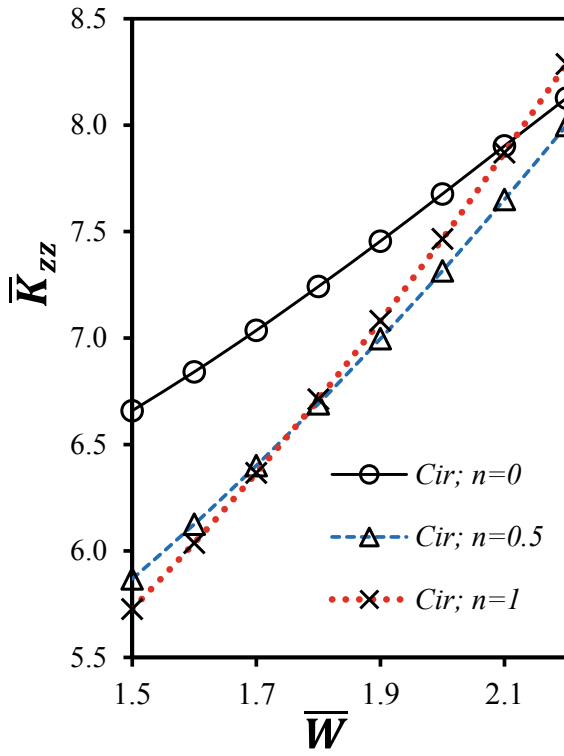
Fig. 8 Stiffness coefficient ($\overline{K}_{zz}$) vs load
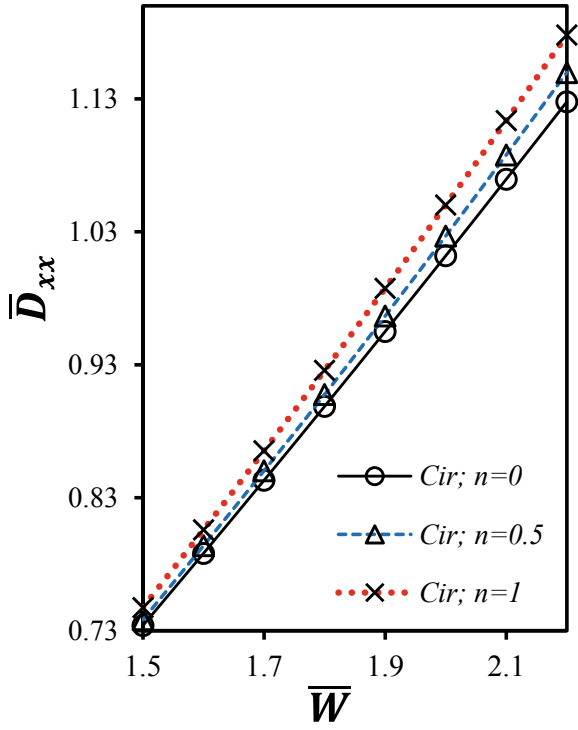
Fig. 9 Damping coefficient ($\overline{D}_{xx}$) versus load
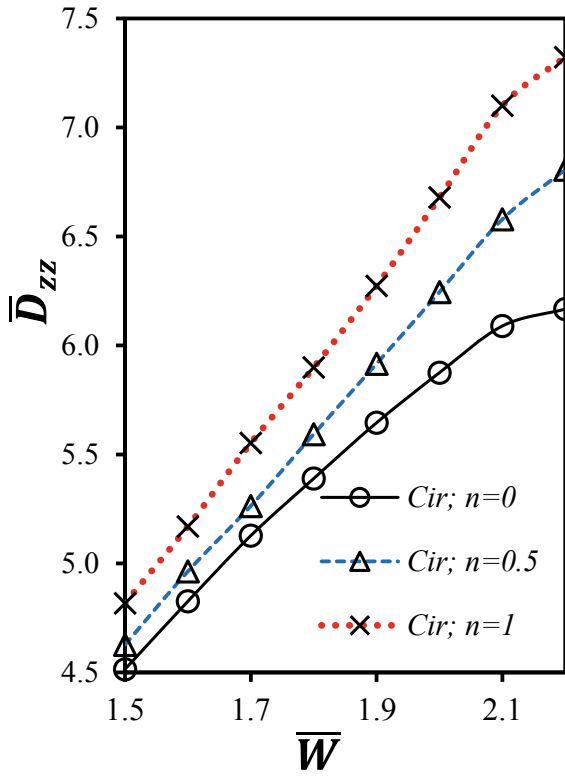
Fig. 10 Damping coefficient ($\overline{D}_{zz}$) versus load
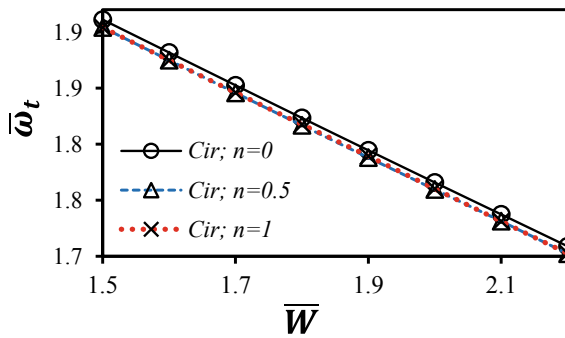
Fig. 11 Threshold speed margin (ω_t) versus load

References

1. Bhushan, B.: Introduction to Tribology. Wiley, New York (2013)
2. Khonsari, M.M., Booser, E.R.: Applied Tribology: Bearing Design and Lubrication. Wiley, West Sussex (2017)
3. Tower, B.: First report on friction experiments. Proc. Inst. Mech. Eng. **34**(1), 632–659 (1883)
4. Mehta, N.P., Singh, A.: Stability analysis of finite offset-halves pressure dam bearing. J. Tribol. **108**(2), 270–274 (1986)
5. Nair, K.P., Sinhasan, R., Singh, D.V.: Elastohydrodynamic effects in elliptical bearings. Wear **118**(2), 129–145 (1987)
6. Rahmatabadi, A.D., Rashidi, M.R., Nekoeimehr, M.: Preload effects on the static performance of multi-lobe fixed profile journal bearings with micropolar fluids. Proc. Inst. Mech. Eng. Part J: J. Eng. Tribol. **225**(8), 718–730 (1987)
7. Bing, W., Chun-ge, Z.A.N.G., Yu-hao, S.U.N.: Experimental test of dynamic characteristics of tilting pad thrust bearing. Lubr. Eng. **39**(4), 55–60 (2014)
8. Etsion, I.: State of the art in laser surface texturing. J. Tribol. **127**(1), 248–253 (2005)
9. Gropper, D., Wang, L., Harvey, T.J.: Hydrodynamic lubrication of textured surfaces: a review of modeling techniques and key findings. Tribol. Int. **94**, 509–529 (2016)
10. Tala-Ighil, N., Fillon, M., Maspeyrot, P.: Effect of textured area on the performances of a hydrodynamic journal bearing. Tribol. Int. **44**(3), 211–219 (2011)
11. Kumar, V., Sharma, S.C.: Effect of geometric shape of micro-grooves on the performance of textured hybrid thrust pad bearing. J. Braz. Soc. Mech. Sci. Eng. **41**(11), 508 (2019)
12. Cupillard, S., Glavatskih, S., Cervantes, M.J.: Computational fluid dynamics analysis of a journal bearing with surface texturing. Proc. Inst. Mech. Eng. Part J: J. Eng. Tribol. **222**(2), 97–107 (2008)
13. Kumar, V., Sharma, S.C., Narwat, K.: Influence of micro-groove attributes on frictional power loss and load-carrying capacity of hybrid thrust bearing. Ind. Lubr. Tribol. (2019). https://doi.org/10.1108/ILT-07-2019-0278
14. Kumar, V., Sharma, S.C.: Performance analysis of rough surface hybrid thrust bearing with elliptical dimples. Proc. Inst. Mech. Eng. Part J: J. Eng. Tribol. (2020). https://doi.org/10.1177/1350650120931981
15. Wada, S., Hayashi, H.: Hydrodynamic lubrication of journal bearings by pseudoplastic lubricants (part II, experimental studies). Bull. JSME **14**(69), 279–86 (1971)
16. Oliver, D.R.: Load enhancement effects due to polymer thickening in a short model journal bearing. J. Nonnewton. Fluid Mech. **30**, 185–196 (1988)
17. Spikes, H.A.: The behavior of lubricants in contacts: current understanding and future possibilities. Proc. Inst. Mech. Eng. Part J: J. Eng. Tribol. **28**, 3–15 (1994)
18. Scott, W., Suntiwattana, P.: Effect of oil additives on the performance of a wet friction clutch material. Wear **181**, 850–855 (1995)
19. Lin, J.R.: Effects of couple stresses on the lubrication of finite journal bearings. Wear **206**(1–2), 171–178
20. Kumar, V., Sharma, S.C.: Study of annular recess hydrostatic tilted thrust pad bearing under the influence of couple stress lubricant behaviour. Int. J. Surf. Sci. Eng. **11**(4), 344–369 (2017)
21. Kumar, V., Sharma, S.C.: Magneto-hydrostatic lubrication of thrust bearings considering different configurations of recess. Ind. Lubr. Tribol. **71**(7), 915–923 (2019)
22. Kumar, V., Sharma, S.C.: Combined influence of couple stress lubricant, recess geometry and method of compensation on the performance of hydrostatic circular thrust pad bearing. Proc. Inst. Mech. Eng. Part J: J. Eng. Tribol. **231**(6), 716–733 (2017)
23. Mokhiamer, U., Crosby, W., El-Gamal, H.: A study of a journal bearing lubricated by fluids with couple stress considering the elasticity of the liner. Wear **224**(2), 194–201 (1999)
24. Khonsari, M.M., Brewe, D.E.: On the performance of finite journal bearings lubricated with micropolar fluids. Tribol. Trans. **32**(2), 155–160 (1989)

25. Kango, S., Sharma, R.K.: Studies on the influence of surface texture on the performance of hydrodynamic journal bearing using power law model. Int. J. Surf. Sci. Eng. **4**(4–6), 505–524 (2010)
26. Kumar, V., Sharma, S.C.: Finite element method analysis of hydrostatic thrust pad bearings operating with electrically conducting lubricant. Proc. Inst. Mech. Eng. Part J: J. Eng. Tribol. **232**(10), 1318–1331 (2018)

Design and Comparison of Different Available Model of Prosthetic Knee Joint

Himakshi Pareta and **Manish Chaturvedi**

1 Introduction

The composite materials were as traditional material in many engineering fields, but it was not stable at high temperature conditions. Later a ceramic material was used in place of composite material. It was more stable at high temperature conditions than composite materials but it mechanically unstable due to low toughness. To get rid of this instability, the new material has been invented in 1984 in Japan called as functionally graded material (FGM) [1]. It can withstand at high temperature conditions up to 2000 °C and specially designed for aerospace industries. The FGM is referred as a material with changing porosity, microstructure and composition through the volume of material (1). To perform a set of various functions, the FGM was designed by varying properties with the volume of bulk material regarding their area of application in which they can be used [2]. There are different types of FGM available include.

2 Literature Survey

Shah et al. [3] represented a study on natural human knee joint through FEM simulation-based analysis. The aim was to study ligaments under the loads ranging from 10 to 1010 N. The conclusion of the study is that any increment of force from 10 to 1010 N leads to decrement in fatigue life of human knee joint. High performance and low-cost prosthetic knee joint (PKJ) were developed by Fu et al. [4] by using experimental and simulation-based analysis. The material used for designing PKJ model with parallel spring and damping mechanism is 7075 aluminium alloy.

H. Pareta (✉) · M. Chaturvedi
Department of Mechanical Engineering, Rajasthan Technical University, Kota, Rajasthan, India
e-mail: hamnshi42576@gmail.com

The testing was done by applying a 2500 N vertical force on PKJ modal. It was observed that the displacement is 0.2593 mm and max. stress is 1.1765×108 N/m^2, and parallel spring buffers flexion angle and damper regulate the swing speed of the shank. Simulation-based FEM analysis was studied to designed four-bar linkage transfemoral AKP model by Alhakim et al. [5]. The aim of the study is to find out the stress analysis of AKP transfemoral model in gait cycle. The material used for this AKP modal is Al-alloy 6061. The load of 1000 N has been applied on the modal at three moment position, i.e., 00-150, 150-00, and 00-300. Maximum von Mises occurs at 14.570 and minimum at 00 at the face of initial contact. Microcontroller-based transfemural PKJ was developed by Purba and Pudjilaksono [6]. To improve the passive functionality of PKJ model and also reducing manufacturing cost and weight, simulation-based FEM analysis is used. The materials used for developing model are Al-alloy 6061, Al-alloy 7075, AISI 4103 steel. The testing was done at 1200 N vertical load. As a result, the best material selected for manufacturing PKJ was Al-alloy 6061.

3 Prosthetic Knee Joint Specifications and Materials

The knee joint should be capable to withstand during shocks, and transient loads occur under human walking conditions. The prosthetic knee joint should be capable to bear approximately three times the patient's bodyweight. All prosthetic knee joint models are assumed to be made up from aluminium alloy Al-T6061 [7]. Aluminium alloy is used to develop all the parts of prosthetic knee joints because aluminium is easily available at low cost, easy to machine, has a high strength-to-weight ratio and acceptable safety. Easy machining process of aluminium saves the manufacturing time thus helps to reduce manufacturing cost. Table 1 illustrates the material and mechanical properties used for the current study purpose.

4 Methodology

The present study be based on two steps, firstly the process of modelling and secondly, the stress analysis. All of them are performed using SOLIDWORKS 15 and ANSYS 18.1. Three types of prosthetic knee models were used on this current work named as D1, D2, D3. The stress analysis of all 3D models based on finite element method is performed to determine the stress distribution. The fine meshing of 2 mm size has been used for model in study (Fig. 1).

Table 1 Material and mechanical properties of Al-T6061

No.	Property	Values (Al-T6061)	Unit
1	Density	2.77	g/cm3
Isotropic elasticity			
2	Young's modulus	68,900	MPa
3	Poisson ratio	0.33	-
4	Bulk modulus	6.7549E+10	Pa
5	Shear modulus	2.5902E+10	Pa
Strength properties			
6	Tensile yield strength	276	MPa
7	Compressive yield strength	276	MPa
8	Tensile ultimate strength	310	MPa
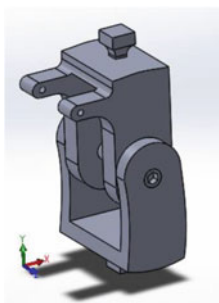
D1 Single point prosthetic knee joint
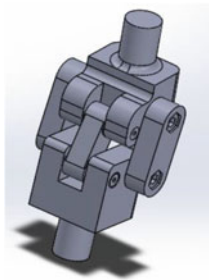
D2 Polycentric Jaipur Stanford knee joint
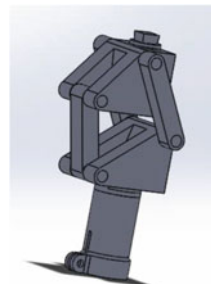
D3 Polycentric Above knee prosthetic joint

Fig. 1 Geometry of three different prosthetic knee joints

5   Boundary Condition for Analysis Model of Knee Joint

The boundary condition used for performing analysis on prosthetic knee joint model includes two points application, at one point the load was applied while the other end was kept fixed. A vertical load of 1000 N was applied at tip of upper part of femoral component while the bottom part of tibial component was kept fixed. All 3D models of prosthetic knee joints were simulated the load when the prosthetic knee joint model moves at an angle of 0.140, 4.60, 14.270, 14.570. Figure 2 illustrates the boundary conditions applied to single axis PKJ model for all four angles. All the boundary conditions were applied to the angle positions that form during the initial phase of contact, loading response and mid-stance. Similar boundary conditions and

Single axis PKJ (Load = 1000N)	
Angle = 0.17^0	Angle = 4.6^0
Angle = 14.27^0	Angle = 14.57^0
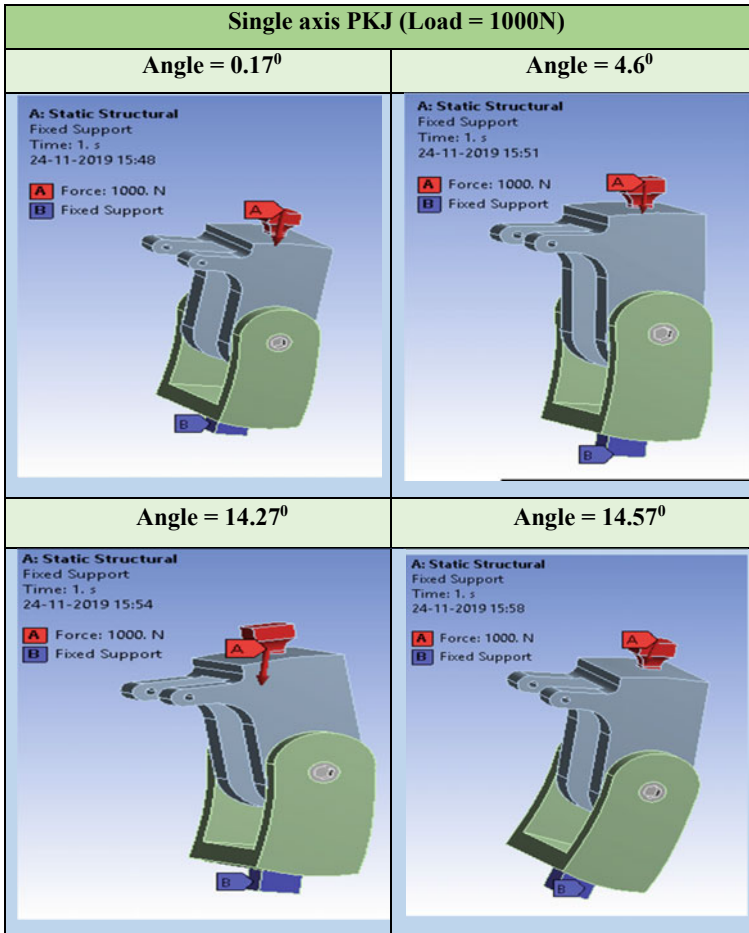
Fig. 2 Boundary conditions applied on single axis prosthetic knee joint validation study

motion angles were taken for all the prosthetic knee joint models for performing finite element analysis using ANSYS WORKBENCH 18.1.

Design I prosthetic knee joint was validated against the work done by Kadhim et al. under similar loading as mentioned in paper [8]. Prosthetic knee design I model was developed of approximately similar dimensions as that of reference model mentioned in [8]. Figure 3 shows the maximum von Mises stresses developed in the reference model and design model I. The material assignment for both the models was similar that of aluminium alloy 6061 and both the models were subjected to similar loading conditions. Figure 3 clearly illustrates that the maximum stress developed in design I was 38.76 MPa which was close enough to the reference model stresses (40.85 MPa).

Fig. 3 Stress distribution in reference model and prosthetic knee design I
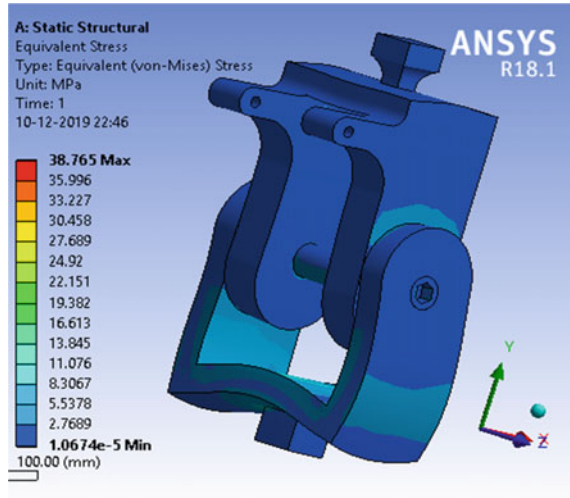
6 Parametric Study

This study involves the comparison between the three prosthetic knee joint models at different angles. All the prosthetic knee joints are compared and analysed by using ANSYS WORKBENCH 18.1. The observed maximum von Mises stresses in all model at different angles have been summarized in Table 2.

The weight of design I including the assembly parts is 1.19 kg and the overall weight of design II including the assembly parts is 1.42 kg and weight of design III is 1.26 kg. So, on the comparison basis on weight, the design III will be best. Though the single axis PKJ is seen to have lightest be simple among all the three designs, it may be difficult in single-axis PKJ to control or if locked and result a different gait from the natural gait. Polycentric knee designs for prostheses can offer a more similar or mimic of natural gait by permitting the knee to flex during walking while allowing the user to control the joint with less effort. An appropriately designed polycentric knee, due to the changing position of the instantaneous centre of rotation (ICR), can

Table 2 Observed maximum von Mises stresses in all model at different angles

Design/Phase at different position	Phase of the initial contact angle 0.170 maximum von Mises stress (MPa)	Phase of loading angle 4.60 maximum von Mises stress (MPa)	Phase of mid-stance angle 14.270 maximum von Mises stress (MPa)	Phase of terminal stance angle 14.570 maximum von Mises stress (MPa)
Design I	**28.776**	40.361	**68.622**	69.514
Design II	53.298	46.008	69.747	76.536
Design III	**44.002**	**40.169**	**30.263**	**28.505**

help an amputee user to have better voluntary control—that is, the user may utilize the residual thigh musculature more effectively to provide stable load bearing with lower effort than a hinge knee (when knee flexes a curve is traced by the ICR which is known as centrode) (Fig. 4).

There are also some more advantages of a polycentric PKJ that is high knee flexion angles and good clearance of toe during swing due to limb length shortening. A four-bar mechanism is the simplest and mostly used solution for a polycentric PKJ. The polycentric knee design III is seen to be optimum through the point of functionality and weight of model. The final results are:

1.   Initial phase at 0.170: D2 > D3 > D1
2.   Phase of loading at 4.6: D2 > D1 > D3
3.   Mid-stance phase at 14.270: D2 > D1 > D3
4.   Terminal phase at 14.570: D2 > D1 > D3

7   Conclusion

Hence, on the basis of above results, it was clear that the knee joint design D3 is the optimum design on the basis of maximum stresses, manoeuvrability and weight reduction parameters. Though D1 design is simple and has minimum stress in initial phase of walking but as it works on the single-axis mechanism and restricts the motion of prosthetic knee joint, it is locked and requires large effort to control it. D2 and D3 both prosthetic knee designs work on the multi-axis principle but it was found that D3 design requires the less machining processes in comparison to D2 design. Thus, D3 design seen to be optimum design among all current prosthetic knee designs under given loading conditions.

Angle= 0.17⁰

Angle =4.6⁰

Angle =14.27⁰

Angle= 14.57⁰
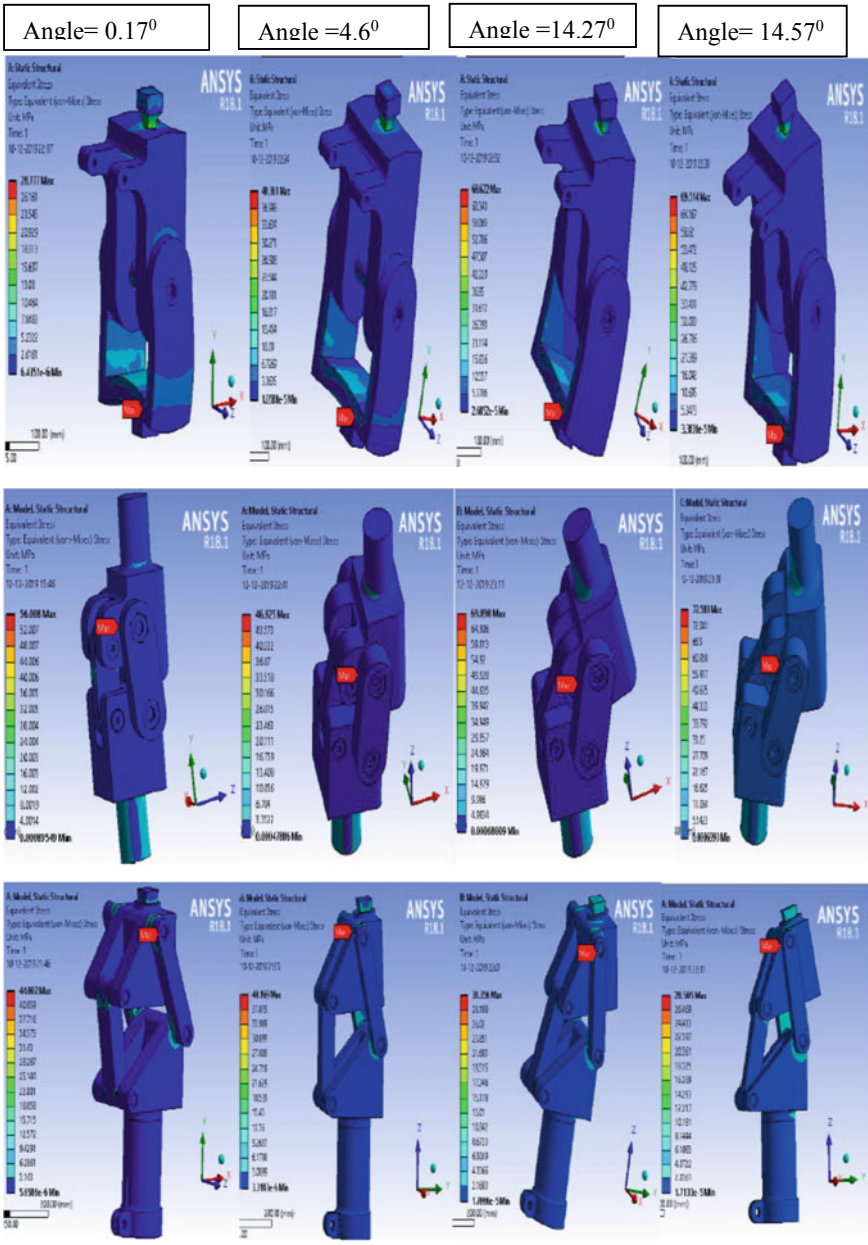
Fig. 4 Stress distribution of three different models at different phase angle

References

1. Lambrecht, B.G.A.: Design of a Hybrid Passive-Active Prosthesis for Above-Knee Amputees (2005)
2. Arya, A.P., Lees, A., Nirula, H.C., Klenerman, L.: A biomechanical comparison of the SACH, Seattle and Jaipur feet using ground reaction forces (1995)
3. Shah, Y., Bhave, A., Sonetha, V.: Fatigue analysis of the knee joint. Int. Conf. Adv. Comput. Technol. Appl. (2015)
4. Fu, H., Zhang, X., Wang, X., Yang, R., Li, J., Wang, L., Zhang, N., Li, G., Liu, T., Fan, B., Inoue, Y.: A novel prosthetic knee joint with a parallel spring and damping mechanism. Int. J. Adv. Robot. Syst. 1–9 (2016)
5. Alhakim, S.B.P., Setiana, B., Ismail, R., Tauviqirrahman, M.: Stress analysis of four-bar linkage transfemoral prosthetic in gait cycle. Int. J. Appl. Eng. Res. **12**(20), 9333–9337 (2017). ISSN 0973-4562
6. Purba, S.E., Pudjilaksono, L.: Experiment and fem simulation of static test of knee joint prostheses. AIP Conf. Proc. **1983**, 030019 (2018)
7. Borjian, R., Lim, J., Khamesee, M.B., Melek, W.: The design of an intelligent mechanical active prosthetic knee. IEEE (2008)
8. Kadhim, F.M., Chiad, J.S., Takhakh, A.M.: Design and manufacturing knee joint for smart transfemoral prosthetic. IOP Conf. Ser. Mater. Sci. Eng. **454**, 012078 (2018)

Numerical Investigations on Steady-State Dynamic and Transient Rolling of Automobile Tire

Subhajit Konar and **Vijay Gautam**

1 Introduction

Numerical analysis (FEA) of an automotive tire has become an inevitable aspect of the tire design coupled with failure analysis for almost all the automotive industries dealing in tire design and manufacturing. Tire modeling with Abaqus is generally a complicated process involving complex material models comprising of hyper-elastic rubber and textile reinforcements, large model size data, too lengthy simulation time, and various convergence issues. FEA is a powerful simulation software solution which is adopted in many automotive and tire industries, for understanding the efficient behavior of engineering systems under a variety of loading conditions. An FE model provides fairly accurate results as has been shown by many researchers. An FE analysis helps in accurately simulating the actual conditions without performing the experiment. CAE is one of the FE tools that has been mostly employed in the tire industry due to its versatile capability in modeling composite material layers with a considerable focus on the tire structure to a bigger scenario than is available in other numerical analysis software [1]. Hall et al. presented a paper [2] with explicit finite element results for the transient macroscopic behavior of an automotive tire with the objective to develop a methodology for modeling for an advanced LS-DYNA finite element simulation of a rolling tire that can be used to provide internal transient stresses and strains to address the design and development of sensor systems technology for the industry. Xia [3] developed a three-dimensional finite element model for tire and terrain interaction as well as a finite strain hyper-elasticity model for material modeling of rubber using kinematic behavior.

S. Konar (✉) · V. Gautam
Department of Mechanical, Production & Industrial and Automobile Engineering, Delhi
Technological University, North West Delhi, Delhi 110042, India
e-mail: subhokonar94@gmail.com

V. Gautam
e-mail: vijaygautam@dce.ac.in

The tire-body is generally analyzed and understood to have a longer fiber composite material where there is an interaction of the elastomeric matrix of rubber with enforcing steel wires as well as other non-metallic reinforcements, known as textile cords (such as PA 6.6, PES textile fibers). The tire-body behaves as a specific composite material with different cord angles, thicknesses of various layered plies, cord materials, cord constructions, and the base materials (different chemical compositions of rubbers as a matrix). The composite structural parts of the tire-body are steel wire/cord belts, textile carcass, and also a belt made of textile. The material used in tire is also investigated by many papers. For material modeling, there exist a number of material models which have been used to evaluate and describe a nonlinear behavior of stress–strain in rubbers, out of which the most important models are Arruda–Boyce [4], Marlow [5], Ogden, Polynomial, Van der Waals (Kilian Model), and Yeoh. Mooney-Rivlin model and Ogden model are the most popular. These models were found to be more accurate than other models for FE analysis of tire on Abaqus.

Tire with road interaction is being studied and optimized to enhance the ease of handling of a vehicle to ensure the safety and comfort of the occupants under challenging circumstances. Conradie studied behavior of off-road tires due to radial loading conditions [6]. Tires are the only parts of a vehicle which are in intimate contact with the variety of road surfaces. The required safety during acceleration, intermittent braking, frequent steering, and cornering all depend on a relatively small area of contact presented between the road surface and the tires. Due to these reasons, tires are considered the most important components of vehicles as far as the safety is concerned. These are designed to accomplish the fundamental sets of various functions such as offering damping with cushioning, stability on the different terrains, and quite often a better steering response, at the same time reducing rolling resistance and resulting of low noise and vibration. Tires also must withstand stresses due to contact with stones, sharp objects on the road, besides frictional forces due to rolling. Due to these, the probability of failure of tires becomes extremely high. Therefore, the design engineers are taking specific interest in determination of behavior of tires in the area of dynamics of vehicles. Many researchers and investigators have tested and tried to solve intricate and robust mathematical models during the past years to explain the kinematics and dynamics of the rolling of tires on the rigid and deformable surfaces. The simulations of deformations of tire can be utilized as a tool to compare the behavior of tires being operated under a wider range of operating conditions. A lot of research has been carried out on car tires considering calculation of rolling resistance [7], cornering characteristics [8], and tire/terrain interaction [3]. But very few papers are available which discuss the stresses generated due to perforations in a tire.

1.1 Automobile Tire

Tire plays an inevitable role in case of a vehicle movement. It seems to be an unavoidable part of an automobile wheel assembly. Tire acts as a mechanical shock absorber that acts as a cushioning system. It is a rubber casing with steel reinforcement inside gets attached to the wheel rim. It is solely responsible for generating the required amount of friction force. Generally, the tires that are in automobile applications are pneumatic ones. A pneumatic tire is held under high internal air pressure to carry the required amount of load. Usually, a rubber tube is used inside the tire casing for holding air pressure, but nowadays automobile companies are more interested in tubeless tires (Fig. 1).

Forces and Moments Acting on Tires. The coordinate system helps in determining the forces and moments acting on the tire. The force acting along the X-axis is known as longitudinal force (F_x), and the moment acting about X-axis is called overturning couple. The force acting along the Y-axis is known as lateral force (F_y), and the moment acting about Y-axis is called rolling resistance moment. The force acting along the Z-axis is known as vertical force (F_z), and the moment acting about Z-axis is called self-aligning torque. Side drifting is also a phenomenon that is occurred due to the lateral force. The angle between tire direction and traveling direction is called slip angle (α) as shown in Fig. 2.

2 Simulation

Abaqus (version 6.14-5) is used for the simulations of the engineering real-life problems. The software uses three different stages that are preprocessing, solution, and post-processing to solve problems.
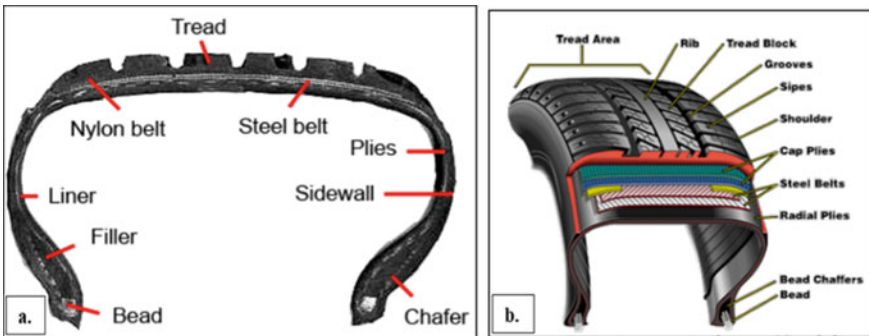
Fig. 1 **a** Cross section of a tire indicating various components, **b** cut section view of an automobile tire

Fig. 2 Forces and moments acting on a tire in three dimensions [6]
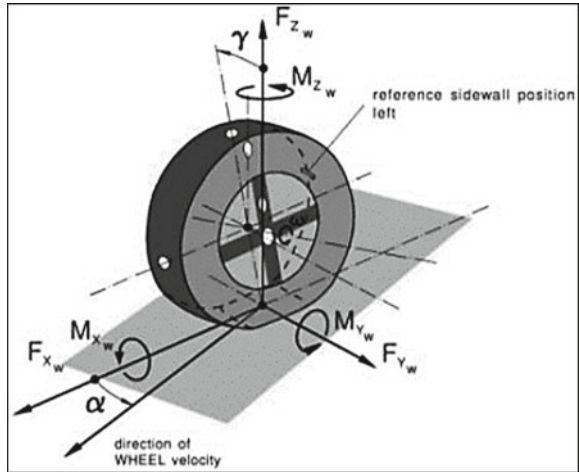
2.1 Part Module

A 2D axis-symmetric model of tire has been created in this module. The entire 3D model has been generated by mirroring the partially generated model with respect to a vertical line situated on the symmetry plane of the tire model. The dimensions of the radial tubeless tire used are **175/80 R14**, as given in Table 1.

The geometry of the part and the 3D model is shown in Fig. 3.

Table 1 Dimensions of the tire used

Parameters	Dimensions
Width if the tire	175 mm
Height of sidewall	140 mm
Diameter of the rim	14 in.
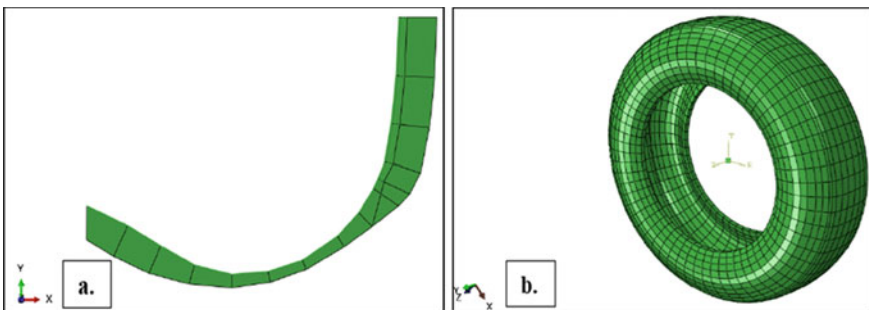
Fig. 3 **a** Axis-symmetric model of the tire and **b** full 3D model of the tire

Table 2 Properties of the carcass

Density (kg/m^3)	Young's modulus (Pa)	Poisson's ratio
1500	9.87×10^9	0.3

Table 3 Properties of belt material

Density (kg/m^3)	Young's modulus (Pa)	Poisson's ratio
5900	172.2×10^9	0.3

2.2 Property Module

Three materials are to be defined by their properties, and then, materials are assigned to the sections, and then, the sections are assigned to the parts, respectively. The rubber is modeled as an incompressible hyper-elastic material and includes a time domain visco-elastic component that is mentioned with the help of Prony series. For an incompressible material, a 1-term Prony series is defined by using shear relaxation modulus ratio, g, and associated relaxation time, T_1. In this paper, the used variables are $g = 0.3$ and $T_1 = 0.1$.

Hyper-Elastic Material Models. Large deformation behavior of materials can be represented by using hyper-elastic materials models. They are commonly used to model mechanical behaviors of unfilled elastomer or filled elastomers, polymeric foams, etc. Hyper-elastic materials are described with the help of a strain-energy density function. The strain-energy density can be used to derive a nonlinear constitutive model (i.e., stresses as a function of large strain deformation measures like deformation gradient or Cauchy–Green tensors, etc.).

Carcass Material. Table 2 shows the properties of the carcass.

Belt Material. AISI S13800 stainless steel is used as the material for the belts. Table 3 shows the properties of this material. The stress–strain graph of rubber is further shown in Fig. 4.

Rubber. Table 4 shows the properties of the hyper-elastic rubber. The stress–strain graph of rubber is further shown in Figs. 4 and 5.

2.3 Step Module

First step is initial step which is auto generated to solve the boundary conditions first without loading. Then according to problem, we can select number of steps mentioned as period of 60 s, max. number of increments of 100, initial increment size of 0.25, minimum increment size of 0.00001, and maximum increment size of 1.
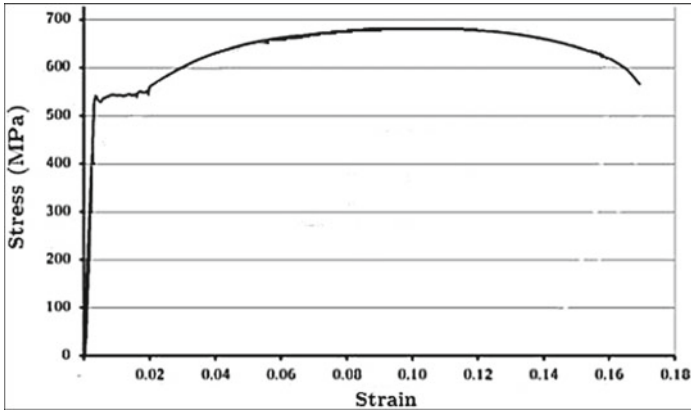
Fig. 4 Stress–strain behavior of belt material (stainless steel)

Table 4 Properties of the hyper-elastic rubber

Density (kg/m³)	Hyper-elastic properties			Viscoelastic properties		
	C10	C01	D1	g_i (shear relaxation modulus ratio)	k_i (bulk relaxation modulus ratio)	tau_i (relaxation time)
1100	1,000,000	0	0	0.3	0	0.1
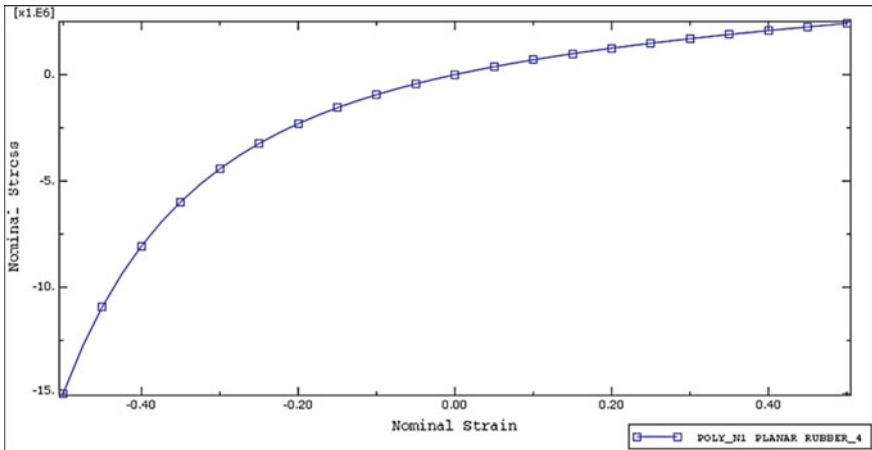
Fig. 5 Stress versus strain graph of hyper-elastic rubber

Table 5 Interaction properties used in simulation

Interaction	Contact property	Friction formulation	Friction coeff.
Tire/road surface	Tangential behavior	Penalty	1

Field Output. Select the output variables in this manager which are required as results are mentioned as stress components and invariants, logarithmic strain components, translation and rotation, translational and rotational velocities, translational and rotational accelerations, contact stresses, slip velocity magnitude, and accumulated slip displacement.

History Output. History output can be mentioned as reaction forces and moments, translation and rotation, and translational and rotational velocities.

2.4 Interaction Module

Define the interaction between the mating parts. In transient analysis of tire, frictional contact is defined between the tire and road surface, and the properties of interaction are also defined like friction coefficient, normal, and tangential behavior. Constraints are also defined in this module.

Interaction Property. Normal behavior—This property is defined for all three types of boundary conditions which is hard contact type. Tangential behavior—It is defined separately for all three conditions as given in Table 5.

2.5 Load Module

In this module, loads and boundary conditions are to be defined for the analysis. The axisymmetric partially generated tire model is loaded with an inflation load of 200 kPa and a footprint load of 1650 N. The rolling analysis is performed with a translational velocity of 10 km/h. Inertia and viscoelasticity are considered in this analysis. During the transient dynamic analysis, the vehicle load is applied to the reference node of the rim. Load distribution on the tire is shown in Fig. 6.

2.6 Meshing

The mechanical model has been presented having meshing elements to be specified as CGAX4H and CGAX3H. The road which has been taken for experiment is defined as analytical rigid body. Meshing of the tire is shown in Fig. 7.

Fig. 6 Load distribution on the tire
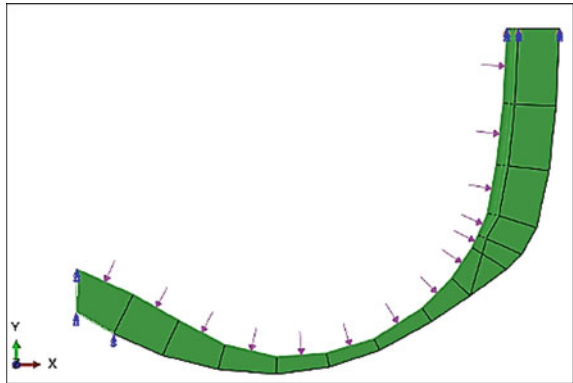
Fig. 7 Meshing of the tire
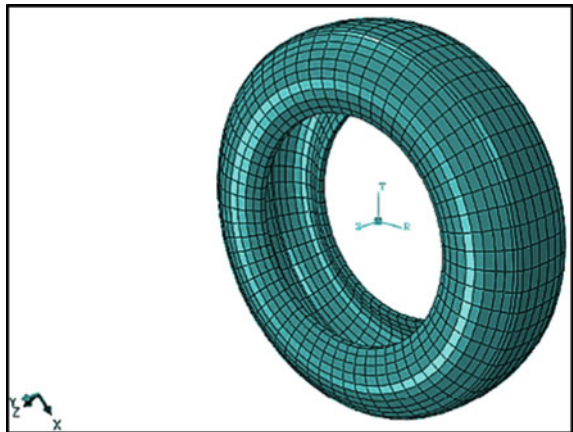
2.7 Job Module

In this module, analysis of the solution is done by solution technique full newton method. Solution of the problem is done in incremental steps.

2.8 Virtualization Module

In this module, the result of output variables is shown by the image, animation, and graphs for every node and element. The result of temperature and contact pressure is shown on the animation.
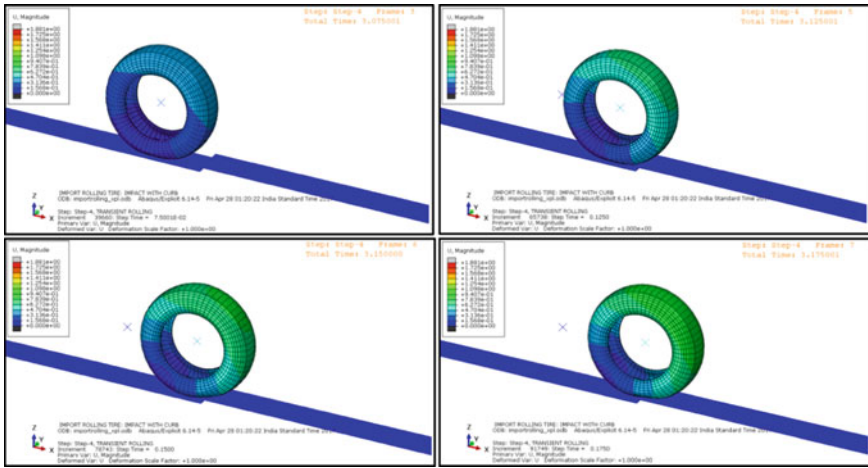
Fig. 8 Total displacement of the tire at different frames

3 Results and Discussion

This project analyzes the impact on a tire due to a curb. The steel-belted tire contains the AISI S13800 stainless steel wires wound closely around the tire. The yield strength of the steel is 550 MPa, and a tensile strength of 680 MPa. The dynamic impact on the tire due to the unevenness of the road is responsible for the high frequency noise. This high frequency noise is revealed from the high values of reaction forces on the rim. The use of visco-elastic material in the matrix enhances the damping property that eventually reduces the high frequency noise.

The following images show the displacement of the tire as it moves forward. The total displacement is the vector sum of the displacements in the X-, Y-, and Z-directions (Fig. 8).

The maximum stress before hitting the curb is 327 MPa. After hitting the curb, the simulation shows an increase in the stress to a maximum value of 366 MPa. The impact with irregularities on the road can induce extremely high stresses which can lead to cracks on the tire and weakening of the belt material. The tire starts to move over the curb generating a maximum stress of 333.3 MPa at the point of contact with the curb as shown in Fig. 9.

4 Conclusions

The stress–strain relationship obtained by tensile testing of material results was fitted to select the suitable constitutive model. The numerical analysis is performed, and the results are compared to the physical experiment to validate the hyper-elastic material
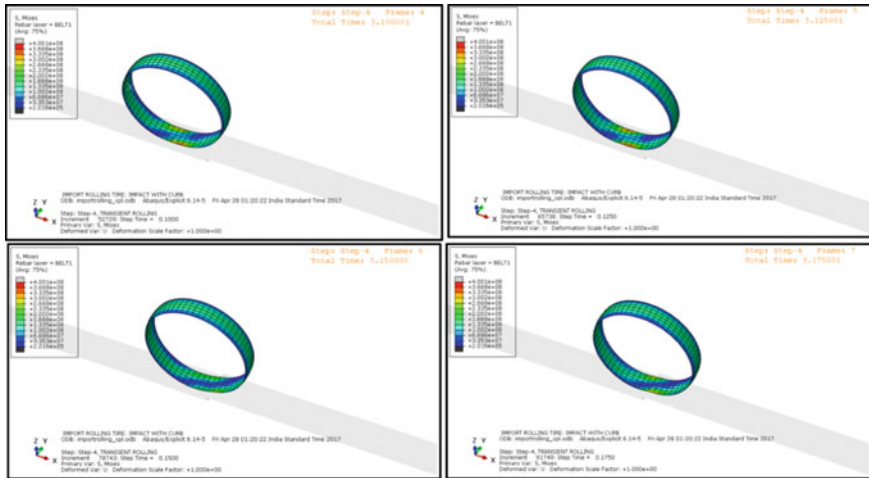
Fig. 9 The von-Mises stress distribution in belt 1 at different frames

model. The maximum stress generated in the belts of SS is 366 MPa, whereas the tensile yield strength of the material is 550 MPa. Hence, the stresses in the belts are well within their limits. The maximum stress before hitting the curb is 327 MPa. After hitting the curb, the simulation shows an increase in the stress to a maximum value of 366 MPa. The impact with irregularities on the road can induce extremely high stresses which can lead to cracks on the tire and weakening of the belt material.

The cyclic application and removal of stresses can lead to fatigue in the belt. After permissible number of cycles, the compression and elongation of material can lead to its failure due to fatigue. Thus, we have computed the results with acceptable errors by using a method which resulted in significant computational and time savings.

References

1. Behroozi, M., Olatunbosun, O.A., Ding, W.: Finite element analysis of aircraft tyre–effect of model complexity on tyre performance characteristics. Mater. Des. **35**, 810–819 (2012)
2. Marlow, R.S.: A general first-invariant hyperelastic constitutive model. Const. Models Rubber, 157–160 (2003)
3. Ogden, R.W., Saccomandi, G., Sgura, I.: Fitting hyperelastic models to experimental data. Comput. Mech. **34**(6), 484–502 (2004)
4. Kilian, H.G.: Equation of state of real networks. Polymer **22**(2), 209–217 (1981)
5. Yeoh, O.H., Fleming, P.D.: A new attempt to reconcile the statistical and phenomenological theories of rubber elasticity. J. Polym. Sci. Part B: Polym. Phys. **35**(12), 1919–1931 (1997)
6. Ebbott, T.G., Hohman, R.L., Jeusette, J.P., Kerchman, V.: Tire temperature and rolling resistance prediction with finite element analysis. Tire Sci. Technol. **27**(1), 2–21 (1999)
7. Erşahin, M. A.: Finite element analysis of cornering characteristics of rotating tires (Doctoral dissertation, METU). (2003)

8. Hall, W., Mottram, J.T., Jones, R.P.: Finite element simulation of a rolling automobile tyre to understand its transient macroscopic behavior. Proc. Inst. Mech. Eng., Part D: J. Automob. Eng. **218**(12), 1393–1408 (2004)

Design and FEA Analysis of Polycaprolactone Based Bio-resorbable Cardiovascular Stent

Hrishabh Dubey [ID]**, Nidhi Dixit** [ID]**, and Prashant K. Jain** [ID]

1 Introduction

Percutaneous coronary intervention (PCI) is the most commonly used non-surgical procedure and currently used alternative to coronary artery bypass grafting (CABG). CABG is a procedure which includes replacement of the existing damaged artery with other grafting vessels from somewhere else in the body [1]. Stents made up of nitinol alloy, titanium, and stainless steel are being used by the medical practitioners for PCI. However, these metal stents sometimes induce an inflammatory response that can lead to hyperplasia. The other problems related to metallic stents also include development of blood clots at the site of stenting which can eventually lead to a cardiac arrest [2]. On the other hand, bio-resorbable drug eluting stents can eliminate the problems associated with the presently used stents. These bio-resorbable stents can be used for stenting of the coronary arteries for sufficient period of time needed for the recovery of the narrowed artery to its original shape [3].

The various early designs that include Wallstent by Schneider, Palmaz-Schatz by Johnson & Johnson, and Wiktor by Medtronic have now given way to the multilink, micro, and multiple other designs [4–6]. The selection of the material for metals stents depends on properties such as strength, elasticity, and malleability. Properties like shape memory and biocompatibility are also taken into account while selecting the material [7]. Various materials that are found compatible to be used for the fabrication of stents include stainless steel, tantalum, and nitinol alloys. Nitinol possess thermal shape memory property that allows self-expansion and thermally induced collapse during deployment and removal process, respectively. In addition to this, nitinol also possess superelastic property [8, 9]. The surfaces of the metal stents

H. Dubey (✉)
Faculty of Engineering, Global Nature Care Sangthan's Group of Institution, Jabalpur, India
e-mail: me171049@global.org.in

N. Dixit · P. K. Jain
PDPM Indian Institute of Information Technology, Design and Manufacturing, Jabalpur, India

Table 1 Properties of polycaprolactone

Property	Value
Glass transition temperature	$-60\ °C$
Maximum temperature: mechanical	40 °C
Density	1.1 g/cm³
Young's modulus	1.2 GPa
Poisson's ratio	0.3
Bulk modulus	1E±09 Pa
Shear modulus	4.615E±08 Pa
Ultimate tensile strength	10 MPa
Elongation at break	300%

are mildly thrombogenic and require anticoagulant or antiplatelet procedure in short term. However, the limitation of using metal stents is that these metallic stents are impossible to remove practically [6].

Presently, several reports have appeared regarding biodegradable as well as non-biodegradable polymeric stents having easy loading of drug. Several polymers displaying shape memory behavior have been introduced with increasing trends in shape memory polymers. Aliphatic polyesters such as poly-L-lactic acid (PLLA), polycaprolactone (PCL), poly-D, L-lactic acid (PDLLA), and polyglycolic (PGA) acid are presently being used for the fabrication of bio-resorbable stents [8]. The principle of degradation for polymeric stents is the hydrolysis in the polymer backbone of ester bond. However, it has been reported that in few cases due to improper sterilization, the stents sometimes also show inflammatory response, thus leading to abnormal behavior and functioning of the associated organ [6]. In this study, the analysis for deformation and stresses at stenting site were analyzed using computational numerical methods. This study summarizes the use of PCL as a bio-resorbable material for stents (Table 1).

2 Materials and Methods

2.1 Material

Polycaprolactone (PCL), due to its medical approval as a material for drug delivery devices, is used in this study despite of having low strength but better flexibility. PCL is having a degradation time of 18–24 months which is sufficient time for the artery to regain its normal shape [10]. It also has low specific heat and conductivity making it feasible and ideal for small-scale modeling and fabrication of part using rapid prototyping [11–13]. The balloon used for inflation was defined using hyperelastic Mooney-Rivlin 2 parameter [14] (Table 2).

Table 2 Properties of balloon material

Property	Value
Mooney-Rivlin 2 property	–
Material constant C10	1.06 MPa
Material constant C01	0.71 MPa
Incompressibility parameter D1	$0 \, Pa^{-1}$

2.2 Stent Design

The cardiovascular stent was modeled using SoildWorks as shown in Fig. 1, using hexagonal approach. The length of the stent was kept 10.81 mm, the outer diameter 3.74 mm, strut thickness minimum 0.1 mm, and maximum strut thickness 0.25 mm. The maximal diagonal length was kept 1.71 mm, number of units along circumference were kept 6, and the maximum width of the strut was kept at 0.15 mm [14].

(A) Front View

(B) Top View

(C) Side View

(D) Isometric View
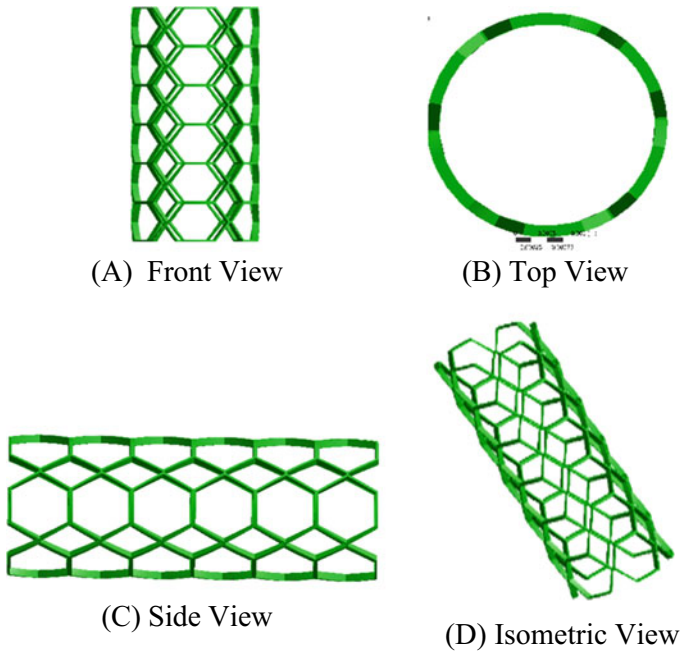
Fig. 1 Various views of modeled stent

2.3 Analysis and Input Parameters

The finite element analysis is a numerical approach in solving engineering problems and mathematical physics. FEA is not only limited to the structural strength and heat and mass transfer analysis but also applicable on vast fields. The static structural analysis of stent was done using ANSYS Workbench. The designed and modeled stent was imported in STEP format. Only one ring of the stent was taken into account for lesser consumption of time and resources, using asymmetrical approach. Large deflection was switched on due to hyperelastic behavior of balloon. The stent was analyzed for the instance at which the balloon has inflated to its maximum. The meshing was done using ANSYS meshing, the default mesh was generated with elements behavior set to quadratic, and refinement was applied. The total number of nodes and elements were 10,187 and 51,113, respectively. The material was taken as polycaprolactone. The pressure of 0.6 MPa was applied at the wall of balloon. Fixed support at the ends with no slip condition was assumed as shown in Fig. 2 [12].

(A) Stent During Inflation

(B) Meshed Stent

(C) Analysis Conditions
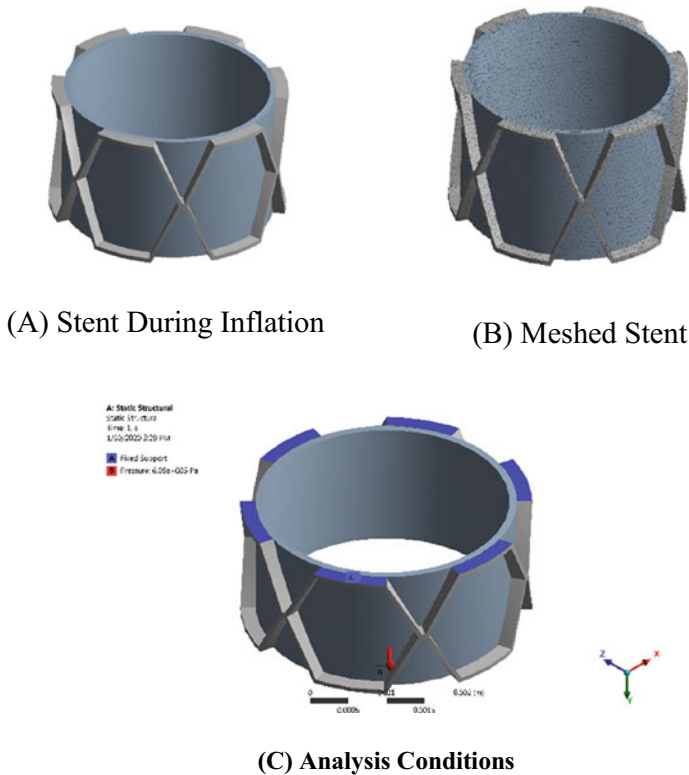
Fig. 2 Analysis setup

S. No.	Time(s)	Minimum (Pa)	Maximum (MPa)
Table 3 Equivalent stress (von-Mises stress)			
1	0.2	85.215	6.2827E±00
2	0.4	348.51	1.2147 E±01
3	0.6	362.81	1.8052 E±01
4	0.9	411.31	2.671 E±01
5	1	436.68	2.9578 E±01

The results were analyzed for total deformation and equivalent stresses (von-Mises stresses).

3 Results and Discussion

3.1 Finite Element Analysis

For testing the compressive and effective tensile modulus of the modeled stent geometry, finite element analysis was used.

It generally gives an error of about 30%. The designed model was tested for its structural strength at the instant of maximum inflation of balloon. The minimum and maximum stress was 85.215 Pa and 2.95E07 Pa at an instant of 0.2 s and 1 s, respectively, as given in Table 3, an increase in stress is observed with respect to increase in time.

The stress versus time curve was plotted and found approximately linear as shown in Fig. 3.
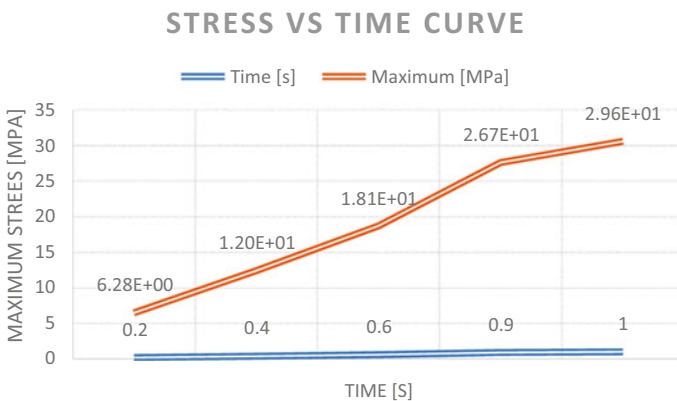
Fig. 3 Stress versus time curve

Table 4 Total deformation

S. No.	Time(s)	Minimum (mm)	Maximum (mm)
1	0.2	0	5.5691E−06
2	0.4	0	2.4185E−05
3	0.6	0	4.2087E−05
4	0.9	0	7.762E−05
5	1	0	1.138E−04

The maximum deformation of 0.1381 mm at time 1 s and minimum deformation of 0.0055 mm as given in Table 4 were observed due to the flow of blood over the site of stenting. The graph of time versus deformation was plotted, and the curve obtained is shown in Fig. 4.

Figures 5 and 6 represent equivalent von-Mises stress and total deformation that occurs at the time of maximum inflation of balloon during angioplasty. Only a single ring of the stent was analyzed for minimum consumption of resources and time.
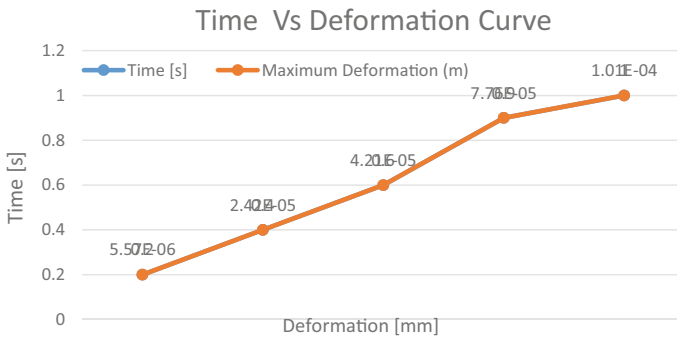
Fig. 4 Time versus deformation curve

Fig. 5 Equivalent stress (von-Mises stress)
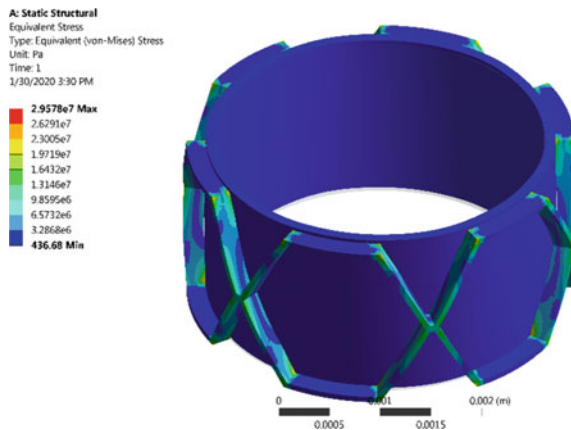
Fig. 6 Total deformation in stent
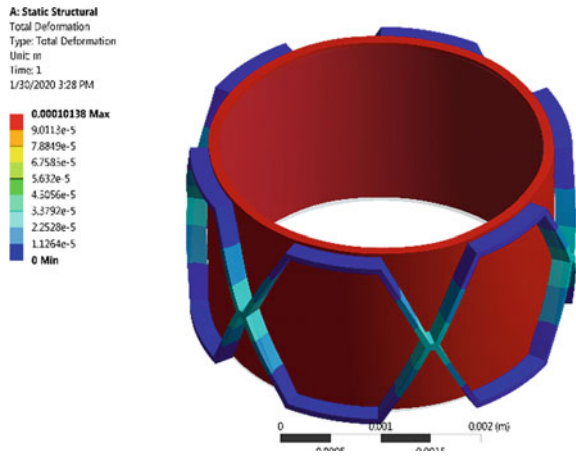
4 Conclusion

The stent was modeled using polycaprolactone for its application as a material based on its nature ideal for small-sized rapid prototyping biomedical devices. The computer-aided design of the stent was developed as per the actual dimensions. The structural analysis of the stent was done using ANSYS Workbench for finding out the mechanical properties like equivalent stress and total deformation of the designed stent. After analyzing the obtained results from computational finite element analysis, it is concluded that the bio-resorbable stent made from polycaprolactone has the maximum von-Mises stress of 29.57 MPa and a total deformation of 1.01 mm. The mechanical strength is defined by the pressure exerted by the balloon on the wall of the stent at maximum inflation, also the mechanical properties of the stent are majorly dependent on the material and the design of the stent.

References

1. Serruys, P.W., de Jaegere, P., Kiemeneij, F., Macaya, C., Rutsch, W., Heyndrickx, G., Morel, M.: A comparison of balloon-expandable-stent implantation with balloon angioplasty in patients with coronary artery disease (1994)
2. Hoffmann, R., Mintz, G.S.: Coronary in-stent restenosis—predictors, treatment and prevention. Eur. Heart J. **21**(21), 1739–1749 (2000)
3. Eberhart, R.C., et al.: Bioresorbable polymeric stents: current status and future promise. J. Biomater. Sci. Polym. Ed. **14**(4), 299–312 (2003)
4. Thrinayan, M., Mishra, S., Murali, C., Mahesh, N., Muthu, P.: Patient specific coronary stent designing and its computational analysis using ANSYS patient specific coronary stent designing and its computational analysis using ANSYS (2019)
5. Escaned, et al.: Propensity and mechanisms of restenosis in different coronary stent designs. J. Am. Coll. Cardiol. **34**(5), 1490–1497 (1999)
6. Kastrati, A., et al.: Restenosis after coronary placement of various stent types. Am. J. Cardiol. **87**(1), 34–39 (2001)
7. Kokot, G., Kuś, W., Dobrzyński, P., Sobota, M., Smola, A., Kasperczyk, J.: A project of bioresorbable self-expanding vascular stents. The crimping process numerical simulation. AIP Conf. Proc. **1922**, 1–7 (2018)
8. Wen C., et al.: Mechanical behaviors and biomedical applications of shape memory materials: a review **5**(4) (2018)
9. Wen, C.E., Xiong, J.Y., Li, Y.C., Hodgson, P.D.: Porous shape memory alloy scaffolds for biomedical applications: a review. Phys. Scr. T, **T139** (2010)
10. Bassi, A.K., Gough, J.E., Zakikhani, M., Downes, S.: The chemical and physical properties of poly (ε-caprolactone) Scaffolds functionalised with poly (vinyl phosphonic acid-co-acrylic acid) **2011** (2011)
11. Al-abassi, A.: Finite element analysis of shape memory alloy NiTi stent in (2017)
12. Engineering, M., Engineering, F.: Computational material analysis of structural and hemo-dynamic model of coronary stent by CFD/FEA in computer aided mechanical engineering approach. **130**(1), 249–251 (2016)
13. Martin, D.: ARROW @ TU Dublin computational structural modelling of coronary stent deployment : a review (2011)
14. Alagarsamy, K., Fortier, A., Kumar, N., Mohammad, A., Banerjee, S., Carolina, N.: Computational modeling of stent implant procedure and comparison of different stent materials **1**, 1–10 (2016)

Mathematical Analysis of a Spiral Passive Micromixer

Syed Farhan Javed [iD]**, Mohammad Zunaid** [iD]**,
and Mubashshir Ahmad Ansari** [iD]

1 Introduction

The micromixing depends on the contact surface area and the characteristic mixing length (diffusion length), and in order to increase the mixing efficiency of the fluids, contact surface area must be increased, and the characteristic mixing length should be reduced. This can also be done by either modifying the given microchannel geometry or putting obstacles inside the micromixer channel. By modifying the micromixer geometry, we do not always achieve better micromixing efficiency. We need to first analyze the flow regimes inside the micromixer.

In past few recent years, various passive micromixers have been reported. The proposed passive micromixer design uses topology optimization technique [1]. Circular (TMC_x) structures have been used which increases mixing efficiently. Mixing efficiency comes out to be 95.9%. The design can also be modified with ridges [2]. The mixing index and pressure drop at the outlet is observed. An analysis using Taguchi method was performed [3]. Three passive micromixers designs are studied, namely active, passive, and active-passive. Mixing index was observed for different parameters of frequency, velocity, and voltage. At time of 0.2 s, an efficiency of about 99.6% is observed. The triangular-shaped ridges enhance the micromixer efficiency. The study inside simple T shaped micromixers is done [4]. Higher pressure drop is observed in case of water-ethanol mixing. The two layer serpentine microchannel is fabricated for low Reynolds number [5]. Another technique is applying optimization method on zigzag channels [6]. For Reynolds number less than 0.5 and greater than 5, mixing index of about 93% is observed. And also between 0.5 and 5, mixing index of

S. F. Javed (✉) · M. Zunaid
Department of Mechanical Engineering, Delhi Technological University, North West Delhi, Delhi 110042, India
e-mail: s.farhanjaved@gmail.com

M. A. Ansari
Department of Mechanical Engineering, Aligarh Muslim University, Aligarh 202002, India

90% is found. Similar technique is the use of topological micromixers with reversed flow TMRFx (x have different values) [7]. TMRF$_{0.75}$ shows great mixing performance between Reynolds number 0.1 and 10 and becomes better beyond mentioned values. A newly designed HC micromixer is compared to tear drop and chain micromixer [8]. The mixing efficiency achieved is greater than 90%. The passive micromixer in the form of 3D over bridge is fabricated to enhance mixing efficiency [9]. An efficiency of up to 90% is achieved between Reynolds number 0.01 and 200. An efficiency of greater than 90% can also be obtained by varying flow rates.

A new design with trapezoidal zigzag channels is also suggested [10]. The mixing performance is analyzed at three different Reynolds number 0.5, 5, and 50. Mixing efficiency greater than 85% is achieved throughout. Another three-dimensional Tesla model is developed for bio-applications [11]. It showed great mixing performance ranging from 0.1 to 100 Reynolds number. Its mixing effectiveness in the binding reaction of antibodies for detecting antigens of lung cancer is appreciable. The simple T shape micromixer with different geometrical aspect ratio (width to height ratio) is observed [12]. By varying the ratio and with increasing Re, it shows completely different results. Another case of T shape but with obstacles is observed [13]. The numerical results show improved mixing index in T shaped micromixer with obstacles and grooved micromixer than that of the basic design by 37.2% and 43.8%, respectively. The geometry of cross-linked dual helical is also developed and analyzed [14] for low Reynolds number. It shows excellent efficiency up to 99% in a very short length of about four cycles. A new type of multimixing mechanism is developed for novel micromixer [15] for high efficiency at low Re. An efficiency of 80–85% is attained. Another novel micromixer with trapezoidal blades is developed for mixing at low Re [16]. In the range of Re ranging from 0.5 to 60, high mixing efficiency is observed irrespective of the Re. Very high improvement in percentage of mixing as compared to rhombic mixers. Another passive micromixer for bio-applications is developed with elliptical micropillars for human blood mixing [17]. For Re less than 1, it shows an efficiency of greater than 80%. This is a very useful method in blood sample handling. With the periodic variation of velocity profile, multi-objective optimization is done in passive micromixer [18]. Mixing performance is observed with respect to geometrical changes. Another case for spiral micromixing is developed which makes use of logarithmic spiral channels. The mixing performance is analyzed between 0.2 and 100 Reynolds number [19]. The mixer is found to be suitable for Re > 5. The new design with unbalanced three split rhombic sub-channels is proposed and developed [20]. The micromixer is found to be effective for Reynolds number ranging from 30 to 80. Another case is of asymmetric split and recombine mixer with sub-channels [21]. For Re ranging 1–100, it shows better mixing performance due to increased width ratio but also shows higher pressure drop. The use of triangular obstacles or rather baffles is incorporated again [22]. The results of mixing performance is compared with common Y mixer. It shows better performance at Re equals 100 and much better at Re equals 500. In a curved microchannel, circular obstruction is created for mixing between water and ethanol [23]. An efficiency of 88% is observed at Re = 0.1. Minimum efficiency of 72% is observed at Re = 5. The microchannel walls given the shape of semi-elliptical sides
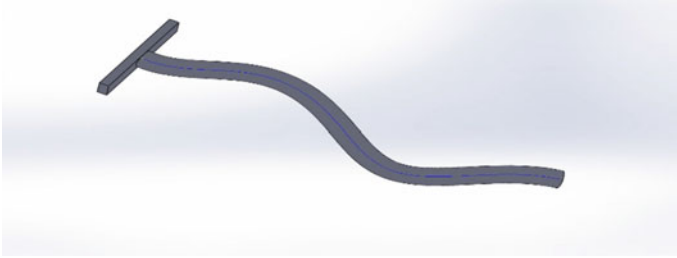
Fig. 1 Geometry of spiral *T* shaped micromixer (same characteristic cross section areas)

is developed [24]. A better mixing efficiency is observed for large expansion ratio. The planar micromixer using circular chambers and crossing constriction channels is developed [25]. It has eight mixing chambers/zones. It has achieved an efficiency of 88% at Re = 10 but is ineffective for Re greater than 10.

2 Geometrical Modeling

In this research, newly designed micromixer in the shape of spiral is fabricated in an effort to increase the micromixer efficiency at significant low Reynolds number. The geometry is made in SolidWorks. The mixing characteristic of water and dye is analyzed at different lengths and at the outlet of mixing channel. The mixing characteristics and efficiency are compared with that of simple *T* shaped micromixer (see validation section). In order to have the same mass flow rate, we have to assign same inflow area at the inlets of the spiral. The mixing channel is given the shape of the spiral with almost two revolutions. The diameter of the mixing spiral channel is made such to accommodate the two fluids gushing toward the channel. The mixing channel is appropriately adjusted to have the same mixing length (Fig. 1). Therefore, the inlet faces are of rectangular cross section, and outlet is circular cross section, i.e., at the end of spiral mixing channel. The specifications of the simple *T* shaped and spiral *T* shaped micromixers are given below (see Table 1). The meshing grid of about 2.4 million elements is generated using ANSYS solver technique (Fig. 2). The subsequent simulation results are analyzed and calculated in ANSYS Fluent.

The meshing model obtained in ANSYS is shown (Fig. 2).

3 Validation

The simplest of passive micromixers is either *T* shape or *Y* shape which is easy to fabricate and analyze. In this research, *T* shaped micromixer (Fig. 3) is taken as the reference geometry and is validated with the published paper [26]. The two fluids,

Table 1 Geometry details of simple and spiral T shaped

Type	Simple T shape (dimensions)[a]	Spiral T shape (dimensions)[a]
Inlet cross section	100 * 100	159.5769 * 62.6657
Non mixing channel length	800	800
Mixing channel diameter (d_h)	133.3333	159.5769
Mixing channel length	3000	~3000
Spiral diameter (D)	–	400
Spiral pitch (p)	–	2000
Spiral turns (n)	–	~1.25

[a] All dimensions are in microns
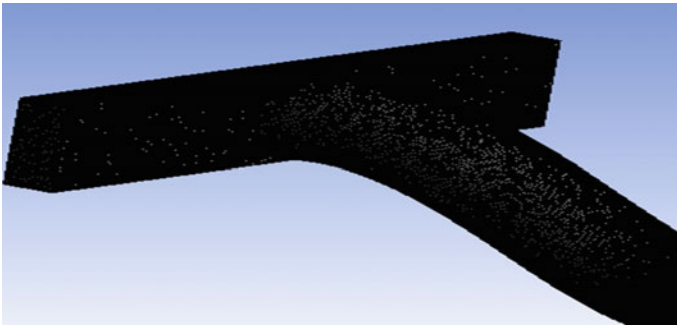
Fig. 2 Spiral T shape micromixer mesh
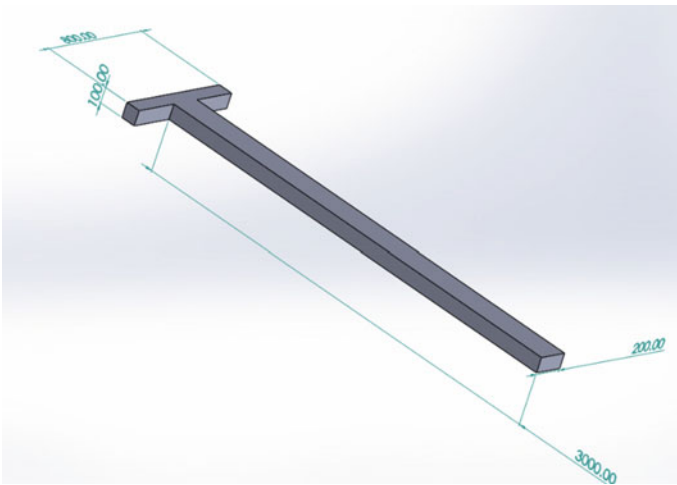
Fig. 3 Simple T shaped micromixer
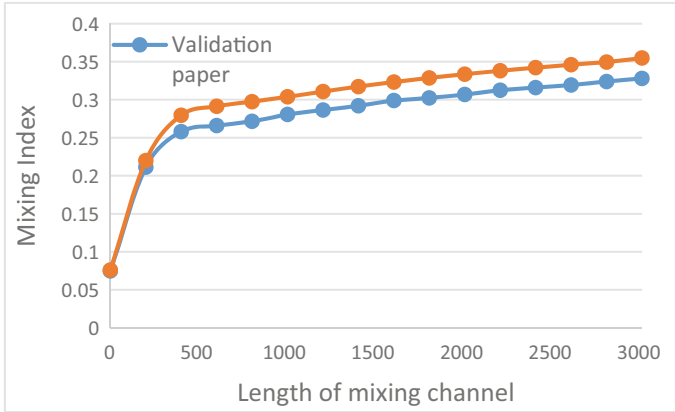
Fig. 4 Comparison of mixing index inside fabricated T shaped micromixer with the validation paper at Re = 266 at various lengths across the channel

namely water and dye (same props. as of water), is given at the two inlets. The boundary condition for concentration is given as 'one' at the left inlet and 'zero' at the right inlet in terms of mass fraction of same species.

The mixing characteristic is analyzed throughout the entire channel. The micromixing efficiency is calculated at the various sections across the length of channel for Re equals 266 and compared with the computational results obtained (Fig. 4).

4 Results and Discussion

The kinds of results achieved from a CFD simulation are engineering quantities of interest in the analyzed flow case. Micromixing index/efficiency is the bone of contention for the above computational analysis. The two fluids are allowed to fuse into one another, and their mixing behavior at different Re has been observed. Mass fractions contours and mixing index are calculated at Re = 266 for spiral-shaped micromixer also. The mass fraction contour has been observed throughout the channel at Re = 266 for spiral shaped (Fig. 5). The mixing mass fraction contour is also compared with that of simple T shaped (Fig. 6).

The variation of mixing index with Reynolds number at the outlets of simple T shaped and spiral T shaped micromixer is given below (Fig. 7). The results are obtained for a wide variety of Reynolds number ranging from 5 to 350.

Fig. 5 Mass fraction
contour of water and dye in
spiral-shaped micromixer at
Re = 266

(a)   (b)
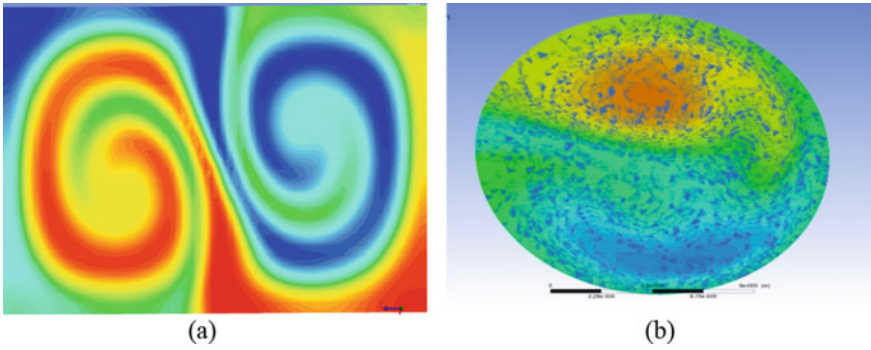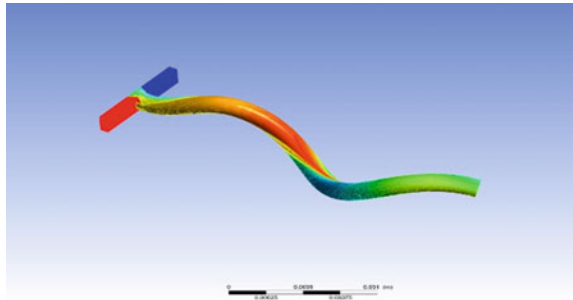
Fig. 6 Comparison of mass fraction contours of water and dye at the outlets of T shaped (**a**) and spiral-shaped (**b**) micromixer at Re = 266
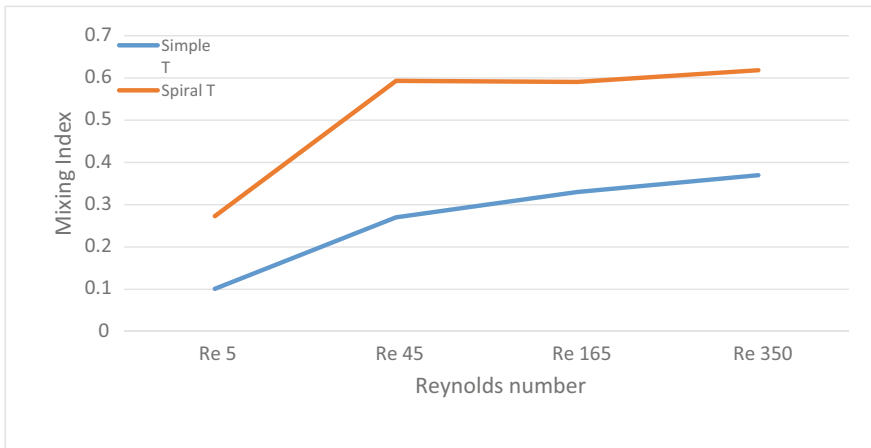
Fig. 7 Mixing index comparison at the outlets

5 Conclusions

It can be concluded that with the increase in Re, we can achieve better mixing at the outlets. There is significant increase in mixing efficiency at low Reynolds number but beyond Re = 100, only a small percentage increase is observed in efficiency. It is also evident from the graph that micromixing efficiency of water and dye is better in case of spiral-shaped micromixer as compared to T shaped micromixer. The increase in mixing index might be due to the swirling effect in spiral T passive micromixer. Thus, just by modifying the geometry to spiral/helical shaped micromixer, we can get a much improved mixing performance between the fluids. From the wide range of Re ranging from 5 to 350, least efficiency (27.3%) is observed at Re = 5, and maximum efficiency (61.84%) is observed at Re = 350.

References

1. Chen, Yao, Chen, Xueye: An improved design for passive micromixer based on topology optimization method. Chem. Phys. Lett. **734**, 136706 (2019)
2. Vijayanandh, V., Pradeep, A., Suneesh, P.V., Satheesh Babu, T.G.: Design and simulation of passive micromixers with ridges for enhanced efficiency. IOP Conf. Ser.: Mater. Sci. Eng., **577**(1), 012106 (2019)
3. Shah, I., Su Jeon, H., M., Ali, H., Hoi Yang, D., Choi, K.-H.: Optimal parametric mixing analysis of active and passive micromixers using Taguchi method. Proc. Inst. Mech. Eng., Part E: J. Process Mech. Eng. **233**(6), 1292–1303 (2019)
4. Lobasov Alexander, S., Shebeleva, A.A., Minakov, A.V.: The study of ethanol and water mixing modes in the T-shaped micromixers. *Журнал Сибирского федерального университета. Математика и физика* **12**(2) (2019)
5. Hossain, S., Lee, I., Min Kim, S., Kim K.-Y.: A micromixer with two-layer serpentine crossing channels having excellent mixing performance at low Reynolds numbers. Chem. Eng. J. **327**, 268–277 (2017)
6. Chen, Xueye, Li, Tiechuan: A novel passive micromixer designed by applying an optimization algorithm to the zigzag microchannel. Chem. Eng. J. **313**, 1406–1414 (2017)
7. Chen, Xueye, Li, Tiechuan: A novel design for passive misscromixers based on topology optimization method. Biomed. Microdevice **18**(4), 57 (2016)
8. Viktorov, V., Readul Mahmud, M., Visconte, C.: Numerical study of fluid mixing at different inlet flow-rate ratios in Tear-drop and Chain micromixers compared to a new HC passive micromixer. Eng. Appl. Comput. Fluid Mech. **10**(1), 182–192 (2016)
9. Li, Xiaoping, Chang, Honglong, Liu, Xiaocheng, Ye, Fang, Yuan, Weizheng: A 3-D overbridge-shaped micromixer for fast mixing over a wide range of reynolds numbers. J. Microelectromech. Syst. **24**(5), 1391–1399 (2015)
10. Ta, B.Q., Lê Thanh, H., Dong, T., Nguyen Thoi, T., Karlsen, F.: Geometric effects on mixing performance in a novel passive micromixer with trapezoidal-zigzag channels. J. Micromech. Microeng. **25**(9), 094004 (2015)
11. Yang, An-Shik, Chuang, Feng-Chao, Chen, Chi-Kuan, Lee, Mei-Hui, Chen, Shih-Wei, Tsai-Lung, Su, Yang, Yung-Chun: A high-performance micromixer using three-dimensional Tesla structures for bio-applications. Chem. Eng. J. **263**, 444–451 (2015)
12. Andreussi, T., Galletti, C., Mauri, R., Camarri, S., Vittoria Salvetti, M.: Flow regimes in T-shaped micro-mixers. Comput. Chem. Eng. **76**, 150–159 (2015)

13. Rasouli, M.R., Abouei Mehrizi, A., Lashkaripour, A.: Numerical study on low Reynolds mixing oft-shaped micro-mixers with obstacles. Transp. Phenom Nano Micro Scales **3**(2), 68–76 (2015)
14. Liu, K., Yang, Q., Chen, F., Zhao, Y., Meng, X., Shan, C., Li, Y.: Design and analysis of the cross-linked dual helical micromixer for rapid mixing at low Reynolds numbers. Microfluid. Nanofluid. **19**(1), 169–180 (2015)
15. Le The, H., Tran-Minh, N., Le-Thanh, H., Karlsen, F.: A novel micromixer with multimixing mechanisms for high mixing efficiency at low Reynolds number. In: The 9th IEEE International Conference on Nano/Micro Engineered and Molecular Systems (NEMS), pp. 651–654. IEEE, 2014
16. Le The, H., Le-Thanh, H., Tran-Minh, N., Karlsen. F.: A novel passive micromixer with trapezoidal blades for high mixing efficiency at low Reynolds number flow. In: 2nd Middle East Conference on Biomedical Engineering, pp. 25–28. IEEE, 2014
17. Tran-Minh, N., Dong, T., Karlsen, F.: An efficient passive planar micromixer with ellipse-like micropillars for continuous mixing of human blood. Comput. Methods Programs Biomed. **117**(1), 20–29 (2014)
18. Afzal, A., Kim, K.-Y.: Multi-objective optimization of a passive micromixer based on periodic variation of velocity profile. Chem. Eng. Commun. **202**(3), 322–331 (2015)
19. He, X., Wei, D., Deng, Z., Yang, S., Cai, S.: Mixing performance of a novel passive micromixer with logarithmic spiral channel. J. Drain. Irrigation Mach. Eng. **32**(11), 968–972 (2014)
20. Hossain, S., Kim, K.-Y.: Mixing analysis of passive micromixer with unbalanced three-split rhombic sub-channels. Micromachines **5**(4), 913–928 (2014)
21. Li, J., Xia, G., Li, Y.: Numerical and experimental analyses of planar asymmetric split-and-recombine micromixer with dislocation sub-channels. J. Chem. Technol. Biotechnol. **88**(9), 1757–1765 (2013)
22. Wang, L., Ma, S., Wang, X., Bi, H., Han, X.: Mixing enhancement of a passive microfluidic mixer containing triangle baffles. Asia-Pac. J. Chem. Eng. **9**(6), 877–885 (2014)
23. Alam, A., Afzal, A., Kim, K.-Y.: Mixing performance of a planar micromixer with circular obstructions in a curved microchannel. Chem. Eng. Res. Des. **92**(3), 423–434 (2014)
24. Wu, C.-Y., Tsai, R.-T.: Fluid mixing via multidirectional vortices in converging–diverging meandering microchannels with semi-elliptical side walls. Chem. Eng. J. **217**, 320–328 (2013)
25. Alam, A., Kim, K.-Y.: Mixing performance of a planar micromixer with circular chambers and crossing constriction channels. Sens. Actuators B: Chem. **176**, 639–652 (2013)
26. Dundi, T.M., Raju, V.R.K., Chandramohan, V.P.: Numerical evaluation of swirl effect on liquid mixing in a passive T-micromixer. Aust. J. Mech. Eng. 1–15 (2019)

Design of a Low-Cost ARM-Based CNC Plotter Machine

Prabhkirat Singh, Randheer Kumar, Rakesh Kumar Dhammi, and Charu Gaur

1 Introduction

The concept of computer numerical control emerged during the World War II era to automate various machine tools. The NC machine tools operated on punched tape, which made it difficult to modify the program once stored. Although NC machines had low installation and maintenance cost, but they were less flexible, less accurate, had limited computational capability and required highly skilled operators. This led to the development of the concept of computer numerical control. First CNC milling machine was developed, in the early 1950s, by Richard Kegg. The primary difference between NC and CNC machine is on the basis of storage of the part program code. While the NC machines store the part program on punched tape cards, the CNC machines enabled the operator to input the part program in G-code format using a keyboard which was further converted into machine-understandable form by MCU, which further generated corresponding control signals to actuate the drive systems. Also, feedback systems were provided for giving position and velocity feedback of the machine tool to the MCU. For a detailed description of the working of CNC machines, the reader is advised to refer [1, 2].

Researchers [3] provide a description of Arduino-based low-cost CNC milling machine, using Easel software to convert design image/G-codes to corresponding stepper signals. The mentioned components establish the main components used to build a CNC plotter machine and are similar to the components used by other literatures reviewed in this section, with a few minor changes. Researchers [4] developed a low-cost, flexible plotter machine. The operator provides input either in G-code format or in speech input through microphone. The motion in *x*-, *y*-, and *z*-axes is achieved through two stepper motors and one servo motor, respectively. The authors [5] have investigated the application of CNC plotter for printing signature of Persons

P. Singh (✉) · R. Kumar · R. K. Dhammi · C. Gaur
Delhi Institute of Tool Engineering, New Delhi 110020, India
e-mail: prabhkirats@gmail.com

with Disability (PwD) through thumb authentication system. The system is based on Raspberry Pi 3B model microcomputer and has a fingerprint module for thumbprint authentication. The drive system used is, although, similar to the previous paper. Researchers [6, 7] have worked on the design and development of a low-cost CNC plotter machine for applications such as design of mechanical parts of a machine and 2D design. The methodology involves sending the G-codes via the computer, which is intercepted by the Arduino microcontroller and converted into pulses that are fed to stepper motor drivers mounted on the CNC shield (powered by SMPS to receive 12 V input) to operate the stepper motor.

Researchers [8–10] used Inkscape software, to convert image into G-code format. Also, authors [8] and [10] used the processing programming software to transfer the G-code from the user interface to the plotter machine. The authors [8] have used spare parts to develop the plotter and a wooden structure is used to mount the various components. Two stepper motors are used for x-axis and y-axis motion whereas the pen movement is given by a servo motor.

Researchers [11] have worked on the development of an Arduino-based CNC plotter machine. It transfers G-code from computer to ATmega328 using FTDI cable, which are converted by the user into pulses to be fed to the three stepper motor drivers to actuate the motors. The authors [12] have also used three stepper motors for x-, y-, z-axes along with a CNC shield to operate the stepper motors. Easel software tool has been used to convert design into G-code. A similar approach has been used by authors [13] to build Arduino UNO-based plotter using CNC shield (with A4988 drivers) to control the two stepper motors to enable the operator to successfully plot designs and sketches have been put forward.

The authors [14] have proposed and built two kinds of systems that may be used to develop a CNC plotter machine. In the first kind, the image made using express PCB or Autodesk Eagle Software is converted to G-code using Benbox software and CNC shield has been used to send control signal to motors; while in the second kind, Inkscape software is used along with processing software to convert image into G-code and L293D is used to issue control signal to motors. The authors used a conductive pen in z-axis, operated by servo motor, to draw circuits using the conductive ink. The researchers [15] have used an ARM cortex M3-based microcontroller, LPC1769 which is programmed in embedded C in LPCXpresso. Inkscape has been used for conversion of image to G-code and processing software has been used for building GUI for serial transmission of G-codes to ARM using FT232 module.

In the present paper, authors attempt to develop a cost-effective design of plotter using base structures made of acrylic sheets, designed in AutoCAD and machined using laser machining process. This design provides a distinct advantage to choose the desired dimensions of work volume. The authors have used programming to convert G-codes for controlling signals for motors rather than using existing options like CNC shield or GRBL software. Focus has been primarily on achieving faster processing speed and flexibility, thus concept of interrupts driven programming and the manipulation of register bits has been utilized in the modular programming approach. Also, a modified form of double slider mechanism and a proportional control have been

Fig. 1 Block diagram for mechanical motion transmission
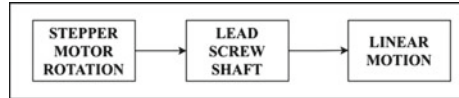
implemented to achieve precise control of servo motor and hence the pen along the z-axis.

2 Methodology

The CNC plotter designed in this paper converts the GUI commands inputted by the user to machine-understandable form to actuate the stepper motors and servo motor. The methodology used has been described in this section.

2.1 *Mechanical*

The mechanical section consists of two mechanisms. One mechanism is used for **controlling the motion of the stepper motors** to provide linear motion in x- and y-axes. It uses the leadscrew mechanism to convert rotational motion to translational motion. Figure 1 depicts the conversion of motion from rotational to linear. The other mechanism is used for **controlling the motion of a servo motor** to provide linear motion to pen in the z-axis. A modified form of double slider mechanism has been implemented to achieve linear motion of servo motor.

2.2 *Electronics*

The electronic section describes the power circuit and the computational circuit used in the model. The **power circuit** takes 220V from AC mains and converts it into three voltage variants, i.e., 5 V, 12 V, and 27 V used to operate different components of the circuit, shown in Fig. 2. The **computational circuit** consists primarily of the microcontroller (STM32F103) [16] which plays a vital role in the overall operation of the CNC plotter. It receives the commands sent by the user via the custom-built GUI, that are decoded by the microcontroller. The necessary control signals are then sent to the drivers and L293D IC, which actuate the motors. It also implements a proportional control to actuate the servo motor, taking feedback from the built-in potentiometer of the servo motor. The block diagram for flow of data is shown in Fig. 3.
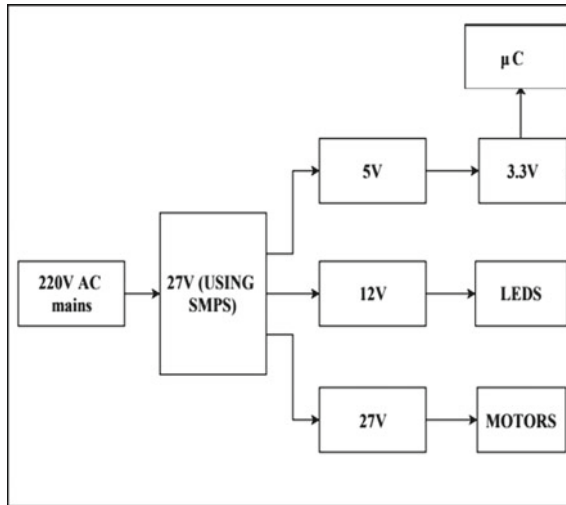
Fig. 2 Block diagram for electronic power distribution
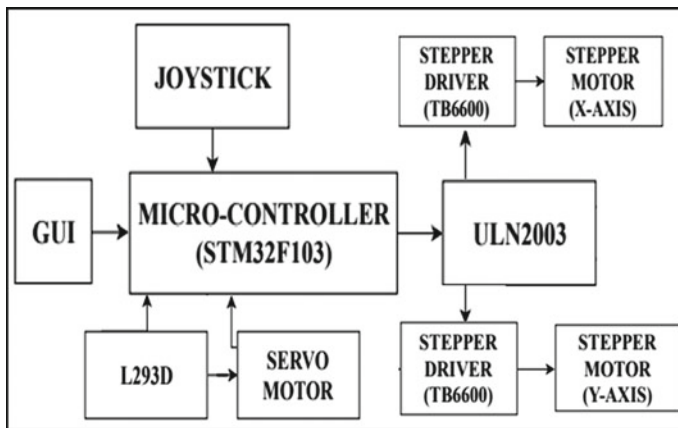
Fig. 3 Computational circuit of the CNC plotter

2.3 Programming

This section describes the programming for building a GUI that provides the user with a platform to send commands to the microcontroller via the USB connection. The GUI is built in the Microsoft Visual Studio using C# (sharp) programming language. It also includes the programming of the microcontroller to perform the tasks such as decoding the user commands, coming either from joystick or GUI, and generating the corresponding control signals to actuate the various motors. The

microcontroller programming allows the user to choose between two different operating modes namely, Manual Mode and Automatic Mode. The flow charts for GUI programming (Fig. 4) and microcontroller programming (Fig. 5) provide a basic depiction of the flow of information and its processing. However, detailed description of the programming is discussed in the next section.
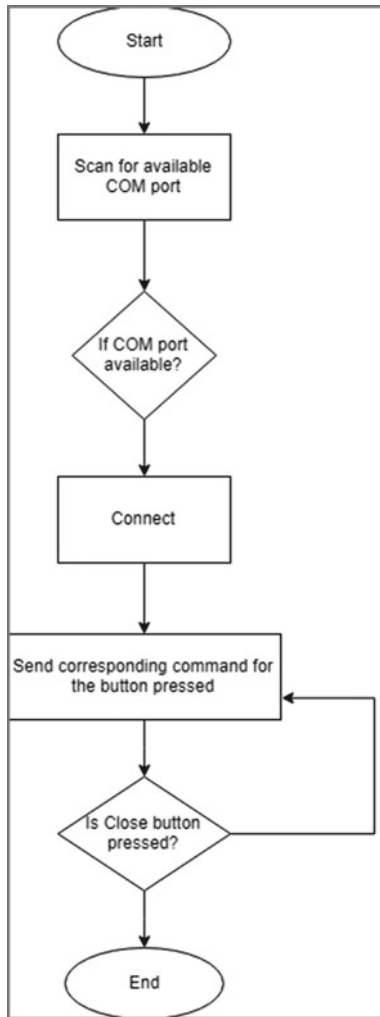
Fig. 4 Flowchart for GUI programming
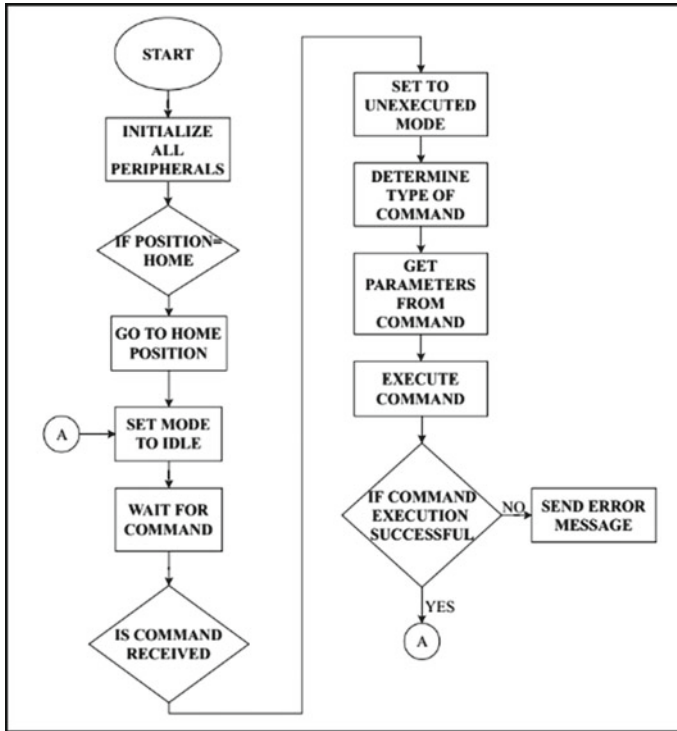
Fig. 5 Flowchart for microcontroller programming

3 Implementation

3.1 *Mechanical*

The mechanical structure consists of the main base (Base I) upon which the rest of the components are mounted. Primary stepper motor along with lead screw vertical brackets is mounted upon this base, supporting the lead screw arrangement for the x-axis movement. Over this arrangement, a second base (Base II) is supported which mounts a similar arrangement for another stepper motor for movement in y-axis. On the lead screw for Base II, the pen mechanism is mounted and it is operated by a servo motor. Both the bases (Base I and II) and the pen mechanism structure are made of acrylic sheet boards. As described earlier, mechanical subsection is divided into two mechanisms. First mechanism is used for controlling the motion of the stepper motors to provide linear motion in x- and y-axes. It utilizes two stepper motors controlled by the microcontroller which provides rotational motion. This rotational motion is further converted into linear motion by coupling stepper motor shaft to a lead screw shaft using 5–8 mm coupler. The lead screw converts the rotational
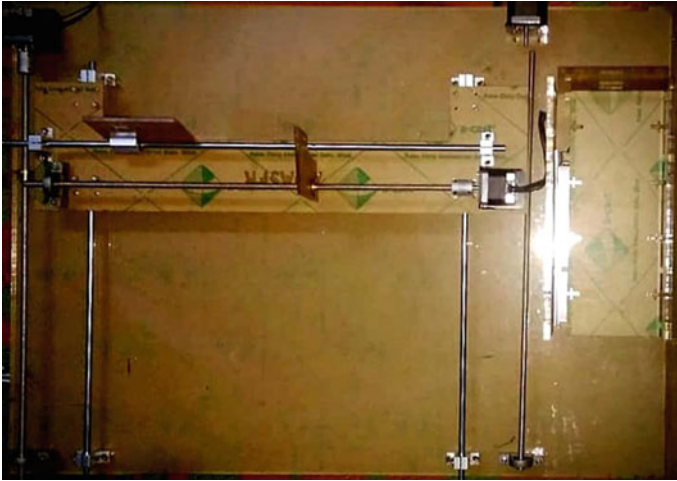
Fig. 6 Mechanical assembly

motion to translational motion using copper nut, which moves the Base II (based upon which pen mechanism is mounted), thus providing the *x*-axis movement. A similar arrangement is used with a stepper motor mounted on the Base II which provides the linear motion in *y*-axis. This is depicted in Fig. 6. The copper nut on the lead screw of this axis provides support for mounting the pen mechanism.

The pen mechanism is used for controlling the motion of the servo motor to provide linear vertical motion to pen in the *z*-axis. A modified form of double slider mechanism has been implemented to achieve linear motion of the servo motor. This mechanism is illustrated in Fig. 7a whereas Fig. 7b provides CAD representation of the mechanism.

3.2 Electronics

The electronic section can be divided into two circuits. The first circuit is the power circuit to power the various electronic components of the CNC plotter. The power circuit takes 220 V from AC mains as input which is converted to 27 V using SMPS. This 27 V supply is used in three voltage forms. The first form uses the 27 V directly to operate the stepper motor drivers which further drive the stepper motors. The second form converts the 27 V to 5 V using a Buck converter (LM 2576). This 5 V is further converted to 3.3 V by the in-built buck converter of the STM32F103 microcontroller. This 3.3 V powers the microcontroller.

The third form converts the 27 V to 12 V using a Linear Voltage Regulator IC (LM7812) to power the Status LEDs. The voltage distribution is depicted in the form of chart in Fig. 2.
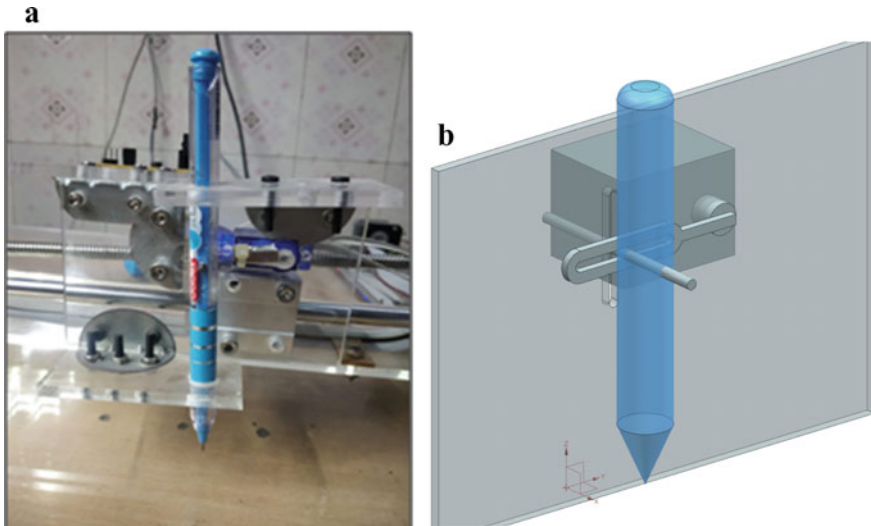
Fig. 7 **a** Pen mechanism, **b** Pen mechanism CAD model

The second circuit is the computational circuit responsible for the actual operation of the CNC plotter. The microcontroller decodes the received input from the user, which acts as an actuating signal for both the stepper motors and servo motor. The microcontroller provides three signals, namely STEP, DIR, ENABLE, for operating the two stepper motors individually. The logic level of these signals is 3.3 V but that of stepper motor driver is 5 V. Thus the Darlington Transistor Array IC (ULN 2803) is used to raise the logic level of these signals to 5 V. This signal is further sent to stepper motor drivers which drive the stepper motors accordingly. The microcontroller also issues signal for the actuation of the servo motor used to operate the pen mechanism. A feedback is provided from the servo motor's in-built potentiometer to the microcontroller. The Joystick Module is to provide the functionality to the user to operate the CNC plotter in manual mode. However, the program also provides the functionality to operate the CNC plotter machine in automatic mode by the user. The development of a PCB upon which the power and computational circuits are mounted was also undertaken. The actual circuit is shown in Fig. 8 while the schematic of various circuits is shown in Fig. 9.

3.3 Programming

A modular programming approach has been utilized in the paper. The programming has been divided into individual Application Program Interface (APIs). The APIs are software intermediaries constituting set of instructions, which are called in the main function to perform specific operations. So, rather than building one program
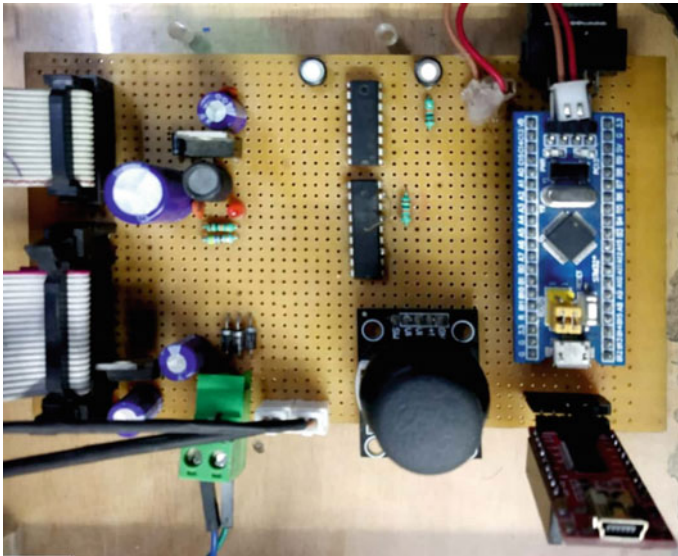
Fig. 8 Electronic assembly

having all the functions, multiple programs are written. This provides flexibility to easily change blocks of program. Use of APIs enables speeding up of the program development process, and provides a feature to add extra functionality to the program. The APIs used in the programming are listed below along with their functions:

i. In the **System API**, implementation of the programming and calling of all the APIs for the successful operation of the CNC plotter machine are done.

ii. In **RCC API**, an external clock source is selected as a clock source for PLL. PLL is set in such a way that it outputs a frequency of 72 MHz. It sets the frequency of all individual peripherals using its pre-scaler/clock divider. Two different functions are defined, namely delay milliseconds and microseconds, which provide the operation of delay in the program.

iii. In the **Analog API**, the initialization of ADC is done. In this API, a function analog Read is defined. It is linked to the following three ADC channels: x-axis, y-axis, and servo pot, one of which is passed as parameters. It returns the value at various channels into the function.

iv. In the **Serial API**, UART is initialized. Interrupt setting is done for receiving data. In this API, three functions are defined – char sending function, string sending function, data read function. The char sending function is used to transmit character type of data. The string sending function is used to transmit string type of data. The data read function is to read the data from the computer.

v. In the **Button API**, it scans whether a button is pressed or not. The buttons could be either on the GUI or the pushbuttons present physically on the PCB of the CNC machine. In the **LED API**, the status of the machine is judged and the
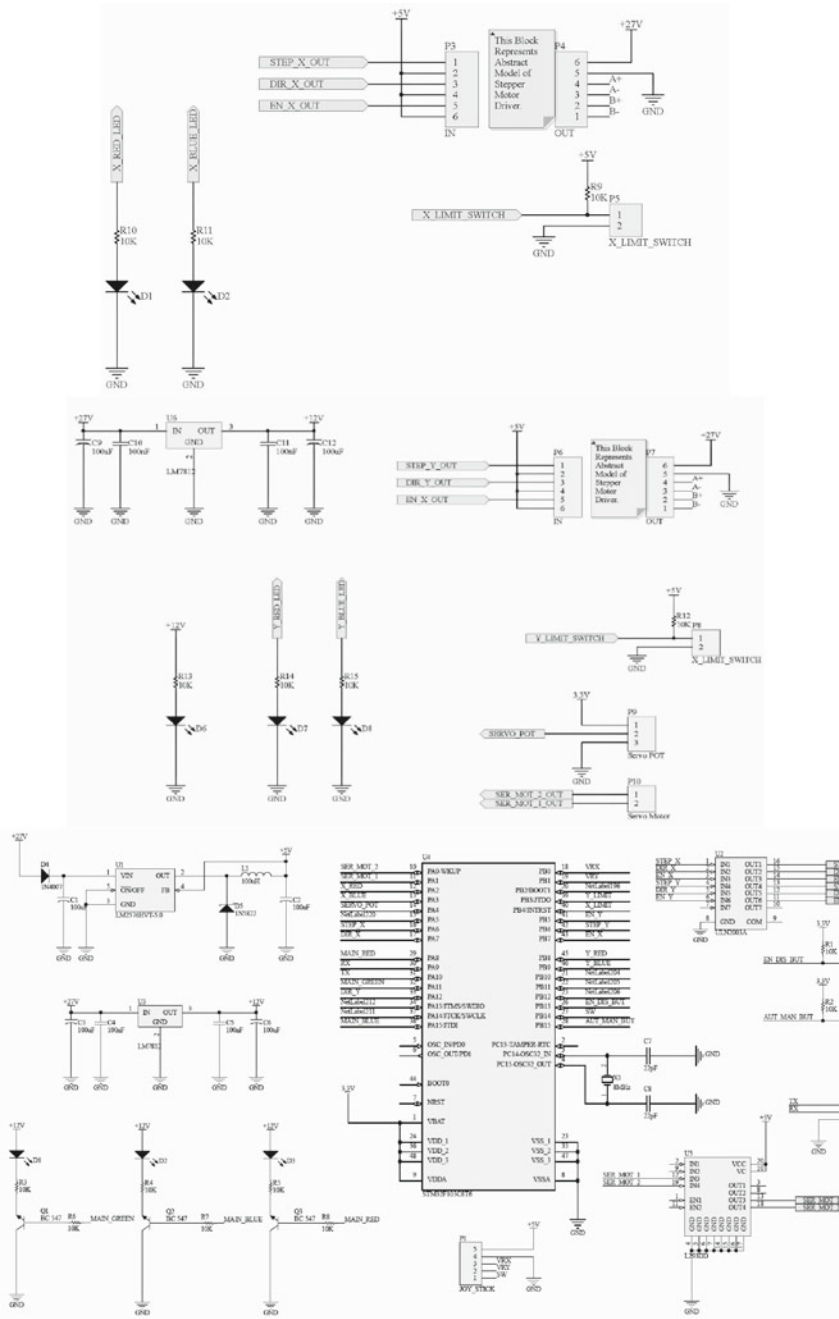
Fig. 9 Schematic of controller and *x*- and *y*-axes motors

corresponding LED is enabled or disabled. The LEDs used for illumination of the workspace are also enabled or disabled in this API.

vi. In the **Millis API**, the delay microseconds and milliseconds function are used. This API has a specific task of calling handlers which need to be called, repetitively, in the program. It also performs the function of holding the task that needs to be delayed while keeping the rest of the program running continuously.

vii. In the **Stepper API**, timers and I/O pins to operate stepper motor are initialized. The function stepper write is defined which requires four parameters to be passed. The parameters passed are the number of steps in the x-axis, the number of steps in y-axis, speed in x-axis, and speed in the y-axis. In the **Servo API**, proportional control on the servo motor is implemented so that it operates between two angles corresponding to the positions of pen, i.e., pen up and pen down.

viii. In the **Coordinate API**, the number of steps taken by the stepper motor is recorded, converted into coordinate and returned to the microcontroller. The pen vectoral velocity is fixed to get the respective stepper motor x- and y-axes velocity using Jacobian matrix [17].

Further, the development of GUI has been undertaken. GUI is built in Microsoft Visual Studio using C# (C sharp). It acts as the display panel for the operator (Fig. 11) and has buttons built on it to send corresponding signal via the computer to the controller, which decodes the commands and acts accordingly. In the programming, a set of new list of commands has been defined. These commands are written in the text box and the 'SEND' button is pressed to send the commands via the FTDI cable to the microcontroller. The microcontroller program is written to intercept the commands and convert them into a control signal for the actuation of the drive system. The actual model is depicted in Fig. 10 and the Graphical User Interface (GUI) for control of machine is shown in Fig. 11.

4 Applications

The primary field of application of the plotter is in engineering drawing or blueprint drawing. The machine can also perform scaled plotting operations. It can also be used in PCB prototyping where it poses a distinct advantage over traditional printers by providing high-resolution prints irrespective of the plotting area. With slight modifications, this machine can be used in many other applications. It can be used for laser engraving and cutting operations if pen is replaced by laser engraver. On replacing the pen with a laser welding torch, it can be used for welding operations. Also, it can be used as coordinate measuring machine, if the pen is replaced by a stylus and thus, can be used to measure distance.

Although plotters provide numerous applications, yet there may be a few constraints. They may be slower in plotting as compared to traditional printers, since

Fig. 10 Actual model
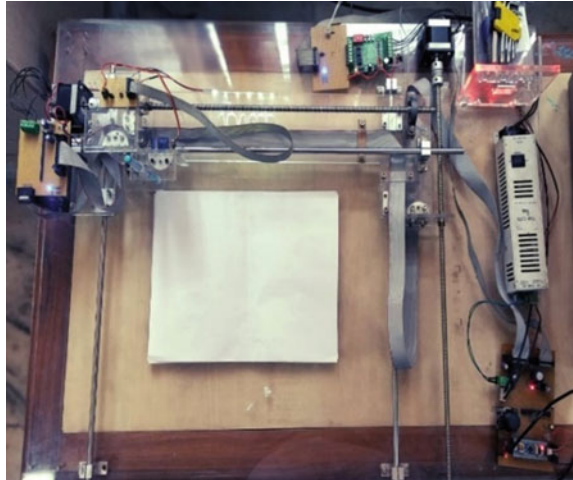
Fig. 11 GUI front panel
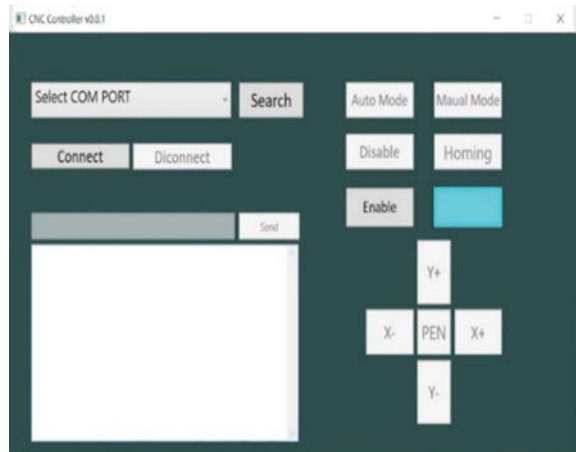
they plot each line separately. In terms of housing space, plotters require more space to accommodate as compared to printers. Moreover, in case of mass printing, plotters may be more expensive compared to printers, since printers can directly scan images for printing whereas the use of plotters requires conversion of the material into vector format before printing.

5 Outcome

In this paper, a new and innovative way to develop a CNC plotter machine has been put forward. The structure of the CNC plotter machine is made of Polymethyl Methacrylate (PMMA) which not only provides an aesthetically pleasing look but is rigid at the same time. The ability of a CNC plotter to operate in both manual and automatic mode is quite unique. The G-codes are sent through GUI built using C# programming. No readymade modules have been used. The programming of GUI in C# and modular programming of microcontroller are done through register level programming. This provides accuracy to the motion of motors and flexibility in operation and, thus, enables building a robust custom-built system for the application. The machine uses limit switches for origin setting. The ARM microcontroller (as opposed to other alternatives [5], thus reducing cost further) has been used due to a number of advantages like faster computation speed, sophisticated functionality, a greater number of peripherals, higher resolution of timers, etc. A proportional control has been implemented to achieve a precise vertical control over the motion of pen in z-axis as opposed to using a stepper motor [12] which saves cost. The technique involved in the development of this machine has several advantages over the existing machines like low cost, ease of use, and operable by anyone with knowledge of the few control commands of the machine.

The CNC plotter was successfully able to draw alphabets and simple designs. Also it was able to draw moderate designs if the G-code of the design are inputted by the operator as in a conventional CNC machine. It can also be used for layout plotting.

One of the focus areas of the project was to achieve the above outcomes at lowest possible cost. The microcontroller used (STM32F103) is lower in cost compared to Raspberry Pi [5] and other AMR used by other researchers [15], yet provides quite remarkable functionality. The model uses two stepper motors instead of three [7, 11, 12], and a servo motor in pen mechanism. Here a P-control has been implemented on the servo motor, thus making it more precise and cost friendly. The choice of Acrylic instead of metal advances two main advantages. On one hand, the easy workability of acrylic reduces the cost of manufacturing parts relative to the expensive processes of metals like metal cutting. On the other hand, acrylic being lighter than metal, reduces the cost for various other components like lower power stepper motor and its driver, SMPS, other active and passive components, etc. Small machining operations like drilling and the whole PCB designing process have been carried out in house, thus no cost has been incurred on these processes. Linear shafts and bearings have been used instead of linear rails, which are comparatively inexpensive.

6 Conclusion

The authors have undertaken a detailed review of the literature on the design and development of CNC plotter. This paper attempts to design, fabricate and develop a cost-effective ARM-based CNC plotter which can be operated in both manual and automatic mode. The mechanical and electronic principles behind the design have been explained along with the programming. The various Application Programming Interfaces developed by the authors have been discussed in the paper. On implementation of these principles, the CNC Plotter thus developed was successfully able to draw sample alphabets and simple designs. It can be extended to draw moderate designs as per user input. The applications of this plotter are widespread ranging from engineering drawing to welding operations. The future extensions of this project would be to implement the principles of digital image processing for the conversion of the image into G-code to make the CNC plotter machine fully sophisticated. This does not involve any further cost to be incurred.

References

1. Ramesh Mamilla, V., Prasad, M.N.: Study on computer numerical control (CNC) machines. Int. J. Adv. Sci. Res. **1**, 13–17 (2016). www.newresearchjournal.com/scientific
2. Ansar, A.H., Hussain, M.A., Alamoodi, S.M., et al.: Features and applications of Cnc machines and systems. Int. J. Sci. Eng. Technol. Res. **5**, 717–726 (2016)
3. Deshpande, S.V., Karthik, P.U., Naveen Kumar, D. et al.: Design and fabrication of 3-axis CNC milling machine. **6**, 34–38 (2018)
4. Joshi, H., Kulkarni, N.: A review on pen plotter, 44–46 (2018)
5. Keche, K.A., Kate, D.M.: A real time design and development of pen plotter machine for authentication system and signature plotting, 1350–1353 (2018)
6. Pandey, U., Sharma, S.R.: Model and fabrication of CNC plotter machine. Ijarcce **6**, 336–339 (2017). https://doi.org/10.17148/ijarcce.2017.6659
7. Abd-alstar, S., Yahya, A.: Design and analysis mini CNC plotter machine (2018)
8. Khan Prince, M.K, Mukaddem Ansary, M.-A., Mondol, A.S.: Implementation of a low-cost CNC plotter using spare parts. Int. J. Eng. Trends Technol. **43**, 333–339 (2017). https://doi.org/10.14445/22315381/ijett-v43p256
9. Nsayef, A.I., Mahmood, A.L.: Microcontroller-based plotter machine. Al-Nahrain J. Eng. Sci. **21**, 350–355 (2018). https://doi.org/10.29194/njes.21030350
10. Ranjan, S., Rani, M., Ranjan, S., Singh, M.: Design and Implementation of low-cost 2D plotter computer numeric control (CNC) machine. Int. J. Eng. Res. Technol. **7**, 99–101 (2018). 2278-0181
11. Girhe, P., Yenkar, S., Chirde, A.: Arduino based cost effective CNC plotter machine. **6**, 6–9 (2018)
12. Hasan, Y.M., Shakir, L.F., Naji, H.H.: Implementation and manufacturing of a 3-axes plotter machine by Arduino and CNC shield. Int. Iraqi Conf. Eng. Technol. Its Appl. IICETA **2018**, 25–29 (2018). https://doi.org/10.1109/IICETA.2018.8458071
13. Pal, T.K., Mandal, D.K., Ebadattulla, S. et al.: Modeling of portable CNC plotter machine/3D printer. V:73–76 (2018)
14. Kamble, P., Khoje, S., Lele, J.: Implementation of paper PCB using conductive ink 2D plotter. In: Proceedings—2018 4th International Conference on Computing Communication Control

and Automation ICCUBEA 2018 1–6 (2018). https://doi.org/10.1109/ICCUBEA.2018.869 7781
15. Saji, N.A., Athanasius, M.: An ARM based CNC plotter, 434–438 (2018)
16. Technology S, Jose S (2008) Reference Manual. Technology 1. https://doi.org/10.1093/cid/ciq238
17. Saha, S.K.: Introduction to Robotics, 2e. Tata McGraw-Hill Education

Failure Analysis of Alloy Steel Connecting Rod

Abhinav Gautam, K. Priya Ajit, Pramod Kumar Sharma , **Atul Gautam** ,
Vilas Warudkar , **and J. L. Bhagoria**

1 Introduction

Connecting rod acts as a device to change the reciprocating motion of the piston to
the rotary motion of the crankshaft converting gas thrust at combustion to desired
turning moment at the shaft. It undergoes high cyclic load, level ranging from high
compressive load during power stroke to high tensile load arising from inertia [1,
2]. Design of the rod is primarily based on the maximum compressive load of the
power stroke. The small end connects the piston through gudgeon pin, working
under hydrodynamic lubrication. With the seizure of lubrication, the pin will rub
the bearing lining material at a fluctuating load rate. Also, there is impulsive force
imparting dynamic load. All these make the actual force and stress pattern quiet
complex at the bearing lining–pin interface of the rod [1].

Ilia et al. [2] in their study talk about two methods or two different technologies,
those are used in manufacturing of connecting rod. These methods are fracture-
split drop forging and fracture-split powder forging; both these methods are used at
present. Two interesting but contradictory results were reported by Afzal and Fatemi
[3] and by Ilia et al. [2] regarding the two methods of manufacturing of connecting rod.
The study of Afzal and Fatemi [3] states that the fatigue strength of connecting rod
manufactured through drop-forged is higher than that of a powder forged connecting
rod. While Ilia et al. [2] claim that the reverse is correct, they claim that "the higher
performance, superior raw material utilization and lower total cost of the finished

A. Gautam
Department of Mechatronics Engineering, Indian Institute of Information Technology Bhagalpur,
Bhagalpur, India

K. Priya Ajit
Department of Mining Machinery Engineering, IIT (ISM) Dhanbad, Dhanbad, India

P. K. Sharma · A. Gautam (✉) · V. Warudkar · J. L. Bhagoria
Department of Mechanical Engineering, MANIT, Bhopal, India
e-mail: atul1993gautam@gmail.com

machine and assembled product are the main reasons why the use of powder forged connecting rods has significantly increased in the last two decades, taking away the market share of drop forged connecting rods."

Failure of connecting rod is catastrophic in nature. Reported literatures indicate events of total destruction of the engine arising from connecting rod failure and they predict the cause in a diverse way. Fracture of rod is analyzed by Bai-yan et al. [4] with the help of experimental observations from fractography, metallography also testing hardness and stress-strain behavior. For crack growth analysis, they used ABAQUS software. A failure investigation is reported by Xiao and Zhi [5] of a diesel engine connecting rod, used in a truck, fractured in service (only 1200 km), and destroyed the entire engine. The fracture occurred at the small end of the connecting rod. Their visual and scanning electron microscopy observations show a lot of axial grooves on the internal surface close to the fracture and fatigue cracks initiated from such axial grooves. Fractography observations indicate multiple-origin fatigue fracture as the dominant failure mechanism. The machining or assembling process as suggested by the authors is responsible for the formation of the axial grooves. Nonlinear finite element analysis conducted by Khare et al. [6] observes failure to occur by wear at pin and bearing interface of the rod. Son et al. [7] use FEM to predict fretting damage at the upper split of the marine-head type diesel engine's connecting rod treating it as a multi-body flexible dynamic system. Many researchers [8–12] reported failure analysis of different mechanical components following almost a common route of tests, viz., visual inspection, fractography, metallography, mechanical property testing, and testing of chemical composition.

In view of the procedures in literature present investigation is carried out in the following steps: (1) SEM to reveal the crack initiation, their propagation, and type of failure, (2) Optical emission spectroscopy (OES) to identify the chemical composition of rod material, (3) Hardness test to obtain a qualitative estimate of the material, (4) Tensile test to understand its ductility response in addition to its characteristic value of yield strength (σ_y), tensile strength(σ_u), and elasticity modulus (E) to categorize the material property in AISI scale. (5) To identify the location of maximum stress, a finite element analysis is performed. The maximum stress is found to arise around the oil hole region.

The fractured connecting rod is shown in Fig. 1a. Figure 1b focuses on two different areas, marked as 1 and 2, used for SEM test samples preparation.
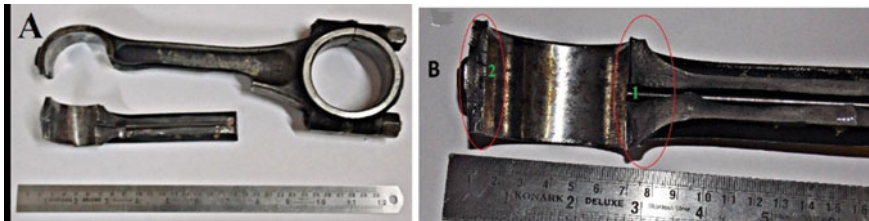
Fig. 1 **a** and **b** Photograph of fractured connecting rod as received

2 Materials and Methods

To identify the cause of failure samples for the first four steps, stated above, are prepared by wire EDM cutting to minimize any damage during machining and are chosen from its relevant portions only. Samples for SEM, OES observations, and hardness testing are taken from the marked portion, 1 and 2, in Fig. 1b. The test samples are shown in Fig. 2. For FEA, the input data are considered from Table 1, stating the engine specifications, and measured tensile test properties, Table 3.

2.1 Visual Inspection

A connecting rod, fractured from small end, is received from a local workshop of Ashok Leyland. Its chemical composition and working history were unknown. The broken in two parts of the rod, as received, is shown in Fig. 1a. The bearing lining surface has many scratching marks and shining smooth bearing surface near the oil

Fig. 2 Sample used for microscopic analysis
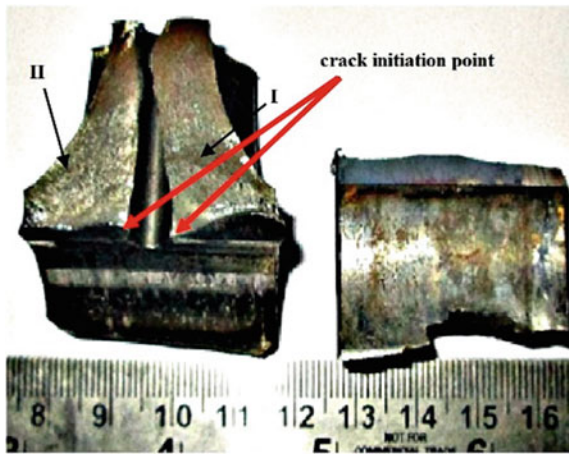
Table 1 Engine specification (Ashok Leyland ALM–402 marine diesel engine)

Crank shaft radius (mm)	60.32
Connecting rod length (mm)	285
Piston diameter (mm)	107.18
Mass of connecting rod (kg)	2.56
Maximum gas pressure (MPa)	3.5
Power rating	66.2 kW @ 1500 rpm, 80.9 kW @ 1800 rpm, 86.8 kW @ 2000 rpm

hole symbolizing seizure of lubrication, rubbing of pin on lining that in presence of fluctuating load may lead to fretting fatigue rupture. Shear lip formation is visible on either side of the oil hole at the small end suggests severe erosion of lining material. Final separation occurred by splitting of the rod. Crack initiation location could not be resolved with naked eye, but fracture pattern directs it to be initiated from around the oil hole region. Accordingly, micro-observations are carried out selecting samples from the indicated fractured region to identify the exact location of crack initiation and propagation mechanism involved.

2.2 Microscopic Examination

SEM investigation reveals the fracture mechanism and surface morphology of sample shown in Fig. 2. After appropriate surface preparation, different images at reforming resolution and magnification are captured. Sample areas prepared from fracture region are marked as I and II in Fig. 2. The images from SEM are given in Fig. 3. Crack is observable to initiate from multiple sources around the oil hole giving trace of slant fracture and shear lips on its either side. Thinning of the bearing lining by high frequency impact and rubbing of the pin gave way for fretting fatigue crack initiation as in Fig. 3a. Cyclic high thrust resulted in high-stress intensities at crack tip that has grown during each cycle leaving striation marks of wavy appearance presented in Fig. 3b–d. This stage of crack propagation was stable growth. Subsequently, dimple morphology and nodal formations in the sample region with disappearing striations are observable [13, 14] in Fig. 3e, f, large enough crack propagation and sequence of impacts can decrease stress intensities and ductile crack extension takes on the course. Unstable crack propagation occurred as soon as the shear lips could meet the edge of the bearing surface ending the small end boundary. This resulted in split of the rod in two parts.

2.3 Chemical Composition

Analysis for chemical composition is carried out by optical emission spectroscopy (OES), a method to identify the constituents of the sample. The weight % of different elements present in the sample are given in Table 2. The chemical composition matches very closely with those of AISI 4140 Steel.

2.4 Hardness Test

Hardness test is carried out at 750 Kgf load with 10 mm steel ball on a Brinell Hardness Testing machine. Four test points are chosen on the surface of the sample.
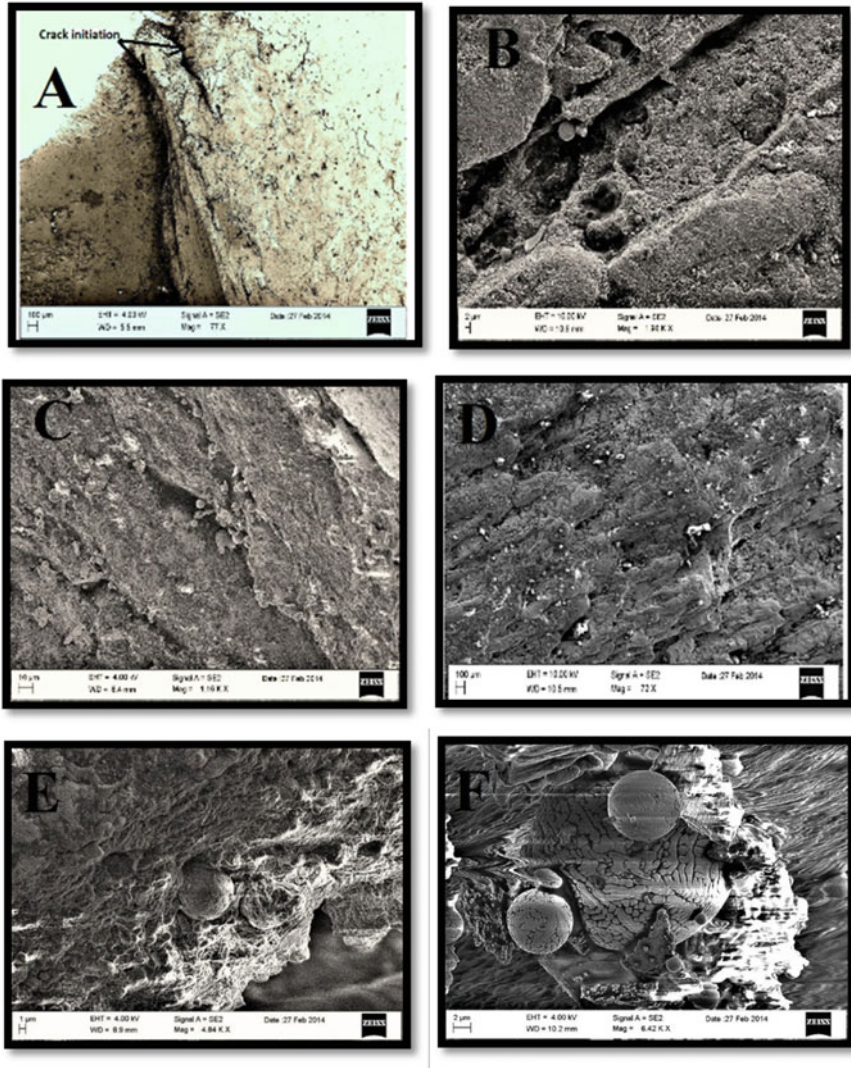
Fig. 3 SEM observation, **a** crack initiation, **b**, **c**, and **d** striation marks, **e** dimple morphology, and **f** nodal formation

Table 2 Chemical composition (weight %) of fractured connecting rod sample

Elements	C	Si	Mn	P	S	Cr	Ni	Ti	Cu	W
Concentration (wt%)	0.47	0.26	2.05	0.007	0.35	1.05	1.33	0.01	0.06	0.29

Table 3 Mechanical property of connecting rod material results

Tensile property

Material	Ultimate (σ_U) strength (MPa)	Yield strength (σ_Y) (MPa)	Young's modulus (E) (GPa)	Elongation (%)	Reduction of area (%)
Connecting rod	856.06	733.25	208.75	13.98	39.83

Hardness property (BHN)

Test points	1	2	3	4	Mean
Connecting rod	262	270	269	267	267

Hardness results are presented in Table 3. The average value obtained is BHN 267 that closely matches with the values of AISI 4140 series steel (BHN279). Very little variation in hardness value is observed for different positions of the sample representing consistency of its property.

2.5 Tensile Test

Tensile tests are performed at room temperature using five standard samples taken from beam area of the connecting rod. Tests are carried out obeying ASTM E8/E8M-2015 standard standards [14]. Specimen was obtained from connecting rod beam area using wire electrode discharged machining. Drawing of specimen and machined sample are shown in Fig. 4. Thickness of a specimen is 2 mm. An average of five sample tests is shown in Table 3. A typical experimental stress–strain curve is shown in Fig. 5. Elongation of gauge length and contraction of cross-section indicate good ductility and toughness of the parent material.

3 Finite Element Analysis of Connecting Rod

A 3D nonlinear finite element analysis is employed to estimate the stress field solution for the complex force distribution prevalent at the small end of the rod. In line with the method indicated in [15, 16] boundary conditions, material property and loading conditions as available in manufacturer's catalogue and current test results of the material are implemented in the FEA. Location of extreme stress magnitude is found on the small end around the oil hole, shown in Fig. 9. The maximum stress locations match with the crack initiation sites.
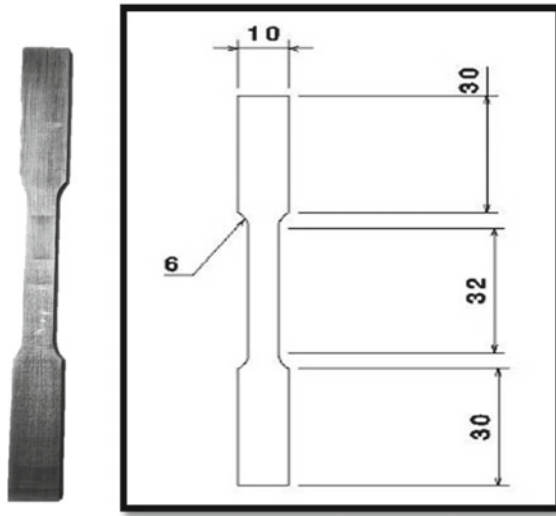
Fig. 4 Specimen drawing and machined sample
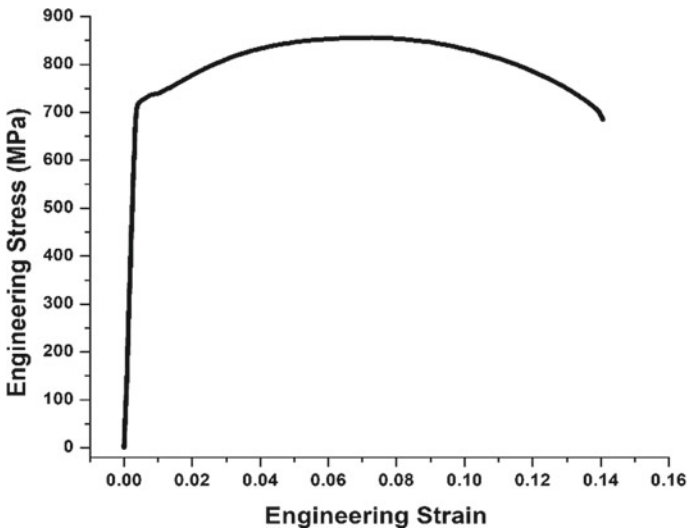
Fig. 5 Engineering stress–strain plot of connecting rod specimen

3.1 Modeling and Preprocessing

For estimation of stress distribution in the connecting rod, ANSYS 14.0 WORK-BENCH platform is used. Static stress analysis of connecting rod is considered keeping big end section restrained while Hartzian contact force and thrust load caused

by fuel combustion are applied at the small end. Implementation of boundary conditions and load application is shown in Fig. 6a. Material property data obtained from tensile test (Table 3) are used in the analysis. Maximum gas pressure of 3.5 MPa is considered from Table 1. The arrangement of analysis is shown in Fig. 6a, and its mesh model in Fig. 6b. 3D tetrahedral element is used. Refine meshing closer to lubricating oil hole is used for better accuracy in result. 114,624 numbers of elements comprising 171,079 nodes with 3 mm element size are used.

Corresponding deformation and equivalent von-Mises stress distribution are shown in Figs. 7 and 8. Both the deformation and stress near small end section are relatively high. A magnified image of maximum stress region is shown in Fig. 9.
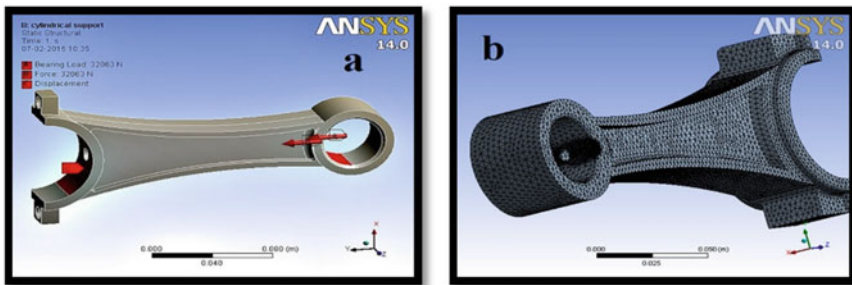
Fig. 6 **a** stress analysis arrangement, static Hartzian contact, and bearing load distribution over 180° at small end and crank end fully restrained over 120°, **b** meshed image of connecting rod
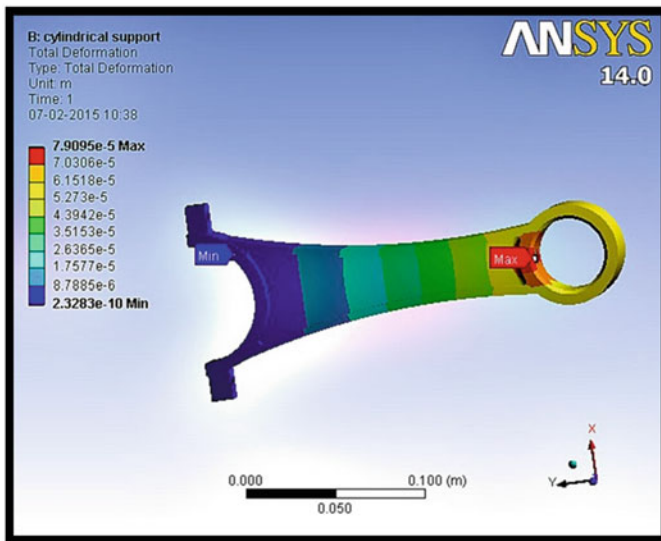
Fig. 7 Deformation plot
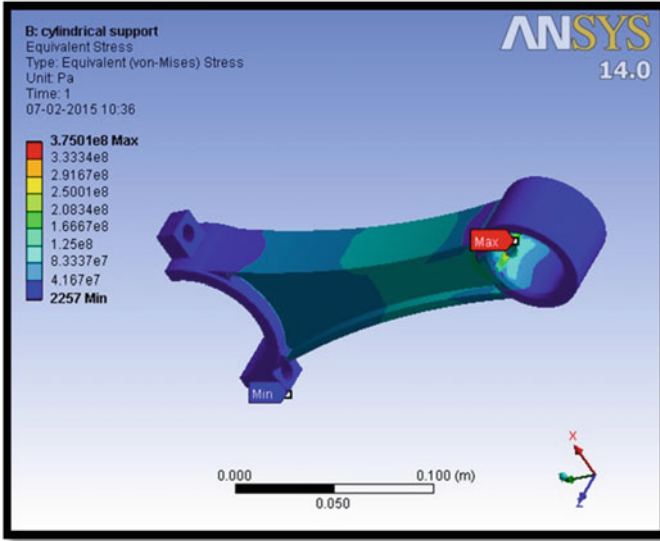
Fig. 8 Stress plot
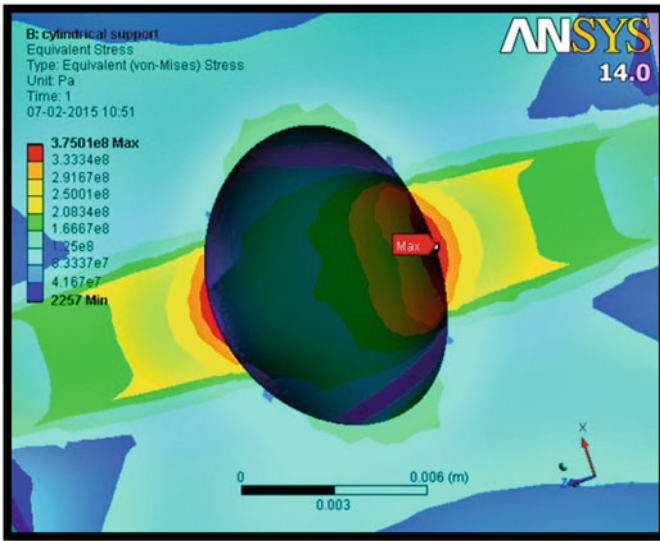
Fig. 9 Magnified image of maximum stress region

Maximum deformation is observed to be about 0.079 mm, while maximum stress reaches near to 375 MPa. Both occur in the vicinity of the lubricating oil hole.

4 Result and Discussion

Since the composition and other material property features of the considered fracture sample were not available, OES, hardness, and tensile tests are performed to verify composition and mechanical properties of the material. Results are stated in Tables 1 and 2. They closely conform to AISI 4140 steel [14] giving an average hardness value of BHN 267, an average of Young's modulus of 209 GPa, with percentage elongation of about 14%.

Visual inspection shows frictional polishing of lining surface with shear lips on either side of the oil hole and slant fracture an indication of fretting fatigue. Fretting is a form of wear, which occurs in the contact area between two metals under fluctuating load with small relative displacement in the range of 5–50 μm [7, 17]. A magnified image (Fig. 10) of the bearing surface shows scoring and scratching marks. These marks indicate development of contact stress between the gudgeon pin and bearing lining of small end and their relative rubbing due to depletion of lubricating oil film. This formed wear debris trapped in contact area, which further reduced the lining
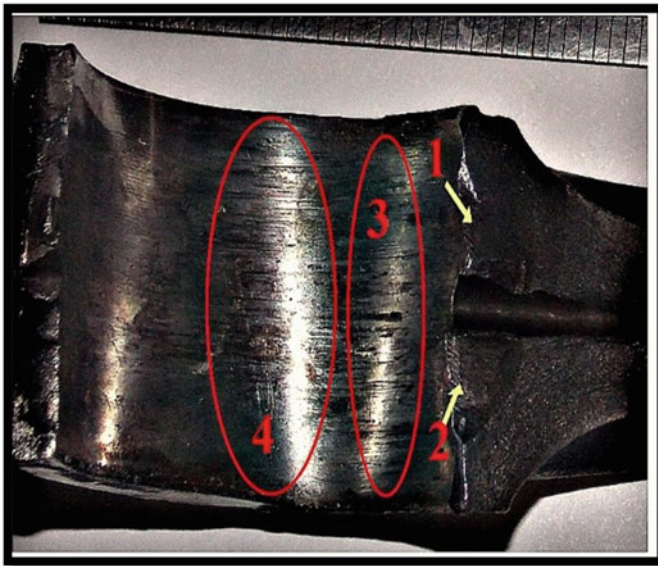
Fig. 10 Points (1 and 2) give signature of shear lip formation while areas 3 and 4 indicate scoring and wear marks

thickness by successive fluctuating loading cycles. These favored crack initiation condition.

SEM observations show crack to initiate from multiple sources of scratched region on lining surface in oil hole vicinity. Just below the shear lips, the wavy striation marks are indication of fatigue crack growth, ahead of which dimple and nodal morphologies indicate ductile crack extension. These support the fretting fatigue crack initiation and propagation mechanism to be active in the sample case of study.

FEM analysis helped to estimate the stress distribution in the rod and to locate the points of maximum stress and deformation magnitudes. These arise around the oil hole at two diametrically opposite points on its periphery. The peak stress magnitude is about 375 MPa with extreme deformation of 7.9×10^{-5} m. Crack initiation from its vicinity is reasonable.

5 Conclusion

The cause of failure of a marine type diesel engine connecting rod is analyzed. Material characterization indicates that the properties of the connecting rod are very near to AISI 4140 steel. Multiple cracks are found to originate by fretting fatigue from the vicinity of the lubricating oil hole in small end under SEM. FEM-based analysis indicates extreme magnitude of stress and deformation to situate on two diametrically opposite sites on the hole periphery. This is due to stress concentration factor at these points. Due to the combined effect of lubricating oil seizure and stress concentration factor, micro-crack initiation takes place at the vicinity of lubrication oil hole. The crack surface morphology shows slant fracture surface with wavy striation marks. This infers steady fatigue growth mechanism was active during propagation of the cracks. Then, it has dimpled and nodal microstructures signifying ductile fracture to follow steady fatigue crack growth.

References

1. Shenoy, P.S., Fatemi, A.: Dynamic analysis of loads and stresses in connecting rods. Proc. Inst. Mech. Eng. Part C: J. Mech. Eng. Sci. **220**, 615–624 (2006)
2. Ilia, E., O˝Neill, M., Tutton, K., Lanni, G., Letourneau, S., Haehnel, M.: Benchmarking the Industry: Powder Makes a Better Connecting Rod. SAE Technical Paper 2005-01-0713 (2005)
3. Afzal, A., Fatemi, A.: A Comparative Study of Fatigue Behavior and Life Predictions of Forged Steel and PM Connecting Rods, SAE Technical Paper 2004-01-1529 (2004)
4. He, B.Y., Shi, G.D., Sun, J.B., Chen, S.Z., Nie, R.: Crack analysis on the toothed mating surfaces of a diesel engine connecting rod. Eng. Fail. Anal. **34**, 443–450 (2013)
5. Xu, X.L., Yu, Z.W.: Failure analysis of a diesel engine connecting rod. J. Fail. Anal. Prev. **7**, 316–320 (2007)
6. Khare, S., Singh, O.P., Dora, K.B., Sasun, C.: Spalling investigation of connecting rod. Eng. Fail. Anal. **19**, 77–86 (2012)

7. Son, J.H., Ahn, S.C., Bae, J.G., Ha, M.Y.: Fretting damage prediction of connecting rod of marine diesel engine. J. Mech. Sci. Technol. **25**(2), 441–447 (2011)
8. Yu, Z., Xu, X.: Fatigue fracture of truck diesel engine connecting-rods. J. Fail. Anal. Prev. **15**, 311–319 (2015)
9. Lancha, A.M., Lapena, J., Serranoa, M., Gorrochategui, I.: Metallurgical failure analysis of a BWR recirculation pump shaft. Eng. Fail. Anal. **7**, 333–346 (2000)
10. Osman, A.: Failure analysis of a crankshaft made from ductile cast iron. Eng. Fail. Anal. **13**, 1260–1267 (2006)
11. Muralidharan, N.G., Kaul, R., Kasiviswanathan, K., Jayakurnar, V., Raj E.B.: Failure analysis of an ammonia refrigerant condenser tube. J. Mater. Eng. Perform. **5**, 241–246 (1996)
12. Juarez, C., Rumiche, F., Rozas, A., Cuisano, J., Lean, P.: Failure analysis of a diesel generator connecting rod. Case Stud. Eng. Failure Anal. **7**, 24–31 (2016)
13. Harding, S., Stafford, S.W.: AISI/SAE Alloy Steels: Atlas of Fractographs. In: ASM Handbook Fractography, vol. 12, ASM International, PP. 540–545 (1987)
14. Gautam, A., Sarkar, P.K.: Continuum damage mechanics-based ductile behavior and fatigue life estimation of low carbon steels: AISI 1020 and AISI 1030. Proc. Inst. Mech. Eng., Part L: J. Mater.: Des. Appl. **233**(10), 2057–2071 (2019)
15. Cook, R.D., David, S.M., Michae, E.P., Robert, J.W.: Concepts and Applications of Finite Element Analysis, 4th edn. Wiley (2002)
16. Szabo, B.A., Babuska, I.: Finite Element Analysis, 1st edn. Wiley (1991)
17. Andresen, P.L.: Corrosion fatigue testing. In: ASM Handbook. Fatigue and Fracture, vol. 19, ASM International, pp. 498–500 (1996)
18. Rabb, R.: Fatigue failure of a connecting rod. Eng. Fail. Anal. **3**(1), 13–28 (1996)

Thermal and Fluid Flow Modelling of a Heating Bed for Application in Metal AM Process

Gourav K. Sharma , **Piyush Pant** , **Prashant K. Jain** ,
Pavan Kumar Kankar , **and Puneet Tandon**

1 Introduction

Heating bed has variety of applications in manufacturing space. The purpose of providing a heating bed is to uniformly and evenly control the heating of the surface and at the same time removes the excess of heat. In the presented heating bed, the substrate is heated using conduction heating from heating bed. The substrate is kept in close contact with top surface of the bed. The heating bed consists of resistance coils in a serpentine pattern and cooling unit. A zigzag pattern duct with coolant flow takes away the excess heat from the bed [1]. The cooling unit provided in heating bed prevents the heat to be transported to the part of the axis, which would suffer distortion otherwise.

A crucial application of heating bed is seen in additive manufacturing for keeping the substrate at high temperature, which allows smaller thermal gradients during the deposition. In additive manufacturing, layer-by-layer stacking of material is done in a defined fashion to produce a part [2–4]. The temperature and temperature gradients involved during the deposition decides the final behaviour of the fabricated component. Fang et al. [5] performed the heat transfer analysis on fused coated additive manufacturing of tin alloy, they demonstrated the key role of substrate heating on printing uniformity and surface morphology of metal lines. The stable heating of heat bed could be an alternate to the warping problem commonly encountered in 3D printing [6]. In additive manufacturing technologies which utilise a focused energy source like laser and electron beam, excessive local heat input causes thermal stresses and distortion of the part [7, 8]. A preheated substrate significantly reduces the part

G. K. Sharma · P. Pant · P. K. Jain (✉) · P. Tandon
Mechanical Engineering Discipline, PDPM Indian Institute of Information Technology, Design and Manufacturing, Jabalpur, India
e-mail: pkjain@iiitdmj.ac.in

P. K. Kankar
Mechanical Engineering Department, Indian Institute of Technology, Indore, India

distortion and eliminates crack formation across deposited material [9, 10]. Residual
stresses control during weld deposition was demonstrated by controlling temperature
by implementing a heat sink [11]. Bulk substrate heating to reduce the part distortion
was suggested in research [12, 13].

From the above-reviewed literatures, heating of substrate is an important factor for
sound deposition. Consequently, it has received a lot of attention over the years. To
mitigate the above issues of heating the substrate, a heating bed design is simulated
for heat analysis to uniformly heat the substrate in contact with the heating bed. The
presented study performs a heat and fluid transport analysis of heating bed with one
inlet and one outlet cooling domain.

2 Numerical Model

2.1 Heating Bed Description

The heat bed platform's dimensions are 200 mm × 200 mm × 12 mm. The heat bed
surface plate is of cast iron of dimensions 200 mm × 200 mm. The three-dimensional
geometry model in Fig. 1 consists of subdomains: a heating bed, a heating coil, a
base plate, fluid region, and an interface between the fluid and the heating coil. The
heating bed surface is of cast iron material, interface plate and base plate are of
aluminium material (Al 6061), and the fluid region is a serpentine water flowing slot,
while the heating coil is a type of tubular heater stainless steel shielded and 8 mm
diameter. For bed base, aluminium material was selected specifically for its inherent
thermal properties and lightweight. The material properties input to the simulation
are shown in Table 1. Since the purpose of a heated platform is to transfer energy to
the printed part to raise the parts' temperature, efficient energy transfer is imperative
[14].
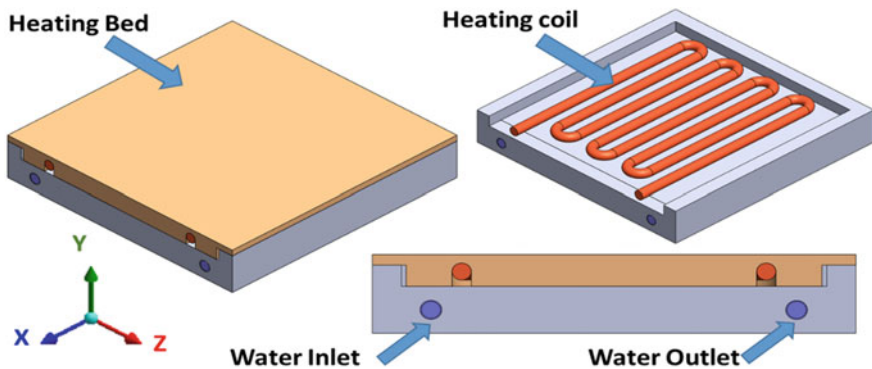
Fig. 1 CAD model of the heating bed for AM application

Table 1 Thermo-physical properties of materials used for numerical simulation [15]

Property	Material (aluminum-Al 6061)	Material (cast iron-ASTM 40)
Density (kg/m^3)	2700	7100
Thermal conductivity (W/m K)	167	46
Specific heat capacity (kJ/kg K)	896	490

2.2 Model Analysis and Assumptions

Thermal and fluid flow analysis is performed using ANSYS Workbench module and the temperature distribution on the heating bed is obtained. The heating bed assembly with cooling configuration having one inlet and one outlet is considered and shown in Fig. 2. The configuration is solved for two parametric variations of inlet water flow velocity based on the pump flow rate. The computational domain is discretized into 895,145 tetrahedral cells, fair enough to grasp the grid independence solution. A typical computational domain and model mesh is presented in Fig. 3. The study considers following assumptions:

- The flow is steady and turbulent.
- The considered fluid is water and incompressible.
- Heating coils were given a constant temperature.
- Radiative heat transfer is considered from coil surface with a constant emissivity of 0.6.

Fig. 2 Water domain with one inlet one outlet configuration of cooling channels
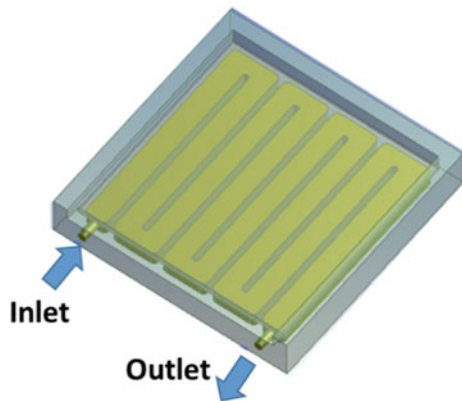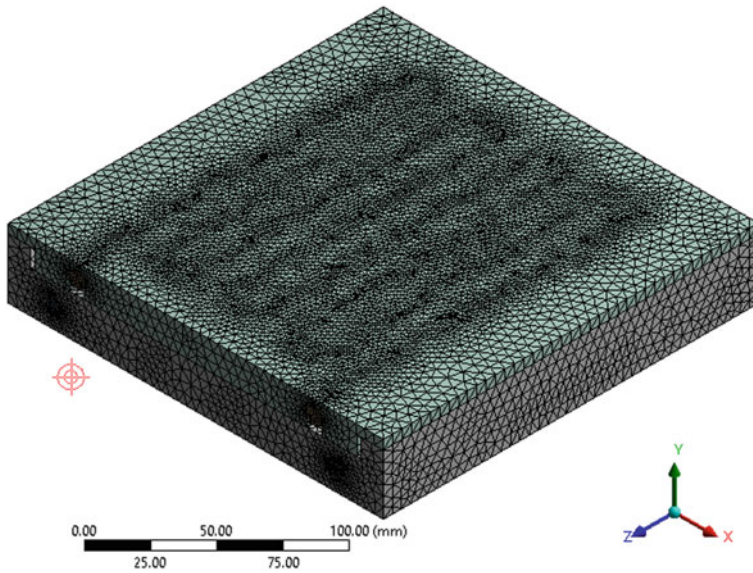
Fig. 3 3D computational domain along with mesh used for simulation

2.3 Governing Equations and Boundary Conditions

In the computational domain, the continuity, momentum and energy equations are solved for calculation of pressure, velocity and temperature. Additionally, the popular Reynolds Average Navier–Stokes (*RANS*)-based standard k–ε turbulence model is implemented for fluidic transport, due to the high Reynold's number (*Re* ~ 8500) pertaining to the physical condition of problem. Notably, k and ε are the turbulent kinetic energy and dissipation rate of kinetic energy respectively. The k and ε equations were solved to obtain turbulent viscosity. Details of the turbulence equations are not discussed here for the purpose of brevity and can be referred from literature [16, 17]. Surroundings of heating bed are exposed to convective ambience. The fluid flow is given as velocity boundary condition at inlet and pressure outlet is considered at the flow outlet. Velocity inlet condition is decided based on the flow rate and pumping capacity from water pump. The heating coils are subjected to a fixed bed temperature based on the temperature required during deposition and is governed by controlled electrical input power to coil. The generalised form of governing equation is given in the below form [17, 18].

$$\frac{\partial}{\partial t}(\rho \emptyset) + \mathrm{div}(\rho U \emptyset) = \mathrm{div}(\Gamma_\emptyset \mathrm{grad}\emptyset) + S_\emptyset \tag{1}$$

where $\emptyset$ can take the form of u, v and w velocity, temperature field, T and turbulence moderator's k and ε. ρ is the density and $\Gamma_\emptyset$ is the diffusion coefficient. Since the

Table 2 Imposed boundary and initial conditions

Water inlet velocity, V	0.75 m/s, 1.5 m/s
Heater temperature	500 °C
Water inlet temperature	25 °C
Local heat convection coefficient	20 W/m^2 K

problem is a time independent, the first term on left-hand side of Eq. 1 is negotiated. The boundary conditions were imposed to the model and their numerical values are represented in Table 2.

3 Results and Discussion

However, the proposed heating bed simultaneously serves the two purposes. Firstly, heating the deposition substrate kept atop of heating bed apex surface and secondly, cooling the heating bed base which resists the heat transfer to the bed movement unit. So, a particular interest of this study is to observe the temperature distribution at the apex, bottom and at the sidewalls of the heating bed assembly.

3.1 Temperature Distribution at Apex

The thermal field lines are visualised after solving the necessary transport equations to study the heat distribution in the heating bed. The heat distribution provides the insight for uniformity of temperature in heated surface. Figure 4a, c shows the temperature at the plane located at the apex of the heating bed. In Fig. 4a, which represents the temperature distribution for water flow velocity 1.5 m/s, the temperature of apex surface varies from 120 to 476 °C. With the flow velocity of 0.75 m/s, the temperature variation is between 162 and 481 °C. To observe a region of heating uniformity, both the above conditions identify a printing region of almost equal area, having isothermal temperature, hence suitable for deposition. This temperature uniformity sustains metal printing and can induce smaller thermal gradients resulting in smoother clad deposition without warp in single track clad. Also, this will prohibit the introduction of residual stresses, imparted majorly due the larger temperature difference between the molten metal and substrate.

3.2 Temperature Distribution at Bottom

Figure 4 also shows the temperature at the plane located at the bottom of the heating bed. In Fig. 4b, which represents the temperature distribution for water inflow velocity
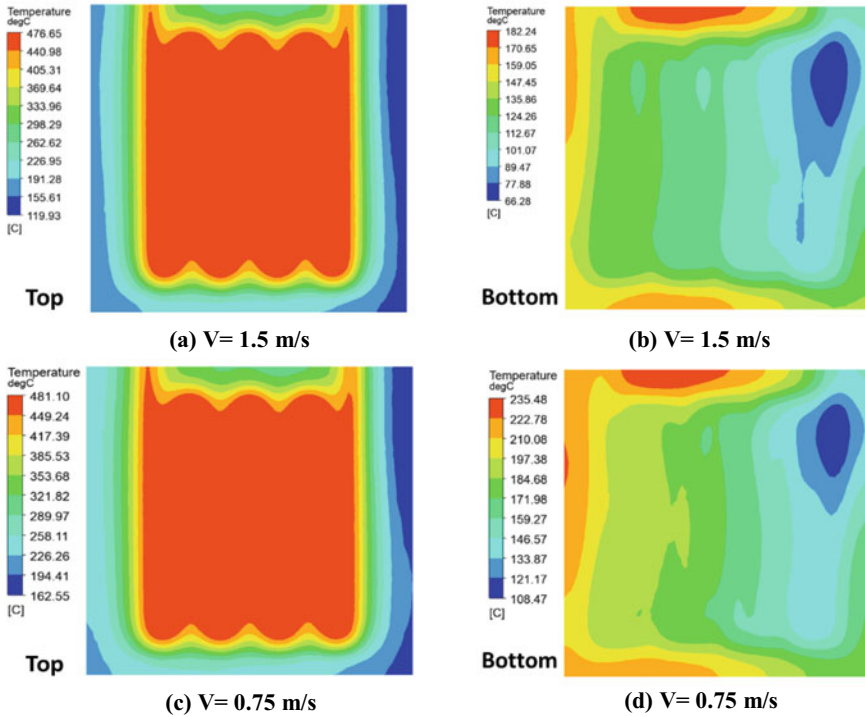
Fig. 4 Temperature distribution (°C) in heating bed; for water inlet velocity, $V = 1.5$ m/s **a** Top surface, **b** bottom surface, for water inlet velocity, $V = 0.75$ m/s, **c** top surface, **d** bottom surface

of 1.5 m/s, the thermal distribution is not uniform with the temperature ranging from 67 to 182 °C and the average surface temperature of 94 °C. With the water inlet velocity of 0.75 m/s, the maximum temperature reaches to 235 °C, while the average surface temperature is 154 °C (refer Fig. 4d). With the lower average temperature of the bed bottom, condition following water inlet velocity of 1.5 m/s is found to be more suitable for the presented design of heating bed. High temperature at the bottom of the heating bed is likely to transfer the heat to the positioning and traversing unit via conduction mode, thus causing deformation to the machine parts.

3.3 Temperature Distribution at Sidewalls and Water Domain

The heat dissipation of the heated bed should be constrained to the heating bed apex surface. So, it is necessary to know the heat conducted to the sidewalls. Figure 5 shows the temperature at the two side's namely left and right walls of the heating bed. Figure 5a represents the temperature distribution for water inlet velocity, $V = 1.5$ m/s, the temperature varies from 91.7 to 150.4 °C and 148.3 to 186 °C for
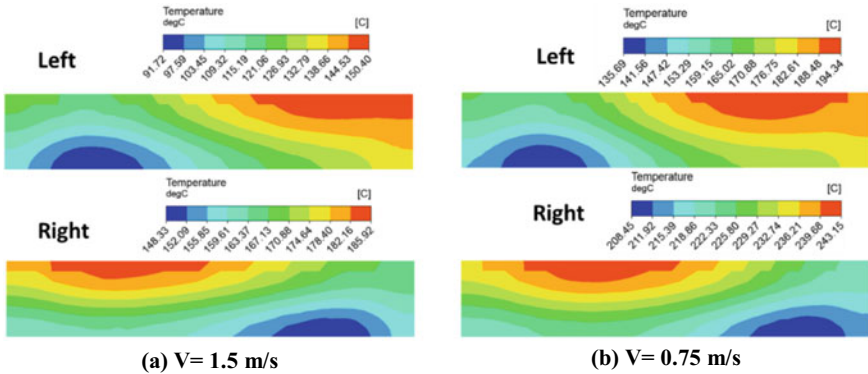
(a) V= 1.5 m/s   (b) V= 0.75 m/s

Fig. 5 Temperature distribution on sidewalls of heating bed for **a** $V = 1.5$ m/s, **b** $V = 0.75$ m/s

left and right walls, respectively. With the second input condition (refer Fig. 5b), the temperature variation is between 135.7 and 194.3 °C and 208.4 to 243.1 °C for left and right walls, respectively. The significant difference of temperature in the two walls is due to the water inflowing near the left wall and carrying the heat of the system when exiting the near right wall. From Fig. 6a, b shows the heat carried by the water for the two inflow conditions, from which it can be deduced that the turbulent flow resulting from high velocity of water helps in maintaining low temperature of the heating bed base. Thus from numerical observations, high inlet velocity condition for one inlet one outlet heating bed could be a promising design parameter of heating bed.

Based on the above simulation study, a heating bed is fabricated for application in additive manufacturing process as shown in Fig. 7. The heating bed can be uniformly heated to a manifested temperature as required, depending on the selection of depositing material. The temperature of the bed can be controlled by a Proportional Integral Derivative (PID) controller.
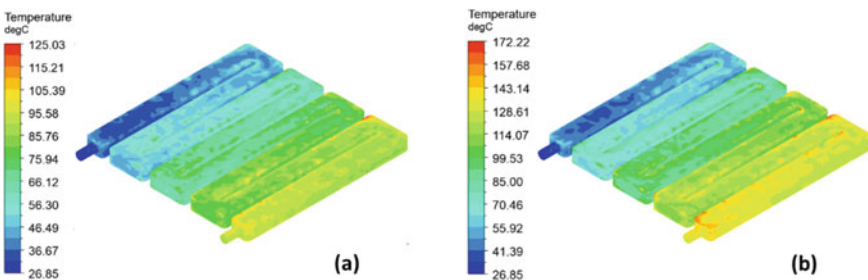
Fig. 6 Distribution of temperature (°C) in water domain of the heating bed for **a** $V = 1.5$ m/s, **b** $V = 0.75$ m/s

Fig. 7 Fabricated heating bed based for application in AM process
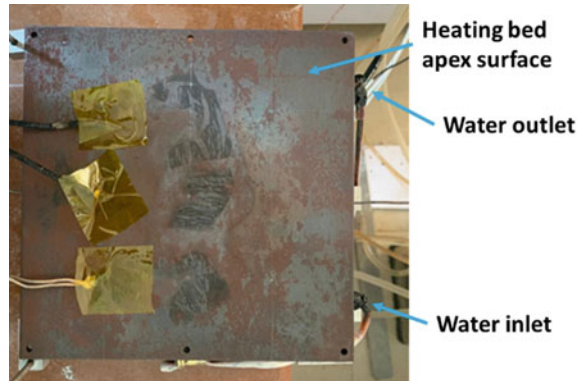
4 Conclusion

In this study, a novel heating bed design is presented based on the thermal process simulations. The simulation model solves the heat transfer and fluid flow equations using Ansys Fluent platform. The heat dissipation of bed and the effect on the substrate were analysed by a CFD simulation, and the simulation results were compared for two water inflow conditions. The conclusions of this article can be directly applied under the same working conditions, and for different conditions, it can be used as a reference. The following conclusions can be drawn from the results of this study:

- Water inflow velocity of 1.5 m/s results in ideal heating of bed apex surface and significantly cooling the bed bottom surface.
- The presented work could find its probabilistic application in the additive manufacturing, wherein substrate heating is required for isothermal deposition of every layer, so as to ensure less residual stresses and reduced distortions in the final part. Such, a heating bed is fabricated and demonstrated.
- Since the outlet temperature of water reaches around 90 °C, the provision of a radiator would ensure the cooling of water and recirculate in the cooling unit of heating bed.

References

1. Karunakaran, K.P., Suryakumar, S., Pushpa, V., Akula, S.: Low cost integration of additive and subtractive processes for hybrid layered manufacturing. Robot. Comput.-Integr. Manuf. **26**(5), 490–499 (2010)
2. Sharma, G.K., Pant, P., Jain, P.K., Kankar, P.K. Tandon, P.: On the suitability of induction heating system for metal additive manufacturing. In: Proceedings of the Institution of Mechanical Engineers, Part B: Journal of Engineering Manufacture (2020). https://doi.org/10.1177/0954405420937854
3. Jain, P.K., Pandey, P.M., Rao, P.V.M.: Experimental investigations for improving part strength in selective laser sintering. Virtual Phys. Prototyp. **3**(3), 177–188 (2008)
4. Francis, V., Jain, P.K.: Effect of stage-dependent addition of nanoparticles in additive manufacturing. J. Thermoplast. Compos. Mater. **33**(3), 357–376 (2020). https://doi.org/10.1177/0892705718805528
5. Fang, X., Du, J., Wei, Z., He, P., Bai, H., Wang, X., Lu, B.: An investigation on effects of process parameters in fused-coating based metal additive manufacturing. J. Manuf. Processes **28**, 383–389 (2017)
6. Keşkekçi, A.B., Şenol, R., Bayrakci, H.C.: Fuzzy logic approach for warping problem in 3D printing. Int. J. Comput. Exp. Sci. Eng. **6**(1), 75–77 (2020)
7. Shamsaei, N., Yadollahi, A., Bian, L., Thompson, S.M.: An overview of direct laser deposition for additive manufacturing; part II: mechanical behavior, process parameter optimization and control. Addit. Manuf. **8**, 12–35 (2015)
8. Pant, P., Chatterjee, D., Samanta, S.K., Nandi, T., Lohar, A.K.: A bottom-up approach to experimentally investigate the deposition of austenitic stainless steel in laser direct metal deposition system. J. Braz. Soc. Mech. Sci. Eng. **42**(2), 1–10 (2020)
9. Corbin, D.J., Nassar, A.R., Reutzel, E.W., Beese, A.M., Michaleris, P.: Effect of substrate thickness and preheating on the distortion of laser deposited Ti–6Al–4V. J. Manuf. Sci. Eng. **140**(6), 061009(1–10) (2018)
10. Alimardani, M., Fallah, V., Khajepour, A., Toyserkani, E.: The effect of localized dynamic surface preheating in laser cladding of Stellite 1. Surf. Coat. Technol. **204**, 3911–3919 (2010)
11. Bajpei, T., Chelladurai, H., Ansari, M.Z.: Mitigation of residual stresses and distortions in thin aluminium alloy GMAW plates using different heat sink models. J. Manuf. Processes **22**, 199–210 (2016)
12. Jendrzejewski, R., Śliwiński, G., Krawczuk, M., Ostachowicz, W.: Temperature and stress fields induced during laser cladding. Comput. Struct. **82**(7–8), 653–658 (2004)
13. Klingbeil, N.W., Beuth, J.L., Chin, R.K., Amon, C.H.: Residual stress-induced warping in direct metal solid freeform fabrication. Int. J. Mech. Sci. **44**(1), 57–77 (2002)
14. Wang, D., Wang, X., Liu, Y., Chen, P., Liu, J.: A study on the heat dissipation and thermal environment of a novel heated bed. J. Build. Phys. **42**(5), 629–651 (2019)
15. Mechanical Properties of Gray Irons, Cast Iron Science and Technology. In: Stefanescu, D.M. (ed.) ASM Handbook, vol. 1A, pp. 430–455. ASM International (2017). https://doi.org/10.31399/asm.hb.v01a.a0006344
16. Nayak, B.B., Chatterjee, D.: Convective heat transfer in slurry flow in a horizontal Y-shaped branch pipe. Powder Technol. **318**, 46–61 (2017)
17. Argyropoulos, C.D., Markatos, N.C.: Recent advances on the numerical modelling of turbulent flows. Appl. Math. Model. **39**(2), 693–732 (2015)
18. Rictor, A., Riley, B.: Optimization of a heated platform based on statistical annealing of critical design parameters in a 3D printing application. Procedia Comput. Sci. **83**, 712–716 (2016)

Numerical Analysis of Inclined Jet Micro-channel Heat Sink Using Nanofluids

Mohammad Zunaid , **Prakash Singh** , **and Afzal Husain**

1   Introduction

Due to decrease in the size of the electronics, the power density has increased drastically. This led to increase in heat fluxes and thus needed better heat dissipation system. The high heat flux in the microelectronic devices makes it difficult to cool. It is one of the major challenges regarding the dense packaging of the microelectronics devices. This problem has to be fixed in order to further decrease the size of microchips. Hence, new tools should be developed for better thermal management. The micro-channels have become quite important in scientific community and industry and have received a lot of attention from them. One of the creative works of this field was completed by Tuckerman and Pease [1]. They showed that microchannels had very effective cooling potential. The microchips will work properly only if there is proper heat dissipation and the surface temperature of the microchip is within the permissible limits. The nanofluids can maintain the required temperature of such systems. The use of nanoparticles in the base fluid increases the effective thermal conductivity of the resulting nanofluid. The nanofluid removes more heat as compared to single-phase base liquid used as a coolant.

It also helps to overcome space constraints and provides great design flexibility. Tuckerman and Pease [1] investigated as mass flow rate decreases maximum thermal resistance of downstream fluid increases. Yeh [2] said hydraulic diameter and the aspect ratio of micro-channel have serious effects not only on Reynolds number but also on the friction factor and coefficient of heat transfer. Garimella and Rice [3] found out that as Reynolds number and nozzle diameter of micro-channel increase,

M. Zunaid (✉) · P. Singh
Department of Mechanical Engineering, Delhi Technological University, North West Delhi, Delhi
110042, India
e-mail: mzunaid3k@gmail.com; graaaaa0@gmail.com

A. Husain
Department Mechanical and Industrial Engineering, Sultan Qaboos University, Muscat, Oman

the rate of heat transfer also increases. Peng and Peterson [4] analyzed the micro-channels and investigated the convection heat transfer dependence on the aspect ratio. Mala, Li and Dale [5] numerically analyzed the micro-channel and detected that as complicacy of micro-channel increases, it is tougher to find out correct value of heat transfer. Wu et al. [6] found that a micro-impinging jet can provide effective cooling, greater driving pressure gives improved cooling, but lesser efficiency. Lee and Vafai [7] presented comparative study of jet impingement and micro-channel cooling. He investigated jet impingement analysis and gave better results in comparison to micro-channel cooling for a large plate. Fedorov and Viskanta [8] concluded that the thermo-properties are temperature dependent. Ambatipudi and Rahman [9] and Liu and Garimella [10] showed that as channel length increases, the local temperature of fluid also increases. Qu and Mudawar [11] and [12] concluded that reduction of the pressure in micro-channel increases with an increase in Reynolds number. Khanafer et al. [13] explained the formulae to find out thermal expansion and coefficient of nanofluids. Wen and Ding [14] found out that it was beneficial to use nanofluid as it improved the convective heat transfer rate of fluid by improving its thermal conductivity. Yang et al. [15] and [16] performed an experiment using graphite as nanoparticle, and thermal conductivity of the fluid increased significantly by adding graphite as a nanoparticles. Foli et al. [17] found out that the heat transfer of a micro-channel depends on its dimensional factors. Husain and Kim [18] investigated that overall thermal resistance of micro-channel decreases with increase the fluid mass flow rate. Samad et al. [19] concluded as rate of heat transfer increases, drop in pressure also increases. Michna et al. [20] said average heater surface temperature drops with rise in resistance of the heater. Chein and Chen [21] proposed a numerical study on micro-channel heat sink. They concluded that highest temperature occurs at the edge of the micro-channel and lowest at the entry side of the plate. Husain and Kim [22] found that thermal resistance decreases with increase in the pumping power. De Paz and Jubran [23] and Husain et al. [24] said that overall average heat transfer decreases with increase in the height to jet diameter of nozzle. Brinkman [25] and Hamilton [26] explained relation to find out thermal conductivity and viscosity of mixture of two phases. Husain et al. [27] say difference between inlet and outlet fluid temperature decreases with increase in the number of jets. Ali and Arshad [28] and [29] reported as Reynolds number increases, micro-channel outlet water temperature decreases in both staggered and inline geometry. Husain et al. [24] proposed a novel hybrid design of micro-channel having jets and pillars. They investigated rate of heat transfer in channel increases with increase in number of pillars. Arshad and Ali [29] and [30] found that Nusselt number increases with increase in velocity of water. Wei Wang et al. [31] investigated the relationship between the enhanced thermal conductivity and nanoparticle size, volume fraction and temperature. Zunaid et al. [32] and [33] found pressure drop in micro-channel heat sink increases with increase in Reynolds number. Hou et al. [34] investigated as the volume fraction of nanoparticles increased in base fluid, the heat transfer performance of micro-channel heat sink improved.

As these case studies show, there are a lot of diverse mathematical solutions to the Navier–Stokes equation; they have been applied magnificently on the simple

micro-channels as well as in jet impingement models with different thermo-physical properties and designing parameters like Reynolds number, jet diameter, mass flow rate, number of jets and type of cooling fluid. The recent challenges are caused due to decrease in the size of electronic device demands' improvement in heat dissipation. Hence, this paper is directed toward addressing improvement in heat transfer by performing a thermal and fluid flow analysis in an inclined jet impingement model with different nanofluids.

2 Description of Problem

A schematic diagram of copper based micro-jets impingement heat sink model is shown in Fig. 1. The analysis was performed on the fluid flow domain and solid domain. Inclined inlet jets are provided at top of fluid channel. The fluid domain was created to allow water and nanofluids to pass through micro-channel. The constant heat flux (50,000 W/m^2) was taken through the bottom of the solid substrate. In order to provide a cooling effect, the micro-jet impingement was used. The base fluid (water) is mixed with nanoparticles of aluminium oxide (Al$_2$O$_3$) and titanium oxide (T$_i$O$_2$) in solid volume fraction of 0.1, 0.5 and 1%. The mass flow rate of pure water and nanofluids were taken as 0.000062, 0.000122 and 0.000182 kg/s. The study is simulated for 6, 10, 14, 18 jets with diameters, i.e., 0.1 mm. Figure 2a–d shows micro-channels having 6, 10, 14 and 18 jets, respectively. Figure 2 also shows that half of the jets are placed at an inclination of 45° and remaining half are inclined at 135° from upper surface of the micro-channel. Copper is used as the solid material. The depth of the fluid domain which interacts with solid material is 0.3 mm. The geometric parameters, e.g., cross-sectional area, thickness of the solid substrate base, height of the fluid domain, length of nozzle, are constant throughout the analysis.
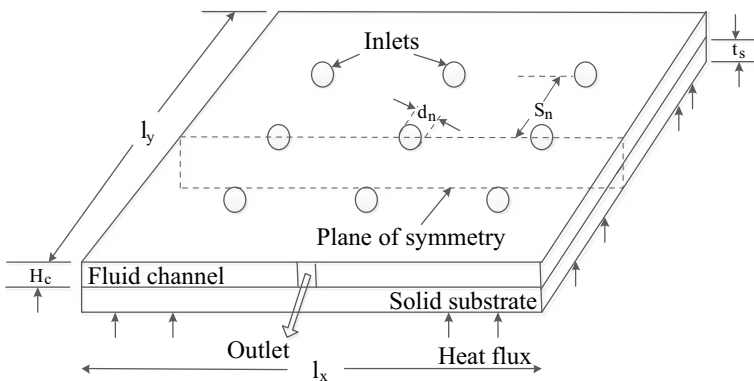
Fig. 1 Schematic diagram of multiple micro-jet impingements heat sink
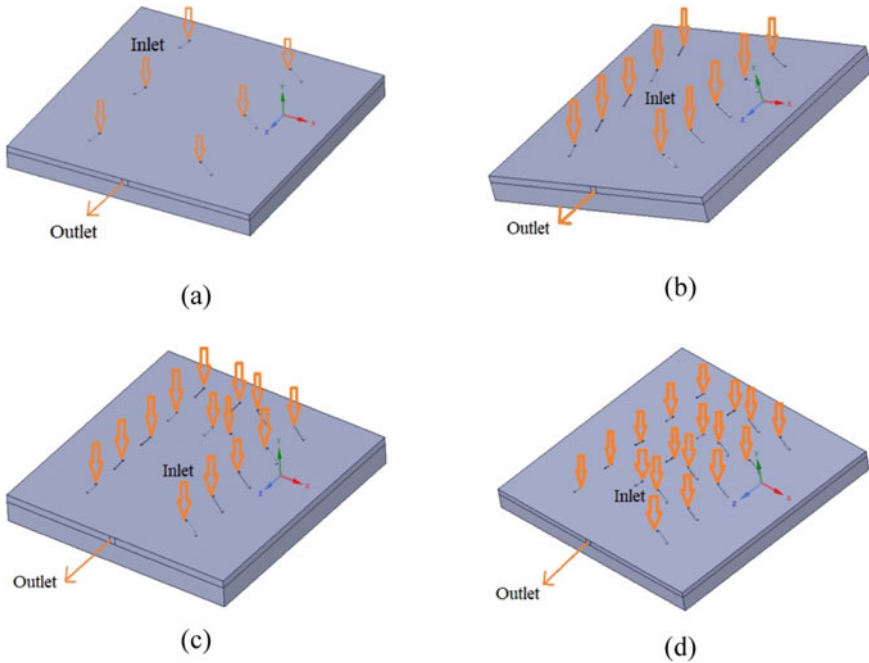
Fig. 2 Geometry of inclined jets micro-channel heat sinks **a** 6 jets, **b** 10 jets, **c** 14 jets and **d** 18 jets

3　Validation

In this mathematical analysis, authentication is done for 45° inclined four micro-jets impingement heat sink and the outcomes are plotted for maximum temperature rise of cooling fluid. Four different values of heat flux are supplied at the bottom surface of the heat sink for a particular mass flow rate. The validation of the present scheme was carried out for a laminar flow of fluid in micro-channel. The validation results were compared with the benchmark solutions reported in Husain et al. [27]. The maximum percentage errors ΔT are 4%, 2.91%, 1.86% and 1.32% for 5, 10, 15 and 20 W/cm² heat flux, respectively (Table 1).

Table 1 Dimensions of the inclined micro-jets heat sink

S. No.	No. of jets	A_{cs} (mm²)	H_c (mm)	t_s (mm)	d_n (mm)	l_n (mm)	S_n (mm)
1.	6	12 × 12	0.3	0.8	0.1	0.5	3
2.	10	12 × 12	0.3	0.1	0.1	0.5	2
3.	14	12 × 12	0.3	0.1	0.1	0.5	2
4.	18	12 × 12	0.3	0.1	0.1	0.5	2

4   Simulation Results

In this study, parameters such as mass flow rate, number of jets and fraction of nanoparticles, affect heat transfer and outlet bulk mean temperature. The CFD analysis is used to simulate 6, 10, 14 and 18 jets; these jets are inclined at 45° and 135° from upper surface of the micro-channel. The temperature contour for 1% T_iO_2 and 0.000062 kg/s mass flow rate for 6, 10, 14 and 18 jets is shown in Fig. 3. The variation of outlet bulk mean temperature of pure water and nanofluids with number of jets (6–18) for constant mass flow rate of 0.000062, 0.000122, 0.000182 kg/s are shown in Fig. 4a–c. It was observed that outlet bulk mean temperature of pure water and nanofluids increased with increase in number of jets (Table 2).

In Fig. 4a, it is clear that nanofluid having solid volume fraction of 0.1%, 0.5% and 1% Al_2O_3 obtains maximum temperature 328.011, 328.371 and 328.822 K, respectively, and nanofluid having 0.1%, 0.5%, 1% TiO_2 obtained maximum temperature 328.017, 328.401, 328.881 K, respectively for 18-jet microchannel and 0.000062 kg/s mass flow rate.
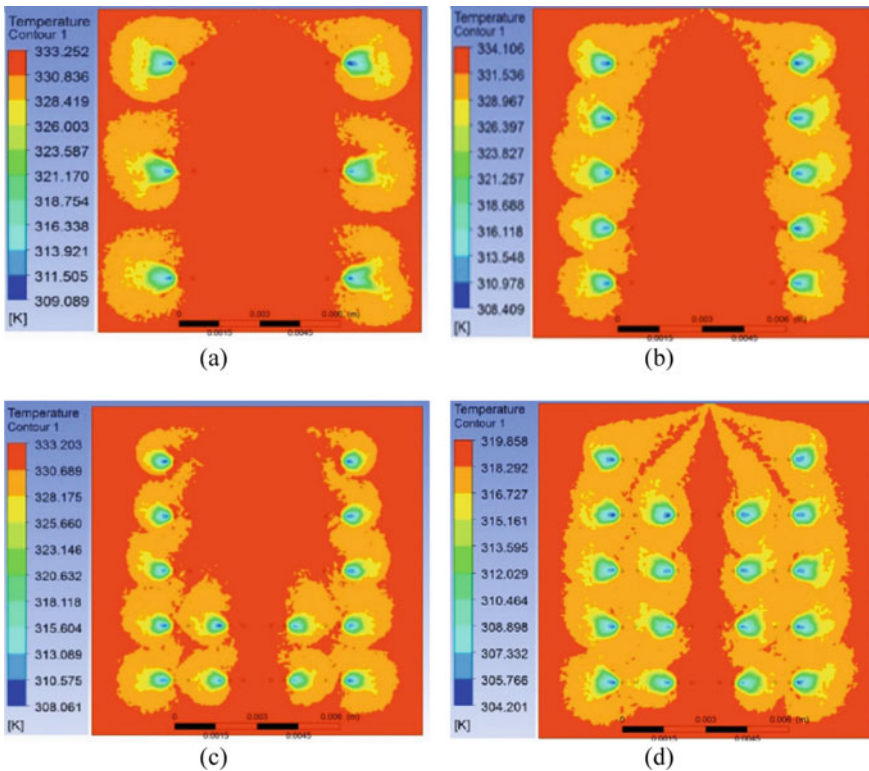
Fig. 3 Temperature contour for 1% TiO_2 and 0.000062 kg/s mass flow rate for **a** 6 jets, **b** 10 jets, **c** 14 jets and **d** 18 jets
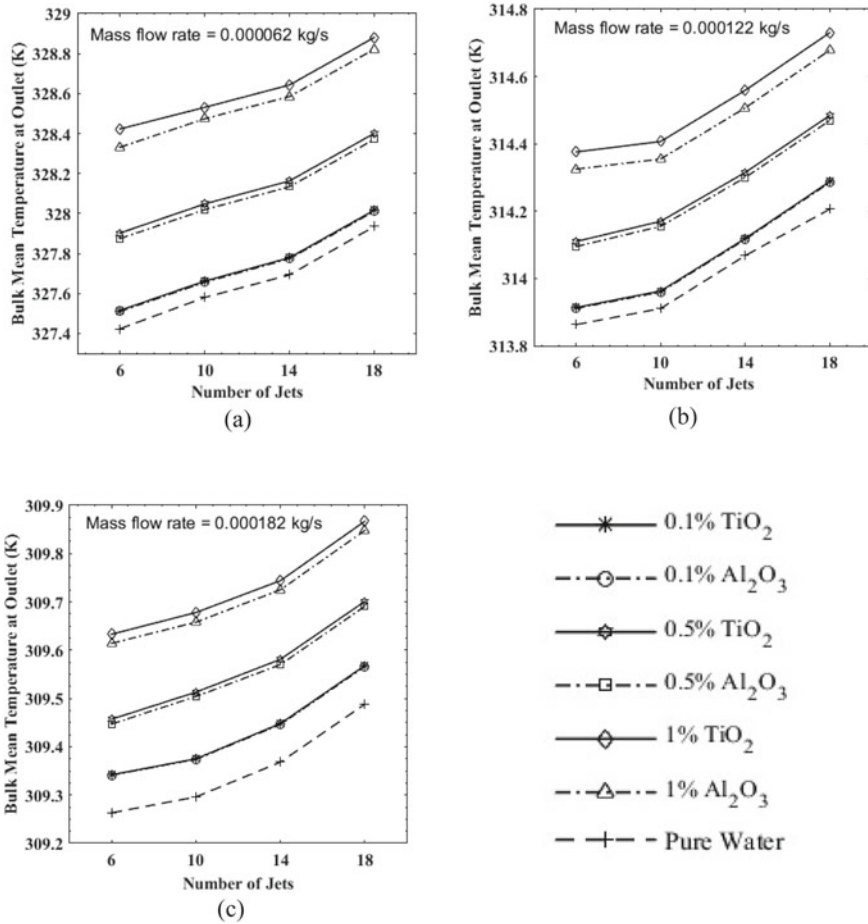
Fig. 4 Variation of bulk mean temperature with number of jets at mass flow rate of **a** 0.000062 kg/s, **b** 0.000122 kg/s, **c** 0.000182 kg/s

Table 2 Values of maximum temperature rise of cooling fluid

Heat flux (W/cm^2)	ΔT (K), Husain et al. [27]	ΔT (K), Present	% Error
5	5	5.2	4.00
10	10.3	10.6	2.91
15	21.5	21.9	1.86
20	38	38.5	1.32

The exit temperature obtained by Al_2O_3 and TiO_2 nanofluids is increased by increasing the volume fraction of nanoparticles because heat transfer coefficient of nanofluid increases with increase in the volume fraction of nanoparticles in base fluid. In Fig. 4a, nanofluid containing 1% TiO_2 gives the highest bulk mean temperature. Bulk mean temperature 328.423, 328.531, 328.643 and 328.881 K is observed at exit of micro-channel for constant mass flow rate of 0.000062 kg/s and 6, 10, 14 and 18 jets, respectively.

In Fig. 4b, 18-jet micro-channel containing 0.1%, 0.5% and 1% solid volume fraction of Al_2O_3 achieves maximum temperature of 314.285, 314.469 and 314.678 K, respectively, and 0.1%, 0.5%, 1% solid volume fraction of TiO_2 achieve maximum temperature of 314.288, 314.484 and 314.73 K, respectively, for a fixed mass flow rate of 0.000122 kg/s. Figure 4b also indicates that nanofluid containing 1% TiO_2 gives highest bulk mean temperature of 314.73 K at outlet for 6, 10, 14 and 18 jets, respectively, for mass flow rate of 0.000122 kg/s.

In Fig. 4c, it is clear that for 18-jet micro-channel containing 0.1%, 0.5% and 1% Al_2O_3 obtains maximum temperature of 309.566, 309.691, and 309.848 K, respectively, and having 0.1%, 0.5%, 1% TiO_2 obtains maximum temperature of 309.568, 309.701, 309.867 K, respectively, for constant mass flow rate of 0.000182 kg/s. Figure 4c also displays that nanofluid having 1% TiO_2 has highest bulk mean temperature at outlet.

Figure 4a–c dictates that maximum outlet bulk mean temperature for pure water and nanofluids at constant mass flow rate of 0.000062, 0.000122, 0.000182 kg/s is for 18-jet micro-channel. These figures also reveal that outlet bulk mean temperature of nanofluid is more than that of water. Figure 4a–c also indicate that as the concentration of nanoparticles in the base fluid is increased, the bulk mean temperature of fluid at the outlet also increases while keeping mass flow rate constant. As mass flow rate increases, the bulk mean temperature at the outlet decreases. The simulation carried out on nanofluid gave better heat transfer than pure water.

5 Conclusions

This numerical simulation can be used to analyze the behavior of Al_2O_3/water and TiO_2/water nanofluids. The study has been conducted under steady laminar flow for micro-channel geometry. The nanofluid is considered homogenous throughout with modified thermo-physical properties. These modified properties are taken into account while performing simulation. Nanofluids show an increase in the heat transfer with respect to the base fluid. Results showed that as mass flow rate of nanofluid was increased, the bulk mean temperature at outlet decreased. It was observed that bulk mean temperature of both nanofluids at the outlet increased with increase in percentage concentration of the nanoparticles in base fluid. The results for both nanofluids indicate that the heat transfer of nanofluids improves with increase in number of jets. It was observed that for all the concentration of nanoparticle, the outlet bulk mean temperature of nanofluid containing TiO_2 is more than Al_2O_3.

When mass flow rate was increased keeping number of jets constant, then bulk mean temperature at outlet decreased thus decreasing the heat transfer rate. The 18-jet arrangement used during simulation dictated maximum bulk mean temperature at outlet while keeping mass flow rate constant.

References

1. D. B. Tuckerman and R. F. W. Pease, "High-Performance Heat Sinking for VLSI," *IEEE Electron Device Lett.*, vol. EDL-2, no. 5, pp. 126–129, 1981, https://doi.org/10.1109/edl.1981.25367

2. Yeh, L.T.: Review of heat transfer technologies in electronic equipment. J. Electron. Packag. Trans. ASME **117**(4), 333–339 (1995). https://doi.org/10.1115/1.2792113

3. Garimella, S.V., Rice, R.A.: Confined and submerged liquid jet impingement heat transfer. J. Heat Transfer **117**(4), 871–877 (1995). https://doi.org/10.1115/1.2836304

4. Peng, X.F., Peterson, G.P.: Convective heat transfer and flow friction for water flow in microchannel structures. Int. J. Heat Mass Transf. **39**(12), 2599–2608 (1996). https://doi.org/10.1016/0017-9310(95)00327-4

5. Mala, G.M., Li, D., Dale, J.D.: Heat transfer and fluid flow in microchannels. Int. J. Heat Mass Transf. **40**(13), 3079–3088 (1997). https://doi.org/10.1016/s0017-9310(96)00356-0

6. S. Wu, J. Mai, Y. C. Tai, and C. M. Ho, "Micro heat exchanger by using MEMS impinging jets," *Proc. IEEE Micro Electro Mech. Syst.*, pp. 171–176, 1999, https://doi.org/10.1109/memsys.1999.746799

7. Lee, D.Y., Vafai, K.: Comparative analysis of jet impingement and microchannel cooling for high heat flux applications. Int. J. Heat Mass Transf. **42**(9), 1555–1568 (1999). https://doi.org/10.1016/S0017-9310(98)00265-8

8. Fedorov, A.G., Viskanta, R.: Three-dimensional conjugate heat transfer in the microchannel heat sink for electronic packaging. Int. J. Heat Mass Transf. **43**(3), 399–415 (2000). https://doi.org/10.1016/S0017-9310(99)00151-9

9. Ambatipudi, K.K., Rahman, M.M.: Analysis of conjugate heat transfer in microchannel heat sinks. Numer. Heat Transf. Part A Appl. **37**(7), 711–731 (2000). https://doi.org/10.1080/104077800274046

10. Liu, D., Garimella, S.V.: Analysis and optimization of the thermal performance of microchannel heat sinks. Int. J. Numer. Methods Heat Fluid Flow **15**(1), 7–26 (2005). https://doi.org/10.1108/09615530510571921

11. Qu, W., Mudawar, I.: Analysis of three-dimensional heat transfer in micro-channel heat sinks. Int. J. Heat Mass Transf. **45**(19), 3973–3985 (2002). https://doi.org/10.1016/S0017-9310(02)00101-1

12. Qu, W., Mudawar, I.: Experimental and numerical study of pressure drop and heat transfer in a single-phase micro-channel heat sink. Int. J. Heat Mass Transf. **45**(12), 2549–2565 (2002). https://doi.org/10.1016/S0017-9310(01)00337-4

13. Khanafer, K., Vafai, K., Lightstone, M.: Buoyancy-driven heat transfer enhancement in a two-dimensional enclosure utilizing nanofluids. Int. J. Heat Mass Transf. **46**(19), 3639–3653 (2003). https://doi.org/10.1016/S0017-9310(03)00156-X

14. Wen, D., Ding, Y.: Experimental investigation into convective heat transfer of nanofluids at the entrance region under laminar flow conditions. Int. J. Heat Mass Transf. **47**(24), 5181–5188 (2004). https://doi.org/10.1016/j.ijheatmasstransfer.2004.07.012

15. Yang, Y., Zhang, Z.G., Grulke, E.A., Anderson, W.B., Wu, G.: Heat transfer properties of nanoparticle-in-fluid dispersions (nanofluids) in laminar flow. Int. J. Heat Mass Transf. **48**(6), 1107–1116 (2005). https://doi.org/10.1016/j.ijheatmasstransfer.2004.09.038

16. S. El Bécaye Maïga, S. J. Palm, C. T. Nguyen, G. Roy, and N. Galanis, "Heat transfer enhancement by using nanofluids in forced convection flows," *Int. J. Heat Fluid Flow*, vol. 26, no. 4 SPEC. ISS., pp. 530–546, 2005, https://doi.org/10.1016/j.ijheatfluidflow.2005.02.004

17. Foli, K., Okabe, T., Olhofer, M., Jin, Y., Sendhoff, B.: Optimization of micro heat exchanger: CFD, analytical approach and multi-objective evolutionary algorithms. Int. J. Heat Mass Transf. **49**(5–6), 1090–1099 (2006). https://doi.org/10.1016/j.ijheatmasstransfer.2005.08.032

18. A. Husain and K. Y. Kim, "Shape optimization of micro-channel heat sink for micro-electronic cooling," *IEEE Trans. Components Packag. Technol.*, vol. 31, no. 2 SPEC. ISS., pp. 322–330, 2008, https://doi.org/10.1109/tcapt.2008.916791

19. Samad, A., Lee, K.D., Kim, K.Y.: Multi-objective optimization of a dimpled channel for heat transfer augmentation. Heat Mass Transf. und Stoffuebertragung **45**(2), 207–217 (2008). https://doi.org/10.1007/s00231-008-0420-6

20. Michna, G.J., Browne, E.A., Peles, Y., Jensen, M.K.: Single-phase microscale jet stagnation point heat transfer. J. Heat Transfer **131**(11), 1–8 (2009). https://doi.org/10.1115/1.3154750

21. Chein, R., Chen, J.: Numerical study of the inlet/outlet arrangement effect on microchannel heat sink performance. Int. J. Therm. Sci. **48**(8), 1627–1638 (2009). https://doi.org/10.1016/j.ijthermalsci.2008.12.019

22. Husain, A., Kim, K.Y.: Enhanced multi-objective optimization of a microchannel heat sink through evolutionary algorithm coupled with multiple surrogate models. Appl. Therm. Eng. **30**(13), 1683–1691 (2010). https://doi.org/10.1016/j.applthermaleng.2010.03.027

23. De Paz, M.L., Jubran, B.A.: Numerical modeling of multi micro jet impingement cooling of a three dimensional turbine vane. Heat Mass Transf. und Stoffuebertragung **47**(12), 1561–1579 (2011). https://doi.org/10.1007/s00231-011-0819-3

24. Husain, A., Ariz, M., Al-Rawahi, N.Z.H., Ansari, M.Z.: Thermal performance analysis of a hybrid micro-channel, -pillar and -jet impingement heat sink. Appl. Therm. Eng. **102**, 989–1000 (2016). https://doi.org/10.1016/j.applthermaleng.2016.03.048

25. Brinkman, H.C.: The viscosity of concentrated suspensions and solutions. J. Chem. Phys. **20**(4), 571 (1952). https://doi.org/10.1063/1.1700493

26. Hamilton, R.L.: Thermal conductivity of heterogeneous two-component systems. Ind. Eng. Chem. Fundam. **1**(3), 187–191 (1962). https://doi.org/10.1021/i160003a005

27. Husain, A., Kim, S.M., Kim, K.Y.: Performance analysis and design optimization of micro-jet impingement heat sink. Heat Mass Transf. und Stoffuebertragung **49**(11), 1613–1624 (2013). https://doi.org/10.1007/s00231-013-1202-3

28. Ali, H.M., Arshad, W.: Thermal performance investigation of staggered and inline pin fin heat sinks using water based rutile and anatase TiO_2 nanofluids. Energy Convers. Manag. **106**, 793–803 (2015). https://doi.org/10.1016/j.enconman.2015.10.015

29. Arshad, W., Ali, H.M.: Experimental investigation of heat transfer and pressure drop in a straight minichannel heat sink using TiO_2 nanofluid. Int. J. Heat Mass Transf. **110**, 248–256 (2017). https://doi.org/10.1016/j.ijheatmasstransfer.2017.03.032

30. Duangthongsuk, W., Wongwises, S.: An experimental investigation on the heat transfer and pressure drop characteristics of nanofluid flowing in microchannel heat sink with multiple zigzag flow channel structures. Exp. Therm. Fluid Sci. **87**, 30–39 (2017). https://doi.org/10.1016/j.expthermflusci.2017.04.013

31. Wei Wang, Lin Lin, Zhou XiaoFeng, and ShengYue Wang, "A comprehensive model for the enhanced thermal conductivity of nanofluids," *J. Adv. Res. Phys.*, vol. 3, no. 2, pp. 1–5, 2017, [Online]. Available: http://stoner.phys.uaic.ro/jarp/index.php?journal=jarp&page=article&op=view&path%5B%5D=70

32. Zunaid, M., Jindal, A., Gakhar, D., Sinha, A.: Numerical study of pressure drop and heat transfer in a straight rectangular and semi cylindrical projections microchannel heat sink. J. Therm. Eng. **3**(5), 1453–1465 (2017). https://doi.org/10.18186/journal-of-thermal-engineering.338903

33. Zunaid, M., Cho, H.M., Husain, A., Jindal, A., Kumar, R., Chauhan, B.S.: Computational Analysis of Liquid Jet Impingement Microchannel Cooling. Mater. Today Proc. **5**(14), 27877–27883 (2018). https://doi.org/10.1016/j.matpr.2018.10.026
34. Y. Hou, J. Yang, and W. Zhang, "Numerical Study of Enhanced Heat Transfer of MicroChannel Heat Sink with Nanofluids," *IOP Conf. Ser. Mater. Sci. Eng.*, vol. 721, no. 1, 2020, https://doi.org/10.1088/1757-899x/721/1/012052

Industrial and Production Engineering

Study of Effects of Part Commonality on Stochastically Variable Product Demand

Shubha , **Shivam Singh** , **Shubham Sharma** , **and M. S. Niranjan**

1 Introduction

Part commonality refers to the condition of product families which have similar bill of materials [1]. The list of parts a product is composed of is bill of materials. Bi and Zhang [2] define modularity as higher instances of independence and usability among components that configure the products. Higher levels of commonality lead to utilization of economy of scale as a tool for business advantage through improvement in manufacturing, design and inventory performance. The modular products are devised through a product architecture that helps to achieve products as a combination of part subassemblies. Commonality helps in conceiving multiple product configurations by way of various possible combinations of some unique parts over common subassembly in a way maximizing the product variety with limited number of part assortments.

In terms of statistical theory, higher level of part commonality helps to optimize inventory cost for a required level of demand fulfilment. Another managerial advantage associated with common parts is the reduction in the inventory profile of the warehouse, which in effect reduces the capital bind-up within the inventory system. It also helps to simplify the planning and scheduling systems in the production units. Collier [3] emphasizes positive influence of commonality on manufacturing system performance. Higher level of part demand from the supplier as a result of part commonality across multiple products helps in reduction in order variability. The final cascading effect goes into reduction in uncertainty. Furthermore, Vishkaei et al. [4] developed a bi-objective inventory model which minimized the total stock-out costs by considering stock-out time as a separate objective. This reduces the

Shubha (✉) · S. Singh · S. Sharma · M. S. Niranjan
Department of Mechanical, Production & Industrial and Automobile Engineering, Delhi Technological University, Shahbad Daulatpur, Main Bawana Road, Delhi 110042, India
e-mail: shubha22dtu@gmail.com

863

safety stocks and improves productivity [5]. Some studies [6] indicate drawbacks associated with too much commonality.

In terms of enterprise supply chain performance, demand variability induces supply chain uncertainly which introduces the Bullwhip effect in inventory stocks at its upstream tiers. Statistically, common parts across multiple products help to suppress demand variance [5]. Gerchak and Henig [7] validate this for a three-level supply chain with distribution center serving product demands which have varying levels of part commonality. Similarly, Catena [8] provided models for safety stock for common components for assemble/manufacture to order systems. Persona [9] applied this in industries and show reduction in safety stock. The method for calculating safety stocks for components that are used in modular products in continuous review inventory policy is proposed by Chopra and Meindl [5], while Hernández [10] uses a method to calculate safety inventory considering commonality and the replacement of components under a Make to Order strategy.

1.1 Part Commonality

With regard to product design and manufacturing, component commonality is defined as the instance in which two or more products possess common components in their product structures. In manufacturing industries, the management of inventory is carried out to segregate different class of inventory (viz. A, B and C) on the basis of their cost. Appropriate inventory control strategies are applied to these items for both cost consideration and process simplification. For a type inventory items, the cost of carrying inventory is appreciably higher than the other two and for these items, strict inventory management policies are necessary to control manufacturing cost [11]. Commonality helps in utilizing principles of statistics in optimizing inventory levels of common components. It is possible as common parts reduce inventory types so this improves planning and scheduling systems. Increase in volume of component items due to commonality helps in economy of scale and reduction in order variability, which helps in continuous replenishment.

In continuous review inventory management systems, the decision variables are the cycle inventory and safety inventory. While safety inventory level guarantees a minimum level of confidence against stock-out during the period between initiation of procurement orders and delivery of items in the store. A higher safety inventory provides higher level of confidence against stock-out, but it also increases holding inventory. The opportunity of cost savings thus will accrue due to the management of these common part inventories.

2 Literature Review

2.1 Research Gap

Based on the above, this research undertakes demand variability during lead time as the basis to evaluate the impact of part commonality to control shortages through development of a simulation test bed for experimentation.

Analytical models that help in the study of effect of part commonality on manufacturing performance are not found in literature in vogue. It is because the treatment of such models for industrial scenario becomes mathematically unwieldy and so simulation modelling offer opportunity in these cases to elucidate research underlining under different scenario. Simulation models that depict product manufacturing during lead times thus become the framework for evaluating benefits of part commonality on stock-out performance.

2.2 Research Objective

This paper uses discrete event simulation to underline:

- The benefit of part commonality on manufacturing performance by way of optimization of inventory of common components.
- For evaluating benefits of part commonality on stock-out performance—Demand variability and lead time uncertainty are responsible for stock-out during the lead time of inventory procurement. As such studies of inventory performance against shortages are monitored during the lead time period.

2.3 Research Connotations of Part Commonality

The aspect of component commonality that relates it with inventory management is the fact that demand variability across product family induces magnification in supply chain uncertainly for parts at upstream tiers. Common parts across multiple products help in the reduction of order variability; as statistical data streams that are composed of multiple datasets suppress variance as compared with the summation of individual variances [5]. Brennan and Gupta [12] examined the performance of manufacturing environment under demand and lead-time uncertainties. Similarly, effect of late delivery of raw materials has been examined by Kanet and Sridharan [13], while Matsuura [14] used this to model demand. Liao and Shyu [15] studied inventory systems with probabilistic variables to identify lead time demand parameters. Ben-Daya and Raouf [16] extended Liao and Shyu [15] model with lead time and ordering quantity as decision variables. This work was extended by Ouyang [17] while considering backorders during shortages. Moon and Choi [18] and further

Hariga and Ben-Daya [19] improved this to evaluate reorder point. Keller and Noori [20] worked with probabilistic lead time demand with stock-out. Sinha et al. [21] performed sensitivity analysis by changing various process variables and analysed its impact on total supply chain cost. The modularity of a product allows for the typological changes through interchangeable modules which can vary the functionality of such configured products according to the number of modules in them. Bi and Zhang [2] define modularity as higher instances of independence and usability among components that configure the products.

Collier [3] has pointed that increase in the extent of commonality positively influence system performance. This idea is further reinforced in research as it is observed that stock levels decrease with increase in part commonality [1]. Gerchak and Henig [7] validates this for a three-level supply chain with distribution center serving product demands which have varying levels of part commonality. Similarly, Catena [8] provided models for safety stock for common components for assemble/manufacture to order systems. Persona [9] applied this in industries and show reduction in safety stock. The method for calculating safety stock for components that are used in modular products in continuous review inventory policy is proposed by Chopra and Meindl [5], while Hernández [10] proposes a method to calculate safety inventory considering commonality and the replacement of components under a Make to Order strategy.

3 Continuous Review Inventory Model

Safety inventory is carried to satisfy demand that exceeds the amount forecasted during the lead-time period of inventory procurement (Fig. 1). Raising the level of safety inventory increases product availability, and thus, it has the potential to improve the margin captured from customer purchases. While it ensures higher service levels, the flip side is that it increases inventory holding costs. Thus, a trade-off issue is to be addressed as to what should be the appropriate level of product availability? Conversely, if desired level of product availability is to be ensured, what should be the safety inventory?

Fig. 1 Continuous review inventory model [5]
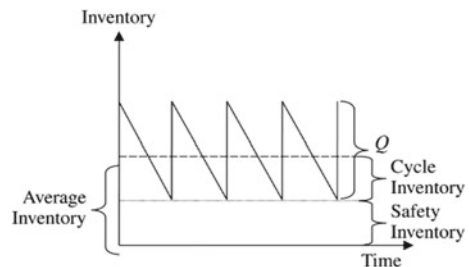
In addition, the knowledge of the relationship among the decision parameters that helps to achieve reduction in safety inventory while improving the product availability can create a competitive advantage. Singha et al. [22] determined an optimal cycle service level for continuously stocked items under a continuous review policy. For a continuous review inventory system, the formulations for the inventory models are given below [5]. The same will be used in the development of simulation model later.

3.1 Characteristics of Demand During Lead Time

For a normally varying demand per period,

D_i Average demand for period i
σ_i^2 Demand variance for period i
L Lead time
ROP   Reorder point
ρ_{ij} Correlation coefficient.

Average demand during lead time $= D_L$ and variance $= \sigma_L^2$ are as

$$D_L = \sum_{i=1}^{L} D_i \tag{1}$$

$$\sigma_L = \sqrt{\sum_{i=1}^{L} \sigma_i^2 + 2 \sum_{i>j} \rho_{ij}\sigma_i\sigma_j} \tag{2}$$

D_i and σ_i are all identical for each period:

$$D_L = DL \tag{3}$$

$$\sigma_L = \sigma_D \sqrt{L} \tag{4}$$

$$\text{Lead Time Demand(DL)} + \text{Safety Stock(SS)} = \text{Reorder Point(ROP)} \tag{5}$$

Cycle Service Level (CSL) given a Replenishment Policy

$$\text{CSL} = \text{Prob(ddlt of } L \text{ weeks} \leq \text{ROP)} \tag{6}$$

$$\text{CSL} = F(\text{ROP}, D_L, \sigma_L) = \text{NORMDIST}(\text{ROP}, D_L, \sigma_L, 1) \tag{7}$$

According to the continuous review policy, as commonality increases the mean demand for common component also increases. The demand for common component

is the sum of demand across all the products. The standard deviation for the common component follows Eq. (4), thus is more than the standard deviation of any other component which is not common. Thus, the overall safety stock for a given value of CSL increases. The relation between CSL and safety stock is given below:

$$ss = F_s^{-1}(\text{CSL}) * \sigma_L \tag{8}$$

ss = safety stock.

4 Component Commonality Model

4.1 Case Background

Here, to investigate the effect of part commonality, two different products are considered each of which is assembled by three parts. We are taking two cases with part commonality = 0 and 1, i.e., in 1st case with (defined as commonality = 0) no common components i.e. all the components for both the products are different (indicated in Fig. 2a, b), whereas in the 2nd case (defined as commonality = 1) 1 component (C1) in both the products is taken common (indicated in Fig. 3 a, b). The product configuration is as given below. When none of the parts are common, P1 is assembled with components C1, C2 and C3, while P2 is assembled with C4, C5 and C6.

The simulation modeling for the above product configurations has been undertaken on a simulation platform Arena® [23]. This is discussed below.

Fig. 2 **a** Product 1, **b** Product 2

No component is common
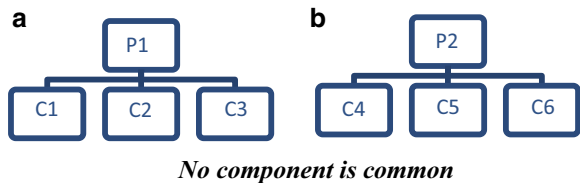
Fig. 3 **a** Product 1, **b** Product 2

Component C1 is common
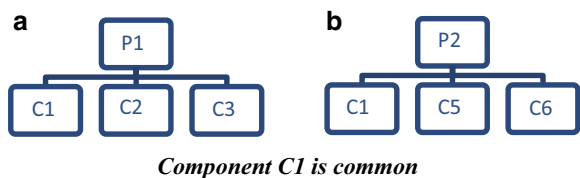
5 Development of Simulation Model

5.1 Explanation of the Model Created

In arena modeling platform entities depict modeling elements which flows through different modules. While these move through the modules, the system parameters and changes in the system variables are assigned as per the actual system parameters. The data stream is thus generated which depict the behaviors of the simulated system. Entities in the simulation model may depict some entity of actual system or these are used to undertake parametric changes as per the model devised.

This is illustrated with the help of modules given in arena [23]. Demand for Product P2 is generated with the help of CREATE module as indicated in Fig. 4a. This module creates product P2 depicted as entity type distridemandP2 daily with further details as illustrated in the module description. Some attributes and variable value are assigned to entity through assign module as given in Fig. 4b. In this case, attributes like demand quantity and picture are assigned. As detailed in Fig. 4b, the demand is assigned a normal variate with parameters DmeanP2 and DstdP2. Arena [23] allows for many types of distribution function in assignment.

The entity then flows through the decide module where the part inventories for C4, C5 and C6 are compared with the demand. This is depicted in the following figure. In case part inventories are available, product P2 is configured and inventories of the related parts are decremented by the amount equal to the demand. In case the part inventories are not sufficient for any part shortage is evaluated as count in the instances of stock-out is assigned. Similarly, at review periods each part inventory is reassigned a value equal to the respective ROP and the process is repeated till the simulation period is over. Multiple experiments for cycle service level at different safety inventory is undertaken to profile the CSL against safety inventory. After which data is tabulated as saved. The snapshot of the detailed model is given in Fig. 7. Figure 6 depicts the animation of some of the model variables (Figs. 5, 6 and 7).
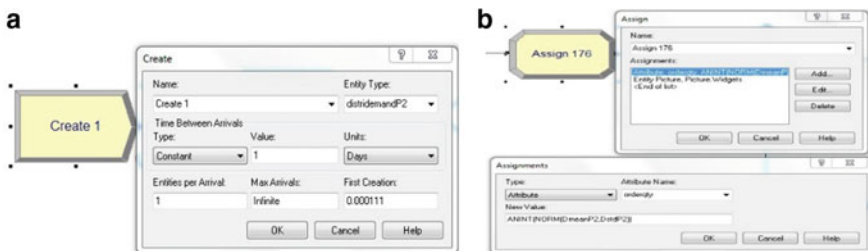
Fig. 4 **a** Create module used in arena [23], **b** assign module used in arena [23]
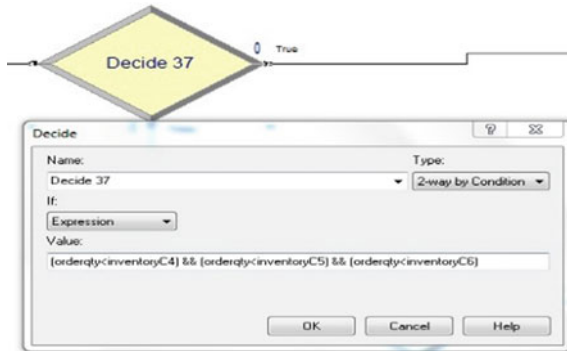
Fig. 5 Decision module used in arena [23]
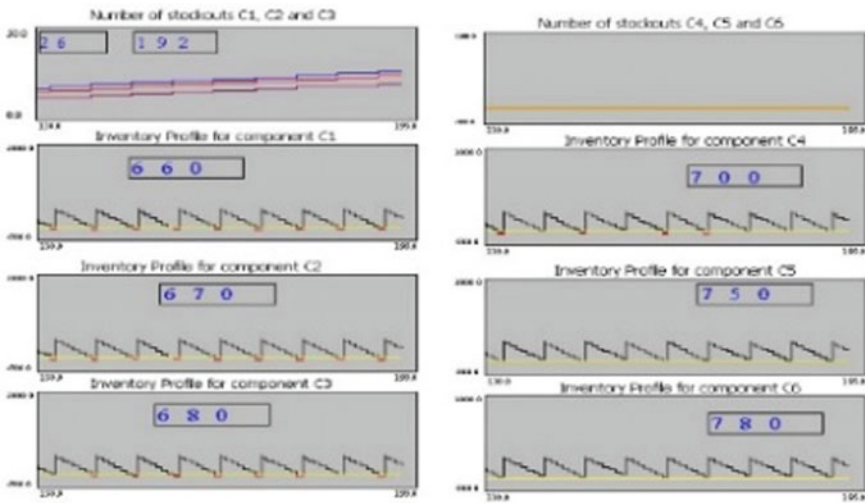
Fig. 6 Animation of the model variables

5.2 Determining Outputs

Demands for products P1 and P2 are considered normal variates. These demands generate normal variate demands for individual components. The aggregate demands of each component thus can be calculated as the demand streams from the individual product streams.

In case the demand data streams are not normal variates as well as when periodic demand and lead times belong to different distribution function, the models given above cannot be used without introducing error in the estimation of safety inventory for required service level. Under such conditions, simulation modeling can be
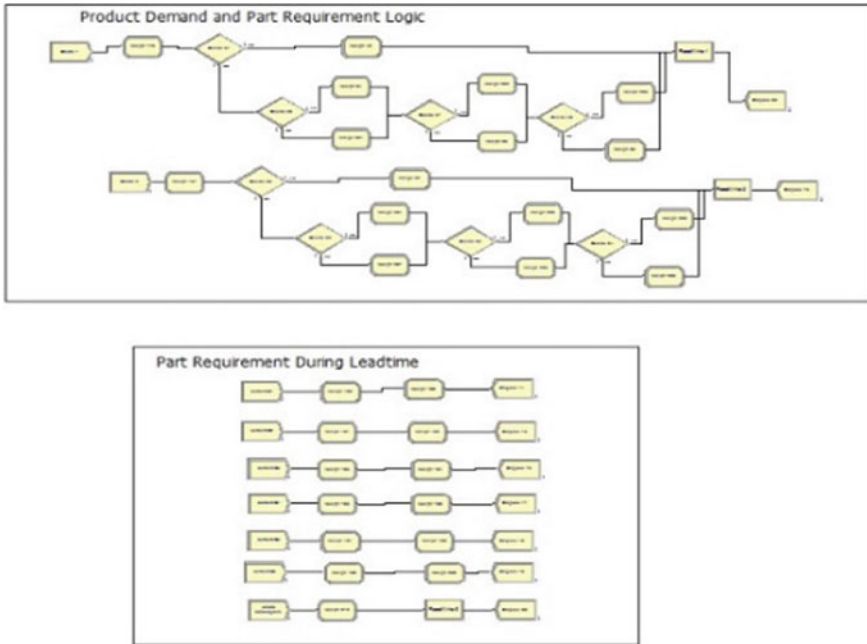
Fig. 7 Simulation model (arena)

applied to estimate safety inventory. Appropriate experimental design for simulation can provide acceptable estimate of safety inventory before the same scheme is implemented in industrial scenario.

According to Eq. (7) ROP, D_L, σ_L are needed to equate CSL, and thus the outputs from the simulation model are aimed to extract the above-mentioned variables. [5] Based on estimates of demand distribution for the future, instances of demands for different components are generated. Instance of demand mentioned above refers to random demand obtained from a demand distribution. These variables are then used to compute the CSL using the NORMDIST function in Excel.

This simulation experiment is carried out for sufficient length of time and repeated multiple times such that the dataset for performance is sufficient enough for statistical validation. In the present case, the simulation run length was 3865 days which was found sufficient.

6 Analysis of Simulation Results

The simulation results for different simulation runs are compiled in the following two tables. Table 1 depicts the cycle service level at different safety inventories for each component when there are no common components, i.e., when P1 and P2 separately

Table 1 Dataset for no component common

Safety inv.	Cycle serv. level
0.00	53.54
5.00	60.25
10.00	66.61
15.00	70.60
20.00	78.77
25.00	83.85
30.00	87.11
35.00	92.01
40.00	94.74
45.00	96.73
50.00	98.37
55.00	98.55
60.00	99.09
65.00	99.64
70.00	99.82
75.00	100.00
80.00	100.00

require unique components. Table 2 represents the CSL at different safety inventories of C1 when it is common to both P1 and P2. The result is depicted in Fig. 8.

It is observed from the result as given in Fig. 8 that when the component commonality is increased from 0 to 1, then cycle service level for components improves at the same safety stock level. Conversely, for a required cycle service level, the equivalent safety stock level for common components decreases. This validates the results of analytical model (given in Sect. 3.1).

7 Conclusion

It is now important to mention that simulation modeling for evaluating safety inventory under common components can examine different types of product configurations as well as different types of data stream representing the periodic demand and lead time.

By introduction of component commonality, the simulation results showed that cycle service level increased considerably. Existing literatures indicate that the increase in CSL is characterized by increase in the performance of supply chain, i.e., parameters like delivery dependability, supply chain profitability show positive changes. This also helps in optimizing inventory levels and thus issues such as order variability, inventory holding cost, delays in providing services reduce.

Table 2 Dataset for 1 component common

Safety inv.	Cycle serv. level	Safety inv.	Cycle serv. level
2.5	58.08	45	99.09
5	63.88	47.5	99.64
7.5	69.87	50	99.82
10	73.87	52.5	100.00
12.5	78.58	55	100.00
15	82.58	57.5	100.00
17.5	86.03	60	100.00
20	88.75	80	100.00
22.5	89.66	100	100.00
25	91.83	120	100.00
27.5	94.37		
30	95.46		
32.5	96.73		
35	97.64		
37.5	98.00		
40	98.00		
42.5	98.55		
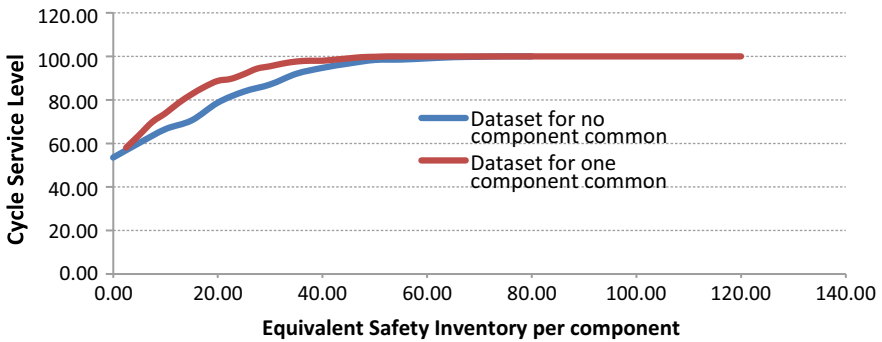
Fig. 8 Safety inventory versus cycle service level for different datasets

This simulation platform can further be extended to accommodate stochastic nature of part substitution as an extension of present research. The capability to accommodate different types of discrete variables and their interaction is one of the novelties of the present research framework.

References

1. Baker, K.R.: Safety stocks and component commonality. J. Oper. Manag.ment **6**(1), 13–22 (1985)
2. Bi, Z.M., Zhang, W.J.: Modularity technology in manufacturing: taxonomy and issues. The Int. J. Adv. Manuf. Technol. **18**(5), 381–390 (2001)
3. Collier, D.A.: The measurement and operating benefits of component part commonality. Decis. Sci. **12**(1), 85–96 (1981)
4. Vishkaei, B.M., Khorram, E., Farhangi, M., Niaki, S.T.A.: A Bi-objective inventory model to Minimiaw cost and stock out time under backorder shortages and screening. Int. J. Ind. Eng. **26**(5), 707–718 (2019)
5. Chopra S., Meindl P., Kalra D.V.: Supply Chain Management: Strategy Planning and Operation; 6e, Pearson India Education, Chennai (2017)
6. Wazed, MdA, Ahmed, S., Yusoff, N.: Commonality in manufacturing resources planning—issues and models: a review. Eur. J. Ind. Eng. **4**(2), 167–188 (2010)
7. Gerchak, Y., Henig, M.: An inventory model with component commonality. Oper. Res. Lett. **5**(3), 157–160 (1986)
8. Catena M., Ferrari E., Manzini R., Persona A.: Quantitative models for evaluating safety stocks in case of modular products. In: 17th International Conference of Production Research (ICPR) 17th August 3–7, Blacksburg, Virginia USA (2003)
9. Persona, A., Battini, D., Manzini, R., Pareschi, A.: Optimal safety stock levels of subassemblies and manufacturing components. Int. J. Prod. Econ. **110**(1–2), 147–159 (2007)
10. Hernández, K.E., Olivares-Benítez, E., Zuñiga, C.A.: Safety stock levels in modular product system using commonality and part families. IFAC-Papers-On-Line **48**(3), 1387–1392 (2015)
11. Mirchandani, P., Mishra, A.K.: Component commonality: models with product-specific service constraints. Prod. Oper. Manage. **11**, 199–215 (2002)
12. Brennan, I., Gupta, S.M.: A structured analysis of material requirements planning systems under combined demand and supply uncertainty. Int. J. Prod. Res. **31**, 1689–1707 (1993)
13. Kanet, J.J., Sridharan, S.V.: The value of using scheduling information in planning material requirements. Decis. Sci. **29**(2), 479–496 (1998)
14. Matsuura, H., Tsubone, H., Kataoka, K.: Comparison between simple infinite loading and loading considering a workload status under uncertainty in job operation times. Int. J. Prod. Econ. **40**, 45–55 (1995)
15. Liao, C.J., Shyu, C.H.: An analytical determination of lead time with normal demand. Int. J. Oper. Prod. Manage. **11**, 72–78 (1991)
16. Ben-Daya, M., Raouf, A.: Inventory models involving lead time as a decision variable. J. Oper. Res. Soc. **45**, 579–582 (1994)
17. Ouyang, I.Y., Yeh, N.C., Wu, K.S.: Mixture inventory model with backorders and lost sales for variable lead time. J. Oper. Res. Soc. **47**, 829–832 (1996)
18. Moon, I., Choi, S.: A note on lead time and distributional assumptions in continuous review inventory models. Comput. Oper. Res. **25**, 1007–1012 (1998)
19. Hariga, M., Ben-Daya, M.: Some stochastic inventory models with deterministic variable lead time. Eur. J. Oper. Res. **113**, 42–51 (1999)
20. Keller, G., Noori, H.: Impact of investing in quality improvement on the lot size model. Omega Int. J. Manage. Sci. **15**, 595–601 (1988)
21. Sinha, A.K., Anand, A.: Lot sizing problem for fast moving perishable product: modeling and solution approach. Int. J. Ind. Eng. **25**(6), 757–778 (2019)
22. Singha K., Buddhakulsomsiri J., P. Parthana.: Optimal cycle service level for continuos stocked items with limited storage capacity, In: The 3rd International Conference on Agro-Industry 2016, pp. 82–88, Knowledge E, Thailand (2018)
23. Arena® V 14.00.00000, Application Pack (Student edition and Product manual), Rockwell Automation, Inc., USA

Application of Goal Programming to Optimize the Schedule and Frequency of Product Advertisement in Telemedia

Oikantik Sinha, Parth Dharmarha, and Pravin Kumar

1 Introduction and Background

The period of 2013–2015 witnessed the growth story of television as an advertising medium. By 2013, India became the third-largest TV market with 161 million television households, a 15.7-billion-dollar revenue industry. The TV advertisement market in India increased by 2.84 billion dollars between 2015 and 2018; this is the fifth-largest advertisement expenditure growth in the world during this time period. In 2019, the Indian television industry grew at 13.8% to a size of 20 billion dollars. Compared to all the other categories, the highest spender on TV advertisements was the FMCG sector. The Indian advertising industry is projected to grow at close to 13% in the coming years. The growth of Indian tele-advertising industry in India is shown in Fig. 1.

The United States has the highest advertising revenue all over the world. Presently, 71 billion U.S. dollars TV advertising revenue is generated in the United States alone, and it is estimated to grow to 72 billion in 2023. The TV advertisement in the world has been projected to increase from \$173 billion to \$192 billion between 2018 and 2022 [2]. This shows that television media is one of the important mediums to share the product knowledge with the target customer. Now, the main problem is to determine the frequency of a product advertisement and finding the slots, so that advertisement cost can be minimized with increased effectiveness and viewership of the target customer.

O. Sinha · P. Dharmarha (✉) · P. Kumar
Department of Mechanical, Production & Industrial and Automobile Engineering, Delhi Technological University, Bawana Road, North West Delhi, Delhi 110042, India
e-mail: pddharmarha@gmail.com

O. Sinha
e-mail: oikantik.sinha@gmail.com

P. Kumar
e-mail: pravin.papers@gmail.com

Fig. 1 Annual growth of Indian television industry (bn ₹) [1]

Deciding the slots and the frequency of the advertisement on television is very difficult. The complexity arises from sophisticated show structure, limited number of advertising slots, audience demographics, and show preferences. To find the solution of this problem, many researchers have used the different optimization tools and techniques. Rubinson [3] conducted a survey to check whether the effectiveness of the television advertising has declined over the time. But just opposite to this hypothesis, he observed that TV advertising is more effective. Barajas et al. [4] projected the impact of telemarketing on daily sales using time series-based approached. They presented the relationship between ad impressions and commercial actions on log-scale and observed it as the effective way to describe the scenario. Results indicated that television marketing continues to be the most effective among other options.

Barajas et al. [5] used linear programming for the media section and allocation of the advertisement. They provided the different weights to the viewership data to be used in linear programs and observed their impact. Charnes et al. [6] proposed the use of goal programming for the media planning. They presented the goal programming model for media selection by changing the objectives and extending the previous media allocation models by accounting for cumulative duplicating audiences over a variety of time periods. Cornelis and Kluyver [7] examined the formulation of goal programming for media selection. To assess the impact of goal programming formulation on the resulting solutions, the different scheduling with actual data has been used repeatedly. Kwak et al. [8] used a mixed integer goal programming model for finding the right advertisement media. Jha and Aggarwal [9] used a fuzzy goal programming approach to achieve a compromised solution for advertisement media allocation. They identified the satisfactory solution and analyzed by performing the sensitivity analysis. The sensitivity analysis was used for model flexibility by providing different weights combinations of different products in each segment, so as to meet the aspiration levels of management for each advertisement.

Fleming and Pashkevich [10] formulated a model from the advertising agency's perspective, to optimize the reach of each brand for multiple clients, using a modified multi-objective genetic algorithm (MOGA). Regis and Evangelista [11] presented a modified format of the Fleming and Pashkevich model, wherein it reformulates the objective functions and constraints into a multi-objective binary integer programming

format. Mihiotis and Tsakiris [12] presented an integer programming model with the goal of maximizing gross rating points (GRP), under a cost constraint, from the perspective of an advertising agency. It considers a television program as a straight line, with each point on it has two characteristics, namely viewership and unit cost of commercial time. TV networks also need to optimally schedule their commercials and allocate advertising time to meet their clients' demands and maximize their profits. Ghassemi and Alaei [13] presented a winner determination problem in a multi-unit combinatorial auction mechanism for allocation of advertising time to advertisers, with a goal of maximizing the revenue generated. Bollapragada and Garbiras [14] presented a model from a TV network's perspective for the scheduling of commercial ads and have used heuristics modeling to solve effectively the formulated integer programming problem.

The researches have also been performed from the perspectives of different companies. Brown and Warshaw [15] presented a linear programming model formulated with the objective function incorporating several parameters to reflect the effectiveness of the advertisement. Linear and nonlinear models for response to promotional inputs have also been presented and incorporated into the objective function. Bhattacharya [16] presented a model from the perspective of a company, in which he formulated a chance constraints goal programming model with the goal of maximizing the desired reach under a cost constraint with a limit on the maximum and minimum number of advertisements for different time slots and channels. The goal programming is one of the unique methods for multi-objective linear programming. It allows to incorporate the multiple conflicting objectives in finding the solution in the range of the already decided/fixed goals. More accurately, it can be said that the goal programming is designed to minimize the deviation between the achievement level and the goals set. Based on the evidence of its effectiveness, goal programming has been used to solve the formulated multi-objective problem. In this paper, we have formulated a goal programming optimization model for achieving target effective impressions generated under a budget with maximum and minimum advertisement frequency as constraints from the perspective of the company.

2 Problem Description and Model Formulation

One of the primary goals of any television advertisement campaign of a company is to achieve its target of effective exposure or impressions. Effective impressions are those impressions which are generated by the company's target audience. The company intends to expose the ad to as many new people as possible, while exposing each ad enough number of times to the people to increase their chances of recognition of the brand during purchasing decisions. The companies are also restricted under a budget and have a goal to restrict the cost of advertising to its budget limit.

In this paper, the optimum number of the advertisement on different television channel has been decided considering the budget constraint. The main aim is to achieve the target number of effective impressions generated by the possible

customers. The cost of advertisement varies from one time slot to another. The cost aspects for the different time slots in a day of the television channels have been given due attention. The goal programming is used to formulate the problem providing the weights to the certain demographic, so as to advertise the product maximum to the potential target customer base. Constraints on the maximum and minimum number of advertisements that can be allocated per time slot in different time slots in each channel have also been considered. Some of the basic terminology used in the paper is discussed below:

Spot: A spot is defined as one broadcast of an advertisement.
Reach: It is defined as the number of unique people who will be exposed to one spot.
Impressions: Impressions are the total number of exposures to an advertisement. Impressions generated in each time slot are calculated by multiplying the number of spots by the number of viewers in that time slot.

2.1   Model Formulation

A multiple-objective linear programming model has been formulated to determine the optimal frequency of advertisements. A multi-objective linear programming can be solved by the formulation of goal programming, which enables us to efficiently solve many real-world decision problems. This approach also allows the decision maker to consider the individual importance of various conflicting objectives. To formulate this problem, we have used lexicographic goal programming for finding the solution. In lexicographic goal programming, the minimization of a deviation in a higher priority goal is infinitely more important than any other deviations in lower priority goals. Some of the important parameters considered in this model formulation are summarized in Table 1.

Table 1   Parameters used in goal programming

Code	Descriptions
x_{ij}	Frequency of advertisement in the ith time slot in the jth channel
C_{ij}	Cost of one 10 s advertisement in the ith time slot in the jth channel
V_{ij}	Viewership in the ith time slot in the jth channel
P_j	Target audience percentage in the jth channel
U_{ij}	Total ad slots available in the ith time slot in the jth channel
R_n	Percentage of the total viewers in the nth category
W_n	Weightage assigned to the nth category
i	Time slots
j	Channels

To determine the target audience percentage in the ith time slot in jth channel, the weighted mean approach has been used as illustrated in Brown and Warshaw (1965). At first, the characteristics of the target audience are decided, and the percentage of the total viewers that fall within that category (R_n) are determined. The suitable weights (W_n) to the different categories of viewers are assigned. Now, the weighted mean of is calculated to determine the target audience percentage (P_j).

Let us consider the percentage of the total viewers in each category are as gender $= R\_1$; age group $= R\_2$; income level $= R\_3$; and weights assigned to each category are gender $= W\_1$; age group $= W\_2$; and income level $= W\_3$. Now, the target audience percentage can be determined by:

$$P_j = \frac{R_1 \times W_1 + R_2 \times W_2 + R_3 \times W_3}{W_1 + W_2 + W_3} \tag{1}$$

There are two goals in the tele-advertising process: one is to achieve the total impression target, and other is to minimize the total cost of the advertisement as discussed below:

Minimizing the total cost of the advertisement. The cost of the advertisement depends on the frequency and the time slots chosen for the advertisement. Here, the product of frequency x_{ij} and the cost of that time slot C_{ij} indicates the cost of advertisement as shown in Eq. (2). Its target is fixed as T_1.

$$\sum_{j=1}^{5}\sum_{i=1}^{5} x_{ij} \times C_{ij} \leq T_1 \tag{2}$$

Achieving the total impressions target. In this model, total impressions generated by the ad within the target audience are considered as the objective function which is to be maximized. The product of V_{ij} ⟦ and P⟧ $_{ij}$ and x_{ij} shows the total impressions. Our goal is to achieve the total effective impressions greater than the specified target value T_2 as shown in Eq. (3).

$$\sum_{j=1}^{5}\sum_{i=1}^{5} x_{ij} \times V_{ij} \times P_j \geq T_2 \tag{3}$$

Now, there are two constraints as discussed below:

Ad slot constraint. In this model, we have considered a limit of ad slots that are available per time slot per channel, to imitate the real-world scenario. The frequency of advertisement per time slot per channel cannot exceed this value. This is represented by Eq. (4).

$$x_{ij} \leq U_{ij} \tag{4}$$

Minimum advertisements constraint. We have considered the minimum value of frequency of advertisement per time slot per channel x_{ij} as 1, to maximize the number of unique people who will watch the advertisement, which hence increases reach. This is given by Eq. (5).

$$x_{ij} \geq 1 \forall \tag{5}$$

Now, lexicographic goal programming is applied to solve this model. The lexicographic goal programming provides infinitely more importance to the highest priority goal than the goals of subsequent priority levels. Here, the objective function is to minimize the underachievement $[\![(d)]\!]_2^-$) and overachievement (d_1^+).

The model after simplifying can now be represented as:

$$\text{Lex min} \left(d_2^-, d_1^+ \right) \tag{6}$$

Subject to

$$\sum_{j=1}^{5} \sum_{i=1}^{5} x_{ij} \times C_{ij} + d_1^- - d_1^+ = T_1 \tag{7}$$

$$\sum_{j=1}^{5} \sum_{i=1}^{5} x_{ij} \times V_{ij} \times P_j + d_2^- - d_2^+ = T_2 \tag{8}$$

$$x_{ij} \leq U_{ij} \tag{9}$$

$$x_{ij} \geq 1 \forall I \tag{10}$$

d_1^+ and d_2^+ are the over achievements and d_1^- and d_2^- are the under achievements of the target level of the two objectives, respectively. This model can be solved using linear programming model in which Eq. (6) shows the objective function and Eqs. (7)–(10) show the constraints.

3 Case Study

A company (*XYZ*) desires to advertise its newly launched cologne brand for men, in five prominent television channels of India. The name of the company and the channels are not disclosed in this study to maintain the privacy of the company. Its goal is to maximize the exposure of this brand in its target audience. The target audience for this company are the men aged between 18 and 60 years, and having an annual income of more than ₹ 5,00,000. It has a goal of achieving 4,50,00,000 effective impressions from the advertising campaign and has a budget of ₹ 5,50,000.

Table 2 Cost and viewership for each time slot and channel

Time slot	Cost of 10 s ad (in 1000 ₹) (C_{ij})					Number of viewership (per week) (in millions) (V_{ij})				
	Ch_1	Ch_2	Ch_3	Ch_4	Ch_5	Ch_1	Ch_2	Ch_3	Ch_4	Ch_5
8:00AM–11:00AM	6	5	4	2	3	0.6	1	0.9	0.1	0.2
11:00PM–2:00PM	7	6	2	2	6	0.8	1.3	0.4	0.15	1.2
2:00PM–5:00PM	8.5	6	2.5	3	12	0.7	0.9	0.5	0.2	1.5
5:00PM–8:00PM	10	8	4.5	3.5	18	1.2	1.3	0.8	0.3	1.9
8:00PM–11:00PM	12	17	10	7	34	1.9	1.6	1	0.45	2.5

It has been assumed that the company wants to advertise in five prominent television channels of India corresponding to $j = 1, 2, ..., 5$. Television channels' airtimes have been split into five time slots corresponding to $i = 1, 2, ..., 5$. These time slots are 8:00AM–11:00AM, 11:00PM–2:00PM, 2:00PM–5:00PM, 5:00PM–8:00PM, and 8:00PM–11:00PM, respectively. The cost (₹ 1000) and the viewership (million) in different time slots for all the five different channels are summarized in Table 2.

Some assumptions made in the model are discussed below as:

- The demographic across different time slots of the same channel is the same.
- The duration of all ads is considered as 10 s.
- The values of total ad slots available per time slot per channel are assumed as any suitable value in relation to that slot's cost and viewership.
- Due to unavailability of current data, the parameter for percentage of total viewers in each category has been suitably assumed.
- The weights assigned to each characteristic category, and target values of effective impressions, and budget have also been suitably assumed.

To find the target audience percentage, we use the weighted mean approach as mentioned in Eq. (1). The data for the percentage of total viewers of each channel falling in the required categories has been suitably assumed and represented in Table 3.

Table 3 Categories of the viewers on the different television channels

Channels	Gender (male)(R_{1j}) (%)	Age group (18–60) (R_{2j}) (%)	Income level (₹ 5,00,000+) (R_{3j}) (%)
Channel 1	50	60	70
Channel 2	52	65	72
Channel 3	60	65	76
Channel 4	65	70	72
Channel 5	58	60	75

The weights for the characteristic categories were assigned, after consulting with experts in the field of television advertising. For a cologne brand for men, the target audience is predominant and almost exclusively male. So, a higher weight of 0.5 was assigned to this category. Next, the target audience's age group was identified to be between 18 and 50 years. This is also an important factor as the brand does not appeal to audiences not in this age group. Hence, it was assigned a weight of 0.4. Finally, income level of the audience was also taken into account. Though, it was assigned a weight of only 0.1, as income level does not influence the sale of this product to a large extent, due to its easy affordability. Weights assumed for each category is as W_1 (GENDER) $= 0.5$; W_2 (AGE GROUP) $= 0.4$; W_3 (INCOME LEVEL) $= 0.1$.

Now, Using Eq. (1), we get $P_1 = 56\%$, $P_2 = 59.2\%$, $P_3 = 63.6\%$, $P_4 = 67.7\%$, and $P_5 = 60.5\%$.

The target audience percentage and the total ad slots available in different channel for different time slots are summarized in Table 4.

Solving the linear programming model from Eqs. (6)–(10) using LINGO software, we get the optimal values for the different variables as shown below. Thus, the optimal distribution of the frequencies in different time slots on different channels is obtained and summarized in Table 5. Total cost incurred in the advertisement is ₹ 5,50,000, and the effective impression generated is 4,51,90,950.

$$x_{11} = 1; \ x_{12} = 1; \ x_{13} = 1; \ x_{14} = 1; \ x_{15} = 1;$$
$$x_{21} = 1; \ x_{22} = 4; \ x_{23} = 6; \ x_{24} = 1; \ x_{25} = 6;$$

Table 4 Data of target audience % and total ad slots available for each time slot and channel

Time slot	Target audience % (P_{ij})					Total ad slots available (U_{ij})				
	Ch_1	Ch_2	Ch_3	Ch_4	Ch_5	Ch_1	Ch_2	Ch_3	Ch_4	Ch_5
8:00AM–11:00AM	56	59.2	63.6	67.7	60.5	4	6	3	8	7
11:00PM–2:00PM	56	59.2	63.6	67.7	60.5	5	4	6	6	6
2:00PM–5:00PM	56	59.2	63.6	67.7	60.5	6	7	8	5	5
5:00PM–8:00PM	56	59.2	63.6	67.7	60.5	4	5	4	5	5
8:00PM–11:00PM	56	59.2	63.6	67.7	60.5	3	3	4	4	2

Table 5 Frequency distribution of ad in different time slots on different channel

Time slot	Frequency of advertisements (x_{ij})				
	Ch1	Ch2	Ch3	Ch4	Ch5
8:00AM–11:00AM	1	1	1	1	1
11:00PM–2:00PM	1	4	6	1	6
2:00PM–5:00PM	1	7	8	1	5
5:00PM–8:00PM	1	5	4	1	4
8:00PM–11:00PM	2	3	1	4	1

$$x_{31} = 1; \; x_{32} = 7; \; x_{33} = 8; \; x_{34} = 1; \; x_{35} = 5;$$
$$x_{41} = 1; \; x_{42} = 5; \; x_{43} = 4; \; x_{44} = 1; \; x_{45} = 4;$$
$$x_{51} = 2; \; x_{52} = 3; \; x_{53} = 1; \; x_{54} = 4; \; x_{55} = 1;$$
$$d_2^- = 0; \; d_2^+ = 0; \; d_1^- = 0; \; d_1^+ = 0 = 0.19095.$$

4 Conclusions

This study is based on the optimization of the impressions generated for the specific brand of a product and the cost of the advertisement. A multi-objective linear programming model was developed for finding the optimum number of ad frequencies in different slots in different television media for the minimum cost. This was solved with the help of lexicographic goal programming. This case study has been performed replicating real-world scenarios to test for the effectiveness of the formulated model. This study has also some limitations, which may be incorporated in the future research. One of the main limitations is the fatigue of the viewers and decrease in effectiveness of an advertisement, as the audience is exposed to the same advertisement again and again. It may irritate the viewers. However, since the numbers of advertisement slots available are limited in most television channels, this problem can be ignored easily. Another limitation is that the study is based on only five channels. For the broad study, some more channels may be included. These limitations may be addressed in future research.

References

1. Statista: Revenue of TV Industry in India (2019). https://www.statista.com/statistics/243879/revenue-of-the-tv-industry-in-india-by-source/. Retrived May 27, 2020
2. Guttmann, A.: TV advertising revenue in the U.S. 2018–2023 (2019). https://www.statista.com/statistics/259974/tv-advertising-revenue-in-the-us/. Retrived April 8, 2020
3. Rubinson, J.: Empirical evidence of TV advertising effectiveness. J. Advert. Res.arch **49**(2), 220–226 (2009)
4. Barajas, J., Akella, R., Holtan, M., Kwon, J., Null, B.: Measuring the effectiveness of display advertising: a time series approach. In: Proceedings of the 20th International Conference Companion on the World Wide Web, pp. 7–8 (2011). ISBN: 978-1-4503-0637-9
5. Bass, F.M., Lonsdale, R.T.: An exploration of linear programming in media selection. J. Mark. Res. **3**(2), 179–188 (1966)
6. Charnes, A., Cooper, W.W., DeVoe, J.K., Learner, D.B., Reinecke, W.: A goal programming model for media planning. Manag. Sci. **14**(8), B-423 (1968)
7. De Kluyver, C.A.: Hard and soft constraints in media scheduling. J. Advert. Res. **18**(3), 27–31 (1978)
8. Kwak, N.K., Lee, C.W., Kim, J.H.: An MCDM model for media selection in the dual consumer/industrial market. Eur. J. Oper. Res. **166**(1), 255–265 (2005)
9. Jha, P.C., Aggarwal, R.: Optimal advertising media allocation under fuzzy environment for a multi-product segmented market. Turk. J. Fuzzy Syst. **3**(1), 45–64 (2012)

10. Fleming, P.J., Pashkevich, M.A.: Optimal advertising campaign generation for multiple brands using MOGA. IEEE Trans. Syst. Man Cybern. Part C Appl. Rev. **37**(6), 1190–1201 (2007)
11. Regis, R.G., Evangelista, V.M.: A multi-objective approach to optimal TV advertising. In Canadian Operational Research Society (CORS) 58th Annual Conference, Banff Centre, Banff, Alberta, Canada, May 30–June 1, 2016
12. Mihiotis, A., Tsakiris, I.: A mathematical programming study of advertising allocation problem. Appl. Math. Comput. **148**(2), 373–379 (2004)
13. Ghassemi Tari, F., Alaei, R.: Scheduling TV commercials using genetic algorithms. Int. J. Prod. Res. **51**(16), 4921–4929 (2013)
14. Bollapragada, S., Garbiras, M.: Scheduling commercials on broadcast television. Oper. Res. **52**(3), 337–345 (2004)
15. Brown, D.B., Warshaw, M.R.: Media selection by linear programming. J. Mark. Res. **2**(1), 83–88 (1965)
16. Bhattacharya, U.K.: A chance constraints goal programming model for the advertising planning problem. Eur. J. Oper. Res. **192**(2), 382–395 (2009)

Impact of Wall Angle, Step Size and Spindle Speed on Forming Force in Single Point Incremental Forming

Ajay Kumar [ID], Parveen Kumar, Deepak Kumar, and Ravi Kant Mittal

1 Introduction

Manufacturing sectors seek the upgrade of their business by producing customized and low-cost objects to satisfy the cutting edge needs of customers. To satisfy these requirements, the best suitable approach of production is batch-type that has potential to manufacture the complex shapes of sheet metals with lower cycle-time and cost of setup. Sheet material forming methods produce components for various sectors with lowest wastages. Although, traditional methods of sheet forming seek the use of specific tools and dies for a particular shape to be produced that becomes a barrier for satisfying the need of customized production. In addition, the force required to manufacture components is quite large during these methods which demand the use of heavy machinery and hardware [1]. The use of forming hardware of high capacity leads to the increase in cost of process that makes the process uneconomical if components are not produced up to the quantity that reaches at least breakeven point of the process [2].

A. Kumar (✉)
Department of Mechanical Engineering, Faculty of Engineering & Technology, Shree Guru Gobind Singh Tricentenary University, Gurugram 122505, India
e-mail: ajay.kumar.30886@gmail.com

P. Kumar
Department of Mechanical Engineering, National Institute of Technology, Kurukshetra 136119, India

D. Kumar
Department of Computer Science and Engineering, Guru Jambheshwar University of Science and Technology, Hisar, India

R. K. Mittal
Department of Mechanical Engineering, Birla Institute of Technology and Science, Pilani 333031, India

Therefore, the necessity of evolving a creative and adjustable forming technique becomes stronger and compelling that enables the customized production and rapid prototyping of sheet material components economically [3]. In addition, the agile and flexible sheet forming techniques have potential to bridge the demand of requirements of rapid prototyping and customized production by producing the complex sheet material parts to fulfill the need of various frontier sectors. Incremental sheet forming (ISF) is a flexible and agile technique of forming the customized parts of sheet material economically and efficiently. This method of forming excludes the use of forming dies and punches which makes it economically suitable for batch-type and customized production [4]. In ISF, a single forming tool, normally hemispherical-ended, is capable of producing variety of complex shapes by deforming the sheet material locally, layer by layer, using the predetermined numerical instructions on forming machinery, normally CNC milling machine or industrial robot. The CAD model of desired shape is normally used for generating the numerical instructions using suitable CAM package [5, 6]. This concept of forming the sheet material was envisaged by two patents [7, 8], both issued in 1967. By back-tracking the publications on ISF, Mason's [9] work can be considered as the origin of the true ISF process. The applications of ISF include, but not limited to, automobile components, aerofoil and fuselage parts, ankle and knee implants, cranial plate, customized channels, etc. [10].

Single point incremental forming (SPIF) is a subclass of ISF process which is also known as "negative incremental forming" or "die-less forming". SPIF technique eliminates the use of any kind of dies for producing components of sheet material. Since the deformation is accomplished locally during SPIF method, the forces required to produce deformation are quite small as compared to traditional sheet forming techniques [11, 12]. In addition, the viability of this die-less technique of forming is enhanced by the absence of devoted punches and dies making this novel technique flexible, agile and versatile for rapid prototyping [13]. Figure 1 shows the schematic of SPIF technique.

The nature of deformation during SPIF, which is absolutely local, allows deforming the material at quiet reduced forces as compared to traditional sheet forming techniques. Moreover, SPIF is a green process as it directly saves energy
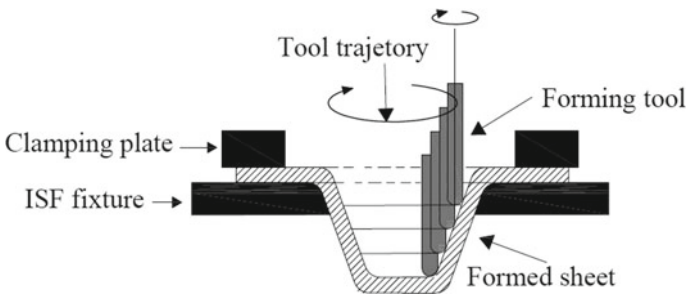
Fig. 1 Single point incremental forming [1]
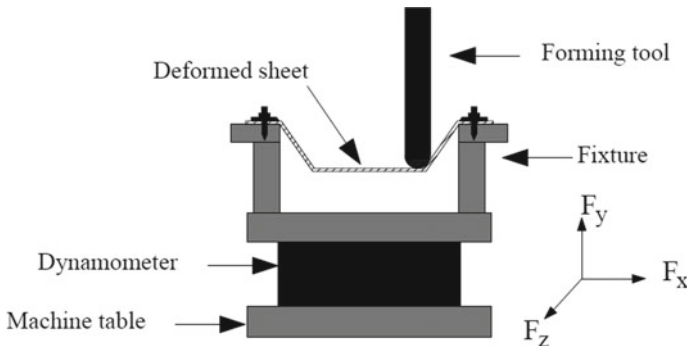
Fig. 2 Schematic of measurement of forming force during SPIF

up to large extent by producing parts with forming machinery of small size and capacity. Moreover, the particular combination of parameters delineates the capacity of forming machinery required for executing SPIF process by determining the maximal forces for specific material. Hence, investigation and delineation of maximal forces can ensure the effective utilization of forming setup [14].

The procedure of measurement of forming force has been a matter of choice for researchers during SPIF. A majority of researchers [13–22] has employed table type force dynamometer or load cell due to its simplicity and effectiveness taking setup conditions of SPIF into account. This kind of dynamometer can be simply placed between clamping device and machine table (Fig. 2).

Kumar et al. [13] studied impact of various process variables on axial forming forces on AA2024 sheets using forming tool of hemispherical shape. Conical frustums of various wall angles (52°, 56°, 60°, 64°) were formed using helical tool path. Forming forces were raised by 20.03% when tool radius was raised from 3.76 to 7.83 mm for a wall angle of 64°. Kumar et al. [14] focused on the influence of interactions of tool radius–tool shape and wall angle–tool shape on forming forces on AA2024 sheets. The increase in tool radius (from 3.76 to 7.83 mm) resulted in the decrement of forces by 35.49%. Use of flat-end tool with higher wall angle led to increase in axial forces and sheet failure. Uheida et al. [15] studied the impact of feed rate and spindle speed on vertical forming forces on titanium grade 2 sheets of 0.8 mm thickness using hemispherical-end forming tool of 10 mm to produce varying wall angle conical frustum (VWACF). Results showed that, although, forming force decreased with the increase in spindle speed but sheet fracture was noticed after spindle speed of 4000 rpm. Ali et al. [16] optimized the SPIF process for forming forces taking step size, feed rate, sheet thickness and tool radius into account on AA1050-H14 sheets. Furthermore, a model was established to estimate the forces by artificial intelligence techniques. Sakhtemanian et al. [17] developed a theoretical model for predicting the energy that can be transferred to heat from the ultrasonic vibrations used in the study. The forming forces were decreased significantly when ultrasonic vibrations were used.

Long et al. [18] studied the influence of feed rate, material of sheet (AA1050-H14, AA5052-H34), vibration amplitude (0, 6, 9, 12, 15, 18 µm), ultrasonic power and tool radius on forming force and temperature induced during ultrasonic-assisted SPIF process. The reduction in forming forces was lower when higher feed rate was used because less ultrasonic energy could be transmitted into work material per unit time. Honarpisheh et al. [19] investigated the forming force of bimetal sheets of AA1050 and copper (C-10100). The results showed that the axial forming forces increased from 1464 and 1357 N to 1636 and 1730 N for numerical and experimental tests, respectively, when tool diameter was raised form 10 mm to 16 mm. Zhai et al. [20] investigated the effects of spindle speed, sheet thickness and step size on forming forces during ultrasonic-assisted ISF (U-ISF) and ISF on AA1050-O sheets to produce pyramidal frustums. Forming forces were found to reduce up to 40% when ultrasonic amplitude was increased from 0 to 10 µm. Moreover, the forming forces increased gradually in the initial stages because of work hardening effects and then became stable, and this is in accordance with [21]. Kumar et al. [21] studied impact of various process variables for axial forming forces and optimized the SPIF process using Taguchi method for AA6063 and AA2024 sheets. Results showed that forming forces were found to be reduced by 14.20% when hemispherical tool of 11.60 mm was used in place of flat-end tool of same diameter keeping other factors constant. A statistical model was also developed for estimating the axial forming forces which was validated with further experimentation work. Authors also explored the gradient of force curve that could be employed as a spy variable for safe implementation of SPIF operation. Kumar and Gulati [22] studied impact of various process variables for axial forming forces and thickness reduction and optimized the SPIF process using Taguchi method on AA2014 sheets. Conical frustums were formed using two different tool path approaches viz. profile and helical, and these are well described by [1, 12, 21]. Forming forces were observed to be raised when tool radius, step size and sheet thickness were increased. A statistical model was proposed for predicting the forming which was further validated experimentally. Chang et al. [23] developed an analytical model for predicting forming forces in single pass SPIF, multi-pass SPIF and incremental hole flanging processes and validated the same with experimental results by varying impact factors like sheet thickness, wall angle, step size and tool diameter for AA5052 and AA3003 alloys sheets to produce VWACF and VWAPF.

Literature [12, 24], and [25] also reports that vertical downward forces (F_z, in Fig. 2) are of greater intensity as compared to horizontal forces (F_x and F_y, in Fig. 2). Hence, delineation and calculation of F_z would secure the safe employment of forming tools and machine for SPIF process. Moreover, the failure of material and forming machine can be well estimated by determining the influence of input variables on forming force during this die-less process. Hence, the estimation of F_z can also ensure the energy required by forming machine so that the process can be controlled online.

In the current work, an attempt has been made to investigate the impacts of wall angle, step size and spindle speed on maximal downward forces. In addition, the impacts of interactions of these factors have also been studied. These input variables and their interactions have not been explored on AA2024 alloy sheets to the best of

Table 1 Chemical compositions of AA2024 sheet

Element	Al	Cr	Cu	Fe	Mg	Mn	Si	Ti	Zn
Weight %	91.50	0.10	4.60	0.30	1.70	0.80	0.50	0.10	0.20

Table 2 Levels of input variables under investigation

Variable	Level 1	Level 2	Level 3	Level 4
Wall angle (°)	60	64	68	–
Step size (mm)	0.2	0.5	0.8	1.2
Spindle speed (rpm)	Free	500	1000	1500

authors' knowledge so far. AA2024 is a popular aluminum alloy which is known for its favorable characteristics in sheet metal applications like lightweight, high strength, corrosion resistance, etc. The chemical compositions of this alloy are represented in Table 1. The procedure and instrument used for measuring these compositions are well explained in previous studies [2, 14, 21]. Table 2 depicts the varied impact factors and their levels. While varying the set of input factors, other parameters were kept constant according to previous work [14].

2 Materials and Methods

Figure 3 depicts the experimental setup installed on CNC milling machine. Forming tool was firmly mounted on spindle to provide rotation to it. In addition, SPIF fixture (which is hollow) was mounted on the machine table to clamp the sheet firmly and to provide relative motion between tool and sheet. A load cell was also placed between the machine table and SPIF fixture to measure vertical downward force. Data logger system, installed to support the load cell, was assisted by MicroSCADAa software to store the real-time values of force. The working area of fixture was 200 mm × 200 mm. To produce conical frustums of 120 mm major diameter and 70 mm height, CAD model was designed in SolidWorks® software, and the same was imported to Delcam™ software for generating numerical instructions for CNC milling machine taking helical tool path into consideration. Castrol Alpha SP 320 oil has been used as lubricant during forming operation.

3 Results and Discussion

The recorded values of the maximal vertical downward forces (F_z_max.) are depicted in Table 3. The influence of interaction of wall angle and step size is depicted by Fig. 4. The maximal axial force was increased dramatically when the amount of wall
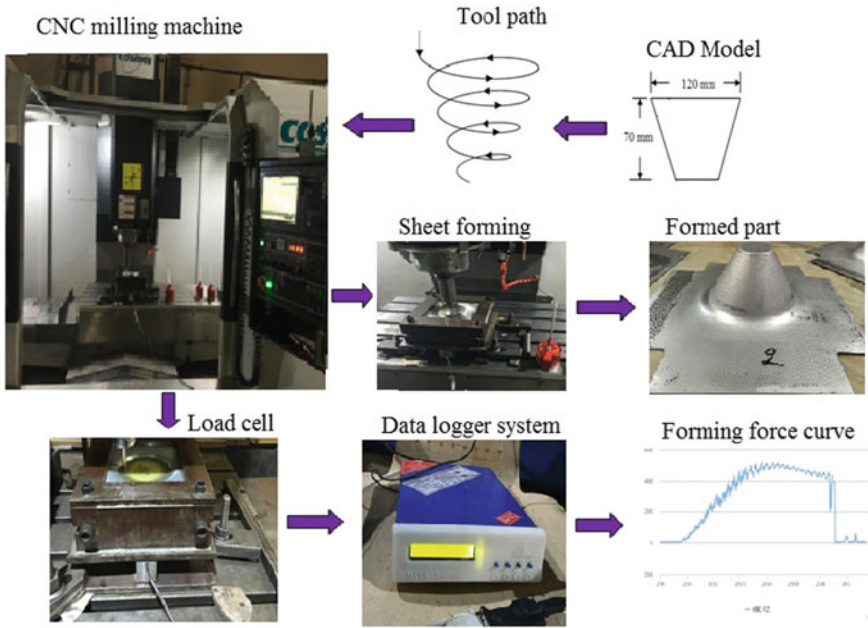
Fig. 3 Experimental setup and measurement of forming force

Table 3 Experimental results of maximum axial force for the experimented conditions

(a) Effects of step size and wall angle				(b) Effects of spindle speed and wall angle			
Run	Step size	Wall angle	F_z_max. (N)	Run	Spindle speed	Wall angle	F_z_max. (N)
1	0.2	60	863	1	Free	60	1032
2	0.2	64	910	2	Free	64	1152
3	0.2	68	988	3	Free	68	1314
4	0.5	60	907	4	500	60	971
5	0.5	64	1001	5	500	64	1076
6	0.5	68	1121	6	500	68	1221
7	0.8	60	988	7	1000	60	901
8	0.8	64	1122	8	1000	64	992
9	0.8	68	1274	9	1000	68	1123
10	1.2	60	1126	10	1500	60	843
11	1.2	64	1276	11	1500	64	914
12	1.2	68	1458	12	1500	68	1018
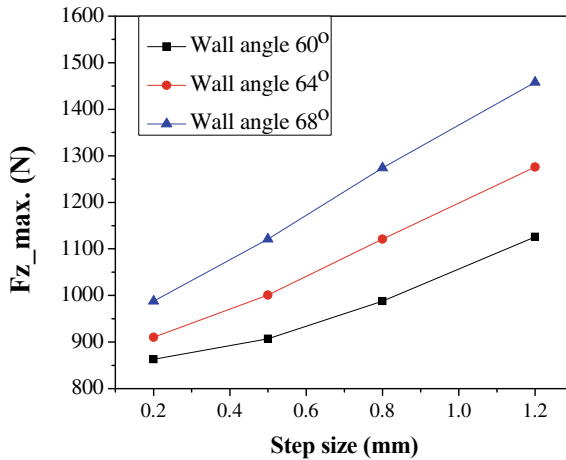
Fig. 4 Influence of wall angle and step size on maximal axial forces

angle and step size was raised because the larger step size and wall angle result in deforming the material in large amount at an instant. When combination of higher levels of these two factors is employed, the forming force increases very rapidly and hence becomes the limiting factor of forming tool and machinery that should obviously be avoided. On the other hand, employment of higher wall angle resulted in the fracture of sheet material well before achieving the designed height of conical frustums. Sheet material was fractured at a height of 53.3 mm when combination of moderate step size (0.5 mm, in this case) and wall angle (68°, in this case) was employed. When same wall angle (68°) was employed with higher level of step size (1.2 mm, in this case), sheet fractured at a relatively lower height (35.7 mm). This is because excessive thinning of sheet is occurred when wall angle increases (according to sine law [26]). This effect of thinning the sheet becomes severe when large step size is combined with higher wall angle. On the other hand, the implementation of higher step size leads to reduction in forming time since larger step size can finish the required depth in lesser contours.

The influence of interaction of wall angle and spindle speed is depicted in Fig. 5. The maximal axial force was found to reduce dramatically when the spindle speed was raised because the high spindle speed led to increment in friction at tool–sheet interface. Hence, ductility of material is raised due to increase in temperature caused by increased friction. This trend of reducing forces continued with all levels of spindle speed. It was also be noticed that higher spindle speed (1500 rpm, in this case) resulted in producing chips during forming operation which led to the deterioration of surface quality of formed components. It can be observed that the axial peak force obtained at "68° wall angle and 1500 rpm" is much lower (1018 N, in this case) than that observed at "60° wall angle and free to rotate condition of spindle" which is 1032 N. This depicts that components having higher wall angles can be formed at reduced forming forces by employing higher spindle speed at the expense of surface quality.
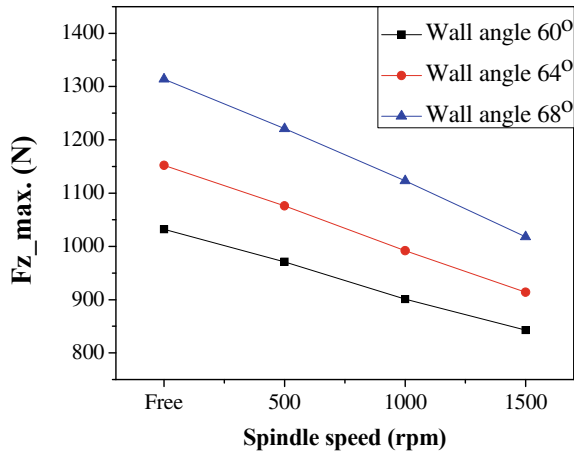
Fig. 5 Influence of wall angle and spindle speed on maximal axial forces

4 Conclusion

The objective of current work was to explore the impacts of interactions of step size and tool rotation with wall angle on AA2024 sheets during SPIF technique. Conical frustums were formed as a benchmark shape using helical tool path. It was observed that the investigated factors were of great significance that can affect and control the process. When combination of higher levels of these two factors is employed, the forming force increases very rapidly and hence becomes the limiting factor of forming tool and machinery that should obviously be avoided. On the other hand, the implementation of higher step size leads to reduction in forming time since larger step size can finish the required depth in lesser contours. This depicts that components having higher wall angles can be formed at reduced forming forces by employing higher spindle speed at the expense of surface quality. Future work would target the investigation of effects of interactions of input variables on formability and surface roughness of formed components.

References

1. Kumar, A., Mittal, R.K.: Incremental Sheet Forming Technologies: Principles, Merits, Limitations, and Applications, 1st edn. CRC Press, Taylor and Francis. United States (2020). ISBN: 978-0-367-27674-4
2. Kumar, A., Gulati, V.: Experimental investigation and optimization of surface roughness in negative incremental forming. Meas.: J. Int. Meas. Confed. **131**, 419–430 (2019)
3. Kumar, A., Gulati, V., Kumar, P.: Investigation of surface roughness in incremental sheet forming. In: Procedia Computer Science, International Conference on Robotics and Smart Manufacturing 2018, vol. 133, pp. 1014–1020. Elsevier (2018)

4. Kumar, A., Gulati, V., Kumar, P.: Effects of process parameters on surface roughness in incremental sheet forming. In: Materials Today Proceedings, International Conference on Composite Materials, Manufacturing, Experimental Techniques, Modeling and Simulation 2018, vol. 5(14), pp. 28026–28032. Elsevier (2018)
5. Gulati, V., Kumar, A.: Investigation of some process parameters on forming force in single point incremental forming. Int. Res. J. Eng. Technol. **4**(4), 784–791 (2018)
6. Manju, Gulati, V., Kumar, A.: Process parameters and thickness reduction in single point incremental forming. Int. Res. J. Eng. Technol. **7**(1), 473–476 (2020)
7. Leszak, E., Ave, H.: Apparatus and process for incremental dieless forming. United States Patent, United States (1967)
8. Berghahn, W. G., Murray, G. F.:Method of dielessforming surfaces of revolution. United States Patent, New York (1967)
9. Mason, B.: Sheet metal forming for small batches. PhD Thesis, University of Nottingham (1978)
10. Kumar, A., Gulati, V., Kumar, P., Singh, V., Kumar, B., Singh, H.: Parametric effects on formability of AA2024-O aluminum alloy sheets in single point incremental forming. J. Mater. Res. Technol. **8**(1), 1461–1469 (2019)
11. Kumar, A., Gulati, V., Kumar, P., Singh, H., Singh, V., Kumar, S., Haleem, A.: Parametric investigation of forming forces in single point incremental forming. In: International Conference on "Advances in Materials and Manufacturing Applications (IConAMMA 2018)" Amrita Vishwa Vidyapeetham, Bengaluru Campus, Karnataka, India. 16–18 Aug 2018
12. Kumar, A.,Gulati, V.: Forming force in incremental sheet forming: a comparative analysis of the state of the art. J. Braz. Soc. Mech. Sci. Eng., **41** (2019)
13. Kumar, A., Gulati, V., Kumar, P.: Investigation of process variables on forming forces in incremental sheet forming. Int. J. Eng. Technol. **10**(3), 680–684 (2018)
14. Kumar, A., Gulati, V., Kumar, P.: Experimental Investigation of forming forces in single point incremental forming. In: Shanker, K., Shankar, R., Sindhwani, R. (eds.) International Conference on Future Learning Aspects of Mechanical Engineering 2018, LNME, pp. 423–430. Springer, (2019)
15. Uheida, E.H., Oosthuizen, G.A., Dimitrov, D.: Investigating the impact of tool velocity on the process conditions in incremental forming of titanium sheets. In: Procedia Manufacturing, vol. 7, pp. 345–350. Elsevier (2017)
16. Ali, A., Ragab, A.E., Dabwan, A., Mustafa M., Hidri, L.: Prediction of formation force during single-point incremental sheet metal forming using artificial intelligence techniques, PloS one **14**(8) (2019)
17. Sakhtemanian, M.R., Honarpisheh, M., Amini, S.: A novel material modeling technique in the single-point incremental forming assisted by the ultrasonic vibration of low carbon steel/commercially pure titanium bimetal sheet. The Int. J. Adv. Manuf. Technol. **102**, 473–486 (2019)
18. Lon, Y., Li, Y., Sun, J., Ille, I., Li, J., Twiefel, J.: Effects of process parameters on force reduction and temperature variation during ultrasonic assisted incremental sheet forming process. The Int. J. Adv. Manuf. Technol. **97**, 13–24 (2018)
19. Honarpisheh, M., Keimasi, M., Alinaghian, I.: Numerical and experimental study on incremental forming process of Al/Cu bimetals: influence of process parameters on the forming force, dimensional accuracy and thickness. J. Mech. Mater. Struct. **13**(1), 35–51 (2018)
20. Zhai, W., Li, Y., Cheng, Z., Sun, L., Li, F., Li, J.: Investigation on the forming force and surface quality during ultrasonic-assisted incremental sheet forming process. The Int. J. Adv. Manuf. Technol. **106**, 2703–2719 (2020)
21. Kumar, A., Gulati, V.: Experimental investigations and optimization of forming force in incremental sheet forming. Sādhanā **43**, 159 (2018)
22. Kumar and Gulati, Optimization and investigation of process parameters in single point incremental forming. Indian J. Eng. Mater. Sci. (2020), ISSN: 0975-1017 (Online); 0971-4588 (Print), Accepted

23. Chang, Z., Li, M., Chen, J.: Analytical modeling and experimental validation of the forming force in several typical incremental sheet forming processes. Int. J. Mach. Tools Manuf **140**, 62–76 (2019)
24. Oleksik, V., Pascu, A., Gavrus, A., Oleksik, M.: Experimental studies regarding the single point incremental forming process. Acad. J. Manuf. Eng. **8**, 51–56 (2010)
25. Fiorentino, A., Ceretti, E., Attanasio, A., Mazzoni, L., Giardini, C.: Analysis of forces, accuracy and formability in positive die sheet incremental forming. Int. J. Mater. Form. **2**, 805–808 (2009)
26. Jeswiet, J., Micari, F., Hirt, G., Bramley, A., Duflou, J., Allwood, J.: Asymmetric single point incremental forming of sheet metal. CIRP Ann.—Manuf. Technol. **54**, 88–114 (2005)

Location and Capacity Allocation Decisions to Mitigate the Impacts of Unexpected Man-Made Disasters in Delhi: A Goal Programming Approach

Sahil Shah, Abhishek Bhardwaj, Kartik Dahiya, and Pravin Kumar

1 Introduction

The World Health Organization defined the term disaster as "any occurrence that causes damage, ecological disruption, loss of human life, deterioration of health and health services on a scale sufficient to warrant an extraordinary response from outside the affected community or area" [1]. An effective humanitarian supply chain may reduce the after effects of the disaster up to some extent. The researchers have already proposed and developed many mathematical models to tackle such type of uncertainties and minimize the losses. According to Sheu [2], the humanitarian logistics can be defined as managing the flows of relief, information and services from the points of origin to the disaster location to fulfill the requirements of the affected people under the emergency situations. There is difference between the performance measurement of commercial and humanitarian logistics systems. In the commercial logistics systems, the main focus is given to minimizing the cost and reducing the lead time of supply. But, in the humanitarian logistics systems, effectiveness of flow of relief with high efficiency is given more priority [3–5]. Some of the major terrorist attacks in India are shown in Fig. 1.

The disaster may be classified as natural disaster, technological and man-made disaster. All the terrorist attacks, burning the public and private properties, communal

S. Shah · A. Bhardwaj · K. Dahiya · P. Kumar (✉)
Department of Mechanical, Production & Industrial and Automobile Engineering, Delhi
Technological University, Delhi 110042, India
e-mail: pravin@dce.ac.in

S. Shah
e-mail: sahils983@gmail.com

A. Bhardwaj
e-mail: abhishek.bh.17@gmail.com

K. Dahiya
e-mail: kartikdahiya805@gmail.com

Fig. 1 Few major terrorist attacks in India in the last one decade [6]

riots, bioterrorism, political and social disturbances due to some issues are more prone in India. Recently, it is not clear that Covid-19 pandemic is man-made disaster or natural disaster. Each year, millions of people are affected by man-made/natural disasters in the world. The man-made disasters are increasing day by day due to the complexity of geopolitics between two countries and domestic or local issues in a country. Some of the major terrorist attacks in India have been summarized as shown in Table 1.

Domestic or local issues are also responsible for the man-made disasters and violence. In the recent years, we have seen many disturbances in terms of burning the public and private properties and killing the innocent people due to domestic issues, such as social disturbances, demand for reservation in jobs and professional education, arrest of religious gurus, issues of temple/mosque, resistance to bills like Citizenship Amendment Act, etc. In addition, many cities of India such as Delhi, Mumbai, Varanasi, Ahmadabad, Chennai and Hyderabad have been on the terrorists target (Table 1). The uncertainty associated with the prediction of the attacks makes it very difficult to deploy the human forces to control the situation exactly at the same time. In this situation, we have to optimize the use of the existing number of human forces to control the situation and simultaneously make the relief operations.

Considering the number of attacks in the major Indian cities, it becomes very necessary to consider the preparedness and response to the man-made disaster in

Table 1 Some major terrorist attacks in India [7–9]

S. No	Attacks and description	Location	Number of persons Killed	Number of persons Injured	Date
1	13 blasts across the city	Mumbai	257	713	March 12, 1993
2	Mulund Railway Station	Mumbai	11	80	March 13, 2003
3	Gateway of India and Zaveri Bazaar	Mumbai	52	160	August 25, 2003
4	Seven blasts at seven locations in local trains across the city	Mumbai	181	890	July 11, 2006
5	Multiple terrorist attacks across the city	Mumbai	175	300	November 26, 2008
6	Serial blasts in Mumbai	Mumbai	26	131	July 13, 2011
7	Nine bomb blasts along six areas in Jaipur	Jaipur	71	200	May 13, 2008
8	17 serial bomb blasts in Ahmedabad	Ahmedabad	56	200	July 26, 2008
9	Lajpat Nagar blast	Delhi	13	39	May 21, 1996
10	Indian Parliament attack in New Delhi	Delhi	7	18	December 13, 2001
11	Serial blasts in New Delhi	Delhi	70	250	October 29, 2005
12	Three synchronized terrorist attacks in Varanasi	Varanasi	28	101	March 7, 2006
13	Two blasts in Hyderabad's Lumbini park and Gokul Ghat	Hyderabad	42	54	August 25, 2007
14	Five bomb blasts in Delhi markets	Delhi	33	130	September 13, 2008
15	Delhi bombing	Delhi	15	79	September 7, 2011
16	Uri attack	Uri, J&K	23	8	September 18, 2016

(continued)

Table 1 (continued)

S. No	Attacks and description	Location	Number of persons Killed	Number of persons Injured	Date
17	Pulwama attack	J & K	46	-	February 14, 2019

an effective manner. McLoughlin [10] divided the literature related to humanitarian logistics into four categories. First two categories are related to preparedness and mitigation of disaster, i.e., pre-disaster phase. Rest two categorizes are related to response and recovery after the disaster, i.e., post-disaster phase. In post-disaster relief operations, lack of integration in humanitarian logistics was the main observation of Vitoriano et al. [11]. Matisziw et al. [12] examined the restoration problem of a telecommunication network during the recovery phase using decision variables related to disrupted nodes and arcs in a multi-period environment.

The authors have focused this study on the preparedness and response to the man-made disaster in Delhi considering few sensitive locations and a rough estimate of the resources such as availability of police force, firemen and doctors in the different locations.

2 Literature Review

Huang et al. [13] observed that humanitarian relief is not only concerned with minimization of cost, it has multiple objectives such as save the life of people, send the relief within the limited time, selection of alternate route to avoid the delay and disruption of supply network. Holguín-Veras et al. [14] observed that in a commercial supply chain minimization of the cost is the primary objective, but in humanitarian aid, the main motivation is to reduce the human suffering and minimize the impact [15]. Humanitarian aid is an assistance provided for humanitarian purposes during the crisis, especially natural and man-made disasters. Rekik et al. [16] presented four models of humanitarian network design and distribution problems: number of facilities to be opened, the location of the facilities, allocation of the resources among the different facilities and the distribution of humanitarian aid. Finally, describe a network design and humanitarian aid distribution problem in the aftermath of a disaster. They focused on two objectives: One is to maximize the coverage of affected people, and other is to minimize the total transportation time. Kanoun et al. [17] also emphasized the objectives, as maximization of coverage of the affected people and minimization of the travel time for the best location of the police stations, firefighters and ambulance services. They also highlighted the importance of fire and emergency services which are crucial in saving lives and reducing the injuries.

Ransikarbum and Mason [18] presented a goal programming model incorporating multiple objective of integrated response and recovery model in network restoration decisions. The model gives the compromise solutions for user-desired goals, under limited capacity, budget and available resources. Barzinpour and Esmaeili [19] developed a multi-objective mixed-integer linear programming model for preparation planning phase of disaster management. In urban areas, local organizations such as municipal authorities are responsible for disaster-related relief operations. They have to provide emergency shelters, food, clothes and medicine to the affected people to reduce the human sufferings. Ortuño et al. [20] used a lexicographical goal programming model for relief operations in the disaster affected areas. The main objective was to deliver the planned quantity of goods with the constraints of minimum operation cost and time of response. Noham and Tzur [21] used a heuristic algorithm based on the Tabu-search method for post-disaster decisions considering a set of humanitarian constraints. They tested the both randomly generated data and real data obtained from the Geophysical Institute of Israel.

Gralla et al. [22] proposed the three criteria for the performance measurement: maximization of the ratio of units distributed to their delivery time, efficiency (cost) and equity. Yu et al. [23] proposed an approach for effective and equitable resource allocation in humanitarian logistics considering human suffering. They used dynamic programming for multi-period resource allocation dispatch problem to represent the disaster response phase considering the human suffering due to the delayed delivery. Thomas [24] emphasized to develop the infrastructure to reduce the impact and cost of the disaster. The minimizing loss of life and alleviating the human suffering have been considered as the main goal of humanitarian aid [25]. Holguín-Veraset al. [14] and Sheu [26] also considered the human suffering as the main criteria of effectiveness of the emergency logistics. Paul and MacDonald [27] developed a stochastic model to determine the location of point of distributions and capacities of distribution centers for emergency stockpiles to enhance the preparedness in the event of a disaster. They applied the proposed model to a region prone to earthquake incorporating the various sources of uncertainties.

Chong et al. [28] focused their study on the optimal asset distribution, reduced human suffering, optimal warehouse locations, distribution points, inventory levels and cost considering a wide range of uncertainties. They implemented the model in a landslide and flood area in Peruvian city. Many researchers have already proposed the goal programming in humanitarian logistics as discussed in this section, and many developments in this area are going on. We have observed that only few researches are focused on distributing manpower, most of the studies on humanitarian supply chain deal with distribution of logistics and setting up distribution centers. In this study, the authors have proposed a model, which considers the deployment of the human resources during the emergency situation. The main objective of this study is to propose the goal programming model to optimize the resource allocation in terms of human resources and quick response to the man-made disasters in Delhi.

3 Model Formulation and Case Discussion

The latest terrorist attack took place on Wednesday, September 7, 2011, at 10:14 local time outside Gate No. 5 of the Delhi High Court, which is also known as Delhi Bombing of 2011. A briefcase bomb was planted which resulted in death of 15 people and 79 people were injured. Before this incident, a low-intensity bomb blast also occurred at the High Court outside Gate No. 7 on May 25 without any casualty [29]. The attack took place, while Indian Prime Minister Manmohan Singh was on a historic two-day visit to Bangladesh, to discuss Bangladesh–India relations.

In this study, a hypothetical situation has been created incorporating the vulnerable areas of Delhi and one location as the disaster point. Akshardham Temple is considered as the disaster point and other five locations, such as New Delhi, Red Fort, Nizamuddin and Inter State Bus Terminal, Kashmiri Gate as the vulnerable location in Delhi. Some human forces are also reserved for sealing of the other areas and containment of the terrorists. The attack locations are required to be supplied with the sufficient number of policemen, firemen and medical staff to control and contain the terrorist by sealing the areas, minimize the human suffering and provide medical aid to the sufferers and reduce the losses due to burning of public and private properties. While the potential attack locations need policemen and fire staff in addition to the police force reserved for barricading and other operations. Some medical staffs are required to attend to the victims of attack in addition to the regular patients in the hospitals. The number of firemen is required according to the number of firefighting trucks required for the particular location. The constraints include the availability of the firemen, policemen and doctors in the different location in Delhi.

Model Description

Following parameters are used in the model development:

$$i \rightarrow 1, 2, \ldots, 5 \text{indicate the attack locations}$$

$1 -$ Akshardham (the location of Disaster/attack);

$2 -$ NewDelhi (Vulnerable area)

$3 -$ Nizamuddin (Vulnerable area);

$4 -$ Red Fort (Vulnerable area);

$5 -$ I.S.B.T. Kashmiri Gate (Vulnerable area)

$6 -$ Other high alert area/regular requirement

(Area to be sealed for containment of terrorists)

$$P_i \rightarrow \text{Polishmen required in} i\text{th location}$$
$$F_i \rightarrow \text{Firemen required in} i\text{th location}$$
$$H_i \rightarrow \text{Health/Medical staff in} i\text{th location}$$

The goal programming model is formulated as

$$
\text{Minimize}
$$

$$
\begin{cases}
\{W_1 D_1^- + W_2 D_2^- + W_3 D_3^- + W_4 D_4^- + W_5 D_5^- + W_6 D_6^- + W_7 D_7^- + W_8 D_8^- + W_9 D_9^+ \\
+ W_{10} D_{10}^+ + W_{11} D_{11}^+ + W_{12} D_{12}^- + W_{13} D_{13}^- + W_{14} D_{14}^- + W_{15} D_{15}^- + W_{16} D_{16}^- + W_{17} D_{17}^- \\
+ W_{18} D_{18}^+ + W_{19} D_{19}^+ + W_{20} D_{20}^+ + W_{21} D_{21}^+ + W_{22} D_{22}^- + W_{23} D_{23}^+ + W_{24} D_{24}^+ + W_{25} D_{25}^+ \\
+ W_{26} D_{26}^+\}
\end{cases}
\tag{1}
$$

Subject to:

$$
P_1 + H_1 + F_1 - D_1^+ + D_1^- = K_1 \tag{2}
$$

$$
P_2 + H_2 + F_2 - D_2^+ + D_2^- = K_2 \tag{3}
$$

$$
P_3 + H_3 + F_3 - D_3^+ + D_3^- = K_3 \tag{4}
$$

$$
P_4 + H_4 + F_4 - D_4^+ + D_4^- = K_4 \tag{5}
$$

$$
P_5 + H_5 + F_5 - D_5^+ + D_5^- = K_5 \tag{6}
$$

$$
P_6 - D_6^+ + D_6^- = K_{P6} \tag{7}
$$

$$
H_6 - D_7^+ + D_7^- = K_{H6} \tag{8}
$$

$$
F_6 - D_8^+ + D_8^- = K_{F6} \tag{9}
$$

$$
\sum_{n=1}^{6} P_n - D_{11}^+ + D_{11}^- = K_P \tag{10}
$$

$$
\sum_{n=1}^{6} H_n - D_{11}^+ + D_{11}^- = K_H \tag{11}
$$

$$
\sum_{n=1}^{6} F_n - D_{11}^+ + D_{11}^- = K_F \tag{12}
$$

$$
P_i - D_J^+ + D_J^- = K_{Pi}; \ \forall \ \ i \le 5, \quad 12 \le j \le 16 \tag{13}
$$

$$
H_i - D_J^+ + D_J^- = K_{Hi}; \ \forall \ \ 1 \le i \le 5, \ 18 \le j \le 21 \tag{14}
$$

$$
F_i - D_J^+ + D_J^- = K_{Fi}; \ \forall \ \ 1 \le i \le 5, \ 22 \le j \le 26 \tag{15}
$$

where j represents the specific number of deviations in goals for Eqs. (12–15) from D12 to D26.

Equation (1) represents the objective functions which lead to minimization of the deviations, i.e., overachievement and under achievements. Equations (2–6) represent the total number of human forces required in the different affected and vulnerable areas. Equations (7–9) represent the number of human resources required for regular need and other high alert areas. Equations (10–12) represent the constraints related to availability of the total police force, medical staff and firemen in Delhi, respectively. Equations (13–15) represents the total number of police force, medical staff and fireman required individually in the attack areas. A minimum requirement of the human resources as police force, firemen, medical staff in the different locations in Delhi during crisis is given below:

$$K_1 = 600; \; K_2 = 140; \; K_3 = 140; \; K_4 = 180; K_5 = 120;$$
$$K_P = 1,00,000; \; K_H = 10,000; \; K_F = 3280$$
$$K_{P1} = 400; \; K_{P2} = 115; \; K_{P3} = 115; \; K_{P4} = 150; K_{P5} = 95$$
$$K_{P6} = 80000$$

$$K_{H1} = 100; \; K_{H2} = 5; \; K_{H3} = 5; \; K_{H4} = 5; \; K_{H5} = 5; \; K_{H6} = 11.000$$
$$K_{F1} = 80; \; K_{F2} = 32; \; K_{F3} = 32; \; K_{F4} = 32; \; K_{F5} = 32; \; K_{F6} = 2960$$

The proposed model is solved using linear programming software (QM) for Windows V5. The model results are shown in Table 2 gives the optimum number of policemen, firemen and doctors in location "i" (where $i = 1, 2, 3, 4, 5$) in man-made disaster. After optimization, we get the optimal number of the various human resources that can be employed in the different areas during the crisis.

The above proposed model is devoted to minimize the response time for better control and containment of the disaster factor such as terrorists. The main purpose is to reduce the loss of lives and damage to the property. India has been suffering from the terrorist attacks from the decade of the 90s, and Delhi and Mumbai are prone

Table 2 Optimal values of the human resources in the different effected areas

Type of human resources	Effected areas					
	Akshardham	New Delhi	Nizamuddin	Red Fort	ISBT Kashmiri Gate	Other high alert zone
Police force	420	115	115	150	95	80,000
Medical Staff	100	0	0	0	0	9900
Firemen	80	25	25	30	25	2960

to the terrorist attack. The making of dedicated anti-terror organization in a large country like India and to deploy them on time on the site of disaster is a very difficult task. The effective utilization of the existing resources may be one of the most viable and relatively faster approaches.

4 Conclusion

In this study, five sensitive locations of Delhi have been considered for the fast response, relief operations including the other high alert zone. It has been observed that when the man-made disaster occurs in some specific locations in Delhi, sufficient number of security forces could not be deputed on time. Due to shortage of security forces, medical facilities, firefighting devices, the loss of human lives and properties could not be avoided. This study is based on the available resources that how it can be utilized optimally to minimize the various losses. This concept may be utilized during the earthquake, flooding the lower part of Delhi and terrorist attack including the communal rights.

In this study, goal programming is used for optimum utilization of the resources, especially police force, medical staff and fireman. An approx estimation of availability of these resources in Delhi has been used, and model is proposed to solve the problem. It may help in minimizing the casualties during the crisis. We have observed the huge loss of lives of people in different terrorist attacks in Delhi such as parliament attack, serial bombing in Sarojini Nagar market, Lajpat Nagar, and in DTC buses, communal riot in northeast Delhi, etc. This paper may help the administration to control the situation and make the relief during the disaster.

Limitations: The main focus of the study is deployment of human resources. The relief materials, shelters, food, clothes, etc., may be incorporated in the future research. Also, the availability of human resources is based on an approximate estimation. Some variation in availability of the human forces may be considered using fuzzy sets.

References

1. Najafi, M., Eshghi, K., Dullaert, W.: A multi-objective robust optimization model for logistics planning in the earthquake response phase. Trans. Res. Part E: Log. Transp Rev. **49**(1), 217–249 (2013)
2. Sheu, J.B.: Challenges of emergency logistics management. Transp. Res. Part E: Logist. Transp. Rev. **43**(6), 655–659 (2007)
3. Beamon, B.M., Balcik, B.: Performance measurement in humanitarian relief chains. Int. J. Public Sector Manage. **21**(1), 4–25 (2008)
4. Tatham, P., & Christopher, M. (Eds.).: Humanitarian logistics: Meeting the challenge of preparing for and responding to disasters. Kogan Page Publishers (2018)

5. Celik, M., Ergun, O., Johnson, B., Keskinocak, P., Lorca, A., Pekgun, P., Swann, J.: Human-itarian logistics, tutorials in operations research. In: Institute for Annual Operations Research and the Management Sciences (INFORMS) conference (pp. 14–17) (2012, October).
6. The Economics Time (February 15, 2020). Six terror attacks that shook India. https://econom ictimes.indiatimes.com/news/defence/six-terror-attacks-that-shook-india/1993-bombay-bla sts/slideshow/74146291.cms. Retrieved April 20, 2020.
7. SATP: Terrorist attacks in Mumbai since 1993. South Asia Terrorism Portal, https://www.satp. org/satporgtp/countries/india/database/mumbai_blast.htm (2011)
8. TOI: Since 2005, terror has claimed lives of 707 Indians (2005). https://timesofindia.ind iatimes.com/india/Since-2005-terror-has-claimed-lives-of-707-Indians/articleshow/532342 26.cms. Retrieved April 20, 2020.
9. The Hindu: The explosions killed 71 people and left 200 injured in the Walled City. https://www.thehindu.com/news/national/other-states/four-sentenced-to-death-in-2008-jaipur-serial-blasts-case/article30358914.ece. Retrieved April 20, 2020.
10. McLoughlin, D.: A framework for integrated emergency management. Public Administration Review **45**, 165–172 (1985)
11. Vitoriano, B., Ortuño, M.T., Tirado, G., Montero, J.: A multi-criteria optimization model for humanitarian aid distribution. J. Global Optim. **51**(2), 189–208 (2011)
12. Matisziw, T.C., Murray, A.T., Grubesic, T.H.: Strategic network restoration. Networks Spat. Econom. **10**(3), 345–361 (2010)
13. Huang, M., Smilowitz, K., Balcik, B.: Models for relief routing: equity, efficiency and efficacy. Trans. Res. Part E: Log. Transp. Rev. **48**(1), 2–18 (2012)
14. Holguín-Veras, J., Pérez, N., Jaller, M., Van Wassenhove, L.N., Aros-Vera, F.: On the appro-priate objective function for post-disaster humanitarian logistics models. Journal of Operations Management **31**(5), 262–280 (2013)
15. Gutjahr, W.J., Nolz, P.C.: Multicriteria optimization in humanitarian aid. Eur. J. Oper. Res. **252**(2), 351–366 (2016)
16. Rekik, M., Ruiz, A., Renaud, J., Berkoune, D., Paquet, S.: A decision support system for human-itarian network design and distribution operations. In: Humanitarian and Relief Logistics, pp. 1–20. Springer, New York, NY (2013)
17. Kanoun, I., Chabchoub, H., Aouni, B.: Goal programming model for fire and emergency service facilities site selection. INFOR: Inf. Syst. Oper. Res. **48**(3), 143–153 (2010)
18. Ransikarbum, K., Mason, S.J.: Goal programming-based post-disaster decision making for integrated relief distribution and early-stage network restoration. Int. J. Prod. Econ. **182**, 324–341 (2016)
19. Barzinpour, F., Esmaeili, V.: A multi-objective relief chain location distribution model for urban disaster management. Int. J. Adv. Manuf. Technol. **70**(5–8), 1291–1302 (2014)
20. Ortuño, M.T., Tirado, G., Vitoriano, B.: A lexicographical goal programming based decision support system for logistics of Humanitarian Aid. Top **19**(2), 464–479 (2011)
21. Noham, R., Tzur, M.: Designing humanitarian supply chains by incorporating actual post-disaster decisions. Eur. J. Oper. Res. **265**(3), 1064–1077 (2018)
22. Gralla, E., Goentzel, J., Fine, C.: Assessing trade-offs among multiple objectives for humanitarian aid delivery using expert preferences. Prod. Oper. Manage. **23**(6), 978–989 (2014)
23. Yu, L., Zhang, C., Yang, H., Miao, L.: Novel methods for resource allocation in humanitarian logistics considering human suffering. Comput. Ind. Eng. **119**, 1–20 (2018)
24. Thomas, A.: Humanitarian logistics: enabling disaster response. Fritz Inst. **15** (2003)
25. Apte, A.: Humanitarian logistics: A new field of research and action. Found. Trends Technol. Inf. Oper. Manage. **3**(1), 1–100 (2010)
26. Sheu, J.B.: Post-disaster relief–service centralized logistics distribution with survivor resilience maximization. Transportation Research Part B: Methodological **68**, 288–314 (2014)
27. Paul, J.A., MacDonald, L.: Location and capacity allocations decisions to mitigate the impacts of unexpected disasters. Eur. J. Oper. Res. **251**(1), 252–263 (2016)
28. Chong, M., Lazo, J.G.L., Pereda, M.C., De Pina, J.M.M.: Goal programming optimiza-tion model under uncertainty and the critical areas characterization in humanitarian logistics

management. Journal of Humanitarian Logistics and Supply Chain Management. **9**(1), 82–107 (2019)

29. NDTV: Minor explosion outside Delhi High Court, no casualties (2011). https://www.ndtv.com/india-news/minor-explosion-outside-delhi-high-court-no-casualties-456713. retrieved on May 26, 2020.

Comparative Studies on Microstructure and Hardness of Plasma-Sprayed Al$_2$TiO$_5$, ZrO$_2$ and Cr$_2$O$_3$ Ceramic Coatings on Al-Silicon (LM13)

Adil Wazeer, Vishal Mondal, and Sarangapani Kennedy

1 Introduction

LM13 alloy retains higher mechanical properties such as high strength and high hardness even at the higher operating temperatures. This makes LM13 as a suitable material for IC engine components and aerospace materials because of its low weight and high specific strength. Present emerging technologies contain most protruding constant developments, advances, and modernizations in different engineering and scientific areas to improve the surface characteristics by the utilization of modern techniques. There are a variety of characteristics that are improved by implementing surface alteration methodologies such as mechanical, thermo-mechanical, tribological, electrical, and optical properties. Aluminium alloys have attractive physical and mechanical properties. They are lightweight, low costs production (with sand casting technology), easy to machine, and have good recycling possibilities (up to 95%) [1]. Due to these facts, their application in automotive and other industries is increasing. One of the applications in automotive industry is replacing of material for engine blocks, which has been traditionally made entirely of grey cast iron. Today, more than 60% of the engines for passenger cars are produced in cast aluminium alloys [2] with some concrete examples [3]. Over the last 10 years, there has been intensive development in methods to coat the cylinder bore of aluminium cast engine blocks for the automotive industry [4–9]. Several thermal spray processes were developed for the cylinder bore application during the last 15 years [4–9]. The typical bond strength according to ASTM C 633–79 is 40 to 50 MPa for aluminium cast alloy and 50–70 MPa on grey cast iron substrate. The typical as sprayed thickness is between

A. Wazeer (✉) · S. Kennedy
School of Mechanical Engineering, Galgotias University, Greater Noida 201310, India
e-mail: wazeeradil@gmail.com

V. Mondal
Symbiosis International University, Nagpur, Maharashtra 440008, India

160 and 240 μm and 80 and 150 μm after finishing. For coating performance, a thickness of 80 μm is enough [10–12]. The high thermal energy density available within a plasma for melting powders coupled with the ability to manufacture powders and design plasma guns with short spray distances for specific applications has rapidly promoted the use of plasma spraying [13–17].

2 Experimental

Commercially available metal Aluminium alloy LM13 is chosen as a substrate material. LM13 is chosen for its well-known characteristics of wear resistance and corrosion resistance under atmospheric conditions and is a major material for the construction of cylinders and pistons in IC Engine. EDX graph of substrate material evidently demonstrates that the material is only Al-Silicon (LM13) and no other grade of aluminium. The substrate material is in the form of small cylindrical rods having the dimensions of 10 mm diameter and 40 mm length. Stand-off distance was taken between 4 and 5 inches for purpose of blasting. The specimen surface which was grit blasted is prepared using acetone in an ultrasonic environment. Plasma spraying was proximately carried out after cleaning. The plasma spray deposition was performed at Ashok Plasma Sprayers, Surat, Gujarat, India, 50 kW DC non-transferred arc mode plasma spraying was used, and the powders were also supplied by the same. In the plasma torch, the input power limits were ranged from 11 to 21 kW, by monitoring the voltage, gas flow rate, and also arc current. The powder injection stood exterior to nozzle and concentrating in the direction of plasma. Carrier gas used was a mixture of hydrogen and argon gas. Scanning electron microscope studies were done at Jeol India Pvt. Ltd, New Delhi, India, by Jeol JSM-IT200LV scanning electron microscope. The microstructure of the uncoated and coated specimens was examined. The surface morphology, along with the coating-substrate interface morphology of coating, was studied under the microscope. The hardness test of the coated specimen was carried out at Narang Metallurgical and Spectro Services, New Delhi, India. More than two readings were recorded on each specimen, and mean value is described as the data point. The sprayed coatings are more brittle in comparison with corresponding compact materials and powders of hard materials (Fig. 1).

3 Results and Discussions

Thermal plasma coatings of three different ceramics are deposited on the substrate sample of Aluminium alloy LM13. Characterization of the coatings is carried out along with the hardness test of coated ceramics. SEM images of the top surface were recorded.

Fig. 1 Actual arrangement of the plasma spray set-up installed at Ashok Plasma Sprayers, Surat, Gujarat, India

3.1 Surface Morphology of Uncoated Specimen

The uncoated sample of LM13 Aluminium alloy was studied via SEM images obtained. The images showed a higher rate of machining surface irregularities of the order of 1–2 µm raised during the turning, milling, and surface finishing operations performed during the conversion of the LM13 Aluminium alloy bar into small cylindrical billets of the required dimensions. SEM micrographs were captured at 20 kV, at a high vacuum, and different magnifications. The formation of oxides on the surface of the alloy is visible and is characterized by white regions on the SEM images. The oxides formed on the surface range in the order of 0.1–1 microns. The SEM micrographs showing the surface morphology of the uncoated specimen at different micron levels and magnifications are shown in Fig. 2.
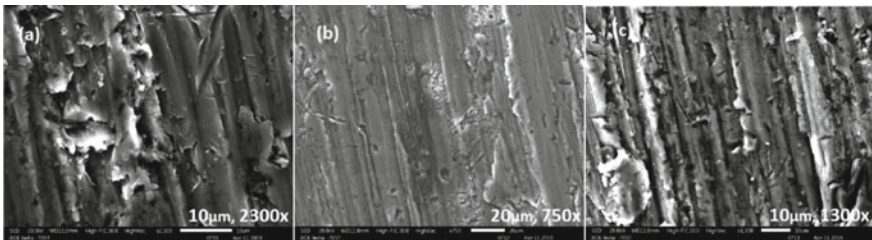
Fig. 2 SEM micrographs of LM13 Aluminium alloy specimen prior to coatings
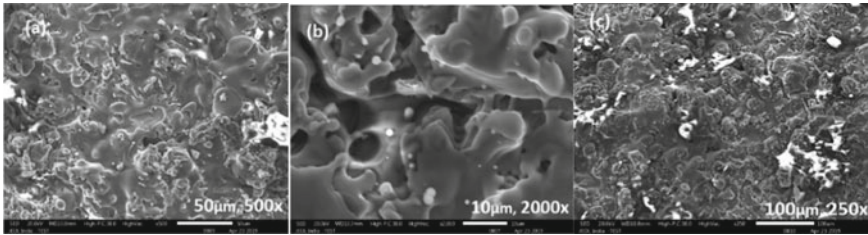
Fig. 3 SEM micrographs of specimen with Al$_2$TiO$_5$ coating

3.2 *Surface Morphology of Al$_2$TiO$_5$-coated Specimen*

The Al$_2$TiO$_5$ coating is deposited at 20 kV and a high vacuum on alloy specimens. Porosity on the coated surface is observed which is found in the order of 1–6 microns (Fig. 3a). The size of the powder particle ranges between 23.20 and 53 µm. Coating thickness ranges between 200 and 250 µm which is analysed through SEM micrographs. When the image is slightly enlarged, then cracks are also visible (Fig. 3b) which might be formed due to sudden cooling of the specimen after the plasma spray was done because the temperature of the plasma spray is around 2000 °C which alters the surface characteristics of the coated specimen. Some oxide formation is also visible on the surface of the Al$_2$TiO$_5$-coated alloy (Fig. 3c) which is characterized by large white spots or regions scattered on the surface and visible in the SEM micrograph. During the coating process, the temperature of the coating is very high which in turn raises the temperature of the specimen also. The occurrence of the cracks on the coated surface is the evidence that the material after the coating has turned brittle and can lead to fracture if load above its plastic limit is applied which is assumed to be low.

3.3 *Surface Morphology of ZrO$_2$-coated Specimen*

The zirconium oxide coating is deposited at 20 kV and a high vacuum on LM13 alloy. The size of the powder particle ranges between 23.20 and 53 µm. Under the SEM examination, it is found that a lot of cracks are formed on the surface (Fig. 4a) which might be formed due to sudden cooling of the specimen after the plasma spray was done because the temperature of the plasma spray is around 2000 °C which alters the surface characteristics of the coated specimen. The porosity is also observed on the surface in the order of 2–4 microns (Fig. 4b) which is very small. Also, less amount of oxide formation is observed on the zirconium oxide-coated surface (Fig. 4c).
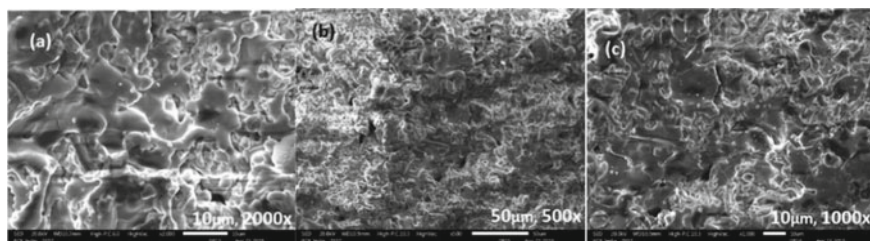
Fig. 4 SEM micrographs of specimen with ZrO_2 coating
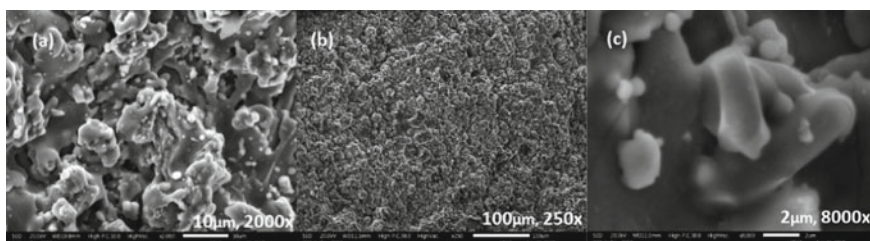
Fig. 5 SEM micrographs of specimen with Cr_2O_3 coating

3.4 Surface Morphology of Cr_2O_3-coated Specimen

The chromium oxide coating is deposited at 20 kV and a high vacuum on LM13 alloy. The size of the powder particle ranges between 23.20 and 53 µm. Under the SEM examination, it is observed that the coated surface has a uniform pore size (Fig. 5a). Fine grains of coating are seen which look like dimple structure (Fig. 5b). The minimum amount of cracks is visible on the surface which directs that the strength of the coating is better in comparison with aluminium–titanium oxide coating and zirconium coating. Oxide formation results in the range of 1–2 microns (Fig. 5c).

3.5 EDX Analysis of Uncoated Specimen

The elemental composition of the substrate material is carried out by the technique of energy dispersive X-ray or EDX analysis. The data produced by EDX analysis consist of spectra showing peaks equivalent to the elements making up the exact composition of the sample under consideration (Fig. 6).

Highest peak of EDX graph visibly states the dominating percentage of aluminium in the substrate material. The percentage of carbon is also appreciable in the aluminium alloy seen as the first peak of the graph. The quantity of silicon present is one of the differentiating factors among the grades of aluminium alloys. In the case of LM13, it is found to be 5.59 wt. % .
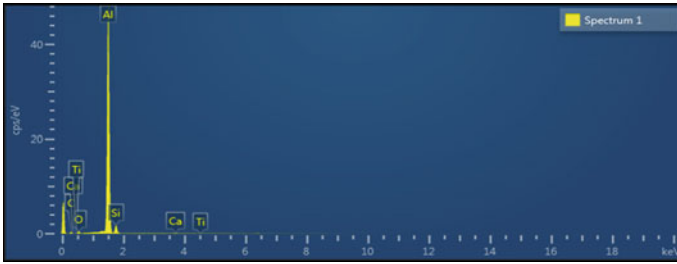
Fig. 6 EDX analysis graph of the uncoated specimen
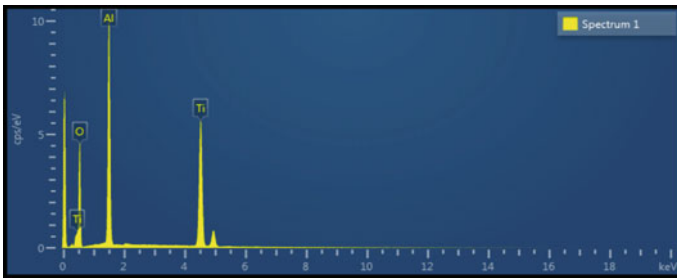
Fig. 7 EDX analysis graph of the Al_2TiO_5-coated specimen

3.6   EDX Analysis of Al_2TiO_5 Specimen

The highest peak corresponds to the aluminium and points to 16.97 atomic %. The presence of oxygen appears more important corresponding to 71.14 atomic %. Titanium peaks are also scattered and can be seen varying from short to middle range peaks. The weight % of titanium in the inspected sample is found to be around 26.28 weight % (Fig. 7).

3.7   EDX Analysis of ZrO_2 Specimen

The highest signals from Zr were detected in this sample, but the smallest peaks also correspond to Zr depending upon the concentration of Zr on the testing surface. Oxygen composition matches to about 40.67 weight % in the entire composition of the coated ceramic. Although some impurities were also found that they are unaccountable in comparison with the major elemental compositions of the ceramic coating (Fig. 8).
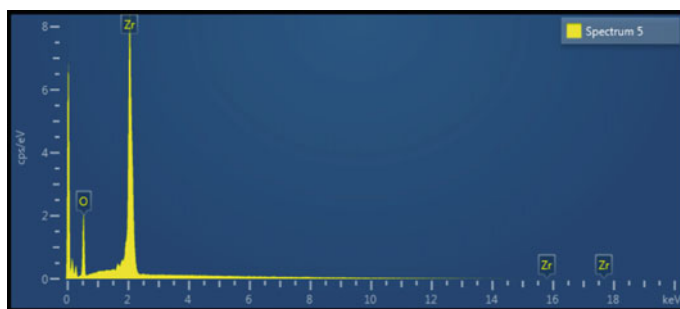
Fig. 8 EDX analysis graph of the ZrO_2-coated specimen
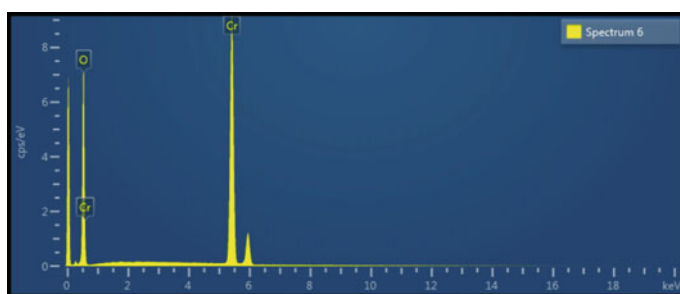
Fig. 9 EDX analysis graph of the Cr_2O_3-coated specimen

3.8 EDX Analysis of Cr_2O_3 Specimen

The analysed specimen is rich in chromium accounting to about 71.20 weight % in the composition of the coated ceramic. Cr peaks were also the smallest ones but clear. Another major constituent of the coating, i.e. oxygen also appears with long-range peaks in the analysis contributing to about 56.80 atomic % in the composition of the ceramic. Small peaks of impurities were neglected (Fig. 9).

3.9 Hardness Studies

The hardness test of the coated and uncoated specimens was carried out at Narang Metallurgical & Spectro Services, New Delhi, India. About two or more observations were considered on the respective sample, and the mean value is stated as a data point.

The hardness of the uncoated sample was found to be 73 Hardness Rockwell B (HRB) during the hardness test on the surface of the LM13 Aluminium alloy. This test was carried out without any surface modification and coating. The surface morphology is not changed at this point. Al_2TiO_5 when tested for hardness gives the
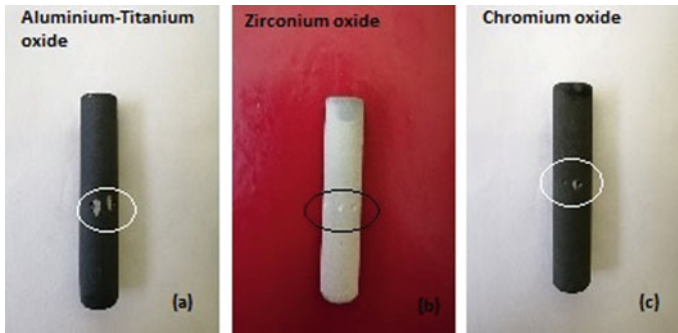
Fig. 10 Encircled areas showing the indented regions on the coated specimens used for hardness test

value of 43–44 HRB. The coated surface showed cracks and porosity, thereby making the material brittle which in turn decreases the hardness of the sample coated with aluminium–titanium oxide. From the hardness test, it is evident that if the material is coated with aluminium–titanium oxide coating, then it will result in fracture soon under a small amount of load when working in aggressive conditions like a cylinder of internal combustion engines. The value 43–44 HRB is not by the uncoated sample, and thus, it decreases its hardness (Fig. 10).

The hardness value of samples coated with zirconium oxide falls in the range of uncoated sample, i.e. 73–74 HRB, thus not proving to be efficient for the surface modification of the LM13 alloy. A lot of cracks and small size of pores make the material a little brittle and thus not suitable to be coated for surface modification of the aluminium alloy. The hardness test shows that if the load unbearable to its limit will be applied, then it will fail very soon, and the purpose of coating will also fail. The hardness value of the sample coated with chromium oxide fits with the hardness analysis when compared between the three samples. The hardness value of the chromium oxide-coated sample is found to be in the range of 79–80 HRB. This value of hardness shows that the hardness of the Aluminium alloy LM13 is increased when it is coated with chromium oxide coating by plasma spray technique. In this investigation, it is found that the surface modification of Aluminium alloy LM13 shows variations as per the different coatings sprayed onto it. In the surface morphology, examination of the sample coated with aluminium–titanium oxide porosity on the coated surface is observed which is found in the order of 1–6 microns. Cracks are also visible which might be formed due to sudden cooling of the specimen after the plasma spray. The occurrence of the cracks on the coated surface is the evidence that the material after the coating has turned brittle and can lead to fracture, and thereby, its hardness decreases to a non-considerable value of 43–44 HRB and making the coated material unfit for further usage in the coating. In specimen coated with zirconium oxide, it is found that a lot of cracks are formed on the surface. The porosity is also observed on the surface in the order of 2–4 microns which is very small. Also, less amount of oxide formation is observed on the zirconium oxide-coated surface.

The zirconium oxide coating does not affect the hardness of the LM13 alloy appreciably and also did not find its application as a coating material to be used on LM13 alloy. Chromium oxide-coated material shows that the coated surface has a uniform pore size. Fine grains of coating are seen which look like dimple structure. Oxide formation results in the range of 1–2 microns. This results in the increased hardness of the material which is in the range of 79–80 HRB and found to be suitable as a coating material for Aluminium alloy LM13.

4   Conclusions

Following conclusions are drawn from present study:

1. Al_2TiO_5, ZrO_2, and Cr_2O_3 coatings can be coated for the surface modification purpose, but the substrate material should be suitable for the coating.
2. Such coatings certainly have budding coating characteristics namely good adhesion strength, porosity, hardness, etc.
3. Coatings microstructure moreover depends upon the physical properties such as hardness and phase transformations during spraying at altered power levels.
4. SEM images reveal the thickness of the coated ceramic ranging between 200 and 250 microns and the particle size to be in range of 23–55 microns.
5. Coatings developed are much harder and also weaker than substrate metals on which they are deposited. Hence, only chromium oxide-coated material can be recommended for tribological applications.
6. Sudden cooling of the coated specimen after plasma spraying results in the formation of cracks on the surface of the coated specimen, and also, it is irrespective of the coating material.
7. Chromium oxide coating hardness increases when it is sprayed via a plasma spray technique and is suitable for coating applications.
8. Some amount of oxide formation is also observed on the surface of all the coated specimens which is expected to be unavoidable.

References

1. https://www.eaa.net/downloads/auto.pdf—Aluminium in Automotive Industry, European Aluminium Association, Brochure.
2. Barbezat, G.: Advanced thermal spray technology and coating for lightweight engine blocks for the automotive industry. Surf. Coat. Technol. **200**(5–6), 1990–1993 (2005)
3. http//www.autoaluminum.org/engines.htm
4. Barbezat, G., Keller, S., Wegner, K.H.: Rotaplasma application in the automotive industry. ITSC 95, Kobe, 1995 Proceeding, pp. 9–13
5. Mc. Cune, Weld. J. (August 1, 1995) 41.
6. Rao, V.D.N., Kabat, D.M., Rose, R., Leong, D.Y.: Proceeding SAE Conference, Detroit, March (1997)

7. Byrnes, M.: Kramer, p. 39. Proceeding NTSC, Boston (1994)
8. G. Barbezat, G. Wuest, Surf. Eng., Lond. **14**(2) (1998) 113.
9. Rao, D.M., V.D.N., Cikaneth, H.A., Wuest, G.: Proceeding SAE Conference, Detroit, (March 1997)
10. Barbezat, G., Schmid, J.: Plasma spray coating and subsequent honing of cylinder bores. MTZ, Mot.tech. Z. **62**(4), 314 (2001)
11. Barbezat, G.: Int. J. Automot. Technol. **2**, 47 (2001)
12. Barbezat, G.: Proceeding, ITSC (2003) 139 Orlando
13. Byrnes, L., Kramer, M.: Proceeding 6th Natl Thermal Spray Conference, Boston, MA, USA, June 1994, ASM International.
14. Barbezat, G., Keller, S., Wegner, K.H.: Proceeding ITSC '95, Kobe, J pan, May 1995, ASM International Thermal Spray Society, 9–13
15. Barbezat, G.: Schweissen Schneiden **48**, 127–131 (1996)
16. Barbezat, G., Keller, S. Wegner, K.H.: Proceeding '96, Essen, Germany, March 1996, DVS, German Welding Society, pp. 114–117
17. Wuest, G., Barbezat, G., Keller, S.: Proceeding SAE International Congress, Detroit, MI, USA, February 1997, SAE International, 97–0016

Lean Implementation Barriers in Indian MSMEs: An Interpretive Structural Modeling

Waseem Akhtar [ID]**, Bhim Singh, and Vineet Kumar**

1 Introduction

Lean manufacturing (LM) is a creative style of manufacturing that always concern about improving manufacturing efficiency by eliminating the muda from entire value stream. The idea of LM was supervised by a Japanese organization "Toyota" during Second World War, which was famous as lean manufacturing. But lean manufacturing is not restricted to the automobile industries; as a substitute of that other sectors such as process, service, building, medical science, have also implemented LM and benefited from that philosophy [2]. It focuses on working with lower inventory, eliminating defects, and make products only when the customer needs it. LM philosophy highlighted the value-added and non-value-added activities in that organization. On the other hand, LM emphasizes on the removal of non-value-added activities [3, 4]. The key principle of lean manufacturing is to assist the organization to provide cheapest and high-quality products to the end customer [5]. The main principle of LM is to support the organization to provide low-cost and high-quality products to the end customer [5].

MSMEs are considered as the backbone of emerging economies, and these industries are significantly contributed to developing employment [6, 7]. According to [8] the implementation of Lean–Kaizen, it eliminates the waste, variation inside the procedure, achieves customer pleasure and zero defects products, and reduces production time, and Lean–Kaizen tool reduces the rejection price of 1250/rupees per day.

Nowadays, the Indian MSMEs are facing various challenges associated with productivity, quality, customer need fulfillment, inventory, waste, and delivery. As we know, the large industries successfully implemented LM, by the motivation of that, MSMEs also started adopting lean manufacturing. Even with the inspiring situations,

W. Akhtar (✉) · B. Singh · V. Kumar
Department of Mechanical Engineering, SET, Sharda University, Greater Noida 201310, India
e-mail: waseemalig20@yahoo.com

MSMEs endure to meeting barriers that hinder from the executing LM. According to [9], only 10% of the organization has successfully implemented lean manufacturing.

In the present study, an effort has been examined on the LM implementation barriers for the Indian MSMEs and to structure a hierarchical model that displays the interrelationship between the LM barriers. The on-hand study has the objective as follows:

1. To identify the barriers/challenges associated with LM implementation in Indian MSMEs.
2. To find the relationship between the identified barriers/challenges.
3. To develop the ISM model on the basis of their relationship.

2 Literature Review

However, the organization realized that the LM is a suitable system in getting improvement in productivity, improvement in quality, minimization in inventory ration, it is also capable of decreasing the lead time, and it eliminates the waste from the entire value stream [10]. Absence of implementation strategy and absence of knowledge about the lean philosophy may also restrict the implementation of LM [11]. According to [12], there are various noticeable and untouchable benefits of LM implementation. Only a few parts of work focused on other imperative variable such as barriers of LM implementation in the Indian MSMEs, performance improvement initiatives [13].

A few authors have studied on examination of LM implementation barriers in the Indian MSMEs. Hu et al. [14] argued that lean implementation barriers for the large-scale industries differ from the lean implementation barriers from the SMEs. In a study, there are 20 barriers are identified in the Indian industries context, namely absence of knowledge, and absence of top management commitment has identified main barriers [15]. According to [16], absence of commitment from top management is the main barrier of LM implementation. The features of MSMEs are unlike from large industries; so it is probable that the LM implementation barriers are also different [17]. Furthermore, SMEs typically hire the staff with imperfect skills and frequently regard training as a blessing [18], but LM needs a great level of skill and exercise. Commitment and authorization of employees are also a key point in the lean driving [19]. According to [20], there is a lack of financial support to SMEs, which is shown as a biggest restriction in the implementation of lean philosophy. LM also requires an effective and transparent communication at all levels in the organization [19, 21]. Value stream mapping (VSM) is the most prominent gears in LM, and by the help of VSM, the lead time, processing time and WIP inventory have been significantly reduced in an Indian industry [22]. After reviewing the literature, a set of lean implementation barriers has been identified as shown in Table 4.

2.1 Micro, Small, and Medium Enterprises

MSMEs play crucial character in the advancement of the economics in the developing and developed countries across the world. MSMEs serve as the basic training for entrepreneurship and innovation in India. Nowadays, MSMEs have become the heart of the industrial revolution in India. During deep study about MSMEs, it examined that 55% of the employees are found in the urban cities and 45% of the employees are found in the rural areas [24]. MSMEs are governed under the MSMEs Act 2006, and the key role of this act is to promote and advance the competitiveness of MSMEs and facilitate the overall development of the MSMEs sector in the country and identify all related issue to MSMEs sectors. The Ministry of MSMEs has classified the MSMEs on the basis of three categories (Tables 1, 2, 3 and 4).

Table 1 Based on manufacturing sector classification

Enterprises	Investment in manufacturing sector
Micro enterprises	Funding is fewer more than 25 lakhs INR
Small enterprises	Funding is above 25 lakh and fewer than 5 crore INR
Medium enterprises	Funding is above 5 crore but fewer than 10 crore INR

Table 2 Based on service sector classification

Enterprises	Investment in services sector
Micro enterprises	Funding is fewer than 10 lakhs INR
Small enterprises	Funding is above 10 lakhs but fewer than 2 crore INR
Medium enterprises	Funding is above 2 crore and below5 crore INR

Table 3 Based on turnover of the organization

Enterprises	Turnover from the industries
Micro enterprises	If the turnover of the industries is up to 5 crore INR
Small enterprises	If the turnover of the industries is more than 5 crore but less than 75 crore INR
Medium enterprises	If the turnover of the industries is more than 75 core but less than 150 crore INR

Table 4 Lean manufacturing implementation barriers

Barriers	References/sources
Scarcity of financial resources	[25, 18, 10, 6]
Poor pledge and support from top administration	[14, 10, 19]
Deficiency of technical knowledge	[8]
Workers resistance to change	[8, 26, 13]
Absence of planning	[2]
Absence of training and skills	[6, 12, 14, 18, 13]
Organizational culture	[9, 10, 14, 13]
Deficiency of effective and transparent communication	[19, 10, 14]
Absence of employees involvement	[10, 19, 16, 8]
Lack of supplier involvement	[10]
Difference of opinion about lean manufacturing	[8, 13]
Absence of resources to implement lean manufacturing	[24, 22]
Absence of implementation know-how	[16, 10]

3   Research Methodology

The goal of on-study is to examine the lean implementation barriers in relation to the Indian MSMEs and to explain the relationship among the identify barriers and to structure a hierarchical model among them. These barriers are examined for the interrelationship with other barriers of LM implementation in the Indian MSMEs. Informative structural modeling (ISM) is used in the study. Thirteen barriers are considered for this study.

In the second stage, the available works of literature are arranged in useful references, the concept of LM, barriers, MSMEs, and ISM methodology were reviewed from the materials. The background of LM with its mechanism, principle, and its implementation barriers was studied (Fig. 1).

4   Interpretive Structural Modeling (ISM)

ISM method is used for recognizing and analyzing interrelationship between one variable to another which affects the system under study [27]. This methodology was developed by [27]. ISM methodology provides the hierarchal level of the variable in order of their driving and dependent power. The most important benefit of ISM is to decide if variables are interrelated or not, and if yes, then how they are related it identifies. There are following steps that are involved in this methodology:

1.   Barriers of LM implementation in the Indian MSMEs are examined.
2.   Evaluate the couple of relationship among the barriers.
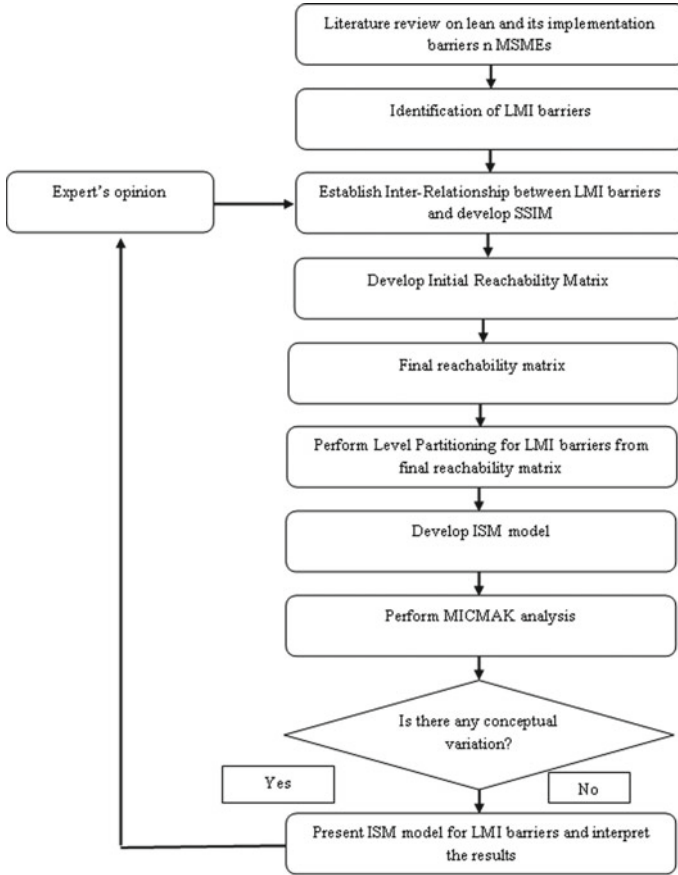
Fig. 1 Research methodology

3. Evaluate structural self-interaction matrix for the barriers.
4. Develop initial reachability matrix by the entry of P, Q, R, and S, then checked for the transitivity, and final matrix is derived. "Here V is replaced by P, A is replaced by Q, X is replaced by R, ad O is replaced by S".
5. Separating the final reachability matrix into different level.
6. Drawing a directed diagram on the basis of final reachability and eliminating the transitivity link in the diagram.
7. Translate the resulted diagram into ISM model.
8. Check the developed ISM diagram for conceptual inconsistency and applying essential change (Table 5).

Table 5 Structural self-interaction matrix (SSIM)

	13	12	11	10	9	8	7	6	5	4	3	2
1	P	P	Q	P	P	P	Q	P	P	P	Q	Q
2	P	P	P	P	P	P	P	P	P	P	P	–
3	R	P	Q	P	S	P	Q	P	P	P	–	
4	R	V	Q	P	S	P	Q	P	P	–		
5	P	V	R	P	P	P	R	P	–			
6	P	V	S	P	P	P	R	–				
7	Q	Q	Q	Q	Q	Q	–					
8	Q	P	Q	Q	Q	–						
9	Q	P	Q	Q	–							
10	P	Q	R	–								
11	Q	P	–									
12	S											

4.1 Initial Reachability Matrix

Binary matrix is the formulation basis of self-interaction matrix (SSIM), by replacing P, Q, R, S with 1 and 0 with respect to ISM rules.

1. Reachability matrix of the (j, i) entrance becomes 0, when the (i, j) entrance in SSIM is P and the (i, j) entrance in reachability matrix is 1.
2. Reachability matrix of the (j, i) entrance becomes 1, when the (i, j) entrance in SSIM is Q and (i, j) entrance in reachability matrix is 0.
3. Reachability matrix of the (j, i) becomes 1, when the (i, j) entrance in SSIM is R and (i, j) entrance in reachability is 1.
4. Reachability matrix of the (j, i) becomes 0, when the (i, j) entrance in SSIM is S and (i, j) entrance in reachability is 0.

From Table 6, it is clear that there is no issue of transitivity found in the initial reachability matrix. So, the initial reachability matrix could be accepted as the final reachability matrix (FRM). Value of each row is known as driving power, and value of each column is known as dependent power.

4.2 Level Partitioning

On the basis of FRM, the reachability and antecedent set for each variable are created. The reachability sets (all one in row of Table 6) and antecedent set (all one in columns of Table 6) were found for each variable. The variable of which reachability and interaction set are matched is given the highest-level variable in the ISM structure. When the highest-level barrier is assigned, it will be removed from the remaining

Table 6 Initial reachability matrix (IRM) (it is accepted as final reachability matrix)

Barriers	13	12	11	10	9	8	7	6	5	4	3	2	1	Driving power
1	1	1	0	1	1	1	0	1	1	1	0	0	1	9
2	1	1	1	1	1	1	1	1	1	1	1	1	1	13
3	1	1	0	1	0	1	0	1	1	1	0	0	1	8
4	1	1	0	1	0	1	1	1	1	1	0	0	1	9
5	1	1	1	1	1	1	1	1	1	1	0	1	1	12
6	1	1	0	1	1	1	1	1	1	1	1	0	1	11
7	0	0	0	0	0	0	0	0	0	1	0	0	0	1
8	0	1	0	0	0	0	0	0	1	1	0	0	0	3
9	0	1	0	0	0	1	0	1	0	1	0	0	0	4
10	1	1	1	1	1	1	1	1	1	1	1	1	1	13
11	0	1	0	0	0	1	0	1	0	1	0	1	0	5
12	0	1	0	1	1	0	0	1	1	1	0	0	0	6
13	0	1	0	1	0	1	0	1	1	1	0	0	0	6
Dependence power	7	12	3	9	6	10	5	11	10	13	3	4	7	100/100

challenges. Reachability sets, antecedent sets, and interaction sets and the final level partition for each barrier are shown in Tables 6, 7 and 8.

4.3 MICMAC Analysis

For analyzing the driving and dependent power of each barrier, MICMAC analysis is used. In MICMAC analysis, the barriers are divided into four sections based on their driving and dependent power shown in Fig. 2. The first section is called autonomous section, and it consists of the barriers having the lowest driving and lowest dependent power. The second section is called dependent section, and it consists of the barriers having the lowest driving power and having the highest dependent power. The third section is called linkage section, and it consists of the barriers having strong driving and dependent power, and the last cluster is called independent section, it consists of the barrier having strong driving power but the lowest dependent power. In this study, it finds that the first, second, and third barriers are the key barriers as shown in Fig. 3. In Fig. 3, lean barriers were classified into four sections as follows: First section, independent barriers which carry: 1, 2, and 3. Second section, linkage barriers: 4, 5, 6, and 10. Third section: dependent barriers: 8, 12, and 13. Fourth section: autonomous section: 7, 9, and 11.

Table 7 Iteration 1

Barriers	Reachability set	Antecedent set	Interaction set	Level
1	1, 4, 5, 6, 8, 9, 10, 12, 13	1, 2, 3, 4, 5, 6, 10	1, 4, 5, 6, 10	
2	1, 2, 3, 4, 5, 6, 7, 8, 9, 10, 11, 12, 3	2, 5, 10	2, 5, 10	
3	1, 4, 5, 6, 8, 10, 12, 13	2, 6, 10	6, 10	
4	1, 4, 5, 6, 8, 10, 12, 13	1, 2, 3, 4, 5, 6, 7, 8, 9, 10, 11, 12, 13	1, 4, 5, 6, 8, 10, 12, 13	I
5	1, 2, 4, 5, 6, 7, 8, 9, 10, 11, 12, 13	1, 2, 3, 4, 5, 6, 10, 12, 13	1, 2, 4, 5, 6, 10, 12, 13	
6	1, 3, 4, 5, 6, 7, 8, 9, 10, 12, 13	1, 2, 3, 4, 5, 6, 9, 10, 11, 12, 13	1, 3, 4, 5, 6, 9, 10, 12, 13	
7	4	2, 4, 5, 6, 10	4	I
8	4, 5, 12	1, 2, 3, 4, 5, 6, 9, 10, 11, 13	4, 5,	
9	4, 6, 8, 12	1, 2, 5, 6, 10, 12	6, 12	
10	1, 2, 3, 4, 5, 6, 7, 8, 9, 10, 11, 12, 13	1, 2, 3, 4, 5, 6, 10, 12, 13	1, 2, 3, 4, 5, 6, 10, 12, 13	
11	2, 4, 6, 8, 12	2, 5, 10	2	
12	4, 5, 6, 7, 9, 10, 12	1, 2, 3, 4, 5, 6, 8, 9, 10, 11, 12, 13	4, 5, 6, 9, 10, 12	
13	4, 5, 6, 8, 10, 12	1, 2, 3, 4, 5, 6, 10	4, 5, 6, 10	

Table 8 Final level partitioning

Barriers	Reachability set	Antecedent set	Interaction set	Level
1	1, 5, 10	1, 2, 3, 5, 10	1, 5, 10	V
2	2, 3, 5, 10	2, 5, 10	2, 5, 10	VII
3	5, 10	2, 10	10	VI
4	1, 4, 5, 6, 8, 10, 12, 13	1, 2, 3, 4, 5, 6, 7, 8, 9, 10, 11, 12, 13	1, 4, 5, 6, 8, 10, 12, 13	I
5	2, 5, 10	2, 3, 5, 10	2, 5, 10	VI
6	1, 3, 5, 7, 10, 13	1, 2, 3, 5, 10, 11	1, 3, 5, 6,9, 10, 13	IV
7	4	2, 4, , 5, 6, 10	4	I
8	5	1, 2, 3, 5, 6, 9, 10, 11, 13	5	III
9	6	1, 2, 5, 6, 10	6	IV
10	2, 3, 5, 10	2, 3, 5, 10	2, 3, 5, 10	VI
11	2	2, 5, 10	2	V
12	5, 6, 9, 10	1, 2, 3, 5, 6, 9, 10, 11, 13	5, 6, 9, 10	II
13	5, 6, 10	1, 2, 3, 5, 6, 10	5, 6, 10	IV
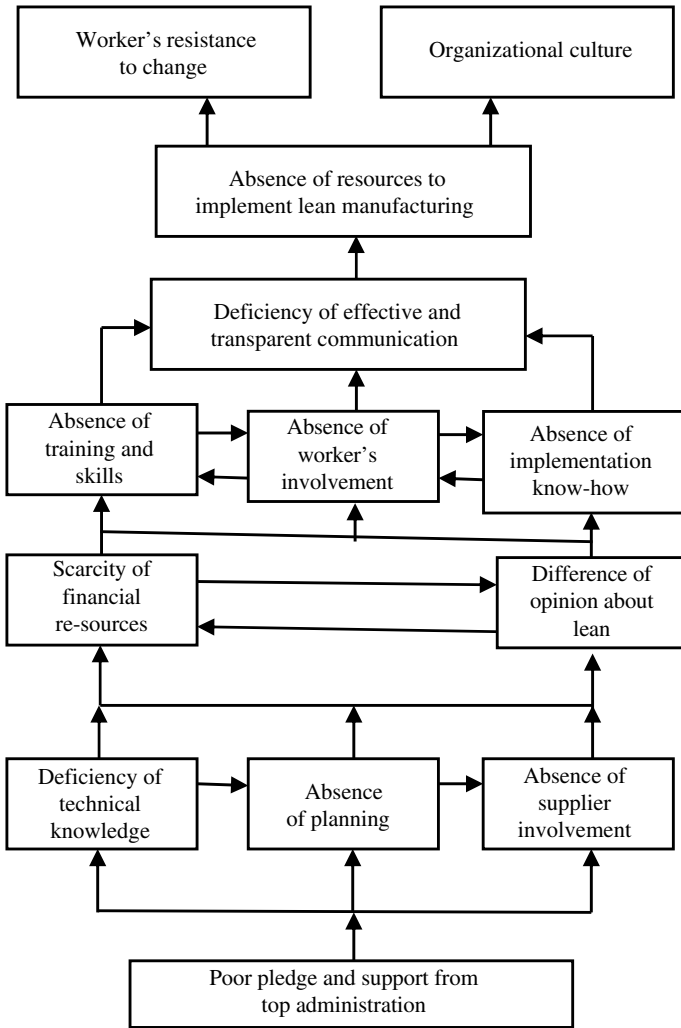
Fig. 2 ISM model

5 Discussion

After having gone through rigorous literature review, thirteen barriers of lean implementation in the Indian MSMEs are identified. The structural graph obtained with the application of ISM methodology gives a platform to explore the interactions among the barriers. ISM graph explains that the lean barriers in the Indian MSMEs can be prioritized into four main groups as follows:

First, independent barriers include poor commitment and support from top management, deficiency of technical knowledge, and scarcity of financial resources.
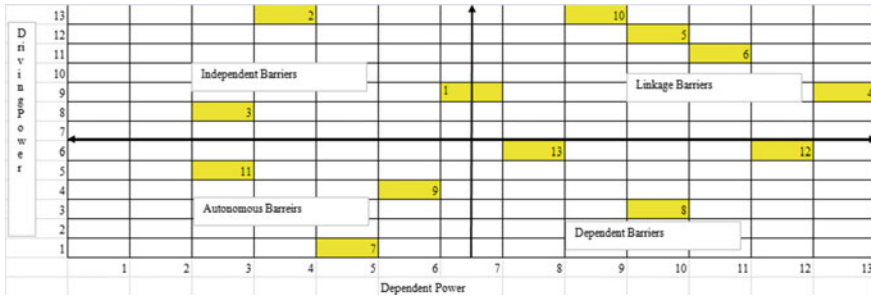
Fig. 3 MICMAC diagram

These proved to be the strongest barriers of lean implementation, and these need maximum attention concerning other barriers. The second, linkage barriers which carry employee's resistance to change, absence of planning, absence of training and skills, and absence of supplier involvement, followed by the third, dependent barriers consist lack of effective and transparent communication, absence of resources to implement lean, and absence of employee's know-how need moderate attention. Dependent barriers are driven by the remaining three groups. Fourth, autonomous barriers which are organizational culture, absence of worker involvement, and differences of opinion about LM are shown to be in the middle of the model. Poor pledges from top administration, lack of knowledge, and deficiency of effective and transparent communication have been proved to be the key obstacles in the implementation of LM in the Indian MSMEs.

6 Conclusion

It has been found that MSMEs are still not able to enjoy the full benefits of LM due to many impediments that need immediate attention of practitioners and professionals working there. This paper is a piece of research, which will guide them to identify, prioritize, and eliminate the lean implementation barriers. An effort has been made to identify these impediments from the extant literature. ISM and MICMAC analyses are used for emphasizing and prioritizing the lean barriers in the Indian MSMEs. The most critical barriers of lean implementation in the Indian MSMEs are poor pledge and lack of support from top administration, deficiency of technical knowledge, and scarcity of financial resources which are the main hindrance in the process of lean implementation. If practitioners, researchers, and professionals put their effort to mitigate the effect of LM barriers, then the Indian MSMEs will have much more to contribute to the Indian economy. This paper provides an initial finding, and more research needs to be in context to the Indian MSMEs.

References

1. Bhasin, S., Burcher, P.: Lean viewed as a philosophy. J. Manuf. Technol. Manag. **17**, 56–72 (2006). https://doi.org/10.1108/17410380610639506
2. Bhamu, J., Sangwan, K.S.: Lean manufacturing: Literature review and research issues. Int. J. Oper. Prod. Manag. **34**, 876–940 (2014). https://doi.org/10.1108/IJOPM-08-2012-0315
3. Deif, A.: Assessing lean systems using variability mapping. Procedia CIRP **3**, 2–7 (2012). https://doi.org/10.1016/j.procir.2012.07.002
4. Shah, R., Ward, P.T.: Defining and developing measures of lean production. J. Oper. Manag. **25**, 785–805 (2007). https://doi.org/10.1016/j.jom.2007.01.019
5. Bhasin, S.: An appropriate change strategy for lean success. Manag. Decis. **50**, 439–458 (2012). https://doi.org/10.1108/00251741211216223
6. Dhingra, A.K., Kumar, S., Singh, B.: Cost reduction and quality improvement through Lean-Kaizen concept using value stream map in Indian manufacturing firms. Int. J. Syst. Assur. Eng. Manag. **10**, 792–800 (2019). https://doi.org/10.1007/s13198-019-00810-z
7. Chaple, A.P., Narkhede, B.E., Akarte, M.M., Raut, R.: Modeling the lean barriers for successful lean implementation: TISM approach. Int. J. Lean. Six Sigma. (2018). https://doi.org/10.1108/IJLSS-10-2016-0063
8. Powell, D., Riezebos, J., Strandhagen, J.O.: Lean production and ERP systems in small- and medium-sized enterprises: ERP support for pull production. Int. J. Prod. Res. **51**, 395–409 (2013). https://doi.org/10.1080/00207543.2011.645954
9. Authors F.: Benchmarking: An International Journal (2017)
10. Jagdish, R.J., Shankar, S.M., Santosh, B.R.: Exploring barriers in lean implementation. Int. J. Lean Six Sigma **5**, 122–148 (2014). https://doi.org/10.1108/IJLSS-12-2012-0014Permanent
11. Singh, B., Garg, S.K., Sharma, S.K., Grewal, C.: Lean implementation and its benefits to production industry. Int. J. Lean Six Sigma **1**, 157–168 (2010). https://doi.org/10.1108/20401461011049520
12. Mazzocato, P., Holden, R.J., Brommels, M., et al.: How does lean work in emergency care? A case study of a lean-inspired intervention at the Astrid Lindgren Children's hospital, Stockholm, Sweden. BMC Health Serv Res **12**. https://doi.org/10.1186/1472-6963-12-28 (2012)
13. Almeida Marodin, G., Saurin, T.A.: Managing barriers to lean production implementation: context matters. Int. J. Prod. Res. **53**, 3947–3962 (2015). https://doi.org/10.1080/00207543.2014.980454
14. Hu, Q., Mason, R., Williams, S.J., Found, P.: Lean implementation within SMEs: a literature review. J. Manuf. Technol. Manag. **26**, 980–1012 (2015). https://doi.org/10.1108/JMTM-02-2014-0013
15. Achanga, P., Shehab, E., Roy, R., Nelder, G.: Critical success factors for lean implementation within SMEs. J. Manuf. Technol. Manag. **17**, 460–471 (2006). https://doi.org/10.1108/17410380610662889
16. Radnor, Z.J., Holweg, M., Waring, J.: Lean in healthcare: the unfilled promise? Soc. Sci. Med. **74**, 364–371 (2012). https://doi.org/10.1016/j.socscimed.2011.02.011
17. Panwar, A., Nepal, B.P., Jain, R., Rathore, A.P.S.: On the adoption of lean manufacturing principles in process industries. Prod. Plan Control **26**, 564–587 (2015). https://doi.org/10.1080/09537287.2014.936532
18. Jaiswal, P., Kumar, A.: Analyzing barriers of lean manufacturing adoption in Indian SMEs using an integrated approach of grey decision making trial and evaluation laboratory (DEMATEL). Lect. Notes Eng. Comput. Sci. **2224**, 688–691 (2016)
19. Kleszcz, D.: Barriers and opportunities in implementation of Lean Manufacturing tools in the ceramic industry. Prod. Eng. Arch. **19**, 48–52. https://doi.org/10.30657/pea.2018.19.10 (2018)
20. Bajjou, M.S., Chafi, A.: Lean construction implementation in the Moroccan construction industry: awareness, benefits and barriers. J. Eng. Des. Technol. **16**, 533–556 (2018). https://doi.org/10.1108/JEDT-02-2018-0031

21. Panizzolo, R., Garengo, P., Sharma, M.K., Gore, A.: Lean manufacturing in developing countries: evidence from Indian SMEs. Prod. Plan Control **23**, 769–788 (2012). https://doi.org/10.1080/09537287.2011.642155
22. Shrimali, A.K., Soni, V.K.: Barriers to lean implementation in small and Medium-Sized Indian enterprises. Int. J. Mech. Eng. Technol. **8**, 1–9 (2017)
23. Upadhye, N., Deshmukh, S.G., Garg, S.: Lean manufacturing system for medium size manufacturing enterprises: An indian case. Int. J. Manag. Sci. Eng. Manag. **5**, 362–375 (2010). https://doi.org/10.1080/17509653.2010.10671127
24. Anand, G., Kodali, R.: Selection of lean manufacturing systems using the PROMETHEE. J. Model Manag. **3**, 40–70 (2008). https://doi.org/10.1108/17465660810860372
25. Mukherjee, D.: Lean manufacturing and six sigma: challenges for SME' s. Int. J. Eng. Technol. Sci. Res. **4**, 1644–1649 (2017)
26. Gade, S.: MSMEs' Role in Economic growth—a study on India' s perspective introduction: Int. J. Pure Appl. Math. **118**, 1727–1741 (2018)
27. Kumar, R., Kumar, V.: Barriers in implementation of lean manufacturing system in Indian industry: a survey. Int. J. Latest Trends. Eng. Technol. **4**, 243–251 (2014)
28. Singh, B., Sharma, S.: Value stream mapping as a versatile tool for lean implementation: an Indian case study of a manufacturing firm. Meas. Bus Excell. **13**, 58–68 (2009). https://doi.org/10.1108/13683040910984338

Evolution and Future of Sustainable Project Management

Chakshu Malik , **Shahnil Samantara** , **and Ashok Kumar Madan**

1 Introduction

Sustainability is a property that will define the development in all fields of engineering and management in the upcoming years. Contrary to popular belief, sustainability does not mean that only the future should be taken into consideration while making decisions regarding any project. It implies that the current needs of the human population are met in a satisfactory manner without having an impact on the future generations and their ability to be able to fulfill their demands. Therefore, sustainability allows to meet the persisting objective of environmental, communal and commercial success of any project and warrants a good quality of life in the future as well [1].

Project management skills of a project manager and the implementation of sustainable resources and the laws of sustainability implemented in the ongoing and upcoming projects define the success rate of the organization pursuing the project. These resources can vary from equipment to monetary resources and assist in completing a predefined objective within a limited period of time [2]. A popular topic is among the government and private organizations, and there is a rising demand to undertake initiative that would help in the amalgamation of sustainability with management of projects in all fields [3].

Present-day project managers play an important role in the implementation of sustainable project management. They need to possess general management skills along with technical skills that extend past just the realm of their work. A project manager attains his capabilities by acquiring knowledge, developing skills and applying the said knowledge and skills in the real-world situation. Project managers possess two types of skills. First type is a set of specific skills which are applicable directly to the project they are working on, and the second is a set of general skills

C. Malik (✉) · S. Samantara · A. K. Madan
Department of Mechanical Engineering, Delhi Technological University, Delhi 110042, India
e-mail: chakshu.cm@gmail.com

which are skills that can be used on almost any project that the project manager may work on [4].

The triple bottom line approach (TBLA) comprises, as the name suggests, three factors when evaluating the success of a project. It focusses on the environmental, economic and the social aspects of any project. Although this approach was initially used just to help organizations achieve their corporate social responsibility, it has quickly become a way to measure the attainment of sustainable project management. To succeed in this, efforts to practice sustainability during the project need to be made from the very beginning. From the planning of the project to the acquisition of raw material to the final delivery, all need to be done keeping in mind the sustainability factor [5]. The financial, social and environmental aspects, all need to be taken into consideration while coming up with solutions and evaluation criteria that will help in achieving the long-term goal of sustainability [6].

The United Nations is consistently working on the science behind sustainable development. In this paper, we hope to be able to provide information that can help national and local level governments to be able to make significant changes in their governance and implementation of laws so that they are in compliance with the aim of sustainable development as the United Nations proposes. This will ensure even development of countries across the globe by the target year of 2030.

2   Motivation for Research

The main aim of this paper is to recognize the gaps in sustainability in projects undertaken by the Government of India and suggest changes that can be made in order to fill those gaps. This has been done by first reviewing literature to understand what sustainability, project management and the different criteria affecting sustainable project management are. The literature review is followed by a study that compares the different levels of sustainable development goals (SDGs) that have been attained by the Indian Government by an indexing method that is defined later in the paper. Comparison between India and Denmark is done to better understand the exact points where India is lacking in achieving SDGs. Ultimately, suggestions to attain sustainable development goals by 2030 are made, and the importance of integration of sustainability in government projects is defined.

3 Sustainability, Project Management and Sustainability Criteria

3.1 Sustainability

Gro Harlem Brundtland, in 1987, first put forward the concept of sustainability at the World Commission on Environment and Development. She said sustainability or sustainable development can be defined as "development that meets the needs of the present without compromising the ability of the future generations to meet their own needs" [5]. Sustainability can be measured based on various factors such as quality of the product, social factors, financial factors and use of non-renewable resources efficiently which in turn effects the environment [7]. The Brundtland model states that the collaboration of environmental, social and economic factors results in sustainability. A representation of the Brundtland model can be seen in Fig. 1.

In 2002, Giddings put forward another model which is portrayed in Fig. 2. According to him, economic, social and environmental impacts are not unique entities that intersect each other. In fact, they are all interdependent and not one can be removed if sustainability is to persist. Economic factors are usually given the highest priority when defining policies for any project followed by social and environmental factors. Economic factors are usually considered to affect humans the most, and the environmental factors are considered apart from humans. The social factors bridge the gap and interconnect the two. The economy is dependent on the society and the environment, whereas humans and the society are dependent on the environment. When all these factors are considered together, they help in maintaining diversity and sustaining communities [7].

Fig. 1 Visual representation of the Brundtland model
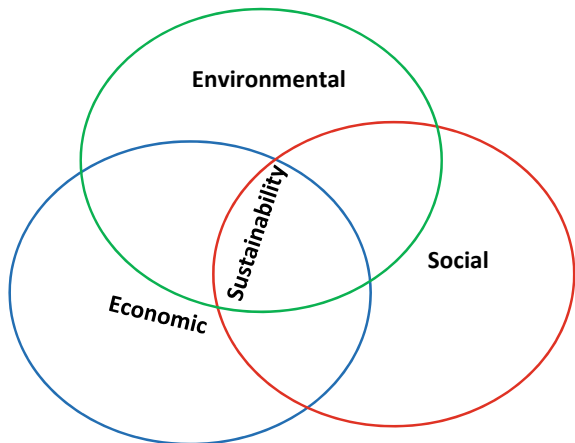
Fig. 2 Visual representation of the Giddings model
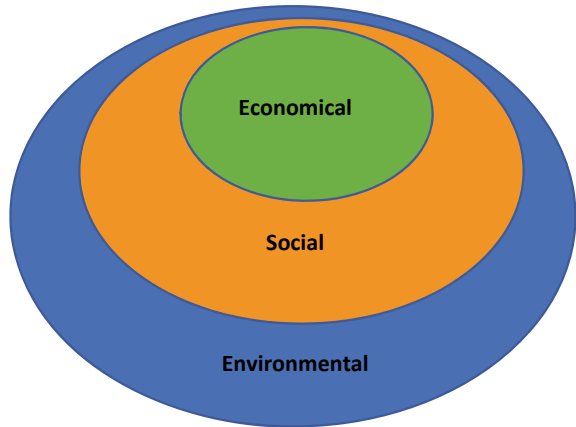
3.2 Application of Sustainability in Project Management

Project management involves meeting predefined goals in a specific period of time by applying skills and knowledge applicable to the project. With the growing demand for renewable resources and renewability in all aspects of industries, it becomes increasingly important for project managers to come up with solutions that will drive their projects toward sustainability. This is applicable to all bits of work, from materials to machinery. Many applications of sustainability in various fields of work can be seen in our daily lives. Table 1 shows a few examples of sustainability measures taken in different projects.

Table 1 Sustainability measures taken by certain organizations

S. No.	Project/organization	Sustainability Measure
1	Delhi Metro (DMRC) [8]	• Optimized energy consumption • Managing greenhouse gas emissions • Sustainable water consumption • Assessment of biodiversity loss and compensatory afforestation • Inventorization and management of waste
2	Hero Motocorp Ltd. [9]	• Lean manufacturing • Replaced oil lamps with 7 W LEDs saving over 30 million units of electricity per annum • Put solar street lights in over 250 villages • Does not use single use plastic in any of its locations
3	Kirloskar [10]	• Pumping energy audit • Environmental compliance while procurement of material
4	Samsung [11]	• Nordic Swan Ecolabel • TCO certification

3.3 Sustainability Criteria

Below are a few factors and their effects on projects and sustainability that can be taken into consideration for project management:

Scheduling

Scheduling is the part of project management where all activities and goals that need to be completed in a project are put together in an orderly manner and planned from the start date to the finish date of the project with duration for each activity clearly assigned. The project scheduling technique is crucial to attain the best performance of each process [12].

Quality

To attain a high-quality product and sustainability simultaneously, an organization needs to keep in mind that any unnecessary processes and excess waste including energy, water, greenhouse gases, machinery and material used are removed from the process altogether. In case there are any fallbacks on the organizations part in terms of quality, they must be willing to come up with feasible solutions to overcome the problem. And lastly, there must be quality checks at each step of the production to make sure there are minimum faults which in turn will ensure that unnecessary production does not need to be done [13].

Cost and Economic Assets

Cost is one of the most important factors that affects any business or manufacturing process. Without economic support, any project would not be possible. Sustainable materials, machines and processes are usually more expensive and require a high capital investment initially. Therefore, the cost of the final product is also high. Despite being so expensive, demand for sustainably produced products is growing fast. The external environment must always be observed in order to allow changes that may affect the cost, trends and risks that come with a project [13]. Sustainable alternatives, especially ones that are around the environmental laws, usually result in a higher capital cost due to the limited availability of the raw material and the complex designs used in implementation of the project [4]. Although high in cost, these designs usually do not need to be replaced or refurbished for long periods and thus result in great return on the investment and have an extremely positive impact on the environment.

Stakeholder Satisfaction

A project manager's biggest task is probably to communicate and keep in touch with the stakeholders. The biggest problem is that there are many stakeholders and all of them have different demands that according to them must be fulfilled. Thus, managing stakeholders is a crucial skill that every project manager must possess since only the demands that are beneficial and feasible during the project can and must be fulfilled [14]. The feasibility, acquisition and review of the project must be performed by both

the manager and the stakeholders together in order to be able to get an innovative solution to the problems that might come up [15]. The stakeholders and the project manager must agree upon a means to assess the sustainability, performance and the feasibility of the project [3].

Performance of Business

The performance of a business can be measured easily by setting goals and defining key performance indicators (KPIs). The goals and the indicators may vary drastically depending upon the project and the field of work. There are two broad ways to measure success: one that checks if the original idea of the project is met and another that checks if the KPIs and the various goals within the project are met successfully [16]. Business models of these projects need to be such that they take into consideration the environmental impact the project might have, the economic funds that the project might need and the social contribution it will make through the profits generated by it or with its final product. The projects must be finished all while taking ethical norms and social values into consideration [6].

Environmental Policies and Resources

An important part of sustainability environment and the policies made to sustain it needs to be implemented in every upcoming project. The products manufactured or the services offered by the business/project need to enhance the environment and be within the defined criteria of environmental protection [17]. The work methods used in the project must be such that the environment does not get affected.

4 Implementation of Sustainability by the Government of India

Implementation of sustainability in project management is the future of every country and organization. Therefore, the government needs to implement laws that make it easier for all government and non-government organizations to integrate sustainability in any project that they take up. To do so, analysis of all the data available through the government needs to be done and segregated based on economic, social and environmental problems. Then, the problems in each individual region need to be recognized and more projects and initiatives related to the respective problems need to be taken up. The projects in must be overseen by respected and accomplished project managers.

4.1 Sustainable Development Goals of India

The data used is from SDG India Index & Dashboard 2019–2020. The graph represents 15 sustainable development goals (SDG) for 2030 proposed by the United Nations on the horizontal axis and the number of states and union territories in India that have achieved the said goals up to various indexing levels. The total number of states/union territories is 36, and the maximum index that a goal can be achieved up to is 100. The index was defined using a five-step method [18].

Method to Calculate the Index

- The process starts with the collection of raw data and forecasting of the missing data based on the already available data.
- The Government of India then sets a judicious target value to achieve by 2030 for each indicator.
- The raw values are then scaled to a score between 0 and 100. The normalization of data is done using the following formulae:

Equation (1) represents indicators that imply higher value means higher performance.

$$y' = \frac{y - \min(y)}{T(y) - \min(y)} \times 100 \tag{1}$$

where

y	raw data value
$\min(y)$	minimum observed value of the indicator in the dataset
$T(y)$	national target value for indicator
y	$'$normalized value after rescaling.

Equation (2) represents indicators which imply higher value means lower performance.

$$y' = \left[1 - \frac{y - \min(y)}{\max(y) - T(y)}\right] \times 100 \tag{2}$$

where $\max(y)$ = maximum observed value of the indicator in the dataset.

Equation (3) represents indicators where increasing value means higher performance.

$$y' = \frac{y - \min(y)}{\max(y) - \min(y)} \times 100 \tag{3}$$

Equation (4) represents indicators where increasing value means lower performance.

$$y = \left[1 - \frac{y - \min(y)}{\max(y) - \min(y)}\right] \times 100 \tag{4}$$

- After scaling, arithmetic mean of the normalized score is calculated to set a goal score for each SDG using the following formula:

$$I_{ij}\left(N_{ij}, I_{ij}\right) = \sum_{k=1}^{N_{ij}} \frac{1}{N_{ij}} I_{ijk} \tag{5}$$

where

I_{ij} goal score for state/UT i under SDG j.
N_{ij} number of non-null indicators for state/UT i under SDG j.
I_{ijk} normalized value for state/UT i of indicator k under SDG j.

- This is followed by averaging all goal scores to get a composite SDG index for India using the following formula:

$$I_i\left(N_i, N_{ij}, I_{ijk}\right) = \frac{1}{N_i} \sum_{j=1}^{N_{ij}} I_{ij}(N_{ij}, I_{ijk}) \tag{6}$$

where

I_i composite SDG index score of state/UT i
N_i no. of goal scores for which a state/UT has non-null data
I_{ij} goal score of state/UT I under SDG j.

Analysis of SDGs of India

From Fig. 3, we can conclude that the government needs to focus the most on projects that benefit social factors such as gender equality and eradication of poverty since most gap in achievement can be seen there. These projects can be focused on providing equal opportunities to both genders in school and workplace. Trends related to pay difference between the gender can be studied by collecting data, and after the analysis of the data, pay grades for both the genders can be normalized. The government is already taking steps to have equality in opportunities to study.

Economic goals such as decent work and economic growth and industry innovation and infrastructure are being worked upon already but can have certain sustainable measures taken to improve them. A suggestion to improve economic factors is to promote sustainable ways to produce all goods within India. Certain sustainable actions that can be taken are to manufacture machinery that will use energy optimally and produce minimal waste. These machines can then be used in production lines.
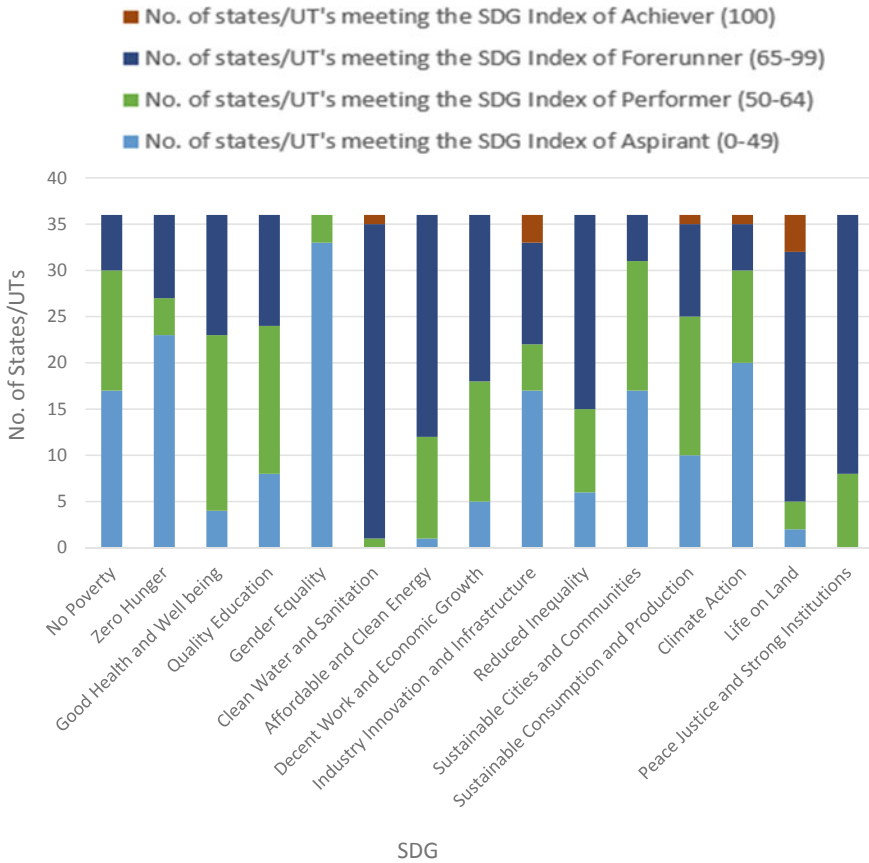
Fig. 3 Graphical representation of various sustainable development goals index met by no. of states/UT's out of the total of 36

The environmental aspect of the SDG's is well in reach of the government. There is considerable work being done on climate action already, and clean water is being provided almost all over India except in Delhi. To maximize the effect of the environmental factors and to achieve the goals surrounding the environment before 2030, campaigns to educate everyone in urban as well as rural areas, about the importance of clean water and energy must be undertaken by the governments at central and state level so that measures to attain these SDGs can be taken up on a personal as well as a community level.
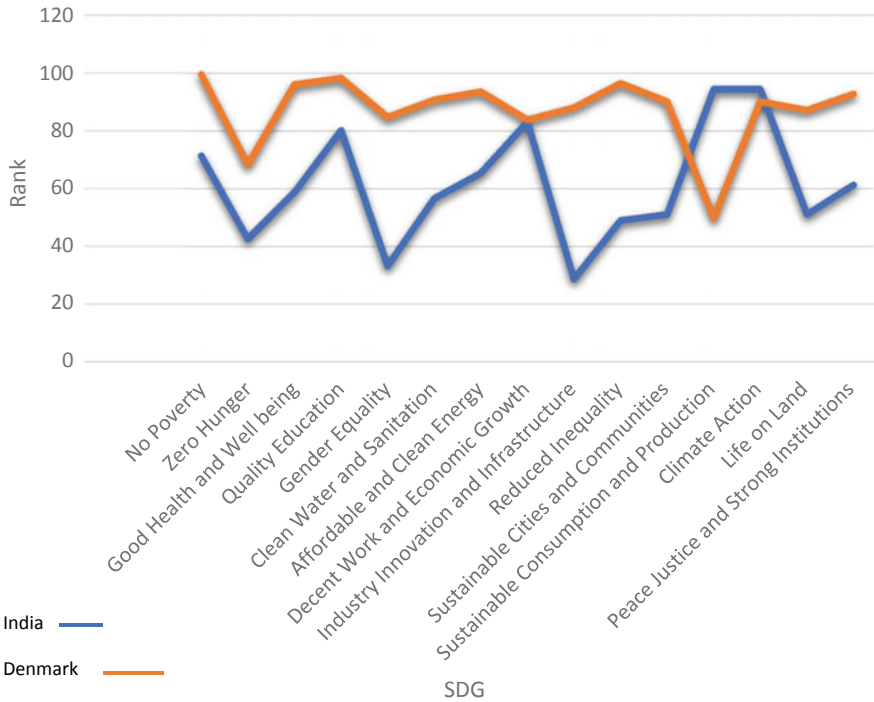
Fig. 4 Graphical comparison of SDG indices achieved by India and Denmark

4.2 Comparison of Sustainable Development Goals

The SDGs of Denmark and India are compared in Fig. 4. The blue line represents the SDGs achieved by India, and the orange line represents the SDGs achieved by Denmark. Denmark was chosen as a means of comparison because according to the United Nations' Sustainable Development Report, Denmark is currently the most sustainable country overall. India ranks at 115 out of the 162 countries for which the data was available [19]. This itself tells us that the Government of India needs to take up more projects that will drive India toward sustainability in all three spheres. From the graph in Fig. 4, we can see that Denmark has a higher index of achievement in all SDGs except sustainable consumption and production and climate actions. We can also conclude from the graph that the educational system, allowance of growth of economy, availability of clean water and energy and equality of all individuals contribute a lot to the sustainability achieved by Denmark. The Government of India can implement policies similar to the ones applied in Denmark to allow a fast, efficient and sustainable growth of the nation. The Government of India must continuously assess how implementing projects in various parts of the country is profitable for the people and the country and makes the required changes based on the feedback. The government should also proactively seek partnerships with private organizations so

that the responsibilities of the government can be divided and thus the work done is of high quality. These steps can help India become a sustainable nation faster and achieve most of its SDGs by 2030.

5 Conclusion and Suggestions

Project management is a part of every industry and requires expertise of project managers who are fluent in technical as well as soft skills. The field of project management requires work to be done in an efficient and effective manner while meeting predefined goals within a set time limit. In this paper, a literature review on how sustainability can be incorporated in various aspects of project management is put together in a concise manner. The literature used to analyze the different parts of project management ranges from 2010 to 2020. It can be seen that the steps taken to implement sustainable project management have been quite similar throughout the decade.

The suggestions given below clearly state that integration of various parts of sustainability is extremely important in order for a country to grow in social, economic and environmental aspects.

- The Government of India must collaborate with private organizations that have expertise in the required fields to make significant changes in a short span of time. By joining forces with multiple private organizations, the government can implement more projects in a shorter span of time. This will also ensure better implementation of the project since these organizations are well equipped to handle any difficulties that might come up during any stage of the project.
- The local governments, while implementing sustainability projects, must involve the people of the community so that they are better aware of the positive consequences that sustainable development can result in.
- Education up till secondary school must be provided free of cost so that it is easily accessible for everyone and people have a better understanding of the importance of pursuing higher education. This will not only result in higher literacy rates, but will also add to the economic growth of the country and reduce gender inequality and poverty.

Sustainability and its implementation in projects that affect India and the world are yet to be exploited to its fullest. The suggestions given above are in alignment with the data represented in Figs. 3 and 4. With new research being done constantly, new ideas and technology can be used to implement sustainability faster than before all the while maintaining the quality of the product and satisfying customers and stakeholders alike.

References

1. Ihuah, P.W., Kakulu, I.I., Eaton, D.: A review of critical project management success factors (CPMSF) for sustainable social housing in Nigeria. Int. J. Sustain. Built Environ. **3**(1), 62–71
2. Mishra, P., Dangayach, G.S., Mittal, M.L.: An ethical approach towards sustainable project Success. Procedia-Soc. Behav. Sci. **25**, 338–344 (2011)
3. Otegi-Olaso, J.R., et al.: Towards sustainable project management. A Lit. Rev. (2015)
4. Hwang, B.-G., Ng, W.J.: Project management knowledge and skills for green construction: overcoming challenges. Int. J. Proj. Manage. **31**(2), 272–284 (2013)
5. Kivilä, J., Martinsuo, M., Vuorinen, L.: Sustainable project management through project control in infrastructure projects. Int. J. Project Manage. **35**(6), 1167–1183 (2017)
6. Chawla, V., et al.: The sustainable project management: a review and future possibilities. J. Project Manage. **3**(3), 157–170 (2018)
7. Giddings, B., Hopwood, B., O'brien, G.: Environment, economy and society: fitting them together into sustainable development. Sustain. Devel. **10**(4), 187–196 (2002)
8. DMRC Sustainability Report, 2015–2016. http://delhimetrorail.com/otherdocuments/Sustainability-Report.pdf. Last accessed 17 May 2020
9. Rathore, H., et al.: Examining the mediating role of innovative capabilities in the interplay between lean processes and sustainable performance. Int. J. Prod. Econ. (2018)
10. Integrated Sustainability Report, Kirloskar, 2015–16. http://www.kirloskarpumps.com/control/content/Pdf_8312016124920PMIntegratedSustainabilityReport2015-16.pdf. Last accessed 17 May 2020
11. Samsung Electronics Sustainability Report (2017). https://images.samsung.com/is/content/samsung/p5/se/innovation/sustainability/sustainability/samsung-sustainability-report-en-V2.pdf. Last accessed 17 May 2020
12. Demeulemeester, E., Kolisch, R., Salo, A.: Project management and scheduling, 1–5 (2013)
13. Jasiulewicz-Kaczmarek, M.: Is sustainable development an issue for quality management? Found. Manage. **6**(2), 51–66 (2014)
14. Li, T.H.Y., Thomas S.N., Skitmore, M.: Evaluating stakeholder satisfaction during public participation in major infrastructure and construction projects: A fuzzy approach. Auto. Constr. **29**, 123–135 (2013)
15. Pade-Khene, C., Mallinson, B., Sewry, D.: Sustainable rural ICT project management practice for developing countries: investigating the Dwesa and RUMEP projects. Inf. Technol. for Dev. **17**(3), 187–212 (2011)
16. Ogunlana, S.O.: Beyond the 'iron triangle': Stakeholder perception of key performance indicators (KPIs) for large-scale public sector development projects. Int. J. Project Manage. **28**(3), 228–236 (2010)
17. Tam, G.: The program management process with sustainability considerations. J. Proj. Prog. Portfolio Manage. **1**(1), 17–27 (2010)
18. SDG India Index and Dashboard. 2019–2020. https://niti.gov.in/sites/default/files/2019-12/SDG-India-Index-2.0_27-Dec.pdf. Last accessed 17 May 2020
19. Sustainable Development Report Dashboard 2019, https://dashboards.sdgindex.org/#/. Last accessed 17 May 2020

Implementation of Blockchain Technology in Supply Chain Management

N. Yuvraj [iD]**, Bharat Bhutani** [iD]**, Krishna Lohiya** [iD]**, and Shikhar Mittal** [iD]

1 Introduction

Blockchain technology is the one of the most innovative technologies developed in the recent years. It has been accepted widely. While the current data follows the CRUD (Create-Read-Update-Delete) methodology, in blockchain, data is instead decentralized, i.e., rather than storing the data centrally, it stores data across its peer-to-peer network thereby eliminating the risk which comes along with storing data centrally, instead of being manipulated the data it appended (joined at the end). Supply chain management on the other hand includes all the activities involved from the time of procuring the raw material to the time the finished goods are produced, along with that it also includes the flow of these finished products from the point of manufacture to the end customer. Integration of blockchain technology and supply chain management is a topic gaining increased momentum in the recent years. Various applications of the combination of blockchain technology with supply chain management have been addressed in different industries, such as in the food, the shipping industry, the healthcare industry (e.g., [1, 4, 7]) and many more have attracted attention; hence, it is prominent that blockchain has various applications in supply chain management. Thus, the primary purpose of this research is to focus on blockchain and supply chain management integration and to study how blockchain technology can improve the efficiency of supply chain management.

The rest of this research paper is organized as, we will start by introducing some basic concepts of supply chain management and blockchain technology in Sect. 2. Section 3 describes the research methodology. Section 4 analyzes the case of OPaL plant in Dahej, Gujarat. Section 5 includes the conclusion, limitations and findings followed by references.

N. Yuvraj · B. Bhutani (✉) · K. Lohiya · S. Mittal
Department of Mechanical Engineering, Delhi Technological University, Delhi 110042, India
e-mail: bharat.bhutani97@gmail.com

2 Supply Chain Management and Blockchains: Basic Concepts

2.1 Supply Chain Management

According to CSCMP, supply chain management can be defined as the process that takes place between two points, the procurement of raw materials and the delivery of the finished product to the customer. All the procedures that take place in between these two points, like collaboration between the supplier and distributors, the involvement of contracts including any third party, related to logistics, inventory, etc., as well as the customers, also form a part of the supply chain. Hence, supply chain management is the sum total of these starting and ending points as well as all the processes that lie in between [3].

In a basic supply chain, there are three components, namely the supplier of raw materials, the producer and the consumer. The supplier supplies the raw materials to the producer which in turn produces the finished goods, from there the finished good reaches to the consumer. Let us take a simple example of the newspaper industry to understand supply chain management. The newspaper industry first acquires the paper and ink required to publish newspapers from a source. Then they also need a factory where they can print the papers. Also, they will need an inventory to store extra paper and ink. Finally, when the papers for the day have been printed, they will need a logistics department to transport these papers from their factory to the distributors, i.e., newspaper stands. Furthermore, these newspaper stands will also require a logistics team of bike riders to deliver papers to the customers. Now, all these procedures starting from acquiring the raw materials for the production of newspaper to the delivery to customers come under the supply chain of the newspaper industry. And the efficient management of these to gain a competitive edge over others in the industry to maximize profits as well as to achieve and increase customer satisfaction is called supply chain management.

2.2 Blockchain Technology

Blockchain technology is essentially seen as a very important tool to provide accessibility, verification as well as security to the information provided by supply chains at different levels [2]. A widely accept accepted definition of blockchain was given by Treiblmaier, i.e., "a ledger which is digital, distributed and decentralized in which various transactions can be lodged and added in a chronological order with the ultimate goal of creating tamperproof and permanent records" [8, p. 547]. Blockchain technology is widely used to store data in an decentralized manner, i.e., it converts data into hash pointers and stores it in multiple computers rather than storing everything on the same computer, thereby reducing the possibility of failure at a single

point as data is stored on multiple nodes rather than on a single node. Blockchain technology is gaining increased popularity in various industries, such as in the healthcare industry, medical records of different patients are widely scattered, and this forces the medical staff to work with incomplete records of the patients and can sometimes lead to various problems. In order to tackle this challenge, various projects have been launched with the primary aim of using blockchain technology as a means of providing data sharing with proper authentication and at the same time maintaining confidentiality. Blockchain is also being used by the LGBT community in order to φht for their rights, as this technology is in building the "pink economy," enabling them to fight for their rights without revealing their identities. This also helps them by protecting them against the hate crimes especially in countries where abusing of the human rights is a common issue or where homosexuality is outlawed. There are many other different applications of blockchain technology but only a few are discussed above. Blockchain is also used in SCM because it has a unique ability to eliminate the use to middlemen, hence enabling the work to be completed faster and in a more efficient manner.

A blockchain, as the name suggests, is a chain of various blocks which are interconnected to one and other. Once data is stored in a block, it is next to impossible to change the data without hampering the entire chain of blocks. A single block in a blockchain contains three values, i.e., the data, hash and hash of the previous block. Hash of the block is unique for different blocks, and used to identify the block as well as its content. Changing something inside the block also changes the hash of the block, in other words in order to find data of which block has been changed one can always look at the hash if it is changed or not. If the hash of the block changes, then it no longer is the same block. Different blocks can only be appended in a blockchain, i.e., added to the end of the last block. Initially, the use of blockchain was only limited to cryptocurrencies but now people have started experimenting its use outside of finance, such as its use in supply chain management.

2.3 Smart Contracts

Smart contract was an idea proposed by Szabo [6]. They, in many ways, can be compared to the legal contracts. They have the capability to function on their own. The idea behind the application of smart contracts was that the blockchain network would automatically be terminated if any violation of the smart contracts was revealed. This also helps in the reduction of any further damage or loss in the network.

A smart contract is basically a self-operating contract in which the terms and conditions of a contract between two different parties (i.e., buyer and seller) are typed down directly into lines of code on a digital platform in a blockchain. Basically, they are a form of automatic generated agreements in which electronic algorithms are used to implement the process of carrying out various transactions that are processed by the two parties. Smart contract not only enforces the contract but also eliminates the requirement of a third-party involvement.

For example, in the real estate sector when a seller wants to sell a particular house and a buyer wants to buy that house, if a smart contract is used the terms and conditions decided by the two parties cannot be changed by either of them. If a fixed price is mentioned in the smart contract by the seller, then the buyer will be able to purchase the house only after paying that respective amount. It also eliminates the need of the middleman as the terms and conditions are set by the two involved parties. This helps to ensure proper transparency while carrying out the deal. Hence, in smart contracts, if any of the parties try to manipulate the code, then it will not be masked, but instead fully visible to all the parties involved. Therefore, it offers transparency.

2.4   Blockchain Technology in Supply Chain Management

Earlier the use of blockchain was only limited to finance until recently when people have started experimenting the use of blockchain outside finance. Different promising applications of blockchain outside finance include those in SCM, health care, power, food and agriculture. For example, as reported by Lehmacher in 2017, using blockchain technology in supply chain could potentially eliminate 25 cm high paperwork originating from just dispatching roses from Holland to Kenya [5]. These are some of the areas where it is expected that using blockchain will deliver return on investment in the early stages. For example, in most simple businesses, the process includes manufacturing and then delivering finished goods to the consumer. The supply chain of this process will include procurement of resources for manufacturing, followed by delivery, retail and warehousing. The supply chain will have problems like tracking the materials, procurement costs as well as distrust between the two parties as well as the party and middleman. To tackle this, blockchain can be used as it can help create a permanent record of every transaction that happens, from manufacture to sale. This not only reduces time delays and man-made errors, but also eliminates unnecessary audits and paperwork. It can be used to link various physical items to serial numbers, bar codes and tags like RFID, etc. Since everything is permanently documented in blockchain, it creates trust between both parties and also eliminates the need of a middleman because all the data is visible for everyone to see. Also, geographical location does not create any limitation on the blockchain network as anyone can access it from anywhere. Also, the immutability that blockchain offers makes sure that the transactions are corruption free and free from any cyber threat.

Other examples where blockchain technology can be used in various supply chain management scenarios are as follows:

Coffee

In coffee supply chain management, the product is grown in remote areas and not in mainlands. Also, there is abuse of laborers and lack of fair price for farmers. Blockchain technology offers transparency as well as traceability which ensure that

the customer can track where the coffee is coming from and also the farmer does not have to depend on an intermediary for a fair price.

Counterfeit Drugs

In the current pharmaceutical scenario, there is an increase in counterfeit drugs in which area risk to human life. Using blockchain technology, each drug packet can be given a unique code which is stored on the platform and cannot be corrupted. Hence, the retailer as well as the customer can track the shipment and make sure that only verified drugs are being sold.

Automotive Industry

The problem of spare parts lies in the automotive industry as well. This causes accidents which leads to distrust toward the manufacturer. The parts can be given a unique incorruptible code and can be tracked in real time, ensuring delivery and shelving of only real spare parts.

There are various benefits to using blockchain technology in supply chain management. It ensures transparency because the data cannot be changed in a blockchain. And any changes made to a smart contract will be visible to all parties involved. Furthermore, blockchain can be used in collaboration with other technologies, like IoT, which allows for real-time tracking of not only location, but also temperature pressure and other physical and chemical factors in case of sensitive shipments. Also, due to the transparency blockchain offers, there is elimination of intermediaries as well as a paper trail which increases the trust between the parties involved.

The challenges blockchain technology faces in the current scenario are mostly the acceptability of this technology. Not many industries are ready to shift from their current enterprise resource platform systems (ERP) to blockchain technology yet. Also, management software developers have not yet given the blockchain technology the preference it needs to be developed as an ERP yet. Once blockchain technology is accepted in various industries, it will pave way for a better supply chain management system.

3   Research Methodology

The main goal of this paper is to systematically identify the restraints in the current scenario of supply chain management and then tackle them using blockchain technology. First a review of current papers in the field of blockchain technology application in supply chain management was done to help us identify the aforementioned.

A case study was conducted in ONGC Petro Additives Limited (OPaL) where the flow of material from its production in the factory to its delivery to the customer was studied and divided in steps, and finally a blockchain platform was used to tackle the bottlenecks found in the entire supply chain. Finally, the results from the above

studies conducted are cumulated and condensed to clearly show how blockchain technology brought about a change in the current supply chain scenario.

4 Case Study

This case study is about the dispatch system and vehicle turnaround time in ONGC Petro Additives Limited (OPaL). It was carried out during the summer of 2018. The following are the inferences from what was observed.

4.1 About OPaL

ONGC Petro Additives Limited (OPaL) is a joint venture company which comes under the partnership of ONGC, GAIL and GSPC. The company was incorporated under the Companies Act' 1956 in November 15, 2006, as Public Limited Company. The mega petro chemical complex was built with a total investment of about Rs. 30,000 Cr. and was inaugurated by PM Shri. Narendra Modi on March 07, 2017.

The OPaL plant is located at Dahej Special Economic Zone (SEZ 1), Gulf of Khambhat, and has a total area of 508 Ha. The industrial complex is surrounded by Arabian Sea at South, SEZ internal road at North, Gujarat Fluorochemical Limited (GFL) and Deepak Phenolics Ltd. at West and Suva village at East. OPaL has the single largest Dual Feed Cracker unit in India and has an annual production capacity of 1.4 million tonnes of polymers and 0.5 million tonnes of chemicals. The complex has been designed by Linde (Germany), Lurgi (Germany), Ineos (USA), Ineos (Europe), Mitsui chemicals (Japan) and Axens (France). It is expected that OPaL will acquire about 13% of the total polymer share in the country.

The flow of finished product was tracked in the compound for 6 weeks. It is explained in the following:

Checking at Gate

There are two types of transporting vehicles that arrive at OPaL, trucks for solid finished products and tankers for chemicals, licensed by the authorized transporter. The entry and also the exit of these vehicles happen at gate number 4. Before the vehicle is allowed to enter, the security check post outside gate number 4 checks the vehicle for the authorization letter issued to the driver by the transporter. Then the driver is given a checklist by the security at this check post, a tanker checklist for the tanker and a truck checklist for the trucks. In case of discrepancy in any of the checks, the vehicle is rejected.

Main Gate Entry (MGN)

Once cleared, the driver then takes this checklist to the main gate, where he provides certain details, like his license number, etc., to the security officer at the main gate. His

details are then entered in the SAP. If the driver has, in the past, delivered goods for OPaL, his information is already stored in the SAP system. In case of any discrepancy like an expired license, or if the driver has been blacklisted due to criminal record, the SAP notifies the security officer, and they reject the driver. Once the driver is cleared by the security officials, he is then allowed to take his vehicle in the plant premises for further activity. This is called main gate entry (MGN).

Weight Bridge Entry (WBN): Capturing of Tare Weight

The vehicle then proceeds to the weigh bridge, where the tare weight is taken (weight of the vehicle without any material). This is taken so that when the vehicle is weighed again with the finished goods, permissible weight can be determined, and it is decided whether the vehicle is carrying the right amount of finished goods. Weigh bridges 4 and 5 are for trucks, and weigh bridges 6 and 7 are for tankers. Once the tare weight has been captured, SAP entry is done, and the vehicles then proceed to the product warehouse for issuing of loading slip.

Issuing of Loading Slip

The driver reports at the office window or he reports to the authorized transporter representative about his arrival. The operations team then issues a loading slip on the basis of the order that has been placed. SAP entry is done. Then the truck proceeds to the loading bay in the product warehouse itself while the tankers proceed to the gantry.

Loading of Finished Material

The product warehouse at OPaL has 60 loading bays. The truck comes to the product warehouse and is parked until the loading slip is issued to it. Once the loading slip is issued, the truck is sent to the designated loading bay. The loading of the truck is done by a gang of three workers. Once loaded, the truck is then covered with tarpaulin. The truck then goes to the weigh bridge for gross weight. If the gross weight is according to the specified need, then the truck moves back to the warehouse to collect the invoice and then to the main gate for exit and finally dispatch to customer. Once loading has been done, the driver notifies the logistics team and SAP entry is done again.

Weight Bridge Exit (WBX): Capturing of Gross Weight

Once the trucks and tankers have been loaded, they are sent to the weigh bridge again for calculating net weight. The tare weight is subtracted from the net weight to calculate the gross weight. If the gross weight is within limits of the specified allowance for tankers and trucks, respectively, entry is done in the SAP system, and they are then sent back to the warehouse to collect the invoice (Fig. 1).
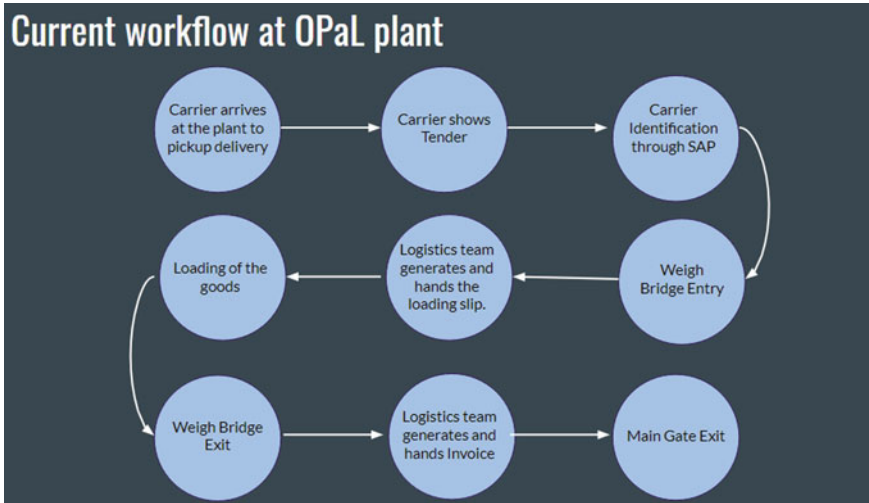
Fig. 1 Flowchart representing the work flow of material from the plant to the truck which then transports the plastic to the customer

4.2 Time Recorded and Analysis

On analysis of cycle time of 1039 vehicles (June 1, 2018–June 7, 2018), the following graph shows the distribution of time taken percentage wise (Fig. 2).
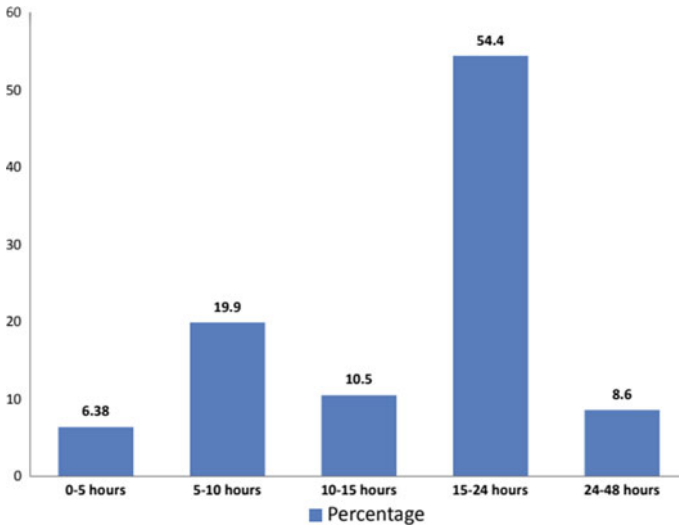
Fig. 2 Distribution of time taken by each truck percentage wise

Ideally, cycle time should not be more than 10 h. But from the above graph, it is clear that around 54% of vehicles have a cycle time between 15 and 24 h. The area of improvement has been marked by the red box in the graph below. In order to optimize the cycle time, OPaL should focus on ways to **reduce the vehicles in** between the time bracket of 10–48 h (Fig. 3).

The following time is recorded in the SAP system:

1. MGN-WBT (main gate entry to tare weight).
2. WBT-DOC (tare weight to issuing of loading slip).
3. DOC-LDG (issuing and handing of loading to driver).
4. LDG-WBG (loading of vehicle to gross weight measurement).
5. WBG-INV (gross weight measurement to issuing of invoice).
6. INV-MGX (handing of invoice to driver to exit from main gate).

Further analysis of the time taken is as follows (Table 1; Fig. 4).
The bottlenecks identified in vehicle turnaround time are as follows.
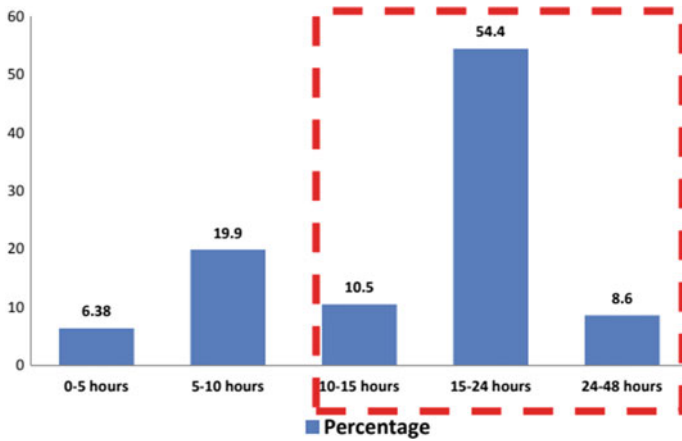
Fig. 3 Distribution of time taken by each truck percentage wise

Table 1 Time taken by different activities in the OPAL plant

Sr. No.	From-To	Time taken (h)
1	MGN-WBT	0.5
2	WBT-DOC	1.3
3	DOC-LDG	10.3
4	LDG-WBG	2.3
5	WBG-INV	3.5
6	INV-MGX	4.3
7	Time taken	16
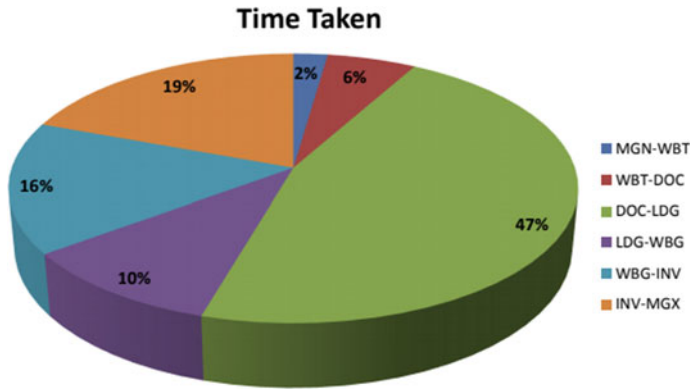
Time Taken

Fig. 4 Pie chart representing percentage of time taken by different activities

High Reliance on Paper as a Medium of Communication and Proof

From the pie chart, it is clear that most of the time (47%) is consumed in issuing and delivery of loading slip and invoice to the driver (DOC-MGX). Hence, this is the area which should be given prime importance for improvement. On observing the processes in the product warehouse, it was noticed that once the driver has reported to the logistics team, instead of being handed the loading slip on the spot, he has to wait. This happens because there is no seamless method of issuing and handing of loading slip. A bunch of 15–20 loading slips and invoices is created first in the invoice room which is then sent to the person responsible for circulating it further. This entire procedure takes a minimum of 30 min usually for the first few vehicles. Due to the vehicles being made to wait, the ones that follow them have to wait more and thus create a lag. Sometimes, they may have to stay in the industry premise for a whole evening and loading starts next morning.

No Transparency Between Stakeholders

Since data about sales, purchases and other transactions is stored in a centralized platform completely under the control of OPaL, they are prone to manipulation from anyone in OPaL. This creates a distrust between the two parties.

Vulnerable to Cyber Threats

Storage of all data in one centralized platform means all of it is susceptible to cyber threats. The data can be changed, deleted or manipulated in any other way.

4.3 Implementation of Blockchain in Current Scenario

After condensing the problems in the current supply chain procedure, a theoretical implementation of blockchain technology was done. The various ways in which the bottlenecks are tackled are as follows:

Elimination of Paper Trail

A private or open blockchain can store shipment data, i.e., its order, delivery transactions as well as tender data in the form of a serial number which can then be converted into a QR code. This QR code is scanned at the weighing bridge as well as the loading bay to verify the shipment instead of generating two documents. This saves a lot of time as compared to the previous process, hence creating a seamless and efficient system of delivery.

Create an Immutable Ledger of All Shipments of the Plant

In a centralized data system, data can be manipulated and even destroyed. But in blockchain technology, for every data element, for example, a transaction, a cryptographic hash is created which cannot be used to recreate the original transaction. Hence, it protects the integrity of the consensus between the consumer and service/goods provider.

Data Visibility to Stakeholders for Effective Auditing

Since blockchain uses smart contracts, which ensure that any change made to the program in the blockchain is visible to all the nodes, it ensures for the stakeholder that no manipulation is being done. Hence, this creates trust between both the parties.

Possibility of Geo Locating and Tracking of Shipment Using Internet of Things (IoT)

The blockchain platform can be integrated with Internet of things (IoT) to track where the shipment has reached and also keep a track of the conditions under which the chemical is stored, like temperature and pressure. This is very useful when transporting hazardous material, especially in bulk. The following flowchart depicts the workflow in the same scenario if blockchain is integrated in supply chain management at OPaL (Fig. 5).

5 Conclusion, Limitations and Findings

The purpose of this study was to find out how BCT can transform the way we look at SCM. BCT is relatively new and a novel technology. From the face value, it is evident that it can remove various bottlenecks in supply chain, thereby increasing the efficiency of the supply chain management.
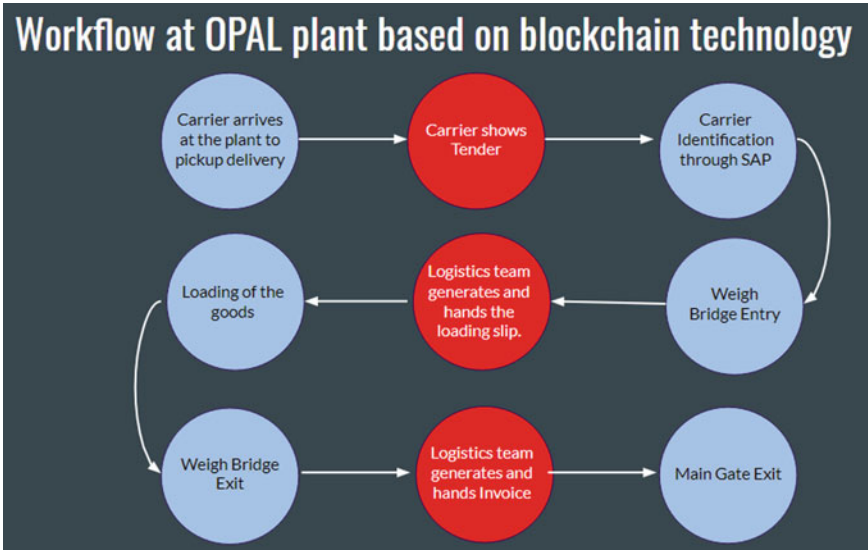
Fig. 5 Workflow at OPAL plant based on blockchain technology

Many companies are investing millions of dollars in the research and development as to determine how this technology can benefit their respective businesses. **IBM** unveiled its "Blockchain as a Service" in March 2017 (Tech Crunch 2017), which is based on the open-source Hyperledger Fabric, version 1.0 from The Linux Foundation. **IBM blockchain** is a public cloud service that customers can use to build secure blockchain networks.

Also, supply chain needs to be revised not as an independent theory, but as a culmination of blockchain technology and existing theories for proper and problem less implementation in the industry.

Now, from a social change perspective, block chains are already remodeling the relationship between customers and organizations, as well as business to business without intermediary to validate the transaction.

Not only can blockchain be just integrated with supply chain, it also opens up new avenues for implementation of other technologies with BCT as their carrier. For example, Internet of things (IoT) can be integrated on a blockchain platform with supply chain to geo locate shipments and track temperatures for sensitive products.

Thus, we would finally like to conclude by saying that blockchain technology, although relatively new and unexplored to its fullest potential, is the next industry disrupter and will bring about a change in how we visualize and practice supply chain management today.

References

1. Bocek, T., Rodrigues, B.B., Strasser, T., Stiller, B.: "Blockchains everywhere—a use case of blockchains in the pharma supply-chain. In: IFIP/IEEE Symposium on Integrated Network and Service Management, pp. 772–777 (2017)
2. Cottrill, K.: The benefits of blockchain: fact or wishful thinking? Supply Chain Manage. Rev. **22**(1), 20–25 (2018)
3. Council of Supply Chain Management Professionals (CSCMP): "CSCMP's definition of supply chain management. (2018). Available at: www.cscmp.org/CSCMP/Educate/SCM_Definitions_ and_Glossary_of_Terms/CSCMP/Educate/SCM_Definitions_and_Glossary_of_Terms.aspx? hkey=60879588-f65f-4ab5-8c4b-6878815ef921. Accessed 10 July 2018
4. Coyne, A.: Food giants Nestlè and Unilever link up with IBM on blockchain project. Aroq-Just-Food.Com (Global News), p. 13 (2017)
5. Lehmacher, W.: Why blockchain should be global trade's next port of call (2017) Available at: www.weforum.org/agenda/2017/05/blockchain-ports-global-trades/. Accessed 21 Jan 2019
6. Szabo, N.: Smart contracts (1994). Available at: www.fon.hum.uva.nl/rob/Courses/Informati onInSpeech/CDROM/Literature/LOTwinterschool2006/szabo.best.vwh.net/smart.contracts. html. Accessed 30 Sept 2018
7. Tirschwell, P.: Maersk charts new future with IBM blockchain pact. (2018) Joc Online, 27 January, p. 1, available at: www.joc.com/technology/maersk-ibm-blockchain-deal-statement-techs-role-industrychange_20180127.html/. Accessed 15 Nov 2018
8. Treiblmaier, H.: The impact of the blockchain on the supply chain: a theory based research framework and a call for action. Supply Chain Manage. An Int. J. **23**(6), 545–559 (2018)

Vendor Managed Inventory: Issues and Challenges in a Single Vendor Multiple Retailer Supply Chain

Aditya Anand , **Arnuv Mishra** , **S. K. Garg, and Reeta Wattal**

1 Introduction

The supply chain entities are increasingly adopting vendor managed inventory (VMI) framework to augment operations efficiency. This transition was catalysed with the advent of the phenomenon of information sharing. In a single vendor multiple retailer supply chain, under VMI, the retailer at the lower echelon of the supply chain provides demand information of the consumer to the upper echelon vendor. The vendor assumes accountability of the retailer's inventory considerations rather than simply replenishing material [1, 2]. The vendor inspects the retailer's stock (physically or via electronic messaging) periodically and take replenishment decisions accordingly. These decisions concern factors such as order quantities, transportation and service levels. Hence, the purchasing agreements conventionally initiated by the retailers are now initiated by the vendor. After the vendor approval of the purchase order, an advance shipping notice (ASN) apprises the retailers of the goods in transit [3]. Vendor managed inventory (VMI) also known as consignment inventory has been increasingly used in a plethora of applications. Material management in the healthcare industry has shown a rising trend towards the adoption of VMI. The conspicuousness of VMI is more than just-in-time and stockless frameworks in such a case [4]. A prediction has been done by a survey regarding the multiplying effect of VMI in the retail industry in the coming years [5]. Main retail players like Wal-Mart, Kmart, Dillard Department Stores and JCPenney were among the first to the transition to VMI. The contemporary interest towards VMI has led to the claim that VMI as a concept would prove indispensable in recasting the efficiency of the distribution

A. Anand · A. Mishra (✉) · S. K. Garg · R. Wattal
Department of Mechanical Engineering, Delhi Technological University, Delhi 110042, India
e-mail: arnuvmishradtu@gmail.com

A. Anand
e-mail: adityaanand1697@gmail.com

channel [6, 7]. Vendor managed inventory (VMI) can augment customer service efficiency by mitigating stock levels and increasing fill rates [8]. VMI is imperative in providing new business opportunities to both tiers in the supply chain by optimizing costs and increasing service levels [9]. In spite of having ample amount of benefits, VMI also comes with its own set of limitations especially in a single vendor multiple retailers' framework [10–13]. The unequal benefit distribution between the vendor and retailers remains the primary impediment. In many instances, the retailer tends to avail higher profits in such an arrangement [14–16]. The vendor will reap benefits from the VMI collaboration when the stock levels maintained by the retailers are less than the inventory in VMI [17]. Responding to Mishra et al. [14] work, Kim HS [18] disputed the claim that the retailer increases its profits under the guise of brand competition in the VMI system. Kim HS [18] suggests that the retailer instead might have to let go of the profits when adopting VMI if it deals with less holding cost and small profit margins [13]. In such a case, it becomes imperative to understand the trade-offs between the benefits and limitations from both the stakeholder's paradigm before making an informed decision as shown in Table 1.

Table 1 Benefits and limitations of implementing vendor managed inventory model in a single vendor multiple retailer supply chain

Benefits		Limitations
For retailer	*Vendor managed inventory*	Inequitable profit sharing [2, 12]
Effective inventory management [1, 5, 10, 17]		Unreliable information sharing [5, 16]
Less uncertainty regarding inventory turnover [1, 15]		Information sharing delay [9, 11]
Better forecasting practices [6, 11]		Uncertain demand of the customers [8, 13]
Improved customer service levels [3, 4, 6]		High Administrative costs [11]
For vendor		Supply chain of perishable products [7, 16]
Increased availability of brand in retail stores [14, 18]		Ineffective storage [13, 17]
Effective control of retailer's inflated orders [5, 7, 10]		Imperfect production process [15, 17]
Better production planning [9, 12]		Pricing and promotion conflict [3, 12, 18]

2 Analysis of Issues and Challenges in a Single Vendor and Multiple Retailer Supply Chain

A single vendor multiple retailer supply chain incorporates a lone upstream vendor who supplies the goods to the downstream retailers depending on the demand patterns decided by the consumer. The stock keeping units are managed by the vendor in the retailer's warehouses. The SKUs may be common goods or customized to the consumer's requirements. The goods can also be perishable in nature which again raises the concern of effective storage and warehousing. For effective integration and efficiency of the supply chain, the timing of production should be in synchronization with the demand of the customers. Hence, production is also an integral part of this system. Proper information sharing becomes imperative in such a scenario. All these factors must be considered to evaluate the feasibility of implementation of vendor managed inventory model in such a system. To understand the intricacies of the issues and the challenges involved within, we divide the single vendor multiple retailers supply chain in individual blocks and analyse these issues thoroughly. These issues considered are depicted in Table 2.

2.1 Uncertain Demand of Consumer

Conventionally, in the production and delivery problem, the market demand and transit time were assumed to be invariable. Pragmatically, this is not possible in the contemporary single vendor multiple retailer supply chains. The fluctuation in the variables of the system like time is a critical factor in commercial applications. It not only causes transportation lag but also compromises the reliability of the complete supply chain. Hence, lead time is an unavoidable issue in the stochastic demand situations [19, 23].

2.1.1 Stochastic Lead Time Demand

In this specific case of uncertain consumer demand, the inventory model for a commodity is evolved from a stochastic environment involving a price-dependent demand over a finite time limit. The shortages are allowed (if they occur), and probabilistic lead time is taken into account [48]. Preparing the order, transportation, supplier lag time and setup time combines to form the lead time of the system [49]. Lead time may be shortened by using additional expenses in many situations. Hence, the practitioners can vary the customer service level, safety stock and the loss of stock-out by controlling the lead time [19]. Lead time is normally distributed in a stochastic lead time model, and hence, this factor comes to play while taking decisions. A multi-SKU multi-chance constrained joint single vendor multi-buyer inventory situation was considered by [23]. In this problem, the demand follows a

Table 2 Issues in a single vendor multiple retailer supply chain from literature

Issues	References	Remarks
Uncertain demand of consumer	[19–24]	The reasons behind the ambiguities due to this demand are addressed by analysing various types of uncertain demand like stochastic and stock-dependent demands.
Product type	[25–27]	The difference in the management of perishable (consumable) items from the non-perishable items is discussed in a supply chain.
Environmental issues	[28–30]	The issues affecting sustainability of a supply chain are discussed, incorporating factors like pollution, raw materials wastage, packaging etc.
Production	[19, 20, 22, 31–36]	The problems in the production process are discussed which prevents optimizing the inventory costs and compromises the quality of goods produced.
Storage	[37, 38]	Constraints in storage of goods are discussed with the aim of minimizing holding costs and optimizing lead times.
Transportation	[22, 36, 37, 39, 40]	The bottlenecks in transportation procedure including scheduling deliveries and ineffective stock transportation are studied.
Quality control	[41–44]	The mitigation of quality due to increasing production rate and ineffective inspection is reviewed.
Information sharing	[45]	The time lag in shipments is mentioned which compromises timely information sharing.
Pricing and promotion	[25, 46, 47]	The discounts and pricing strategies are discussed which compromises the optimization of the complete supply chain by catering to the profit margins of individual players.

uniform distribution, the lead time is considered linear with respect to the lot size, and shortages are considered in the form of lost sales and backorder.

2.1.2 Stock-Dependent Demand

It is commonly experienced in the market that the stock exhibited in the shops allures more consumers. Hence, the inventory affects the demand generated. Various studies have investigated and analysed inventory models considering some functional inter-relationship between on-hand stock level and demand rate [20]. There is a positive dependency of the number of items displayed on the demand rate. Spices, cloths, cards and sugar are some real-life examples of items displaying stock-dependent demand [21, 50].

2.2 Product Type

The type of product or stock keeping unit directly influences the production planning and control in a supply chain. It also influences the inventory management of the product and transportation mechanisms.

2.2.1 Perishable Products

Deterioration refers to the phenomenon in which certain consumable or volatile products like dairy, fruits, vegetables and chemicals are decayed, damaged or spoilt as time progresses. Mitigation of the usable volume and shrinkage of the effective value of goods are some of the consequences of deterioration [25]. Deterioration cannot be overlooked in inventory modelling; in fact, it is an integral part of it. Items such as electronics, edibles and clothing lose their quality, value and utility with time [26].

2.3 Production

The production process is responsible for producing goods at a rate which can be consumed for maximum service level, catering to the needs of the consumers. The issues of scheduling and capacity optimization are indispensable for proper functioning of the production machinery.

2.3.1 Imperfect Production Process

Many works of the production inventory literature suppose that the production process always generates goods of satisfactory quality. Pragmatic truth is far from this assumption. The stock delivered to the retailer almost always comprises some proportion of non-conforming items. This lack of compliance to quality standards is

a consequence of lack of facility maintenance, locomotive damage, transportation lag and other defects of the process. These defectives adversely impact customer satisfaction, profit margins and the goodwill of the supply chain stakeholders. Hence, it becomes imperative to analyse the effect of such products on inventory decisions. The retailers may also rely on a complete screening of products received from the vendor before taking it out to the market [20, 32].

2.3.2 Stochastic Machine Unavailability Time

The facilities used in production process may also experience a stochastic break down due to which the production may get affected. Theoretically, the machine initiates production after the stock level drops down to nil. The production runs may also get postponed due to machine unavailability, insufficient stock and equipment. The fluctuating production due to the underlying inefficiencies makes the vendor unable to meet the predetermined orders causing lost sales [34, 35].

2.4 Storage

Storage of the inventory is an integral part for matching the supply and demand of the goods. It is imperative to minimize the holding costs of the inventory while maintaining quality in order to provide the right goods to the consumers at the right time and right costs.

2.4.1 Warehouse Capacity Constraint

An increased attention in a supply chain is directed towards storage and warehousing capacity. This factor is indispensable for optimum decision-making and cost reduction policies. Altering the capacity of a warehouse is a long-term decision having wide ramifications on the supply chain. This strategic decision should be backed up by a prediction of substantial demand increase. A peak of demand may also arise in a supply chain due to short-term measures like discounts, seasonality, promotions and emergencies. The supplier may enter into contractual agreements with third parties for strengthening their inventory management policies [37]. It is redundant for practitioners to expend in increased warehousing which cannot be made use of in the long run. Additionally, renting the warehouses for a short time, such as one month, is also not economically viable in many cases [38].

2.5　Environmental Issues

For a long-term smooth functioning of a supply chain, it is imperative that all the stakeholders involved are concerned about the environmental effects of the processes involved. It not only induces sustainability within the supply chain but also puts the stakeholders on a good side of customer goodwill and government policies.

2.5.1　Raw Material Wastage and Air Pollution

Rising environmental consciousness among the masses has instilled in businesses a need of inducing sustainability in their working. [30]. The novel initiatives and practices consider the complete life cycle of a product from design to end of life [51, 52]. The taxing measures and cost mechanisms have also been introduced to limit the ecological impact of human activities (i.e. greenhouse gas—GHG emissions) [28].

2.5.2　Unsustainable Packaging

The packaging of the products may pollute the environment and prove to be a limitation in efficient transportation and consumption by the end-user. The packaging of products should be efficient and resource optimal. These are a variety of secondary packaging material and can be reused in the same form. Some examples of returnable containers are crates, bins, pallets or boxes [53]. These assist in inducing longevity in the supply chain by enhancing green variables of the system. They have a distinguishable benefit of reducing carbon dioxide emissions as well [29, 54].

2.6　Transportation

The timely delivery of goods from one supply chain entity to another for value addition happens by using modes of transportation in between. Transportation problem involves optimizing the transit time for maximum profit generation in the supply chain.

2.6.1　Ineffective Stock Transportation Between Retailers

Non-optimal frequency and sizes of shipment to retailers and trans-shipments between retailers result in high system-wide cost in a supply chain. Ineffective stock transportation of shipments leads to stock shortages and stock-outs at various retailers in a supply chain [37].

2.6.2 Scheduling Deliveries to Retailers

A single vendor often implements independent optimization strategy with multiple retailers to deliver products to them rather than having an integrated delivery strategy. Consequently, having independent delivery schedule (number of deliveries and their timings) and optimal lot size sent to different retailers raises the joint ordering and inventory holding costs [22].

2.7 Quality Control

The primary aim of any supply chain is to provide quality products to the end-user. The product should be reliable, aesthetic, durable and safe to use or consume.

2.7.1 Degrading Quality with Increasing Production Rate

The increase in rate of production gradually increases the probability of process failure, consequently, causing deterioration in the quality of product at a certain percentage [42].

2.7.2 Quality and Inspection Errors

Defectives produced during a cycle are inevitable. Defectives occur due to out of control process, inconsistent inspection procedure, etc. Defectives can be scraped or reworked, thus increasing the cost.

2.8 Pricing and Promotion

The issue of pricing is primarily responsible for providing the valuable cash flows which the product generates. It is dependent on all other issues of the supply chain. The issues of promotions, quantity discounts and seasonal demand have a huge say on what the pricing of the product would be.

2.8.1 Low Channel Profit

High competition among retailers in a market leads to low-driven profit margins. Non-optimal sales quantity, sales price and contract price between vendor and multiple retailers often result in low profit for a retailer [46].

2.8.2 High Joint Total Cost of a Supply Chain

As far as conventional approach of inventory control is concerned, both vendors and retailers employ their own inventory control strategies to deal with instability in domestic demand or supply chain uncertainties, such that to ensure occurrence of repeated inventory in a supply chain. This independent inventory control policies of vendors and buyers significantly increase the joint total cost of the supply chain [47].

2.9 Information Sharing

It is essential that all entities of a supply chain be it the vendor, manufacturer, transporter or the retailers are well connected throughout the process with seamless information sharing between them. This would lead to lesser lead time and less wastage of resources in the supply chain.

2.9.1 Time Lag in Communication and Shipment

Time lag in communication of information and movement of materials contributes to the need for inventory in order to prevent stock shortages and stock-outs. As a result, incurring high system-wide costs in a supply chain [45] (Table 3).

Table 3 Issues and challenges in a single vendor multiple retailer supply chain

Issues	Challenges
Uncertain demand of consumer	Stochastic lead time demand Stock-dependent demand
Product type	Perishable products
Production	Imperfect production process Stochastic machine unavailability time
Storage	Warehouse capacity constraint
Environmental issues	Raw material wastage and air pollution Unsustainable packaging
Transportation	Ineffective stock transportation between retailers, scheduling deliveries to retailers
Quality control	Degrading quality with increasing production rate, quality and inspection errors
Pricing and promotion	Low channel profit High joint total cost of a supply chain
Information sharing	Time lag in communication and shipment

3 Successfully Implemented VMI Models

3.1 Consignment Stock Policy VMI Model

Tarhini et al. [37] developed a consignment stock (CS) agreement for a vendor and multiple retailers allowing trans-shipments among the retailers. Limited storage capacity of retailers and restricted shipment size between two locations is taken into consideration. CS policy accounts for the vendor's assurance to replenish the inventory at the retailer's location. When a vendor replenishes the stock at retailer's location, no amount is levied on the retailer upon replenishment rather it only has to pay for the depleted items from its inventory. As a result, this policy of storing items at a cheaper location proves beneficial for the vendor. Furthermore, this framework determines the optimal strategy that results in a minimum system-wide cost per unit time.

3.2 Ordering Cost Reduction and Shipment VMI Model

Tu et al. [47] proposed that an integrated approach for simultaneous replenishment of the retailers' inventory with goods in one cycle in a single vendor and multiple retailer supply chain is formulated. The proposed framework incorporates VMI, ordering cost reduction strategy and optimal shipment policy in an integrated model. Substantial savings in the system-wide costs per unit time of the supply chain can be achieved by integrating the policies rather than employing them individually.

3.3 Just-in-Time Shipment Policy VMI Model

A new decision model with a novel approach of conceptualizing a demand function is employed by [25]. This involved the proposition of a brand competition ratio and dual promotion cost strategies, i.e. the promotion cost distributed between the vendor and retailers and the other which was incurred by the retailers only. The increase in the wholesale price and sharing of the promotion cost directly influences the decision-making in such a scenario.

3.4 Integrated Quality Inspection VMI Model

A VMI integrated model of the quality inspection approach and production inventory control in a single vendor multiple retailer supply chain was ideated by [43]. The vendor coordinates with multiple retailers in a combined vendor managed inventory

and consignment stock (VMI–CS) agreement. The quality aspect of this model constituted two types of inspection inaccuracies, i.e. either accepting a non-conforming unit or rejecting a conforming unit. The mathematical model proposed amply put forth that the inspection errors cause both the vendor and retailers cost to rise, with vendor's cost taking a more substantial hit.

4 Managerial Implications

The paper has attempted to provide the practitioners, a tool to get a holistic purview of the concept of vendor managed inventory and enable them to take a right decision based on various issues and challenges faced in implementing it in a single vendor multiple retailers setting. It has also crunched the previous information in the literature of VMI into a potent gist which could be a readily available one-point source for decision-making. A trade-off between the benefits and initial investment towards transition to a vendor managed inventory framework has to be made (e.g. labour and technology costs have to be made) to determine the feasibility and sustainability of the new system.

5 Conclusions

The coordination of the vendor and retailer through information sharing, in which the vendor assumes control of the retailer's inventory, leads to the arrangement of vendor managed inventory. This paper analyses the intricacies of such an arrangement in a single vendor multiple retailer supply chain to its core by elaborating upon the bottlenecks and issues which the stakeholders may need to face in transitioning to or upkeeping such a system. The trade-offs between the benefits and limitations of VMI are discussed in the early part of the paper, both from the perspective of vendor and retailers. A comprehensive analysis has been done on the issues and challenges of implementing VMI system from the paradigm of a single vendor multiple retailers system. Finally, successful models of the VMI arrangement have been put forth to the readers from the past literature. These models were developed to counteract specific challenges the stakeholders faced before implementing the VMI model.

References

1. Chen, X., Sim, M., Simchi-Levi, D., Sun, P.: Risk aversion in inventory management. Oper. Res. **55**(5), 828–842 (2007). https://doi.org/10.1287/opre.1070.0429
2. Ru, J., Shi, R., Zhang, J.: When does a supply chain member benefit from vendor-managed inventory? Prod. Oper. Manage. **27**(5), 807–821 (2018). https://doi.org/10.1111/poms.12828

3. Waller, M., Johnson, M.E., Davis, T.: Vendor-managed inventory in the retail supply chain. J. Bus. Log. **20**, 183–204 (1999)
4. Gerber, N.: Objective comparisons of consignment, just-in-time, and stockless. Hosp. Mater. Manage. Q. **13**(1), 10 (1991)
5. Andel, T.: Manage inventory, own information. Trans. Distrib. (1996)
6. Burke, M.: It's time for vendor managed inventory. Ind. Distrib. **85**(2), 90–90 (1996)
7. Cottrill, K.: Reforging the supply chain. J. Bus. Strategy **18**(6), 35–40 (1997)
8. Dong, Y., Xu, K.: A supply chain model of vendor managed inventory. Trans. Res. part E: logistics Trans. Rev. **38**(2), 75–95 (2002). https://doi.org/10.1016/S1366-5545(01)00014-X
9. Niranjan, T.T., Wagner, S.M., Nguyen, S.M.: Prerequisites to vendor-managed inventory. Int. J. Prod. Res. **50**(4), 939–951 (2012). https://doi.org/10.1080/00207543.2011.556153
10. Sari, K.: Inventory inaccuracy and performance of collaborative supply chain practices. Ind. Manage. Data Syst. (2008). https://doi.org/10.1108/02635570810868353
11. Levi, D.S., Kaminsky, P., Levi, E.S.: Designing and Managing the Supply chain: Concepts, Strategies, and Case Studies. McGraw-Hill (2003)
12. Fiddis, C.: Manufacturer-Retailer Relationships in the Food and Drink Industry: Strategies and Tactics in the Battle for Power. FT Retail & Consumer Publishing, Pearson Professional London (1997)
13. Govindan, K.: Vendor-managed inventory: a review based on dimensions. Int. J. Prod. Res. **51**(13), 3808–3835 (2013). https://doi.org/10.1080/00207543.2012.751511
14. Mishra, B.K., & Raghunathan, S.: Retailer-vs. vendor-managed inventory and brand competition. Manage. Sci. **50**(4), 445–457. https://doi.org/10.1287/mnsc.1030.0174
15. Pasandideh, S.H.R., Niaki, S.T.A., Nia, A.R.: An investigation of vendor-managed inventory application in supply chain: the EOQ model with shortage. Int. J. Adv. Manufact. Technol. **49**(1–4), 329–339 (2010). https://doi.org/10.1007/s00170-009-2364-5
16. Zavanella, L., Zanoni, S.: A one-vendor multi-buyer integrated production-inventory model: the 'Consignment stock' case. Int. J. Prod. Econ. **118**(1), 225–232 (2009). https://doi.org/10.1016/j.ijpe.2008.08.044
17. Lee, C.C., Chu, W.H.J.: Who should control inventory in a supply chain? Eur. J. Oper. Res. **164**(1), 158–172 (2005). https://doi.org/10.1016/j.ejor.2003.11.009
18. Kim, H.S.: Research note—revisiting "retailer-vs. vendor-managed inventory and brand competition. Manage. Sci. **54**(3), 623–626
19. Sun, X.: The single-vendor multibuyer integrated production-delivery model with production capacity under stochastic lead time demand. Math. Prob. Eng. 2020 (2020). https://doi.org/10.1155/2020/2309073
20. Mandal, P., Giri, B.C.: A two-warehouse integrated inventory model with imperfect production process under stock-dependent demand and quantity discount offer. Int. J. Syst. Sci. Oper. Log. **6**(1), 15–26. (2019). https://doi.org/10.1080/23302674.2017.1335806
21. Omar, M., Zulkipli. H.: A single-vendor multi-buyer integrated production-inventory system with stock- dependent demand. Int. J. Syst. Sci.: Operat. Log. **5**(3), 204–210 (2018). https://doi.org/10.1080/23302674.2016.1248522
22. Hariga, M., Gumus, M., Ben-Daya, M., Hassini, E.: Scheduling and lot sizing models for the single-vendor multi-buyer problem under consignment stock partnership. J. Oper. Res. Soc. **64**(7), 995–1009 (2013). https://doi.org/10.1057/jors.2012.101
23. Taleizadeh, A.A., Niaki, S.T.A., Makui, A.: Multiproduct multiple-buyer single-vendor supply chain problem with stochastic demand, variable lead-time, and multi-chance constraint. Expert Syst. Appl. **39**(5), 5338–5348 (2012). https://doi.org/10.1016/j.eswa.2011.11.001
24. Shah, N.H., Gor, A.S., Jhaveri, C.: Single vendor and multiple buyers integrated inventory system when demand is quadratic. Int. J. Business Perform. Supply Chain Modell. **2**(2), 171–182 (2010). https://doi.org/10.1504/IJBPSCM.2010.036168
25. Chen, Z.: Reprint of "Optimization of production inventory with pricing and promotion effort for a single-vendor multi-buyer system of perishable products". Int. J. Prod. Econ. **209**, 285–301 (2019). https://doi.org/10.1016/j.ijpe.2019.01.040

26. Sana, S.S.: A two-echelon inventory model for ameliorating/deteriorating items with single vendor and multi-buyers. Proc. Nat. Acad. Sci. India Section A: Phys. Sci. 1–14 (2019). https://doi.org/10.1007/s40010-018-0568-5

27. Yang, P.C., Wee, H.M.: A single-vendor and multiple-buyers production–inventory policy for a deteriorating item. Eur. J. Oper. Res. **143**(3), 570–581 (2002). https://doi.org/10.1016/S0377-2217(01)00345-9

28. Castellano, D., Gallo, M., Grassi, A., Santillo, L.C.: The effect of GHG emissions on production, inventory replenishment and routing decisions in a single vendor-multiple buyers supply chain. Int. J. Prod. Econ. **218**, 30–42 (2019). https://doi.org/10.1016/j.ijpe.2019.04.010

29. Fan, X., Xu, X., Zou, B., Bai, Q.: Returnable containers management in a single-vendor multi-buyer supply chain with investment in reducing the loss fraction. Measurement **143**, 93–102 (2019). https://doi.org/10.1016/j.measurement.2018.12.003

30. Chan, C.K., Lee, Y.C.E., Campbell, J.F.: Environmental performance—Impacts of vendor–buyer coordination. Int. J. Prod. Econ. **145**(2), 683–695 (2013). https://doi.org/10.1016/j.ijpe.2013.05.023

31. Majumder, A., Jaggi, C.K., Sarkar, B.: A multi-retailer supply chain model with backorder and variable production cost. RAIRO-Oper. Res. **52**(3), 943–954 (2018). https://doi.org/10.1051/ro/2017013

32. Cheng, Y.L., Wang, W.T., Wei, C.C., Lee, K.L.: An integrated lot-sizing model for imperfect production with multiple disposals of defective items. Scientia Iranica **25**(2), 852–867 (2018)

33. Chiu, Y., Lin, H., Wu, M., Chiu, S.: Alternative fabrication scheme to study effects of rework of nonconforming products and delayed differentiation on a multiproduct supply-chain system. Int. J. Ind. Eng. Comput. **9**(2), 235–248 (2018). https://doi.org/10.5267/j.ijiec.2017.6.001

34. Taleizadeh, A.A., Samimi, H., Sarkar, B., Mohammadi, B.: Stochastic machine breakdown and discrete delivery in an imperfect inventory-production system. J. Ind. Manage. Optim. **13**(3), 1511–1535 (2017). https://doi.org/10.3934/jimo.2017005

35. Wee, H.M., Widyadana, G.A.: Single-vendor single-buyer inventory model with discrete delivery order, random machine unavailability time and lost sales. Int. J. Prod. Econ. **143**(2), 574–579 (2013). https://doi.org/10.1016/j.ijpe.2011.11.019

36. Yang, M.F., Lin, Y.: Integrated cooperative inventory models with one vendor and multiple buyers in the supply chain. Eur. J. Ind. Eng. **6**(2), 153–176 (2012). https://doi.org/10.1504/EJIE.2012.045603

37. Tarhini, H., Karam, M., Jaber, M.Y.: An integrated single-vendor multi-buyer production inventory model with transshipments between buyers. Int. J. Prod. Econom. **107568** (2019) https://doi.org/10.1016/j.ijpe.2019.107568

38. Feng, X., Moon, I., Ryu, K.: Warehouse capacity sharing via transshipment for an integrated two-echelon supply chain. Trans. Res. Part E: Log. Transportation Review **104**, 17–35 (2017). https://doi.org/10.1016/j.tre.2017.04.014

39. Wong, K.H., Chan, C.K., Lee, Y.C.E.: Optimal parameter selection problem with application to the synchronization of delivery cycles in a supply chain with Wiener process. Opt. Control Appl. Methods **40**(5), 914–937 (2019). https://doi.org/10.1002/oca.2524

40. Siajadi, H., Ibrahim, R.N., Lochert, P.B.: A single-vendor multiple-buyer inventory model with a multiple- shipment policy. Int. J. Adv. Manuf. Technol. **27**(9–10), 1030–1037 (2006). https://doi.org/10.1007/s00170-004-2267-4

41. Rahman, T., Wirdianto, E., Muluk, A.: An integrated production and inventory model considering reworks and two types of demand simultaneously in a two level supply chain network. In: IOP Conference Series: Materials Science and Engineering, vol. 505, No. 1, p. 012071. IOP Publishing (2019)

42. Sarkar, B., Majumder, A., Sarkar, M., Kim, N., Ullah, M.: Effects of variable production rate on quality of products in a single-vendor multi-buyer supply chain management. Int. J. Adv. Manuf. Technol. **99**(1–4), 567–581 (2018). https://doi.org/10.1007/s00170-018-2527-3

43. Alfares, H.K., Attia, A.M.: A supply chain model with vendor-managed inventory, consignment, and quality inspection errors. Int. J. Prod. Res. **55**(19), 5706–5727 (2017). https://doi.org/10.1080/00207543.2017.1330566

44. Wu, C.W., Wang, Z.H.: Developing a variables multiple dependent state sampling plan with simultaneous consideration of process yield and quality loss. Int. J. Prod. Res. **55**(8), 2351–2364 (2017). https://doi.org/10.1080/00207543.2016.1244360

45. Banerjee, A., Banerjee, S.: A coordinated order-up-to inventory control policy for a single supplier and multiple buyers using electronic data interchange. Int. J. Prod. Econ. **35**(1–3), 85–91 (1994). https://doi.org/10.1016/0925-5273(94)90068-X

46. Sue-Ann, G., Ponnambalam, S.G., Jawahar, N.: Evolutionary algorithms for optimal operating parameters of vendor managed inventory systems in a two-echelon supply chain. Adv. Eng. Softw. **52**, 47–54 (2012). https://doi.org/10.1016/j.advengsoft.2012.06.003

47. Tu, Z., Liu, X.: (ICAMS 2010) A new integrated VMI-based model for single vendor and multiple buyers with ordering cost reduction. In: 2010 IEEE International Conference on Advanced Management Science. https://doi.org/10.1109/icams.20https://doi.org/10.5553234

48. Maiti, A.K., Maiti, M.K., Maiti, M.: Inventory model with stochastic lead-time and price dependent demand incorporating advance payment. Appl. Math. Model. **33**(5), 2433–2443 (2009). https://doi.org/10.1016/j.apm.2008.07.024

49. Tersine, R.J.: Principles of Inventory and Materials Management. PTR Prentice Hall. Inc., New Jersey (1994)

50. Sarkar, B.: An EOQ model with delay in payments and stock dependent demand in the presence of imperfect production. Appl. Math. Comput. **218**(17), 8295–8308 (2012). https://doi.org/10.1016/j.amc.2012.01.053

51. de Sousa Jabbour, A.B.L., de Oliveira Frascareli, F.C., Jabbour, C.J.C.: Green supply chain management and firms' performance: Understanding potential relationships and the role of green sourcing and some other green practices. Resour. Conserv. Recycl. **104**(366), 74 (2015). https://doi.org/10.1016/j.resconrec.2015.07.017

52. Kaur, J., Sidhu, R., Awasthi, A., Chauhan, S., Goyal, S.: A DEMATEL based approach for investigating barriers in green supply chain management in Canadian manufacturing firms. Int. J. Prod. Res. **56**(1–2), 312–332 (2018). https://doi.org/10.1080/00207543.2017.1395522

53. Kroon, L., Vrijens, G.: Returnable containers: an example of reverse logistics. Int. J. Phys. Distrib. Log. Manage. (1995). https://doi.org/10.1108/09600039510083934

54. Hellström, D., Johansson, O.: The impact of control strategies on the management of returnable transport items. Transp. Res. Part E: Log. Trans. Rev. **46**(6), 1128–1139 (2010). https://doi.org/10.1016/j.tre.2010.05.006

Modelling of Shoe Polishing Machine Through Adaptive Neuro-Fuzzy Inference System

Fuzail Ahmad and **Vikrant Mishra**

1 Introduction

Industrial revolution has given birth to automation. The revolution of automation is evolving rapidly to replace simple processes such as dish washer to highly complex integrated mechanisms including automatic assembly line in the huge automobile industries. This resulted in creating an ease for the human efforts which in turn brought uniformity and standardization of products as well as provided an opportunity of exploring new regimes of science and technology to bring comfort for human beings on earth. Previous decades have experienced automation of various mechanisms and processes across simple household mechanisms to huge industrial processes.

The extent of automation which must be induced in simple machinery and industry has been rigorously reported in the scientific literature available. A commonly accepted framework to decide the extent and what system functions to be automated consists of four basic levels. Appropriate choice is always important in the selection of the extent of automation, Parasuraman and Sheridan [1] proposed that automation can be applied to four broad classes of functions: (i) information acquisition, (ii) information analysis, (iii) decision and action selection and (iv) action implementation. There is full propelled scope of automation in each of these four classes. Systems can vary from fully manual to fully automatic in each domain. One common misconception about automation is that the human interaction is diminished by it, and automation just changes the way human interacts in case of easily comprehensible work [2]. Also, the change sometimes is in areas unintended and unexpected to the designers. As a result, this is bound to open more areas of expertise required for the human operators [3].

F. Ahmad (✉) · V. Mishra
Rajkiya Engineering College Mainpuri, Dr. A. P. J. Abdul Kalam Technical University, Lucknow, India
e-mail: ahmadfuz007@gmail.com

Automation in the recent oxfords dictionary refers to as "the use of machines and computers to do the work that was previously done by people" [4]. This implies directly that automation is a direct attempt to replace the physical work performed by humans, but there is more to it, humans merely do not work with just physical efforts, and there is a lot more than the physical effort in the process of mental cognition going on. Simply automation can never get the jobs done which work beyond just an ON and OFF commands. For example, an automated blower can be just switched ON when required but it always reaches a fixed rpm. The dryness fraction may be required on a lesser rpm, to which manual handling is to be done. Here is where the artificial intelligence comes to play. The application of fuzzy inference systems solves many such problems by providing the intermediates stages between a classic ON and OFF or between 0 and 1.

In this project, we take up on another very common and simple process and develop a working model to ease the jobs. Automated shoe polishing program, if applied to any basic simple machine, has the potential to be a revolutionary household simple machine. This can be further applied into the mass production. The data set is made using the common human cognition and observations of various shoe polishing operations and surveying different cobblers. The observations simplified in the form of matrix table for both the parameters emphasized are shown.

The first thing to consider is the brush force required to apply on the shoe to clean the dirt. This is varied from gentle to harsh with medium being the middle ground. This model will be very useful while we are working on designing a completely automated shoe polishing machine to practically implement this model. Modelling of an automated shoe polishing programme using the inputs of quality of shoe material is based on hardness and the brightness of shine required, which in turn gives the force to be applied by the brush on the shoe and amount of liquid polish to be applied to get the required amount of shine.

The literature provides a good insight into how various researchers have contributed towards the idea of developing an automated shoe polishing machine. Considerable amount of work is available on the hardware design of the machine. Amogh et al. designed and fabricated a shoe polishing device which was mechanized through a motor driver circuit and a programmable Arduino microcontroller. In this device, various sizes of shoes can be placed at carriage and then input signal is sent to microcontroller after gripping the shoe on the carriage. Lead screw mechanism is actuated by microcontroller. The motion of the carriage can be controlled in both forward and reverse direction with lead screw. The shoe is polished when the carriage comes closer to the polishing brush during its forward motion. At the extreme point of the forward motion of carriage, the push button switch is actuated which alters the direction of lead screw, and the rest shining process is performed due to fast rotating brush [5]. D. Srihari et al. designed a portable coin operated machine applying the Raspberry Pi and open-source computer vision library (Open CV). This work aimed at bringing practicality in shoe polishing machines to be self-operated at public places [6]. Gouda et al. demonstrated a shoe sole cleaning and buffing machine using the gear train mechanism [7]. Liu et al. presented a control system for automated ceramic polishing machine [8].

Adaptive neuro-fuzzy inference system (ANFIS) builds a fuzzy inference system (FIS) by means of the toolbox function or the input/output data set. Its membership function parameters are estimated with a back-propagation algorithm alone or with a combination of back-propagation and least squares method. ANFIS is jointly based on the principles of fuzzy logic and neural networks both [9]. Shibendu Shekhar Roy estimated surface roughness in turning operation by designing an adaptive neuro-fuzzy interface system. In this work, two shapes (bell-shaped and triangle) of membership functions were considered for estimating roughness using ANFIS. The results depicted that both membership function attained suitable accuracy, still the accuracy of bell-shaped membership function is somewhat higher [10].

2 Methodology

Modelling of an automated shoe polishing programme is based on inputs of quality of the shoe material and the brightness of shine required over the shoes. This provides force to be applied by the brush on the shoe and amount of liquid polish to be applied to get the required amount of shine.

This above situation can be generally described as shown in Fig. 1. On the one hand, the shine on the shoe can be varied from dull to bright in the given condition. On the other hand, shoe surface can be varied from soft to rough depending upon the material quality of the shoe. The matrix in Fig. 1 provides intensity of the brush force required based on the two parameters by, namely material quality of the surface and shine of the shoes. From the real-life observations and expert opinions obtained from boot polishers, the amount of polishing required for glittering shine of the surface is an important factor which must be considered while designing such device. In general cases, the shoes are monochromatic and get the shine by the continuous and careful rubbing of the surface along with small amount of lubrication to soften the surface (Fig. 2).

In the matrix shown in above figures, the shine of the shoe (SH) is in increasing order from dull to bright. Also, the vertical direction is the material quality (MQ) in increasing order from top to bottom that includes soft, med and rough categories. The

Fig. 1 Brush force variation

SH MQ	DULL	MED	BRIGHT
SOFT	MILD	GENTLE	GENTLE
MED	HARSH	MILD	GENTLE
ROUGH	HARSH	HARSH	MILD

Fig. 2 Volume of polish variation

matter provides the volume of polish or rubbing required to be applied varying from very low (VL) to very high (VH). The point selection plays a very important role as it reflects the accuracy of data set points and formation of membership functions which will be used further.

2.1 Modelling Methods

Recent advances in soft computing techniques have given rise to various application-based modelling tools. Neural networks and fuzzy-based modelling tools are very effective modelling methods for automating mechanisms based on artificial intelligence. Data-based statistics are applied to form the rule bases from the models to predict the precise outcomes based on the input conditions.

2.2 Fuzzy Modelling

A very convenient method to map input spaces to the output spaces is using the fuzzy logic. The method to formulate the mapping or a given input to an output applying the fuzzy logic is known as fuzzy inference. This involves the membership functions, fuzzy logic operators and if–then rules set. A curve that designates how each point in input space is related to a degree of membership (also known as membership value) between 0 and 1 is known as membership function. Fuzzy inference systems are divided into two ways generally, the Mamdani-type and Sugeno-type. These two types of inference systems vary somewhat in the way outputs are determined [11].

The most common fuzzy inference methodology is the Mamdani's fuzzy inference system. Mamdani's method was the very initial control systems developed using fuzzy set theory, which was proposed in 1975 by Ebrahim Mamdani [12] in an attempt to develop a control system for a steam engine coupled with boiler by synthesizing a set of linguistic rules obtained by experienced human operators. Ebrahim Mamdani's
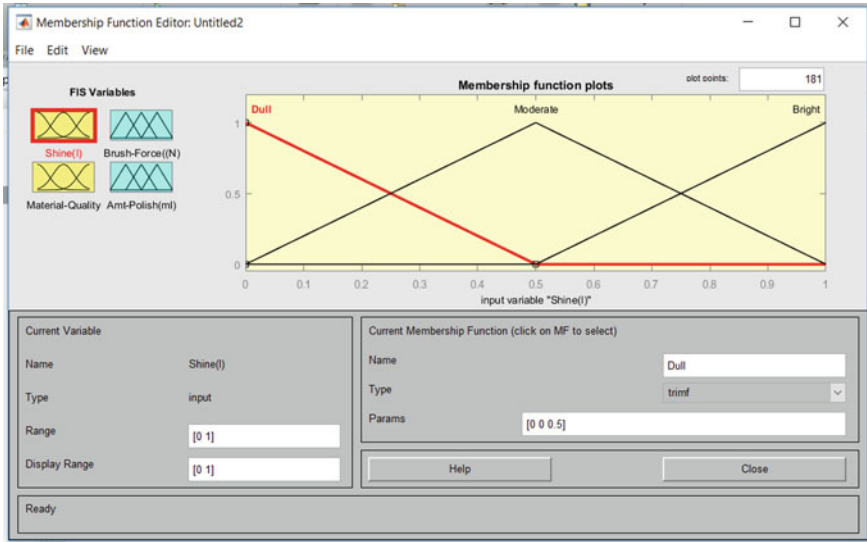
Fig. 3 Input 1 (Shine)

work was based on Lotfi Zadeh's 1973 paper on fuzzy algorithms for complex systems and decision processes [13].

The Mamdani-type inference is used to predict the output membership functions to be fuzzy sets. After the aggregation of the process, the outcome in the form of fuzzy set for each variable is to be passed through defuzzification. It is possible to have either a singleton output membership function as output or multiple sets of membership functions.

To completely specify the working of fuzzy inference system, we divide the working into three main parts.

- **Input**: The input includes the operators such as AND operator and OR operator to combine the multiple input membership functions.
- **Process**: The processing part where the calculations takes place using the membership functions.
- **Output**: The output is given out in membership functions, and the defuzzified form of it gives the exact values of output.

2.3 Modelling Steps

The steps involved to develop the final model are as follows:

Inputs. There are dual inputs. The first input is the shine of shoes which is present on the shoes. It varies from dull to bright. Here we have used the triangular membership
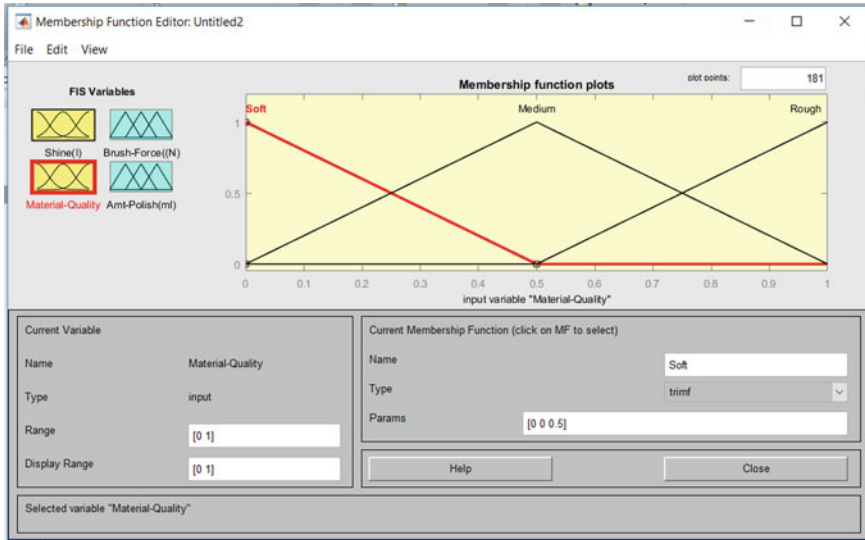
Fig. 4 Input 2 (material quality)

function (Fig. 3). The second one is the material quality of the shoes. This varies from soft to rough. The triangular membership is applied here too (Fig. 4).

The triangular membership functions defining the first input shine. Three triangular membership functions are used to complete the set: the dull set, moderate set and the bright set.

Outputs. The outputs are also dual. The first output is the brush force required for polishing. It varies from gentle to harsh (Fig. 5). The second output which we get will be the amount of polish required to apply. It varies from very low to very high (Fig. 6).

Rule base. The formation of rule base is using the operators. Here the basic equation is applied using the AND operator. The general equation being of the form. If p is A and q is B, then r is C and s is D, where 'A' and 'B' are the fuzzy sets in the antecedent (here the *shine* and *material quality*) and C and D are the fuzzy sets in the subsequent (here *brush force* and *amount of liquid*).

The rule base is defined as follows:

- If shine is dull and material quality is soft, then brush force is mild, and amount of polish is medium.
- If shine is dull and material quality is medium, then brush force is harsh, and amount of polish is high.
- If shine is dull and material quality is rough, then brush force is harsh, and amount of polish is very high.
- If shine is moderate and material quality is soft, then brush force is mild, and amount of polish is low.
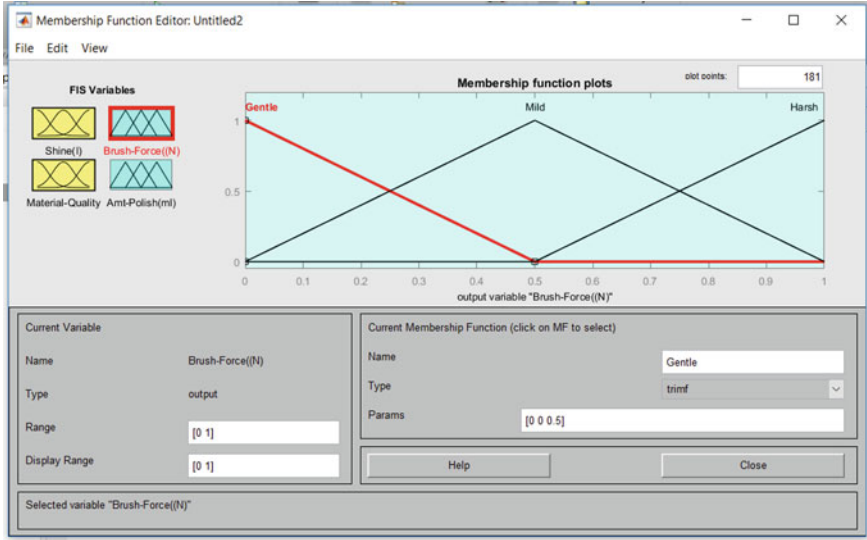
Fig. 5 Output 1 (brush force required for polishing in Newton)
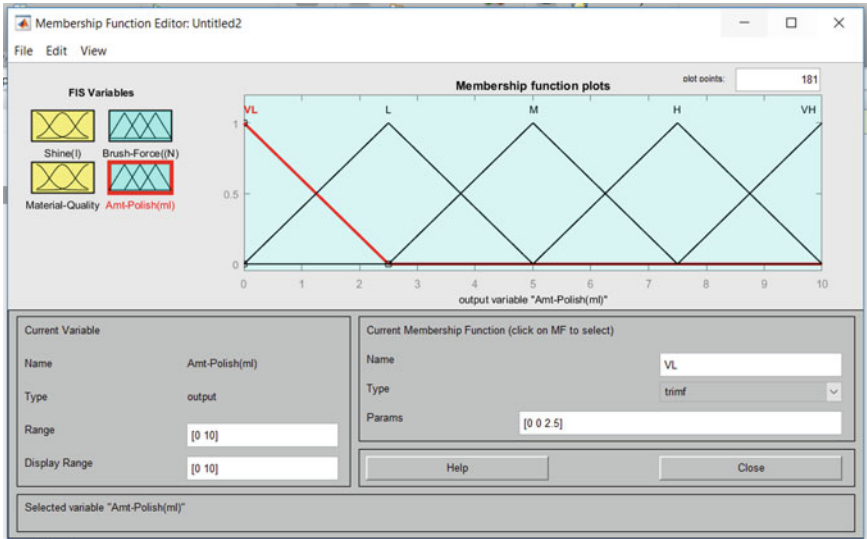
Fig. 6 Amount of polishing liquid required (in ml)

- If shine is moderate and material quality is medium, then brush force is mild, and amount of polish is medium.
- If shine is moderate and material quality is rough, then brush force is mild, and amount of polish is high.
- If shine is bright and material quality is soft, then brush force is gentle, and amount of polish is very low.
- If shine is bright and material quality is medium, then brush force is gentle, and amount of polish is low.
- If shine is bright and material quality is rough, then brush force is mild, and amount of polish is medium.

The rule base table used in the M-ANFIS model used here is shown in Fig. 7.
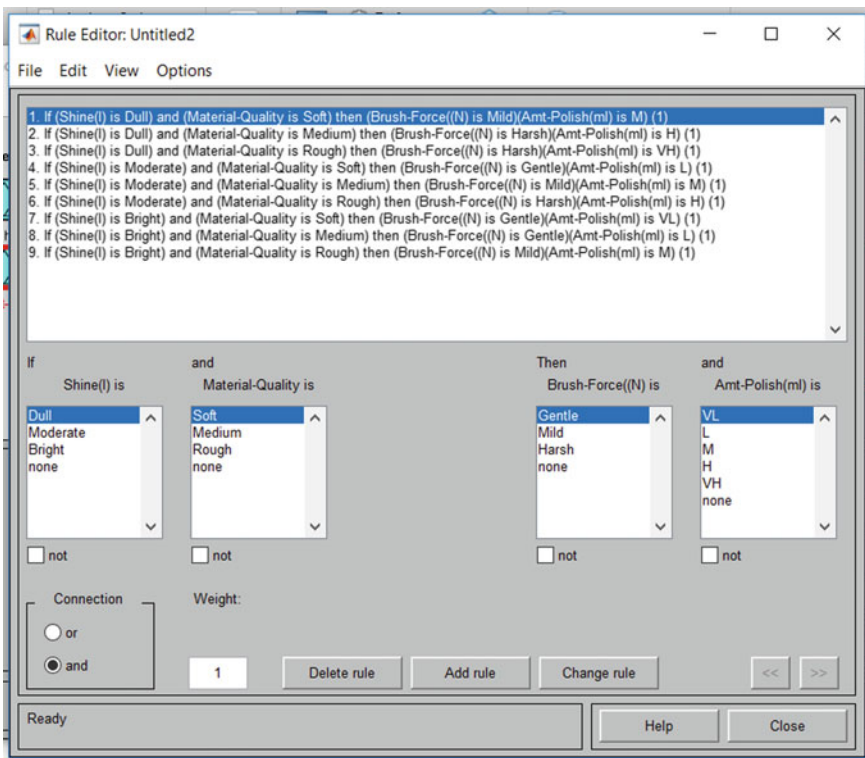
Fig. 7 Rule base used in the model

3 Result

The results obtained using this model were very effective closely compatible with the data set. The model gives results closely linked with practical observations, and outputs obtained are very close to the general human cognition process. The results are depicted in Fig. 5 for the brush force required and in Fig. 6 for the amount of polishing liquid required. The rule base shown in Fig. 7 also depicts the application of ANFIS for different input condition. For example, if material of the shoe is soft, the required brush force will be of gentle grade and lesser amount of polishing liquid will be required.

4 Conclusion

In this paper, adaptive neuro-fuzzy inference system (ANFIS) was used to demonstrate an automatic shoe polishing machine. This ANFIS helped in regulating the required force of the polishing brush and the amount of polishing liquid. The current available machines have brush designed to rotate at fixed rpm, whereas applying this model it can be varied as per the requirement. Here, we get the brush force which can also be compatible for reciprocating brush mechanisms. The rpm can easily be calculated using the power and torque equation by defining the radius. The novelty of this model is that it is very close to a common human cognition based on experience that makes the machines working on this model optimum in use and close to the actual output which is best polishing of the shoes. Future researches should be concentrated on the automation of similar kinds of domestic and industrial process.

References

1. Parasuraman R., Sheridan T.B., Wickens, C.D.: A model for types and levels of human interaction with automation. IEEE Transactions on Systems, Man, and Cybernetics Part A: Systems and Humans (2000).
2. Parasuraman, R., Riley, V.A.: Humans and automation: Use, misuse, disuse, abuse. Hum. Factors **39**, 230–253 (1997)
3. Woods, D.: Decomposing automation: apparent simplicity, real complexity, Human Performance in Automated Systems: Current Research and Trends (1994)
4. https://www.oxfordlearnersdictionaries.com/definition/english/automation. Last accessed 30 April 2020
5. Neermarga, A.A., Chirag V.R., Martis, D.P.: Design and fabrication of automatic shoe polishing machine. Nat. Conf. Adv. Mech. Eng. Sci. (2016)
6. Srihari, D., Ravi Kumar, B., Yuvaraj, K.: Development of Indian coin based automatic shoe polishing machine using raspberry pi with open CV. Int. J. Adv. Res. Elect. Elect. Inst. Eng. **1**(3), 228–234 (2012)
7. H.T., S., Gouda, S.: Design of shoe sole cleaning with polishing machine. Int. J. Innovat. Res. Sci. Eng. Technol. **2**(9), 5022–5029 (2013)

8. Liu, W., Chi, Y., Li, M., Tong, H.: Research on control system of new type ceramic polishing machine. In: Mechanic Automation and Control Engineering (MACE), Second International Conference IEEE Hohhot, pp. 1529–1532 (2011).

9. Jang, J.S.R., Sun, C.T., Mizutani, E.: Neuro-fuzzy and soft computing-a computational approach to learning and machine intelligence. Autom. Control, IEEE Trans. **42**(10), 1482–1484 (1997)

10. Shibendu Shekhar Roy: Design of adaptive neuro fuzzy interface system for predicting surface roughness in turning operation. J. Sci. Ind. Res. **64**, 653–659 (2005)

11. Jang, J.S.R., Sun, C.T.: Neuro-Fizzy modeling and control. Proc. IEEE **83**(3) (1995)

12. Mamdani, E. H., & Assilian, S.: An experiment in linguistic synthesis with fuzzy logic controller. Int. J. Man–Mach. Stud. **7**(1), 1–13 (1975)

13. Zadeh, L.A.: Outline of a new approach to the analysis of complex systems and decision processes. IEEE Transactions on Systems, Man and Cybernetics **3**(1), 28–44 (1973)

Development and Properties of Aluminium-Based Metal Matrix Composite: A Review

Sourav Kumar Gupta [ORCID] **, Siddharth Chauhan, Shivam, and Ravi Butola**

1 Introduction

Friction stir processing (FSP) uses the equivalent principles as friction stir welding (FSW) [1]. The difference is, instead of mixing the samples, this method modifies the local microstructure of monolithic samples to absorb specific and desired properties by altering the surface of the microstructure. As in FSW, the tool induces plastic flow during the method. The choice of process parameters, such as applied force, travel speed and rotational speed, gives the fabric flow a modified microstructure that is beneficial to the fabric's functionality. Introduced by Mishra in 2000, this innovative process can be relatively new for microstructural development and modification.

In FSP process, the pin is submerged in the processed material towards the rotating tool that rotates the final metals. The tool (Fig. 1a) crosses the revised direction, rotating the shoulder under the applied load effect and heating the metal around the revised area and flowing and forming the metal from each section with the rotating action of the pin, to cause localized microstructural modification for improved specific and required enhancement of properties [2]. For example, a fine-grained microstructure for increased strain rate super plasticity was fabricated in the commercial 7075Al alloy through FSP [3, 4]. Also, for surface composite on aluminium substrate fabrication, FSP technology is widely used [5]. The first important area of FSW is the turbulent region, and they are often identified as first in the differences between FSP and FSW processes. The second main differentiation is that the main area of the FSP is the zone directly under the pin, and the FSW does not matter because the welding technique with material thickness is common [6].

S. K. Gupta (✉) · S. Chauhan · Shivam · R. Butola
Department of Mechanical, Production & Industrial and Automobile Engineering, Delhi Technological University, North West Delhi, Delhi 110042, India
e-mail: souravkgupta999@gmail.com
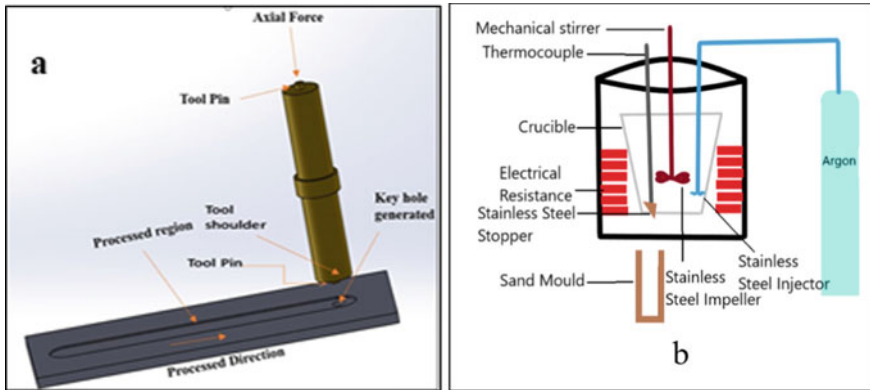
Fig. 1 **a** Schematic of friction stir processing **b** Schematic of stir casting [2, 7]

2 Literature Survey on Experimental Details

Ramezani et al. (2019) cited the dimensions of base plate of Al 7075 as 100 mm x 200 mm × 10 mm. A groove was made of the dimension of 100 mm × 2 mm × 4 mm. SiC nano powder was used as reinforcement having an average size of 45–65 nm and with a purity approaching to 100% [8]. Input parameters were selected according to screening tests, literature reviews and previous studies [9–12]. Azimi et al. (2017) used 5-mm-thick rolled 1050 aluminium alloy as base material and filled with milled powder mixture of Fe_2O_3-Al. The groove was having dimension of 1.4 mm width and 3.5 mm depth. The ratio of Fe_2O_3 to Al powder was 2.2 wt% [13]. Jafari et al. (2014) [12] used carbon nanotubes (CNT) of mean size of 20–30 nm and purity of more than 95% as reinforcement and cold rolled copper of dimensions 70 mm × 100 mm × 6 mm as base material, and the effect of inclusion of CNT into pure copper was studied via friction stir processing. In this, using different shoulders, a change in temperature peak of one-pass FSP was recorded. The processing tool had a tilt of an angle of 2.5° [14]. Khademi et al. (2016) used TiB_2 particles with 99.9% purity and size of about 200 nm as the reinforcement and rolled carbon steel plates having dimensions of 200 mm × 75 mm × 5.6 mm to fabricate surface MMC of low carbon steel and mechanical and microstructural properties were compared. The groove had dimensions of a 1 mm width and depth of 2 mm. The rotational speed of 1000 rpm and two traversing speeds (4 and 8 mm/s) were selected. The angle of separation was chosen 3° [15]. Yoshihiko et al. (2011) fabricated A1050-A6061 aluminium alloy and formed A1050-A6061 aluminium foam using FSP, the rotation speed was set at 1000 rpm, and the speed of welding speed was set at 100 mm/min with an angle of tilt angle of 3°, was used in accordance with a previous study on fabricating aluminium foam [16] and A6061 aluminium foam [17]. Naik et al. (2019) used 4-mm-thick plates of Cu with 0.18 wt% Zr alloy as the base metal. FSP was done on the surfaces of the plates, with the help of a pin tool having cylindrical shape of diameter 3 mm and length of 6 mm. Tool shoulder was having diameter 18 mm. The tool's

rotational speed was fixed as 600 rpm, and the traversing speed ranged between 50 and 200 mm/min with gaps of 50 mm/min. A solution was prepared that contained 5 ml of $FeCl_3$, 2 ml HNO_3, and 93 ml distilled water so as to observe the specimen's microstructure with the help of electron microscope [18]. Rana et al. used the Al7075 plates as base metals of dimensions $100 \times 100 \times 6.5$ mm. Dimensions of 1.2 mm $\times$ 2.5 mm $\times$ 100 mm were used to make a groove on the base plate. B_4C having size 12–15 μm was used. The groove cavity was closed using a pin less tool, and pin possessing a taper cylindrical profile was used for stirring passes. The traverse speed of tool was varied, and the rotational speed of the tool was kept constant at 545 rpm [19]. Ramesh et al. calculated the mean hardness of the surface composite fabricated after FSP, and it was concluded that it was 61–62% higher compared to the base metal of Al7075-T651. Al7075-T651 was used as base metal (matrix), and B_4C particles were used as reinforcement. The increased hardness was found due to the uniform distribution of B_4C particles. A groove of dimension 0.5 mm $\times$ 2.5 mm $\times$ 100 mm was produced on the base plate. The tool used was made up of high carbon chromium steel having the cylindrical profile surface [20]. Akash et al. analysed the defects due to two different feed rates, i.e. 40 and 50 mm/min and studied the effect of tool profiles like cylindrical and truncated probe tool. It was found that the defects produced by the cylindrical tool are greater than those produced by truncated tool profiles. AZ31 magnesium alloy having a very good strength to weight ratio was chosen for FSP. H13 having shoulder diameter 18 mm, pin diameter 6 mm and length of pin 5.36 mm was chosen as tool material. For stirring action, a tilt angle of 1.80° was kept constant, and rubbing action of leading edge of shoulder was avoided [21]. Mahmud et al. found that there was uniform distribution of reinforcement particles in the matrix and did not have any defects except for the small voids present about the Al_2O_3 particles [22]. Chen et al. fabricated rods of length 85 mm and diameter of 45 mm as ingots and then thixoforming was done. Finally, a plate of dimensions 100 mm $\times$ 40 mm $\times$ 15 mm was produced. For comparison purpose, plates of dimension 200 mm $\times$ 200 mm $\times$ 15 mm were also produced [23]. The dimensions of the tool pin were 7 mm diameter and height of 5 mm. The diameter of the shoulder was 20 mm, and a constant tilt angle of 3° was employed. The rotational speed of tool was kept constant at 450 rpm, and traverse speed was set at 60 mm/min [24]. Butola et al. use pure Al6061 as the matrix in the process of fabrication of composite. Banana ash, coconut ash and sugarcane ash with SiC were used as reinforcement for three different samples and their hardness, and yield strength was calculated.
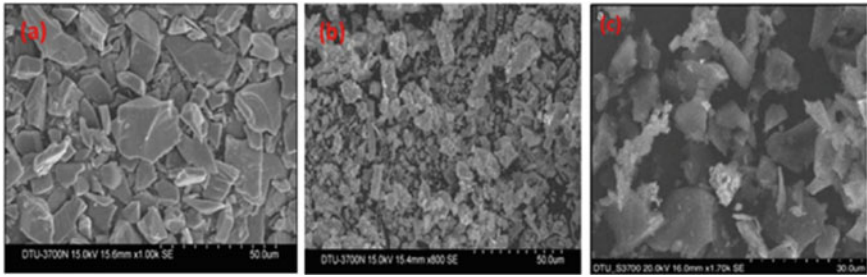
Fig. 2 Scanning electron microscope image of **a** SiC at 50 microns, **b** Rice Husk Ash at 50 microns and **c** B$_4$C at 30 microns [2]

3   Review and Discussion

3.1   *Microstructural Characteristics*

Chen et al. The grain refinement was seen ue to plastic deformation [23–27]. Four different zones were found, namely nugget zone, heat-affected zone, thermo-mechanically affected zone and parent material [12, 24]. It was reported that there was improvement in material microstructure, and homogeneity was observed due to severe plastic deformation [28, 29]. It was found that due to the huge role of dynamic recrystallization, the grain size became very fine as compared to base material [29–31]. Naik et al. [18] found that the grain size got reduced when the travel speed was increased. The least was found to be 4.6 microns [31]. Vipin et al. [32] fabricated a composite having aluminium as base metal and graphite as reinforcement using three different concentrations of graphite particles, viz. 2%, 4% and 6%. The composite was fabricated using the stir casting method. The stir casting set-up in shown in Fig. 1b [7]. Ravi et al. performed tensile testing on four different composites of Al6061. Figure 2 shows the SEM image of SiC at 50 microns, RHA particles at 50 microns and B$_4$C at 30 microns [2].

3.2   *Microhardness*

Mahmud et al. came out with the conclusion that base metal's average hardness is directly proportional to amount of SiC added and inversely to the Al$_2$O$_3$ particles [22]. Ramezani et al. [8] found that at best, the microhardness increased to 156% of the base metal. The best microhardness level was found to be 127.24 when the rotational speed was 900 rpm, traverse speed was 50 mm/min, and three passes were performed [9, 33]. Ghasem et al. concluded that there was little increase in hardness of base material [13, 33]. UTS of FSPed Al 1050 aluminium came out 97 MPa. Percentage elongation was found to be 64%. Chen T et al. [34, 35] also

reported the same result on the FSP of Al 1060 alloy. Rana et al. used Vickers hardness tester working at a load of 300 gm for a still time of 10 s, reported that there was an increment in hardness for about 40-70% as compared to the base metal. It was also found that increment in traverse speed and decrement in stirring speed have resulted in the reduction of hardness [19]. [Ravi et al.] Two results of hardness number and yield strength of each composite were obtained, and it was concluded that the sequence of hardness number and the yield strength in decreasing order were aluminium with banana ash, aluminium with coconut ash, aluminium with sugarcane ash and aluminium. Bar graph displaying mean hardness number and mean yield strength is shown in Fig. 3a, b, respectively. Graph showing comparison between the variance of hardness number and yield strength of all specimen is shown in Fig. 3c. It was deduced that due to role of different components and uncontrollable factors like temperature caused the variations in different composites [36]. Abhishek et al. prepared a nanocomposite of Al6061-SiC-graphite using friction stir processing and reported hardness and Young's modulus of the nanocomposite at 2200 rpm. Figure 4 shows the comparison of hardness, Young modulus and a curve between load and displacement [37]. Ravi et al. prepared five samples with a range of concentration of reinforcements. Coconut ash, sugarcane ash, groundnut shell ash and rice husk ash were used as reinforcements. It was found that the composite is with composition as rice husk ash 4% and aluminium 96%. Maximum hardness and maximum yield strength were found in composite with composition as coconut shell ash 4% and aluminium 96% [38].
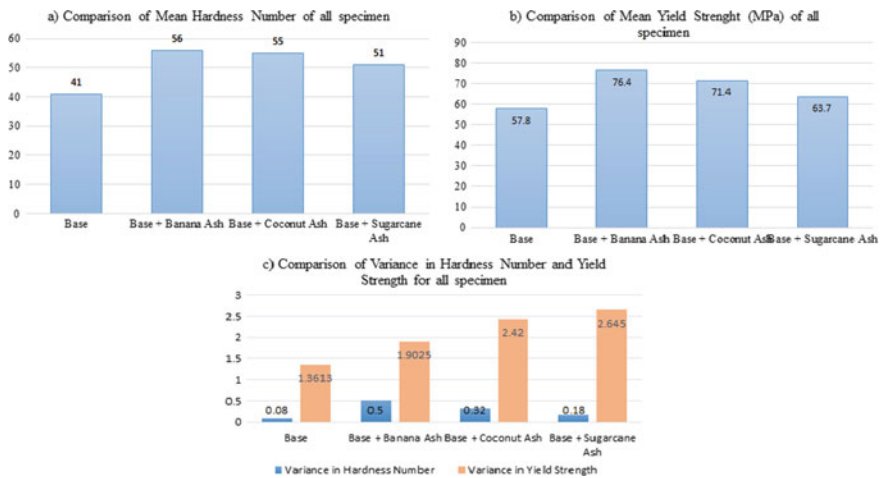
Fig. 3 Comparison of **a** mean hardness number and **b** mean yield strength of **c** comparison of variance for hardness number and yield number for four specimens [36]
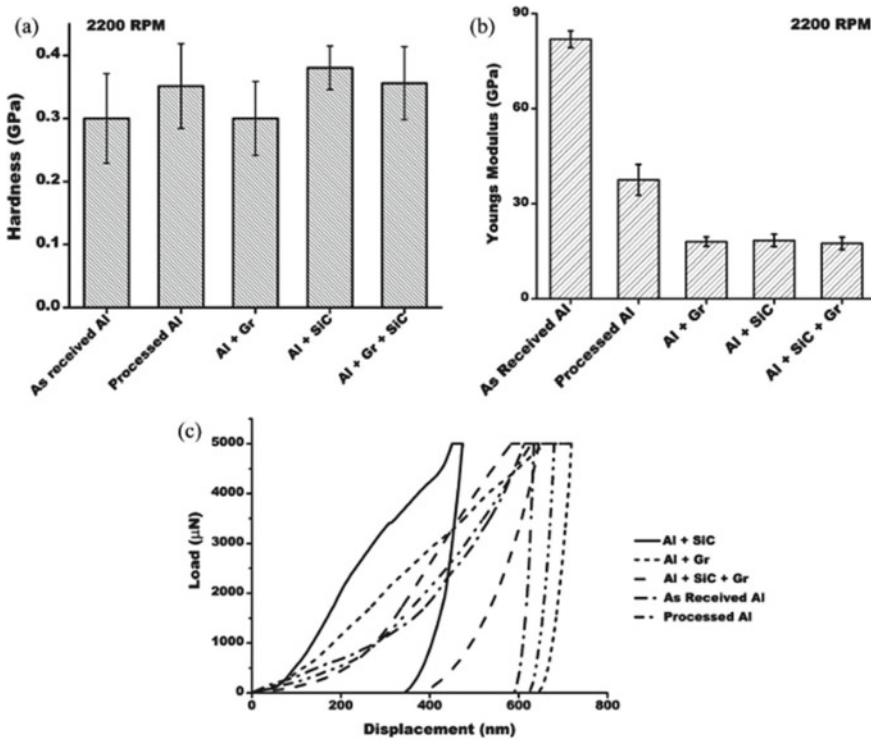
Fig. 4 Graphs of **a** hardness **b** Young's modulus and **c** load vs displacement curve [37]

3.3 Composite and Wear Resistance

It was found that the wear resistance of the FSPed alloy was far better than that fabricated through casting [24] and the friction coefficient decreased [12, 34]. It was observed that the wear resistance of thrice passed FSPed composite comes out to be three times that of pure copper. This is due to the formation of the graphite layer that acted as lubricant due to application of shear stress and hence reducing wear resistance and coefficient of friction [18, 39–41]. It was found that there was sudden increase in wear resistance after the FSP of the processed alloys because of the increment in the hardness of the alloy [32, 42–44]. Wear sensor was used to record the wear in micrometre units as a function of the length of the pin and plotted for sliding distance and is shown in Fig. 5a. Figure 5b shows the specific wear rate of the three samples. Initially, negative wear was indicated by the sensor, and then because of the breakdown of the wear particles, abrupt wear was recorded, as far as the coefficient of friction is concerned. It is shown in Fig. 6. After 200 m of starting running distance, this was because initially smeared layer was thin and resulting in metallic contact and hence friction coefficient increased. But when inclusion of graphite increased, that caused smeared layer to grow thick resulting in decrease in
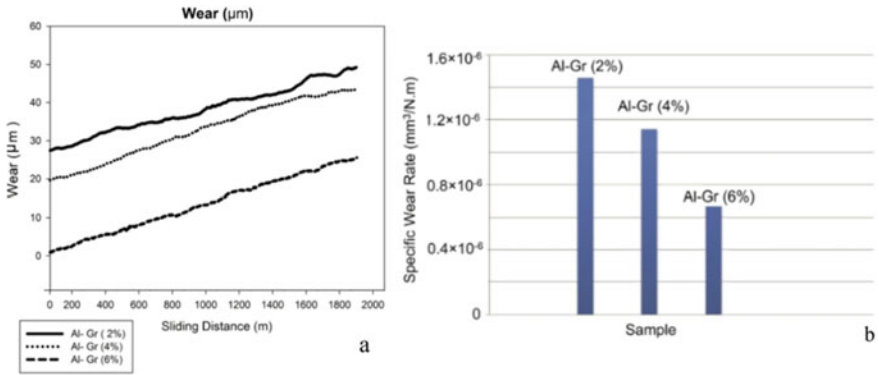
Fig. 5 Variation of **a** wear for Al-Gr of all 3, **b** specific wear rate for Al-Gr of all 3 samples [32]

Fig. 6 Curve of coefficient of friction vs distance [32]
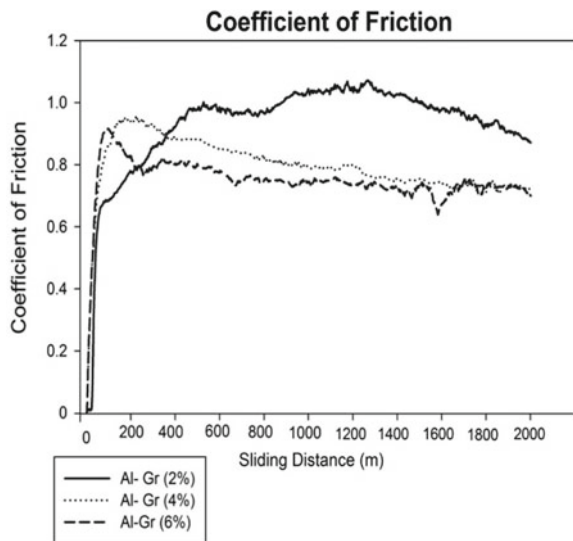
friction coefficient. Thus, it was seen that the higher the concentration of graphite leads to lesser the coefficient of friction. Ranganath et al. observed that the wear resistance increases and reached the maximum after second pass and then decreased for Al–Si hypoeutectic A356 alloy. Increase in ductility started after the third pass for same [45].

4   Conclusion

In this review paper, the mechanical, microstructural and wear properties of aluminium-based composites were discussed. It was found that the composites fabricated were showing improved properties than aluminium. After a review of the properties of composites, it can be concluded that

1. An increase in reinforcement particles increases the hardness number, yield strength and ultimate tensile strength of the aluminium-based metal matrix composites but it was seen that the variations in values were due to uncontrollable factors like temperature.
2. Microstructural properties improved because of dynamic recrystallization and homogeneity because of vigorous plastic deformation.
3. An increase in reinforcement leads to a decrease in wear and specific wear rates of the AMMCs as the wear and specific wear rates are inversely proportional to the amount of reinforcement added.
4. It was found that the coefficient of friction decreased on increasing the reinforcement after a running distance of 200 m in Al–Gr composite because of variation in thickness of smeared layer.

5   Future Scope

1. Discontinuous reinforcement can be used and compared with continuous ones.
2. Other mechanical test should be performed for more generalized results.
3. Reinforcement particles shapes and size could be an area of research.

References

1. Thomas, W.M., Nicholas, E.D., et al.: GB Patent Application No. 9125978.8 (1991)
2. Butola, R., Ranganath, M.S., Murtaza, Q.: 'Fabrication and optimization of AA7075 matrix surface composites using Taguchi technique via friction stir processing (FSP). Eng. Res. Express (2019). https://doi.org/10.1088/2631-8695/ab4b005
3. Mishra, R.S., Mahoney, M.W., McFadden, S.X., Mara, N.A., Mukherjee, A.K.: Scripta Mater. **42**, 163–168 (2000)
4. Ma, Z.Y., Mishra, R.S., Mahoney, M.W.: Acta Mater. **50**, 4419–4430 (2002)
5. Mishra, R.S., Ma, Z.Y., Charit, I.: Mater. Sci. Eng., A, **A341**, 307–10 (2002)
6. Węglowski, M.S.: Friction stir processing—state of the art. Arch. Civ. Mech. Eng. **18**(1), 114–129 (2018). https://doi.org/10.1016/j.acme.2017.06.002
7. Coyal, A., Yuvaraj, N., Butola, R., Tyagi, L.: An experimental analysis of tensile, hardness and wear properties of aluminium metal matrix composite through stir casting process. SN Appl. Sci. **2**(5) (2020). https://doi.org/10.1007/s42452-020-2657-8
8. Ramezani, N.M., Davoodi, B., Aberoumand, M., Hajideh, M.R.: Assessment of tool wear and mechanical properties of Al 7075 nanocomposite in friction stir processing (FSP). J. Braz. Soc. Mech. Sci. Eng. **41**, 182 (2019)

9. Asadi, P., Faraji, G., Besharati, M.K.: Producing of AZ91/SiC composite by friction stir processing (FSP). Int. J. Adv. Manuf. Technol. **51**(1–4), 247–26030 (2010)
10. Asadi, P., et al.: On the role of cooling and tool rotational direction on microstructure and mechanical properties of friction stir processed AZ91. Int. J. Adv. Manuf. Technol. **63**(9–12), 987–99731 (2012)
11. Asadi, P., et al.: Predicting the grain size and hardness of AZ91/SiC nanocomposite by artificial neural networks. Int. J. Adv. Manuf. Technol. **63**(9–12), 1095–110732 (2012)
12. Jafari, J., Givi, M.K.B., Barmouz, M.: Mechanical and micro-structural characterization of Cu/CNT nanocomposite layers fabricated via friction stir processing. Int. J. Adv. Manuf. Technol. **78**(1–4), 199–209 (2015)
13. Azimi-Roeen, G., Kashani-Bozorg, S.F., Nosko, M., Nagy, Š., Maťko, I.: Formation of Al/(Al$_{13}$Fe$_4$ + Al$_2$O$_3$) Nano-composites via Mechanical Alloying and Friction Stir Processing. J. Mater. Eng. Perform. **27**(2), 471–482 (2018)
14. Khosravi, J., Beshrati Givi, M.K., et al.: Microstructural, mechanical, and thermophysical characterization of Cu/WC composite layers fabricated via friction stir processing. Int. J. Adv. Manuf. Tech. (2014). https://doi.org/10.1007/s00170-014-6050-x
15. Khademi, A.R., Afsari, A.: Fabrications of surface nanocomposite by friction stir processing to improve mechanical and microstructural properties of low carbon steel. Trans. Indian Inst. Met. **70**(5), 1193–1198 (2016). https://doi.org/10.1007/s12666-016-0912-x
16. Hangai, Y., Utsunomiya, Y., Hasegawa, M.: J. Mater. Process. Technol. **210**, 288–292 (2010)
17. Utsunomiya, T., Tamura, K., Hangai, Y., Kuwazuru, O., Yoshikawa, N.: Mater. Trans. **51**, 542–47 (2010)
18. Bheekya Naik, R., Venkateswara Reddy, K., Madhusudhan Reddy, G., Arockia Kumar, R.: Development of high-strength and high-electrical conductivity Cu–Zr alloy through friction stir processing. Trans. Indian Inst. Met. (2019). https://doi.org/10.1007/s12666-019-01623-1
19. H.G. Rana,V.J. Badheka, A. Kumar, Fabrication of Al7075/B4C surface composite by novel friction stir processing and investigation on wear properties. Proc Technol. **23**, 519–528 (2016)
20. R. Ramesh, Murugan, N., Production and characterization of aluminum 7075-T651/B 4 C surface composite by friction stir processing. IJEAT **2**(1) (2012). ISSN: 2249-8958
21. Gupta, Akash, Singh, Prabhoj, Gulati, Piyush, Shukla, Dinesh Kumar: Effect of tool rotational speed and feed rate on the formation of tunnel defect in friction stirs processing of AZ31 Magnesium alloy. Mater. Today Proc. **2**, 3463–3470 (2015)
22. Essam, R.I.Mahmoud, Takahash, Makoto, Shibayanagi, Toshiya, Ikeuchi, Kenji: Wear characteristics of surface hybrid MMCs layer fabricated on aluminum plate by friction stir processing. Wear **268**, 1111–1121 (2010)
23. Chang, C.I., Dua, X.H., Huang, J.C.: Achieving ultrafine grain size in Mg–Al–Zn alloy by friction stir processing. Scripta Mater. **57**, 209–212 (2007)
24. Chen, T., Zhu, Z., Ma, Y., Li, Y., Hao, Y.: Friction stir processing of thixoformed AZ91D magnesium alloy and fabrication of surface composite reinforced by SiCps. Journal of Wuhan University of Technology-Mater. Sci. Ed., 25(2), 223–227 (2010). https://doi.org/10.1007/s11595-010-2223-0
25. Charit, I., Mishra, R.S.: Low temperature superplasticity in a friction-stir-processed ultrafine grained Al–Zn–Mg–Sc Al–loy. Acta Mater. **53**, 4211–4223 (2005)
26. Feng, A.H., Ma, Z.Y.: Enhanced Mechanical Properties of Mg–Al–Zn Cast Alloy via Friction Stir Processing. Scripta Mater. **56**, 397–400 (2007)
27. Sato, Y.S., Park, S.H.C., Matsunaga, A., et al.: A novel production for highly formable mg alloy plate. J. Mater. Sci. **40**, 637–642 (2005)
28. Liu, L., Nakayama, H., Fukumoto, S., Yamamoto, A., Tsubakino, H.: Microstructural evolution in friction stir welded 1050 aluminum and 6061 aluminum alloy. Mater. Trans. **45**(8), 2665–2668 (2004)
29. Barmouz, M., Besharati Givi, M.K., Seyfi, J.: On the role ofprocessing parameters in producing Cu/SiC metal matrix composites via friction stir processing: investigating microstructure, microhardness, wear and tensile behavior. Mater. Charact. **62**, 108–117 (2011)

30. Khosravi, J, Beshrati Givi, M.K., et al.: Microstructural, mechan-ical, and thermophysical characterization of Cu/WC composite layersfabricated via friction stir processing. Int. J. Adv. Manuf. Tech. (2014). https://doi.org/10.1007/s00170-014-6050-x

31. Barmouz, M., Asadi, P., Besharati Givi, M.K., Taherishargh, M.: Mater Sci Eng **A528**, 740 (2011)

32. Sharma, V.K., Singh, R.C., Chaudhary, R.: Wear and friction behaviour of aluminium metal composite reinforced with graphite particles. Int. J. Surf. Sci. Eng. **12**(5/6), 419 (2018). https://doi.org/10.1504/ijsurfse.2018.096753

33. Cavaliere, P., De Marco, P.P.: Superplastic behaviour of friction stir processed AZ91 magnesium alloy produced by high pres-sure die cast. J. Mater. Process. Technol. **184**, 77–83 (2007)

34. Chen, T.J., Ma, Y., Li, B., et al.: Wear behavior of thixoformed AZ91D magnesium alloy: a comparison with permanent mould cast alloy. Mater. Sci. Eng., A **445–446**, 477–485 (2007)

35. Bahrami, M., et al.: On the role of pin geometry in micro-structure and mechanical properties of AA7075/SiC nano-com-posite fabricated by friction stir welding technique. Mater. Des. **53**, 519–527 (2014)

36. Butola, R., Pratap, C., Shukla, A., Walia, R.S.: Effect on the mechanical properties of aluminum-based hybrid metal matrix composite using stir casting method. Mater. Sci. Forum **969**, 253–259 (2019). https://doi.org/10.4028/www.scientific.net/msf.969.253

37. Sharma, A., Sharma, V.M., Mewar, S., Pal, S.K., Paul, J.: Friction stir processing of Al6061-SiC-graphite hybrid surface composites. Mater. Manuf. Processes **33**(7), 795–804 (2017). https://doi.org/10.1080/10426914.2017.1401726

38. Butola, R., Malhotra, A., Yadav, M., Singari, R., et al.: Experimental studies on mechanical properties of metal matrix composites reinforced with natural fibres ashes. SAE Technical Paper 2019-01-1123 (2019). https://doi.org/10.4271/2019-01-1123

39. Barmouz, M., Besharati Givi, M.K.: Fabrication of in situ Cu/SiC composites using multi-pass friction stir processing: evaluation ofmicrostructural, porosity, mechanical and electrical behavior. Compos. Part A **42**, 1445–1453 (2011)

40. Barmouz, M., Abrinia, K., Khosravi, J.: Using hardness measurement for dislocation densities determination in FSPed metal in order to evaluation of strain rate effect on the tensile behavior. Mater SciEng. A **559**, 917–919 (2013)

41. Scharf, T.W., Neira, A., et al.: Self-lubricating carbon nanotube reinforced nickel matrix composites. J. Appl. Phys. **106**, 013508–013515 (2009)

42. Surekha, K., Els-Botes, A.: Mater. Des. **32**, 911 (2011)

43. Lee, M., Kang, S.B., Sato, T., Tezuka, H., Kamio, A.: Evolution of Iron aluminide in Al/Fe in situ composites fabricated by plasma synthesis method. Mater. Sci. Eng., A **362**(1), 257–263 (2003)

44. Ke, L., Huang, C., Xing, L., Huang, K.: Al-Ni intermetallic composites produced in situ by friction stir processing. J. Alloys Compd. **503**(2), 494–49930 (2010)

45. Chaudhary, A., Kumar Dev, A., Goel, A., Butola, R., Ranganath, M.S.: The mechanical proper-ties of different alloys in friction stir processing: a review. Mater. Today: Proc. **5**(2), 5553–5562 (2018). https://doi.org/10.1016/j.matpr.2017.12.146

Analysis and Modeling of Value Stream Mapping Success Factors

Lakhan Patidar [ORCID]**, Vimlesh Kumar Soni, and Pradeep Kumar Soni**

1 Introduction

During the First World War, Henry Ford [1] given an evolutionary concept of 'mass production' to industries. After that, 'lean manufacturing' has become more popular than 'mass production'. It is an innovative and effective approach to performance evaluation, documentation, and analysis that is very accepted worldwide [2]. Rother and Shook [3] were the first two researchers to transform the working style of the Toyota Production System (TPS) with value stream mapping into a practical guide called 'Learning to See.' VSM can become an innovative and valuable lean concept in revealing improvement potential for Indian Industries [4]. Developed countries have successfully increased performance of its industries by using VSM practices, while Indian economies still unaware about drastic benefits of effective VSM implementation. One reason behind this fact is that Indian company are so busy with their day-to-day management activity that they do not have the time and resources to devote their strategic understanding of the need for value stream mapping. After the effective implementation of the VSM lean tool, most Indian industries can increase their productivity and remain in a competitive world market for a long time. The role of value stream mapping and its practices needs to be identified and recognized as an important research area. However, some of the important observation found for lacking performance of Indian industries and its growth. They could be summed up as

- Still little study of VSM transformation in Indian industries;

L. Patidar (✉)
Department of Production and Industrial Engineering, M.B.M. Engineering College, JNV University, Jodhpur, India
e-mail: lakhanmanit@rediffmail.com; teqip.lakhan.pi@jnvu.edu.in

V. K. Soni · P. K. Soni
Department of Mechanical Engineering, Maulana Azad National Institute of Technology (MANIT), Bhopal, India

- The status of basic VSM success factors in Indian industries yet to be explored.

  Thus, above gaps can be addressed in the following way:

- The success factors of VSM specific to Indian industries still need to be defined.

  The overall research objective will be achieved through breaking down the research into four sections:

1. Identifying the VSM success factors with the help of domain experts and conducting a systematic review;
2. To establish levels of relationship for identified VSM success factors;
3. To establish contextual relationship for identified VSM success factors;
4. Development of a model and MICMAC analysis for highlighting importance of VSM success factor.

After a brief introduction, the next section reviews the literature on VSM and identifies key success factors. In 'Methodology' section, subsections, 'An ISM based approach to model factors' is presented. A 'MICMAC analysis' of the final ISM model is carried out later to understand the driving power and dependence power of the factors. Finally, the conclusions and contribution of the research have been presented.

2 Literature Review

Value stream mapping differs from traditional recording techniques, as it holds the essential information at manufacturing line about the set-up time, cycle time, WIP inventory, shop-floor space utilization, man power demand, and information flow [5, 6]. VSM incorporates both value-added and non-value-added, but addendum activities [7, 8]. The VSM focuses primarily on the section, sub-section of the production line and, setting targets for areas that actually require improvement [6, 9].

VSM is an effective integration of manpower, materials and machinery, and methods [10]. Khadse et al. [11] identifies key factors responsible for lean tool implementation in Indian enterprises and then incorporates these factors into a framework that can exactly illustrate the current as-in-situation of lean practices in Indian industries. VSM is a well-known visual lean tool that helps a manager to produce more with less resource [4, 12]. In view of the previous year's studies, Indian industries could not perform with its full capacity due to ineffective implementation of lean practices. Hence, a need is felt by industries to re-investigate into the success factors.

In current literature review, many authors are identified the critical factors of VSM in Indian context as presented in Table 1. From Table 1, fourteen factors identified and labeled from F1 to F14 in four review categories.

Success factors are top management commitment (F1), time and training provided by lean expert (F2), clarity of method (F3), organizational culture (F4), all employees' involvement (F5), material and information flow (F6), integration between processes

Table 1 Review of VSM success factors in Indian context

No.	Authors	Review categories[a]	Success factors with application													
			1	2	3	4	5	6	7	8	9	10	11	12	13	14
1	[13]	C3,C2	X	X	X											
2	[14]	C3	X			X					X					
3	[15]	C1			X							X				
4	[16]	C3					X							X	X	
5	[17]	C4, C3	X													X
6	[18]	C4					X			X			X	X		
7	[2]	C1						X	X			X		X		X
8	[19]	C3				X										
9	[20]	C4					X	X						X	X	
10	[21]	C1					X	X				X		X	X	
11	[22]	C1				X			X			X				X

[a]C1: Conceptual study, C2: case study, C3: empirical/modeling study, C4: survey study

(F7), process transparency and stability (F8), resource utilisation (F9), skilled people and work (F10), standardization of best practices (F11), supplier feedback (F12), customer orientation (F13), implementation with small VSM-related projects (F14). Review categories are conceptual study (C1), case study (C2), empirical study (C3), and survey-based study (C4).

3 Methodology

After identified fourteen value stream mapping success factors (14-VSMSFs), a questionnaire designed and conducted pilot test with two domain experts with an aim to maintain the quality of the survey instrument. The number of meetings have been arranged with fifteen domain experts including industry and academia to gather information about the VSM success factors. The primary aim of the study is to explore the interactions between all selected VSMSFs and to analyze the driving power and dependence power for effective execution of VSM practices in Indian small–medium-scale industries. In this study, no invalid responses were founded due to one-to-one interaction. Finally, Table 2 is prepared from an average mean

Table 2 Structural self-interaction matrix (SSIM)

SFs	Name of VSMSFs	14	13	12	11	10	9	8	7	6	5	4	3	2	1
1	Top management commitment	V	A	V	O	O	V	O	X	O	O	X	O	X	–
2	Time and training provided by lean expert	V	O	V	O	O	O	O	V	O	O	A	O	–	
3	Clarity of method/procedure	O	O	O	O	O	O	O	A	V	O	V	–		
4	Organizational culture	V	V	V	O	A	V	O	V	V	O	–			
5	All employees' involvement	O	O	O	A	A	O	V	O	X	–				
6	Smooth material and information flow	O	O	O	A	A	O	V	O	–					
7	Integration between processes	O	X	V	O	O	O	O	–						
8	Process transparency and stability	O	O	O	O	A	O	–							
9	Resource utilisation	V	O	V	O	O	–								
10	Skill people	O	O	O	V	–									
11	Standardization of best practices	O	O	O	–										
12	Supplier feedback	O	A												
13	Customer orientation	V	–												
14	Implementation of small VSM related project	–													

Rule: V: $i \rightarrow j$, A: $i \leftarrow j$, X: $i \leftrightarrow j$, O: $i \nleftrightarrow j$

of reactions of the domain experts. In the approach of ISM-MICMAC analysis, the results of the current study are broken down into two sections:

- Developing a structural model through ISM for VSM success factors;
- Conducting a cluster analysis through MICMAC approach.

3.1 ISM Analysis for VSM Success Factors

For analyzing the various success factors to develop relation matrix (Table 2), the following sign [23] has been applied in the Structural self-interaction matrix (SSIM) to represent the inter-relationships among the VSMSFs (from 'SFi' source to 'SFj' destination):

- V: forward link from SFi to SFj, i.e. Success factor SFi will support/help to achieve factor SFj;
- A: inverse relationship with destination 'SFj' to source 'SFi', that meaning is Success factor 'SFj' will contribute for achieving factor 'SFi';
- X: relationship in both sides, and
- O: both success factor having no relation to each other. Here, *i*th row = *j*th column = 1, 2, 3, …, 14.

According to the binary matrix conversion rule, structural self-interaction matrix (SSIM) relationships have been transformed into Initial Reachability binary format [4]. Table 3 shows the pair-wise binary relationship of 1 and 0. The transitivity is checked in Table 3 by using transitivity assumption [24]. If '*a*' is related to '*b*' and '*b*' is related to '*c*', then according to transitive assumption both '*a*' and '*c*' will have interrelationship with each other. Then, a final reachability matrix (Table 4) has been evolved by applying transitivity notation of '1*'.

There are numbers of transitive relationship found in final reachability matrix. Reachability sets and antecedent sets have been developed and are shown in Table 5. Reachability sets are the sets of those factors that have allotted the cells '1' for various *i*th rows (row 1 to row 14) in Table 4. The antecedent set is laid down for each factor containing VSMSFs that cells in column associated with each factor are assigned '1' in Table 4.

Further, Table 5 has been developed different levels and each level has a similar set of VSM factors. These levels are separated from Table 4 of final reachability matrix. However, a number of iterations are conducted for the purpose of levels partitions and are developed in Table 5 [25]. Initial iteration level is developed through comparing the reachability set and intersection sets value. If both sets are found same VSM factors, then assigned those factors as the level-I on the top of the framework.

Further, second level is developed by eliminating the row and column of those factors that were already occupied in level-I. In addition, the next iteration table is generated by removing the same factors from the antecedent set, reachability set, and intersection sets.

Table 3 Initial reachability matrix (IRM)

SFs	Name of VSMSFs	1	2	3	4	5	6	7	8	9	10	11	12	13	14
1	Top management commitment	1	1	0	1	0	0	1	0	1	0	0	1	0	1
2	Time and training provided by lean expert	1	1	0	0	0	0	1	0	0	0	0	1	0	1
3	Clarity of method/procedure	0	0	1	1	0	1	0	0	0	0	0	0	0	0
4	Organizational culture	1	1	0	1	0	1	1	0	1	0	0	1	1	1
5	All employees' involvement	0	0	0	0	1	1	0	1	0	0	0	0	0	0
6	Smooth material and information flow	0	0	0	0	1	1	0	1	0	0	0	0	0	0
7	Integration between processes	1	0	1	0	0	0	1	0	0	0	0	1	1	0
8	Process transparency and stability	0	0	0	0	0	0	0	1	0	0	0	0	0	0
9	Resource utilisation	0	0	0	0	0	0	0	0	1	0	0	1	0	1
10	Skill people	0	0	0	1	1	1	0	1	0	1	1	0	0	0
11	Standardization of best practices	0	0	0	0	1	1	0	0	0	0	1	0	0	0
12	Supplier feedback	0	0	0	0	0	0	0	0	0	0	0	1	0	0
13	Customer orientation	1	0	0	0	0	0	1	0	0	0	0	1	1	1
14	Implementation of small VSM related project	0	0	0	0	0	0	0	0	0	0	0	0	0	1

Binary matrix conversion rule: 'V' = '1', 'A' = '0', 'X' = '1', 'O' = '0'
Source Researcher's self calculation

Similarly, the third level is obtained by removing VSMSFs from second level. Thus, several iterations are developed until the final level is reached. The final iteration is developed and level-IV showed that all three sets of VSMSFs (antecedent set, reachability set, and intersection sets) are the same.

Further, Table 6 is presented the conical matrix that has been obtained by grouping the same levels of VSMSFs. For this, an iterative action is needed across the rows and columns of the final reachability matrix of VSM success factors. Also, levels are clubbed and modified by driving and dependent power. According to Table 6, the level-1 set includes four factors that tend to have lower driving power and higher dependence power. In addition, level-II contains two factors with moderate driving and dependent power. Similarly, level-III includes seven factors with moderately high driving and moderately low dependent power. Levels-IV includes single factor as 'skill people' that has high driving but very low dependence power.

Similarly, the third level is obtained by removing VSMSFs from second level. Thus, several iterations are developed until the final level is reached. The final iteration is developed and level-IV showed that all three sets of VSMSFs (antecedent set, reachability set, and intersection sets) are the same.

Further, Table 6 is presented the conical matrix that has been obtained by grouping the same levels of VSMSFs. For this, an iterative action is needed across the rows and columns of the final reachability matrix of VSM success factors. Also, levels are clubbed and modified by driving and dependent power. According to Table 6,

Table 4 Final reachability matrix (FRM)

SFs	Name of VSMSFs	1	2	3	4	5	6	7	8	9	10	11	12	13	14	DrP
1	Top management commitment	1	1	1*	1	0	1	1	0	1	0	0	1	1*	1	10
2	Time and training provided by lean expert	1	1	1*	1*	0	1	1	0	1*	0	0	1	1*	1	10
3	Clarity of method/procedure	1*	1*	1	1	1*	1	1*	1	1*	0	0	1*	1*	1*	12
4	Organizational culture	1	1	1*	1	1*	1	1	1	1	0	0	1	1	1	12
5	All employees' involvement	0	0	0	0	1	1	0	1	0	0	0	0	0	0	3
6	Smooth material and information flow	0	0	0	0	1	1	0	1	0	0	0	0	0	0	3
7	Integration between processes	1	1*	1	1*	1*	1*	1	1	1*	0	0	1	1	1*	12
8	Process transparency and stability	0	0	0	0	0	0	0	1	0	0	0	0	0	0	1
9	Resource utilisation	0	0	0	0	0	0	0	0	1	0	0	1	0	1	3
10	Skill people	1*	1*	1*	1	1	1	1*	1	1*	1	1	1*	1*	1*	14
11	Standardization of best practices	0	0	0	0	1	1	0	1*	0	0	1	0	0	0	4
12	Supplier feedback	0	0	0	0	0	0	0	0	0	0	0	1	0	0	1
13	Customer orientation	1	1*	1*	1*	1*	1*	1	1*	1*	0	0	1	1	1	12
14	Implementation of small VSM related project	0	0	0	0	0	0	0	0	0	0	0	0	0	1	1
	DeP	7	7	7	7	8	10	7	9	8	1	2	9	7	9	98/98

Note *Used in matrix for "rule of transitivity", SFs means "success factors", DeP means "dependents power", and DrP means "driving power"

Table 5 Level partition of the VSMSFs (iteration 1–4)

SFs	Name of VSMSFs	Reachability set	Antecedent set	Intersection	Level
1	Top management commitment	1,2,3,4,6,7,9,12,13,14	1,2,3,4,7,10,13	1,2,3,4,7,13	III
2	Time and training provided by lean expert	1,2,3,4,6,7,9,12,13,14	1,2,3,4,7,10,13	1,2,3,4,7,13	III
3	Clarity of method/procedure	1,2,3,4,5,6,7,8,9,12,13,14	1,2,3,4,7,10,13	1,2,3,4,7,13	III
4	Organizational culture	1,2,3,4,5,6,7,8,9,12,13,14	1,2,3,4,7,10,13	1,2,3,4,7,13	III
5	All employees' involvement	5,6,8	3,4,5,6,7,10,11,13	5,6	II
6	Smooth material and information flow	5,6,8	1,2,3,4,5,6,7,10,11,13	5,6	II
7	Integration between processes	1,2,3,4,5,6,7,8,9,12,13,14	1,2,3,4,7,10,13	1,2,3,4,7,13	III
8	Process transparency and stability	8	3,4,5,6,7,8,10,11,13	8	I
9	Resource utilisation	9,12,14	1,2,3,4,7,10,13	9	I
10	Skill people	1,2,3,4,5,6,7,8,9,10,11,12,13,14	10	10	IV
11	Standardization of best practices	5,6,8,11	10,11	11	III
12	Supplier feedback	12	1,2,3,4,7,9,10,12,13	12	I
13	Customer orientation	1,2,3,4,5,6,7,8,9,12,13,14	1,2,3,4,7,10,13	1,2,3,4,7,13	III
14	Implementation of small VSM related project	14	1,2,3,4,7,9,10,13,14	14	I

Table 6 Level partition of the VSMSFs (iteration 1–4)

SFs	VSM Success factors	14	8	12	9	5	6	11	1	2 4	7	13	3	10	DrP	Levels
14	Implementation of small VSM related project	1	0	0	0	0	0	0	0	0	0	0	0	0	1	I
8	Process transparency and stability	0	1	0	0	0	0	0	0	0 0	0	0	0	0	1	I
12	Supplier feedback	0	0	1	0	0	0	0	0	0 0	0	0	0	0	1	I
9	Resource utilisation	1	0	1	1	0	0	0	0	0 0	0	0	0	0	3	I
5	All employees' involvement	0	1	0	0	1	1	0	0	0 0	0	0	0	0	3	II
6	Smooth material and information flow	0	1	0	0	1	1	0	0	0 0	0	0	0	0	3	II
11	Standardization of best practices	0	1*	0	0	1	1	1	0	0 0	0	0	0	0	4	III
1	Top management commitment	1	0	1	1	0	1*	0	1	1	1	1*	1*	0	10	III
2	Time and training provided by lean expert	1	0	1	1*	0	1*	0	1	1	*1	1*	1*	0	10	III
4	Organizational culture	1	1*	1	1	1*	1	0	1	1	1	1	1*	0	12	III
7	Integration between processes	1*	1*	1	1*	1*	1*	0	1	1*1	*1	1	1	0	12	III
13	Customer orientation	1	1*	1	1*	1*	1*	0	1	1*1	*1	1	1*	0	12	III
3	Clarity of method/procedure	1*	1*	1*	1*	1*	1	0	1*	1*1	1*	1*	1	0	12	III
10	Skill people	1*	1	1*	1*	1	1	1	1*	1*1	1*	1*	1*	1	14	IV
	DeP	9	9	9	8	8	10	2	7	7 7 7	7	7	7	1	98/98	

*Used in matrix for "rule of transitivity". DeP means dependents power and DrP means Driving power
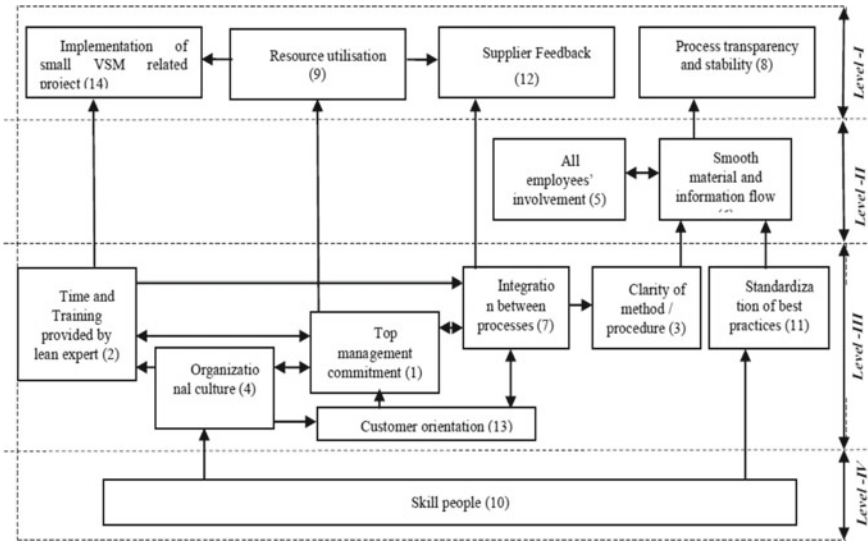
Fig. 1 ISM based framework represents the levels of VSM success factor

the level-1 set includes four factors that tend to have lower driving power and higher dependence power. In addition, level-II contains two factors with moderate driving and dependent power. Similarly, level-III includes seven factors with moderately high driving and moderately low dependent power. Level-IV includes single factor as 'skill people' that has high driving but very low dependence power.

Further, a directional graph is drawn by considering the interrelationship between VSM success factors from the final reachability matrix (Table 4). In addition, the transitivity of success factors is removed from the directional graph by changing the nodes with relationship statements. The relationship statements are examined by verifying the conceptual inconsistencies (if any) and the necessary modifications are made accordingly. However, the process is repeated till the inconsistency is removed from the final reachability matrix.

Finally, the ISM-based model (Fig. 1) is developed to set out the relationship statement into a framework for the VSM success factors.

4 Results and Discussions

4.1 Effectiveness and Rank of VSM Success Factors

The effectiveness of VSM success factors is the subtraction value of dependence power on the driver power in canonical matrix (Table 6). It is presented in Fig. 2. VSM success factors are set out on top of the framework while having low effectiveness. It is
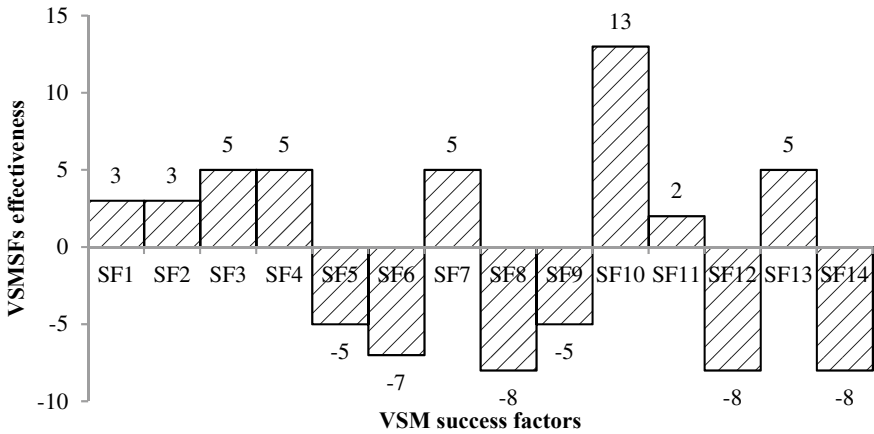
Fig. 2 Effectiveness of VSM success factors in Indian industries

represented that such type of factors is highly dependent on other factors and they may be affected by other factors. Similarly, factors having high effectiveness are put on the bottom of the framework. It indicates that such types of factors are independent from other factors and they cannot be influenced by other factors. A skill person (SF10) has high effectiveness hence given the rank one and put in foundation level in the models. Further, clarity of method (SF3), organizational culture (SF4), integration between processes (SF7), and customer orientation (SF13) have the effectiveness value five and given the rank two. Top management commitment (SF1), time and training provided by lean expert (SF2) have the effectiveness value three and given the rank three. Standardization of best practices (SF11) has the effectiveness value two and given the rank four. All employees' involvement (SF5) and resource utilisation (SF9) have the effectiveness value negatively five and given the rank five. Smooth material and information flow (SF6) have the effectiveness value negatively seven and given the rank six. Finally, process transparency and stability (SF8), supplier feedback (SF12), implementation of small VSM-related project (SF14) have the effectiveness value negatively eight and given the rank seven.

4.2 Cross-Impact Matrix Multiplication Applied to Classification (MICMAC) Analysis

In MICMAC analysis, success factors of VSM are classified into four groups named autonomous, dependent, linkage, and driver or independent [25], based on their driving power and dependency power as shown in Fig. 3. The results from the model help us in concluding that all the chosen factors are shown the significance of value stream mapping, and no factors is an autonomous factors except standardization of
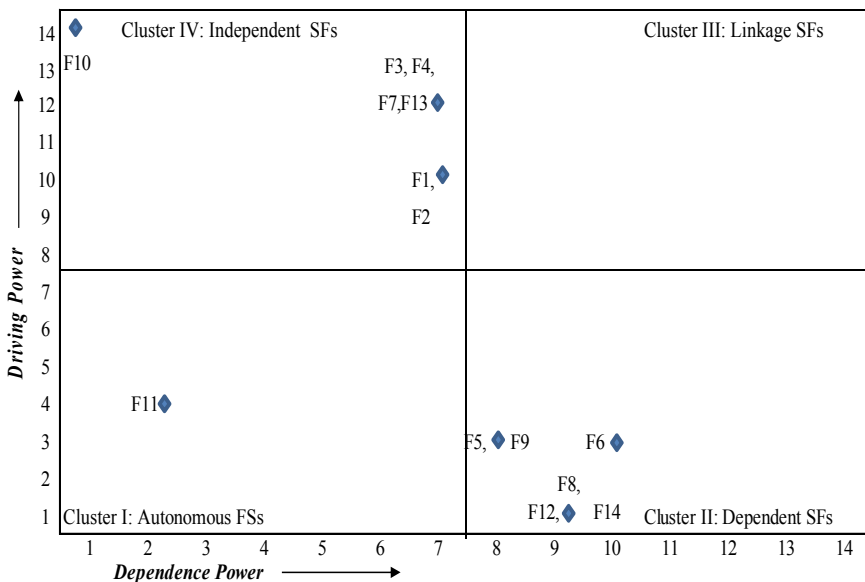
Fig. 3 MICMAC graph

best practices (F11) lies in cluster I. Autonomous group indicated only one dominant factor of VSM that has both low dependency as well as low independency. It reveals that the success factors have been chosen after keen review and due care. Six VSM success factors like all employees' involvement (F5); smooth material and information flow (F6); process transparency and stability (F8); resource utilisation (F9); supplier feedback (F12); and implementation of small VSM-related project (F14) are in the second quadrant as dependent factors. Process transparency and stability (F8), supplier feedback (F12), and implementation of small VSM-related project (F14) are not driving any other factors but driven by other factors. However, smooth material and information flow (F6) was identified as the most dependent factor while all employees' involvement (F5) and resource utilisation (F9) had moderate driving but high dependence power.

On the other hand, top management commitment (F1), time and training provided by lean expert (F2), clarity of method (F3), organizational culture (F4), integration between processes (F7), skill people (F10), and customer orientation (F13) are categorized in fourth group. Industry people can achieve their goals by focusing on these independent factors. Skill people (F10) is not driven by any other factors and has high driving power among other factors. Top management commitment (F1), time and training provided by lean expert (F2), clarity of method (F3), organizational culture (F4), integration between processes (F7), and customer orientation (F13) have high driving power but moderator dependency. Cluster 4 factors are highly independent and play an important role for industries. Therefore, action on these

factors may impact on others. Thus, the industry people/manager should pay more attention to these factors in the context of effective VSM implementation.

5 Conclusions

This study has provided a detailed description of the analysis, results, discussions, and the way in which the relationship models were developed. It gave specific purge and relevance of the results used for the various analysis. Various results have been analysed and verified by domain experts. An ISM-MICMAC analysis was conducted for justify the effectiveness of success factor for efficient implementation of VSM. Relation between fourteen factors was examined by ISM-MICMAC approach. Further, fourteen factors rank and levels identified. The VSM factors are structured into four levels. The result of the research reveals that skill people was the first need of Indian industries for better implementation of VSM. Finally, a relationship model was developed for Indian industries to identify which factor becomes more suitable for effective VSM implementation. Cluster analysis is revealing a lot of informatics insights and interrelationship between the success factors of VSM with the help of Cross-Impact Matrix Multiplication Applied to Classification.

This study could help higher authority of government as well as private organization in decision making.

References

1. Batchelor, R.: Henry Ford, Mass Production, Modernism, and Design, vol. 1. Manchester University Press (1994)
2. Liker, J.K.: The Toyota Way. Esensi (2004)
3. Rother, M., Shook, J.: Learning to See: Value Stream Mapping to Create Value and Eliminate Muda. v. 1.1. Oct., The Lean Enterprise Inst., Brookline (1998)
4. Patidar, L., Soni, V.K., Soni, P.K.: Manufacturing wastes analysis in lean environment: an integrated ISM-fuzzy MICMAC approach. Int. J. Syst. Assur. Eng. Manage. **8**(2), 1783–1809 (2017)
5. Singh, B., Garg, S.K., Sharma, S.K.: Value stream mapping: literature review and implications for Indian industry. Int. J. Adv. Manuf. Technol. **53**(5), 799–809 (2011)
6. Liu, Q., Yang, H., Xin, Y.: Applying value stream mapping in an unbalanced production line: a case study of a Chinese food processing enterprise. Qual. Eng. **32**(1), 111–123 (2020)
7. Seth, D., Seth, N., Dhariwal, P.: Application of value stream mapping (VSM) for lean and cycle time reduction in complex production environments: a case study. Prod. Plann. Control **28**(5), 398–419 (2017)
8. Tapping, D., Shuker, T.: Value Stream Management for the Lean Office: Eight Steps to Planning, Mapping, & Sustaining Lean Improvements in Administrative Areas. Productivity Press (2018)

9. Das, B., Venkatadri, U., Pandey, P.: Applying lean manufacturing system to improving productivity of airconditioning coil manufacturing. Int. J. Adv. Manuf. Technol. **71**(1–4), 307–323 (2014)

10. Dadashnejad, A.-A., Valmohammadi, C.: Investigating the effect of value stream mapping on overall equipment effectiveness: a case study. Total Qual. Manage. Bus. Excellence **30**(3–4), 466–482 (2019)

11. Khadse, P.B., Sarode, A.D., Wasu, R.: Lean manufacturing in Indian industries a review. Int. J. Latest Trends Eng. Technol. **3**(1), 175–181 (2013)

12. Balaji, V., et al.: DVSMS: dynamic value stream mapping solution by applying IIoT. Sādhanā **45**(1), 38 (2020)

13. Ainul Azyan, Z.H., Pulakanam, V., Pons, D.: Success factors and barriers to implementing lean in the printing industry: a case study and theoretical framework. J. Manuf. Technol. Manage. **28**(4), 458–484 (2017)

14. Almeida Marodin, G., Saurin, T.A.: Managing barriers to lean production implementation: context matters. Int. J. Prod. Res. **53**(13), 3947–3962 (2015)

15. Ferenhofa, H.A., Durstb, S., Seliga, P.M.: Knowledge waste in organizations: a review of previous studies. Braz. J. Oper. Prod. Manage. **12**(1), 160–178 (2015)

16. Hofer, C., Eroglu, C., Hofer, A.R.: The effect of lean production on financial performance: the mediating role of inventory leanness. Int. J. Prod. Econ. **138**(2), 242–253 (2012)

17. Kumar, N., et al.: Implementing lean manufacturing system: ISM approach. J. Ind. Eng. Manage. **6**(4), 996–1012 (2013)

18. Kumar, R., Kumar, V.: Lean manufacturing in Indian context: a survey. Manage. Sci. Lett. **5**(4), 321–330 (2015)

19. Losonci, D., et al.: The impact of shop floor culture and subculture on lean production practices. Int. J. Oper. Prod. Manage. **37**(2), 205–225 (2017)

20. Sanders, A., Elangeswaran, C., Wulfsberg, J.: Industry 4.0 implies lean manufacturing: research activities in industry 4.0 function as enablers for lean manufacturing. J. Ind. Eng. Manage. **9**(3), 811–833 (2016)

21. Shah, R., Ward, P.T.: Defining and developing measures of lean production. J. Oper. Manage. **25**(4), 785–805 (2007)

22. Womack, J.P., Jones, D.T.: Lean Thinking: Banish Waste and Create Wealth in Your Corporation. Simon and Schuster, New York (1996)

23. Sindhwani, R., Malhotra, V.: Modelling and analysis of agile manufacturing system by ISM and MICMAC analysis. Int. J. Syst. Assur. Eng. Manage. **8**(2), 253–263 (2017)

24. Kannan, G., Pokharel, S., Kumar, P.S.: A hybrid approach using ISM and fuzzy TOPSIS for the selection of reverse logistics provider. Resour. Conserv. Recycl. **54**(1), 28–36 (2009)

25. Patidar, L., Soni, P., Soni, V.: Development of a framework for implementation of maintenance tools and techniques using interpretive structural modeling. Mater. Today Proc. **4**(8), 8158–8166 (2017)

Reliability and Availability Analysis of Degrading Systems Under Imperfect Repair Scenario

Varun Kumar [ID]**, Girish Kumar** [ID]**, and Umang Soni** [ID]

1 Introduction

In global competitive era, the industrialists are striving hard to run the industries round the clock for meeting the customer's requirements. The ultimate objective of producing quality products and in time delivery has forced the modernization of industrial systems. Although the modernization of these systems makes them more sophisticated and helps in increasing the productivity, but simultaneously the complexity of the system gets increased and hence the risk of failure. The ultimate goal of failure-free operation becomes unachievable because failure is an unavoidable phenomenon associated with these technological systems. The failure of complex automated production systems might result in disastrous consequences. Therefore, the reliability and availability of complex systems have emerged as a thrust area in system planning, design, development and operational phase. Reliability engineering has become one of the essential tools which can benefit industries in terms of higher productivity at lower maintenance costs. Thus, higher system availability and reliability are desirable in many industries where downtime adversely affects the production cost [1].

Modern mechanical systems are the integral part of various industries such as refineries, power plant and manufacturing systems. These are intended to perform the specific function for the time; the plant is being operated which is not possible without

V. Kumar (✉) · U. Soni
Division of Manufacturing Processes and Automation Engineering, Netaji Subhas Institute of Technology, Delhi, India
e-mail: varunkumar3793@yahoo.in

U. Soni
e-mail: umangsoni.1@gmail.com

G. Kumar
Department of Mechanical, Production & Industrial and Automobile Engineering, Delhi Technological University, Delhi, India
e-mail: girish.kumar154@gmail.com

having proper maintenance policies. If not followed with given safety requirements, it can cause risk to the personnel, public or the environment. However, it is unfortunate that a threat of deteriorating process involved in components or machine parts is always present, therefore, maintenance measures are to be followed to control the deterioration of the machine components and also to increase the performance of the system during its life time. The incidence of failures in any component not only causes loss of system output but also adversely effects the consistency and smooth operations of the system [2]. When maintenance options other than system replacement are available, these systems shall be referred to as a repairable system [3]. When a failure occurs, any repair process may restore the repairable system to the operating state, therefore, it is not appropriate to replace the whole system [4]. A mechanical system is not a single unit system, but consists of units which work together to perform desired task. While working together, it results in wear out of the mating components which cause system failure. Failure is due to wear, fracture or fatigue or sometimes due to manufacturing errors and occurs randomly. The restoration method will take into consideration both the normal ageing of the system and the efficiency of the repair operation. These two elements provide a better view of the actions on the system behaviour and the maintenance strategy can be modified accordingly [5].

Maintenance activities improve the productivity and profitability of a company through improving availability of production systems, maintaining the quality of products and keeping the safety of working environments [6]. It is important to make the system work at least for the time and it is intended to work. These days proper maintenance actions are necessary for the industries to make the system work in a prescribed manner. Maintenance eventually increases system reliability and availability. The traditional maintenance approaches include corrective and preventive repair of subsystems. Corrective repair is effectively illustrated by the theory "if it is not broken, do not fix it" while preventive maintenance consists of certain scheduled procedures that are carried out while the system is already in service. These maintenance strategies do not work in the current industrial scenario. As a result, even more effective maintenance strategies, such as opportunistic maintenance is applied in the modelling and analysis of degrading system to enhance system performance. Opportunistic maintenance is sometimes referred to as taking a maintenance action at or during an opportunity. These opportunity types can be classified as internal opportunities in the sense that opportunity originates within the system itself. In contrast, external opportunities are external factors that can yield considerable cost saving such as stops due to weather conditions, production outage, etc. It allows full use of time required to do corrective maintenance on subsystem, using that period to conduct proactive maintenance on subsystems which have deteriorated [7]. Opportunistic maintenance can also be defined as combined or group of maintenance activities of some components of the system that reduce the maintenance cost and time [8]. There are two main benefits of opportunistic maintenance over traditional maintenance approaches: (1) The savings of setup cost when initiating a maintenance action and (2) reduced downtime cost which is caused by frequent preventive maintenance activities if applied [9]. The most challenging aspect of opportunistic

maintenance is the nature of uncertainty of opportunity occurrence. The subsystem selection/choice for the opportunistic maintenance should be done based on the condition of subsystem and by satisfying the time constraint [10].

Traditionally, the maintenance used in power plants was breakdown maintenance that is also called fire-fighting maintenance or failure maintenance or corrective maintenance. Breakdown maintenance can only be carried out until a failure of component or machine occurs. Breakdown maintenance is widely accepted by default in power plants and therefore becomes costly. It is important for a power system to work as per the requirements, but due to the unpredictable nature of failure of components, it is not possible to give a continuous supply to the consumers. However, in this paper, corrective maintenance is coupled with opportunistic maintenance whenever the system enters the repair phase and the benefit of opportunistic maintenance is quantified in terms of increased system availability.

Maintenance engineers should have knowledge of efficiency indicators on the basis of reliability–availability characterization for the effective running of such systems [11]. Traditionally, reliability block diagram, fault tree analysis and reliability graph were used for reliability and availability analysis [12]. These techniques are simple and exact, but because of their static nature complex systems which include repairs sequences cannot be solved with these techniques. Therefore, the advancement to such methods is a Markov approach. In this work, the degraded system model is developed and analysis is carried out to determine reliability and availability of a series system using Markov approach.

The remaining paper is structured as follows. Section 2 describes the Markov approach in brief. Section 3 defines system modelling to integrate multi-level degradation. The solutions of the Markov-based models are discussed in Sect. 4. Finally, Sect. 5 concludes the work.

2 Markov Approach

The Markov model proves to be a powerful modelling and analysis technique with strong application in reliability–availability analysis of various industrial systems. The reliability–availability behaviour of the system has been represented using a state transition diagram, which consists of a set of discrete states that a system can have, and also defines the speed with which the transition between these states takes place. It is a stochastic process in which at any given time, the subsequent course of process is affected only by the state at the given time and does not depend on the behaviour of the process at any preceding time. Markov model is the function of two random variables, the state of the system and the time of observation. A Markov model needs identification of possible states of the system, their transition paths and the rate parameters of the transitions [13]. Each state represents the different condition of the system. A Markov graph consists of nodes and branches, the nodes represent the states of a system and the branches depict the respective transition probabilities [14]. In order to find the reliability–availability of the system, one has to form a set of
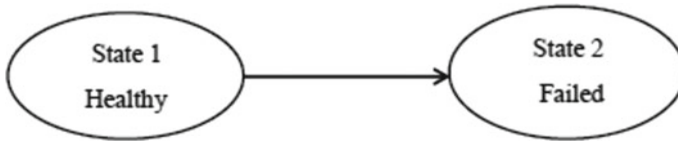
Fig. 1 Two states, i.e., healthy and failed

linear differential equations. The formulation of the model starts with the definition of the states of the system, as the state is an exact description of the circumstances existing in the system at a particular time. The proposed approach is much better in representing the deterioration process of physical systems in terms of mathematical simplification and extension ability. Figure 1 represents a two-state Markov model.

The symbol λ denotes the transition rate from State 1 to State 2. In addition, $P_i(t)$, denotes the probability of the system being in ith state at time t. Refer Fig. 1 for a two-state Markov model. The equations for a two-state Markov model are expressed below [7]:

$$\mathrm{d}P_1/\mathrm{d}t = -\lambda P_1 \tag{1}$$

$$\mathrm{d}P_2/\mathrm{d}t = \lambda P_2 \tag{2}$$

Also,

$$P_1 + P_2 = 1 \tag{3}$$

For a complex system with large number of constituent components and units, the number of states and the number of rate equations increases exponentially. For such a system model, manual solution of set of large number differential equations is cumbersome. Therefore, these differential equations can be solved using MATLAB software and the availability of the system is obtained by adding the operating states probabilities.

3 System Modelling

3.1 System Description

A system is characterized as a set of subsystems/components working together towards achieving some logical end. The two-stage reciprocating air compressor system with serially configured components is selected for this paper as shown in Fig. 2. Being a series system, it should be highly available when called to function so that the power plant operations do not suffer.
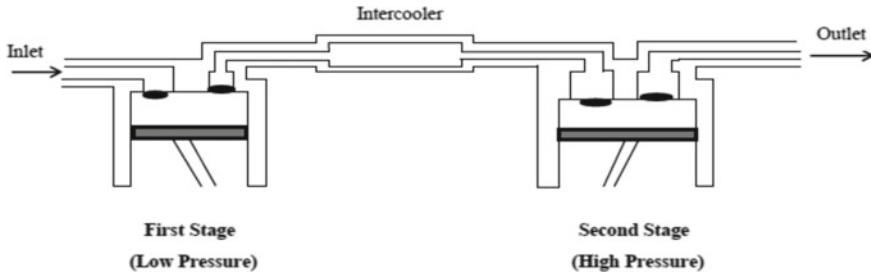
Fig. 2 Multi-stage reciprocating air compressor system

Degradation modelling and simulation are a crucial and difficult aspect of the execution of an effective maintenance plan. The failure process for the system must be interpreted in such a manner that an effective failure model is built and implemented in operation. Degradation is not sudden but gradual. Whenever a system is in working, it is always degrading with time. Firstly, the system is in new state then with time it starts degrading. The system with gradual degradation is considered for this work. In addition, random failure is also considered which will stop the working of the system and hence can cause a major break down. The repair rates are defined as per the condition of the system and amount of resource employed.

In the system model development, state O is considered as the original operating state, i.e. "as good as new" state, D as degraded state and F as the failed state at the subsystem level as shown in Fig. 3. A maintenance action, i.e. imperfect repair is considered, which restores the subsystem from its failed state F to the degraded state D and from degraded state D to operating state O, respectively. The states of the subsystem represented by O and D are considered as working states, while F is the repair state due to performance below the unacceptable level.

The following assumptions are made for developing system model:

- Simultaneous failure of two or more subsystems is not considered.
- Subsystems are expected to undergo gradual degradation.
- Failure or maintenance of any subsystem disables the system.
- Imperfect repair restores the subsystem to the state just before the failed state, i.e. degraded state.
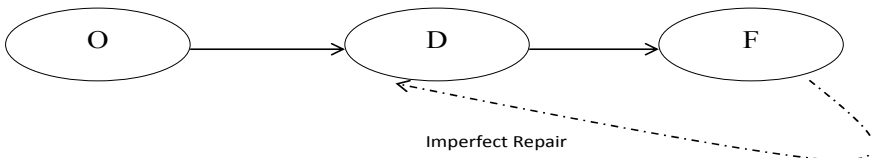
Fig. 3 Degradation stages of subsystem and corrective imperfect repair

3.2   Models with Imperfect Repair

In this section, system models are developed considering imperfect repair. Modelling imperfect repair of a multi-component device is a way that captures a repair effect that lies somewhere between as good as new (perfect repair) and as bad as old (minimum repair) [15]. In all, two models for the system have been developed as discussed in the following subsections.

3.2.1   System Model Based on Imperfect Repair Without Opportunistic Maintenance

Modelling and analysis of degrading systems may prove beneficial in evaluating system performance and the degree of interaction between the constituent subsystems. To express the system performance in quantitative terms, it is necessary to develop a mathematical model of real existing systems and analyse their performance under actual operating conditions. The work presented here is mainly concerned with the imperfect repair actions carried out whenever the system enters the repair phase. The system comprises of three subsystems each with the potential to be in one of the three states at a given moment of time. Their series combination gives a total of twenty feasible states that the entire system can maintain during its lifetime. Twelve states are the "under repair" system states, while the remaining eight states are the "working states" as shown in Table 1. A system model is developed taking into account subsystem degradation represented by black line; imperfect repair without opportunistic maintenance represented by continuous dotted black line and is shown in Fig. 4.

Markov's approach solves the system model developed as shown in Fig. 4 following the discussion is in Sect. 2. The transition graph represents the change in state for a system. A system crosses from one state to the next with a certain transition probability.

Following symbols are used for developing the mathematical model:

$P_i(t)$—Probability of system being in ith state at time t.
dP_i/dt—Rate of change of ith state at time t.
λ_{ij}—Degradation transition rate from state i to j.
μ_{ij}—Repair transition rate from state i to j.

The twenty equations are developed correspond to the number of states as shown in Table 1 and for the system model as shown in Fig. 4. A change in state probability can be calculated by the addition of all transition probabilities. These transition probabilities can be obtained from the multiplication of the state probabilities with the corresponding transition rates. All arrows pointing away from a state are negative and all arrows pointing to a state are positive. This results in the following twenty differential equations for the developed system model.

Table 1 System states and their corresponding transitions

System state		State of subsystem 1	State of subsystem 2	State of subsystem 3	Transition to	Maintenance possibility	
S. No.	Status					C.M.*	O.M.*
1	Working	O	O	O	2 4 9	–	–
2	Working	O	O	D	3 5 10	–	–
3	UR	O	O	F	2	Yes (S3)	No
4	Working	O	D	O	5 7 12	–	–
5	Working	O	D	D	6 8 13	–	–
6	UR	O	D	F	5	Yes (S3)	Yes (S2)
7	UR	O	F	O	4	Yes (S2)	No
8	UR	O	F	D	5	Yes (S2)	Yes (S3)
9	Working	D	O	O	17 12 10	–	–
10	Working	D	O	D	18 13 11	–	–
11	UR	D	O	F	10	Yes (S3)	Yes (S1)
12	Working	D	D	O	19 15 13	–	–
13	Working	D	D	D	20 16 14	–	–
14	UR	D	D	F	13	Yes (S3)	Yes (S1, 2)
15	UR	D	F	O	12	Yes (S2)	Yes (S1)
16	UR	D	F	D	13	Yes (S2)	Yes (S1,3)
17	UR	F	O	O	9	Yes (S1)	No
18	UR	F	O	D	10	Yes (S1)	Yes (S3)
19	UR	F	D	O	12	Yes (S1)	Yes (S2)
20	UR	F	D	D	13	Yes (S1)	Yes (S2,3)

*C.M.—Corrective maintenance, O.M.—opportunistic maintenance, UR—under repair

$$dP_1/dt = -(\lambda_{12} + \lambda_{14} + \lambda_{19})P_1(t)$$
$$dP_2/dt = -(\lambda_{25} + \lambda_{23} + \lambda_{210})P_2(t) + \lambda_{12} P_1(t) + \mu_{32} P_3(t)$$
$$dP_3/dt = \lambda_{23} P_2(t) - \mu_{32} P_3(t)$$
$$dP_4/dt = -(\lambda_{45} + \lambda_{47} + \lambda_{412})P_4(t) + \lambda_{14} P_1(t) + \mu_{74} P_7(t)$$
$$dP_5/dt = -(\lambda_{56} + \lambda_{58} + \lambda_{513})P_5(t) + \lambda_{25} P_2(t) + \lambda_{45} P_4(t)$$
$$+ \mu_{65} P_6(t) + \mu_{85} P_8(t)$$
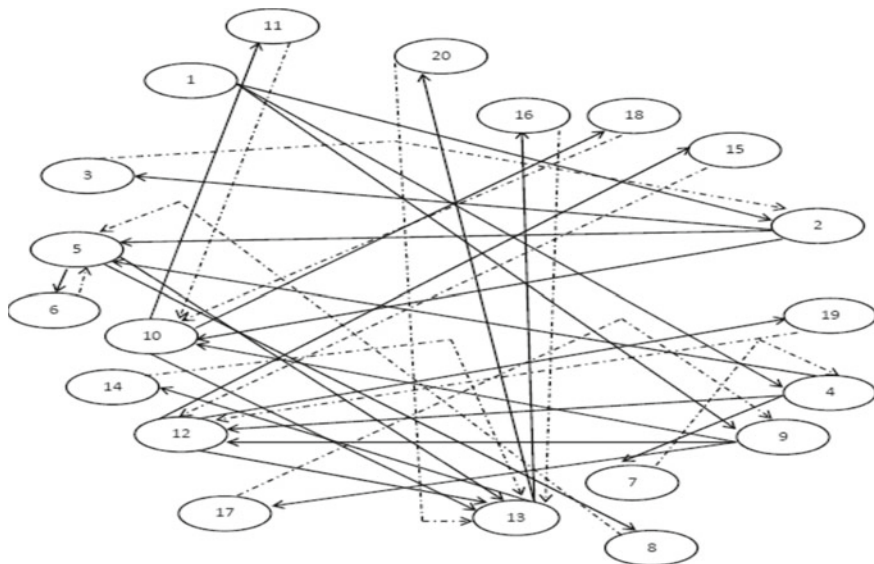
Fig. 4 Markov model for the system undergoing imperfect repair only

$$\mathrm{d}P_6/\mathrm{d}t = \lambda_{56}\, P_5(t) - \mu_{65}\, P_6(t)$$

$$\mathrm{d}P_7/\mathrm{d}t = \lambda_{47}\, P_4(t) - \mu_{74}\, P_7(t)$$

$$\mathrm{d}P_8/\mathrm{d}t = \lambda_{58}\, P_5(t) - \mu_{85}\, P_8(t)$$

$$\mathrm{d}P_9/\mathrm{d}t = -(\lambda_{910} + \lambda_{912} + \lambda_{917})P_9(t) + \lambda_{19}\, P_1(t) + \mu_{179}\, P_{17}(t)$$

$$\mathrm{d}P_{10}/\mathrm{d}t = -(\lambda_{1011} + \lambda_{1013} + \lambda_{1018})P_{10}(t) + \lambda_{210}\, P_2(t) + \lambda_{910}\, P_9(t)$$
$$\qquad\qquad + \mu_{1110}\, P_{11}(t) + \mu_{1810}\, P_{18}(t)$$

$$\mathrm{d}P_{11}/\mathrm{d}t = \lambda_{1011}\, P_{10}(t) - \mu_{1110}\, P_{11}(t)$$

$$\mathrm{d}P_{12}/\mathrm{d}t = -(\lambda_{1213} + \lambda_{1215} + \lambda_{1219})P_{12}(t) + \lambda_{412}\, P_4(t)$$
$$\qquad\qquad + \lambda_{912}\, P_9(t) + \mu_{1512}\, P_{15}(t) + \mu_{1912}\, P_{19}(t)$$

$$\mathrm{d}P_{13}/\mathrm{d}t = -(\lambda_{1314} + \lambda_{1316} + \lambda_{1320})P_{13}(t) + \lambda_{513}\, P_5(t) + \lambda_{1013}\, P_{10}(t)$$
$$\qquad\qquad + \lambda_{1213}\, P_{12}(t) + \mu_{1413}\, P_{14}(t) + \mu_{1613}\, P_{16}(t) + \mu_{2013}\, P_{20}(t)$$

$$\mathrm{d}P_{14}/\mathrm{d}t = \lambda_{1314}\, P_{13}(t) - \mu_{1413}\, P_{14}(t)$$

$$\mathrm{d}P_{15}/\mathrm{d}t = \lambda_{1215}\, P_{12}(t) - \mu_{1512}\, P_{15}(t)$$

$$\mathrm{d}P_{16}/\mathrm{d}t = \lambda_{1316}\, P_{13}(t) - \mu_{1613}\, P_{16}(t)$$

$$\mathrm{d}P_{17}/\mathrm{d}t = \lambda_{917}\, P_9(t) - \mu_{179}\, P_{17}(t)$$

$$\mathrm{d}P_{18}/\mathrm{d}t = \lambda_{1018}\, P_{10}(t) - \mu_{1810}\, P_{18}(t)$$

$$\mathrm{d}P_{19}/\mathrm{d}t = \lambda_{1219}\, P_{12}(t) - \mu_{1912}\, P_{19}(t)$$

$$\mathrm{d}P_{20}/\mathrm{d}t = \lambda_{1320}\, P_{13}(t) - \mu_{2013}\, P_{20}(t)$$

These set of equations are solved using MATLAB software and the solution is discussed in Sect. 4.

3.2.2 System Model Based on Imperfect Repair with Opportunistic Maintenance

The work presented in this section is related to the imperfect repair actions coupled with opportunistic maintenance whenever the system enters the repair phase. System model based on imperfect repair with opportunistic maintenance is developed as shown in Fig. 5, with removal of the lines 6-5, 8-5, 11-10, 14-13, 15-12, 16-13, 18-10, 19-12, 20-13, from the model developed in the previous section as these nine lines represent imperfect repair only and do not include opportunistic maintenance, restoring the subsystem from state F to D. Also, new lines 6-2, 8-4, 11-2, 14-2, 15-4, 16-4, 18-9, 19-9 and 20-9 representing imperfect repair coupled with opportunistic maintenance are included in the model.

The twenty equations are developed correspond to the number of states as shown in Table 1 and for the system model as shown in Fig. 5.

$$\mathrm{d}P_1/\mathrm{d}t = -(\lambda_{12} + \lambda_{14} + \lambda_{19})P_1(t)$$
$$\mathrm{d}P_2/\mathrm{d}t = -(\lambda_{25} + \lambda_{23} + \lambda_{210})P_2(t) + \lambda_{12}\,P_1(t) + \mu_{32}\,P_3(t)$$
$$+ \mu_{62}\,P_6(t) + \mu_{112}\,P_{11}(t) + \mu_{142}\,P_{14}(t)$$
$$\mathrm{d}P_3/\mathrm{d}t = \lambda_{23}\,P_2(t) - \mu_{32}\,P_3(t)$$
$$\mathrm{d}P_4/\mathrm{d}t = -(\lambda_{45} + \lambda_{47} + \lambda_{412})P_4(t) + \lambda_{14}\,P_1(t) + \mu_{74}\,P_7(t)$$
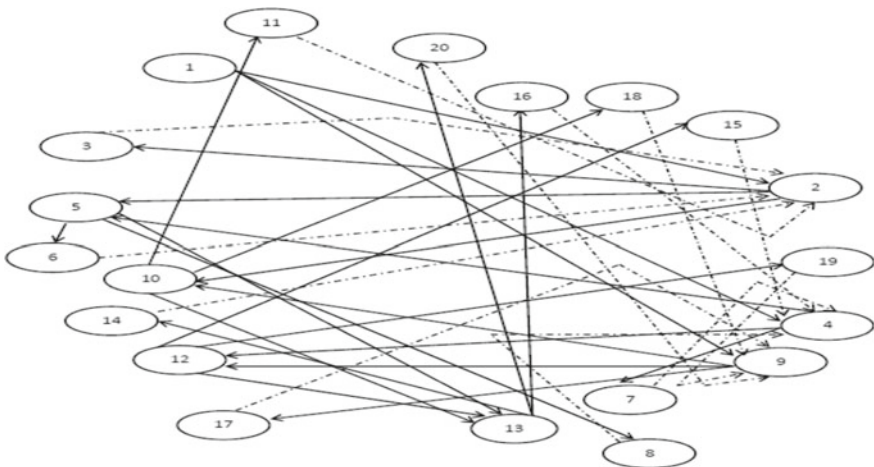
Fig. 5 Markov model for the system undergoing imperfect repair coupled with opportunistic maintenance

$$+ \mu_{84}\, P_8(t) + \mu_{154}\, P_{15}(t) + \mu_{164}\, P_{16}(t)$$

$$\mathrm{d}P_5/\mathrm{d}t = -(\lambda_{56} + \lambda_{58} + \lambda_{513})P_5(t) + \lambda_{25}\, P_2(t) + \lambda_{45}\, P_4(t)$$

$$\mathrm{d}P_6/\mathrm{d}t = \lambda_{56}\, P_5(\mathrm{t}) - \mu_{62}\, P_6(t)$$

$$\mathrm{d}P_7/\mathrm{d}t = \lambda_{47}\, P_4(\mathrm{t}) - \mu_{74}\, P_7(t)$$

$$\mathrm{d}P_8/\mathrm{d}t = \lambda_{58}\, P_5(t) - \mu_{84}\, P_8(t)$$

$$\mathrm{d}P_9/\mathrm{d}t = -(\lambda_{910} + \lambda_{912} + \lambda_{917})P_9(t) + \lambda_{19}\, P_1(t)$$
$$+ \mu_{179}\, P_{17}(t) + \mu_{189}\, P_{18}(t) + \mu_{199}\, P_{19}(t) + \mu_{209}\, P_{20}(t)$$

$$\mathrm{d}P_{10}/\mathrm{d}t = -(\lambda_{1011} + \lambda_{1013} + \lambda_{1018})P_{10}(t) + \lambda_{210}\, P_2(t) + \lambda_{910}\, P_9(t)$$

$$\mathrm{d}P_{11}/\mathrm{d}t = \lambda_{1011}\, P_{10}(t) - \mu_{112}\, P_{11}(t)$$

$$\mathrm{d}P_{12}/\mathrm{d}t = -(\lambda_{1213} + \lambda_{1215} + \lambda_{1219})P_{12}(t) + \lambda_{412}\, P_4(t) + \lambda_{912}\, P_9(t)$$

$$\mathrm{d}P_{13}/\mathrm{d}t = -(\lambda_{1314} + \lambda_{1316} + \lambda_{1320})\, P_{13}(t) + \lambda_{513}\, P_5(t)$$
$$+ \lambda_{1013}\, P_{10}(t) + \lambda_{1213}\, P_{12}(t)$$

$$\mathrm{d}P_{14}/\mathrm{d}t = \lambda_{1314}\, P_{13}(t) - \mu_{142}\, P_{14}(t)$$

$$\mathrm{d}P_{15}/\mathrm{d}t = \lambda_{1215}\, P_{12}(t) - \mu_{154}\, P_{15}(t)$$

$$\mathrm{d}P_{16}/\mathrm{d}t = \lambda_{1316}\, P_{13}(t) - \mu_{164}\, P_{16}(t)$$

$$\mathrm{d}P_{17}/\mathrm{d}t = \lambda_{917}\, P_9(t) - \mu_{179}\, P_{17}(t)$$

$$\mathrm{d}P_{18}/\mathrm{d}t = \lambda_{1018}\, P_{10}(t) - \mu_{189}\, P_{18}(t)$$

$$\mathrm{d}P_{19}/\mathrm{d}t = \lambda_{1219}\, P_{12}(t) - \mu_{199}\, P_{19}(t)$$

$$\mathrm{d}P_{20}/\mathrm{d}t = \lambda_{1320}\, P_{13}(t) - \mu_{209}\, P_{20}(t)$$

These set of equations are solved using MATLAB software and the solution is discussed in Sect. 4.

4 Solution of the System Model

The following steps have been taken to get the solution of system model using the Markov approach:

- Develop a state transition diagram for the system that represents all feasible states of the system.
- Model the differential equations for each feasible state of the system as discussed in Sect. 2.
- The set of differential equations for each model are simultaneously solved using MATLAB with initial conditions and for a required mission time.

The nature of repairable system can be described in terms of reliability, availability and maintainability which may be evaluated at different points of time in the working life of a system to observe its evolution. In the absence of repair or replacement, reliability and availability metrics are the same. These are different when maintenance

Table 2 Distribution parameters of two-stage reciprocating compressor system

Parameter	Value	Parameter	Value	Parameter	Value
λ_{12}	0.000111	μ_{85}	0.0022	μ_{1512}	0.0022
λ_{14}	0.000167	λ_{910}	0.000111	μ_{1613}	0.0022
λ_{19}	0.0000667	λ_{912}	0.000167	μ_{179}	0.0022
λ_{23}	0.000223	λ_{917}	0.00019204	μ_{1810}	0.0022
λ_{25}	0.000167	λ_{1011}	0.000223	μ_{1912}	0.0022
λ_{210}	0.0000667	λ_{1013}	0.000167	μ_{2013}	0.0022
μ_{32}	0.0022	λ_{1018}	0.00019204	μ_{62}	0.0022
λ_{45}	0.000111	μ_{1110}	0.0022	μ_{84}	0.0022
λ_{47}	0.0002936	λ_{1213}	0.000111	μ_{112}	0.0022
λ_{412}	0.0000667	λ_{1215}	0.0002936	μ_{142}	0.0022
λ_{56}	0.000223	λ_{1219}	0.00019204	μ_{154}	0.0022
λ_{58}	0.0002936	λ_{1314}	0.000223	μ_{164}	0.0022
λ_{513}	0.0000667	λ_{1316}	0.0002936	μ_{189}	0.0022
μ_{65}	0.0022	λ_{1320}	0.00019204	μ_{199}	0.0022
μ_{74}	0.0022	μ_{1413}	0.0022	μ_{209}	0.0022

is considered for the system. Availability is often greater than reliability. Availability of the system is obtained by summing up all working state probabilities. The overall performance of the system depends on its various subsystems and on their malfunction and repair levels, which depend on the working conditions and the maintenance activities of the industry [16]. The Markov model is adjusted for reliability evaluation by removing the repair arcs from the model's absorbing states [17]. The time to failure and the time to repair of mechanical subsystems are assumed to follow exponential distribution for assessment of system availability and their values are listed down in Table 2 [18].

The system of equations for two models, i.e. system model based on imperfect repair without opportunistic (Sect. 3.2.1) and with opportunistic maintenance (Sect. 3.2.2) is solved using MATLAB software for a mission time of 50,000 h. For the solution, it is assumed that initially (at time $t = 0$) the system is in state "1" with probability value 1 in both models and exponential distribution parameters are applied as per Table 2. The results obtained are presented in Fig. 6 and these results provide a definite indication of the trend in the system reliability and availability. These statistical results can be quantitatively analysed to assess the relative change in the performance of the system in different scenarios. The availability shows the increasing trend for the same mission time when opportunistic maintenance is integrated with the corrective imperfect repair.

This explicitly supports the possibility of performing opportunistic maintenance to improve system availability. The impact of opportunistic maintenance on availability is very small, as shown in Fig. 6, but it increases with time until the steady state is reached. Analysing the availability under different conditions is therefore a critical
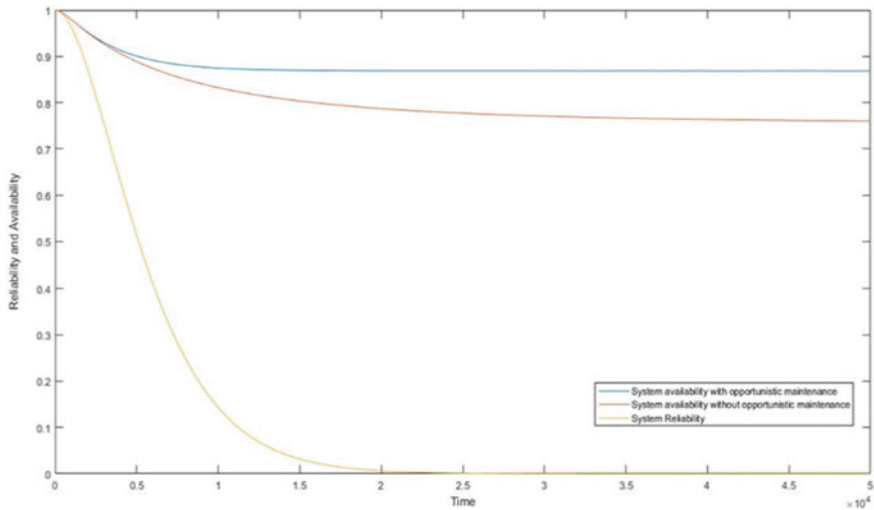
Fig. 6 Reliability and availability analysis of the system

method for developing a policy to conduct opportunistic maintenance to optimize system performance. Unlike the previous studies, this work involves degradation modelling incorporating the real-life factors which affect a subsystem during its working lifecycle to make it closer to reality. Thus, it makes the developed model more practical, thereby ensuring the results obtained from analysis are more accurate.

5 Conclusion

In this study, Markov approach has been proposed for reliability and availability analysis of degrading systems. The approach suggested reflect dependencies that are not feasible in traditional techniques such as RBD and FTA. The research involves degradation-based modelling, the derivation of transitions of each feasible state and the solution of system model for reliability and availability assessment. The suggested method is demonstrated for a two-stage reciprocating air compressor system with intercooler in between, system is series configuration. In this series configured system, the gain in steady-state system availability is evaluated. The findings indicate that when opportunistic maintenance is utilized, there is gain in availability. For a 50,000 h mission period, there is a gain of 10.84% in system availability when opportunistic maintenance is coupled with imperfect repair. The research has its limitations since it is believed that repair and failure time obey exponential distribution. Consequently, the present analysis may be expanded to involve the non-exponential distribution in the simulation. This analysis is predicted to allow

researchers, analysts, consultants and others to establish effective maintenance policy considering the gain in system availability.

References

1. Kumar, G., Jain, V., Soni, U.: Modelling and simulation of repairable mechanical systems reliability and availability. Int. J. Syst. Assur. Eng. Manage. **10**(5), 1221–1233 (2019)
2. Jain, M., Meena, R.K.: Availability analysis and cost optimization of M/G/1 fault-tolerant machining system with imperfect fault coverage. Arab. J. Sci. Eng. **45**(3), 2281–2295 (2020)
3. Alaswad, S., Cassady, R., Pohl, E., Li, X.: A model of system limiting availability under imperfect maintenance. J. Qual. Maintenance Eng. (2017, Oct 9)
4. Dietrich, S., Kahle, W.: Optimal imperfect maintenance in a multi-state system. In: Recent Advances in Multi-state Systems Reliability, pp. 179–193. Springer, Cham (2018)
5. Nguyen, D.T., Dijoux, Y., Fouladirad, M.: Analytical properties of an imperfect repair model and application in preventive maintenance scheduling. Eur. J. Oper. Res. **256**(2), 439–453 (2017)
6. Alsyouf, I.: The role of maintenance in improving companies' productivity and profitability. Int. J. Prod. Econ. **105**(1), 70–78 (2007)
7. Varghese, J.P., Kumar, G.: Availability analysis with opportunistic maintenance of a two component deteriorating system. Int. J. Mater. Mech. Manuf. **2**(2) (2014)
8. Pham, H., Wang, H.: Optimal (τ, T) opportunistic maintenance of a k-out-of-n: G system with imperfect PM and partial failure. Naval Res. Logistics (NRL) **47**(3), 223–239 (2000)
9. Ab-Samat, H., Kamaruddin, S.: Opportunistic maintenance (OM) as a new advancement in maintenance approaches: a review. J. Qual. Maintenance Eng. **20**(2), 98–121 (2014)
10. Kumar, G., Jain, V., Gandhi, O.P.: Steady-state availability analysis of repairable mechanical systems with opportunistic maintenance by using semi-Markov process. Int. J. Syst. Assur. Eng. Manage. **5**(4), 664–678 (2014)
11. Jain, M.: Reliability prediction of repairable redundant system with imperfect switching and repair. Arab. J. Sci. Eng. **41**(9), 3717–3725 (2016)
12. Asjad, M., Kulkarni, M.S., Gandhi, O.P.: An insight to availability for O&M support of mechanical systems. Int. J. Prod. Qual. Manage. **16**(4), 462–472 (2015)
13. Yang, L., Yan, X.: Design for reliability of solid state lighting products. In: Solid State Lighting Reliability, pp. 497–556. Springer, New York (2013)
14. Son, K.S., Kim, D.H., Kim, C.H., Kang, H.G.: Study on the systematic approach of Markov modeling for dependability analysis of complex fault-tolerant features with voting logics. Reliab. Eng. Syst. Saf. **1**(150), 44–57 (2016)
15. Nafisah, I., Shrahili, M., Alotaibi, N., Scarf, P.: Virtual series-system models of imperfect repair. Reliab. Eng. Syst. Saf. **1**(188), 604–613 (2019)
16. Modgil, V., Sharma, S.K., Singh, J.: Performance modeling and availability analysis of shoe upper manufacturing unit. Int. J. Qual. Reliab. Manage. (2013, Aug 30)
17. Kumar, G., Jain, V., Gandhi, O.P.: Reliability and availability analysis of mechanical systems using stochastic petri net modeling based on decomposition approach. Int. J. Reliab. Qual. Saf. Eng. **19**(01), 1250005 (2012)
18. Barringer: Weibull Database (2018). https://www.barringer1.com/wdbase

Prioritization of Wheel Materials Using MCDM Techniques (TOPSIS) for Automobile Wheels

Aditya Bhatia [ID]**, Sahil Kumar** [ID]**, Sarthak Bhatt** [ID]**,
Mukesh Shamrao Dadge, and Mohd Shuaib**

1 Introduction

Vehicles have a significant job in influence of our day-to-day life. This makes it important to attempt to decrease their creation cost in accordance with the advancement of creation apparatus. But today, we also have different materials like magnesium, aluminium at our disposal. In-build applications, where weight assumes a significant job, choosing magnesium is a decent decision. Its recyclable property likewise gives an edge. The utilization of magnesium and its combinations in car parts was restricted in the mid-sixties and seventies; however, today the mindfulness on fuel reserve funds and natural insurance through diminished CO_2 discharges makes this material alluring [1]. Automobile manufacturers are additionally trying a wide assortment of cutting-edge materials in new vehicle models.[2]. The utilization of finite element technique for better understanding pressure and displacement arrangement in an Al alloy car rim-wheel combo subject to the combined impact of rising pressure and spiral load has likewise been contemplated [3]. An analysis can also be done to examine the change in shape of the automobile tyre rim when exposed to varying static loading, giving us an insight into the performance of different materials in different conditions, along with their alloys [4]. The wheel rim is utilized to give a stable foundation on which to position the tyre. Its specifications, contour must be appropriate to sufficiently adjust the specified tyre suitable for the automobile [5]. Such analysis helps to understand importance of material in absorbing the load and performing effectively [6]. Relative investigation will support any creator while choosing materials for wheels of a ground automobile [7]. Such studies across various properties and domains, of different materials and their alloys, help us reach the optimal material required for certain tasks in the industry, as done in this paper.

A. Bhatia (✉) · S. Kumar · S. Bhatt · M. S. Dadge · M. Shuaib
Department of Mechanical, Production & Industrial and Automobile Engineering, Delhi
Technological University, Delhi 110042, India
e-mail: adityabhatia.dtu@gmail.com

MCDM is a procedure to settle on choices within the sight of numerous, typically clashing rules or criteria. The issues of MCDM are grouped into two classifications: MADM and MODM, contingent upon whether the issue being a determination issue or an issue in design. MADM is a methodology utilized to take care of issues including choice from among a limited number of choices. An MADM strategy determines how ascribe data is to be prepared so as to show up at a decision. MCDM is a famous methodology which is efficiently useful in selection of one choice from a number of muddled choices. MCDM methods are applicable in taking care of genuine and day-to-day issues such as motorcycle, selection of cars with clashing alternatives and because of their extraordinary highlights and objective connection which is shown by the past investigations of different researches. For the best solution among different situations, the criteria can be solved by applying more than one MCDM method. There are a great number of MCDM techniques such as TOPSIS (The Technique for Order of Preference by Similarity to Ideal Solution), AHP(Analytic Hierarchy Process), and MOORA (Multi-Objective Optimization by Ratio Analysis) including many others which are used at a great scale across the globe to solve various issues over the last numerous years.

TOPSIS technique is selected in this problem in deciding the best alloy alternative among the given alloys of various metals such as aluminium, magnesium and Titanium.

2 Literature Review

The choosing of a composite matter for the purpose of alloy wheel is as vital as knowing the wheel geometry for its fabrication. Many benefits and drawbacks of each material may be perceived in a trail of work composite structures for standard antimonial structures [8]. Commonly, steel has been used for such purposes, due to its desirable qualities. We can check the press-forming features of multiple grades of HSLA (high-strength and low-alloy) steels [9]. Also, top standard steels have been extensively used on automobile bodies to increase crashworthiness without expanding the unit's weight under a big load of the necessities for fuel utilization, energy conservation, and withstanding of crashes [10]. However, these sometimes come with some disadvantages. Periodic plasticity, pressure accumulation is examined in periodic pressuring of less alloyed and LC steels used in the automotive industry [11]. The various properties of such new alloy combinations (Titanium-Aluminium) have been studied extensively. Steel having rigidity of 600 MPa at least, joined with great formability, has been created. The steel, consequently created, has been effectively applied to manufacturing of car wheel discs [12]. The business enthusiasm for titanium and its compounds was incited by the moderately low density of this metal. Consequently, titanium and its combinations are utilized fundamentally in two territories of uses: erosion safe regions, for example, the chemical business, and in regions where weight-saving and high quality are prevalent, for example, in

airplane and aviation uses [13]. Apart from using materials like aluminium and titanium, magnesium and its alloys have also been tried for automobile applications [14]. Apart from the individual analysis of each domain, they have also been coalesced into a single study to examine their various properties parallely [15]. First, the properties of commonly used material have been assimilated to have a comprehensive overview and collection of the desired properties and their values. [16]. A twofold control shaping innovation of cruiser wheel was right off the bat created to frame the non-simple parts with high mechanical features [17] (Tables 1, 2 and 3).

3 Methodology

The study conducted which is mentioned below points at introducing a procedure in determining the selection criteria issues while selecting the optimum automobile wheel materials among various alloys, where many conflicting decisions are involved. To achieve this, traditional TOPSIS (Technique-for-Order-Preference-by-Similarity-to-Ideal-Solution) is utilized.

3.1 TOPSIS Method

The methodology TOPSIS is adopted from [22] the preliminary idea in which the selection starts from identifying various properties of alloy materials such as density, UTS, percentage elongation and hardness as the evaluation criteria with detailed literature for search and gathering of the data. The different steps for TOPSIS are shown mathematically as (Fig. 1):

Step-1: The first stage includes the establishment of decision matrix (DM).

$$
\text{DM} = \begin{array}{c} \\ C_1 \\ C_2 \\ \cdots \\ C_n \end{array} \overset{\displaystyle L_1 \quad L_2 \quad \ldots \quad L_n}{\left[\begin{array}{cccc} X_{11} & X_{12} & \ldots & X_{1n} \\ X_{21} & X_{22} & \ldots & X_{2n} \\ . & . & . & . \\ X_{m1} & X_{m2} & \ldots & X_{mn} \end{array} \right]} \tag{1}
$$

Or

$$
\text{DM} = [x_{ii}]_{m \times n}
$$

Here, 'j' ($j = 1, 2, 3, 4, 5, \ldots, m$) is the criteria index; 'm' denotes the number of potential sites available in the DM and 'i' refers to alternative index ($i = 1, 2, 3, 4, 5, \ldots, n$). The elements ($L_1, L_2, \ldots, L_n$) denotes different criteria and the elements ($C_1, C_2, \ldots, C_n$) points to the alternative locations.

Table 1 Aluminium alloy materials and its properties [18, 19]

S.No.	Material	Composition	Density (g/cm³)	Them. cond. (W/mK)	U-T-S (MPa)	Y-T-S (MPa)	F-S (MPa)	Hardness (BHN)	Percent elong. at break	Specific Δ (J/g °C)	Coeff. of them. exp. (μm/m–C)
1	AA6016-T4	Al: 96–98 Si: 1.2 Cu: 0.4	2.7	190	200	110	68	55	27	0.88	23
2	AA6061-T6	Al: 96–98 Mg: 1 Si: 0.4–0.8 Cu: 0.15–0.4	2.7	170	310	270	96	93	10	0.9	24
3	AA5182-O	Al: 93–96 Mg: 4.5 Mn: 0.4	2.65	130	280	130	130	69	12	0.9	24
4	AA5754-O	Al: 94–97 Mg: 3	2.67	130	210	90	96	52	19	0.9	24
5	AA5454-O	Al: 94–97 Mg: 3 Mn: 0.5–1	2.69	130	240	100	120	61	17	0.9	23.6
6	AA5052	Al: 96–98 Mg: 2.5	2.68	138	190	79	117	47	22	0.88	25.7
7	AA5454	Al: 94–97 Mg: 3 Mn: 0.5–1	2.69	130	240	100	83	61	17	0.9	24
8	AA5154	Al: 94–97 Mg: 3–4 Cr: 0.15–0.35	2.66	130	240	94	100	58	20	0.9	24

(continued)

Table 1 (continued)

S.No.	Material	Composition	Density (g/cm³)	Them. cond. (W/mK)	U-T-S (MPa)	Y-T-S (MPa)	F-S (MPa)	Hardness (BHN)	Percent elong. at break	Specific Δ (J/g °C)	Coeff. of them. exp. (μm/m-C)
9	AA 6061-T4	Al:96–98 Mg: 1 Si: 0.4–0.8 Cu: 0.15–0.4	2.7	170	230	130	96	63	18	0.9	24

Table 2 Properties of Mg alloy materials [20]

S. No.	Material	Composition	Density (g/cm³)	Them. cond. (W/mK)	U-T-S (MPa)	Y–T-S (MPa)	F-S (MPa)	Hardness (BHN)	Per cent elong. at break	Specific Δ (J/g °C)	Coeff. of them. exp. (μm/m-C)
1	AZ91	Mg: 88–91 Àl: 8.3–9.7 Zn: 0.3–1 Mn: 0.13–0.5	1.81	72.7	230	150	97	63	3	0.8	26
2	AM60	Mg: 92–94 Al: 5.5–6.5 Mn: 0.1–0.6	1.79	62	241	131	80	65	13	1	26
3	AM50	Mg: 93–95 Al: 4.4–5.4 Mn: 0.2–0.6	1.77	65	228	124	75	60	15	1.02	26
4	AZ31	Mg: 93–97 Al: 2.4–3.6 Zn: 1 Mn: 0.05–1	1.771	96	260	200	90	49	15	1	26
5	ZE41	Mg: 91–95 Zn: 3.5–5 Zr: 0.4–1	1.84	113	205	140	63	62	3.5	1	26
6	EZ33	Mg: 91–95 Zn: 2–3 Zr: 0.5–1	1.8	99.5	200	140	40	50	3.1	1.04	26.4
7	ZE63	Mg: 89–92 Zn-5.5–6 Zr: 0.4–1	1.87	109	295	190	79	75	7	0.96	27

(continued)

Table 2 (continued)

S. No.	Material	Composition	Density (g/cm³)	Them. cond. (W/mK)	U-T-S (MPa)	Y–T-S (MPa)	F-S (MPa)	Hardness (BHN)	Per cent elong. at break	Specific Δ (J/g °C)	Coeff. of them. exp. (μm/m-C)
8	ZC63	Mg: 89–92 Zn: 5.5–6.5 Cu: 2.4–3 Mn: 0.25–0.75	1.87	122	240	125	93	60	4.5	1	26

Table 3 Titanium alloy materials and its properties [21]

S. No.	Material	Composition	Density (g/cm³)	Them. cond. (W/mK)	U-T-S (MPa)	Y-T-S (MPa)	F-S (MPa)	Hardness (BHN)	Percent elong. at break	Specific Δ (J/g °C)	Coeff. of them. exp. (μm/m-C)
1	Grade 1	(cp-Ti: 0.2 Fe, 0.18 O)	4.51	16	240	180	170	122	24	0.52	8.7
2	Grade 4	(cp-Ti: 0.5 Fe–0.40 O)	4.51	17.2	550	480	250	280	15	0.53	9.2
3	Grade 6	(Ti-5Al-2.5 Sn-0.5 Fe)	4.507	8.66	890	840	290	297	11	0.55	9.4
4	Near-α titanium alloys: Ti-6-2-4-2-S	Ti-6 Al-2 Sn-4 Zr-2 Mo-0.1 Si	4.54	7	1110	1050	320	333	3	0.46	7.7
5	TIMETAL 1100	Ti-6 Al-2.7 Sn-4 Zr-0.4 Mo-0.4 Si	4.5	7	1034	924	655	337	4	0.545	8.5
6	TIMETAL 685	Ti-6 Al-5 Zr-0.5 Mo-0.25 Si	4.45	4.15	1030	900	440	355	10	0.5	9.7
7	TIMETAL 834	Ti-5.8 Al-4 Sn-3.5 Zr-0.5 Mo 0.7 Nb-0.35 Si-0.06 C	4.55	7.06	1050	930	560	342	11	0.52	10.6
8	α + β titanium alloys: Ti-6-4	Ti-6 Al-4 V	4.43	6.7	950	880	240	334	14	0.53	9.2

(continued)

Table 3 (continued)

S. No.	Material	Composition	Density (g/cm³)	Them. cond. (W/mK)	U-T-S (MPa)	Y-T-S (MPa)	F-S (MPa)	Hardness (BHN)	Percent elong. at break	Specific Δ (J/g °C)	Coeff. of them. exp. (μm/m-C)
9	Ti-6-6-2	Ti-6 Al-6 V-2 Sn	4.54	6.6	1050	980	190	367	14	0.67	9.4
10	Ti-6-2-4-6	Ti-6 Al-2 Sn-4 Zr-6 Mo	4.64	7.61	1199	1047	262	360	7	0.5	9
11	Ti-17	Ti-5 Al-2 Sn-2 Zr-4 Mo-4 Cr	4.65	7.8	1170	1034	621	369	11	0.525	8.5
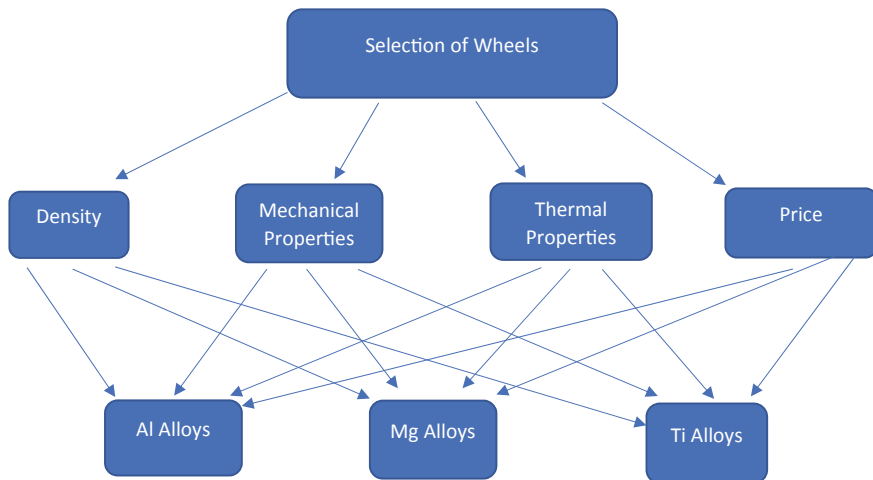
Fig. 1 Flowchart for the properties and materials

Step-2: Calculation of N-D-M (Normalized-Decision-Matrix)

The NDM denotes the relative performance of design choices.

$$\text{NDM} = R_i = \frac{X_{ij}}{\sqrt[2]{\sum_{i=1}^{m} X_{ij}^2}} \tag{2}$$

Step-3: Calculation of WDM (Weighted Decision Matrix)

The WDM is a one which is constructed by multiplication of each and every element of vertical column of N-D-M @@(1) by their respective assigned weights.

$$\text{WDM} = V = V_{ij} = w_j \times R_{ij} \tag{3}$$

Step-4: Identifying P-I-S (Positive-Ideal-Solution) and N-I-S (Negative-Ideal-Solution)

P-I-S and N-I-S are denoted by A^+ and A^-, respectively. Both positive (A^+) and $-$ve (A^-) answers are evaluated using weighted decision matrix (WDM) defined in Eq. (3) above via Eqs. (4) and (5) below.

$$\text{PIS} = A^+ = \left\{ V_1^+, V_2^+, V_3^+, \ldots, V_n^+ \right\}$$

Here:

$$V_j^+ = \left\{ \left(\max i\left(V_{ij} \right) \text{ if } j \in J \right); \left(\min i\left(V_{ij} \right) \text{ if } j \in J' \right) \right\} \tag{4}$$

$$\text{NIS} = A^- = \left\{V_1^-, V_2^-, V_3^-, \ldots, V_n^-\right\}$$

Here:

$$V_j^+ = \left\{\left(\min i\left(V_{ij}\right) \text{ if } j \in J\right); \left(\max(V_{ij}) \text{ if } j \in J'\right)\right\} \tag{5}$$

where J^- in Eqs. (4) and (5) is characterized along with non-beneficial characteristics and J^+ represents beneficial characteristics.

Step-5: In this step, the separation distance of each choice is found from ideal and non-ideal solutions.

$$S^+ = \sqrt[2]{\sum_{j=1}^{n}\left(V_j^+ - V_{ij}\right)^2} \text{ where } i = 1, 2, \ldots, m \tag{6}$$

$$S^- = \sqrt[2]{\sum_{j=1}^{n}\left(V_j^- - V_{ij}\right)^2} \text{ where } i = 1, 2, \ldots, m \tag{7}$$

Here, i = criterion index and j = alternative index.

Step-6: The relative closeness of each location is calculated from the ideal solution. The relative closeness of ith choice is given as:

$$R = S_i^- / S_i^+ + S_i^- \tag{8}$$

Here, $0 \leq R \leq 1$, $i = 1, 2, 3, \ldots, m$.

Step-7: The preferences order obtained is ranked or the highest alternative among them is selected. A group of different alternatives can be arranged in decreasing order by C values from Eq. 8.

4 Result and Discussion

The results of various metals are given below one by one using the TOPSIS technique. Also after identifying which alloy is best among various alloys taken, further results are found out among the best ones which we have got and accordingly by taking two of its applications which are heavy weight vehicles and expensive vehicles, one alloy is chosen which can be feasibly used in both these applications.

Table 4 Ranking table for Mg

Ranking	Alloy name
1	AZ31
2	AM50
3	AM60
4	ZE63
5	ZC63
6	AZ91
7	ZE41
8	EZ33

Table 5 Ranking table for Al

Ranking	Alloy name
1	TIMETAL 834
2	Ti-6-6-2
3	TIMETAL 685
4	TIMETAL 1100
5	Ti-6-4
6	Grade 4
7	Grade 1
8	Ti-6-2-4-6
9	Grade 6
10	Ti-17
11	Ti-6-2-4-2-S

4.1 Aluminium Alloys

After applying the steps involved in TOPSIS process, below is the ranking Tables 4 and 5, and for Magnesium alloys (Figs. 2 and 3).

4.2 Magnesium Alloys

See Figs. 4 and 5; Table 6.
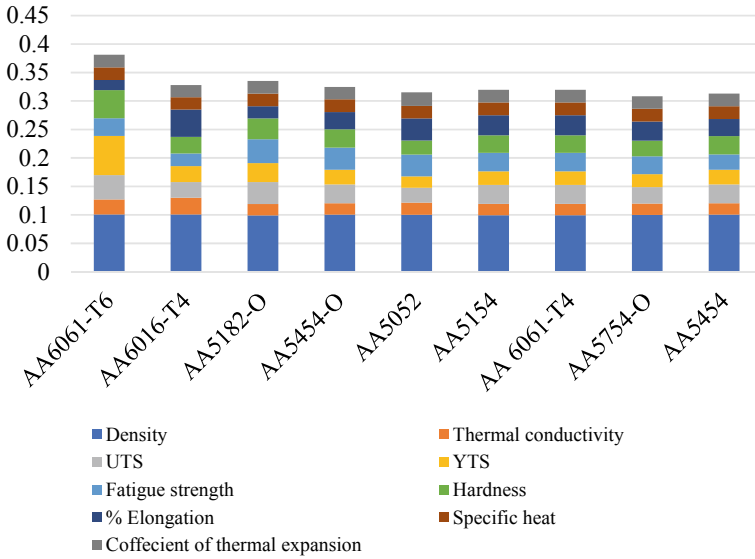
Fig. 2 Weighted value chart for Al Alloys
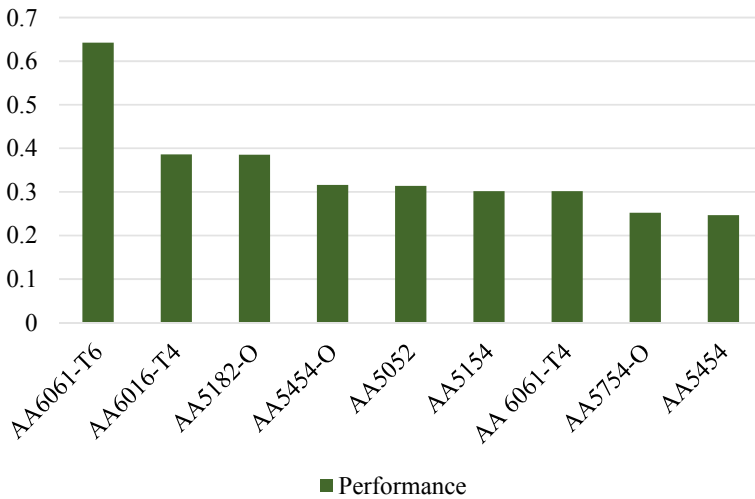
Fig. 3 Relative closeness chart for Al alloys

4.3 Titanium Alloys

Using the TOPSIS technique, we find that AA6061-T6 is the best alternative to use among aluminium alloys, AZ31 is the best alternative among magnesium alloys and TIMETAL 834 is the best alternative among titanium alloys (Figs. 6 and 7).
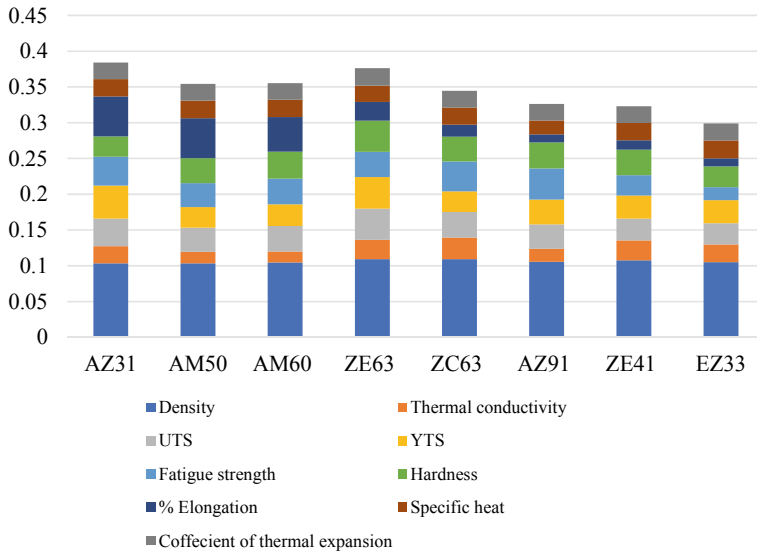
Fig. 4 Weighted value chart for Mg alloys
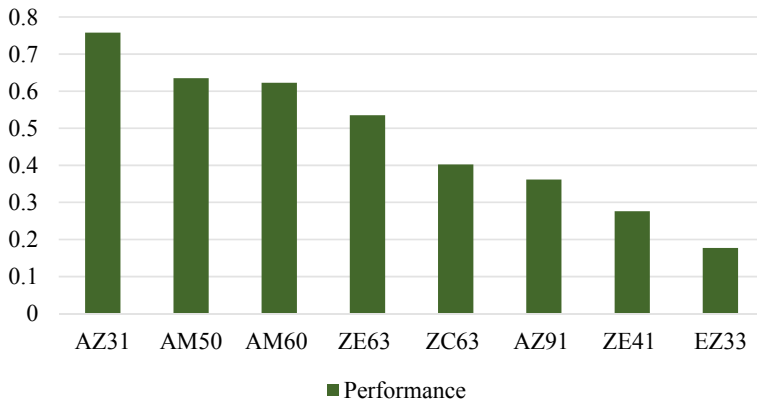
Fig. 5 Relative closeness chart for Mg alloys

We now find out the best alternative among these three alloys for two applications: heavy weight vehicles and expensive vehicles. For this, we have introduced a new column in our table which is price of the metal per kg.

Table 6 Ranking for Ti

Ranking	Alloy name
1	TIMETAL 834
2	Ti-6-6-2
3	TIMETAL 685
4	TIMETAL 1100
5	Ti-6-4
6	Grade 4
7	Grade 1
8	Ti-6-2-4-6
9	Grade 6
10	Ti-17
11	Ti-6-2-4-2-S
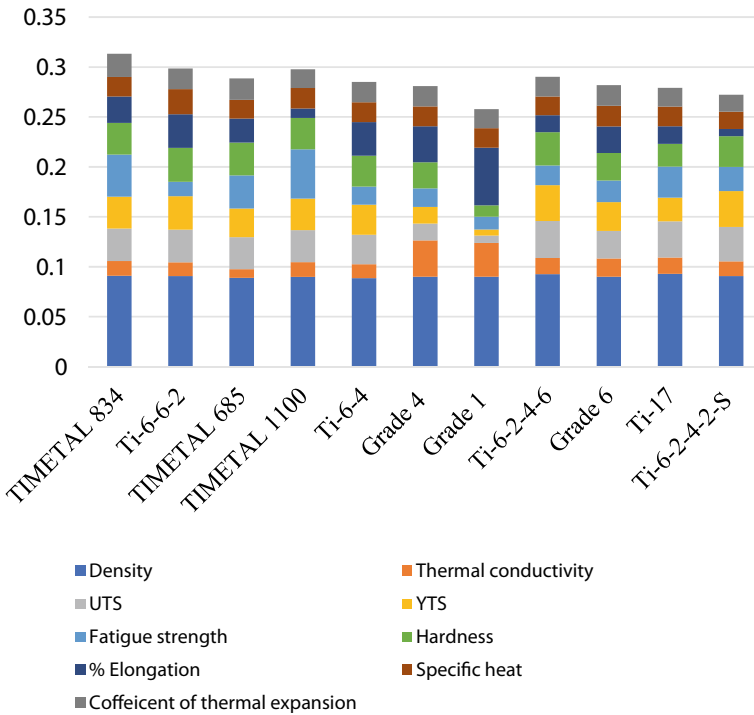
Fig. 6 Weighted value chart for Ti alloys
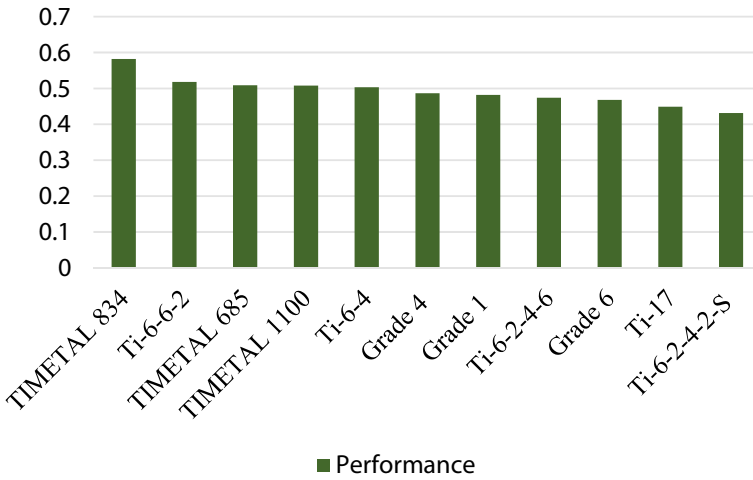
Fig. 7 Relative closeness chart for Ti alloys

4.4 Heavy Weight Vehicles

To obtain weighed value decision matrix using Eq. 3, the properties are divided into three categories and accordingly weights are assigned to them (Figs. 8 and 9; Tables 7, 8 and 9).
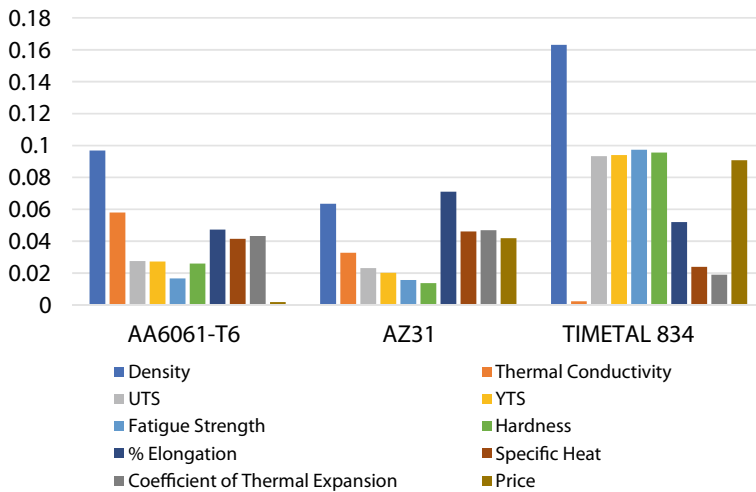
Fig. 8 Weighted value chart for heavy vehicles alloys
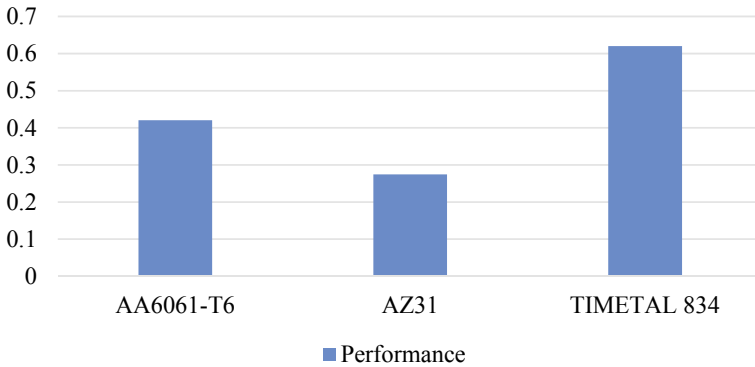
Fig. 9 Relative closeness chart for heavy vehicles alloys

4.5 Expensive Vehicles

See Figs. 10 and 11; Table 10.

5 Conclusion

Using TOPSIS technique, we are able to find an alternative from the given options of alloys of a particular element as a wheel material. In the above study, AA6061-T6 is best among aluminium Alloys, AZ31 is the best among magnesium alloys, and TIMETAL 834 is best among Titanium alloys.

Also, among the best alternatives of each element's alloys, when the application of heavy weight vehicles is taken into consideration, density is considered as a beneficial attribute and hence the 1st best alternative among the three alloys comes out as titanium alloy (TIMETAL 834) and the 2nd best comes out as aluminium alloy (AA6061-T6). Also, when the application of expensive vehicles is considered, the price is included as a beneficial attribute since this attribute has large value and hence the 1st best alternative among the three alloys comes out to be titanium alloy (TIMETAL 834) and the 2nd best comes out as magnesium alloy (AZ31).

Table 7 Properties of three alloys selected from Al, Mg, and Ti groups

S.No.	Density (g/cm³)	Them. cond. (W/m-K)	U-T-S (MPa)	Y-T-S (MPa)	F-S (MPa)	Hardness (BHN)	Percent elong. at break	Specific Δ (J/g °C)	Coeff. of them. exp. (μm/m-C)	Price (/kg)
AA6061-T6	2.7	170	310	270	96	93	10	0.9	24	130
AZ31	1.771	96	260	200	90	49	15	1	26	3000
TIMETAL 834	4.55	7.06	1050	930	560	342	11	0.52	10.6	6500

Table 8 Calculated weights

Properties	Physical properties	Mechanical properties	Price	Thermal properties
Weights	0.2	0.1	0.1	0.0666

Table 9 Ranking of heavy vehicles

Ranking	Alloy name
1.	TIMETAL 834
2.	AA6061-T6
3.	AZ31
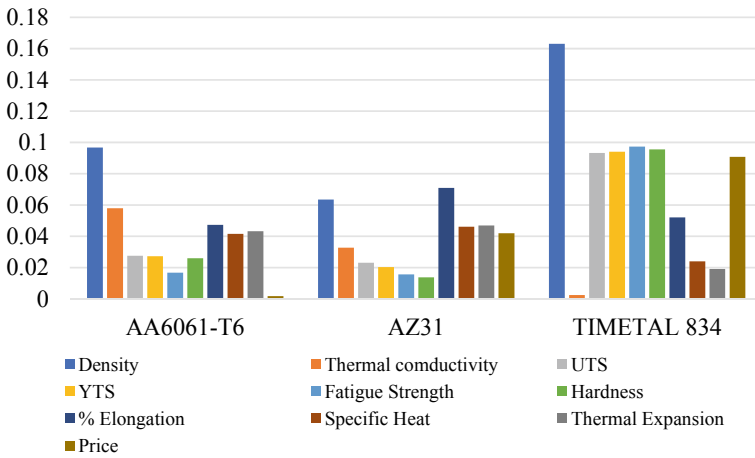
Fig. 10 Weighted value chart for expensive vehicles alloys
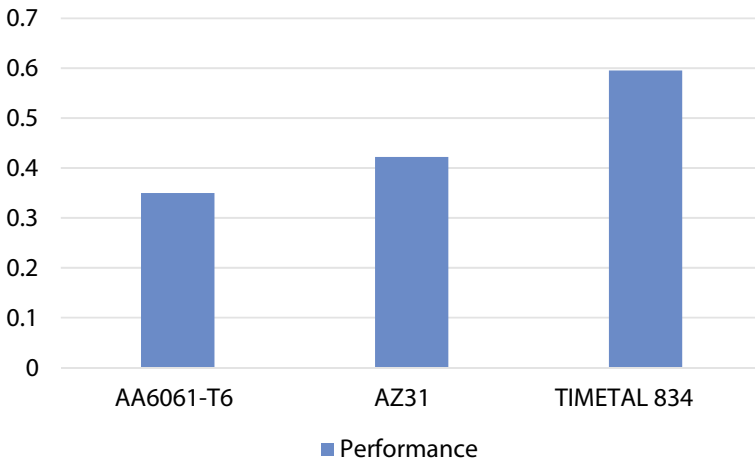
Fig. 11 Relative closeness chart for expensive vehicles alloys

Table 10 Ranking for high-priced automobiles

Ranking	Alloy name
1	TIMETAL 834
2	AZ31
3	AA6061-T6

References

1. Sameer Kumar, D., Tara Sasanka, C., Ravindra, K., Suman, K.N.S.: Magnesium and Its Alloys in Automotive Applications—A Review
2. Lutsey, Nicholas, P.: Review of Technical Literature and Trends Related to Automobile Mass-Reduction Technology
3. Stearns, J., Srivatsan, T.S., Prakash, A., Lam, P.C.: Modeling the Mechanical Response of an Aluminum Alloy Automotive Rim
4. Sabri Sidik, M., Mu'az, A., Shahril, K., Ab-Kadir, A.R., Ihsan, J.: Design Analysis of Car Wheel Rim Deformation Behaviour Under Different Static Loading
5. Patel, M.V., Bhatt, P., Patel, M.: Review Paper on Wheel Rim
6. Stearns, J., Srivatsan, T.S., Gao, X., Lam, P.C.: Understanding the Influence of Pressure and Radial Loads on Stress and Displacement Response of a Rotating Body: The Automobile Wheel
7. Kale, H.N., Dhamejani, C.L., Galhe, D.S.: Comparative Study of Wheel Rim Materials
8. Sai Virinchy, C., Hafeezasif, A., Jayakumar, V., Santhosh Kumar, D., Raviteja Reddy, M.: Review on Selection, Manufacturing and Testing of Composite Materials for Alloy Wheels
9. Lumm, J.A., Hughes, G.M., Bastian, B.J.: Application of High Strength Steels to Wheel Manufacturing
10. Takahashi, M.: Development of High Strength Steels for Automobiles
11. Tsybanev, G.V., Ponomarev, S.L.: Fatigue of low-carbon and low-alloyed steels for the automotive industry. Part 1. The influence of stress concentration and fretting on fatigue life of full-scale automobile wheels and specimens
12. Froes, F.H., Friedrich, H., Kiese, J., Bergoint. D.: Titanium in the Family Automobile: The Cost Challenge
13. Lutjering, G., Williams, J.C.. Gysler, A.: Microstructure and Mechanical Properties of Titanium Alloys
14. Blawert, C., Hort, N., Kainer, K.U.: Automotive Applications of Magnesium and Its Alloys
15. Suguna, M.: Comparative Analysis of Automotive Wheel Rim by Using Different Materials
16. Puncioiu, A.-M., Truţă, M., Marinescu, M., Grosu, D., Vînturiş, V.: Analysing the Uniformity of an Automobile Wheels' Distribution of Slipping and Skidding
17. Jiang, J., Wang, Y., Chen, G., Liu, J., Li, Y., Luo, S.: Comparison of Mechanical Properties and Microstructure of AZ91D Alloy Motorcycle Wheels Formed by Die Casting and Double Control Forming
18. Swapna, D., Srinivasa Rao, Ch., Sameer Kumar, D., Radhika, S.: AHP and TOPSIS based selection of aluminium alloy for automobile panels. J. Mech. Energy Eng. (2019)
19. https://www.makeitfrom.com/material-properties/6061-T6-Aluminum
20. Sameer Kumar, D., Suman, K.N.S.: Selection of magnesium alloy by MADM methods for automobile wheels. Int. J. Eng. Manuf. **2**, 31–41 (2014)
21. https://www.azom.com/properties.aspx?ArticleID=1641
22. Sri Krishna, S., et al.: A new car selection in the market using TOPSIS technique. Int. J. Eng. Res. Generic Sci. (IJERGS) (2014)

A Study on Comfort in Higher Education

Sameen Mustafa , **Mubashshir Ahmad Ansari, and Qasim Murtaza**

Nomenclature

Symbol	Description
AC	Acoustic comfort
BB	Black or green board
CL	Cleanliness
CR	Colour of room
DO	Doors
HV	Heat ventilation
IQ	Illumination quality
PT	Projector technique
SA	Seating arrangement
TC	Table and chair
WW	Window

S. Mustafa (✉)
Department of Mechanical and Aerospace Engineering, Politecnico di Torino, Turin, Italy
e-mail: sameenmustafa4@gmail.com

M. A. Ansari
Mechanical Engineering Department, Aligarh Muslim University, Aligarh 202002, India

Q. Murtaza
Department of Mechanical, Production & Industrial and Automobile Engineering, Delhi Technological University, Delhi 110042, India

1   Introduction

Globally, the highest heat load occurs in subtropical and arid places. High levels of heat and humidity prevail round the year in equatorial regions. In tropical climates of mountains (altitudes between 1600 and 1900 m above sea level), there is a minimal stress because of either heat or cold. In these climates however, for a person in a street at noon, discomfort increases drastically due to high levels of radiation [1]. Wong and Khoo [2] conducted a field study in classrooms ventilated by fans in Singapore during the lesson hours. It was shown that the classroom occupants generally acknowledged cool thermal sensations rather than warm thermal sensations. Their study showed that the tolerable temperatures range was 27.1–29.3 °C which implied that the ASHRAE standard 55–92 [3] was improbable to free running buildings in their respective local climates.

Adult musculoskeletal disorders (MSDs) like pain in back and neck are a major health concern in places where the working/sitting hours are longer. Khanam et al. [4] presented a review under five categories: vision, posture, computer usage, pain reporting, anthropometrics and furniture. They suggested that MSD among school children could be reduced by incorporating integrated ergonomics approach such as posture education, classroom furniture design, backpack weight as well as load carrying capability. Low back pain has been of significant concern over health and economy in advanced and industrialized countries [5, 6]. Yeats reported that the classroom in schools is like a workplace and that its workers are its pupils and that they are the adult workers of tomorrow [7]. According to Grimes and Legg [8], in adult workplace, major focus should be laid upon ergonomically designed seating and proper positioning in certain working environments.

Norbäck and Nordström [9] studied the effects of ventilation in computer classrooms on university students in a blinded study. It was observed that higher air exchange resulted in a perception of low temperature, greater air movement and improved air quality. Also, increasing ventilation from 7 l/s to 10–13 l/s per person could provide better thermal comfort and good air quality. They demonstrated that increasing air exchange in computer classrooms, from mean CO_2 levels in the range of 830–930 ppm to 1040–1200 ppm, provided better thermal comfort and indoor air quality (IAQ). Another review impressed that better IAQ could be achieved by plummeting CO_2 levels to 800 ppm [10]. Still another study on health, productivity and ventilation, EUROVENT, concluded that a low ventilation was related to ill effects on health and degraded the performance in offices [11]. One study suggested that increasing the personal outdoor airflow rate from 1.3 to 11.5 l/s lowered the risk of symptoms of asthma in school children [12]. Dense indoor environments like classrooms can provide both thermal discomfort and poor indoor air quality.

Frontczak and Wargocki [13] made a literature survey in which they considered the following comfort factors: thermal, visual, acoustic and air quality. They suggested that in order to design systems for the control of indoor environment, the building type and outdoor climate need to be considered. It was also reported that thermal comfort is of greater importance than visual and acoustic comforts.

About 5–12% of students suffer at least moderate signs of hypersensitivity to brightness and high-contrast repetitive patterns. This condition leads to symptoms of visual discomfort and visual perceptual distortions when reading [14, 15]. Haverinen-Shaughnessy et al. conducted a study in which it was found that a considerable amount of energy was used to provide thermal comfort in educational buildings. Significant associations were found between satisfactory scores in mathematics and reading tests and indoor temperature, ventilation rate and hygiene of high contact surfaces [16].

This paper aims at studying the methods used in different studies for human comfort in education. Various suggestions given by different authors in their reviews have been discussed. There is a further scope of continuing this study by incorporating questioners from students studying in newly designed or renovated rooms and rating their comfort. In future, this type of study can help to recommend prototypes for modern and smart classrooms in the age of technology.

2 Methodology

This study mainly focusses on reviews from tropical and subtropical regions. A literature search has been carried out for articles showing the results of studies on how thermal comfort, IAQ, ergonomic furniture, thermal comfort between genders and variation in climatic zones affect the perception of comfort and performance of occupants in educational buildings. A survey incorporating 300 students using questioners is also included in this study. Throughout this article, comfort deals with satisfying aspects such as IAQ, acoustic and visual comfort, furniture design and comfort between genders. The effect of each factor on comfort has been studied in detail, and proper choice of these factors has been suggested to gain the optimal condition of human comfort and efficiency. Relevant study articles were found in electronic databases of Google Scholar, Science Direct, John Wiley and Sons, Taylor and Francis and Springer. Twenty-two articles in the period from 1987 to 2017 have been included in the present survey. The results of some studies are shown in Table 1.

3 Result and Discussion

3.1 Thermal Comfort

Human body is like a thermodynamic machine. About 115 W of thermal energy is emitted due to metabolism of body. The human body must dissipate the heat generated from metabolism, and it is like a thermodynamic machine whose efficiency η is given by [21, 22]:

Table 1 Overview of some studies showing factors effecting comfort of students

Study	Nature of study	Results
[17]	Measurements and questioners held in 14 schools each with different ventilation and heating	Application of Thermo Active Building systems (TABS) could improve the perceived thermal comfort for students in winter. TABS give better result than any other traditional heating system.
[18]	Review examining effect of different gender on internal thermal comfort	Females experience more discomfort than males while being in same thermal environments. They have lower tolerances to deviations from optimal thermal environments.
[19]	Review on building energy consumption implications and thermal comfort	Reduction in cold stress and increasing heat stress would lead to less space heating requirement in cold seasons and risk the increase of summer overheating, respectively. Proper analysis of combined cooling, heating and power (CCHP) systems is important for catering cooling and heating requirements in different climatic zones.
[20]	Review on thermal comfort in educational buildings	Human adaptability is influenced both by indoor and outdoor climates. Thermal comfort evaluations for both climates lead to better outcomes. Students prefer cooler environments and are more sensitive to warmer conditions.

$$\eta = 1 - \frac{T_1}{T_2}$$

where T_1 is the ambient temperature (in °C) and T_2 is the body temperature (in °C). The reference datum for the comfort sensation is skin temperature. Thus, the air conditioning of classrooms should be done in accordance with the heat losses shown in Fig. 1a and the comfort zone shown in Fig. 1b so that the pupils learn and work with greater efficiency.

In conditions of higher ambient temperature than the body temperature, the body heat is not dissipated properly, and thus, the thermal discomfort sets in leading to sweating. Comfort can be provided by ensuring proper ventilation through fans and blowers. However, in tropical and subtropical climates where the humidity is very high, proper air-condoning systems should be installed to ensure comfort. Proper clothing is important to achieve thermal comfort in different climatic conditions. Therefore, the college dress code must be such that it recommends cotton clothing in high temperature and humid conditions. On the other hand, woolen and insulated clothes should be recommended in cold conditions.

(a)

(b)
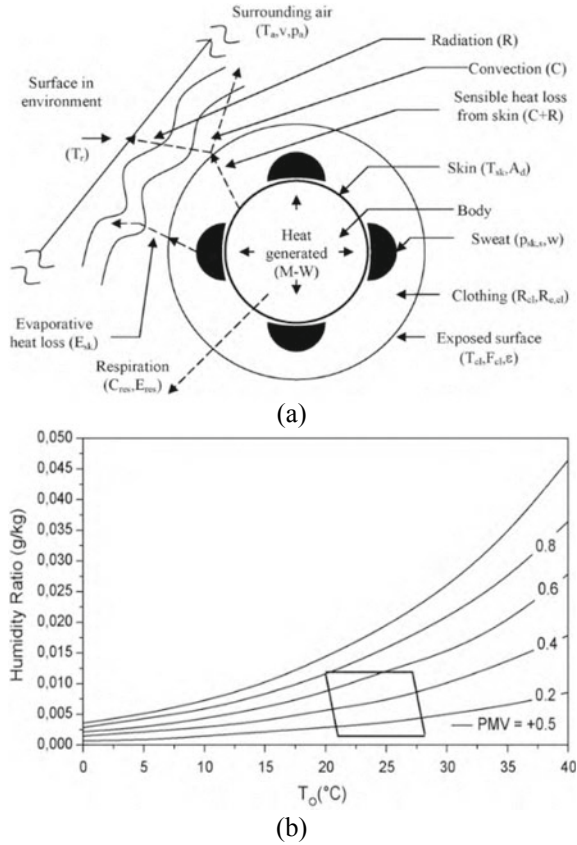
Both the indoor and outdoor climates influence human adaptability [20]. Studies have shown that students prefer cooler environments [17, 18, 20]. As a result of providing daylight in classrooms through large windows, excess heat load occurs during noon. This leads to discomfort in students. To check discomfort due to high incoming heat, proper insulating curtains should be installed in classrooms. In places where temperatures are very high during the day, study light should be provided to compensate for the natural light. However, cool daylights must be used in classrooms, else, heat load might increase.

3.2 Furniture, Visual and Acoustic Comfort

The definition of visual comfort is, "a subjective condition of visual well-being induced by the visual environment" [13]. Factors like luminance, illuminance, glare, flicker rate, colour of light and amount of daylight effect the visual conditions and hence the comfort. Thus, classrooms should be designed such that there is plenty of

light available for students; moreover, the lights should be positioned in such a way that glare is prevented.

Acoustic comfort is defined as "a state of contentment with acoustic conditions" [13]. It is influenced by factors such as reverberation time, absorption and sound insulation. Other factors influencing listening in an environment are classroom style and seating arrangements. The use of classroom amplification systems will aid to better understanding of teacher speech. Studies from some developed countries suggest that providing a good classroom acoustic environment is a challenging task. A good acoustic environment can be achieved by employing sound field amplification and better sound absorbing materials in lecture rooms, noise issues when designing schools should also be considered. The use of slotted timber panels can aid to acoustic comfort considerably.

From these studies, it can be observed that visual and aural comfort is not as critical for students as the thermal comfort. Further, less literature was available as to how the thermal comfort is influenced by visual and aural factors. For example, if a classroom is well air-conditioned, the students feel comfortable to compromise with the noise coming from fans and air conditioners. These details are needed in carrying out remedial and renovating actions in buildings. The design of school furniture should be allowing comfortable body posture and preventing MSDs. The clearance between desk and chair should be adequate to allow a student to move into or out of it comfortably. A student sitting on low seat slouches and pushes the feet forward and thus becomes a disturbance to others. Legs freely hanging of high seats can too cause discomfort. The height of the back rest of chairs, angle of the back rest and its dimensions should be such that it stabilizes the lumbar region. Cushioned seats provide more human comfort. An optimum anthropometrical design of educational furniture is that of chair with arm tablet and sled desk [8]. Hence, adopting these designs can prevent pack pain and lethargy among the students.

3.3 Short Survey

The authors took a short survey in the classrooms of Zakir Hussain College of Engineering and Technology (Aligarh). This included all the comfort factors that were possibly present in classrooms. The survey was conducted among 300 students to find about relevant comfort factor and performance. In this survey, out of 300 students, 250 are boys, and 50 are girls, and every student has given opinion. Survey was conducted by distributing questionnaires among students. After arranging the selected comfort factor, a rating was collected corresponding to each factor. The result of survey is shown in Fig. 2.

The furniture and colour of room received average rating, while the projecting technique and cleanliness received a good rating. However, the seating arrangement and acoustic conditions were not up to the mark. Therefore, care should be taken to place sled desks which are of utmost comfort for students [4]. The aural and visual comfort should be addressed according to the study provided by Frontczak

	IQ	TC	BB	CR	HV	PT	CL	AC	SA	DO	WW
■ Very Good	35	0	0	10	3	120	201	0	0	13	21
■ Good	138	0	51	92	21	74	35	0	91	105	28
■ Average	127	151	126	181	50	30	51	132	163	125	73
■ Bad	0	92	62	5	120	76	5	65	3	21	33
■ Very Bad	0	57	61	12	106	0	8	103	43	36	145

■ Very Good   ■ Good   ■ Average   ■ Bad   ■ Very Bad
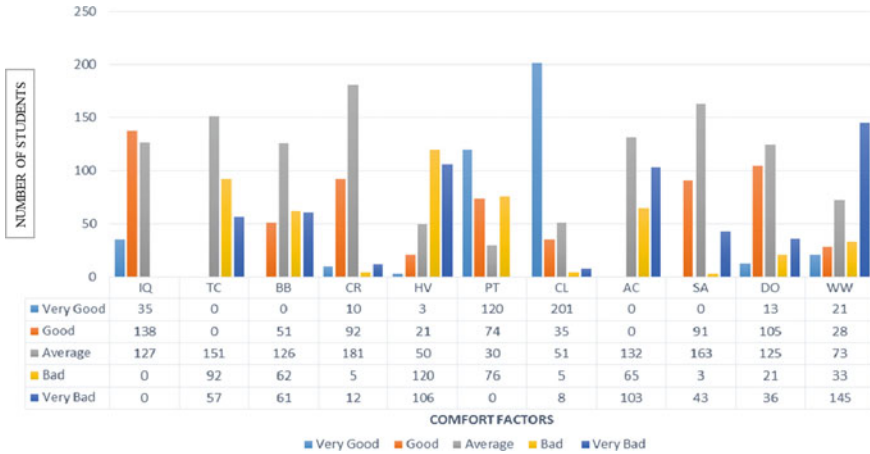
Fig. 2 Survey of comfort factor

and Wargocki [13]. It can be suggested that most of the students find it comfortable to read if they are exposed to full spectrum fluorescent light. Thus, classroom must be made well in terms of quantity (300 lx) as well as quality of the light for providing the comfort to students and teachers. Some LED lights can now function as a warm light, bright light and full spectrum light by varying the temperature of the filament as 2700 K, 3500 K and 5600 K, respectively.

4   Conclusion

This paper shows how different comfort factors in classrooms are responsible for increase in the students' performances. The efficiency of students can be maximized by providing them a perfect working environment. As the academic load is more on the students of higher class (undergraduate to post-doctorate), their studying and working conditions require more attention by the researchers. Providing classrooms with optimum air conditioning based on the local climate and proper spacing between the furniture will provide a relaxed environment. To enhance the output of the students, judicious choice of furniture, insulation, proper arrangement of lights and application of TABS will be required in classrooms as the students of today are the workers of tomorrow. To ensure the visual and aural comfort, rooms should incorporate smart LED lights as well as sound insulators like acoustic timber panels. Planners should keep it in mind that while designing the systems for controlling the indoor environment, the possibility of customizing environmental conditions according to the occupier's need may be offered in order to reflect their preferences.

References

1. Jauregui, E.: The human climate of tropical cities: an overview. Int. J. Biometeorol. **35**(3), 151–160 (1991)
2. Wong, N.H., Khoo, S.S.: Thermal comfort in classrooms in the tropics. Energy Build. **35**(4), 337–351 (2003)
3. ASHRAE, ASHRAE Standard 55: Thermal Environmental Conditions for Human Occupancy, America Society of Heating, Refrigerating and Air-conditioning Engineers (1992)
4. Khanam, C.N., Reddy, M.V., Mrunalini, A.: Designing student's seating furniture for classroom environment. J. Hum. Ecol. **20**(4), 241–248 (2006)
5. Legg, S.J., Trevelyan, F.I., Carpentier, M.-P., Fuchs, B.: Musculoskeletal discomfort in New Zealand intermediate school students. In: Ergonomics for Children in Educational Environments Symposium at the 15th Congress of the International Ergonomics Association in Seoul, Korea, pp. 24–29 (2003, Aug)
6. Troup, J.D.G., Foreman, T.K., Baxter, C.E., Brown, D.: The perception of back pain and the role of psychosocial tests of lifting capacity. Spine **12**, 645–657 (1987)
7. Yeats, B.: Factors that may influence the postural health of schoolchildren (K-12). Work J. Prev. Assess. Rehabil. **9**(1), 45–55 (1997)
8. Grimes, P., Legg, S.: Musculoskeletal disorders (MSD) in school students as a risk factor for adult MSD: a review of the multiple factors affecting posture, comfort and health in classroom environments. J. Human-Environ. Syst. **7**(1), 1–9 (2004)
9. Norbäck, D., Nordström, K.: An experimental study on effects of increased ventilation flow on students' perception of indoor environment in computer classrooms. Indoor Air **18**(4), 293–300 (2008)
10. Seppänen, O.A., Fisk, W.J.: Summary of human responses to ventilation. Indoor Air **14**(Suppl. 7), 102–118 (2004)
11. Wargocki, P., et al.: Ventilation and health in non-industrial indoor environments: report from a European multidisciplinary scientific consensus meeting (EUROVENT). Indoor Air **12**, 113–128 (2002)
12. Smedje, G., Norbäck, D.: New ventilation systems at selected schools in Sweden-effects on asthma and exposure. Arch. Environ. Health **55**, 18–25 (2000)
13. Frontczak, M., Wargocki, P.: Literature survey on how different factors influence human comfort in indoor environments. Build. Environ. **46**(4), 922–937 (2011)
14. Evans, B.J., et al.: A Delphi study to develop practical diagnostic guidelines for visual stress (pattern-related visual stress). **10**(3), 161–168 (2017)
15. Uccula, A., et al.: Colors, colored overlays, and reading skills. **5**, 833 (2014)
16. Haverinen-Shaughnessy, U., et al.: An assessment of indoor environmental quality in schools and its association with health and performance. **93**, 35–40 (2015)
17. Zeiler, W., Boxem, G.: Effects of thermal activated building systems in schools on thermal comfort in winter. Build. Environ. **44**(11), 2308–2317 (2009)
18. Karjalainen, S.: Thermal comfort and gender: a literature review. Indoor Air **22**(2), 96–109 (2012)
19. Yang, L., Yan, H., Lam, J.C.: Thermal comfort and building energy consumption implications–a review. Appl. Energy **115**, 164–173 (2014)
20. Zomorodian, Z.S., Tahsildoost, M., Hafezi, M.: Thermal comfort in educational buildings: a review article. Renew. Sustain. Energy Rev. **59**, 895–906 (2016)
21. Djongyang, N., Tchinda, R., Njomo, D.: Thermal comfort: a review paper. Renew. Sustain. Energy Rev. **14**(9), 2626–2640 (2010)
22. Zingano, B.W.: A discussion on thermal comfort with reference to bath water temperature to deduce a midpoint of the thermal comfort temperature zone. Renew. Energy **23**(1), 41–47 (2001)

Investigation on Prediction Capability of Artificial Neural Network on Responses of Wire Electro Discharge Machining

Hargovind Soni and **P. M. Mashinini**

1 Introduction

The TiNi-based alloy is highly recommended for biomedical, robotics, aerospace applications for their popular properties [1]. TiNi-based alloys itself unique class of material; however, if third alloying element is added into TiNi, then the internal properties of these material can be increased as per the requirements [2]. For example, adding Co in TiNi, transformation temperature and biocompatibility can be increased of the TiNi alloy [3]. However, these materials are highly sensitive material and very difficult to handle with the conventionally available manufacturing techniques. It is mandatory to handle without losing the inherent properties of the material during machining. Hence, demand has risen to develop unconventional manufacturing process with a suitable process condition [4]. Because there is no direct contact between tool and work material during the non-conventional machining processes result; there is very less chance to affect their internal properties of these materials. WEDM is one of the appropriate processes to handle difficult-to-cut materials like Ti alloy, TiNi alloy and combinations of TiNiCo alloys [5]. To obtain the best surface roughness during this machining process, many researchers have been carried out the parametric study of this machining process and they found that pulse on time and servo voltage were affect mostly the surface roughness [6–8]. The data achieved from the experimental investigations are suggested to compare with the mathematically simulated data, further the experimental results and simulated data are compared to predict the error. Artificial neural network (ANN), response surface method (RSM) and gray wolf prediction techniques, etc. [9–12] were adopted by researchers for the comparative study. It has been noticed that neural-based networking model found more suitable and accurate than the other common simulated techniques. Hence,

H. Soni (✉) · P. M. Mashinini
Department of Mechanical and Industrial Engineering Technology, University of Johannesburg, Johannesburg, South Africa
e-mail: hargovindsoni2002@gmail.com

machining of $Ti_{50}Ni_{49}Co_1$ has been carried out with varying pulse one time and servo voltage and measured the surface roughness in present study. Moreover, ANN was used to predict outputs, and error analysis has been carried out in current research work.

2 Materials and Methods

The vacuum arc melting process is used to develop the TiNiCo-based alloy. The alloying element of the $Ti_{50}Ni_{49}Co_1$ is confirmed through the spectra analysis using energy-dispersive spectroscope, and the results achieved are given in Fig. 1. Experiments are designed with reference to the standard orthogonal array having twenty-five set (combination) of experiments. The WEDM process has been performed with the 0.25-mm-diameter wire, and de-ionized water was used as a dielectric fluid. Surface roughness was measured using surface roughness tester and presented in Table 1.

2.1 Artificial Neural Network (ANN)

An ANN is a biological networking model simulating the brain neuro (human neuro) systems. It is an interpolation of set of input data driven from the experimental results having an order of mathematical formulas for information processing. The NN system is a clause of nonlinear data processing system simulating the neuro systems. Each set holds a weightage for connections and processing of information

Element	Wt.%	At. %
Ti	44.92	50
Co	1.1	1
Ni	53.98	49
Totals	100	100

Full Scale 13848 cts Cursor: 10.330 (77 cts)
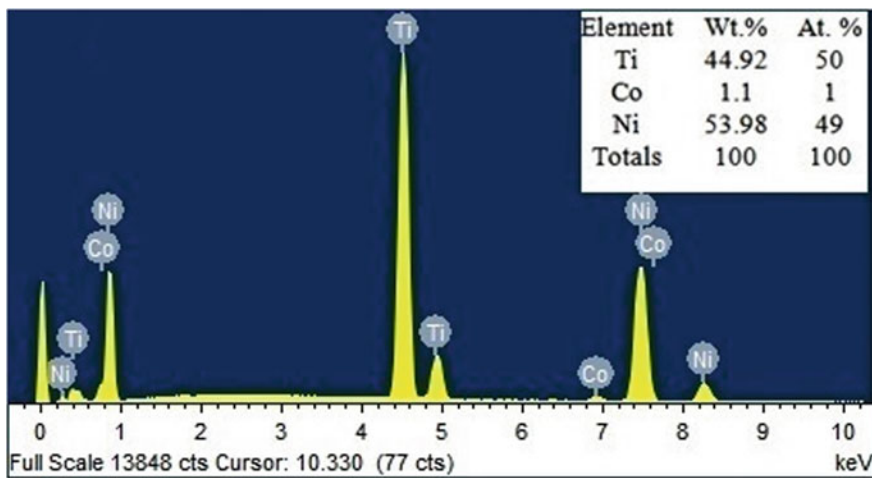
Fig. 1 EDX analysis of developed alloy

Table 1 Experimental and predicted values of surface roughness

Trial No.	Pulse on time (μs)	Servo voltage (V)	Experimental surface roughness	Predicted surface roughness
1	105	20	1.68	1.67
2	105	30	1.61	1.59
3	105	40	1.48	1.47
4	105	50	1.27	1.25
5	105	60	1.04	1.02
6	110	20	2.1	2.09
7	110	30	2.07	1.91
8	110	40	1.89	1.86
9	110	50	1.68	1.679
10	110	60	1.18	1.17
11	115	20	2.63	2.61
12	115	30	2.51	2.49
13	115	40	2.13	2.12
14	115	50	1.85	1.86
15	115	60	1.73	1.70
16	120	20	2.82	2.81
17	120	30	2.76	2.73
18	120	40	2.4	2.39
19	120	50	2.4	2.35
20	120	60	2.27	2.14
21	125	20	3.87	3.77
22	125	30	3.63	3.59
23	125	40	3.25	3.24
24	125	50	2.66	2.65
25	125	60	2.31	2.14

from one branch to others. The data processing is a feed-forward system operating with back-propagation model. There may be a greater number of input data with a combination of number of neurons to produced particular output. In this paper, two highly influential input process parameters, namely pulse duration and voltage, are used to simulate with NN to predict the minimum roughness of the machined surface roughness. Experimentally calculated data is used to train in a NN tool package available in MATLAB and the simulated to forecast the minimum surface roughness of $Ti_{50}Ni_{49}Co_1$ alloy machined using WEDM process. The data processing is of two; they are as training data and test data. The neuron layers in between the input and output data is constructed with a set of 15 hidden layers as shown in Fig. 2. From the experimentation, the 70% of the data reserved for training and the 30% of the data
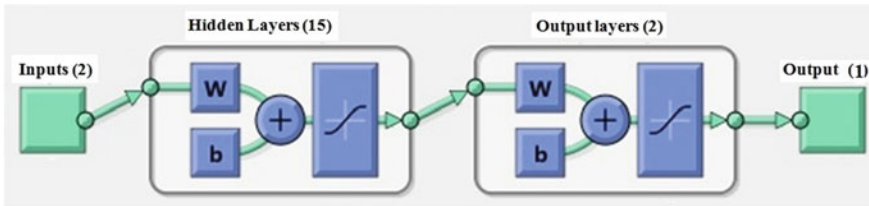
Fig. 2 Architect of the proposed neural network model

was used to compare in testing data [13]. The predicted information from the data simulation is given in Fig. 3.
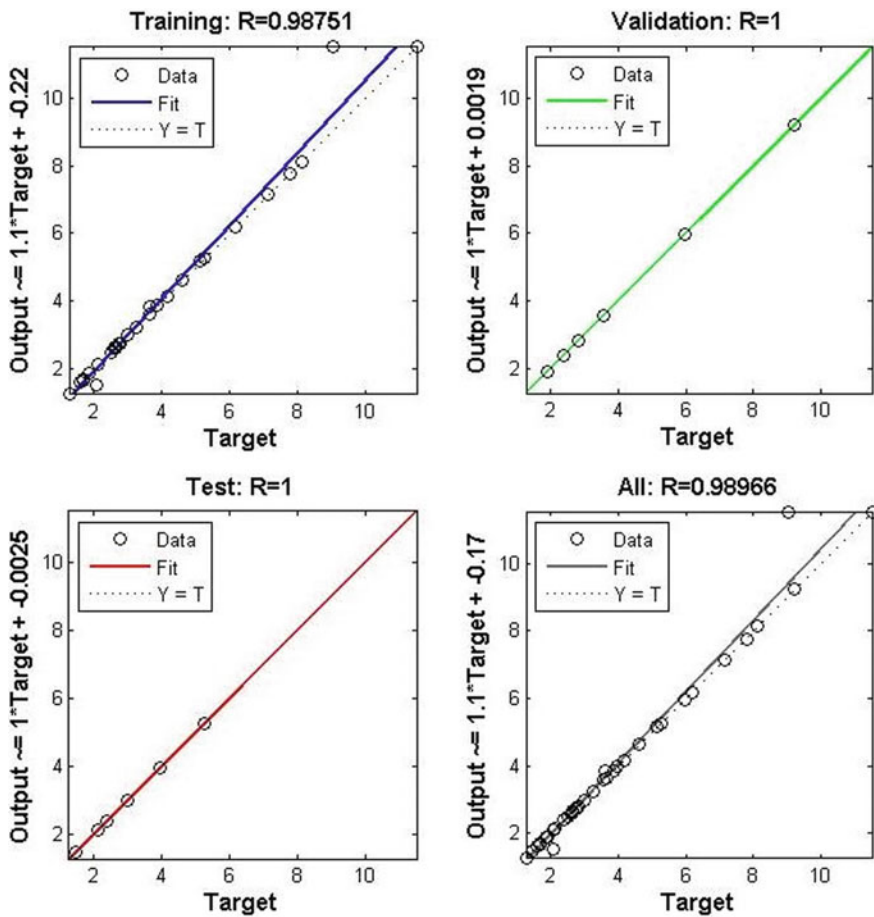
Fig. 3 Output data retrieved from the simulated data

3 Results and Discussion

From the mathematical simulation, the difference in experimental results and predicted results is calculated in the name of error analysis. The error predicted from the neural network is identified for wire electro discharge machining (WEDM) response such as the surface roughness (SR) during the machining of $Ti_{50}Ni_{49}Co_1$. Experimental and predicted surface roughness has been exhibited in Table 1. The absolute error analysis for the proposed mathematical modeling is calculated with the following equations:

$$\text{Absolute error (\%)} = \frac{\text{Experimental Value} - \text{predicted values}}{\text{Experimental value}} \times 100 \quad (1)$$

3.1 Effects of Each Experimental Run on Surface Roughness

As discussed above, that artificial neural network prediction tool is appropriate prediction tool for prediction the output responses. Similar behavior was observed by Karthikeyan et al. [14] that artificial neural network is suitable tool for better and have a higher predictive capability of surface roughness values. The values of surface roughness are predicted by artificial neural network in the present study. The response on each set of proposed design of experiment is validated, and the results are plotted in Fig. 4. The experimental results and the biologically simulated results in adjunct show very similar with negotiable differences. It is clear to infer that the surface roughness found sinusoidal with an increasing trend from the initial trial. The changes in the roughness value are due to the servo voltage and pulse duration. At higher servo voltage, the roughness found increase and decreased with the lower servo voltage. In connection with the spark duration, the effect of energy used to melt the metal is varying. The effect of dielectric fluid is also contributing toward the surface roughness. Research claims the same effect on machine difficult-to-cut hard material [15].

The maximum variation in the error percentage (between the experiments and simulated data) is found to be 8% (Table 2). At the same, the data predicted for the ANN found closer (accurate) and best results. ANN is an effect tool to predict the best result compared to other mathematical modeling concepts [16].
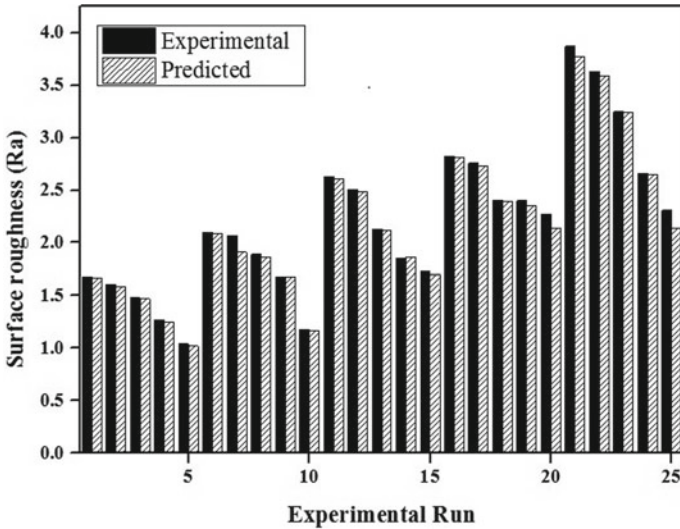
Fig. 4 Experimental and predicted values of SR for $Ti_{50}Ni_{49}Co_1$ alloy

Table 2 Maximum error

Alloy	Maximum error obtained through ANN
	SR
$Ti_{50}Ni_{49}Co_1$	8%

4 Conclusions

It has been confirmed that pulse duration and servo voltage are most influential process parameters for the machining selected alloy for the study of surface roughness. Minimum roughness of surface is found 1.04 μm at the 105 μs pulse on time and 60 V servo voltage, while maximum value 3.87 μm of roughness is found at the 125 pulse on time and 20 V servo voltage. Moreover, ANN gave maximum 8% error which means this prediction technique is most suitable technique for prediction of responses.

References

1. Nolan, M., Tofail, S.A.M.: Density functional theory simulation of titanium migration and reaction with oxygen in the early stages of oxidation of equiatomic NiTi alloy. Biomaterials **31**, 3439–3448 (2010)
2. Mohammad Sharifi, E., Kermanpur, A., Karimzadeh, F.: The effect of thermomechanical processing on the microstructure and mechanical properties of the nanocrystalline TiNiCo shape memory alloy. Mater. Sci. Eng. A **598**, 183–189 (2014)

3. Rui-rui, J., Fu-shun, L.I.U.: The influence of Co addition on phase transformation behavior and mechanical properties of TiNi alloys. **20**, 153–156 (2007)
4. Soni, H., Narendranath, S., Ramesh, M.R.: Evaluation of wire electro discharge machining characteristics of $Ti_{50}Ni_{45}Co_5$ shape memory alloy. In: Proceedings of the COPEN 10, 2017 Conference at IIT Chennai India (2017)
5. Soni, H., Mashinni, P.M.: Wire electro spark machining and characterization studies on $Ti_{50}Ni_{49}Co_1$, $Ti_{50}Ni_{45}Co_5$ and $Ti_{50}Ni_{40}Co_{10}$ alloys. **7**(1), 1–12 (2020)
6. Zhu, L., Guan, Y., Wang, Y., Xie, Z., Lin, J., Zhai, J.: Influence of process parameters of ultrasonic shot peening on surface roughness and hydrophilicity of pure titanium. Surf. Coatings Technol. **317**, 38–53 (2017)
7. Pant, P., Pandey, N., Rajesha, S., Jain, G.: Prediction of surface roughness in WEDM process using feed forward back propagation neural. Network **4**, 667–674 (2014)
8. Aspinwall, D.K., Soo, S.L., Berrisford, A.E., Walder, G.: Workpiece surface roughness and integrity after WEDM of Ti–6Al–4V and Inconel 718 using minimum damage generator technology. CIRP Ann. Manuf. Technol. **57**, 187–190 (2008)
9. Sharma, A., Garg, M.P., Goyal, K.K.: Prediction of optimal conditions for WEDM of Al 6063/ZrSiO$_4$(p) MMC. Procedia Mater. Sci. **6**, 1024–1033 (2014)
10. Rao, S.S.M., Rao, K.V., Reddy, K.H., Ch, V., Rao, S.P.: Prediction and optimization of process parameters in wire cut electric discharge machining for high-speed steel (HSS). Int. J. Comput. Appl. **7074**, 1–8 (2017)
11. Surya, V.R., Kumar, K.M.V., Keshavamurthy, R., Ugrasen, G., Ravindra, H.V.: Prediction of machining characteristics using artificial neural network in wire EDM of Al7075 based in-situ composite. Mater. Today Proc. **4**, 203–2012 (2017)
12. Lee, W.M., Liao, Y.S.: Self-tuning fuzzy control with a grey prediction for wire rupture prevention in WEDM. Int. J. Adv. Manuf. Technol. **22**, 481–490 (2003)
13. Ugrasen, G., Ravindra, H.V., Prakash, G.V.N., Keshavamurthy, R.: Estimation of machining performances using MRA, GMDH and artificial neural network in wire EDM of EN-31. Procedia Mater. Sci. **6**, 1788–1797 (2014)
14. Karthikeyan, R., Lakshmi Narayanan, P., Naagarazan, R.: Mathematical modelling for electric discharge machining of aluminium–silicon carbide particulate composites. J. Mater. Process. Technol. **87**, 59–63 (1999)
15. Sharma, P., Chakradhar, D., Narendranath, S.: Evaluation of WEDM performance characteristics of Inconel 706 for turbine disk application. Mater. Des. **88**, 558–566 (2015)
16. Shandilya, P., Jain, P.K., Jain, N.K.: RSM and ANN modeling approaches for predicting average cutting speed during WEDM of SiCp/6061 Al MMC. Procedia Eng. **64**, 767–774 (2013)

Integrated Approach of Green Lean with Six Sigma for Improving Quality Issues in Small-Scale Industries

Nivedika Saroha, Tanmay Agarwal, Girish Kumar , and Umang Soni

1 Introduction

The Micro, Small and Medium Enterprises (MSME) sector has transformed a lot over the last fifty years. It has been playing a significant role in the economic and social development of various developing countries by promoting entrepreneurship and providing large employment opportunities. In Indian context, compliance with the Micro, Small and Medium Enterprises Development (MSMED) Act, 2006 the MSME for manufacturing sector can be classified based on investment in plant and machinery. If the investment cost in an enterprise is in a range of 0 to 35,000 USD, 35,000 USD to 700,000 USD, and 700,000 USD to 1,500,000 USD, then it is a micro, small and medium enterprise, respectively. Further, according to 6th economic census by National sample survey (NSS) conducted in India, there are about 633.88 lakh MSME at present. Therefore, MSME sector plays a crucial role in an economy.

In most of the cases, these industries are unable to realize even half of their production capabilities as some portion of the capital remains blocked and some of the machinery remain idle most of the time. Such circumstances arise because of poorly qualified entrepreneurs who lack in skill and experience. Resource optimization is not profitably executable in most of the SMEs as they do not have that kind of expertise nor they can afford such kind of expenditures. Moreover, they do

N. Saroha · T. Agarwal (✉) · G. Kumar
Department of Mechanical, Production & Industrial and Automobile Engineering, Delhi
Technological University, Delhi, India
e-mail: tanmayagarwal_bt2k16@dtu.ac.in

G. Kumar
e-mail: girish.kumar154@gmail.com

U. Soni
Manufacturing Processes and Automation Engineering, Netaji Subhas University of Technology,
Delhi, India
e-mail: umangsoni.1@gmail.com

not contemplate on various factors viz. location of the plant, financial availability, product demand, production level and capacity of the plant, etc. MSME sector does not receive enough funds from the government due to which they are incapable of buying the much-needed resources in order to enhance their production. Since the profit margins are bleak, MSMEs sometimes need funds or low interest loans from govt controlled financial bodies in order to bear their operating costs, some new technology or for some other similar functionalities. Majority of the SME (Small and Medium Enterprise) still use primitive technology which leads to poor quality and low productivity of the product [1]. Lack of funds leaves them with no choice but to continue with their traditional trends as neither are they able to research and develop new technologies nor are they affluent enough to acquire it from other firms. This lack of awareness throws such growing industries out of the competition. Additionally, they lose value among the consumers due to their incapability in delivering quality products in given time. Several studies have been conducted which aim at alleviating problems related to quality and efficiency in the MSME sector. Researchers have investigated this problem in different ways [2].

Six sigma is used heavily in various industrial sectors; however, it is also having applications in healthcare logistics. Researchers worked on increasing factors to be taken in project selection. Al-Qatawneh et al. [3] showed the importance of otherwise considered less important parameters namely, performance and criticality of each item in a logistics system. The paper discusses how these factors when added into the define phase of a typical six sigma methodology makes it greatly beneficial for healthcare logistics.

In industrial applications of six sigma, it has been used to optimize various processes. Nabiyouni and Franchetti [4] conducted full process analysis of red bag waste management including human, environmental and economic factors by implementing lean six sigma. This way, they were able to optimize red bag waste management programme, essentially increasing value by decreasing defects and managing disposal frequency.

Industries today are extensively using the DMAIC approach to enhance the product quality. Agriculturae et al. [5] used six sigma to control the product quality and avoid increase in internal costs on a metallurgical operation. They concluded that using pareto diagram, histogram, FMEA and, Ishikawa diagram the sigma level was improved by 13%. Kubilius et al. [6] utilized change management tools in addition to DMAIC methodology to reduce the rate of STFs (slips, trips and falls) for joint commission field staff. The source of data included workmen's compensation claims data and an online survey administered to field staff who reported STFs. Setyawan and Lugo-telles [7] applied DMAIC approach to minimize the defective products in bridge and rib department. The sigma level average value is equal to 4125 and the possibility of defects by 4639 units based on DPMO (Defect per million opportunities) value calculation. Hakim et al. [8] aimed to increase production flexibility on highest unmatching ratio products in an Indonesian company using six sigma. Q-model calculations were done on a weekly basis on the absorption scheme fluctuations order. The results were a decrease in unmatching ratio from 4.9 to 1.2% and profits of IDR 431,635,851. Kaid et al. [9] incorporated DMAIC methodology to

find the solution to the problem of increased demand of flour in biscuit production in a Y company. Authors defined root causes using Ishikawa diagram. In addition to this, selection of major important causes was done using pareto chart. Lastly, brainstorming was done with experts from various departments to formulate necessary solutions. Gupta and Kumar [10] used DMAIC approach of six sigma to examine the problem of damage of HDPE bags in carbon black industry which resulted in both economic loss to the manufacturer and damage to the company's brand image. AHP (analytic hierarchy process) was applied to each root cause identified using ishikawa diagram. Finally, a pareto chart helped focus attention on the prime root causes. DMAIC was able to reduce the deviation rate of flour material usage from 27.55 to 10.45% on the production line. However, six sigma is not the only methodology used by scholars to improve quality. Sundar et al. [11] attempted to create a lean route map for an organization to implement lean manufacturing system. Most of the study focuses on single aspect but for successful implementation in an organization emphasis on all aspects should be done. An exploratory survey was conducted, and its results were unified to create a theory to be implemented on lean elements.

Sagnak and Kazancoglu [12] integrated a GLEAN (green lean approach) with conventional six sigma. The author proposed measurement system analysis and gage control techniques as measurement systems and stressed the need for a GLEAN six sigma-based approach. Further, limitations arising due to incorporation of green and lean were overcome by adopting tools from the original six sigma approach. Sulong et al. [13] introduced Material flow cost accounting (MFCA) to five Malaysian companies. It was seen that these companies benefited both economically and environmentally. The author discussed the case study of one of the companies and showed that MFCA can be successfully applied in a SME. Therefore, overthrowing the traditional view that investment in eco-friendly benefits can reduce financial performance in a SME. Dekamin and Barmaki [14] applied MFCA on soybean production to assist farmers in understanding the various energy waste in different stages of crop production. MFCA greatly increased the energy use efficiency and material efficiency by balancing the environment and economy. Tsung et al. [15] applied the SPC in multistage scenario in quality improvement in manufacturing and service sector by comprehensively comparing the existing techniques and also provided with some possible future scope for newer technique. Park et al. [16] combined a damping process controller with SPC to reduce process variability. Further, this integration was compared with routine APC and SPC integration and the former one resulted in better variability control.

As seen from the literature review, limited work has been done so far on optimization of manufacturing processes and production cost. Additionally, work on MFCA and GLEAN has been done explicitly. Therefore, the current study proposes a novel methodology which contributes mainly towards integration of lean six sigma and MFCA. This methodology later has been illustrated by applying it on a small-scale industry which achieved benefits in terms of economic gains and helped it in sustaining the environment. Moreover, MFCA has been used here as a diagnostic accounting method whereas lean with DMAIC approach of six sigma (LSS) has been used for identification of losses. Root causes for major losses for the SME have been

identified using fishbone diagram and thereafter, they have been prioritized using AHP. The remaining organization of the paper is as follows: Sect. 2 explains the proposed methodology. Thereafter, in Sect. 3 methodology is illustrated through an industrial problem. Further, results are discussed in Sect. 4. Finally, Sect. 5 concludes the work with its future scope, limitations and recommendations.

2 Methodology

2.1 Six Sigma: Overview

Six sigma towards process control was conceptualized by a Motorola engineer named Bill Smith in 1986. Six sigma's potential in improving quality, reducing costs and defects, and expanding corporate business performance has helped it evolve beyond Motorola. The main motivation of applying six sigma is variability reduction in key product quality characteristics around target values which are specified beforehand. This process is completed to a point where chances of a defect or failure are highly improbable. A six sigma process produces up to 3.4 parts per million (ppm). It has a five-step problem-solving approach namely—Define, Measure, Analyse, Improve and Control (DMAIC). The DMAIC framework utilizes control charts, designed experiments, process capability analysis, measurement systems capability studies, and many other basic statistical tools [17].

2.2 Lean: Overview

An extension to six sigma concepts is lean methodology which is a technique that deals with the elimination of inefficient steps in a process that do not add value to it. This methodology guarantees high-quality products and consumer satisfaction. This approach involves five steps viz. identify value (from the point of the customer), measure the value stream, pull on customer demand, create flow and achieve perfection. Lean methodology aims at waste reduction, while six sigma aims at reduction of process variation [18].

2.3 Lean Six Sigma: Overview

A combined version of the above two techniques is lean six sigma, capturing best of both the methodologies. LSS values defect prevention over detection is fact-based and essentially a data driven philosophy. It creates a competitive advantage to other techniques by reducing variation, waste and cycle time. It promotes the use of work standardization and flow, resulting in customer satisfaction and bottom-line results.

Fig. 1 Lean six sigma
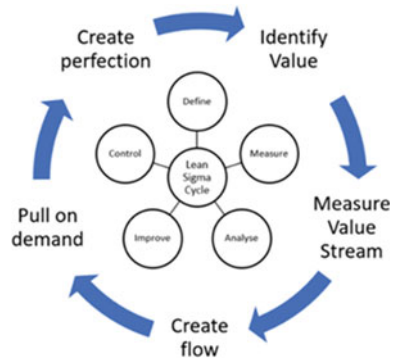
The main phases of the integrated LSS approach are shown in Fig. 1. It includes ten stages, five of which are DMAIC and remaining are identification of value, application of value stream mapping, redesign to remove waste and improve value stream, redesign manufacturing system. This supports manufacturing functions and achieves single unit flow and applications of total productive maintenance (TPM) [19].

2.4 Glean with Six Sigma

LSS has been used for identification of incurred losses and their root causes. Prior to application part of LSS, remedies are suggested. MFCA has been used as a diagnostic accounting technique. MFCA supports organizations in understanding the imminent environment and financial consequences of energy and material and thus acts as a management tool. It also helps the organization improve them by making changes in those practices [20]. It can be applied in three steps, i.e., identification and visualization of flow of physical material (in units), consideration of involved monetary aspects. The execution starts with a structured model that provides with the limitations of the involved quantity centres (QC). MFCA helps in differentiating between desired (material flow that tend to become a part of finished goods) and undesired material flow. Last step involves converting physical units into monetary equivalents. Thus material, system and energy costs are assessed. This assessment enables organizations to identify all the process inefficiencies and process wastes. Thereby provides an opportunity to improve their environmental and financial performance. It also provides them to learn more about their losses due to undesired material flow.

Here in this study MFCA has been used for the identification and quantification of losses at different QCs in the production of injector pins. Thus, a combined technique consisting of LSS and MFCA has been used here under the umbrella name-Green lean (GLEAN). It is an integration of MFCA with LSS to achieve higher process efficiency. MFCA is a technique to differentiate undesirable wastes and negative

outputs from desired material flow. Here, these negative outputs are lost opportunities and the process efficiency can be improved if these are handled prudently but the problem of residual losses cannot be resolved through this technique. However, it is essential to identify and eliminate the causes for losses so that zero defect and zero effect can be achieved. This problem is solved here with the implementation of GLEAN that helps in identifying the underlying losses. The main concern here is to incorporate environmental principles in LEAN methodology for minimization of wastes, such that the current state of material and energy flow is analysed continuously for improvement potential [21].

Steps involved in GLEAN are graphically represented in Fig. 2. It includes identification of QCs, identification and quantification of inputs and outputs, flow costing which includes material costs, energy costs and system costs, analysis of material

Fig. 2 Flow chart for GLEAN
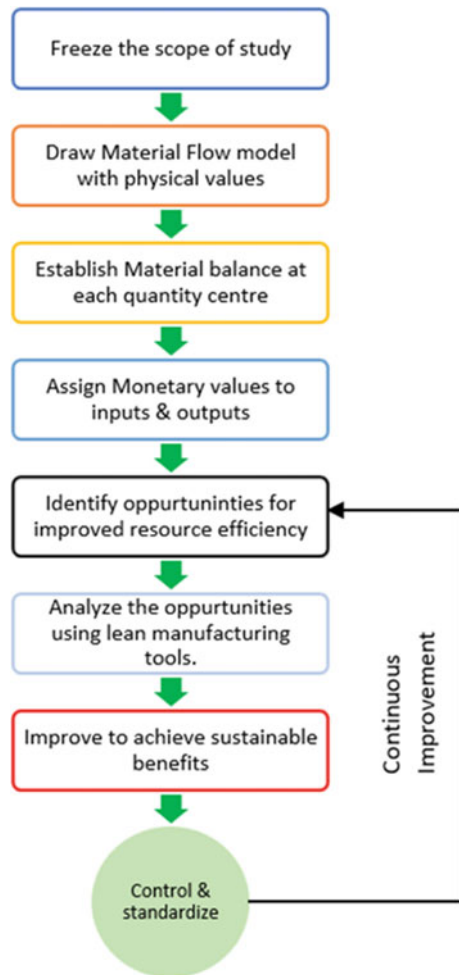
flow, prioritization of critical QCs, and finally analysis and improvement. Thus, all the decisions regarding enhancements are well supported by LEAN framework such that lesser environmental wastes are produced along with cost reduction.

The following section deals with the application of GLEAN in an SME.

3 Illustration

The proposed methodology, as discussed in Sect. 3, has been illustrated here by using an industrial problem provided by a small-scale enterprise-ABC. It manufactures injector pins for automobiles, where most of the QCs are in house while the rest are on a contract basis with some other SME. This enterprise provides its finished products to different automobile manufacturers as a third party. Due to lack of time management, machinery and skilled labour, it has been incurring tremendous amount of total losses for some time, as a result of which its adopted manufacturing processes have become inefficient and are delivering poor performance. All this is leading the enterprise to lose its profits, orders and value among its customers. This work has been done on the inputs provided by the enterprise. Firstly, different QCs identified in the production of injector pins have been quantified and a process flow diagram is schematized for the production steps, which were involved in the manufacturing of injector pins. These were sawing, turning, heat treatment, grinding, lapping and packing. A schematic diagram is shown in Fig. 3.

As soon as all the major manufacturing steps are identified, different processing units are classified as different QCs. A QC is a processing unit, performing identical manufacturing processes on different lots of a product. QCs. Here in this case, there are eleven QCs in total. These processing units are raw material storage, inspection-1, sawing, inspection-2, turning and facing, inspection-3, heat treatment, grinding and finishing, packing, storage and dispatch. These QCs are shown in Table 1.

Here in the material flow model inputs and outputs have been first identified for each QCs. Inputs are positive products as material and energy while outputs are negative products as material, monetary and energy losses. After the identification step, inputs and outputs are quantified in terms of physical units viz. mass, length, volume or number of species.

Percentage material losses for every QC has been calculated using the outputs from the same and are mentioned in Table 2.

A pareto analysis has been performed using material losses from different QCs, to identify those 20% of the QCs that are causing 80% of the material losses. Pareto chart for this problem is shown in Fig. 4.

QC-5, QC-7 and QC-3 contribute towards 80% (approx.) of the total material losses, individual material loss being 29.54, 8.02 and 6.9%. Therefore, in order to alleviate this problem of material losses, these three QCs viz. turning and facing, heat treatment, and sawing have been selectively targeted so that major portion of the problem can be solved. Ishikawa diagram has been used to identify root causes for the material losses at each of these QCs. These root causes were identified through
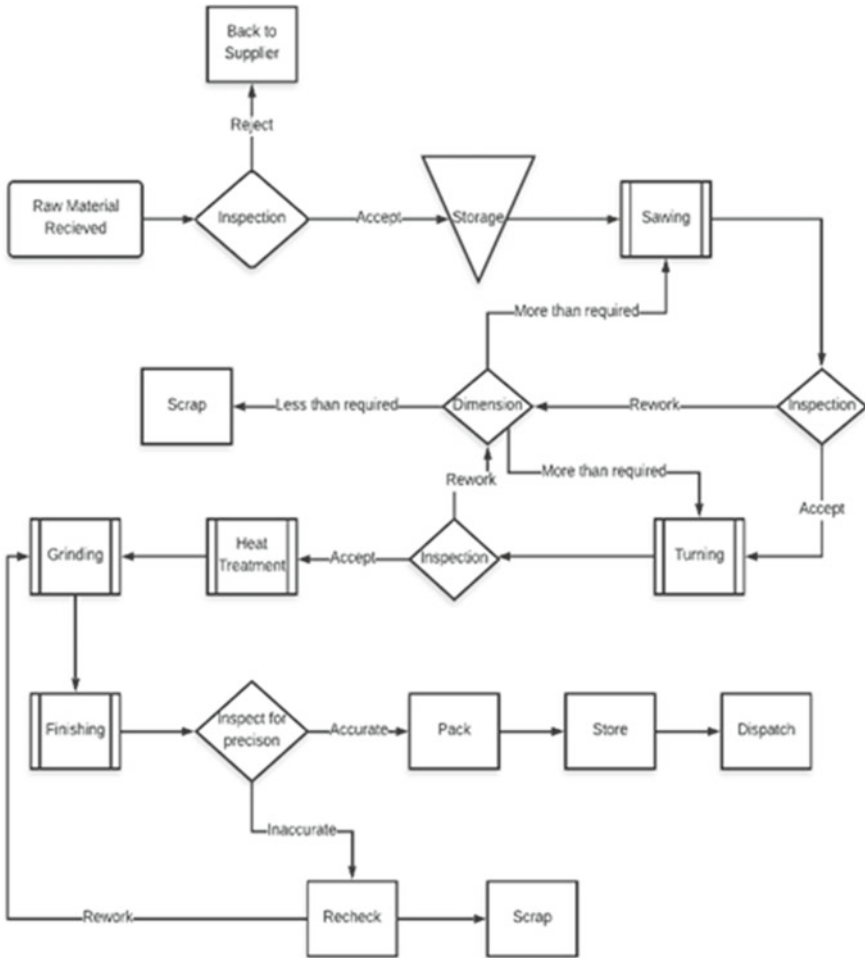
Fig. 3 Process flow chart

joint brainstorming sessions with the management of the SME. The major root causes were classified into tool, man, machine, environment, material finish, oil and furnace. Among these classifications, root causes have been allocated for each of the three QC considering the experience of the production and quality control workforce. Fishbone diagram for the concerned QCs is shown in Figs. 5, 6 and 7.

Additionally, root causes along with potential solutions are shown in Table 3. Further, the root causes for each QC are used to construct relative weight matrix. Thereafter this relative weight matrix is used to obtain priority matrix by using AHP. It is one of the multi-criteria decision-making methods which is used to derive ratio scales from paired comparisons. Decision matrix and priority matrix for QC-5, QC-7 and QC-3 are shown in Table 4a–c, respectively. In case of QC-5 tool came out to be

Table 1 Material flow sequence

Input	Quality Centre	Output	Material loss
Steel rods	QC-1 Raw material storage	–	–
Stored rods	QC-2 Inspection Quality gate 1	Rejected material	–
Rod, hack saw, white marker, cutting oil	QC-3 Sawing using hack saw	Cutting oil, white marker, end pieces, scrap	6.90%
Cut rod	QC-4 Inspection Quality gate 2	Rejected parts	3%
Lathe, cutting oil, Tool	QC-5 Turning and facing using lathe	Cutting oil, scrap metal chips, facing tool	29.54%
Semi-finished injector pin	QC-6 Inspection Quality gate 3	Rejected parts	4%
Injector pin, quenching oil	QC-7 Heat treatment	Quenching oil, heat losses, deformed pins	8.02%
Hardened injector pin, lubricant oil, grinder, emery paper	QC-8 Grinding and lapping	Scrap metal, cutting oil	1.4%
Sub assembles, carton box, bubble wrap	QC-9 Packing	Carton box, bubble wrap	0.06%
Finished goods	QC-10 Storage	Boxes, thermocol	0.07%
Warehouse goods	QC-11 Dispatch	Carton box	0.07%

Table 2 % Material losses in different quantity centres

Quality centre	Material loss (in %)
QC-5	29.54
QC-7	8.02
QC- 3	6.9
QC- 6	4
QC-4	3
QC-8	1.4
QC-10	0.07
QC-11	0.07
QC-9	0.06
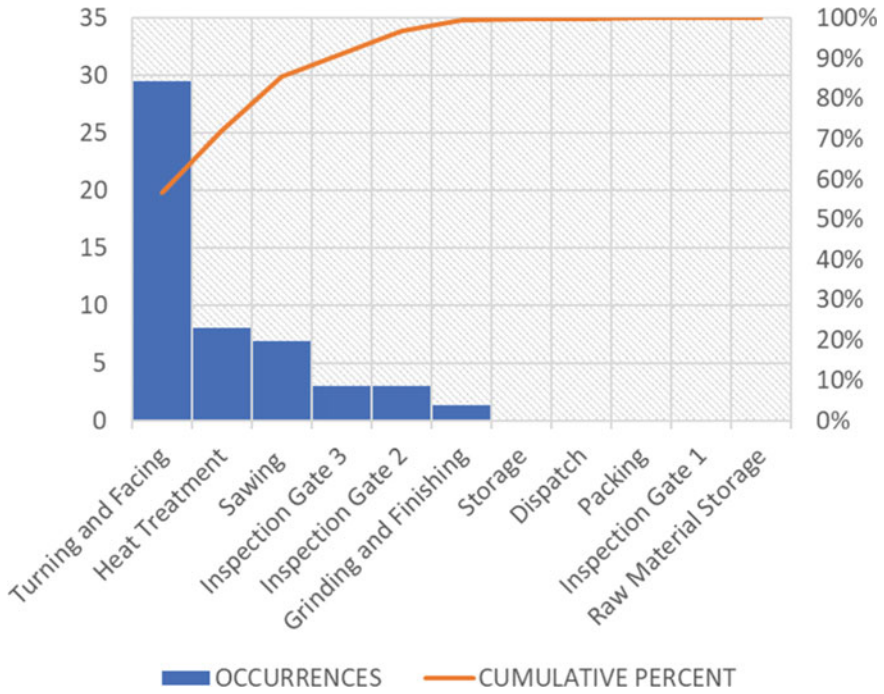
Fig. 4 Pareto chart analysis
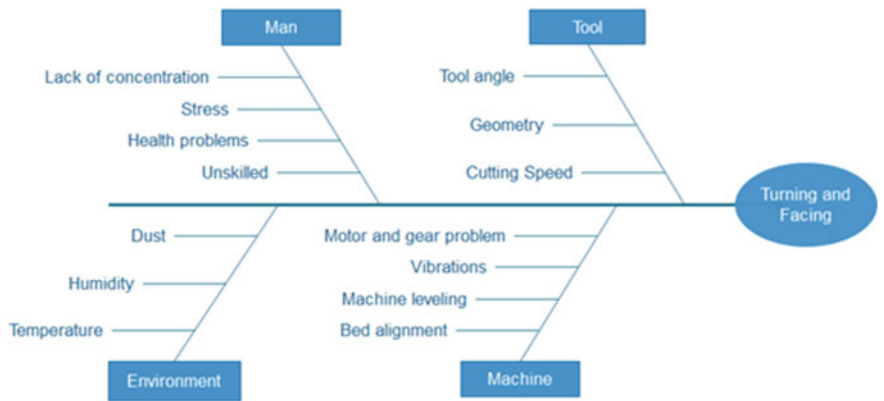
Fig. 5 Fishbone diagrams for turning and facing

the most significant factor in deterring the problem followed by machine, man and environment. Similarly, for QC-7 the order came out to be man, furnace, material finish, oil and environment. Finally, in case of QC-3 machine factor contributed the most followed by man, tool and environment. Thereafter, the remedial steps should
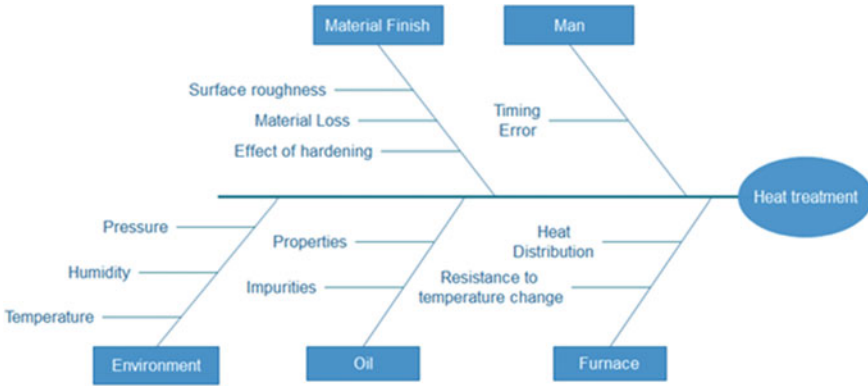
Fig. 6 Fishbone diagrams for heat treatment
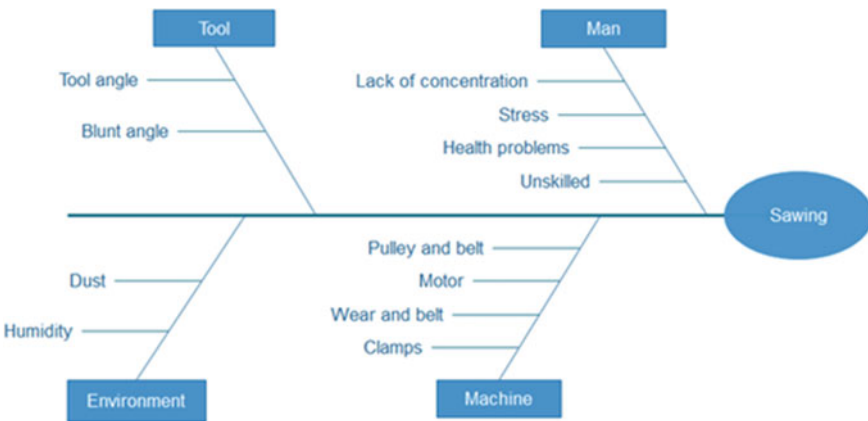
Fig. 7 Fishbone diagrams for sawing

be executed in these orders only so that the ratio of process improvement to no. of remedial actions taken can be maximized.

4 Result

Application of the proposed methodology helped in resolving the quality, losses and defects related issues in ABC enterprise. MFCA helped in identifying QC which were contributing about 80% towards total material losses. QC-5, QC-7 and QC-3 came out to be most inefficient QCs. These QCs were selectively targeted for improvement, causes were identified via fishbone diagram as shown in Figs. 5, 6 and 7. Further, AHP generated a priority matrix which resulted in different orders for each of the

Table 3 Root cause solution table

Problem	Solution
Tool	• Proper tool should be used with proper geometry for turning and facing operation • Operations should be carried out at proper cutting speed
Machine	• Maintenance tech like TPM (Total Productive maintenance) should be incorporated • It should be set properly before carrying out any operation to avoid vibrations, poor alignment, etc.
Man	• Good working environment should be provided • Proper hygiene should be maintained • Workload should be properly divided
Environment	• Humidity can be controlled using moisture absorbent like silica gel • Temperature can be controlled using water cooling
Oil	• Oil should be purified before reusing it

Table 4 **a** Priority vector matrix for QCs turning and facing. **b** Priority vector matrix for sawing. **c** Priority vector matrix for heat treatment

(a)

Turning and facing	T	Mc	M	E	Priority
T	1	3	2	7	0.462
Mc	0.33	1	2	9	0.29
M	0.5	0.5	1	6	0.20
E	0.142	0.11	0.167	1	0.043

(b)

Sawing	T	Mc	M	E	Priority
T	1	0.33	0.25	7	0.167
Mc	3	1	2	9	0.464
M	4	0.5	1	6	0.325
E	0.142	0.11	0.167	1	0.042

(c)

Heat treatment	M	F	O	Mat	E	Priority vector
M	1	1	4	3	6	0.36
F	1	1	3	2	6	0.32
O	0.25	0.33	1	0.5	1	0.084
Mat	0.33	0.5	2	1	4	0.168
E	0.167	0.167	1	0.25	1	0.06

three QC. Further, as per these orders remedial actions should be taken. Thus, the firm effectively utilized its capital by channelling it on priority basis.

5 Conclusion

This study was conducted to propose a methodology which is an integration of GLEAN with six sigma. Green is implemented through MFCA. It is used to identify faulty QCs. Later, lean with six sigma is employed for providing remedies. Further, the causes are identified using fishbone diagram. Thereafter, they are prioritized using AHP methodology. This resulted in the order in which remedial action should be executed to maximize the ratio of process improvement to no. of remedial actions taken. Additionally, this methodology has been illustrated by resolving a quality-related problem faced by an SME (ABC enterprise) 2as here QC-5, QC-7 and QC-3 came out to be the most inefficient QCs with 29.54%, 8.02% and 6.9% total percentage loss, respectively. Here, improvement process was streamlined for these three QCs only so as to minimize process improvement expenditure. However, this study compares energy, material and monetary losses while such losses cannot be directly associated without an equating factor. This arises future scope in this study. Therefore, the methodology can be extended among all sectors of SMEs, namely chemicals, sheet metal, forging, etc. Thus, their unique requirements and improvement opportunities can be dealt efficiently. Sustainable product manufacturing can be achieved using this novel integration of lean, six sigma and MFCA (GLEAN) without harming the environment. Although this is an early attempt aiming at an integration of GLEAN with six sigma, various practitioners and academician are recommended to use this study for future study in other industries where quality, defects and losses related problems are to be solved expeditiously.

References

1. Rao Chalapati, C.V.: Environmental Status of India—C. V. Chalapati Rao—Google Books. https://books.google.co.in/books?id=nwbPwZF1Gw4C&printsec=frontcover#v=one page&q&f=false. Accessed 10 July 2020
2. What are the Problems Faced by Small Scale Industries in India? https://accountlearning.com/what-are-the-problems-faced-by-small-scale-industries-in-india/. Accessed 25 Feb 2019
3. Al-Qatawneh, L., Abdallah, A.A.A., Zalloum, S.S.Z.: Six sigma application in healthcare logistics: a framework and a case study. J. Healthc. Eng. **2019** (2019). https://doi.org/10.1155/2019/9691568
4. Nabiyouni, N., Franchetti, M.J.: Applying lean six sigma methods to improve infectious waste management in hospitals. Int. J. Six Sigma Compet. Advantage **11**(1), 1–22 (2019). https://doi.org/10.1504/IJSSCA.2019.098706
5. Agriculturae, A.T., Girmanová, L., Šolc, M., Kliment, J., Divoková, A., Mikloš, V.: Application of six sigma using DMAIC methodology in the process of product quality control in metallurgical operation, 104–109 (2017). https://doi.org/10.1515/ata-2017-0020

6. Kubilius, A., Winfrey, K., Mayer, C., Johnson, G., Wilson, T.: Applying lean six sigma tools to reduce the rate of slips, trips and falls for Joint Commission field staff. Int. J. Six Sigma Compet. Advantage **9**(1), 37–55 (2015). https://doi.org/10.1504/IJSSCA.2015.070089

7. Setyawan, D., Lugo-telles, R.: Minimization of defective products in the department of press bridge & rib through six sigma DMAIC phases minimization of defective products in the department of press bridge & rib through six sigma DMAIC phases (2017). https://doi.org/10.1088/1757-899X/215/1/012035

8. Hakim, I.M., Wahyuningtyas, R., Kusuma, N.: Planning to increasing production flexibility on highest unmatching ratio products in automotive company with DMAIC approach. **04029**, 0–5 (2018)

9. Kaid, H., Noman, M.A., Nasr, E.A., Alkahtani, M.: Six sigma DMAIC phases application in Y company: a case study six sigma DMAIC phases application in Y company: a case study. (March 2017) (2016). https://doi.org/10.1504/IJCENT.2016.082330

10. Gupta, K., Kumar, G.: Six sigma application in warehouse for damaged bags: a case study. In: Proceedings—2014 3rd International Conference on Reliability, Infocom Technologies and Optimization: Trends and Future Directions, ICRITO 2014 (Jan 2015). https://doi.org/10.1109/ICRITO.2014.7014736

11. Sundar, R., Balaji, A.N., Kumar, R.M.S.: A review on lean manufacturing implementation techniques. Procedia Eng. **97**, 1875–1885 (2014). https://doi.org/10.1016/j.proeng.2014.12.341

12. Sagnak, M., Kazancoglu, Y.: Integration of green lean approach with six sigma: an application for flue gas emissions. J. Clean. Prod. **127**, 112–118 (2016). https://doi.org/10.1016/j.jclepro.2016.04.016

13. Sulong, F., Sulaiman, M., Norhayati, M.A.: Material flow cost accounting (MFCA) enablers and barriers: the case of a Malaysian small and medium-sized enterprise (SME). J. Clean. Prod. **108**, 1365–1374 (2015). https://doi.org/10.1016/j.jclepro.2014.08.038

14. Dekamin, M., Barmaki, M.: Implementation of material flow cost accounting (MFCA) in soybean production. J. Clean. Prod. **210**, 459–465 (2019). https://doi.org/10.1016/j.jclepro.2018.11.057

15. Tsung, F., Li, Y., Jin, M.: Statistical process control for multistage manufacturing and service operations: a review and some extensions. Int. J. Serv. Oper. Inform. **3**(2), 191–204 (2008). https://doi.org/10.1504/IJSOI.2008.019333

16. Park, M., Lee, M.L., Lee, J.: Integrated process control by combining controllers and monitoring charts. Int. J. Reliab. Qual. Saf. Eng. (2019). https://doi.org/10.1142/S0218539320500138

17. Montgomery, D.C., Woodall, W.H..: An overview of six sigma. Int. Stat. Rev. **76**(3), 329–346 (2008). https://doi.org/10.1111/j.1751-5823.2008.00061.x

18. Liker, J.K., Hoseus, M.: Center for Quality People and Organizations. Toyota Culture: The Heart and Soul of the Toyota Way. McGraw-Hill (2008)

19. Wheat, B., Mills, C., Carnell, M.: Leaning into Six Sigma: the Path to Integration of Lean Enterprise and Six Sigma. Pub. Partners, Boulder City, Colorado (2001)

20. Environmental Management—Material Flow Cost Accounting—General Framework. BSI Standards Publication (2011)

21. Kurdve, M., Shahbazi, S., Wendin, M., Bengtsson, C., Wiktorsson, M.: Waste flow mapping to improve sustainability of waste management: a case study approach. J. Clean. Prod. **98**(October 2017), 304–315 (2015). https://doi.org/10.1016/j.jclepro.2014.06.076

Role of Nanostructured Hardfacing Alloy on Steel for Enhanced Wear Behavior

Kumari Archana, Pratibha Kumari, Dhananjay Pradhan, Krishna Vijay Ojha, and Kuldeep Singh

1 Introduction

Hardfacing is largely used to enhance the life of the worn-out structural components and gaining popularity these days for reducing the cost of replacement [1]. Wear is one of the most important reason along with impact adhesion, oxidation and fatigue for early failure of machine component. Various industries like agriculture, cement, hammers, cutters, drills, etc. are facing failure of components mainly due to abrasion wear [1, 2]. To improve wear resistance of the material two approaches are used, firstly by making an alloy of existing material with other and secondly by improving surface property of material [1, 2]. Use of hardfacing improved the life span of the worn-out components and thereby reduce the replacement cost and also reduces downtime by extending the service life. A variety of coatings are nowadays available which are in practice to enhance the resistance against corrosion and wear of materials [1, 3]. The improved resistance to wear of a hardfaced alloy depends on many aspects like toughness and strain hardfacing behavior of the matrix. Other important factors in the abrasion resistance are the carbides orientation and the size of particle [3, 4]. The AISI 316L coatings were thermally sprayed by WSF and HVOF processes. The coating made of HVOF is more compact than that of WSF and the hardness was improved by 40% in HVOF coating compared to WSF coating and that had great influence on its wear properties along with WSF coating had outstanding corrosion resistance compared with the HVOF deposited coating [5, 6]. Coating of chromium nitride had been used on SS specimens for the wear resistance and also CrN coating on stainless steel sample was mainly constituted of chromium on nitrogen, i.e., CrN in the chromium matrix with little quantity of carbide and oxide of chromium [7, 8]. NiCrBSiC (Fe) is a potential alternative of hard Cr with improved hardness after

K. Archana (✉) · P. Kumari · D. Pradhan · K. V. Ojha · K. Singh
Department of Mechanical Engineering, KIET Group of Institutions, Delhi-NCR, Ghaziabad 201206, India
e-mail: kumari.archana@kiet.edu

cyclic heat treatment and as it shows excellent resistance to corrosion, erosion, friction and good adhesion to steel [4, 6, 8–14]. There is scope of using statistical technique for better prediction analysis and optimization of results. Thus, this investigation deals with use of design of experiment (DOE) using a multi-technique with an objective to optimize the various process parameters of wear.

2 Experimental Procedure

2.1 Base Material and Sample Preparation

In this work IS 2062 steel plate of 10 mm thickness was selected as base material and over one side of this plate a single layer of chromium coated wire material was deposited by the help of thermal spraying (HVOF). The typical standard chemical composition of the base material (IS 2062) is as follows

$$0.23\,C - 0.40\,Si - 1.50\,Mn - 0.012\,N - 0.045\,P - 0.045\,S - 0.025\,Cr - 0.01\,M$$

2.2 Coating Material

For the purpose of coating 140 MXC Chromium nanostructured wire is selected. The composition of different element present in this wire is

$$20.8\,Cr - 2.84\,C - 2.1\,Mo - 0.64\,B - 1.79\,W - 0.54\,Si - 0.8\,Nb - Balance\,Fe$$

Hardfacing coating is performed on substrate by HVOF processes and hardness was measured using Brinell Hardness tester, the hardness of the base plate was 80 HRB and after hardfacing it was increased by 7.5%. After the hardfacing, eight test specimens of 10 mm× 10 mm cross section of each test level were sectioned by wire EDM. The sectioned specimens were welded to cylindrical pin of diameter 8 mm on the opposite face of hardfaced surface to camp on it on the pin of disk machine. The coated and uncoated specimen are in Figs. 1 and 2.

2.3 Wear Testing

The pin on disk wear test was carried out on the specimen with the condition that instruments have to obtain linear measures of wear that should have a sensitivity of 2.5 μm or better. The wear test specimens were sonicated using acetone and then

Fig. 1 Uncoated specimen

Fig. 2 Uncoated specimen
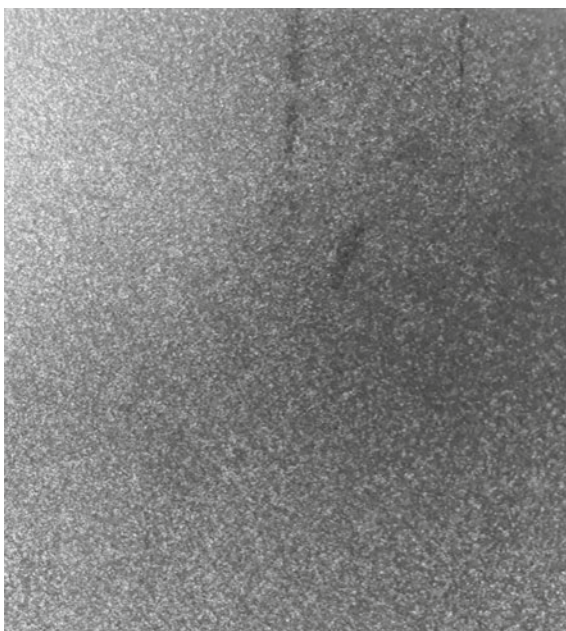
Table 1 2^3 factorial design for non-hardfaced and hardfaced wear test

Run order	S.V.	Load	Temp.
1	1	50	50
2	1	50	100
3	2	50	50
4	2	15	50
5	1	15	100
6	2	15	100
7	2	50	100
8	1	15	50

dried before performing test, thereafter each specimens were weighed on microbalance with sensitivity up to 5 decimal. The test specimens were clamped on the pin tribometer for the selected process parameters. After the test, the specimens were again sonicated and dried and weighed. The wear was evaluated using [12]

$$W_v = W_i - W_f$$

where

W_v = Weight of weared specimen.
W_i = Initial weight.
W_f = Final weight.

2.4 Response Surface Methodology (RSM)

A very cost-effective method of optimization, i.e., design of experiment, was employed in the study. The DOE reduced the number of iterations to 8 by using the processes parameter at two different parameters at two different levels as per 2^3 factorial design for non-hardfaced. Table 1, MINITAB software package, was used to analyze the result.

3 Results and Discussion

3.1 Graphical Representation of Wear Without Hardfacing

3.1.1 Scatter Plot

The scatter plot as shown in Fig. 3 shows the variance in the value of wear obtained by experiment and modeled wear obtained by response surface methodology (RSM)
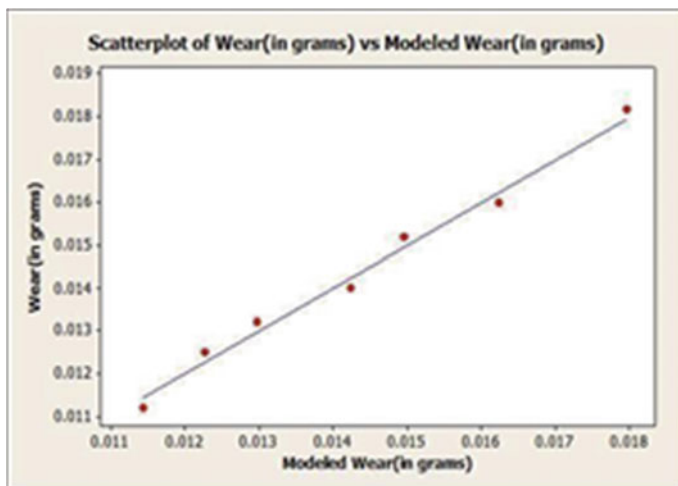
Fig. 3 Scatter plot of wear (in grams) versus modeled wear (in grams) before hardfacing

method before the application of the hardfacing. Closeness of the modeled value shows the accuracy of the experiment.
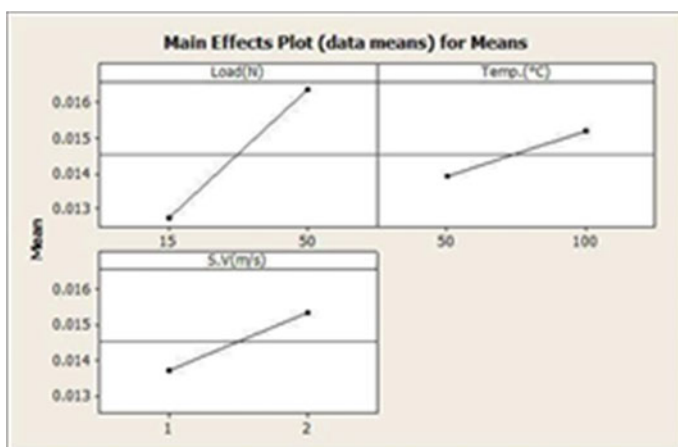
Fig. 4 Plot of wear versus selected parameters before hardfacing

3.1.2 Main Effect Plot

Figure 4 show effect of individual parameters on the wear of specimen. Hence, contribution of each parameter toward wear can be seen separately from the plot between wear and different selected parameters, before the application of hardfacing.

3.1.3 Interaction Between Different Variables

The effect of interaction between different parameters, e.g., load and sliding velocity, load and temperature & temperature and sliding velocity on the sample of wear specimen, is shown in Fig. 5. This graph was plotted before hardfacing process.

3.1.4 Contour Plot Between Different Variable

Figure 6 shows the variation of load and sliding velocity on wear before hardfacing. For higher values of sliding velocity and load the value of wear obtained is higher which can be seen from the change in color. Figure 7 shows the contour plot for the effect of load and temperature on the process of wear before hardfacing. Figure 8 shows the contour plot for the effect of sliding velocity and temperature on wear process before hardfacing.

3.1.5 Scatter Plot

The scatter plot as shown in Fig. 9 shows the variance in the value of wear obtained by experiment and modeled wear obtained by response surface methodology (RSM)
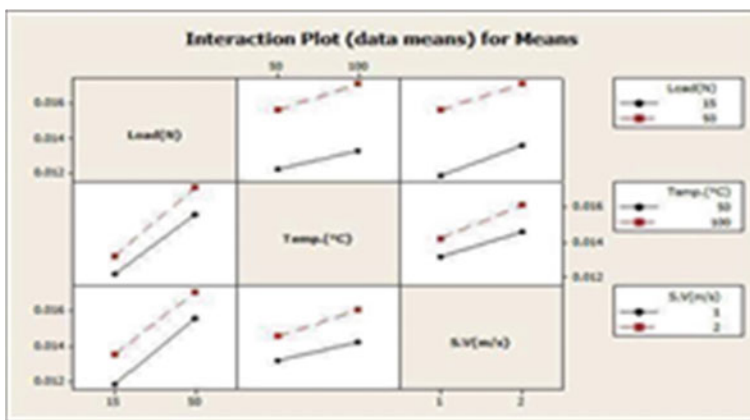
Fig. 5 Plot for interaction between different parameters before hardfacing
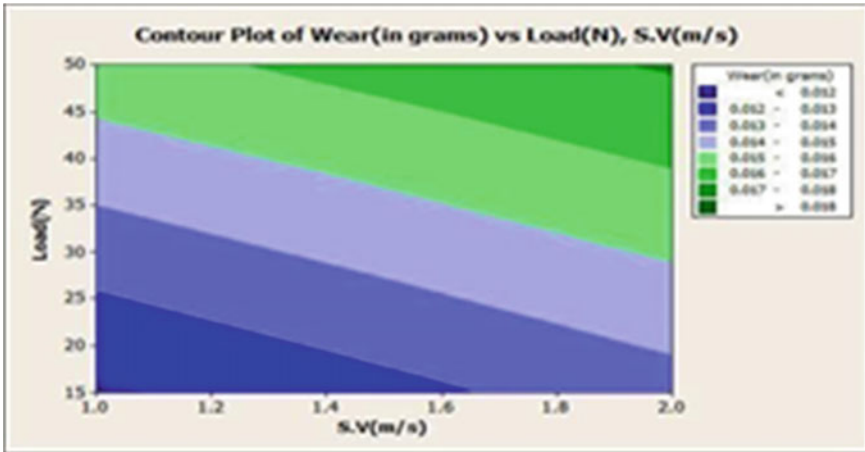
Fig. 6 Contour plot of wear (in grams) versus load (N), S.V (m/s) before hardfacing
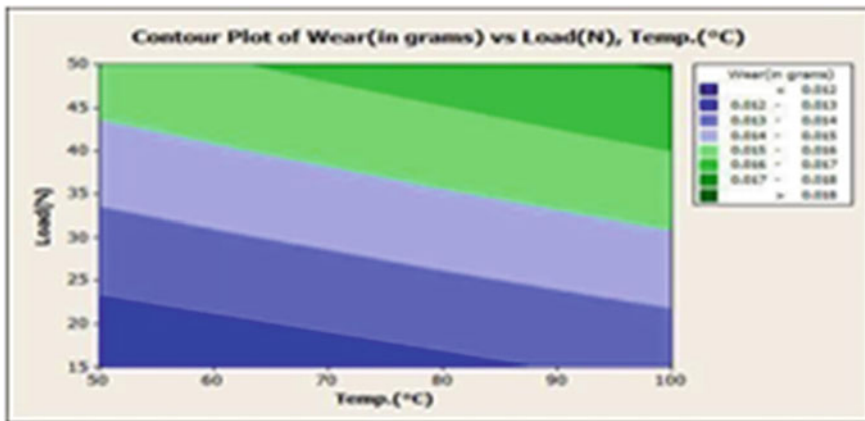
Fig. 7 Contour plot for wear (in grams) versus load (N), temp. (°C) before hardfacing

method after the application of the hardfacing. Closeness of the modeled value shows the accuracy of the experiment.

3.1.6   Main Effect Plot

Figure 10 shows effect of individual parameters on the wear of specimen. Hence contribution of each parameter toward wear can be seen separately from the plot between wear and different selected parameters, before the application of hardfacing.
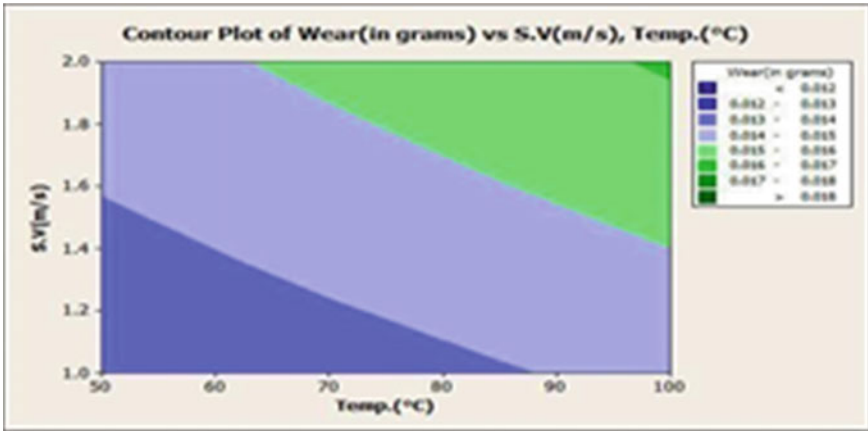
Fig. 8 Contour plot for wear (in grams) versus S.V (m/s), temp. (°C) before hardfacing
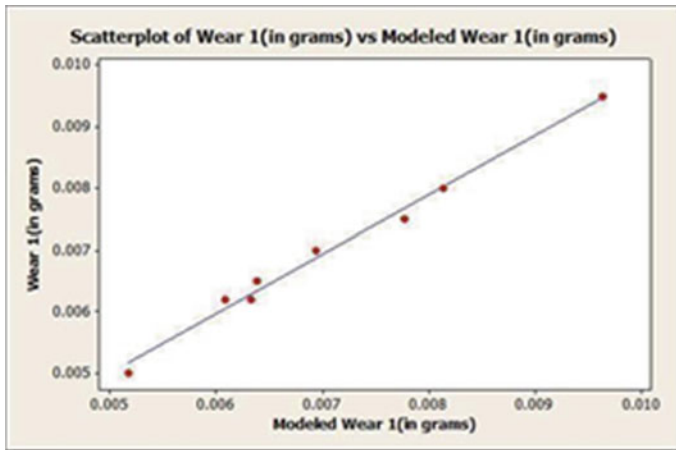
Fig. 9 Scatter plot of wear (in grams) versus modeled wear (in grams) after hardfacing

3.1.7 Interaction Plot

The effect of interaction between different parameters, e.g., load & sliding velocity, load & temperature & sliding velocity, on the wear of the specimen is shown in Fig. 11. This graph was plotted after hardfacing process.
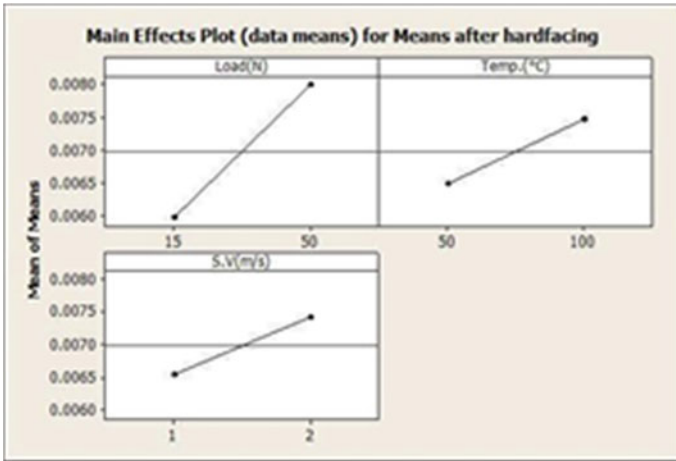
Fig. 10 Plot for means versus selected parameters after hardfacing
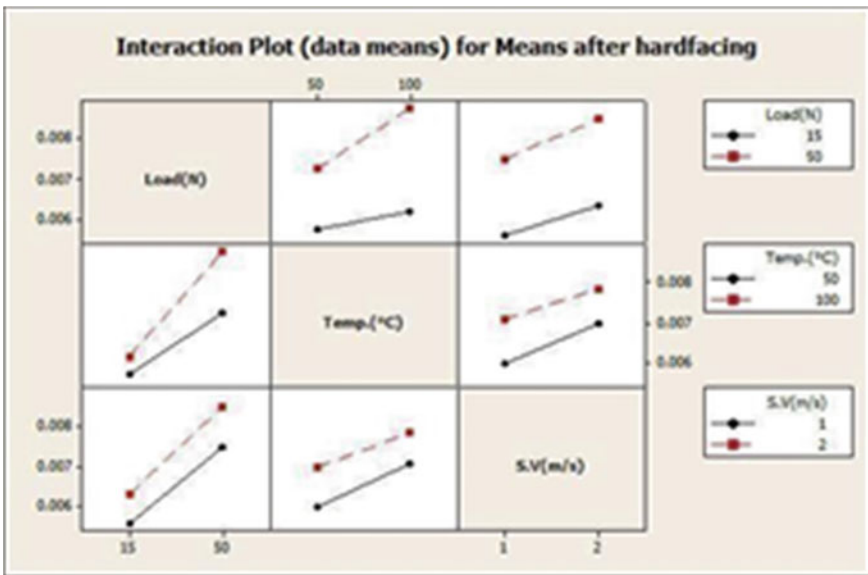
Fig. 11 Plot for wear versus interaction between selected parameters

3.1.8 Contour Plot Between Different Variables After Hardfacing

The effect of combined change in load and sliding velocity on the process of wear is shown after hardfacing in Fig. 12. For higher values of sliding velocity and load the value of wear obtained is higher which can be seen from the change in color.
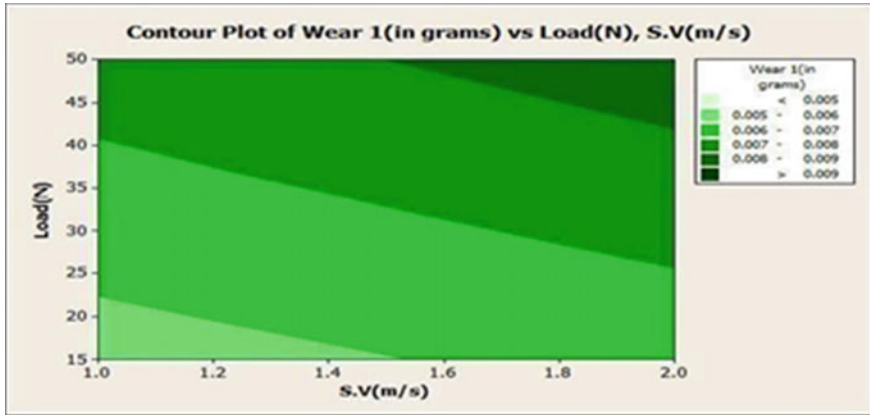
Fig. 12 Contour plot of wear (in grams) versus load (N), S.V (m/s) after hardfacing
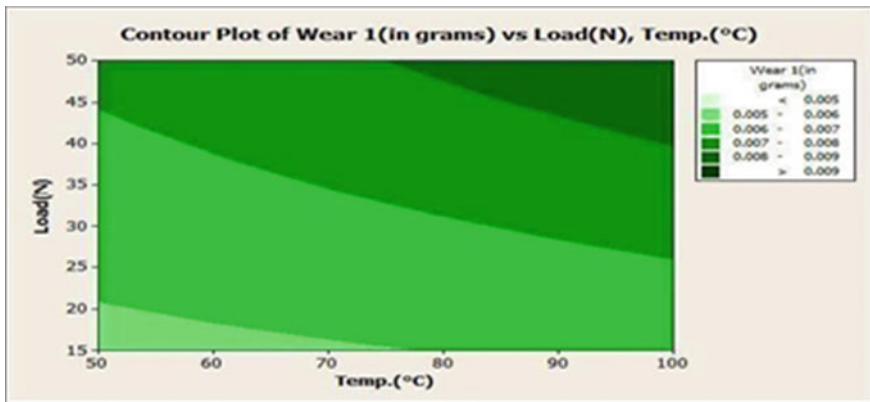
Fig. 13 Contour plot for wear (in grams) versus load (N), temp. (°C)

Figure 13 shows the contour plot for the effect of load and temperature on the process of wear after hardfacing.

Figure 14 shows the contour plot for the effect of load and temperature on the process of wear before hardfacing.

4 Conclusion

The conclusions drawn from this study on effect of hardfacing on IS 2062 steel plate by nanostructured materials 140 MXC Chromium wire by thermal spraying are as follows:
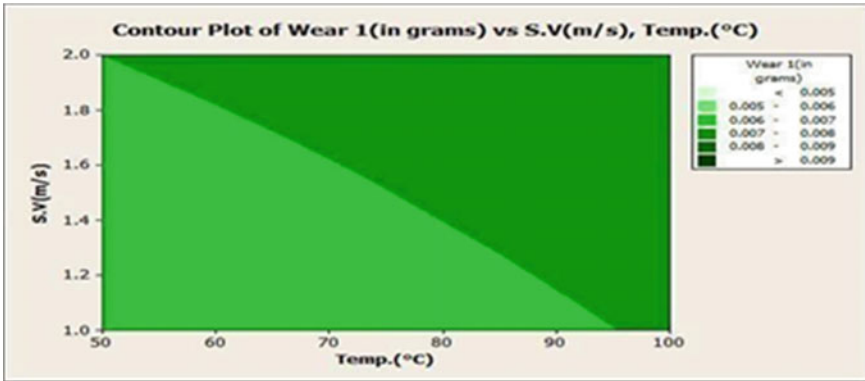
Fig. 14 Contour plot for wear (in grams) versus (m/s), temp. (°C) after hardfacing

- Hardness of the base plate before and after hardfacing by thermal spraying was increased by nearly 7.5%.
- The wear rate is dependent on sliding velocity, load, temperature and sliding distance.
- Scatter diagram certifies precision of the model.
- The wear resistance of hardfacing layer enhanced by 50%.

References

1. Venkatesha B., Srikera K., Prabhakar V.S.V.: Wear characteristics of hardfacing alloys, state-of-the-art. Procedia Mater. Sci. (2015)
2. Ahn, D.G.: Hardfacing technologies for improvement of wear characteristics of hot working tools. Int. J. Precis. Eng. Manuf. **14**(7) (2009)
3. Kumar, S., Mondal, D.P., Jha, A.K.: Effect of microstructure and chemical composition of hardfacing alloy on abrasive wear behavior. J. Mater. Eng. Perform. **9**(6) (2000)
4. Kear, B.H. : Factors controlling decarburization in hvof sprayed nano-wc/co hardcoatings. Scripta Mater. **44**, 1703–1707 (2001)
5. Tkachenko, S., Wang, X.: Wear on Grinding Rotors with Thermally Sprayed Coating in a High Speed Mill. The welding Institute, Abington Hall, pp. 32–39 (2018)
6. Barber, J., Hume, A.H.: The Development of Sub-surface Damage High Energy Solid Particle Erosion of a Thermally Sprayed WC-Co-Cr Coating. Department of Mechanical Engineering, Karlsruhe Institute of Technology, Germany (2005)
7. Sheppard, P., Buchanan, V.E.: Effect of W dissolution in NiCrBSi-WC and NiBSi-WC arc sprayed on wear behaviors. Surf. Coat. Technol., **202**(8), 1502–1509 (2014)
8. Al-Mutairi, S.: Microstructural characterization of HVOF/plasma thermal spray of micro/nano WC-12%Co powders. Surf. Coat. Technol. S0257-8972 (14)01194-3 (2014)
9. Ahn, D.G.: Microhardness and abrasive wear resistance of metallic glasses and nanostructured composite materials. Int. J. Precis. Eng. Manuf., **14**(7) (2009)
10. Mindivan, H., Rao, S., Shettyand R., Nayak, R.: A Comparative Study of Thermal Sprayed AISI 316L Stainless Steel Coating. Department of Aeronautical and Automobile Engineering,

Manipal Institute of technology, Manipal, India. Department of Mechanical Engineering, National Institute of Technology Karnataka, Suratkal, India (2017)

11. Vackel, A., Sampath, S.: Fatigue behavior of thermal sprayed WC- CoCr- steel systems: role of process and deposition parameters. Surf. Coat. Technol. **315**, 408–416 (2017)
12. Hajare, A.S.: Comparative study of wear behavior of thermal spray HVOF coating on 304 S. Mater. Today: Proc. **5**, 6924–6933 (2018)
13. Gkomoza, P.: Comparative study of structure and properties of thermal spray coatings using conventional and nanostructured hydroxyapatite powder, for applications in medical implants. Surf. Coat. Technol. S0257-8972(18)311514 (2018)
14. Amin, S., Panchalet, H.: A review on thermal spray coating processes. Int. J. Curr. Trends Eng. Res. (IJCTER) **2** (2016). e-ISSN 2455–1392

Challenges for Mass Customization in Industry 4.0 Environment: An Analysis Using Fuzzy TOPSIS Approach

Praveen Kumar Dwivedi[ID] **, Girish Kumar**[ID] **, and R. C. Singh**[ID]

1 Introduction

In past, designers designed the product with minimal input from customers. There were limited interactions among customers, designers and manufactures. However, it is possible now to satisfy the demand of individual customer and designing it right too. With the advent of 1990s, mass customization (MC) evolution started to satisfy customer demand for the variety of products [1]. Information and automation technology became the main drivers of MC. Industrial robots, computer integrated systems and flexible manufacturing systems which are basically numerically controlled machines, could be reprogrammed faster now. As a result, flexible production systems were developed to ensure high productivity, large varieties at low cost.

Effective implementation of MC is still a challenge, although it is in practice for years. Flexible tooling and processes are required to switch efficiently between product variants [2]. Industry 4.0, the fourth industrial revolution, encircles traditional industrial platforms and manufacturing practices with the latest smart technology. Mass customization with the help of Industry 4.0 technologies can manufacture variety of products on same production floor with flexible production processes. Interchangeable tooling sets and dynamically programmed robots facilitate manufacturing to be effective with minimum efficiency loss.

Machines equipped with sensors can communicate record and issue instructions over the production line. Integration of supply chain and other business units can make system even more efficient. Industry 4.0 enables manufacturing of individual products at the cost of mass production. Now, it is possible to coordinate among

P. K. Dwivedi (✉) · G. Kumar · R. C. Singh
Department of Mechanical, Production & Industrial and Automobile Engineering, Delhi Technological University, North West Delhi, Delhi 110042, India
e-mail: praveendwivedi05@gmail.com

product development, production and rest of the product life. In this way, value can be added as per the requirements of customer.

Industry 4.0 integrates across three dimensions of high process digitization, smart production and communication between companies. Analysis of high volume of statistical and managerial data is the main driver of Industry 4.0. Big data analysis tools help in new product development and services aligned as per consumer preference [3].

Mass customization (MC) can be defined as "a strategy that creates value by some form of company–customer interaction at the fabrication/assembly stage of the operations level to create customized products with production cost and monetary price similar to those of mass produced-products".

2 Identifying Mass Customization Barriers

Many researchers have investigated mass customization from different perspectives and observed that MC concept has not gained much popularity among industries to a satisfactory extent until now. Limited studies are available on factors that affect the success of the adoption of MC. Therefore, it becomes necessary to discuss the difficulties in implementing this strategy in Industry 4.0 scenario. Presently, research is mainly focussed on technical aspects of technology. There is a missing link to highlight the barriers at organization level. Limited research is available to mark prerequisites and hindrance in the path to adopt mass customization strategy in Industry 4.0 environment. Following subsection discusses the main barriers in implementing MC in Industry 4.0 environment.

2.1 Inaccuracy in Demand Forecast

Forecasting has never been easy task in manufacturing and it becomes more complicated in mass customized manufacturing. Generally, suppliers systems are optimized towards producing pre-arranged quantities of products. Mostly, companies forecast each option individually. Planning bills instead of bill of material are used and quantities are expressed as a percentage rather than unit quantity. With the help of planning bills, forecasting is simplified up to a certain level. With right coordination of operations with engineering, it is possible to overcome issues related to forecasting as organization moves to MC. Cost of mass customization is a big problem organizations face and it increases exponentially in case of unplanned demand. For example, in automobile industry, if a customer orders certain style of sunroof which need to be installed during an upstream manufacturing, the automaker would have to halt the production flow which increase the price.

The current forecasting approach does not forecast for options which results in high inventories and customer dissatisfaction. Right demand forecast helps in maintaining the quality of sales and operation planning (S&OP) which enables better

corporate management. Even employing all the available methods the forecast for mass customization is still a challenge that need to be taken in future researches.

2.2 Internal Complexity

High product variety which is responsible for decreased efficiency and high cost with slow supply chain is the main source of internal complexity. The difference between internal and external variety are discussed in the literature [4]. External variety is faced by end user, whereas internal variety is felt during manufacturing and supply chain management. Therefore, any system should maintain sufficient internal variety in terms of processes, tools, components to compliment the external variety. This results in high variety at shop floor level. However, there are many studies to optimize variety and complexity; there is little insight into how to implement in organization successfully.

2.3 External Complexity

Offering large variety increases customer base and let them select optimal product but it also creates confusion among them to decide. This confusion is termed as external complexity. There are many factors which are responsible for external complexity. Comparing many options require processing capabilities which often customer does not have and nothing can be done for this. Lack of knowledge about product is also work like a barrier in selecting right configuration. In some cases, customers do not know their real requirements or they are unable to express their needs and it makes confusion in deciding. A model of MC environment where orders do not compliment customer's needs was suggested. A good support system is always required during customer interaction process.

2.4 Inventory Management

Many studies have identified inventory management as the most crucial issues in MC [5] An inefficient inventory management will harm environment and society. Higher returns due to poor quality and higher unsold products will hamper the organization profit and environment. Furthermore, these returns and unsold inventories will hamper the brand image as today's customer also cares for sustainability and social responsibility. Inventory management is a tedious task for mass customization implementation.

2.5 Lack of Standardization

Use of common components and modules in production, purchasing, research and development activities is called standardization [6]. It is necessary to apply standardization at every level in an organization to achieve MC efficiently. For example, at network level, standard interface and protocol should be used across all type of network technologies. Standardization is being practiced in most of the fields. However, there are many violations in adopting standardization in true spirit.

2.6 Inadequate Broadband Infrastructure

A good broadband infrastructure has pivotal role with the success of Industry 4.0 technologies. Not only good speed with reliability is required but its cost also should be affordable. As the use of Internet of things (IoT) is increasing, wireless connections will increase abruptly within organization. Attention should be given to wired network where ever possible. Broadband infrastructure should be capable enough to handle the internal data flow. Devices are integrated from suppliers to distributors including manufacturing plant via wireless and Internet technologies [7]. Reliably should be high of communication networks to fully unlash the benefits of Industry 4.0. Also, the expansion of broadband infrastructure is necessary wherever required [8]. An efficient networking of interconnected devices forms the base of self-organized decentralized operation of cyber physical system.

2.7 Cyber Security

Cyber attacks are common nowadays and a fully automated business can be hacked for confidential data resulting huge financial losses. Growing cyber security sector is a hint about this challenge which Industry 4.0-based organizations are facing. According to Nasdaq (an US financial market index), USD 105.45 billion cyber security market in 2015 is going to be USD 181.77 billion in 2021 with an increase rate of 9.5 per cent [9].

In MC environment, intelligent manufacturing systems are used which work with the help of cyber physical system. CPS are capable to record, interpret and communicate data. Cyber physical production systems are enabler of interaction opportunities between human and manufacturing system. Collaboration of human and robot on factory floor will emerge as a new dimension in manufacturing. Establishing such systems may seem insecure and vulnerable to cyber attacks.

2.8 Uncertain Environment for Supply Chain Management

Supply chain management enables enterprises to source the raw materials necessary to create a product or service and deliver that product or service to customers. Present structure of supply chain in business models is inclined towards push system, whereas mass customization production system need pull system to compliment. Unforeseen demands cannot be satisfied with this kind of supply chain structures. Latest supply chain applications like automated planning and just in time are needed for high flexibility and visibility in MC.

Partial customization can be implemented by manufacturing standard products and configuring them when needed. Partial customization can cater advantages to manufacturers. Even with partial customization, product scope increases and it helps to target different segments of market.

Nowadays, practitioners and researcher are giving more attention towards supply chain quality management. However, it is required to investigate the relation between product design and production capabilities with supply chain quality management. Integration of manufacturing processes with vendors and customers can make positive impact on competitive performance [10].

2.9 Return of Customized Product

MC creates a lot of problems for the manufacturers when the products get returned. Mostly this does not happen as the product is created according to the likes of the customer but some products returns will always be there. In such cases, businesses that do not have mechanisms to reverse the customization tend to face many issues. In MC, the chances of another client wanting the same product as someone else are too narrow, which can put the business in a tricky situation. Therefore, the majority of such companies do not have any return policies or simply bear the loss of return in case it allows it.

2.10 Maintaining Quality

Sustained high quality is one of the prerequisite for mass customization and maintaining it when every product is of different configuration is difficult. It is not possible for manufacturer to test every combination of modules or assembly sub-sets. That is why, it is required to integrate quality practices with production planning. All employees must be trained in a way so that top-notch quality can be ensured [11].

2.11 Unavailability of Skilled Manpower

Skilled work force is of prime importance to guarantee the success of any business model. In a technology intensive environment like Industry 4.0, creativity of human can result in the form of better results. To make this fourth industrial revolution sustainable and successful, it is required to train people. More skilled workforce is required as these technologies are recently developed. Training should focus to develop skills of decision making and ability to take on new responsibilities with a vision of world class manufacturing. Organizations need to understand the role of continuous training to cope up technology-related challenges.

3 Methodology

The main purpose of this study is to prioritize the challenges for mass customization in Industry 4.0 environment. There are many multi-criteria decision-making (MCDM) methods like AHP, ELECTRE, PROMETHEE, etc. available for ranking of barriers. Each technique has their own advantages and limitations. AHP is time consuming in case of large criteria. ELECTRE method needs another MCDM technique to select the best alternative after discarding some alternatives. Fuzzy TOPSIS technique is used for this study. Linguistic variable is used for the rating of criteria. Expressing the judgement with linguistic variable is more convenient. Fuzzy TOPSIS method is easy to programme as it is rational. Fuzzy theory can precisely model difficult problems. "Technique for order performance by similarity to ideal solution (TOPSIS)" was proposed by Hwang and Yoon (1981). It is based upon the concept that positive ideal solution should have shortest distance from selected alternative for maximizing benefit criteria and minimizing cost criteria, whereas negative-ideal solution should have maximum distance from selected alternative for minimizing benefit criteria and maximizing cost criteria [12]. To deal ambiguity and vagueness of human judgement, fuzzy TOPSIS was first introduced by Zadeh in 1965. Fuzzy systems have ability to give better performance in case of approximate reasoning and decision making with uncertain information [13]. Due to these characteristics, fuzzy logic is combined with TOPSIS. This fuzzy TOPSIS methodology is used for the ranking of barriers in implementing mass customization in Industry 4.0 environment [14].

During this study, a brief explanation was given to expert's panel. There are three members in expert's panel. Out of three, one is from automation and manufacturing industry having more than 12 years of experience. The second member is from a technology company which provide services in e-commerce and software technologies and has an experience more than 12 years. Third member is from a leading home appliance company having more than 10 years of experience. The barriers identified through literature review was discussed and validated with expert's opinion. Experts have given their response in linguistic term provided to them.

The steps of methodology are briefly described here:

Step 1: Collect the required data from experts in linguistics terms based on a proper scale to represent data precisely. A five-point scale is selected having the linguistic terms low, fairly low, medium, fairly high and high for the calculations. Triangular fuzzy number (TFNs) value is determined of every linguistic term [14, 15].

Step 2: Evaluate the fuzzy decision matrix, D

$$D = \left[p_{ij}\right] n \times m \tag{1}$$

p_{ij} is the value assigned to ith barrier by the jth expert (R). $i = 1, 2, 3, \ldots, n$ are the number of barriers and $j = 1, 2, 3, \ldots, m$ are the number of experts.

Step 3: Fuzzy unweighted matrix, B is generated by neutralizing weight of decision matrix. Equation (2) is applied as barriers are similar to cost criteria [16].

$$B = \left[r_{ij}\right] n \times m, \ r_{ij} = \left(\frac{a_j^-}{c_{ij}}, \frac{a_j^-}{b_{ij}}, \frac{a_j^-}{a_{ij}}\right). \tag{2}$$

where $a_j^- = \min\{a_{ij}\}, j = 1, 2, \ldots, m.$

Step 4: Weighted normalized decision matrix, C is calculated as

$$C = \left[q_{ij}\right]_{n \times m}, \ i = 1, 2, \ldots, n; \ j = 1, 2, \ldots, m \tag{3}$$

where the weighted normalized value q_{ij} is obtained using Eq. (4)

$$q_{ij} = r_{ij} * l_j; \tag{4}$$

where $l_j = (1, 1, 1) \ \forall \ j \in n$, all ranking are considered of equal weight.

Step 5: Compute the ideal and negative-ideal solution for the barriers

$$E^* = \left(q_1^*, q_2^*, \ldots q_m^*,\right) \text{ where } q_m^* = \max\{q_{ij3}\}. \tag{5}$$

$$E^- = \left(q_1^-, q_2^-, \ldots q_m^-,\right) \text{ where } q_m^- = \min\{q_{ij1}\} \tag{6}$$

Step 6: Calculate the sum of distances of each barrier from fuzzy positive ideal solution (FPIS) [16]

$$Z_j^+ = \frac{\sqrt{\sum_{i=1}^m d\left(q_{ij} - q_i^*\right)}}{m}, \ j = 1, 2, 3, \ldots, m \tag{7}$$

Similarly calculate the sum of distances of each barrier from fuzzy negative-ideal solution (FNIS)

$$Z_j^- = \frac{\sqrt{\sum_{i=1}^m d\left(q_{ij} - q_i^-\right)}}{m}, \ j = 1, 2, 3, \ldots, m \tag{8}$$

Step 7: Closeness coefficient to the ideal solution is calculated with respect to E*
[17]

$$CC_j = Z_j^- / \left(Z_j^+ + Z_j^- \right), \quad j = 1, 2, 3, \ldots, m \tag{9}$$

Step 8: Rank the barriers according to the closeness coefficient (CC_j).

In next section, all the steps are applied and barriers are ranked as per methodology.

4   Results and Discussion

To rank the barriers in implementing mass customization in Industry 4.0 era, eleven
barriers were identified on the basis of literature review and expert discussions. Three
expert ranked these barriers based on their importance using the linguistic terms low
(L), fairly low (FL), medium (M), fairly high (FH), and high (H). Expert's responses
were used to prepare decision matrix.

Refer Sect. 3, triangular fuzzy numbers are used to convert linguistics variable in
fuzzy numbers. Fuzzy weighted normalized decision matrix, D is constructed with
fuzzy numbers (Refer Table 1).

In next step normalized (un-weighted) fuzzy decision matrix, B is obtained the
following procedure detailed in Sect. 3. The matrix, B is used to derive the weighted
normalized decision matrix, C using Eqs. (3) and (4). This matrix is further used to
find ideal (E^*) and negative-ideal (E^-) solutions using Eqs. (5) and (6). The distance
Z^+ and Z^- is calculated as per Eqs. (7) and (8). Closeness coefficient CC_j is also
calculated for each barrier using Eq. (9). The final ranking of barriers has been done
based on fuzzy TOPSIS and is shown in Table 2. Results are also shown graphically
in Fig. 1.

Table 1 Fuzzy decision matrix, D

MC barriers	R1	R2	R3
MCB1	(1, 3, 5)	(1, 3, 5)	(3, 5, 7)
MCB 2	(1, 3, 5)	(5, 7, 9)	(1, 1, 3)
MCB 3	(5, 7, 9)	(3, 5, 7)	(7, 9, 9)
MCB 4	(1, 1, 3)	(3, 5, 7)	(3, 5, 7)
MCB 5	(1, 3, 5)	(5, 7, 9)	(3, 5, 7)
MCB 6	(7, 9, 9)	(7, 9, 9)	(3, 5, 7)
MCB 7	(5, 7, 9)	(7, 9, 9)	(3, 5, 7)
MCB 8	(3, 5, 7)	(1, 1, 3)	(1, 3, 5)
MCB 9	(1, 3, 5)	(1, 3, 5)	(7, 9, 9)
MCB 10	(5, 7, 9)	(7, 9, 9)	(1, 1, 3)
MCB 11	(1, 3, 5)	(5, 7, 9)	(3, 5, 7)

Table 2 Closeness coefficient matrix

MC barriers	Z^+	Z^-	CC_j	Rank
MCB1	1.396253	1.150337	0.451717	4
MCB 2	1.081502	1.275928	0.541237	2
MCB 3	2.024572	0.160474	0.073442	9
MCB 4	1.222416	0.969851	0.442396	6
MCB 5	1.69271	0.674276	0.284867	8
MCB 6	2.059978	0.122733	0.05623	11
MCB 7	2.024572	0.160474	0.073442	9
MCB 8	1.003731	1.36092	0.575527	1
MCB 9	1.50943	1.027604	0.405041	7
MCB 10	1.260995	1.018726	0.446864	5
MCB 11	1.361621	1.167085	0.461534	3

Fig. 1 MC barriers ranking in descending order (bottom to top)

According to analysis, MCB 8 (uncertain environment for supply chain management) is found to be the most challenging barrier and MCB 6 (inadequate broadband infrastructure) is the least challenging barrier in implementing mass customization in the era of Industry 4.0. Top rank of uncertain environment for supply chain management reflects that organizations are still not managing supply chain in a way so that it can provide the required flexibility and responsiveness needed for MC. Traditional supply chain is based on mass production which cannot be effective in customer-driven environment. Industry 4.0 technologies can be beneficial in transforming the present supply chains. Academia and industry can come together to develop programmes for the learning of supply chain professionals.

Internal complexity is ranked as the second most influential barrier. In today's competitive environment, manufacturers are offering high product variety to target more customer segments. However, this variety induced complexity is putting more pressure on production floor. Organizations need to understand that offering too much

variety can delay processes. Even quality will be compromised because it would not be possible to check and verify every combination of components in the form of product desired by the customer. Organizations need to identify that up to what degree of customization is beneficial for them. Organization can start with partial customization and later it can be expanded in a phased manner.

There are few recommendations in the literature about implementing MC in Industry 4.0 environment. This study connects the gap by describing and ranking the barriers which can guide higher management to develop a better approach for the implementation of MC.

The results obtained contribute to the identification of barriers that guides in the implementation of MC for organizations those intend to plan or already implemented.

5   Conclusion

Most of the companies can benefit from mass customization. However, only few companies are following MC strategies. Changing company's strategy from mass production to mass customization needs high capital as well as change in mindset of all employees including top management. A failed mass customization strategy can result huge financial losses as well as can damage the reputation of organization. In Industry 4.0 environment, mass customization needs to be viewed from a different angle both in terms of product and manufacturing flexibility. Ability to treat each individual customer cost effectively is considered core competency. Companies are considering mass customization to be more important in near future. The results of the study give an insight about the barriers in implementing mass customization. All the barriers are identified through literature review and analysed for the better understanding. This paper ranks the barriers with the help of fuzzy TOPSIS method. Uncertain environment of supply chain and internal complexity are identified as the top barriers. All the barriers are discussed in the paper with an insight to overcome them. This study can help managers to understand mass customization strategy and how organizations can get benefit from it. Ranking of barriers will help organizations to focus on them priority basis to get maximum benefit from mass customization.

As the ranking is done purely on the basis of input from the experts, therefore, there may be some bias towards the industries they belong. It will be relevant to incorporate experts from different domains of industries. As the experts belong to India, there is a possibility of biasness of data towards developing countries. In future study, a larger sample for data collection can be implemented by including experts from different industries as well as nations so that chances of biasness of data can be eliminated.

References

1. Fitzgerald, B.: Mass customization—at a profit. World Cl. Des. to Manuf. **2**, 43–46 (1995). https://doi.org/10.1108/09642369310077779
2. Salvador, F., Martin de Holan, P., Piller, F.: Cracking the code of mass customization. MIT Sloan Manag. Rev. **50**, 71–78 (2009)
3. Kolberg, D., Zühlke, D.: Lean automation enabled by Industry 4.0 Technologies. IFAC-PapersOnLine **48**, 1870–1875 (2015). https://doi.org/10.1016/j.ifacol.2015.06.359
4. Anderson, B.D.M.: Mass Customization, the Proactive Management of Variety (2009)
5. Duray, R.: Mass customizers' use of inventory, planning techniques and channel management. Prod. Plan. Control. **15**, 412–421 (2004). https://doi.org/10.1080/0953728042000238791
6. Perera, C., Nagarur, N., Tabucanon, M.: Component part standardization: a way to reduce the life-cycle costs of products. Int. J. Prod. Econ. **60–1**, 109–116 (1999). https://doi.org/10.1016/S0925-5273(98)00179-0
7. Kinzel, H.: Industry 4.0—Where Does This Leave the Human Factor? (2016)
8. Kagermann, H., Wahlster, W., Helbig, J.: Securing the future of German manufacturing industry: recommendations for implementing the strategic initiative INDUSTRIE 4.0. Final Rep. Ind. 4.0 Work. Gr. 1–84 (2013)
9. Fully Autonomous Robots_ The Warehouse Workers of the Near Future
10. Zhang, M., Guo, H., Huo, B., Zhao, X., Huang, J.: Linking supply chain quality integration with mass customization and product modularity. Int. J. Prod. Econ. **207**, 227–235 (2019). https://doi.org/10.1016/j.ijpe.2017.01.011
11. Mouw, R.: How to overcome the challenges of manufacturing customized products. https://www.reliableplant.com/Read/30506/manufacturing-customized-products
12. Wang, Y.-M., Elhag, T.: Fuzzy TOPSIS method based on alpha level sets with an application to bridge risk assessment. Expert Syst. Appl. **31**, 309–319 (2006). https://doi.org/10.1016/j.eswa.2005.09.040
13. Gupta, S., Ahuja, G., Kumar, G.: Identification of optimum locations for charging of electric vehicles. (2018). https://doi.org/10.1109/ICRITO.2018.8748280
14. Manghani, S., Kumar, G.: Automotive composites and polymer material selection for fairing of a human powered vehicle using multi-attribute decision making methodology. (2016). https://doi.org/10.4271/2016-01-0526
15. Gupta, S., Soni, U., Kumar, G.: Green supplier selection using multi-criterion decision making under fuzzy environment: a case study in automotive industry. Comput. Ind. Eng. (2019). https://doi.org/10.1016/j.cie.2019.07.038
16. Almalki, S., Zhuo, Z., Musaad, A., Siyal, Z., Hashmi, H., Ahsan, S., Shah, S.A.A.: A fuzzy multi-criteria analysis of barriers and policy strategies for small and medium enterprises to adopt green innovation. symmetry (Basel). **12**, 116 (2020). https://doi.org/10.3390/sym12010116
17. Kumar, A., Kashyap, H., Malhotra, H., Rawat, K., Kumar, G., Soni, U.: Preferential selection of locations for installing CCTV using fuzzy TOPSIS approach: a case study for North Delhi. (2019). https://doi.org/10.1109/IC3.2019.8844896

Effect of Thickness Stretching on Sandwich Plate with FGM Core and Piezoelectric Face Sheets

S. J. Singh and **S. P. Harsha**

1 Introduction

The sandwich materials enrich the performance of structures by reducing their weight and improving the inherent elastic properties. The conventional sandwich plates consist of soft core and very thin face sheets. But, with the advancement in materials and fabrication processes, the soft core is replaced by functionally graded material (FGM) where the materials are continuously graded in the thickness direction. This will further assist the designers in improving the material properties based on the requirement. Further, homogenous face sheets are replaced by piezoelectric material (PZT) which will assist in actively controlling the vibrating structures and found applications in aerospace, shipbuilding, automotive industries, etc.

The considerable research on the FG sandwich plate [1–4] has been reported in the literature, but limited research has been done on the plate comprising FGM core and PZT outer layers. In the context of the piezoelectric plate, Kulikov et al. [5] implemented the 3D coupled steady-state analysis of functionally graded PZT laminated plates. The free and forced analysis of the FG PZT plate is done by Zhong and Yu [6]. The exponent-law dependent material properties were considered. Zenkour and Hafed [7] performed the bending analysis of an FG PZT plate using a quasi-3D theory. Arefi et al. [8] developed a concept of the neutral surface to analyze the FG PZT plate for bending analysis.

S. J. Singh (✉)
Department of Mechanical Engineering, Pandit Deendayal Petroleum University, Gandhinagar 382421, India
e-mail: simran.singh@sot.pdpu.ac.in

S. P. Harsha
Mechanical and Industrial Engineering Department, Indian Institute of Technology, Roorkee 247667, India
e-mail: surajfme@iitr.ac.in

Thus, in the light of reported literature, it is conceivable that limited work was done on the FGM core sandwich plates. Thus, therefore, the aforementioned plate is analyzed to determine the effect of PZT and thickness stretching effect on the fundamental frequency. The Lagrangian approach is implemented to derive governing equations and an exact solution is obtained using Navier's approach. The plate is assumed to be simply supported along all the edges. The present formulation is validated from the available results and also found to be in good harmony.

2   Problem Formulation

The plate is analyzed using higher-order and normal shear deformation theory. So, to incorporate the effect of piezoelectric on FGM plate, the constitutive relation has been modified and results in the electromechanical coupling. The sandwich plate under analysis is shown in Fig. 1.

2.1   Modeling of Sandwich FGM Plate

The core of the sandwich plate is made up of function graded material in which material property varies according to some mathematical rule [9–11]. In the present study, the material properties vary according to P-FGM. Besides, the face sheets are homogenous and consider as a piezoelectric material in the present study. The plate configuration used in the present formulation is given in Table 1. Thus, the volume

Fig. 1 Sandwich plate with three layers
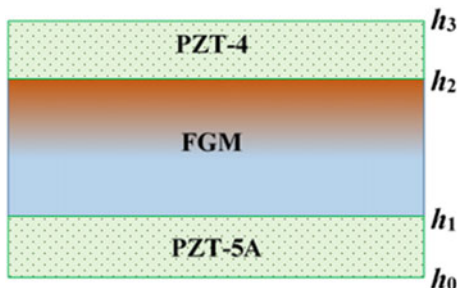
Table 1 Plate configurations

Configuration	Ω_1^*	Ω_2^*
1-1-1	6	6
1-8-1	5/2	5/2

* $h_1 = -h/\Omega_1$, $h_2 = h/\Omega_2$

Fig. 2 Volume fraction variation along the transverse direction
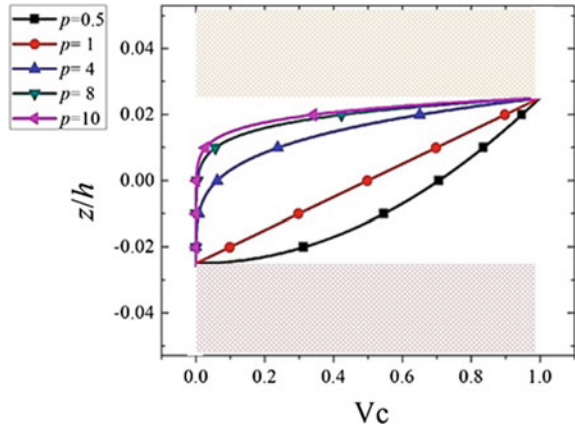
fraction function for the sandwich plate is given by Eq. (1) and variation is shown in Fig. 2.

(a)   Bottom layer

$$PZT - 5A \qquad (1.a)$$

(b)   P-FGM core:

$$V_c = \left(\frac{z - h_1}{h_2 - h_1} \right)^p \quad \text{for } h_1 \leq z \leq h_2 \qquad (1.b)$$

(c)   Top layer:

$$PZT - 4 \qquad (1.c)$$

Thus, the effective material property for the sandwich plate is obtained using the following functional relationship:

$$P(z) = P_2 + (P_1 - P_2)V_c \qquad (2)$$

where P_1 and P_2 are the material properties such as Young's modulus, density, and poison ratio for top and bottom material, respectively. V_c is the volume fraction of material at the top of FGM and given by Eq. (1).

2.2   *Electromechanical Constitutive Relation*

The relation of mechanical and piezoelectric stress and strain relation is given as:

$$\sigma_{ij} = C_{ijkl}\varepsilon_{kl} - e_{kij}E_k$$
$$D_i = e_{ikl}\varepsilon_{kl} + \mu_{ik}E_k \tag{3}$$

$\sigma, \varepsilon, E,$ and D represent stress, strain, electric field, and electric displacement, respectively. $C, e,$ and μ represent material constant, piezoelectric constant, and dielectric constant, respectively.

The electric field (E) is defined in terms of electric potential difference (Φ) by the following relationship:

$$E = -\nabla\Phi \tag{4}$$

2.3 Kinematic Relations

The higher-order and normal shear deformation theory are selected which will capture the realistic displacement field for the present problem. The mathematical relation can be written as:

$$u(x, y, z, t) = \bar{u}(x, y, t) - z\left(\frac{\partial \bar{w}_b(x, y, t)}{\partial x}\right) + f(z)\left(\frac{\partial \bar{w}_s(x, y, t)}{\partial x}\right)$$

$$v(x, y, z, t) = \bar{v}(x, y, t) - z\left(\frac{\partial \bar{w}_b(x, y, t)}{\partial y}\right) + f(z)\left(\frac{\partial \bar{w}_s(x, y, t)}{\partial y}\right)$$

$$w(x, y, z, t) = \bar{w}_b(x, y, t) + \bar{w}_s(x, y, t) + g(z)\varphi_z(x, y, t)$$

$$\Phi(x, y, z, t) = \frac{2z}{h}V_e - g(z)\phi \tag{5}$$

where $\bar{u}$ and $\bar{v}$ are the in-plane displacement in x- and y-directions, respectively. $\bar{w}_b$ and $\bar{w}_s$ are the out-of-plane displacement. V_e and ϕ are the applied voltage and electric potential distribution. $f(z)$ and $g(z)$ represent the shape functions and are given as:

$$f(z) = z - h\sinh\left(\frac{z}{h}\right) + z\cosh\left(\frac{1}{2}\right), \quad g(z) = 1 - f(z) \tag{6}$$

2.4 Energy Equations

The strain energy (U_s) and kinetic energy (K_e) stored in the plate due to initial excitations can be expressed as:

$$U_\mathrm{s} = \frac{1}{2}\sigma_{ij}\varepsilon_{kl} - \frac{1}{2}D_i E_k \tag{7}$$

The above expression in terms of stress resultant can be expressed as:

$$U_\mathrm{s} = \frac{1}{2}\left(\mathbf{N_U}\boldsymbol{\varepsilon}_0^T + \mathbf{M_U^b}\boldsymbol{\varepsilon}_\mathbf{b}^T + \mathbf{M_U^s}\boldsymbol{\varepsilon}_\mathbf{s}^T + \mathbf{Q}_{\mathbf{z}}^T - \mathbf{D\#}^T\right) \tag{8}$$

where

$$\mathbf{N_U} = \{N_{xx}, N_{yy}, N_{xy}\}; \quad \boldsymbol{\varepsilon}_0 = \{\bar{u}_{,x}, \bar{v}_{,y}, \bar{u}_{,y} + \bar{v}_{,x}\}$$

$$\mathbf{M_U^b} = \{M_{xx}^b, M_{yy}^b, M_{xy}^b\}; \quad \boldsymbol{\varepsilon}_\mathbf{b} = \{-\bar{w}_{s,xx}, -\bar{w}_{b,yy}, -2\bar{w}_{b,xy}\}$$

$$\mathbf{M_U^s} = \{M_{xx}^s, M_{yy}^s, M_{xy}^s\}; \quad \boldsymbol{\varepsilon}_\mathbf{s} = \{-\bar{w}_{s,xx}, -\bar{w}_{s,yy}, -2\bar{w}_{s,xy}\}$$

$$\mathbf{Q} = \{Q_{xz}, Q_{yz}, Q_{zz}\}; \quad \boldsymbol{\varepsilon}_\mathbf{z} = \{\bar{w}_{s,x} + \varphi_{z,x}, \bar{w}_{s,y} + \varphi_{z,y}, \varphi_z\}$$

$$\mathbf{D} = \{D_x, D_y, D_z\}; \quad \boldsymbol{\phi} = \{\phi_{,x}, \phi_{,y}, \phi_{,z}\}$$

$$\begin{Bmatrix} \mathbf{N} \\ \mathbf{M^b} \\ \mathbf{M^s} \\ Q_{zz} \\ D_z \end{Bmatrix} = \begin{bmatrix} \mathbf{A} & \mathbf{B} & \mathbf{A^s} & \mathbf{H} & \mathbf{A^e} & -\mathbf{H^e} \\ \mathbf{B} & \mathbf{D} & \mathbf{B^s} & \mathbf{J} & \mathbf{B^e} & -\mathbf{J^e} \\ \mathbf{A^s} & \mathbf{B^s} & \mathbf{D^s} & \mathbf{J^s} & \mathbf{D^e} & -\mathbf{J^{se}} \\ \mathbf{H} & \mathbf{J} & \mathbf{J^s} & \mathbf{K} & \mathbf{L^e} & -\mathbf{K^e} \\ \mathbf{H^e} & \mathbf{J^e} & \mathbf{J^{se}} & \mathbf{K^e} & -\mathbf{L^p} & \mathbf{K^p} \end{bmatrix} \begin{Bmatrix} \boldsymbol{\varepsilon}_0 \\ \boldsymbol{\varepsilon}_\mathbf{b} \\ \boldsymbol{\varepsilon}_\mathbf{s} \\ \varphi_z \\ I \\ \phi \end{Bmatrix},$$

$$\begin{Bmatrix} Q_{xz} \\ Q_{yz} \\ D_x \\ D_y \end{Bmatrix} = \begin{bmatrix} F_{55} & 0 & -F_{15}^e & 0 \\ 0 & F_{44} & 0 & -F_{24}^e \\ F_{15}^e & 0 & F_{11}^p & 0 \\ 0 & F_{24}^e & 0 & F_{22}^p \end{bmatrix} \begin{Bmatrix} \bar{w}_{s,x} + \varphi_{z,x} \\ \bar{w}_{s,y} + \varphi_{z,y} \\ \phi_{,x} \\ \phi_{,y} \end{Bmatrix}$$

$$\{A_{ij}, B_{ij}, D_{ij}, A_{ij}^s, B_{ij}^s, D_{ij}^s, F_{ij}, H_{ij}, J_{ij}, J_{ij}^s, K_{ij}\}$$
$$= \int_{-h/2}^{h/2} C_{ij}(z)\{1, z, z^2, f(z), zf(z), f(z)^2, g^2, g', zg', f(z)g', g'^2\}\mathrm{d}z$$

$$\{A_{ij}^e, B_{ij}^e, D_{ij}^e, L_{ij}^e\} = \int_{-h/2}^{h/2} \frac{2V_e e_{ij}}{h}\{1, z, f(z), g'\}\mathrm{d}z$$

$$\{H_{ij}^e, J_{ij}^e, J_{ij}^{se}\ F_{ij}^e, K_{ij}^e\} = \int_{-h/2}^{h/2} e_{ij}\{g', zg', f(z)g', g^2, g'^2\}\mathrm{d}z$$

$$\left\{ F_{ij}^p, L_{ij}^p, K_{ij}^p P_{ij}^p \right\} = \int_{-h/2}^{h/2} \mu_{ij} \left\{ g^2, \frac{2V_e}{h} g', g'^2, 2\left(\frac{V_e}{h}\right)^2 \right\} dz$$

The kinetic energy (K_e) stored in the plate can be expressed as:

$$K_e = \frac{1}{2}\rho\left(\dot{u}^2 + \dot{v}^2 + \dot{w}^2\right) \tag{8}$$

The kinetic energy in terms of inertia can be written as,

$$K_e$$

$$= \frac{1}{2} \begin{bmatrix} I_0\left(\dot{\bar{u}}^2 + \dot{\bar{v}}^2 + \left(\dot{\bar{w}}_b + \dot{\bar{w}}_s\right)^2\right) - 2I_1\left(\frac{\partial \dot{\bar{w}}_b}{\partial x}\dot{\bar{u}} + \frac{\partial \dot{\bar{w}}_b}{\partial y}\dot{\bar{v}}\right) + I_2\left(\left(\frac{\partial \dot{\bar{w}}_b}{\partial x}\right)^2 + \left(\frac{\partial \dot{\bar{w}}_b}{\partial y}\right)^2\right) \\ -2I_1^s\left(\frac{\partial \dot{\bar{w}}_s}{\partial x}\dot{\bar{u}} + \frac{\partial \dot{\bar{w}}_s}{\partial y}\dot{\bar{v}}\right) + I_2^s\left(\left(\frac{\partial \dot{\bar{w}}_s}{\partial x}\right)^2 + \left(\frac{\partial \dot{\bar{w}}_s}{\partial y}\right)^2\right) + 2I_3\left(\frac{\partial \dot{\bar{w}}_b}{\partial x}\frac{\partial \dot{\bar{w}}_s}{\partial x} + \frac{\partial \dot{\bar{w}}_b}{\partial y}\frac{\partial \dot{\bar{w}}_s}{\partial y}\right) \\ 2I_4\dot{\varphi}_z\left(\dot{\bar{w}}_b + \dot{\bar{w}}_s\right) + I_5\dot{\varphi}_z^2 \end{bmatrix} \tag{9}$$

where $\left\{ I_0, I_1, I_2, I_1^s, I_2^s, I_3, I_4, I_5 \right\} = \int_{-h/2}^{h/2} \rho\{1, z, z^2, f(z), f(z)^2, zf(z), g, g^2\}dz.$

3 Lagrangian Formulation and Exact Solution

The plate is simply supported along all the edges. Mechanical and electrical variables are defined in terms of an unknown $\left(U^{mn}, V^{mn}, W_b^{mn}, W_s^{mn}, \theta_z^{mn}, \theta_e^{mn}\right)$ as:

$$\bar{u}(x, y) = \sum_{m=1}^{\infty}\sum_{n=1}^{\infty} U^{mn} \cos(\alpha x) \sin(\beta y)$$

$$\bar{v}(x, y) = \sum_{m=1}^{\infty}\sum_{n=1}^{\infty} V^{mn} \sin(\alpha x) \cos(\beta y)$$

$$\{\bar{w}_b(x, y), \bar{w}_s(x, y), \varphi_z(x, y), \phi(x, y)\}$$

$$= \sum_{m=1}^{\infty}\sum_{n=1}^{\infty} \left\{ W_b^{mn}, W_s^{mn}, \theta_z^{mn}, \theta_e^{mn} \right\} \sin(\alpha x) \sin(\beta y)$$

where $\alpha = \frac{m\pi}{a}$, $\beta = \frac{n\pi}{b}$.

The Lagrangian equation for the present problem can be defined as,

$$\frac{\mathrm{d}}{\mathrm{d}t}\left(\frac{\partial K_{\mathrm{e}}}{\partial \dot{\zeta}_{mn}}\right) - \frac{\partial K_{\mathrm{e}}}{\partial \zeta_{mn}} + \frac{\partial U_{\mathrm{s}}}{\partial \zeta_{mn}} = 0 \tag{10}$$

where $\zeta_{mn} = \left\{U^{mn}, V^{mn}, W_{\mathrm{b}}^{mn}, W_{\mathrm{s}}^{mn}, \theta_{z}^{mn}, \theta_{\mathrm{e}}^{mn}.\right\}$

Thus, six equations are obtained based on the generalized coordinate (ζ_{mn}). Thus, six coupled equations are obtained and converted to equivalent eigenvalue problem as,

$$\left(K_{ij} - \omega^2 M_{ij}\right)\varsigma_j = 0 \quad (i, j = 1, 2, 3, 4, 5, 6) \tag{11}$$

4   Validation Study

The validation of the present formulation is done by considering the sandwich plate (1-8-1) but with homogenous outer layers. The plate is assumed to be simply supported and consists of aluminum ($E_1 = 70$ GPa, $\rho_1 = 2707$ kg/m^3) on the top layer and alumina ($E_2 = 380$ GPa, $\rho_2 = 3800$ kg/m^3) at the bottom layer. The results for different (a/h) and FGM exponent are obtained and compared with Hadji et al. [12] and Li et al. [13]. The comparison is done by considering plate without thickness stretching effect and results are found to be in good agreement as depicted from Table 2. However, for the sake of completeness, the results for the thickness stretching effect are also calculated. The fundamental frequency is non-dimensionalized using the following relationship:

Table 2 Validation study

a/h	Theory	$p = 0.5$	$p = 1$	$p = 2$	$p = 5$	$p = 10$
5	[13]$_{(\varepsilon zz = 0)}$	1.1958	1.25338	1.31569	1.39567	1.4454
	[12]$_{(\varepsilon zz = 0)}$	1.18682	1.24352	1.30576	1.38736	1.43837
	Present$_{(\varepsilon zz = 0)}$	1.18978	1.2467	1.30854	1.389159	1.439557
	Present$_{(\varepsilon zz \neq 0)}$	1.21782	1.27493	1.33328	1.406959	1.453613
10	[13]$_{(\varepsilon zz = 0)}$	1.29751	1.34847	1.40828	1.49309	1.5498
	[12]$_{(\varepsilon zz = 0)}$	1.29459	1.34533	1.40514	1.49044	1.54754
	Present$_{(\varepsilon zz = 0)}$	1.295643	1.34642	1.40606	1.49102	1.5479
	Present$_{(\varepsilon zz \neq 0)}$	1.325108	1.3752	1.43012	1.5065	1.55872
100	[13] $_{(\varepsilon zz = 0)}$	1.33931	1.38669	1.44491	1.53143	1.59105
	[12] $_{(\varepsilon zz = 0)}$	1.33927	1.38665	1.44487	1.53139	1.59103
	Present$_{(\varepsilon zz = 0)}$	1.33929	1.38667	1.44489	1.53141	1.59104
	Present$_{(\varepsilon zz \neq 0)}$	1.36926	1.41558	1.46856	1.54579	1.60033

$$\tilde{\omega} = \frac{\omega a^2}{\hbar} \sqrt{\frac{\rho_0}{E_0}}, \quad \rho_0 = 1\,\text{kg/m}^3, \ E_0 = 1\,\text{GPa} \qquad (12)$$

5   Results and Discussion

The sandwich plate having a top face sheet of PZT 4 material and bottom face sheet is of PZT-5A material. The mechanical and electrical properties are obtained from Arefi et al. [8]. The core layer is the P-FGM material consisting of alumina ($E_1 = 380\,\text{GPa}$, $\rho_1 = 3800\,\text{kg/m}^3$) and aluminum ($E_2 = 70\,\text{GPa}$, $\rho_2 = 2707\,\text{kg/m}^3$).

   Two different types of plate configurations (1-8-1 and 1-1-1) are considered in the present study depending on the thickness of face sheets and the core layer. In addition, the following parameters are chosen until they are not specified: $p = 4$, $b/a = 1$, $a/h = 10$.

   The effect of (a/h) on fundamental frequency is analyzed based on considering and neglecting the thickness stretching effect. Figure 3 depicts the variation of frequency with the change in (a/h) and it is found that the frequency increases with increase in span to thickness ratio of the plate, whereas the fundamental frequency decreases with increase in volume fraction exponent and aspect ratio as inferred from Figs. 4 and 5, respectively. This decrease in frequency occurs as a result due to overall reduction in stiffness which in turn occurs due to (a) an increase in constituent material with lower Young's modulus (Fig. 4) and (b) reduction in the overall dimension of the plate (Fig. 5). On the contrary, the increase in frequency with an increase in span to thickness ratio occurs due to non-dimensionalizing the frequency which is inversely proportional to the thickness of the plate. Hence, with a reduction in thickness (increase in span to thickness ratio), the non-dimensional frequency increases.

Fig. 3 Effect of span to thickness ratio on non-dimensional fundamental frequency (*solid line-$\varepsilon_{zz} \neq 0$, dash line-$\varepsilon_{zz} = 0$*)
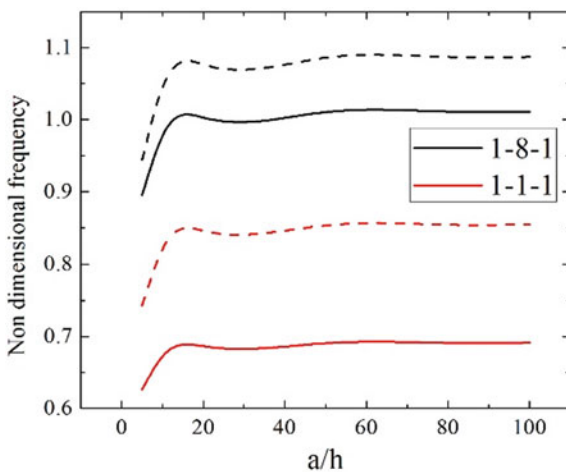
Fig. 4 Effect of volume fraction exponent on non-dimensional fundamental frequency (*solid line-$\varepsilon_{zz} \neq 0$, dash ine-$\varepsilon_{zz} = 0$*)
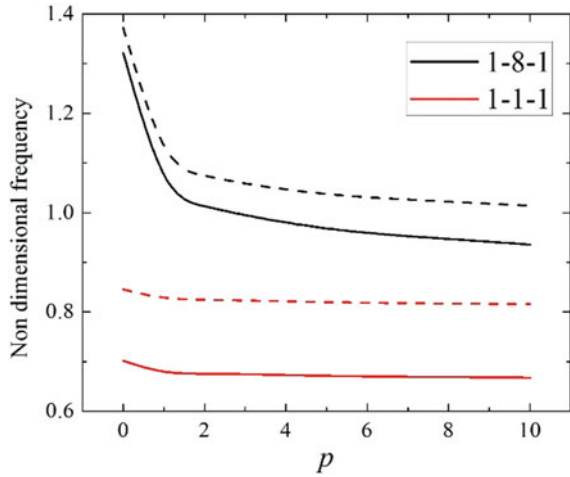
Fig. 5 Effect of aspect ratio on non-dimensional fundamental frequency (*solid line-$\varepsilon_{zz} \neq 0$, dash line-$\varepsilon_{zz} = 0$*)
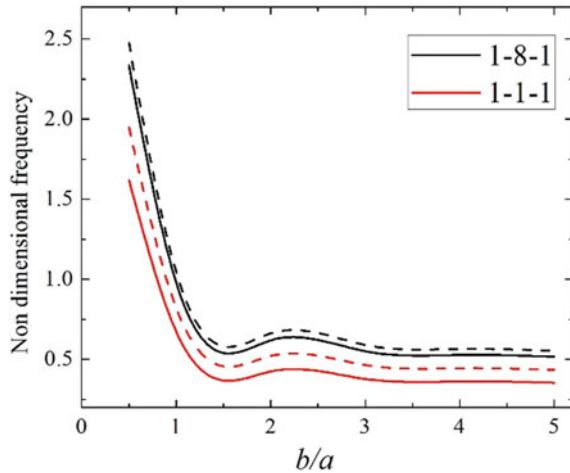
Nevertheless, as depicted in Figs. 3, 4 and 5, 1-8-1 plate configuration always possesses maximum fundamental frequency in comparison with 1-1-1 plate configuration which occurs as a result of large core thickness in 1-8-1 plate in comparison with 1-1-1 plate which in turn increases the overall stiffness of the plate. Also, the thickness stretching effect reduces the fundamental frequency of the plate irrespective of the plate configuration and other geometrical parameters. However, it is also observed that 1-1-1 plate configuration is largely affected by the thickness stretching effect.

6 Conclusions

The free vibration analysis is performed to study the dynamic behavior of the sandwich FGM plate with the PZT effect. The thickness stretching effect is introduced in the formulation by considering the displacement field as higher-order and normal deformation theory [4]. The equation of motion is derived using the Lagrangian approach. The present formulation is validated from the available results and found to be in good harmony. It is observed that

- The introduction of the thickness stretching effect results in the reduction of the fundamental frequency of the plate when outer layers consist of PZT materials.
- 1-8-1 plate configuration always possesses maximum fundamental frequency in comparison with 1-1-1 plate configuration.
- plate configuration is largely affected by the thickness stretching effect.

References

1. Di Sciuva, M., Sorrenti, M.: Bending and free vibration analysis of functionally graded sandwich plates: an assessment of the refined zigzag theory. J. Sandwich Struct. Mater., p. 109963621984397 (2019)
2. Singh, S.J., Harsha, S.P.: Exact solution for free vibration and buckling of sandwich S-FGM plates on Pasternak elastic foundation with various boundary conditions. Int. J. Struct. Stab. Dyn. **19**(3), S0219455419500287 (2018)
3. Singh, S.J., Harsha, S.P.: Nonlinear vibration analysis of sigmoid functionally graded sandwich plate with ceramic-FGM-metal layers. J. Vib. Eng. Technol., p. 18 (2018)
4. Bessaim, A., Houari, M.S.A., Tounsi, A., Mahmoud, S., Bedia, E.A.A.: A new higher-order shear and normal deformation theory for the static and free vibration analysis of sandwich plates with functionally graded isotropic face sheets. J. Sandwich Struct. Mater. **15**(6), 671–703 (2013)
5. Kulikov, G.M., Plotnikova, S.V.: An analytical approach to three-dimensional coupled thermo-electroelastic analysis of functionally graded piezoelectric plates. J. Intell. Mater. Syst. Struct. **28**(4), 435–450 (2017)
6. Zhong, Z., Yu, T.: Vibration of a simply supported functionally graded piezoelectric rectangular plate. Smart Mater. Struct. **15**(5), 1404–1412 (2006)
7. Zenkour A.M., Hafed, Z.S.: Bending analysis of functionally graded piezoelectric plates via quasi-3D trigonometric theory. Mech. Adv. Mater. Struct., 0(0), 1–12 (2019)
8. Arefi, M., Mohammad-Rezaei E., Bidgoli, Dimitri, R., Bacciocchi, M., Tornabene, F.: Application of sinusoidal shear deformation theory and physical neutral surface to analysis of functionally graded piezoelectric plate. Compo. Part B: Eng. 151, pp. 35–50 (2018)
9. Singh, S.J., Harsha, S.P.: Static analysis of functionally graded plate using nonlinear classical plate theory with Von-Karman strains. Int. J. Appl. Mech. Eng. **23**(3), 707–726 (2018)
10. Singh S.J., Harsha, S.P.: Static Analysis of Functionally Graded Plate Using Nonlinear Classical Plate Theory with von Karman Strains: A Complex Solution Analysis (2019)
11. Singh, S.J., Harsha, S.P.: Buckling analysis of FGM plates under uniform, linear and non-linear in-plane loading. J. Mech. Sci. Technol. **33**(4), 1761–1767 (2019)

12. Hadji, L., Atmane, H.A., Tounsi, A., Mechab, I., Addabedia, E.A.: Free vibration of functionally graded sandwich plates using four-variable refined plate theory. Appl. Math. Mech. (English Edition) **32**(7), 925–942 (2011)
13. Li, Q., Iu, V.P., Kou, K.P.: Three-dimensional vibration analysis of functionally graded material sandwich plates. J. Sound Vib. (2008)

Selection of a Vehicle Using Multi-attribute Decision Making

Kiran Pal [ID]**, Lal Bahadur Singh** [ID]**, and Sanjeev Kumar** [ID]

1 Introduction

Most of the vehicle buyers in India are confused while selecting a vehicle of their requirement and capability. Due to this, they take too much time in this process, consult their friends or colleagues in an unscientific manner. A large section regrets after buying about their wrong selection. Even in some cases, they sell their vehicle for unsatisfactory performance. It is therefore necessary to propose a scientific decision-making framework to assist them in proper selection of the vehicle of their choice. Every individual has a different mindset to purchase the products and obtain services, and also it varies for different products. However, Mahatma Gandhi already talked earlier about customer importance but with the emergence of the Internet, there are more choices and the market can be dominated by smart customers. But the selection of an ideal one out of the several available choices is not an easy task for the general consumer. Consumer behavior is influenced with so many reasons, i.e., individual, occasional, psychological, and somehow social. Today, there is an abundance of advertisements appearing on TVs or Web pages, to influence consumers, but each of them describes the merits and advantages while demerits are not shown. Further marketing managers often play with the psychology of the customers and often try to influence them with effects they can manage for example music, alignment and ease of use of products, cost and publicity, etc. Walker et al. [1] concluded in their study that income of family is the prime reason for the purchasing of the number, size and

K. Pal (✉)
Department of Mathematics, Delhi Institute of Tool Engineering, Okhla, New Delhi 110020, India
e-mail: kiranpaldite@gmail.com

L. Bahadur Singh
Department of Mathematics, BIT, Sonipat, India

S. Kumar
Department of Mechanical Engineering, Delhi Technological University, North West Delhi, Delhi 111042, India
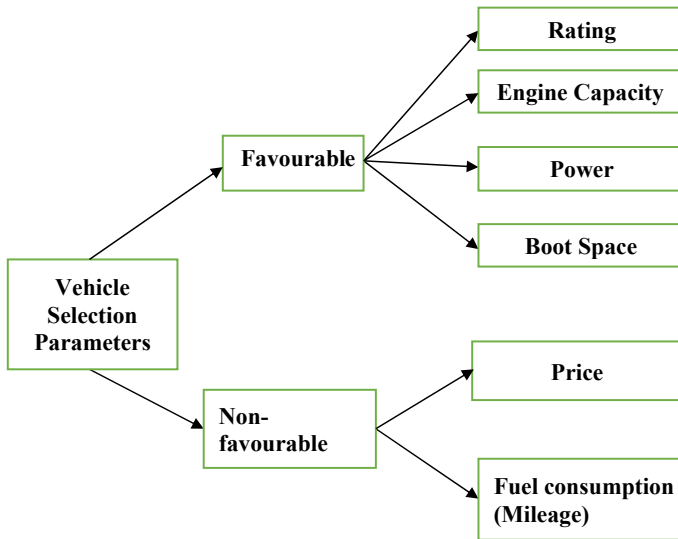
Fig. 1 Vehicle selection parameters

brand of cars; in addition, that family size is not so appropriate parameter because it was observed in many cases that larger vehicles were preferred even by smaller family and vice versa [1]. The study by Shehzad et al. [2] explained the important factors playing a crucial role in choice of vehicle buyers, life stage of buyer (choice of young generation is accordingly), impact of children and women in case of complete family. Figure 1 shows the vehicle selection parameters commonly used [2]. However, it was the matter of great confusion for a person with no technical background to select a vehicle because so many parameters are there, some of them required in more amount like aesthetics, power, boot space, while some other should be in lesser, e.g., cost, insurance amount. In this study, petrol cars of different brands were chosen for study because from various surveys; it was found that petrol cars are being used more in comparison of diesel. Monga [3] concluded about that there are various parameters of vehicle selection, i.e., provision of service after sale, cost, maintenance cost and availability and spare parts issues. Further, the image build-up of a brand into the mind of customer is greatly dependant mostly on the parameters given earlier [3]. Shende [4] compiled various parameters in terms of economic and technological, social and demographical, which affects the customer behaviour, while purchasing a vehicle. But the customers of lower middle and middle class from Delhi like city mainly emphasize on price-, technological- and performance-related parameters. These mainly include price, exotic colours, boot space, music system, mileage, pick up, maximum speed, torque, engine capacity [4]. There are some Web sites also available to compare the features of the available cars of different brands. Similarly, Web site of Zigwheel provides the comparison of various parameters among almost brand of different segments [5]. For every added feature, one has to pay for that;

hence, two categories of parameters are there, i.e., favorable and non-favorable—in this study, price, fuel consumption, rating, engine capacity, power, boot space and dimension of the vehicle. The parameters are shown in Fig. 1. SAW and TOPSIS methods are applied to rank the alternative cars on the basis of their features.

2 Multiple Attribute Decision-Making Approach

MCDM is a scientific tool that motivates the decision maker to make a well-calculated choice. Multiple Criterion Decision-Making tools are applied when there are conflicting criterions, and this technique makes a choice or ranks the alternatives on the basis of their preference level. MCDM can be subdivided into Multiple Objective Decision Making and Multiple Attribute Decision Making [6].

MODM looks at the problem through a design approach, that is, there is some objective behind the choice that needs to be chosen, whereas MADM is applied to get the rankings of the alternatives present. The value of decision variables lies in the integer or continuous range for MODM, and there are infinite or a large number of choices, whereas for MADM, there are a specific number of choices and the values of decision variables are discrete [7].

Due to this biasness in MODM technique, MADM is preferred for this work. The decision-making process through the MADM method involves a number of choices called alternatives and the criterions on which the choices are based called attributes. These attributes may have different weights, that is, varying level of preference of a criterion.

Mark and Patrick [8] observed that SAW has the ability to balance among the available criteria. Its computation is easy, and there is no need for multifarious computer programs as such [8]. Adriyendi [9] utilized SAW and WP to provide the selection of best food choice from the available alternatives of rice, potato, sorghum, wheat and some others. Swapna et al. [10] applied TOPSIS method with AHP to obtain best aluminium alloy from various compositions for automobile panels and explained the benefit of TOPSIS as its easiness in application, whether the size of problem is large or small. Mark and Patrick [8] explained that TOPSIS has an uncomplicated procedure and is programmable too. Dagdeviren et al. [11] applied TOPSIS weapon selection in combination with AHP. AHP technique was utilized to explain and evaluate the arrangement of the problem and to locate criteria of weights, while the final ranking was provided by TOPSIS [11]. Mohammadi (2018) applied SAW, TOPSIS and fuzzy TOPSIS methods for cultivation priority planning of maize, rapeseed and soybean crops in land units [12]. Hence, the combination of SAW and TOPSIS were applied in this work. SAW method was applied to obtain preferences among the different models of same brand, and TOPSIS method was applied to obtain preferences among the best model of the cars of different brand.

The deployment of any MCDM tool for problem solving involves the following basic steps- (a) identification and determination of the choices called alternatives and the criterion known as the attributes for evaluation, (b) measurement of relative

importance of the attributes and the alternatives, and (c) calculation of performance measures of the alternatives for ranking. There are various tools for the decision making in MADMs: SAW and TOPSIS have been discussed below and then applied in Sect. 3 to get the preferred vehicle for the selected alternatives.

2.1 Simple Additive Weighing Method

The Simple Additive Weighing (SAW) method is an easy method to apply. In this, initially, weights (W_j) are allotted to each one of the attributes such that $\sum_{j=1}^{M} W_j = 1$, where j is the number of attributes. The attributes are separated on the basis of beneficial and non-beneficial attributes. Subsequently, a normalized matrix is obtained in terms of ratio. For beneficial attributes, divide with highest value of the attribute for the various alternatives from each one of them; however, for the non-beneficial attributes, the lowest value is considered for division. Finally, SAW score Q_i can be obtained as per the following Eq. 1 (Adriyendi 2015) [8, 13].

For favorable attribute:

$$N_{ij} = \frac{Z_{ij}}{Z_{ij}\text{Max}} \tag{1}$$

For non-favorable attribute:

$$N_{ij} = \frac{Z_{ij}\text{Min}}{Z_{ij}}$$

$$Q_i = \sum_{j=1}^{M} N_{ij} W_j, \tag{2}$$

where Z_{ij} is the normalized value for each attribute. The alternative with the highest value of Q_i is considered as the best solution.

2.2 TOPSIS Method

In the Technique for Order Preference by Similarity to Ideal Solution (TOPSIS) method, the initial matrix design is such that the attribute values are in the rows and alternatives in the columns. The normalization of the matrix is carried out by Sayedmohammedi [12], Zavadskas et al. [14].

$$N_{ij} = Z_{ij} / \left[\sum_{i=1}^{M} (Z_{ij})^2 \right]^{1/2} \tag{3}$$

The weights for the attributes are same to the ones used in SAW method. However, here we calculate the weighted normalized matrix P_{ij},

$$P_{ij} = W_j \times R_{ij}. \tag{4}$$

Then, the best, P+, and the worst, P−, value for an attribute with different alternatives. Therefore, if there are M attributes, M number of P+ and P− values are obtained. Note that when considering beneficial traits, the P_j^+ indicates the highest value of the attribute, whereas in non-beneficial trait, it indicates the lower value of the trait. Similarly, for P_j^-, the lowest value for beneficial trait and the highest value for non-beneficial trait are to be considered.

After this, the separational measures are found by (Mohammedi, 2018; Zavadskas et al. [14] [12].

$$S_i+ = \left\{ \sum_{j=1}^{M} (P_{ij} - P_j+)^2 \right\}^{0.5} \quad \text{and} \quad S_j- = \left\{ \sum_{j=1}^{M} (P_{ij} - P_j-)^2 \right\}^{0.5} \tag{5}$$

Finally, the TOPSIS score, Q_i, can be calculated by Rao [7],

$$Q_i = (S_i-)/\{(S_i+) + (S_i-)\} \tag{6}$$

This score arranged in decreasing order which gives the ranking for the alternatives.

3   Problem Formulation

In this paper, different MADM techniques were also used. Popular brands of petrol cars were selected as per the trends because in India, the percentage of petrol cars is very high in comparison of diesel cars. Values of parameters were collected from Web sites of various vehicle manufacturers and Zigwheels to obtain the characteristics of the cars. SAW method was applied to obtain preferences among the different models of same brand. Then TOPSIS method was applied to obtain preferences among the best model of the cars of different brand.

Step 1: Five popular brands are available in India, and their six models of lower segments were chosen keeping in view the lower-middle and middle-income group people. Selected brands are Maruti, Tata, Hyundai, Renault and Honda, and six models with the feature are presented in Tables 1, 2, 3, 4 and 5 [5].

Step 2: Normalized matrix was obtained by using Eq. (2) for all brands of vehicle, and normalized matrix of Maruti for its every model is obtained using SAW method and presented in Table 6. Similarly, normalized matrix for other brands was calculated.

Table 1 Various models of Maruti cars and their features

Features	Vitara Brezza LXI	Celerio LXI	Wagon R LXI	Alto 800 STD	Celerio ZXI AMT optional	Swift LXI
Ex-Showroom Price	Rs. 7.34 lakh	Rs. 4.41 lakh	Rs. 4.46 lakh	Rs. 2.95 lakh	Rs. 5.58 lakh	Rs. 5.19 lakh
Length Width Height	3995*1790*1640	3695*1600*1560	3655*1620*1675	3445*1490*1475	3695*1600*1560	3840*1735*1530
Boot space-litres	328	235	341	177	235	268
Fuel consumption (ARAI) kmpl	17.03	21.63	21.79	22.05	21.63	21.21
Engine displacement	1462 cc	998 cc	998 cc	796 cc	998 cc	1197 cc
Power	103.2bhp@6000 rpm	67.04bhp@6000 rpm	67.04bhp@5500 rpm	47.3bhp@6000 rpm	67.04bhp@6000 rpm	81.80bhp@6000 rpm
Safety rating	3.9 (588 ratings)	3.8 (48 ratings)	3.8 (2053 ratings)	3.6(1578 rating)	3.9(588 rating)	4.0(3596 rating)

Table 2 Various models of Tata cars and their features

Overview	Tiago Petrol	Tigor XM	Altroz XE	Nexon XE	Nexon XM	Tiago XZ Plus
Ex-showroom price	Rs. 4.60 lakh	Rs. 6.10 lakh	Rs. 5.29 lakh	Rs. 6.95 lakh	Rs. 7.70 lakh	Rs. 5.99 lakh
Length width height	3765 * 1677 * 1535	3993 * 1677 * 1532	3990 * 1755 * 1523	3993 * 1811 * 1606	3993 * 1811 * 1606	3765 * 1677 * 1535
Boot space	242	419 l	345	350	350	242
Fuel Consumption (ARAI) kmpl	...	20.3 kmpl	...	17 kmpl	17 kmpl	23.84 kmpl
Engine displacement	1199 cc	1199 cc	1199 cc	1199 cc	1199 cc	1199 cc
Power	84.48bhp@6000 rpm	84.48bhp@6000 rpm	84.82bhp@6000 rpm	118.3bhp@5500 rpm	118.3bhp@5500 rpm	84.48bhp@6000 rpm
Safety rating	4.2	4.4	4.6	4.5	4.5	4.2

Table 3 Various models of Hyundai cars and their features

Overview	Grand i10 Nios Magna	Elite i20 Magna Plus	Santro Era executive	Grand i10 Sportz	Santro Magna AMT	Venue E
Ex-Showroom Price	Rs. 5.92 lakh	Rs. 6.50 lakh	Rs. 4.57 lakh	Rs. 6.00 lakh	Rs. 5.53 lakh	Rs. 6.70 lakh
Length width Height	3805 * 1680 * 1520	3985 * 1734 * 1505	3610 * 1645 * 1560	3765 * 1660 * 1520	3610 * 1645 * 1560	3995 * 1770 * 1605
Boot Space	260	285	235	256	235	350
Mileage (ARAI) kmpl	20.7 kmpl	18.6 kmpl	20.3 kmpl	18.9 kmpl	20.3 kmpl	17.52 kmpl
Engine Displacement	1197 cc	1197 cc	1086 cc	1197 cc	1086 cc	1197 cc
Power	81.86bhp@6000 rpm	81.86bhp@6000 rpm	68bhp@5500 rpm	81.86bhp@6000 rpm	68bhp@5500 rpm	81.86bhp@6000 rpm
Safety Rating	4.1	4.2	3.8	4.0	3.8	4.2

Table 4 Various models of Renault Cars and their features

Overview	KWID RXE	KWID RXT	KWID STD	Redi-GO T Option	KWID Climber 1.0	Triber RXE
Ex-showroom price	Rs. 3.62 lakh	Rs. 4.22 lakh	Rs. 2.92 lakh	Rs. 4.16 lakh	Rs. 4.71 lakh	Rs. 4.99 lakh
Length width height	3731 * 1579 * 1474	3731 * 1579 * 1474	3731 * 1579 * 1474	3435 * 1574 * 1546	3731 * 1579 * 1474	3990 * 1739 * 1643
Boot Space	279	279	279	222	279	84
Mileage (ARAI) kmpl	25.17 kmpl	25.17 kmpl	25.17 kmpl	25.17kmpl	23.01 kmpl	19 kmpl
Engine displacement	799 cc	799 cc	799 cc	799 cc	999 cc	999 cc
Power	53.26bhp@5678 rpm	53.3bhp@5678 rpm	53.3bhp@5678 rpm	53.64bhp@5600 rpm	67bhp@5500 rpm	71bhp@6250 rpm
Safety rating	3.8	3.8	3.8	4.5	3.8	4.2

Table 5 Various models of Honda cars and their features

Overview	Amaze E Petrol	Amaze V Petrol	Jazz V	Amaze V Petrol	Jazz VX	WRV Edge Edition i-VTEC S
Ex-showroom price	Rs. 6.10 lakh	Rs. 7.45 lakh	Rs. 7.45 lakh	Rs. 7.45 lakh	Rs. 7.89 lakh	Rs. 8.08 lakh
Length width height	3995*1695*1498	3995*1695*1501	3955*1694*1544	3995*1695*1501	3955*1694*1544	3999*1734*1601
Boot space	420	420	354-litres	420	354-litres	363 Litres
Mileage (ARAI) kmpl	18.6 kmpl	18.6 kmpl	18.2 kmpl	18.9 kmpl	20.3 kmpl	17.52 kmpl
Engine displacement	1199 cc	1199 cc	1199 cc	1199 cc	1199 cc	1199 cc
Power	88.76bhp@6000 rpm	88.76bhp@6000 rpm	88.76bhp@6000 rpm	88.7bhp@6000 rpm	88.7bhp@6000 rpm	88.76bhp@6000 rpm
Safety rating	3.9	3.9	4.2	3.9	4.2	4.2

Table 6 Normalized matrix (MARUTI) for different models

Manufacturer	Ex-showroom price	Length width height	Boot space	Mileage (ARAI) kmpl	Engine displacement	Power	Safety rating
*Weightage of each attributes (W_i)	0.10	0.15	0.15	0.10	0.20	0.20	0.10
Maruti Vitara Brezza LXI	0.4019	1	1	0.7712	3	0.9619	0.9750
Celerio LXI	0.6689	0.6496	0.6826	0.9809	0.8289	0.6891	0.9500
Wagon R LXI	0.6614	0.6496	0.6826	0.9882	0.8457	1	09,500
Alto 800 SID	1	0.04583	0.5444	1	0.6456	0.5191	09,000
Celerio ZXI	0.5287	0.6496	0.6826	09,809	0.7864	0.6891	0.9750
Swift LXI	0.4990	0.7926	0.8187	09,619	0.8692	0.7859	1

For favorable attribute:

$$N_{ij} = \frac{Z_{ij}}{Z_{ij}\text{Max}}$$

For non-favorable attribute:

$$N_{ij} = \frac{Z_{ij}\text{Min}}{Z_{ij}}$$

where Z_{ij} is the element value of decision matrix and N_{ij} is the values of different properties for different technologies.

Step 3: The performance scores are calculated using Eq. (2), and the alternative with the highest value of Q_i is considered as the best solution (highest ranking). The performance scores and ranking of each model are shown in Table 7.

Step 4: Normalized matrix of short-listed cars of different brands by Eq. (3) by TOPSIS method and given in Table 8.

Step 5: Weighted normalized matrix is obtained by Eq. (4) by TOPSIS method and shown in Table 9.

Step 6: The beneficial traits, P_j^+ indicate the highest value of the attribute, whereas in non-beneficial trait, it indicates the lower value of the trait. Similarly, for P_j^-, the lowest value for beneficial trait and the highest value for non-beneficial trait are to be considered. Benefit traits and non-benefit traits calculated are shown in Table 10.

Step 7: The best separation measures, $S+$, and the worst separation measures, $S-$, value for an attribute with different alternatives are obtained by using Eq. (5); these are shown in Table 11

Table 7 Performance score of each attribute and ranking by SAW method

Maruti		Honda		Tata		Hyundai		Renault	
Score	Rank	Score	Rank	Score	Rank	Score	Rank	Score	Rank
$Q_1 = 0.90920$	1	$Q_1 = 0.9715$	1	$Q_1 = 0.7021$	6	$Q_1 = 0.91467$	2	$Q_1 = 0.839335$	3
$Q_2 = 0.7541$	4	$Q_2 = 0.95366$	3	$Q_2 = 0.9381$	1	$Q_2 = 0.9047$	3	$Q_2 = 0.82798$	4
$Q_3 = 0.8032$	3	$Q_3 = 0.9391$	6	$Q_3 = 0.9327$	2	$Q_3 = 0.8593$	5	$Q_3 = 0.8587$	2
$Q_4 = 0.6652$	6	$Q_4 = 0.9550$	2	$Q_4 = 0.85296$	4	$Q_4 = 0.8979$	4	$Q_4 = 0.81058$	6
$Q_5 = 0.7362$	5	$Q_5 = 0.94477$	4	$Q_5 = 0.8465$	5	$Q_5 = 0.8418$	6	$Q_5 = 0.8988$	1
$Q_6 = 0.8166$	2	$Q_6 = 0.94144$	5	$Q_6 = 0.8704$	3	$Q_6 = 0.9528$	1	$Q_6 = 0.82250$	5

Table 8 Normalized matrix of short-listed cars of different brands

Manufacturer	Ex-showroom price	Length width height	Boot space	Mileage (ARAI) kmpl	Engine displacement	Power	Safety rating
Maruti Vitara Brezza LXI	0.6417	1	0.78095	0.7401	1	1	0.8864
Honda Amaze	0.7721	0.8649	1	0.8083	0.8201	0.8601	0.8864
Tata Tigor XM	0.7721	0.8747	0.9976	0.8822	0.8201	0.8186	1
Hyundai Venue E	0.70298	0.9677	0.8381	0.7614	0.8187	0.7932	0.9545
Renault Kwid Climber	1	0.7404	0.6643	1	0.6833	0.6492	0.8636

Table 9 Weighted normalized matrix of short-listed cars

Manufacturer	Ex-showroom price	Length width height	Boot space	Mileage (ARAI) kmpl	Engine displacement	Power	Safety rating
Maruti Vitara Brezza LXi	0.02773	0.064815	0.050625	0.03198	0.08642	0.08642	0.03830
Honda Amaze	0.03381	0.05682	0.0657	0.03540	0.07184	0.07534	0.0382
Tata Tigor XM	0.3299	0.056055	0.063915	0.03769	0.07008	0.06996	0.04273
Hyundai Venue E	0.3168	0.065415	0.056655	0.03431	0.07378	0.07150	0.04302
Renault Kwid Climber	0.04651	0.05166	0.5844	0.04651	0.06356	0.06038	0.04017

Table 10 Benefit traits and non-benefit traits

P^+ benefit trait	0.02773	0.6545	0.657	0.4651	0.4651	0.8642	0.4302
P^- Non-benefit trait	0.04651	0.05166	0.050625	0.03198	0.6356	0.06038	0.0382

Table 11 Separation measures

S_i^+	$S_1^+ = 1.1462$	$S_2 = 1.5148$	$S_3 = 1.3971$	$S_4 = 1.394$	$S_5 = 1.4082$
S_i^-	$S_1 = 0.8434$	$S_2 = 0.5643$	$S_3 = 0.56598$	$S_4 = 0.8864$	$S_5 = 0.7825$

Table 12 Score value and ranking of different model vehicle

Score value	$Q_1 = 0.4239$	$Q_2 = 0.2714$	$Q_3 = 0.28831$	$Q_4 = 0.3887$	$Q_5 = 0.35719$
Ranking	1	5	4	2	3
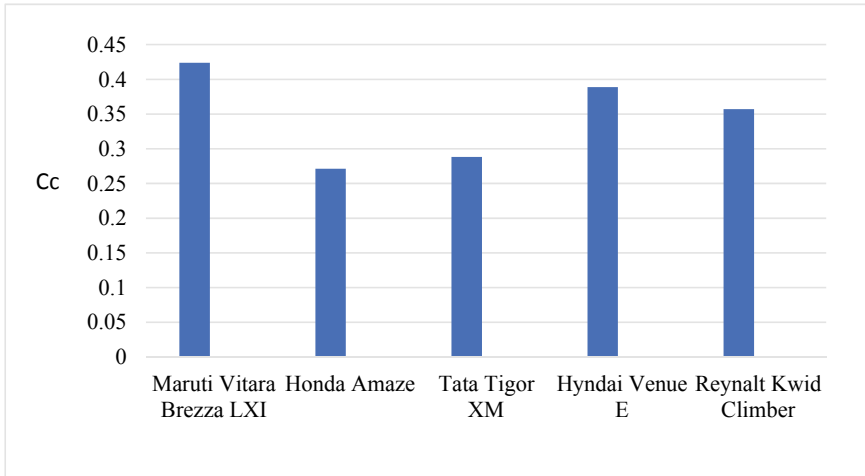
Fig. 2 Graphical representation of ranking of the cars

4 Results and Discussion

The value of score is obtained by using Eq. (6). The ranking of alternatives with the highest score value Q_i is considered as the best solution. These are shown in Table 12. Here for the values considered Maruti Vitara Brezza LXI comes as the best choice, and others are ranked accordingly and shown in Fig. 2.

5 Conclusions

SAW and TOPSIS MADM techniques have been applied for the selection of vehicle considering seven attributes of the available alternatives, i.e., different models of various vehicle brands. SAW method was applied to obtain the ranking of the different vehicle models of same brand. One vehicle having maximum score value of top ranked vehicle from every brand was selected. Selected best models of different brands are Maruti Vitara Brezza LXI, Honda Amaze, Tata Tigor XM, Hyundai VenueE and Renault Kwid Climber. TOPSIS method was applied to find the best vehicle from these short-listed cars, and Maruti Vitara Brezza LXI is found the best choice among the available alternatives. This algorithm can be utilized to obtain the best selection as per the weight choices of any different vehicle buyer. Thus, this

study may be useful for vehicle buyers and prove to be a more scientific way of vehicle selection.

References

1. Walker, J.L., Emily, E., Banerjee, I., Dugundji, E.R.: Correcting for endogeneity in behavioral choice models with social influence variables. Transp. Res. Part A: Policy Pract. **45**(4), 362–374 (2011). https://doi.org/10.1016/j.tra.2011.01.003
2. Shehzad, U., Ahmad, S., Iqbal, K.., Nawaz, M., Usman S.: Influence of brand name on consumer choice & decision. IOSR J. Bus. Manag.. **16**(6)72–76 (2014). Ver. III,
3. Monga, N.: Vehicle market and buying behaviour—a study of consumer perception. Int. J. Res. Manag., Econ. Commer. www.indusedu.org 44. IJRMEC 2(2) (2012). ISSN: 2250-057X
4. Shende, V.: Analysis of Research in Consumer Behaviour of Automobile Passenger vehicle Customer. Int. J. Sci. Res. Publ., **4**(21) (2014). ISSN 2250-3153
5. ZIGWHEEL Homepage: https://www.zigwheels.com/compare-cars, last accessed 2020/04/23
6. Vyas, S., Misal, S.: Comparative study of different multi-criteria decision-making methods. Int. J. Adv. Comput. Theory Eng., **2**(4), 9–12. (2013)
7. Rao, V.: Decision Making in the Manufacturing Environment using Graph Theory and Fuzzy Multiple Attribute Decision Making Methods. Springer London Limited (2007)
8. Mark, V., Patrick, T.H.: An analysis of multi-criteria decision making methods. Int. J. Oper. Res. **10**(2), 56–66 (2013)
9. Adriyendi.: Multi-attribute decision making using simple additive weighting and weighted product in food choice. I. J. Inf. Eng. Electron. Bus. **6**, 8–14. https://doi.org/10.5815/ijieeb. (2015). 06.02
10. Swapna, D., Srinivasa, R.C., Kumar, S., Radhika, S.: AHP and TOPSIS based selection of aluminium alloy for automobile panels. J. Mech. Energy Eng., **3**(43), (1), 43–50 (2019). https://doi.org/10.30464/jmee.2019.3.1.43
11. Dagdeviren, M., Yavuz, S., Kilinc, N.: Weapon selection using the AHP and TOPSIS methods under fuzzy environment. Expert Syst. Appl. **36**(4), 8143–8151 (2009). https://doi.org/10.1016/j.eswa.2008.10.016
12. Sayedmohammedi, J., Sarmadian, F., Jafarzadeh, A.A., Ghorbani, M.A., Shahbazi, F.: Application of SAW, TOPSIS and fuzzy TOPSIS models in cultivation priority planning for maize, rapeseed and soybean crops. Geoderma **310**, 178–190 (2018). https://doi.org/10.1016/j.geoderma.2017.09.012
13. Venkateswarlu, P., Sharma, B.D.: Selection of supplier by using SAW and VIKOR Methods. Int. J. Eng. Res. Appl. **6**(9), (Part-3), 80–88 (2016) www.ijera.com 80
14. Zavadskas, E.K., Vilutiene, T., Turskis, Z., Tamosaitiene, J.: Contractor selection for construction works by applying saw-g and TOPSIS grey techniques. J. Bus. Econ. Manag. www.jbem.vgtu.lt, **11**(1): 34–55 (2010). https://doi.org/10.3846/jbem.20

Analyzing the Barriers of Green Construction Using Interpretive Structural Modeling

Niranjan Sahoo and **Anil Kumar**

1 Introduction

Green construction is the art of making building systems safer and more resource-effective [1]. Sometimes, it is also referred to as green building or sustainable building. This green construction process, therefore, supports the production of a more favorable and eco-friendlier environment and this is achievable with the collaboration and coordination of various team members associated with a green construction project. The green building also provides the same satisfaction, strength, and value of design as traditionally constructed buildings. The green building movement also provides numerous business chances to individuals associated with the construction industry. Although there is an excellent advantage in green construction, its adaption is not possible because of certain hindrances [2, 3]. One of the major obstacles is that there are no proper guidelines for green construction.

Therefore, it is essential to analyze the critical barriers of green construction. It is also essential to investigate the barriers while implementing the green building concept. Based on a comprehensive literature review, the impediments to green buildings can be classified into six categories. The barriers like financial, regulatory, management/leadership, technical, socio-cultural, and knowledge/awareness are taken as key barriers for green construction. The above-mentioned six categories influence the operation and implementation of green construction. The top

N. Sahoo
Department of Mechanical Engineering, Galgotias College of Engineering and Technology, Greater Noida, India
e-mail: niranjan.sahoo@galgotiacollege.edu

N. Sahoo · A. Kumar (✉)
Department of Mechanical, Production & Industrial and Automobile Engineering, Delhi Technological University, Delhi, India
e-mail: anilkumar76@dtu.ac.in

A. Kumar
Centre for Energy and Environment, Delhi Technological University, Delhi, India

management of a construction project must be aware of the green construction barriers.

The factors which characterize an issue can be best analyzed with the help of interpretive structural modeling (ISM) [4, 5]. It also indicates the nature of the complication of such barriers [6, 7]. This methodology also identifies the levels of the barriers of green construction and ranking them according to their driving and dependence power. From the literature survey and expert's idea on green construction, six key barriers have been selected. Further, a relationship matrix was developed, and finally, an ISM model developed from the relationship matrix.

The objective of this paper is to investigate about the critical barriers of green construction. The modeling technique is used to identify the rank as well as the relationship status among the critical barriers of green construction. And finally, the driver-dependence diagram is drawn with the help of MICMAC analysis.

2   Green Construction Barriers

The green construction practices have helped a lot in protecting the environment. But there is a lot of barriers associated with green construction. To identify the barriers and understand, the influence is a must for successful implementations of green construction. For this, six key barriers have been identified, and it is shown in Table 1. The financial barrier includes many factors like the fear of higher initial investment costs, consumer worries about the benefit, no idea about the profit, and the pay-back period. Many authors also proposed that the additional cost required for implementing GC is a significant financial barrier. The regulatory barrier includes insufficient government policies, green building codes, and government regulation. It is also documented that the government must put some legislation and policies for the successful implementation of the GC concept [8]. Excellent administration and leadership have a crucial role in the success of GC. This barrier includes poor leadership quality, no proper division of market according to customer potential, lack of motivated managers, and lag in decision making. The higher authority of the construction sector, like managers and leaders, has the leading role to play in attaining the successful implementation of GC [9]. Without management support, it is very

Table 1 Identified key barriers of green construction

	Key barrier	Authors
FB	Financial barriers	[12, 13]
RB	Regulatory barriers	[8–10, 13, 14]
MB	Management/leadership barriers	[9, 10, 14]
TB	Technical barriers	[9, 10, 13, 14]
SB	Socio-cultural barriers	[9, 10, 13, 14]
KB	Knowledge/awareness barriers	[12, 11]

tough to achieve the concept of GC. The role of a technical barrier for the success of the GC project cannot be underestimated. This barrier includes the unavailability of proper sustainable materials, sustainable measurement tools, lack of demonstrated green projects, and lack of technical knowledge. The successes of any GC project have a direct relationship with technical barriers. Rydin et al. [10] claimed that when concerns arise regarding sustainable construction design, designers in the construction sector are not optimistic. Therefore, the designers must be thoroughly familiar with the concepts of sustainable architecture to incorporate in their practice. It is also documented that there is a lack of adequate guidance for the designers working in sustainable construction projects [9]. The required technical knowledge for sustainable construction must be available in a proper format for easy understanding of the design professionals and contractors. The conventional construction companies have operated in a specific manner for an extended time period; therefore, it is challenging to change the pattern. Such change-resistance happens if the consumers and stakeholders will not demand a green building. It is also documented that the loss of demand for sustainable products is also a barrier for GC implementation [11]. A proper understanding and knowledge are required for the implementation of GC, and it has been well documented [11, 12]. The knowledge/awareness barrier includes inadequate expert's knowledge, lack of information about the benefits of GC, confusion about sustainability, inadequate knowledge as the foremost obstacles for the implementation of GC [12].

3 ISM Methodology

ISM is a technique used to characterize among specific variables of a matter [4]. ISM methodology may be used as a tool for analyzing the nature of relationships between system variables [15, 16]. It is documented that an ISM technique is used to create a model for achieving India's waste management target [17]. ISM enables the establishment of relationships between different items/elements depending on their power of driving and dependency [18, 19]. Currently, many researchers began the use of the ISM method of their environmental associated decision making [20].

There are many obstacles to green building implementation. Therefore, examining the direct and indirect linkage among the constraints of green construction will provide a better photograph of the situation than examining the constraints individually in isolation. The ISM approach is interpretive in nature and it interprets the fact from the expert's comments. It is also relational, as with the notion of courting, it derives a basic structure from the selected variables. It is an approach that describes the relationship among variables and creates a digraph for illustrating the structure of the system. ISM is mainly meant as a group mastering system. Figure 1 represents the steps required for creating an ISM model.
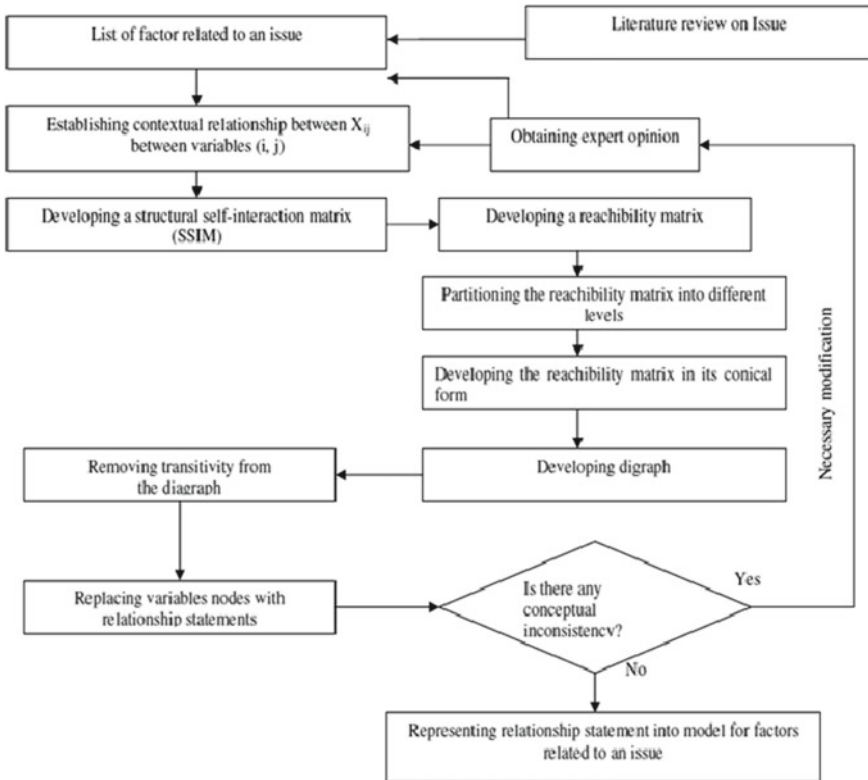
Fig. 1 Structural outline to prepare an ISM model

3.1 Structural Self-Interaction Matrix (SSIM)

The current work identified significant barriers as variables to implement toward green construction. Six variables were finalized from the literature survey to implement green construction.

ISM technique uses the expert critiques in establishing the contextual relationship between most of the variables under consideration [21, 22]. Due to this, a number of elements need to be consulted with industry experts and academic professionals to find out the nature of the contextual relationship. Those industry and academia experts have to be well informed of the underlying issue. A contextual courting of the type 'leads to' or 'influences' has to be selected for reading the factors. That means one element is influencing every other element. To the premise of this, contextual dating is advanced among the factors identified. The degree of association between any factors (i and j) is decided by keeping the contextual relationship in mind. The notations used for representing the degree of association between two factors are V, A, X, and O.

Table 2 SSIM of selected key barriers of green construction

Barriers	KB	SB	TB	MB	RB	FB
FB	A	V	O	A	A	
RB	V	V	V	V		
MB	X	V	A			
TB	V	V				
SB	A					
KB						

where
V: Accomplishment of barrier *i* by *j*.
A: Accomplishment of barrier *j* by *i*.
X: Allow accomplishing each other.
O: The barriers unrelated to each other.
The SSIM is developed from the relevant linkage among the key barriers (Table 2).

3.2 Reachability Matrix

The next step is to develop an initial reachability matrix (IRM) by replacing the symbols V, A, X, or O to 1 and 0 in SSIM. The guidelines for creating IRM are:
Replace V by 1 for (i, j) and 0 for (j, i).
Replace A by 0 for (i, j) and 1 for (j, i).
Replace X by 1 for both (i, j) and (j, i).
Replace O by 0 for both (i, j) and (j, i).
The IRM is prepared in accordance with the rules. The final reachability matrix is prepared after finding the transitive links with the help of experts (Tables 3 and 4).

Table 3 Initial reachability matrix

Barriers	FB	RB	MB	TB	SB	KB
FB	1	0	0	0	1	0
RB	1	1	1	1	1	1
MB	1	0	1	0	1	1
TB	0	0	1	1	1	1
SB	0	0	0	0	1	0
KB	1	0	1	0	1	1

Table 4 Final reachability matrix

Barriers	FB	RB	MB	TB	SB	KB	Driver power
FB	1	0	0	0	1	0	2
RB	1	1	1	1	1	1	6
MB	1	0	1	0	1	1	4
TB	1*	0	1	1	1	1	5
SB	0	0	0	0	1	0	1
KB	1	0	1	0	1	1	4
Dependence power	5	1	4	2	6	4	

*Entries after incorporating the transitivities

3.3 Level Partitioning

In this step, the barriers are partitioned at different levels. The rules are as follows:

First rule: Find out the reachability and the antecedent set of each barrier.

Second rule: Find out the intersection set for each barriers.

Third rule: Find out the barriers whose reachability set and intersection set are equal and leveled them as first.

Fourth rule: Remove the first level barriers from the matrix for further consideration.

Fifth rule: Continues the process of iteration until figured out the levels for each element.

Tables 5, 6, 7 and 8 represent the process of iteration.

Table 5 First iteration

Barriers	Reachability set	Antecedent set	Intersection set	Level
FB	1,5	1,2,3,4,6	1	
RB	1,2,3,4,5,6	2	2	
MB	1,3,5,6	2,3,4,6	3	
TB	1,3,4,5,6	1,2,3,4,5,6	1,3,4,5,6	I
SB	5	1,2,3,4,5,6	5	I
KB	1,2,5,6	2,3,4,6	2,6	

Table 6 Second iteration

Barriers	Reachability set	Antecedent set	Intersection set	Level
FB	1	1,2,3,6	1	II
RB	1,2,3,6	2	2	
MB	1,3,6	2,3,6	3,6	
KB	1,2,6	2,3,6	2,6	

Table 7 Third iteration

Barriers	Reachability set	Antecedent set	Intersection set	Level
RB	2, 3, 6	2	2	
MB	3, 6	2, 3, 6	3, 6	III
KB	2, 6	2, 3, 6	2, 6	III

Table 8 Fourth iteration

Barriers	Reachability set	Antecedent set	Intersection set	Level
RB	2	2	2	IV

3.4   ISM Model

An ISM model is finally developed for the barriers of green construction, and it is shown in Fig. 2.
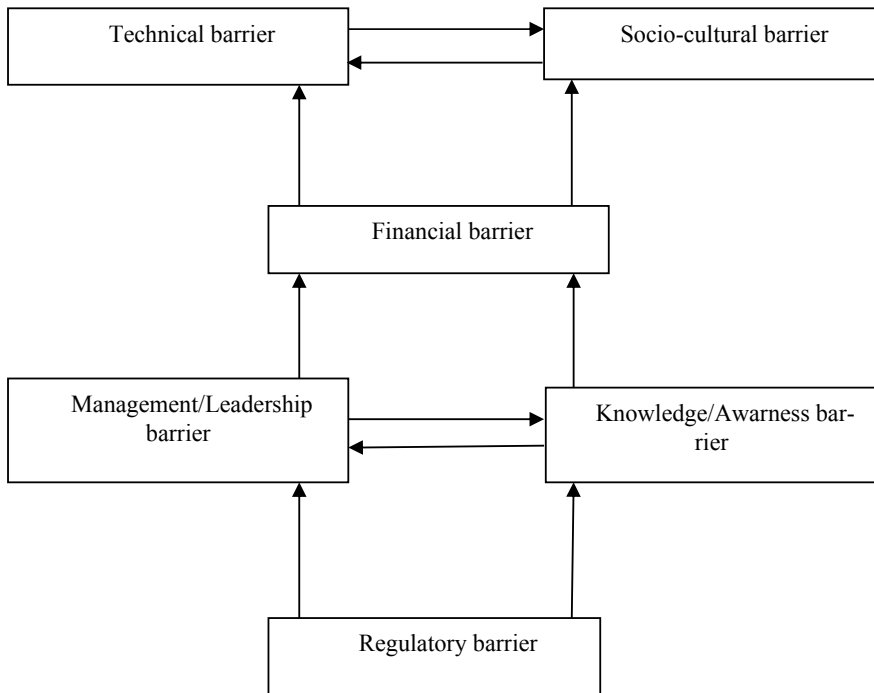
Fig. 2   ISM-based model for the barriers of green construction
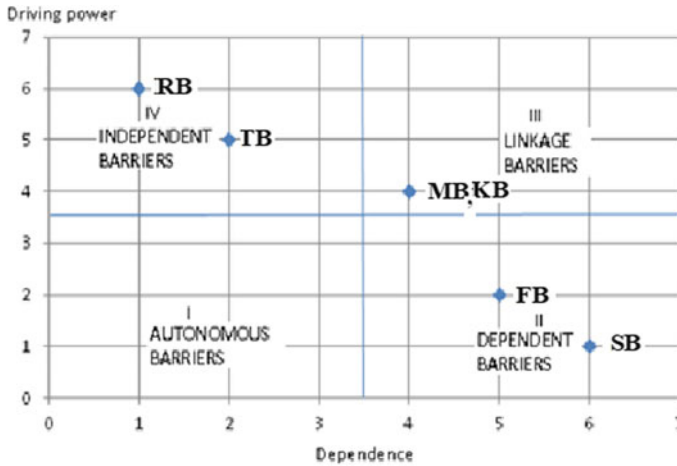
Fig. 3 Driving power and dependence power diagram

4 MICMAC Analysis

The primary purpose of this analysis is to find out the type of barriers depending on driver power and the dependence power. According to this analysis, the barriers are divided into four categories as independent, linkage, autonomous, and dependent barriers, as presented in Fig. 3. The methodology for MICMAC analysis is given as:

Step-1: Determine the driving power and dependence power of each barrier.

Step-2: Classify the barriers into four categories.

Step-3: Determine the dominant barriers of green construction.

5 Results and Discussion

Figure 2 shows the relationships among the barriers of green construction. The barriers are organized in four levels in a hierarchical structure. The regulatory barrier (RB) is placed at the lowest level of the ISM model. It represents that the regulatory barrier (RB) having higher driving power though it is placed at the lowest level. Therefore, the government should establish some policies/approach and pressurize the management of the construction companies to implement the use of green practices. The driver-dependence diagram does not pose any autonomous barriers (Fig. 3). It means that all the six barriers have some influences while implementing the green construction project. It is also observed that the financial barrier (FB) and socio-cultural barrier (SB) come under the dependent barriers. They are having weak driving power but strong dependence power. Regulatory barrier (RB) and technical

barrier (TB) are found as independent barriers. Hence, no barrier is unstable among all the six green construction barriers picked.

6 Conclusion

Construction companies are facing a lot of problems implementing green practice. The key barriers for the success of green construction practice have been identified. Modeling has been done to form a model that shows the relationships among the key barriers. The conclusions made from the study are discussed below. The lowest level is occupied by the regulatory barrier (RB). The regulatory barrier (RB) also drives the other barriers of green construction. The financial barrier (FB) and socio-cultural barrier (SB) are depending on the other barriers. It is observed that all the considered six barriers are having reliable driving power and can be responsible for most of the other barriers. In the construction companies, the decision-maker should theoretically address the barriers that hinder green building so that the desired targets could be achieved.

The major drawback of ISM model is that it purely depends on the expert's comment and may fail due to the biasness of the experts. In the present work, the model is not tested practically. The limitations may give a chance for the future work. The validity and reliability of the ISM model may be checked through structural equation modeling (SEM).

References

1. Council, U.G.B.: Building Design Leaders Collaborating on Carbon-Neutral Buildings by 2030. Press Release, May, 7 (2007)
2. Lam, P.T., Chan, E.H., Poon, C.S., Chau, C.K., Chun, K.P.: Factors affecting the implementation of green specifications in construction. J. Environ. Manage. **91**(3), 654–661 (2010)
3. Ofori, G., Kien, H.L.: Translating Singapore architects' environmental awareness into decision making. Build. Res. Inf. **32**(1), 27–37 (2004)
4. Warfield, J.N.: Developing interconnection matrices in structural modeling. IEEE Trans. Syst. Man Cybern. **1**, 81–87 (1974)
5. Sage, A. P. Methodology for large-scale systems (1977).
6. Mandal, A., Deshmukh, S.G.: Vendor selection using interpretive structural modelling (ISM). Int. J. Oper. Prod. Manage. **14** (6), 52–59 (1994)
7. Jharkharia, S., Shankar, R.: IT-enablement of supply chains: understanding the barriers. J. Enterp. Inf. Manage. **18**(1), 11–27 (2005)
8. Dzokoto, S.D., Dadzie, J.: Barriers to sustainable construction in the Ghanaian construction industry: consultant's perspectives In: Laryea. In: Agyepong, S.(eds) Procs 5th West Africa Built Environment Research (WABER) Conference, pp. 12–14 (2013).
9. Osaily, N.Z.: The key Barriers to Implementing Sustainable Construction in West Bank–Palestine, p. 63. University of Wales, UK (2010)
10. Rydin, Y., Amjad, U., Nye, M., Moore, S., Whitaker, M.: Sustainable Construction and Planning: The Academic Report. Centre for Environmental Policy and Governance, The LSE SusCon Project, CEPG, London School of Economics, London (2006)

11. Williams, K., Dair, C.: What is stopping sustainable building in England? Barriers experienced by stakeholders in delivering sustainable developments. Sustain. Dev. **15**(3), 135–147 (2007)
12. Häkkinen, T., Belloni, K.: Barriers and drivers for sustainable building. Build. Res. Inf. **39**(3), 239–255 (2011)
13. Hydes, K.R., Creech, L.: Reducing mechanical equipment cost: the economics of green design. Build. Res. Inf. **28**(5–6), 403–407 (2000)
14. Nelms, C., Russell, A.D., Lence, B.J.: Assessing the performance of sustainable technologies for building projects. Can. J. Civ. Eng. **32**(1), 114–128 (2005)
15. Sage, A. P. Methodology for Large-scale System, pp. 91–164. McGraw-Hill, New York, NY (1977).
16. Saxena, J.P., Vrat, P.: Scenario building: a critical study of energy conservation in the Indian cement industry. Technol. Forecast. Soc. Chang. **41**(2), 121–146 (1992)
17. Sharma, H.D., Gupta, A.D.: The objectives of waste management in India: a futures inquiry. Technol. Forecast. Soc. Chang. **48**(3), 285–309 (1995)
18. Mandal, A., Deshmukh, S.G.: Vendor selection using interpretive structural modelling (ISM). Int. J. Oper. Prod. Manage. **14**(6), 52–59 (1994)
19. Mangla, S., Madaan, J., Chan, F.T.: Analysis of flexible decision strategies for sustainability-focused green product recovery system. Int. J. Prod. Res. **51**(11), 3428–3442 (2013)
20. Jia, P., Diabat, A., Mathiyazhagan, K.: Analyzing the SSCM practices in the mining and mineral industry by ISM approach. Res. Policy **46**, 76–85 (2015)
21. Ravi, V., Shankar, R., Tiwari, M.K.: Productivity improvement of a computer hardware supply chain. Int. J. Prod. Perform. Manage. **54**(4), 239–255 (2005)
22. Hasan, M.A., Shankar, R., Sarkis, J.: A study of barriers to agile manufacturing. Int. J. Agile Syst. Manage. **2**(1), 1–22 (2007)
23. Shankar, R., Narain, R., Agarwal, A.: An interpretive structural modeling of knowledge management in engineering industries. J. Adv. Manage. Res. **1**(1), 28–40 (2003)
24. Luthra, S., Kumar, V., Kumar, S., Haleem, A.: Barriers to implement green supply chain management in automobile industry using interpretive structural modeling technique: an Indian perspective. J. Ind. Eng. Manage. (JIEM) **4**(2), 231–257 (2011)
25. Barve, A., Kanda, A., Shankar, R.: Analysis of interaction among the barriers of third party logistics. Int. J. Agile Syst. Manage. **2**(1), 109–129 (2007)

Challenges of Battery Production: A Case Study of Electrical Vehicles in India

Sanjeev Kumar and **Amit Pal**

1 Introduction

Today, world is facing severe environmental problems of greenhouse gas emissions, urban pollution, and fossil fuel exhaustion directing energy security issues, for which electromobility possibly will be a preeminent option to counter these problems, as a road transport system in which vehicles utilize electricity for propulsion. In this transport system, power is obtained from a battery to drive the electric motor, which finally propels the vehicle. Hence, high-performance batteries of reasonable cost are the fundamental requirement for transferring the transport system from conventional (vehicles using IC engines for power requirement) to newer, i.e., electric vehicles (EVs). Amjad et al. [1]; Peng et al. [2]; Tie and Tan [3] and Andwari et al. [4] revealed benefits of battery electric vehicles (BEVs), first as its principle is simple and secondly removal of the internal combustion engine (ICE) and the fuel tank. Andwari et al. [4] explained various advantages of BEVs as highly efficient, zero tailpipe emissions, advantageous for local air quality, higher acceleration, charging during the night (home stay) on low-cost electricity, which is produced by power station, situated far from residential areas, using any type of fuel together with renewables. Today, a wide range of successful models of BEVs runs on the road, ranging the low-cost to the high-cost brands. Also, a huge investment is being made by the government in infrastructure, due to which possibilities of adoption of BEVs have increased. Conventional IC-engine-driven vehicle obtains power through burning of petroleum fuel, unlike in BEVs power is supplied by a rechargeable aboard battery system. Primary requirement of batteries in BEVs is to grasp high amount of energy from single charge to facilitate longer range. To enable such property, specific materials are used for constructing the batteries, consequential in elevated cost. Batteries used

S. Kumar (✉) · A. Pal
Department of Mechanical, Production & Industrial and Automobile Engineering, Delhi Technological University, Delhi 110042, India
e-mail: ersanjeevkumar124@gmail.com

Table 1 Battery manufacturers in India

Name of industry	Lead–acid	Li-ion	References
Exide Industries Ltd	Yes	No	https://www.exideindustries.com/about/about-exide.aspx [18]
Amara Raja Batteries Ltd	Yes	Yes	https://www.amararajabatteries.com/about/technology-focus [19]
HBL Power Systems Ltd	Yes	No	https://www.hbl.in/product-1-batteries [20]
Okaya Power Ltd	Yes	Yes	https://www.okayapower.com/e-rickshaw-batteries.php [21]
Southern Batteries Pvt Ltd	Yes	No	http://www.southernbatteries.com/about_profile.htm [22]
Artheon Electronics Ltd	Yes	No	http://www.artheonelec.com/aboutus.asp [23]
TATA Green Batteries	Yes	No	https://www.tatagreenbattery.com/cms/products [24]

for propulsion of BEVs are different from the batteries used for starting, lighting, and ignition because they supply power above-sustained periods of time. These batteries have comparatively more power/weight (lightweight), specific energy (more range) for improved performance. Specific energy of presently available battery systems is nether in comparison with petroleum fuel, and its impacts reflect on most of the electric range of the vehicles. Commonly, batteries used in electric vehicles include lead–acid battery, nickel–cadmium (Ni-Cd), nickel–metal Hydride (NiMH), lithium-ion (Li-ion), zinc–air, and sodium–nickel chloride (NaNiCl2). But on searching Web sites of different brands of battery electrical vehicles manufacturers, such as Tesla, Hyundai, and Tata, it was found that most of the BEVs are equipped with either lithium-ion or lithium polymer batteries, due to the property of their high energy density in comparison with their weight. In Table 1, a list of some of the important global manufacturers of BEVs is compiled, and it can be concluded that most of the models of BEVs utilize lithium-ion batteries for the power requirement to propel the vehicle. However, in India, usually lead–acid batteries are being utilized for propulsion in E-rickshaws (electrical-rickshaw).

2 Research Methodology

The researcher gave consideration for BEVs since at the end of the twentieth century or start of twenty-first century, but battery production was being considered an important subject due to the requirement of an energy storage device for various applications for long time. Hence, the researcher papers of previous decade were of prime concerns, but earlier papers were also studied with focused on the type of battery technologies utilized for vehicle propulsion purpose and challenges of battery production.

Web sites of battery manufacturers in India were searched aiming to know the types of battery technologies produced in India and that of BEVs manufacturers globally to know the types of batteries utilized by the various brands of cars. Simple additive weighing (SAW) method was used to obtain the ranking of various battery technologies.

3 Battery Technology

Andwari et al. [4] observed the important predicaments in the expansion in addition to market infiltration of electrical vehicles, as the technological keenness of batteries and the energy storage system. Burke et al. [5] compiled the important parameters for batteries as energy density (range and weight determination), the power density (acceleration requirement), the battery life (cycle as well as calendar both), and cost in addition to protection. Fotouhi et al. [6] told that while designing any technology or battery, a transaction between energy and power density is followed. Manzetti and Mariasiu [7] revealed that the size of battery is normally determined through its energy necessities for the purpose of allowing a definite range to be reached along with the adoption of advanced technology and material composition. Budde-Meiwes et al. [8] explained various important characteristics for classification of the battery technologies, as given as.

1. Power density: Elevated values of power density both of gravimetric and volumetric insinuate less electrical resistance, which consequential in less energy losses in addition to high-power capability.
2. Energy density: Elevated values of energy density both of gravimetric and volumetric of batteries are the key requirement.
3. Energy efficiency. It is the ratio of energy, which can be retrieved to the energy supplied for charging. It is essential to evade overheating.
4. Battery life: Both calendar as well as cycle lifetime are considered.
5. Costs: It is an important parameter for selection of the battery. The particular necessities of battery and quality features determine the cost.

Budde-Meiwes et al. [8]; Tie and Tan [3]; Andwari et al. [4] gave an overview of various battery technologies, and some are explained briefly as following.

3.1 Lead–Acid Battery

In spite of broad and unremitting hard work, "lead–acid" battery was invented in 1859, by Gaston Plante. Miller [9] told about its lesser specific energy, ranging from 20 and 40 Wh/kg. Budde-Meiwes [10] observed the various problems in lead–acid batteries, due to which, these are installed with BEVs if the operating distance is less and not varying, weight is not so important and a stumpy price is critical. There is

a liquid electrolyte or an electrolyte duly adsorbed in a mat of glass-fiber in these batteries. Potentials of lead–acid batteries are considered as the stumpy substance expenditure, inherent protection, and elevated salvage quotes (>95%, the maximum of the entire battery technologies). Lead–acid batteries are considered as a capable alternative and for future development too. Budde-Meiwes et al. [8] told that in every electric vehicle, a small lead–acid battery is also fixed for safekeeping. In case of accident with BEV, this battery can supply power.

3.2   Ni–Cd Battery

These batteries have a diminutive superior energy density in comparison of lead–acid batteries, but power density is much advanced, at the lot of prominent specific battery costs. Also, Ni–Cd batteries provide security necessities at the time of accident. Manzetti and Mariasiu [7] observed major disadvantage of this battery as the utilization of cadmium (heavy metal) in the manufacturing, by means of detrimental effects on the ambiance and living things and European Union (EU) directives already limited the utilization of Ni–Cd batteries.

3.3   NiMH Battery

According to Manzetti and Mariasiu [7], production and operation of NiMH batteries are similar to Ni–Cd, and it is an improvement of nickel–cadmium batteries, focusing devoid of toxic cadmium and keeping the benefits of nickel–cadmium batteries. Budde-Meiwes et al. [8] stated that absence of memory effect is considered as the major benefit of NiMH batteries, due to which these batteries have maximum load capacity. Major favorable characteristics are its energy density (approximately twice as compared to Ni–Cd batteries), elevated power density, and the adequate battery life; however, deep temperature execution is reduced comparatively.

3.4   Sodium–Nickel Chloride Battery

This battery is also identified as the "ZEBRA battery," and ZEBRA stands for zero-emission battery research activities. Manzetti and Mariasiu [7] explained that in this battery, liquid salt at the working temperature of 270–350 °C and a solid ceramic electrolyte are utilized. Solid electrolyte also performs the function of separator. Main strength of this battery is its elevated hoarded energy density. According to Budde-Meiwes et al. [8], the most important drawbacks are associated to its workable security and the repository capacity for prolonged duration, which includes its high working temperature approximately 300 °C, and for that good separation is

needed. A lowering of temperature tends to an elevated thermo-mechanical stress for solid ceramic electrolyte. Other drawbacks are the constricted power and the self-discharge. Therefore, ZEBRA batteries utilization in personal vehicles is intricate due to its low range and thermal losses. Expenses are approximately similar to lithium-ion batteries. Budde-Meiwes et al. [8] further added that the research on these batteries is relatively insufficient and only two companies are involved in developing these batteries globally.

3.5 Lithium-Ion Batteries

Li-ion batteries remain acknowledged for their excellent uses from lower and higher power devices in addition to moveable electronics gadgets due to their elevated energy density and efficiency. Leadbetter [11]; Suberu [12] described that carbon graphite is used to manufacture the anode and lithiated metallic oxide for cathode of Li-ion battery. The energy storage material comprises a blend of lithium salts along with organic carbonates. Important features of Li-ion batteries can be summarized as its extended life cycle more than 3000, high-speed charge and discharge potential, elevated energy density, specific energy, the low fraction of self-discharge, manufactured in different configurations and dimensions, light and more operating characteristic curve (OCV) in comparison with other batteries and essentially safe from environmental point of view. The main disadvantage is its excess manufacturing cost. Because of the absence of internal overcharge process, every cell has to be managed independently to shun overcharging of any individual cell because this would lastly direct to the demolition of that particular cell. For the sake of cells, charging and discharging process stopped, while any cell attains full state of charge or discharge. An additional benefit that makes its suitability of its utilization for battery electric vehicles is the high-capacity use still on high current rates.

3.6 Supercapacitors

Supercapacitors are also called electrochemical twofold capacitors, which can accumulate and dispatch energy hastily on large current rates instantly. Supercapacitors contain an extremely high-power density as well as surpass almost every battery technology for the cycle lifetime. But supercapacitors have very lower energy density in comparison with batteries, which is why they are suitable for buffers only to be used jointly with other energy storage system. Karden et al. [13] explained that supercapacitors are used to compensate the property of less power density and hybridization of energy storage system, particularly to provide pulse power. Commercial supercapacitors typically include two actuated carbon electrodes with carbon-based electrolyte. Burke [8]; Budde-Meiwes et al. [14] wrote that chemical reaction does not take place

while charging and discharging process; hence, these processes are highly reversible, which provide an extensive cycle lifetime, beyond five lac full cycles.

3.7 Lithium–Carbon Capacitors

These are the coalescence of a supercapacitor with a lithium-ion battery also known as hybrid capacitors focusing to combine the beneficent traits of both. Cericola and Kotz [15] explained that in this combination, power density as well as cycle lifetime increases in comparison with lithium-ion batteries, and also energy density increases twice more than supercapacitors. In this combination usually, one electrode is taken of supercapacitor while others of battery and electrolyte used are organic. Further, these capacitors permit superior cell voltages of cell up to 4 V and acquire a superior power density. However, cycle life time is more than batteries till now, but it is limited with the battery electrode. It was also told that lithium capacitors are in initial phase of commercialization.

3.8 Future Research

One of the future technologies is lithium–sulfur, in which for active matter on the anode is made of Li metal and cathode is a combination of basic sulfur alongside carbon. Kolosnitsyn and Karaseva [16] told the advantages of this concept as higher energy density, i.e., greater than 2500 Wh/kg, can be attained. Further some of these cells can perform well at the temperatures lower than -30 °C, which makes its utilization suitable in automotive applications, higher efficiency, i.e., over 80%, and charging and discharging efficiency is also fairly good.

In another technology, oxygen of atmosphere is to be utilized for active material in cathode side and pure metal at anode. Due to which oxygen is obtainable universally, we have to store merely metal in the battery. An electrolyte is provided amid permeable membrane and lithium like metal anode. The porous membrane remains in the contact of atmosphere, and electrolyte transfers the solvate lithium cations to that membrane where reaction takes place with the oxygen. Due to this membrane, it is considered as a combination of a battery with a fuel cell. According to Kolosnitsyn and Karaseva [8]; Budde-Meiwes et al. [16], energy density of 13 KWh/kg can be attained by a lithium–air battery. Main challenges includes the life cycles, the security concerns, and the lifetime. Apart from these battery technologies, researchers and industries from all over the world are engaged to develop the energy storage system with utmost potential.

4   Battery Production in India

The battery production has been the core issue as the energy storage device for various applications. Mohanty and Kotak [17] told that there is a wide scope for India in research and development of battery technologies as well as battery management system (BMS) that will propel affordability and acceptance. Modification of battery systems according to local weather conditions in addition to transport infrastructure will give better performance. One of the causes for leisurely succession of BEVs into India is to be short of manufacturers, particularly in four-wheeler area. Further Faster Adoption and Manufacturing of (Hybrid &) Electric Vehicles in India (FAME) plan launched by Indian government for development, manufacturing, and rapid adoption of electrical vehicles is accommodating local companies exclusively for incentives, which can be taken as opportunity by Indian manufacturers.

Various Web sites are searched aiming to know that which types of batteries are produced by Indian manufacturers. It can be seen from Table 1, nearly most of the manufacturers are producing mostly lead–acid batteries, while Amara Raja Batteries Ltd and Okaya are manufacturing lead–acid battery and also Li-ion battery. It was also studied that manufacturers of batteries are interesting to collaborate with BEVs manufacturing industries.

4.1   Assessment of Parameters

On the basis of literature review, various parameters were identified which are given in Table 2.

5   Evaluation of Battery Technologies Using MCDM Tool

Chaitanya and Srinivas [30] explained that MCDMs may be referred as the tools or techniques utilized to make the decision when multiple, mostly contradictory, criteria. These methods are broadly utilized to calculate different type of quantitative and qualitative problems. Further, these techniques are utilized to make orders or groups of the available alternatives. Kaur and Kadam [31] told that MADMs approach considers both static and dynamic attributes and can provide ranking to the twinned reference. The SAW method of MADMs was utilized to find out the top-quality resources among all the available matching resources. MADM method involves a number of choices called alternatives, and the criteria on which the choices are based called attributes. These attributes may have different weights, that is, varying level of preference of a criterion. Any MCDM tool includes the basic steps as given below (i) identification and determination of the choices called alternatives and the criterion known as the attributes for evaluation, (ii) measurement of

Table 2 Battery manufacturing challenging parameters

Parameters		References
1	Production costs	Kwade et al. [25]; Vayrynen and Salminen [26]; Deng [27]; Knoche and Reinhart [28]
2	Scale up issue	Kwade et al. [25]; Vayrynen and Salminen [26]; Deng [27]; Knoche and Reinhart [28]
3	Availability of lithium reserve	Kwade et al. [25]; Mohanty and Kotak [17]; Deng [27]
4	Fast charging requirement	Deng [27]; Schnell et al. [29]; Knoche and Reinhart [28]
5	FAME plan supports to Indian company exclusive	Mohanty and Kotak [17]
6	Safety concern	Deng [27]; Kwade et al. [25]; Schnell et al. [29];
7	Handling of toxic materials	Vayrynen and Salminen [26]; Schnell et al. [29]
8	Recycling of materials	Vayrynen and Salminen [26]; Deng [27]; Knoche and Reinhart [28]
9	Mechanical stability	Schnell et al. [29]; Kwade et al. [25]
10	Handling of large volumes of contaminated waste	Deng [27]; Kwade et al. [25]
11	Battery swelling	Kwade et al. [25]

relative importance of the attributes and the alternatives, and (iii) calculation of performance measures of the alternatives for ranking. There are various MADM techniques, i.e., SAW, weighted product model (WPM), analytical hierarchy process (AHP), analytical network process (ANP), technique for order of preference by similarity to ideal solution (TOPSIS), Vise Kriterijumska Optimizacija I Kompromisno Resenje (VIKOR which means: multi-criteria optimization and compromise solution, with pronunciation), etc. Out of various MADMs, SAW method is an easy method to apply. Adriyendi [32] told that in SAW method, weights are given to each attribute. The attributes are alienated on the basis of favorable and non-favorable attributes. Consequently, a normalized matrix is obtained in terms of proportion. For favorable attributes, all value divided by max value, however, particular element of normalized value for cost criteria is obtained by dividing the minimum value of cost criteria by that particular element value. Allocated weight is multiplied to each criterion, and then, sum of rows are obtained which give the SAW score. On the basis of SAW score, ranks of the alternatives are obtained.

Step 1: Construction of Decision Matrix

As per the values of chosen six characteristics of the selected batteries in Table 3, a decision matrix was made as given in Table 4.

Table 3 Collected data for different batteries parameters

Parameters → Type of battery↓	Specific power (W/kg)	Specific energy Wh/kg	Energy efficiency %	Power/weight	Cycle life time (no. charging)	[a]Cost (USD/kWh)
Lead–acid battery	180	35	80	180	1000	100
Ni-Cd	200	70	75	150	2000	225-675
NiMH	200–300[a]	80	70	1000	3000	700–800
NaNiCl$_2$	150.	90–120	80	1500	1200	200–250
Li-ion	300	150	80	1800	1000	700

[a]Maximum values are taken for calculation

Table 4 Decision matrix

	Crt1	Crt2	Crt3	Crt4	Crt5	Crt6
Alt1	180	35	80	180	1000	100
Alt 2	200	70	75	150	2000	675
Alt 3	300	80	70	1000	3000	800
Alt 4	150	120	80	1500	1200	250
Alt 5	300	150	80	1800	1000	700

From the available battery technologies, Lead–acid (Alt$_1$), nickel–cadmium (Alt $_2$), nickel–metal hydride (Alt$_3$), sodium–nickel chloride (Alt$_4$), and lithium-ion (Alt$_5$) batteries were chosen as alternatives (Alts), and the six properties are taken as the criteria, i.e., specific power (Crt$_1$), specific energy (Crt$_2$), energy efficiency (Crt$_3$), power/weight (Crt$_4$), cycle life time (Crt$_5$), and cost (Crt$_6$). Values of these properties for the particular battery technology are given in Table 3. These values are on the basis of various research paper, i.e., Andwari et al. [4] Tie and Tan [3], Manzetti and Mariasiu [7], and Suberu et al. [14].

Step 2: Construct the normalized decision matrix

$$\text{For favorable attribute}: E_{ij} = \frac{V_{ij}}{V_{ij}\text{Max}} \tag{1}$$

$$\text{For non nonfavorable attribute}: E_{ij} = \frac{V_{ij}\text{Min}}{V_{ij}} \tag{2}$$

where E_{ij} is the element value of decision matrix and V_{ij} is the values of different properties for different technologies (Table 5).

Weights for different criteria are taken as given in Table 6 with the condition of $\sum W = 1$.

Step 3: Construction of normalized decision matrix with weight.

Table 5 Normalized decision matrix

	Crt1	Crt2	Crt3	Crt4	Crt5	Crt6
Alt1	0.6000	0.2333	1.0000	0.1000	0.3333	1.0000
Alt 2	0.6667	0.4667	0.9375	0.0833	0.6667	0.1481
Alt 3	1.0000	0.5333	0.8750	0.5556	1.0000	0.1250
Alt 4	0.5000	0.8000	1.0000	0.8333	0.4000	0.4000
Alt 5	1.0000	1.0000	1.0000	1.0000	0.3333	0.1429

Table 6 Weight of parameters

Crt1	Crt2	Crt3	Crt4	Crt5	Crt6
0.15	0.2	0.2	0.15	0.15	0.15

$$T_{ij} = W_{ij} \times E_{ij}$$

where T_{ij} is elemental value of normalized decision matrix with weight (Table 7).

Step 4: Obtain the score of chosen alternatives

Step 5: Ranking of the alternative

On the basis of score in Table 8, ranks of the alternatives were determined as given in Table 9. Alternatives 1, 2, 3, 4, and 5 obtained the rank as 4, 5, 2, 3, and 1, respectively.

Table 7 Normalized decision matrix (weighted)

	Crt1	Crt2	Crt3	Crt4	Crt5	Crt6
Alt1	0.09	0.04666	0.2	0.015	0.049995	0.15
Alt 2	0.100005	0.09334	0.1875	0.01249	0.100005	0.02221
Alt 3	0.15	0.10666	0.175	0.08334	0.15	0.01875
Alt 4	0.075	0.16	0.2	0.12495	0.06	0.06
Alt 5	0.15	0.2	0.2	0.15	0.049995	0.02143

Table 8 Score matrix

	Crt1	Crt2	Crt3	Crt4	Crt5	Crt6	Score
Alt1	0.0900	0.0467	0.2000	0.0150	0.0500	0.1500	0.5517
Alt 2	0.1000	0.0933	0.1875	0.0125	0.1000	0.0222	0.5156
Alt 3	0.1500	0.1067	0.1750	0.0833	0.1500	0.0188	0.6838
Alt 4	0.0750	0.1600	0.2000	0.1250	0.0600	0.0600	0.6800
Alt 5	0.1500	0.2000	0.2000	0.1500	0.0500	0.0214	0.7714

Table 9 Rank of alternatives

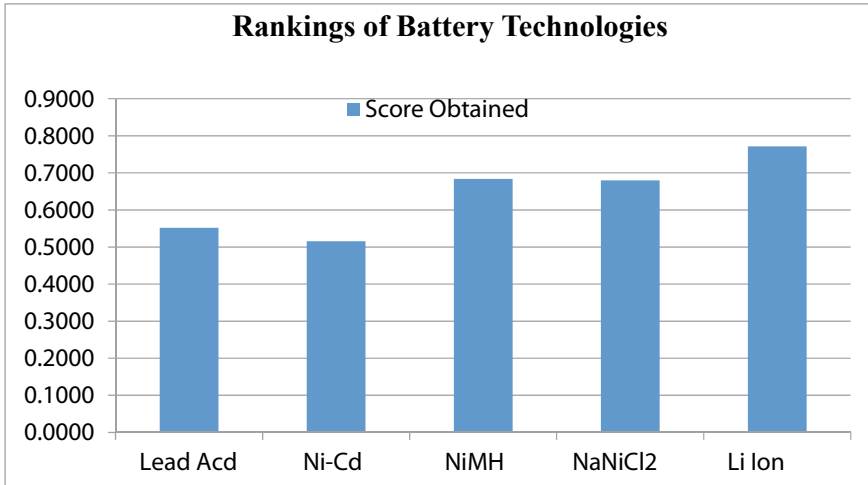|	Crt1	Crt2	Crt3	Crt4	Crt5	Crt6	Score	Rank
Alt1	0.0900	0.0467	0.2000	0.0150	0.0500	0.1500	0.5517	4
Alt 2	0.1000	0.0933	0.1875	0.0125	0.1000	0.0222	0.5156	5
Alt 3	0.1500	0.1067	0.1750	0.0833	0.1500	0.0188	0.6838	2
Alt 4	0.0750	0.1600	0.2000	0.1250	0.0600	0.0600	0.6800	3
Alt 5	0.1500	0.2000	0.2000	0.1500	0.0500	0.0214	0.7714	1

Fig. 1 Score obtained by chosen battery technology through SAW method

Hence, on the basis of ranking obtained through the SAW method, Li-ion battery technology stood first followed by NiMH. Score obtained by chosen battery technology was also described with the help of bar graph in Fig. 1. However, sodium nickel chloride (ZEBRA) battery also scored very near to NiMH. Further in actual practice, various automobile manufacturers use Li-ion battery, as given in Table 10. Therefore, it can be concluded that Li-ion battery technology should be considered as the best battery technology at present situation. But use of NiMH and ZEBRA batteries may also be an attractive alternative to Li-ion batteries.

6   Conclusion

In this work, challenging parameters for production of batteries for BEVs were identified. Evaluation of battery technologies was performed by applying SAW method, and the ranking of various battery technologies was obtained. According to ranking,

Table 10 Type of battery installed in top brands of passenger cars

S. No.	Model/Brand of BEV	Type of battery pack installed	References
1	Tata Nexon EV	Lithium-ion battery	https://www.indiatoday.in/auto/latest-auto-news/story/tata-nexon-ev-launch-today-price-features-specifications-battery-range-warranty-all-other-details-explained-1640744-2020-01-28 [33]
2	Tesla Model 3	Lithium-ion battery	https://en.wikipedia.org/wiki/Tesla_Model_3 [34]
3	KONA Electric	Lithium-ion polymer	https://www.hyundai.com/content/dam/hyundai/in/en/data/brochure/Hyundai_KONA_SUV_brochure.pdf [35]
4	MG ZS EV	Lithium-ion battery	https://www.zigwheels.com/news-eatures/news/mg-zs-electric-suv-could-come-with-a-73kwh-battery-in-two-years/36325/#leadform [36]
5	Tata Tigor EV	Lithium-ion battery	https://www.zigwheels.com/newcars/Tata/tigor-ev/xe-plus#leadform [37]
6	Mahindra E Verito	Lithium-ion battery	https://www.cardekho.com/mahindra/e-verito/specs [38]
7	Honda e	Lithium-ion battery	https://www.honda.co.uk/content/dam/local/uk/brochures/cars/Honda-e-Brochure-20YM.pdf [39]

Li-ion battery technology was found best among the chosen alternatives. But it was also revealed through the study that NiMH and ZEBRA batteries may also prove the potential alternative to Li-ion batteries.

References

1. Amjad, S., Neelakrishnan, S., Rudramoorthy, R.: Review of design considerations and technological challenges for successful development and deployment of plug-in hybrid electric vehicles (2010). https://doi.org/10.1016/j.rser.2009.11.001
2. Peng, M., Liu, L., Jiang, C.: A review on the economic dispatch and risk management of the large-scale plug-in electric vehicles (PHEVs)-penetrated power systems (2012). https://doi.org/10.1016/j.rser.2011.12.009
3. Tie, S.F., Tan, C.W.: Rev. Energ. Sources Eergy Manage Syst Electric Veh. (2013). https://doi.org/10.1016/j.rser.2012.11.077
4. Andwari, A.M., Pesiridis, A., Rajoo, S., Botas, R.M., Esfahanian, V.: A review of battery electric vehicle technology and readiness levels: renewable and sustainable. Energ. Rev. (2017). https://

doi.org/10.1016/j.rser.2017.03.138

5. Burke, A., Jungers, B., Yang, C., Ogden, J.: Battery Electric Vehicles: An Assessment of the Technology and Factors Influencing Market Readiness. Institute of Transportation Studies, Davis, CA, USA (2007)

6. Fotouhi, A., Auger, D.J., Propp, K., Longo, S., Wild, M.: A review on electric vehicle battery modelling: From Lithium-ion toward Lithium-Sulphur (2016). https://doi.org/10.1016/j.rser.2015.12.009

7. Manzetti, S., Mariasiu, F.: Electric vehicle battery technologies: From present state to future systems, (2015). https://doi.org/10.1016/j.rser.2015.07.010.

8. Budde-Meiwes, H., Drillkens, J., Lunz, B., Muennix, J., Rothgang, S., Kowal, J., Sauer, D.U.: A review of current automotive battery technology and future prospects (2013). https://doi.org/10.1177/0954407013485567

9. Miller, J.M.: Energy storage system technology challenges facing strong hybrid, plugin and battery electric vehicles. In: 5th IEEE Vehicle Power and Propulsion Conference, VPPC'09 (2009). https://doi.org/10.1109/VPPC.2009.5289879

10. Budde-Meiwes, H., Schulte, D., Kowal, J., Sauer, D.U., Hecke, R., Karden, E.: Dynamic charge acceptance of lead-acid batteries: Comparison of methods for conditioning and testing. J. Power Sources (2012). https://doi.org/10.1016/j.jpowsour.2011.12.045

11. Leadbetter, J., Swan, L.G.: Selection of battery technology to support grid-integrated renewable electricity. J. Power Sources (2012). https://doi.org/10.1016/j.jpowsour.2012.05.081

12. Suberu, Y.M., Wazir Mustafa, M., Bashir, N.: Energy storage systems for renewable energy power sector integration and mitigation of intermittency (2014). https://doi.org/10.1016/j.rser.2014.04.009

13. Karden, E., Ploumen, S., Fricke, B., Miller, T., Snyder, K.: Energy storage devices for future hybrid electric vehicles. J. Power Sources (2007). https://doi.org/10.1016/j.jpowsour.2006.10.090

14. Burke, A.: Ultracapacitors: why, how, and where is the technology. J. Power Sources (2000). https://doi.org/10.1016/S0378-7753(00)00485-7

15. Cericola, D., Kotz, R.: Hybridization of rechargeable batteries and electrochemical capacitors: Principles Limits (2012). https://doi.org/10.1016/j.electacta.2012.03.151

16. Kolosnitsyn, V.S., Karaseva, E.V.: Lithium-sulfur batteries: Problems and solutions. Russ. J. Electrochem. (2008). https://doi.org/10.1134/S1023193508050029

17. Mohanty, P., Kotak, Y.: Electric vehicles: status and roadmap for India. In: Electric Vehicles: Prospects and Challenges (2017). https://doi.org/10.1016/B978-0-12-803021-9.00011-2

18. Exide Homepage, https://www.exideindustries.com/about/about-exide.aspx. Last accessed on 21 April 2020

19. Amara Raja Battery Limited Homepage. https://www.amararajabatteries.com/about/technology-focus. Last accessed on 21 April 2020

20. HBL Homepage. https://www.hbl.in/product-1-batteries. Last accessed on 21 April 2020

21. Okaya Homepage. https://www.okayapower.com/e-rickshaw-batteries.php. Last accessed on 21 April 2020

22. Southern Batteries Homepage. http://www.southernbatteries.com/about_profile.htm. Last accessed on 21 April 2020

23. ARTHEON Homepage. http://www.artheonelec.com/aboutus.asp. Last accessed on 21 April 2020

24. Tata Green Batteries Homepage. https://www.tatagreenbattery.com/cms/products. Last accessed on 21 April 2020

25. Kwade, A., Haselrieder, W., Leithoff, R., Modlinger, A., Dietrich, F., Droeder, K.: Current status and challenges for automotive battery production technologies (2018). https://doi.org/10.1038/s41560-018-0130-3

26. Vayrynen, A., Salminen, J.: Lithium ion battery production. J. Chem. Thermodyn. (2012). https://doi.org/10.1016/j.jct.2011.09.005

27. Deng, D.: Li-ion batteries: basics, progress, and challenges. Energ. Sci. Eng. **3**(5), 385–418 (2015). https://doi.org/10.1002/ese3.95

28. Knoche, T., Reinhart, G.: Electrolyte filling of large-scale lithium-ion batteries: main influences and challenges for production technology. Appl. Mech. Mater. **794**, 11–18 (2015). https://doi.org/10.4028/www.scientific.net/AMM.794.11

29. Schnella, J., Gunthera, T., Knoche, T., Vieider, C., Kohler, L., Just, A., Keller, M., Passerini, S., Reinhart, G.: All-solid-state lithium-ion and lithium metal batteries—paving the way to large-scale production. J. Power Sources **382**, 160–175 (2018). https://doi.org/10.1016/j.jpowsour.2018.02.062

30. Chaitanya, K.L., Srinivas K.: Sensitive analysis on selection of piston material using madm techniques. Strojníckyčasopis. J. Mech. Eng. **69**(4), 45–56 (2019) https://doi.org/10.2478/scjme-2019-0042

31. Kaur, M., Kadam, S.S.: Discovery of resources using MADM approaches for parallel and distributed computing, Eng. Sci. Tech., Int. J. (2017). http://dx.doi.org/10.1016/j.jestch.2017.04.006

32. Adriyendi: Multi-attribute decision making using simple additive weighting and weighted product in food choice. Int. J. Inf. Eng. Electron. Bus. (2015). https://doi.org/10.5815/ijieeb.2015.06.02

33. India Today Homepage, https://www.indiatoday.in/auto/latest-auto-news/story/tata-nexon-ev-launch-today-price-features-specifications-battery-range-warranty-all-other-details-explained-1640744-2020-01-28. Accessed on 21 May 2020

34. Wikipedia Homepage, https://en.wikipedia.org/wiki/Tesla_Model_3. Accessed on 19 May 2020

35. Hyundai Homepage. https://www.hyundai.com/content/dam/hyundai/in/en/data/brochure/Hyundai_KONA_SUV_brochure.pdf. Accessed on 19 May 2020

36. ZIGWHEELS. https://www.zigwheels.com/news-features/news/mg-zs-electric-suv-could-come-with-a-73kwh-battery-in-two-years/36325/#leadform. Accessed on 19 May 2020

37. ZIGWHEELS Homepage, https://www.zigwheels.com/newcars/Tata/tigor-ev/xe-plus#leadform. Accessed on 19 May 2020

38. Cardekho Homepage, https://www.cardekho.com/mahindra/e-verito/specs. Accessed on 19 May 2020

39. Honda e Homepage. https://www.honda.co.uk/content/dam/local/uk/brochures/cars/Honda-e-Brochure-20YM.pdf. Accessed on 21 May 2020

Solid Waste Management Practices in Indian Cities

Priyanka Goyal and **Amit Pal**

1 Introduction

Solid wastes are the wastes originating from human and animals activities that are usually discarded as unwanted. The discarded wastes are often reusable and considered a resource in another process. Solid waste management refers to all the activities which are associated with the handling of discarded materials from generation to the ultimate residual disposition of solid wastes. Solid waste management is one of the primary concerns of both the developed and developing countries [1, 2]. The management process operates under a range of formal and informal sectors with different level of efficiency. Inefficiency in waste management and other issues associated with it greatly obstruct not only economic and physical development but also social development in growing cities [3, 4].

The municipal solid waste is a heterogeneous blend of cloth, metal glass, plastic, paper, organic waste demolition and construction debris, etc., which generates from household, market, road cleaning and various commercial activities. In India, about 62 million tons of municipal solid waste generated annually, 82% is being collected, and remaining 18% is littered; only 28% is being treated and disposed out of the total collected waste. In India, municipal solid waste (MSW) generation rate for small cities is 200–300 gm/capita, for medium cities, rate is about 300–400 gm/capita, and for large cities, generation rate is 400–600 gm/capita [5].

P. Goyal (✉) · A. Pal
Department of Mechanical, Production & Industrial and Automobile Engineering, Delhi Technological University, Delhi 110042, India
e-mail: priyankagoel03@gmail.com

A. Pal
e-mail: amitpal@dce.ac.in

S. No.	States	Waste quantity generated (TPD)	Waste collected (TPD)	% of waste collected	Waste treated (TPD)	% of treated waste
1	Andhra Pradesh and Telangana	11,500	10,656	93	9418	82
2	Arunachal Pradesh	110	82	82	74	74
3	Chandigarh	340	330	97	250	74
4	Chhattisgarh	1896	1704	90	168	9
5	Delhi	8390	7000	83	4150	49
6	Gujarat	9227	9227	100	1354	15
7	Haryana	3490	3440	99	570	16
8	Himachal Pradesh	300	240	80	150	50
9	Jammu & Kashmir	1792	1322	74	320	18
10	Karnataka	8784	7602	87	2000	23
11	Kerala	1576	776	49	470	30
12	Madhya Pradesh	5079	4298	85	802	16
13	Maharashtra	26,820	14,900	56	4700	18
14	Orissa	2460	2107	86	30	1
15	Punjab	3900	3853	99	32	1
16	Rajasthan	5037	2491	49	490	10
17	Tamil Nadu	14,532	14,234	98	1607	11
18	Uttar Pradesh	19,180	19,180	100	5197	27
20	West Bengal	8674	7196	83	1415	16
	Total	134,100	111,651	–	33,197	–

Management of municipal solid waste (MSW) in metropolitan areas has come out as one of the biggest challenges faced by our country not only in terms of environmental and aesthetic impact but also the potential threat to public health, resulting from improper and non-scientific handling of municipal waste. There is an urgent need to put up extra efforts to achieve 100% scientific treatment and disposal of MSW by 2019.

1.1 Sources of MSW

MSW is usually consists of street sweeping, garden wastes, rubbish, food wastes, demolition and construction wastes as shown in Fig. 1. Numbers of factors which
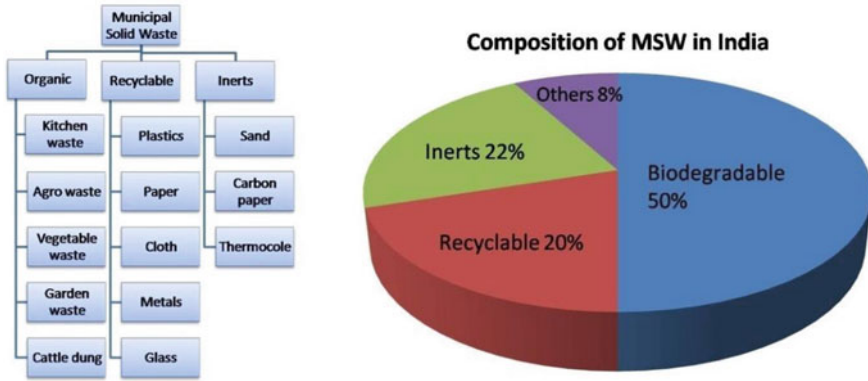
Fig. 1 Composition of Municipal Solid Waste in India [7]

affect the properties of municipal solid waste are climate, per capita income, degree of industrialization and urbanization [6].

2 Integrated Municipal Solid Waste Management

The hierarchy is shown in Fig. 2 for the integrated waste management system.

Fig. 2 Integrated solid waste management hierarchy [6]

2.1 Collection of Municipal Solid Wastes

"Collection and transportation of solid waste include the storage at the source level and various pick-up locations, collection by the workers, trucks moving near the locality and transportation of the waste to the transfer points or stations or to a disposal area." Waste collection is a more costly and complex process. It consumes approximately 60–80% of the total solid waste budget of the community. Therefore, there is a requirement for advancement in the collection system which can overall cut the cost effectively [6–8].

Following mentioned steps need to be taken by the urban local bodies to forbid littering and to ease compliance [9, 15].

- House-to-house collection, central or community bin collection and collection by using musical bell of the vehicle should be organized to collect the municipal solid wastes.
- Hazardous waste such as biomedical wastes, construction and demolition wastes and industrial wastes must follow the rules to dispose off and shall not be mixed with the municipal solid waste.
- Strict norms shall be regulated for the burning of waste.

2.2 Segregation at Source Level

Segregation of waste is the more specific art of separating dry waste which may include glass, metal, etc., from wet waste including organic waste. Segregation at source level involves the separation of waste into various streams at the time of disposing [10, 11].

Segregation of solid waste at generation level is important to manage the waste effectively as it.

- Reduces municipal efforts and resources spent for post collection segregation.
- Avoids the mixing of recyclable waste with wet and hazardous waste during discarding.
- Ensures the good health and dignity of waste collection workers.
- Enhances the processes to recycle and reuse of waste materials.
- Reduces the landfilling.

Source segregation is completely a manual process as it requires the involvement of an individual in the act of segregation. Municipal authorities should take the initiative to encourage the individuals to segregate the waste into dry and wet waste streams at source level itself. In Indian cities, collection of papers, plastics and other waste by "kabaris" is also very effective in keeping away a dry waste from landfills.

2.3 Segregated Waste Collection and Its Transportation

Segregated collection of waste from the source is a very important step in the solid waste management system. Segregated waste collection improves the potential of an effective treatment of waste in terms of cost [12, 13].

Waste collection is categorized into two following groups:

- **Primary collection**: It is the process of collection of waste from institutions, markets, households and the various commercial units and transfer the waste to the disposal site.
- **Secondary collection**: It is the process of collection of waste from central bins, storage site or transfer stations and taking it to waste processing site or the landfill. There should be synchronization in primary and secondary collection system to avoid waste littering on streets and roads.

3 Waste Processing and Treatment

The process of remanufacturing and processing collected waste is known as recycling and recovery. It reduces adverse environmental impact and the burden of managing waste by diverting a significant amount of municipal, business and institutional waste. The revenues generated through this result in reducing the overall cost of MSWM [1, 14, 15].

4 Processing Technology

Organics are separated from recyclables and other high calorific waste using pre-processing facilities at an ISWM plants. Manure or energy is produced depending on whether the organic waste is processed anaerobically or composted aerobically. High calorific wastes can be co-processed in cement plants or as a fuel after being baled or processed. Number of techniques are available for processing of waste as shown in Fig. 3.

4.1 Material Recovery Facility

In material recovery facility, recyclable and non-biodegradable solid waste collected is sorted. Waste is segregated into different domains (bottles, plastics, etc.) and is then sold to intermediaries. MRFs can be classified as manual or mechanized based on the level of mechanization and scale [12, 21]. Small-scale MRFs are operated and managed by informal sector, whereas the latter has sophisticated systems and
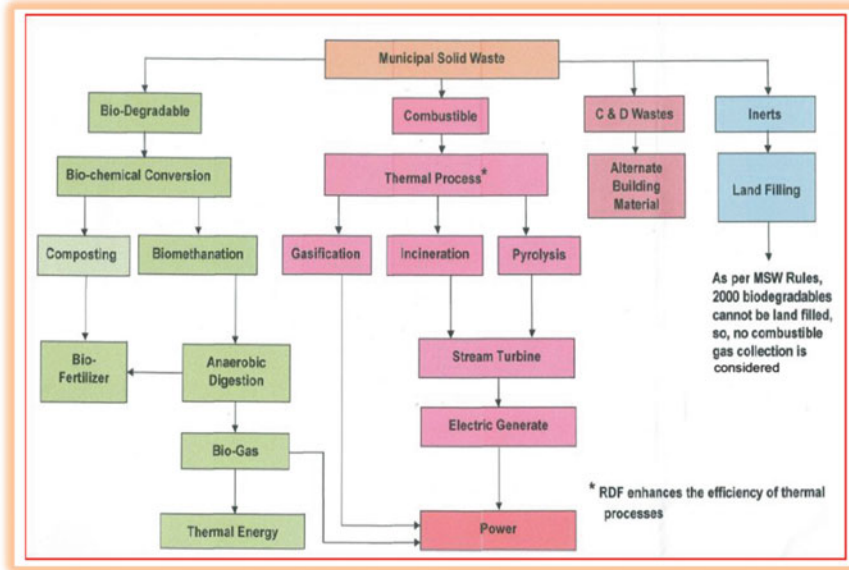
Fig. 3 Waste to wealth technologies [16]

Category	Type of bag/container	Type of waste	Treatment disposal options
Yellow	Non chlorinated colour coded bags in coloured bins Separate collection system leading to ETP	• Human anatomical waste • Animal anatomical waste • Soiled waste • Expired or discarded medicines • Chemical waste • Micro, biotech & clinical lab waste • Chemical liquid waste	Incineration/deep burial
Red	Non chlorinated plastic bags in coloured bins/containers	Contaminated waste (recyclable) tubing, bottles, urine bags, syringes (without needles) and gloves	Auto/micro/hydro and then sent to recycling
White	Translucent, puncture, leak & tamper proof	Waste sharps including metals	Auto/dry heat sterilization followed by shredding /mutilation/encapsulation
Blue	Water proof card board boxes/containers	Glassware waste	Disinfection or auto/micro /hydro then sent to recycling

*Disposal by deep burial is permitted only in rural or remote areas where there is no access to common bio-medical waste treatment facility. This will be carried out with prior approval from the prescribed authority

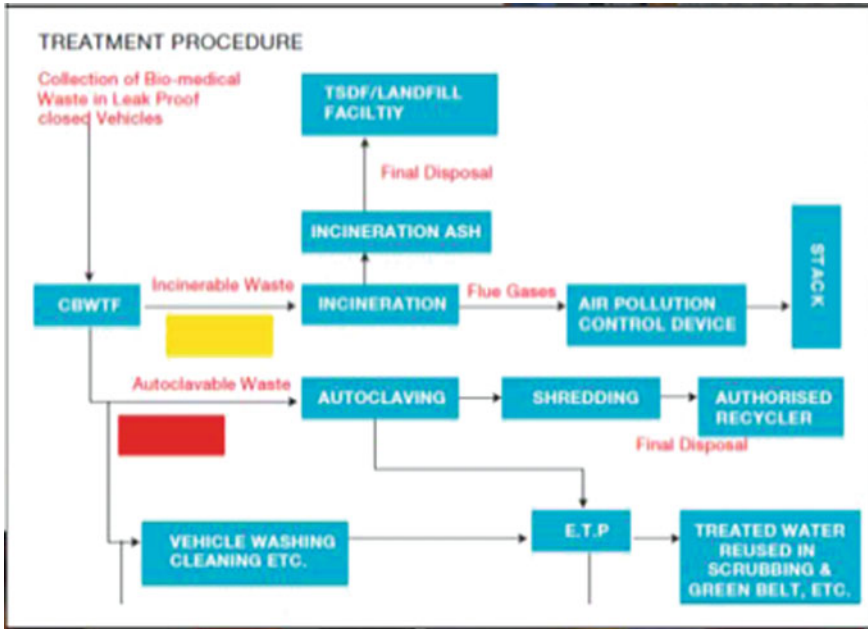**Fig. 4** Colour coding based on type of waste [17]

Fig. 5 Treatment procedure of biomedical waste [17]

equipment that offer a highly efficient segregation of materials into the different domain.

4.2 Composting

It refers to "digesting" the MSW biologically under the controlled aerobic condition, so it may be recycled for other purposes. It can be carried out at either decentralized level or a centralized level based on the feasibility of implementation [1, 3]. However, at both centralized and decentralized level, significant pre-processing is required, and only segregated organic matter can be composed.

4.3 Waste to Energy

Energy recovery from municipal solid waste is recommended as a feasible alternative in case of composting, and material recovery is not possible as desired. High calorific value domain is either processed anaerobically or biodegraded. The resultant energy which is either biogas or heat can be used directly or can be converted to electricity.

Financial viability of waste to energy systems should be outmatched during the sale of this energy. A tipping fee maybe considered by ULB when the tariff of power is not high [1, 2, 6].

4.4   Incineration

"The process of waste treatment involves combustion of waste material at a high temperature in the presence of oxygen". It results in the generation of heat, flue gases and ash. It is reasonable for the high calorific waste domain and minimally processed or unprocessed waste. The amount of energy generated depends on composition, density, a presence of inert and moisture content. It is an option to be considered when other options are not realistic and the availability of land is a major problem. It is desirable for cities that supply minimum of 1000 tons per day (TPD) of waste. They, however, can cause adverse environmental impacts through emission. Also if not operated efficiently, they may fly ash, thus polluting the environment [14, 13, 15].

4.5   Gasification

Fossil-based or organic materials are being converted into hydrogen, carbon monoxide and carbon dioxide in the presence of oxygen at elevated temperature are known as gasification [14].

4.6   Pyrolysis

The breakdown of organic material using heat in the absence of oxygen is known as pyrolysis. It results in the formation of mixture of various combustible gases like mainly methane, hydrogen, complex hydrocarbons and carbon monoxide, solid residues and liquids [18, 19].

4.7   Bio-methanation

The anaerobic digestion of biodegradable organic waste in controlled conditions like moisture, pH and temperature in an enclosed space is known as bio-methanation. Due to MSWs high organic and moisture content, this process is considered to be the technically most feasible option for the solid waste management in the Indian cities mainly due to its high organic content and moisture present. An appropriate source of degradable organic matter needs to be free from an inert matter. The input

feed specifications greatly affect the plant's overall performance. For optimal plant performance, segregated biodegradable MSW is required. [14, 13, 20].

4.8 Disposal of Municipal Solid Waste

Incineration, conversion processes or resource recovery greatly reduces the volume of municipal solid waste. There is a residue in all cases which should be disposed of to eliminate any hazard to the society. Sanitary landfills are the most acceptable land disposal method of MSW and residues. The most common method of solid waste disposal in India is sanitary landfilling [1, 6]. The most difficult part of disposal by landfilling is proper site selection. It requires the compressing of solid waste into the layers, which are afterwards covered with a layer of soil regularly after the day-to-day operation.

5 Covid-19 Biomedical Waste Management

Waste which is in vicinity is in the facility of a Covid-19 patient who has been in contact or exposed to the coronavirus treated as a medical waste. There is an increasing concern about how to manage waste in 2020 arising due to Covid-19 outbreak as it expands globally. The repercussions of this excess will have an intense impact on sustainable medical waste management practices. There is a critical need for an effective and better management of the waste arising from the infectious area, laboratories, hospitals or patients, which is now a global challenge.

The World Health Organization (WHO) advises that system which practices for infectious waste will be able to manage waste infected with Covid-19. Segregation system will also remain the same [17–21].

- Segregation of waste at source level.
- Treat Covid waste as an infectious waste.
- Infectious waste bin or container should be properly colour-coded and labelled with the bio-hazardous symbol.
- Transport the waste in a leak-proof container.
- Storage areas should be secure and protected.
- Best waste management practices indicate that the waste should be disinfected by steam-based treatment like microwaving or autoclaving not by incinerating.
- All technologies should be properly tested, checked and validated.
- After the disinfection process, waste can be sent for recycling or disposal.

The Central Pollution Control Board (CPCB) of India has issued a special guideline to ensure safe disposal of medical waste which is generated during the diagnosis, treatment and quarantine of infectious patients with the Covid-19. The CPCB guidelines provide a step for the safe disposal and treatment of waste generated in testing

centres, medical laboratories and isolation wards for Covid-19 patients including quarantine facilities and homes of a suspected patients also, although it becomes a major challenge in the overcrowded hospitals.

5.1 Biomedical Waste Management (BMWM) 2016

BMWM 2016 rules which were amended in 2018 and 2019 cater the following:

- Environment (Protection) Act, 1986.
- Applicable to all who generate, collect and involve in a transportation and treatment of biomedical waste.
- Proper identification, handling, storage and disposal of medical waste are responsibility of an administrator who is having a control over the premises generating the medical waste.

5.2 Segregation, Transportation and Storage of Biomedical Waste

- Biomedical waste should not be mixed or packed with other wastes.
- Segregation of biomedical waste shall be done into bags or containers at the point of waste generation only.
- Waste bags or containers must be labelled with biohazard symbol or with any other details which are required.
- Untreated medical waste must not be stored for more than 48 h.
- There is no spillage during transit and handling of waste.

5.3 Waste Management at Home Due to Covid-19

Waste generated at home by the Covid-19 positive people during quarantine or during the recovery period should be properly collected and closed in black bags before disposal to the municipal services. They should take all precautionary measures when handling their waste, should follow instructions or guidelines for safe handling, collection and disposal to the municipal services.

In addition to requiring households with Covid-19 positive people or people in mandatory quarantine to take precautionary measures when handling their waste, it is appropriate that all citizens are encouraged to follow instructions on safe handling and delivering of waste for collection, in particular:

- Waste like masks and tissues should be collected in a disposable plastics bag.
- When bag is about ¾ full, it should be properly closed.

- People should strictly follow the procedure disinfect or wash their hands after handling the waste bags.
- Pets should be kept away from the waste bags.

5.4 Responsibilities of Municipal Waste Providers and Local Authorities

- Identification of interface.
- Develop measures to focus on the identified interface.
- Proper implementation of health and safety norms for all workers.
- To ensure the availability of personal protective equipment (PPE).
- Immediate prohibition of all manual segregation of mixed waste.
- Expansion of the current operations for sorting the waste coming from household as well as from the business as a separate collection systems.
- To ensure the elimination of manual contact at the interface wherever possible.
- Communicate precautionary measures for safety and additional hygiene of the interface unambiguously in all languages.
- Implementation of sanitization process and provide hand washing facilities at recycling areas.

5.5 Disposal and Treatment of Biomedical Waste

- Waste handling staff should be properly trained and should be protected with the use PPE.
- Staff should be provided with a proper vaccination against hepatitis, tetanus, etc.
- Give preference to the paper bag until the pandemic is over as the virus survives for longer time on plastic and metal than the paper.
- Store the recyclable materials for at least three days before disposal.
- WHO has endorsed steam-based methods over the incineration for disinfection because of the persistent organic pollutants POP which is produced by incineration.
- Incineration technologies are costlier than the steam-based technologies.
- Incineration technologies have higher carbon footprint also.
- Trapping energy from burning waste is the expensive form of energy generation and polluting also.

Many developing countries still lack proper infrastructure facility to treat hazardous and infectious waste. In those cases, it is important to take an exceptional measures, and waste produced during Covid-19 pandemic must be sent to be stored in landfills on a separated area which is separate from the regular waste with immediate daily cover. So, the healthcare workers will not be exposed to the infectious waste [22].

6   Conclusions

The amount of waste generated is increasing due to the change in life style and population explosion in Indian cities. The government and ULBs should work more in the direction of promoting the awareness for source segregation, waste treatment like waste recycling/reuse and to produce high quality compost from organics. Practices like waste disposal in an open area cause major health issues and result in a degradation of environment also. Such inadequate practices result in economic losses, which need to be modified in a designed way. Major barriers in the proper or effective waste management are the lack of planning, facility data and majorly finances.

The Government of India and ULBs should work in order to promote the segregation of waste at source level to achieve the high percentage of recycling and to produce a good quality of compost. Non-recyclable waste must be properly controlled and managed. Energy recovery is the best option for waste management. Medical waste has been increased number of times than the normal due to Covid-19 pandemic. Huge amount of medical waste cannot be managed properly, so it is required to follow the guidelines strictly. Treatment of biomedical waste must be done by the steam-based technologies as much as possible. Development of newer and eco-friendly approaches must be encouraged.

References

1. Mor, S., Ravindra, K., Visscher, A.D., Dahiya, R.P., Chandra, A.: Municipal solid waste characterization and its assessment for potential methane generation: a case study. J. Sci. Total Environ. **371**(1), 1–10 (2006)
2. Siddiqui, T.Z., Siddiqui, F.Z., Khan, E.: Sustainable development through integrated municipal solid waste management (MSWM) approach—a case study of Aligarh District. In: Proceedings of national conference of advanced in mechanical engineering, Jamia Millia Islamia, New Delhi, India, pp. 1168–1175 (2006)
3. Ministry of Environment and Forests (MoEF): The Gazette of India. Municipal Solid Waste (Management and Handling) Rules, New Delhi, India (2000)
4. Ahsan, N.: Solid waste management plan for Indian megacities. Indian J. Environ. Prot. **19**(2), 90–95 (1999)
5. CPCB: Status of Solid Waste Generation, Collection, Treatment and Disposal in Metrocities, Series: CUPS/46/1999–2000 (2000)
6. Sharholy, M., Ahmad, K., Mahmood, G., Trivedi, R.C.: Analysis of municipal solid waste management systems in Delhi—a review. In: Book of Proceedings for the Second International Congress of Chemistry and Environment, pp. 773–777. Indore, India (2005)
7. Sharholy, M., Ahmad, K., Mahmood, G., Trivedi, R.C.: Development of prediction models for municipal solid waste generation for Delhi city. In: Proceedings of National Conference of Advanced in Mechanical Engineering (AIME-2006), Jamia Millia Islamia, New Delhi, India, pp. 1176–1186 (2006)
8. Central Pollution Control Board (CPCB): Management of Municipal Solid Waste. Ministry of Environment and Forests, New Delhi, India. https://www.cpcbenvis.nic.in/cpcb_newsletter/SOLID%20WASTE.pdf(2004)
9. Singh, S.K., Singh, R.S.: A study on municipal solid waste and its management practices in Dhanbad-Jharia coalfield. Indian J. Environ. Prot. **18**(11), 850–852 (1998)

10. Colon, M., Fawcett, B.: Community-based household waste management: lessons learnt from EXNOR's zero waste management scheme in two south Indian cities. J. Habitat Int. **30**(4), 916–931 (2006)
11. Malviya, R., Chaudhary, R., Buddhi, D.: Study on solid waste assessment and management—Indore city. Indian J. Environ. Prot. **22**(8), 841–846 (2002)
12. Gupta, P.K., Jha, A.K., Koul, S., Sharma, P., Pradhan, V., Gupta, V., Sharma, C., Singh, N.: Methane and nitrous oxide emission from bovine manure management practices in India. J. Environ. Pollut. **146**(1), 219–224 (2007)
13. Khan, R.R.: Environmental management of municipal solid wastes. Indian J. Environ. Prot. **14**(1), 26–30 (1994)
14. Kansal, A.: Solid waste management strategies for India. Indian J. Environ. Prot. **22**(4), 444–448 (2002)
15. Chakrabarty, P., Srivastava, V.K., Chakrabarti, S.N.: Solid waste disposal and the environment—a review. Indian J. Environ. Prot. **15**(1), 39–43 (1995)
16. CPCB: Status of municipal solid waste generation, collection, treatment and disposal in class I Cities, Series: ADSORBS/31/1999–2000 (2012)
17. UNEP.: Technical Guidelines on the Environmentally Sound Management of Biomedical and Healthcare (2003). https://digitallibrary.un.org/record/475506?ln=enanddoa22.05.2020
18. Chang, N.B., Davila, E.: Siting and routing assessment for solid waste management under uncertainty using the grey mini-max regret criterion. Environ. Manage. **38**, 654–672 (2006)
19. Morrissey, A., Browne, J.: Waste management models and their application to sustainable waste management. Waste Manage. **24**, 297–308 (2004)
20. Mor, S., Ravindra, K., De Visscher, A., Dahiya, R.P., Chandra, A.: Municipal solid waste characterization and its assessment for potential methane generation: a case study. Sci. Total Environ. **371**(1), 1–10
21. WHO: Water, sanitation, hygiene and waste management for COVID19. (2020) https://www.who.int/publications/i/item/water-sanitation-hygiene-and-waste-management-for-the-covid-19-virus-interim-guidanceanddoa20.06.2020
22. Chartier, Y., Emmanuel, J., Pieper, U., et al.: Safe management of wastes from health-care activities. WHO, Geneva, Switzerland (2014)
23. Rathi, S.: Alternative approaches for better municipal solid waste management in Mumbai India. J. Waste Manage. **26**(10), 1192–1200 (2006)
24. Ray, M.R., Roychoudhury, S., Mukherjee, G., Roy, S., Lahiri, T.: Respiratory and general health impairments of workers employed in a municipal solid waste disposal at open landfill site in Delhi. Int. J. Hyg. Environ. Health **108**(4), 255–262 (2005)
25. Jha, M.K., Sondhi, O.A.K., Pansare, M.: Solid waste management—a case study. Indian J. Environ. Prot. **23**(10), 1153–1160 (2003)
26. Kansal, A., Prasad, R.K., Gupta, S.: Delhi municipal solid waste and environment—an appraisal. Indian J. Environ. Prot. **18**(2), 123–128 (1998)
27. Das, D., Srinivasu, M., Bandyopadhyay, M.: Solid state acidification of vegetable waste. Indian J. Environ. Health **40**(4), 333–342 (1998)
28. WHO: Safe management of wastes from health-care activities (2014). https://www.who.int/water_sanitation_health/publications/wastemanag/en/anddoa07.05.2020

Study of Hardness in Sand Casting of SG Iron

Abhishek Mukhija and Surendra Kumar Saini

1 Introduction

Manufacturing processes play a significant role in manufacturing industries [1–4]. Casting is one of the essential procedures for manufacturing of automotive parts, space craft components, jewelry and ornaments [5]. Casting of components is a common activity, but quality of sand casted parts hampered mainly due to different defects like misrun, cold shut, blowhole, sand inclusion, shrinkage, etc. Each and every step in the sand molding process is very critical for production of good-quality castings. Therefore, the best possible characterization and distinguishing proof of a specific defect is the fundamental essential to address and control quality of casting. A standard quality management methodology has to be designed to achieve the optimum quality improvement through better control on the process. Patil et al. [6] observed that the improper control of different factor involved in casting practice leads to the defects in the casting and resulted in the imperfection. Siddaling Swami et al. [7] found that it was extremely hard to create castings without defects.

The optimum values of casting process parameters obtained using conventional and artificial intelligence-based techniques [8, 9]. Achamyeleh et al. [10] stated that Pareto chart is an exceptional kind of visual diagram that can be utilized to demonstrate the general recurrence of various problems. Sama and Manogharan [11] did experimental and numerical study for printing and sand casting of impeller part. Kuo et al. [12] did sand casting of stainless steel and studied the various defects. The motivation behind present research work is to diminishing of the casting defect and enhance production yield. Spheroidal graphite iron (i.e., ductile cast iron) is a sort of cast iron incorporates automotive components, impellers, agricultural equipment, machineries, etc. Objective of the present research paper is to control hardness variation in sand casted parts of spheroidal graphite iron using bar chart.

A. Mukhija · S. K. Saini (✉)
Mechanical Engineering Department, Poornima College of Engineering, Jaipur, Rajasthan, India
e-mail: surendra1feb@gmail.com

Fig. 1 Photograph of sand
casted part of spheroidal
graphite iron

2 Experimentation

Sand casting is old process of manufacturing metallic components for different applications. The mold is prepared with green sand (75–85%), water (2–4%), bentonite clay (5–11%), and remaining (3–5%). Casting of spheroidal graphite (SG) iron has been done at Hariom Precision Alloys (Private Limited) at Alwar, Rajasthan, as shown in Fig. 1. Hardness along length of casted parts has been measured at different position. Hardness is defined as the ability of a material to resist plastic deformation, usually by indentation. The SG iron is good material for metal castings due to its specific characteristics. However, microstructure, hardness and chemical composition variation cause metallurgical defects into sand casted parts. The lower and upper hardness values are found less than 207 brinell hardness number (BHN) and greater than 262 BHN, respectively. Hence, parts found out of specified ranges, i.e., 207–262 BHN, have been rejected.

3 Results and Analysis

Table 1 shows the experimental results (part rejection data of three months, i.e., January, February and March). Bar charts are used to analyze casting defect in casted parts. The purpose of using bar chart is to identify the number of rejections due to corresponding factors. Different responsible defects for casting rejection of three months are shown by Figs. 2, 3 and 4. The possible defects, i.e., sand drop, swelling, slag, shifting, cold metal, mold break and hardness, are presented in sand casted parts of SG iron. Maximum rejection 16.69% is found in month of February followed by 15.37% and 14.54% in March and January, respectively. Hardness variations are high compared to other defects in casted parts as shown in Figs. 2, 3 and 4. The sand casted parts are divided into groups—one lower hardness and other higher hardness. Further to control hardness variation within specified ranges, i.e., 207–262 HBN. The percentage of copper in the chemical composition of cast materials has

Table 1 Summary of rejected parts

Month	Quantity	Rejection quantity	Total rejection (%)
January	2125	309	14.54
February	2642	441	16.69
March	3142	483	15.37

JANUARY REJECTION (14.54%)
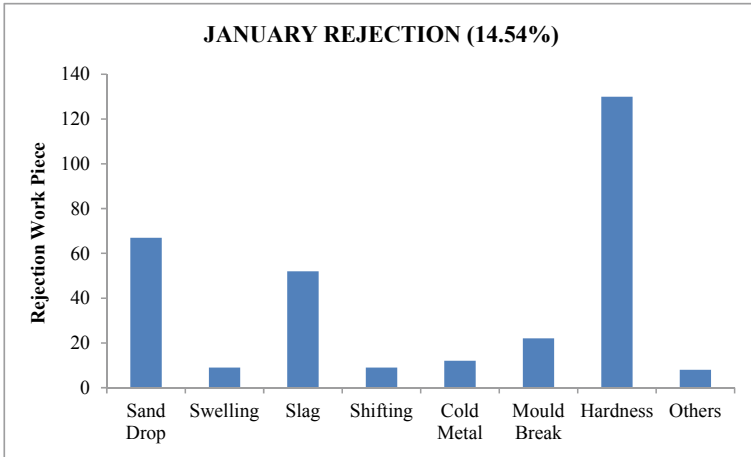
Fig. 2   Bar chart showing the rejection components in the month of January
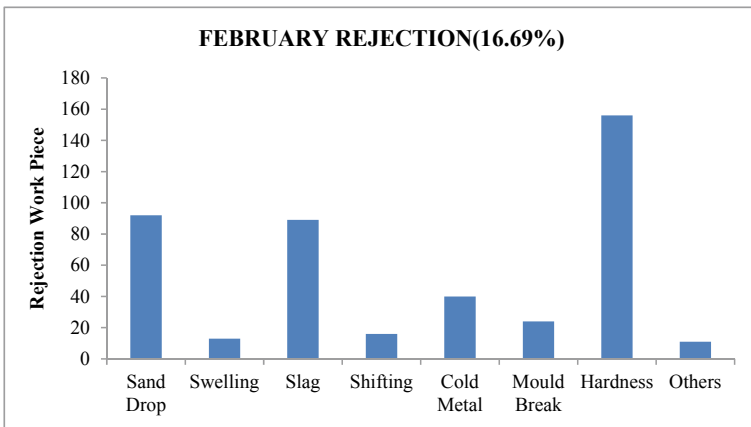
FEBRUARY REJECTION(16.69%)

Fig. 3   Bar chart showing the rejection components in the month of February

increased from 0.047 to 0.327%, while rest silicon (2.25%) and phosphorus (0.02%) kept constant. Then, it is found that hardness variation was reduced up to 16% in sand casted parts.

4   Conclusion

Study of different defects on sand casted of SG iron has done successfully. The major rejection of SG iron sand casted parts was due to high hardness variation in
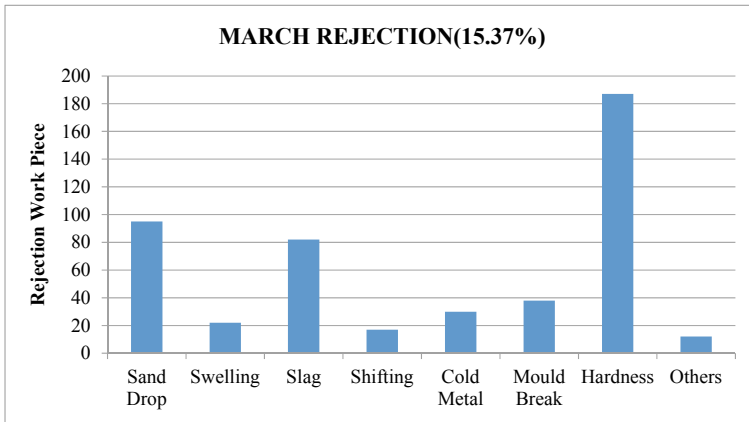
Fig. 4 Bar chart showing the rejection components in the month of March

compared to other defects. Further control in hardness variation has been done by increasing the percentage of copper from 0.047% to 0.327%, while silicon (2.25%) and phosphorus (0.02%) kept constant in the chemical composition of cast material. It is observed that hardness variation was reduced up to 16% by increase of copper.

References

 1. Pandey, N.L.: Sand casting-a basic review. Int. J. Innovative Res. Technol. **7**, 477–483 (2015)
 2. Kenawy, M.A., Abdel-Fattah, A.M., Okasha, N., Gazery, M.: Mechanical and structural properties of ductile cast Iron. Egypt. J. Basic Appl. Sci. **7**, 151–159 (2001)
 3. Saini, S.K., Pradhan, S.K.: Soft computing techniques for the optimization of machining parameter in CNC turning operation. Int. J. Emerg. Technol. Adv. Eng. **4**, 117–124 (2014)
 4. Saini, S.K., Pradhan, S.K.: Optimization of multi-objective response during CNC turning using taguchi-fuzzy application. Procedia Eng. **97**, 141–149 (2014)
 5. Landage, M.G.: Sand moulded castings defects, causes, remedies—review paper. Int. J. Theoret. Appl. Res. Mech. Eng. **6**, 2319–3182 (2017)
 6. Patil, R.T., Veena S.M., Shubhangi, S.T.: Causes of casting defects with remedies. Int. J. Eng. Res. Technol. **4**, 639–644 (2015)
 7. Swami, S., Hiremath, S., Dulange, S.R.: Advanced techniques in castings and rejection analysis: a study in an industry. Int. J. Innovative Eng. Res. Technol. **9**, 1–9 (2015)
 8. Pradhan, S.K., Saini, S.K.: Multi-objective optimization of CNC turning machining parameters. J. Adv. Mater. Res. **1016**, 172–176 (2014)
 9. Saini, S.K., Pradhan, S.K.: Optimization of machining parameters for CNC turning of different materials. J. Appl. Mech. Mater. **592–594**, 605–609 (2014)
10. Kassie, A.A., Samuel, B.A.: Minimization of casting defects. IOSR J. Eng. **3** (2013)

11. Sama, S.R., Manogharan, G.: Case studies on integrating 3d sand-printing technology into the production portfolio of a sand-casting foundry. Int. J. Metalcast. **14**, 12–24 (2020)
12. Kuo, J.K., Huang, P.H., Lai, H.Y., Wu, W.J.: Design of casting systems for stainless steel exhaust manifold based on defective prediction model and experimental verification. Int. J. Adv. Manuf. Technol. **100**, 529–540 (2019)